CYSENI 2011 Conference of Young Scientists on ENergy Issues

# Conference of Young Scientists on Energy Issues

ISSN 1822-7554

Conference proceedings
www.cyseni.com
26—27 May, 2011

Dear Reader of the proceedings,

Conference of Young Scientists on Energy Issues 2011 is already an eighth conference. Initiative came from young, enthusiastic researchers who realised that around ourselves we do have young, smart and science-oriented young people in the energy field, who need an event to come together and share their views, ideas, and success and disappointment stories. The very beginning was year 2004, when young researchers with the supervision of experienced scientists from only Lithuanian Energy Institute organised a conference. In 2005 it became a national conference with participants from Kaunas University of Technology, Vilnius Gediminas Technical University, Vilnius University, Vytautas Magnus University – in fact from all science and education institutions of Lithuania involved in energy-related topics. Year 2006 was devoted to strengthen status of the conference among young researchers and their experienced supervisors and bring the message that only joint efforts in a small country we can reach our targets. In 2007 organising committee decided to put emphasis on regional and international dimension. In the conference we had papers from neighbouring countries – Belarus and Poland. We realised that facing challenges in energy research we have to bring together as many young researchers as possible to create a critical mass to be competent and competitive for the future research. Thus, conference is not only increasing the competence with involvement of best experienced scientists as peer reviewers, involving the review process participants of the conference as educational exercise, but also expanding geographically. In 2008 we already had papers and participants from Belarus, Estonia, India, Latvia, Lithuania and Russia. In 2009 we had papers from Belarus, Estonia, Italy, Latvia, Lithuania, Nigeria, and Ukraine. Young scientists in the conference of Young Scientists on Energy Issues 2009 have an auditorium to share their views and findings of the research, a possibility to evaluate achievements and hear critical comments for the improvements. In 2010 we had papers from various Lithuanian science and research institutions and that foreign institutions Belarus, Estonia, Germany, Italy, Latvia, Nigeria, Norway and Ukraine. In 2011 we had 69 young scientists' papers from various Lithuanian science and research institutions and that foreign institutions Belarus (5 papers), Estonia (2 papers), Germany (1 paper), Latvia (11 papers), Nigeria (1 paper), Poland (2 papers), Taiwan (2 papers) and Ukraine (3 papers).

We will keep this momentum in the future Young Scientists on Energy Issues conferences as well. Thus, we already now invite you to conference of Young Scientists on Energy Issues 2012, which will be held in 24-25 May, 2012 in Kaunas, Lithuania.

Organisers

1. **Hydrogen and fuel cells**

Dr. Darius Milčius
(Lietuvos energetikos institutas, Lietuva) (Lithuanian Energy Institute, Lithuania)
http://www.lei.lt/main.php?m=418&k=1

Prof. Bjørn C. Hauback
(Fizikos departamentas, Energetinių technologijų institutas, Norvegija)
(Physics Department, Institute for Energy Technology, Norway)
http://www.science24.com/person/19239

2. **Renewable energy sources and their use**

Dr. Mantas Marčiukaitis
(Lietuvos energetikos institutas, Lietuva) (Lithuanian Energy Institute, Lithuania)
http://www.lei.lt/main.php?m=142&k=1&l=&surname=Mar%C4%8Diukaitis&title=&publication=&date=visi&pubType=visi&B1=Ie%C5%A1koti

3. **Smart energy networks**

Prof. Dr. Panos M. Pardalos
(Floridos Universitetas, JAV) (University of Florida, USA)
http://www.ise.ufl.edu/pardalos/index.html

Dr. Virginijus Radziukynas
(Lietuvos energetikos institutas, Lietuva) (Lithuanian Energy Institute, Lithuania)
http://www.lei.lt/main.php?m=158&k=1

4. **Energy efficiency and savings**

Prof. Dr. Namejs Zeltins
(Fizikinės energetikos institutas, Latvija) (Institute of Physical energetics, Latvia)
http://www.lza.lv/scientists/zeltinshn.htm

Prof. Habil. Dr. Vytautas Martinaitis
(Vilniaus Gedimino technikos universitetas, Lietuva) (Vilnius Gediminas Technical University, Lithuania)
http://www.svk.ap.vgtu.lt/?did=8869&page=DARBUOTOJO_CV

Prof. Dr. Andres Siirde
(Talino technologijos universitetas, Estija) (Tallinn University of Technology, Estonia)
https://www.etis.ee/portaal/isikuCV.aspx?LastNameFirstLetter=s&PersonVID=38322&FromUrl0=isikud.aspx&lang=en

5. **Knowledges for energy policy making**

Prof. Dr. Andris Kreslins
(Rygos technikos universitetas, Latvija) (Riga Technical University, Latvia)
http://www.lza.lv/scientists/KreslinsA.htm

Habil. Dr. Vaclovas Miškinis
(Lietuvos energetikos institutas, Lietuva) (Lithuanian Energy Institute, Lithuania)
http://www.lei.lt/main.php?m=159&k=1

6. **Investigations in the fields of thermal physics, fluid mechanics and metrology**

Academician prof. Habil. Dr. Sergej Zhdanok
(A. V. Lykovo Šilumos ir masės mainų institutas, Baltarusija)
(A. V. Luikov Heat & Mass Transfer Institute, Belarus)
http://www.itmo.by/

Ass. Prof. Dr. Myriam Lazard
Institut PPrime, ENSIP
Ecole Nationale Supérieure des Ingénieurs de Poitiers, FRANCE
http://ensip.univ-poitiers.fr/; http://www.let.ensma.fr/

7. **Nanosciences and Nanotechnologies, investigations on multifunction materials**

Prof. Dr. Enn Mellikov
(Mokslo akademijos narys, Estija) (Member of the Estonian Academy of Sciences, Estonia)
(http://www.akadeemia.ee/en/membership/_members/mellikov/)

8. **Investigations of combustion and plasma processes**

Dr. Victor A. Zhovyansky
(Nacionalinė mokslų akademija, Ukraina) (National Academy of Sciences of Ukraine, Ukraine)
http://www.ingas.org.ua/index.files/Page5004.htm

Dr. Bernhard Peters
(Luksemburgo universitetas, Liuksemburgas) (University of Luxembourg, Luxemburg)
http://wwwen.uni.lu/

9. **Global change and ecosystems**

Prof. Habil. Dr. Ralf Ebinghaus
(Luneburg‘o universitetas, Vokietija) (Lüneburg University, Germany)
http://coast.gkss.de/aos/staff/ebinghaus/index.html

Prof. Dr. Sten Bergström
(Švedijos meteorologijos ir hidrologijos institutas, Švedija)
(Swedish Meteorological and Hydrological Institute, Sweden)
http://www.espon.eu/mmp/online/website/content/network/94/754_EN.html

10. **Fusion energy**

Dr. Sigitas Rimkevičius
(Lietuvos energetikos institutas, Lietuva) (Lithuanian Energy Institute, Lithuania)
http://www.lei.lt/main.php?m=417&k=1

Prof. Dr. Finn Ravndal
(Oslo universitetas, Norvegija) (University of Oslo, Norway)
http://folk.uio.no/finnr/, http://en.scientificcommons.org/finn_ravndal

Dr. Luis E. Herranz
(UPSO universitetas, Ispanija) (UPCO University, Spain)
http://www.ciemat.es/portal.do

Dr. Alessandro Petruzzi
(Pizos universitetas, Italija) (University of Pisa, Italy)
http://www.unipi.it/english/index.htm

11. **Nuclear fission and radiation protection**

Prof. Habil. Dr. Eugenijus Ušpuras
(Lietuvos energetikos institutas, Lietuva) (Lithuanian Energy Institute, Lithuania)
http://www.lei.lt/main.php?m=137&k=1

Prof. Dr. Pierre-Etienne Labeau
(Briuselio universitetas, Belgija) (Briussels University, Belgium)
http://mntek3.ulb.ac.be/pub/pel/perso.html

---

By countries:

- Lithuania – 7 members;
- Latvia – 2 members;
- Estonia – 2 member;
- Belgium –1 member;
- USA – 1 member;
- Germany – 1 member;
- Sweden – 1 member;
- Norway – 2 members;
- Belarus – 1 member;
- France – 1member
- Ukraine – 1 member
- Luxembourg – 1 member
- Spain – 1 member
- Italy – 1member

Total: 23 members.

# CONTENT

## I. HYDROGEN AND FUEL CELLS (4)

## II. RENEWABLE ENERGY SOURCES AND THEIR USE (9)

## III. SMART ENERGY NETWORKS (5)

## IV. ENERGY EFFICIENCY AND SAVINGS (5)

## V. KNOWLEDGES FOR ENERGY POLICY MAKING (5)

## VI. INVESTIGATIONS IN THE FIELDS OF THERMAL PHYSICS, FLUID MECHANICS AND METROLOGY (4)

## VII. NANOSCIENCES AND NANOTECHNOLOGIES, INVESTIGATIONS ON MULTIFUNCTION MATERIALS (4)

## VIII. INVESTIGATIONS OF COMBUSTION AND PLASMA PROCESSES (4)

## IX. GLOBAL CHANGE AND ECOSYSTEMS (7)

## X. FUSION ENERGY (3)

## XI. NUCLEAR FISSION AND RADIATION PROTECTION (10)

CYSENI 2011, May 26–27, Kaunas, Lithuania
ISSN 1822-7554, www.cyseni.com

# SELF-IGNITION OF A HIGH-PRESSURE HYDROGEN JET OUTFLOWING INTO THE ENCUMBERED SPACE

**D.G. Ignatenko, V.N. Mironov, O.G. Penyazkov, A.V. Skilandz**
*A.V. Luikov Heat and Mass Transfer Institute*
*P. Brovka str. 15, 220072 Minsk – Belarus*
*Phone +37517-2841520*
*E-mail: IgnatenkoDG@gmail.com*

ABSTRACT

The determination of possible regimes of propagation of the explosive process in encumbered space is an imprortant problem of the hydrogen safety. This can be associated particularly either with pipeline breaking or with failure of locking and controlling fittings existed close to operating equipment. It become the reason of experimental studies. Experimental results on ignition initiation involving the interaction of a shock wave with different-configuration obstacles are given in the present work. The shock wave was generated by a high-pressure hydrogen jet outflowing from a chamber after breaking a diaphragm. Experiments were conducted at four diameters of an outflowing jet: 6, 9, 12 and 15 mm and at initial pressures 12–13.5 MPa. The possibility for self-ingnition of a pulse hydrogen jet outflowing into the encumbered space due to the concentration of shock wave disturbances and flame dynamics is studied.

It has been shown that the self-ignition of a high-pressure hydrogen jet outflowing into the encumbered space can occur. Moreover the self-ignition of a pulse hydrogen jet and explosion in the system of obtacles focusing and swirling the flow can take place. The performed study allowed working out a criteria of hydrogen safety.

Keywords: hydrogen, high pressure, ignition, safety, detonation.

## 1. INTRODUCTION

Hydrogen is of interest as a fuel for various engine systems. Burning rate, the limits of self-ignition and detonation of hydrogen is higher than that of hydrocarbon fuels. Thus, hydrogen can accelerate ignition, flame propagation and detonation, and therefore can be used to improve performance of gas engine, gasoline, air-jet and detonation engines.

However, hydrogen is one of the most inflammable and explosive gases, technological use, transportation, storing and production of which could be done only with strict observing special safety rules. In particular, there are cases discribed in literatural sources in which crack of the high-pressure hydrogen lines leads to self-ignition which could cause human death or material losses [1].

Development of hydrogen energy infrastructure requires high attention to the operation safety of hydrogen equipment, its transportation and distribution lines and storage facilities. One of the biggest practical issues in hydrogen safety is determination of possible ignition conditions and propagation of hydrogen explosion process when hydrogen is rapidly released into encumbered space [1] which could be caused, for example, by pipeline break, high-pressure tank crack or control valves breakdown.

In the paper conditions for spontaneous self-ignition of high-pressure hydrogen jet (up to 15 MPa) interacting with barriers of different types and configurations are studied experimentally.

## 2. EXPERIMENTAL SETUP

Efflux of the hydrogen jet from cylindrical chamber is initiated by cracking a multilayer membrane at the top end of the chamber. The membrane was made from the brass and is 100 μm thickness. Breaking the membrane is made by force impact on pein by rod of the air cylinder installed in the chamber. As a result of the impact, peaces of the membrane are torn away and the cross section of the outflow becomes equal to the cross section of the outlet which is controlled and is varied from 6 to 15 mm. Efflux picture is visualized by shadow unit IAB-451 (ИАБ-451) and high speed photo camera PCO Dicam Pro with minimum exposure time of 20 ns. Measurement of pressure inside the chamber and at different control points of the blast is made with piezoelectric pressure sensors PCB «Piezotronics» 113B32. The signals are recorded by using oscilloscope Techtronics. The processes of hydrogen ignition and conbustion are registered by using digital photo camera Casio EX-F1 with shooting speed of 600 frames per second. Temperature and air humidity are measured right before the experiment by using thermal hygrometer TGC-MG 4.01 (ТГЦ-МГ 4.01) (precision for temperature – ± 0.5 C, for relative humidity – ±3%).

## 3. RESULTS AND DISCUSSIONS

### 3.1. Analysis of high-pressure hydrogen jet efflux

Efflux of hydrogen jet interacting with plane, wedge and hemisphere of different radius is studied. The barriers are set at different distances from the membrane. Representative pictures of the flow at the first stage of the jet impulse formation are shown in Fig. 1.

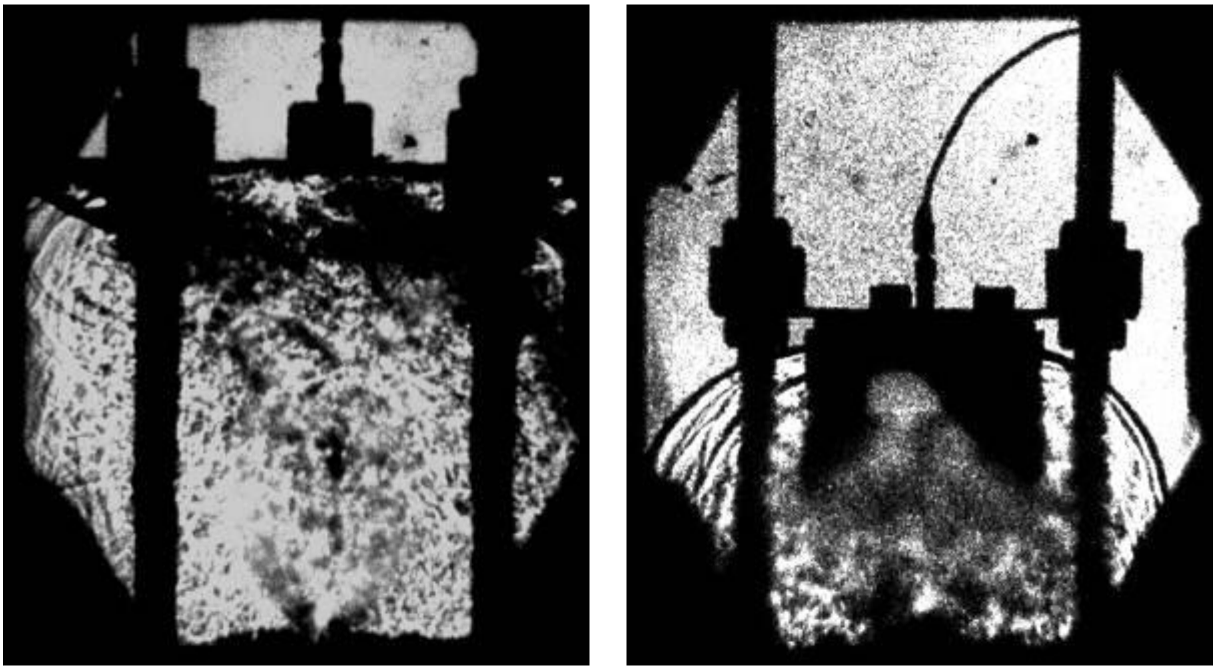

a b

Fig. 1. Processes inside the hydrogen jet impulse at the first formation stage right after the membrane break. a – plane, $P_0$ = 12.5 MPa; d = 9 mm, t = 350 μs; b - inner wage d = 75 mm, $P_0$ = 13.1 MPa; d = 15 mm, t = 191 μs

Note that because of high density gradients in the controlled field of the shadow unit, the shadow method with spot light source is used. In this case the shadow effect is the second derivative with respect to density and the jet wave is registered as border line between light and dark areas [2].

Time dependences for pressure on the reflection surfaces and jet waves speeds are compared with those in the case of hydrogen release into free space. Fig. 2.

Despite the fact that in some experiments, because of the jet focalization, pressure variations are considerably higher that those for the free flow scenario, none of the experiments reveals the hydrogen self-ignition, except for the case with reflection from the 37 mm hemisphere. In the case with the 37 mm hemisphere, the highest magnitude of the pressure variation is registered. And the pressure level is highly dependent from the distance of the focusing barrier from the membrane. Thus, when the initial pressure is about 1.25–1.27 MPa, the pressure on the focusing surface axis, for the 60 mm distance (4 flux gages) from the membrane, is 2.6 MPa; for 5, 6, 7 and 8 flux gages – 3.7; 14.8; 10.1 and 4.0 MPa correspondingly (Fig. 2, c). In the last mentioned cases, on the photos made in the dark room, with the camera shutter opened, glowing at the bottom edge of the focusing surface is clearly seen.

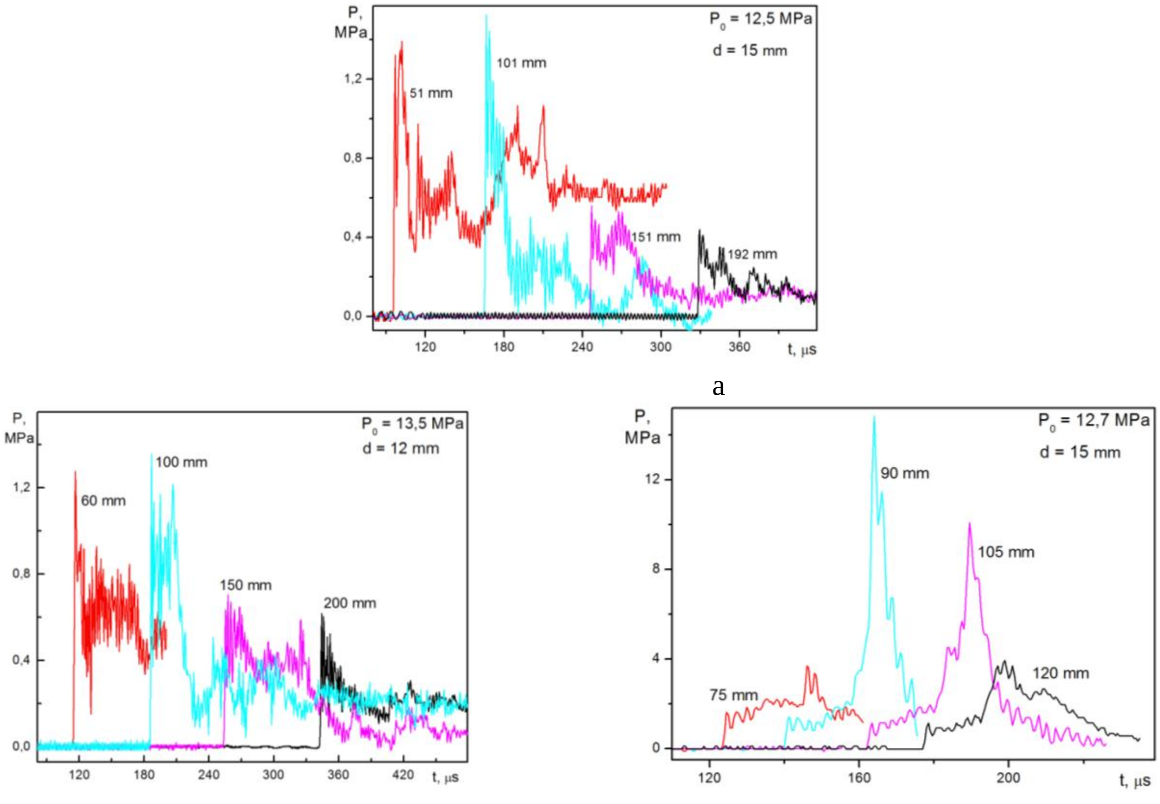

a

b

c

Fig. 2. The pressure at the hydrogen jet axis with different barrier configurations (figures near the curves are distances from the membrane to the sensor): a – with no barrier; b – plane barrier: c – inner hemisphere, r = 37 mm

Nevertheless, flame of the air-hydrogen mixture is not exceeding the volume of the cavity. For explosion process propagation the additional unit perpendicular to the jet axis for turbulence creation is needed. This unit, in our opinion, makes possible the fire areas to be transferred from the focusing surface into external volume. The recorded size of the fire area correlates well with the calculated volume of products of combustion. Therefore, the possibility of hydrogen pulse jet self-ignition in the system with focusing and turbulence creating barriers is shown experimentally.

### 3.2. Hydrogen self-ignition experiments

The experiments are held for four different diameters of the outlet hole that forms the hydrogen jet: 6 ,9, 12 and 15 mm; and for driving pressure $P_0$ = 12–13.5 MPa. Turbulence creating rod diameter – D = 5 mm.

In Table 1 results of the most interesting experimental sets are shown (for the barriers provide considerable and stable pressure rise) for outlet diameters of 9, 12 and 15 mm. Note: $H$ – distance from the membrane to the bottom surface of the barrier (where the pressure sensor is flush-mounted); $h$ – distance from the membrane to the turbulence creating unit; $P_{sen}$ – maximum pressure registered by the sensor inside the cavity; $t$,$w$ and $\rho$ – air parameters: temperature, relative humidity and water vapour density correspondingly; $r$ – hemisphere radius; $R$ – external radius of the barrier; $D$ – diameter of the turbulence creating unit.

For $d$ = 6 mm, there are no evidences of ignition process for all the configurations of the focusing barriers, For $d$ = 9 and 12 mm, *glowing from the cavity* is registered once for each case (is not colored with yellow-orange colour which is typical for *local self-ignition phenomenon*). Therefore, only $d$ = 15 mm reveals constant cases of the local self-ignition phenomenon (Fig. 3) together with volume self-ignition and combustion (external area, Fig. 4).

Nevertheless, foregoing does not mean that hydrogen self-ignition is impossible for smaller diameters of the outlet hole. The study shows that even with determined geometry of the jet that should provide steady conditions for early explosive self-ignition phenomenon of hydrogen, it is difficult to repeat such a result of just obtain repeatedly self-ignition and combustion of hydrogen. Thus, at the moment, we can say that self-ignition phenomenon in pulse jet of high-pressure hydrogen released into encumbered space has stochastic nature with probability rising for bigger outlet hole diameter.

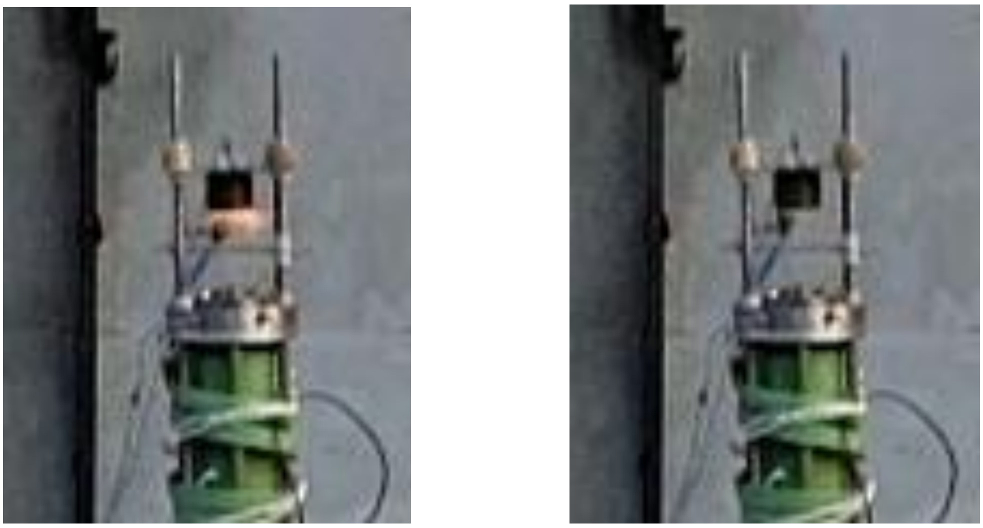
1.333 µs
2.667 µs

Fig. 3. Local self-ignition in the cavity and near area (N 124)

Table 1. Hydrogen self-ignition experiments: conditions and results

| No | d, mm | $P_0$, MPa | Barrier type | H, mm | $\frac{H}{d}$ | h, mm | $P_{sen}$ , MPa | Air parameters | | | Combustion index |
|---|---|---|---|---|---|---|---|---|---|---|---|
| | | | | | | | | t, $^0C$ | w, % | $\rho$ , $g/m^3$ | |
| 119 | 9 | 11.8 | Hemispherical cavity, r-25 mm | 54 | 6 | 22 | 2.72 | 16.8 | 56 | 7.9 | no |
| 121 | | 12.3 | | 45 | 5 | 14 | 2.24 | 16.0 | 62 | 8.4 | 1 |
| 106 | 12 | 13.0 | | 84 | 7 | 36 | | 23.4 | 46 | 9.6 | 1 |
| 107 | | 13.0 | | 72 | 6 | 36 | 2.28 | 25.6 | 46 | 11.0 | no |
| 108 | | 13.0 | | 60 | 5 | 30 | 1.81 | 22.2 | 57 | 11.3 | no |
| 105 | 12 | 12.7 | Hemispherical cavity, r = 37 mm | 84 | 7 | 30 | | 23.5 | 52 | 11.0 | no |
| 68 | 15 | 13.1 | Inner wedge with 900 angle , R = 75 мм | 81 | 5.4 | - | 4.4 | 20 | | <17.3 | no |
| 66 | 15 | 11.3 | Hemispherical cavity, r = 25 mm | 78 | 5.2 | - | 5.4 | 20 | | <17.3 | no |
| 78 | 15 | 12.8 | Hemispherical cavity, r = 37 mm | 60 | 4 | - | 2.6 | 19 | | <16.3 | no |
| 69 | | 13.2 | | 75 | 5 | - | | 20 | | <17.3 | 3 |
| 71 | | 13.0 | | 75 | 5 | - | 2.7 | 18 | | <15.3 | no |
| 77 | | 12.8 | | 75 | 5 | - | 3.7 | 19 | | <16.3 | no |
| 79 | | 12.7 | | 90 | 6 | - | 14.8 | 20 | | <17.3 | 2, a |
| 80 | | 12.7 | | 105 | 7 | - | 10.1 | 20 | | <17.3 | 2, a |
| 81 | | 12.6 | | 120 | 8 | - | 4.0 | 20 | | <17.3 | 2, a |
| 82 | 15 | 12.5 | Hemispherical cavity, r = 37 mm | 90 | 6 | 30 | 2.7 | 19 | | <16.3 | 3 |
| 93 | | 13.2 | | 90 | 6 | 30 | >3.0 | 13.8 | 90 | 10.7 | no |
| 94 | | 13.2 | | 90 | 6 | 30 | >3.0 | 13.2 | 90 | 10.4 | no |
| 95 | | 13.0 | | 90 | 6 | 30 | 2.4 | 17.6 | 67 | 10.3 | 2, a |
| 96 | | 13.0 | | 75 | 5 | 36 | 2.6 | 17.7 | 68 | 10.6 | no |
| 97 | | 13.0 | | 105 | 7 | 43 | | 17.3 | 46 | 6.6 | 3 |
| 98 | | 13.0 | | 105 | 7 | 43 | 5.1 | 17.5 | 46 | 6.7 | 3 |
| 99 | | 13.0 | | 105 | 7 | 43 | 3.3 | 17.6 | 48 | 7.1 | 2, a |
| 109 | | 13.0 | | 90 | 6 | 43 | 2.7 | 21.5 | 64 | 12.2 | 1 |
| 113 | | 13.0 | | 90 | 6 | 33 | 2.5 | 8.7 | 100 | 8.5 | 2, a |
| 110 | | 13.0 | | 120 | 8 | 58 | 3.2 | 20.7 | 66 | 12.0 | 2, a |
| 111 | | 13.0 | | 135 | 9 | 73 | 2.6 | 19.3 | 73 | 12.0 | no |
| 112 | | 13.0 | | 120 | 8 | 58 | 2.4 | 16.5 | 63 | 8.7 | no |
| 129 | 15 | 12.6 | Hemispherical cavity, r = 37 mm material: polimethyl methacrylate | 90 | 6 | - | 1.8 | 6.0 | 75 | 5.5 | no |
| 117 | | 13.0 | | 105 | 7 | 43 | 6.1 | 17.6 | 58 | 8.6 | 2, b |
| 123 | | 12.1 | Hemispherical cavity, r = 37 mm | 105 | 7 | 43 | | 5.5 | 55 | 3.4 | 2, b |
| 114 | 15 | 13.0 | Wedge plane with 900 angle , R = 75 мм | 90 | 6 | 33 | 5.2 | 11.9 | 84 | 8.8 | no |
| 115 | 15 | 13.0 | Hemispherical cavity, r = 25 mm | 90 | 6 | 43 | 3.9 | 13.8 | 68 | 8.1 | no |
| 116 | | 13.0 | | 90 | 6 | 43 | 2.2 | 15.0 | 63 | 8.0 | no |
| 124 | | 12.1 | | 105 | 7 | 43 | 2.7 | 4.1 | 52 | 3.3 | 2, b |
| 125 | | 12.6 | | 105 | 7* | 43 | 3.5 | 4.3 | 80 | 5.2 | no |

Combustion index: 1 – glowing from the cavity; 2 – local self-ignition (a – in the cavity, b – in the cavity and in volume); 3 – self-ignitino in volume

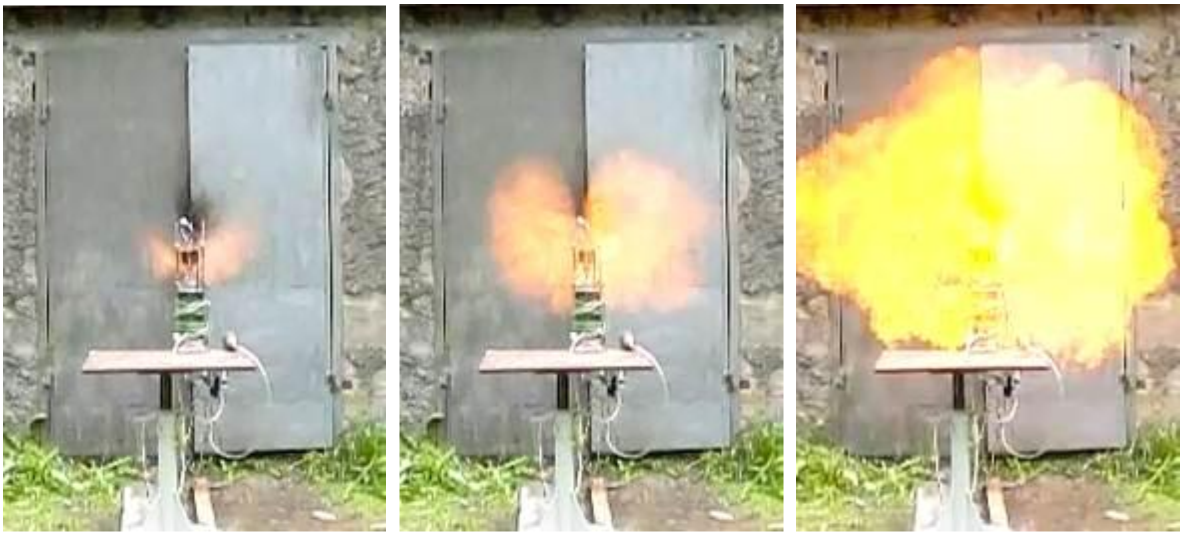

2.667 μs 4.000 μs 40.000 μs

Fig. 4. Self-ignition and combustion in volume (N 98)

Let’s determine basic stages of process of the membrane brake and interaction of a jet with a barrier:

**Formation of the primary air shock weaves.**

In Fig. 5, distribution of Mach number (M) along the axis of the shock wave (H) obtained as a result of hydrogen jet released into free space volume through the outlet hole of d = 15 mm is shown (rectangles and triangles are for different result processing methods and two curves – for different results approximation methods). It could be seen that the highest wave intensity is at the distance of 70–80 mm from the membrane brake (about 5 flux gages). As a result of the study, distances from the outlet to the barrier surfaces are selected.

**Focalization of pressure variation and mixing of the shocked air inside the cavity with high-pressure hydrogen (driving gas of the primary flow).**

Time dependences for pressure variation at the focusing surface axis for different barriers are shown in Fig. 2, maximum pressure levels – in Table 1. This values are probably lower than those in the focal spot of the pressure variations (except for the cases with cone and wedge).

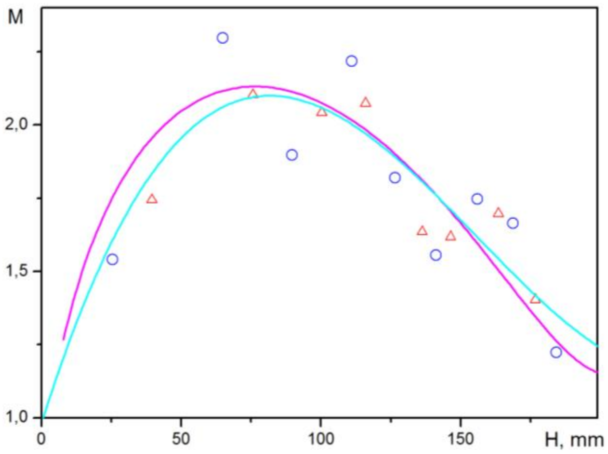

Fig. 5. Distribution of the shock wave Mach number along the jet axis

**Local self-ignition** (with necessary conditions are observed) **of air-hydrogen mixture inside the cavity** (and in the near area - with big volume of the primary combustion mixture).

**Forced ignition of air-hydrogen mixture in the area of forming jet interacting with combustion sources exported from the cavity.**

Analysis of the results in Table 1 shows that pressure of $P_{sen}$ = 2.4–2.5 MPa could be enough for local self-ignition (N 95 and N 113), while at pressures of $P_{sen}$ = 5.4 MPa (N 66) and $P_{sen}$ = 3.9 MPa (N 115) there is even no glowing from the cavity observed. Let's take a detail look at the reasons for such instability.

One of the factors that determine the delay of hydrogen self-ignition is concentration of water vapour in the air-hydrogen mixture [3, 4]. In [3] the study based on numeric analysis of hydrogen self-ignition kinetic models shows that different volume concentrations could both increase or decrease self-ignition delay time. For water vapour concentration of 1.5% (it is a critical concentration) promotion and inhibition features compensate each other, while for higher concentrations thermal inhibition features prevail.

Mentioned critical water vapour concentration is equal to water vapour density of $\rho \approx 16$ g/m$^3$ in the experiments (for air-hydrogen mixture with stoichiometric index $\phi = 1$); for poor mixture, bottom self-ignition level of this critical concentration is equal to water vapour density about 12 g/m$^3$. From the results in Table 1, it could be seen that the recorded values $\rho$ are lower than before mentioned critical values. Therefore, for the conditions of the experiments water vapour density can't lead to the ignition delay increase (compared to the conditions of dry air).

Meanwhile, with the water vapor density decrease (becoming more distant from the critical value), hydrogen ignition induction time decreases and, by that manner, probability of its self-ignition increases. Results in Tale 1 also support such a conclusion.

Lets take a detail look at reasons for increase of probability of hydrogen combustion outside the focusing cavity. As it is described above, for these purposes turbulators are used. That provides opportunity for the combustion areas to be transferred from the cavity into external area. Without turbulator unit, combustion in the external area outside the focusing barrier is observed in only one experiment (N69).

On the other hand, several experiments with turbulators with local self-ignition process don't lead to combustion in the external area even with variable high of the turbulators. It is probable, that for the flame propagation into area of high-speed flow of nonstoichiometric air-gas mixture, it is necessary to have low water concentration to provide very small self-ignition delay time. Thus, both cases of volume combustion with controlled air humidity are observed for low water vapour density – $\rho$ = 6.7 g/m$^3$ (N 97 and N 98).

Note that according to [3], minimum time of self-ignition delay is observed for water vapour density of $\rho \lesssim 1$ g/m$^3$. In experiments N 123 and N 124, $\rho$ = 3.4 g/m$^3$ > 1 g/m$^3$ . That's why local combustion spots don't lead to fire propagation into external area. Probably, there are another, unrevealed eat, factors that determine this process.

The attempt to force the fire area transfer from the cavity by shifting the axis of the barrier from the axis of the jet is made in experiment N125. It is supposed that central, high-pressure part of the jet will force the self-ignition area out of the cavity towards mixing area with lower flow speeds and air-hydrogen mixture parameters closer to stoichiometry. But we failed to check this theory because of no hydrogen self-ignition in these experiments which, probably, could be caused by decrease of the pressure variations level because of asymmetry of the primary shock wave impact on the hemispherical cavity.

Distribution of visible speed of diffusion flame V over fire base radius $R_f$ (in horizontal plane) obtained after processing of video recordings of experiments N 97 and N 98 are shown in Fig. 6. The show results are well correlated with each other which indicates good reproducibility of the studied combustion process in case of its successful ignition. Maximum visible speed levels (105–115 m/s) are observed for distances of 0.2–0.4 m from the jet axis. Such high speeds are determined in particular by high-pressure hydrogen jet flowing around the barrier with high radial component of the velocity vector. This factor should be taken into account during assessment of ignition probability in case of accident release of hydrogen pulse jet.

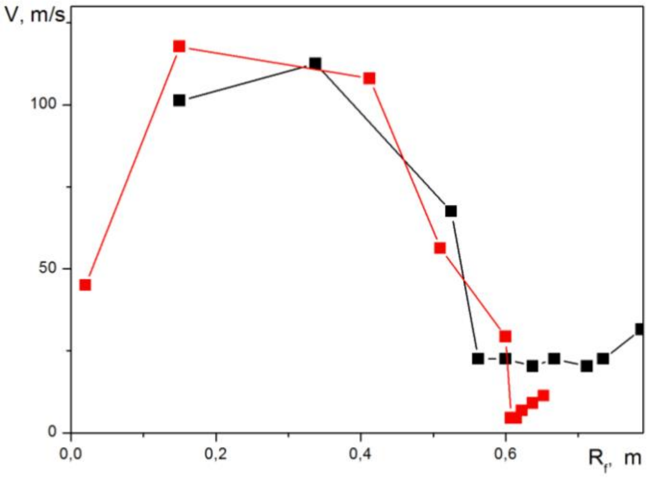

Fig. 6. Distribution of air-hydrogen mixture combustion velocity over fire spot radius (rectangles for exp. N 97, triangles – for exp. N 98)

## 4. CONCLUSIONS

As a conclusion, during the study we didn't obtain reproducibility of self-ignition and combustion processes in pulse jet of hydrogen released into encumbered space. But possibility of such phenomena is proved and conditions for occurrence of these processes in emergency situations and accidents should be eliminated. In the discussed cases, safety criterion is absence of elements and parts that could serve as flow turbulators and pressure variation focusing planes near potentially hazardous technological units (from the point of potential breakdown of hydrogen tanks or transportation lines).

## ACKNOWLEDGMENTS

The study has been completed within the framework projects GPII Vodorod (Belarus) by order of Vodorod 14.

## REFERENCES

1. HELFAND, B.E., POPOV, O.E., CHAYVANOV B.B. Vodorod: parametry gorenija I vzryva. – M.: FML. 2008. 288 p.
2. LIEPMANN, H.W., ROSHKO, A. Elements of Gas Dynamics. Paperback. 2002 456 p. ISBN 13: 9780486419633.
3. GOLOVICHEV, V.I., DIMITROV, V.I., SOLOUKHIN, R.I. Chislennyj analiz modelej vosplamenenija vodoroda. FGV. 1973. V. 9, N 1. p. 95–101.
4. HELFAND, B.E., SILNIKOV, M.V., MEDVEDEV, S.P., HOMIK, S.V. Dinamika gorenija I vzryva vodoroda. SPb. 2009. 584 p.

CYSENI 2011, May 26–27, Kaunas, Lithuania
ISSN 1822-7554, www.cyseni.com

# SUBSTRATE EFFECTS ON FORMATION AND HYDROGENATION OF MG-NI FILMS

**M. Lelis, D. Milčius, S. Tučkutė**
*Lithuanian Energy Institute*
*Breslaujos st. 3, LT-44403 Kaunas – Lithuania*
*Phone +370 37 401 904*
*Email: Martynas@hydrogen.lt*

**M. Lelis, S. Tučkutė**
*Vytautas Magnus University*
*Vileikos st. 8, LT-44404 Kaunas – Lithuania*
*Phone +370 37 327 910*
*Email: fk@gmf.vdu.lt*

## ABSTRACT

Usually thin metallic films for metal hydrides research applications are synthesised on hard and flat substrates such as silicon, magnesium oxide, fused silica or quartz glass. When film thickness increases all films during hydrogenation deals with typical problems such as film brittleness and cracking. In this paper we demonstrate that metal Mg-Ni films for hydrogen storage can be successfully deposited on to the flexible low surface energy teflon substrates. The received results for soft substrates are compared to films deposited on pure silica films with and without plasma pretreatment. It is observed that different interface zone between substrate and film has great affect on both film crystallinity and its reaction with hydrogen. It is also demonstrated that modifying substrate surface has crucial affect on film microstructure before and after hydrogenation. Metallic films were tested for hydrogen adsorbtion - desorbtion cycling and arising differences in film microstructure were revealed by scanning electron microscopy. Several physical insights and basic theoretical models for the received results are also provided.

Keywords: Hydrogen energy, hydrogen storage, metal hydride, film, substrate, interaction.

## 1. INTRODUCTION

At the beginning of the second decade of the twenty first century all of the modern economies including USA, Japan, China and countries of European Union are highly depended on fossil resources. Furthermore, International Energy Agency (IEA) in its World Energy Outlook 2010 gives intimidating statement that the world of energetics faces unprecedented uncertainty [1]. This outlook was released at the end of the year 2010 and at that time IEA experts predicted that if global policies would have stayed the same as they were at the end of the year 2010 then average crude oil price would rise steadily from 75 Dollars per barrel (as they were at November, 2010) till 100 Dollars per barrel in 2018 and 120 Dollars per barrel in 2025. This predicted rising of crude oil prices was already seen as a big challenge for global economical situation. However, in the beginning of the 2011 we have witnessed the beginning of the civil disorders in North Africa and near East countries and then civil disorder began in Libya (which has around 3.2% of global oil reserves [1] and currently produces around 1% of the global oil demand [2]) crude oil prices has skyrocketed and in just few weeks has reached almost 120 Dollars per barrel [3]. Still and all high oil price is only one side of the coin, meanwhile on the other side we have even bigger chalanges such as rapid depletion of oil reserves, unacceptable environmental changes and the risk of new global or at least wide spread socio-economical crysis. Either of these issues is serious enough to initiate immediate action and modern world has no choice but to look for all kinds of alternative energy solutions. In this light investigation of every single alternative for energy generation and storage is very important and hydrogen based energy systems can be one of the solutions.

During the last decade a lot of efforts have been made to find a perfect solid state hydrogen storage material which would have high hydrogen storage capacity, proper thermodynamic properties and good cycling stability [4–6]. However, no single material was able to meet the requirement and it became clear that different sortes of material engineering is needed. Probably the biggest step forward at improving hydrogen storage properties of known hydrides was achieved by Bogdanavic when he added titanium chloride to sodium alanate [7–8]. Unfortunately, this progress was not enough and further advances are still needed.

During current research we wanted to test if manipulation of thin film-substrate interaction zone and controlling free surface energy could have significant effects on hydrogenation properties of thin films deposited by magnetron sputtering. F or this purpose we have chosen to use $Mg_2Ni$ alloy and its coresponding $Mg_2NiH_4$ hydride. This material was chosen for several reasons. First of all, since its discovery by Reilly and Wiswall in 1968 [9] $Mg_2Ni_4$ became a target for many studies, therefore there is a lot of information on this hydride at different literature sources. It was revealed that in powder form $Mg_2NiH_4$ has three crystal phases: LT-1 and LT-2 are both monoclinic low temperature (below 510 K) phases respectively without and with microtwinings [10–11], and HT is FCC non-conducting high temperature (above 510 K) phase. For $Mg_2NiH_4$ powders, phase transition between low temperature and high temperature phases is reversible. On the other hand, it was shown that $Mg_2NiH_4$ in thin film form on quartz and calcium fluorite substrates does not undergo any phase transitions and always stays at some intermediate pseudo cubic phase [12]. Furthermore, extensive studies have demonstrated that both for powders and thin film material crystallographic, electrical and optical properties of $Mg_2NiH_4$ hydride strongly depend on residual stresses as well as contaminants. These facts make magnesium nickel hydride very attractive candidate for investigations of new approaches for bulk hydride properties modification just by modifying film-substrate interaction forces.

## 2. METHODOLOGY

For current experiments we used Kurt J. Lesker company PVD-75 magnetron sputtering system with two independent 3” DC powered magnetrons. The system was equipped with cryopump which allows to achieve a base vacuum level down to $5 \cdot 10^{-8}$ mbar ($5.05 \cdot 10^{-6}$ Pa). For sputtering we used 99.99% pure magnesium and 99.999% pure nickel targets. During our earlier experiments [12] as substrates we have used amorphous quartz and polycristaline calcium fluorite. Therefore, in order to check if we can manipulate hydride properties by changing film-substrate interaction forces we have chosen two types of substrate with completely opposing properties from those which were used during earlier experiments. First of them was precisely polished prime grade silicon wafers with strict (111) surface orientation. In contrast to quartz and $CaF_2$, silicon wafers have flat and periodical surface even at the atomic scale which is guaranteed by (111) crystalline orientation. Furthermore, it is known that at higher temperatures (around 600° C) magnesium and silicon can form magnesium silicates [13] which can suppose much higher Mg-Ni film and substrate interaction comparing to earlier studies. On the other hand for the second substrate we were looking for substrate with as low surface energy as possible. Probably the most suitable candidate was Teflon (100 % expanded PTFE ($-(CF_2)_n-$) with multidirectional strength) from Gore Company. Teflon is widely known for very low free surface energy and apart that it also i) exhibits very good temperature stability in -268 °C to +315 °C temperature range; ii) is dimensionally stable with no aging or degradation; iii) chemically inert – resistant to all media in the 0-14 pH range, except molten alkali metals and element fluorine; iv) possible operating pressure vacuum to 200 bar [14].

For both types of substrates we have used three different surface pre-treatment procedures: i) Si and Teflon substrates were washed in acetone at ultrasonic bath, dried out under dry air flow and then additionally washed with cloth rinsed in ethyl alcohol; ii) in addition to washing as described above before film deposition substrates were affected by DC power source generated plasma (no contact with air between plasma treatment and thin film deposition); iii) washed and treated with pulsed DC power source generated plasma. Further experimental details are provided in table 1.

Table 1. Experimental condition of thin film deposition

| Sample | Substrates | Substrate cleaning with acetone and alcohol | Substrate cleaning-activation with DC source generated plasma | Substrate cleaning-activation with pulsed DC source generated plasma | Thin film deposition parameters (deposition time - 15 minutes, pressure - $6\cdot10^{-3}$ mbar (0.606 Pa)) | |
|---|---|---|---|---|---|---|
| | | | | | Mg | Ni |
| 1 | For each experiment two subtrates were used:<br>one 20 x 10 mm piece of prime grade Si (111) wafer<br>one 15 x 6 mm piece of Teflon | + | - | - | I = 0.5 A<br>U = 237 V | I = 0.175 A<br>U = 329 V |
| 2 | | + | **Ar pressure:**<br>P = $2\cdot10^{-2}$ mbar (2.02 Pa)<br>**DC power source parameters:**<br>U = 900 V<br>I = 0–10 mA<br>t = 15 min | - | I = 0.5 A<br>U = 233 V | I = 0.175 A<br>U = 333 V |
| 3 | | + | - | **Ar pressure:**<br>P = $2\cdot10^{-2}$ mbar (2.02 Pa)<br>**Pulsed DC power source parameters:**<br>U = 650 V<br>I = 350–360 mA<br>t = 15 min | I = 0.,5 A<br>U = 230 V | I = 0.175 A<br>U = 330 V |

All as-deposited thin films were analysed by X-ray diffraction (XRD) and Scanning Electron Microscopy (SEM) methods and then hydrogenated for 72 hours at 20 bar hydrogen pressure and constant 180° C temperature. After hydrogenation thin films analysis with XRD and SEM techniques was repeated. Received data was analysed in two aspects: i) how films have changed compared to the initial samples and ii) can we receive the low temperature phase (LT-1 and/or LT-2) magnesium nickel hydride which was not achievable during earlier experiments then films were deposited on quartz and calcium fluoride substrates [12].

## 3. RESULTS AND DISCUSIONS

Before thin film deposition we took silicon and Teflon substrates and analysed them with SEM. Substrates were analysed at two stages: after they were washed with acetone/alcohol and after pulsed DC plasma treatment. As it might be expected prime grade silicon wafers with and without plasma treatment were so flat that SEM did not reveal any topographical information. Meanwhile, SEM analysis of Teflon substrates with and without plasma treatment shows extensive changes (Fig. 1). These observations indicates that chosen method for substrate surface modification is effective and it is reasonable to assume that in total we will have six samples with different size film-substrate interaction forces.

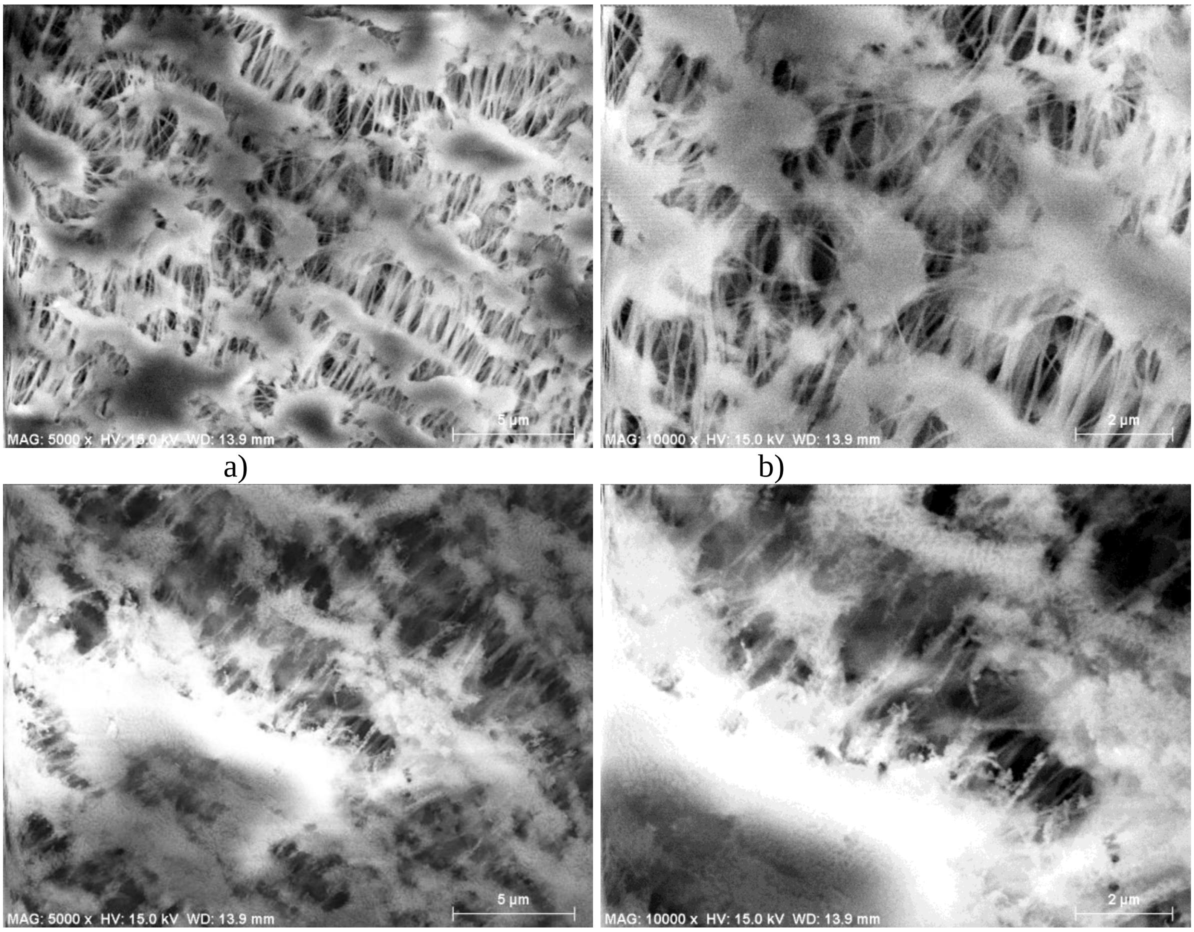

a) b)

c) d)

Fig. 1. SEM images of Teflon substrates: a) and b) Teflon substrate was washed with acetone/alcohol; c) and d) Teflon substrate was washed with acetone/alcohol and treated with pulsed DC plasma

SEM images of metallic Mg-Ni films deposited on silicon and Teflon substrates are shown in Fig. 2. These images show that different substrate pre-treatment has significant influence on thin film growing. Looking at Mg-Ni films deposited on silicon we can identify that plasma treatment has observable effect on film topography. In Fig. 2a we can see that Mg-Ni thin film rugged and that it has small (50–100 nm) ridges. These ridges can still be identified in Fig 2c and are completely absent in Fig. 2e. Altogether, SEM image analysis allows making qualitative assumptions that plasma treatment significantly improves film homogeneity, density and makes it flatter which means it repeats silicon substrate surface better than plasma untreated sample.

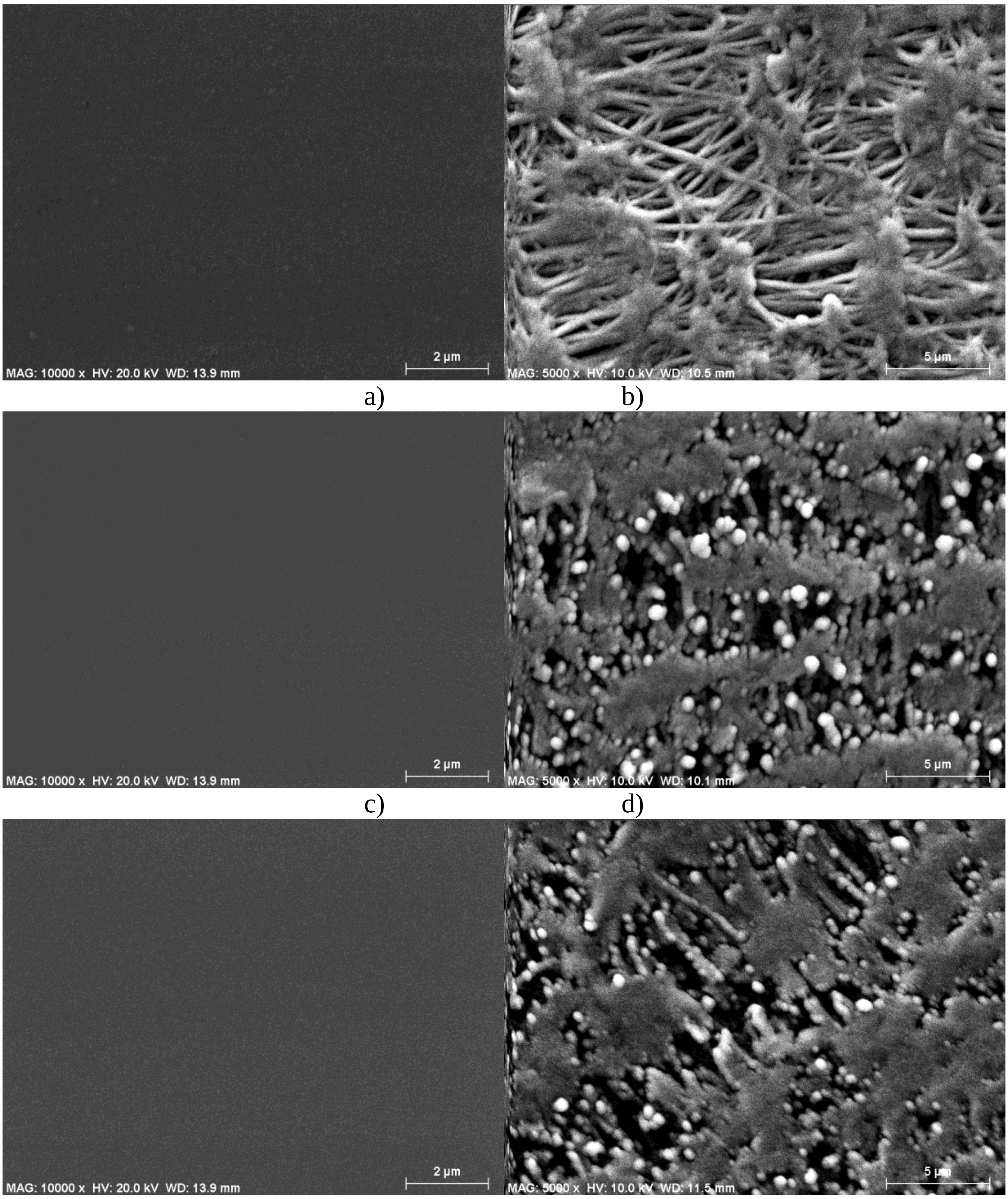

a) b)

c) d)

e) f)

Fig. 2. SEM images of as deposited Mg-Ni thin films on different substrates: a) Mg-Ni thin film on washed silicon, b) Mg-Ni thin film on washed Teflon, c) Mg-Ni thin film on washed and DC plasma treated silicon, d) Mg-Ni thin film on washed and DC plasma treated Teflon, e) Mg-Ni thin film on washed and pulsed DC plasma treated silicon, f) Mg-Ni thin film on washed and pulsed DC plasma treated Teflon

Quantitative analysis of film density and surface investigations with atomic force microscope could be useful in order to confirm or deny these assumptions, however we did not have possibilities to do either of these analysis. On the other hand plasma treatment of Teflon substrates not only brakes structural “strings” but also significantly improves film adhesion to the substrate which is clearly indicated by better surface coverage with the film. For elemental microanalysis of deposited thin films we have used Energy Dispersive Spectroscope (EDS) which was connected to SEM equipment. EDS measurements revealed that for all samples Mg and Ni atomic concentration respectively were close to the 65 at. % and 35 at. % respectively.

X-ray diffraction analysis of as-deposited Mg-Ni thin films on silicon and teflon substrates has revealed that in all cases deposited Mg-Ni film is formed in amorphous phase. XRD data for Mg-Ni films on Teflon substrates with different pre-treatment is shown in Fig. 3. Because of the limited space the corresponding XRD data for films deposited on silicon substrate is not shown here.

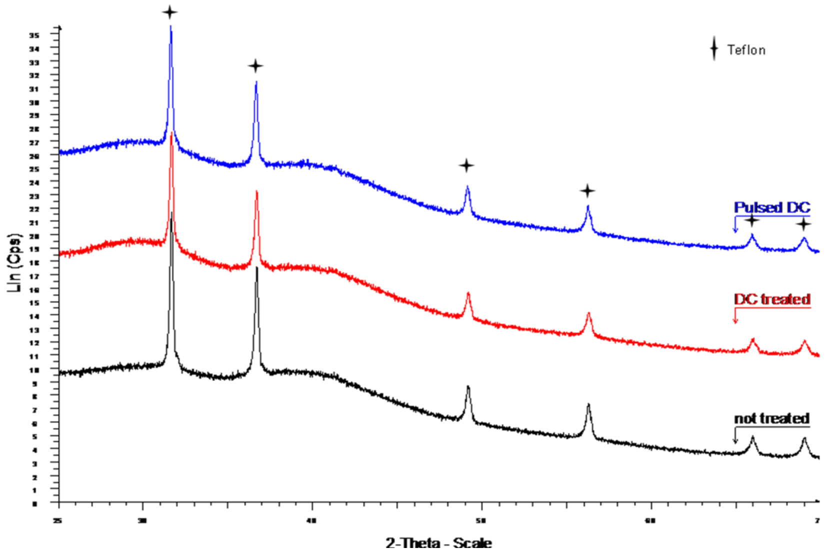

Fig. 3. X-ray diffractograms of Mg-Ni thin films deposited on Teflon substrates

SEM images of Mg-Ni thin films after hydrogenation are shown in Fig. 4. Here we can see that after hydrogenation surface characteristics of Mg-Ni films on silicon substrates have changed drastically. For the substrate which did not had any plasma pre-treatment we can see that the film is even more homogeneous and more flat than it was before the hydrogenation, meanwhile SEM images of Mg-Ni films on plasma pre-treated silicon substrates presuppose that during hydrogenation they have undergone through much higher mass transport phenomena and therefore it is reasonable to assume that these two samples have adsorbed more hydrogen that the first one. Also by the surface topography changes we can predict that DC plasma treatment was a little more favourable for the formation of magnesium nickel hydride.

Looking at SEM images of hydrogenated Mg-Ni films which were deposited on Teflon substrates we can clearly indicate high level of thin film expansion. This means that Mg-Ni films on Teflon substrate have much lower adhesion, therefore they can expand more freely. This observation can be very useful trying to find proper substrates for the films in order to avoid film cracking and falling off of the substrate during the hydrogenation and/or dehydrogenation processes.

X-ray diffraction data for hydrogenated Mg-Ni thin films on silicon and Teflon substrates are shown in Fig. 5 and 6. Looking at Fig. 5 we can see that according to crystal phase information the highest hydrogen content (beta hydride) is received for the sample which was deposited on DC plasma treated silicon substrate. This is in good agreement with predictions which were made looking at SEM images (Fig. 2).

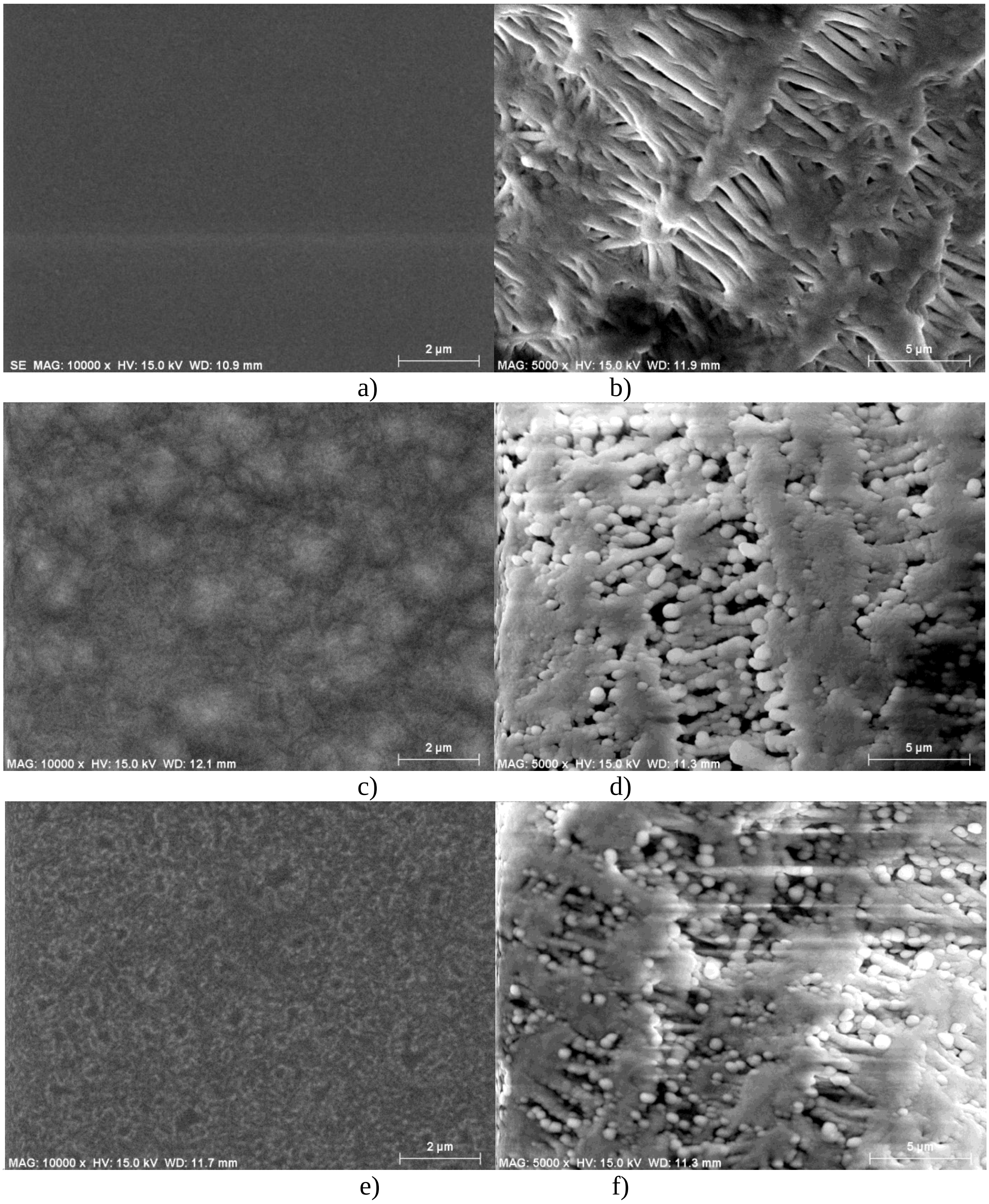

a) b)

c) d)

e) f)

Fig. 4. SEM images of as hydrogenated Mg-Ni thin films on different substrates: a) Mg-Ni thin film on washed silicon, b) Mg-Ni thin film on washed Teflon, c) Mg-Ni thin film on washed and DC plasma treated silicon, d) Mg-Ni thin film on washed and DC plasma treated Teflon, e) Mg-Ni thin film on washed and pulsed DC plasma treated silicon, f) Mg-Ni thin film on washed and pulsed DC plasma treated Teflon.

It is important to point up that full magnesium nickel hydride (beta phase) is formed only for the sample which was deposited on DC plasma pre-treated substrate and no beta hydride formation was observed for other two samples which were deposited on other two silicon substrates. Another striking result is that after DC plasma pre-treatment we were able to form low temperature monoclinic $Mg_2NiH_4$ hydride which was not observed on other samples.

Furthermore, as it can be seen from Fig. 6 beta phase hydride was not observed on neither of the samples deposited on Teflon substrate. This indicates that probably there is optimal strength of adhesion (interaction force between film and the substrate) under which we have best conditions for formation of $Mg_2NiH_4$ hydride.

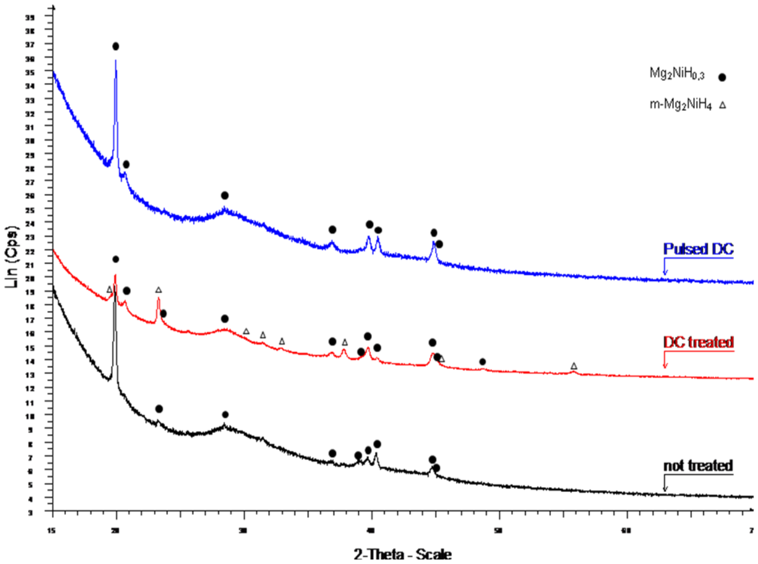

Fig. 5. X-ray diffractograms of hydrogenated Mg-Ni thin films deposited on silicon substrates with different pre-treatment

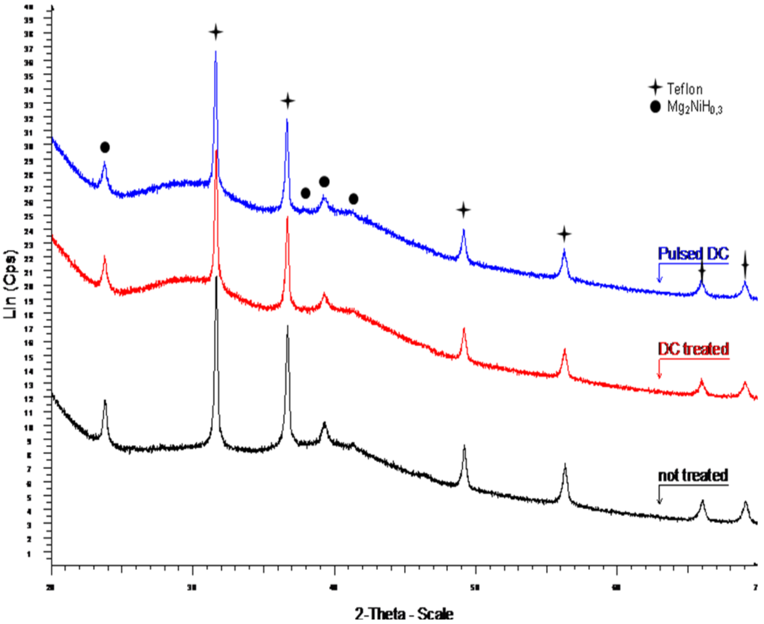

Fig. 6. X-ray diffractograms of hydrogenated Mg-Ni thin films deposited on teflon substrates with different pre-treatment

## 4. CONCLUSIONS

During our research we have qualitatively demonstrated that at least for Mg-Ni thin films we can use substrates with opposing properties and various preparation methods and consequently generate different interaction forces between substrate and the thin film which could lead to completely different properties of hydride formation. Quantitative SEM analysis shows significant changes in surface topology and can be interpreted as an outcome of received film densification. Furthermore, hydrogenation experiments and formation of dissimilar hydride phases (particularly alfa and beta) indicates that in order to have fast formation of the particular hydride we might need to search for optimal substrate material and its preparation. In summary, we can conclude that observed results reveals new possibilities how we can manipulate hydride properties and make them more attractive for the alternative energy system applications.

## REFERENCES

1. http://www.eia.gov/oiaf/ieo/pdf/0484%282010%29.pdf
2. http://www.eia.doe.gov/cabs/Libya/Oil.html
3. http://oilprice.com/
4. B. SAKINTUNA, F. LAMARI-DARKRIM, M. HIRSCHER, Metal hydride materials for solid hydrogen storage: A review, International Journal of Hydrogen Energy, Volume 32, Issue 9, June 2007, p. 1121–1140.
5. P. JAIN, P. JAIN, A. JAIN, Novel hydrogen storage materials: A review of lightweight complex hydrides, Journal of Alloys and Compounds, Volume 503, Issue 2, 6 August 2010, p. 303–339.
6. R. B. BINIWALE, S. RAYALU, S. DEVOTTA, M. ICHIKAWA, Chemical hydrides: A solution to high capacity hydrogen storage and supply, International Journal of Hydrogen Energy, Volume 33, Issue 1, January 2008, p. 360–365.
7. German patent application 195 26 434.7, 1995.
8. B. BOGDANOVIC, R.A. BRAND, A. MARJANOVIC, M. SCHWICKARDI, J. TOLLE, Metal-doped sodium aluminium hydrides as potential new hydrogen storage materials, Journal of Alloys and Compounds, Volume 302, Issues 1–2, 28 April 2000, p. 36–58.
9. J. REILLY, R. H. Jr. WISWALL, Reaction of hydrogen with alloys of magnesium and nickel and the formation of $Mg_2NiH_4$, Inorganic Chemistry, 7, 1968, 2254.
10. D. NORÉUS and L.G. OLSSON, The structure and dynamics of hydrogen in $Mg_2NiH_4$ studied by elastic and inelastic neutron scattering, Journal of Chemical Physics, 78 (1983), p. 2219.
11. D. NORÉUS and L. KIHLBORG, Twinning at the unit cell level in the low temperature phase of $Mg_2NiH_4$ studied by electron microscopy, Journal of the Less Common Metals, Volume 123, Issues 1-2, September 1986, p. 233–239.
12. M. LELIS, D. MILCIUS, E. WIRTH, U. HÅLENIUS, L. ERIKSSON, K. JANSSON, K. KADIR, J. RUAN, T. SATO, T. YOKOSAWA, D. NORÉUS, A mechanically switchable metal–insulator transition in $Mg_2NiH_4$ discovers a strain sensitive, nanoscale modulated resistivity connected to a stacking fault, Journal of Alloys and Compounds, Volume 496, Issues 1-2, 30 April 2010, p. 81–86.
13. T. MITSUDA, H. TAGUCHI, Formation of magnesium silicate hydrate and its crystallization to talc, Cement and Concrete Research, Volume 7, Issue 3, May 1977, p. 223–230.
14. http://www.gore.com/en_xx/products/sealants/gaskets/gore-tex_gr_sheet_gasketing.html

CYSENI 2011, May 26–27, Kaunas, Lithuania
ISSN 1822-7554, www.cyseni.com

# EXPERIMENTAL STUDY OF Ti FILMS HYDROGENATION USING MAGNETRON WATER VAPOUR PLASMA

**L. Pranevicius, M. Urbonavicius**
*Vytautas Magnus University*
*Vileikos str.8, LT-44404 Kaunas – Lithuania*
*Phone +370 643 63871*
*Email: marius.urbonavcius@fc.vdu.lt*

ABSTRACT

The goal of this research is to separate hydrogen from water molecules using ion implantation method. The plasma has been generated in the water vapour at 10 – 100 Pa pressure using DC and RF magnetrons with titanium cathode. Positive ions have been extracted from water vapour plasma, accelerated by electric field and directed to the Ti sample. The energetic water ions entering the Ti film are broken into its components: hydrogen and oxygen. After plasma treatment all samples have been analyzed by SEM (scanning electron microscopy), EDS (energy dispersive X – ray spectroscopy), GDOES (glow discharge optical emission spectroscopy) and XRD (X - ray diffraction) methods. GDOES distribution profiles show that hydrogen separated from water is transported deeply into the bulk of Ti. XRD patterns include the diffraction peaks of titanium hydrogen oxide hydrate. Separated hydrogen atoms predominantly stay at interstitials and form solid solution without formation of hydrides in the bulk.

*Keywords*: hydrogen, water vapour, plasma, ion implantation.

## 1. INTRODUCTION

Hydrogen as an energy carrier has potential to address many aspects of the energy problem, particularly in the transportation sector [1]. One of the biggest hydrogen sources is water. Efficient and economical water splitting would be a key technology component of hydrogen economy.

Various methods for splitting of water molecule are issued. It is electrolysis, thermo chemical decomposition, radiolysis and photocatalysis. But all these methods are not widely used in the world. Currently, 96% of hydrogen is produced from steam methane reformation from hydrocarbons. Only 4% of hydrogen produced is from electrolysis. Hydrogen produced from electrolysis is still more expensive and less efficient than produced from reformation methods [1].

The goal of this work is to separate hydrogen from water molecules by using water vapor plasma as a source of water molecular ions and plasma immersion ion implantation (PIII) as a method to split water molecules. Furthermore, the water PIII may yield a better surface oxide layer that can offer better enhancement in the surface electrochemical properties [2].

For studies, the titanium (Ti) was selected as a material for interaction with incident ions. Recent studies [3-5] have shown that titanium dioxide is used as catalyst in photocatalytic water splitting method.

# 2. EXPERIMENTAL

## 2.1. Hydrogenation technique

The 0.5 μm thick titanium films were deposited on 2 mm thick stainless steel and silicon substrates employing sputter deposition in vacuum technique. The same PVD – 75 system (Kurt J. Lesker company) was used for film deposition and PIII. Samples were located at different sites of vacuum chamber as shown in Fig. 1: (I) at distance 1–2 cm from magneron outside its sputtering zone (sample A), and (II) on the surface of Ti magnetron cathode (sample B). Two areas of sample located on the cathode have been distinguished: low and high-flux irradiation. In case A, ion current density was in the range of 1-10 μA/cm$^2$, in case B: 1–2 mA/cm$^2$ – for the area of low flux irradiation, and about 10 mA/cm$^2$ – for the area of high flux irradiation.

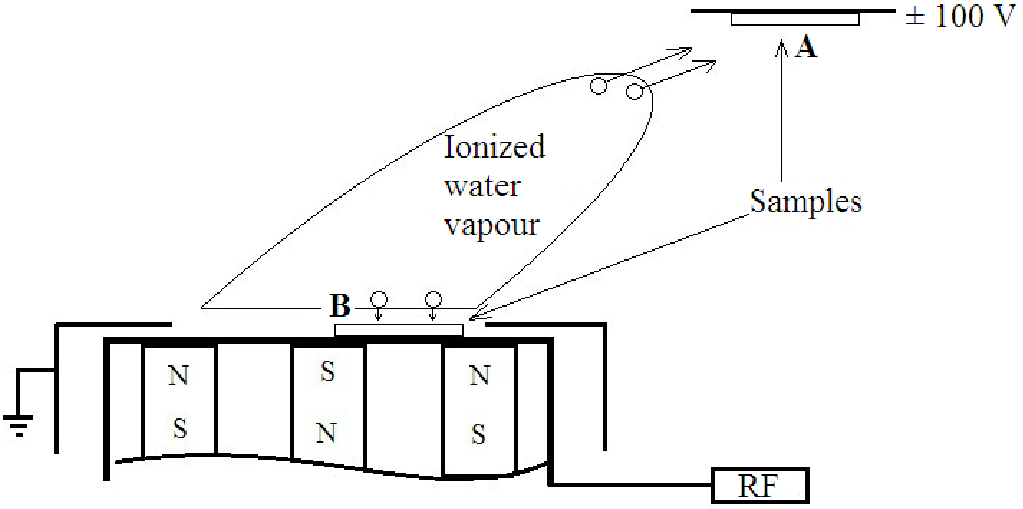

Fig. 1. The layout of samples in vacuum chamber

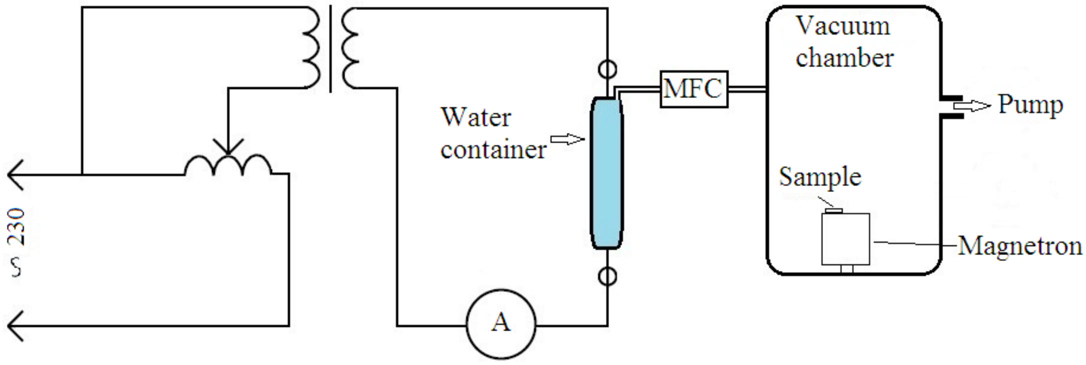

Fig. 2. The scheme of the experimental technique

A vacuum system including rotary and cryogenic pumps enabled a base pressure of $2 \cdot 10^{-4}$ Pa. Water vapour was injected into vacuum chamber from heated water container (Fig. 2). Pure water (pH = 7) was a source of water vapour. PIII was performed at 10 Pa pressure of water vapour. Flow and pressure of water vapour were controlled by mass flow controller. The plasma was ignited by using DC and RF energy sources. The power dissipated in plasma was equal to 100–300 W.

## 2.2. Analysis methods

The microstructure of the samples was analyzed by X - ray diffraction method using Bruker diffractometer (Bruker D8). The measurements were performed using $\theta$–$2\theta$ configuration and Cu K$\alpha$ radiation with $2\theta$ angle in steps of 0.01°. The identification of peaks has been done using EVA *Search – Match* software. The thickness and surface topography of Ti films were measured using the nanoprofilometer (AMBIOS XP 200). The surface views after hydrogenation were investigated by a scanning electron microscopy (SEM, JEOL JSM – 5600). The elemental composition of plasma treated films was analyzed by energy dispersive X–ray spectroscopy (EDS, Bruker Quad 5040). The distribution profiles of hydrogen in titanium films after hydrogenation were measured by glow discharge optical emission spectroscopy (Spectruma Analytic GMBH; GDA 750 Analyzer) analysis.

## 3. RESULTS

### 3.1. Ti film on stainless steel substrate

Fig. 3 shows the XRD patterns of Ti films on stainless steel substrate (sample B) treated by water plasma after different time of plasma treatment: curve 1 - 1 min, and curve 2 - 3 min. Titanium peak Ti (002) at $2\theta = 38.38°$ ($\theta$ is the diffraction angle [6]) and peak of substrate at $2\theta = 44.12°$ were registered. One more peak was identified at $2\theta = 37.57°$. It is peak of titanium hydrogen oxide hydrate (Ti4H209 · 1.9H2O). Sample before hydrogenation is curve 3, where Ti (002) peak was identified at $2\theta = 38.38°$.

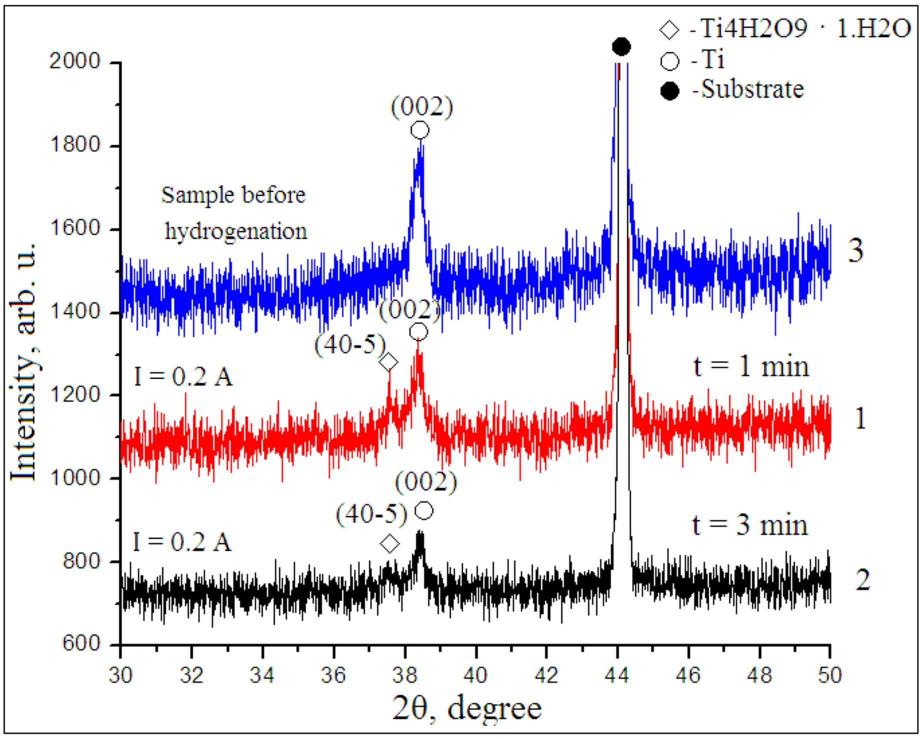

Fig. 3. XRD patterns before and after different durations of hydrogenation

Fig. 4 includes SEM surface views of Ti film after high (Fig. 4a) and low (Fig. 4b) flux irradiation by ions extracted from water vapour plasma. The registered surface topography irregularities may be attributed to the defects of the stainless steel substrate after its mechanical polishing. The surface view after high and low flux irradiation looks the same as well as surface before hydrogenation.

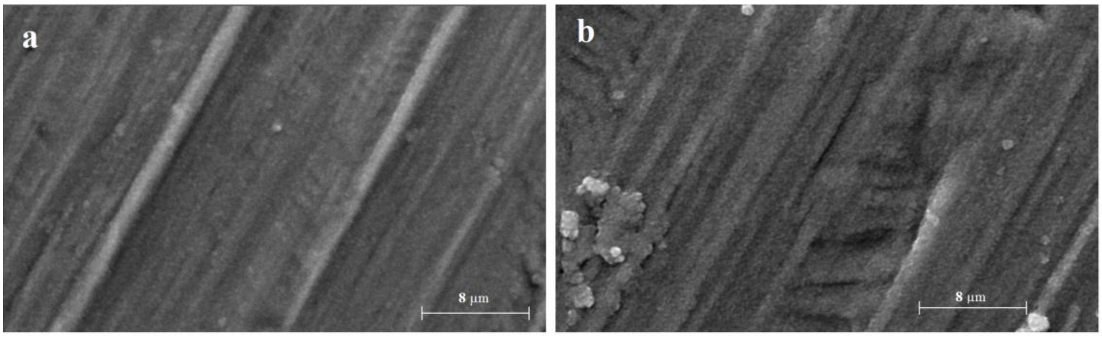

Fig. 4. SEM surface views of Ti film on stainless steel substrate: a – after high-flux, and b – low-flux ion irradiation

### 3.2. Ti film on silicon substrate

Ti films deposited on silicon substrate were treated in RF plasma. Sample A was attached to the holder in front of magnetron and sample B was located on the magnetron cathode (Fig. 1). The thickness of as-deposited Ti was measured by nanoprofilometer (Fig. 5a). It is equal to approximately 625 nm. Nanoprofilometer was used to measure the difference of thickness between two areas (high and low dose-irradiated) of the sample after treatment in water vapor plasma. Hence, it is important to note that Ti surface does not erode under ion irradiation by ions from water vapour plasma. After treatment in water vapor plasma during 60 min surface stays flat (with 10-20 nm accuracy) as is shown in Fig. 5b.

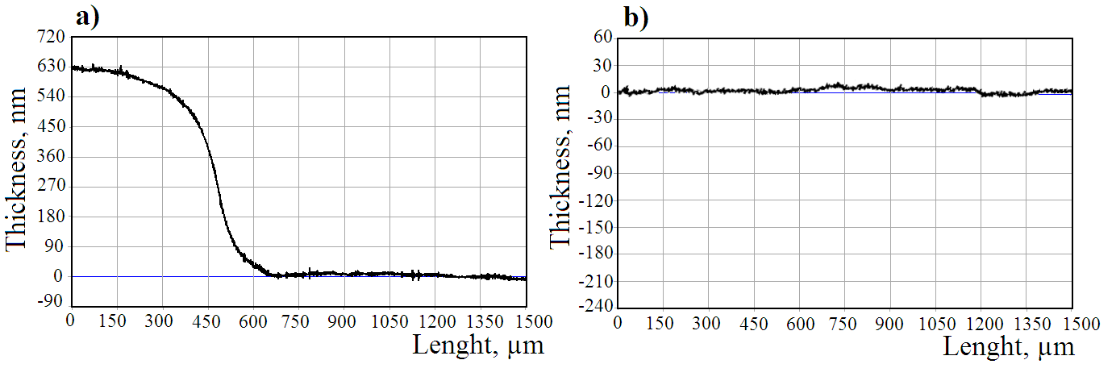

Fig. 5. The profiles of surface topography: a – at the boundary between deposited Ti film and silicon substrate, and b – at the boundary between high and low-dose irradiated areas

Fig.6 includes SEM surface views of Ti film after high (Fig. 6a) and low flux (Fig. 6b) irradiation by ions extracted from water vapor plasma. It is registered that surface roughness is a bit less after high flux ion irradiation. Surface view before hydrogenation is the same as view of low-dose irradiated area (Fig. 6b). EDX analysis shows that oxygen concentration is higher in the area affected by low-flux irradiation (56.18 at. %). The oxygen concentration in the area of Ti film affected by high-flux irradiation is equal to 30.90 at. %.

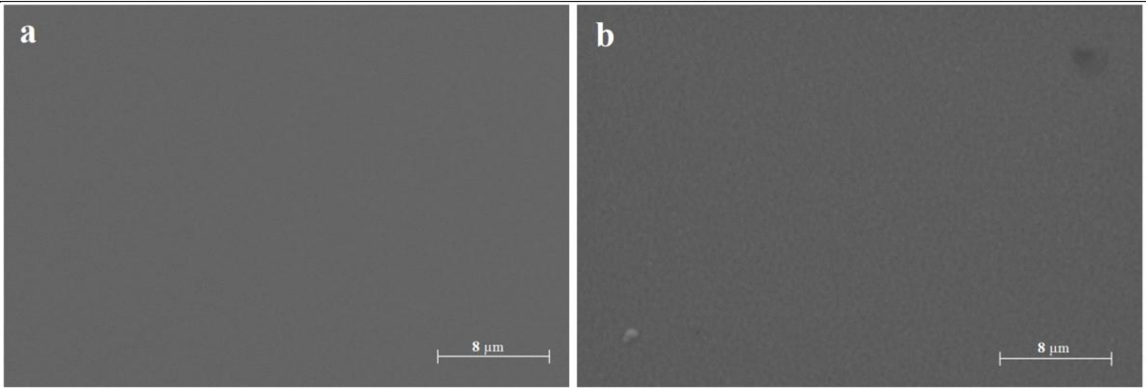

Fig. 6. SEM surface views of Ti film on silicon substrate: a – after high-flux, and b – low-flux ion irradiation

The results of microstructure analysis (using EVA *Search – Match* software) are shown in Fig. 7 for A and B samples, and for the sample before hydrogenation. The peak Si (111) at $2\theta = 28.37^\circ$ is attributed to the substrate. Characteristic peak of Ti (111) is identified at $2\theta = 38.28^\circ$. The peak is assymetrical. It is result of overlapping of two peaks: Ti at $2\theta = 38.28^\circ$ with TiO (101) at $2\theta = 37.47^\circ$. Other peaks of Ti5Si3 (002) and Ti5Si3 (221) were registered at $2\theta = 27.27^\circ$ and $2\theta = 51.82^\circ$, respectively. Small peaks characteristic for titanium hydride phase were identified for the Ti film after intensive ion irradiation: TiH (111) at $2\theta = 35.59^\circ$, TiH (002) and TiH (113) at $2\theta = 39.39^\circ$ and $2\theta = 69.10^\circ$, respectively.

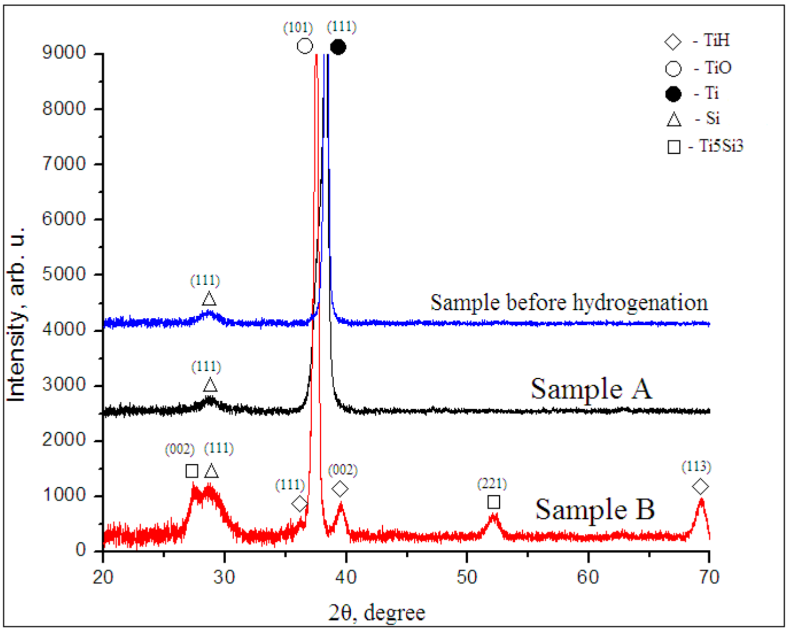

Fig. 7. XRD paterns of Ti film on silicon substrate: sample A, sample B and sample before hydrogenation

Fig. 8 includes the distribution profiles of hydrogen across the thickness of Ti film irradiated by water plasma ions under different intensities of irradiation: a-sample B – high-flux irradiation (10 mA/cm$^2$), b-sample B – low-flux irradiation (1-2 mA/cm$^2$) and c-sample A (1-10 μA/cm$^2$). It is seen that hydrogen depth distribution in Ti film depends on the irradiation intensity.

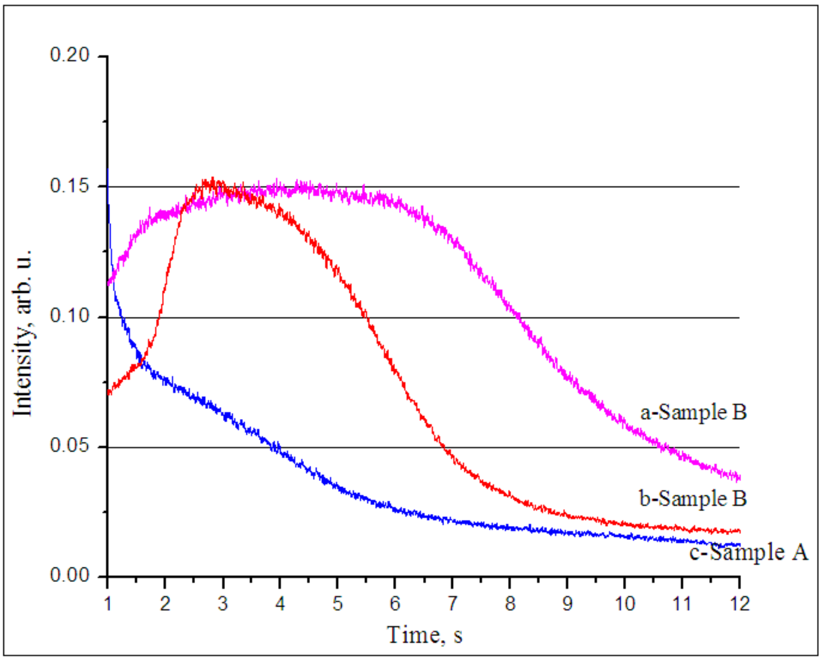

Fig. 8. The distribution profiles of H across the thickness of Ti film after water plasma treatment under different intensities of irradiation: a – sample B for high flux irradiation, b – sample B for low flux irradiation and c – sample A

Fig. 9. shows the distribution profiles of carbon, oxygen and hydrogen across the thickness of Ti film. Fig. 9a. is a distribution after high flux irradiation and fig. 9b. – after low flux irradiation. GDOES did not identified oxygen and identified carbon due to rotational pump. Looking at the distribution profile after low flux irradiation (Fig. 9b) we can say that hydrocarbons possibly could be formed and located in this sample area. It should be mentioned that GDOES method is not the quantitative one.

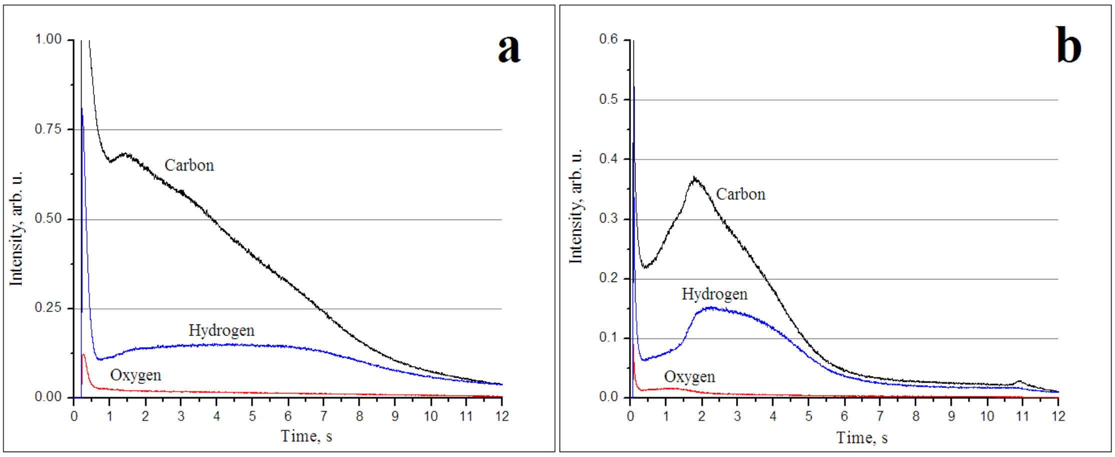

Fig. 9. Distribution profiles of carbon, hydrogen and oxygen under different intensities of irradiation: a – after high flux and b – after low flux irradiation

## 4. DISCUSSION

The experimental trapping efficiency of 1 keV hydrogen ions in titanium is about 90% up to doses $10^{19}$ ions/cm$^2$ [7]. In case of water molecular ion implantation the energy of incident molecular ions is shared between its elements [8, 9]. Ti atoms react with separated oxygen atoms and surface of Ti film is covered by thin titania film with oxygen atoms located on the surface, as it is schematically shown in Fig. 9a. Splitted hydrogen atoms move into the bulk where they stay in interstitials. Under ion irradiation the surface is dynamic [10]. Oxygen atoms sputtered from the surface are replaced by surface adatoms (Fig. 9a). At steady state the balance between the fluxes of sputtered and adsorbed oxygen atoms is established and the resulting surface erosion rate becomes equal to zero. This fact is in agreement with surface topography profiling experimental results (Fig. 5b).

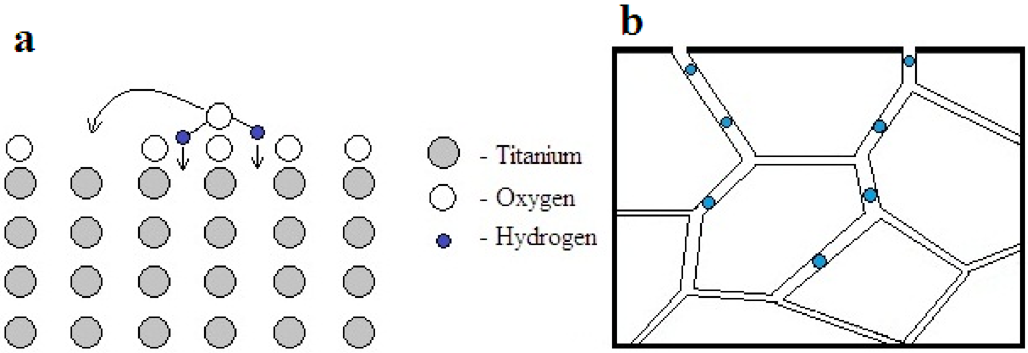

Fig. 9. Schematic presentation of the mechanism of water splitting: a – split of water molecule, and b – transport of hydrogen into the bulk

Liberated hydrogen atoms flow from interstitials into the grain boundaries of nanocrystalline Ti film. The diffusion coefficient of H along grain boundaries is 2-3 orders higher than in the bulk. In that case the H atoms move deeply into the bulk without formation of hidrides (Fig. 9b). If concentration of hydrogen is low, the hydrogen forms α phase which is not registered by XRD (Fig. 3). However, hydrogen has been registered by GDOES technique (Fig. 8). The β phase of titanium hydride (not full hydride) was registered in XRD paterns (Fig. 7, sample B) when concentration of hydrogen exceeded the limit of solubility in Ti.

The concentration of H in Ti film depends on the iradiation dose and intensity of irradiation. Estimations show that in that cases when irradiation time is short (less than 60 min) and irradiation intensity is low (less than 1 mA/cm2) the implanted hydrogen begin to form hidrides.

## 5. CONCLUSIONS

According to the results of the present study (Fig. 8), the technique and method of plasma implantation are capable of splitting water molecules into their constituent atoms and hydrogen separation. The XRD data show that separated hydrogen mainly occupy the interstitials without formation of hidrides. The GDOES distribution profiles show that implanted H is driven into the bulk along the entire thickness of Ti film presumably by diffusion along grain boundaries of nanocrystalline Ti. It is shown that the behavior of H atoms in Ti film depends on the irradiation intensity. Hydrogen penetration depth increases with the increase of irradiation intensity. The obtained results will be used for molecular hydrogen production employing membrane technologies.

## REFERENCES

1. V.T. NGUYEN S., FOSTER J., GALLIMORE A. Operating a radio-frequency plasma source on water vapour. Review of scientific instruments, 2009, Vol. 80.

2. LIU X.M., WU S.L., CHU PAUL K., CHUNG C. Y. Effects of water plasma immersion ion implantation on surface electrochemical behavior of NiTi shape memory alloys in simulated body fluids. Applied surface science, 2007, Vol. 253, p. 3154–3159.
3. SUN H., WANG S., MING Ang H., LI Q. Halogen element modified titanium dioxide for visible light photocatalysis. Chemical Engineering Journal, 2010, Vol. 162, p. 437–447.
4. RAVELLI D., DONDI D., FAGNONI M., ALBINI A. Titanium dioxide photocatalysis: An assessment of environmental compatibility for the case of the functionalization of heterocyclics. Applied Catalysis B: Environmental, 2010, Vol. 99, p. 442–447.
5. ANG YING SHAN, TINIA IDITY MOHD. GHAZI, SURAYA ABDUL RASHID. Immobilisation of titanium dioxide onto supporting materials in heterogeneous photocatalysis: A review. Applied Catalysis A: General, 2010, Vol. 389, p. 1–8.
6. <http://www.spec2000.net/09-xrd.htm>
7. MCCRACKEN G. M. The beaviour of surfaces under ion bombardment. Reports on Progress in Physics, 1975, Vol. 38, p. 241–327.
8. < http://www.iue.tuwien.ac.at/phd/hoessinger/node65.html >.
9. < http://www.iue.tuwien.ac.at/phd/hoessinger/node67.html>.
10. PRANEVICIUS L., MILCIUS D., PRANEVICIUS L.L., THOMAS G. Plasma hydrogenation of Al, Mg and MgAl films under high-flux ion irradiation at elevated temperature. Journal of Alloys and Compounds, 2004, Vol. 373, p. 9–14.

## Acknowledgement

This research was funded by a grant (Nr. ATE-02/2010) from the Research Council of Lithuania. The authors also are grateful to S.Tučkute for her contribution in experimental investigations.

# MODELING OF WATER MOLECULAR ION IMPLANTATION

**M. Televičiūtė, A. Švaikovskij, S. Tučkutė**
*Vytautas Magnus University*
*Vileikos str. 8, LT-44404 Kaunas – Lithuania*
*Email: Andros_281@hotmail.com*

ABSTRACT

In this paper, we have studied theoretically the split of $H_2O$ molecules and separation of H atoms by the molecular ion implantation. It is shown by an analytical estimation of the projected ranges for hydrogen and oxygen atoms, and then, by the computer simulation by SRIM, that energetic water molecules are broken upon the entrance into Ti film and separated oxygen and hydrogen atoms are distributed in the near surface region with the similar depth distribution profiles. The modeling results are compared with the experimental ones. Registered discrepancies show that hydrogen diffusion processes have to be included.

The formation of hydrogen from the water vapor by the molecular ion implantation has two main advantages: 1) hydrogen separation takes place in the range of low temperatures, and 2) process may be verified changing energy and intensity of ion irradiation.

Keywords: Hydrogen, Water vapor, Plasma, Ion implantation.

## 1. INTRODUCTION

The dominant technology for direct hydrogen production is steam reforming from hydrocarbons [1]. Many other methods are known including electrolysis and thermolysis [2]. Water splitting by nanophotocatalysis is one of the most promising and attractive methods for direct hydrogen generation. The problem is that it consumes a significant amount of electricity.

Previous works have recognized the use of plasma for hydrogen production, but only to break up hydrocarbons or as a catalyst. Plasma in water vapor [3] is used to produce hydrogen, when the O-H bonds are mainly dissociated by electrons collisions with water molecules or radicals. However, hydrogen purification remains unsolved problem for many practical applications. The discovery and development of less expensive methods of production of hydrogen is relevant to the establishment of a hydrogen economy.

Recently the plasma ion implantation is introduced as a method for hydrogen production and separation. Energetic incident water ions are injected into the near-surface region of a substrate. They are broken into elements upon entrance into the solid if the ion energy is higher than the dissociation energy of the molecule which is of the order of 10 eV/atom.

The development of practical methods for the implantation of molecular ions requires a better understanding of interaction of energetic molecules with materials. In this paper, the split of $H_2O$ molecules and separation of H atoms under molecular ion implantation is studied theoretically.

# 2. MODELING OF WATER MOLECULAR ION IMPLANTATION

## 2.1. The split and space separation of H atoms from $H_2O^+$ and $OH^+$ ions

With molecular ions dissociating upon an entrance into the solid within a few near surface atomic layers, the energy of an *i*th element is given by

$$\varepsilon_i = \left(\frac{m_i}{M_0}\right) \cdot E_0, \tag{1}$$

where $\varepsilon_i$ and $E_0$ are the respective energies of the element and the molecular ion and $m_i$ and $M_0$ are their respective masses. The relationship obtained from the energy conservation law. energy goes to the item molecular ion. This relationship is valid at the molecular ion implantation. also, when implantation takes place during element division of the ions.

Theoretical difficulties in studies of atomic processes induced by ion implantation justify the use of simplified models. The sizes and configurations of the atoms and molecules are not considered. Assume that dissociation occurs if the energy lost by the molecule due to electronics interaction is higher than the dissociation energy ($E_{H_2O} > E_{\text{dis}}$). Plasma in water vapor includes many different positive ions. In the present work, the behavior of $H_2O^+$ and $OH^+$ ions in Ti is considered.

Fig. 1 includes dependences of the average penetration depth of hydrogen (a) and oxygen (b) atoms in Ti as a function of the energy of incident water molecular ions calculated using SRIM program [4].

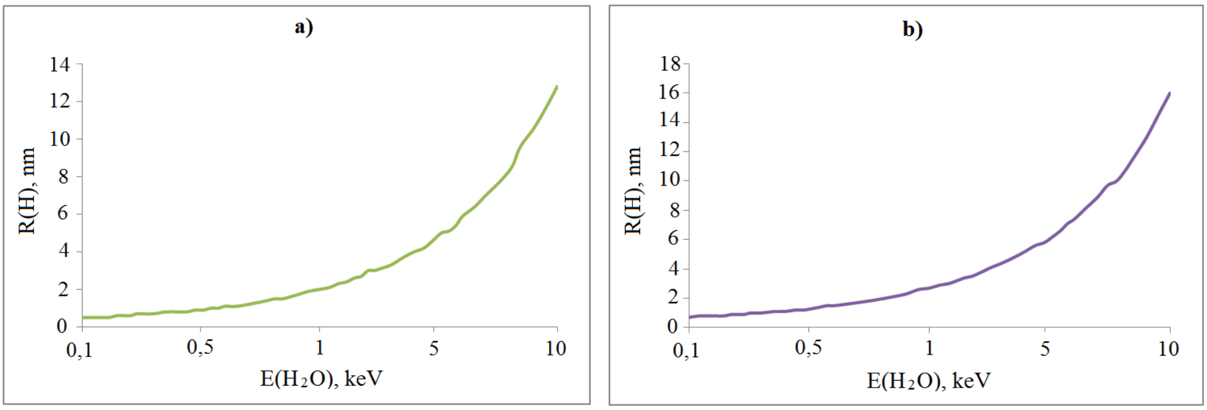

Fig. 1. Dependences of the average penetration depth of hydrogen (a) and oxygen (b) atoms on the energy of incident water molecular ions

The broken elements (O and H atoms) occupy lattice interstitials and interact with surrounding atoms. Oxygen having high affinity to form oxides make M-O bonds, and in the range of low concentrations hydrogen form solid solutions [5]. After molecular ion implantation, the implanted species are located in the near surface region. The ratio of the average penetration depths for hydrogen and oxygen atoms as a function of the energy of incident species is shown in Fig. 2. It increases with the increase of energy of incident water molecules and approaches 1 in the range of tens keV (Fig. 2 a). For $OH^+$ (Fig. 2 b), the average penetration depth of O atoms is two times more than H.

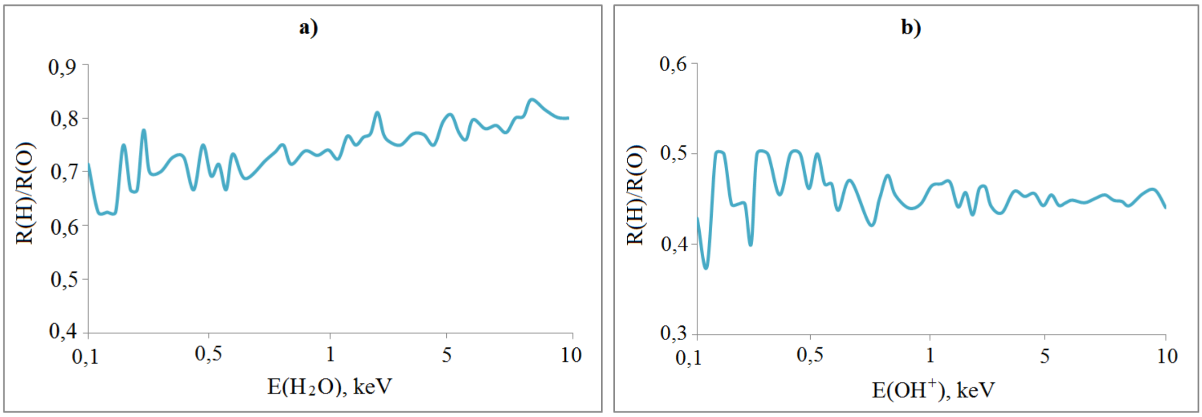

Fig. 2. The dependences of the ratio of average penetration depths of H and O atoms on the energy of incident ions for $H_2O^+$ (a), and $OH^+$ (b)

## 2.2. The calculated distribution profiles of implanted species

### *2.2.1. Low dose water molecular ion implantation*

In the range of low implantation doses when surface sputtering effects may be neglected, the distribution of the implanted ions about the average penetration depth can be approximated as Gaussian with a standard deviation $\Delta R_p$ [4].

$$N(x) = \frac{D}{\sqrt{2\pi}\Delta R_p} e^{-\frac{(x-R_p)^2}{2\Delta R_p^2}}, \qquad (2)$$

where *D* is the implantation dose.

Fig. 3 includes calculated distribution profiles of H (curve 1) and O (curve 2) atoms after molecular ion implantation for implantation dose equal to $8*10^{16}$ ions/cm$^2$ and ion energy – 1 keV for $H_2O^+$ (a) and $OH^+$ (b). The maximums are well expressed in all curves. The locations of maximums for O and H atoms approximately coincides for $H_2O^+$. For $OH^+$, separated H atoms are located closer to the surface than O atoms; however, distribution profiles are overlapping.

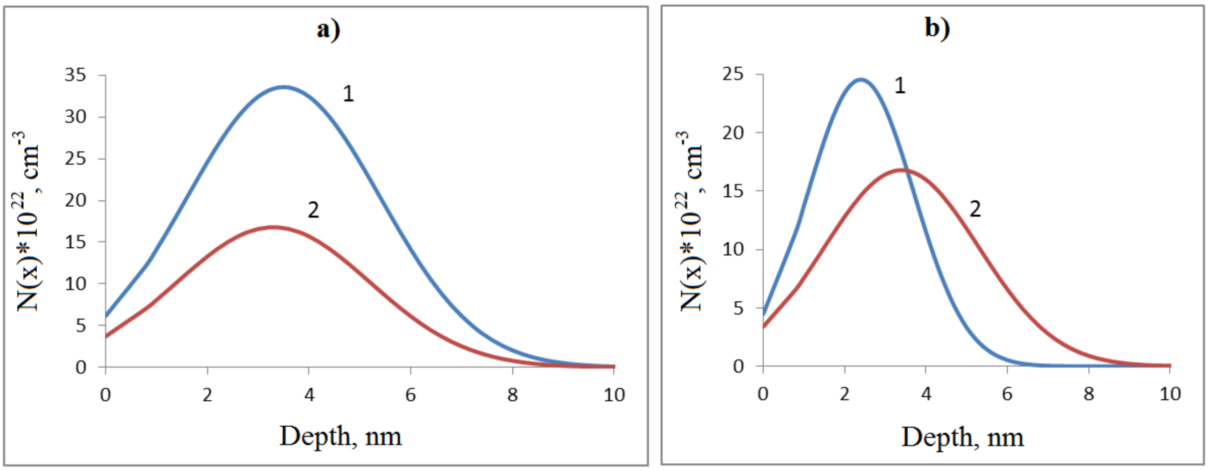

Fig. 3. Calculated distribution profiles of H (curve 1) and O (curve 2) atoms in Ti implanted by 1 keV $H_2O^+$ (a) and $OH^+$ (b) for low dose of irradiation

### *2.2.2. High dose water molecular ion implantation*

In the range of high implantation doses when surface sputtering effects are considered, the distribution of the implanted ions about the average penetration depth can be approximated as [4].

$$N(x) = \frac{N}{2Y}\left[ erf\,\frac{(x - R_p + DY/N)}{\sqrt{2}\Delta R_p} - erf\,\frac{(x - R_p)}{\sqrt{2}\Delta R_p} \right]. \tag{3}$$

Fig. 4 includes calculated distribution profiles of H (a) and O (b) atoms after molecular ion implantation for implantation doses equal to 8.0*$10^{16}$ ions/cm$^2$ (curve 1) and 1.0*$10^{17}$ ions/cm$^2$ (curve 2) for HO$^+$ ion energy – 1 keV. It is seen that the saturation is reached for doses higher than 5*$10^{17}$ ions/cm$^2$ for O atoms and 1.0*$10^{17}$ ions/cm$^2$ for H atoms. It denotes that the fluxes of implanted and sputtered species become equal. The sputtering yields used in calculations were extracted from SRIM program. The sputtering yield of Ti by 1 keV oxygen ions is equal to 0.408.

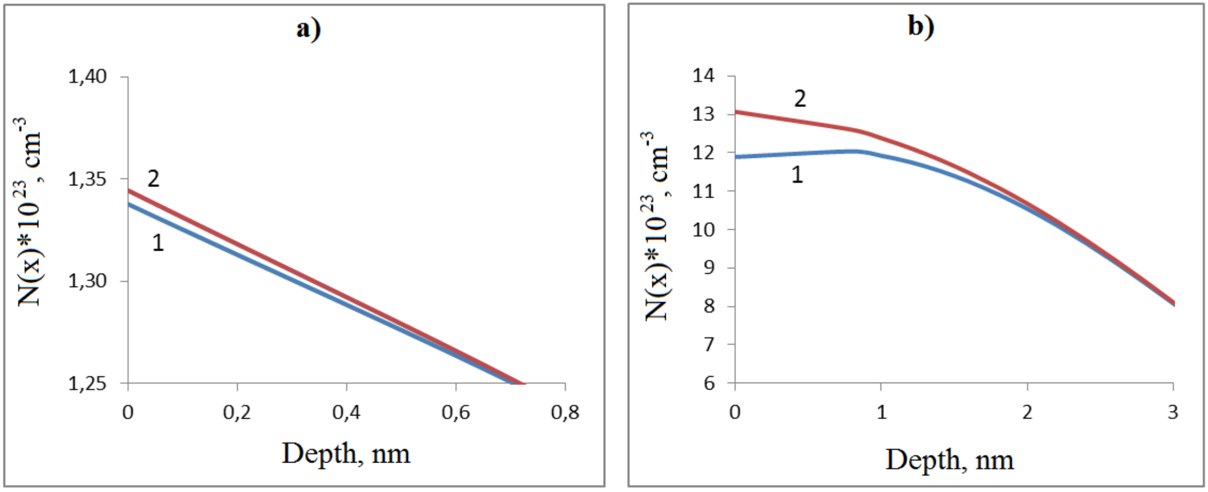

Fig. 4. Calculated distribution profiles of H (a) and O (b) atoms in the implanted Ti by 1 keV OH$^+$ for implantation doses:8.0*$10^{16}$ ions/cm$^2$ – curve 1 and 1.0*$10^{17}$ ions/cm$^2$ – curve 2

## 2.3. Comparison with experimental data

The experimental distribution profiles of H across 0.6 μm thick Ti film measured by glow discharge optical spectroscopy technique (GDOES, SPECTRUMA ANALYTIK GMBH) is shown in Fig. 5. We can see that the concentration of H atoms in Ti film depends on the irradiation dose and intensity of irradiation. In Fig. 5 is shown hydrogen penetration depth when irradiation intensity is low (less than 1 mA/cm$^2$) and high (10 mA/cm$^2$). Respectively in this different irradiation intensities areas we have low and high dose water molecular ion implantation (exact numerical dose values were not estimated). More experimental details are presented in publication [6].

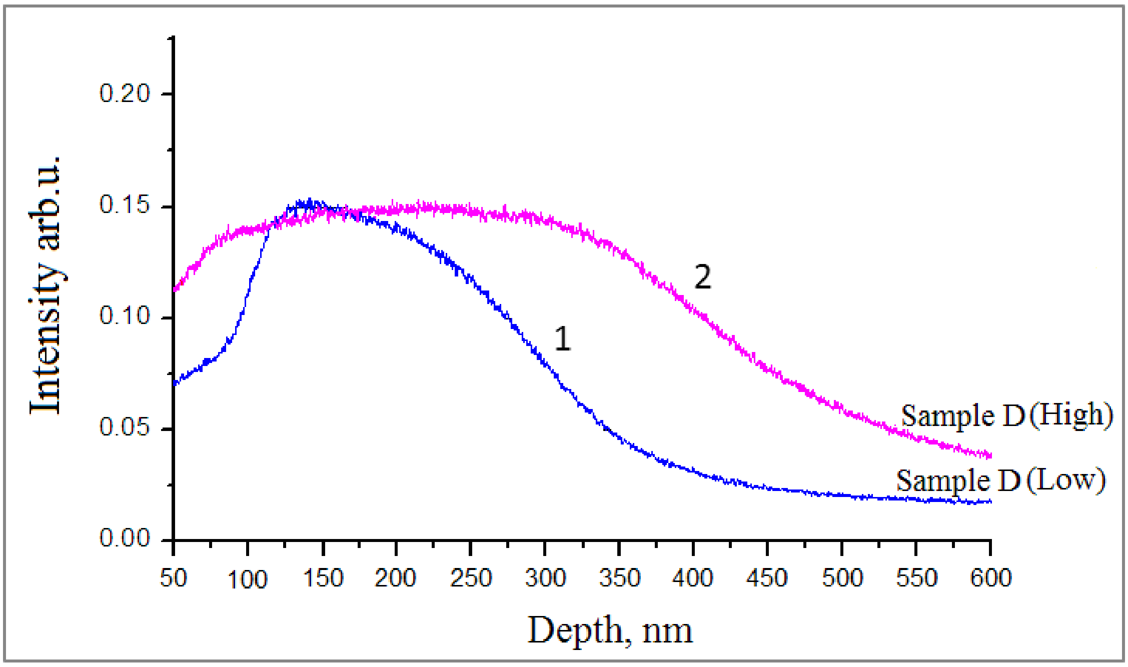

Fig. 5. Experimental distribution profiles of H atoms in Ti film after water plasma treatment under low (1) and high (2) intensities areas

It is seen that calculated distribution profiles of H atoms in Ti (Fig. 3 and Fig. 4) are in qualitative, however, not in quantitative agreement with the experimental ones presented in Fig. 5. The discrepancies in penetration depth of H may be explained assuming that process of hydrogen diffusion is considered.

## 3. CONCLUSIONS

In this study, the model of water molecular ion implantation was used to study the hydrogen separation from water molecules. Also, the model was developed to simulate the behavior of implanted hydrogen and oxygen in Ti. It enables to calculate the distribution profiles of broken hydrogen and oxygen atoms for low and high-dose water molecular ion implantation. Based on this study, the following conclusions can be drawn: (1) the distribution profiles of separated hydrogen and oxygen atoms despite of differences in their masses are overlapping in the near-surface region after molecular implantation of $H_2O+$ and OH+ ions; (2) the modeling results are in qualitative agreement with experimental ones. For quantitative agreement, the diffusion of hydrogen has to be considered. The scarcity of experimental results limits the scope of investigation. In Fig. 3 is only the implantation, in fig. 4 and includes erosion. The values obtained for different ion content does not match, which interferes in the material. Comparing graphs 3 and 4 received mismatch. Fig. 4 supplied implantation, including the erosion coefficient, which resulted in discrepancies. Whereas oxygen erosion coefficient are higher than hydrogen and therefore its variation increased.

## 4. ACKNOWLEDGEMENTS

This research was funded by a grant (Nr. ATE-02/2010) from the Research Council of Lithuania. The authors express theirs appreciation to prof. L. L. Pranevicius and graduate student M. Urbonavicius for the experimental data and useful discussions. Student A.Švaikovsky was supported by the special grant of the Research Council for students.

## REFERENCES

1. ROSEN M. A. Advances in hydrogen production by thermochemical water decomposition: A review. *Energy*, 2010, Vol. 35, No. 2, p. 1068–1076.
2. PETITPAS G, ROLLIER J.-D., DARMON A, GONZALEZ-AGUILAR J, METKEMEIJER R, FULCHERI L. A comparative study of non-thermal plasma assisted reforming technologies. *International Journal of Hydrogen Energy*, 2007, Vol. 32, No. 14, p. 2848–2867.
3. SERRANO E, RUS G, GARCÍA-MARTÍNEZ J. Nanotechnology for sustainable energy. *Renewable and Sustainable Energy Reviews*, 2009; Vol. 13, No. 9, p. 2373–2384.
4. ZIEGLER J.F., BIERSACK J.P. and LITTMARK U. The Stopping and Range of Ions in Solids, Pergamon Press, New York, 1985, Bibliography: p. 308–315.
5. GAMBINI M, MANNO M, VELLINI M. Numerical analysis and performance assessment of metal hydride-based hydrogen storage systems. *International Journal of Hydrogen Energy*, 2008; Vol. 33, No. 21, p. 6178–6187.
6. PRANEVIČIUS L., URBONAVIČIUS M. Experimental study of hydrogenation of Ti films using magnetron water vapour plasma. Submitted for publication in *Conference of Young Scientists on Energy Issues*, 2011.

# ECONOMICAL AND ECOLOGICAL ASPECTS OF BIOENERGY PROJECTS IN UKRAINE

**A.V. Epik, S.M. Chaplygin, E.N. Oleynik**
*Institute of Engineering Thermophysics of National Academy of Sciences*
*Zhelyabova str. 2a, P.O. Box 66, 03067, Kyiv-67 – Ukraine*
*Phone : +3 044 453 28 56; +3 044 456 94 62*
*Email: epik@biomass.kiev.ua*

ABSTRACT

The work is dedicated to the investigation of the most applicable biomass-to-energy technologies for heat and power production under Ukrainian circumstances. Each technology is ranked by the separately determined applicability factors. Total potential of renewable energy sources over Ukraine is used with aim of limitation and proper distribution of the individual projects implementation under local conditions. The work includes a complex analysis of factors for each biomass utilization technology. The principal ranking factors are: technological availability (commercialization rate), access to the state support, legislative and economical incentives, legislative peculiarities (namely, for “green” tariff receiving, sector of implementation, etc.), greenhouse gases emission reductions input, quantity of already realized projects, positive socio-economic factors. Performed economical analysis result in the determination of number of most priority directions of biomass technologies implementation for Ukrainian energy sector. The brief analysis of peculiarities of biomass as a fuel has been performed with aim to find out key barriers and bottlenecks on the way of biomass utilization in already operated equipment. The electricity production from biomass has been briefly overviewed with the conclusion of total feasibility of electricity production from raw biomass. As a result the recommendations for acceleration of bioenergy projects realization has been proposed in form of political moves and private initiatives.

Keywords: bioenergy technologies, biomass boilers, ranking, applicability factors, commercialization rate.

## 1. INTRODUCTION

The reduction of natural gas consumption, development of energy saving and solving of the ecological problems are the major priority tasks, which Ukraine encounters nowadays. The efficiency of energy utilization in the country is highly dependent to the degree of diversity of used energy resources. The main energy resource traditionally used in Ukraine is natural gas (NG): the share of its utilization in the total balance of primary energy resources is 40% (Table 1). In addition, Ukraine’s internal natural gas production supplies own needs of the country only approximately on 35% and another 65% are imported, mainly from Russia. The input of renewable energy sources (RES) is on the level of 2.7% with biomass share of 0.5% from total primary energy consumption of Ukraine. Such situation creates huge energy dependence and lowers energy security of Ukraine.

From the other side the price of the imported natural gas is constantly growing. This price increased five times in 5 years: from 60 USD in 2005 to 305 USD in the first quarter of 2010 [1]. The dramatic increase of natural gas price from one side and its sufficiently large share in the energy consumption balance of Ukraine on the other side are the driving force on the way of renewable energy sources implementation.

Meanwhile Ukraine has a sufficient potential of renewable energy sources, mainly biomass. The total biomass potential in Ukraine is estimated on the level of 27–35 mio tce (tones of coal equivalent) depending on annual crop yield [2], covering approximately 15% of total primary energy consumption of the country in 2009. Because the major part of Ukrainian territory is located in the forest-steppe and steppe zones (average percentage of forest land is 14.7% [3]) and traditionally Ukraine is agriculturally developed country, the principal source of biomass comprises farm waste and in future energy cultures. That is why current work focuses mainly on the consideration and comparison of biomass energy utilization technologies.

Table 1. Structure of energy consumption in Ukraine and other world in 2009

| Fuel Type | World | Ukraine | EU-15 Countries | USA |
|---|---|---|---|---|
| Natural gas | 21% | 39.5% | 22% | 24% |
| Oil | 35% | 11.8% | 41% | 28% |
| Coal | 23% | 28% | 16% | 23% |
| Uranium | 7% | 18% | 15% | 8% |
| RES | 14% | 2.7% | 6% | 7% |

## 2. PECULIARITIES OF BIOMASS UTILIZATION

Biomass is a renewable and $CO_2$-neutral fuel, which has no greenhouse effect and utilization of which improves the ecological situation in comparison with fossil fuels combustion. One of the advantages of biomass is its relative cheapness in comparison with other fossil fuels, namely natural gas. To illustrate this, let’s calculate the cost of the energy unit for each type of fuel (UAH/GJ) using standard values of net calorific value and cost of biofuel established between producers and consumers within Ukraine. Table 2 presents the results of such analysis.

Table 2. Cost comparison of solid biomass and natural gas

| Fuel type | Price | Lower heat value | Cost of energy in the fuel | The ratio of energy cost in NG to the energy cost from other fuels | | | |
|---|---|---|---|---|---|---|---|
| | UAH/t | MJ/kg | UAH/GJ* | NG for industry and government-financed organizations | | NG for housing and communal services sector | |
| | | | | before 1/08/10 | to 1/08/10 | before 1/08/10 | to 1/08/10 |
| Wood wastes | 50 | 11 | 4.5 | 15.2 | 16.5 | 5.5 | 8.2 |
| Fuel wood (chip) | 250 | 11 | 22.7 | 3.0 | 3.3 | 1.1 | 1.6 |
| Wood pellets | 800 | 17 | 47.1 | 1.5 | 1.6 | 0.5 | 0.8 |
| Wood briquettes | 700 | 15 | 46.7 | 1.5 | 1.6 | 0.5 | 0.8 |
| Straw in bales | 300 | 13 | 23.1 | 3.0 | 3.2 | 1.1 | 1.6 |

* - 1 UAH = 0.1 €

The structure of the table is the following: the left part of the table represents fuel types ranged by the cost of energy for each type. The right part of the table illustrates the ratio of energy cost due to natural gas combustion and biofuels utilization ranging them by the cost of natural gas for different options. In Ukrainian conditions natural gas price varies a lot depending on the sector of its utilization. For example, the price of natural gas for housing and communal services before 1st of August 2010 was on the level of 900 UAH/1000 $m^3$ and for the industry and state-financed organizations – more than 2400 UAH/1000 $m^3$. The columns “before” and “to” 1st of August 2010 mean the increasing of natural gas price in Ukraine on 50% for housing and communal services after mentioned date. From the practical point of view the ratio between natural gas and biofuel prices in energy equivalents should be more than 2.5 to make the option of biofuel utilization economically attractive and applicable. Such figure corresponds to the maximal commercialization rate (which equals 1.0 or 100%) and payback period of the technology due to natural gas economy of less than 4 years. It could be seen, that before the increase of natural gas cost the utilization of own wood wastes, fuel wood and baled straw only in the industry and governmental sector was economically feasible. As for housing and communal services sector even after 50 % increasing of natural gas price the only feasible option of biomass waste utilization is use of wood wastes with price of fuel 5 Euro/t. Such price of fuel is impossible in the market conditions. So the only case when it could be attractive is the case of the own waste utilization for energy production (with the free price of fuel) or industrial waste utilization. All other options are not economically attractive and their commercialization may be expected after natural gas price increase by more than two times in comparison with current level. It is interesting to mention, that such analysis clearly defines the main reason why pellets and briquettes are exported from Ukraine to EU – it is more economically feasible option in comparison with utilization inside Ukraine.

It should be mentioned, that here we do not include the impact of biomass logistics and organizational process, stockpiling, etc., which will additionally increase the energy cost of biomass. So one can conclude, that biomass should be utilized nearly the places of harvesting and stockpiling. According to the expert estimation the maximal practically applied distance of raw biomass transportation due to its low energy density should not exceed 50–100 km [4].

The most applicable technologies for Ukrainian conditions being identified in this section will be considered in details in the next sections.

## 3. ECONOMIC INDEXES OF BIOMASS UTILIZATION IN HEATING BOILERS

The previous section summarized, that implementation of straw- and wood-fired boilers is most feasible alternative of biomass utilization under current Ukrainian conditions and fossil fuel pricing practically for all heat and power objects. The next section will provide brief overview of the number of most feasible technologies of biomass utilization for heating.

### 3.1. Wood-fired boilers for domestic heating

The first option is domestic heating boiler working on fuel wood. The principal characteristics of the boiler are presented in the Table 3. It is assumed, that the average capacity needed for thermal energy supply per one household is 10 kW. Recalculation on the energy equivalent using low heat value shows fuel consumption per year and consequently the volume of natural gas substitution. Bearing in mind current natural gas price for population of 1098 UAH/1000$m^3$, the effect of the technology implementation only due to natural gas economy is estimated on the level of 3200 UAH annually. However, one-time capital costs for the installation of wood-fired boiler with mentioned capacity assumed on the level of commercial value (6200 UAH) are relatively high for the typical resident of Ukraine.

In addition, fuel expenses and maintenance costs according to the real commercial values of wood fuel producers in Ukraine are estimated on the level of 2100 UAH/year. Thus, the payback period of such technology only due to the natural gas substitution is 5.6 years. Obviously, only limited share of residents in Ukraine could allow themselves such technology, bringing us to the conclusion that state support in the form of first loan or provision of tax privileges to the population for implementation of such activity is crucial. Another strategic action for the enhancing of commercialization of such projects may be the state programme on promotion of domestic straw boiler implementation or increasing of natural gas price for population by 50 % (through cancellation of subsidies for natural gas purchase for population) as well as combination of these measures.

Table 3. Economic indexes of fuel wood application for domestic heating (with gas substitution)

| Name | Measure unit | Value |
|---|---|---|
| Boiler capacity | kW | 10 |
| Lower heat value | MJ/kg | 14 |
| Fuel consumption | tons/year | 8.6 |
| equivalent gas consumption | th.m$^3$/year | 3.0 |
| Fuel wood price* | UAH/t | 250 |
| The price of gas for population | UAH/1000m$^3$ | 1 098 |
| Capital investments | th.UAH | 6.2 |
| Fuel expenses (fuel wood) | th.UAH/year | 2.1 |
| gas for population | th.UAH/year | 3.2 |
| Cost cutout on the fuel purchase | th.UAH/year | 1.1 |
| Payback period | years | 5.6 |

* – The fuel wood price does not include expenses of preparing the wood for combustion

### 3.2. Baled straw-fired boilers for farms

The second option is heating boiler with thermal capacity under 1 MW$_{th}$ working on the baled straw for medium households and farms. The principal characteristics of this alternative are presented in Table 4. The estimation has been done for two capacities: 250 kW and 860 kW. Both prototypes with such capacities have been successfully implemented in Ukraine and are operational defining the choice of capacity for analyzed options. All input values used in calculation were based on the real market conditions from practice. This technology may be introduced to: budget funded organizations, industry and housing and communal services. The sector of implementation has a dramatic influence on the economical indexes and payback periods for considered technologies because of the huge range of natural gas price variation. For example, if straw-fired boiler with heat capacity 250 kW is implemented in the housing and communal services sector, the payback period will be 6.7 years and for the budget-financed organizations sector – 1.7 years. This data totally correlates with the natural gas prices for these two sectors in Ukraine: 1309 UAH/1000m$^3$ for housing and communal services and 2624 UAH/1000m$^3$ for industry and budget organizations. Due to the decrease of capital costs per kW with the increasing of thermal capacity of equipment the payback period for a 860 kW straw boiler (if applied for budget-financed objects' heat supply) is 1 heating season (0.9 years) being the most applicable commercial technology of solid biomass utilization under current Ukrainian conditions. According to the estimations of Institute of Engineering Thermophysics of NASU [5] the market volume of considered boiler types (with capacity range of 0.1–1 $MW_{th}$) is quantified in more than 10 000 units with average total installed capacity of 2 $GW_{th}$.

Table 4. Economic indexes of baled straw utilization in heating boilers (with gas substitution)

| Name | Measure unit | Value | |
|---|---|---|---|
| Boiler Capacity | kW | 250 | 860 |
| Lower heat value | MJ/kg | 13 | |
| Fuel consumption (straw) | tons/year | 275 | 947 |
| equivalent gas consumption | th.$m^3$/year | 98 | 336 |
| Straw price | UAH/ton | 300 | |
| Gas price for housing and communal services sector | UAH/th.$m^3$ | 1 309 | |
| Gas price for industry and government-financed organizations | UAH/th.$m^3$ | 2 624 | |
| Capital investments (facility + project + installation)* | th.UAH | 300 | 535 |
| Fuel expenses (straw) | th.UAH/year | 83 | 284 |
| Gas for housing and communal services sector | th.UAH/year | 128 | 439 |
| Gas for industry and government-financed organizations | th.UAH/year | 256 | 880 |
| Cost cutout on the purchase of fuel, with gas substitution | | | |
| housing and communal services sector | th.UAH/year | 45 | 155 |
| government-financed organizations | th.UAH/year | 173 | 596 |
| Payback period | | | |
| housing and communal services sector | years | 6.7 | 3.4 |
| government-financed organizations | years | 1.7 | 0.9 |

* – Capital expenditures do not include the cost of building fuel storage, purchase of vehicles, cost of maintenance and improvement of the territory

## 4. BIOMASS UTILIZATION FOR ELECTRICITY PRODUCTION

Previously we have considered technologies of biomass utilization for heating. The principal source of economical feasibility of such projects was natural gas substitution with the straight correlation between natural gas price and payback period. In spite of the high economical feasibility and commercialization potential of such technologies, another alternative of biomass utilization has been appeared since the “green” feed-in tariff law adoption in Ukraine on the 1st of April 2009. This alternative is electricity production from renewable and alternative energy sources including biomass. The production of electricity from biomass may be even more attractive from financial point of view due to artificial increasing of tariff on electricity from RES. Therefore in current work we can not pass over this problem and will present the typical economical studies for the most appropriate and practically sound technologies of biomass-to-electricity utilization.

The fixed minimal “green” tariff for installations, which burn biomass, is 13.4 Eurocent/kWh$_{el}$. Despite the imperfection and the number of mistakes and misapplications of the law of “green” tariff it establishes one of the highest tariffs on renewable electricity in Europe. For example, in Germany one of the leading EU states in bioenergy utilization and development “green” tariff for biomass electricity is established on the level of 7.0–14.5 Eurocents/kWh$_{el}$. The general tariff for industrial consumers in Ukraine to 01/01/2011 was 7.2 Eurocents/kWh$_{el}$. Thus, the “green” tariff is two times higher in comparison with standard value of electricity tariff in Ukraine. Using these values as a basis we perform the analysis of the technologies of electricity production from biomass.

Considered options are: full or partial reconstruction of existing fossil fuel CHP to the biomass CHP as well as construction of new CHP on biomass. First option is especially important in Ukrainian circumstances due to overtime operation of existing CHP and outdated technical equipment used. The brief economical analysis is presented in the Table 5.

Table 5. Feasibility study of CHP reconstruction/construction with gas substitution

| Name | Measure units | Reconstruction of the existing CHP | | New CHP on biomass |
|---|---|---|---|---|
| Electric capacity of generator | MW | 12.0 | | |
| Thermal capacity | MW | 40 | 0 | 40 |
| Lower heat value | MJ/kg | 12 | | |
| Fuel consumption (chips/ milled straw) | tons/year | 230 040 | 118 973 | 230 040 |
| equivalent gas substitution | th.m$^3$/year | 72 870 | 37 687 | 72 870 |
| The amount of the produced “green” electricity | (MWh)/year | 77 760 | | |
| The amount of purchased electricity for own needs | (MWh)/year | 13 997 | 13 997 | 13 997 |
| Reducing emissions $CO_2$-eqv. | tons $CO_2$-eq./year | 133 198 | 62 833 | 133 198 |
| The electricity sales “green” tariff, without VAT | UAH/(MWh) | 1 344.6 | | |
| The price of purchasing electricity from the network, without VAT | UAH/(MWh) | 679.0 | | |
| Fuel cost (chips/ milled straw) | UAH/t | 250 | | |
| The tariff of thermal energy sales | UAH/Gcal | 200 | | |
| Capital investments* | th.UAH | 120 000 | | 300 000 |
| specific capital investments | €/kW$_{el}$ | 1 000 | | 2 500 |
| Operating costs | th.UAH/year | 67 375 | 39 608 | 67 375 |
| Income** | th.UAH/year | 149 130 | 104 556 | 149 130 |
| Simple payback period | years | 1.5 | 1.8 | 3.7 |

* – Capital investment for renovation involves the biomass boiler installation, fuel storage construction, construction of systems for fuel supply, ash removal, flue gas cleaning.

** – Profits from the Emission Reduction Units (ERUs) sales are not taken into account.

The estimation is performed for the capacity of 12 $MW_{el}$. The first option as more practically applied is divided into two sub-options: reconstruction in CHP regime and Thermal power plant working in the condensing regime, which is reflected in the figures of “Heat capacity” (second line of Table 5). Obviously the CHP regime is more feasible due to additional heat sales and natural gas economy, but the influence is not crucial, because the cumulative income from electricity sales by “green” tariff overlap the revenues from heat component. It should be mentioned that CHP and TPP regimes has different electrical efficiency because of the technological peculiarities of equipment performance (for example, due to different turbine types: condensing for TPP and back-pressure turbine for CHP), but here for simplification this impact was not taken into account. It can be seen, that specific capital investments for CHP reconstruction are on the level of 1000 Euro/$kW_{el}$. The simple payback period for such assumptions is 1.8 years for TPP and 1.5 years for CHP.

New biomass CHP as the alternative to the reconstruction is considered as less practically applied option, but still feasible and realistic. It is expected, that it will be implemented after CHP reconstruction for biomass utilization will start in the industry sector. The estimation was done on the basis of optimistic value of 2500 Euro/$kW_{el}$ specific capital investments. Even in this case the payback period is 3.7 years. The real cost of biomass CHP construction in current conditions may two times exceed mentioned value with the appropriate impact on the payback and investments return. The emission reduction sales if accounted for, may somewhat improve the economical indexes of both measures but still the share of additional investments from Kyoto Protocol quotas selling is low for such types of projects. Hereby, it could be summarized that three analyzed alternatives of biomass-to-electricity conversion have all necessary conditions for implementation in current circumstances.

## 5. CONCLUSIONS

Ukraine has a good background and sufficient potential for the dynamic bioenergy sector development. The main drivers of this process are rapid growth of fossil fuels prices and availability of large biomass potential for energy utilization. The legal part of incentives also is not empty: the law of “green” tariff creates a plenty of possibilities for the biomass-to-electricity utilization.

Performed analysis of alternatives of biomass-to-energy utilization shows, that in current Ukrainian conditions:

- biomass utilization for heating is feasible in the budget and industrial economical sectors due to higher natural gas price for these sectors in comparison with housing and communal services sector and population; for population the usage of small domestic heating boilers is recommended;
- electricity production from biomass is feasible for all alternatives, even for construction of new CHP; the payback period of new biomass CHP is 3.7 years due to high long-term established “green” tariff; in case of cheaper measure “existing CHP reconstruction” the priority sectors of biomass-to-electricity utilization are industry and energy sector where the most outdated equipment with necessity of urgent modernization is operated.

According to the results of the economical analysis the following political measures for acceleration of bioenergy utilization could be proposed: state subsidies (compensations) for enterprises which plan to use biomass as a fuel on the level of 20% from total capital cost; tax incentives, for example, releasing from VAT or releasing from income tax for all producers and consumers of bioenergy equipment; providing of simplified loan procedure for population which implements bioenergy projects; adoption of the state target programme on bioenergy development with the strict indexes of bioenergy input in total energy balance, at least for 5 years; stopping of the artificial reduction of the natural gas prices for population and housing and communal services sector by cancellation of subsidies for the natural gas purchase. The wise combination of all mentioned measures may provide fast, environmentally friendly and sustainable development of bioenergy sector of Ukraine in long-term future.

## REFERENCES

1. *Statistical yearbook of Ukraine for 2010.* Under edition of Osaulenko O.G.: State Committee of Statistics of Ukraine, 2011. 569 p.
2. *Agriculture in Ukraine*. *Statistical yearbook for 2009*. Under edition of Ostapchuk Ju. M.: State Committee of Statistics of Ukraine, 2010. 370 p.
3. PRISTAYA O. Forest policy for the wood energy development. Equipment and enginery for professionals, 2010, No.3/2010, p. 52–54.
4. MARTIN VIS. Harmonization of biomass resource assessments. Volume I: *Best practices and methods handbook*. Report on WP5 of the EC FP7 Project “Biomass Energy Europe”, 2010. BTG Biomass Technology Group B.V., the Netherlands.
5. GELETUKHA G., ZHELYEZNA T.A. Current status and perspectives of bioenergy development in Ukraine. Part 2. Industrial Heat Engineering, 2010, Vol. 32, No. 4, p. 94–100.

CYSENI 2011, May 26–27, Kaunas, Lithuania
ISSN 1822-7554, www.cyseni.com

# CONTINUOUS BIOHYDROGEN PRODUCTION FROM SWEET POTATO FERMENTATION USING MIXED ANAEROBIC BACTERIA

**C.H. Lay, C.W. Lee, Gopalakrishnan K., C.Y. Lin**
*Department of Environmental Engineering and Science*
*Green Energy Development Center*
*Feng Chia University, Taiwan*
*Email: cylin@fcu.edu.tw*

**J.J. Chang**
*Genomics Research Center*
*Academia Sinica*, Taiwan

**S.Y. Kuo**
*Master Program of Green Energy Science and Technology*
*Feng Chia University, Taiwan*

**C.C. Chen**
*Department of Landscape Architecture*
*Chungchou Institute of Technology, Taiwan*

ABSTRACT

Global environmental pollution problems are increasing at an alarming rate due to the use of fossil fuels as a primary energy source. Hydrogen is an ideal clean energy source, produces only water by-product during its combustion. Biohydrogen can be produced by anaerobic fermentation of organic feedstocks. At present the biomass from crops like sweet sorghum, potato, sugarcane, soybean and palm oil have been used as raw materials for biohydrogen production. Sweet potato could be considered as a suitable substrate for producing biohydrogen and bioethanol due to its high starch content (sugar content is more than 35%), cold-resistant, high growth rate and suitable to grow even in poor soil. In order to maintain the crop price, about 220,000 hectares of farm land which is not used for any purposes has been allotted aside in Taiwan could be used to grow sweet potato for bioenergy production.

A CSTR (continuously-stirred tank reactor) lab-scale hydrogen fermenter (working volume, 1.0 L) was operated at hydraulic retention times (HRT) of 1-12 h and an influent concentration of 15 g/L. A pH decreasing strategy was used to optimize the pH for hydrogen production. The suitable operation pH 6.0 was obtained with higher hydrogen production rate (HPR) of 20 mmol $H_2$/L/d during the start-up period. Shortening HRT was a good strategy for improving hydrogen production performance. Peak HPR 930 mmol $H_2$/L/d was obtained at HRT 2 h. Ethanol and acetate were the main soluble metabolic products (SMPs) with low concentration (690 mg COD/L) during start-up period. However, the metabolic pathway shifted to acetate and butyrate fermentation with an increase in the SMP concentration of 13.2 - 28.5 g COD/L while the HRT was shortened to 8-2 h. The microbial diversity was investigated by the molecular techniques of genomic DNA fingerprint analysis of 16S-rDNA. Microorganisms in the fermentor included *Acetobacter indonesiensts*, *Actinomyces* sp., *Bifidobacterium* sp., *Clostridium vincentii*, *Pseudomonas* sp., *Serratia* sp., uncultured *Clostridium* sp., *Bacillus* sp., *Endophyte bacterium*, *Enterobacter aerogenes* and *Erwinia rhapontici*.

Keywords: sweet potato, biohydrogen production, anaerobic fermentation.

## 1. INTRODUCTION

Energy is vital to global prosperity. Nowadays, global energy supply is mostly dependent on fossil fuels, which eventually lead to foreseeable depletion due to limited sources [1, 2]. Now we have faced significant energy challenges. The concept of sustainable development is evolved for a livable future where human needs are met while keeping the balance with nature. Driving the global energy system into a sustainable path is progressively becoming a major concern and policy objective. The world's energy requirements are being fulfilled by fossil fuels, which serve as a primary energy source. Fossil fuel has delivered energy and convenience, in our homes, for transportation and industry. However the overwhelming scientific evidence is that the unfettered use of fossils is causing the world's climate to change, with potential disastrous effects. In recent years a great deal of attention is being paid to the utilization of hydrogen as alternative and ecofriendly fuel throughout the world. Hydrogen is a promising energy alternative because of its clean, efficient, renewable and non-polluting characteristics. Biohydrogen is attractive because of its energy saving production process as compared with chemical processes.

Generally CSTR (continuously-stirred tank reactor) fermentation system is used for continuous hydrogen production due to their easy operation. This system's complete mixing operation allows intimate contact between the substrate and micoflora, as well as effective pH and temperature control. The substrates used for fermentative hydrogen production are generally rich in carbohydrates like glucose [3, 4], sucrose [5, 6] and starch [7, 8].

Many biomasses like agricultural by-products or crops (corn, rice, potato, sweet potato etc.) are rich in starch which is being converted biologically into hydrogen using pure cultures [8]. Sweet potato is rich in carbohydrates which are readily converted anaerobically into hydrogen/ethanol using pure cultures. Moreover, sweet potato contains indigenous bacteria which might convert the sweet potato component into valuable bioenergy.

Using mixed cultures in anaerobic fermentative hydrogen process has the advantage of being simpler to operate and easier to control [9]. Mixed cultures can be obtained from a large variety of sources, including soil. The soil can simply be thermally treated to selectively target for hydrogen-producing bacteria. Mixed cultures are ideal for bio$H_2$ production from wastewaters for a few reasons. The feed source intended for use in mixed cultures can be very complex, as the mixed microbial community have the ability to adapt to a variety of carbon sources and nutrients from a domestic or industrial waste stream for bio$H_2$ production.

Based on the above considerations, this work aimed at investigating the hydrogen production from sweet potato in CSTR by using mixed anaerobic microflora.

## 2. MATERIALS AND METHODS

### 2.1. Seed sludge and substrate

The seed sludge was obtained from a municipal sewage treatment plant in central Taiwan. The collected sludge was screened with a No. 8 mesh (dia. 2.35 mm) and heated at 100°C for 45 minutes (to inhibit hydrogen consuming methanogen bioactivity). The pH, volatile suspended solids (VSS, to express the biomass concentrations), total chemical oxygen demand (COD) and total carbohydrate concentrations of the seed sludge were 7.32, 9.1 g/L, 36.8 g COD/L, and 0.12 g/L, respectively.

The tested sweet potato was bought from a supermarket in central Taiwan. The sweet potato was washed by tap water and sliced in to a particle size of about 5 cm then mixed with DI water and stirred to make the sweet potato solution of 150 g/L. The total COD and sugar concentrations in the solution were 54.9 g COD/L and 26.2 g/L, respectively.

### 2.2. Operation strategy and hydrogen production in the fermentor

A CSTR hydrogen fermentor (1 L) (Fig. 1) with a working volume of 0.9 L was operated at a temperature of $35^{o}C$ and hydraulic retention times (HRTs) of 1–24 h. The fermentor was mixed at 125 rpm with a flow level controller. A pH of 6.7 was maintained using a pH controller and 6 N NaOH for starting-up the fermentor. The biogas amount produced was measured using a gas meter (Ritter, Germany, TG 1/5). When a steady-state condition reached and the desired data were obtained the HRT was reduced. Steady-state conditions reached when the product concentrations such as hydrogen gas content and biogas production were constant.

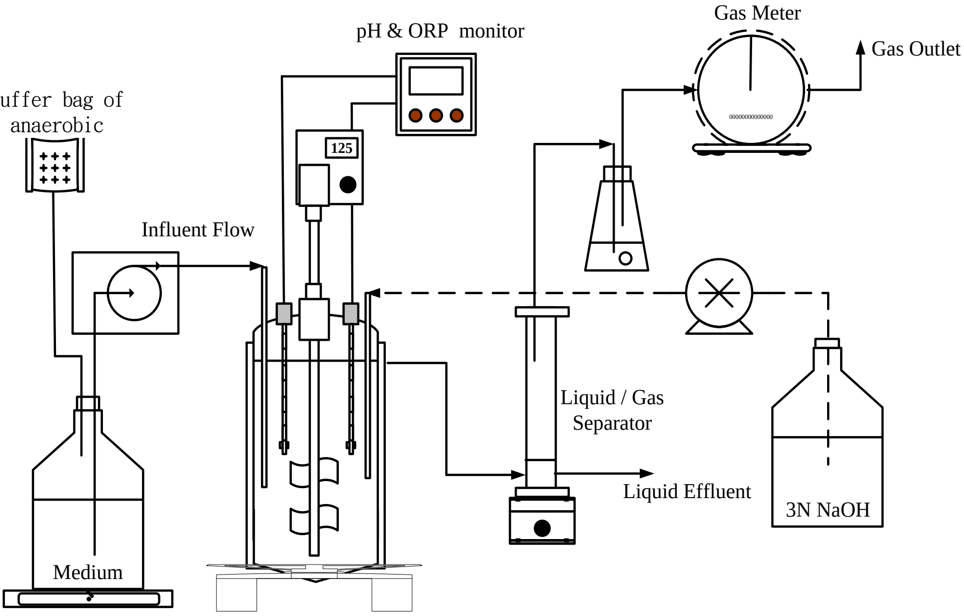

Fig. 1. A Schematic diagram of the CSTR for continuous biohydrogen production

## 2.3. 16S rDNA gene based bacteria community structure analysis

Total genomic DNA samples were derived from the system and purified using the Blood & Tissue Genomic DNA Extraction Miniprep System (Viogene, Taiwan) following the manufacturer’s instructions. For analysis of bacterial diversity, primer pair EUB968F (5’-CGC CCG GGG CGC GCC CCG GGC GGG GCG GGG GCA CGG GGG GAA CGC GAA GAA CCT TAC-3’) and UNIV1392R (5’-ACG GGC GGT GTG TRC-3’) were used to amplify partial 16S rRNA gene to create a DNA fragment suitable for DGGE analysis [10]. PCR (polymerase chain reaction) mixtures (50 μL) contained each 200 μM deoxynucleoside triphosphate, 1.5 mM $MgCl_2$, 0.4 μM each primer sets, 1.25 U of Taq DNA polymerase (Promega, USA). The amplification was performed with an automatic thermocycler iCyclerTM (Bio-Rad, U.S.A.), and consisted of a DNA denaturing step at 95°C for 5 min, followed by 35 cycles of denaturation at 94°C for 1 min, annealing at 55°C for 1 min, extension at 72°C for 1 min, and a final extension step at 72°C for 3 min. The PCR-amplified extracted rDNA fragments were assessed using DGGE by using a DCodeTM Universal Mutation Detection System (BioRad, U.S.A.). The 6% (w/v) acrylamide solution was used to cast a gel with denaturant gradients ranging from 35 to 65%. Electrophoresis was conducted in a 1 × TAE (Tris/acetic acid/EDTA) buffer solution at 100 V and 60°C for 16 h. The gels were stained for 10 min with ethidium bromide and visualized with UV radiation. The number of operational taxonomic units in each sample was defined as the number of DGGE bands. The PCR products were extracted and purified from the gel bands by using the Centrilutor microelectroeluter system (Millipore, Rockville, MD, USA). After re-amplification under the reaction conditions described above, the resulting PCR products were cloned for sequencing. And the searches were performed in NCBI web site using BLAST to determine each band’s similar species.

### 2.4. Monitoring and analyses

During the hydrogen production experiments, the monitoring parameters were pH, ORP (oxidation- reduction potential), alkalinity, volatile fatty acid (VFA) distribution and gas production. The hydrogen production efficiency was evaluated using the hydrogen content in the biogas, hydrogen yield (the ability of converting glucose into hydrogen, HY), hydrogen production rate (the rate of hydrogen production from the reactor, HPR) and specific HPR (the hydrogen production ability of the biomass in the reactor, SHPR).

The Standard Methods [11] analytical procedures were used to determine the liquid contents. Ethanol and VFA concentrations were analyzed with a gas chromatograph having a flame ionization detector (glass column, 145$^{o}$C; injection temperature, 175$^{o}$C; carrier gas, $N_2$; packing, FON 10%). Gas composition was analyzed with a gas chromatogra having a thermal conductivity detector (column, 55$^{o}$C; injection temperature, 90$^{o}$C; carrier gas, Argon; packing, Porapak Q, mesh 80/100). Anthrone-sufuric acid method was used to measure the hexose concentration [12].

## 3. RESULTS AND DISCUSSION

### 3.1. Start-up strategy and fermentor performance

pH is an important environmental factor in anaerobic hydrogen fermentation [13]. Our previous study showed that the suitable pHs for hydrogen production ranged from 4.5 to 6.7 [14]. During the start-up period, the operation pH was controlled at 6.7 with low and unstable hydrogen production. Therefore, a pH decrease strategy was used to optimize the pH. Fig. 2 illustrates the pH adjustment during 27 days cultivation. Low hydrogen production rate (HPR, ca 5 mmol $H_2$/L/d) was obtained at pH 6.7 (Tabe 1).

Table 1. Fermentation performance under steady-state conditions at each HRT

| **HRT (h)** | **Start-up** | **12** | **8** | **6** | **4** | **2** | **1** |
|---|---|---|---|---|---|---|---|
| **OLR (g sweet potato/L/d)** | | **267** | **400.5** | **534** | **801** | **1602** | **3204** |
| $H_2$ content (%) | 13.2±10.5 | 13.5±6.7 | 35.1±7.9 | 32.8±6.3 | 40.2±11.8 | 29.2±12.5 | 8.8±7.7 |
| HPR (mmol $H_2$/L/d) | - | 5±1 | 60±9 | 135±18 | 238±12 | 929±35 | 328±26 |
| SHPR (mmol $H_2$/g VSS/d) | - | 0.8±0.2 | 8.2±2.0 | 25.2±1.1 | 31.6±1.8 | 72.2±2.5 | 11.6±0.1 |
| HY (mmol $H_2$/mol hexose) | - | 40±1 | 291±10 | 505±6 | 604±10 | 1451±115 | 3516±148 |
| VSS (g/L) | 23.4±15 | 6.84±6 | 7.33±2 | 5.36±2 | 7.54±4 | 12.9±3.8 | 20.3±5 |
| ORP (mV) | -519±58 | -445±49 | -446±35 | -444±36 | -439±47 | -389±83 | -208±137 |
| Alkalinity (mg/L as $CaCO_3$) | 5.1±1.8 | 11.0±2.6 | 10.2±2.4 | 9.7±1.2 | 9.0±1.0 | 5.9±0.9 | 3.1±4.8 |
| Hexose degradation (%) | - | 81.9±15.0 | 82.7±10.0 | 80.3±9.0 | 78.9±18.0 | 71.4±0.9 | 4.7±0.1 |
| SCOD (g/L) | - | 20.25±1.6 | 27.95±1.8 | 26.60±2 | 25.07±6 | 26.06±5 | 26.49±10 |
| TCOD (g/L) | 36.39±9 | 26.99±2.5 | 32.69±5.1 | 35.18±1.6 | 36.87±11 | 36.62±1.5 | 42.29±10 |
| SCOD/TCOD | NA | 0.75 | 0.86 | 0.76 | 0.68 | 0.71 | 0.63 |

- HPR, Maximum hydrogen production rate; SHPR, Specific maximum hydrogen production rate; HY, Hydrogen yield.

HPR increased to 20 mmol $H_2$/L/d at pH 6.0. However, pH 5.0 was not suitable for hydrogen producing bacteria with decreasing HPR. This was similar to some reports of using *Clostridium* sp. to produce hydrogen with a suitable pH of 6.0. and *Clostridial* activity being inhibited at pH lower than 5.0 [15, 16]. Therefore, the continuous system was cultivated at pH 6.0 for optimizing the HRT.

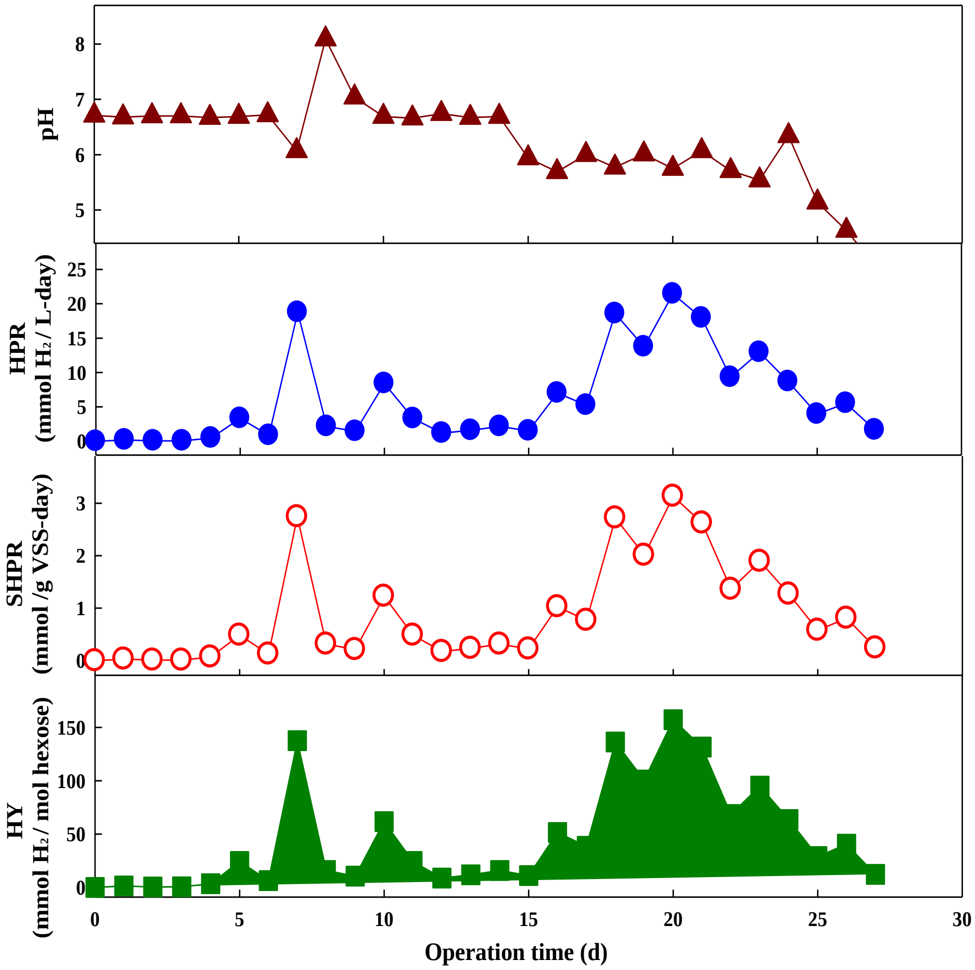

Fig. 2. $H_2$ production performance for the hydrogen fermentation system at various pHs during start-up period

### 3.2. Biogas production and fermentor performance during the continuous operation

Fig. 3 and Table 1 show the daily hydrogen production performance at HRTs 12 h to 1h. HPR increased from 5.4 to 60 mmol $H_2$/L-d when HRT was decreased from 12 to 8 h. When HRT was shortened from 8 h to 6 h, HPR increased to 135 mmol $H_2$/L-d. Shortening the HRT to 4 h resulted in a HPR of 238 mmol/L-d which value is 1.8 times of that at HRT 6 h. Peak HPR of 929 mmol $H_2$/L-d was obtained at HRT 2 h. The hydrogen producing bacteria were washed-out at HRT 1 h with lower HPR of 328 mmol $H_2$/L-d.

Table 1 shows that the hexose degradation decreased with shortening HRT. The hexose degradations ranged from 70 to 80% at HRTs 12–2 h but was less than 5% at HRT 1 h with low HPR values. The biogas production stopped when alkalinity was 1.54 g/L at day 207 (Fig. 3). The reason could be that too high organic loading rate (OLR) inhibited the hydrogen producer activity to reduce the hexose degradation.

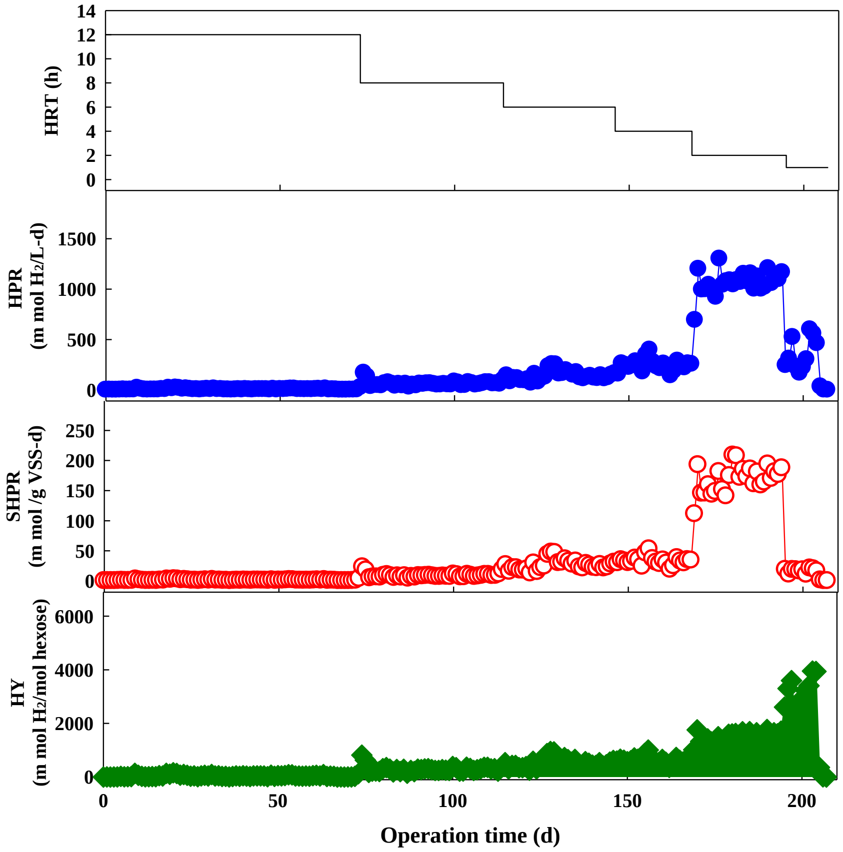

Fig. 3. $H_2$ production performance for the fermentation system at various HRTs

The variation of fermentor operation parameters during the start-up period was quite large. The VSS concentrations ranged from 5.36–7.54 g/L during steady-state at HRTs 12–4 h. When the HRT was shortened to 2 h, the VSS concentration and biogas production rate increased. ORP values (-445 to -519 mV) at HRTs 12–2 h were in the range favorable to biohydrogen generation (Table 1 and Fig. 3). Peak HPR and SHPR were 929±35 mmol $H_2$/L-d and 72.2±2.5 mmol $H_2$/g VSS-d, respectively. These values at HRT 2 h were about 2-4 times of that at HRT 4 h. However, the hydrogen production performance decreased with HPR 328±26 mmol $H_2$/L-d, SHPR 11.6±0.1 mmol $H_2$/g VSS-d and hydrogen content 14%. This resulted from that hydrogen producing bacteria were washed-out from the reactor. Chen and Lin [17] reported that the maximum specific growth rate of biohydrogen producers for glucose and condensed molasses fermentation solubles were 0.333–0.345 $h^{-1}$. The fermentor was operated at HRT 2 h which was shorter than the growth rate of hydrogen producers. The hexose degradation value of 4.6% shows that there was low carbohydrate conversion in the reactor.

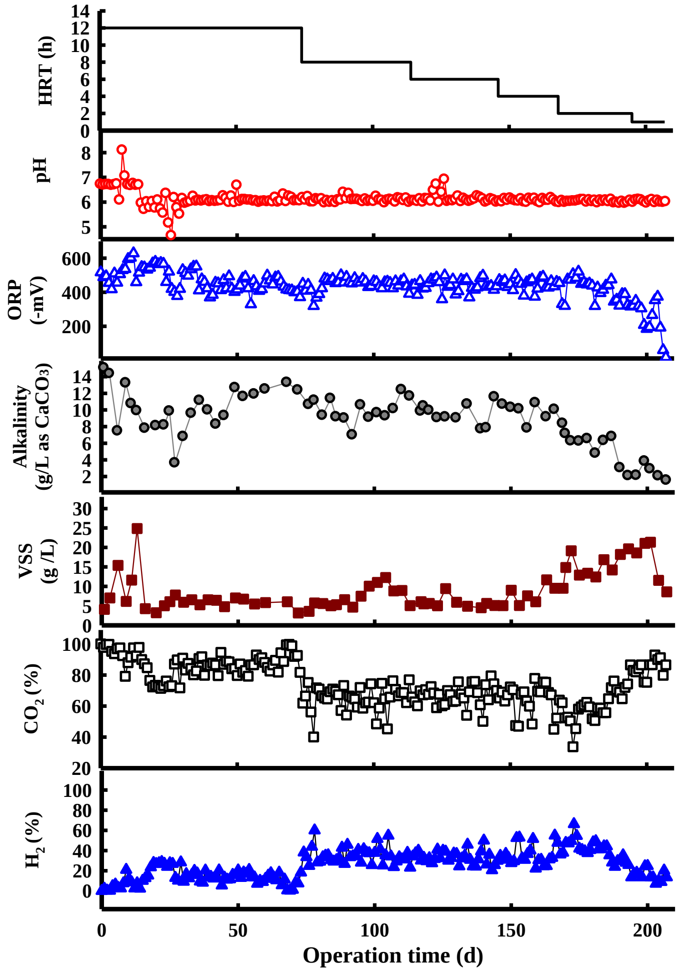

Fig. 4. The performance of the hydrogen fermentation system at various HRTs

Fig. 5 illustrates the VSS concentrations at various HRTs and shows that the increasing VSS concentration was obviously affected by the increasing OLR. Since the VSS concentration values denoted sweet potato and bacterial biomass, high OLR resulted in high bacterial biomass.

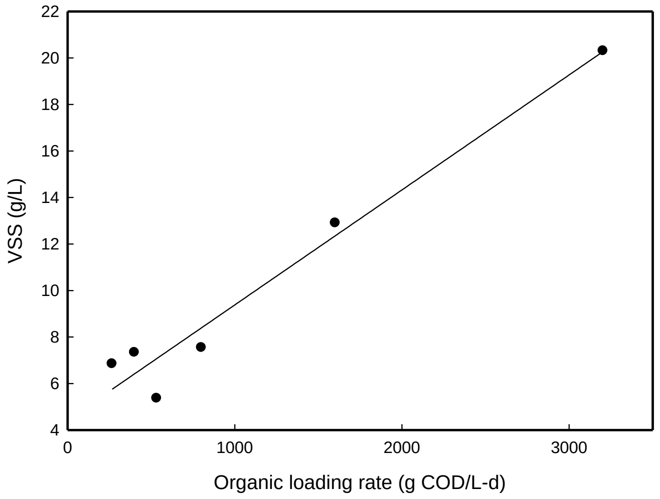

Fig. 5. The relationship between organic loading rate and VSS concentrations

### 3.3. Production of volatile fatty acids (VFAs) and ethanol

Table 2 summarizes the variation of soluble metabolites content under steady-state conditions at each HRT. The main SMP were ethanol, acetate and iso-butyrate during start-up and long HRT (12 h). When the HRT was shortened to 8 h, the metobolic pathway shifted to acetate and n-butyrate fermentation with concentrations of 2936±139 and 6397±346 mg COD/L, respectively. Peak total VFA (TVFA) of 11408±989 mg COD/L was obtained at HRT 4 h with acetate 2715±254 mg COD/L, propinate 689±107 mg COD/L, i-butyrate 236±68 mg COD/L, n-Butyrate 5485±351 mg COD/L and n-valerate 775±101 mg COD/L. However, the SMP and TVFA concentrations with the peak hydrogen production performance decreased to 19746±798 and 18438±811 mg COD/L, respectively, at HRT 2 h. The maximum reduction of 40% was butyrate concentration comparing those values at HRTs 4 and 2 h. Moreover, the butyrate/acetate (HBu/HAc) concentration ratio decreased from 0.61 at HRT 4 h to 0.45 at HRT 2 h.

Hawkes et al. [18] reported that acetate and butyrate fermentative pathway was suitable for hydrogen production. However, high hydrogen production accompanies with low ethanol production. High ethanol concentration of 2579±338 mg COD/L was obtained with lower acetate (4110±346 mg COD/L) and butyrate (7304±514 mg COD/L) concentrations and an HBu/HAc ratio of 0.72 at HRT 1 h.

Table 2. Variation of soluble metabolites content under steady-state conditions at each HRT

| **HRT (h)** | **Start-up** | **12** | **8** | **6** | **4** | **2** | **1** |
|---|---|---|---|---|---|---|---|
| **OLR (g sweet potato /L/d)** | | **267** | **400.5** | **534** | **801** | **1602** | **3204** |
| TVFA (mg COD/L) | 497± 51 | 6833± 644 | 11408± 989 | 9900± 792 | 27136± 954 | 18438± 811 | 13802± 659 |
| SMP (mg COD/L) | 692± 20 | 8637± 514 | 13248± 821 | 11147± 421 | 28512± 378 | 19746± 798 | 16381± 841 |
| Ethanol (mg COD/L) | 196± 25 | 1804± 66 | 1840± 129 | 1248± 350 | 1376± 214 | 1308± 165 | 2579± 338 |
| Acetate (mg COD/L) | 170± 95 | 2565± 139 | 2936± 340 | 2715± 254 | 9721± 658 | 7458± 423 | 4110± 346 |
| Propionate (mg COD/L) | 146± 31 | 1772± 250 | 1021± 121 | 689± 107 | 1824± 364 | 2057± 321 | 1416± 256 |
| i-Butyrate (mg COD/L) | 180± 42 | 2495± 411 | 235± 116 | 236± 68 | 73± 35 | 151± 67 | ND |
| n- Butyrate (mg COD/L) | ND | ND | 6397± 346 | 5485± 351 | 14645± 544 | 8309± 105 | 7304± 514 |
| n-Valerate (mg COD/L) | ND | ND | 818± 135 | 775± 101 | 873± 91 | 464± 84 | 971± 120 |
| Butyrate/Acetate (mol/mol) | 0.42 | 0.39 | 0.90 | 0.84 | 0.61 | 0.45 | 0.71 |

* TVFA (total volatile fatty acids) = acetate + propionate + butyrate + valerate; SMP (soluble microbial products) = ethanol + TVFA

### 3.4. Microbial community

For analyzing the bacterial community structure in the CSTR with sweet potato substrate, the genomic DNA samples were purified for different HRT operations and analyzed by 16S rRNA DGGE. The DGGE pattern shows a consistent bacterial community comprising of *Acetobacter indonesiensis, Bacillus sp., Bifidobacterium sp., Enterobacter aerogenes, and Endophyte bacterium* at HRT ranged from 12 to 4 h (Fig. 6) (Table 3). *Acetobacter* strain has been reported as an acetate-producer which can convert the alcohol into acetate as well [19]

*Bifidobacterium* is also an anaerobic bacterium which contributes to the lactate and acetate production [20]. *Enterobacter aerogenes* can ferment cellulose, starch, and glucose into organic acid and butandiol. It possesses the formate hydrogen-lyase activity of degrading the acetate into hydrogen and carbon dioxide [21].

Both *Bacillus* and *Endophyte bacterium* presented in the sweet potato substrate, but the population was withered and replaced by other predominant bacteria such as *Actinomyces* sp., *Bifidobacterium* sp., *Pseudomonas*, *Serratia* sp. and *Clostridium* species when the HRT was shorter than 8 h (Fig. 6). *Clostridium* has the potential of conducting Acetone–Butanol–Ethanol (ABE) fermentation and biohydrogen production by degrading crystalline cellulose and plant cell wall polysaccharides [22]. *Actinomyces* sp. can decompose cellulose, hemi-cellulose and lignin and might act as one of the disintegrators for degrading the sweet potato. Furthermore, the presence of *Serratia* sp. resulted in a red flux colour of the system and then significantly lowered the hydrogen performance of the system (data not shown).

A group of new species such as *Bifidobacterium psychroaerophilum*, *Clostridium butyricum* and *Clostridium vincentii* was determined at very short HRT conditions (Fig. 7). This bacterial community structure was close to that of the seed inoculum (Fig. 7). The best hydrogen performance was obtained at HRT 2 h with *Clostridium* species being the predominant bacteria. The decrease of hydrogen productivity at HRT 1 h might result from the wash-out of the contributors. Figure 8 depicts the scanning electron microscope (SEM) results for the sweet potato degrading process. The sweet potato particle surface was attached by rod-shape *Clostridium*-like microorganisms with 0.5–2 $\mu$m in diameter and 3.0 $\mu$m in length.

Table 3. The microbial communities during fermentation

| **Microbes/HRT (h)** | **Raw sweet potato** | **Initial** | **12** | **8** | **6** | **4** | **2** | **1** |
|---|---|---|---|---|---|---|---|---|
| *Acetobacter indonesiensts* | ˇ | ˇ | ˇ | ˇ | ˇ | ˇ | — | — |
| *Acetobacter sp* | — | — | — | ˇ | ˇ | ˇ | — | — |
| *Actinomyces sp.* | — | — | — | ˇ | ˇ | ˇ | — | — |
| *Bacillus sp.* | ˇ | ˇ | ˇ | — | — | — | ˇ | — |
| *Bifidobacterium sp.* | ˇ | ˇ | ˇ | ˇ | ˇ | ˇ | ˇ | ˇ |
| *Bifidobacterium psychroaerophilum* | — | — | — | ˇ | ˇ | ˇ | ˇ | ˇ |
| *Clostridium butyricum* | — | — | — | — | — | — | ˇ | ˇ |
| *Clostridium pasteurianum* | — | — | — | — | — | — | ˇ | — |
| *Clostridium vincentii* | — | — | — | ˇ | ˇ | ˇ | ˇ | ˇ |
| *Endophyte bacterium* | ˇ | ˇ | ˇ | — | — | — | — | — |
| *Enterobacter aerogenes* | ˇ | ˇ | ˇ | — | — | — | — | — |
| *Erwinia rhapontici* | — | — | ˇ | — | — | — | — | — |
| *Pseudomonas sp.* | — | — | — | ˇ | ˇ | ˇ | — | — |
| *Serratia sp.* | — | — | — | ˇ | ˇ | — | — | — |
| *Uncultured bacterium* | — | ˇ | ˇ | ˇ | ˇ | ˇ | — | — |
| *Uncultured Clostridium sp.* | — | — | — | ˇ | ˇ | ˇ | — | — |

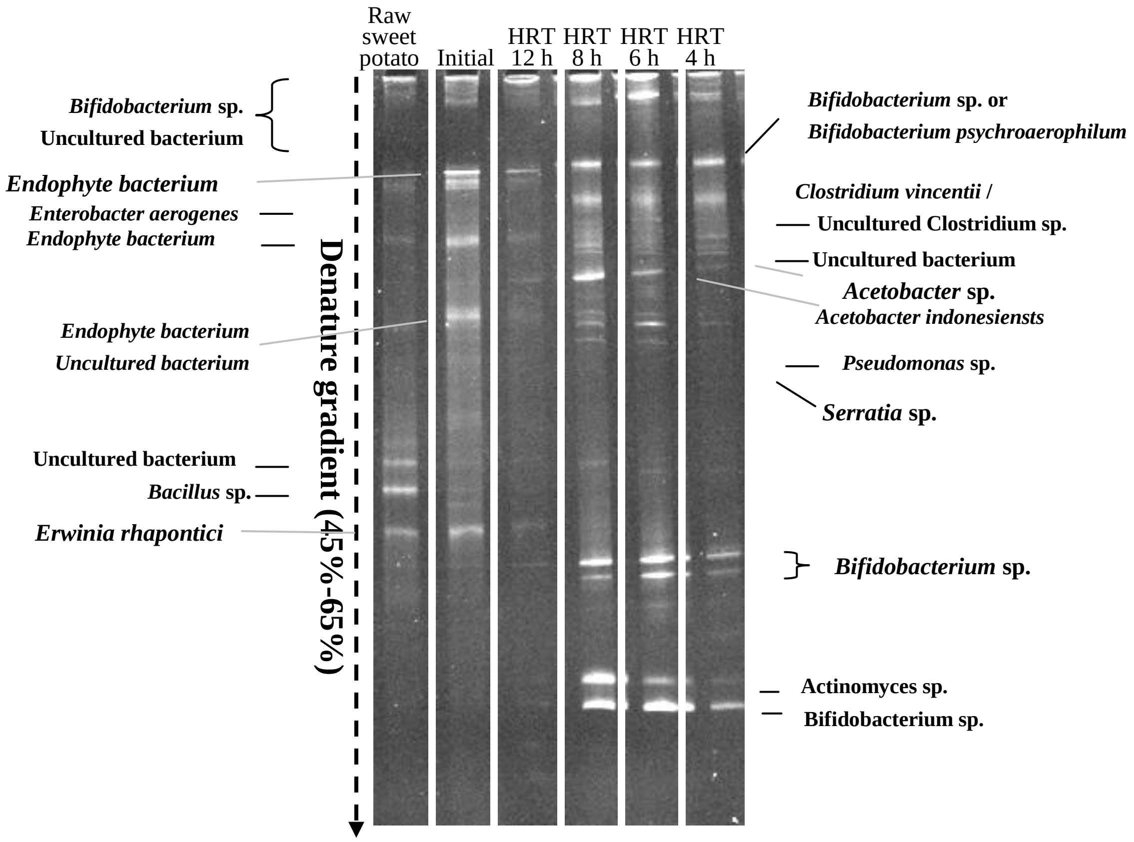

Fig. 6. A DGGE pattern showing bacterial community structure of the raw sweet potato, initial and HRTs 12, 8, 6 h in the CSTR system

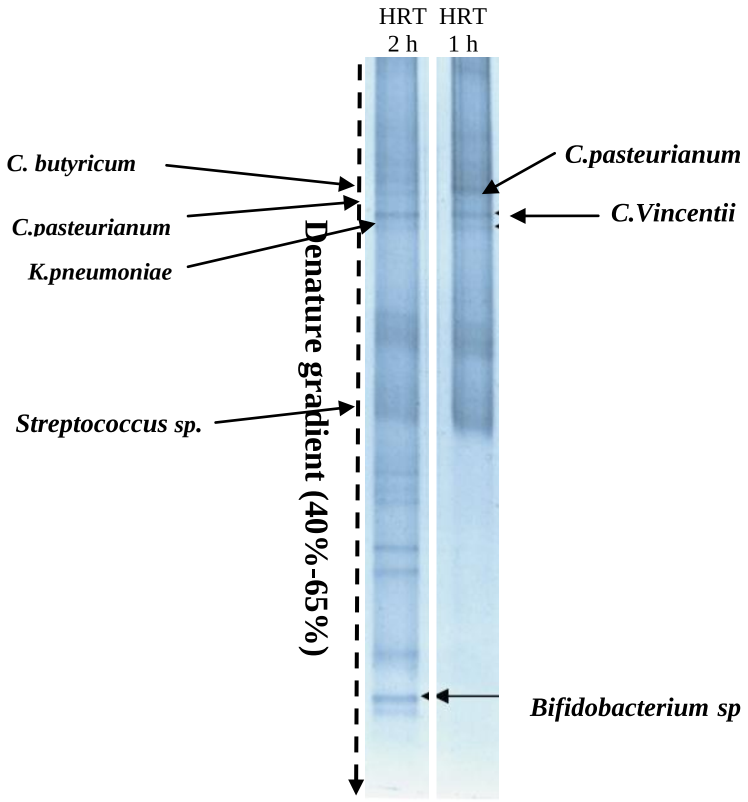

Fig. 7. A DGGE pattern showing bacterial community structures at HRTs 2 and 1 h

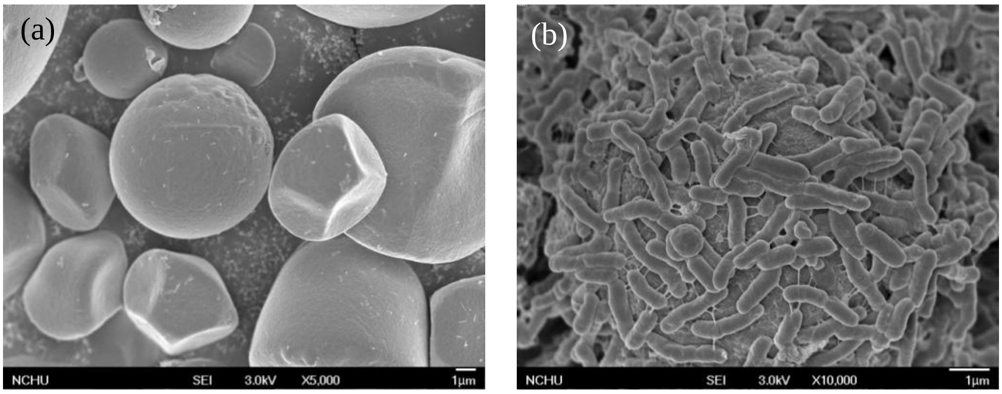

Fig. 8. SEM photos of (a) the raw sweet potato being meshed and (b) sweet potato fermented at HRT 2 h

## 4. CONCLUSIONS

This study shows that during sweet potato fermentation the indigenous potato bacteria can hydrolyze the starch into carbohydrates and good natural mixed microflora seed enhances hydrogen production.The hydrogen yield peaks at the suitable pH 6.0 in a CSTR system and shortening HRT improves the hydrogen production. Peak hydrogen production rate of 929 mmol $H_2$/L-d was obtained at HRT 2 h accompanying with growing predominant hydrogen-producing bacteria such as *Bifidobacterium psychroaerophilum*, *Clostridium butyricum*, and *Clostridium vincentii*. Unlike the butanol fermentation of food waste substrate, acetate (37~57%) and ethanol (5~28%) were the major metabolites in fermentative biohydrogen production from sweet potato substrate.

## ACKNOWLEDGEMENTS

The authors gratefully acknowledge the financial supports by Taiwan’s Bureau of Energy (grant no. 99-D0204-3), Taiwan’s National Science Council (NSC-99-2221-E-035 -024 –MY3, NSC-99-2221-E-035 -025 -MY3, NSC-99-2632-E-035 -001 -MY3), Feng Chia University (FCU-09G27102) and APEC Research Center for Advanced Biohydrogen Technology.

## REFERENCES

1. HART, D. *Hydrogen Power: The Commercial Future of the Ultimate Fuel*. Financial Times Energy Publishing: London, 1997. ISBN 1-85334-760-4.
2. OH, S. and LOGAN, B.E. Hydrogen and electricity production from a food processing wastewater using fermentation and microbial fuel cell technologies. *Water Research*, 2001, Vol. 39, p. 4673–4682.
3. LIN, C.Y., CHANG, R.C. Hydrogen production during the anaerobic acidogenic conversion of glucose. *J. Chem. Technol. Biotech.*, 1999, Vol. 74, p. 498–500.
4. MIZUNO, O., DINSDALE, R., HAWKES, F.R., HAWKES, D.L., NOIKE, T. Enhancement of hydrogen production from glucose by nitrogen gas sparging. *Bioresource Technol.*, 2000, Vol. 73, p. 59–65.
5. CHEN, C.C. and LIN, C.Y. Kinetics characteristics of hydrogen production with continuous anaerobic cultures utilizing glucose as the limiting substrate. Proceedings of Asian Waterqual, Bangkok, Thailand, 2003 October 20–22.

6. KIM, S.H., HAN, S.K., SHIN, H.S. Effect of substrate concentration on hydrogen production and 16S rDNA-based analysis of the microbial community in a continuous fermenter. *Process Biochem.*, 2006, Vol. 41, p. 199–207.
7. LAY J.J. Modeling and optimization of anaerobic digested sludge converting starch to hydrogen. *Biotechnol. Bioeng.*, 2000, Vol. 68, p. 269–278.
8. LIN, C.Y., CHANG, C.C., HUNG, C.H. Fermentative hydrogen production from starch using natural mixed cultures. *Int. J. Hydrogen Energy,* 2008, Vol. 33, p. 2445–2453.
9. WANG, J., WAN, W. Factors influencing fermentative hydrogen production: A review. *Int. J. Hydrogen Energy,* 2009, Vol. 34, p. 799–811.
10. NIELSEN, A.T., LIU, W.T., FILIPE, L. Jr. GRADY, MOLIN, S., Stahl, D.A. Identification of a novel group of bacteria in sludge from a deteriorated biological phosphorus removal reactor. *Appl. Environ. Microbiol.*, 1999, Vol. 65, p. 1251–1258.
11. APHA. Standard Methods for the Examination of Water and Wastewater, 19th ed, American Public Health Association, New York, USA, 1995, ISBN 8755-3554.
12. LAY, C.H., CHEN, C.C., LIN, H.C., LIN, C.Y., LEE, C.W., LIN, C.Y. Optimal pH and substrate concentration for fermentative hydrogen production from preserved fruits soaking solution. *J. Environ. Eng. Manage.*, 2010, Vol. 20, p. 35–41.
13. LIN, C.Y., HUNG, C.H., CHEN, C.H., CHUNG, W.T., CHEN, L.H. Effects of initial pH on fermentative hydrogen production from xylose using natural mixed cultures. *Process Biochem.*, 2006, Vol. 41, No. 6, p. 1383–1390.
14. LI, C. and FANG, H.H.P., Fermentative hydrogen production from wastewater and solid wastes by mixed cultures. *Crit. Rev. Env. Sci. Technol.*, 2007, Vol. 37, p. 1–39.
15. TAGUCHI, F., HASEGAWA, K., SAITO-TAKI, T., HARA, K. Simultaneous Production of Xylanase and Hydrogen Using Xylan in Batch Culture of *Clostridium* sp. Strain X53. *J. Ferment. Bioeng.*, 1996, Vol. 81, No. 2, p. 178–181.
16. KASHKET, E.R. and COA, Z.Y. Clostridial strain degenerateion. *FEMS Microbiology Reviews*, 1995, Vol. 24, No. 17, p. 307–315.
17. CHEN, C.C., LIN, C.Y. Using sucrose as a substrate in an anaerobic hydrogen producing reactor. *Adv. Environ. Res.*, 2003, Vol. 7, p. 695–699.
18. HAWKES, F.R., DINSDALE, R., HAWKES, D.L., HUSSY, I. Sustainable fermentative hydrogen production : Challenges for processs optimization. *Int. J.Hydrogen Energy,* 2002, Vol. 27, p. 1339–1347.
19. GARRIDO-VIDAL, D., PIZARRO, C., GONZÁLEZ-SÁIZ, J.M. Study of process variables in industrial acetic fermentation by a continuous pilot fermentor and response surfaces. *Biotechnol Prog.*, 2003, Vol. 19, No. 5, p. 1468–79.
20. WOLIN, M.J., YERRY, S., MILLER, T.L., ZHANG, Y., BANK, S. Changes introduction of ethanol, acids and $H_2$ from glucose by the fecal flora of a 16- to 158-d-old breast-fed infant. *J. Nutr. Jan,* 1998, Vol. 128, No. 1, p. 85–90.
21. LICHSTEIN, H.C. and BOYD, R.B. Studies on the formic hydrogenlyase system of bacteria. *J Bacteriol.*, 1954, Vol. 67, No. 3, p. 335–41.
22. CHANG, J.J., CHOU, C.H., HSU, P.C., YU, S.J., CHEN, W.E., LAY, J.J. Flow-FISH analysis and isolation of clostridial strains in an anaerobic semi-solid bio-hydrogen producing system by hydrogenase gene target. *Appl Microbiol. Biotechnol.*, 2007, Vol. 74, p. 1126–34.

# POTENTIAL OF BIOLOGICAL HYDROGEN PRODUCTION FROM BEVERAGE WASTEWATER

**Y.C. Li, C.Y. Chu, S.Y. Wu, C.Y. Lin, C.C. Wu, S.R. Huang**
*Feng Chia University*
*No. 100, Wenhwa Rd., Seatwen, Taichung – Taiwan*
*Phone +886-4-24517250 ext. 3679*
*Email: sywu@fcu.edu.tw*

## ABSTRACT

The immobilized cell of silicone gel (SC) entraped with *Clostridium* sp. was used as seed sludge in a continuously-stirred anaerobic bioreactor (CSABR). The effects of substrate concentration and hydraulic retention time (HRT) on the hydrogen production performance, hydrogen production rate (HPR) and yield were investigated for anaerobic hydrogen fermentation using beverage wastewater under different influent substrate concentrations ($C_{S0}$ 20, 30, and 40 g COD/L; COD is chemical oxidation demand) and hydraulic retention times (HRT 8 and 4 h). The pH and temperature values were controlled at 5.5 and 37°C, respectively. The hydrogen production rate and yield decreased when influent substrate concentration increased from 20 to 30 g COD/L then leveled off when influent substrate concentration increased from 30 to 40 g COD/L due to inhibiting effects appeared at higher substrate concentrations. The hydrogen production rates were 12.51 ± 1.89 and 12.13 ± 1.08 L/d/L when initial substrate concentrations were 30 and 40 g COD/L, respectively. However, when influent substrate concentration was 20 g COD/L the steady state values of the hydrogen production and yield at HRT of 4 h were higher than those of HRT 8 h. The maximum values obtained for substrate utilization, hydrogen production rate and yield and were 92.03 ± 0.52%, 18.87 ± 0.90 L/d/L and 15.73±0.72 mmol $H_2$/g hexose, respectively, at HRT 4 h, substrate concentration 20 g COD/L, pH 5.5 and temperature 37°C. The HPR value of this beverage wastewater is 3 times higher when compared to the reported value of condensed molasses substrate of HPR 6.17 L/d/L and yield 4.19 mmol $H_2$/g COD substrate at 37°C, pH 5.5, HRT 4 h and the substrate concentration 40 g COD/L.

Keywords: beverage wastewater; immobilized cell; continuously stirred anaerobic bioreactor (CSABR).

## 1. INTRODUCTION

The promising green energy, hydrogen, has been considered as an alternative energy to substitute fossil fuels in the future due to its ideal and clean characteristics. Thus, developing sustainable energy chains based on the contemporary sunlight-like application of biofuels and hydrogen from renewable sources is indispensable. $H_2$ offers tremendous potential as a sustainable energy source because it produces only water when it combusts, generating an energy yield (122 kJ/g) 2.75 times higher than hydrocarbon fuels [1]. In addition, $H_2$ can be easily converted to electricity through fuel cells [2].

Numerous ways exist to produce $H_2$, but the steam reforming of hydrocarbons is widely used due to its cost advantage. However, the reaction occurs at high temperature and pressure condition which require a lot of external energy from fossil fuels, thereby rendering the process environmentally unfriendly. On the other hand, in nature, various microorganisms have capabilities to produce $H_2$ from different sources [3].

The beverage industry is one of the biggest industries in the world and produces a large amount of high strength organic wastewater (189.288 $m^3$/year of a beverage factory in Taiwan) The beverage wastewater has high organic-content which can be used to obtain the biohydrogen energy by anaerobic fermentative hydrogen production system to increase the total energy recovery efficiency. In the present work, therefore, beverage manufacturing wastewater (BMW) was chosen as a substrate in CSABR.

There were many previously studies of using waste as the substrate for fermentative biohydrogen, such as food waste, wastewater, and others on biohydrogen with mixed cultures and batch reactor in the literatures [4–6]. Zhang et al. [4], Mohan et al. [5], Skonieczny et al. [6] carried out the batch experiment by using wastewater as the substrate to obtain the maximum $H_2$ yield of 92 ml/g-starch, 1.25 mmol $H_2$/g COD, 10.3 mL $H_2$/g COD/L, 249.3 mL $H_2$/g starch, and 0.097 mmol $H_2$/g cellulose, respectivily. Besides there were few advantages of using waste as substrate for fermentative with continuous system in the literature [7–10]. Gustavo et al. [7] and Zhu et al. [8], carried out the continuous experiment by using cheese PTA wastewater as the substrate, Kim et al. [9], carried out the continuous experiment by using tofu-processing waste as the substrate, and Jung et al. [10], carried out the continuous experiment by using crude coffee wastes the substrate.

The addition of immobilized cell in the reactor could prevent the hydrogenase bacteria been washed out, enhanced the biomass concentration and increased the hydrogen production rate. High speed anaerobic fermentation biohydrogen production rate had been achieved in the bioreactor by using immobilized cell in many investigations [11–15].

The immobilized cell bioreactor system was used as a hydrogen production bioreactor in this study. The feedstock of beverage wastewater was used to replace the high-cost feedstock such as sucrose, glucose, and starch that were used as a substrate in the several studies for the anaerobic fermentation of hydrogen production [16–19]. An attempt of this study was developed a high-rate biohydrogen production and low-cost feedstock system for further commercialized design.

## 2. METHODOLOGY

### 2.1 Seed sludge and substrate

The seed sludge was taken from Li-Ming Municipal Sewage Treatment Plant in Taichung, Taiwan and pretreated by 0.1 N HCl to pH 3.0–4.0, then adjusted to pH 7.0 by NaOH after 24 hours [20]. The thermal pretreatment was also used to inhibit the growth of methanogens and enhancebiohydrogen production [21]. The immobilized cell particles were made by activated sludge and the silica gel after cultivation of bacteria source then adding 10% working volume of the bioreactor [22]. The average height and diameter of the immobilized cell were 3 mm and 6 mm, respectively with particle density of $1.12 \pm 0.05$ g/cm$^3$.

The BMW used in this study was obtained from north area of Taiwan with a high organic original concentration of $669.00 \pm 46.67$ g COD/L and a carbohydrate composition of 73.88%. The total sugar concentration and pH were $494.23 \pm 18.99$ g/L and 1.80, respectively. The substrate concentration was adjusted to 20 g COD/L by RO water dilution, the pH adjusted to 6.8 by using 1–3 N HCl and stored in the refrigerator at temperature of 4 °C.

### 2.2 CSABR operation

This study was carried out by continuously stirred anaerobic bioreactor (CSABR) (working volume 1.2 L, reactor high of 500 mm and internal diameter of 55 mm) for anaerobic bio-hydrogen production. The CASBR was made from acryl and jacketed with water bath and a heater was used to control the system temperature at 37°C. The schematic diagram of the continuously stirred anaerobic bioreactor system is shown in Fig. 1. The CSABR was seeded with the heat-treated immobilized cell equivalent to 10% of the working volume, and filled with the substrate. It was purged with Ar gas for 5 min to provide an anaerobic condition and agitated at 50 rpm. The initial and operation pH was maintained at 6.8±0.1 and 5.5±0.1, respectively, using pH sensors, pH controllers, and 1–3 N NaOH. The

HRT was progressively decreased from 8 to 2 h. The substrate concentration was progressively decreased from 40 to 20 g COD/L. All experiments were controlled in a temperature at 37°C and gas production was monitored using a wet gas meter.

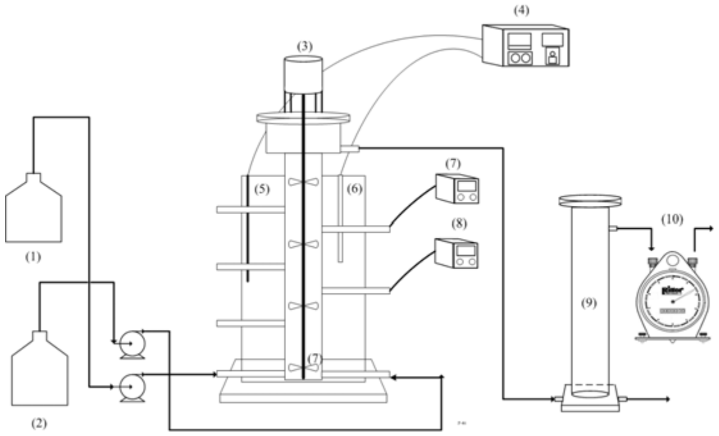

Fig.1. Schematic diagram of the continuously stirred anaerobic bioreactor systems: (1) Medium tank (2) NaOH (3) Stir (4) Temperature and stirred controller (5) Temperature sensor (6) Heater (7) ORP detector (8) pH detector (9) Gas-liquid separator (10) Wet gas meter

## 2.3 Analysis

The component of biogas in the headspace including hydrogen, nitrogen and carbon dioxide was determined using gas chromatography (SHIMADZU GC-14B with TCD). Volatile fatty acids (VFAs) of fermentation was filtered through 0.22 μm filter and analyzed by liquid chromatography (SHIMADZU LC-10AT with RID) and the same was used for glucose, xylose, arabinose, lactic acid (HLa), acetic acid (HAc), propionic acid (HPr), butyric acid (HBu) and ethanol (EtOH).

The biomass content was measured by the APHA method [23]. The method takes 10 mL liquid of biomass, filtered by Whatman 47 mm filter paper as the sample, then put into the oven at 105°C for 24 h. After that, the dry filter paper with biomass is weighed and put in the oven again, but the temperature is set at 550°C for 8 h. Then the sample is weighed again. The biomass content is the weight difference between the two temperatures and sample weights.

## 3. RESULTS AND DISCUSSION

### 3.1 Effect of substrate concentration

The hydrogen yield, hydrogen production rate (HPR) and hydrogen content were obtained in CSABR using beverage wastewater. These experimental data is shown in Fig. 2 with substrate concentrations from 20 to 40 g COD/L at HRT of 8 h, pH of 5.5 and temperature of 37°C. The performance under steady-state for substrate concentration and the liquid phase compositions are shown in Tables 1 and 2. As shown in Fig. 2 and Table 1, the hydrogen production rates were ranged from 11.57 to 12.51 L/d/L, the hydrogen yields and the total sugar utilization were increased with substrate concentration was varied from 40 to 20 g COD/L.

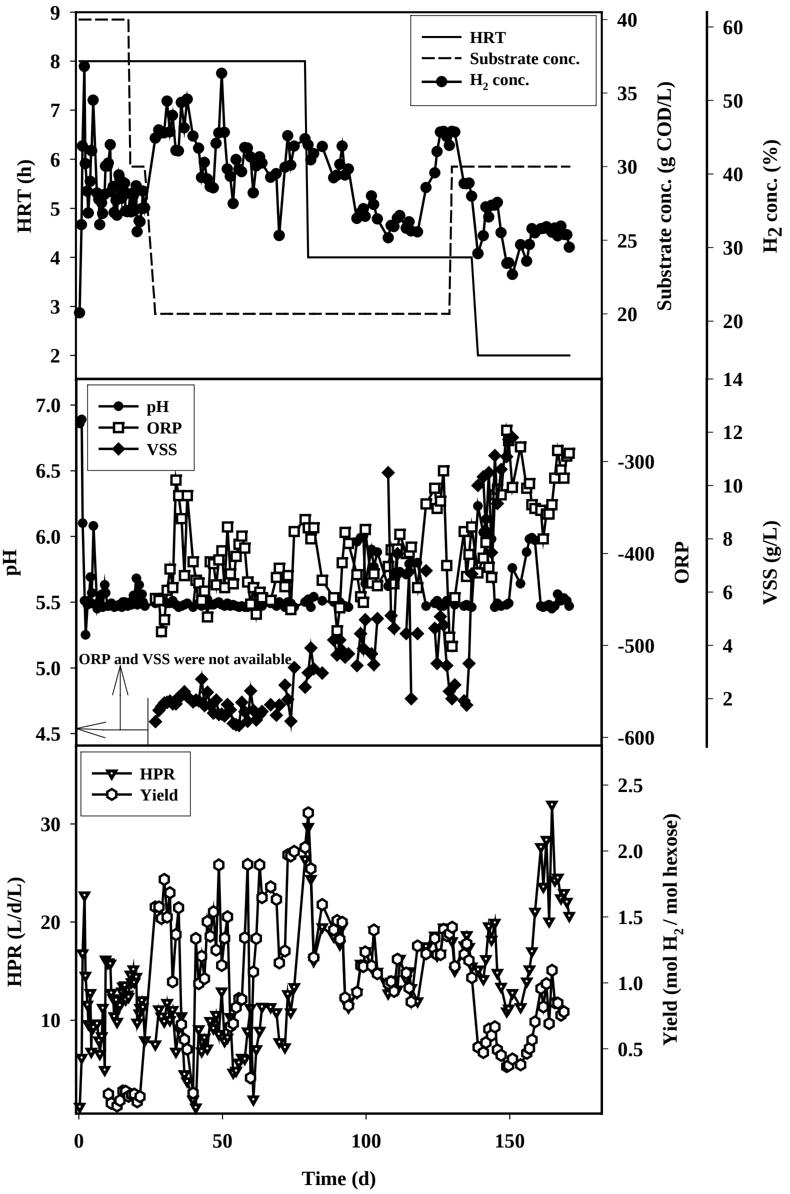

Fig. 2. Hydrogen yield, hydrogen production rate and hydrogen concentration of different substrate concentration and HRT in CSABR

Table 1. The performance of different substrate concentrations at HRT 8 h

| **Substrate conc. (g COD/L)** | **Total sugar (g/L)** | **$H_2$ conc. (%)** | **$H_2$ production rate (L/d/L)** | **$H_2$ yield (mol $H_2$ / mol hexose)** | **Total sugar utilization (%)** | **Biomass conc. (g VSS/L)** |
|---|---|---|---|---|---|---|
| 40 | 36.50 | 36.83±1.92 | 12.13±1.08 | 1.25±0.17 | 52.74±10.54 | N.A. |
| 30 | 27.38 | 35.28±2.07 | 12.51±1.89 | 1.16±0.02 | 74.93±5.60 | N.A. |
| 20 | 14.78 | 41.96±1.86 | 11.57±0.95 | 1.98±0.02 | 87.03±5.94 | 1.98±0.02 |

Table 2. Liquid phase compositions of different substrate concentrations at HRT 8 h

| **Substrate conc.** | **Lactic acid** | **Formic acid** | **Acetic acid** | **Propionic acid** | **Ethanol** | **Butyric acid** | **(HAc+HBu)/SMP %** | **TVFA** | **SMP** | **TVFA/SMP** |
|---|---|---|---|---|---|---|---|---|---|---|
| 40 g COD/L | 121 | 119 | 3384 | 1211 | 3095 | 17304 | 81.98 | 22142 | 25237 | 0.88 |
| 30 g COD/L | 89 | 86 | 4318 | 1117 | 3027 | 16869 | 83.06 | 22481 | 25508 | 0.88 |
| 20 g COD/L | 10 | 38 | 907 | 167 | 518 | 4112 | 87.23 | 5235 | 5754 | 0.91 |

HLa: lactic acid; HAc: acetic acid; HPr: propionic acid; HBu: butyric acid; EtOH: ethanol
TVFA(total volatile fatty acid) = HLa + HAc + HPr + HBu
SMP(soluble microbial products) = TVFA + HLa+EtOH
Unit : mg COD/L

The substrate concentration of 20 g COD/L has the maximum hydrogen yield of 1.98 ± 0.02 mmol $H_2$/mol hexose with a hydrogen production rate of 11.57 ± 0.95 L/d/L when the total sugar utilization was 87.03 ± 5.94% and biomass concentration of 1.56 ± 0.19 g VSS/L. A lower hydrogen production rate and hydrogen production yield at substrate concentration of 40 g COD/L, could be due to an inhibitory effect of high substrate concentration occurs in the fermentation process depending on the sugar utilization of substrates.

### 3.2 Effect of hydraulic retention time (HRT)

The experimental data with HRTs 4 and 8 h were obtained at pH of 5.5 and temperature of 37°C. The performance of the hydrogen production rate, hydrogen yield and hydrogen content under steady-state at substrate concentration of 20 g COD/L are shown in Fig. 2 and Table 3.

Table 3. The performance of different HRT and OLR in the CSABR system

| **HRT (h)** | **Substrate conc. (g COD/L)** | **Total sugar (g/L)** | **$H_2$ conc. (%)** | **$H_2$ production rate (L/d/L)** | **$H_2$ yield (mol $H_2$ / mol hexose)** | **Total sugar utilization (%)** | **Biomass conc. (g VSS/L)** |
|---|---|---|---|---|---|---|---|
| 8 | 20 | 14.78 | 41.96±1.86 | 11.57±0.95 | 1.98±0.02 | 87.03±5.94 | 1.56±0.19 |
| 4 | 20 | 14.78 | 44.20±2.08 | 18.16±1.07 | 1.33±0.09 | 95.27±0.91 | 4.21±0.86 |
| 2 | 30 | 16.05 | 32.34±0.50 | 27.37±3.17 | 0.95±0.11 | 91.93±0.89 | 11.53±0.39 |

The soluble metabolites is shown in Table 4. The biohydrogen production rate at HRT 4 h was higher than HRT 8 h, but the hydrogen yield was inversely. The hydrogen production yield of 1.98±0.02 mmol $H_2$/mol hexose with a hydrogen production rate of 11.57±0.95 L/d/L when the total sugar utilization was 87.03±5.94% and biomass concentration of 1.56±0.19 g VSS/L at HRT 8 h. The hydrogen production rate of 18.16±1.07 L/d/L with a hydrogen production yield of 1.33±0.09 mmol $H_2$/mol hexose when the total sugar utilization was 95.27 ± 0.91% and biomass concentration of 4.21±0.80 g VSS/L at HRT 4 h.

Table 4. Liquid phase compositions of different HRT in CSABR system

| **HRT (h)** | **Lactic acid** | **Formic acid** | **Acetic acid** | **Propionic acid** | **Ethanol** | **Butyric acid** | **(HAc+HBu)/SMP %** | **TVFA** | **SMP** | **TVFA/SMP** |
|---|---|---|---|---|---|---|---|---|---|---|
| 8 | 10 | 38 | 907 | 167 | 518 | 4112 | 87.23 | 5235 | 5754 | 0.91 |
| 4 | N.D. | N.D. | 2983 | 599 | 707 | 10354 | 91.08 | 11149 | 14644 | 0.95 |
| 2 | N.D. | N.D. | 2199 | 206 | 525 | 5545 | 91.37 | 7951 | 8476 | 0.94 |

HLa: lactic acid; HAc: acetic acid; HPr: propionic acid; HBu: butyric acid; EtOH: ethanol
TVFA(total volatile fatty acid) = HLa + HAc + HPr + HBu
SMP(soluble microbial products) = TVFA + HLa+EtOH
Unit : mg COD/L

Table 5 shows comparison of hydrogen production rate and hydrogen yield from organic wastewater by continuously fermentative reactors. There are numerous wastewaters which test by continuously fermentative reactors such as cheese whey, crude coffee waste, molasses, synthesis wastewater and tofu-processing waste with HRTs 2–24 h (Table 5). As shown in Table 5, this study obtained a HPR of 27.37 L/d/L, which is the highest data never found by using high organic wastewater as a substrate from continuously fermentative hydrogen production reactors in the literatures. Although the highest hydrogen yield of 1.98 mol $H_2$/mol hexose in this study is lower than 2.25 mol $H_2$/mol hexose (Barros et al. [26]). The reason could be due to that the experiment in their study was used the glucose as the carbon source to simulate the microbial consortia, thus resulted in their high yield. Moreover, CSABR has an additional advantage because of the reactor was seeded with 10% immobilize cell which can avoid the bacteria wash out and enrich the biomass concentration in the bioreactor. Therefore, the CSABR system could operate steady in low HRTs, it could enhance the hydrogen production rate by feeding with a high organic loading rate.

Table 5. Comparison of hydrogen production rate and hydrogen yield from organic wastewater by continuously fermentative system reactors

| **Reactor type** | **HRT (h)** | **Substrate type** | **Substrate conc.** | **Microorganism** | **$H_2$ production rate (L/d/L)** | **$H_2$ yield (mol $H_2$ / mol hexose)** | **Reference** |
|---|---|---|---|---|---|---|---|
| CSTR | 12 | Starch | $20^b$ | Seed sludge | - | 0.92 | Arooj et al. [28] |
| CSTR | 12 | Tequila vinase | $3^b$ | Granular sludge | 1.21 | - | Buitron et al. [24] |
| USABR | 6 | Crude coffee | $184^b$ | Seed sludge | - | 1.29 | Jung et al. [3] |
| CSTR | 4 | Tofu-processing waste | $10.4^a$ | Sludge | 12.00 | - | Kim et al. [9] |
| AGSBR (pilot scale) | 4 | Sucrose | $40^b$ | Seed sludge | 15.59 | - | Lin et al. [25] |
| AFBR | 4 | Synthesis wastewater | $20^c$ | Activated sludge | - | 1.16 | Zhang et al. [27] |
| AFBR | 2 | Synthesis wastewater | $40^c$ | Sludge | - | 2.25 | Barros et al. [26] |
| CSABR | 8 | Beverage wastewater | $14.78^a$ | Seed sludge +Immobilized cell(10% v/v) | 11.57 | 1.98 | This study |
| CSABR | 4 | Beverage wastewater | $14.78^a$ | Seed sludge +Immobilized cell(10% v/v) | 18.16 | 1.33 | This study |
| CSABR | 2 | Beverage wastewater | $16.05^a$ | Seed sludge +Immobilized cell(10% v/v) | 27.37 | 0.95 | This study |
| a: g carbohydrates/L; b: g COD/L; c: g glucose/L | | | | | | | |

### 3.3 The soluble metabolites composition

The composition of soluble metabolites produced during a dark fermentation biohydrogen production process is usually used as an indicator to confirm the efficiency of the bioreactor [25, 32–33]. As shown in Tables 2 and 4, the major soluble metabolites produced from the bioreactors were acetate and butyrate, accounting for 81.98–91.37% of total SMP. The total volatile fatty acid (TVFA) and SMP increased as HRT decreased from 8 to 2 h. The production of acetic acid (HAc) and butyric acid (HBu) contributed to 13.41–25.94% and 65.43–71.47% of SMP, whereas the alcohol to SMP (EtOH/SMP) ratio was 4.83–12.26%. The high HAc/SMP and HBu/SMP and low EtOH/SMP ratios indicate an efficient biohydrogen generation system, since HAc and HBu production is in general positively correlated to $H_2$ production, whereas generation of solvents (e.g. alcohol) consume free electron derived from NADH, and leads to unfavorable conditions for $H_2$ production [29, 30]. However, when the HRT was shortened from 8 to 2 h, the HBu was the dominant acid product in the soluble metabolites and the ratio of Ethanol/SMP was lower than 15.1. From the analysis of soluble metabolites, the results confirmed good performance in a continuously stirred anaerobic bioreactor.

### 3.4 The microbial community

The DGGE profile of the CSABR was shown in Fig. 3. Lane M is maker, lane 1 was operated at the HRT 8 h in steasy state, lane 2 is before power failure at HRT 4 h, lane 3 started up after power failue at HRT 4 h, lane 4 was operated at HRT 4 h in steady state and lane 5 was operated at HRT 2 h in steady state. These figure revealed that the major bacteria were *Clostridium butyricum*, *Megaspharea* spp. When the reactor was started up after power failue, there are several undesire bacteria apper compared with lanes 1 and 2. It result in the hydrogen production rate decreased from 16.27 to 8.69 L/d/L with HRT 4 and substrate concentration of 20 g COD/L. Compared with lane 3 and lanes 4–5, it was found that the undesire bacteria were washed out in low HRT and resulted in the hydrogen production rate increased from 11.54 to 18.67 L/d/L. The *Clostridium butyricum* and *Megaspharea* spp. were mainly bacteria in the bioreactor for hydrogen production.

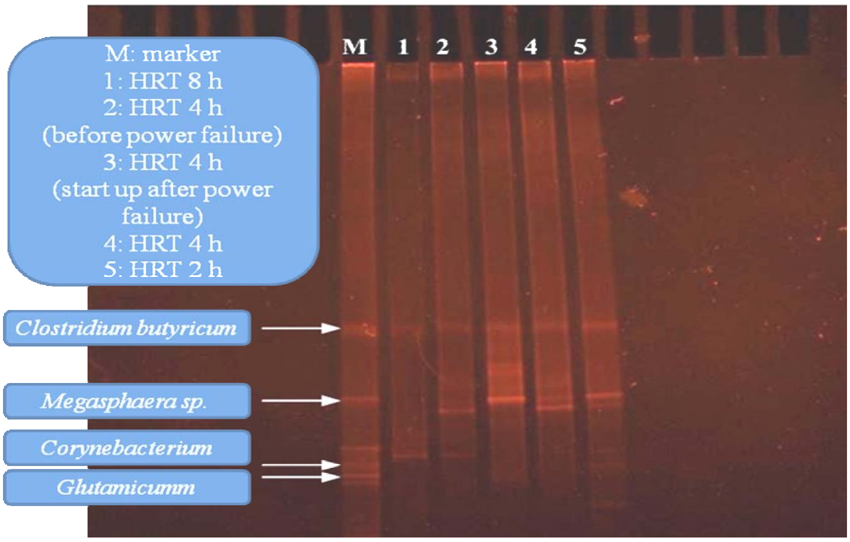

Fig. 3. DGGE profile of the microbial community in CSABR system

## 4. CONCLUSIONS

The biohydrogen production performance of the immobilized cell systems from beverage wastewater fermentation was investigated in this study. The biohydrogen production rate increased with decreasing HRT. The steady-state maximum HPR was 27.37±3.17 L/d/L at HRT 2 h. The HLa concentration decreased with decreasing HRT. A higher feeding rate could wash out the undesired bacteria and remained the hydrogen production bacteria in CSABR system. Therefore, the CSABR system could operate steady in low HRTs, it could enhance the hydrogen production rate by feeding with a high organic loading rate. Finally, the highest HPR value of 27.37 L/d/L has never found using high organic wastewater from continuously fermentative hydrogen production reactors in the literatures.

## 5. ACKNOWLEDGEMENTS

The authors gratefully acknowledge the financial support by National Science Council of Taiwan (grant no. NSC 99-2632-E-035-001-MY3; NSC 99-2811-E-035-001), Taiwan's Bureau of Energy (grant no. 99-D0204-3), and Feng Chia University (grant no. FCU-10G27101).

## REFERENCES

1. SCOTT DS. Hydrogen - the case for inevitability. *Int J Hydrogen Energy*, 2004, Vol. 29, p. 225–227.
2. NEELIS ML., KOOI HJ., GEERLINGS JJC. Exergetic life cycle analysis of hydrogen production and storage systems for automotive applications. *Int J Hydrogen Energy*, 2004, Vol. 29, p. 537–545.
3. JUNG Kyung W., KIM Dong H., SHIN Hang S. Continuous fermentative hydrogen production from coffee drink manufacturing wastewater by applying UASB reactor. *International Journal of Hydrogen Energy*, 2010, Vol. 35, p. 13370–13378.
4. ZHANG T., LIU H., HERBERT H.P. Fang. Biohydrogen production from starch in wastewater under thermophilic condition. *Journal of Environmental Management*, 2010, Vol. 69, p. 149–156.
5. MOHAN SV., BHASKAR YV., KRISHNA PM., RAO NC., BABU VL., SARMA PN.. Biohydrogen production from chemicalwastewater as substrate by selectively enriched anaerobic mixed consortia: Influence of fermentation pH and substrate composition. *International Journal of Hydrogen Energy*, 2007, Vol. 32, p. 2286–2295.
6. SKONIECZNY Monika T., YARGEAU V. Biohydrogen production from wastewater by Clostridium beijerinckii: Effect of pH and substrate concentration. *International Journal of Hydrogen Energy*, 2009, Vol. 34, p. 3288–3294.
7. GUSTAVO DV., CIRIA Berenice CN., LUIS Manuel RC., de LEO´N-RODRI´GUEZ A., RAZO-FLORES E. Continuous biohydrogen production using cheese whey: Improving the hydrogen production rate. *International Journal of Hydrogen Energy*, 2009, Vol. 34, p. 6–4304.
8. ZHU Ge F., WU P., WEI Qun S., LIN Jian y., GAO Yan L., LIU Hai N.. Biohydrogen production from purified terephthalic acid (PTA) processing wastewater by anaerobic fermentation using mixed microbial communities. *International Journal of Hydrogen Energy*, 2010, Vol. 35, p. 8350–8356.
9. KIM Mi S., LEE Dong Y. Fermentative hydrogen production from tofu-processing waste and anaerobic digester sludge using microbial consortium. *Bioresource Technology*, 2010, Vol. 101, p. S48–S52.
10. JUN KW., KIM DH., SHIN HS. Continuous fermentative hydrogen production from coffee drink manufacturing wastewater by applying UASB reactor. *International Journal of Hydrogen Energy*, 2010, Vol. 35, p. 13370–13378.
11. WU SY., LIN CY., CHANG JS., LEE KS., LIN PJ. Microbial hydrogen production with immobilized sewage sludge. *Biotechnol Prog* , 2002, Vol. 18, p. 921–926.
12. Wu SY., Lin CN., Chang JS. Hydrogen production with immobilized sewage sludge in three-phase fluidized beds. *Biotechnol Prog*, 2003, Vol. 19, p. 828–832.
13. WU SY., LIN CN., CHANG JS. Biohydrogen production with anaerobic sludge immobilized by ethylene-vinyl acetate copolymer. *Int. J. Hydrogen Energy*, 2005, Vol. 30, p. 1375–1381.
14. WU SY., HUNG CH., LIN CN., CHEN HW., LEE AS., CHANG, JS. Fermentative hydrogen production and bacterial community structure in high-rate anaerobic bioreactors containing silicone-immobilized and self-flocculated sludge. *Biotechnol Bioeng*, 2006, Vol. 93, No. 5, p. 934–946.
15. LIN CN., WU SY., CHANG JS. Biohydrogen production in a three-phase fluidized bed bioreactor using sewage sludge immobilized by eyhylene-vinyl acetate copolymer. *Bioresource Technology*, 2009, Vol. 100, p. 3298–3301.

16. KATAOKA N., MIYA A. and KIRIYAMA K. Studies on Hydrogen Production by Continuous Culture System of Hydrogen Producing Anaerobic Bacteria. Proc. *Of the 8th International Conference on Anaerobic Digestion*, 1997, Vol. 2, p. 383–390.
17. LIN CY. and CHANG RC. Hydrogen production during the anaerobic acidogenic conversion of glucose. *J. Chem Technol Biotechnol*, 1999, Vol. 74, p. 498–500.
18. CHEN CC., LIN CY., CHANG JS. Kinetics of hydrogen production with continuous anaerobic cultures utilizing sucrose as the limiting substrate. *Appl Microbiol Biotechnol*, 2001, Vol. 57, p. 56–64.
19. ZHANG T., LIU H., FANG HHP. Biohydrogen production from starch in wastewater under thermophilic condition. *J. Environ Manage*, 2003, Vol., p. 149–156.
20. CHEN CC., LIN CY. and LIN MC. Acid-base Enrichment Enhances Anaerobic Hydrogen Production Process. *Appl. Microbiol. Biotechnol*, 2002, Vol. 58, p. 224–228.
21. LIN CY., CHEN CC. and LIN MC. Production in Aanaerobic Acidogenesis Process – Influences of Thermal Isolation and Acclimation Environment. *J. Chin. Inst. Environ. Eng.*, 2000, Vol. 10, No. 3, p. 163–168.
22. WU SY., LIN CN., CHANG JS. Biohydrogen production with anaerobic sludge immobilized by ethylene-vinyl acetate copolymer. *Int. J. Hydrogen Energy*, 2005, Vol. 30, p. 1375–1381.
23. APHA. Standard methods for the examination of water and waste water. 19th ed. New York, USA: *American Public Health Association* 1995.
24. BUITRON G., CARVAJAL C. Biohydrogen production from Tequila vinasses in an anaerobic sequencing batch reactor: Effect of initial substrate concentration, temperature and hydraulic retention time. *Bioresource Technology*, 2010, Vol. 101, p. 9071–9077.
25. LIN Chiu Y., WU Shu Y., LIN Ping J., CHANG Jo S., HUNG Chun H., LEE Kuo S., LAY Chyi H., CHU Chen Y., CHENG Chin H., CHANG Alex C., WU Jou H., Feng-Yuan Chang, Lee-Hao Yang, Chia-Wen Lee, Yi-Chun Lin. A pilot-scale high-rate biohydrogen production system with mixed microflora. *International Journal of Hydrogen Energy*, 2010, doi:10.1016/j.ijhydene.2010.07.115.
26. BARROS Aruana R., ADORNO Maria AT., SAKAMOTO Isabel K., MAINTINGUER Sandra I., VARESCHE Maria BA., SILVA Edson L. Performance evaluation and phylogenetic characterization of anaerobic fluidized bed reactors using ground tire and pet as support materials for biohydrogen production. *Bioresource Technology*, 2011, Vol. 102, p. 3840–3847.
27. ZHANG Zhen P., TAY Joo H., SHOW Kuan Y., YAN R., LIANG David T., LEE Duu J., JIANG Wen J. Biohydrogen production in a granular activated carbon anaerobic fluidized bed reactor. *International Journal of Hydrogen Energy*, 2007, Vol. 32, p. 185–191.
28. AROOJ Muhammad F., HAN Sun K., KIM Sang H., KIM Dong H., SHIN Hang S.. Continuous biohydrogen production in a CSTR using starch as a substrate. *International Journal of Hydrogen Energy*, 2008, Vol. 33, p. 3289–3294.
29. DAS D., VEZIROGLU TN. Hydrogen production by biological process: a survey of literature. *Int J Hydrogen Energy*, 2001, Vol. 26, p. 13–28.
30. LAY JJ., LEE YJ., NOIKE T. Feasibility of biological hydrogen production from organic fraction of municipal solid waste.*Water Res*, 1999, Vol. 33, p. 2579–2586.

# ELABORATION OF SHORT-TERM WIND SPEED AND POWER PREDICTION MODEL FOR WIND FARMS IN LITHUANIA

**M. Marčiukaitis**
*Lithuanian Energy Institute*
*Breslaujos str. 3, LT-44403 Kaunas – Lithuania*
*Phone +370 37 401847*
*Email: mantas@mail.lei.lt*

## ABSTRACT

Wind power fully depends on the wind volatility and it is one of the most important issues compared to the traditional means of power generation. When wind power share in the electricity system is significant, balancing of the system becomes complicated as certain amount of reserve power (spinning reserve) must be constantly kept to compensate wind variations. This problem is usually solved by using short-term wind power prediction systems. Lithuanian wind farms generate about 2 % of total consumed electricity, and power system operator may face some network balancing problems, therefore wind farm power prediction becomes relevant. In this paper short-term wind power prediction model based on numerical weather prediction model HIRLAM data is developed and presented, impact of local topography on the accuracy of wind power predictions has been estimated. It has been determined that overall mean absolute prediction error (MAE) reaches about 10 % of Laukžemės wind farms' installed power, and the developed model can be used to evaluate wind power prediction accuracy for other wind farms.

## INTRODUCTION

Wind power share in electrical systems is increasing rapidly in most countries of the world, including Lithuania. There are more than 100 wind turbines (WT) installed in Lithuania with total power exceeding 160 MW. Most WT are installed in the western part of Lithuania (Kretingos, Skuodo, Tauragės, Mažeikių districts). In 2008 wind power comprised about 1%, in 2009–2010 – about 2% of country‘s gross electricity consumption.

Currently electricity generation from renewable energy sources comprises about 6% of all consumed electricity in Lithuania. EU directive 2001/77/EC obliged Lithuania to increase this share to 7% till 2010, but this target was not reached. New target is 23 % of primary energy to be produced using renewable energy sources till 2020. Future increase of electricity generation from renewable energy is mostly related with wind energy development. National Renewable Energy Development Strategy states that 500 MW of wind power should be installed till 2020. However, there is still no legal basis for the promotion and development of wind power and other renewable energy sources. New Law on Renewable Energy is pending at the Seimas of Lithuania.

As wind share in Lithuanian electricity system is increasing, system power operators are facing problems related to network balancing. These problems arise because wind is an intermittent source of power and fully depends on the meteorological conditions. Prediction of wind farms' power is a much more complicated task comparing to traditional power stations. Electrical utilities all over the world are beginning to realize the need for reliable wind power predictions, as it helps to cope with balancing issues and to allocate necessary spinning reserve power thus facilitating the dispatchers' work and scheduling of the total power production in the electricity grid. Also the experience of other countries has shown that in the liberalized markets wind power prediction influences the price of electricity generated from wind and allows wind power to compete with traditional means of power generation.

There are many short-term wind power prediction models and systems developed and currently operating in other countries [1, 2]. In general, these models can be classified as either using input data from a Numerical Weather Prediction (NWP) model or not using. Whether the inclusion of a NWP model data is necessary, depends on the prediction horizon required by the utility. Typically, prediction models using NWP forecasts outperform time series models after 3–6 hours look-ahead time [1]. Therefore, all models used by the utilities are based on this approach.

The aim of this work is to develop a short-term wind speed and power prediction model for wind farms and to carry out complex estimation of the influence of local topography and atmospheric stability conditions on the model accuracy.

## METHODS OF THE RESEARCH

**Characteristics of the object.** Laukžemės wind farm has been chosen for the development of short-term wind speed prediction model. Wind farm is located in Kretinga district and consists of 6 VESTAS V100 turbines: five turbines with nominal power of 2.75 MW and one with 2.25 MW. Wind farm is situated 12 km from the Baltic sea (Fig. 1).

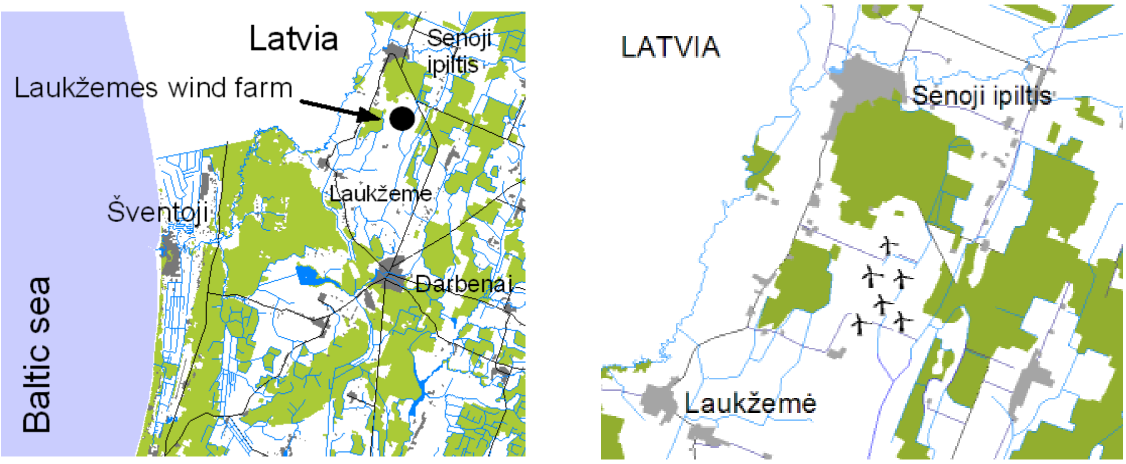

Fig. 1. Location of Laukžemės wind farm

Wind farm began its operation in May 2007. Wind speed measurement data (10 min averages) were taken from the cup anemometers on the nacelle. Power data was provided by Lithuanian electricity transmission system operator SC "LITGRID". Measurement period covers three months (from the 1st of June 2009 till the 30th of August 2009).

Physical method has been chosen for the analysis of short-term wind speed prediction accuracy requiring wind speed, direction, air temperature and other atmospheric parameters' data from a NWP model. These data were provided by the Lithuanian Hydrometeorological Service, where HIRLAM (High Resolution Limited Area Model) model has been used since 2006. Structure of the model used in this work is given in Fig. 2.

Wind speed prediction consists of several stages. First the best performing HIRLAM level is determined, and data from the four HIRLAM grid points are interpolated for the location of the wind farm. Then influence of local topography and atmospheric stability conditions on the accuracy of wind speed predictions is evaluated. Each factor is evaluated separately which allows to determine the most important factors and to adjust the model for a new wind farm. Then complex estimation of local effects is carried out. Model output statistics module uses multiple linear regression, which is a part of the statistical approach of the evaluation of the influence of atmospheric conditions on the prediction accuracy.

After these stages predicted wind speed for the hub-height is obtained. This wind is then converted to power with a power curve.

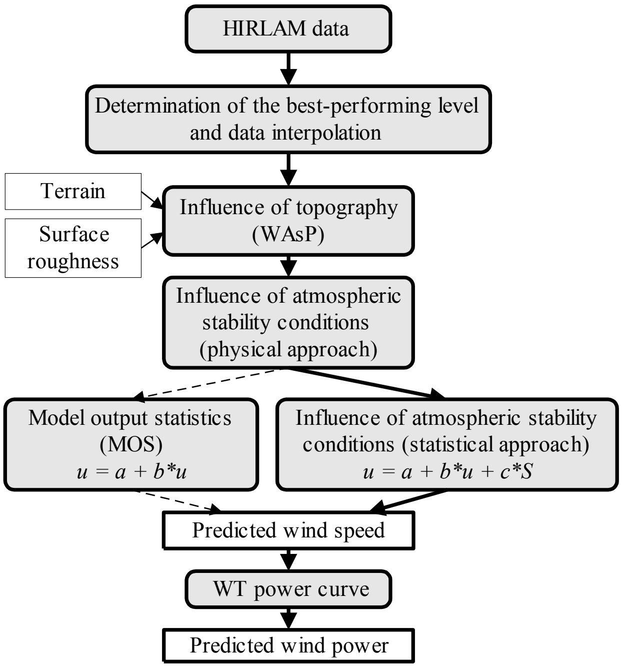

Fig. 2. Structure of the short-term wind speed and power prediction model

**Comparison of short-term wind speed prediction data and wind speed measurement data.** MATLAB software was used for the development of non-operational short-term power prediction model and for comparison of short-term wind speed prediction data and measured data and for the error calculation.

Two types of errors were used for the evaluation of wind speed prediction accuracy [4]: mean absolute error (MAE) and root mean squared error (RMSE):

$$MAE = \frac{1}{N}\sum_{1}^{N}\left|U_{meas} - U_{pred}\right| \; ; RMSE = \sqrt{\frac{1}{N}\sum_{1}^{N}(U_{meas} - U_{pred})^2} \, , \qquad (1)$$

where $N$ – number of data values; $U_{meas}$ – measured wind speed; $U_{pred}$ – predicted wind speed.

**Estimation of the influence of topography and atmospheric stability conditions on the wind profile.** Influence of topography on the wind speed prediction accuracy was estimated twofold: by using WAsP estimated effective roughness length $z_0$ for 12 direction sectors (30° each) and by multiplying predicted wind speed with the correction coefficients estimated by WAsP thus eliminating the influence of topography on the wind flow.

Influence of atmospheric stability conditions was estimated twofold as well: by physical and statistical methods. Physical method uses the same logarithmic profile, adding a function based on Monin-Obuchov similarity theory [5, 6]:

$$u(z) = \frac{u_*}{\kappa}\left(ln\frac{z}{z_0} - \psi\left(\frac{z}{L}\right)\right), \qquad (2)$$

where: $\psi$ – function of $\frac{z}{L}$; $L$ – Obuchov length parameter given as [5, 7]:

$$L = \frac{T_0 c_p u_*^3}{\kappa g H_0}, \tag{3}$$

where $T_0$ – surface temperature; $c_p$ – specific heat of air under constant atmospheric pressure (1004 $JK^{-1}kg^{-1}$); $u_*$ – friction velocity; $g$ – acceleration due to gravity; $H_0$ – heat flux towards the ground.

Functions for $\psi$ have been chosen as proposed by Badger et al. [5] and Jensen et al. [8].

$$\psi\left(\frac{z}{L}\right) = \begin{cases} \left(1-16\frac{z}{L}\right)^{\frac{1}{4}} - 1, & \text{when } L<0 \\ 0, & \text{when } L=\infty \\ -4{,}7\frac{z}{L}, & \text{when } L>0 \end{cases} \tag{4}$$

In neutrally stratified conditions the heat flux is zero, and wind speed at the desired height is calculated from the logarithmic profile.

The importance of atmospheric stability information was also tested statistically, using multiple regression. General expression is given as:

$$u_{corr} = a + b * u_{HIRLAM} + c * S_{HIRLAM}, \tag{5}$$

where $u_{corr}$ – corrected wind speed; $u_{HIRLAM}$ – HIRLAM wind speed; $S_{HIRLAM}$ – stability parameter; *a*, *b* and *c* – statistical parameters.

Atmospheric stability parameters tested are given as [5]:

$$\text{wind speed gradient} \quad S_u = \frac{u_h - u_l}{z_h - z_l}, \tag{6}$$

$$\text{potential temperature gradient} \quad S_\theta = \frac{\theta_h - \theta_l}{z_h - z_l}, \tag{7}$$

$$\text{Brunt-Väisala frequency} \quad N^2 = \frac{g}{\theta_h + \theta_l}\frac{(\theta_h - \theta_l)}{z_h - z_l}, \tag{8}$$

$$\text{wind speed average} \quad u_z = \frac{u_l + u_h}{2}, \tag{9}$$

where: *u* – wind speed; *g* – acceleration due to gravity; indices *h* and *l* refer to “higher” and “lower” HIRLAM levels; $\theta$ – potential temperature, given as:

$$\theta = T\left(\frac{p_0}{p}\right)^{\frac{R}{c_p}}, \tag{10}$$

where *T* and *p* – air temperature and atmospheric pressure of the air of interest; $p_0$ – standard pressure; *R* – universal gas constant (287 $JK^{-1}kg^{-1}$); $c_p$ – specific heat of air.

Systematic errors of the model were eliminated using a simple linear regression:

$$u_{corr} = a + b \cdot U_{HIRLAM} , \qquad (11)$$

where $u_{corr}$ – corrected wind speed; $a$ and $b$ – statistical parameters; $U_{HIRLAM}$ – HIRLAM wind speed. It should be noted that this expression was used for the elimination of systematic errors when estimating the impact of topography and applying physical method for estimation of the influence of atmospheric stability conditions. Multiple regression equation was used when estimating the influence of atmospheric stability conditions statistically (equation 5).

**Persistence model.** Errors obtained were compared with errors of the so-called *persistence model*. In this model, the forecast for all times ahead is set to the value now. Hence, by definition the error for zero time steps ahead is zero. For short prediction horizons (e.g., a few minutes or hours), this model is the benchmark all other prediction models have to beat. This is because the time scales in the atmosphere are in the order of days.

**HIRLAM data.** Data from the HIRLAM model were used for the development of the non-operational wind power prediction model. HIRLAM model is run every six hours (00, 06, 12 and 18 hour of the day). Every time predictions are generated for the horizon of 54 hours typically with 1-hour interval. Each time series of 54 hours length was compared with wind speed and power data by matching the corresponding dates.

## RESULTS AND DISCUSSION

The main purpose of the wind power prediction model development was to find factors leading to the smallest prediction errors. For this reason the influence of topography and atmospheric stability conditions on the accuracy of the predictions was evaluated. The reduction of errors indicates that the method applied was successful.

**HIRLAM data analysis.** HIRLAM model generates wind speed predictions in 60 vertical levels, therefore the best performing level had to be determined for the further analysis. Data from 6 lowest HIRLAM levels (up to 282 m) were used for the comparison of their prediction errors. Data from the HIRLAM point, closest to the wind farm were used.

Mean absolute error calculations were made in two cases. In the first case raw HIRLAM data were used, in the second case HIRLAM wind speed was transformed to the hub-height of wind farm's turbines (100 m) with a log-profile. Roughness value $z_0$ = 0.1 was used. In both cases model output statistics (MOS) was used for the elimination of systematic errors (equation 11). Results have shown that the smallest MAE was obtained when 90 m HIRLAM level was used (Fig. 3).

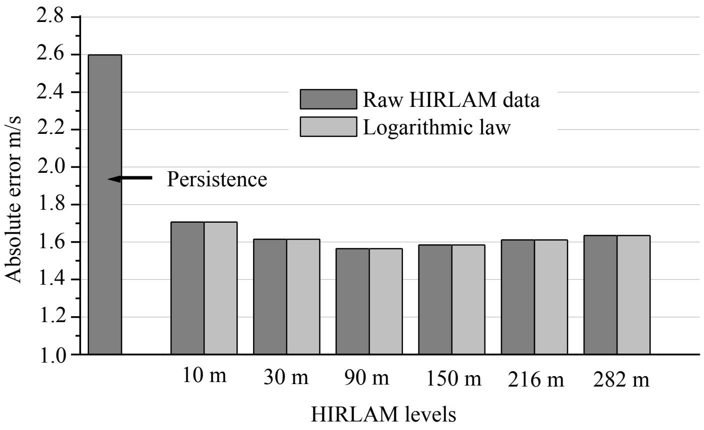

Fig. 3. Mean absolute wind speed prediction errors using data from different HIRLAM levels for Laukžemės wind farm

The most accurate predictions are obtained using data from the 90 m level – mean absolute error is 1.564 m/s. This error is significantly smaller than the error of persistence. Data from the 90 m HIRLAM level is used for further calculations.

As it was expected, mean errors increase with height. At the height of 10 m wind speed is strongly influenced by the topography, and due to HIRLAM resolution limitations wind flows are not simulated sufficiently well.

It should be noted that errors obtained using raw HIRLAM data and those transformed with logarithmic law are equal, because there is a linear relationship between wind speed at two heights. Therefore MOS, which is linear too, in both cases does all the job, and only regression function parameters are different.

HIRLAM model horizontal resolution is 7 km, which means that wind speed predictions are valid for an area of 49 km$^2$. Laukžemės wind farm is located in a relatively small area, therefore using data from the HIRLAM point closest to the wind farm contributes to the general prediction error. In order to eliminate this source of inaccuracy horizontal bilinear interpolation was performed which evaluates the contribution of wind speed prediction data from each of four HIRLAM points according to their distance from the wind farm. Results have shown that interpolation has reduced the mean error of the prediction by 2.6 % to the value of 1.524 m/s. Therefore interpolated prediction data are used in further analysis.

**Influence of topography and atmospheric stability conditions on the accuracy of wind speed predictions.** As mentioned above, values of surface roughness due to HIRLAM model resolution are calculated only every 7 km, and terrain height variation or roughness differences between grid points are “covered” under the average values, therefore smaller scale flow variations are not considered. For this purpose local scale terrain and surface roughness variation effects on the wind flow were estimated with WAsP9 software, which evaluates wind speed and direction changes caused by local topography variation. Coefficients of wind speed changes were calculated for 12 direction sectors (30º each).

Influence of topography was evaluated by multiplying raw HIRLAM data with WAsP coefficients and by using WAsP estimated $z_0$ for wind speed transformation to the hub-height.

Logarithmic law is valid mostly for neutral atmosphere stratification, but in reality atmospheric conditions often are far from neutral and change the shape of the vertical wind speed profile. Therefore it may be expected that without taking into account atmospheric stability conditions an additional error will be introduced when extrapolating wind speed from one height to another [5].

The influence of atmospheric stability conditions on the accuracy of wind speed predictions was evaluated using physical and statistical method. Physical method involves introducing stability function to the logarithmic profile (equation 2). This function contains Monin-Obuchov length $L$, which was calculated with the (3) formula. Statistical method uses multiple regression involving coefficients describing atmospheric stability conditions (equation 5).

Not all environmental effects may have a positive influence to prediction errors. As the main purpose of the analysis is to get the smallest errors, only the combinations of the effects leading to the best error improvement were selected. Calculated MAE errors were compared with those obtained without influence estimation (Table 1).

Results have shown that the error improvements are small (~ 1 %), but any change in average error indicates that these effects have influence on the prediction accuracy. Analysis has shown that multiple regression method has reduced prediction errors by 0.98%, while physical method – by 0.2 %, which suggests that statistical method, is more effective than the physical one. Possible reason is that atmospheric stability conditions are better described by wind speed and potential temperature gradients used in the statistical method.

Table 1. Influence of local topography and atmospheric stability conditions on the mean absolute errors of short-term wind speed prediction

| | Influence not estimated | Influence of topography | Influence of atmospheric stability conditions | |
|---|---|---|---|---|
| | | | Physical method | Statistical method |
| MAE m/s | 1.524 | 1.502 | 1.521 | 1.509 |
| Error improvement | - | -1.4% * | -0. % * | -0.9 % * |

* Minus sign means that error was reduced

In order to increase the error improvement, the evaluations of all effects were integrated in one algorithm, which makes the basis of the short-term wind power prediction model. Average mean absolute errors for all horizons are given in Fig. 4.

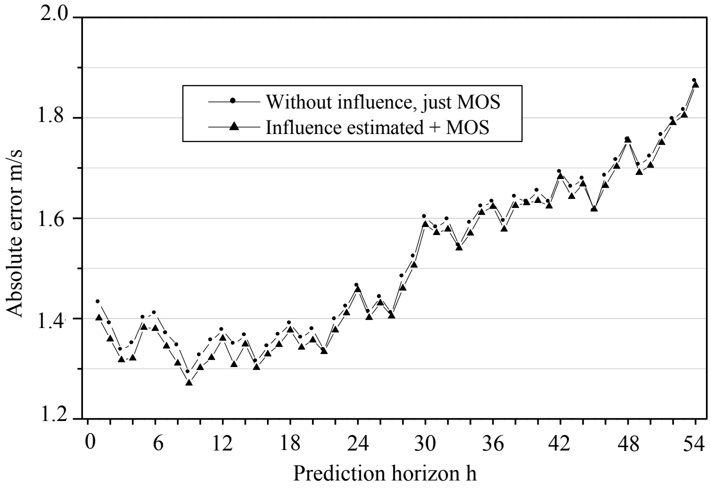

Fig. 4. Comparison of short-term wind speed mean absolute errors before and after the estimation of the general influence of topography and atmospheric stability conditions

It is seen from the Fig. 4 that estimation of the general influence of topography and atmospheric stability conditions has reduced MAE errors mostly for the horizons up to 18 hours. Mean absolute error of all prediction horizons decreased to the value of 1.498 m/s (1.7 % error improvement). It should be noted that mean prediction errors depend on the length of time series used for error calculation. The use of longer time series would lead to more reliable error estimates and smoother curves.

**The importance of model output statistics.** Systematic errors comprise part of short-term wind speed prediction errors. They were eliminated using simple linear regression. Regression function parameters were calculated using all available measurement data and corresponding raw HIRLAM data. Calculated MAE for all prediction horizons are given in Fig. 5.

After application of MOS mean absolute error of wind speed prediction has decreased by about 13 %, comparing with raw HIRLAM data scaled to the hub-height. Also it can be seen that model outperforms persistence only after 3 hours look-ahead time. This is typical for most wind power prediction models [1].

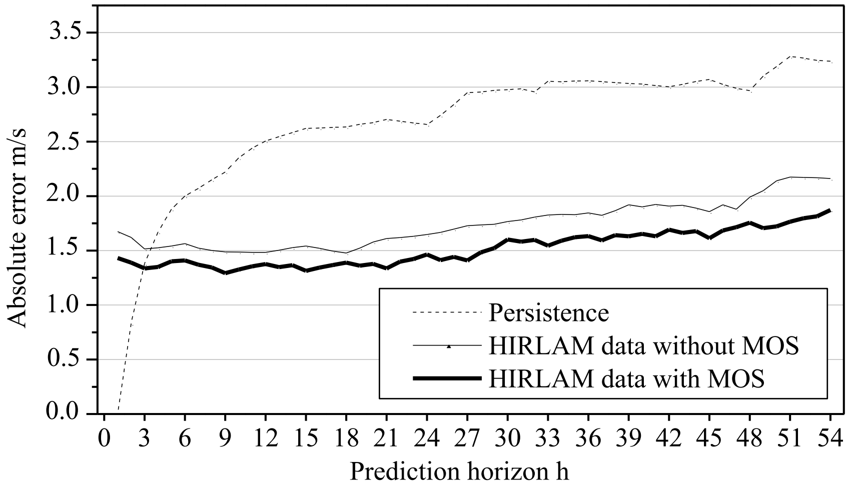

Fig. 5. Importance of MOS to mean wind speed prediction errors

**Conversion of the predicted wind speed to wind power.** Having evaluated the influence of topography and atmospheric stability conditions on the accuracy of short-term wind speed prediction, the last stage is conversion of the predicted wind speed to wind farm power. Theoretical (manufacturer's) power curve of wind farm was used for this purpose.

Predicted power was compared with measured Laukžemės wind farm power data. MAE as well as RMSE errors were calculated for every prediction horizon from 0 to 54 hours and averaged over full measurement period (3 months). Errors are expressed in percentage of the nominal wind farm power (Fig. 6).

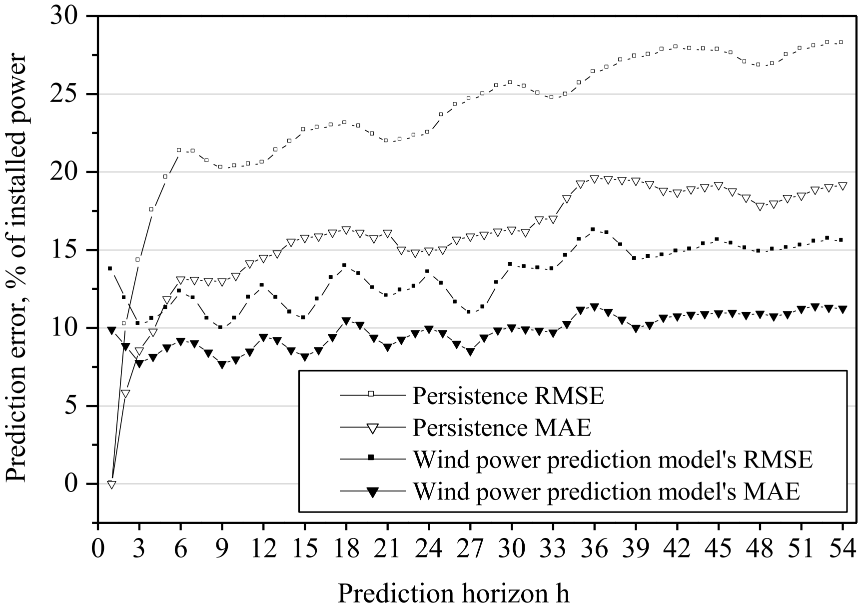

Fig. 6. Short-term wind power prediction errors for Laukžemės wind farm

Results show that wind power prediction average MAE error of all horizons equals to 9.8 % of nominal wind farm power (16 MW). These results agree with the results obtained by other authors, declaring MAE errors of about 10 % [9–13]. This confirms the suitability of the developed model to the prediction of Laukžemės wind farm's power and suggests that model can be applied to other wind farms in Lithuania. RMSE error varies from 10 to 17 %.

It is seen from Fig. 6 that for the horizon of 0–3 hours persistence model's MAE error is smaller than the error of the developed model. This is related with the processes in the atmosphere. It takes a few days for an air system to cross the Europe, therefore wind power prediction according to the last measured value is relatively accurate for the first few hours. However, when horizon exceeds 4–6 hours, even raw HIRLAM predictions are better.

Quality of the short-term wind power prediction model is also evaluated by estimating the error improvement with respect to the persistence model [4]. In order to quantify the error improvement, the improvement score was calculated:

$$IS = \frac{MAE_{pers.} - MAE_{model}}{MAE_{pers.}} \times 100\%, \tag{12}$$

where $IS$ is improvement score, $MAE_{pers}$ – MAE error of the persistence, $MAE_{model}$ – MAE error of the model. Improvement score was calculated for all prediction horizons (Fig. 7).

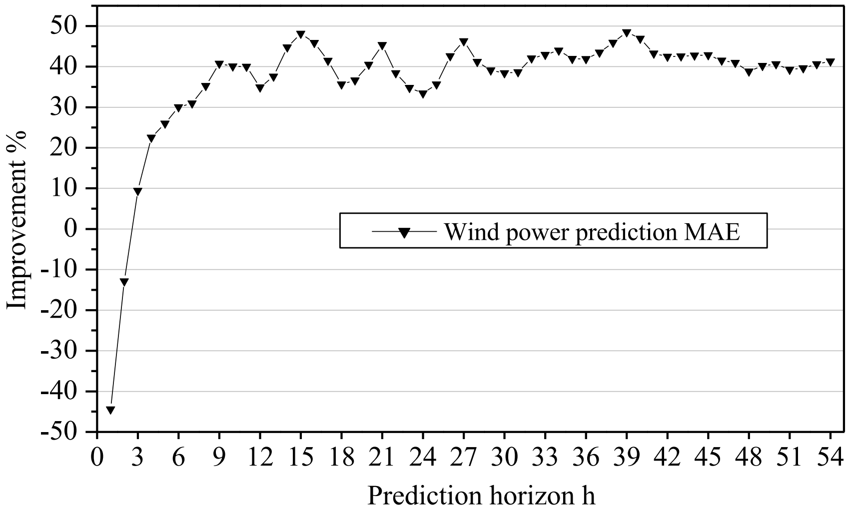

Fig. 7. Improvement of the developed short-term wind power prediction model over the persistence

Data in Fig. 7 show that mean error improvement for the first 3 hours is only 10%. Similar results for this horizon were achieved by other authors [1, 3, 14]. When prediction horizon exceeds 6 hours, MAE error improvement of 30-48 % over persistence is observed. This achievement is relatively low, which most likely was caused by the short time series used in the analysis. However, Madsen et al. [4] states that if prediction model is better than persistence, it can be used for wind power prediction and further improved.

Short-term wind power prediction model described in this work can be adjusted for other wind farms according to their local conditions. Also this model can be further improved by using longer time series of measurement data, directional statistical parameters, by modeling WT power curves, etc.

## CONCLUSIONS

1. A short-term wind speed prediction model has been developed for Lithuanian wind farms with the prediction mean absolute error of 1.498 m/s for Laukžemės wind farm. Such accuracy is typical for most wind speed prediction models in other countries.
2. Analysis of HIRLAM data application to short-term wind speed prediction has shown that model output statistics has the biggest influence on the reduction of mean prediction error. After the application of linear regression wind speed mean absolute errors reduced by 13 % for Laukžemės wind farm.

3. Results have shown that the influence of surrounding topography is more important than atmospheric stability conditions when predicting wind speed for Laukžemės wind farm. Consideration of these effects has reduced mean absolute prediction error by 1.41 % and 0.98 %, respectively.
4. Application of the short-term wind power prediction model to the prediction of Laukžemės wind farm power has revealed that mean absolute error averaged through all prediction horizons is 9.8 % of wind farm's nominal capacity. This achievement is similar to the errors of wind power prediction models in other countries and thus implies that the developed model is suitable for the prediction of other Lithuanian wind farms.

## REFERENCES

1. GIEBEL, G. *The State-Of-The-Art in Short-Term Prediction of Wind Power. A Literature Overwiev*. Project ANEMOS „Development of a Next Generation Wind Resource Forecasting System for the Large-Scale Integration of Onshore and Offshore Wind Farms“. Risø National Laboratory, Roskilde, Denmark. 2003. 36 p.
2. COSTA A, et al. A review on the young history of the wind power short-term prediction. Renewable and Sustainable Energy Reviews, 2007.
3. JOENSEN A. *Short-term wind power prediction.* PhD-Thsesis. Technical university of Denmark. 2002. 256 p.
4. MADSEN, H., PINSON, P., KARINIOTAKIS, G., NIELSEN, H.A., NIELSEN, T.S. Standardizing the Performance Evaluation of ShortTerm Wind Power Prediction Models. *Wind Engineering*, 2005, Vol. 29, No. 6, p. 475–489.
5. BADGER, J., et al. *Report on the use of stability parameters and mesoscale modelling in short-term prediction*. Risø-R-Report. Wind Energy Department, Risø National Laboratory, Technical University of Denmark. Roskilde, Denmark, 2007, 32 p.
6. FOCKEN, U., Heineman, D. Influence of Thermal Stratification on Wind Profiles for Heights up to 140 m. In *Proceedings from European Wind Energy Conference EWEC*, Madrid, 2003.
7. DYER, A.J. A review of flux-profile relationships. *Boundary Layer Meteorology*, 1974, No. 7, P. 363–372.
8. JENSEN, N. O., PETERSEN, E. L., TROEN I. Extrapolation of mean wind statistics with special regerd to wind energy applications. World Meteorological Organization, 1984.
9. COSTELLO, R. et al. Potential Benefits of Wind Forecasting and the Application of More CARE in Ireland. In *CD-Proceedings of the 3rd MED POWER Conference*, November 4–6, 2002, Athens, Greece.
10. GIEBEL, G., et al. Relative Performance of different Numerical Weather Prediction Models for Short Term Prediction of Wind Energy. In *Proceedings of the European Wind Energy Conference EWEC'1999*, March 1–5, 1999, Nice, France, p. 1078–1081.
11. DUTTON, A.G., et al. Load and Wind Power Forecasting Methods for the Optimal Management of Isolated Power Systems with High Wind Penetration. *Wind Engineering*, 1999, No. 23 (2), p. 69–87.
12. GIEBEL, G., et al. *Wind Power Prediction using Ensembles*. Risø-R Report. Risø National Laboratory, Roskilde, Denmark, 2005. 43 p.
13. JOENSEN, A., et al. Model Output Statistics Applied to Wind Power Prediction. In *Proceedings of the European Wind Energy Conference*, March 1–5, 1999, Nice, France, p. 1177–1180.
14. LANGE, M., FOCKEN, U. Physical approach to short-term wind power prediction. Report. Springer-Verlag, Berlin, 2006.

# IRON AND ALUMINIUM AS INHIBITORS OF ANAEROBIC DIGESTION OF PRIMARY-WASTE ACTIVATED SLUDGE MIXTURE

**S. Ofverstrom, I.Sapkaitė, R.Dauknys**
*Vilnius Gediminas technical university*
*Sauletekio av.11, LT-10223 Vilnius – Lithuania*
*Phone +370 605 27927*
*Email: svetlana.ofverstrom@vgtu.lt*

## ABSTRACT

Anaerobic digestion produces relatively stable biosolids at moderate cost and, as added benefit, produces biogas – renewable energy. Anaerobic digestion has wild variety of inhibitory substances, which could be cause of anaerobic digester upset or failure. Iron and aluminium salts are used at the treatment plants to reduce phosphorus in wastewater. As a consequence of chemical phosphorus removal, the volume of sludge increases, between approximately 37% and 97%. Laboratory analyses with anaerobic digestion model W8 (Armfield Ltd, UK) were made to investigate inhibition effect of iron and aluminium ions on anaerobic digestion of primary-waste activated sludge. Results showed that iron and aluminium negatively impacted anaerobic digestion process by reducing the volume of biogas produced. Fe-dosed sludge produced 20–50% less biogas and Al-Fe-dosed sludge produced 30-40% less biogas in comparison to the same un-dosed sludge. Volatile solids (VS) destruction decreased during dosing of Fe or/and Al salt. Biogas composition was not measured during the experiments.

Keywords: aluminium, anaerobic digestion, biogas, chemical phosphorus removal, inhibition, iron, primary-waste activated sludge, volatile solids destruction.

## 1. INTRODUCTION

Municipal and industrial wastewaters often have high concentrations of phosphorous containing compounds. Orthophosphates, polyphosphates, and organic phosphates are the main forms of phosphorous that are present in wastewaters. If these wastewaters are not treated to remove phosphorous, nutrient enrichment of both groundwater and surface waters may occur leading to detrimental effects on water quality and eutrophication of surface water bodies. For this reason, many countries have adopted strict discharge limits concerning phosphorous in wastewaters [1].

The most common chemicals used for chemical phosphorus reduction are aluminium and iron salts. Ferric chloride ($FeCl_3$) and ferrous sulphate ($FeSO_4$) are the most used iron salts to remove phosphorous. [1, 2] Iron is essential or the growth of microorganisms as it forms an important component of many of the enzymes involved in the metabolic pathways of the bacteria. Methanogens have a specific growth requirement or iron. However, in more than trace amounts, iron is generally considered to be one of the toxic heavy metals [3]. Information in the literature about the effect of aluminium on anaerobic digestion is minimal. The mechanism of aluminium inhibition was reported to be due to its competition with iron and manganese or to its adhesion to the microbial cell membrane or wall, which may affect microbial growth [4, 5]. $Al^{3+}$ could be tolerated by anaerobes after acclimation [6].

Chemical phosphorus removal can produce three times more sludge (by mass) in comparison to an un-dosed depending on the dosing location (more sludge is generated from pre-precipitation than from post-precipitation [7].

Anaerobic digestion produces relatively stable biosolids at moderate cost and, as added benefit, produces biogas – renewable energy. Recent changes in our economy, especially the high prices of fossil fuels, was increased interest in use o RES including biogas. In Lithuania there are above 50 wastewater and sewage treatment plants and only several had special tanks for anaerobic digestion [3]. Nowadays a lot of anaerobic digesters will be built over the Lithuania. As produced by digestion, biogas is a clean and environmentally friendly fuel, although it contains only about 55–65% of $CH_4$. Other constituents include 30–40% of $CO_2$, fractions of water vapour, traces of $H_2S$ and $H_2$, and possibly other contaminants. Without further treatment, it can only be used at the place of production. There is a great need to increase the energy content of the biogas, thus making it transportable over larger distances if economically and energy sensible. Ultimately, the compression and use of gas cylinders or introduction into the gas network are targets. This enrichment and enhanced potential of use can only be achieved after removing the $CO_2$ and contaminants [7].

The effect of both iron and aluminium on anaerobic digestion efficiency has been studied by a number of investigators with conflicting results [8, 9, 10, 11]. Present study was undertaken to investigate possible inhibition effect of iron and aluminium ions on anaerobic digestion of primary-waste activated sludge mixture.

## 2. MATERIALS AND METHODS

The primary and waste activated sludge were collected from Vilnius waste water plant (Lithuania) with nitrogen removal technology. Primary sludge was taken from the primary sludge pumping station before thickening and waste activated sludge was collected from the distribution chamber of secondary sedimentation tank. Fresh sludge was taken from the plant every 5th day to avoid changes in sludge characterization and then stored in a refrigerator at +4°C. The proportion was 1:2 (volume basis) primary and waste activated sludge. The average characteristics of the primary-waste activated sludge mixture feed are shown in Table 1.

Table 1. Average characteristics of the sludge mixture fed to digesters

| **Parameter** | **Total solids (TS), g/L** | **Volatile solids (VS), g/L** | **pH** | **VS loading, gVS/L/d** |
|---|---|---|---|---|
| Sludge mixture | 15.8–23.8 | 11.6–17.4 | 6.03–6.34 | 0.67–0.88 |

The feed was screened with a sieve to avoid large particles and was not thickened due to narrow tubes (4 mm) of peristaltic pumps. Total solids (TS) concentration in sludge mixture was 1.6–2.4%. Regular analysis was performed to determine the characteristics and consistency of the feed material.

Experiments were performed at Vilnius Gediminas technical university (Lithuania) using the anaerobic digestion model W8 (Armfield Ltd, UK). This model consist of two separate high-rate digesters 4.8 L each. Reactors were continually mixed using internal mechanical stirrer. The flow rates to the vessels are set and controlled by calibrated peristaltic pumps. The temperature of each reactor was controlled by an electric heating mat wrapped around the external wall. The gas off-take from each reactor was taken into a volumetrically calibrated collector vessel (300 ml) operating by water displacement (see Fig. 1.).

Each reactor was inoculated with anaerobic inoculum obtained from the previous experiment with anaerobic digestion of primary-waste activated sludge mixture [12]. During feeding 0.24 L of sludge mixture was pumped through the system simultaneously using peristaltic pumps, volatile solids loading was 0.67-0.88 gVS/l/d with average 0.76gVS/d). Sludge was not thickened due to small diameter of tubes of pumps. The reactors were fed daily 6 hours per day. Anaerobic digestion was made under mesophilic conditions at 35°C with a solids retention time (SRT) of 20 days.

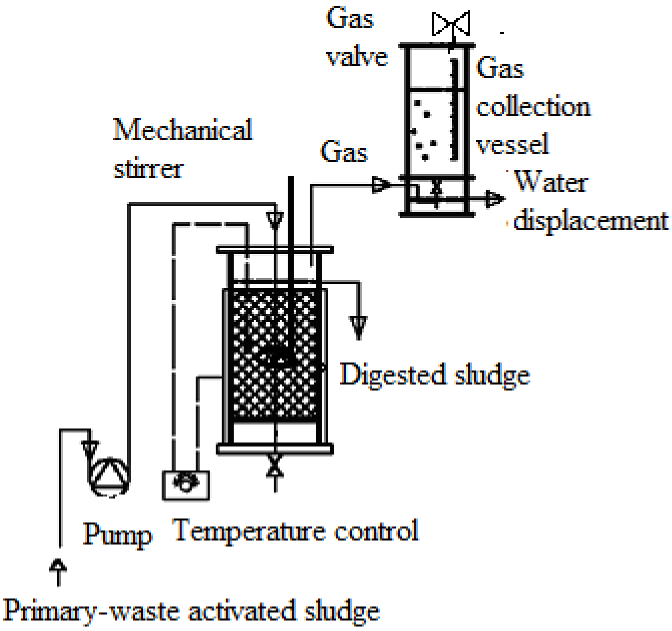

Fig. 1. cheme of anaerobic digestion model W8 (Armfield Ltd, UK)

Laboratory analyses were made during April-June 2010 period. Total amount of experiments were three – anaerobic digestion of un-dosed, Fe-dosed and Al-Fe-dosed sludge mixtures. Doses of Fe and Al were selected according to Gothenborg (Sweden) WWTP average amounts of Fe and Al in digested sludge during 2008 year. It was obtained that the amount of Fe was 52–81 mgFe/gTS and Al was 13–29 mgAl/gTS. Minimum and maximum doses selected were 50 and 100 mgFe/gTS and 15 and 30 mgAl/gTS. The average concentration of TS in digested sludge mixture was 16.8gTS/L. Selected Fe and Al salts for experiment were $FeCl_3 \cdot 6H_2O$ and $Al_2(SO_4)_3 \cdot 18H_2O$ and they were dosed daily into the feed sludge mixture (See Table 2).

Table 2. Selected experimental doses of Al and Fe salts

| **Reactor** | **Fe (III), mg/gTS** | **$FeCl_3 \cdot 6H_2O$, g/L** | **Al (III), mg/gTS** | **$Al_2(SO_4)_3 \cdot 18H_2O$, g/L** |
|---|---|---|---|---|
| I | 50 | 4.17 | 15 | 0.19 |
| II | 100 | 8.34 | 30 | 0.37 |

Process performance was routinely monitored by measurement of pH, influent and effluent TS and VS, alkalinity (ALK), volatile fatty acids (VFA), biogas production. The composition of biogas produced was measured in the beginning of the experiment but stopped due to problems with equipment. Volatile solids destruction (%) was calculated during experiment. During anaerobic digestion process, volatile solids are degraded to a certain extent and converted into biogas. The sludge volume is hereby reduced. The degree of stabilization is often expressed as the percent reduction of volatile solids. Volatile fatty acids (VFA) are the most important intermediates in the AD digestion process, where they are degraded by proton-reducing acetogens in association with hydrogen consuming methanogenic bacteria. All the analysis performed according to Standard Methods [13].

## 3. RESULTS AND DISCUSSION

An examination of digested sludge mixture alkalinity, volatile fatty acid and pH data showed that there was significant reduction of alkalinity in digesters receiving chemically derived sludge with maximum dose of Fe or Al-Fe (see Table 3). That could be probably because of $FeCO_{3(s)}$ precipitation:

$$FeCl_3 + CO_3^{2-} \Leftrightarrow FeCO_{3(s)} + 3Cl^- \quad (1)$$

Associated with this lower alkalinity (500–650 mg/L for Fe-dosed and 300–400 mg/L for Fe-Al dosed sludge mixture) pH was lower than in control digester.

Table 3. Average characteristics of the anaerobic sludge

| **Parameter** | **Control digester** | **Fe-dosed sludge (min)** | **Fe-dosed sludge (max)** | **Fe-Al-dosed sludge (min)** | **Fe-Al-dosed sludge (max)** |
|---|---|---|---|---|---|
| ALK, mg/L | 1250-1750 | 900-1350 | 500-650 | 700-1000 | 300-400 |
| VFA, mg/L | 120-300 | 180-240 | 120-180 | 180-300 | 180-250 |
| pH | 6.80-7.07 | 6.52-6.72 | 6.25-6.32 | 6.52-6.80 | 6.06-6.26 |
| TS, g/L | 17.8-23.8 | 17.6-23.2 | 24.4-32.2 | 22.2-22.5 | 24.0-24.5 |
| VS, g/L | 12.2-19.4 | 12.2-14.4 | 18.0-19.8 | 15.6-16.8 | 15.4-17.0 |
| VS destruction, % | 21-32 | 14-18 | 13-14 | 12-17 | 13-14 |
| Biogas production, ml/gVS | 132-197 | 105-163 | 64-103 | 142-164 | 109-125 |

During digestion of un-dosed sludge mixture VS destruction calculated was 21–32%. VS destruction of VS destruction of Fe-dosed sludge was from 14–18% and 13–14% for minimum and maximum dosed sludge. VS destruction of Al-Fe-dosed sludge mixture was 12–17% and 13–14% for minimum and maximum doses accordingly.

Daily biogas productions (ml/gVS) from un-dosed and Fe-dosed sludge mixture are shown in Fig. 1 as 4-days running averages. Biogas production from un-dosed primary and waste-activated sludge mixture was from 132 mL/gVS to 197 mL/gVS, depending on VS load of fed sludge mixture. The other reason for this variation - primary sludge could vary considerably, depending on the characteristics of the solids in the wastewater, the types of units etc. Within first days of addition of Fe salt to fed sludge mixture biogas production decreased to about 20–25% and 50% for Fe-dosed sludge with minimum and maximum doses. Biogas production varied less from Fe-dosed sludge (maximum dose) and remained depressed during all the experiment. Biogas production from Fe-dosed sludge with minimum dose of Fe salt increased from approx. 12–15 day of experiment and until the end of experiment was close to biogas production from un-dosed sludge mixture.

The same dosed of Fe salt were dosed to feed sludge continuously during the third experiment. At the same time addition of Al salt started. During addition of both Al and Fe salts to feed sludge mixture biogas production from Al-Fe-dosed sludge increased approx. 10–20% compare to biogas production from Fe-dosed sludge (see Fig. 3). Fig. 3 shows weak correlation between dosing of Al and Fe salts and produced biogas possibly because of decreased pH during the experiment. This was able to effect biogas production.

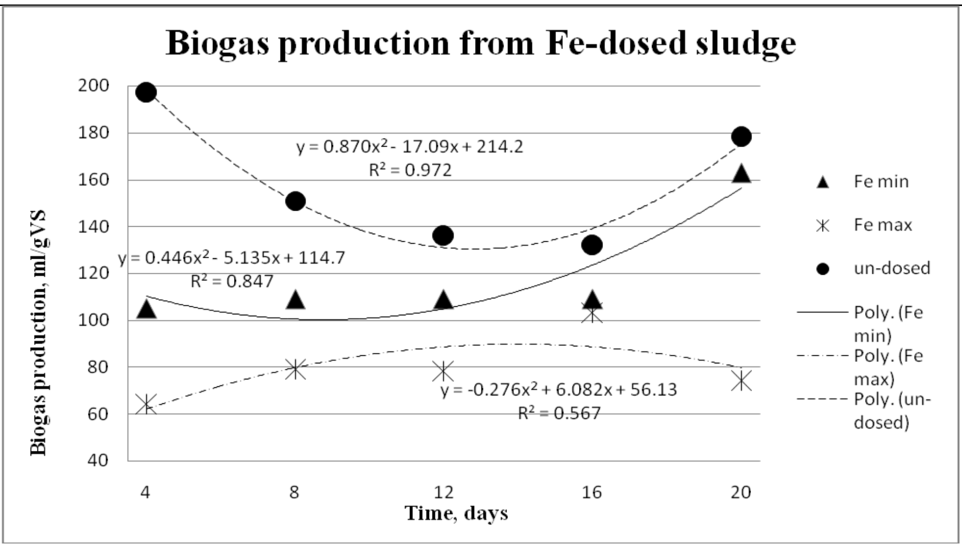

Fig. 2. Biogas production from un-dosed and Fe-dosed sludge mixture

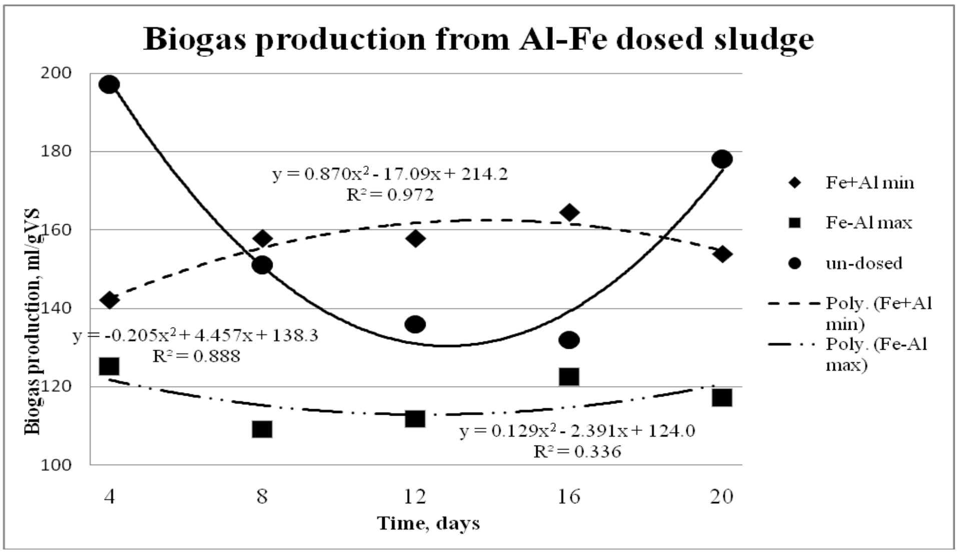

Fig. 3. Biogas production from un-dosed and Al-Fe-dosed sludge mixture

## 4. CONCLUSIONS

The effects of iron and aluminium salt addition to primary-waste activated sludge mixture were investigated through experimental studies. The following conclusions are drawn from this study:

- The addition of Fe salt for chemical phosphorus control may inhibit anaerobic digestion process.
- Results showed that iron and aluminium negatively impacted anaerobic digestion process by reducing the volume of biogas produced.
- Fe-dosed sludge produced 20–50% less biogas and Al-Fe-dosed sludge produced 30–40% less biogas in comparison to the same un-dosed sludge.
- Volatile solids destruction decreased during dosing of Fe or/and Al salt. VS destruction from Fe-dosed sludge mixture was up to 30%.
- Addition of $Al_2(SO_4)_3 \cdot 18H_2O$ raised biogas production up to 10–20% compare to biogas production from Fe-dosed sludge.

- For better understanding of inhibition effect of Al and Fe ions on anaerobic digestion process of primary-waste activated sludge mixture it‘s necessary to make biogas composition analysis.

## REFERENCES

1. CARLIELL-MARQUET, C., SMITH, J., OIKONOMIDIS, I., WHEATLEY, A. Inorganic profiles of chemical phosphorus removal sludge. *Water Management*, 2010, Vol. 163, Nr. 2, p. 65–77.
2. JACKSON-MOSS, C. A.; DUNCAN, J. R. The effect of iron on anaerobic digestion. *Biotechnology Letters*,1990, Vol. 12, Nr. 2, p. 149–154.
3. KATINAS, V., MARKEVICIUS, A., KAVALIAUSKAS, A. Current status and prospects of biomass resources for energy production in Lithuania. *Renewable Energy*, 2007, Vol. 32, p. 884–894.
4. CHEN, Y., CHENG, J.J., CREAMER, K.S. Inhibition of anaerobic digestion process: A review. *Bioresource Technology*, 2008, Vol. 99, p. 4044–4064.
5. CABIROL, N., BARRAGÁN, E.J., DURÁN, A., NOYOLA, A. Effect of aluminium and sulphate on anaerobic digestion of sludge from wastewater enhanced primary treatment. Water Science and Technology, 2003, Vol. 48, Nr. 6, p. 235–240.
6. JACKSON-MOSS, C.A., DUNCAN, J.R. The effect of aluminium on anaerobic digestion. *Biotechnology Letters*, 1991, Vol. 13, Nr. 2, p. 143–148.
7. APPELS, L., BAEYENS, J., DEGRÈVE, J., DEWIL, R. Principles and potential of the anaerobic digestion of waste-activated sludge. 2008, Vol. 34, p. 143–148.
8. NOVAK, J. T., VERMA, N., MULLER, C.D. The role of iron and aluminium in digestion and odor formation. *Water Science and Technology*, 2007, Vol. 56, Nr. 9, p. 59–65.
9. NOVAK, J.T., PARK, C.M. The effect of iron and aluminium for phosphorus removal on anaerobic digestion and organic sulfur generation. *Water Science and Technology*, 2010, Vol. 62, Nr. 2, p. 419–426.
10. SMITH, J. A., CARLIELL-MARQUET, C. M. 2009. A novel laboratory method to determine the biogas potential of iron-dosed activated sludge. *Bioresource Technology*, 100: 1767–1774.
11. SMITH, J. A., CARLIELL-MARQUET, C. M. The digestibility of iron-dosed activated sludge. *Bioresource Technology*, 2008, Vol. 99, p. 8585–8592.
12. OFVERSTROM, S., SAPKAITĖ, I., DAUKNYS, R. Research and analyses of anaerobic digestion of Vilnius WWTP sludge mix. 2010. Proceedings of the 13th conference of Lithuanian Junior Researches Science for the Future: Engineering Systems for Buildings. Vilnius: Lithuania, Technika. 2010 April 15–16, p. 72–75.
13. APHA. 2000. Standard Methods for the Examination of Water and Waste water. 18th ed. Washington DC. USA: American Public Health Association/American Water Works Association. Water Environment Federation.

CYSENI 2011, May 26–27, Kaunas, Lithuania
ISSN 1822-7554, www.cyseni.com

# WIND ENERGY PARAMETER VARIATION REGULARITIES IN LITHUANIAN COASTAL ZONE

**D. Sankauskas**
*Lithuanian Energy Institute*
*Breslaujos str. 3, LT-44403 Kaunas – Lithuania*
*Phone +370 616 25100*
*Email: d.sankauskas@mail.lei.lt*

## ABSTRACT

The primary meteorological station data summary shows that the maximum wind speeds are in the coastal area of Lithuania. A wind measurement station "WICOM-C (made in Germany), which allows to capture wind speed and direction each second, was installed for evaluation of wind power plant construction potential. Measurements were taken 25, 45 and 65 m above ground. Wind direction measured at a height of 30 m.

A correlation analysis of meteorological stations and measurement data was collected, and assessment of the region's suitability for wind power station construction was performed. Investigations were carried out according to the West European standards, consequently, results can be used to select optimal wind turbine sites, predict their energy output, create operation schedules, and to predict possibilities of their use and evaluate the payback period.

Keywords: Wind energy, wind speed measurement, wind power plants.

## 1. INTRODUCTION

Distribution of wind energy resources in Lithuania has not been suitably analysed. Primary evaluation of wind energy resources has been performed, and data from earlier works enable making only approximate evaluations of average wind speed variation receding from the Baltic Sea. Therefore, considering increasing popularity of wind energy, systemic investigations of wind energy resources are needed, especially in the coastal region, where development of wind power plant parks is foreseen. In the investigation of loads on rotors and lifetime of wind power plants, variation of wind parameters, formation of wind speed profiles must be analysed, considering harshness of earth surface and density of constructions in the territory and formation of wind fluxes behind natural and urban barriers.

## 2. RESEARCH AND METHODOLOGY

For evaluation of wind flow parameter variation, a wind parameter measurement station was installed in Giruliai. A wind speed and direction measurement installation “WICOM-C” [1, 2] containing three cup anemometers, one direction measurer and a data registration computer, was constructed in 1.5 km from the Baltic sea.

This measurement installation enables wind speed and direction measurements in one second intervals. For calculations and statistical analysis to be performed in this work, wind parameters were measured in 10 second intervals, averaged and recorded in the computer. Measurements are performed in 25, 45 and 65 m above the earth surface. Wind direction is measured in 30 meters above the earth surface. For evaluation of wind turbulence parameters, wind speed measurements results of a few months were used. A statistical analysis of measurement data is performed and research results are presented.

Measurements are performed according to requirements of European standards, therefore, wind power plants of optimal capacity can be selected and energy output and payback period can be evaluated.

The average wind speed of 10 minutes is given by the formula [1]:

$$V_{vid.} = \frac{\sum_{i=1}^{k} V_i}{k} \tag{1}$$

$V_i$ – instant measured value of wind speed in the fixed moment (m/s); $k$ – number of fixed values, $k$ = 1, 2,..., 60.

Standard deviation of wind speed is calculated according to the formula:

$$\sigma = \sqrt{\frac{\sum_{i=1}^{k} \left(V_{vid.} - V_i\right)^2}{(k-1)}} \tag{2}$$

The level of wind flow turbulence (Tu) is expressed:

$$Tu = \frac{\sigma}{V_{vid.}} \cdot 100, \quad \% \tag{3}$$

## 3. RESEARCH RESULTS

Various urban objects (buildings etc.), natural barriers, relief of earth surface (flat or hilly) and sprouts (high grass, bushes, single trees, forests) have quite large influence for calculations of wind speed and direction in the selected area. Having measurement data in various heights, main statistical wind characteristics were calculated, namely, minimum, average and maximum wind speed in a month. As the Fig. 2 shows, day wind speed variation in a month is not large, however, when a longer term is analysed, larger wind speed pulsations can be noticed (Fig. 1).

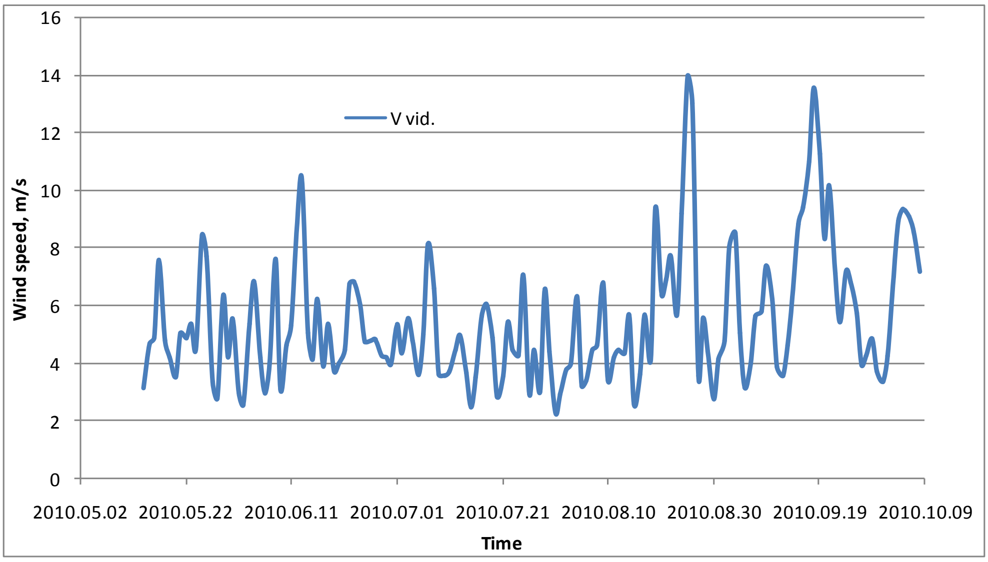

Fig. 1. Average wind speed in 65 m height (Giruliai, 2010)

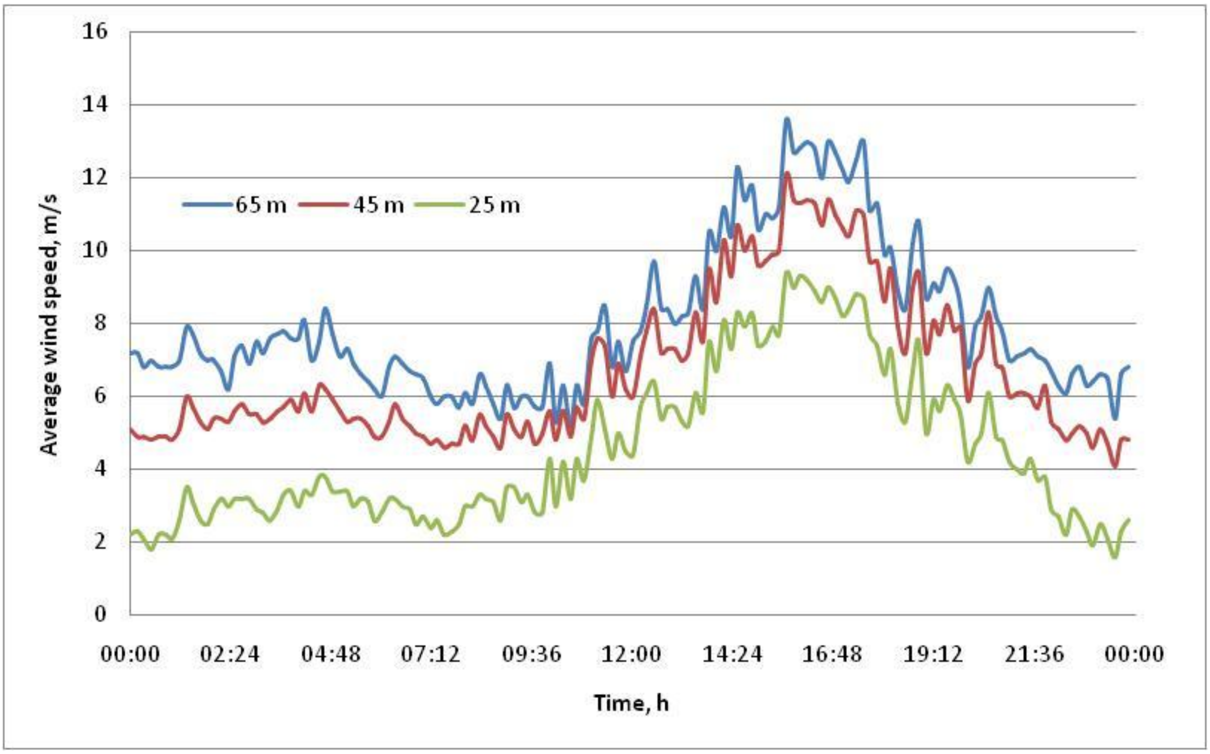

Fig. 2. One day average wind speed at different heights (Giruliai, September 2010)

Processed measurement results show that wind speed in different heights is layered orderly, i.e., the average wind speed at the same time instant is getting higher with growing elevation. It must be noted that wind speed in 25 m elevation is much lower than in other elevations. This means that local topographic conditions have larger impact for wind flow in 25 m elevation, and the impact of earth surface harshness and barriers is lower in higher elevations.

The zone from 1 p.m. to 7 p.m. is clearly distinguished in the wind speed profile. This is partially related to processes in the atmospheric bounder layer during the day: earth surface is heated more in the day time than in the night time; consequently, flows are influencing wind speed more intense.

Measurement data show that wind speed is fluctuating constantly and is characterized by various pulsations, which have negative impact on the work of a wind power plant rotor and decrease life time of the whole wind power plant installation. In case of a turbulent wind flow, its kinetic energy is variating, an unevenly distributed wind flow around rotor blades unevenly, consequently, dynamic loads affecting the rotor and decrease energy performance parameters of the wind power plant. Wind speed pulsations are defined by the average standard deviation and the turbulence (Fig. 3, 4, 5).

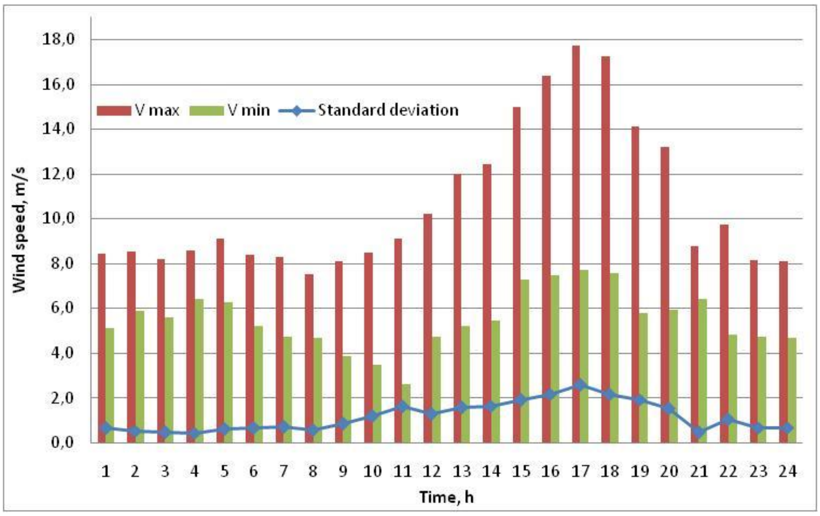

Fig. 3. Maximum and minimum wind speeds and standard deviation of a day (Giruliai, September 2010)

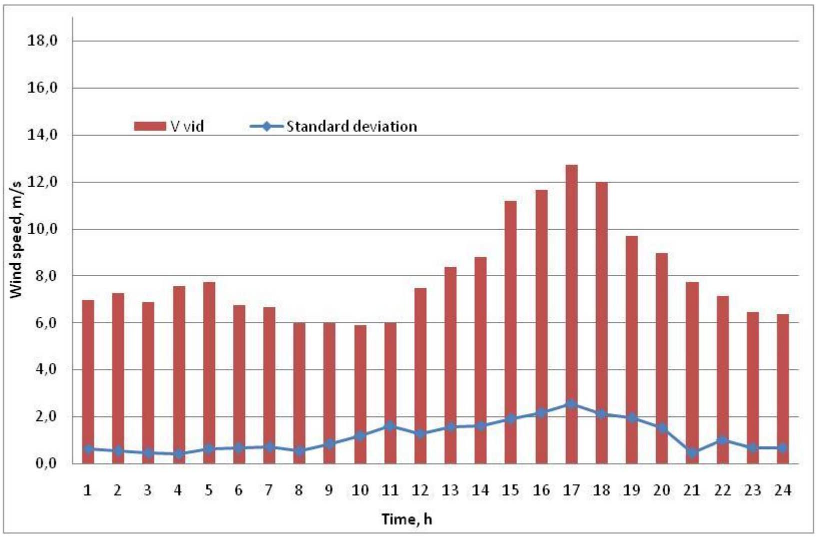

Fig. 4. Average wind speed and standard deviation of a day (Giruliai, September 2010)

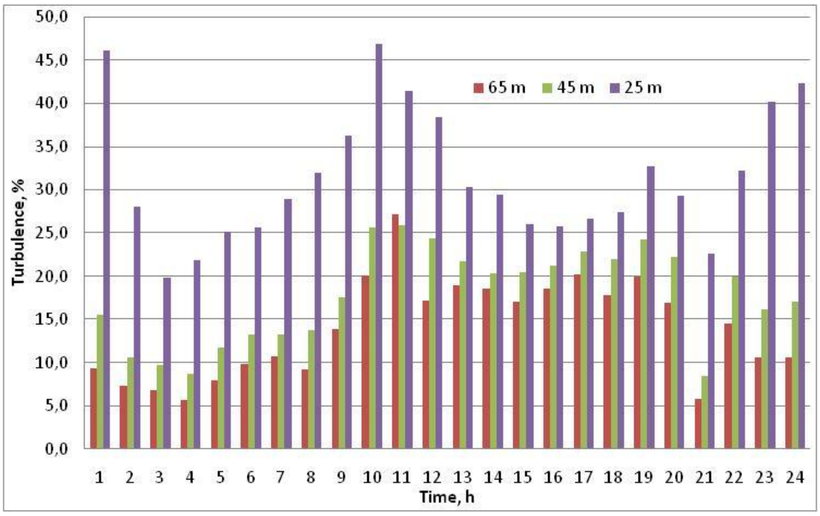

Fig. 5. Wind turbulence level at the different elevations (Giruliai, September 2010)

Flow turbulence is higher closer to the earth surface than in higher elevations due to local barriers. Wind speeds at 25 m of heights is much lower, and wind speed difference is lower in higher elevations. The graph of wind turbulence (Fig. 5) shows these analogies, however, the difference of turbulence is even large than wind speed difference. In higher elevations, turbulence changes slower with changing elevation, though the change of turbulence in a day is larger in higher elevations (turbulence can differ in 4 to 5 times in 60 m elevation, while it varies up to two times in 25 m elevation).

Most often occurring wind speeds in the month period are from 4 to 7 m/s (Fig. 6). Such distribution of wind speed can be described best by the Weibull cumulative distribution function [3]:

$$f(v) = 1 - e^{-\left(\frac{v}{a}\right)^{k}} = 1 - e^{-Av^{k}}; \tag{4}$$

here $A = \frac{1}{a^k}$; $a$ and $k$ – parameters of the function of Weibull cumulative distribution function.

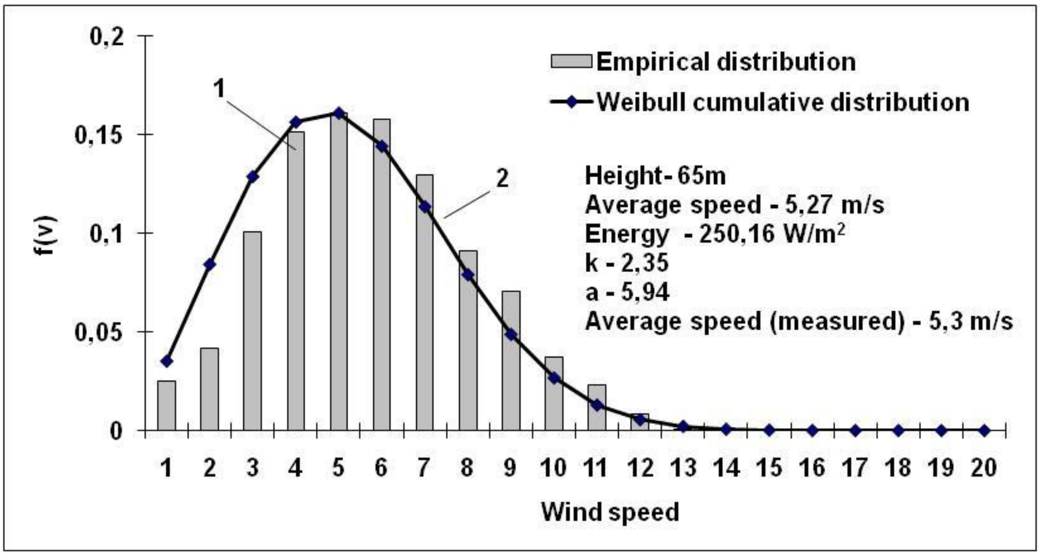

Fig. 6. Generalization of wind speed variations using Weibull distribution

Various calculation methods can be used for calculation of Weibull distribution parameters, though the method of least squares estimation is used most often. The empiric distribution function is defined using wind speed measurement results in the selected area of a few years calculated using this method.

In order to estimate wind speed in the selected elevation, an assumption is made that probability distribution of wind speed in different elevations depends for the same type of Weibull distribution function. In this case, the association between Weibull parameters $(a_{h1}, k_{h1})$ and $(a_{h2}, k_{h2})$ is an expressed using following equation:

$$a_2 = \alpha \cdot a_1^{\beta}; \tag{5}$$

$$k_2 = \frac{k_1}{\beta}; \tag{6}$$

$$\text{Here: } \alpha = \left(\frac{h_2}{h_1}\right)^{B_0}; \tag{7}$$

$$\beta = 1 + B_1 \cdot \ln\left(\frac{h_2}{h_1}\right). \tag{8}$$

$\alpha$ = $V_2/V_1$ – parameter for the characteration of the wind profile power law relationship, where

$V_2$ – the wind speed (m/s) at height $h_2$, m;
$V_1$ – the known wind speed at a reference height $h_1$, m;
$B_0$, $\beta$, $B_1$ – empirically derived coefficients. For neutral stability conditions, $B_0$ is approximately 1/7.

Based on the measurement data of wind parameter investigations, the energy flow delivered to the rotor and its variation can be estimated. This would enable estimation of wind flow impact for the wind power plant rotor, selection of the wind power plant model most suitable for the evaluated region, estimation of the planned lifetime of the wind power plant, annual energy generation and calculation of the economical effect of the wind mill.

## 4. CONCLUSIONS

Wind flow speed is measured, and wind speed changes with changing height from the earth surface. The change of wind speed is faster in layers located closer to the earth surface due to the influence of roughness of the earth surface and other factors.

The change of wind flow turbulence changes analogically, as the wind speed. The essential difference is that the change of turbulence in a day period is lower than in layers located higher.

As wind speeds are distributed in such way that most often occurring wind speeds are 4 to 7 m/s, this distribution can be described best using Weibull distribution density function. When Weibul parameters are found in one height, wind speed can be calculated for other heights.

## REFERENCES

1. Wicom–C datalogger // Ammonit Gesellschaft fur Messtechnik. Berlin, 1994. 63 p.
2. Ammonit // http://www.ammonit.de/english/page2.html.
3. Fortus M. I. Methods of statistical description of wind regions annexing to wind energy. Preprint No. 6. Moscow: USSR Academy of sciences. Institute of atmospheric physics. 1990. 72 p.

CYSENI 2011, May 26–27, Kaunas, Lithuania
ISSN 1822-7554, www.cyseni.com

# DETERMINATION OF COST-EFFECTIVE PIPELINES INSULATION OF SOLAR THERMAL SYSTEM

**P. Shipkovs, A. Snegirjovs, M. Vanags**
*Institute of Physical Energetics*
*Aizkraukles 21, LV-1006 Riga – Latvia*
*Phone +371 67 558620*
*Email: shipkovs@edi.lv*

**L. Migla**
*Riga Technical University*
*Azenes 16/20, LV-1048 Riga – Latvia*

## ABSTRACT

Solar radiation intensity in the Baltic region is lower in comparison with the average European values. The average solar radiation intensity reaches 1100 kWh/m$^2$ per year in Baltic region. And outdoor air temperature range is below average values in Europe. Range of outdoor air temperature in the Baltic region is -3 $^o$C in winter and +16 $^o$C in summer. Therefore, there is a particular need to optimize the solar thermal system in the Baltic region.

A certain proportion of the solar thermal system generated energy is consumed as the heat loss in pipes between the solar energy absorbing devices to the heat-accumulation tank.

Pipeline isolation of solar thermal system is necessary for both outdoor and indoor pipes. Outdoor heat pipe isolation reduces systems heat losses in the environment. While, indoor heat pipe isolation reduces value of unnecessary energy distribution indoors in the summer period.

The amount of pipeline heat energy losses dependence on the pipeline isolation type of solar thermal system was determined with the PolySun simulation program models.

The most popular heat pipe insulation materials in Baltic region were inspected and compared. They were compared and shown in table form by the thermal conductivity coefficient and the price.

The amount of absorbing energy value and heat losses are calculated and displayed in the graphic form.

As a result the method was created. The method can determine most cost-effective solar thermal systems pipe insulation type.

Keywords: Renewable Energy; Solar thermal systems; efficiency increasing, Heat loss.

## 1. INTRODUCTION

The Baltic States climate is colder than the average European climate, and solar radiation amount is less. This gives an increased need to optimize the overall solar thermal system for the Baltic States conditions.

A significant part of the solar thermal system generated energy is consumed as heat losses in pipelines, in stage from the solar energy absorbing devices to the heat-accumulating tank. Pipe isolation is necessary for both an outdoor and indoor pipes of solar energy heating system. Outdoor pipes insulation reduces heat output to the environment. Indoor pipes insulation reduces an additional heat release in indoor in hot period.

Solar thermal system manufacturers and vendors emphasize attention to solar energy absorption unit, but the rest of the system components remain in your choice.The publication describes a method for selection energy-cost effective pipe insulation type in solar thermal systems.

## 2. METHODS AND RESULTS

Companies of Solar collector installation were interviewed to determine pipe insulation types used in solar thermal systems. Questionnaire was determined that Stone wool insulation types with different thickness are most used in solar thermal systems. As well as, special for solar thermal systems, pre- insulated copper pipes are used in some cases. 20 mm and 30 mm Stone wool insulation types are most often used for solar collector circuit in indoor part, and 30 mm Stone wool insulation type the most commonly used in outdoor part. 4, 5, 6, 8 and 10 cm thick rock wool insulation types were included in the research list for deeper and wider issues research.

Amount of pipe heat losses mostly depends of pipe diameter, heat carrier temperature, air temperature of the room or environment. Solar systems for heating temperature depends on solar radiation intensity in a given period, and the outside air temperature changes throughout the year. Instantaneous pipeline heat losses are calculated according to the instantaneous heat carrier, environment and room air temperature. Calculation of average values is not correct. Therefore, it is necessary to use modeling programs with accurate meteorological data.

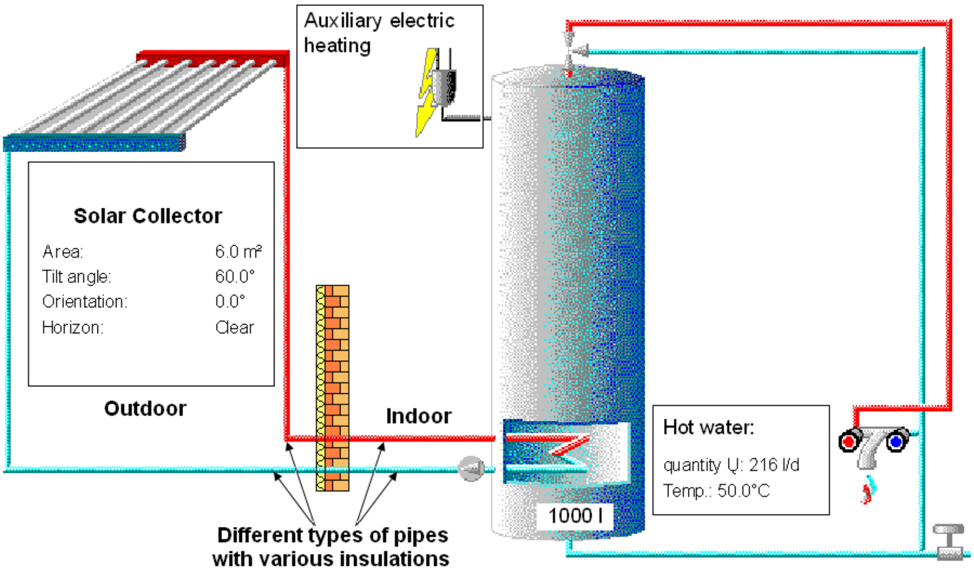

Fig. 1. Principal scheme of solar thermal system

Values of pipe heat losses were determined with the PolySun program modules for each type of pipe insulation and for three diameter dimensions. Model was created for hot water pre-heating with Solar thermal system in typical single-family house. The main elements of the Solar thermal system: 6 m$^2$ area of absorbent (2 vacuum tube Solar collectors); 1 m$^3$ accumulation tank; 15, 18 and 22 mm diameter dimension pipes, length of indoor pipeline are 10 m and outdoor- 10 m. Hot water consumption was created with inconstant daily water demand and without the breaks in holidays. Hot water is heated from 10 to 50 ºC in this model. Solar collectors can provide up to 65% [5]of the hot water heats on consumption in the Baltic States under the climatic conditions, it is therefore necessary in addition to the heater. Hot water have extra heating with electricial heater. Electric heater placement does not affect the pipe heat losses in Solar collector contour.

Latvian meteorological data of several years entered into the program. Program results can be suitable for other neighboring countries, such as Lithuania and Estonia.

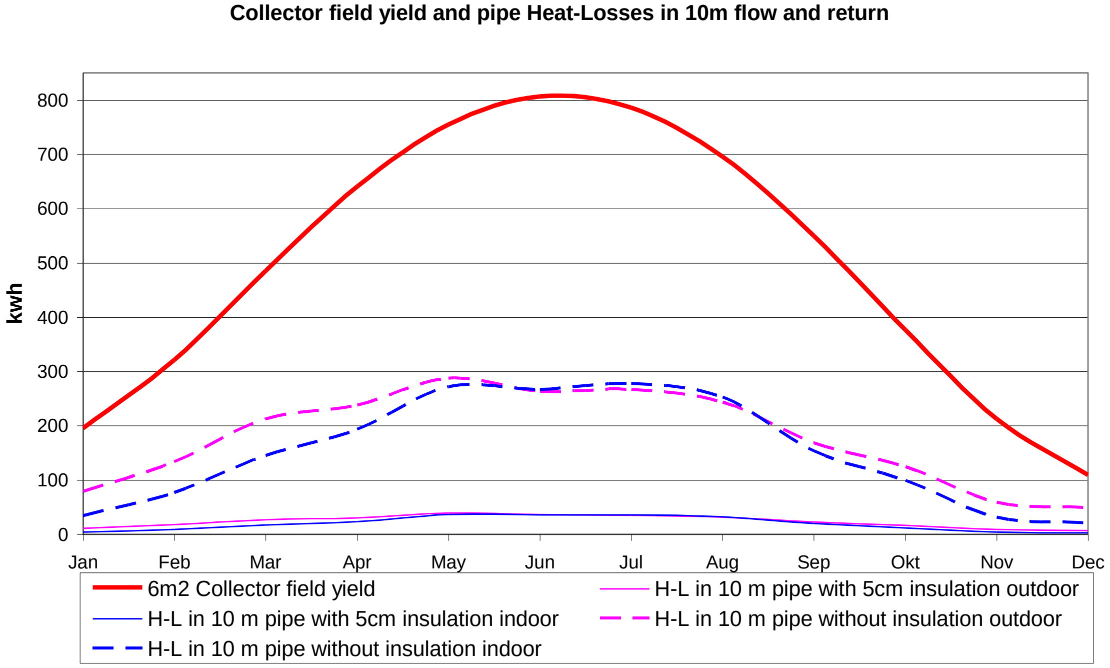

Fig. 2. Monthly comparison of amount of absorbing energy with heat losses (H-L) in Dn18 pipelines

Pipe diameters adopt after solar thermal systems hydraulic calculations. 15, 18 and 22 Dn pipes can be used in this case. 2 types of materials are used for pipe insulation in program models. The first is the rock wool with a coefficient of thermal conductivity λ = 0.039W/m*K. The second is the porous material of synthetic rubber with thermal conductivity λ = 0.037W/m*K for pre-insulated pipes.

Table 1. Heat loses in pipe per year

| Insulation Type | | Non insulation | Pre- insulated | | | Stone wool | | | | | | |
|---|---|---|---|---|---|---|---|---|---|---|---|---|
| Thickness | | | 14 mm | 19 mm | 26 mm | 20 mm | 30 mm | 40 mm | 50 mm | 60 mm | 80 mm | 100 mm |
| | Pipe Ø | kWh/m*year | | | | | | | | | | |
| Outdoor pipe | 15 mm | 90.72 | 18.31 | 15.08 | 13.39 | 16.43 | 14.14 | 12.83 | 11.98 | 11.35 | 10.49 | 9.92 |
| | 18 mm | 103.37 | 21.37 | 17.59 | 15.59 | 19.11 | 16.37 | 14.87 | 13.87 | 13.16 | 12.19 | 11.54 |
| | 22 mm | 117.97 | 25.49 | 21.11 | 18.73 | 22.78 | 19.54 | 17.72 | 16.54 | 15.73 | 14.61 | 13.86 |
| Indoor pipe | 15 mm | 77.58 | 15.35 | 12.57 | 11.15 | 13.77 | 11.79 | 10.66 | 9.92 | 9.38 | 8.64 | 8.14 |
| | 18 mm | 88.24 | 17.81 | 14.58 | 12.82 | 15.83 | 13.48 | 12.20 | 11.36 | 10.74 | 9.90 | 9.34 |
| | 22 mm | 100.45 | 21.03 | 17.26 | 15.20 | 18.70 | 15.88 | 14.35 | 13.32 | 12.63 | 11.67 | 11.03 |

Table 1 shows pipe insulation main effect on the system from viewpoint of energy consumption. This table displays average value of flow and return heat losses for each pipeline meters.

Results of Table 1 show that heat losses from 1m non insulated pipelines are equal to heat losses from 9m good insulated pipelines.

Negligible change of Solar heat systems structure may affect the total energy production. But it not much effect values of pipeline heat losses in solar collector contour. Therefore, it can be used also in similar projects.

50 mm is the maximum thickness of the standard stone wool insulation for copper pipes with 15 mm diameter dimensions, and 60 mm for copper pipes with 18 and 22 mm diameter dimensions. It is difficult to find the stone wool pipe insulation with a higher thickness in this case, so it should be rendered on order.

Table 2. Price for pipe insulation types included insulation put up job in Latvia (Feb. 2011)

| Insulation Type | *Pre- insulated | | | Stone wool | | | | | | |
|---|---|---|---|---|---|---|---|---|---|---|
| Thickness | 14 mm | 19 mm | 26 mm | 20mm | 30mm | 40mm | 50mm | 60mm | 80mm | 100mm |
| | EUR/m | | | | | | | | | |
| Dn 15 mm | 12.80 | 15.41 | 19.13 | 6.77 | 7.05 | 8.18 | 9.23 | 10.48 | 14.31 | 20.48 |
| Dn 18 mm | 13.13 | 16.25 | 20.6 | 8.24 | 8.51 | 9.85 | 10.88 | 12.59 | 17.12 | 24.92 |
| Dn 22 mm | 13.63 | 17.51 | 22.81 | 9.90 | 10.11 | 12.06 | 12.75 | 14.38 | 19.40 | 27.58 |

* prices for pre- insulated pipes are without cupper pipe and put up prices.

As previously mentioned, the solar thermal systems require an additional heat source in Baltic state conditions. It makes hot water after heating. The more energy is spent on the pipeline in the form of heat loss, the more energy it takes to further heating of the water. Therefore, heat losses energy prices are equal to the energy prices from auxiliary heat source.

Most energy- cost profitable type of insulation can be calculated having regard: price for pipe insulation with put up job; annual amount of energy consumption in the form of heat losses; and energy price volatility for auxiliary heater in calculated time period.

The cost of certain type of insulation and operating costs in calculated time period is:

$$P_{i,j} = p_{0i} + E_i \times \sum_{n=1}^{j} f_{(j)} \tag{1}$$

*i – type of pipe insulation; j – a calculation time period;* $E_{0i}$ *– pipe insulation price;* $b_i$ *– annual amount of energy consumption in the form of heat losses;* $f_{(j)}$ *– energy price volatility for auxiliary heater.*

Most energy- cost effective insulation type has the smallest amount spent in a certain time.

Example: Ø 18 mm copper pipe; fixed energy prices ($f_{(j)}$ =const ), and it is equal with Latvenergo enegy price (Apr 2011g. with VAT) 152.77 EUR/MWh [9]; 20 -year time period.

$$P_{Dn18i,20} = p_{0Dn18i} + E_{Dn18i} \times \sum_{n=1}^{20} 152.77\ \text{EUR/MWh} \tag{2}$$

Table 3. Amount of consumed money for different type of insulation and operating costs in 20-years time period

| | | Non insulation | Pre- insulated | | | Stone wool | | | | | | |
|---|---|---|---|---|---|---|---|---|---|---|---|---|
| | | | 14 mm | 19 mm | 26 mm | 20 mm | 30 mm | 40 mm | 50 mm | 60 mm | 80 mm | 100 mm |
| | | EUR | | | | | | | | | | |
| $P_{Dn18, 20}$ | Outdoor | 315.83 | 78.08 | 69.16 | 66.76 | 65.16 | 57.05 | 53.60 | 51.61 | 50.67 | 51.54 | 55.74 |
| | Indoor | 269.60 | 67.22 | 59.94 | 58.30 | 55.14 | 48.24 | 45.46 | 43.92 | 43.30 | 44.56 | 49.00 |

Table 3 show operating cost for non-insulated pipes. And it can be concluded from this table, that 60mm stone wool insulation type is the most energy- cost profitable in this case for outdoor and indoor copper pipes with 18 mm diameter dimension.

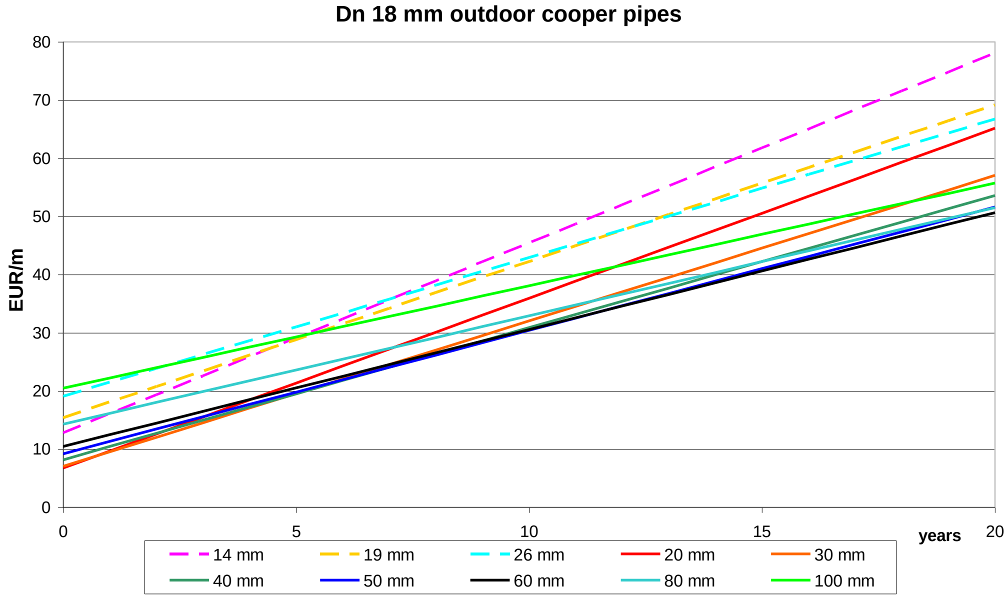

Fig. 3 Price and operating costs for different type of insulation

Fig. 3 describe flow of money for each type of pipe insulation in 20 years. Insulation Selection can affect the repayment more than 25 Euro per pipe meter in this example. It can be conclude from Figure 3 and table 3. Pipe is flow and return. Therefore repayment increases two times for each double pipeline meter.

Double pipe line length is up to 20 m for standard Solar thermal system. Amplitude of repayment different can reach 1100 Euro in 20-years.

## 3. CONCLUSION

There is increased need to optimize the overall solar thermal system for the Baltic States conditions. It is due to colder climate than the average European climate value and lower amount of solar radiation intensity in Baltic States.

Balancing investments and operating costs can increase reimbursement system within a specified period.

Most energy- cost profitable type of insulation can be calculated with this method. This method takes into account important factors:

1) Heat losses energy prices are equal to the energy prices from auxiliary heat source. And energy prices are volatility for auxiliary heater;
2) Prices of Insulation type can vary depending on supplier;
3) But values of heat losses not change over the time.

Calculation results show that heat losses from 1m non insulated pipelines are equal to heat losses from 9m good insulated pipelines.

This Method, for calculation of most energy- cost profitable type of pipe insulation, is useful for all solar thermal systems designer, manufacturers and vendors.

## REFERENCES

1. ANDREN L. *Solar installations* - James&James, 2003, 123 p.
2. *Planning and Installing Solar Thermal Systems*, United Kingdom: James & James, 2005, 300 p.
3. *Planning and Installing Photovoltaic Systems*, United Kingdom: James & James, 2008, 388 p.
4. *RAMILOW B.;* NUSZ B. *Solar water heating*, A comprehensive guide to solar water and space heating systems.- New Society Publishers, 2006, 288 p.
5. SHIPKOVS P.,*Saules kolektoru potenciālās pielietojuma iespējas siltumapgādē*,REA vēstnesis Nr.2 , Rīgas enerģētikas aģentūras, 2008, p. 8–21.
6. MUNKUND R., *Wind and solar power systems: design, analysis, and operation*, UK, 2006, 448 p.
7. WEISS W. *Solar heating system for houses*, A design handbook for solar combisystems. – James & James, 2003, 310 p.
8. FURBO S.; JORDAN U. *Solar energy State of the art*.- Danmarks Tehniske Universitet, 2003.
9. WEISS W. Comparison of systems design for solar combisystems, Proceeding Solar World Congress – Gōteborg, 2003.
10. *Latvenergo Portal.* Electricity tariffs in Latvia. [referred on the 21th of February in 2011 y.]. Link to the internet <http://www.latvenergo.lv/portal/page?_pageid=80,291151&_dad=portal&_schema=PORTAL>
11. *Europe's Energy Portal.* Natural Gas Prices, Electricity Rates, Diesel & Unleaded Fuel Costs [referred on the 21th of February in 2011 y.].Link to the internet <http://www.energy.eu/>

CYSENI 2011, May 26–27, Kaunas, Lithuania
ISSN 1822-7554, www.cyseni.com

# INVESTIGATION OF EMISSIONS REDUCTION OF LOW CAPACITY BOILER WHICH BURNS THE FUEL ON THE GRATE

**A. Grigula, T. Vonžodas**
*Lithuanian Energy Institute*
*Breslaujos g. 3, LT-44403 Kaunas – Lithuania*
*Phone +370 37 401864*
*Email: grigula@mail.lei.lt, vonzodast@mail.lei.lt*

## ABSTRACT

The consumption of renewable energy sources is constantly increasing because of the increasing prices of fossil fuels and the necessity to reduce pollutants' emissions into the atmosphere which originate from the combustion process and cause the greenhouse effect. This complex of tasks is so important that majority of developed countries have undertaken certain obligations which are summarized in the directive documents of the EU. These documents regulate the obligatory actions in alternative energy sources sector. The directive (2009/28/EB) which is newly approved by the European Parliament and Council and concerns the incentive to use the renewable energy sources foresees not only the obligatory incentives but also the tools that must ensure the usage of renewable sources match to the established sustainability criteria.

In Lithuania, the biggest part of renewable energy sources is comprised of various types of solid biofuel – wood fuel, straw and other vegetative biomass. The wood fuel is one of the main and most widely used in the households and central heating boiler houses because of the sufficient stock in the country. It is estimated that the potential of this fuel reaches 840 ktoe and it is now used about 735 ktoe. Over the past 15 years, the use of wood fuel has been constantly increasing due to the increase of demand of this fuel to use in the households for house heating and food preparation, and greater use in central heating boiler houses. According to the data of 2009, more than 50% of the total quantity of wood fuel were consumed in households, 23.2% 0150 in central heating boiler houses and 7.3% – in cogeneration power plants. The remaining quantity was consumed for heating in industrial, service and agriculture sectors.

The investigations of grate boiler fired by biofuel are performed in a laboratory in order to evaluate its efficiency and pollution while it is operating at nominal and minimal output rated capacity.

Keywords: combustion, biomass, combustion chamber.

## 1. INTRODUCTION

The growing public concern about environmental pollution and the strict requirements of the new EU normative documents for the sources of pollution encourage searching an effective tools to reduce pollution by improving the construction of the equipment fired with various types of fuel, including wood fuel.

In the last twenty years the use of biofuel is increasing in Lithuania. But the pace of the increase is declining because the consumption of biofuel jumped by 73% from 1992 till 1996 and only by 24% from 1996 till 2000. Even lesser increase of the consumption of biofuel was from 2000 till 2004. The increase was only 12% in that year. The consumption of biofuel increased only 5.8% from 2004 till 2008. This kind of increase of the consumption of biofuel can be simply explained. The resources of biofuel were consumed only in households for heating and food preparation till 1992. But after 1992, it was started to consume the fuel in central heating boiler houses more rapidly [1–3]. Gradually it was started to use it more and more.

The same tendency should remain with the use of straw fuel. Nowadays, the consumption of straw fuel is very poor, but the resources of this kind of fuel are large. Third of straw residue or 12–15% of total harvest of straw can be used for fuel. This would be about 400 kton or 100 ktoe.

There are still much resources of biofuel in Lithuania. These resources can be enlarged by planting quick rotation plants into unused area of soil. In Fig. 1 the diagram shows the dynamics of the consumption of solid fuel in Lithuania.

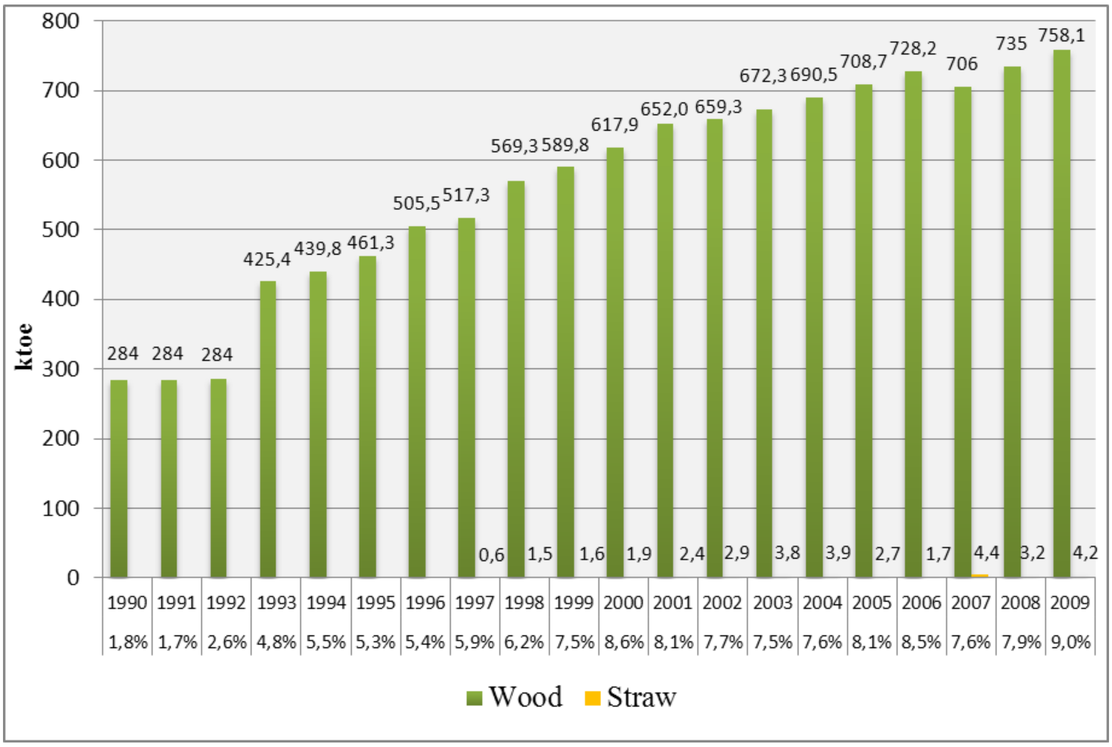

Fig. 1. Consumption of solid biofuel in Lithuanian [1–3]

The consumption of wood fuel should change because of the accepted directive of renewable energy resources. This directive declares that the consumption of biofuel should create 23% of final balance of energy till 2020. This should stimulate the increase of the consumption of wood fuel.

In Lithuania, the main part of wood fuel (< 50%) is consumed in the households, and only about 20–30% – in central heating boiler houses. About 70% of private households in Lithuania use biomass (wood, pellets, briquettes of wood waste) for heat production. Fig. 2 shows that the consumption of wood fuel is quite constant in Lithuanian. While the number of public heat plants which combust biofuel is increasing, the more and more biofuel will be combusted in them. In that case, the part of biofuel which is combusted in households is becoming smaller every year.

Therefore, it is very important to provide effective operation and minimal emissions from low capacity boilers fired with wood fuel. The investigations and tests of low capacity boilers are performed in Lithuanian Energy Institute in order to achieve these goals.

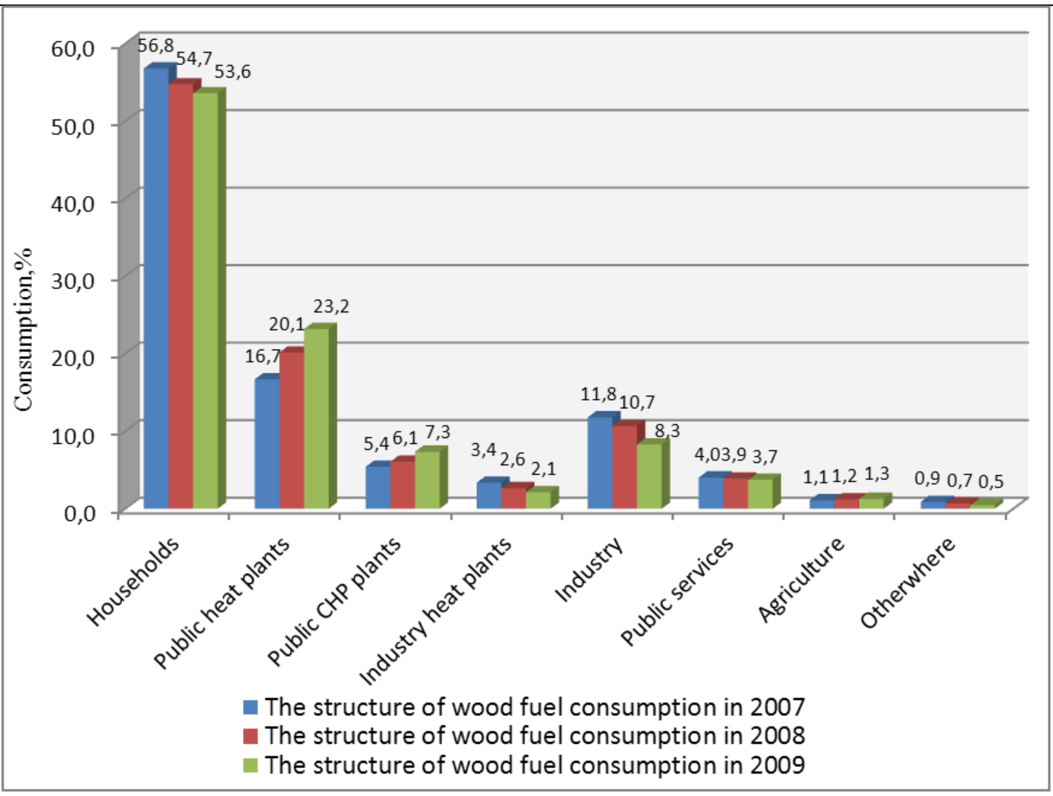

Fig. 2. The structure of wood fuel consumption in 2007–2009 [1–3]

## 2. RESEARCH METHODS

Tests of boilers fired by solid fuel were performed in the Heat equipment research and testing laboratory in Lithuanian Energy Institute. It was done by using the accredited test bench. This appliance is used to test boilers and other similar equipments fired by solid, liquid and gaseous fuel (central heating boilers, momentary and volume water heaters, air heaters, stoves, etc.).

Nominal heat rating of these equipments should be less than 300 kW, water temperature in working conditions should not exceed 95 °C, working pressure in the water system should be not exceed 6 bar. The equipments can be with natural or forced draft air burners and air distention fans. Combustion products that are ejected by these equipments can be condensed or not (in these investigations – not condensed).

By using test bench it can be determined:

- thermal parameters: consumption of fuel, thermal power, thermal effectiveness, thermal loss;
- pollutants' level: $O_2/CO_2$, CO, $C_xH_y$;
- hydraulic parameters: tightness and hardness of water system;
- tightness of gaseous system and tightness of combustion's products exhaustion system;
- temperature of equipment's surface, electrical and safety parameters.

While performing boilers‘ conformity assessment according to the standard „LST EN 303-5:2000 [4]", boilers fired by solid fuel are divided into three classes by the limits of pollutants‘ emission, feeding of fuel, type of fuel and nominal heat output (Table 1). Permissible limits of emission are different in all of classes. The first class is the worst and the third one is the highest (best).

Table 1. Permissible limits of emission of boilers fired by solid fuel [4]

| Stoking | Fuel | Nominal heat output kW | Emission limits | | | | | | | | |
|---|---|---|---|---|---|---|---|---|---|---|---|
| | | | CO | | | $H_xC_y$ | | | Dust | | |
| | | | mg/m$^3$at 10 % $O_2$ * | | | | | | | | |
| | | | class 1 | class 2 | class 3 | class 1 | class 2 | class 3 | class 1 | class 2 | class 3 |
| Manual | biogenic | ≤50 | 25000 | 8000 | 5000 | 2000 | 300 | 150 | 200 | 180 | 150 |
| | | >50 till 150 | 12500 | 5000 | 2500 | 1500 | 200 | 100 | 200 | 180 | 150 |
| | | >150 till 300 | 12500 | 2000 | 1200 | 1500 | 200 | 100 | 200 | 180 | 150 |
| | fossil | ≤50 | 25000 | 8000 | 5000 | 2000 | 300 | 150 | 180 | 150 | 125 |
| | | >50 till 150 | 12500 | 5000 | 2500 | 1500 | 200 | 100 | 180 | 150 | 125 |
| | | >150 till 300 | 12500 | 2000 | 1200 | 1500 | 200 | 100 | 180 | 150 | 125 |
| Auto-matic | biogenic | ≤50 | 15000 | 5000 | 3000 | 1750 | 200 | 100 | 200 | 180 | 150 |
| | | >50 till 150 | 12500 | 4500 | 2500 | 1250 | 150 | 80 | 200 | 180 | 150 |
| | | >150 till 300 | 12500 | 2000 | 1200 | 1250 | 150 | 80 | 200 | 180 | 150 |
| | fossil | ≤50 | 15000 | 5000 | 3000 | 1750 | 200 | 100 | 180 | 150 | 125 |
| | | >50 till 150 | 12500 | 4500 | 2500 | 1250 | 150 | 80 | 180 | 150 | 125 |
| | | >150 till 300 | 12500 | 2000 | 1200 | 1250 | 150 | 80 | 180 | 150 | 125 |

* referred to dry exit flue gas, $0^0$ C, 1013 mbar

Grate boiler was chosen for this investigation because this kind of boilers is spread most widely nowadays. Its scheme is shown in Fig. 3. After the primary test of the boiler it was determined that the boiler didn’t meet the requirements of the worst class according to the standard [4]. Therefore, the investigation and tests of boiler’s improvement were done.

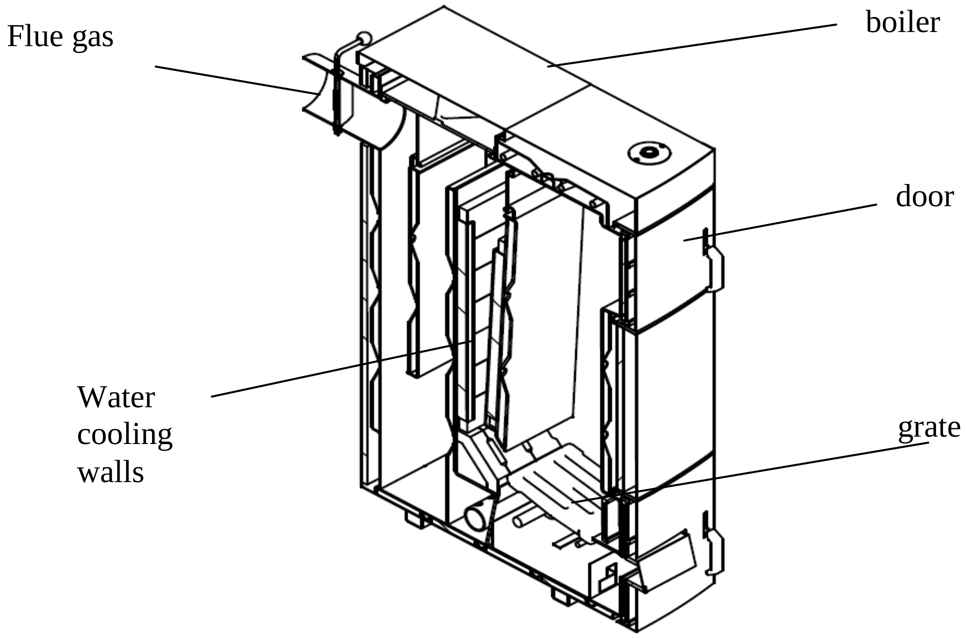

Fig. 3. The cross-section of the grate boiler

The fuel calorific value was determined by using the calorimeter bomb IKA-C5000. It was investigated that wood of net calorific value was 15.901 MJ/kg and water moisture – 12.1%.

## 3. RESULTS

After the primary test of the grate boiler it was determined that the level of pollutants emission was very high (CO – 7694.5 ppm and $C_xH_y$ – 2170.1 ppm; for permissible limits view Table 1). That‘s why the boiler didn’t meet the requirements of the worst class according to the standard. In that case, the investigation and tests of boiler’s improvement were done. After those tests it was determined that the incomplete combustion products appear in the smoke because of the few reasons:

- badly organised, not stable combustion;
- not properly provided air for combustion;
- the lack of air or substechiometric combustion;
- low temperature in a furnace.

After primary tests it was determined that during the combustion process the required temperature in the combustion chamber was not attained. In that case, the construction of combustion chamber was modified. By modeling a new combustion chamber, a high priority was taken for a good mixing of combustion products with secondary air and maintenance of the highest combustion temperature. Therefore, it was designed curved shape combustion chamber which was made of firestone and had two channels of the secondary air. Firestone can withstand high temperature, so the new chamber significantly increased the combustion temperature. Additional secondary air supply channels were introduced into combustion chamber for better mixing of combustion products with air to achieve complete combustion. New tests of the boiler were made after its modification. While implementing further researches, it was investigated that the emission of CO decreased by 55% and $C_xH_y$ – by 34 percent. Boiler’s coefficient of efficiency increased by 3.3%. But according to the standard [4], boiler fulfilled only middle-class requirements. Therefore re-modeling of the combustion chamber was needed. After the repeated modeling, combustion chamber was heightened and narrowed, and a third secondary air supply channel was introduced into it. The boiler’s cross-section before and after improvements is shown in Fig. 4.

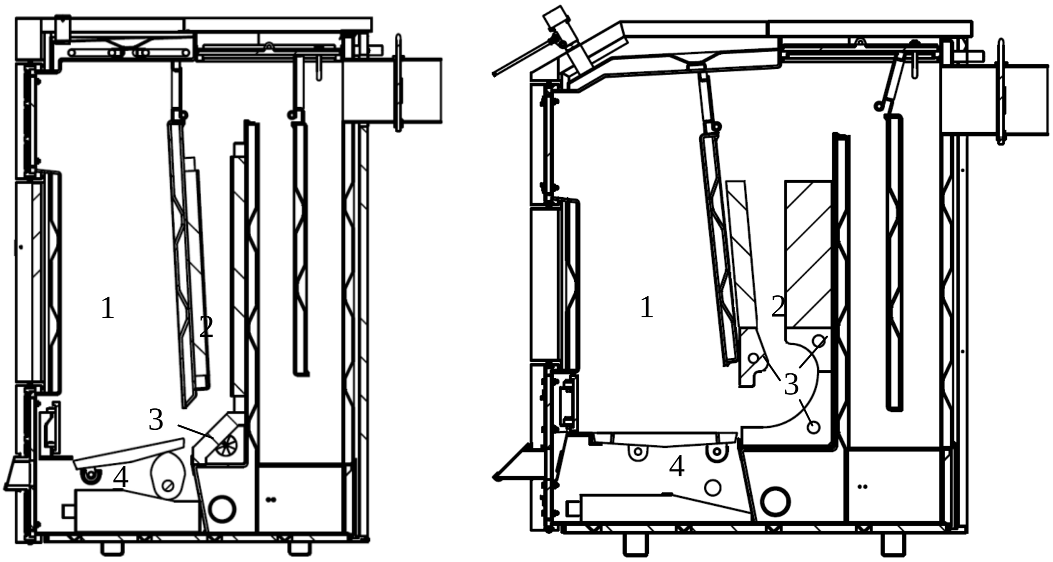

Fig. 4. Boiler’s cross-section before and after improvements: 1- container of fuel, 2 – combustion chamber, 3 – secondary air supply channels, 4 – grate

After the recent changes of the boiler it was investigated that the emission of CO further decreased by 43 percent and $C_xH_y$ – further by 28 percent. Efficiency of the boiler also increased further by 3 percent. After those final improvements, the boiler fulfilled the requirements of the highest class.

Fig. 5 shows the concentrations of carbon dioxide ($CO_2$) of which it can be seen that $CO_2$ concentration during the test of the first version of the boiler is almost 1% lower than the rest. The difference of $CO_2$ concentrations were determined by the inappropriate amount of supplied primary air and wrong choice of place where combustion products are mixing with secondary air. During the second and third tests, the dynamics of $CO_2$ concentrations do not differ sharply from each other. Throughout all the test period they remain almost the same, with exception of some periods of time and the end of the test when the difference of the concentrations appears because of the not stable combustion.

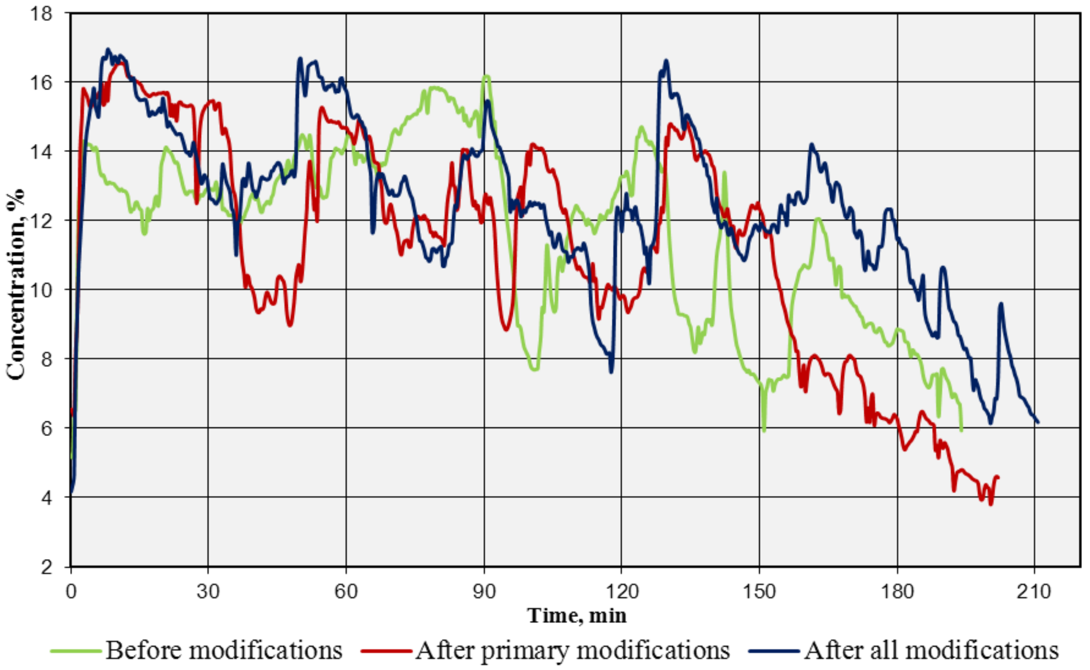

Fig. 5. The concentration of carbon dioxide ($CO_2$) before and after modifications of boiler

Fig. 6 shows the dynamics of carbon monoxide (CO) concentrations. The emission of CO in grate boiler highly depends on temperature in a combustion chamber and also on the supply of primary and secondary air. After the first test, it was disclosed that the construction of combustion chamber wasn’t suitable for reaching and maintaining high temperature. For this reason high concentration of CO emerged. During the second experiment, after the first changes of boiler’s construction, CO concentration was high in the first half of testing period. This showed that bigger amount of primary air and wrong place of secondary air supply in combustion chamber cools down the combustion products and in that case these products can’t burn completely. In the third experiment, after introducing modifications in attachments of primary and secondary air channels, the amount of CO concentration differed significantly from previous tests.

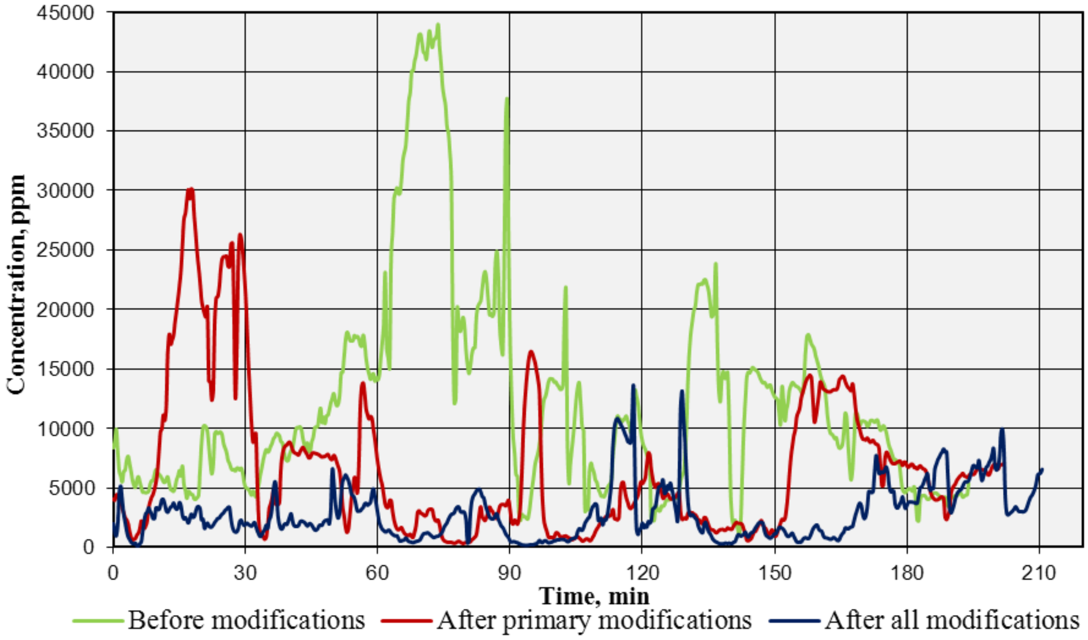

Fig. 6. The concentration of carbon monoxide (CO) before and after modifications of boiler

The diagram of hydrocarbons ($C_xH_y$) concentration dynamics is presented in Fig. 7. It can be seen from it, that the same tendency remains for hydrocarbons ($C_xH_y$) concentration dynamics as for CO concentration dynamics. The above mentioned reasons determined the differences of concentrations, which distinguish significantly during the first test.

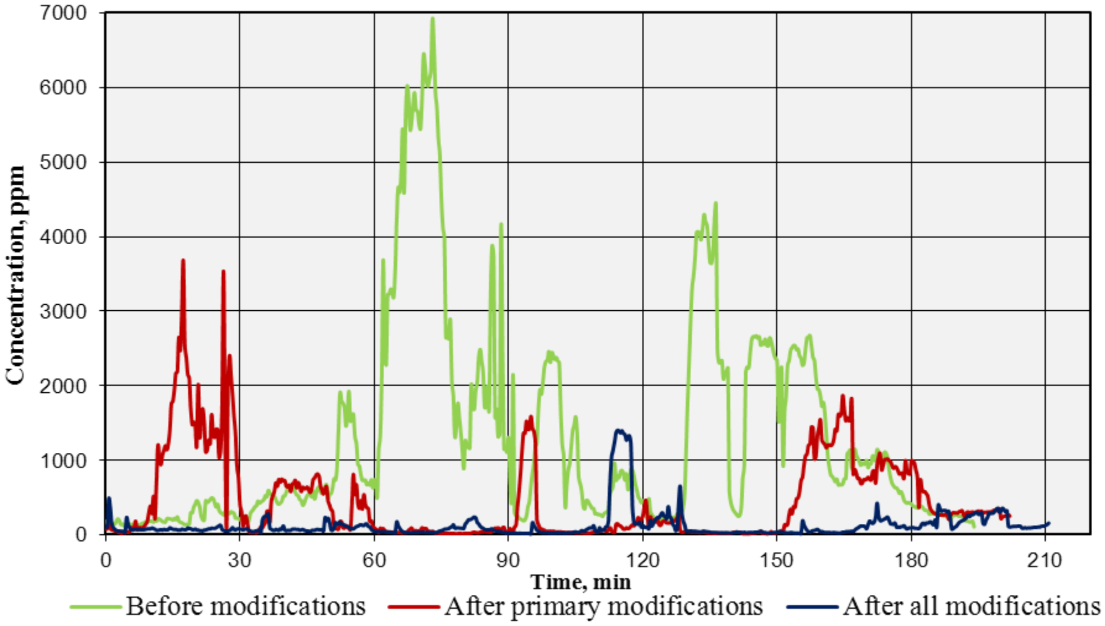

Fig. 7. The concentration of hydrocarbons ($C_xH_y$) before and after modifications of boiler

Table 2 reflects all previously discussed results. The better construction of combustion chamber and more effective combustion of fuel in it determined the highest coefficient of efficiency during the third test which reached 82%.

Table 2. Results of boiler's testing, before and after modifications

| **Modifications of boiler** | **CO concentrations, ppm** | **$C_xH_y$ concentrations, ppm** | **Efficiency, %** |
|---|---|---|---|
| Primary version of the boiler | 12115 | 1296 | 75.6 |
| Construction of combustion chamber was modified and two additional channels of secondary air supply were introduced | 6647 | 449 | 78.9 |
| Combustion chamber was heightened and narrowed, and a third secondary air supply channel was introduced into it | 2887 | 125 | 82 |

## 4. CONCLUSIONS

1. After the modifications of the boiler's construction, the emission of CO was lowered more than four times, the emission of $C_xH_y$ – more than ten times and the coefficient of efficiency was heightened by more than 6%.
2. It could be stated that the parameters of boiler could be improved by modifying the construction of combustion chamber.
3. It could be said that the manufacturers in Lithuania should guarantee that their products fulfil the requirements of the second or third class of boilers by the standard [4] in order to keep competitive in the market of boilers.

## REFERENCES

1. Energy Balance 2009. – Statistics Lithuania. Vilnius, 2010.
2. Energy Balance 2008. – Statistics Lithuania. Vilnius, 2009.
3. Energy Balance 2007. – Statistics Lithuania. Vilnius, 2008.
4. LST EN 303-5:2000 heating boilers – part 5: heating boilers for solid fuels, hand and automatically stocked, nominal heat output of up to 300 kW – terminology, general requirements, testing and marking / European standard.
5. R. BAUER, M. GOLLES, T. BRUNNER, N. DOURDOUMAS, I. OBERNBERGER. *Modelling of grate combustion in a medium scale biomass furnace for control purposes* // Biomass and bioenergy, Vol. 30, 2010, p. 1–11.
6. VONŽODAS T., GRIGULA A. *Investigation of the performance of low capacity boilers (up to 300 kW) fired with biofuel* // 7th annual conference of young scientists on energy issues CYSENI 2010, ISSN 1822-7554, p. 89–96.

CYSENI 2011, May 26–27, Kaunas, Lithuania
ISSN 1822-7554, www.cyseni.com

# THERMAL DECOMPOSITION OF BIOMASS AND ANALYSIS OF TARS DESTRUCTION

**K. Zakarauskas, N. Striugas, G. Stravinskas**
*Lithuanian Energy Institute*
*Laboratory of Combustion Processes*
*Breslaujos str. 3, LT-44403 Kaunas – Lithuania*
*Phone +370 37 401 830*
*Email: zakarauskas@mail.lei.lt*

ABSTRACT

Gasification of biomass and various bio-wastes is a promising method for heat and power generation. The biggest obstacle that paralyzes the development of gasification processes is the tar presence in synthesis gas. Dirty gas, that access the turbine blades, moving parts of internal combustion engines, and other technological equipment, condense, stick, burn and otherwise affect economical and long-term operation of equipment. In order to optimize gasification process the world is looking for new ways of removing tars from the gas. One of these is the catalytic thermal decomposition of tars, when hydrocarbons that form tar are repeatedly gasified till final reaction products of CO and $H_2$, which in turn increases the overall gas output.

The paper reviewed the nature and causes of tars formation during the biomass gasification process, the selection effect of temperature, pressure, reaction time and the gasification process. And tars thermal destruction processes, resulting from gasification of biomass, taking place in nature at different temperatures, in the presence of different catalysts, oxidizing agents (steam, air) and reaction time. The paper also presents the analysis of tars generated during the initial thermal decomposition of biomass, determines the tars composition and compares results of other authors. Generalization will formulate a direction for future research, for effective biogas treatment from tars.

Keywords: biomass gasification, tars, steam reforming, benzene, naphthalene, catalyst, dolomite, char.

## 1. INTRODUCTION

One of the most viable sources of renewable energy is biomass. This includes wood, firewood, wood chips, sawdust, briquettes, waste of logging, manufacture of wood processing and agriculture. Biomass gasification is one of the alternatives, seeking to improve its usability possibilities, when compared to direct combustion. During gasification the carboniferous substances are converted to carbon monoxide, hydrogen, water vapour and small quantity of methane, and higher hydrocarbons by treating the initial substances with high temperature.

Synthesis gas, obtained during gasification, also includes some ash particles, volatile alkali metals and tars (a mixture of aromatic hydrocarbons). Tars concentration in the gas is from 5 to 75 g/m$^3$ [1, 2]. It depends on a number of gasification parameters: oxygen quantity, vapour and biomass ratio, pressure, temperature and time of presence of solid and gaseous substances in reactor. The mentioned tars concentration exceeds the permissible standard for gas turbines, internal combustion engines and other technological equipment, thus, it limits the usage of synthesis gas. Currently synthesis gas is cleaned from tars by primitive methods, it is condensed in scrubbers. This cleaning method is quite effective, but it is uneconomical, and a part of calorific substances is got out [3]. Seeking the optimization of gasification processes, the new ways of removing tars from the gas are being sought. One of these is the catalytic thermal decomposition of tars, when the hydrocarbons, forming tars, are further decomposed, using water vapour and catalyst in 700–900°C. During thermal decomposition all hydrocarbons, higher than methane, react and decompose to the final reaction products, which in turn increases the overall gas output.

$$C_nH_m + nH_2O \Leftrightarrow nCO + \left(n + \frac{m}{2}\right)H_2 \qquad (1)$$

Seeking to create the technology of tar decomposition, the studies of two directions have been carried out in the world:

- Using the main substances, forming the tar, i.e., benzene, toluene, naphthalene, etc. This research is based on the model of aromatic compounds as the compound of biomass tar, therefore, may be applied for real gas in practice;
- Using real biomass gas.

The literature shows [1, 2] that one the most important hydrocarbons, forming the tar, are benzene and naphthalene, which have an aromatic ring and thermally hardly decompose, therefore, it has been decided to carry out the studies of processes of thermal destruction of these hydrocarbons, taking place at different temperatures, in the presence of different catalysts and water vapour.

## 2. METHODOLOGY

The experimental stand consists of the following main parts: the system of making a gas mixture with tar, the catalytic reactor and tar condensers. The experimental tests, modeling the thermal destruction of substances, forming the tar, are carried out in the following way: the heated nitrogen is supplied to the heating chambers 2, where the evaporators 3 and 4 are equipped. Naphthalene or benzene and water are evaporated at a constant temperature in evaporators. Nitrogen flow, flowing through the evaporator, brings out a certain quantity of substance. In order to avoid a condensation of tar and water vapour in the supply line, the temperature of 250°C is maintained till the tar decomposition reactor 11 and tar condenser. When implementing the process of thermal decomposition, the mixtures of nitrogen – tar and nitrogen – water vapour are mixed before catalytic reactor. The resulting gas mixture is placed into the tar decomposition reactor. The catalyst bed 10 is placed into reactor. Type K thermocouple is installed in the reactor, according to which the constant temperature is maintained.

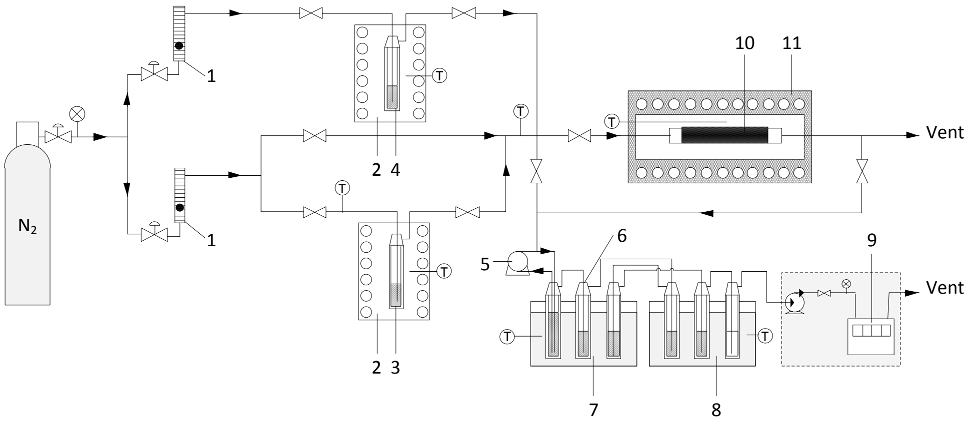

Fig. 1. Stand of experimental setup: 1 – rotameter; 2 – heater; 3 – water evaporator; 4 – model tar evaporator; 5 – peristaltic pump; 6 – gas washing bottles; 7 – heated bath; 8 – cooled bath; 9 – gas flowmeter; 10 – catalytic bed; 11 – reactor

The standard methodology was followed, when determining the tar concentration, which is based on cold trapping [4–5]. Sampling system consists of six vials, placed in two baths, where the appropriate temperature is maintained. 150 ml of isopropanol is added to the first condenser, in the next four ones – 100 ml, and the last one is left empty. First, the solvent (isopropanol) is injected to the gas flow with tar, which circulates in a closed circle from the first bottle (see Fig. 1). During this process the gas is cooled and a part of tar condenses in the solvent. The mixture of gas and solvent gets into the first vial, where the gas is separated from the solvent, and the gas is scrubbed. Gas scrubbing is carried out in the first five vials, at different temperatures, following this way: 1 vial (+40°C) → 2 – (+40°C) → 3 – (-16°C) → 4 – (+40°C) → 5 – (-16°C). The sixth vial (with a temperature of -16°C) collects the drops of tar and the remaining drops of solvent in the gas, which are brought out by gas flow after scrubbing. The quantity of passed gas flow is recorded by gas meter 9 during the experiment. The obtained samples are weighed and analyzed, following the method of gas chromatography. Sample analysis was performed, using Varian GC-3800 gas chromatograph.

## 3. RESULTS AND CONSIDERATIONS

### 3.1. Analysis of Benzene

When analyzing the thermal decomposability of benzene, the experimental tests of two types were carried out, using different dolomite and tyre char catalyst. The activity of each catalyst is analyzed at three different temperatures (700, 800 and 900°C) and at constant concentration of benzene in the gas mixture (47.0 g/m$^3$).

Fig. 2 shows, how the concentration of benzene in gas changes after passing the dolomite catalyst bed, depending on a temperature and at a constant ratio of water vapour/carbon. The presented results demonstrate that the concentration of benzene drops to 3.80 g/m$^3$ as the temperature increases.

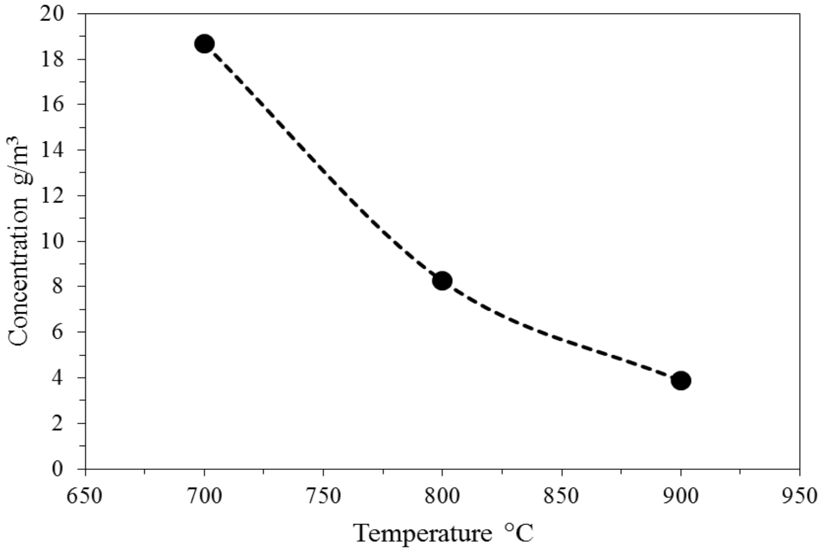

Fig. 2. Concentration of benzene after dolomite catalyst

The further experimental tests were carried out using a tyre char as a catalyst. The initial conditions and the quantity of catalyst remained the same as in the case of dolomite. Fig. 3 shows, how the concentration of benzene in gas changes after passing the activated char catalyst bed, depending on a temperature and at a constant ratio of water vapour/carbon. The presented results demonstrate that the thermal destruction of benzene increases as the temperature increases, and the concentration drops to 5.5 g/m$^3$ at 900°C.

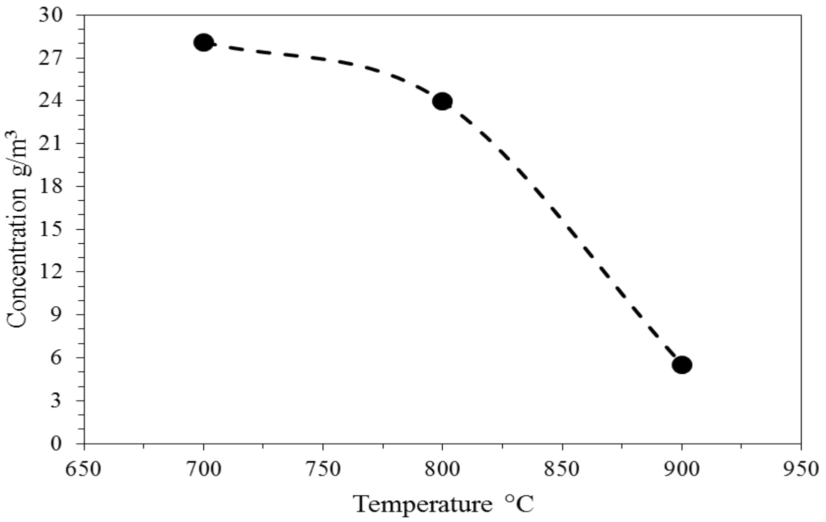

Fig. 3. Concentration of benzene after activated char catalyst

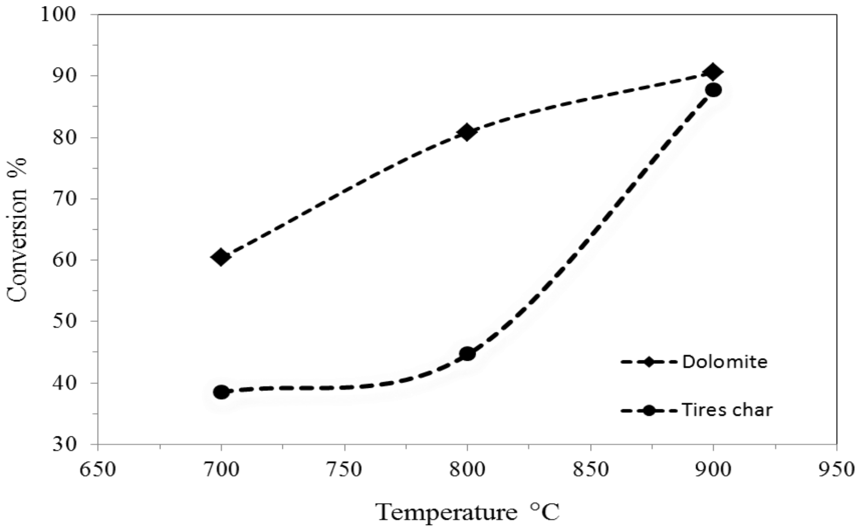

Fig. 4. Efficiency of benzene conversion

In order to assess the efficiency of benzene conversion, calculations with different catalysts were carried out. The obtained results of calculations are presented graphically in Fig. 4, depending on the temperature. The figure shows that when using the dolomite catalyst, the benzene conversion at 700°C was 60.4%, while at 900°C – 90.6%. And when using the tyre char catalyst, the benzene conversion at 700 ° C was only 38.5% and was twice at 900°C – 87.8%. Unlike dolomite, tyre char activity occurred only at higher temperatures near 900 ° C and is not worse than dolomite by its activity in thermal decomposition of benzene.

### 3.2. Analysis of Naphthalene

Naphthalene is the second compound in the tar, according to quantity, therefore, the analysis of thermal decomposition of this compound is of the same relevance and of benzene. When analyzing the thermal decomposability of naphthalene, the experimental tests of two types were carried out, using different dolomite and tyre char catalyst. The activity of each catalyst for destruction of naphthalene is analyzed at three different temperatures (700, 800 and 900°C) and at constant concentration of benzene in the gas mixture (18.0 g/m$^3$).

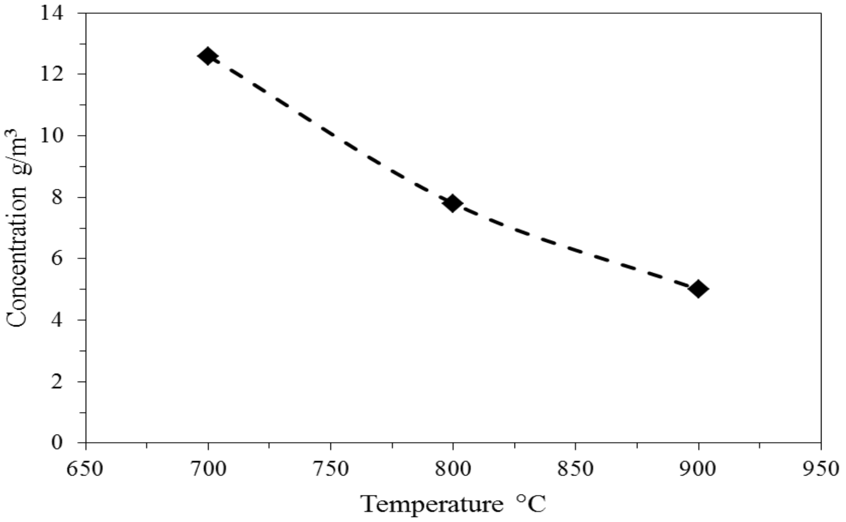

Fig. 5. Concentration of Naphthalene after dolomite catalyst

Fig. 5 shows, how the concentration of naphthalene in gas changes after passing the dolomite catalyst bed, depending on a temperature and at a constant ratio of water vapour/carbon (Fig. 5). The presented results demonstrate that as in the case of benzene the thermal destruction of naphthalene increases and the concentration drops to 5 g/m$^3$ as the temperature increases. The obtained results show that naphthalene is more stable at higher temperature and its full destruction requires a larger quantity of catalyst. Using the tyre char catalyst it was determined that the lowest concentration of naphthalene in gas was 3 g/m$^3$, when the reaction temperature was 900°C ( Fig. 6).

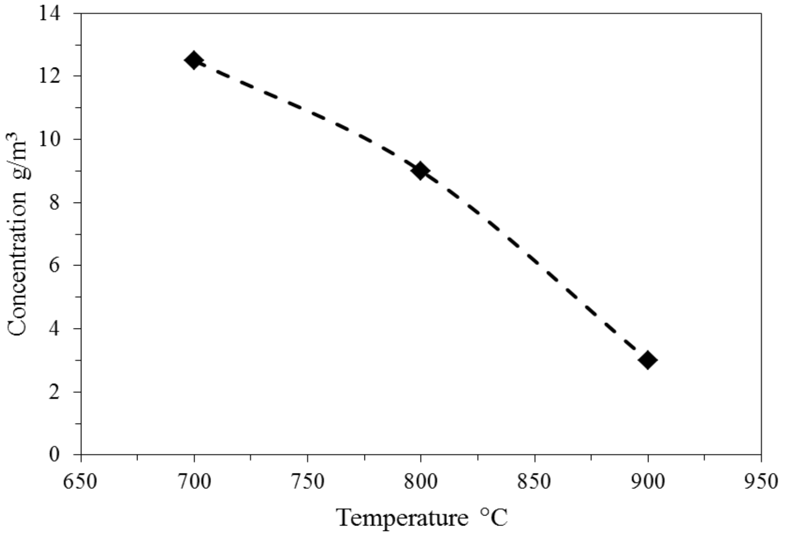

Fig. 6. Concentration of Naphthalene after Activated char Catalyst

Seeking to compare the obtained results with different catalysts, as in the case of benzene, the obtained concentrations are recalculated to naphthalene conversion (Fig. 7). The figure shows that when using the dolomite catalyst, the naphthalene conversion at 700 °C was 30%, and at 900°C – 72%. And when using the tyre char catalyst, the naphthalene conversion at 700 ° C was only 31% and at 900 ° C – 83%. When comparing with the case of dolomite, the usage of tyre carbon intensifies the destruction of naphthalene, the difference is 10%.

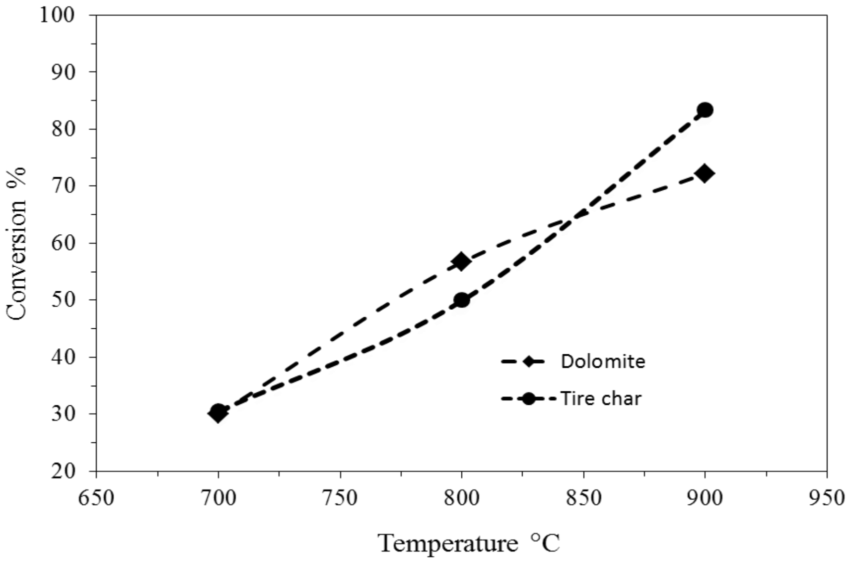

Fig. 7. Efficiency of Naphthalene Conversion

## 4. CONCLUSIONS

1. The catalytic analysis of thermal destruction of benzene and naphthalene at three different temperatures (700, 800 and 900°C) and at a constant ratio of water vapour/carbon was carried out. It was determined that the thermal destruction of benzene is the most intensive, when using the dolomite catalyst, and of naphthalene – when using the tyre carbon catalyst at 900°C. The concentration of benzene decreases from 47.0 to 3.8g/m$^3$, and naphtalene– from 18.0 to 3.0g/m$^3$ at these points.
2. When comparing the activity of dolomite and tyre char catalyst in decomposition of compounds, forming the tar, it is possible to state that both substances are active for tar destruction. However, it is noticed that dolomite is more efficient, when decomposing the light hydrocarbons ($C_6H_6$), and char – the hard ones ($C_{10}H_8$).

## REFERENCES

1. COLL, R., SALVADO, J., FARRIOL, X., MONTANE, D. Steam reforming model compounds of biomass gasification tars: conversion at different operating conditions and tendency towards coke formation. *Fuel processing technology*, 2001, Vol. 74, p. 19–31.
2. HASLER, P., NUSSBAUMER, T. Gas Cleaning for IC Engine Applications from Fixed Bed Biomass Gasification. *Biomass and bioenergy*, 1999. Vol. 16, p. 385–395.
3. DEVI, L., PTASINSKI, J.K., JANSSEN, J.J.G.F., VAN PAASEN., V.B.S., BERGMAN, C.A.P., KIEL, H.A.J. Catalytic decomposition of biomass tars: use of dolomite and untreated olivine. *Renewable Energy*, 2005 Vol. 30, p. 565–587.
4. SURRATT, Kaye; PETERS, Cathy; *Standard operating procedure for the analysis of PAHs and atrazine by GC/Ion trap MS*. Chicago: Environmental Protection Agency, Great Lakes National Program Office, 1995, p. 167–190
5. KONDIOYA, N., BERDAQUE, J.L., A Compilation of Relative Retention Indices for the Anglysis of Aromatic Compounds. Laboratorie Flaveur, Station de Recherches sur la Viande INRA de THEIX, France, 1996.

CYSENI 2011, May 26–27, Kaunas, Lithuania
ISSN 1822-7554, www.cyseni.com

# OPTIMAL RELIABILITY LEVEL ESTIMATION FOR DISTRIBUTION NETWORK CONSIDERING DIFFERENT TYPES OF LOAD

**A. Ļvovs, A. Mutule**
*Riga Technical University*
*Faculty of Power and Electrical Engineering*
*Kronvalda blvd. 1, LV-1010 – Latvia*
*Phone +371 25 970 020*
*Email: aleksandrs.lvovs@inbox.lv*

ABSTRACT

This work gives methodology for Total Costs of Reliability (TCR) calculation taking into account both customer and utility reliability costs. Previously mentioned methodology of TCR calculations includes new approach for finding electrical power interruption costs depending on the share of customers in electricity consumption and their geographical allocation. As a result of analysis of sectors of customers, substations with typical load or Typical Substations are defined. Definition of such substations is simplifying considering of different types of load that are located in different regions of country. The work shows that the new approach allows one to estimate non-supply costs for customers more precisely comparing with situation when average non-supply costs are used.

Taking into account reliability improvement costs and the share of customers in electricity consumption combined with costs of electrical energy not supplied, TRC calculation methodology allows to find optimal reliability costs with high accuracy and in such way defines optimal reliability level that in its turn increase society benefits.

Keywords: Reliability of power supply, reliability costs, power supply interruptions, optimal reliability level.

## 1. INTRODUCTION

Nowadays electrical energy plays big role in economics of each country. Introduction of new power quality sensitive equipment that lasted for several decades results in higher standards for quality of electricity. Taking into account liberalization processes that occur in recent time in electricity producing, transmitting and distributing companies, quality of electrical energy can go down as Transmission System Operators (TSOs) and Distribution System Operators (DSOs) try to diminish their reliability costs. To prevent such situation, regulating institutions of some countries already introduced some reliability targets, but some countries are still on their way of introduction of such targets. To define appropriate targets (and also some bonuses and penalties for achieving or un achieving targets) deep analysis of reliability of network and reliability-related costs should be performed. Nowadays there have already been performed some calculations with the aim to find reliability costs of customers and to compare them with utility reliability-related costs, but usually all the methods take average value of customer reliability related costs. Such approach is incorrect because it introduces big deviation of customer non-supply costs in resulting calculations in calculations, especially in cases if reliability of power supply for geographically wide region with big number of customers is analysed.

Further given methodology, proposed by authors of the paper, shows how to make reliability related costs calculations precise (comparing with situation when average values are used) and in such way find optimal reliability level area (see Fig. 2). The methodology, applied to the whole power system, can help to find reliability targets and appropriate values of bonuses/penalties for utilities.

## 2. METHODOLOGY

To find optimal reliability level for any network we should define reliability criteria. So, first of all we should set definition of term “reliability” and then define some criteria (indicators), that will be used for finding optimal level of reliability.

Power network`s efficiency (or quality) is determined as the ability of the system to perform needed functions. Such ability can be characterised by such terms: reliability, economy, safety (security) and, sometimes, vitality of the system [1]. According to [2] there is such an explanation of the term „*Reliability*”:

Reliability (performance) (191-02-06) – The ability of an item to perform a required function under given conditions for a given time interval. NOTES: 1 – It is generally assumed that the item is in a state to perform this required function at the beginning of the time interval. 2 – The term “reliability” is also used as a measure of reliability performance (see 191-12-01 explanation in [2]).

All reliability indicators can be divided into 2 big categories – quantitative and qualitative indicators.

In the group of quantitative indicators there are indicators like outage probability $\chi$, failure rate $\lambda$, time of outage state $T_{os}$ and others. Quantitative indicators usually are related with some concrete element of the grid or group of elements.

On the other hand there are qualitative indicators of reliability. Such indicators give us qualitative or indirect quantitative information about whole network or big parts of network. These indicators usually are used to describe reliability of the network. As qualitative indicators of reliability SAIFI, SAIDI, MAIFI, etc. indexes are used.

Fig. 1 illustrates usage of reliability indices by utilities of the United States of America [3].

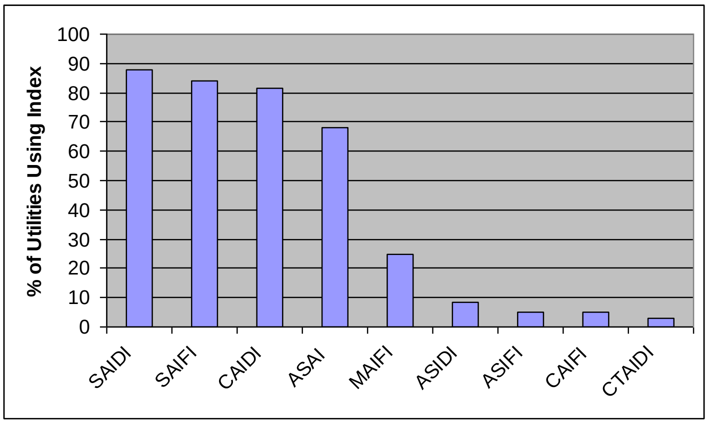

Fig. 1. Usage or reliability indexes by utilities of the United States of America

As we can see, the most popular indexes are SAIDI, SAIFI, CAIDI and ASAI. About 25% of all utilities of the USA also use MAIFI indicator.

Here is the explanation of the indexes:

- SAIFI – System Average Interruption Frequency Index.
  SAIFI = (total number of customer interruptions)/(total number of customers served);
- SAIDI – System Average Interruption Duration Index.
  SAIDI = (Σcustomer interruption duration)/(total number of customers served);
- CAIDI – Customer Average Interruption Duration Index.
- CAIDI = (Σcustomer interruption duration)/(total number of customer interruptions);
- ASAI – Average Service Availability Index.
  ASAI = (customer hours service availability)/(customer hours service demand).

- MAIFI – Momentary Average Interruption Frequency Index. This index shows total number of ALL customer interruptions and is very similar to SAIFI. Difference between MAIFI and SAIFI is in definition of interruption. SAIFI includes only interruption with duration longer than 3 minutes, MAIFI in its turn includes absolutely all interruptions in respect of duration.

To find out the optimal reliability level for the network we should know not only values of these indices, but also costs related to reliability of power supply. In ideal case optimal reliability level is reached when sum of costs of network improvement and costs (expenses) of customers due to power supply interruptions are minimal [10–12]. In real life each participant of electrical energy system tries to minimize his costs without paying attention to the possible effect on the other participants. Besides the previously mentioned fact, it is hard to estimate reliability related costs absolutely precisely. And because of that it is rational to speak not about optimal reliability level point, but about <u>area</u> of optimal reliability level. Fig. 2 schematically shows dependence of utility, customer and total costs depending on reliability level of power supply.

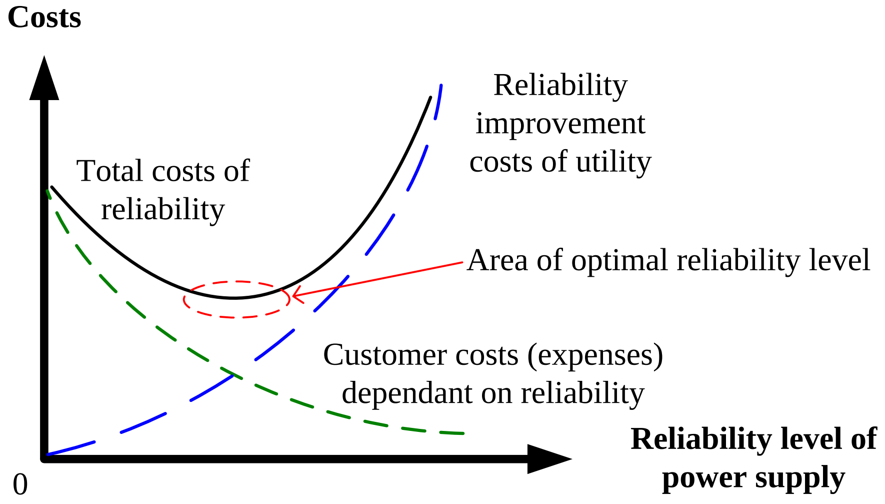

Fig. 2. Utility, customer and total costs depending on reliability level of power supply

Further sections of the paper outline new methodology of assessment of costs for customers and utilities.

## 2.1. Assessment of costs of customers depending on their type and allocation

The main criterion that shows importance of reliability level for customers are power supply interruption costs.

Power supply interruption costs depend on such factors like: a) type of customer; b) interruption duration (costs per unit are different for different durations) and c) type of interruption (if the interruption was scheduled or not). Power supply interruption costs show damage, created by power supply interruption to customer (industry, agriculture, etc.), in money equivalent.

To find out power supply interruption costs different methods (like customer surveys, blackout studies, ratio of gross economic output to energy consumption) usually are applied. Nowadays a lot of studies have been performed to find out costs of power supply interruptions [4], but, unfortunately, usage of just average values of these costs can lead to inadequate assessment of damage size.

Fig. 3 shows costs of power supply interruption for different customers [3].

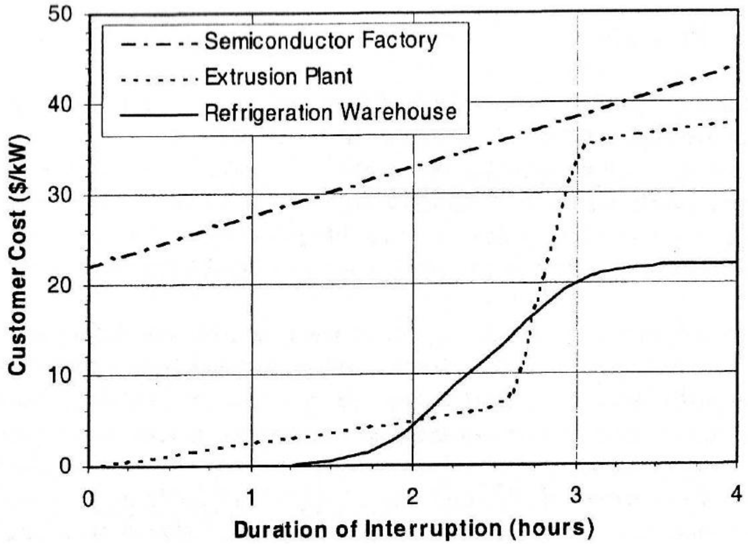

Fig. 3. Time-dependant power supply interruption costs for different types of customers

To find customers' power supply interruption costs more precisely than using just average values of the costs, information about distribution of customers by sectors (Industry, Transport, Households, Services and Construction, Agriculture) and subsectors (like Banking, Shopping, various Subsectors in Services and Construction) is needed. To evaluate non-supply costs for particular substation, information about the distribution of customers over the country, depending on the sector and related substation, is also required.

Table 1 summarises information about electrical energy consumption in GWh by sectors per year for time period from year 2004 to 2008 that was taken from publication of Ministry of Economy of Republic of Latvia "Latvian Energy in Figures" [5]. Information about energy consumption by subsectors (in Latvia) have been taken from [6].

Table 1. Electrical energy consumption by sectors in Latvia [GWh/year]

| **Sector** | **2004** | **2005** | **2006** | **2007** | **2008** |
|---|---|---|---|---|---|
| Industry | 1546 | 1597 | 1640 | 1705 | 1590 |
| Transport | 139 | 148 | 150 | 140 | 138 |
| Households | 1467 | 1572 | 1728 | 1794 | 2031 |
| Services and construction | 2090 | 2256 | 2460 | 2822 | 2730 |
| Agriculture | 162 | 156 | 165 | 145 | 139 |
| In total: | 5404 | 5729 | 6143 | 6606 | 6628 |

On the basis of analysis of geographical allocation of different sectors on consumer level conducted by authors of the paper and on statistical data about consumption by sectors, we defined the following categories of substations or Typical Substations (TS). There can be:

1. City substations;
2. Rural substations;
3. Industrial substations.

City substations have customers from almost all sectors of customers, excepting Agricultural sector. Therefore, shares of energy consumption for city substation by sectors in percentage within the framework of the work were calculated anew. As city substation has no Agricultural load, shares of other sectors grew proportionally to their initial value. For example let's calculate share of Industrial sector for Latvian city substation in year 2008. Share of Industrial sector consumption in overall countries' consumption is

1590/6628=0.2399 or 23.99% (where 6628 is total energy consumption in Latvia in year 2008), but for city substation share of Industrial sector consumption will be1590/(6628-139)=0.245 or 24.5% (where 6628-139 represents total consumption of all sectors in country excluding Agriculture sector).

According to the results of performed analysis, rural substations have only three representatives of the sectors – Households, Agriculture, Services and construction. Because of the fact, shares of energy consumption by sectors (in percentage) for rural substations were calculated anew. Transport sector is not included in rural substation, because representatives of this sector (Railroad, Pipeline and Road transport) consume electricity in cities – because roads are illuminated in cities and at short distances outside cities, electrical railroad lies around cities and due to that take energy from city substations, but pipeline terminals with electrical pumps are located in places of loading (of gas, oil, etc.) – in ports or places of consumption (of gas, oil, etc.)

Energy consumption shares of sectors, according to results of calculations after performed analysis, are given in Table 2.

Table 2. Shares of energy consumption by sectors (in %) for city and rural substations

| **Sector** | **City substation** | **Rural substation** | **Industry substation** |
|---|---|---|---|
| Industry | 24.5 | - | 100 |
| Transport | 2.13 | - | - |
| Households | 31.30 | 41.45 | - |
| Services and construction | 42.07 | 55.71 | - |
| Agriculture | - | 2.84 | - |

Industrial substations usually are specially built substations for a particular factory. As an example, substation “Liepajas metalurgs” near city Liepaja in Latvia can be mentioned. This substation was specially built for metal-fabricating factory.

When shares of typical loads for TS are known, power supply interruption costs (i.e. customer costs of reliability) (due to outages in substations) can be calculated. Equation (1) should be used for calculation of customer costs of reliability due to outages in substations (because it takes into account only number of outages of substation per year), while (2) should be used for calculation of customer costs of reliability due to outages in feeders of the distribution network (because it takes into account only number of outages in sections of feeder).

For calculation of customer costs of reliability (CCR) following equations can be used:

$$CCR(t)_{s-s} = P_{TR\_nom} \cdot n_{TR} \cdot k \cdot \lambda_{s-s} \cdot \sum_{i=1}^{n} S_i \sum_{j=1}^{m} S_{ij} \cdot C(t_{os})_{ij} \tag{1}$$

where *CCR(t)*$_{s\text{-}s}$ – customer costs of reliability due to outages in substation (show damage in money equivalent, created by power supply interruption to customer) [monetary unit/year]. Subindicy *s-s* is abbreviation of “substation”;

$P_{TR\_nom}$ – nominal power of transformer (s) installed at substation (kW);

$n_{TR}$ – number of transformers installed at substation;

*k* – coefficient of load of transformers (shows the ratio of $S_{max\_load}/S_{nom}$. Usually value of this coefficient is 0.7);

$\lambda_{s-s}$ – number of outages of substation per year;

*i* – number of type of sector;

*j* – number of type of subsector;

$n$ – total number of sectors $i$;
$m$ – total number of subsectors $j$ in sector $i$;
$S_i$ – share of sector in electricity consumption of substation [%];
$S_{ij}$ – share of subsector in electricity consumption of sector $S_i$ [%];
$C(t_{os})_{ij}$ – time-dependant costs of energy not supplied for subsector [monetary unit/kW]. These costs are calculated for different durations of power supply interruptions using empiric formulas or diagrams (like in figure 3) for different types of customers;
$t_{os}$ – time of outage state for substation.

$$\begin{aligned}CCR(t)_F = \sum_{f=1}^{F}\sum_{lpf=1}^{LPf} P_{lpf}\cdot\Bigg[\left(\sum_{i=1}^{n} S_{ilpf}\sum_{j=1}^{m} S_{ijlpf}\cdot C(t_{repair})_{ij}\right)\cdot \sum_{L=1(L\in M_{Lf})}^{L=lpf}\cdot\lambda_L + \\ +\left(\sum_{i=1}^{n} S_{ilpf}\sum_{j=1}^{m} S_{ijlpf}\cdot C(t_{switch})_{ij}\right)\cdot \sum_{L=lpf+1(L\in M_{Lf})}^{L=LPf}\cdot\lambda_L\Bigg],\end{aligned} \tag{2}$$

where $CCR(t)_F$ – customer costs of reliability due to unscheduled outages in feeders coming out of substation [monetary unit/year]. Subindicy $F$ is abbreviation of “Feeder”;
$f$ – number of feeder;
$F$ – total number of feeders $f$ in substation;
$lpf$ – number of load point of the feeder $f$;
$LPf$ – total number of load points on a feeder $f$;
$P_{lpf}$ – active load of the load point $lp$ on a feder $f$;
$i$ – number of type of sector;
$j$ – number of type of subsector;
$S_{ilpf}$ – share of sector $i$ in electricity consumption at load point $lp$ on a feeder $f$ [%];
$S_{ilpfj}$ – share of subsector $j$ in electricity consumption of sector $i$ at load point $lp$ on a feeder $f$ [%];
$C(t_{repair})_{ij}$ – costs (time-dependant) of energy not supplied for subsector [monetary unit/kW]. These costs are calculated for duration of power supply interruptions $t_{repair}$ needed for repairing outages in upstream sections of feeder;
$L$ – number of feeder section;
$M_{Lf}$ – set of sections that form a feeder $f$;
$\lambda_L$ – number of section’s $L$ outages per year;
$C(t_{switch})_{ij}$ – the same as $C(t_{repair})_{ij}$, but calculated for duration of power supply interruptions $t_{switch}$ needed for switchings to disconnect damaged downstream section of feeder.

Costs of energy not supplied due to scheduled outages in feeders connected to substations can be calculated using equation similar to equation (2). The only difference will be in value of time-dependant costs. Scheduled outages in downstream section of feeder will not affect costs of energy not supplied for load point placed upstream.

Sum of $\lambda_L$ (for particular load point) and $\lambda_{s-s}$ used in equations (1) and (2) give us value of SAIFI for the load point, because power supply of load point will be interrupted in both cases – when sections of feeder and/or substation has fault. It is important to notice, that for feeders with manual feeder sectionalizing SAIFI for all load points of the feeder will be equal. In case of automatic feeder sectionalizing SAIFI for load points of the feeder will be different. This can be explained by the fact that in case of manual feeder sectionalizing fault in upstream and downstream will cause power supply interruption with duration longer than 3 minutes (manual sectionalising requires longer time to make switchings). In case of automatic feeder sectionalizing load point will be interrupted for more than 3 minutes only due to faults in upstream sections of feeder (faults in downstream feeders will cause interruptions with duration up to 3 minutes, that are related only with MAIFI, but not SAIFI).

## 2.2. The ways of network's reliability improvement and total utility reliability-related costs

According to statistical data [7, 8, 11], power supply interruptions are caused mainly by outages in distribution network. According to [8] 85% of all power supply interruptions are caused by outages in distribution network, 9% due to outages at (high voltage)/(middle voltage) (HV/MV) substations and 4% and 2% due to outages in transmission network and power plants respectively. So, bigger attention should be paid to reliability of HV/MV substations and distribution networks.

### *2.2.1. The ways of network's reliability improvement*

According to results of calculations of reliability level for 110/10(20)kV substations, performed by authors of this paper and published in [9], reliability level of HV/MV substations can be considerably improved by installing circuit breaker between busbars of switchgear. In case of rural substations, important role for reliability level is playing number of overhead lines connected to switchgear. In both cases (rural and city substations) usage of Gas Insulated Switchgears instead of Air Insulated Switchgears improves reliability level dramatically.

In [11, 13] as the main reasons of increasing SAIDI and SAIFI are mentioned scheduled outages, defective equipment, adverse weather, lightning and tree-related interruptions. Taking into account these facts, reliability level can be improved by better planning of scheduled maintenance works, partial cabling of overhead lines placed in woodland, installing additional switches and automation (including fault location detection devices).

Taking into account that distribution network has more possibilities and potential for reliability improvement, reliability-related costs of distribution utility will be discussed in the next sub-paragraph.

### *2.2.2. Reliability-related costs of utility*

Nowadays more and more regulatory authorities introduce bonus-penalty system for utilities with the aim to keep reliability of power supply at allowable level. It means that for power supply there are defined some reliability targets (usually SAIFI and SAIDI indexes are used as targets). In case if utility fulfils reliability targets it can gets bonuses (usually bigger profit is allowed for the next working period as bonus), otherwise it pays penalties (penalties .to customers and allowable profit level for the next period is reduced). Fig 4 illustrates total utility costs that are formed by utility costs and bonuses/penalties [3].

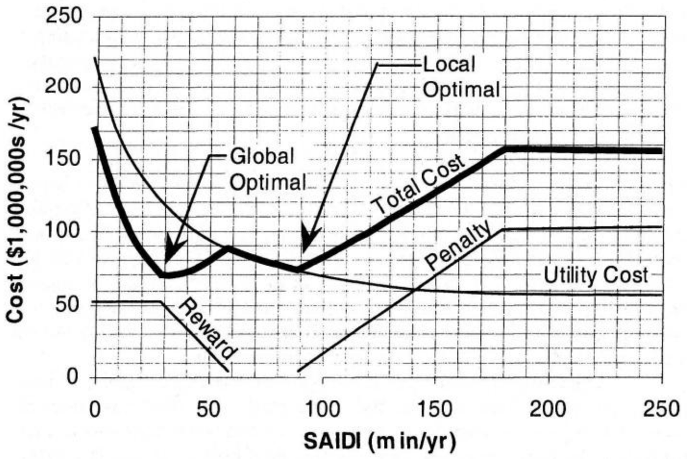

Fig. 4. Formation of total utility costs

In this case power supplying companies (mainly DSOs, because their networks are the main reason for power supply interruptions) should solve optimization problem where from one side are expenses for reliability improvement and bonuses for good reliability level, but from the other side penalties for not meeting the reliability targets. Total utility costs that include expenses for reliability improvement and bonuses/penalties in ideal case should represent total costs of reliability that have been shown at Fig. 2. In such way optimal costs of utility will correspond to overall optimal costs of reliability.

But until relationship between reliability targets (SAIDI and SAIFI indexes) and costs of customers for particular network are not known precisely, we cannot use values of penalties. Due to this reason costs of utility and costs of customers (that normally are used as base for determining value of penalties) are calculated separately.

Utility costs of improvement of reliability (additional costs to existing costs of utility), don’t taking into account penalties and bonuses, can be calculated using equation (3).

$$UCR = \sum_{f=1}^{F} \left[ \sum_{L \in M_{Lf}} \left( N_{sL} \cdot C_{sL} + N_{aL} \cdot C_{aL} + N_{flddL} \cdot C_{flddL} + L_{cL} \cdot C_{cL} + L_{L} \cdot C_{tt} \right) + L_{icf} \cdot C_{ic} \right] + C_{s-s\_imp} \tag{3}$$

where $UCR$ – utility costs of improvement of reliability (additional costs to existing costs of utility) [monetary unit/year];

$N_{sL}$ and $C_{sL}$ – amount and price of sectionalising switches in section $L$;

$N_{aL}$ and $C_{aL}$ – amount and price of automation complects in section $L$;

$N_{flddL}$ and $C_{flddL}$ – amount and price of fault location detecting devices in section $L$;

$L_{cL}$ and $C_{cL}$ – length (km) and price (monetary unit/km) of cable line buried instead of overhead line in section $L$;

$L_{L}$ and $C_{tt}$ – length of lines located in woodland (km) and costs for additional tree trimming (monetary unit/km). If section is located in woodland, then value of $L_L$ is equal to length of the section, otherwise value of $L_L$ is zero;

$L_{icf}$ and $C_{ic}$ – length (km) and price (monetary unit/km) of interconnection for feeder $f$;

$S_{s\text{-}s\_imp}$ – costs of utility for substation’s reliability improvement.

It is important to notice, that costs of additional equipment installed by utility should be represented in equation (3) taking into account lifetime of equipment, e.g. if lifetime of new built cable line is assumed to be 30 years, utility costs of improvement of reliability calculated according (3) should take into account approximately 1/30 of the costs of cable line (whole cost of line estimated for 1 year of lifetime), because calculations are performed for one year.

### 2.3. Total costs of reliability

Total costs of reliability can be calculated using equation (4).

$$TCR = UCR + CCR \tag{4}$$

where $TCR$ – total costs of reliability;
$UCR$ – utility costs of improvement of reliability;
$CCR$ – customer costs of reliability.

Optimal reliability level of power supply is reached when value of TCR is minimal. To find minimal TCR value, values of UCR and CCR should be calculated for different combinations of network reliability improvement ways (steps). So, optimal reliability level can be defined using equation (5):

$$TCR_{opt} = \min_{n \in N_{st}} (UCR_n + CCR_n) \tag{5}$$

where $TCR_{opt}$ – total reliability costs, that correspond to optimal reliability level of power supply;
$n$ – number of network reliability improvement way (step);
$M_{st}$ – set of network reliability improvement ways (steps) $n$;
$UCR_n$ and $CCR_n$ - utility costs of improvement of reliability and customer costs of reliability for network reliability improvement way (step) $n$.

## 3. RESULTS AND DISCUSSIONS

In this paragraph the practical example of calculations is presented. It is is given for rural substation case (when power lines are formed mostly by overhead lines). To simplify example, calculations are performed only for one radial distribution feeder (Fig. 5). Numbers in sqares at Fig.5 show potential places for sectionalising switches installation.

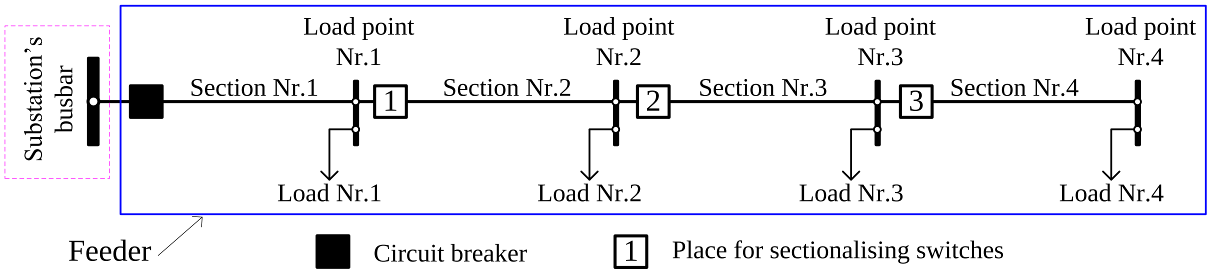

Fig. 5. Feeder scheme used for calculations

Table 3 gives information about used lengths of lines (sections) of feeder and loads in load points.

Table 3. Lengths of lines (sections) of feeder and loads in load points

| | **Number of load point and line** | | | |
|---|---|---|---|---|
| | **1** | **2** | **3** | **4** |
| **Length of line (km)** | 5 | 4 | 4 | 5 |
| **Load of load point (kW)** | 250 | 160 | 200 | 250 |

Calculations have been performed for six different reliability improvement steps, each of the next steps is like supplement to previousely realised steps and each further step consequently improves reliability level of power supply at the feeder. At the first step only circuit braker is installed at the beginning of the feeder and no reliability improvement actions are not performed. At the second step manual sectionalising switches are installed in points for sectionalising switches (see Fig. 5). At the third step automatic sectionalising switches are installed instead of manual sectionalising switches. At the step four, sections 1 and 2 of feeder are additionally trimmed. Overhead line in section 1 is replaced by cable line at fifth step, but at sixth step overhead lines in sections 1 and 2 are replaced by cable lines. Replacement of overhead lines by cable lines, as well as trimming, in sections 1 and 2 was performed, because faults at these sections affect biggest part of consumers. Trimming costs haven't benn taken into account whem cable liones were buried instead of overhead lines in sections 1 and 2.

During calculations it was assumed that life-cycle of switches and cable lines is 30 years. It is assumed, that time needed for repairing fault is 4 hours, but time needed for switching of manual sectionalising switch is 1 hour. Failure rate of overhead line (that shows number of line outages per 100 km during a year) is assumed to be $\lambda = 5$, but for cable line $\lambda = 0.5$.

Table 4 summarizes costs of reliability improvement works. Costs of manual sectionalising switches have been taken from [15]. According to [14], additional trimming of trees reduces number of faults, caused by tree falling, by 47%.

Table 5 summarizes costs of energy not supplied for corresponding types of customer subsectors [4] and gives shares of subsectors in total installed load in every load point. To make calculations more easy, it is assumed, that shares of loads by sectors and subsectors is identical for all load points of the feeder. Shares of sectors in load connected to feeder have been taken from Table 2.

Table 4. Costs of reliability improvement works

| | **Sectionalising switch (US$/unit)** | **Automated sectionalising switch (US$/unit)** | **Additional tree trimming (US$/km)** | **Cable line (US$/km)** |
|---|---|---|---|---|
| **Costs** | 1650 | 3050 | 28 | 49780 |

Table 5. Costs of energy not supplied for corresponding types of customer sectors and corresponding shares of load

| | **Costs of energy not supplied for corresponding types of customer sectors (US$/kW) and corresponding shares of load** | | | | | | |
|---|---|---|---|---|---|---|---|
| | **Services and construction** | | | **Agriculture** | | | **Households** |
| **Duration of interruption** | **Eating and drinking place** | **Hotels, camps, ...** | **Banks and Service** | **Cultivation of grain** | **Animal farms** | **Pig-breeding** | **Residental** |
| **1 hour** | 28.41 | 1.13 | 29.39 | 0.099 | 0.31 | 0.43 | 0.15 |
| **4 hours** | 147.93 | 3.05 | 58.49 | 1.1 | 3.05 | 3.42 | 1.64 |
| **Load (% of sector consumption)** | 56% | 24% | 20% | 27% | 35% | 38% | 100% |

Tables 6 and 7 give results of calculations for customers and utility, and also values of reliability indexes SAIFI and SAIFI after feeder improvement. The last column of Table 6 shows us CCR values for situation when we use just average power supply interruption costs calculated as just average costs for appropriate interruption duration. For example for 1 hour long interruption average costs are equal to (28.41+1.13+23.39+0.099+ 0.31+0.43+0.15)/7= 7.7 US$/kW.

Table 6. Results of calculations of reliability-related costs and reliability indexes for customers

| **Reliability improvement step** | **CCR(t) for load points (thous. US$)** | | | | **Sum of CCR(t) of load points (thous. US$)** | | SAIDI | SAIFI |
|---|---|---|---|---|---|---|---|---|
| | **1** | **2** | **3** | **4** | New method | Using total average costs | | |
| **1** | 12.112 | 7.752 | 9.690 | 12.112 | 41.665 | 24.180 | 4 | 0.9 |
| **2** | 5.373 | 4.766 | 7.616 | 12.112 | 29.866 | 17.727 | 2.59 | 0.9 |
| **3** | 3.364 | 3.876 | 6.998 | 12.112 | 26.350 | 15.292 | 2.25 | 0.56 |
| **4** | 1.682 | 1.938 | 4.576 | 9.084 | 17.280 | 10.028 | 1.9 | 0.48 |
| **5** | 0.336 | 1.076 | 3.499 | 7.738 | 12.650 | 7.341 | 1.8 | 0.45 |
| **6** | 0.336 | 0.387 | 2.637 | 6.661 | 10.023 | 5.817 | 1.62 | 0.4 |

Table 7. Results of calculations of reliability-related costs for utility

| **Reliability improvement step** | **Additional costs to existing costs of utility – UCR (US$)** |
|---|---|
| **1.** Only circuit breaker is installed | 0 |
| **2.** Step 1 + Manual sectionalising switches installed | 165 |
| **3.** Step 2 + Automatic sectionalising switches installed | 305 |
| **4.** Step 3 + Additional tree trimming for sections 1 and 2 | 562 |
| **5.** Step 4 + Cable line instead of overhead line in section 1 | 8715 |
| **6.** Step 5 + Cable lines instead of overhead lines in sections 1 and 2 | 15096 |

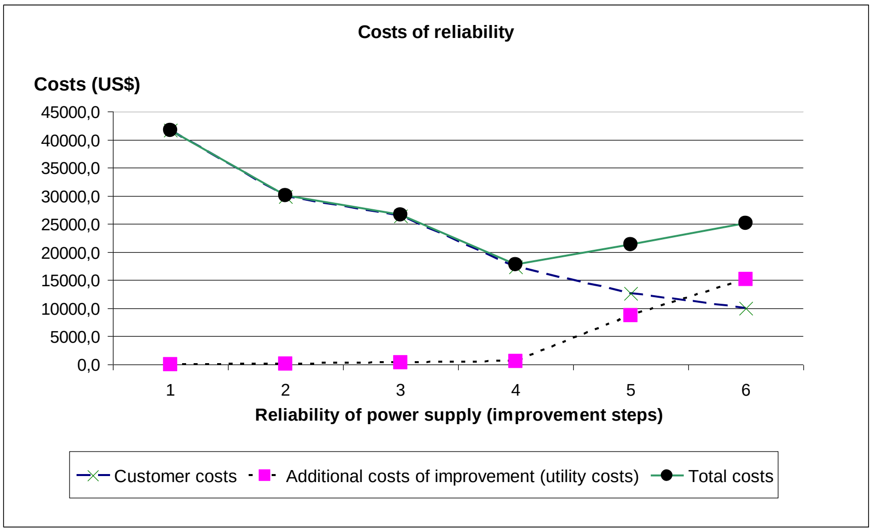

Fig. 6. Utility, customer and total costs depending on reliability improvement steps

Fig. 6 illustrates results of calculations summarised from Tables 6 and 7. Optimal reliability level for the feeder (in our case) corresponds to step 4 – when feeder has all automatic sectionalising switches installed and trees in sections 1 and 2 are being additionally trimmed.

Results of calculations can vary widely depending on loads, types of customers, length of lines placed in woodland, costs of improvement activities, etc. To make precise calculations DSO should know precise information about all components of the network. In different cases the same reliability improvement steps (activities) can give different results. For example, sometimes it can be more economical to install fault location detecting devices at each branch of feeder, instead of installing automatic sectionalising switches. Only after gathering detailed information about different costs and network structure, DSO can make more detailed analysis of network improvement.

## 4. CONCLUSIONS

Methodology for precise estimation of optimal reliability level was developed. For precise estimation of optimal reliability level, methodology allows to include: 1) detailed information about customer costs by sectors and subsectors according their geographical allocation; and 2) detailed information about reliability improvement costs of utility by defining this information for each feeder of substation.

Calculation results summarized showed effectiveness of the new methodology by showing big difference (about 40% for the 1st step – (41.665-24.180/41.665)=0.42) between results that use just average values of power supply interruption costs and results, that have been obtained using new methodology. For particular case improvement step 4 showed optimal reliability level using both – average CCR values and new methodology. But for real networks, with much more possible development variants, possibility of determination of incorrect “optimal” reliability improvement way by using average CCR costs can increase dramatically.

Developed methodology can be realised in different computer software (e.g. Matlab) and in combination with genetic algorithms (for faster finding optimal type of reliability improvement for particular feeder or substation) it could be a powerful tool for optimization of distribution network development taking into account reliability of power supply.

## REFERENCES

1. СКОПИНЦЕВ, В.А.; ЧЕМОДАНОВ, В.И.; ЧИЧИНСКИЙ, М.И. Оценка надёжности работы электрической сети (in Russian). *Трактат* НМЦ НЭС, Moscow, 2004, 37 p.
2. LVS IEC 50-191:1990, Starptautiskā elektrotehnikas vārdnīca, 191. nodaļa: Drošums un pakalpojumu kvalitāte (IEC 50-191:1990, *International Electrotechnical Vocabulary, Chapter 191: Dependability and quality of service)*. Rīga: Latvijas Nacionālais standartizācijas un metroloģijas centrs, 1998. 63 p.
3. RICHARD E. BROWN. *Electric power distribution reliability*. New York: Marcel Dekker Inc., 2002. 365 p. ISBN 0-8247-0798-2.
4. P. J. BALDUCCI; J. M. ROOP; L. A. SCHIENBEIN; J. G. DeSTESSE; M. R. WEIMAR. *Electrical Power Interruption Cost Estimates for Individual Industries, Sectors, and U.S. Economy*. Pacific Northwest National Laboratory, Washington, DC, PNNL-13797, 2002.
5. "Latvian Energy in Figures". Ministry of Economics of the Republic of Latvia, Riga, 2009. [Online]. Available: http://www.em.gov.lv/images/ modules/items/les_2009_.pdf.
6. "EN12. Production, imports, exports and consumption of electricity and production and consumption of heat, in natural units". Data bases of Central Statistical Bureau of Latvia. [Online]. Available: http://data.csb.gov.lv/DATABASEEN/vide/Annual%20statistical%20data/Energy/Energy.asp.

7. HONG-CHAN CHANG; TENG-FA TSAO. Reliability cost/worth analysis of distribution systems considering different topologies. Proceedings of international conference PMAPS 2002. [CD]. Naples. 2002 September 22–26.
8. *Reliability of Electric Utility Distribution Systems: EPRI White Paper*. EPRI, Palo Alto, CA: 2000. 1000424. Final Report, October 2000.
9. ĻVOVS, A, MUTULE, A. Estimation of outage probability of schemes of switchgears for 110kV substations. CYSENI2010. Proceedings of annual conference of young scientists on energy issues. [CD]. Kaunas: Lithuanian Energy Institute. 2010 May 27–28.
10. Z. KRIŠĀNS; I. OĻEINIKOVA; *Elektroenerģētisko uzņēmumu vadības pamati* (in Latvian). Rīga: Rīgas tehniskā universitāte, 2007. 158 p. ISBN 978-9984-32-985-7.
11. ALI A. CHOWDHURY; DON O. KOVAL. *Power Distribution System Reliability: Practical Methods and Applications*. John Wiley & Sons, Inc., Hoboken, New Jersey. 2009. 531 p. ISBN 978-0470-29228-0.
12. G. ROTHWELL; T. GÓMEZ. *ELECTRICITY ECONOMICS: Regulation and Deregulation*. John Wiley& Sons, Inc., 111River Street, Hoboken, NJ. 2003. 304 p. ISBN0-471-23437-0.
13. КАЛЯВИН, В.П.; РЫБАКОВ, Л.М. *Надёжность и диагностика элементов электроустановок.* Санкт-Петербург: Элмор, 2009. 331 p. ISBN 5-7399-0150-2.
14. P. HILBER; R. BERTLING. Multiobjective maintenance policy for a distribution system an application study. Proceedings of international conference PMAPS 2008. [CD]. Puerto Rico. 2008. May 25–29.
15. Web page of JSC "JAUDA" (Latvian electricity equipment producing company). [Referred on the 2nd of December in 2010 y.]. Link to the internet <http://www.jauda.com/html/atdalitaji.html>

CYSENI 2011, May 26–27, Kaunas, Lithuania
ISSN 1822-7554, www.cyseni.com

# MODEL FOR EVALUATION OF LARGE-SCALE POWER SYSTEM INTERCONNECTION COSTS AND BENEFITS

**O. Kochukov, A. Mutule, Z. Krishans, I. Oleinikova**
*Institute of Physical Energetics*
*Aizkraukles 21, LV-1006 – Latvia*
*Phone +371 67558616*
*Email: olegsk@edi.lv*

ABSTRACT

This paper considers the analysis of large-scale power system optimal interconnection concept as well as description of the model for evaluation of its costs and benefits. All existing power systems are willing to connect with other power systems. Power systems of one country merge together, countries developing interconnections and power systems of whole regions are constantly growing up. Developing new bigger power system from several small systems is slow process, but interconnected system has several big advantages – higher stability; higher reliability of power supply, especially in accident situations; better opportunities for optimal allocation of power reserves; better opportunities for optimal utilization of fuel and generation power.

This paper contains the method for comparison different scenarios of interconnection of two world largest power systems - ENTSO-E and IPS/UPS by economical criteria. The research has shown that developed model helps to make deep analysis and is ready for calculation of interconnection links optimal locations, transmission capacities and interconnection type.

Keywords – Large power system interconnection, ENTSO-E, IPS/UPS.

## 1. INTRODUCTION

The development of electric power industry follows closely the increase of the demand on electrical energy. Main driving factors for energy consumption are: technological development, population growth, economical growth, availability of energy. In the early years this increase was extremely fast, also in industrialized countries, many decades with the doubling of energy consumption each 10 years. Nowadays, such fast increase still is present in developing countries, especially in Far-East. In the industrialized countries the increase is, however, only about 1 to 2% per year with an estimated doubling of the demand in 30 to 50 years. In next 20 years, power consumption in developing and emerging countries is expected to more than double, whereas in industrialized countries, it will increase only for about 40%. Fast development and further extension of power systems can therefore be expected mainly in the areas of developing and emerging countries. However, because of a lack on available investments, the development of transmission systems in these countries does not follow the increase in power demand. Hence, there is a gap between transmission capacity and actual power demand, which leads to technical problems in the overloaded transmission systems.

The benefits from power system interconnection are (they are generally valid and do not depend on the kind of the interconnection):

- Possibility to use larger and more economical power plants;
- Reduction of the necessary reserve capacity in the system;
- Utilization of most favorable energy resources;
- Flexibility of building new power plants at favorable locations;
- Increase of reliability in the systems;
- Reduction of losses by an optimized system operation.

## 2. POSSIBLE SCENARIOS OF INTERCONNECTION OF LARGE POWER SYSTEMS

Interconnection of separated grids in the developed countries can solve some of these problems, however, when the interconnections are heavily loaded due to an increasing power exchange, the reliability and availability of the transmission will be reduced. The main question here is finding reliable and cheap way of connecting large power systems.

Possible technical ways of interconnecting two large-scale power systems are shown in Fig. 1. They are: a) AC + AC, b) DC, c) AC + DC.

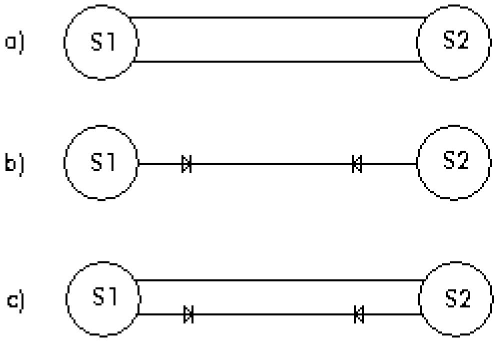

Fig. 1. Possible types of power system interconnection

Considering “AC + AC” interconnection type, only one line cannot keep necessary stability level, that’s why for large-scale power systems it is assumed that more than one AC link between systems is needed. AC link can be a cable or an overhead line.

DC link provides power flow from one power system to another without voltage frequency and level synchronization. DC links is divided into back-to-back and generation-to-load links. Also DC link can be a cable or an overhead line.

In case of hybrid interconnection “AC + DC”, direct current link makes synchronized system more stable and prevent from separate types of accidents.

In the past, the normal way to merge system was making the synchronous interconnections. Best example is the development of the UCTE system in Western Europe, which has been expanded in steps to the today very complex configuration, with the expected further extension to Romania and Bulgaria. Now the situation has changed and HVDC connections have considerable advantages:

- DC cables low capacitance causes fewer losses in comparison to AC (e.g., 250 km Baltic cable, the 600 km NorNed cable, and 290 km Basslink);
- Making HVDC from AC line increases the capacity of an existing power grid (especially profitable in situations where additional wires are difficult or expensive to install);
- Possibilities for power transmission and stabilization between unsynchronized AC systems;
- Possibilities of connecting remote generator to the grid (e.g. Nelson River Bipole);
- Stabilized predominantly AC power-grid, without increasing prospective short circuit current;
- Reduced line cost. HVDC needs fewer conductors as there is no need to support multiple phases. Also, thinner conductors can be used since HVDC does not suffer from the skin effect;
- Possibilities to facilitate power transmission between different countries that use AC at differing voltages and/or frequencies;

- Easiest transmission of energy produced by renewable energy sources.

The disadvantages of HVDC are in conversion, switching, control, availability and equipment maintenance problems.

## 3. COSTS OF INTERCONNECTION OF LARGE-SCALE POWER SYSTEMS

Costs of new electric transmission line consider:

- Total capital investments $K$ (including materials, equipment and construction);
- Annual maintenance costs $C_{main}$;
- Annual losses costs $C_{losses}$;
- Annual non-delivery energy costs $C_{N.D.}$;
- Annual costs for amortization.

According to these costs, it is possible to estimate interconnection types from economical point of view. Table 1 shows relative costs for different interconnection scenarios. “Weak AC connection” scenario considers existing lines without building new. Explanation of costs amount for different scenarios can be found in Section 2.

Table 1. Relative costs of different interconnection scenarios

| Connection type / Relative costs | **AC+AC** | **DC** | **AC+DC** | **Weak AC connection** |
|---|---|---|---|---|
| **High** | $C_{main}$ | $K$ | $K, C_{main}$ | $C_{main}, C_{N.D.}$ |
| **Average** | $C_{losses}, C_{N.D.}$ | $C_{main}, C_{losses}$ | $C_{losses}$ | $C_{losses}$ |
| **Low** | $K$ | $C_{N.D.}$ | $C_{N.D.}$ | |

## 4. METHODOLOGY FOR ENTSO-E AND IPS/UPS POWER SYSTEM INTERCONNECTION COST CALCULATION

Since interconnection cost calculation is complicated task, we propose to utilize information technology LDM-TG’08 for this purpose.

### 4.1. Description of the LDM-TG’08 information technology

LDM-TG’08 software was developed in 2008 in Laboratory of Power System Mathematical Modeling for calculation of optimal sustainable development of power systems. The possibilities of the software include:

- Annual technical-economical criteria calculation;
- Total technical-economical criteria calculation;
- Development plan sensitivity analysis;
- Risk analysis of forecasts;
- Power flows in model;
- Voltages, voltage loses and balance in nodes;
- Network reliability;
- Switchgear reliability;
- Annual energy balance.

### 4.2. ENTSO-E and IPS/UPS model forming

Fig. 2 shows the structure of ENTSO-E and IPS/UPS power system network in LDM-TG'08 software environment.

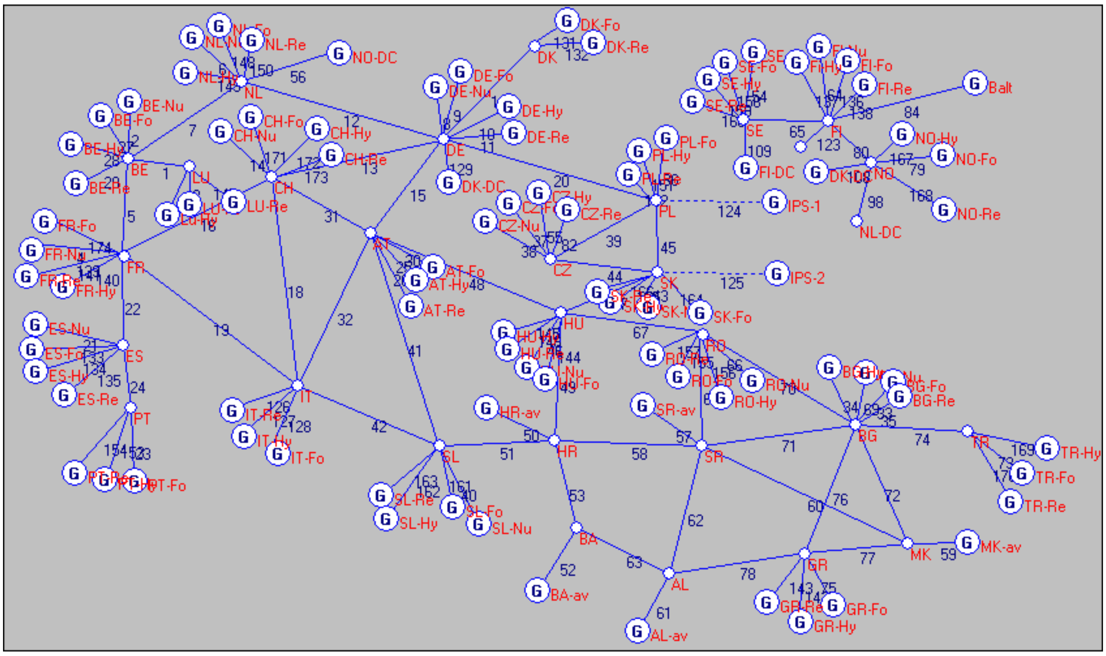

Fig. 2. Structure of the power system model

ENTSO-E power system is modeled with set of countries-members with nominal voltage of 400 kV. IPS/UPS power system is modeled with set generators connected to ENTSO-E network. Place of connection of IPS/UPS system (generator) as well as their power depends on interconnection scenario considered. In example shown in Fig. 2 IPS/UPS generators are connected to Poland and Slovakia. Each country or subsystem is modeled with a load node and several generator nodes (equivalent power plants). Each equivalent power plant corresponds to different power plant type. Number of equivalent power plants depends on types of energy sources that are used in the country. Maximum number of equivalent power plants is four: nuclear, fossil-fired, hydro and renewable. For some countries it can be three or two, for example Italy do not have nuclear power plants at all. Fig. 3 shows load node and power plant forming windows.

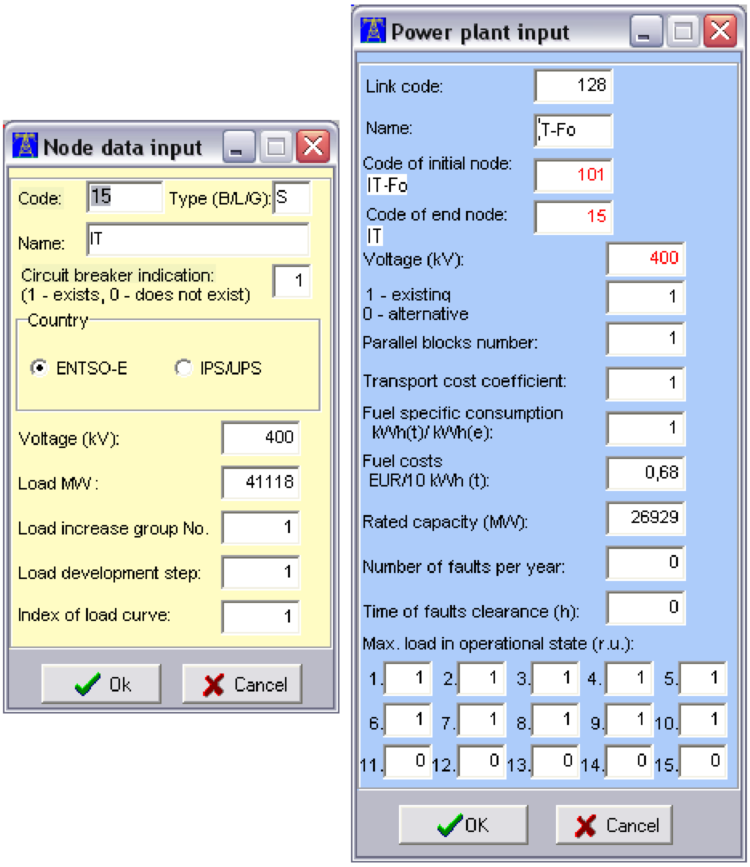

Node data input

Code: 15 Type (B/L/G): S

Name: IT

Circuit breaker indication: (1 - exists, 0 - does not exist): 1

Country: ● ENTSO-E ○ IPS/UPS

Voltage (kV): 400

Load MW: 41118

Load increase group No.: 1

Load development step: 1

Index of load curve: 1

Power plant input

Link code: 128

Name: IT-Fo

Code of initial node: 101 IT-Fo

Code of end node: 15 IT

Voltage (kV): 400

1 - existing 0 - alternative: 1

Parallel blocks number: 1

Transport cost coefficient: 1

Fuel specific consumption kWh(t)/kWh(e): 1

Fuel costs EUR/10 kWh (t): 0,68

Rated capacity (MW): 26929

Number of faults per year: 0

Time of faults clearance (h): 0

Max. load in operational state (r.u.):

1. 1 2. 1 3. 1 4. 1 5. 1
6. 1 7. 1 8. 1 9. 1 10. 1
11. 0 12. 0 13. 0 14. 0 15. 0

Fig. 3. Load node and power plant forming windows

Network member annual generated energy of 2010 ($W_{annual}$) was input data of the model [3]. Since parameter "Relative maximal load in operational state" is set to 1 (power plant non-stop works at set load), power of each equivalent power plant is:

$$P_i = \frac{(\text{annual generated energy})_i}{8760} \tag{1}$$

Average load of nodes in the model are calculated the same way:

$$L_i = \frac{(\text{annual consumed energy})_i}{8760}. \tag{2}$$

Part of calculation results of average power and load of modeled countries are shown in Tab. 2 and Tab. 3. Generated energy, consumed energy and peak demand are given values.

Table 2. Part of calculation results of average power for different equivalent power plants

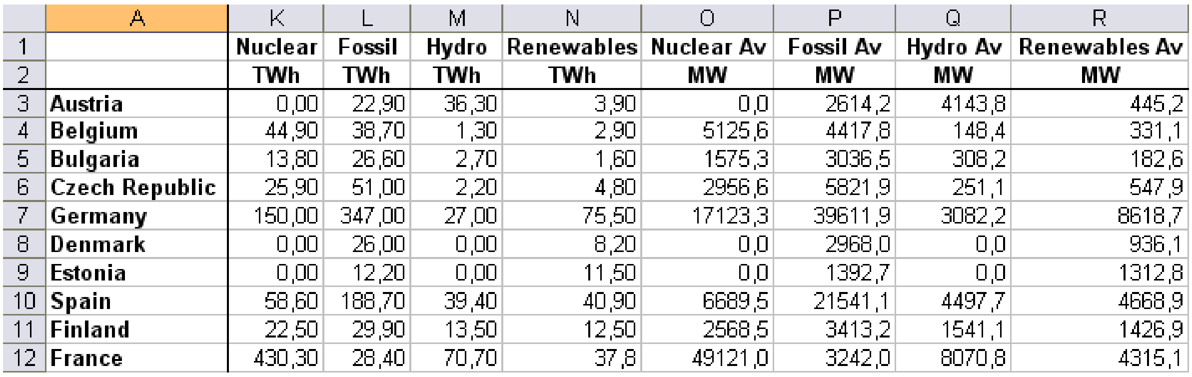

| | A | K | L | M | N | O | P | Q | R |
|---|---|---|---|---|---|---|---|---|---|
| 1 | | **Nuclear** | **Fossil** | **Hydro** | **Renewables** | **Nuclear Av** | **Fossil Av** | **Hydro Av** | **Renewables Av** |
| 2 | | **TWh** | **TWh** | **TWh** | **TWh** | **MW** | **MW** | **MW** | **MW** |
| 3 | **Austria** | 0,00 | 22,90 | 36,30 | 3,90 | 0,0 | 2614,2 | 4143,8 | 445,2 |
| 4 | **Belgium** | 44,90 | 38,70 | 1,30 | 2,90 | 5125,6 | 4417,8 | 148,4 | 331,1 |
| 5 | **Bulgaria** | 13,80 | 26,60 | 2,70 | 1,60 | 1575,3 | 3036,5 | 308,2 | 182,6 |
| 6 | **Czech Republic** | 25,90 | 51,00 | 2,20 | 4,80 | 2956,6 | 5821,9 | 251,1 | 547,9 |
| 7 | **Germany** | 150,00 | 347,00 | 27,00 | 75,50 | 17123,3 | 39611,9 | 3082,2 | 8618,7 |
| 8 | **Denmark** | 0,00 | 26,00 | 0,00 | 8,20 | 0,0 | 2968,0 | 0,0 | 936,1 |
| 9 | **Estonia** | 0,00 | 12,20 | 0,00 | 11,50 | 0,0 | 1392,7 | 0,0 | 1312,8 |
| 10 | **Spain** | 58,60 | 188,70 | 39,40 | 40,90 | 6689,5 | 21541,1 | 4497,7 | 4668,9 |
| 11 | **Finland** | 22,50 | 29,90 | 13,50 | 12,50 | 2568,5 | 3413,2 | 1541,1 | 1426,9 |
| 12 | **France** | 430,30 | 28,40 | 70,70 | 37,8 | 49121,0 | 3242,0 | 8070,8 | 4315,1 |

Table 3. Part of calculation results of average demand for different countries

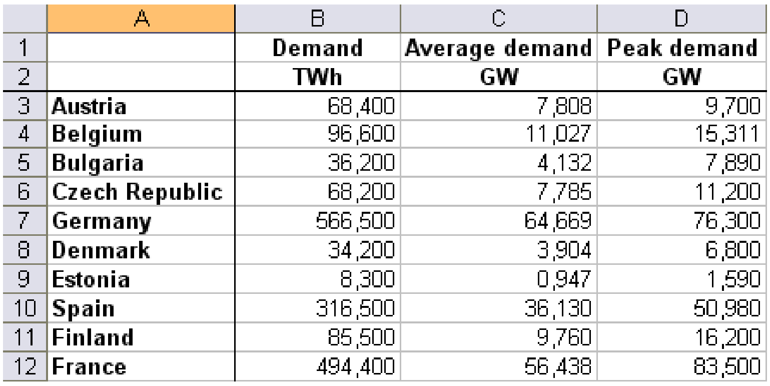

| | A | B | C | D |
|---|---|---|---|---|
| 1 | | **Demand** | **Average demand** | **Peak demand** |
| 2 | | **TWh** | **GW** | **GW** |
| 3 | **Austria** | 68,400 | 7,808 | 9,700 |
| 4 | **Belgium** | 96,600 | 11,027 | 15,311 |
| 5 | **Bulgaria** | 36,200 | 4,132 | 7,890 |
| 6 | **Czech Republic** | 68,200 | 7,785 | 11,200 |
| 7 | **Germany** | 566,500 | 64,669 | 76,300 |
| 8 | **Denmark** | 34,200 | 3,904 | 6,800 |
| 9 | **Estonia** | 8,300 | 0,947 | 1,590 |
| 10 | **Spain** | 316,500 | 36,130 | 50,980 |
| 11 | **Finland** | 85,500 | 9,760 | 16,200 |
| 12 | **France** | 494,400 | 56,438 | 83,500 |

Prices of electrical energy in equivalent power plants of each country were set according to study of International Energy Agency [4]. For countries that didn't provide information about electricity prices from their power plants, average prices from all other countries are assumed. According to our study, average price of electricity production at ENTSO-E power plants is 0,087 EUR per kWh and average price of electricity production at IPS/UPS power plants is 0,058 EUR per kWh. In the model prices of electricity from different energy sources are calculated separately. Relation of electricity prices from different power plants of different countries gives possibility to build the ranking of equivalent power plants in the model (to let the plant with cheapest energy work first).

Links between the countries (nodes) are modeled with overhead lines and cables. It is assumed that mark of these links is the same for each interval of 400 kV ENTSO-E network - 3xAS-400/51 overhead line. Maximal transmission capacity between countries (nodes) is calculated as:

$$P_{MAX} = P_{MAX.SINGLE} \cdot n, \tag{3}$$

where $P_{MAX}$ – maximal transmission capacity between countries (nodes);

$P_{MAX.SINGLE}$ – maximal transmission capacity of single line; $n$ – parallel line number on given interval.

## 5. POWER SYSTEM DEVELOPMENT PLANS AND ITS COMPARISON

LDM-TG'08 software has special block for power system development plan forming and its comparison. Development plan forming starts with development action setting. Development action setting window is shown in Fig. 4.

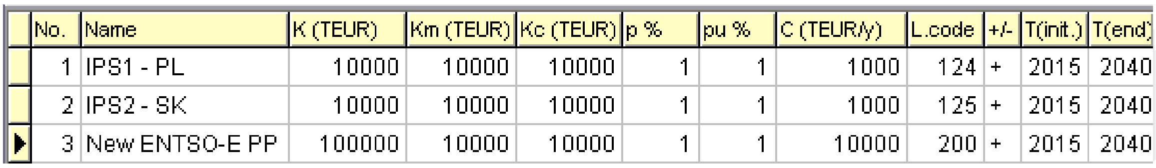

| No. | Name | K (TEUR) | Km (TEUR) | Kc (TEUR) | p % | pu % | C (TEUR/y) | L.code | +/- | T(init.) | T(end) |
|---|---|---|---|---|---|---|---|---|---|---|---|
| 1 | IPS1 - PL | 10000 | 10000 | 10000 | 1 | 1 | 1000 | 124 | + | 2015 | 2040 |
| 2 | IPS2 - SK | 10000 | 10000 | 10000 | 1 | 1 | 1000 | 125 | + | 2015 | 2040 |
| 3 | New ENTSO-E PP | 100000 | 10000 | 10000 | 1 | 1 | 10000 | 200 | + | 2015 | 2040 |

Fig. 4. Development action setting window

This test case has two development actions concerning AC interconnections: IPS/UPS – Poland, IPS/UPS – Slovakia and one development action concerning new power plant building in ENTSO-E system (Italy). As it was already mentioned above, interconnections are modeled with alternative lines from generators, which model IPS/UPS system. In this case we can clearly set generation power and also we can assume that it this case it is transmission power from IPS/UPS to ENTSO-E system. Parameters of the development actions are approximate and considered for testing of the model. It was decided to compare different interconnection scenarios with scenarios of building new power plant in ENTSO-E system. New power plant building scenarios besides will take into account real capital investments for new modern power plant and oil price increment in region. Technical-economic calculation (that our model is ready to perform) results can clearly show benefits of interconnection scenarios.

After setting development actions, plan forming can be performed. Development plan formation window is show in Fig. 5.

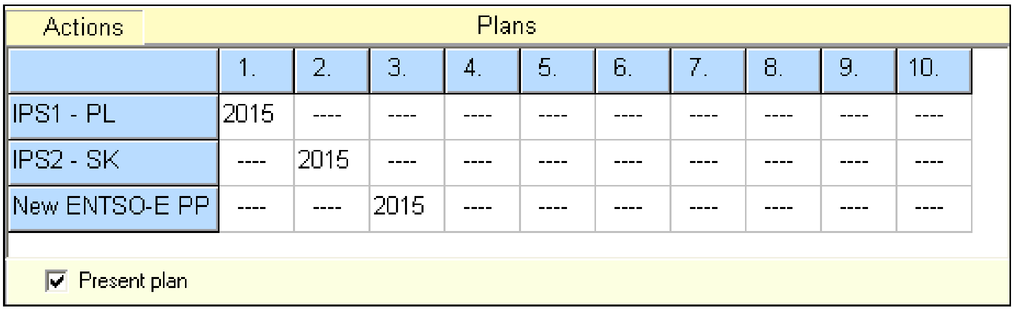

|  | 1. | 2. | 3. | 4. | 5. | 6. | 7. | 8. | 9. | 10. |
|---|---|---|---|---|---|---|---|---|---|---|
| IPS1 - PL | 2015 | ---- | ---- | ---- | ---- | ---- | ---- | ---- | ---- | ---- |
| IPS2 - SK | ---- | 2015 | ---- | ---- | ---- | ---- | ---- | ---- | ---- | ---- |
| New ENTSO-E PP | ---- | ---- | 2015 | ---- | ---- | ---- | ---- | ---- | ---- | ---- |

☑ Present plan

Fig. 5. Development plan formation window

In this test case we form three development plans. First development plan considers IPS/UPS – Poland connection in 2015, second – IPS/UPS – Slovakia connection in 2015 and the third – new power plant building in ENTSO-E system in 2015. Also model considers development plan with no actions.

To perform sustainable development plan analysis, precise load increment forecast should be made. Our calculations showed that in period from 2010–2020 load increment in Europe will be from 0.5% to 10% and average 2.2% annually. In period from 2020–2030 it will be from 0.2% to 2.5% and average 1.5% annually. According to this study, average annual load increment value for period from 2010–2030 for whole ENTSO-E system is 1.9%.

After development actions and plan forming are done, we move on to power balance. Calculation results of power balance for 2010 performed by our model shows no misbalance. However, taking into account load increment that was shown previously, power balance of 2015 shows that ENTSO-E will need additional 27.88 GW of installed power by that time (Fig. 6). At the year of 2020 deficit is already 70 GW. Also, some overloaded lines in ENTSO-E system appear after 2010.

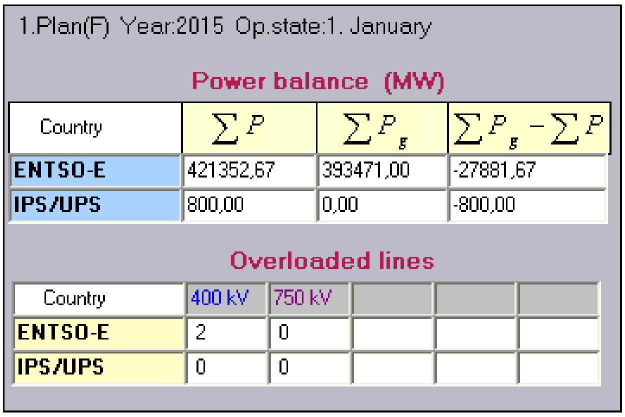

1.Plan(F) Year:2015 Op.state:1. January

Power balance (MW)

| Country | $\sum P$ | $\sum P_g$ | $\sum P_g - \sum P$ |
|---|---|---|---|
| **ENTSO-E** | 421352,67 | 393471,00 | -27881,67 |
| **IPS/UPS** | 800,00 | 0,00 | -800,00 |

Overloaded lines

| Country | 400 kV | 750 kV |  |  |  |
|---|---|---|---|---|---|
| **ENTSO-E** | 2 | 0 |  |  |  |
| **IPS/UPS** | 0 | 0 |  |  |  |

Fig. 6. Power balance in model for 2015

Obvious, to get maximal benefit in future, not only border connections or new power plants should be built, but also inter-system network has to be improved.

This paper provides only model testing. Further, it is possible to examine technically valid ENTSO-E and IPS/UPS interconnection scenarios to figure out interconnection links optimal locations, transmission capacities and interconnection type.

## 6. CONCLUSIONS

Since world's energy consumption and energy needs are constantly growing new generating capacities are essential, as well as, in order to optimally utilize resources, power systems development should include merging into bigger systems.

Developed model is capable and ready to make deep analysis and comparison of ENTSO-E system possible development plans, including different scenarios of new power plants building and interconnection with IPS/UPS system.

Test case calculation results show deficit in ENTSO-E system already in 2015, what proofs the necessity in the system's development. Also, since number of overloaded lines is growing with years, it can be concluded that in order to get maximal benefit from system's development, not only border connections or new power plants should be built, but also inter-system network has to be improved.

## 7. REFERENCES

1. KRISHANS, Z.; MUTULE, A.; MERKURIEV, Y.; OLEINIKOVA, I. *Dynamic Management of Sustainable Development.* Germany: Springer, 2011. 5–6, p. 52–60.
2. KRISHANS, Z.; MUTULE, A.; MERKURIEV, Y.; OLEINIKOVA, I. 10th International Conference on Probabilistic Methods Applied to Power Systems. Symposium Proceedings [CD]. Puerto Rico: Rincón. 2008 May 25–29.
3. *ENTSO-E network online transmission capacity database*. Link to the internet <https://www.entsoe.net/data.aspx?IdMenu=8>
4. INTERNATIONAL ENERGY AGENCY. *Projected costs of generating electricity*. 2010, p. 60–70.

# POWER PLANTS SUSTAINABLE DEVELOPMENT OPTIMIZATION IN LIBERALIZED MARKET CONDITIONS

**M. Turcik, I. Oleinikova, Z. Krishans**
*Institute of Physical Energetics*
*Laboratory of Power System Mathematical Modelling*
*Aizkraukles 21, Riga, LV-1006 – Latvia*

ABSTRACT

This article presents power system development strategy planning and optimization with focus on power generation segment under liberalized market conditions Paper describes requirements of electricity market establishment and proposes methods and principles for Power System Sustainable Development Management.

Keywords: Power plant model, electricity market, power system, development optimization methods.

## 1. INTRODUCTION

Progressive energy policy of European Union (EU) based on competitive environment, security of supply and implementation of renewable energy sources in generation structures brings many new challenges and transform the conventional pattern of energy sector. Planned common European market with electricity calls for reinforcement of transmission systems in member States[1] as well as for cross-border interconnections construction or extension.

Targets of EU Commission with long term energy strategy to 2020 are presented in 20-20-20 EU's Strategy. Regarding to new tendencies in this area, activities for Baltic region are summarized as a Baltic Energy Market Interconnection Plan (BEMIP) [1].

Investments into new infrastructure are not centrally planned anymore. Market prices should give the right incentives for the development of the network and for investing in new electricity generation. [2] Stimulation of investors with reliance only at market signals can be not sufficient for proper, stable sustainable development of power system. Targets and thus investments are often different (opposed) regarding to independent market players. New generating capacity investments in compliance with EU directive 72/2009/EC indicate two main procedures in this area, Authorisation and Tendering.

Solving tasks related with new power generation units moreover, need to take into account condition in new liberalized market environment, especially envisage with requirements for encouraging competitive ambiance between power sources.

Furthermore, power plants development optimization under liberalized market should be simultaneous optimization of generation structure and transmission network.

Considering requirements of new environment this article proposes methods for power system sustainable development optimization with special attention on power generation under liberalized market conditions.

## 2. ELECTRICITY MARKET BALANCE

The Balance in the electricity market means equilibrium of electricity supply and demand in a particular timeframe, without causing a considerable disproportions in any part of the power system, and thus disturbances on electricity market.

---

[1] Implementation of EU Energy legislation cover the whole European Economic Area (EEA)

Unlike the vertically oriented system, in a liberalized market, prediction of consumption is not implemented in nationwide scale directly by supply company that could be at the same time also power producer, operator of the transmission and distribution system, but depends on the contracts between independent market participants. Secure and reliable operation of power system requires utilization of long-term as well as short-term balance calculation.

The main reasons for solving tasks related with Balance and load prediction at the whole-scale transmission system /electricity market level are mostly as follows [3]:

- State intervention in case of deficiency of electricity;
- Power system operational reliability calculation including ancillary services, grid estimation inclusive cross-border interconnections;
- Grid development planning;
- New generation capacity planning;
- Reserve/Regulation capacity estimation;
- Planning of power system operation.

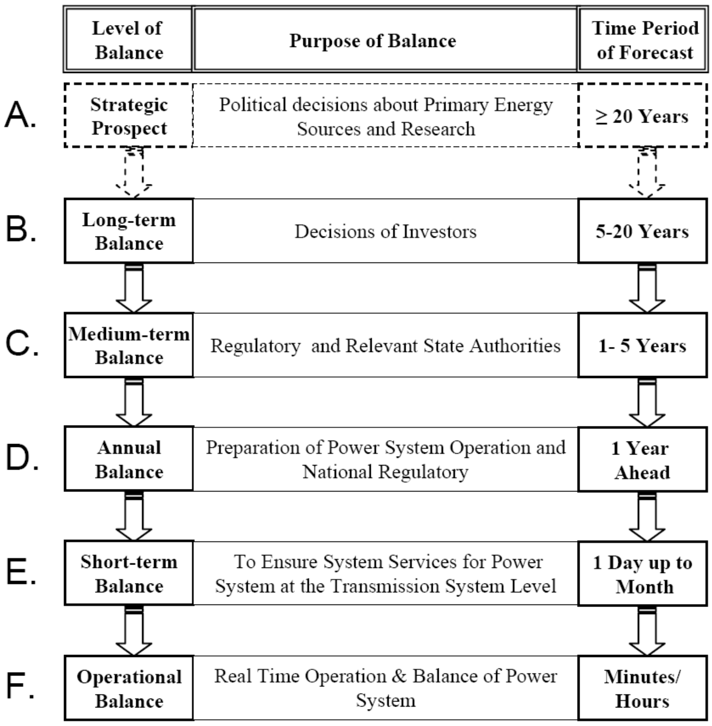

Fig. 1. Levels of power system balance

A strategic prospect serves as a basis for political decisions, future primary energy source determination, State subsidy mechanism creation as well as scientific research purposes. Long-term balance estimation is based on prediction of consumption (5–20 years forward) in order to secure sufficient electricity volume (State production or cross-border transmission).

Medium-term balance assumptions takes into account, that power production is relatively exactly determined as well as requirements of consumers. However, impact of weather on consumption is not determined. None considerable changes in structure or behavior of consumers expected.

In this article we are focused on part depicted in Figure 1. in blocks A and B.

## 3. OPTIMIZATION CRITERA

Optimization methods for Power System development need to take into account new conditions for power sources and networks development process in condition of liberalized market. [4]-[5]. Estimation period is represented as a multi-step development process. Uncertainty of information and conditions need to be considered in decision making process. Power system analysis of sustainable development is performed in compliance with methods for whole economic life cycle of object (20–25 years). Duration of development plan estimation period $T$ is to be considered for interval at least equal to the economic cycle or longer, up to 50 years. The objective function must be calculated for whole estimation period $T$ under information and conditions uncertainty. The final decision must be made specifically for not durable time period, not far perspective. This time interval is designated as decision making period $t_d < T$ and period from $t_d$ up to $T$, adaptation period $t_{ad}$ (see Fig. 2).

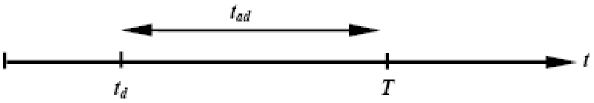

Fig. 2. Estimation ($T$), decision making ($t_d$) and adaptation ($t_{ad}$) period

Criteria for power system sustainable development are presented in Figure 3. *Objective function.* Objective function for PS development plan shall display and integrate technical, economic, power supply reliability, ecological etc. parameters depending on specific technical system [3]. Objective function is system development plan g quality criterion and denoted as $F(T,g)$. Further on, the objective function will be calculated by a formula:

$$\max F(T,g) = \max_{g\in\{G\}} \sum_{t=1}^{T} F(t,e(t)) \qquad (1)$$

T – number of development steps; g – development plan; $\{G\}$ – set of all possible development plans; $e(t)$ - development state in step $t$; $F(t,e(t))$ – objective function part in development step $t$.

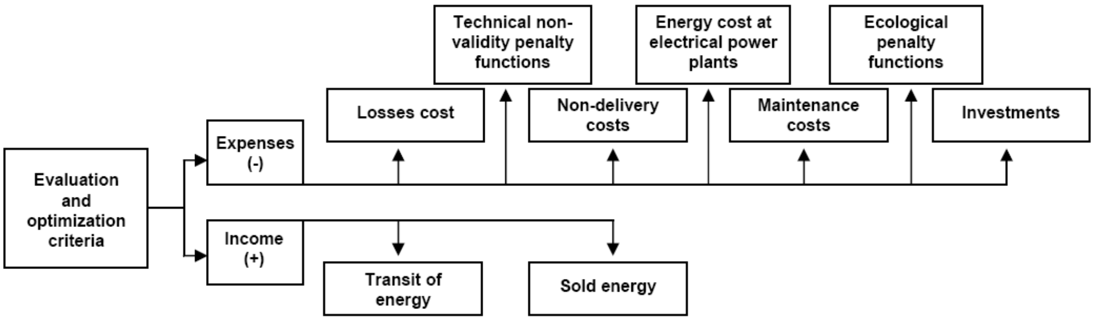

Fig. 3. Evaluation and Optimization criteria of Power system

According to formula (1), the maximum of objective function is the maximal value of sum from $F(t,e(t))$, i.e., an additive function [2]. System graph, consumption and generation are constant values at the development step but development actions are only realized in transition from development step t-1 to development step t. Observing these assumptions, $F(t,e(t))$ model may look as follows:

$$F(t,e(t)) = k(t)\cdot\tau(t)\cdot d(t) \tag{2}$$

$k(t)$ – System quality criterion for the first year of the development step $t$; $\tau(t)$ – Number of years in development step $t$; $d(t)$ - Discount (reduction) coefficient for development step $t$.

$F(t,e(t))$ is not dependent on development plan up to development state $e(t)$. Objective function (1) allows dynamic programming application for task solution on large technical systems sustainable development management. For optimal development plan selection under information uncertainty in power system sustainable development process, we use risk analysis (see Fig 4 and formula 3) [4].

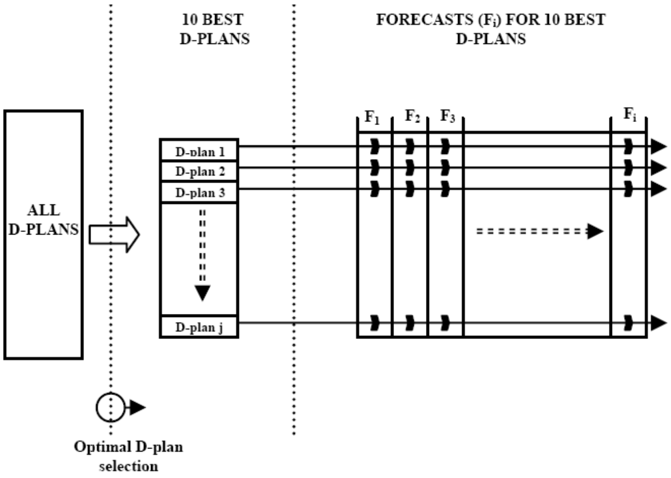

Fig. 4. Principle of development plan risk analysis

Minimal maximal risk is calculated by formula:

$$\min_{j\in\nu} R(j)_{\max} = \min_{j\in\nu}\max_{i\in\mu}\left(F(j,i)-F(i)\right) \tag{3}$$

where $i$ – index of forecast; $j$ – index of development plan; $\mu$ – Set of forecasts; $\nu$ – Set of development plans.

## 4. POWER PLANT DEVELOPMENT OPTIMIZATION

In Power Plant development optimization must be special model of development plan. This model should be described with the following basic concept: 1) development action; 2) development state [4]–[5]. Development action reflects activity related with new system object, e.g. power plant and transmission network construction, as well as existing objects extension, reconstruction or modernization and is assigned along with capital investments and relevant network elements. Development action can be classified as simple or compound (of several simple development actions following logical sequence). During risk analysis development actions which are realized on period $t_d$ are not depending on forecast but only on development plan. Development actions realized on period $t_{ad}$ are acquired by dynamic optimization. Development process of Power System depends on realized development actions. Development action structure is given on Fig. 5.

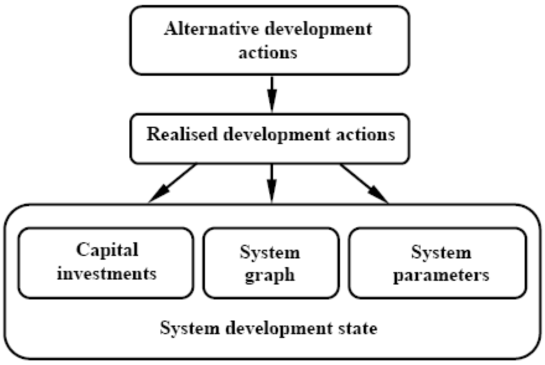

Fig. 5. Formation of development state $e(t)$

Development process of Power System depends on realized development actions. Development state - Generally, development state of Power System is determined by parameters in assumed moment. In optimization task is specified by system graph, its elements parameters and other technical, economic, ecological etc. parameters. Relation between development state and development action is shown on Fig. 6.

Fig. 6. Development state formation

Power system development plan $g$ should be defined as a sequence of development states $e(t)$ on estimation period which is divided into ($T$) development steps.

As a result of selection, best development plans are automatically formed, which are obtained through optimization (10 development plans), so both, technical and economic analysis may be performed for these development plans. Dynamic optimization task to determine optimal development plan $opt\, g$, that has the maximal value of objective function is calculated by formula (1). Development plan is described as states sequence as follows:

$$g = e(1) \subseteq e(2) \ldots e(t-1) \subseteq e(t) \ldots e(T-1) \subseteq e(T) \tag{4}$$

Development process is described by development graph see Fig.7. In Fig. 7 states in step t can be expressed by a set of realized development actions the task is reviewed with two development actions; possible development states are: {0} - none of development actions is realized; {1} - 1st development action is realized; {2} - 2nd development action is realized ;{ α, β} – in state e (t) 1st and 2nd development actions are realized.

Thus, it must be clarified what development actions and where (in which development step) must be realized.

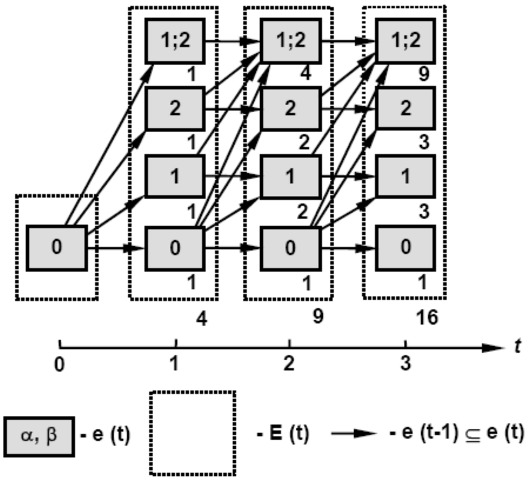

Fig. 7. Development plan graphs

Symbol $e(t-1) \subseteq e(t)$ expresses the meaning that set $e(t)$ contains all set $e(t-1)$ development actions. Possible development plans set can be illustrated with development graphic. Dynamic development optimization software complex can be illustrated with a flowchart (see Fig. 8).

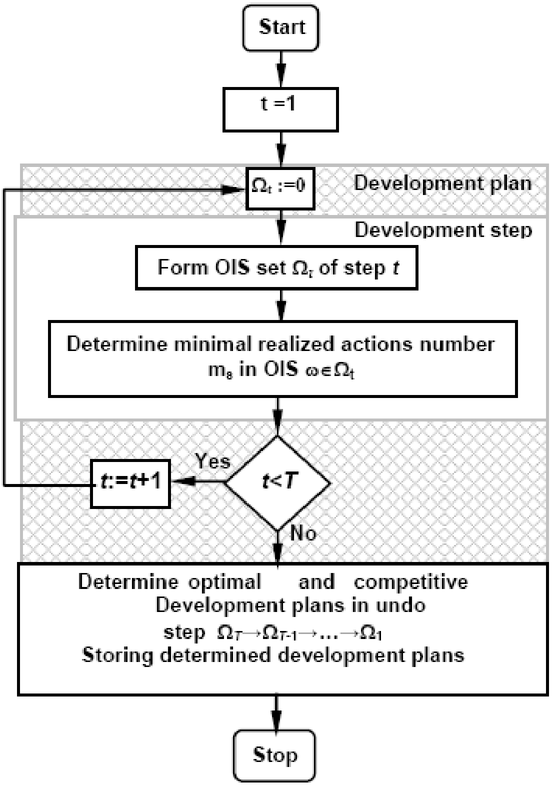

Fig. 8. Dynamic development optimization algorithm

## 5. METHOD FOR LOAD DISTRIBUTION BETWEEN POWER PLANTS IN LIBERALIZED MARKET

For simultaneous optimization of generation system and transmission network load should be distributed optimally between power sources. Composition of power sources in assumed Area varying with different development plan and development step. Thus, as a benchmark for various developments plan comparison is taken into consideration optimal distribution of load between them. The aim of these methods (see Fig. 9) is to calculate $P(n,re)$ for all power plants in development state e(t) in operational state $re$. As well specific electricity price at power plant for $t, e(t), re$ is applied following model of Power Plant under liberalized market conditions:

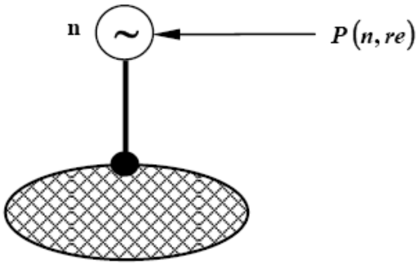

Fig. 9. Model of Power Plant under liberalized market conditions

$n$ – Index of power plant; $re$ – Operational state; $P(n,re)$ – Generation of power plant $n$ in operational state $re$ should be estimated for all power plants.

Power plant $n$ is to be designated with: Power plant nominal capacity $P_{nom}(n)$, MW; Specific electricity costs $C_{ip}(n,re)$ is formed by forecast at development state and operation state $re$ for $re = 1,2,\ldots,rem$ in m.u. /MWh; Capacity factor $Fc(n,re)$ for $re = 1,2,\ldots,rem$, $rem$ - Number of all operational states.

Average Power plant generation in every operational state depend on various factors which have a bearing on output generation schedule formation of assumed source. Factors with direct impact on output generation schedule respect type of Power plant, e.g. for Combine Heat&Power plant ratio of generation heat and power, Hydro Power plant – water condition, reservoir volume, Wind Power plant – wind condition. But also intended temporary service decommissioning (total or reduced power generation) etc. Capacity factor of power plant can be calculated as follows:

$$Fc(n,re) = \frac{W_p}{Tr(re) \cdot P_{nom}(n)} \tag{5}$$

$Tr(re)$ – Duration of operational state in hours; $W_p$ – Volume of generated electricity during $Tr(re)$ in MWh.

Appropriate value of $Tr(re)$ is considered as year (annual capacity factor) or monthly capacity factor For various types of Power plants, estimated average annual outputs are in Table 1 [6].

Limit (maximal value) of power generation at power plant $n$ in operational state $re$:

$$P_m(n,re) = P_{nom}(n) \cdot Fc(n,re), \quad [\text{MW}] \tag{6}$$

Table 1. Annual capacity factors by Power plant type

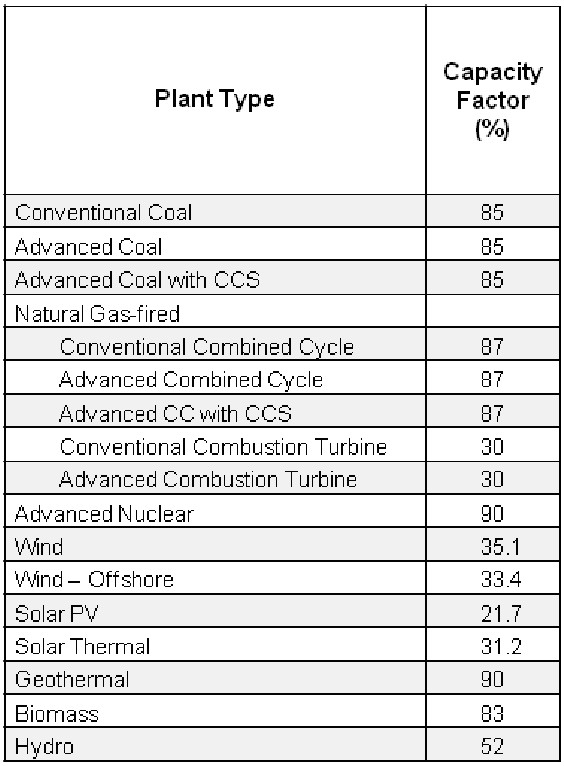

| **Plant Type** | **Capacity Factor (%)** |
|---|---|
| Conventional Coal | 85 |
| Advanced Coal | 85 |
| Advanced Coal with CCS | 85 |
| Natural Gas-fired | |
| Conventional Combined Cycle | 87 |
| Advanced Combined Cycle | 87 |
| Advanced CC with CCS | 87 |
| Conventional Combustion Turbine | 30 |
| Advanced Combustion Turbine | 30 |
| Advanced Nuclear | 90 |
| Wind | 35.1 |
| Wind – Offshore | 33.4 |
| Solar PV | 21.7 |
| Solar Thermal | 31.2 |
| Geothermal | 90 |
| Biomass | 83 |
| Hydro | 52 |

Limit (maximal value) of power generation at power plant $n$ in operational state $re$:

$$P_m(n,re)=P_{nom}(n)\cdot Fc(n,re),\quad [\mathrm{MW}] \tag{6}$$

Calculation of load distribution between power plants is performed for every development plan in all development steps and operational states. In such situation total electricity costs in all development states will be minimal. Objective function is:

$$Cr(t)=\sum_{re=1}^{rem(t)}\sum_{n\in MG}Cr(t,n,re)\rightarrow \min \tag{7}$$

Electricity costs Cr calculation for source $n$ in operational state $re$:

$$Cr(t,n,re)=P(n,re)\cdot Tr(re)\cdot Cip(n,re),\quad [\mathrm{m.u.}] \tag{8}$$

$P(n,re)$ – Source generation in operational state $re$; $Cip$ – Specific electricity price for power plant *n*, in rezime *re*.

Load distribution between power plants in operational state $re$ observes these limitations: $P(n,re)\le P_m(n,re)$; $\sum P(n,re)=Psd(re)$, $Psd(re)$ – Consumption (demand) in operational state $re$, [MW]; $n\in MG$, $MG$ – Set of power sources (power plants).

The flowchart of optimization algorithm for sources in operational state is shown below:

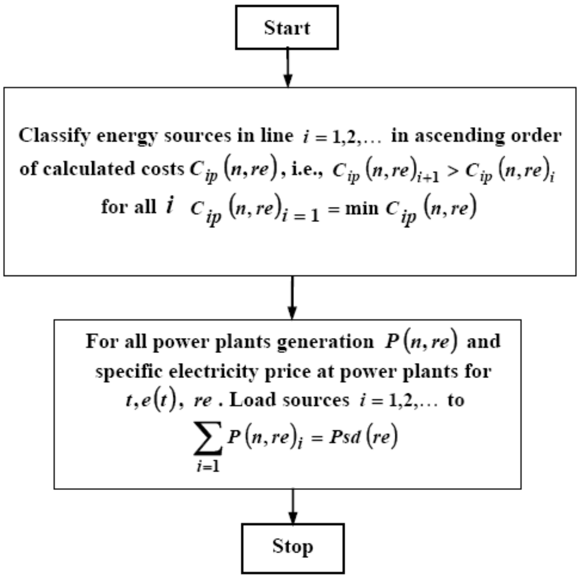

Fig. 10. Optimization algorithm of power sources in operational state $re$

In accordance with optimization algorithm above, price $C_{OP}$ in Area is determined by set of power plants and power demand in operational state. Illustration of results from this algorithm is shown on Fig. 11 [7].

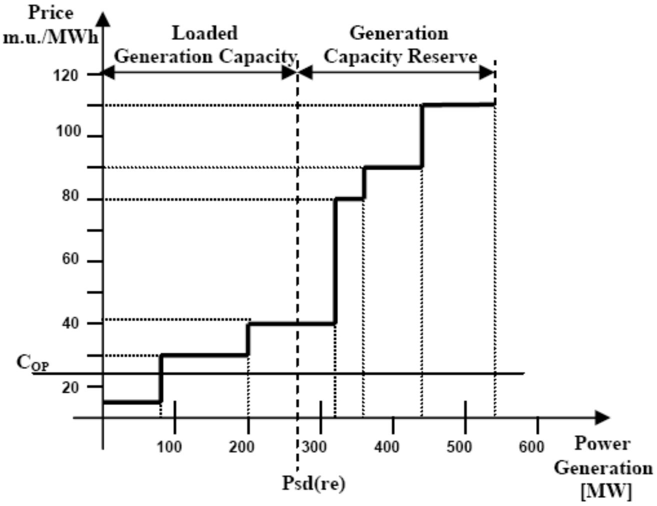

Fig. 11. Average price in Area according to optimization algorithm

In order to obtain annual network capacity calculation, average monthly generation of power sources for 12 operational states is required. With same way is necessary to determine monthly loads schedules, where as a result is computed network capacity. This approach, which calculates the monthly average output from power plants as well as average monthly consumption (load) in network, allows reflect considerable irregularity of generation and also consumption in comparison to average annual values. Thus, operational state is represented as a month (730 h), considering power plant type, in which generation and load are modelled. Set of operational states 1–13, where 13th is post-emergency state for reliability calculation.
In case that as estimation of network overloading is required, calculation must be performed with maximal load. If average load $P_V$ is known, then maximal load is calculated as:

$$P_{MAX} = k \cdot P_V \tag{9}$$

Load maximum coefficient $k$ depends specifically on the Area for which the calculation is performed. The values of the coefficient $k$ for high voltage networks ranging within interval 1.3–1.7 [6, 7].

## 6. CONCLUSIONS

Transformation of the energy sector and attendant new requirements for development projects as well as natural recovery process of power system requires tools to effectively manage these tasks. Methods and principles presented in this Article could contribute in processes of decision making, control and planning in power system. Optimization methods for Power System development need to take into account new conditions for power sources and networks development process in condition of liberalized market.

In competitive environment of liberalized market, in a case of technically equally suitable power generation units (power plants), also assessment of competitiveness must be observed.

## ACKNOWLEDGEMENT

The paper is supported by the European Social Fund Project "Scientific Group Supporting Latvian Activities of the European Strategic Energy Technology Plan", No.1DP/1.1.1.2.0/09/APIA/VIAA/027 and by Scientific Grant Agency of the Ministry of Education of the Slovak Republic and the Slovak Academy of Sciences within the project VEGA 1/0166/10.

## REFERENCES

1. Final Report of the High Level Group: Baltic Energy Market Interconnection Plan, Vilnius, 25 Nov. 2009.
2. Directive 2009/72/EC of the European Parliament and of the Council of 13 July 2009 Concerning Common Rules for the Internal Market in Electricity.
3. CHEMISINEC, I.; MARVAN, M.; NECESANY, J.; SYKORA, T.; TUMA, J. *Obchod s Elektrinou*, 1st Edition, CONTE spol s r.o., 2010, 201 p. ISBN 978-80-254-6695-7.
4. KRISHANS, Z.; MUTULE, A.; MERKURYEV, Y.; OLEINIKOVA, I. *Dynamic Management of Sustainable Development - Methods for Large Technical Systems*, 1st Edition, Springer, 2011, XXIII, 190 p. ISBN: 978-0-85729-055-7, January 2011.
5. KRISHANS, Z.; OLEINIKOVA, I.; MUTULE, A. LDM Family (LDM – Latvian Dynamic Model) for Network Development Optimization, Proceedings of 2nd International Scientific Symposium "Elektroenergetika", Stará Lesná, Slovak Republic, September 16-18, 2003. p. 200–201.
6. Energy Information Administration: Annual Energy Outlook, April 2009 SR-OIAF/ 2009-03.
7. BARKANS, Jekabs. Elektroenergetisko Sistemu Ekspluatacija, 199 p. Riga 2008, Link to the internet <http://www.eef.rtu.lv/doc/studiju_materiali/013.pdf>

CYSENI 2011, May 26–27, Kaunas, Lithuania
ISSN 1822-7554, www.cyseni.com

# AGE-DEPENDENT PROBABILISTIC ANALYSIS OF FAILURES IN GAS PIPELINE NETWORKS

**T. Iešmantas, R. Alzbutas**
*Lithuania Energy Institute*
*Breslaujos g. 3, LT-44403 Kaunas – Lithuania*
*Phone +370 625 37096*
*Email: tomas.iesmantas@gmail.com*

## ABSTRACT

Given that natural gas provides very significant portion of energy it is important to insure that the infrastructure remains as robust and reliable as possible. For this purpose, authors present recent statistical information and probabilistic analysis related to failures of natural gas pipelines in gas transportation networks of Lithuania and European countries, which are members of International Association of Gas & Oil Producers and United Kingdom Onshore Pipeline Operators' Association.

Presented historical failure data is used to model age-dependent reliability of pipelines in terms of Bayesian methods, which have advantages of being capable to manage scarcity and rareness of data and of being easily interpretable for engineers. The performed probabilistic analysis allows investigating failure rates of pipelines when age-dependence is significant and when it is not relevant.

The results of age-dependent modelling and analysis of gas pipeline reliability are applied to estimate frequency of explosions due to natural gas release when pipeline failure occurs. Estimated time-dependent explosion frequency is compared and proposed to be used instead of conservative and time-independent estimate of external events assessment used for nuclear power plants. The results of such analysis may also be incorporated in the development of smart gas networks.

Keywords: Natural Gas Pipelines, Gas Explosions, Age-dependent Reliability, Bayesian Inference

## 1. INTRODUCTION

Uncontrolled release of natural gas or loss of pressure in the system cause unsafe situations due to the potentially explosive mixture of gas and air [1]. Usual practice in assessment of such dangerous events is to consider failures rate of pipelines network as constant value. However, due to improvements in maintenance strategies, due to use of more advanced materials in the construction of new pipelines and in the repair of old ones, due to dynamic operating environment real failure rate is time-dependent.

If actual failure rate is higher than the value used in reliability and explosion assessment, then inferences made from such evaluation is overly optimistic and leads to underestimated risk. If actual failure rate is lower, then this leads to higher economical costs in risk management.

Paper structure is as follows. In section 2 the newest statistical information from international associations is reviewed. In section 3 Bayesian model for time-dependent analysis of statistical information is presented. Further, these models are applied to time-dependent failure rate and explosion accidents analysis in natural gas network.

## 2. REVIEW OF STATISTICAL INFORMATION

UKOP (United Kingdom Onshore Pipeline Operators' Association) in its report for 2008th years [2] presents time-dependent Fig. 1 statistical estimates of failure rate, which were calculated every 5 years in 1969–2008 period.

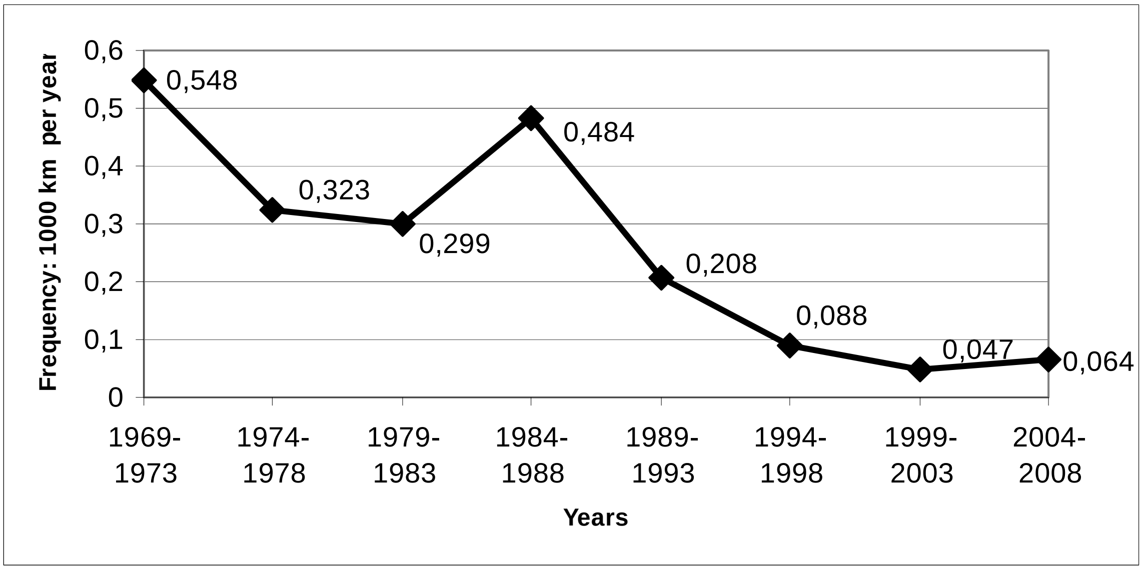

Fig. 1. UKOP failure rate estimates of every 5 years

Failure[1] rate estimate of last 5 years (from 2004 till 2008) is 0.064 events for 1000 km per year, while general estimate of 1962–2008 period is 0.242 events for 1000 km per years. There is an increase over the last 5 year incident rate, but it is within the expected variation shown over the last ten years. An overview of the development of this failure frequency over the period 1962 to 2008 is shown in Fig.2.

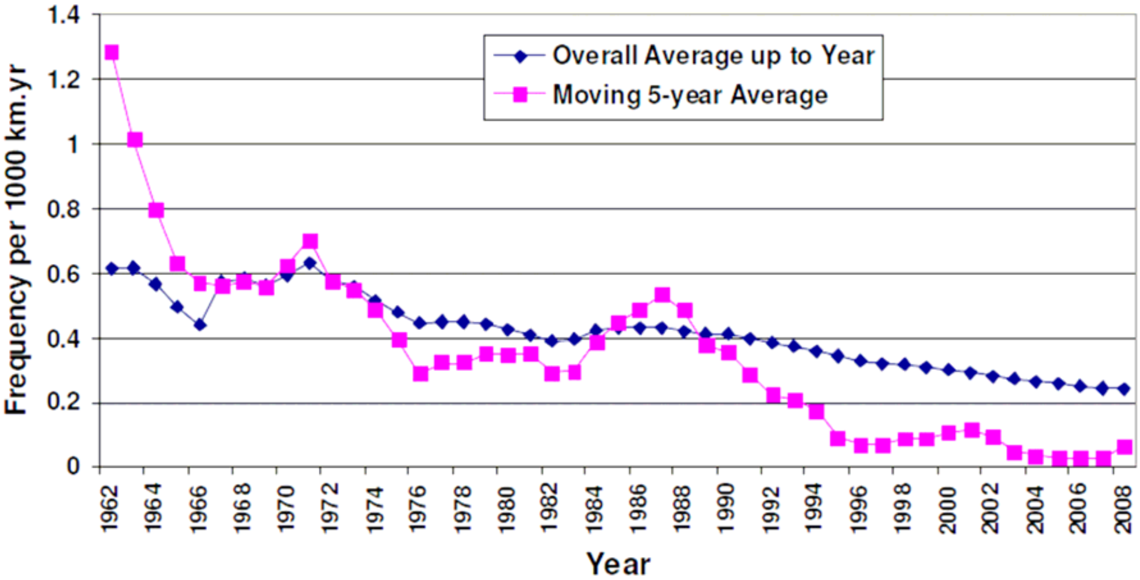

Fig. 2. Development of overall incident frequency [2]

EGIG(European Gas Pipelines Incident Data Group) in its report [3] for period from 1970 till 2007 reports failure frequency equal to 3.7E-4. Overall length of pipeline network was 129719 km.

EGIG has investigated the relationship between the age of the pipelines and their failure frequencies to determine whether older pipelines fail, due to corrosion, more often than more

---

[1] In this paper, pipeline failure is defined as product (natural gas) loss incident, i.e. unintentional loss of product from the pipeline, excluding associated equipment (e.g. valves, compressors) or parts other than the pipeline itselt

recently constructed pipelines. The influence of the age of the pipelines on their failure frequencies has been studied in the ageing analysis presented in Fig. 3.

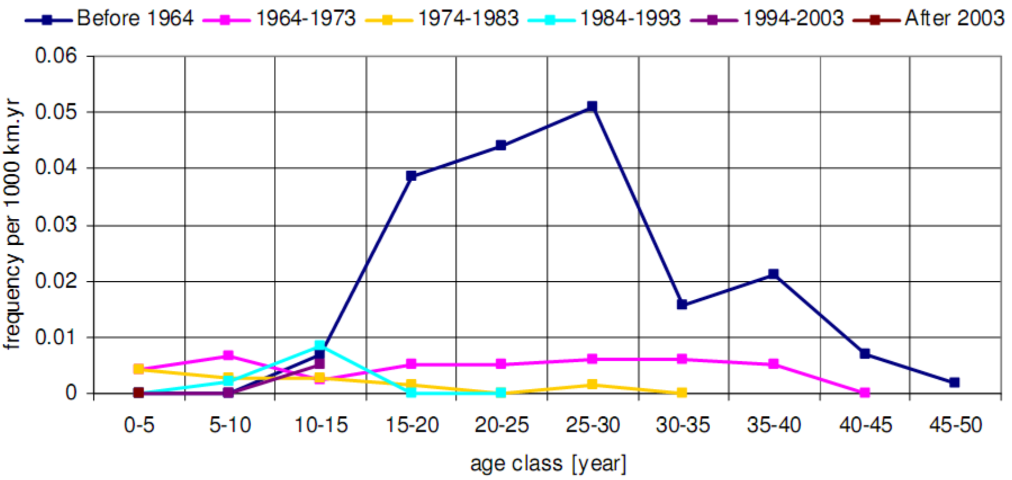

Fig. 3. Ageing analysis (corrosion) relationship between age and construction year class

Early constructed pipelines had a higher failure frequency due to corrosion, in their early years, than recently constructed pipelines. In recent years, due to improved maintenance, pipelines age is no longer a major influence on the occurrence of corrosion failures.

Table 1. Distribution of failure frequencies

| Category | Failure frequency (for 1 kilometer per 1 year) |
|---|---|
| Wall thickness less than 5 mm | 4E-4 |
| Wall thickness less than 10 mm | 1.7E-4 |
| Wall thickness less than 15 mm | 8.1E-5 |
| Wall thickness higher than 15 mm | 4.1E-5 |

Distribution (table) of failure frequencies according to pipe wall thickness is presented in report [4] for 2010th years of The International Association of Oil & Gas Producers. In 1172 events registered in EGIG database 11 ended with human injuries or death.

## 3. BAYESIAN MODELLING

As already been mentioned at the introduction, Bayesian methods are well known to have robustness properties in outliers' problems and are well-suited for analysis of sparse and small data samples. In this chapter, methodology developed by authors [in print] for Bayesian age-dependent failure data analysis will be very briefly presented.

One of the difficulties of Bayesian inference is inability to deal with changes of age-dependant parameter as a continuous process. This problem partially can be overcome by considering ageing (or degradation) as step-wise process, which is constant in some period of time and has value jump in other period. Mathematically this can be expressed as a jump process:

$$d(t)=\sum_{i=1}^{N-1} 1_{\{t_i<t<t_{i+1}\}} d(t_i) \tag{1}$$

where $d(t)$ is any model of characteristic under consideration and constant $d(t_i)$ is value of characteristics at each time period $t_i$; N – number of time intervals.

Model of characteristic $d(t)$ can have any functional form. It can be linear, Weibull, or some other form. Depending on adopted formula, $d(t)$ will be based on vector of parameters $\Theta = \{\theta_1, ..., \theta_m\}$:

$$d(t) = d(t, \Theta) \tag{2}$$

If prior knowledge and beliefs about systems parameters is represented by probability density distribution $\pi(\Theta)$ and statistical observations has likelihood $f(y \mid d(t))$, then, according to Bayes theorem, age-dependent beliefs about systems degradation or failure rate is expressed as posterior distribution:

$$\pi(\Theta \mid y, t) = \frac{\pi(\Theta) f(y \mid d(t, \Theta))}{\int_{\Omega} \pi(\Theta) f(y \mid d(t, \Theta)) d\Theta} \tag{3}$$

## 4. CASE STUDY

In this part of paper age-dependent reliability and explosion assessment is carried out in terms of Bayesian models.

Suppose failure rate (Fig. 1) follows decreasing trend function and data is generated by Gaussian nonlinear regression model with unknown dispersion, then full Bayesian model is as follow:

$$Y_t \sim N\left(d(t, a, b, c), \sigma^2\right)$$

$$d(t, a, b) = a + \frac{b}{1+t} + c^t, t = \overline{1,8},$$

$$a, b, c \sim uniform(0, K)$$

where K is some large constant (we used $K = 1000$), ensuring that large enough space of states is explored by MCMC algorithm (Markov Chains Monte Carlo – is a family of specific algorithms, which allows generation of random number distributed by some distribution, known up to constant [5]). Uniform prior distributions for regression parameters are chose because no prior information is available to make any prior judgments about values of parameters.

In the next two sections calculations and discussion for time-dependent failure rate and explosion probability will be presented separately.

### 4.1. Time-dependent failure rate of natural gas pipelines network

MCMC simulation of stated model allows estimation of posterior distribution of regression parameters (Fig. 4) and of dispersion parameter (Fig. 5). These posterior distributions represent updated state of knowledge about variability of model parameters.

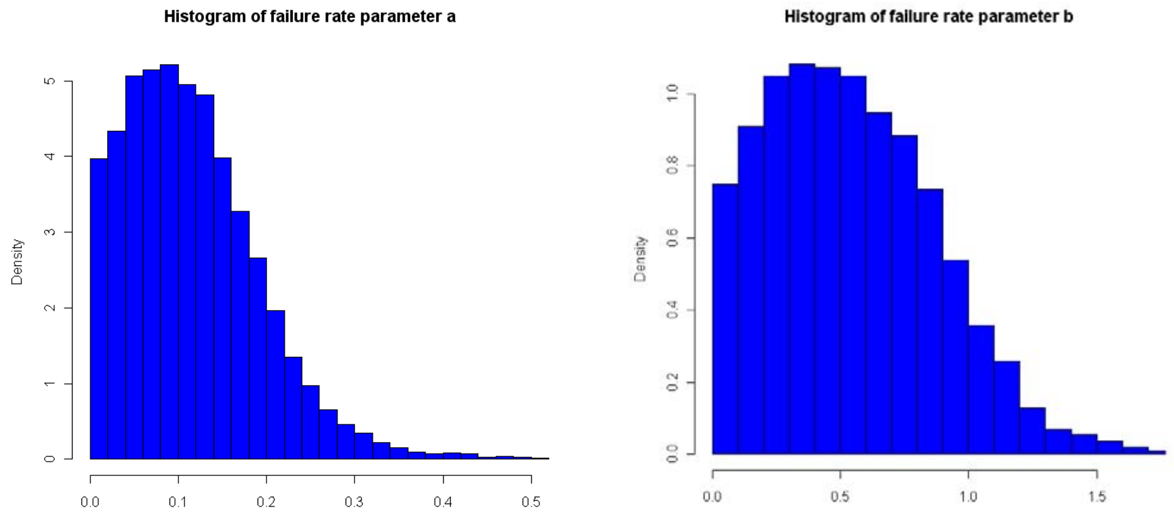

Fig. 4. Posterior distributions of regression parameters a and b

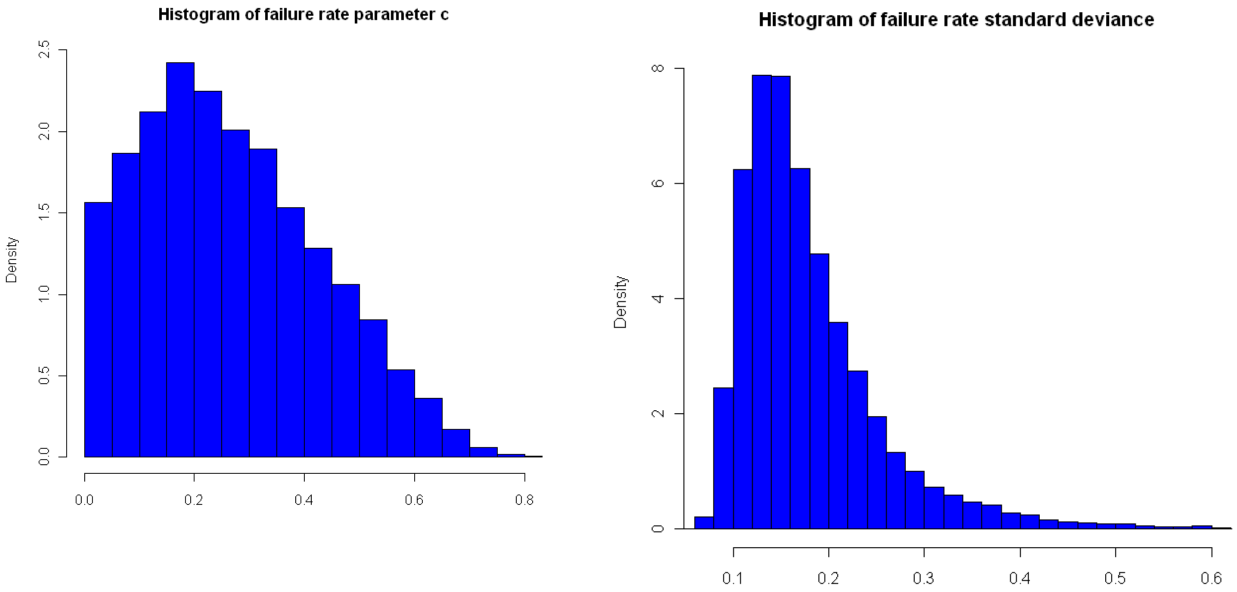

Fig. 5. Posterior distributions of regression parameter c and model standard deviation

Point estimates and Bayesian confidence intervals, representing uncertainty about parameters after data were obtained are presented in Table 2.

Table 2. Bayesian point and interval estimates

| **Parameter** | **Mean** | **95% Confidence interval** |
|---|---|---|
| a | 0.11 | [0.0059;0.2549] |
| b | 0.52 | [0.0350;1.1682] |
| c | 0.26 | [0.0215;0.6112] |
| sigma | 0.16 | [0.0917; 0.2925] |

It is worth to note, that Bayesian intervals have different meaning compared to frequentists confidence intervals: Bayesian intervals reflects probability of being in that interval while frequentists confidence intervals represents long-run frequency to „fall“ into calculated interval. For frequentists, at every new sample probability that parameter will be in previously computed confidence interval is either 1 or 0. Usually, which is a mistake, frequentists confidence intervals are interpreted as Bayesian confidence intervals.

Estimated failure rate of pipeline network under consideration is shown in Fig. 6.

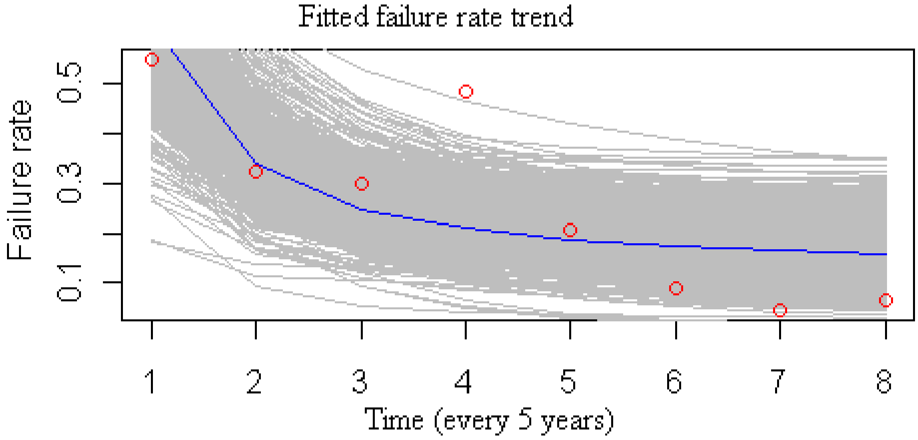

Fig. 6. Age-dependent failure rate regression curve Bayesian and frequentists estimates

Failure rate with one term equal to constant $a$ considered in this analysis were chose deliberately. Despite continuously improving maintenance strategies of natural gas transition network, it is unrealistic that failure rate will become equal to zero, so it is reasonable to analyze failure rate trend function with some limiting constant.

As is usually the case in reliability analysis, useful lifetime is of interest, i.e. system operation with constant failure rate. We will dismiss the case when ageing of system manifests, since it is highly unlikely, because of previously mentioned reasons for decreasing failure rate.

Further, in this section we will estimate time moment $t^*$, when failure rate approaches limiting constant (say, with error $\varepsilon = 0.01$) and whole lifetime of pipeline network can be divided into two sections: with decreasing and constant failure rate.

Time moment $t^*$ is such that $\left|\lambda\left(t^*\right) - a\right| \le \varepsilon$ or $\left|\frac{b}{1+t^*} + c^{t^*}\right| \le 0.01$ and approximate solution is $t^* = 51$ time periods, which is equal to $5 \cdot 51 = 255$ years. These results show, that failure rate of gas grid settles down after quite long time and, since predictions for such time period would be very inaccurate, there is no reason to further analyze constant failure rate segment. Such segmentation would be useful in case when failure rate would approach constant value after relatively short time period (e.g. 10 or 20 years).

Failure rate estimate of UKOP natural gas transmission grid allows more advanced improvement of whole energy network reliability assessment and enables making more accurate predictions decisions. Well established practice to use constant failure rate for whole system lifetime when assessing reliability is harmful in terms of underestimated risk.

Age-dependent analysis presented in this section also allows modification of gas grid maintenance strategies dependent on network age, and, as a consequence, risk related to network accidents (such as gas leakage explosions) is more accurately assessed, as will be shown in next section, where age-dependent natural gas explosion probability will be estimated.

## 4.2. Time-dependent explosion probability of natural gas pipelines network

The ussual practice to calculate explosion probability near to nuclear power plant is to use constant pipeline failure rate [6]:

$$P = \lambda \cdot D \cdot f_s \cdot f_t \cdot f_d \cdot f_w \tag{4}$$

where $\lambda$ is pipeline failure frequency, $D$ is pipeline length, close to nuclear power plant, $f_s$ is hazarduous pipeline accidents frequency, $f_t$ – frequency of accidents related to technical works performed close to site, $f_d$ unnoticed and unrepaired accidents, $f_w$ – ratio of adverse weather conditions.

Further we will use estimates, presented in [3, 6]:

Table 3. Parameter values

| **Parameters** | **Value** |
|---|---|
| $\lambda$ | 3.7E-4 |
| $f_s$ | 0.32 |
| $f_t$ | 0.25 |
| $f_d$ | 0.1 |
| $f_w$ | 0.5 |

Suppose, that $D = 1\text{ km}$, then probability of natural gas explosion near to nuclear power plant site is $P = 3.7 \cdot 10^{-4} \cdot 1 \cdot 0.32 \cdot 0.25 \cdot 0.1 \cdot 0.5 = 1.48 \cdot 10^{-6}$. However, the use of constant pipeline failure frequency can lead to overestimated or underestimated (depending whether actual failure rate is highter or lower than averaged constant value) gas explosion probability. So, to improve accuracy of explosion probability estimate and to better evaluate the risk, pipeline causes to nuclear power plant, time-dependent failure rate, like estimated in previous section, should be used.

Further we will use previously estimated failure rate $\lambda(t) = 0.11 + \frac{0.52}{1+t} + 0.26^t$. So, prediction of time-dependent probability of gas explosion close to (imaginary) nuclear power plant is like in Fig. 7.

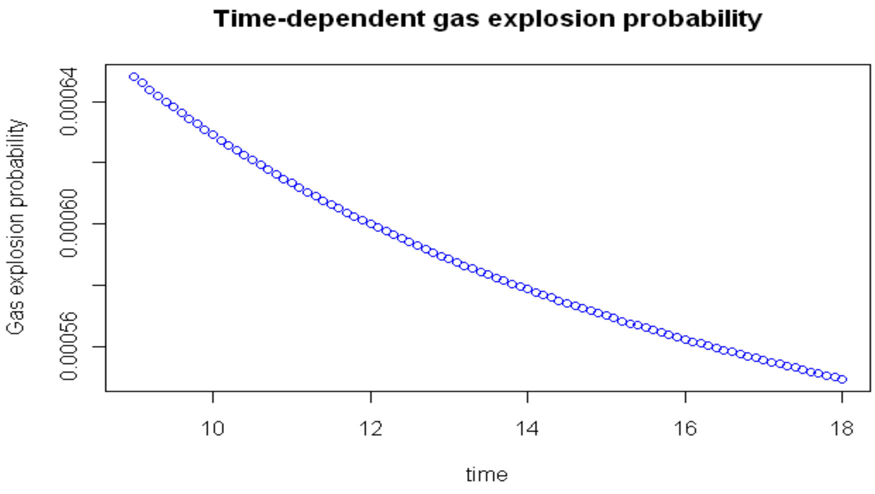

Fig. 7. Time-dependent gas explosion probability near to nuclear power plant

Gas explosion probability estimation approach is quite universal, because the object which is close to pipeline grid can be not necessarily nuclear power plant, it can be factory, houses and other important objects.

## 5. CONCLUSIONS

Up-to-date statistical natural gas pipeline grid data were presented in this paper and used to estimate time-dependent failure rate and gas explosion probability.

Bayesian methods allowed more robust estimation of time-dependent failure rate parameters; furthermore, uncertainties of these parameters were also obtained and used to estimate confidence intervals which are more easily interpretable (compared to frequentists).

Estimated time point when failure rate decreases to constant value (with some error $\varepsilon$) showed that there is no necessity to divide failure rate into two segments: strictly decreasing and constant.

Time-dependent failure rate is advantageous for development of maintenance strategies of pipeline grid, also for evaluating risk at different network points – this can be done by using time-dependent gas explosion probabilities instead of constant.

## REFERENCES

1. HELSETH, A., HOLEN, A.T. Reliability modelling of gas and electric power distribution systems; similarities and differences. Proceedings of 9th International Conference on Probabilistic Methods Applied to Power Systems. Stockholm: KTH, 2006 June 11–15.
2. ARUNAKUMAR, G. UKOPA PIPELINE FAULT DATABASE. Pipeline Product Locc Incidents (1962–2008). 6th Report of the UKOPA Fault Database Management Group. 2009, December.
3. EGIG 2007. 7th EGIG-report 1970-2007 Gas Pipeline Incidents, 7th report of the European Gas Pipeline Incident Data Group, Doc. No. EGIG 08. TV-B.0502, 2007.
4. International Association of Oil & Gas Producers. Riser & pipeline release frequencies. OPG Report No. 434-4, March 2010.
5. GILKS, W.R., RICHARDSON, S., SPIEGELHALTER, D. J. *Markov Chain Monte Carlo in Practice*. Chapman and Hall/CRC, 1996.
6. NUREG-CR-4550 (SAND86-2084), Vol. 3, Rev. 1, Pt. 3, Analysis of Core Damage Frequency: Surry Power Station, Unit 1 External Events, Sandia NL, Albuquerque, NM, 1990.

# ANALYSIS OF METHODS OF POWER FLOWS CALCULATION UNDER OPTIMIZATION OF POWER SYSTEM DEVELOPMENT

**A. Obusevs, I. Oleinikova, Z. Krishans**
*Institute of Physical Energetics*
*Laboratory of Power System Mathematical Modelling*
*Aizkraukles 21, LV-1006 Riga – Latvia*
*Phone +371 22 120 106*
*Email: A.Obusev@gmail.com*

## ABSTRACT

These papers present the analysis of methods of power flows calculation in optimization of power system development tasks. Authors analyze methods of power flow calculation of transmission network: iteration method with base node, iteration method without base node, Gauss elimination method and inverse matrix method. The target of this research is to improve active power flow calculation methods with the aim compare calculation speeds for criterion calculations in development tasks and analyze methods advantages and disadvantages. The results of this can be useful for developing sustainable development management technologies for power system.

Keywords: power flow, mathematical modelling, dynamic optimization.

## 1. INTRODUCTION

A mathematical model of power system (PS) makes it possible to calculate criteria and analysed system with a view to make justified decisions on system sustainable development. To enable computer implementation of the given task, data are required as well as appropriate software providing optimization algorithm and algorithms for calculating generating nodes output and transmission network links load. Active power flow calculation results are used for criterion calculations in development tasks. The major criterion of PS development process is management optimization objective function which shall display and integrate technical, economical, power supply reliability, ecological etc. parameters depending on specific technical system:

$$\max F(T,g)=\sum_{t=1}^{T}F(t,e(t)), \tag{1}$$

where $t$ – development step serial number, $T$ – number of development steps in estimation period, $F(t,e(t))$ – system criteria for development step $t$ and state $e(t)$, $g$ – development plan (process) $e(1),e(2),\ldots,e(t),\ldots,e(T)$.

Each plan is characterized by number of realized development actions $n$ and its realization moment $t$, as well as by each development action realization type. The total number of development plans may be calculated by the following formula:

$$V=\prod_{i=1}^{n}V_i=(T+1)^n\prod_{i=1}^{n}m_i, \tag{2}$$

where $n$ – number of development actions, $m_i$ – development action realization type number, $i$ – development action index, $T$ – number of development steps in estimation period.

Obviously, also in real tasks (for example $m=1$, $n=11$, $T=15$) the number of comparable development plans attains astronomic quantity ($10^{15}$). Therefore, it is required to apply specialized dynamic optimization methods in PS sustainable development management process [1]. Within the frame of electric power system dynamic optimization task, power flow calculation must be performed with high-speed and certain accuracy. Due to that it is necessary to use specialized methods.

This paper presents the four methods: iteration method with base node, iteration method without base node, Gauss elimination method and inverse matrix method for active power flow calculation, with calculation analysis and test results. The target of this research is to improve active power flow calculation methods with the aim compare calculation speeds. The approach is worked out by Laboratory of Electric Power System Simulation, Institute of Physical Energetics.[3]

## 2. POWER FLOW CALCULATION METHODS

### 2.1. Iteration method with base node

Performance is achieved using a simplified power flow model. The voltage moduli for all nodes of transmission network are assumed to be approximately equal and the active resistance − much smaller than the inductive resistance [2]. Then active flow at link $ij$ :

$$P_{ij} = Y_{ij} \cdot (\delta_i - \delta_j), \tag{3}$$

where $Y_{ij}$ – link's $ij$ admittance coefficient, $\delta_i, \delta_j$ – voltage losses from feeding centre up to node.

$$Y_{ij} = \frac{U_{ij}^2}{X_{ij}}, \tag{4}$$

where $U_{ij}$ – link's $ij$ voltage value; $X_{ij}$ - link's $ij$ reactance.

Linear equations system for nodes potential $\delta_i$ calculation [1]:

$$\begin{array}{l} -Y_{11}\delta_1 + Y_{12}\delta_2 + \dots + Y_{1i}\delta_i + \dots + Y_{1j}\delta_j + \dots + Y_{1m}\delta_m = P_1 \\ Y_{21}\delta_1 - Y_{22}\delta_2 + \dots + Y_{2i}\delta_i + \dots + Y_{2j}\delta_j + \dots + Y_{2m}\delta_m = P_2 \\ \dots\dots\dots\dots\dots \quad \dots\dots\dots \quad \dots\dots\dots \quad \dots\dots\dots \\ Y_{i1}\delta_1 + Y_{i2}\delta_2 + \dots - Y_{ii}\delta_i + \dots + Y_{ij}\delta_j + \dots + Y_{im}\delta_m = P_i \\ \dots\dots\dots\dots\dots \quad \dots\dots\dots \quad \dots\dots\dots \quad \dots\dots\dots \\ Y_{m1}\delta_1 + Y_{m2}\delta_2 + \dots + Y_{mi}\delta_i + \dots + Y_{mj}\delta_j + \dots - Y_{mm}\delta_m = P_m \end{array}, \tag{5}$$

where $Y_{ii}$ – node $i$ self-conductivity coefficient; $P_i$ – load in node $i$.

Then in matrix form

$$\mathbf{Y\delta} = \mathbf{P} \tag{6}$$

This flow model („direct current" model) is used in Latvian dynamic model (LDM). The „direct current" model provides an order of magnitude less calculation time than the „alternating current" model (nonlinear system equations with complex values) and accuracy, sufficient for the planned tasks.

However, taking into account large number of variables, it is necessary to use all applicable algorithmic options to reduce calculation time [2]. Iteration methods are simple and fast enough, they are suitable for feasibility analysis and power system networks optimal synthesis tasks in a dynamic statement. Iterations methods that use the principle of relaxation are the most appropriate. The potential node system of equation (5) solved using the expression:

$$\mathbf{R} = \mathbf{P} - \mathbf{Y}\boldsymbol{\delta}, \tag{7}$$

where $R$ - unbalanced power vector.

Substituting the $\delta$ values satisfying the system solution into (7), we obtain $R = 0$. If some $\delta$ values substituted into (7) do not satisfy the system solution, $R \neq 0$. Solution of system (6), using the relaxation principle, is based on the approximate determination of the potential of node, so that for $i = 1, \ldots, q$ the following equation to be accomplished:

$$\left| R_i \right| \leq \varepsilon_i, \tag{8}$$

where $\varepsilon_i$ – allowable power unbalance at node $i$.

Power flow is defined if the first Kirchhoff law is performed with accuracy $\varepsilon_i$ [3]. The Kirchhoff first rule for node $n$ can be expressed in the form:

$$\sum_{ij \in V_n} a_{ij} \cdot P_{ij} + P_n = 0, \tag{9}$$

where $V_n$ – is the whole set of incident links for node $n$; $a_{ij} = 1$ – if $n$ is the first node of link $ij$, otherwise $a_{ij} = -1$; $P_n$ – is the load in node $n$.

The rate of convergence of the iteration process with base node for determining the node potentials strongly depends on the location of base node. Such dependence is shown in Fig. 1. In this example, the range of the number of iterations was $30 - 552$. If the base node is chosen incorrectly then the power flow calculation is not convergence.

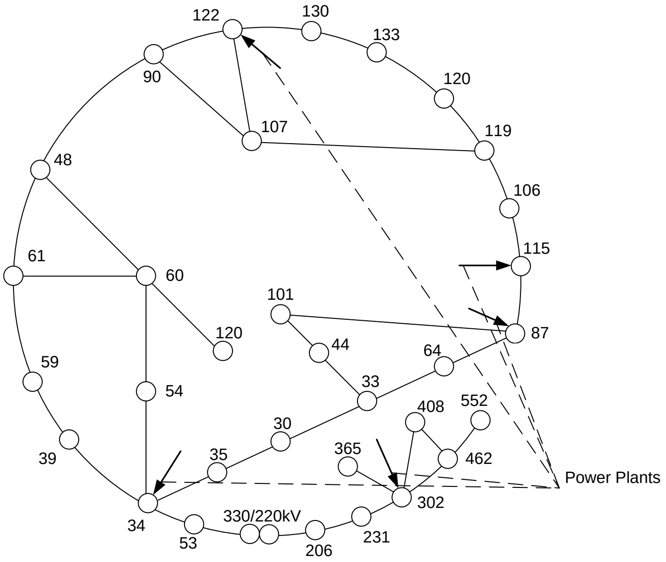

Fig. 1. The dependence of the number of iterations on the location of the base node

## 2.2. Iteration method without base node

Disadvantage of iteration method with base node is dependency number of iterations on position of determined base node in particular scheme. The number of links in these schemes can vary in 1.5 – 2.5 times. This fact has a significant impact on the performance of optimization algorithms for power systems. This main weakness of such method can be solved by employing approach when for calculation base node is not necessary. When using this method the values of nodes potentials varies continuously, but the values of power flows are uniquely determined in accordance with the first and second Kirchhoff's laws to within the permissible unbalance (8). For a network with $q$ nodes and $p$ links a system of linear equations is:

$$R_i = P_{ii} + \sum_{j \in N_i} P_{ij}, \qquad \mathrm{i} = 1, \ldots, q, \tag{10}$$

Limitations:

$$\sum_{ij \in L_k} a_{ij}{}^{k} \frac{P_{ij}}{Y_{ij}} = 0, \qquad \mathrm{k} = 1, \ldots, p - q + 1, \tag{11}$$

where $a_{ij}{}^{k}$ – equal to +1 for match and – 1 if not match the direction of link with the positive direction in loop, $ij \in L_k$ – indicating the membership of links to multiple links that form a closed loop with a given positive direction.

Expression (10) is a record of 1st and (11) record of 2nd Kirchhoff's law. Unknowns are the power flows $P_{ij}$. Search for decisions regarding the power flows $P_{ij}$ is to implement such an unbalance power $R_i$ change process subject to limitations (11), in which $R_i$ reduced to any before given small value $\varepsilon$.

At the beginning of the iteration process there is given an initial approximation for the power flows to satisfy the limitations (11). They are satisfied in the case, if values of power flows are equal to zero. Then the corresponding values of power unbalance are loads of network nodes. Additionally it should be defined the matrix of unbalance power distribution on the incident links (defined as matrix $\alpha$). Algorithm for data preparation is shown in Fig. 3.

After completion of the data preparation, algorithm for calculating power flows, which is presented in Fig. 4, begins. At the beginning of the iteration process unbalance of power with an initially given value $|R_k| > \varepsilon$ is compared. Iterative processes consist two cycles. In the first cycle the searching for the power flows for the incident links at node $i$ is performed. In the second cycle unbalance power in the incident nodes is corrected. In such way a power flows matrix for entire network is formed. The calculation is performed for each node, and then unbalance power vector is checked. The process stops at reaching a given unbalance [3]. After the process we find the nodes difference voltage:

$$\delta_{ij} = \frac{P_{ij}}{Y_{ij}} \tag{12}$$

After that we choose a base node and fix the value of the voltage. Knowing the voltage difference between nodes, we find the potential values in all nodes.

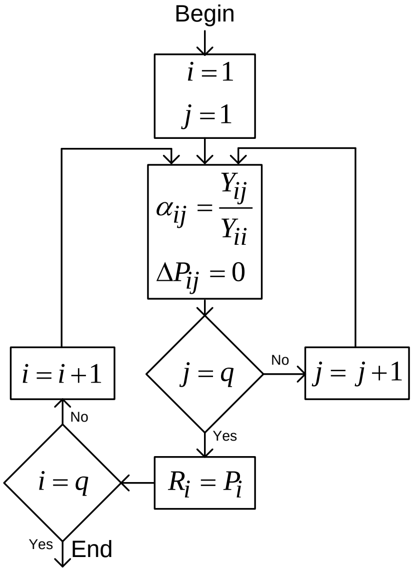

Fig. 2. Algorithm for data preparation (where $\alpha$ - matrix of unbalance power distribution)

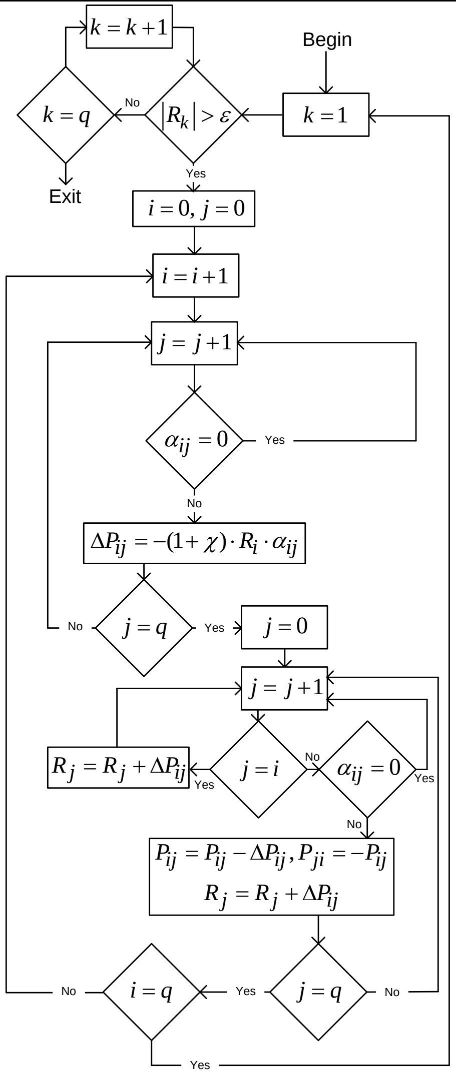

Fig. 3. Algorithm for active power flow calculation without base node

The main feature of the active power calculations used in an optimal development task is the manner of doing them. The usual iteration process can be speeded up if we choose the $\chi$ value within the interval from 0 to 1. At $\chi=0$, in the nodes a monotone convergence of the unbalance power to an acceptable level $\varepsilon$ takes place. In turn, at $\chi>0$ natural fluctuations of the convergence process occur, which leads to a rapid node unbalance decrease in the next iterations and therefore to acceleration of the convergence in an iteration process [3].

## 2.3. Gauss elimination method

Performance of iterative algorithms depends on the number of nodes $q$ in an electrical network, as well as on ratio $p/q$. With an increasing number of nodes the time spent on the calculations increases. In this connection it is expedient to combine iterative methods with methods to reduce the number of unknowns. A general method for solving systems of linear equations with successive elimination of unknowns is the method of Gauss [4]. In the Gauss elimination method of scheme transformation the following steps can be identified: equivalenting parallel links of the graph; scheme transformation, associated with node elimination; calculate node potentials.

Scheme transformation is an iteration process that minimizes network graph. Single step conversion scheme consists of the following operations, for clarity see Fig. 4, where:

a) Elimination node $i$ with minimal degree of incidence;

b) Converting the graph into an equivalent graph in which for the node $i$ corresponding active load is distributed among the incident nodes in proportion to the conductivity coefficient of links:

$$P_j^i = P_j^{i-1} - P_i^{i-1}\cdot\frac{Y_{ij}^{i-1}}{Y_{ii}^{i-1}} \tag{13}$$

The formation of a new link, the coefficient of conductivity is determined by the expression:

$$Y_{jk}^i = Y_{jk}^{i-1} - \frac{Y_{ij}^{i-1}\cdot Y_{ik}^{i-1}}{Y_{ii}^{i-1}} \tag{14}$$

Nodes elimination process is repeated until the graph contains only one node. After direct calculation process, reverse calculation process begins, in which the unfolding of the scheme and step by step determination excluded nodes is performed. Calculation of the nodal potentials begins with equating to zero its value in the remaining node ( $\delta_q = 0$ ).Further, using datas about the excluded branches and nodes, for the nodes potentials calculation in all remaining nodes of the graph such equation used:

$$\delta_i = -\frac{P_i^{i-1}}{Y_{ii}^{i-1}} - \sum_{j=1}^{q}\frac{Y_{ij}^{i-1}}{Y_{ii}^{i-1}}\delta_j \tag{15}$$

After reverse calculation process the active power flows in links are determined [5]. Algorithm for node potential calculation is shown in Fig. 6.

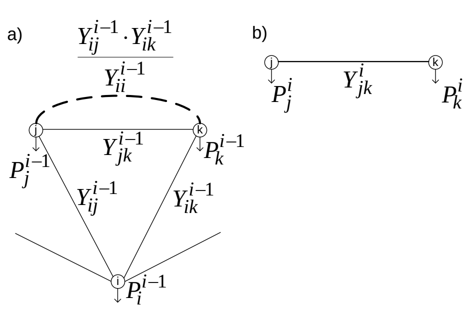

Fig. 4. Node elimination $i$ a) before elimination b) after elimination

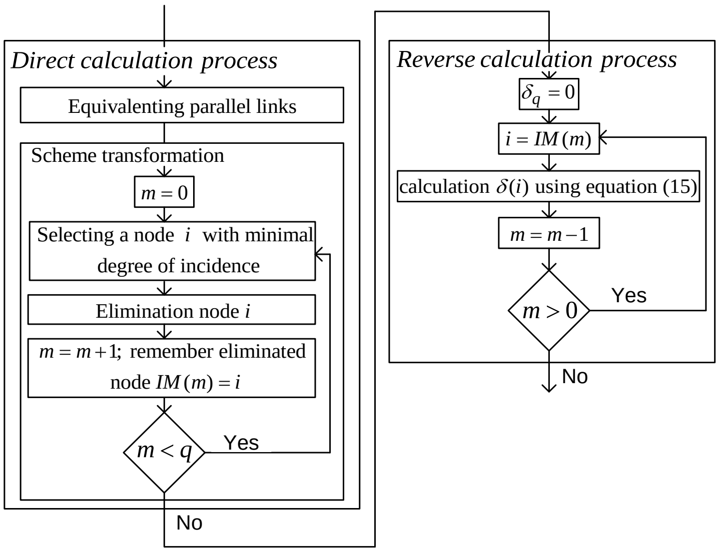

Fig. 5. Algorithm for node potential calculation using Gauss elimination method

## 2.4. Inverse matrix method

Determination of node potentials by inverse matrix method is using expression:

$$\boldsymbol{\delta} = \mathbf{Y}^{-1} \times \mathbf{P} \tag{16}$$

where $\mathbf{Y}^{-1}$ inverse matrix of admittance matrix;

$$\mathbf{Y}^{-1} = \frac{1}{|Y|} \times \mathbf{C}^{\mathbf{T}} \tag{17}$$

where $\mathbf{C}^{\mathrm{T}}$ cofactor matrix, $|Y|$ admittance matrix determinant;

$$C_{ij} = (-1)^{i+j} \cdot M_{ij} \tag{18}$$

where $M_{ij}$ $(i, j)^{th}$ minor of admittance matrix Y.

## 3. TEST RESULTS

This paper is focused on active power flow calculation methods with the aim compare calculation speeds. The calculations were made in the MATLAB software using 1.90 GHz AMD Turion 64 x2 PC with 2048 MB of RAM. For analysis of methods were used MATPOWER (MATLAB power system simulation package) bus test systems [6]. The calculations compare the time, which is necessary for finding the active power flows, spent by each method. For iterative methods allowable power unbalance is taken $\varepsilon = 0{,}001$. Comparing the methods the influence of the acceleration factor $\chi$ for iterative processes is taken into account. For testing were taken following acceleration factors: $\chi_1 = 0; \chi_2 = 0.45; \chi_3 = 0.9$

Table 1. The time needed to solve different schemes

| | 4 bus | | | 9 bus | | | 14 bus | | |
|---|---|---|---|---|---|---|---|---|---|
| $\chi$ | 0 | 0,45 | 0,9 | 0 | 0,45 | 0,9 | 0 | 0,45 | 0,9 |
| I | $11\cdot 10^{-4}$ | $10\cdot 10^{-4}$ | $66\cdot 10^{-4}$ | $15\cdot 10^{-3}$ | $3{,}6\cdot 10^{-3}$ | $17\cdot 10^{-3}$ | $31\cdot 10^{-3}$ | $12\cdot 10^{-3}$ | $26\cdot 10^{-3}$ |
| II | $0{,}64\cdot 10^{-4}$ | $1{,}45\cdot 10^{-4}$ | $11\cdot 10^{-4}$ | $0{,}55\cdot 10^{-3}$ | $0{,}57\cdot 10^{-3}$ | $2{,}7\cdot 10^{-3}$ | $1{,}5\cdot 10^{-3}$ | $0{,}64\cdot 10$ | $4{,}6\cdot 10^{-3}$ |
| III | $0{,}76\cdot 10^{-4}$ | | | $0{,}11\cdot 10^{-3}$ | | | $0{,}158\cdot 10^{-3}$ | | |
| IV | $2\cdot 10^{-4}$ | | | $1{,}1\cdot 10^{-3}$ | | | $3{,}3\cdot 10^{-3}$ | | |
| | 30 bus | | | 39 bus | | | 57 bus | | |
| $\chi$ | 0 | 0,45 | 0,9 | 0 | 0,45 | 0,9 | 0 | 0,45 | 0,9 |
| I | 0,178 | 0,068 | 0,048 | 0,803 | 0,312 | 0,085 | 0,585 | 0,234 | 0,106 |
| II | 0,0083 | 0,0022 | 0,0112 | 0,034 | 0,013 | 0,025 | 0,092 | 0,033 | 0,043 |
| III | 0,000338 | | | 0,000492 | | | 0,000884 | | |
| IV | 0,035 | | | 0,084 | | | 0,35 | | |
| | 118 bus | | | 300 bus | | | | | |
| $\chi$ | 0 | 0,45 | 0,9 | 0 | 0,45 | 0,9 | | | |
| I | 3,029 | 1,22 | 0,262 | 90,09 | 37,79 | 6,25 | | | |
| II | 0,909 | 0,355 | 0,158 | 32,54 | 12,91 | 1,5 | | | |
| III | 0,0036 | | | 0,0312 | | | | | |
| IV | 15,3 | | | -* | | | | | |

where I – iteration method with base node, II – iteration method without base node, III – Gauss elimination method, IV – inverse matrix method.

*Impossible to find $|Y|$ admittance matrix determinant;

The results show that iteration method with base node and inverse matrix method is inappropriate for using it in dynamic optimization tasks. This is due to fact that this methods takes more computer time for calculation. Performance depends on the number of nodes $q$ in an electrical network, as well as on ratio $p/q$. In this connection it is expedient to use methods that are least dependent on these variables. In this case better to use Gauss elimination or iteration method without base node, by using optimal acceleration factor.

Using Gauss elimination method in reverse calculation process we should remember excluded nodes and links parameters, in this connection for large size schemes it is necessary to use large amount of random-access memory. To solve 300 bus scheme size of needed memory (without special methods to decrease size) is 206 Mb.

## 4. CONCLUSIONS

This research reflects one of the many problems, which need to be solved in imminent future and then utilized for power transmission network modelling and development tasks. Increasing integration in the Baltic electricity market and Europe-wide interconnection establishment makes it necessary to consider the networks of higher dimension, with many nodes and links. In this paper is given comparison of four methods: iteration method with base node, iteration method without base node, Gauss elimination method and inverse matrix method for active power flow calculation, with calculation analysis and test results. The target of this research is to improve active power flow calculation methods with the aim compare calculation speeds.

In order to compare time of computation with different methods MATPOWER bus test systems were used. The results show the possibility of greatly reducing computation time by using Gauss elimination or iteration method without base node, by using optimal acceleration factor.

## ACKNOWLEDGMENT

The paper is supported by the European Social Fund Project “Scientific Group Supporting Latvian Activities of the European Strategic Energy Technology Plan”, No.1DP/1.1.1.2.0/09/APIA/VIAA/027.

## REFERENCES

1. KRISHANS Z., MUTULE A., MERKURYEV Y., OLEINIKOVA I. “Dynamic management of Sustainable Development: Methods for Large Technical Systems”, in Hardcover, 1st ed., Springer, 2010.
2. KRISHANS Z., „Modelling and optimization methods”, Riga: RTU, 1998, p. 18–22.
3. DALE V., KRISHANS Z., PAEGLE O. „Dynamic methods for power networks development analysis”, Riga: Zinatne, 1979, p. 81–137.
4. DEMIDOVICH B.P., MARON I.A. "Foundations of computational mathematics", Moscow (1966) (In Russian).
5. DALE V., KRISHANS Z., PAEGLE O., „Dynamic optimization of the development of electrical networks”, Riga: Zinatne, 1990, p. 159–171.
6. RAY D. ZIMMERMAN, CARLOS E. MURILLO-SÁNCHEZ & DEQIANG (DAVID) GAN, MATPOWER v4.0 (MATLAB Power System Simulation Package), Link to the internet: http://www.pserc.cornell.edu/matpower/

CYSENI 2011, May 26–27, Kaunas, Lithuania
ISSN 1822-7554, www.cyseni.com

# REGIONAL ENERGY ECONOMY DEVELOPMENT FROM THE ECOLOGICAL FOOTPRINT PERSPECTIVE

**K. Biekša, A. Klevienė**
*Lithuanian Energy Institute*
*Laboratory of Regional Energy Development*
*Breslaujos str. 3, LT-44403 Kaunas – Lithuania*
*Phone +370 680 16985*
*Email: bieksa@mail.lei.lt*

## ABSTRACT

Sustainable development is a function with many variables where the main factors are environmental, economical, social, moral, ethic and cultural aspects. Nowadays we think about national or even global development targets without enough attention in the regional context. Energy prices are increasing because energy production technologies based on fossil fuels are dominating in the energy economy. Regional – means sustainable, because energy doesn't need transportation and energy avoids losses. However there are hidden costs of energy production which have an impact for development of renewable energy technologies. Sustainable process index methodology as part of the ecological footprint method is a tool to reveal hidden costs of energy production. Energy can be efficiently and effective use locally with enough attention to economical, social and environmental aspects. This can be possible by development of renewable energy technologies. Process network system analysis and a life cycle approach are used for evaluating the best energy production technologies in a regional scale. In the article the sustainable process index methodology as part of ecological footprint methods is investigated. Using process network system analysis tool the energy production technologies are investigated and compared with a traditional fossil fuel burning technologies. Scenarios for regional energy economy development with emphasis for possibilities to use renewable energy technologies are identified.

Keywords: sustainable development, ecological footprint, renewable energy sources, sustainable process index, life cycle approach, process network system analysis.

## 1. INTRODUCTION

One of the paradoxes of prosperity is that people in rich countries don't realize how good things really are [1]. There is a proverb and it says “the best things usually are free”. However nowadays almost everything has a value, costs or price. Even an air has a value in a resort city where you pay for breathing of fresh air. Our economy has a big value in terms of money and economy growth is measured by gross domestic product (GDP). Huge forces (money) move our wellbeing values forward enough far away from our limits to growth because the evaluation of well-being economy is based on consumption measures such as GDP so far. There is an urgent need to develop more precise indexes of our wellbeing life and to correct the obvious drawbacks in using the GDP [1]. Accounting system of energy costs is based on evaluation of direct cost. Tax pollution cost from emission is negligible. Other environmental damages (degradation of land, contamination of soil, water and etc.) are not taking into consideration during accounting of energy prices. The proportion of taxation from green taxes is now lower than it was in the UK in 1997 [1]. A sustained effort by government is now required to design appropriate mechanisms for shifting the burden of taxation from incomes onto resources and emissions [1]. Nowadays economic activities should shift away from measuring economic growth by using GDP factor and try to measure sustainable economic values and include as many variables (not only economic but socials, environment, cultural, moral, ethic and others aspects) as possible. Some damages caused by pollution in the energy conversion processes are reflected (through taxes or penalty fees) in the national accounts. Environmental damage directly affects human welfare and usually the loss of welfare is not reflected in the national accounts. For examples the discomfort of breathing polluted air, use of treated water polluted by industry is defined as loss of welfare. This defensive expenditure (treating of polluted water, air or contaminated soil) does not contribute to welfare, but because it is final expenditure, it is counted as part of GDP. So there is a need to correct GDP by implementing alternative measuring indexes of wellbeing. One of indicator called "Genuine Progress Indicator" (GPI) – is a tool where the cost of restoring environmental damage is counted negative rather than positive as it is in case of calculating GDP index. There is another possibility to replace GDP by Index of Sustainable Economic Welfare (ISEW) which includes more than 20 indicators, such as consumption, distribution of wealth, environmental health, the cost of unemployment and other indicators. The index of human wellbeing (HWI) is also could be as an option for substitution of GDP index. There is so called happy planet index which measures countries' people happiness. The indicator of Sustainable Process Index (SPI) developed by Krotscheck and Narodoslawsky (1995) is based on the assumption that a sustainable economy builds only on solar energy and it evaluates surface area needed for the conversion of energy into products and services. Surface area is a limited resource in a sustainable economy because the Earth has a finite surface. SPI index is could be used as a substitute of GDP for economical appraisal of the best available energy technologies.

## 2. ECOLOGICAL FOOTPRINT

An ecological footprint concept gives priority to environmental aspects of sustainable development. The ecological footprint is measuring human demand on the Earth's ecosystems. It compares human demand with planet Earth's ecological capacity to regenerate. It represents the amount of biologically productive land and water area needed to regenerate the resources a human population consumes and to absorb harmless the corresponding waste. Ecological footprint directly contributes to a tool for measuring $CO_2$ and other emissions in energy conversion processes or other activities. It evaluates a land plot needed for a certain economic activities and because the land area is a limited recourse it is directly contributes to the economical value of the region. Ecological footprint can substitute the GDP index through the value of the land which is allocated for a certain economic, social and other activities.

Today humanity uses the equivalent of 1.3 planets to provide the resources we use and absorb our waste. This means it now takes the Earth one year and four months to regenerate what we use in a year. Moderate UN scenarios suggest that if current population and consumption trends continue, by the mid 2030s we will need the equivalent of two Earths to support us. Turning resources into waste faster than waste can be turned back into resources puts us in global ecological overshoot, depleting the resources on which human life and biodiversity depend.

The ecological footprint can be a useful tool to educate people about carrying capacity and over-consumption and to argue that many current human activities are not sustainable. The footprint does not attempt to include the social or economic dimensions of sustainability however some social and cultural aspects can be included into account with calculating how much land should be utilize renewable resources. This can be a case for local initiatives for a decision making processes, because on regional level a footprint smaller than the locally available area opens up the possibility to "export" bio-capacity in the form of consumer goods [5]. A footprint larger than the available area reveals that trade is required to use a resource hinterland [5]. In the regional level the fossil footprint is defined as the land needed to produce the same amount of energy produced by agricultural resources (f.e. biomass) or it estimates the land area required to sequester the $CO_2$ emitted by burning fossil fuels [5].

The methodology of sustainable energy production process is based on ecological footprint concept. Different energy production technologies and its influence to environment, using SPI index methodology, were investigated in the article. The investigation in the article shows pros and cons of using SPI methodology for evaluating of energy costs.

## 3. SUSTAINABLE PROCESS INDEX

One of the methods for ecological footprint calculation has been developed by Krotscheck and Narodoslawsky in technical university of Graz (Austria) in 1995. This method is called the Sustainable Process Index (SPI). This calculation method is based on the assumption that a sustainable energy economy builds only on solar energy. Surface area is needed for the conversion of energy into products and services but the area is a limited resource because the Earth has a finite surface. Area is the underlying dimension of the SPI. The more area a process needs to fulfill a service, the more it cost from sustainable point of view. The SPI is the fraction of the area per inhabitant related to the delivery of a certain product or service unit. The SPI is calculated with this equation:

$$SPI = \frac{a_{tot}}{a_{in}} \tag{1}$$

where $a_{in}$ is the area per inhabitant in the region being relevant to the process.
$a_{tot}$ is the specific (sustainable) service area and is calculated with equation
*unit* can be kWh, kg, $m^3$ or $m^2$ or other dimension.

$$a_{tot} = \frac{A_{tot}}{S_{tot}} \ (\mathrm{m^2/unit}) \tag{2}$$

$S_{tot}$ is the number of unit-services (e.g. product units) supplied by the process in question for a reference period of normally one year.

The total area $A_{tot}$ is calculated with equation

$$A_{tot} = A_R + A_E + A_\xi + A_S + A_p \, (\mathrm{m^2}) \tag{3}$$

The areas on the right hand side are called a partial area and refer to impacts of different productive aspects.

$A_R$ – the area required for the production of raw materials, is the sum of the renewable raw material area ($A_{RR}$) and the non-renewable raw material area ($A_{RN}$).

$A_\xi$ – the area necessary to provide process energy.

$A_S$ – the area to provide the installation for the process, is the sum of the direct use of land area ($A_{ID}$) and the indirect use of land area ($A_{II}$).

$A_S$ – the area required for the staff.

$A_p$ – the area for sustainable dissipation of products and by-products. The reference period for these partial areas is usually one year.

The sustainable process index (SPI) relates the land area required by a certain process (production, services) to the area of a certain region. Regional sustainability is achieved, if the SPI of all processes of the region does not exceed “Imported” and ”exported” areas are made visible as materials and energy embedded in traded goods and services. The calculation method of the SPI comprises different subareas for material resources, energy, personnel, process installation (e.g. machines for the production process), and product dissipation (assessment of the waste quality and quantity of different material and energy flows and emissions [5].

Scientists G. Stoglehner and M. Narodoslawsky have used SPI methodology for evaluation of different energy development scenarios [5, 6, 7]. According data acquired from Austrian case study [5] and using a life cycle assessment (LCA) approach the different aspects were investigated: the raw material, the process and the size of production facility. Three different process options have been evaluated: (1) ethanol production in combustion with biogas in CHP plant; (2) ethanol production combined with biogas combustion and (3) ethanol production combined with straw combustion. A production capacity of bioethanol (yield) had a range from 1000 t per year (small farmers) to 10’000 t per year (de-central, small scale production units) and 60’000 t per year in large scale production units.

Interesting results have been discovered in an option for a small scale local farms where the increase of footprint size has been discovered. The reason is because it comprises a large biogas plant (only the off-heat is used to supply energy for ethanol production). The larger the plant capacity, the more biogas manure has to be recycled to the fields, leading to considerable increase of transport loads and subsequently increase ecological pressures [5].

The alternatives of medium size decentralize production unit shows the decreasing of footprint size. This is the reason of increasing the technological efficiency, because production technologies are optimized to the capacity [5].

A large scale production unit with a capacity over 60.000 t of bioethanol per year has a footprint almost four times larger than unit with a production capacity of 10.000 t per year. The reason is that the size of utilization of bio-energy becomes problematic because of transport impacts.

The conventional bioethanol plants which use natural gas for process energy have much higher ecological footprint. Alternatives with “conventional” biofuels (biodiesel produced from rapeseed oil in the large scale bioethanol production units) offer only limited advantages. Energy production in this type of units is approximately 30% more efficiently and has less ecological impact compared to fossil fuels. In the case of biodiesel production from utilization of by-products of other sectors (like tallow) or even waste material (used kitchen oil) decreases the ecological footprint dramatically [5]. An impressive reduction of footprint can be achieved by utilizing biogas as biofuel. In this case the higher yield per hectare (including the whole plant for production of bioethanol not only corn grains) is combined with lower agricultural input (less fertilizer, no drying) and low impact conversion process (low heat and moderate electricity requirement). Considering these factors the production of biofuel using biogas has the footprint lower by a factor of 16 compared in the case of using gasoline. In comparison if fossil diesel is used an impressive 13 factor can be achieved [5].

The calculation of footprint in G. Stoglehner study [5] shows that the substitution of fossil through renewable energy carriers reduces the footprint to a much higher degree than thermal insulation of houses [6]. Ecologically optimized thermal insulation can save about 70% of primary energy use for heating houses which were constructed in 1970s but at relatively high cost [6] if the life cycle approach of thermal isolation process (including material flow and work load) is taking into account. Thermal insulation reduces the footprint of energy use for heating by 70% however the substitution of fossil fuel through a woodchip furnace for heating of houses (given a constant energy demand as it is in a case with thermal insulation) is actually reducing the footprint at a rate of about 96%. So in the case with a relatively low budget, it is better to change energy source (carrier) for heating system. To substitute a fossil fuel by renewable energy technologies for heating system is a better solution and more economically valuable rather than to invest in thermal insulation [6].

## 3.1. Ecological footprint for production of solar PV module

In the article the principle of SPI methodology is investigated in the case for energy production using photovoltaic tracking system. Using a program "SPIonexcel" the SPI index was calculated for production of photovoltaic panel (PV) with a tracking system. A photovoltaic element is based on silicon wafer technology which has a huge pressure for environment. A process of production of silicon wafer for PV system needs a lot of chemical process which pollutes environment. Consequently a lot of energy is needed to prevent environment from pollution and for cleaning output products. It was calculated that a footprint for production of 1m$^2$ of solar PV wafer is about 165 thous. m$^2$ or 0,165 km$^{2.}$ The distribution of the ecological pressure from inputs for production of solar PV element and the emission rate from production process is considering 74% from the total emission rate. An extraction process of silicon for making 1m$^2$ of PV elements is a costly process as well. For example to produce 1m$^2$ of solar PV wafer is needed about 0.122 kg of silicon which has a footprint about 20 thous. m$^2$ or 0,02 km$^2$ (9.3% from total footprint for production of 1kWh using 1m$^2$ of solar PV element). To produce 1m$^2$ of solar PV wafer is needed about 2.7 kg of aluminum alloy which has a footprint about 29 thous. m$^2$ or 0.029 km$^2$ (13.11%). The overall footprint for production of 1m$^2$ of solar PV element and its by-products is about 222 thous. m$^2$ or 0.222 km$^2$. The calculated SPI index for production of 1m$^2$ of solar PV element is 6.63.

If the SPI index is smaller than 1 (SPI<1), it means that the product service or production process is sustainable and the influence to the environment is considerable small. If the SPI index value is between zero and one (0.001<SPI<1), it means that product service or production process is sustainable suitable. If the SPI index is greater than 1 (SPI > 1), it means that the product service or production process is too inefficient, benefits too expensive.

Production of 1m$^2$ of solar PV element with a tracking system has the following processes which were included to calculate an overall footprint and SPI index. The processes were as follow:

1. Production of steel high alloyed products need for PV system elements;
2. Production of cooper for PV system elements;
3. Production of polyethylene elements;
4. Production of solar PV wafer at plant site;
5. Production of tracking mechanism and PV platform;
6. Electricity provision;
7. Production and assembling of command and control mechanism;
8. Transport provision for all group of processing (from manufacturing to assembling)
9. Assembling process.

All these elements of the production process chain have their own footprints and SPI indexes. The data acquired through calculation are presented in a table 1 below.

The process chain for production of a single solar PV module with a tracking system is shown in picture below. To produce a single solar PV module roughly is needed about 20 MWh electric power. The overall ecological footprint or an area needed to produce 1 kWh of electricity using 1m$^2$ of solar PV module is around 250 m$^2$. The overall ecological footprint for production of 1 unit (1m$^2$) of solar PV module (including all processes) is 3.1 mln.m$^2$ or 3.10 km$^2$ per unit (1m$^2$). The total SPI index is 92.

Table 1. Ecological footprint and SPI index for production of solar PV module

|  | Process name | Unit | Ecological footprint $m^2$/year/unit | Ecological footprint $m^2$/year/kWh | SPI index |
|---|---|---|---|---|---|
| 1 | Production of steel high alloyed products | kg | 4’854 | 18.60 | 0.14 |
| 2 | Production of cooper for PV system elements | kg | 3’961 | 0.341 | 0.12 |
| 3 | Production of polyethylene elements | kg | 3’156 | 0.010 | 0.09 |
| 4 | Production of solar PV wafer at plant site | $m^2$ | 222’959 | 42.839 | 6.63 |
| 5 | Production of tracking mechanism and PV platform | unit | 9’766’882 | 62.374 | 290.65 |
| 6 | Electricity provision for assembling | kWh | 62 | 0.622 | - |
| 7 | Production command and control mechanism | unit | 1974 | 0.013 | 0.06 |
| 8 | Transport provision for all group of processing (from manufacturing to assembling) | tkm | 190 | 0.171 | - |
| 9 | Assembling process | kWh | 97’388 | 0.622 | 2.90 |
|  | Total | kWh | 20323 | 250 | 92 |

Source: program SPIonexcel 2.0 (http://spionexcel.tugraz.at, 2011)

For calculating SPI indexes and ecological footprint for processes a program “SPIonexcel” is using “Probas” database[1] where the information is gathered by the Federal Environmental Agency (German) and the Öko-Institut (Germany) with the IT-supported project "Process-oriented basic data for environmental management instruments (ProBas)". A program also uses “Ecoinvent” database[2] where information is gathered from the Swiss Centre for Life Cycle Inventories. Databases include different values from energy production, energy provision and other production processes. A program also uses an abbreviation of NACE which means “Nomenclature statistique des Activités économiques dans la Communauté Européenne”. This categorization was applied by the European Union based on the “International Standard Industrial Classification of all Economic Activities” developed by the United Nations. NACE information is calculating the distribution of the footprint along the industrial sectors.

Pictures below (Fig. 1 and Fig. 2) summaries the ecological impact of intermediates along the process chain of production of solar PV element. The numbers represent the environmental pressure from the particularly intermediate processes of production of the end product (in this case – 1kWh of electric energy). The graphic shows the increase of the overall footprint along the process chain as well as the fraction supporting processes.

---

[1] http://www.probas.umweltbundesamt.de

[2] http://www.ecoinvent.org

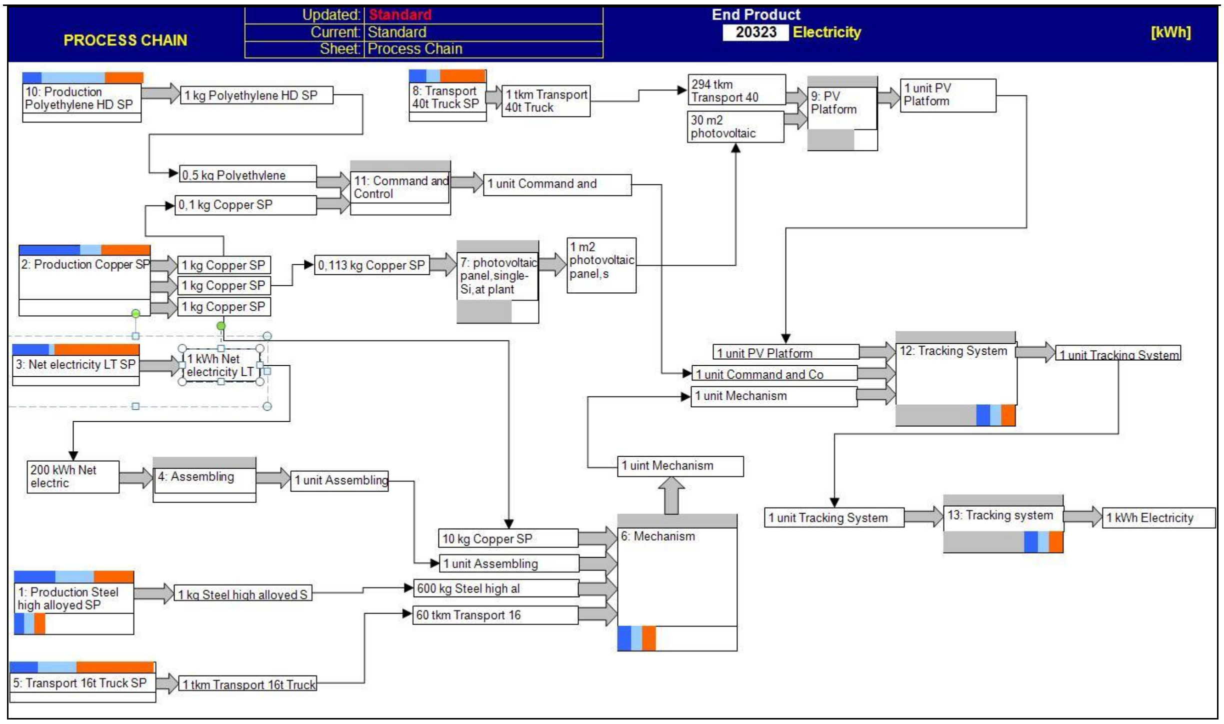

Fig. 1. Sustainable process analysis for solar PV module with tracking system
Source: program SPIonexcel 2.0 (http://spionexcel.tugraz.at, 2011)

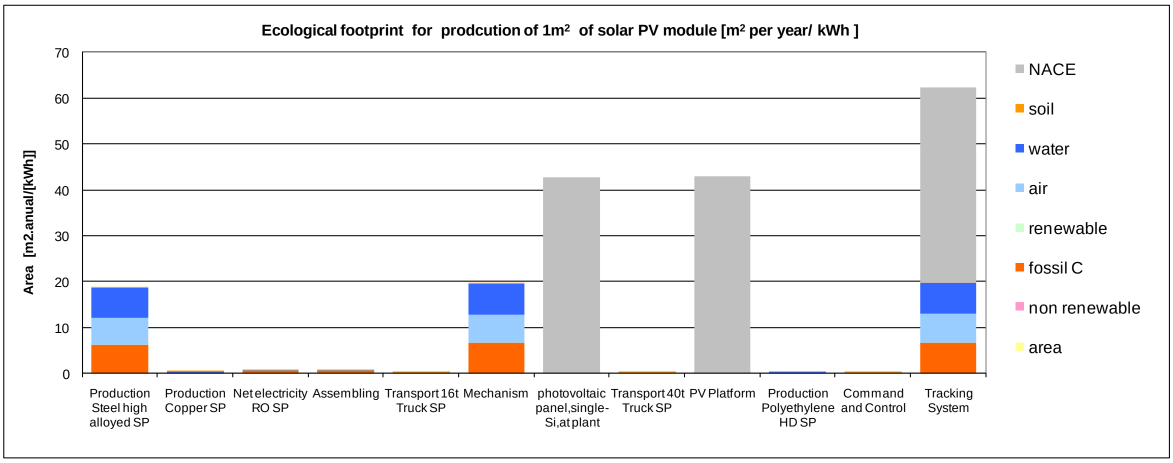

Fig. 2. The ecological impact of intermediates along the process chain
Source: program SPIonexcel 2.0 (http://spionexcel.tugraz.at, 2011)

The graph above (Fig. 2) shows that the biggest contamination arises in the process of production of tracking system because a lot of steel products are involved in the process. Steel production is energy consumed process and it has a huge impact to environment. The large contamination occurs in the production of PV wafer in-situ and PV platform in-situ as well. The processes which have also the largest pressure to environment are production of elements and mechanism components made from steel. These processes contaminate mostly air, water and soil.

The SPI methodology can evaluate the influence to environment using different energy production sources based on SPIonexcel database. According to the database given in SPIonexcel program the ecological footprint for production of 1kWh in the Lithuania power plant is 630 $m^2$/kWh. In the next chapter the principle of SPI methodology for development of regional energy scenarios is investigated.

## 3.2. Ecological footprint of electricity production

There are many good solutions for the development of the best regional energy economy scenarios. One of them is a combination of SPI methodology with a process network synthesis analysis (PNS). It evaluates economical, social and environmental factors, possibilities for development of renewable energy economy, so it helps to find the best solution for development of sustainable regional energy economy.

The SPI index can evaluate the land area required for a certain process and for a certain region. Sustainability level in the regional scale is achieved if the SPI index of all production processes in the region does not exceed 1. “Imported” and ‘‘exported” areas (goods, service and etc.) are visible as materials and energy embedded in traded market of goods and services. The SPI methodology show different subareas for material resources, energy, personal, process installation (e.g. machines for the production process), product dissipation (assessment of the waste quality and quantity of different material and energy flows) and emissions.

Figure below (Fig. 3) shows the comparison of four different technologies for electric energy supply. Wind turbine (3 MW turbine from Vestas Co.), monocristaline photovoltaic panel (“Ecoinvent” database), biogas unit producing heat and power from ethanol mash) and a high performance natural gas combined heat and power system with overall efficiency rate 90% and electricity efficiency rate 45 %, with gas as a major energy input [9]. The impact to environment from using biogas unit is critically depending on the raw material. Footprints may become considerably higher (by a factor of three at least) if biogas production is based on fresh crops [9].

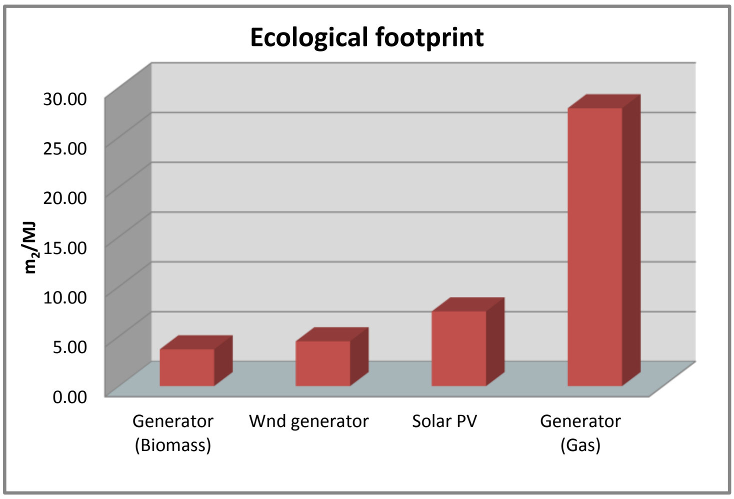

Fig. 3. Ecological footprint for different energy technologies
Source: M. Narodoslawsky, TUG, 2009

The different impact of energy technologies is shown in figure below (Fig.4) with comparison of pressure to environment from wind turbine, PV model and natural gas unit. The influence to climate (represented by the fossil C sector) is strong in all technologies. The large pressure is for the natural gas technology so far. It is interesting to notice that renewable technologies are also having strong influence to environment. For example in the production process of wind turbines and photovoltaic panels there are a lot of energy used in the production of steel elements. The other reason is that our current energy system is still mostly based on fossil fuel and the energy input to production and manufacturing of equipment is also causing pressures in this category [9].

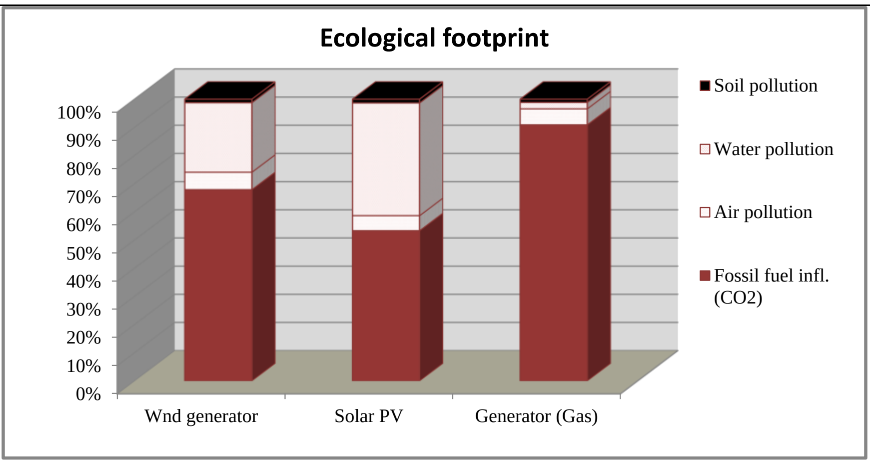

Fig. 4. Ecological footprint for different energy technologies
Source: M. Narodoslawsky, TUG, 2009

The fossil carbon dominates in production process of the wind turbine. It reflects the fossil contribution to steel processing. It cannot be reduced unless fossil coal is replaced by a renewable based alternative (like charcoal) in iron melting [9].

The production of photovoltaic models has quite high pressure on environment as well. Especially the emissions to water are prominent as a result of the complex chemical process needed to produce the semiconductor wafers. It is interesting to notice that the carbon emission pressure predominantly comes from the production of frames for PV modules because it is made from steel. The energy intensive production processes for construction materials is considering as the main factors for harm environment [9].

## 4. CONCLUSIONS

Strongly increased demand for energy and its volatile prices have a tendency to increase over the next years. However impacts to the environment from producing of electric energy and heat energy, as well as use of energy are not properly assessed so far. Existing energy accounting methods in energy economy is mostly based on cost benefit analysis model and it is directly contribute to GDP index. It evaluates the resource consumption rate and treats it as a positive factor. However environmental factors are left aside as a needful and not influencing the production costs. Green accounting methods reveals the hidden costs of energy production and provision services. Ecological footprint is one of the green energy accounting methods and it together with the sustainable process index methodology allows investigating hidden energy values. These values have negative influence on energy price because the energy costs are increasing. However it has a positive effect because renewable energy technologies become a favorable and rival competitor compared to fossil fuel burning technologies. SPI methodology together with life cycle approach and the process network system analysis becoming one of the most prevailing accounting methods for revealing of hidden energy costs. As long as energy prices for fossil fuel burning technologies will be calculated without attention to green accounting methods the RES cannot compete in the market without subsidies or external financial support. As long as RES technologies will be based on fossil fuel the ecological footprint will be considerably high. Energy economy is approaching the development from fossil fuel burning technologies through renewable energy to a sustainable energy economy. Energy is a substantial factor influencing the future development of our society.

## 5. REFERENCES

1. JACKSON, T. *Prosperity without growing. The transition to a sustainable economy*. Earthscan Ltd.: Sustainable development commission, 2009. 286 p. ISBN 1849713235.
2. JUŠKA, F. Renewables and their use in Lithuania. *Report. Ministry of Economy, Division of Energy Development,* 2003.
3. PAULAUSKAS, S. *Savivaldos dialektika*. Klaipėda: Klaipėdos universiteto leidykla, 1999. 25I p. ISBN 9986-505-8-8.
4. RIEWE, R. Sustainable densities. Styrian winter academy 2010. Lecture and presentation for specialist on development sustainable smart cities. Graz, Austria: Graz University of technology. 2010 February 14–18.
5. STOEGLEHNER, G., NARODOSLAWSKY, M. How sustainable are biofuels? Answers and further questions arising from an ecological footprint perspective. *Bioresource technology,* 2009, Vol. 100, p. 3825–3830.
6. STOGLEHNER, G. Ecological footprint – a tool for assessing sustainable energy supplies. *Journal of cleaner production,* 2003, Vol. 11, p. 267–277.
7. STOEGLEHNER, G., NARODOSLAWSKY, M. Implementing ecological footprinting in decision-making processes. *Land use policy*, 2008, Vol. 25, p. 421–431.
8. ŠTREIMIKIENĖ, D., PUŠINAITĖ, R. External cost of electricity generation in Lithuania. *Environmental research, engineering and management*, 2008, No. 2(44), p. 33–40.
9. NARODOSLAWSKY, M. Ecological impact of renewable resource based energy technologies. International conference on process integration, modelling and optimization for energy saving and pollution reduction. Rome, Italy. 2009, 10–13 May.
10. GALINIS, A. Šalies savivaldybėse esamų atsinaujinančių energijos išteklių (Biokuro, Hidroenergijos, Saulės energijos, Geoterminės energijos) ir komunalinių atliekų panaudojimas energijai gaminti. *Galutinė ataskaita*, *LEI*, 2009. p. 357.

# EXTRACT AIR ENERGY UTILIZATION USING HEAT PUMP IN BUILDINGS WITH INDOOR SWIMMING POOLS

**A. Brahmanis, U. Pelīte, A. Lešinskis, D. Kona, T. Bui Kon**
*Riga Technical University*
*Kaļķu iela 1, LV-1658 – Latvia*
*Phone +37129454525*
*Email: Arturs.Brahmanis@rtu.lv*

ABSTRACT

An annual energy consumption simulation is made for one Latvian mansion with swimming pool hall. Building has two main parts: living part (with bedrooms, living room, kitchen, and washing rooms), and a recreation part with 28m² swimming pool, saunas and sports hall.

HVAC system consists of the following elements: heating system with convectors, water-to-water heat pump system cooling / heating concrete slabs in living part, and centralized mechanical extract, with natural outside air intake through the window grilles. Air –conditioning in swimming pool is provided by separate air-handling unit with heat pump - dryer.

In winter the heat pump system heats concrete slabs, utilizing extract air energy through air to water heat exchanger. In summer living room slabs are cooled, and removed heat is used for the swimming pool supply-air preheating.

The annual energy consumption simulation is made with DOE 2.1E core based application, using building's information model (BIM) for the average Latvian meteorological year. Two BIM's are made: for a living part of the mansion and for swimming pool room, using design coefficients for constructions' thermal resistance and indoor air parameters.

Simulation results show, that swimming pool room consumes 77 MWh of heating energy per year. When using heat pump gained energy to preheat swimming pool supply air, annual heat energy consumption decreases to 62 MWh, which means about 20% saving. The heat pump system annual average coefficient of performance (COP) according to manufacturer's data is assumed as 2.5.

Paper results can be used by HVAC engineers and architects for ventilation and air conditioning design in other multi-purpose buildings with indoor swimming pools.

Keywords: HVAC simulation, indoor swimming pool, heat pump.

## 1. INTRODUCTION

### 1.1. The brief of requirements for air exchange in Latvia

According building law rooms has to have balanced ventilation [1, 2]. For residential buildings in Latvia is common using natural or mechanical extract. Mechanical extract in many situations gives a possibility for heat recovery to supply air. However, in buildings with decentralized natural supply air trough the windows, engineers have to find other ways for heat recovery. The aim of this paper is to analyze the energy efficiency of extract air energy utilization using heat pump in buildings with indoor swimming pools.

### 1.2. Heat recovery with heat pump

Several types of air-to-air exchanger recovery devices are available for recovering energy from ventilation. The heat exchanger may transfer sensible heat only or both sensible and latent heat. Over many decades, plate type, regenerative wheels, and heat pipe exchangers were developed and used to transfer heat for a variety of air-to air applications. Typical heat and enthalpy exchange efficiencies range from 55 to 80% [3]. Heat pump energy recuperation technologies are widely used and being researched for decades [45].

As a first step to make heat recovery is to place a heat exchanger in exhaust air flow. Then heat recovery is possible for consumers with lower temperature:

- hot water preheating;
- snow melting on entrance road surfaces outside of the building (not considered as advantage in building energy performance).

When using heat pump it is possible one more potential consumer – heating. Technical data collected in table for building systems - hot water and heating is shown in Table 1:

Table 1. Heat recovery possibilities within the hot water and heating systems

| Nr. | Recovery type | Hot water | Heating |
|---|---|---|---|
| 1 | Heat exchanger | Preheating ~ 7K.<br>Accumulation in buffer tanks is hygienically and technically not reasonable. | Not possible, when all rooms has temperature higher then exhaust air temperature. Limited possibility to cover some part of heat loses in structure. |
| 2 | Heat pump | Preheating ~30K;<br>Heating ~ 45K.<br>Cross-flow or accumulation buffer tanks. | All types of heating, low and high temperature (35ºC and 65ºC). Both – water and airborne heating systems. |

As a special case, in buildings with cooling in summer time, extract air can be used for reversible heat pump heat dissipation, then heat exchanger in air duct is already installed for heat recovery purposes [4].

### 1.3. Recommendations for indoor air parameters in swimming pools

In modern understanding, a swimming pool - is a hydro-technical construction, intended for water sports. Usually temperatures maintained in swimming pool halls are between 28ºC and 32ºC, according to application, preferable 1.1 to 2.2ºC higher than the water temperature. It is suggested, that the indoor air dew point should be held at least 2.7ºC below the coldest surface temperature [10]. A little negative air pressure – about 10 Pa is necessary to keep air out of the rest of the building and out of cold cavities for most of the time.

As a result of a large area of wet surfaces and swimmer's splashes there are high moisture loads on the pool room air ventilation and air – conditioning system. Such maintenance of air parameters as heating and drying, active ventilation and other factors related to water purification and physical parameters maintenance make this type of buildings one of the largest energy consumers in public / multipurpose buildings [7, 8].

## 2. HVAC SYSTEM

The mansion was built in summer 2010 and is located near the Gulf of Riga, the Baltic Sea. Living and recreation parts of the building are separated. Due to the design specifics, it was difficult to install classic supply-exhaust ventilation with heat recuperation, and designers choose to use heat pump for extract air heat utilization. This solution is aimed to provide energy recovery both in winter and in summer seasons.

The living part of building has decentralized extract ventilation system. The fresh air is supplying to rooms through the window grilles and is being extracted from washrooms. The air handling unit (AHU1) is of direct-flow type.

Swimming pool room ventilation is provided by supply – exhaust air handling unit with internal heat pump (AHU2), which consists of the following elements:

- Supply air water heating coil – to utilize the main heat pump produced heat;
- Supply air water post heating coil – to heat the supply air to the room temperature;
- Internal heat pump – to remove moisture from return air;
- Recirculation section;
- Supply and exhaust fans.

Tables 2 and 3 shows air AHU parameters and legend of the symbols used in schemes respectively.

Table 2. Air handling unit parameters

| Description | AHU1 | AHU2 |
|---|---|---|
| Electrical power of supply / exhaust fans, kW | 0.2 | 0.6 / 0.6 |
| Static pressure supply / exhaust fans, Pa | 150 | 250 / 250 |
| Air flow of supply / exhaust fans, $m^3/h$ | 930 | 1500 / 1500 |
| Temperature / humidity efficiency of heat exchanger | - | 50% / 0% |
| Heating power of water heating coil, kW | - | 14 |
| Heating / cooling power of heat utilization coil, kW | 0 / 4.1 | 12.3 / 0 |

Table 3. Scheme legend

| Symbol | Description | Symbol | Description |
|---|---|---|---|
| 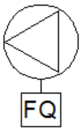 | – Fan with frequency converter | t, fi | – Temperature / humidity sensor |
| ⊕ | – Heating coil | Δp | – Differential pressure gauge |
| ⊖ | – Cooling coil | 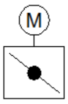 | – Motorized air flow damper |
| 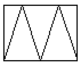 | – Air filter | 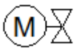 | – Motorized valve |

AHU1 functional scheme is shown in Fig. 1:

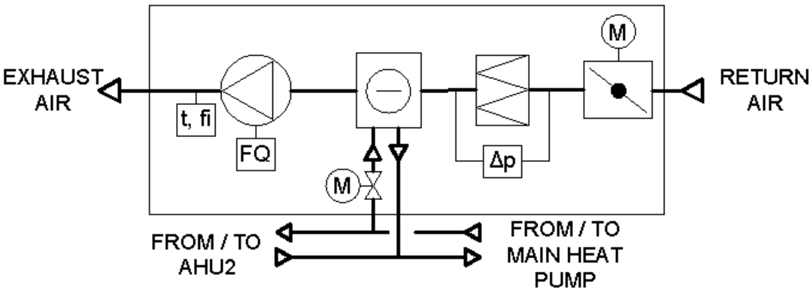

Fig. 1. The functional scheme of AHU1

The AHU1 heat recovery coil utilizes extract air energy during winter periods (heat pump – heating mode). When the heat pump is switching to cooling mode, the motorized valve is turning off and water flow is redirecting to AHU2 heater.

AHU2 functional scheme is shown in Fig. 2:

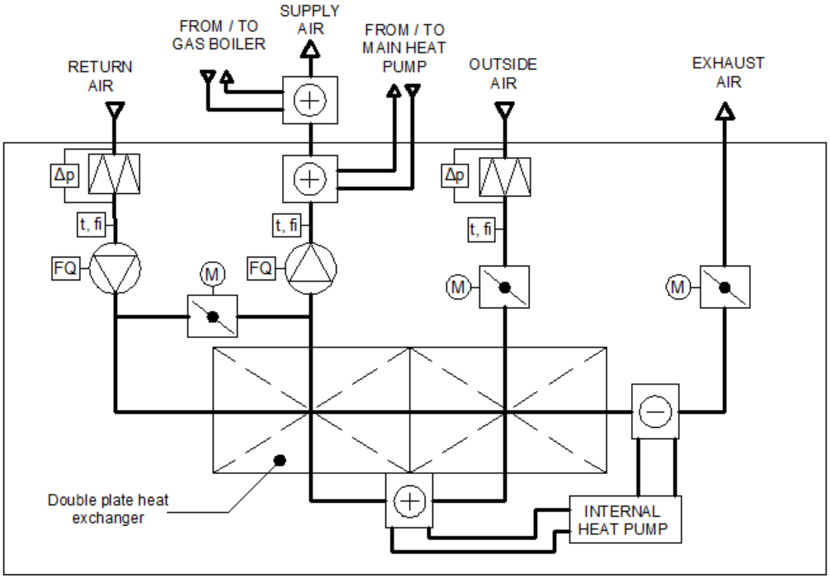

Fig. 2. The functional scheme of AHU2

## 3. METHODS

The building is equipped with minimum energy a counters, that is not usable for deeper research – one gas consumption and electrical consumption counter serves for all the building. Therefore, to evaluate HVAC system efficiency, we have chosen theoretical method – building simulation within the with DOE 2.1E core based application (RIUSKA v.4.6.40). The simulation is performed, using average climate data for Riga, Latvia (the building is located at a distance approximately 80 km from the Capital of Latvia), from the software climatic database. As soon as used program doesn't allow simulating HVAC equipment with reversible cycle, it was made two Room models in CAD program and then exported to simulation software. Room models were transformed to Building Information Models (BIM's). The simulation performed for all rooms with activated concrete slabs (heating / cooling pipes are concreted into the slab, see Fig. 3).

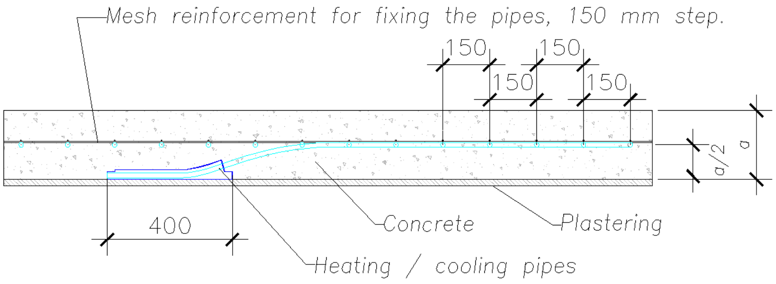

Fig. 3. Principal scheme of the activated concrete slab

Living part model is shown in Fig. 4.

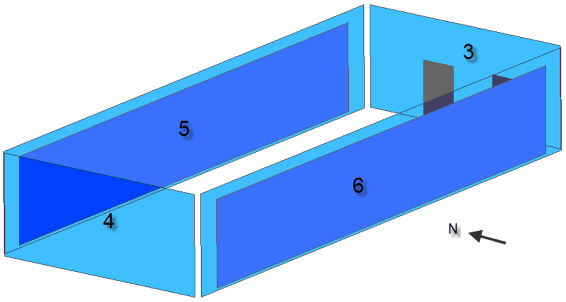

Fig. 4 The model of the Living Part

Living part model, which represents a room, the area of windows and walls of which is the sum of window and wall area in a residential part of the building.

The building envelope characteristics for Living Part are shown in Table 4:

Table 4. The building envelope characteristics for Living Part

| | Name | A, m² | U, W/m²/°C | Azimuth (°) | Window (m²) | Door (m²) |
|---|---|---|---|---|---|---|
| 1 | Ground floor | 151.7 | 0.25 | | | |
| 2 | Roof | 151.7 | 0.16 | 0 | | |
| 3 | EW* | 26.7 | 0.21 | 90 | | 4.8 |
| 4 | EW | 26.7 | 0.21 | 270 | | |
| 5 | EW | 69.0 | 0.21 | 0 | 54.00 | |
| 6 | EW | 69.0 | 0.21 | 180 | 54.00 | |

*External Wall. Brick-faced concrete external wall 330 mm thick (Concrete 100 mm, mineral wool 115 mm, wind shield board 30 mm, brick, perforated, 85 mm). Window type: 2xClear, 6+6 mm, Aluminium frames, U=2.78 W/m²/°C, according to project design.

The model of Swimming pool room is made according to the project (Fig. 5).

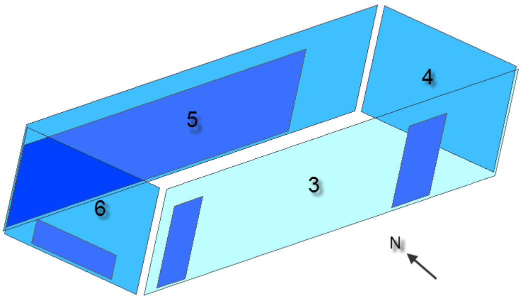

Fig. 5. The model of Swimming pool room

The area of the pool is 32 m². The water temperature is equal to the room air temperature (on 1–2ºC lower), so we didn’t take into account heat losses or gains in this area.

Table 5. The building envelope characteristics for Swimming pool Room

| | **Name** | **A, m²** | **U, W/m²/°C** | **Azimuth (°)** | **Window (m²)** | **Door (m²)** |
|---|---|---|---|---|---|---|
| | **Swimming pool** | | | | | |
| 1 | Ground floor | 71.0 | 0.25 | | | |
| 2 | Roof | 93.0 | 0.16 | 0 | | |
| 3 | EW | 65.5 | 0.21 | 180 | 9.45 | |
| 4 | EW | 17.4 | 0.21 | 90 | | |
| 5 | EW | 65.5 | 0.21 | 0 | 40.50 | |
| 6 | EW | 17.4 | 0.21 | 270 | 2.40 | |

## 4. RESULTS

Simulation results show, that Living part consumes 33 MWh heating energy per year. Cooling electricity, with heat pump COP 2.5 is 4 MWh annually, which is much less than the energy, consumed on heating (Fig. 6).

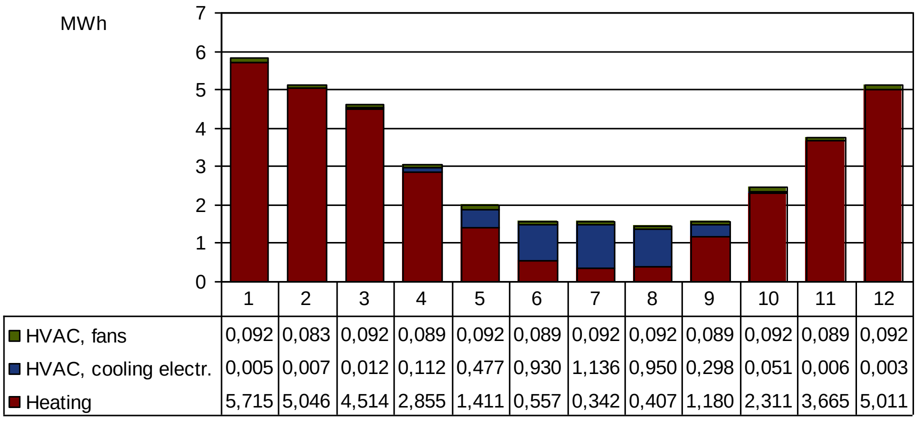

| | 1 | 2 | 3 | 4 | 5 | 6 | 7 | 8 | 9 | 10 | 11 | 12 |
|---|---|---|---|---|---|---|---|---|---|---|---|---|
| 🟩 HVAC, fans | 0,092 | 0,083 | 0,092 | 0,089 | 0,092 | 0,089 | 0,092 | 0,092 | 0,089 | 0,092 | 0,089 | 0,092 |
| 🟦 HVAC, cooling electr. | 0,005 | 0,007 | 0,012 | 0,112 | 0,477 | 0,930 | 1,136 | 0,950 | 0,298 | 0,051 | 0,006 | 0,003 |
| 🟥 Heating | 5,715 | 5,046 | 4,514 | 2,855 | 1,411 | 0,557 | 0,342 | 0,407 | 1,180 | 2,311 | 3,665 | 5,011 |

Fig. 6. HVAC system annual energy consumption in Living Part of the building

Heating energy consumption in Swimming pool is 77.14 MWh per year. Fig. 7 shows, that cooling is not required in this zone, because of high air temperature, maintained all year.

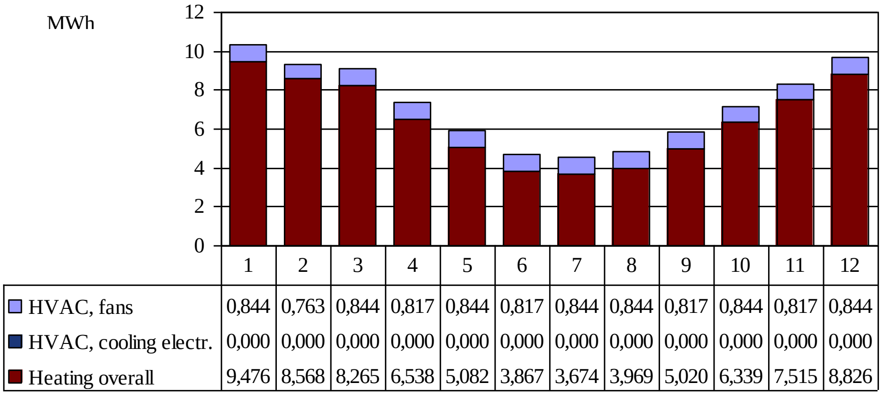

| | 1 | 2 | 3 | 4 | 5 | 6 | 7 | 8 | 9 | 10 | 11 | 12 |
|---|---|---|---|---|---|---|---|---|---|---|---|---|
| ☐ HVAC, fans | 0,844 | 0,763 | 0,844 | 0,817 | 0,844 | 0,817 | 0,844 | 0,844 | 0,817 | 0,844 | 0,817 | 0,844 |
| 🟦 HVAC, cooling electr. | 0,000 | 0,000 | 0,000 | 0,000 | 0,000 | 0,000 | 0,000 | 0,000 | 0,000 | 0,000 | 0,000 | 0,000 |
| 🟥 Heating overall | 9,476 | 8,568 | 8,265 | 6,538 | 5,082 | 3,867 | 3,674 | 3,969 | 5,020 | 6,339 | 7,515 | 8,826 |

Fig. 7. Annual heating energy consumption in swimming pool room

During the cooling period, the amount of heat energy, produced by heat pump, is 15.95 MWh per year. We have summarized Swimming pool room heating demand and heat, produced by heat pump. Fig. 8 shows the ratio of these two variables:

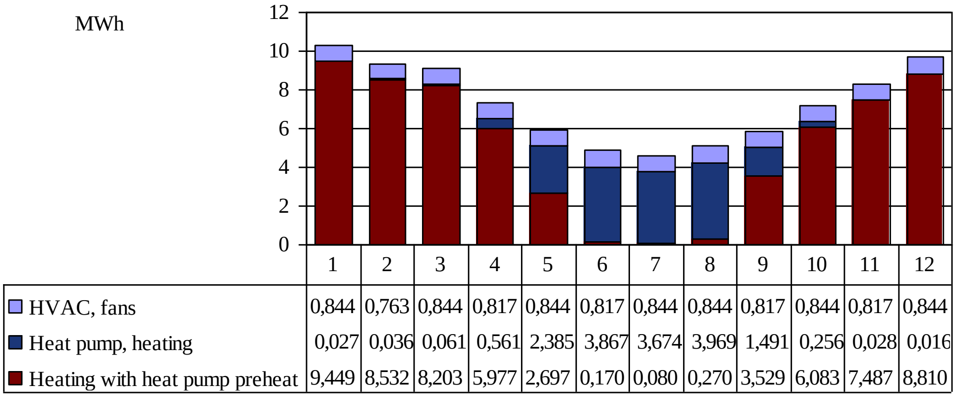

| | 1 | 2 | 3 | 4 | 5 | 6 | 7 | 8 | 9 | 10 | 11 | 12 |
|---|---|---|---|---|---|---|---|---|---|---|---|---|
| ▨ HVAC, fans | 0,844 | 0,763 | 0,844 | 0,817 | 0,844 | 0,817 | 0,844 | 0,844 | 0,817 | 0,844 | 0,817 | 0,844 |
| ■ Heat pump, heating | 0,027 | 0,036 | 0,061 | 0,561 | 2,385 | 3,867 | 3,674 | 3,969 | 1,491 | 0,256 | 0,028 | 0,016 |
| ■ Heating with heat pump preheat | 9,449 | 8,532 | 8,203 | 5,977 | 2,697 | 0,170 | 0,080 | 0,270 | 3,529 | 6,083 | 7,487 | 8,810 |

Fig. 8. Annual heating energy consumption in swimming pool room with heat pump produced energy

In both cases, HVAC fan electricity is less or more constant during the year period. Small variations are explained by the number of month days fluctuations.

## 5. DISCUSSION

The main advantage of the described system is that it provides heat utilization during the summer period. This method is most applicable for building with swimming pools, or other types of warm water storages. Although, heat pump produced heat within the summer period can be used in hot-water pre-heating in building with decentralized water supply, as well as in special-purpose buildings, for example, factories. The highest precision of data obtained could be achieved, if simulation will include condensation in extract air heat recovery coil. Heat losses caused by water evaporation from swimming pool surface also should give some corrections to the results. However, this factor highly depends on the using intensity of swimming pool [8, 10]. The current research focuses on the efficiency of the HVAC system studied. However, further investigations could be dedicated to evaluations of economical aspects in similar systems.

## 6. CONCLUSIONS

The annual energy consumption simulation is made within the average Latvian meteorological year. Two building’s information models (BIM) were created, according to existing site design specifics. Simulation results show, that swimming pool room consumes 77 MWh of heating energy per year, the design value is 85 MWh. When heat pump gained energy is used to preheat swimming pool supply air, annual heat energy consumption decreases to 62 MWh, which means about 20% saving. The paper results can be useful for architects and HVAC system designers in other multipurpose buildings with indoor swimming pools design as an another opportunity to increase the energy efficiency of building heating, ventilation and air-conditioning systems.

## 7. REFERENCES

1. *LBN 208 08. Multi-storey residential buildings*. Latvian building code. Riga, 2008.

2. *LVS EN 15251:2007. Indoor environmental input parameters for design and assessment of energy performance of buildings addressing indoor air quality, thermal environment, lightning and acoustic.* Latvian standard. Riga, 2007.
3. AN NGUYEN, YOUNGIL KIM, YOUNGGY SHIN. Experimental study of sensible heat recovery of heat pump during heating and ventilation. *International Journal of Refrigeration*, 2004, Vol. 28, Elsevier Ltd and IIR, 11 p.
4. R.J. GOLDSTEIN et.al. Heat transfer – a review of 2000 literature. *International Journal of Heat and Mass Transfer,* 2002. Vol. 45, 105 p.
5. S. NOWOTNY. Possibilities of improving the thermodynamic working conditions of heat pumps for heat recovery. *International Journal of Refrigeration*, Volume 2, Issue 3, May 1979, p. 171–175.
6. S. B. RIFFAT and M. C. GILLOTT. Performance of a novel mechanical ventilation heat recovery heat pump system. *Applied Thermal Engineering* Vol. 22, Issue 7, May 2002, p. 839–845.
7. LEWIS G. HARRIMAN III, G.W. BRUNDRETT, R. KITTLER. *Humidity Control Design Guide For Commercial and Industrial Buildings*. Atlanta: ASHRAE, 2001. 180 p. ISBN 978-1883413989.
8. KRUMINS A., PELITE U., BRAHMANIS A., et.al. Optimal control strategy of air handling unit for different microclimates in working and swimming areas of a swimming pool hall. Indoor Air 2008. Proceedings of the 11th International Conference on Indoor Air Quality and Climate. [CD]. 2008 August 17–22.
9. *VDI 2089-1:2006-09. Technische Gebäudeausrüstung von Schwimbädern – Hallenbäder*. Dutch standard. Berlin, 2009.
10. American Society of Heating, Refrigerating and Air-Conditioning Engineers. *ASHRAE Handbook: Applications SI Edition,* Atlanta: ASHRAE, 2004. 400 p. ISBN 1-931862-23-0.

CYSENI 2011, May 26–27, Kaunas, Lithuania
ISSN 1822-7554, www.cyseni.com

# ACTIVE THERMAL NONDESTRUCTIVE TESTING OF BUILDING ENERGY EFFICIENCY

**S.M. Danilova-Tretiak, V.L. Dragun, V.G. Leschenko, T.E. Schelak**
*A. V. Luikov Heat&Mass Transfer Institute of NAS of Belarus*
*Brovki str. 15, Minsk 220072 – Belarus*
*Phone +375 172 841 250*
*Email: dts@hmti.ac.by*

## ABSTRACT

At the present day, the problem of buildings construction and renovation with providing of comfortable living conditions under effective energy use is actual. Express testing on the basis of modern nondestructive methods can help to improve control of construction quality and assess correspondence of standard and estimated parameters.

In this paper, the method of active thermal nondestructive testing is presented. “Activity” of the method implies that the wall surface under investigation undergoes to additional thermal influence in order to create temperature gradient between internal and external surfaces of the wall. Temperature distribution on the object surface is determined by infrared thermography. According to measurements results the qualitative and quantitative analysis is performed. It means analysis of thermograms and modelling of thermal processes in the object under investigation.

The method of active thermal nondestructive testing (ATNDT) was used for examination of apartment building in Rechitsa (Belarus). Such constructive defects as insufficient thermal insulation of building panels` butt joint are easily detected by thermal-vision scanning (thermal camera FLIR P25 was used in represented example). The panels themselves have uniform temperature distributions on thermograms. Their energy efficiency can be estimated by computer modelling. In this investigation the program ELCUT® 5.1 was used to calculate temperature distribution in panel section at preset thermal and technical parameters of the wall and temperature of its internal surface. Conclusion about energy efficiency of building wall is based on analysis of experimental and calculated data of thermal state of external wall surface.

Keywords: active thermal nondestructive testing, energy efficiency, temperature, temperature distribution modelling, thermal insulation

## 1. INTRODUCTION

At the present day the problem of building’s construction and renovation with providing of comfortable living conditions under effective energy use is actual. Express testing on the basis of modern nondestructive methods can help to improve control of construction quality and assessment of standard and estimated parameters correspondence.

The main direction of nondestructive testing of civil and industrial buildings enclosing structures is thermal diagnostics by own infrared radiation of the object under consideration. Survey of building’s wall surface with thermal camera after construction work completion, during exploitation and before renovation allows to detect thermal insulation defects, estimate quality of walls junctions quickly and nondestructively. Surface temperature of building wall is defined not only by interaction with internal and external environment at this moment but by heat transfer for a long period (up to several days) [1]. Thermal image of non-uniform structure (by its properties) shows surface temperature distribution, which reflects properties changing of surface itself and internal layers. These changes cause variations of heat resistance and heat flux from object surface that is registered in infrared spectrum.

Thermal diagnostics allows following:

– to carry out the object pilot survey quickly, during several hours;

- to organize quality control of enclosure structures during building exploitation;
- to define thermal insulation efficiency and to form data base about substandard insulation areas to be reconstructed or changed;
- to form data base about enclosure structure elements inconsistent with standard and requirements.

So, this method is actual as before and its improvement leads to enhance of the objects investigation productivity. Infrared thermography is widely used for buildings inspection [for ex., 2, 3]. The main goal of such researches is to estimate energy efficiency and reliability of building`s wall on the basis of qualitative thermograms analysis or quantitative evaluation of heat fluxes and heat resistance of multilayer wall. The experiment can take several days for results certainty.

For different objects diagnostics thermal testing is used in two ways: passive and active [4–6]. “Activity” of the method implies that the wall surface under investigation is undergone to additional thermal influence in order to create temperature gradient between internal and external surfaces of the wall. Intensification of heat flux through the wall permits to estimate easier its heat-saving properties by infrared thermography. In summer when air temperature inside building is close to ambient one energy efficiency estimation of enclosure structure is almost impossible by passive method. The reason is negligibly small value of heat flux through the structure. However, necessity of such estimation exists because it should be concluded about energy efficiency of new or renovated building before its exploitation begins. For temperature gradient creation either heating or cooling can be used. Both of ways are equal from in the context of physics. Heating is chosen traditionally because of variety of equipment (flash and halogen lamps, radiant and fan heaters). However this equipment is often appropriate in laboratory conditions only and, what is more important, temperature rise due to heating can be not safe in some cases.

We suggest new approach of thermal insulation quality estimation by one measuring of surface thermal field and comparison of the experimental results with calculated ones. Furthermore we develop a cooling technique for temperature gradient creation in summer that is more applicable due to its size, safety and independence on power supply.

## 2. METHODOLOGY

An equipment for temperature gradient creation suggested to carry out active thermal nondestructive testing contains 1) cooling camera which is located in front of inside surface of the object under control without direct contact and 2) thermographic system which allows to measure external surface temperature in the area of cooling. Cooling component consists of tank with cooling agent such as liquid nitrogen or manufactured thermal-electric refrigerator. This component should be made with possibility to maintain temperature regime in definite level during thermografic surveying. Internal wall surface temerature is registered by contact sensors. The equipment suggested is different from other ones used in the same purposes [7–9] for the first by ability to be used in real conditions. In winter period carriage of ATNDT is lighten by heating systems operation which serve as source of heat energy to cause temperature difference between wall surfaces.

Before thermographic surveying it is necessary to analyse the controlled object technical documentation (construction drawings and plans of building facade and enclosure structure components with referencing to geometrical parameters), to detect location of “cold bridges”, heating systems, stacks which influence on temperature distribution through the wall surface. Thermographic investigation is carried out after steady-state heat transfer has settled. One can regard the recurrence of external surface temperature measurements results within measuring device error as indicator of transient process completion. Analysis of the results includes thermograms interpretation (temperature evaluation in several points, plotting of isothermal lines and thermal profiles along chosen line and so on) and reference to external surface images in visible spectrum. Areas of temperature non-uniformity on thermograms can point to constructive peculiarities of the object under investigation, discontinuity of surface emissivity, nonuniformity of heat exchange with ambient due to different internal and external defects of the structure. Such defects as insufficient thermal insulation of panels' junctions are easily detected by thermal vision scanning. Nevertheless, the panels themselves, which have multilayer structure can be characterized by uniform temperature distribution. It leads to the conclusion about absence of any structure defects, however, in some cases, this conclusion may be false. For example, when thermal insulation conditions are not kept up all over wall panel surface (because of insufficient thickness of thermal insulation layer, changing of standard insulation materials to less qualitative ones etc.) energy efficiency of enclosure structure is lower than it should be even if wall temperature distribution visible on thermogram is uniform. Therefore, we consider ATNDT not only as experimental surveying of thermal state of enclosure structure but as complex investigation, which includes computer modelling of temperature distribution in the object under study. For temperature field calculation in multilayer structure the program module for modelling of two-dimensional thermal fields by finite elements method is used. In a case of interest, when temperature distribution on wall surface is uniform but real heat resistance of the structure may differ from required one the model become one-dimensional. External surface temperature is calculated at predetermined wall temperature inside of building and preset thermal and technical parameters of structure according to documentation. Conclusion about energy efficiency of enclosure structure is formed on the basis of calculated and experimental data on temperature of wall panel external surface. In coincidence of the values within 15% one can conclude about correspondence of insulation thermal parameters to standard values for controlled enclosure structure [10]. If coincidence is out of this limit then it can evidence to nonstandard value of moisture in thermal insulation layer of the structure (in this case it is necessary to carry out additional measurements of moisture content in insulation) or to disagreement between thermal conductivity of used insulation material and its standard value.

## 3. THE RESULTS

The method of active thermal nondestructive testing was used for examination of apartment building in Rechitsa (Belarus). Exposed walls are made of assembled three-layer panels with thickness of 300 mm (external layer has thickness 60 mm, insulation layer – 140 mm, internal layer – 100 mm). Expanded polystyrene with discrete expanded-clay concrete junctions is used as a thermal insulation material. Wall panels have textured external surface with decorative marble chips (thickness is 20 mm). Sealing of junctions is made of special two-component paste. The building was investigated in winter period so radiators served as a source of heating. Thermographic surveying was carried out with thermal camera FLIR P25 (measurements accuracy is 2%, temperature sensitivity is 0.08 $^{o}$C) in conditions of high cloudiness at ambient temperature of -2 $^{o}$C.

The results of thermal investigation of the building as well as images in visible spectrum are shown in the Figure 1.

From the results of thermographic survey of enclosure structure we can detect elevated temperature of panels' junctions all over perimeter of the building and in the places of window units connection with wall panels in some parts of the building. Measured temperature of junctions exceeds panels' temperature by 3–4 $^{o}$C; and in most cases junctions have positive temperature value at negative ambient temperature value and internal air temperature no more than 16 $^{o}$C. In some places junction temperature has been more than

+ 4.3 °C. The reason of existence defects in panel junctions is absence of thermal insulation of connections or low heat-saving properties of materials used in junctions. It can be checked after junction uncovering.

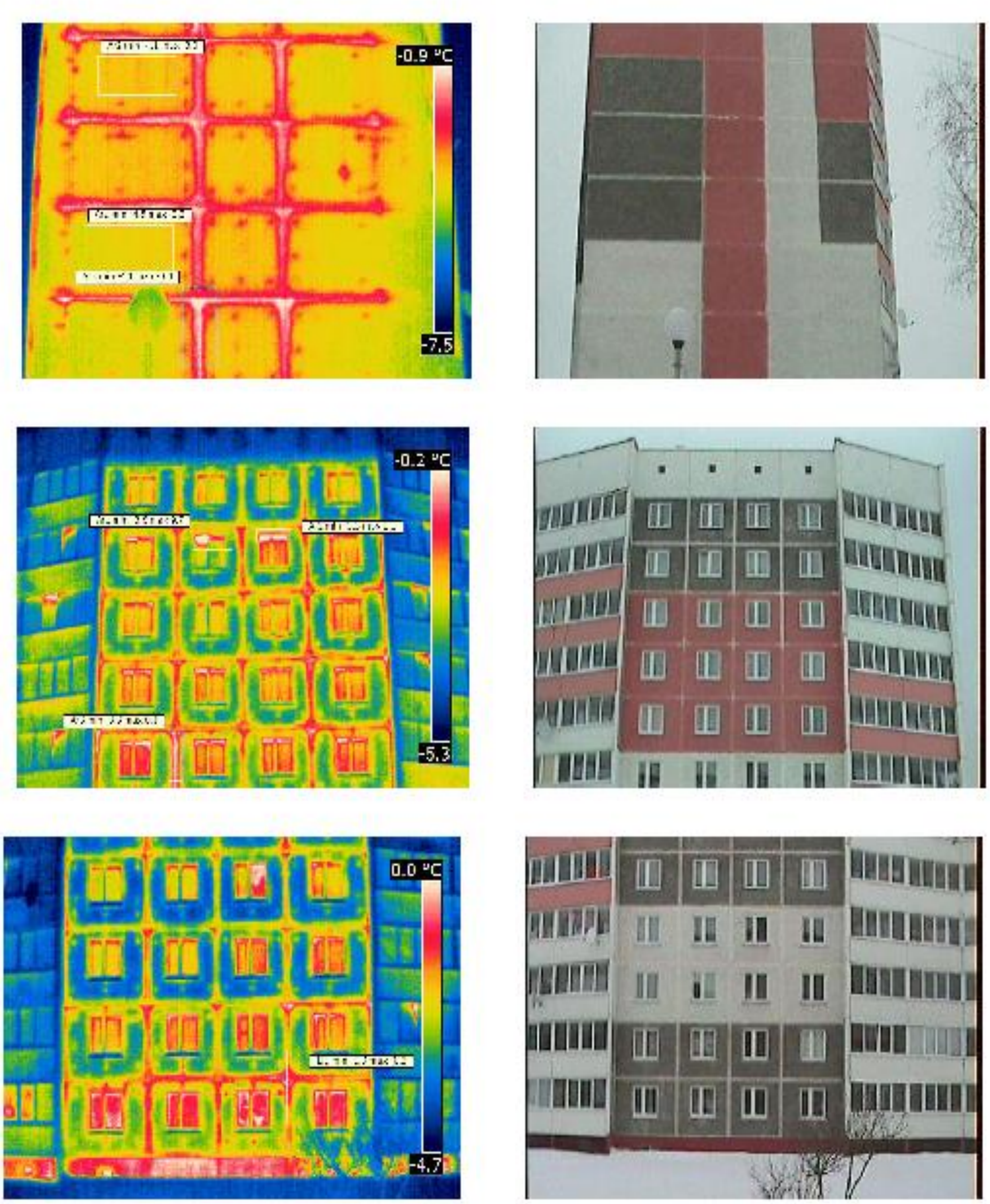

Fig. 1. Images of the building walls in infrared (thermograms) and visible spectrum (Rechitsa, Belarus)

The structure of building panel under investigation and the results of computer modelling of heat transfer through the structure are shown in the Fig. 2 and Fig. 3 correspondingly. Fig. 3 shows that calculated wall temperature corresponds to measured one so it indicates that thermal insulation is quite qualitative and there are no any defects.

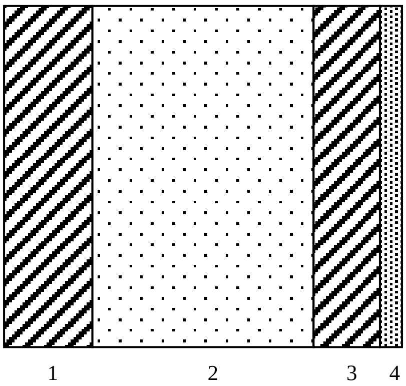

Fig. 2. Structure of building`s multilayer wall:
1, 3 – concrete (100 and 60 mm), thermal conductivity λ = 1.5 W/m·°C;
2 – thermal insulation – expanded polystyrene (140 mm), λ = 0.037 W/m·°C;
4 – stucco (20 mm), λ = 0.93 W/m·°C

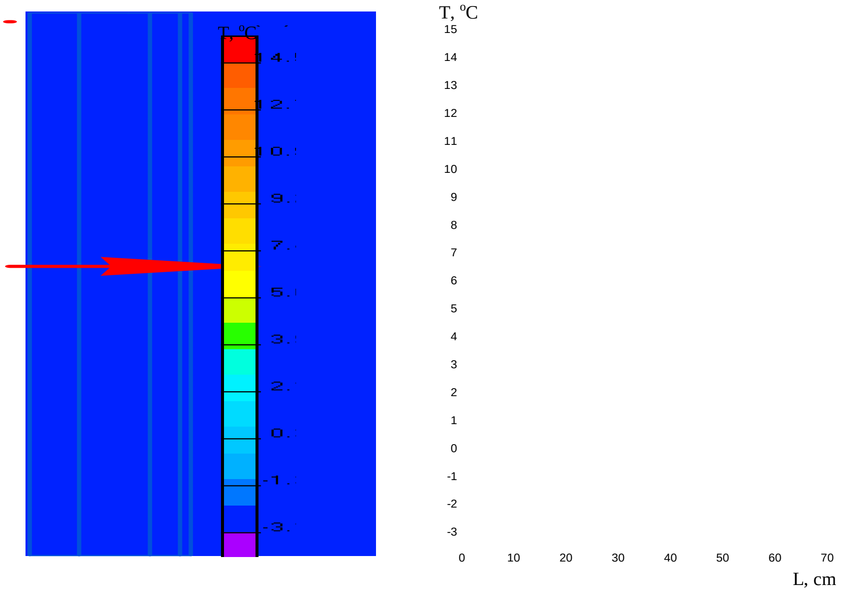

Fig. 3. Computer modelling of temperature distribution in building wall

As an equipment for wall cooling in real conditions is under construction yet, we tested applicabilty of the method in laboratory conditions. Gaseous-silica block with following geometrical parameters was investigated: length is 29 cm, width is 22 cm, height is 12 cm. Three contact thermal sensors were used for temperature measuring on top, underneath and inside of the block. The block was cooled from the underneath by liquid nitrogen placed into tank of 13 cm in diameter. Ambient and initial block surface temperature was 27 $^{o}$C. Temperature field of top surface was registered by infrared camera (Fig. 4). Steady-state regime was riched in one and a half hour. Underneath temperature reduced up to -11.3 $^{o}$C while top temperature became equal to 24 $^{o}$C. Temperature inside of block was -1.5 $^{o}$C. Thus, temperature difference between top and underneath reached the value of 35 $^{o}$C.

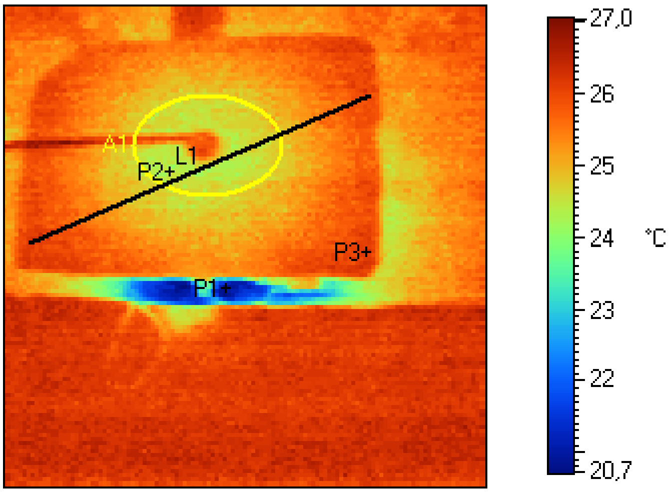

Fig. 4. Temperature field of gaseous-silica block under cooling

The experiment shows applicability of cooling for temperature gradient creation for further estimation of insulation properties of the object.

## 4. CONCLUSIONS

In this paper the method of active thermal nondestructive testing is presented. It implies the following stages of buildings thermal control:

- study of technical documentation of the object under investigation (in particular concerning enclosure structures);
- forming of additional temperature difference in wall panel section;
- survey of external wall surface in infrared and visible spectrum;
- thermograms interpretation;
- computer modelling of temperature distribution in multilayer enclosure structure;
- conclusion about thermal state of the object under investigation or motivation of further additional investigation (for example estimation of moisture).

The main advantages of suggested approach are in one measuring of temperature field (that is required only several hours instead of days) and the way of temperature gradient creation by cooling (that is safe, power independent and benefit in context of equipment size). This diagnostic approach can be used in real conditions and allows detecting of thermal insulation defects not only in junctions but also in the wall panels themselves.

## REFERENCES

1. MALYAVINA, E.G. *Heat losses in building*. Moscow: AVOK-PRESS, 2007. (in Russian).
2. IBOS, L., LARBI YOUCEF, M., MAZIOUD, A., DATCU, S., CANDAU, Y. Nondestructive testing of building walls using active infrared thermography. *8th Int.Conf. on Quantitative InfraRed Thermography*, 2006.
3. MAIERHOFER, Ch., ROELLIG, M. Active thermography for the characterization of surfaces and interfaces of historic masonry structures.Int. Conf. Non-Destructive Testing in Civil Engineering, NDTCE’09.
4. MALDAGUA, X. *Theory and Practice of Infrared Technology for Nondestructive Testing*. Wiley-InterScience, 2001.

5. HAIN, M., BARTL, J., JACKO, V. The use of infrared radiation in measurement and non-destructive testing. *Measurement Science Review*, 2005, Vol. 5, Sec. 3, p. 10–14.
6. AVDELIDIS, N. P., MOROPOULOU, A., ALMOND, D. P. Passive and active thermal nondestructive imaging of materials. *Proc. SPIE*, 2004, Vol. 5612, p. 126–140.
7. Patent US 6000844, 1999. *Method and apparatus for the portable identification of material thickness and defects using spatially controlled heat application*.
8. Patent RU 2086970, 1997. *The equipment for thermal technical testing of enclosure structures of buildings*. (in Russian).
9. Patent RU 2262686, 2005. *The method of thermal nondestructive testing*. (in Russian).
10. Standard 26629-85. *Buildings and constructions. Method of thermal vision control of thermal insulation quality of enclosure structures*. (in Russian).

CYSENI 2011, May 26–27, Kaunas, Lithuania
ISSN 1822-7554, www.cyseni.com

# EFFECT OF FAÇADE INSULATION ON HEATING ENERGY CONSUMPTION, INDOOR AIR QUALITY AND THERMAL COMFORT: CASE STUDY IN SELECTED LATVIAN DAYCARE CENTERS

**G. Stankeviča, A. Lešinskis**
*Department of heat and gas technology*
*Riga Technical University*
*Azenes str. 16, LV-1010 – Latvia*
*Phone +371 28324732*
*Email: galina.stankevica@rtu.lv*

## ABSTRACT

Nowadays the building sector accounts for about 40% of final energy consumption in European countries, contributing greatly to global warming and climate change. Since most of energy in eastern European buildings is used for heating, thermal insulation of building envelope has recently become one of the most commonly implemented energy efficiency measures. However, energy improvement should not compromise health and comfort of building occupants, especially in daycare environments, where children can spend up to 12 hours daily. This study aims to investigate the effect of façade insulation and tightness on heating energy consumption, indoor air quality and thermal comfort in daycare buildings in moderate climate zone of Latvia. Measurements of carbon dioxide, air temperature and relative humidity were carried out in six daycare centers (old, renovated and new-built), and data regarding heating energy consumption as well as daycare center characteristics and maintenance activities was collected via combination of field visits, record analysis and interviews. This field study showed that different types of building construction as well as ventilation strategies employed by daycare centers can cause significant variations in indoor air quality and comfort. It was found that in all facilities temperature and relative humidity was kept in comfort range. Carbon dioxide concentrations exceeded 1000 ppm in 75% of daycare centers studied, with the highest (1356 ppm) measured in a renovated facility with the natural ventilation system. Thus additional insulation of external walls should be accompanied with installation of more efficient ventilation system (mechanical) to account for air tightness.

Key words: Daycare center; heating energy consumption; indoor air quality; thermal comfort; thermal insulation

## 1 INTRODUCTION

Nowadays the building sector in member states of European Union accounts for about 40% of final energy demand and about a third of greenhouse gas emissions, of which about two-thirds are ascribed to residential and one-third to commercial buildings [1]. Since most of energy in eastern European buildings is used for space heating, e.g. about 70% in Latvian households [2], thermal insulation of building envelope has recently become one of the most commonly implemented energy efficiency measures. Since information about typical heating energy usage in European daycare centers is rather limited, this paper presents data for comparison in European school buildings. The mean annual specific heat consumption was reported to be 192 kWh/m$^2$ in Slovenian schools [3] and 157 kWh/m$^2$ in United Kingdom [4]. The Greek study [5] indicated that daycare centers use about 15% more heating energy compared to schools, i.e. by average 119 kWh/m$^2$ and 136 kWh/m$^2$ for schools and daycare centers, respectively.

About 75% of all children under the age of 7 living in Latvian capital Riga spend about 30–60 hours per week in daycare centers. However, research studies indicate that daycare facilities due to the improper indoor air quality (IAQ) may actually be hazardous to children's health. [6, 7] have reported increased risks of asthma and allergies for children spending their time in daycare environments compared to the care obtained at home. Therefore for the last few decades an increased attention has been directed towards creation of appropriate indoor environments in daycare centers.

Carbon dioxide ($CO_2$) is one of the most commonly used indicators of IAQ in spaces, where people are the main pollution source, and it also serves as the determiner for adequate ventilation. $CO_2$ itself is normally not harmful, however its excessive exposure is found to cause headaches, fatigue, increases risk of sick leave [8, 9], and even risks for sudden infant death [10]. The maximum recommended $CO_2$ concentration in a space is 800 ppm (parts per million) above the outdoor according to European standard [11]. The upper limit for $CO_2$ concentration in ASHRAE standard [12] should not exceed 2500 ppm, while 1000 ppm is the recommended value.

Majority of indoor climate studies in daycare environments were conducted in Nordic countries. Mean $CO_2$ levels reported in Scandinavian countries were as follows: 810 ppm in Finnish daycare centers [13], about 1400 ppm in Denmark [14], and as low as 640 ppm in Sweden [15]. [16] investigated IAQ in two Latvian daycare centers and reported the maximum $CO_2$ concentration as high as 1700 and 1450 ppm in rooms with PVC and wooden frame windows respectively.

While $CO_2$ describes IAQ, temperature and relative humidity are usually used to determine thermal comfort level in indoor environments. According to Latvian building norms [17] the minimum acceptable air temperature in daycare centers is at least 20.0°C or 18.0°C for children younger and older than 3 years respectively. ASHRAE standard [12] recommends keeping temperature in the range of 23-26°C and relative humidity between 30 and 60%.

Majority of Latvian daycare centers were constructed in accordance to old Soviet building codes which stated that ventilation should be achieved by natural means, i.e. fresh air supplied through window construction and exhausted through the vents (stack effect). It was presumed that such solution would result in sufficient air exchange. Lately majority of daycare centers in Riga were reconstructed: external walls insulated and wooden frame windows were changed to PVC (polyvinyl chloride) ones. However, these actions alone possess great risk of IAQ problems, since buildings became more airtight leading to insufficient air exchange indoors.

Since very limited data is available regarding indoor air quality in Latvian daycare centers, and being concerned about IAQ children are exposed to in the present construction buildings, the author of this study evaluated the current IAQ and thermal comfort status in six daycare centers in Riga Region. Increased attention has been directed towards renovated buildings in which the facades were additionally insulated.

# 2 MATERIALS AND METHODS

## 2.1 Daycare center selection

Six daycare centers (4%) from a total of 153 were randomly selected from the Education, Youth and Sports Department database of the Riga Council. Facilities differ in the type of construction, i.e. whether the building is old, renovated or new-built (two buildings per each category). All daycare centers were inspected and details of their characteristics were noted, including type of heating and ventilation system, occupant density, building materials etc. In addition, the daycare center personnel were inquired about frequency of window opening, cleaning routines and day regime at their facilities.

## 2.2 Field measurements

$CO_2$ concentration, temperature and relative humidity are convenient and reliable indicators of indoor air quality and comfort level. Measurements of these parameters were carried out simultaneously during the period of one week in October 2010 at all daycare facilities, with the exception of $CO_2$ concentration that was measured only in renovated and new-built daycare centers. Indoor sampling locations were determined prior the measurements through a walkthrough assessment. Since placement of measuring devices close to the breathing zone of children, i.e. at the height of 0.5–0.7 m, was restricted, indoor samplings were performed at the height of 1.5-1.8 m close to the internal perimeter wall. All measurements were conducted continuously from 7 am on Monday to 5 pm on Friday at 5 min intervals.

Indoor air temperature and humidity data was collected by HOBO U12 Family data loggers with the following parameters: temperature -20°C to 70°C (±0.35°C) and relative humidity 10% to 90% with the accuracy (±2.5%). The HOBO loggers were interfaced with $CO_2$ monitors Telaire 7001 measuring in the range of 0 to 10000 ppm (±50 ppm). In addition to HOBO loggers, Testo 175-H2 measuring devices were used, having following parameters: measurement range -20°C to 70°C with resolution 0.1°C, and relative humidity 0 to 100% with resolution of 0.1%.

Since only two measurement sets of HOBO and Telaire were available it was decided to measure simultaneously in one renovated and new built daycare center couple for the first three days and during the last two days at the second couple of renovated and new-built facilities.

Daycare centers in this paper are designated by their type, i.e. new-built, renovated or old, and corresponding number. Three daycare centers (New 2, Renovated 1, Old 2) have a single room for nap and playing; in other daycare centers nap activity and playing is carried out in separate spaces. In the latter case sampling was performed in playing room, where children consequently spend more time.

## 2.3 Data analysis

The measured IAQ and thermal environment parameters among three categories of daycare centers were compared. The means and ± standard deviation (SD) of $CO_2$, room temperature and relative humidity levels were calculated.

The heating energy consumption data, collected from Riga Council [18], was available only for old and renovated daycare centers for the year 2008. This data was further compared between old and renovated building categories based on the average values.

# 3 RESULTS AND DISCUSSION

## 3.1 Daycare center characteristics

The basic data of daycare centers and selected spaces investigated are given in Table 1.

Table 1. Daycare center details

| **Daycare center** | **Area [m$^2$]** | **Ventilation system [-]** | **Heating system [-]** | **Age of children [years]*** | **Floor area per person [m$^2$/pers]*** |
|---|---|---|---|---|---|
| Old 1 | 742 | Natural | Radiators | 6 | 3.2 |
| Old 2 | 1078 | Natural | Radiators | 3–5 | 3.2 |
| Ren. 1 | 2152 | Mechanical | Radiators | 4 | 3.3 |
| Ren. 2 | 2112 | Natural | Radiators | 4–5 | 3.3 |
| New 1 | 3472 | Mechanical | Underfloor | 3 | 5.7 |
| New 2 | 2024 | Mechanical | Underfloor | 4–5 | 3.8 |

* In the measured space

The number of children in one group ranged from 15 to 22 children. The age of children in rooms investigated varied within 3–6 years. The typical daytime regime in daycare centers was as follows: from 7 am to 10:30 am indoor activities in a playing room, 10:30 to 12 am promenade, 12:30 to 15:00 nap-time, and the rest of time is spent indoors.

All daycare facilities have double glazed windows in PVC frames. The maintenance personnel in all daycare centers still relies on natural ventilation for achieving acceptable indoor air quality, and opens the windows every time children are outside.

## 3.2 Heating energy consumption

The specific heating energy consumption in old and renovated daycare centers during the year 2008 is showed in Fig. 1.

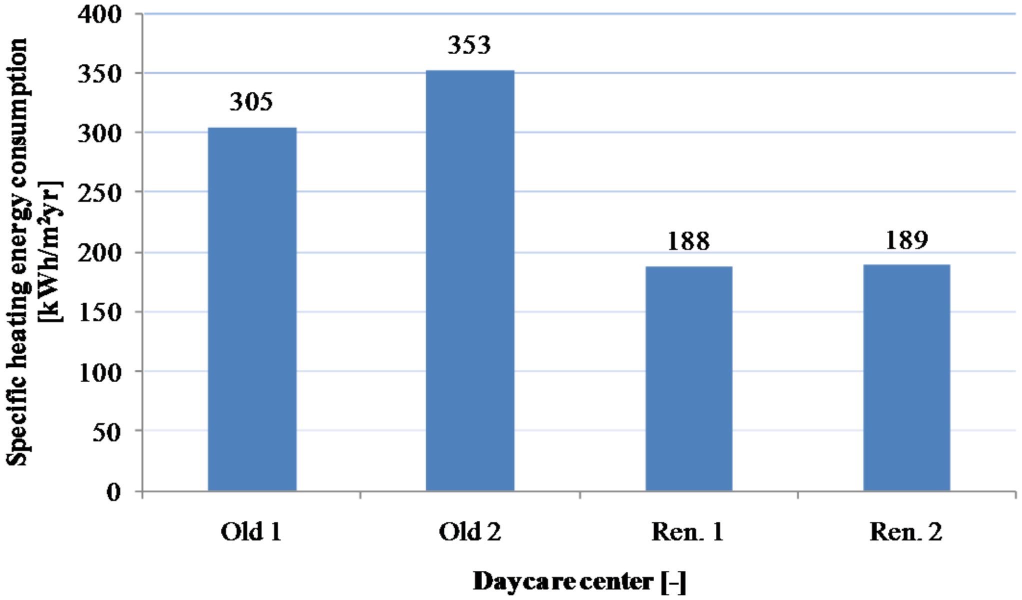

Fig. 1. Specific heating energy consumption in 2008 [18]

The mean heating energy consumption is 329 kWh/m$^2$ and 189 kWh/m$^2$ in old and renovated buildings, respectively. The investigated four (old and renovated) daycare centers were initially constructed pursuant to old Soviet building codes. The external walls consisted of 1.5 leaves of 250 mm brick masonry, and rendering. Such construction had no thermal insulation layer, resulting in a heat transfer coefficient (U-value) of about 0.65 W/m$^2$K. According to Latvian building code LBN 002-01 [19] the normative U-value for daycare centers is 0.3 W/m$^2$K (with external wall mass exceeding 100 kg/m$^2$). Reduction in U-value from 0.65 to 0.3 W/m$^2$K by means of additional thermal insulation of facades, lowered the heating energy consumption on average by 40%. However, resulting mean heating energy consumption is still higher compared to daycare centers in other European countries.

## 3.3 Carbon dioxide

In this study the average indoor $CO_2$ concentration during daytime for all daycare facilities was 730±170 ppm (Table 2).

Table 2. Summary statistics of measured carbon dioxide concentration expressed in parts per million (ppm)

| **Daycare c.** | **Mean (95% CI)** | **Median** | **Min** | **Max** |
|---|---|---|---|---|
| New 1 | 707 (603-811) | 732 | 450 | 1123 |
| New 2 | 609 (470-748) | 601 | 421 | 945 |
| Ren. 1 | 743 (604-882) | 775 | 462 | 1140 |
| Ren. 2 | 864 (651-1077) | 843 | 500 | 1356 |
| Overall | 731 (561-901) | 734 | 421 | 1356 |

In majority of daycare centers (75%) $CO_2$ levels exceeded the ASHRAE recommended value of 1000 ppm. However, this increase was not substantial and maximum values measured were halved ASHRAE's tolerance maximum of 2500 ppm. It was also observed that in multipurpose rooms (for general activities and nap), the nap-time average $CO_2$ level was about 60 ppm higher compared to the non-nap time average $CO_2$ level. This can be explained with the fact, that children were placed in a closed space without adequate air exchange. Even though in the present study $CO_2$ concentration was not measured in sleeping-only rooms, the study conducted in US daycare centers [20] showed 24.3% $CO_2$ increment from non-nap time to nap-time in this type of rooms. Thus it can be expected that Latvian daycare centers might follow the similar tendency, but this should be confirmed by further experiments in sleeping-only rooms.

The highest $CO_2$ concentration was obtained in Renovated 2 daycare center, which has a natural ventilation system as opposed to the other three daycare centers with mechanical ventilation system installed. Even though opening of windows does lower the $CO_2$ concentration, it is still not enough to achieve optimal level since low outdoor air temperature limits the ventilation period. Thus better indoor air quality is achieved in mechanically ventilated spaces with constant supply of fresh air.

## 3.4 Temperature

Outdoor air parameters for October 26, which was a typical mid-week, cold day, are presented in Fig. 2.

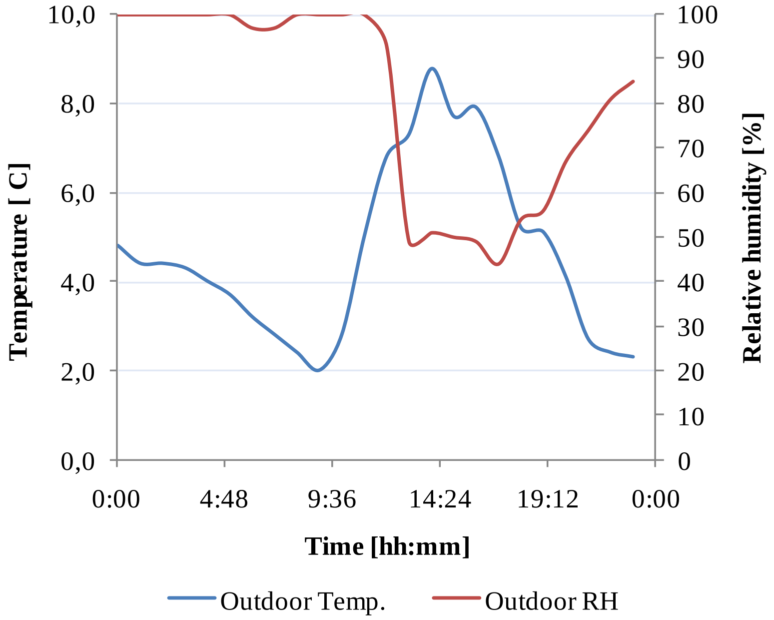

Fig. 2. Atmospheric conditions on 26th October.

Outdoor air temperature varied from 2.0°C to 8.8°C and relative humidity was in a range of 44% to 100%.

The variation of daytime room temperature across daycare centers on 26th October is shown in Fig. 3.

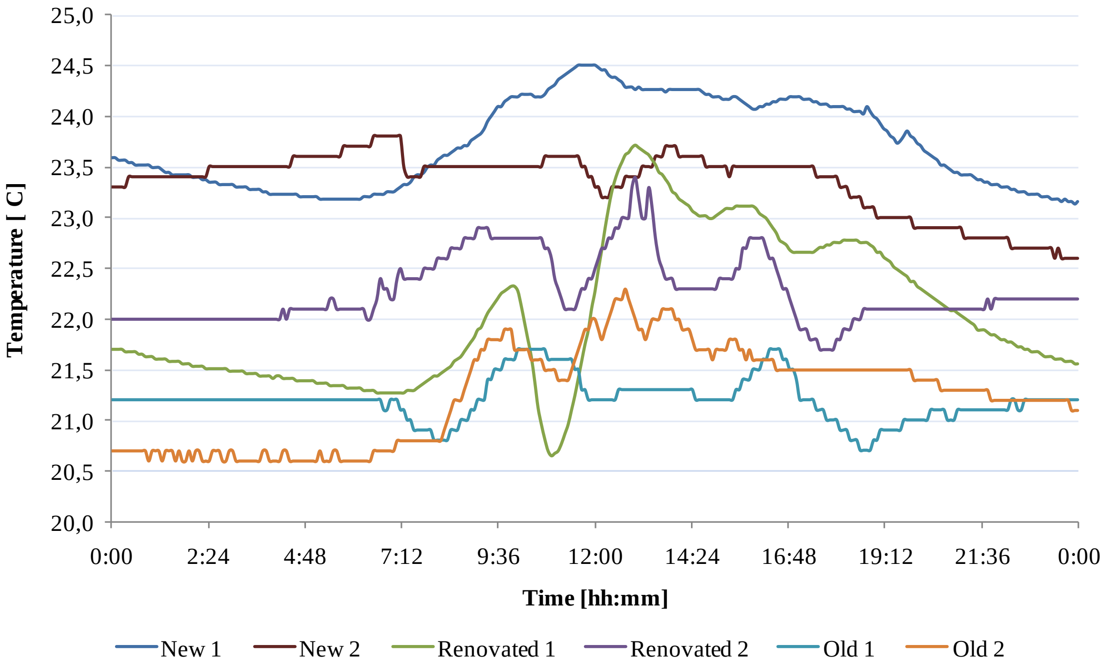

Fig. 3. Temperature variation in six daycare centers on 26th October

The average room temperature in all six daycare centers during the daytime was 22.5±1.1°C. In all facilities the temperature was kept above 20°C, which is the minimum acceptable stipulated by Latvian building norms [17] for children under the age of three. 67% of daycare facilities were outside the ASHRAE recommended comfort range of 23–26°C, having temperatures lower than 23°C.

Temperatures were highest in the new-built daycare centers, that both have underfloor heating system and mechanical ventilation system that explains also not very large temperature fluctuations, i.e. 24.1±0.3°C and 23.5±0.1°C for New 1 and New 2 daycare center, respectively. The greatest temperature fluctuations occurred in the renovated facilities, especially in Renovated 1 (σ = 0.8°C), where temperature ranged from 20.7°C to 23.7°C. Temperature drops are result of extensive airing by opening the windows and consequent creation of draught. However, indoor temperature does not drop rapidly due to the relatively short time of windows being opened.

In all of the facilities there is potential for saving energy by using the night-time temperature setback of up to 3°C.

## 3.5 Relative humidity

The variation in relative humidity across six daycare centers is shown in Fig. 4

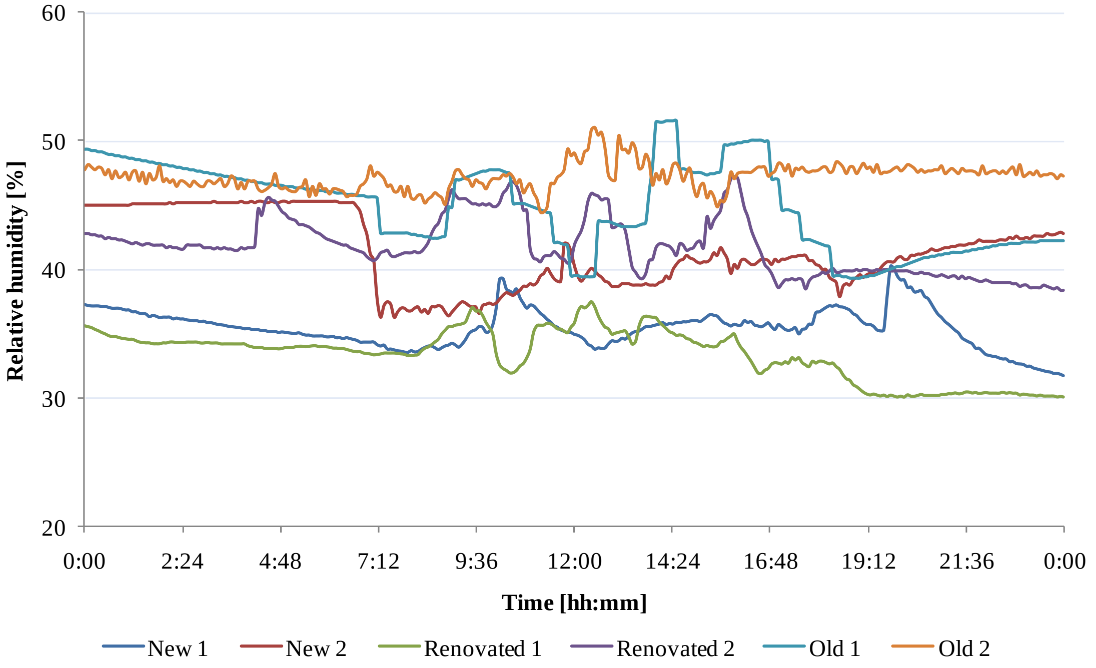

Fig. 4. Relative humidity variation on 26th October.

The average relative humidity of six daycare centers was 40±5% and did not vary to a great extent during the day. All of the facilities had relative humidity in a range of 30 to 60% that is recommended by ASHRAE standard [12]. The relative humidity slightly decreased every time windows were opened. The largest decrement was observed in the first half of the working day. This also corresponds to the rapid outdoor humidity decrease by almost 50% after 12 pm (Fig. 2).

Relatively low humidity levels in the spaces also correspond to no visible signs of any moisture damage or mould growth on indoor surfaces that were examined during the building visits.

## 4 CONCLUSIONS

This study investigates the effect of façade insulation on heating energy consumption, indoor air quality and thermal comfort in selected Latvian daycare centers.

Additional thermal insulation of external walls and replacement of wooden frame windows to PVC ones, reduced heating energy consumption by about 40%, resulting in annual mean specific heat consumption of 189 kWh/m$^2$. However, it is still higher than average consumption in other European countries and thus further energy efficiency improvement measures are recommended to be taken. In addition, in all of the facilities there is potential for saving energy by using the night-time temperature setback of up to 3°C.

The $CO_2$ concentrations exceeded 1000 ppm in 75% of daycare centers studied, with the highest (1356 ppm) measured in Renovated 2 daycare facility with the natural ventilation system. Thus additional insulation of external walls should be accompanied with installation of more efficient ventilation system (mechanical) to account for air tightness. The indoor temperatures in renovated facilities were higher compared to old daycare centers. In all facilities the temperature was kept above 20°C and the average relative humidity was 40 ± 5%, creating comfortable thermal environment for children. The greatest temperature fluctuations were observed in renovated daycare centers and this is another indicator that daycare center personnel still rely entirely on natural ventilation for proper indoor air quality. Therefore Riga Municipality must take actions to educate personnel, and carry out regular inspection and maintenance of ventilation system to ensure its proper operation.

## REFERENCES

1. EC Green-Paper - Towards a European Strategy for the Security of Energy Supply, Commission of the European Communities, 2000- [referred on the 25th of February in 2011 y.]. <http://aei.pitt.edu/1184/1/enegy_supply_security_gp_COM_2000_769.pdf>
2. KLAVS, G., KUDRENICKIS, I. Energy efficiency policies and measures in Latvia. Institute of Physical Energetics, 2009- [referred on the 25th of February in 2011 y.]. <http://www.odyssee-indicators.org/publications/PDF/latvia_nr.pdf>
3. BUTALA, V., NOVAC, P. Energy consumption and potential energy savings in old school buildings. *Energy and Buildings*, 1999, Vol. 29, No. 3, p. 241–246.
4. Good Practice Guide, GPG343, Saving Energy – A Whole School Approach, The Carbon Trust, 2005- [referred on the 25th of February in 2011 y.]. <http://www.fifedirect.org.uk/uploadfiles/publications/c64_GPG343SavingEnergy-AWholeSchoolApproach2.pdf>
5. THEODOSIOU, T.G., ORDOUMPOZANIS, K.T. Energy, comfort and indoor air quality in nursery and elementary school buildings in the cold climatic zone of Greece. *Energy and Buildings*, 2008, Vol. 40, No. 12, p. 2207–2214.
6. HAGERHED-ENGMAN, L., BORNEHAG, C.G., SUNDELL, J., ABERG, N. Day-care attendance and increased risk for respiratory and allergic symptoms in pre-school age. *Allergy*, 2006, Vol. 61, No. 4, p. 447-453.
7. HABY, M.M., MARKS, G.B., PEAT, J.K., LEEDER, S.R. Daycare attendance before the age of two protects against atopy in preschool age children. *Pediatric Pulmonology*, 2000, Vol. 30, No. 5, p. 377–384.
8. ERDMANN, C.A., STEINER, K.C., APTE, M.G. Indoor carbon dioxide concentrations and SBS symptoms in office buildings revisited analyses of the 100 building BASE study dataset. Indoor Air 2002. Proceedings of 9th International Conference on Indoor Air Quality and Climate. Monterey, CA: 2002 June 30–July 5.
9. MILTON, D.K., GLENCROSS, P.M., WALTERS, M.D. Risk of sick leave associated with outdoor ventilation level, humidification, and building-related complaints. *Indoor Air*, 2000, No. 10, p. 212–221.

10. CORBYN, J.A. Sudden infant death due to carbon dioxide and other pollutant accumulation at the face of a sleeping baby. *Medical hypothesis*, 1993, Vol. 41, No. 6, p. 483-494.
11. European Standard EN 13779. Ventilation for non-residential buildings - Performance requirements for ventilation and room-conditioning systems. European Committee for Standardization, Brussels, 2005.
12. ASHRAE Standard 62.1. Ventilation for acceptable indoor air quality. American Society of Heating, Refrigerating and Air Conditioning Engineers, Atlanta, 2004.
13. RUOTSALAINEN, R., JAAKKOLA, J.J. Ventilation and indoor air quality in Finnish daycare centers. *Environment International*, 1993, Vol. 19, No. 2, p. 109–119.
14. PEJTERSEN, J., CLAUSEN, G., SORENSEN, D., QUISTGAARD, D., IWASHITA, G., ZHANG, Y., FANGER, P.O. Air pollution sources in kindergartens. Healthy Buildings 1991. Proceedings of IAQ 1991. Washington DC, Atlanta: 1991 September 4–8.
15. CARS, H., PETERSSON, C., HAKANSSON, A. Infectious diseases and day-care center environment. *Scandinavian Journal of Infectious Diseases*, 1992, Vol. 24, No. 4, p. 525–528.
16. BORODINECS, A., BUDJKO, Z. Indoor air quality in nursery schools in Latvia. Healthy Buildings 2009. Proceedings of Healthy Buildings 2009, Syracuse, NY: 2009 September 13–17.
17. Ministru kabineta noteikumi Nr.596. Higiēnas prasības izglītības iestādēm, kas īsteno pirmsskolas izglītības programmas. Latvijas Vēstnesis, Rīga, 2002.
18. KRUMINS, E. Heating energy consumption in Latvian daycare centers. Riga Council, 2010.
19. Latvijas būvnormatīvs LBN 002-01. Ēku norobežojošo konstrukciju siltumtehnika. Latvijas Vēstnesis, Rīga, 2001.
20. FERNG, S.F., LEE, L.W. Indoor air quality assessment of daycare facilities with carbon dioxide, temperature, and humidity as indicators. *Journal of Environmental Health*, 2002, Vol. 65, p. 14–18.

CYSENI 2011, May 26–27, Kaunas, Lithuania
ISSN 1822-7554, www.cyseni.com

# LINEARIZATION OF PHOTOELECTRIC CELL TRANSFER FUNCTION

**V.V. Lypnytskyy**
*Tallinn University of Technology*
*Ehitajate tee 5, 19086 Tallinn – Estonia*
*Phone +372 53764860*
*Email: Lipkav@ukr.net*

**T.V. Kushnir, Y.V. Lypnytskyy**
*Ternopil Ivan Pul'uy National Technical University*
*Slivenska st. 3/81, 46011 Ternopil – Ukraine*

ABSTRACT

The article is devoted to improving measurement accuracy of luminosity, resolution of the sensors, linearization indications of optical converters, clarifying the conditions for an unambiguous impression device for measuring the luminous flux at different measurement ranges. The device, which is designed by the new scheme, is related to the field of metrology. It can be used for objective measurement and control of natural and artificial lighting and to identify the needs of electricity for artificial lighting. The main purpose of our work is to eliminate shortcomings of the known illuminometer. The reason for the analysis is the current need of energy saving.

Our goal is to improve the accuracy of measurements and operational reliability, to obtain the same performance at different limits, to improve the work of the measuring photocell. Solution of relevant scientific and technical problems occurring will help to eliminate shortcomings of the known illuminometer, to develop a principally new scheme of the device for measuring the flux, which would increase resolution and accuracy of their measurements.

According to the above, the proposed scheme enables us to solve a number of important tasks. The illuminometer has a linear scale, high precision and operational reliability, clarity indications of the device at different limits of measurements. Analysis of the proposed mathematical model of the device for measuring the flux allows an increase in the accuracy of measurements and linearity of indications.

Keywords: photo-electromotive force; photocell; current-meter; short-circuit current; lux-ampere characteristic.

Abbreviations: G – galvanometer, mA – milliammeter, SC – short circuit, PV – photoelectrical cell, LM – illuminometer, lx – lux, CNL – coefficient of natural lighting, EMF - electromotive force, LAC – lux-ampere characteristics.

## INTRODUCTION

Depending on the source of the light, industrial lighting can be: natural created by direct sunlight and diffuse horizon light; artificially created by electric light sources; combined from insufficient natural light supplemented by artificial one.

There are three types of natural lighting: lateral (side one) (single or bilateral) that is coming in through lighting gaps in outside walls; top one that is coming in through electric torches and gaps in the roof and ceiling; combined that is a combination of top and side lighting.

Artificial lighting can be general and combined. General lighting is the lighting where lamps are placed in the upper area of space (not less than 2.5 m above the floor) evenly (general evenly lighting), or with regard to the location of work seats (localized general lighting).

Combined lightning can be main and local. Main combined lighting is used for works with high accuracy, or to create specific or changeable direction of light during the work. Local lighting is created by the lighting appliances. They concentrate the lighting flux on the working place. We cannot use only the local lighting because of high danger of industrial injuries and occupational diseases.

For functional purposes, artificial lighting is divided into operating, emergency, evacuation, security, and regular lighting.

Operating lighting is used for the production process, displacing people and traffic. It is required for all production facilities.

Emergency lighting is used to continue the work when sudden disconnection of operating lighting and related different violations of normal maintenance equipment with it, can cause explosions, fires, poisoning people and the violation process. With emergency lighting the minimum illumination of working surfaces must be 5% of the normalized light of working one, but not less than 2 lx.

Evacuation lighting is appointed to ensure evacuation in the case of an emergency disconnection of working lighting. It must be located in places dangerous for passage of people; in dwellings of satellite buildings where more than 100 people can be found simultaneously; in the aisles; on a staircase; in production facilities employing over 50 people. Minimum illumination on the floor of the main aisles and on the stairs must be at least 0.5 lx, and minimum illumination on outdoor areas must be at least 0.2 lx.

Security lighting is placed along the boundary-line of the territory that is guarded at night by maintenance personnel. The smallest lighting must be 0.5 lx at the ground level.

Regular lighting is provided at non-working hours, in the meantime as a rule, some lighting appliances of other artificial lighting are used.

Natural lighting has a favourable effect on the organ of vision, stimulates different physiological processes, increases metabolism and improves the development of the whole organism. Solar radiation warms and decontaminates air, purging it from the agents of many diseases (e.g. influenza virus). So that natural lighting has a great physiological and hygienic value to employers. In addition, natural light has a psychological effect, creating a sense of direct communication with the environment for the workers.

Nevertheless, natural light has its disadvantages: it is variable in different periods of the day, year and weather; it is unevenly distributed over the area of industrial room; with its unsatisfactory organization it can cause a glare of view.

There are some factors that influence the level of room illumination with the natural lighting: light climate, area and orientation of the light holes, purity of glass in light holes, painting walls and ceiling space, depth of space, and the presence of items preventing window both inside and outside of the premise.

As the natural lighting is variable during the day, quantitative assessment of this type of lighting is carried out by the relative index – the coefficient of natural light (CNL).

Normalized meanings of CNL are determined by the "Building regulations” (SNIP II-4-79). The size of the object of recognition is taken as a basis of determination of CNL. The object of recognition is an object or its part that is considered, or the defect, which must be detected.

To create favourable conditions for visual work that would prevent rapid eye fatigue, the development of occupational accidents and diseases and would contribute to increased productivity of labour and product quality, production lighting must meet the following requirements:

- create the illumination on the work surface that corresponds to the nature of visual work and will not fall below the established standards;

- should not produce a glare of view from the light sources and other items that are under consideration;
- provide sufficient uniformity and consistency on the level of lighting in the industrial premises to avoid frequent re-adaptation of view;
- should not create sharp and deep shadows (especially mobile) on the surface;
- should provide sufficient contrast of surfaces that are lit to distinguish details;
- should not create dangerous and harmful production factors (noise, heat radiation, dangerous electric shock, fire and explosion hazard lights);
- must be reliable and easy, economical and aesthetic to use [1].

This basic amount of light from the lighting device must be within the waves of the visible spectrum, due to which a person receives information about the world. Visible range includes electromagnetic waves in the range of frequencies that are perceived by human eye ($7.6 * 10^{14}$ - $4 * 10^{14}$ Hz), with a wavelength of 400 to 760 nanometres.

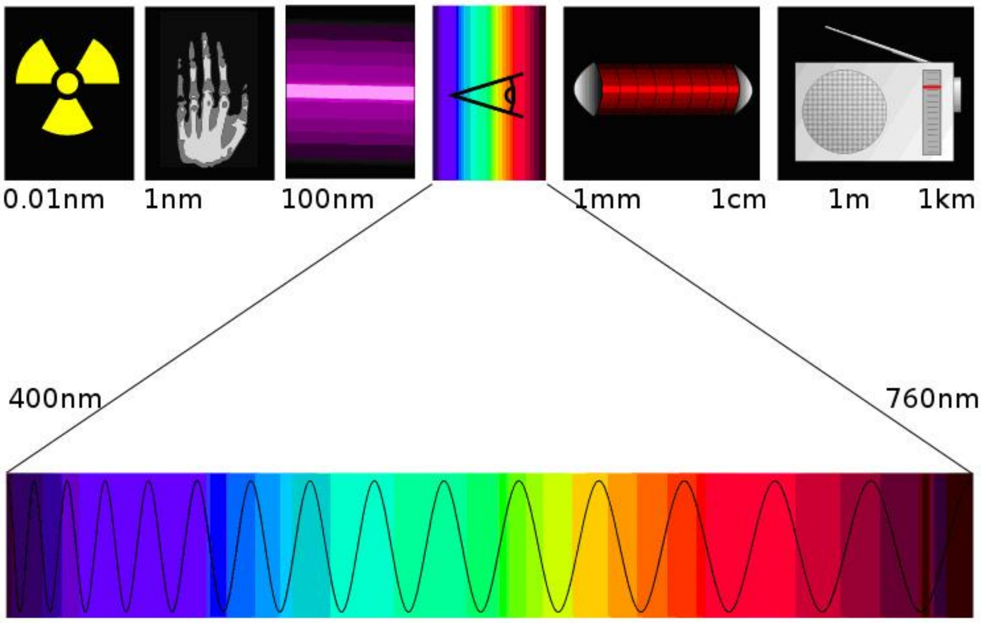

Fig. 1. Visible light spectrum of electromagnetic waves

## ANALYSIS OF RECENT RESEARCH

Illuminometers, photometers, visibility meters and other complex meters are used to measure engineering values of the lighting. Such illuminometers as U-16, U-17, U-116, U-117 and portable digital versatile illuminometer brightness meter TES-0693 are used in production terms to control the lighting of work places and the total luminosity of premises. The work of these devices is based on the photoelectric effect. The light intensity falling on the selenium, germanium or silicium photocell (PV) is converted to electrical energy. Its current strength is measured by milliamperemeter, which scale is graded in lux (lx) [2, 3].

The main advantage of a selenium cell for light measurements is its high integral sensitivity – about 500 μA/lm and characterization of relative spectral sensitivity, which approximates to the curve of the relative spectral sensitivity of organs of vision.

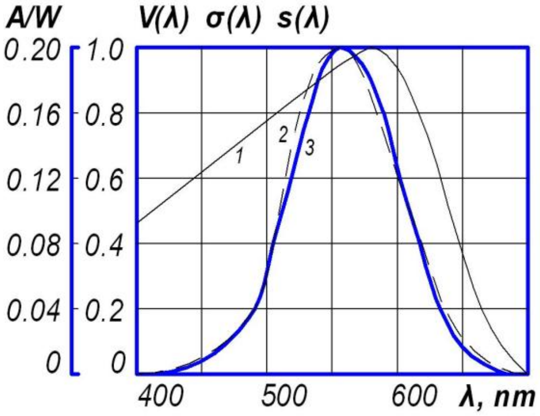

Fig. 2. Curves of the spectral sensitivity of selenium cells (1), medium eye (2) and a photocell with an adjustment filter (3) [6]

Known photovoltaic illuminometers (LM) contain an embedded or removable valve photocell, a magnetoelectric current meter, a scale not evenly graded in lux (lx), a switch of measurements, and all of this is designed on a scheme of direct inclusion of the photocell on the clips of the measuring device (current meter) [4, 5]. If the photocell surface is lit, in a closed circle consisting of the photocell and the magnetoelectrical meter, there is current that dismisses the movable part of the meter. To expand the measurement range the LM has several limits that can be changed by selecting the shunts of the current meter. It has a systematic error caused by the fact that the resistance of the meter has a finite value. As a result, the current in a circuit (contour) “photocell – meter” is not proportional to the lighting of the PV.

There are also known photoelectrical illuminometers in which with order to improve measurement accuracy and improve the working mode of measuring PV, the null indicator is connected in parallel to PV. The source of EMF and the device adjusting current are connected in serial to PV [6].

For the current of the selenium cell to be proportional to the light flux, which falls on its surface (linearity), it is required that the resistance of external circuit to be lower than the internal resistance of the same photocell.

However, the well-known photoelectric LM has some disadvantages:

1. Low accuracy of measurements (for illuminometers U-16, U-17, U-116, U-117, basic error is – ± 10%).
2. Lack of coordination of indications on different limits due to the current in a circuit “photocell- magnetoelectrical meter” that is not proportional to the lighting of the photocell, since the meter has some finite resistance.

Proportionality is only stored for a resistance meter having resistance equal to zero [7]. In addition, during the transition from one measurement limit to another, the load of the PV changes, so identity is not stored on different limits within the measurements. As a result, during the transition from the lower to the higher limits of measurement, the error of measurement increases and the number of instruments relevant to technical conditions decreases [8].

3. Low operational reliability, since LM strongly increases its error, even for one year due to changes in the internal resistance of the PV [9].

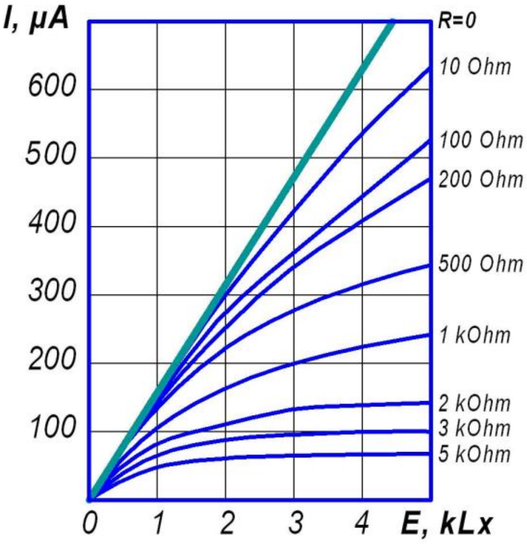

Fig. 3. Integral sensitivity of selenium cells [7]

## PURPOSE OF THE RESEARCH

Our aim is to improve the accuracy of measurements, operational reliability, to obtain the identical exponents on different limits, to improve the work of the measuring photocell.

Thus, our novel approach is aimed at eliminating the shortcomings of the known illuminometers, to develop a principally new scheme of a device for measuring the lighting flux to improve their resolution and accuracy of measurements.

## ACTUAL DISCUSSION AND RESULTS

In order to correct the shortcomings of the known LM, we developed a scheme of an illuminometer that contains an additional valve photocell. The target is achieved by the null indicator connected in parallel to the measuring PV and a switch sequential, a device for current control and an additional valve photocell with a higher short circuit current than in the measuring photocell. Both photocells are simultaneously illuminated by the measured source of light.

Null indicator 2 is connected in parallel to the measuring valve PV 1. Electric circuit consisting of the magnetoelectrical meter of current 3, variable resistors 4 and an additional valve PV 5 is connected in serial to the PV 1 (the positive output of additional is connected to the negative output of the measuring photocell).

If measuring PV 1 and an additional PV 5 are illuminated, the photocurrent appears in the circuit. Moving the regulator of variable resistor 4, we achieve zero reading of the null indicator 2. Under such circumstances the current through the null indicator and, hence, the voltage drop between its connection points are equal to zero.

As a result, we can write the following:

$$Eu + Eq = I(ru + rq + ra + rp) \tag{1}$$

$$Eu - Iru = 0 \tag{2}$$

$$Eq - I(rq + ra + rp) = 0, \tag{3}$$

where: *Eu* – EMF of measuring photocell 1; *Eq* – EMF of extra photocell 5; *ru* – internal resistance of the measuring photocell 1; *rq* – internal resistance of the additional photocell 5;

*I* – current in a circle measured with current meter 3; *rp* - resistance of current meter 3; *ra* – resistance of set variable resistor 4.

Analysis of these equations shows that the measuring photocell 1 will be operating in a regime of short circuit, and a meter of current 3 will be measuring the current that is equal to the current of the short circuit of measuring photocell 1 and is proportional to the lighting on its surface. For proper work it is needed to have the current of short circuit of the additional photocell 5 greater than that of the measuring photocell 1. The scale of the current meter 3 is graded linearly directly in the units of lighting lux (lx).

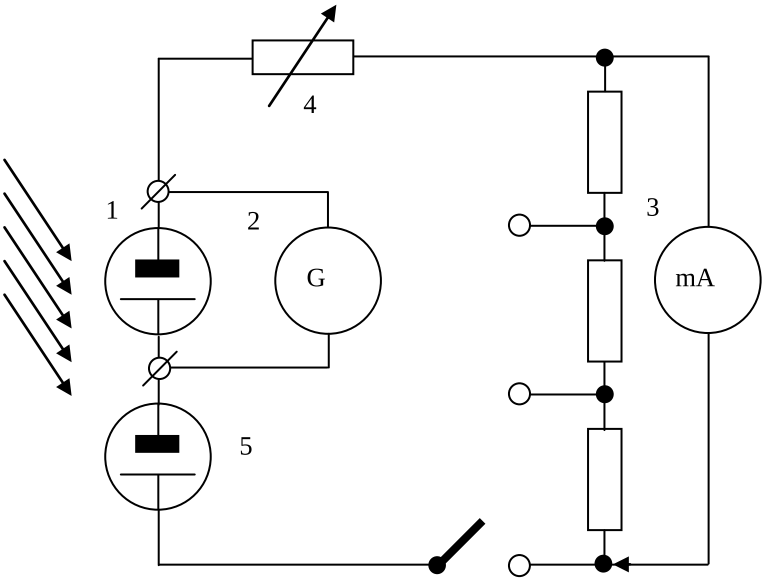

Fig. 4. The proposed scheme of the illuminometer: 1 – measuring photocell, 2 – null indicator, 3 – meter of the current with shunt, 4 – variable resistor, 5 – additional photocell

Known devices for measuring the short circuit current contain one PV. The source of the electromotive force and the galvanometer or lock is connected in serial to the PV. The source of the electromotive force can be changed so as to completely equalize the drop of voltage inside the PV that is equal to its internal electromotive force.

However, there are some disadvantages of these devices:

1. In the initial state in the unlit PV, the scheme can have two positions:
   - if there is voltage in the circuit;
   - if there is no voltage in the circuit.

In the first case the PV and the null indicator are under voltage. As a result, null indicator will be overloaded and “overscaled” and the current will be going through the unlit PV.

2. There are three variants of the scheme at the light PV and to the moment of the balancing scheme (setting null indicator to zero):
   - EMF of the source that acts in a circle is smaller than the EMF of the photocell;
   - EMF of the source that acts in a circle is higher than the EMF of the photocell;
   - EMF of the source that acts in a circle is equal or almost equal to the EMF of the photocell (almost excluded case).

Significant discrepancies are usually possible between the specified types of EMF because of the device that is used as an illuminometer and should measure a wide range of illuminations. This leads to changes in polarity and abrupt changes in the current that breaks the mode of work of the circuit “null indicator – photocell”.

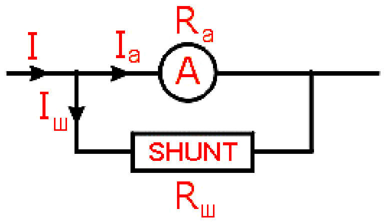

$$I = I_a + I_ш \qquad \underline{I = n \cdot I_a}$$

$$U_a = U_ш$$

$$I_a \cdot R_a = I_ш \cdot R_ш \Rightarrow R_ш = \frac{I_a \cdot R_a}{I_ш}$$

$$\begin{cases} R_ш = \dfrac{I_a \cdot R_a}{I_ш} \\ I_ш = I - I_a \end{cases} \Rightarrow \boxed{R_ш = \frac{I_a \cdot R_a}{I - I_a}}$$

Fig. 5. Calculation of the shunt

The disadvantages above reduce the term of service, work stability, deteriorate the performance of the null indicator and the photocell, and also reduce the accuracy of the measurements.

3. Existence of uncertain correlation between EMF sources and the EMF photocell leads to significant losses of time for balancing (measurement).

4. Using batteries or accumulators with limited lifetime, as a source of EMF requires its periodical replacement that is also inconvenient in operation.

5. If measured illumination changes faster than it is necessary to counterbalance the measuring circuit, the device can not be used.

These shortcommings can be eliminated by replacement of the source of EMF to the source of the photo-EMF on condition that both photocells are simultaneously lit by the measured source of light. Since we use the photo-EMF source instead of the constant power EMF source, it is possible to make almost a full automatic balancing of the scheme. The photo-EMF source produces an EMF value depending on its lighting and raises it to the measuring photocell, on the clips of which the photo-EMF is also created. If the scheme is balanced once, subsequently it will always be near the border balancing.

Shortcomings inherent in the known contrasted devices listed above are completely eliminated in the proposed device.

1. Null indicator and PV operate in an improved mode, shock currents do not occur, moreover, the current always has almost the same direction.

2. Voltage polarity remains virtually constant on the clips of PV, and its sudden change is in general impossible.

3. Periodical replacement of the electromotive force sources that provides a substantial operational advantage is not required.

4. Because the scheme approaches the balancing border, the time of taking measurements is reduced and the productivity of labour increases.

5. During the measurement of the fluctuating lighting, the proposed device is working. It is correct for the operating range of lighting and frequency of the used PV.

All the results proven in laboratory tests of the proposed scheme.

We using an EMF source which changes its value and, in our case, observes for the value of the EMF of the measuring photocell, since both photo-EMF sources are illuminated by the same light source. Instead of a constant source of the EMF, we achieve a qualitatively new scheme, without shortcomings of the known devices. For that purpose photocells were simultaneously lit by the same light, both photocells are mounted in the same frame and connected with a device.

The precision of the lighting measurements is determined by the mode of measuring PV and it is the same in both devices - the mode of the SC. Can not agree with the same precision of measurements of known illuminometers and propose a novel device. That can measure the time variable lighting what is not possible by the known one, i.e. The accuracy of measurement in this case is impossible for comparison.

Known devices do not provide automatic support of the measurement photocell in the SC mode. Measuring by such devices the mode SC for the photocell is set by adjusting the amount of the voltage on the clamps of the source of the electromotive force, reaching a zero display of null indicator. Therefore the manual adjustment is set by changing of the values of resistance of a variable resistor. Then counting is held by the scale of the current meter graded in lux. By using of the photocell in the SC mode, an illuminometer has high linearity of the lux-ampere characteristic (LAC).

The disadvantage of these devices is in their low accuracy because of the small dynamic range, as in the case of significant instability of lighting, the resistance of the photocell changes and it exits the SC mode. Moreover, the accuracy of measurement is insufficient in some cases due to changes in time parameters of the source of the electromotive force and unbalanced circuits.

These shortcomings are eliminated because of replacement of the EMF source to the photo-EMS source, introducing sequentially the additional valve photocell, a positive output of which is connected to the negative output of the measuring photocell, and on condition that both photocells are simultaneously illuminated by light flux measuring. Since we use the photo-EMF source instead of the constant power EMF source it is possible to make almost a full automatic balancing of the scheme. The photo-EMF source produces an EMF value depending on its lighting and raises it to the measuring photocell, on the clips of which photo-EMF is also created from the same luminance. If the scheme is balanced once, subsequently it will be always near the border balancing.

## CONCLUSIONS

As a result of this research a number of important tasks will be solved by the use of the proposed scheme. The illuminometer has a linear scale, high precision, operational reliability and also the clarity of displays on the different limits due to the exclusion of a methodological error, since the regime of short circuit for the measuring photocell is automatically maintained in a wide range of illumination. An essential advantage of the developed scheme of the photoelectric illuminometer is that due to the operation of the measuring photocell in the regime of short circuit the impact resistance of the measuring range of elements measured is completely eliminated. Analysis of the proposed mathematical model of the device for measuring the flux allows an increase in the accuracy of measurements and linearity of indications.

The illuminometer can be implemented if there is a need for objective measurement of natural illumination, to determine the illumination of workplaces, to verify artificial lighting, as well as to identify the needs of electricity for lighting, to control production processes associated with photosynthesis and photocatalysis, for measurements in photography and photo printing, for various lighting and other measurements.

## REFERENCES

1. Types of Lighting http://orbk.net/archives/tag/elektrika (in Ukrainian).
2. Basic Lighting Specifications http://library.if.ua/book/9/947.html (in Ukrainian)
3. Foundations of Work Protection – Basic Lighting Concepts and Units http://buklib.net/index.php?option=com_jbook&catid=177 (in Ukrainian).
4. Catalogue SI-5, Photometric Devices, InformStandartElektro, 1967, p. 5. (in Russian).
5. Illuminometr U-116, U-117 http://www.qrz.ru/schemes/detail/4369.html (in Russian).
6. TIHODEEV P.M. Light Measurements in Light Engineering, M.-L. 1962, p. 210. (in Russian).
7. GUTOROV M.M. Fundamentals of Lighting and Light Sources, M., Energiya, 1968, p. 145. (in Russian).
8. HAZANOV V.S. ect., About the Error of Illuminometer U-16, – SJ Izmeritelnaya Technika, 1971, № 3. (in Russian).
9. HAZANOV V.S. ect., About the Factual Errors of Illuminometers U-16 Type, – SJ Svetotehnika, 1970, № 9 (in Russian).

CYSENI 2011, May 26–27, Kaunas, Lithuania
ISSN 1822-7554, www.cyseni.com

# MODELLING OF REGIONAL SUSTAINABLE ENERGY DEVELOPMENT OPPORTUNITIES: KAUNAS REGION CASE

**E.F. Dzenajavičienė, A. Lisauskas**
*Lithuanian Energy Institute*
*Breslaujos str. 3, LT-44403 Kaunas – Lithuania*
*Phone +370 37 401935*
*Email: farida@mail.lei.lt*

**D. Dzenajavičius**
*Kaunas University of Technology,*
*K. Donelaičio str. 73, LT-44029 Kaunas – Lithuania*

## ABSTRACT

Regional sustainable energy development policy in towns and regions is an integrated part of sustainable regional development, involving environmental, social and economic dimensions from production and use of energy. Sustainable regional energy includes the main areas with the largest potential for reducing greenhouse gas emissions, which are the wider use of renewable energy sources, and improvement of energy efficiency. Among the goals of sustainable development in energy sector is reduction of greenhouse gases emissions in the regions, which will add to national goal of 20% of GHG emissions, 23% of RES share and 20% improvement of energy efficiency by year 2020. Implementation of RES and energy efficiency improvement measures at regional or municipal level gains growing importance for sustainable energy planning and reduction of greenhouse gases emissions, as well as requires simple and easy to use planning tools or, at least available modelling results, provided by energy experts. This paper will overview available models, compare main characteristics, and assess possibilities to use models for regional or local sustainable energy planning needs. It also assesses modeling outcomes in terms of sustainability criteria defined for energy sector. The paper will provide some modelling results for municipalities of Kaunas region, mainly related to the growing share of renewable energy sources, reduction of $CO_2$ emissions and reduction in final energy consumption, which is relevant to the context of sustainable energy development. The paper shows that the results of optimization task on national level cannot be directly transferred to local level, in case implementation of sustainable development is based on local initiatives.

Keywords: sustainable energy development, regional planning, planning models, sustainability criteria.

## 1. INTRODUCTION

Planning of energy sector historically used statistical energy consumption data and planned growth of demand in various consumption areas until the era of qualitative revolution in hardware and software development. More attention to energy forecasting and planning was given after oil crisis. It was evident that former relatively cheap oil will not be able to cover growing energy demand. Investigating various energy supply options in economic terms became the leading axis of the most simulation and optimization energy models.

The evolution and improvement of modeling methodologies reflect above mentioned aspects of planning demand. First models appeared mainly for energy demand forecasting and for analysis of supply options of large national and trans-national energy systems. Later, with energy sector decentralization and introduction of energy markets the need for regional and local level energy planning appeared, which lead to development of regional or local tools. The main planning principles became implementation of national goals and local initiatives in sustainable way i.e. safeguarding social, economic and environmental criteria.

## 2. ANALYSIS OF FOREIGN AND LITHUANIAN ENERGY MODELING EXPERIENCE AND AVAILABLE MODELS

Increased concern in environmental problems brought new impulse to development of energy models, such as reducing greenhouse gases emissions from stationery and mobile sources burning fossil fuel. So-called 3E *(Energy, Environment, Economy)* methodology was developed including optimization of energy consumption, economic costs and reduction of environment pollution [1.]. However, all these factors use different measurement units and need introducing importance (weight) factors in optimizing simulations, which are rather subjective [2.]. Energy demand as well as economic costs may be assessed in different ways, which depends on the restrictions of selected system and period under investigation. Life Cycle Analysis is one of the best-known developed approaches [3.], which evaluates not just operation of the object but also energy consumption and pollution during production of materials and equipment, construction and closure – destroying, disassembling and waste disposal.

### 2.1. Models: types, characteristics and application areas

According to theoretical background and model implementation algorithm energy models can be divided into macroeconomic, energy equilibrium, optimization, simulation and so-called spreadsheets. Every model type can be defined using specific characteristics, restrictions, application, strengths and weaknesses. The main characteristics are provided in Table 1 [4.]. This information may help selecting the best model type appropriate to planning level and goal. It is evident that planning on regional or local levels should not use complicated macroeconomic or energy equilibrium models.

Table 1. Types and characteristics of models [4.]

| | **Macro-economic models** | **Energy equilibrium models** | **Optimization models** | **Simulation models** | **Spreadsheet models** |
|---|---|---|---|---|---|
| **Timeframe** | Short to medium-term | Medium to long-term | Short to long-term | Short to long-term | Medium to long-term |
| **Level of details** | High | Low | High | Partially high | Technically specific |
| **System boundaries** | Entire economy | Entire economy | Energy system | Energy system | Entire economy |
| **Flexibility in terms of technically detailed questions** | Low | Low | High, dependent upon the level of detail of the tech. database | High for limited complexity | High |
| **Theoretical foundation** | Historical analysis of macro-economic interaction matrix | Neo-classical | Optimization with regard to tech.-economic criteria | Primarily tech. determinism of energy systems | Primarily tech. determinism of energy systems |
| **Implementation of the modeling** | Econometric estimation of the interconnections of the matrix | Decisions corresponding to nesting and elasticity | Technological database with optimization algorithms | Technological database, expert knowledge | Technological database |
| **Strengths** | Broad empirical foundation, sectoral disaggregation | Closed theoretical structure | Applicable to tech. total systems. Flexible | Also usable without targeted entities for optimization | Applicable to tech.systems. Flexible application |

| | | | | | |
|---|---|---|---|---|---|
| | | | application possibilities | | possibilities |
| **Weaknesses** | Does not represent specific technologies. No long-term planning | Small empirical basis, often low level of sectoral differentiation | Implicitly rational optimization decisions, strongly influenced by bounds | Economic influences underrepresented, based considerably on the quality of expert knowledge | For local applicability. Variables are indicated exogenously as parameters in future scenarios |

Optimal results could be expected using optimization or simulation models. We can't reject the application of rather simple spreadsheets for very specific planning tasks when planned activity is local and have no significant impact on other more important activities of energy systems in the region. Fig. 1 provides scope and main characteristics of typical modeling tools, suitable for local energy planning.

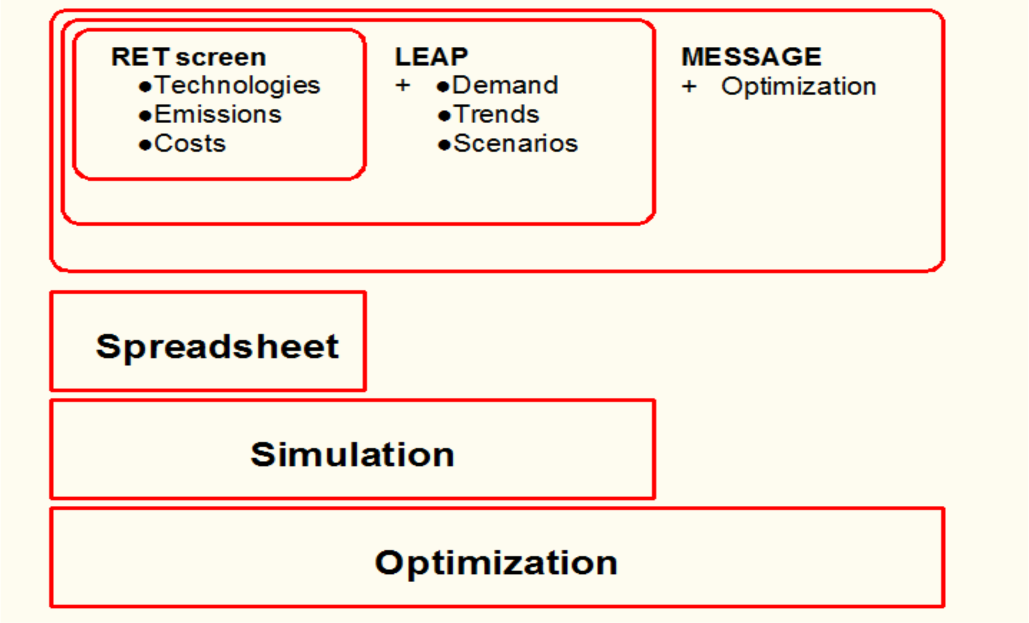

Fig. 1 Characteristics of three typical modeling software tools

Regardless to variety of models applied in energy sector planning, all of them belong to one of the three big groups according to the principles of planning and analysis:

- Using "Bottom-up" methods;
- Using "Top-down" methods; and
- Mixed, joining two above-mentioned methods.

The Fig. 2 presents differences between models formed on "Top-Down" and "Bottom-Up" principles.. Top-down approach typically is used in macroeconomic and energy equilibrium models, while simulation models and spreadsheet calculations uses bottom-up approach. Optimization models often use mixed approach – economic approach in junction with rather detailed technologies.

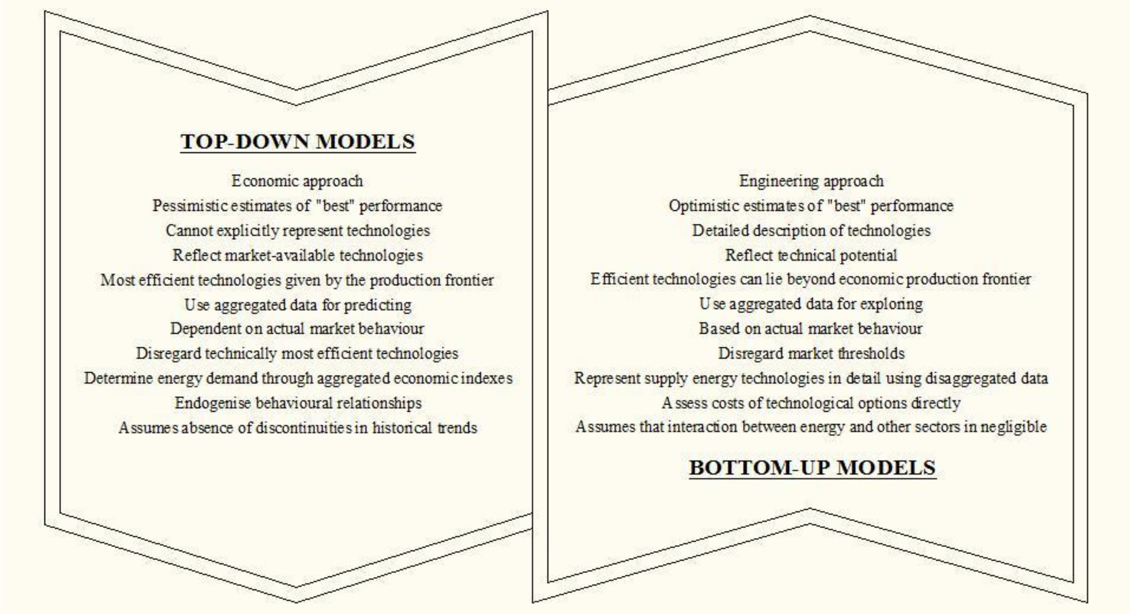

Fig. 2. Differences between models formed on „Top-Down“ and „Bottom-Up“ principles

Integrated energy planning use the same methods as other tasks of mathematical modeling, related to analysis and forecasting of natural, technical and social processes. These methods are screening curves, sequential method, iterative method, and simultaneous optimization. Methods used for energy demand-side planning are trend analysis, end-use method, time series method and econometric method. Methods, employed for supply-side planning are screening curves, iterative method and optimization.

Integrated energy planning use the same methods as other tasks of mathematical modeling, related to analysis and forecasting of natural, technical and social processes. These methods are screening curves, sequential method, iterative method, and simultaneous optimization. Methods used for energy demand-side planning are trend analysis, end-use method, time series method and econometric method. Methods, employed for supply-side planning are screening curves, iterative method and optimization.

## 2.2. Development of energy modeling in Lithuania

### *2.2.1. Energy modeling on national scale*

After retaining independence since 1990 Lithuania was implementing reforms, which were inevitable during transition from planned to market economy. Use of mathematical models was required for assessment of various possible solutions and defining possible economic and social consequences, security and safety of energy supply.

The historical overview of modeling and optimization in Lithuania's energy sector is presented in [5.]. The first implemented model for optimization of energy flows was **EFOM-ENV** with flexible definition of energy systems, energy objects and technologies. Model elaborated the least costs options for development of Lithuania's power sector.

**WASP model** was developed in USA and used for development of nuclear energy. Use of **WASP IV** version and application of **BALANCE** and **VALORAGUA** mathematical models took place while collaborating with IAEA. They were used for revised National Energy Strategies of 1999 and 2002 as well as for assessment of technical, economic and environmental consequences for the closure of Ignalina Nuclear Power Plant.

Mathematical model **MESSAGE** (Model for Energy Supply Strategy Alternatives and their General Environmental Impacts) was further developed in collaboration with IAEA.

Several versions of this model were issued. The models have no restrictions for the number of equations and variables and allow freely select the details of energy sector according to the needs of the consumer. The version adapted for analysis and modeling of energy sector at municipal level and the use of renewable energy sources with cost minimization at national level was used for achieving the modeling results of this paper.

One can see that modeling on national scale already had provided some outcomes related to not just technical, but also economic and environmental consequences of activities in energy sector.

### *2.2.2. Energy modeling on local level*

Different from national energy planning, local modeling (on regional, municipal or local levels) in practice was not performed in Lithuania. Municipalities have the only obligation to elaborate towns' special plans of heat supply. Most simple planning tools, such as SWOT analysis, financial assessment of investment projects, special municipal district heating plans, were used by the regions in their regional development strategies. There is still no uniform methodology and tools for development of such strategies. Widely promoted and developed Integrated Resources Planning (IRP) approach is applied for municipal energy planning rather episodically and mainly under international research and development projects. The same could be said about the development of models for national energy needs.

The importance of implementing sustainable energy approach for regional energy plans is defined by the following main statements of EU energy policy:

- Increase of RES and indigenous energy sources in energy balance;
- Promotion of technological progress for more efficient energy production and end-use;
- Support for initiatives of sustainable energy development in municipalities (communities).

Decentralization of energy market makes regional energy planning some kind of dialogue between stakeholders in planning process who have different interests and priorities. Uncertain future energy prices, lack of financial resources and growing impact to environment makes regional energy planning and modeling more complicated [7.]. Local planning requires optimal software tools for easy use by municipal planners without specific hardware as it does not need to solve macroeconomic tasks. Comprehensive analysis of such models is provided in paper [4.], and the conclusion was made that LEAP model is the optimal tool for small countries. Among the main advantages of the tool is its accessibility and technical support from COMMEND communities. Here we present more detailed overview in terms of sustainability of available models for local/regional planning, which were tested for regional or local planning under various projects.

**SAFIRE$^{LP}$** model was elaborated under EU SAFIRE-LP project [8.] and is to be applied for planning of energy sector at local (municipal) level, and should be used by municipal energy planners or together with energy experts. The main emphasis here was made on extensive use of renewable energy sources, which add to improvement of environmental sustainability of the municipal energy sector. However, experience of exercising in Biržai municipality showed that collecting of required data is complicated even for energy consultants and takes much time. Besides, change of pre-defined values is impossible without creators of this model.

**REAM** – regional energy analysis model, created by Profu (Sweden), and IFE (Norway) under PEE project „3-NITY“ for support of local communities and based on sectoral model KRAM [9.]. REAM model is a modern tool for planning and making investment solutions. **KRAM** model is prototype of REAM model and was used for estimating heat demand and supply; however, it requires detailed statistical data for more detailed analysis. The use of this model mainly adds value to economic sustainability of the projects.

**Balmorel** model is applied for modeling and analysis of energy systems with emphasize on power and combined heat and power (CHP) generation sector. Such analysis usually includes several neighbor countries and investigates energy, environmental and economic aspects of these sectors, which is important to improvement of both economic and environmental sustainability. However, the main idea was to support energy experts, energy companies, network operators and researchers in analysis of future development scenarios, and municipal or regional planners do not use this tool [10.].

**LEAP** model – Long-range Energy Alternatives Planning system is scenarios based modeling tool [11.]. Scenarios are based on detailed information how energy is consumed, transformed and generated in certain region or sector, using the range of assumptions on number of population, economic growth, technologies, prices, etc. Flexible data structure allows introducing of several technologies and demand specifications. This model is constantly improved by filling technological and macroeconomic data bases (years 2000–2008 for Lithuania). The model is considered to be one of the best tools, providing output for development of economic and environmental sustainability in energy sector of local municipalities.

**MESAP** – Modular Energy System Analysis and Planning – is environment-flexible model for energy systems, using modular approach with normalization of information, achieved while separating construction of data basis from algorithms of mathematical modeling [12.].

As experience in local energy sector shows that municipalities are more interested in simple planning tools, which can be used by local planners themselves. Above presented large and complicated models can't position themselves in municipalities or even larger regions. EU Committee of Regions, Covenant of Mayors initiative and IEA initiated projects, which could elaborate methodologies for developing simple tools for local communities and municipalities in EU.

## 3. ASSESSMENT OF MODELLING POSSIBILITIES FOR DEVELOPMENT OF ENERGY SECTOR IN SUSTAINABLE WAY

Besides above mentioned local planning problems in elaborating and adoption of software tools for local planning needs, the only and the best attempt was made by the group of LEI scientists for the order of the Ministry of Energy [13.] Reaching RES and GHG targets was simulated using MESSAGE model and gaining experience in providing data and adapting model for municipal energy needs. The aim of above study was assessment of RES potential and possibilities to use it on municipal level, evaluating the impact from RES use on national level. Optimization model was justified for implementation of such task since it was the best choice for minimization of energy costs with accepted restrictions related to Lithuania's international obligations under RES Directive and Climate-energy package [14.]. Though optimization was performed on national level, energy demand and supply options are presented for each of 60 municipalities.

The most serious problem related to models is filling it with required statistical data. Optimal data volume is usually achieved via introducing default data, such as climate characteristics, technological data and energy resources. Macroeconomic and sectorial data is available in the databases of the Department of Statistics. However the most serious problem is that most data, including energy demand by types of fuel and energy, biomass, waste resources, etc., are hardly available on municipal level. In the best case such data is available in regional statistics.

Collecting technological data for the use of RES requires much time and efforts, as Lithuania has no technologies, which are used in other countries, such as waste incineration, biogas production and purifying, use of forest management waste, etc. Usually we use data and experience of foreign investigations. For this reason modeling data will have to be updated after having received new information applicable for specific situation in Lithuania or even specific municipality.

## 3.1. Assessment of sustainability criteria in development models

Energy development models are usually restricted with cost analysis and optimization (economic criteria); air pollution and input into climate change prevention (environmental criteria). Energy costs and changes in household consumption could be assessed as only social criteria. Modeling and analysis of energy demand can be implemented using various approaches. Energy demand typically is related to forecasted economic development in macroeconomic terms and described by development scenarios for modeling at national level. ,. Integrated resources planning approach includes more detailed analysis of consumption spheres and energy efficiency improvement measures thus allow forecasting not only total energy demand but also energy types to meet energy needs.

Criteria and indicators for sustainable development of energy sector were developed by common efforts of International atomic energy agency, UN Department of Economic and Social Affairs, International Energy Agency, Eurostat and European Environment Agency in 2005 [15.]. Possibilities to assess sustainability criteria using the results of MESSAGE model are presented in Fig. 3. Here we should also mention that model results do not allow evaluating social criteria, just certain share of economic and even less environmental ones (highlighted with green and blue colors).

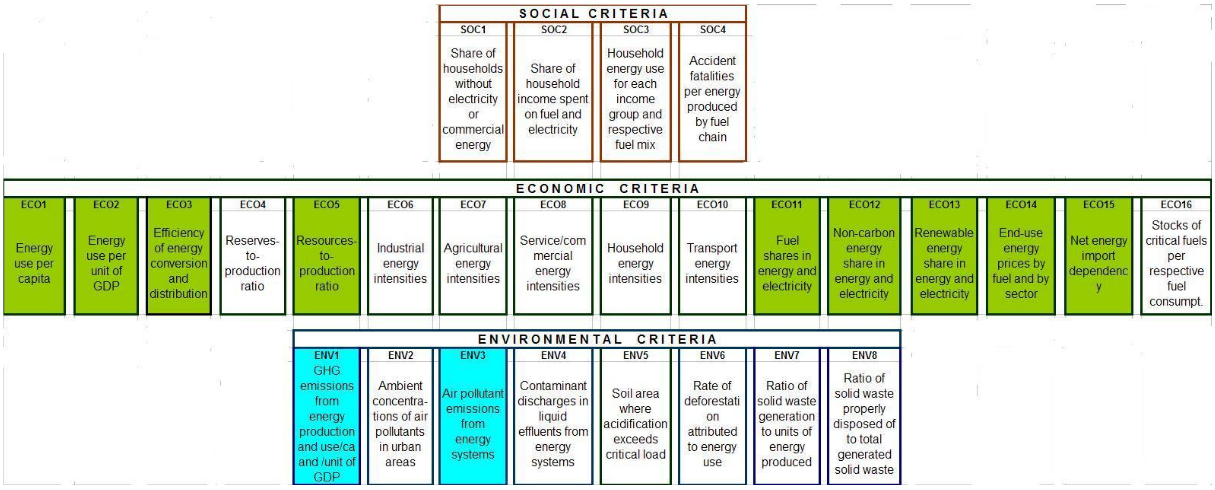

SOCIAL CRITERIA

| SOC1 | SOC2 | SOC3 | SOC4 |
|---|---|---|---|
| Share of households without electricity or commercial energy | Share of household income spent on fuel and electricity | Household energy use for each income group and respective fuel mix | Accident fatalities per energy produced by fuel chain |

ECONOMIC CRITERIA

| ECO1 | ECO2 | ECO3 | ECO4 | ECO5 | ECO6 | ECO7 | ECO8 |
|---|---|---|---|---|---|---|---|
| Energy use per capita | Energy use per unit of GDP | Efficiency of energy conversion and distribution | Reserves-to-production ratio | Resources-to-production ratio | Industrial energy intensities | Agricultural energy intensities | Service/commercial energy intensities |

| ECO9 | ECO10 | ECO11 | ECO12 | ECO13 | ECO14 | ECO15 | ECO16 |
|---|---|---|---|---|---|---|---|
| Household energy intensities | Transport energy intensities | Fuel shares in energy and electricity | Non-carbon energy share in energy and electricity | Renewable energy share in energy and electricity | End-use energy prices by fuel and by sector | Net energy import dependency | Stocks of critical fuels per respective fuel consumpt. |

ENVIRONMENTAL CRITERIA

| ENV1 | ENV2 | ENV3 | ENV4 | ENV5 | ENV6 | ENV7 | ENV8 |
|---|---|---|---|---|---|---|---|
| GHG emissions from energy production and use/ca and /unit of GDP | Ambient concentrations of air pollutants in urban areas | Air pollutant emissions from energy systems | Contaminant discharges in liquid effluents from energy systems | Soil area where acidification exceeds critical load | Rate of deforestation attributed to energy use | Ratio of solid waste generation to units of energy produced | Ratio of solid waste properly disposed of to total generated solid waste |

Fig. 3. Possibilities to assess sustainability criteria using results of MESSAGE model

The goals of RES Directive, EU Climate and Energy package and Covenant of Mayors are introduced into optimization models as restrictions for target function, while in simulation models state policy implementation and sustainable energy development criteria are introduced as scenarios. Use of simulation models requires additional analysis of results for simulated scenarios with regard to defined sustainability criteria (costs, environmental, social).

### 3.2. Modeling results in municipalities of Kaunas Region with regard to energy development in sustainable way

This analysis uses the results of one modeling scenario for 8 municipalities of Kaunas Region. The analysis of the modeling results was performed for three main sustainability indicators – RES share, $CO_2$ emissions at forecasted changes of energy demand, which are in conformity with the targets and tasks of EU Climate and Energy package and RES promotion Directive.

The results of the modeling allowed to compare the fuel demand for district heating (DH) in municipalities of Kaunas region with heat generation using solid and gaseous biofuel and biofuel potential from cutting activities in the forests of Kaunas region in 2008. Birštonas, Kaišiadorys and Raseiniai municipalities cover more than half of their energy demand using biofuel (Fig. 4).

However, total share of biomass fuel used for DH in the regions hardly reach 8%, which is defined by the use of natural gas at Kaunas CHP plant, which covers 80% of DH needs in Kaunas City and Kaunas regional municipality with population over half of that of the whole region. Assessment of forest biomass potential shows that these resources could cover over 70% of DH needs in Kaunas Region.

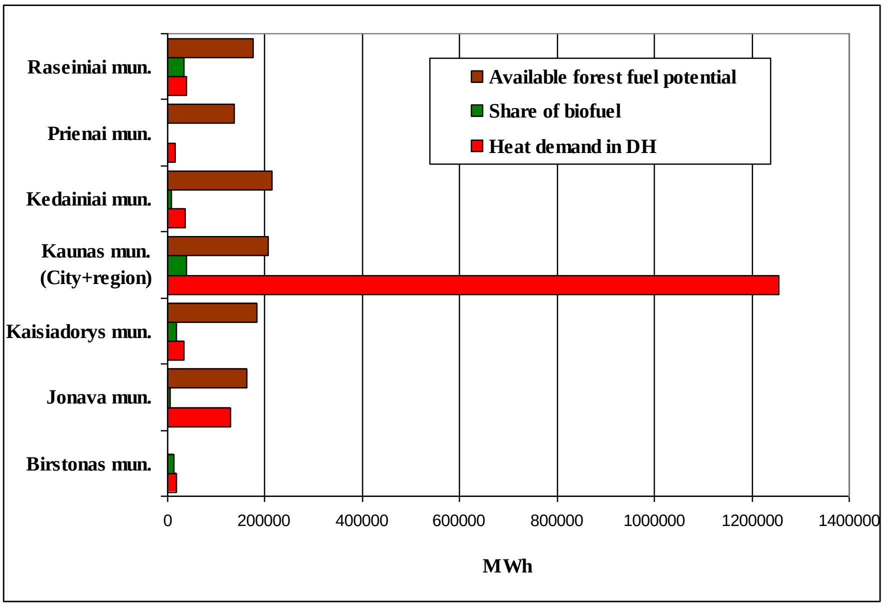

Fig. 4. The use of biofuel and heat demand in 2008 compared to forest fuel potential available for district heating of Kaunas Region

The share of RES in total fuel-energy balance, including decentralized heat generation, reached approximately 11% in 2008. Most of it was used in Raseiniai municipality (there are no natural gas networks in this municipality), and the least in Birštonas municipality, which is the smallest one in the region (Fig. 5. a). The increase of the share of RES in energy balance is shown in Fig. 5 b. Wood, straw and biogas should be considered as the main resources from the least costs attitude. Kaunas City could also use combustible fraction of municipal waste for energy generation.

Modeling results were achieved via applying restriction on target function that the national share of RES in final energy consumption should be not less than target indicator in RES Directive for Lithuania – 23%, and this indicator for Kaunas Region should be 20%.

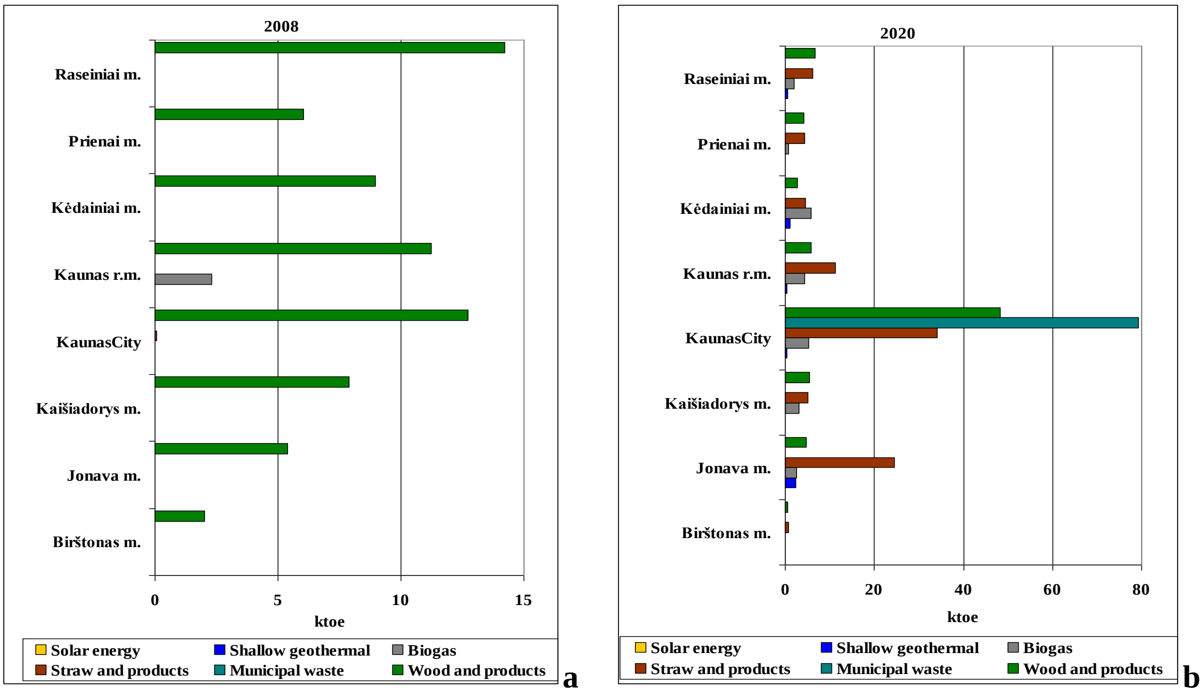

Fig. 5. The use of renewable energy sources in municipalities of Kaunas region in 2008 (a) and in 2020 (b) (modeling results), ktoe

Fuel consumptiondata shows the change of RES and fossil fuel share in energy generation (Fig. 6). This figure also includes biomass from municipal waste which could be used in Kaunas City.

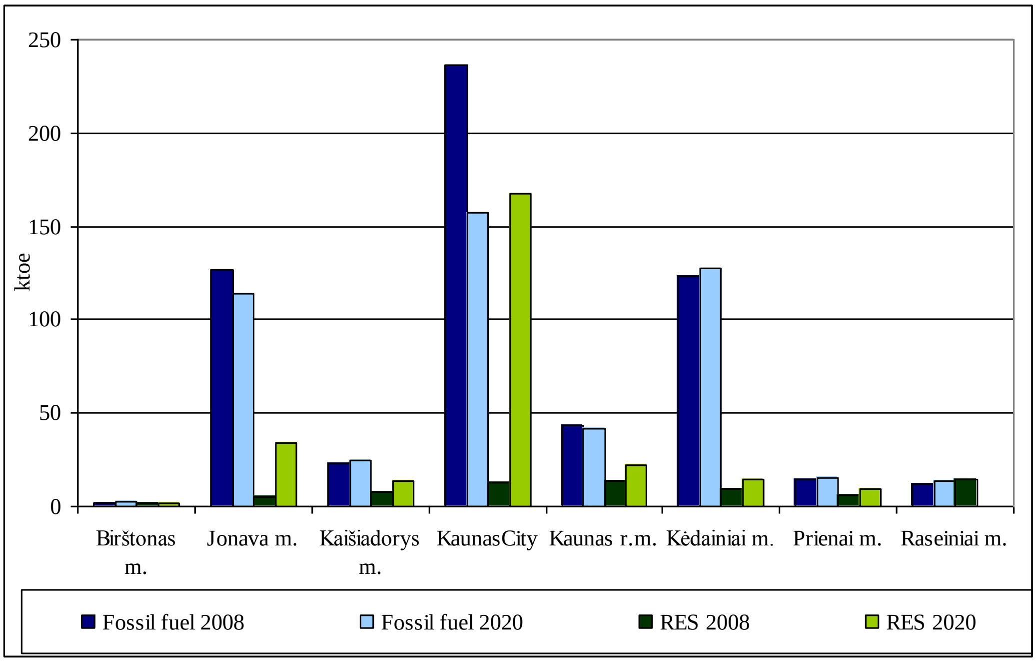

Fig. 6.The changes in the use of fossil fuel and RES in municipalities of Kaunas Region during the period 2008–2020, ktoe

The share of fuel from RES in total primary energy consumption (excluding transport and electricity) could grow from current 25.5% to 35.2% according to the simulation results. Simulation results, showing the change of RES share in fuel balance for municipalities in Kaunas Region are presented in Fig. 7.

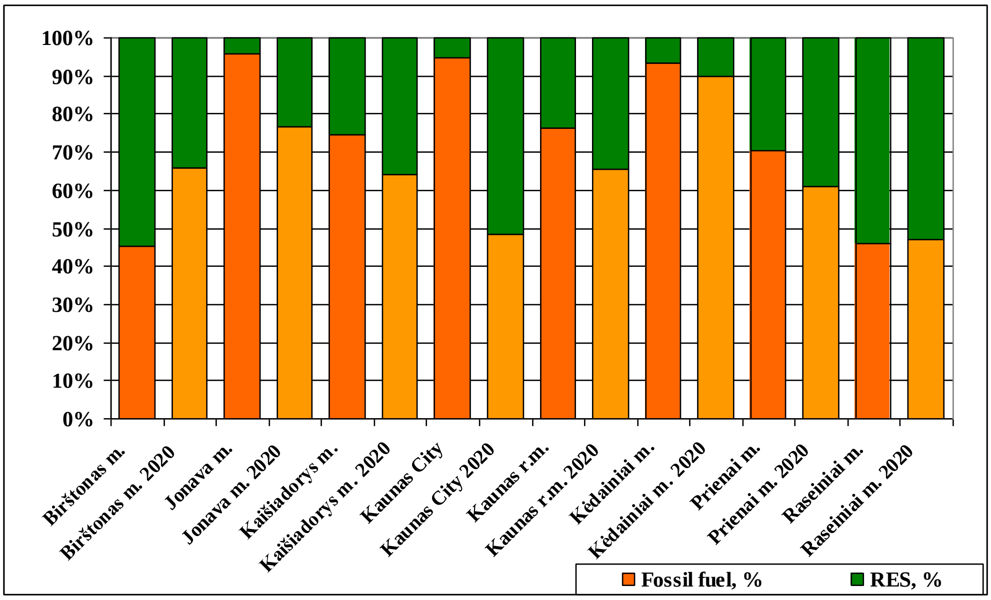

Fig. 7. The share of fossil fuel and RES in fuel balance in years 2008 and 2020 in municipalities of Kaunas Region, %

The other important sustainability criterion – reduction of greenhouse gas (GHG) emissions. It is also one of target functions with regard to EU goals defined in Energy and Climate package, which is reduction of GHG emission by at least 20%. The Covenant of Mayors suggests even more ambitious targets. The results of the modeling and converting of changes in the use of fossil fuel into changes of GHG emissions via $CO_2$ equivalent by municipalities show total reduction of GHG emissions by 20% in Kaunas Region. However, quantitative changes in separate municipalities are not similar, starting with increase of emissions in Birštonas, Kaišiadorys, Prienai and Raseiniai municipalities and showing significant reduction in Kaunas City, Jonava, Kaunas and Kėdainiai regional municipalities (Fig. 8).

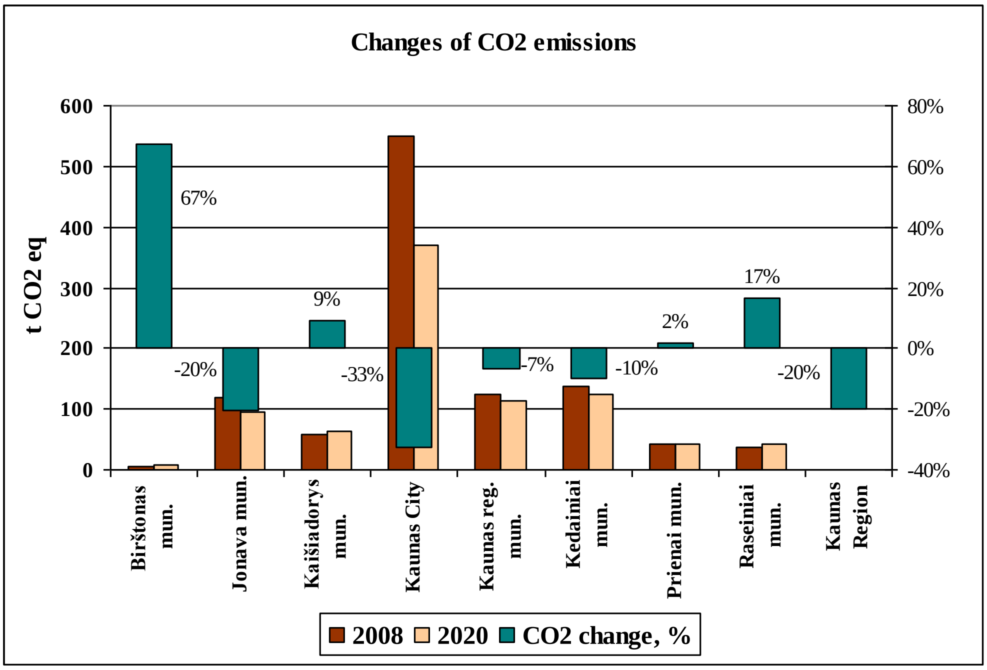

Fig. 8. The change of GHG emissions in Municipalities of Kaunas Region (modeling results)

Growth of $CO_2$ emissions in some municipalities can be related to the growth of energy demand, which is covered using cheaper technologies based on fossil fuel. Besides, in absolute units, this growth is not high as is levered by significant reduction of GHG emission in Kaunas City and Jonava Municipalities.

Reduction of energy demand through improvement of energy efficiency is also one of the targets of energy policy. However, different from reduction of emissions or increasing the share of RES, the defined target of 20% reduction in final energy consumption is related to economic development. This means inevitable growth of energy demand due to economic development, especially in energy intensive sectors of economy. For this reason energy saved from more efficient use is reflected not directly but comparing to the growth of energy demand and unchanged energy efficiency.

For modeling purposes energy demand was elaborated using other methodologies, which evaluate the changes of macro-economic indicators, reduction of energy demand due to autonomous progress effect, impact from the use of energy efficiency measures and other factors (prices elasticity, etc.). The changes of final energy consumption (demand) in municipalities of Kaunas Region are presented in Fig. 9.

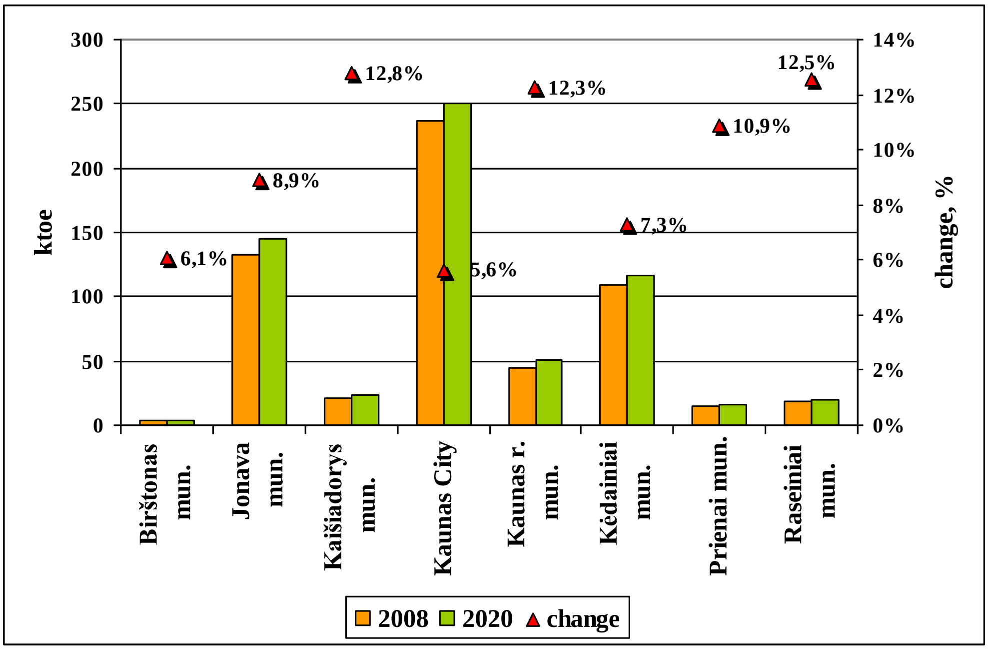

Fig. 9. The changes in final energy consumption used for modeling

The main differences from changing the restrictions of modeling object (in national, regional or municipal levels) could be described in the following conclusions.

## 4. CONCLUSIONS

1. Optimal solution on national level should not be the same as that optimal and meeting sustainability criteria solution for specific municipality or region. Thus, the results of optimization task on national level cannot be directly transferred to local level, in case implementation of sustainable development is based on local initiatives, such as e.g. Covenant of Mayors.
2. Modeling on local level loses internal links of energy market – possible redistribution of fuel and energy resources from one model planning region to another. Simulation models for some types of energy (e.g. electricity, natural gas) introduce category of large energy systems and energy from such systems can be supplied without restrictions.

3. In case decision-making process is based on optimization results achieved on national level, there is always conflict possibility related to inadequacy between input and benefit on local decision-making level, or in other words, territorial aspect of sustainable development is eliminated.

## Acknowledgements

The authors would like to express their acknowledgement to our colleague Dr. Arvydas Galinis and his working group who have performed modeling and kindly provided us with the results for our analysis.

## 5. REFERENCES

1. Capros, P., Integrated Economy / Energy / Environment Models // Int. Symposium on Electricity, Health and the Environment – Comparative assessment in support of Decision Making, IAEA, Vienna, Austria, 16-19 October, 1995.
2. Pollitt, H., Chewpreecha, U., Summerton, P. E3ME: An Energy-Environment-Economy Model for Europe. March 2007. [referred on the 10th of March in 2008]. Link to the internet: http://www.e3me.com
3. Guinée, J., ed:, Handbook on Life Cycle Assessment: Operational Guide to the ISO Standards, Kluwer Academic Publishers, 2002.
4. Dementjeva, N., Smirde, A. Analysis of energy models and their adaptability for Estonian energy market. Energetika. 2009. T. 55, Nr. 2, p. 107–115.
5. Galinis, A., Miškinis, V., Vilemas, J. Energetikos sistemų optimizavimo tyrimai // Mokslas ir technika. ISSN 0134-3165. 2007. Nr. 1, p. 18–19, p. 36–37.
6. Model for Analysis of Energy demand (MAED-2) IAEA, Vienna, 2006, IAEA/CMS/18 © IAEA, 2006 Printed by the IAEA in Austria January 2006.
7. Myrakian, A., Lelait, L., Lewand, N., Isbert, P. The dynamics of regional integrated energy planning and requirements of methods and models // International energy workshop. EIFER, July, 2008 at the IEA, Paris, FRANCE.
8. Report – Strategic assessment framework for the implementation of rational energy - local planning // 5BP Project SAFIRE-LP, 2002–2004.
9. WP3 Report – Sustainable Energy Planning. Final version. // The 3-NITY project under programme Intelligent Energy for Europe. 29th August 2008.
10. Gatautis, R., Ravn, H.,F. Modeling of energy supply systems by the Balmorel model // ENERGETIKA. 2005. Nr. 2, p. 8–20.
11. LEAP – Long-range Energy Alternatives Planning System. Stockholm Environmental Institute in Boston, USA, [referred on the 12th of April in 2010]. Link to the internet: http://www.energycommunity.org
12. Schlenzig, Christoph. Energy planning and environmental management with the information and decision support system MESAP // Institut fur Energiewirtschaft und Rationelle Energieanwendung IER, University of Stuttgart, Pfaffenwaldring 31, 70550 Stuttgart, Germany.
13. GALINIS, A., et al. The use of renewable energy sources (biofuel, hydro, solar, geothermal energy) and municipal waste in municipalities of the country for generation of energy. Lithuanian Energy Institute. Research Study, Kaunas, December 2009 (including data basis and spreadsheets of results).
14. Decision No 406/2009/EC of the European Parliament and of the Council of 23 April 2009 on the effort of Member States to reduce their greenhouse gas emissions to meet the Community's greenhouse gas emission reduction commitments up to 2020.
15. Energy Indicators for sustainable development: guidelines and methodologies. International atomic energy agency, UN Department of Economic and Social Affairs, International Energy Agency, Eurostat and European Environment Agency, Vienna, 2005.

# INPUT-OUTPUT ANALYSIS OF RELATIONSHIPS BETWEEN ENERGY AND OTHER BRANCHES OF LITHUANIAN ECONOMY

**V. Lekavičius**
*Lithuanian Energy Institute*
*Laboratory of Energy Systems Research*
*Breslaujos str. 3, LT-44403 Kaunas – Lithuania*
*Phone +370 615 64334*
*Email: vidas@mail.lei.lt*

ABSTRACT

Energy sector plays a crucial role in the economic development of any contemporary country. Energy resources are used to satisfy final energy demand as well they are intermediate goods to produce other goods and services. The Input–Output analysis is a widely used method to quantify indirect energy consumption in a particular sector and to evaluate the impact of energy-related changes on the economy. One of the main advantages of Input-Output analysis is a possibility to investigate the interdependencies of different sectors of the economy. This method can be applied to all sectors in different countries regardless the specifics of their production processes.

In this paper an input-output analysis is applied for two major aims: to analyse direct and indirect energy demands in particular branches of the Lithuanian economy and to evaluate impact of structural change in energy production on value added, because of shift from imported to local energy resources. Lithuanian input-output table has been modified in order to reflect needs of the analysis. Results of analysis show that an increase in bioenergy use could be beneficial for the development of forestry, transport sectors. Additional investigation should be performed in order to evaluate the impact of energy price changes on competitiveness of energy consuming sectors.

Keywords: input-output analysis, energy demand, indirect energy consumption.

## 1. INTRODUCTION

It is universally agreed that energy sector has an influence on the economy of any contemporary country; however the relationships between the energy sector and the rest of sectors of national economy are different and depend both on country’s features and sectors’ peculiarities. In recent years the issue of relationships between economy and its sectors is becoming highly relevant. On the one hand the importance arises because of year by year increasing price of energy resources and on the other hand new politically essential commitments on wider utilization of renewable energy sources have been accepted.

Energy price development influences on the cost of other sector production. Furthermore, this influence can be both direct (when energy products are used in production processes of other sectors) and indirect (when in production processes are used products that themselves have been produced using a lot of energy).

EU Directive 2009/28/EC on the Promotion of the Use of Energy from Renewable Energy Sources (RES) sets substantially wide use of renewable energy sources. This utilization will influence on extensive changes in the structure of energy sector. Thus it is relevant to evaluate the impact of these changes.

The aims of this article is to quantify direct and indirect energy consumption in the sectors of national economy and to analyze the possible impact of energy sector structural changes caused by extensive use of RES in heat plants on value added and employment in different sectors. These issues are investigated using Input-Output analysis methodology that allows examining the interdependencies between different sectors of the economy.

Research on direct and indirect energy consumption are relevant seeking to solve issues related to energy efficiency or to set application directions of appropriate administrative and other measures. Meanwhile analysis of structural changes in energy sector (i.e., shift from natural gas to biomass in district heating) enables to evaluate a social-economic benefit of these changes at large extent. This is especially relevant seeking to set volume of economic effects and possible amount of support for RES development.

In this article it was considered that energy sector encompasses all economic activities the main product of which is electrical energy, gas, steam or hot water according to CPA 2002 (Statistical Classification of Products by Activity). Full classification of products (sectors) is listed in Appendix 1. Calculations presented in this paper are based on the newest Lithuanian input-output table for 2005 published by Statistics Lithuania in 2009 [1].

## 2. METHODOLOGY AND ASSUMPTIONS

### 2.1. Input-output framework

The main idea of Input-Output analysis is that monetary or physical flows in the economy could be registered in a matrix, where origin and destination of each flow could be recognized. A typical input-output table, which depicts a *n*-sector economy, is shown in Table 1.

Table 1. The basic structure of an input-output table

| | | Intermediate product | | | | | | Final consumption by government, households etc. | Gross fixed capital consumption | Total final demand | Total output (use) |
|---|---|---|---|---|---|---|---|---|---|---|---|
| | | Sector 1 | Sector 2 | … | Sector j | … | Sector n | | | | |
| Intermediate input | Sector 1 | $x_{11}$ | $x_{12}$ | … | $x_{1j}$ | … | $x_{1n}$ | $F_1$ | $GF_1$ | $Y_1$ | $X_1$ |
| | Sector 2 | $x_{21}$ | $x_{22}$ | … | $x_{2j}$ | … | $x_{2n}$ | $F_2$ | $GF_2$ | $Y_2$ | $X_2$ |
| | … | … | … | … | … | … | … | … | … | … | … |
| | Sector i | $x_{i1}$ | $x_{i2}$ | … | $x_{ij}$ | … | $x_{in}$ | $F_i$ | $GF_i$ | $Y_i$ | $X_i$ |
| | … | … | … | … | … | … | … | … | … | … | … |
| | Sector n | $x_{n1}$ | $x_{n2}$ | … | $x_{nj}$ | … | $x_{nn}$ | $F_n$ | $GF_n$ | $Y_n$ | $X_n$ |
| Added value | | $V_1$ | $V_2$ | … | $V_j$ | … | $V_n$ | | | | |
| Total domestic output | | $DO_1$ | $DO_2$ | … | $DO_j$ | … | $DO_n$ | | | | |
| Imports | | $Imp_1$ | $Imp_2$ | … | $Imp_j$ | … | $Imp_n$ | | | | |
| Total input (supply) | | $X_1$ | $X_2$ | … | $X_j$ | … | $X_n$ | | | | |

Rows of input-output table show consumption of production of sector *i*. This consumption can be intermediate (when product is used to produce other products) or final. This can be expressed by the following equation:

$$\sum_{j=1}^{n} x_{ij} + Y_i = X_i, \tag{1}$$

where

$$Y_i = F_i + GF_i. \tag{2}$$

Similar equation explains formation of columns (cost structure of each sector):

$$\sum_{i=1}^{n} \mathrm{x}_{\mathrm{ij}} + \mathrm{V}_{\mathrm{j}} + Imp_{\mathrm{j}} = \mathrm{X}_{\mathrm{j}}. \tag{3}$$

Total input must be equal to total output (sum of rows in the column must be equal to the sum of columns in the row):

$$\mathrm{X}_{\mathrm{i}} = \mathrm{X}_{\mathrm{j}}. \tag{4}$$

It should be noted that formation of each intermediate input can be expressed by the following equation:

$$\mathrm{x}_{\mathrm{ij}} = \mathrm{q}_{\mathrm{ij}} \times \mathrm{p}_{\mathrm{ij}}, \tag{5}$$

where $\mathrm{q}_{\mathrm{ij}}$ is a quantity of products in physical units and $\mathrm{p}_{\mathrm{ij}}$ is a price per physical unit of a particular product. Equation (5) shows that each input-output table covers not only monetary but also physical flows.

In order to analyse possible changes in the economy, technical coefficients $\mathrm{a}_{\mathrm{ij}}$ must be calculated in the following way:

$$\mathrm{a}_{\mathrm{ij}} = \frac{\mathrm{x}_{\mathrm{ij}}}{\mathrm{X}_{\mathrm{j}}}. \tag{7}$$

Because of convenience economic linkages can be expressed in a matrix form:

$$\mathrm{X} = \mathrm{AX} + \mathrm{Y}, \tag{8}$$

where *X* is total output matrix, *A* – technical coefficients matrix and *Y* – total final demand matrix. This equation can be reformulated into the most important equation of an input-output analysis:

$$\mathrm{X} = (\mathrm{I} - \mathrm{A})^{-1} \times Y, \tag{9}$$

where *I* is so called identity matrix (a matrix with ones on the main diagonal and zeros elsewhere). The matrix $(\mathrm{I} - \mathrm{A})^{-1}$ is known as the Leontief inverse or the total requirements matrix [2]. The elements of the total requirements matrix measure the direct and indirect output levels from each sector of the economy required to satisfy the given levels of final demand [3].

It should be noted that Input-Output analysis has some restrictions. Martinez [4] has mentioned four of them:

- intersectoral relationships remain constant over time;
- production of each sector is homogenous;
- returns to scale are constant;
- there are not externalities between the sectors of the economy.

Absence of capacity constraints is mentioned as a limitation of the input-output analysis as well [3].

By developing an Input-Output analysis some of restrictions mentioned above have been solved [2] but in this case Input-Output analysis is going to be similar to much more difficult general equilibrium modelling. In this paper a methodological approach how to analyse changes of intersectoral relationships has been also demonstrated.

## 2.2. Direct and indirect energy consumption

Direct energy consumption can be defined as a direct use of energy in order to produce some quantity of production. Indirect energy consumption counts energy consumption in all products used to produce the same quantity of production. Naturally, indirect energy consumption is always equal or higher than direct energy consumption. In this paper demand analysis based on input-output table has been used in order to evaluate indirect energy consumption in branches of Lithuanian economy.

Demand analysis is one of the main application areas of the input-output method [5]. It is used at various research of indirect energy consumption. Depending on research purposes energy consumption is analysed in monetary terms [3, 6] or monetary units are recalculated into the physical units [7-9]. In order to perform a precise analysis of consumption of electricity or other kind of energy, special input-output tables with energy flows are constructed [10]. This paper is oriented towards economic impacts, therefore analysis in monetary terms has been chosen.

Assuming that the matrix of total requirements remains constant during the enitre simulation, the following expression could be received from the equation (9):

$$\Delta \mathrm{X} = (\mathrm{I} - \mathrm{A})^{-1} \times \Delta Y , \tag{10}$$

where $\Delta \mathrm{X}$ is a difference in the total output and $\Delta Y$ is a difference in the total final demand. Indirect energy consumption (in monetary terms) is analyzed by consistently setting of total final demand per one unit in each sector.

Two approaches can be used when direct and indirect energy consumption is being analyzed:

- energy consumption in the domestic production;
- energy consumption in the total input including import.

As it is showed below, selection of the approach depends on import structure or the particular sector: if that sector imports final production, it is reasonable to analyse energy consumption in the domestic sector, because it allows to analyse domestic production processess in a most detailed way as cost structure of imported products may be unknown. Otherwise, when raw materials or composite materials are imported, more attention should be paid on energy consumption in the total input.

## 2.3. Structural changes in energy sector

In order to analyse structural changes in energy sector (shift from natural gas to biomass in district heating) actual Lithuanian input-output table has been compared with corrected one. This input-output table represents situation after structural change. In order to reflect it some changes in Lithuanian input-output table have been made. First of all, some fictitious sectors have been added to the input-output table as structure of currently existing sectors does not reflect cost structure of biofuel and equipment production precise enough. Fictitious sector could be defined as a sector that does not exist in reality and in statistical classifications. It is created for purposes of the particular analysis and consists of certain elements of the real sectors, but has peculiar structure.

In the Table 2 percentage cost structure of the fictitious biofuel production sector is presented. It shows its linkages to other real sectors as well, because output of this fictitious sector is only used in energy sector. Assumptions about cost structure have been accepted considering information received during discussions with representatives from biomass supplying association.

Table 2. Structural decomposition of the fictitious biofuel production sector

| **Sector code** | **Short name** | **Percentage cost structure** |
|---|---|---|
| 02 | Forest | 70 |
| 20 | Wood | 21 |
| 60 | Land transport | 9 |
| Total | | 100 |

The cost structure of machinery and equipment sector (29) is not fully acceptable for further analysis as import share is high, meanwhile it is expected that the main part of equipment for heat plants will be produced in Lithuania. Because of this reason a fictitious sector of heat plants equipment production has been created. It has been assumed that it has the same intermediate consumption structure as machinery and equipment sector (29) while imports only represent 10% of total input. This fictitious sector has been used to reflect an increase of investment into new equipment.

Secondly, figures in column of energy sector (40) have been adjusted in input-output table. The adjustments have expressed changes of the relationships between energy sector and other sectors which are inputs for energy sector. In order to identify amounts of changes two typical cases of heat production – biomass heat plants and natural gas heat plants – have been analysed. Initial data, calculation assumptions and results of simple calculations are presented in the Table 3.

Table 3. Comparison of technological alternatives

| | **Biomass heat plants** | **Natural gas heat plants** | **Difference** |
|---|---|---|---|
| Fuel | Biomass | Natural gas | |
| Investment cost Lt2005/kW | 1100 | 226 | 874.08 |
| Lifetime, year | 25 | 30 | -5.00 |
| Capacity, MW | 185 | 185 | 0.00 |
| Availability | 0.9 | 0.9 | 0.00 |
| Tmax (working time on maximal power) | 6000 | 6000 | 0.00 |
| Heat production, TWh | 1.00 | 1.00 | 0.00 |
| Amount of fuel used, ktoe | 84.96 | 94.49 | -9.52 |
| Fuel cost, million Lt2005 | **30.76** | **41.48** | -10.72 |
| Total fixed cost, million Lt2005 | 8.97 | 3.78 | **5.18** |
| Total variable cost, million Lt2005 | 6.29 | 3.81 | **2.49** |
| Depreciation, million Lt2005 | 8.15 | 1.39 | **6.75** |
| Total cost, million Lt2005 | 54.17 | 50.46 | 3.70 |

The second column of the Table 3, which is named as “Biomass heat plants”, reflects the new situation after shift to biofuel and the third column “Natural gas plants” describes current technology. It has been chosen a convenient amount of heat production (1 TWh), which makes extrapolation of the results very simple.

Underlined values are the basis for changes of Lithuanian Input-Output table. Naturally, a shift from biomass heat plants to natural gas heat plants has some impact on the cost structure of energy sector (40). Fuel cost of biomass heat plants has been added to energy sector column in the row “Fictitious biofuel production sector”. Thus, fuel cost of natural gas heat plants has been subtracted from value placed in row of sector which includes natural gas (11). Difference of total fixed and variable cost has been distributed to relevant sectors according to existing cost structure in the enterprises. Difference of depreciation has been added to the consumption of fixed capital in the energy sector (40). Furthermore, the value of depreciation cost has been distributed to three rows of the column “Gross fixed capital formation”.

An arguable question about the amount of money added to gross fixed capital formation has arisen. This column is part of final demand, therefore it has an influence on final results of the simulation. As analysis presented in this paper is static, it has been decided to use only part of total investment cost which is equal to one year depreciation. Equal to the total investment cost change in gross final consumption could affect economy (especially activities related to the new investment) in larger scale, but it would be non-recurring. This means that static analysis could show very big changes in the economy, which appears only for one year in reality. In contrast, approach used in this paper assumes gradually shift from one technology type to another and covers average long-term impact of bioenergy investment.

Input-output method allows to analyze not only changes in output or value added of particular sectors but other economic and ecological factors as well [11]. In order to demonstrate this, potential effects on employment have been calculated. Calculations have been based on relationships between sectorial outputs and figures of employed persons presented by Lithuanian Statistics.

## 3. RESULTS

### 3.1. Direct and indirect energy consumption

Large differences have been observed in energy consumption depending on different approaches mentioned in Chapter 2.1. Indirect energy consumption can make up to 16% of the total domestic input in the case of domestic production analysis. Results of calculations are presented in the Fig. 1.

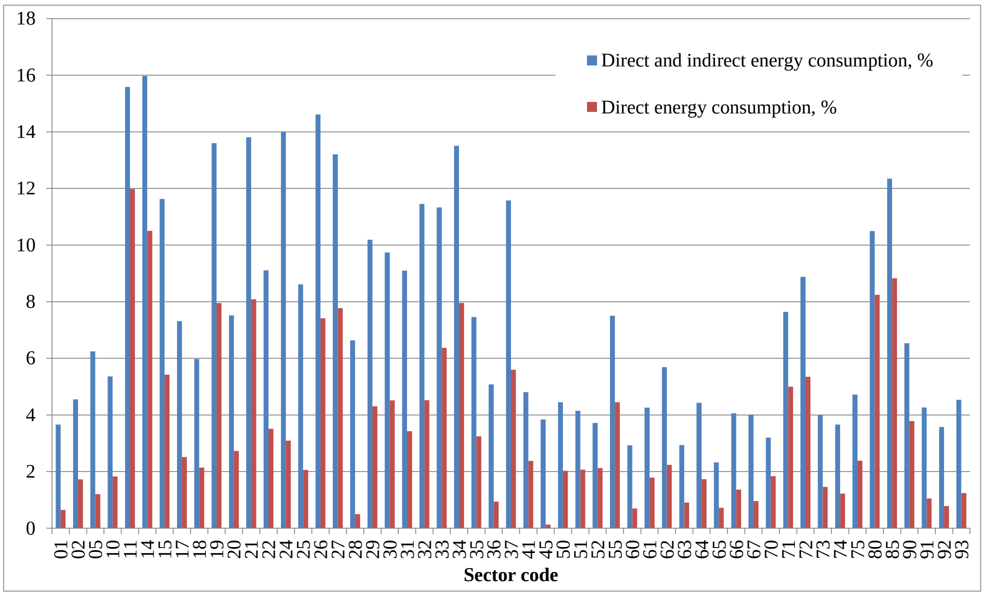

Fig. 1. Energy consumption in economic sectors as part of the total domestic input, %

Fig. 1 is useful for the analysis of products which could be produced from domestic materials. For example, direct energy consumption in the sector of food products and beverages (15) is 5.42% and total energy consumption is 11.62% of the total domestic output. Considering constant linear relationships mentioned in methodological part of this paper, it could be stated that a growth of energy prices by one percent could force food prices to grow up by 0.1162%.

Fig. 1 also shows that sector of chemical products, man-made fibres and coke, refined petroleum products including nuclear fuels (24) have the largest share of “hidden energy”. This situation can be explained by analyzing the main inputs of the sector. This sector uses raw materials (crude petroleum and natural gas) which are mainly imported. Because of this reason energy makes large share of the total intermediate input of sector crude petroleum and natural gas importing sector (11). This analysis shows that in this case approach of energy consumption in the total input should be used. This approach assumes that some share of products must be imported. Results of calculations are presented in the Fig. 2.

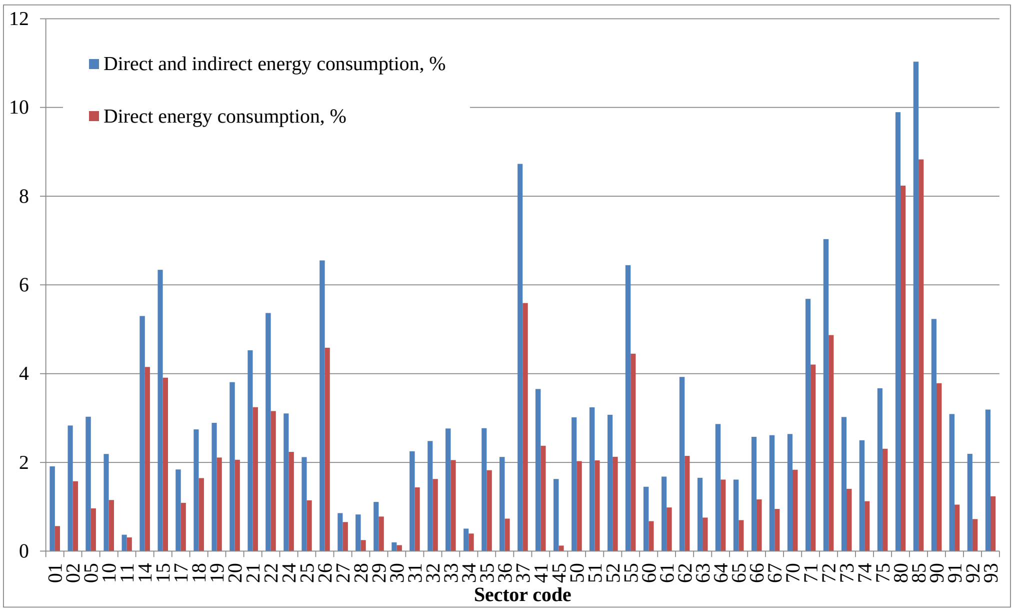

Fig. 2. Energy consumption in economic sectors as part of the total input, %

In this case “domestic sectors” especially related to services at some part supplied by governmental institutions (health and social work services (85), education services (80)) have the highest energy consumption level. In comparison to the previous case, energy consumption in import-based sectors makes smaller share. For example, previously discussed sector (24) in this case shows very moderate energy consumption.

### 3.2. Structural changes in energy sector

Results of simulation of structural changes in energy sector described as a change in heat production from biofuel in 1 TWh are presented in the Table 3.

The table shows that shift to biofuel use in district heating sector taking into account assumptions mentioned above could have a large negative impact on total output of natural gas sector (11). Negative impact on employment and value added in this sector could be very small because it is oriented to import and does not require large number of workers. Strong positive impact could be noticed on output of forestry (02), wood products (20), land transport (60), construction work (45), other business services (74). This shows that most of impacts are related to direct changes (i.e., change of fuel source). If it was assumed wider use of agricultural products (i.e., straw) in district heating sector, analysis would have showed much larger direct impact on agricultural sector (01). Nonetheless, some other indirect effect on value added and employment are observed and presented in the Table 3 as well.

Table 3. Results of analysis of shift to biomass in district heating

| Code of the sector | Effect on total output | Effect on value added, million Lt2005 | Effect on employment, pers. | Code of the sector | Effect on total output | Effect on value added, million Lt2005 | Effect on employment, pers. |
|---|---|---|---|---|---|---|---|
| 01 | 0.040 | 0.018 | 1 | 37 | 0.030 | 0.008 | 0 |
| 02 | 25.011 | 12.690 | 391 | 40 | 4.040 | 5.989 | 14 |
| 05 | 0.003 | 0.001 | 0 | 41 | 0.243 | 0.159 | 5 |
| 10 | 0.055 | 0.017 | 0 | 45 | 2.256 | 1.104 | 30 |
| 11 | -40.438 | -0.675 | -2 | 50 | 0.455 | 0.310 | 8 |
| 12 | 0.000 | 0.000 | 0 | 51 | 2.701 | 1.674 | 14 |
| 13 | 0.000 | 0.000 | 0 | 52 | 0.752 | 0.558 | 13 |
| 14 | 0.090 | 0.014 | 0 | 55 | 0.123 | 0.071 | 2 |
| 15 | 0.088 | 0.017 | 0 | 60 | 3.790 | 2.367 | 33 |
| 17 | 0.311 | 0.045 | 2 | 61 | 0.108 | 0.033 | 0 |
| 16 | 3.242 | 1.077 | 30 | 62 | 0.004 | 0.001 | 0 |
| 18 | 0.066 | 0.024 | 1 | 63 | 0.991 | 0.468 | 3 |
| 19 | 0.027 | 0.002 | 0 | 64 | 0.772 | 0.437 | 4 |
| 20 | 7.479 | 1.879 | 69 | 65 | 1.086 | 0.660 | 5 |
| 21 | 0.272 | 0.038 | 0 | 66 | 0.106 | 0.037 | 1 |
| 22 | 0.251 | 0.102 | 2 | 67 | 0.046 | 0.023 | 0 |
| 24 | 1.323 | 0.197 | 0 | 70 | 0.667 | 0.514 | 2 |
| 25 | 2.062 | 0.389 | 6 | 71 | 0.603 | 0.322 | 2 |
| 26 | 0.253 | 0.059 | 1 | 72 | 0.054 | 0.025 | 1 |
| 27 | 1.290 | 0.049 | 1 | 73 | 0.025 | 0.013 | 2 |
| 28 | 1.065 | 0.203 | 7 | 74 | 3.104 | 1.631 | 23 |
| 29 | 2.308 | 0.154 | 4 | 75 | 0.061 | 0.035 | 1 |
| 30 | 0.097 | 0.001 | 0 | 80 | 0.095 | 0.074 | 3 |
| 31 | 0.602 | 0.096 | 2 | 85 | 0.010 | 0.006 | 0 |
| 32 | 0.172 | 0.017 | 1 | 90 | 0.168 | 0.106 | 2 |
| 33 | 0.400 | 0.058 | 2 | 91 | 0.035 | 0.010 | 1 |
| 34 | 0.444 | 0.009 | 0 | 92 | 0.075 | 0.036 | 1 |
| 35 | 0.081 | 0.022 | 0 | 93 | 0.102 | 0.044 | 2 |
| 36 | 0.400 | 0.133 | 3 | **Total effects:** | **29.494** | **33.351** | **699** |

Positive impact on retail (50) and wholesale (51) trade sectors could be considered as an example of indirect benefits that are determined by wider use of biofuel in district heating sector.

## 4. CONCLUSIONS

Input-Output analysis is a useful tool for evaluation of economic impacts of various changes in energy and other economic sectors. Nonetheless, it has serious shortcomings, mainly related to its unflexibility and incapability to reflect complicated non-linear relations.

Analysis of direct and indirect energy consumption should take into account what part and which type of products is imported. If particular sector imports final production, it is reasonable to analyse energy consumption in the domestic production. Otherwise, when raw materials or composite materials are imported, more attention should be paid on energy consumption in the total input.

It has been found out that food products, products of some industries and health, social work and education services have the largest ”energy content” (direct and indirect energy consumption).

Shifting to wider biofuel usage could be useful for Lithuanian economy, since 1 TWh of “green” heat could give growth of the total value added by 33.35 million $\mathrm{Lt}_{2005}$ and create almost seven hundred work places.

## REFERENCES

1. Statistikos departamentas prie Lietuvos Respublikos Vyriausybės, *Lietuvos sąnaudų ir produkcijos lentelės 2005*. 2009, Vilnius: Statistikos departamentas prie Lietuvos Respublikos Vyriausybės.
2. MILLER, R.E. and P.D. BLAIR, *Input–Output Analysis: Foundations and Extensions*. Second edition ed. 2009, Cambridge: Cambridge University Press.
3. KARKACIER, O. and Z. GOKALPGOKTOLGA, *Input-output analysis of energy use in agriculture*. Energy Conversion and Management, 2005. 46(9-10): p. 1513–1521.
4. MARTINEZ, J.C.C., *Quantification of the Socio-economic Effects of Renewable Energy Technologies in Southern Mediterranean Countries: an Input-Output Evaluation*. 1998.
5. AKHABBAR, A., et al., *Input-Output in Europe: Trends in Research and Application*. 2011, Munich Personal RePEc Archive.
6. AMADOR, J., *Energy content in manufacturing exports: A cross-country analysis*. Working Papers. Vol. 10/11. 2011, Lisbon: Banco de Portugal.
7. LIU, H.-T., et al., *Comprehensive evaluation of household indirect energy consumption and impacts of alternative energy policies in China by input–output analysis*. Energy Policy, 2009. 37(8): p. 3194–3204.
8. PARK, H. and E. HEO, *The direct and indirect household energy requirements in the Republic of Korea from 1980 to 2000—An input–output analysis*. Energy Policy, 2007. 35(5): p. 2839–2851.
9. PACHAURI, S. and D. SPRENG, *Direct and indirect energy requirements of households in India*. Energy Policy, 2002. 30(6): p. 511–523.
10. MU, T., Q. XIA, and C. KANG, *Input-output table of electricity demand and its application*. Energy, 2010. 35(1): p. 326-331.
11. *Handbook of Input-Output Economics in Industrial Ecology*, ed. S. Suh. Vol. 23. 2009: Springer Netherlands.

## APPENDIX 1. CLASSIFICATION OF PRODUCTS (SECTORS) IN THE ANALYSIS

| Code | Product |
|---|---|
| 01 | Products of agriculture, hunting and related services |
| 02 | Products of forestry, logging and related services |
| 05 | Fish and other fishing products; services incidental of fishing |
| 10 | Coal and lignite; peat |
| 11 | Crude petroleum and natural gas; services incidental to oil and gas extraction excluding surveying |
| 12 | Uranium and thorium ores |
| 13 | Metal ores |
| 14 | Other mining and quarrying products |
| 15 | Food products and beverages; Tobacco products |
| 17 | Textiles |
| 18 | Wearing apparel; furs |
| 19 | Leather and leather products |
| 20 | Wood and products of wood and cork (except furniture); articles of straw and plaiting materials |
| 21 | Pulp, paper and paper products |
| 22 | Printed matter and recorded media |
| 24 | Chemicals, chemical products and man-made fibres; Coke, refined petroleum products and nuclear fuels |
| 25 | Rubber and plastic products |
| 26 | Other non-metallic mineral products |
| 27 | Basic metals |
| 28 | Fabricated metal products, except machinery and equipment |
| 29 | Machinery and equipment n.e.c. |
| 30 | Office machinery and computers |
| 31 | Electrical machinery and apparatus n.e.c. |
| 32 | Radio, television and communication equipment and apparatus |
| 33 | Medical, precision and optical instruments, watches and clocks |
| 34 | Motor vehicles, trailers and semi-trailers |
| 35 | Other transport equipment |
| 36 | Furniture; other manufactured goods n.e.c. |
| 37 | Secondary raw materials |
| 40 | Electrical energy, gas, steam and hot water |
| 41 | Collected and purified water, distribution services of water |
| 45 | Construction work |
| 50 | Trade, maintenance and repair services of motor vehicles and motorcycles; retail sale of automotive fuel |
| 51 | Wholesale trade and commission trade services, except of motor vehicles and motorcycles |
| 52 | Retail trade services, except of motor vehicles and motorcycles; repair services of personal and household goods |
| 55 | Hotel and restaurant services |
| 60 | Land transport; transport via pipeline services |
| 61 | Water transport services |
| 62 | Air transport services |
| 63 | Supporting and auxiliary transport services; travel agency services |

| Code | Product |
|---|---|
| 64 | Post and telecommunication services |
| 65 | Financial intermediation services, except insurance and pension funding services |
| 66 | Insurance and pension funding services, except compulsory social security services |
| 67 | Services auxiliary to financial intermediation |
| 70 | Real estate services |
| 71 | Renting services of machinery and equipment without operator and of personal and household goods |
| 72 | Computer and related services |
| 73 | Research and development services |
| 74 | Other business services |
| 75 | Public administration and defence services; compulsory social security services |
| 80 | Education services |
| 85 | Health and social work services |
| 90 | Sewage and refuse disposal services, sanitation and similar services |
| 91 | Membership organisation services n.e.c. |
| 92 | Recreational, cultural and sporting services |
| 93 | Other services |
| 95 | Private households with employed persons |

CYSENI 2011, May 26–27, Kaunas, Lithuania
ISSN 1822-7554, www.cyseni.com

# THE INFLUENCE OF ENERGY SUPPLY DISTURBANCES TO ENERGY SYSTEM

**L. Martišauskas, J. Augutis**
*Lithuanian Energy Institute*
*Laboratory of Nuclear Installation Safety*
*Breslaujos str. 3, LT-44403, Kaunas – Lithuania*
*Phone: +370 37 401938, +370 37 401973*
*Email: linasm@mail.lei.lt , juozas@mail.lei.lt*

**J. Augutis**
*Vytautas Magnus University*
*K. Donelaičio str. 58, LT-44248, Kaunas – Lithuania*
*Phone +370 37 203775*
*Email: j.augutis@adm.vdu.lt*

## ABSTRACT

Energy plays an important role in the national security of any given country as a fuel to power the economic engine. Hence threats to energy security can also result from physical damage to the energy infrastructure either of the supplier, or of the importer as a result of natural events, misfortune, terrorism or warfare. The political and economic instability caused by war or other factors such as strike action can also prevent the proper functioning of the energy industry in a supplier country. All mentioned threats could cause energy supply disturbances affecting the whole energy system and infrastructure.

The paper examines the influence of energy supply disturbances to energy system. A single integrated mathematical framework of the whole energy system comprising electricity, gas, and heat networks is formulated using a network flow concept. The mathematical model of energy system as a network defined by a collection of nodes and arcs with energy flowing from node to node along paths in the network and energy supply disturbances affecting this network is proposed. The paper focuses on three elements: energy supply (production), generation, and consumption. The influence of disturbances to energy system is analysed in respect of fuel accessibility, price changes of fuel, and energy, available generation capacity, meeting the demand of consumers. A numerical example of pilot case is presented to highlight the benefits of the methodology and illustrate how energy supply disturbances influence the network of energy system.

Keywords: energy security, energy systems, mathematical modelling, energy supply disturbances

## 1. INTRODUCTION

There are numerous definitions of what constitutes energy supply security, depending on national or regional circumstances. The International Atomic Energy Agency (IAEA) experts in the reference [1] as goals of energy security include one or more of the following elements: adequate supply to meet basic needs and development aspirations, self-sufficiency, protection against supply disruptions and price volatility, physical plant and infrastructure reliability, diversity of technologies and sources, threats to and/or from neighbouring states, energy markets that function well, economic sustainability of supply (profitability), and environmental benignity. EU Standards for Energy Security of Supply [2] refers the importance of energy supply security risks. The supply shortage or disruption (in presented methodology defined as disturbance) affects the energy consumers that were supposed to receive the supplies. From the consumer's point of view it is less relevant what causes the supply shortage or disruption and which part in the energy supply chain is giving the trouble. The standards [2] security of supply risks points out in the short term and the long term. A sudden shortage in energy supply or disruption can be overcome by measures such as emergency stocks, fuel switching, demand rationing, and reserve capacities. The probability of an energy supply risk and the impact on economy and society depends to a large extent on the structure of the energy system (fuel mix, origin of primary energy sources, energy transport infrastructure, conversions into secondary energy, energy demand, etc.). Changes in the energy system structure will influence country's security of supply risk, i.e. in the future the probability and impact of a sudden shortage can be different from today.

Mentioned reviews indicate the importance of sustainable functioning of energy system when analysing the security of energy supply. The disturbances make it vulnerable, so it is important not only to simulate the functioning of energy system, but also to evaluate its vulnerability to the potential disturbances of the energy supply caused by internal or external events. The paper is dealing with this problem as well.

There are some optimization modelling tools for the analysis of energy system functioning and development. Few well-known optimization modelling tools such as EFOM (Energy Flow Optimisation Model) and MARKAL (MARKet Allocation) [3] are more convenient for the analysis of the national energy systems. BALMOREL (Baltic Model of Regional Energy Market Liberalisation) is a model for analysing the electricity and combined heat and power sectors in the international perspective [4]. BALMOREL is developed in the GAMS language, and the source code is readily available, thus providing complete documentation of the functionalities. Moreover, the user may modify the model according to specific requirements, making the model suited for any purpose within the focus parts of the energy system. MESSAGE (Model for Energy Supply Strategy Alternatives and their General Environmental Impacts) is designed to formulate and evaluate alternative energy supply strategies consonant with user defined constraints on new investment, market penetration rates for new technologies, fuel availability and trade, and environmental emissions [5].

However all of the described tools directly are not adapted to evaluate potential disturbance affect to the energy system. If the modelled energy system is unable to satisfy the given demand, then this problem in all mentioned tools is infeasible. The main objective of the proposed methodology is to develop such mathematical models that would allow not only to simulate operation of the energy system (simplified in most cases), but would be able to assess the influence of the disturbances affecting energy supply indicating the level of unserved demand or the percentage of unsatisfied consumers and what consequences this might cause. Consequences of the supply disturbance defined in the model are technical, economical and socio-political, but are not analysed in more detail. In the future researches we are not discounting the possibility to evaluate the whole energy system with one or more modelling tools mentioned before, but it would constitute only one segment of the model. The next segment would include the proposed methodology of analysing disturbances effect to the energy system. The complete model would allow analysing the performance of entire energy system in terms of energy supply security.

## 2. PROBABILISTIC MODEL OF ENERGY SUPPLY DISTURBANCES

The importance, concept, parameters, and types of energy supply disturbances have been demonstrated by Augutis et al. [6, 7]. The disturbances of energy supply that may result from both external and domestic events create a threat for whole energy system. This paper focuses on both types of energy supply disturbances: external and internal.

The disturbances of energy supply are characterized in various parameters. The values of disturbance parameters and its degrees of severity vary depending on the energy system, i.e. values of parameters can be different in separate energy system e.g. supplied or produced fuel or primary energy resources usually are different in various countries.

The concept of basic scenario, that is needed to describe disturbance parameters, has been determined in the previous papers [6].

### 2.1. Parameters of external disturbances of energy supply

This type of energy supply disturbances is more concerned with the supply of fuel or primary energy resources to energy system. They mainly include the fuel accessibility and price changes that is why the fuel type or primary energy resource of restricted supply is one of the energy supply disturbance parameter. Let's denote it as $\varphi_i$, $i = 1,2,\ldots,N_\varphi$, where $N_\varphi$ – number of fuel types.

Primary energy is understandable as energy found in nature that has not been subjected to any conversion or transformation process. It is energy contained in raw fuels as well as other forms of energy received as input to a system [8].

There are three distinct groups of primary energy resources: fossil fuels (coal, oil, natural gas, etc.), nuclear power (fission and fusion), and renewable energy (hydropower, biomass, wind power, solar power, geothermal, wave, and tidal power).

These three groups of primary energy resources compose any of energy system in general. Primary energy is transformed in energy conversion processes to more convenient forms of energy, such as electrical energy, refined fuels, or synthetic fuels such as hydrogen. In energy statistics these forms are called secondary energy.

One of the most important parameter describing the disturbance of energy supply is a part of primary energy supply deviation in percent from basic supply scenario. For each type of primary energy potential supply reduction is from 0 to 100 percent compared with the supply amounts of the basic scenario in the appropriate period. Let's denote $\delta_i$ – a part of energy supply deviation of basic supply scenario, where $i = 1,2,\ldots,N_\delta$ and $N_\delta$ – number of parameter values.

Another important parameter of energy supply disturbances is duration of primary energy resources or fuel supply disruption. This parameter indicates the continuation of energy supply disturbance. Denote this parameter as $t_i$, where $0 \le t_i < \infty$, $i = 1,2,\ldots,N_t$ and $N_t$ is a number of parameter values.

The next parameter is the fuel or primary energy price deviation from projected price in the basic scenario. Duration of price deviation is expected from the previous energy supply disturbance parameter. Denote this parameter as $\sigma_i$, where $i = 1,2,\ldots,N_\sigma$ and $N_\sigma$ is a number of parameter values.

The last parameter is the starting moment of disturbance. This parameter is important for installation of new technologies, such as construction of new power plants, networks, or grid connections, the connection of new consumers, etc. Summary of energy supply external disturbance parameters is presented in Table 1.

Table 1. Summary of energy supply external disturbance parameters

| Parameter | Notation |
|---|---|
| Fuel type or primary energy resource of restricted supply | $\varphi$ |
| Part of primary energy supply deviation in percent from basic supply scenario | $\delta$ |
| Duration of primary energy resources or fuel supply disruption | $t$ |
| Fuel or primary energy price deviation from projected price in the basic scenario | $\sigma$ |
| Starting moment of disturbance | $\tau$ |

Determining the probabilities of parameter values the real situation of the particular analysed energy system should be taken into account: for example, the probability of natural gas supply restriction is higher than the oil or its products supply restriction to Lithuania, because the reasons of supply restriction are very similar for both fuel types, but the oil supply is possible from the various global markets through Butinge terminal, while the natural gas can be supplied almost exclusively from Russia. Energy resource supply may be disrupted for some time due to technical or natural accidents also.

Some parameters are distributed by the probability distributions and probability distribution function $F(x)$ of these parameters should be defined.

### 2.2. Parameters of internal disturbances of energy supply

This type of energy supply disturbances is related to reliability characteristics. Such disturbances are more of technical nature that occurs within the energy system.

Parameters of internal disturbance of energy supply are the starting moment of disturbance, duration ($t$) and reliability factor in this methodology expressed as availability ($\lambda$). The first two parameters are widely described in the subsection 2.1. The third parameter is associated with the generators and supply networks. It indicates their reliability parameters. Availability parameter shows the maximum share of generator or network capacity available at the disturbance moment. Due to this parameter $\lambda$ has limits: $0 \le \lambda \le 1$. If $\lambda = 0$, then the generator or some network chain is unavailable at the disturbance moment and if $\lambda = 1$, then aforesaid is operating in the normal conditions without any disruptions or failures.

Internal and external disturbances of energy supply are independent, e.g. natural gas supply restriction due to the political decisions is not dependent on the random failure of generating unit. However, internal and external disturbances can occur at the same time and worsen the situation in the rare cases.

### 2.3. Stochastic treatment of energy supply disturbances

The disturbances of energy supply are characterized as a stochastic (random) process $X = \{X(t), t \in T\}$ within or outside the energy system. Realization $x(t)$ is the individual disturbance of energy supply with particular set of parameters at the time moment $t$, where $T$ is the set of time moments $t$. Random vector $(X(t_1), X(t_2), \ldots, X(t_n))$ of energy supply disturbances has the probability distribution. The disturbance turns into realization with the probability of this distribution according to probabilistic distribution of this vector. A set of various energy supply disturbances is obtained from this probability distribution. Probabilistic distributions of disturbance parameter are necessary to evaluate probability of disturbance occurrence. These probabilistic distributions should be assessed by experts and/or obtained from available statistical data.

## 3. MATHEMATICAL FRAMEWORK OF THE ENERGY SYSTEM

The methodology proposes the energy system modelling that includes three types of energy networks – electricity, district heating, and natural gas. The energy networks are described as interconnected graph – the system of nodes and arcs, with energy flowing from node to node along paths in the network. Such structure is a convenient form to use the network flow approach [9, 10]. Arcs in the system represent physical networks (pipelines, cables, air lines, etc.) and their components. Nodes have several functions in the system and are divided into three types – supply (production), generation, and consumption (more about functions of nodes are described in the 3.1 subsection). Nodes correspond to energy supply, generation technologies, storage elements, consumers, and demand. The total interconnected energy system composed of the networks of different energy types proposes Supply – Generation – Consumption approach.

### 3.1. Nodes of the energy network

Two types of node sets are used in the mathematical model of energy system. The first one includes three sets that define the type of energy flowing or transported in the network: electricity, heat, or gas. However, the same node may be included in the different sets of the first type of nodes. Node, that is common to several networks, has related to its energy conversion technology. The same node may be associated with multiple technologies simultaneously. Furthermore, any node in the model can be linked to energy import, generation, storage, and consumption technologies. Therefore it is needed to define the second type of node sets. The following types are used:

1) **The set of supply nodes** includes energy or fuel extraction plants (coal mines, gas wells, etc.), storages of coal, gas, or other type of energy. The imported energy is defined in this set of nodes also. Generally it is set of nodes supplying energy or primary energy resources for energy conversion or generation processes.

The most important parameters of this type set of nodes are quantities of fuel or primary energy supply, imported energy, and storage capacity over the time. The costs of fuel are significant parameters as well.

2) **The set of generation nodes** includes energy conversion or generation technologies (mostly power plants like hydro or pumped storage, nuclear power, CHP, etc.).

Parameters involve power plant characteristics that is necessary for this type of nodes: type, minimal and maximal capacities, efficiency, availability, fuel type, quantity of generated electric power per hour (MWh, for example), and ratio of generating heat and electricity (if it is CHP unit) of power plant. Some characteristics will depend on the season of the year and may vary over the time.

3) **The set of consumption nodes** includes the demand centers in the regions and is characterized as the needs of consumers. Generally this set of nodes involves the end users. The most important parameter is the energy demand of the consumers in the regions over the time.

An unlimited amount of nodes, associated with the producers and consumers, can exist in each region. The end users can be electricity, heat, and gas consumers. Generation technology that uses natural gas from the network and heat pumps using electricity from the network are not considered as end users. It should be noted that both types of node sets may be overlapping.

### 3.2. Arcs of the energy network

Flows between network nodes are distributed by arcs connecting the network nodes. The type of arc sets depends on the energy type, flowing in the arc from one node to other. Arcs represent the transmission and distribution lines in the electricity sector; pipelines and other transportation forms in the sectors of heat and gas.

### 3.3. Mathematical model formulation

#### *3.3.1. Network flow approach*

The energy networks are described as interconnected graph – the system of nodes and arcs, with energy flowing from node to node along paths in the network. Such structure is a convenient form to use the network flow approach. Networks are usually modelled as graphs, including the set of nodes $M$ and the set of arcs $L$ connecting the network nodes. For any node $i \in M$ in the network, the sum of all arc outflows from this node must be equal to the power inflow to node $i$:

$$\sum_{i\in M} F_i^{in} - \sum_{i\in M} F_i^{out} = 0 . \tag{1}$$

The flow from one node to other can be transmitted in both directions, i.e. from node *i* to node *j* and vice versa, from node *j* to node *i*. However, parameters of different direction flows may differ. The result of this leads to the situation of two cases: first, when parameters of the arc $(i,j)$ are identical to the parameters of opposite direction arc $(j,i)$. Second, parameters are different for both flow directions.

In the first case, when parameters of the arc $(i,j)$ are identical to the parameters of the arc $(j,i)$ and when network links are assumed to transmit energy without losses, flows are equal on either side:

$$F_{ij} = -F_{ji} ,\ \forall i,j \in M . \tag{2}$$

Energy losses on arcs can be considered as the difference between inflow and outflow:

$$F_j^{in} = F_j^{out} + \Delta F_{ij} ,\ \forall i,j \in M . \tag{3}$$

Due to losses in the arc $(i,j)$ inequality $F_j^{in} \geq F_j^{out}$ is satisfied. If $\eta_{ij}$ $(0 \leq \eta_{ij} \leq 1)$ are losses in the arc $(i,j)$, then $F_j^{out} = \eta_{ij} F_j^{in}$, because losses in the arc are estimated in the location of inflow to node *j*. If there are no losses in the arc $(i,j)$ equality $\eta_{ij} = 1$ is correct.

The efficiency $\eta_{ij}$ indicates the share of energy is transmitted from node i to node j.
For the case of no physical connection between two nodes *i* and *j* efficiency $\eta_{ij} = 0$:

$$\forall F_{ij} = 0 \Rightarrow \eta_{ij} = 0 . \tag{4}$$

Network arc can be expressed as function of the flows. For example, each arc can be characterized by its transportation cost including cost of investment, capital, maintenance, operation, etc.

A vector of all energy type flows is defined:

$$F_{ij} = \begin{pmatrix} F_{ij,\alpha} & \ldots & F_{ij,\omega} \end{pmatrix}^T ,\quad \forall i,j \in M . \tag{5}$$

For ease of application vector (5) can be identified for each energy type $\alpha$, thus obtaining a number of vectors that reflect a different energy type:

$$F_{ij}^{\alpha} = \begin{pmatrix} F_{1j}^{\alpha} & F_{2j}^{\alpha} & \ldots & F_{ij}^{\alpha} \end{pmatrix}^T ,\quad \forall i,j \in M, \forall \alpha \in E . \tag{6}$$

The number of these vectors is equal to the number of energy types in the network.

Network flows between the network nodes may have certain constraints, i.e. the network arcs have capacities. This parameter is included in the model as two values: lower $F_{ij}^{\min}$ and upper $F_{ij}^{\max}$ bounds on the flow. Then the inequality should be satisfied:

$$0 \leq F_{ij}^{\min} \leq F_{ij} \leq F_{ij}^{\max} ,\ \forall i,j \in M . \tag{7}$$

Each node can be associated with more than one arc. The incoming flows to the node can be more than one as well. The sums of all inflows and outflows should be defined to meet the total power flow into each node of the network.

The sum of all inflows $F_i^{in}$ of one energy type into the node *i* is equal to the total incoming power $G_i^{in}$ to the node *i* of that energy form:

$$G_i^{in} = \sum_{\forall i \in M} F_i^{in} . \tag{8}$$

The sum of all outflows $F_i^{out}$ of one energy type from the node *i* is equal to the total outcoming power $G_i^{out}$ (which is satisfying demand or is transmitted to the other network nodes) from the node *i* of that energy form:

$$G_i^{out} = \sum_{\forall i \in M} F_i^{out} . \tag{9}$$

In order to determine the connections between each node and arc of the network, the node connection matrix *A* of size $N_M \times N_M$ is defined:

$$A = \begin{pmatrix} a_{11} & a_{12} & \cdots & a_{1N_M} \\ a_{21} & a_{22} & \cdots & a_{2N_M} \\ \vdots & \vdots & \ddots & \vdots \\ a_{N_M 1} & a_{N_M 2} & \cdots & a_{N_M N_M} \end{pmatrix}, \tag{10}$$

where elements of this matrix are:

$$a_{ij} = \begin{cases} 1, & if \ (i, j) \in L, \\ 0, & if \ (i, j) \notin L. \end{cases} \tag{11}$$

If $a_{ij} = 1$, it means that the flow from the node *i* to the node *j* in the arc $(i, j)$ exists. If $a_{ij} = 0$, then there is no physical connection between the nodes *i* and *j* in the network. Since the node to itself has no flow, then $a_{ij} = 0$, when $i = j$. Hence the diagonal elements of the node connection matrix (10) are equal to zero.

Each row of matrix (10) indicates the outflows of each node outcoming from that node (when matrix element is equal to 1) and each matrix column indicates the inflows of each node incoming to that node (when matrix element is equal to 1).

The node connection matrix needs to include efficiency coefficients $\eta_{ij}$ when energy flows are with losses. Then the elements of the matrix (10) will be calculated as follows:

$$a_{ij} = \begin{cases} 1 \cdot \eta_{ij} = \eta_{ij}, & if \ (i, j) \in L, \\ 0 \cdot \eta_{ij} = 0, & if \ (i, j) \notin L. \end{cases} \tag{12}$$

The final expression of the node connection matrix is obtained:

$$A_{ij} = \begin{pmatrix} 0 & a_{12} & \cdots & a_{1N_M} \\ a_{21} & 0 & \cdots & a_{2N_M} \\ \vdots & \vdots & \ddots & \vdots \\ a_{N_M 1} & a_{N_M 2} & \cdots & 0 \end{pmatrix}, \tag{13}$$

where:

$$a_{ij} = \begin{cases} \eta_{ij}, & if \ (i, j) \in L, \\ 0, & if \ (i, j) \notin L. \end{cases} \tag{14}$$

Knowing the energy flows between the network nodes (the vector $F_{ij}^{\alpha}$ (6) for each energy type) and the node connection matrix, is a possibility to calculate the distribution of energy flows between the network nodes at time moment *t*. Then:

$$F^{\alpha}(t) = A_{ij}(t) \cdot F_{ij}^{\alpha}(t), \forall i, j \in M, \forall \alpha \in E, \forall t \in T. \tag{15}$$

Matrix $F^{\alpha}(t)$ shows the distribution of flows of energy type $\alpha$ in the network at time moment *t*.

### *3.3.2. Costs*

Every energy production or generation technology is characterized not only by technical parameters like fuel used, capacities, and availability, but also by investment, operating, and maintenance costs. Every arc includes operation and maintenance, investment, and transportation costs as well. The investment costs are estimated for a new generation technologies and arcs only. Let’s define $c_{ij}$ as a total cost per unit of the energy flowing from node *i* to node *j*. The total costs considered are the fuel production, transportation and storage costs, the energy conversion (electricity and heat generation) costs expressed as the operation and maintenance cost associated with energy generating units operations, and the energy transmission costs.

### 3.4. Optimization

There are a number of reasonable objectives that can be used for optimizing energy systems. Energy cost is probably the most common criterion employed in the operational optimization of energy systems. The goal of the network flow problem is to satisfy energy demands with available fuel supplies at the minimal total cost without violating the specified bounds. The formulated problem falls into the category of generalized minimum cost flow problem [9] and can be solved by applying some efficient algorithms [10].

In general considering not only a single time period of the energy system but multiple time periods $t \in \{1, 2, \ldots, N_t\}$ results in multi-period optimization. Some general problems of multi-period and continuous optimization can be found in [9] and [10].

## 4. DISTURBANCES AFFECTING THE ENERGY SYSTEM

From the security of energy supply point of view optimization of the energy system should not only confine to the costs, but also it should include vulnerability of the energy system expressed in the reliability and security terms. It directly leads to optimization with multiple objectives and can be performed by stating a composite objective function as a weighted linear combination of individual objectives. In this paper only objective function minimizing the total costs are used.

Which is why in the methodology we include the level of unserved demand $u(\alpha)$ and its costs $c^{u(\alpha)}$, where $\alpha \in E$. The unserved demand is possible due to the energy supply disturbances. The effect of supply disturbances to the energy system leads to unserved demand level and shows the percentage of consumers that are not satisfied with the energy needs. As a result the unserved demand criterion should be included in the optimization.

Mathematically, in this case the proposed model can be solved as an optimization model that can be formulated as follows:

$$\text{Minimize } \Psi = \sum_{t \in T} \sum_{(i,j) \in L} \sum_{\alpha \in E} \left( c_{ij}(\alpha, t) \cdot F_{ij}(\alpha, t) + c^{u}(\alpha, t) \cdot u(\alpha, t) \right) \tag{16}$$

subject to:

$$\sum_{i\in M} F_i^{in}(\alpha,t) - \sum_{i\in M} F_i^{in}(\alpha,t) = 0\,,\ \forall\alpha\in E\,,\ \forall t\in T\,, \tag{17}$$

$$F_{ij}^{\min} \le F_{ij}(t) \le F_{ij}^{\max}\,,\ \forall(i,j)\in L\,,\ \forall t\in T\,, \tag{18}$$

$$\sum_{\alpha\in E} F^{\alpha}(t) = \sum_{\alpha\in E}\sum_{t\in T} A_{ij}(t)\cdot F_{ij}^{\alpha}(t),\ \forall(i,j)\in L\,. \tag{19}$$

The main results should include the total electricity and heat generation capacities, demand, unserved demand, percentage of the unsatisfied consumers, fuel consumption, total investment, operational costs of the generation technologies and total costs of the energy system. Further section examines the numerical calculation of the pilot case and illustrates how energy supply disturbances influence the network of energy system.

## 5. NUMERICAL EXAMPLE AND RESULTS

Numerical example demonstrates application of the proposed methodology. Pilot case of an example, but not a real situation is analysed. All attention in the paper is paid to the methodology rather than numerical example and results.

Suppose an energy system composed of two areas or two cities. The first one operates three generating units: two combined heat and power (CHP) plants generating both electricity and heat and one biomass fired plant generating only electricity. One of CHP plant is oil fired and the other can use both oil and natural gas as a fuel. The second area operates three generating units also: CHP burning natural gas or oil, CHP burning natural gas, and power plant generating only electricity burning natural gas. All these units are satisfying heat demand of each area and general electricity demand. The data for the system are presented in Table 2. For simplicity we assume that the fuel costs are fixed. A single time step of 24 hours period for the entire energy system is considered.

Table 2. Data for numerical example

| **Area** | **Generation unit** | **Fuel** | **Maximum capacity (MW)** | **Fuel output** | **Average demand (MWh)** | |
|---|---|---|---|---|---|---|
| | | | | | Heat | Electricity |
| 1 | CHP plant (G1) | Natural gas | 1000 | 200 m$^3$ for 1 MWh | 14400 | 38400 |
| | | Oil | | 0.45 t for 1 MWh | | |
| | CHP plant (G2) | Oil | 400 | 0.4 t for 1 MWh | | |
| | Biomass fired plant (G3) | Biomass | 200 | 0.7 t or 1 MWh | | |
| 2 | CHP plant (G4) | Natural gas | 800 | 250 m$^3$ for 1 MWh | 9600 | |
| | | Oil | | 0.5 t for 1 MWh | | |
| | CHP plant (G5) | Natural gas | 300 | 180 m$^3$ for 1 MWh | | |
| | Natural gas fired plant (G6) | Natural gas | 300 | 180 m$^3$ for 1 MWh | | |

The fuel costs for simulated energy system are 500 € for 1 thousand m$^3$ of natural gas, 170 € for 1 tone of fuel oil, 50 € for 1 tone of biomass and all fuel costs are fixed.

The objective is to satisfy the demands at the minimum total operating costs, subjected to the conservation of energy constrains at all nodes ant the units' operating ranges.

### 5.1. Scenarios

Several scenarios were simulated to illustrate the influence of each energy supply disturbance to the energy system. Four scenarios were pointed out – base scenario, low disturbance, medium disturbance, and high disturbance. Assumptions for these scenarios are the following:

- Base scenario – normal operation of energy system, there are no limitations on the fuel transportation and energy losses are neglected;
- Low disturbance – assumptions as in the base scenario, but in this case natural gas costs increase 100% and fuel oil costs increase 50%;
- Medium disturbance – assumptions as in the base scenario, but in this case fuel oil supply is interrupted to 80% from consumption in the base scenario and it means that only 20% of required fuel is available. At the same time G1 unit (CHP plant in the first area) availability is 50%, i.e. it can operate only in a half of its capacity;
- High disturbance – assumptions as in the base scenario, but in this case natural gas and fuel oil supply is interrupted to 100% and 30% respectively from consumption in the base scenario and it means that 70% of required fuel oil is available and natural gas as a fuel is not available at this time moment. At the same time G4 unit (CHP plant in the second area) availability is 50%.

### 5.2. Results

All the results were obtained using the GAMS (General Algebraic Modelling System) software [11] specifically designed for modelling linear, nonlinear and mixed integer optimization problems. This system was used due to its integrated high-performance solvers for optimization and has high level modelling system for mathematical programming and optimization. GAMS is not a solution to solve security of energy supply tasks, but is very useful to solve optimization problems. User by itself should develop the model and implement in the system. The computing time is negligible for all cases that are analysed. Fig. 1 presents the total operating costs of each scenario.

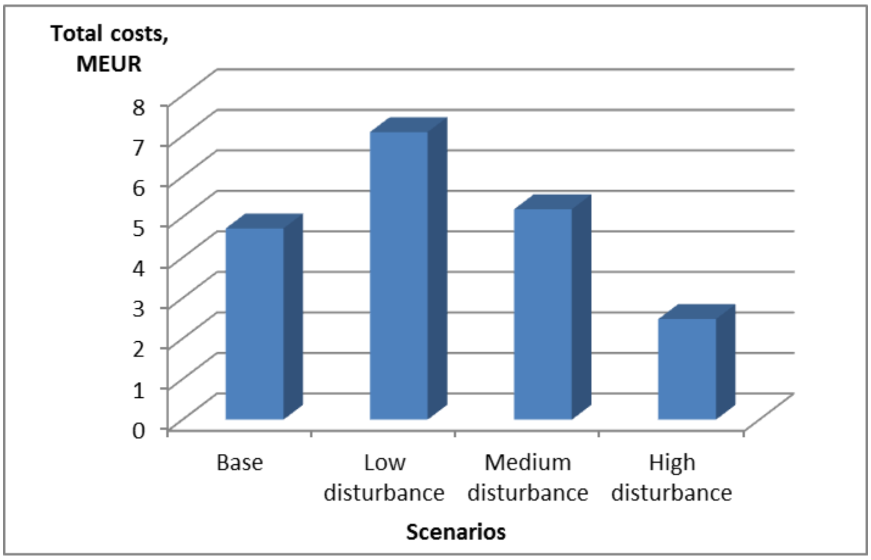

Fig. 1. The total operating costs of simulated scenarios

As it is shown in the Fig. 1, the total operating costs for all the scenarios are different. High costs of the low disturbance are due to the fuel costs increase in this scenario. However, in the medium and high disturbances we have got the total operating costs that are lower and this fact leads to the discussion. The result of these costs is that not all generating units were in operation in these scenarios due to occurred disturbances leading some generators to outages and the demand wasn't satisfied. If we will be able to assess the costs of unserved demand, than the costs of these two scenarios would be much higher.

Fig. 2 presents the served and unserved demands in each scenario. The base and low disturbance scenarios satisfy both heat and electricity demands but in different operating costs. In the other two scenarios due to energy supply disturbances generating units are not able to satisfy the total demand and some consumers leave without necessary amount of energy: in the medium disturbance scenario – 2% of heat and 25% of electricity end-users, in the high disturbance scenario – 12% of heat and 64% of electricity end-users are not satisfied. The total percent of unsatisfied consumers constitute 16% and 44% of medium and high disturbance scenarios respectively. The reasons of this are shortages of fuel and generating units capacity and non-existence of reserves. Results show vulnerability of the energy system in analysed scenarios.

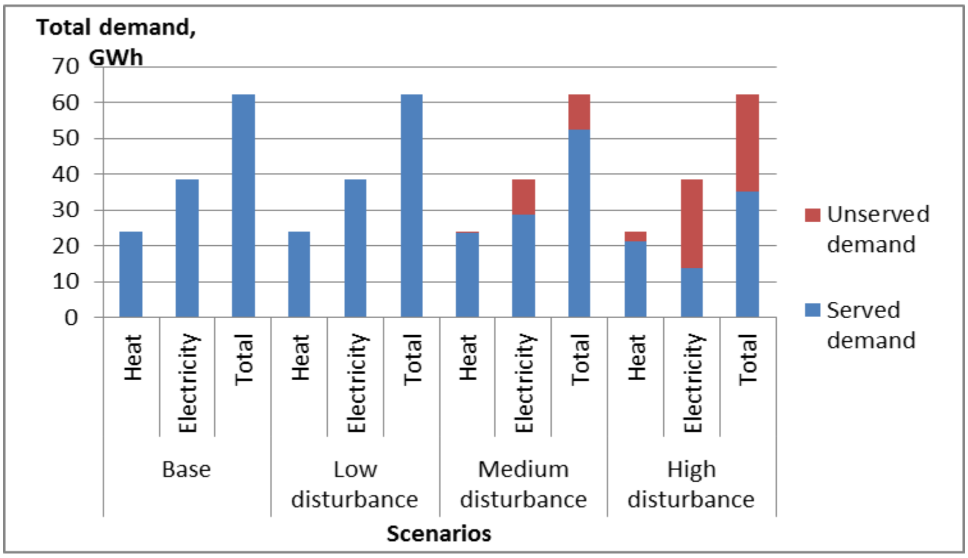

Fig. 2. Served and unserved demand of simulated scenarios

Fig. 3 presents the total generating capacity of each generating unit in all simulated scenarios.

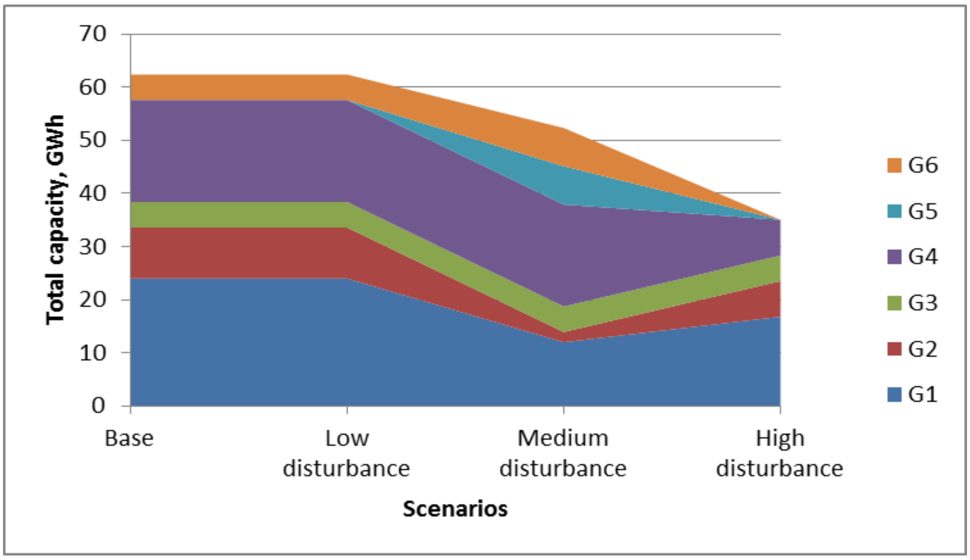

Fig. 3. Capacities of the generating units of simulated scenarios

As it is shown in the Fig. 3, the considerable share of generated energy is from the first and fourth generating units in all the scenarios. The biomass fired power plant generates consistent amount of energy in all the scenarios and disturbances are not affecting it. In the medium and high disturbance scenarios we can see the total amount of unsatisfied energy.

From these results we observe that in this numerical example only medium and high disturbances of energy supply can affect energy system considerably. Significant influence to the simulated energy system have fuel supply interruptions, especially when generating units are fired by one fuel type, and capacity shortages. The percent of interrupted fuel from projected consumption is very significant as well. If both internal and external disturbances occur at the same time period in the energy system, then this effect can cause significant unserved demand. But these conclusions can be done only to this energy system analysed by four scenarios. On purpose to analyse the real energy system lots of input parameters and statistical data are required and more scenarios should be simulated. Authors of the paper are not refusing this idea in the future researches.

From the energy supply security point of view vulnerability of the energy system highlights threats to the energy security. The weak points of the energy system can indicate some solutions to the decision makers: what should or could be done to improve energy security. To achieve this task the model should be extended including alternative or new generators, networks, storages, etc. and investment costs. Simulation should be done not only in a single, but in multiple time steps. The developed model is planned to be extended in the near future.

## 6. SUMMARY AND CONCLUSIONS

A single integrated mathematical framework was formulated in the paper. The model proposed can optimize operation of the energy system with energy supply disturbances affecting it. The theoretical case of the influence of energy supply disturbances to energy system was examined. A numerical example of pilot case was presented to highlight the benefits of the methodology and four scenarios were simulated. According to the obtained results some conclusions could be drawn:

1. Taking into account analysed scenarios only medium and high disturbances of energy supply can affect energy system considerably.
2. Most significant influence to the simulated energy system have fuel supply interruptions and capacity shortages.
3. The energy system becomes very vulnerable if both internal and external energy supply disturbances occur at the same time period. This effect causes significant unserved demand.
4. The developed methodology can be used to identify the weak points of the energy system and determine its vulnerability due to energy supply disturbances. This highlights threats to the energy security.

## REFERENCES

1. INTERNATINAL ATOMIC ENERGY AGENCY, Analyses of Energy Supply Options and Security of Energy Supply in the Baltic States. IAEA-TECDOC-1541, IAEA, Vienna, 2007.
2. SCHEEPERS, M., SEEBREGTS A., de JONG, J., MATERS, H. (2006): EU Standards for Energy Security of Supply, ECN-C-06-039/CIEP, ECN, Petten, the Netherlands.
3. *Energy Technology Systems Analysis Programme*. [referred on the 2nd of March 2011]. Link to the internet <http://www.etsap.org/Tools/MARKAL.htm>

4. RAVN, H.F., Balmorel: A Model for Analyses of The Electricity and CHP Markets in the Baltic Sea Region, 2001- [referred on the 2nd of March 2011]. Link to the internet <http://www.balmorel.com/>
5. *Model for Energy Supply Strategy Alternatives and their General Environmental Impacts (MESSAGE),* [referred on the 2nd of March 2011]. Link to the internet <http://www.iiasa.ac.at/Research/ECS/docs/models.html#MESSAGE>
6. AUGUTIS J., KRIKŠTOLAITIS R., MATUZIENĖ V., PEČIULYTĖ S. Assessment of Lithuanian power supply security depending on nuclear energy. *Safety and Security Engineering III.* Information and Communication Technologies, Vol. 108. WIT Press, Online ISSN 1743-3517, Print ISBN 1-84564-193-1. 2009, p. 235–247.
7. AUGUTIS, A., KRIKŠTOLAITIS, R., ŠIDLAUSKAS, K., MARTIŠAUSKAS, L., MATUZIENĖ, V. Modelling of energy supply disturbances in network systems // Reliability, risk and safety: theory and applications. London: Taylor & Francis Group, 2010. Vol. 3. ISBN 978-0-415-55509-8, p. 1035–1041.
8. KYDES, A., CUTLER, J. Primary energy, In: Encyclopaedia of Earth. Eds. Cutler J. Cleveland (Washington, D.C.: Environmental Information Coalition, National Council for Science and the Environment), 2007- [referred on the 2nd of March 2011]. Link to the internet <http://www.eoearth.org/article/Primary_energy>
9. AHUJA, R.K., MAGNANTI, T.L., ORLIN, J.B. *Network Flows*, Prentice-Hall, Inc., Englewood Cliffs, NJ, 1993.
10. BERTSEKAS, D.P., *Network Optimization: Continuous and Discrete Models*. Massachusetts Institute of Technology, ISBN 1-886529-02-7, 1998.
11. The General Algebraic Modeling System (GAMS), [referred on the 2nd of March 2011]. Link to the internet <http://www.gams.com/>

# ANALYSIS OF ENVIRONMENTAL IMPACT ASSESSMENT OF POWER ENERGY PROJECTS IN LATVIA

**J. Pubule, F. Romagonli, D. Blumberga**
*Riga Technical University*
*Institute of Energy Systems and Environment*
*Kronvalda bulvaris -1, LV-1010 Riga – Latvia*
*Phone +37129485141*
*Email: jelena.pubule@rtu.lv*

## ABSTRACT

Every industrial activity and procedure influences the environment and climate change: each to a lesser or greater extent. In Latvia, the Environmental Impact Assessment (EIA) procedure has been carried out for more than ten years and during these years impact assessments of many projects have been conducted. The main purpose of EIA is to assess the possible impact of the implementation of intended activities, or a planning document, on the environment and to consequently develop proposals for the prevention or decreasing of negative effects in order to avert violation of the requirements specified in regulatory enactments. Latvia is a country with limited resources. The development of the national economy is unthinkable without an increase in the production sector. In turn, the development of the production sector is connected with the intensification of production capacity and the resulting consequences – impact to environment. Power industry in Latvia has acquired a stable position in the national economy. Life Cycle Assessment (LCA) is a specific procedure for product or process impact assessment. LCA differs from EIA in its primary holistic approach that is referenced not on the evaluation of the impacts of a particular site or facility but on the entire environmental effects (direct and indirect) of a certain product or system among all their single life processes (cradle-to-grave thinking). The work concludes with the suggestions how to include principles of LCA in the EIA procedure for the improvement of the power energy projects impact assessment.

Keywords: energy projects, environmental impact assessment, climate change, life cycle assessment, sustainability.

## 1. INTRODUCTION

In order to satisfy increasing needs of humanity, increasingly more resources are being used, natural territories are being changed and natural balance among ecosystems is being broken. Interference in these natural processes enables changes in eco-systems and their transformation.

Nowadays, the concept of “natural environment” shall be considered utopian since the economic growth is inconceivable without development of national economy and industry. Thus, implementation of principles of sustainable development shall be one of the most significant expert tasks.

Currently, particular global attention, including Latvia, is being paid to two aspects of energy crisis – energy dependency and climate changes. Global experience has proven that with increase in consumption of energy, deficiency of energy occurs, and public officials consider increasing of import of energy resources rather than reduction of consumption, and this even more extends dependency of the state from the imported energy resources. At the same time, scientists work on research of alternative energy resources and development of new technologies.

Transfer from fossil fuel economy to economy of renewable energy sources (RES) is a complicated process, which requires a long term development strategy and serious attitude towards its implementation. It is complicated to think in long term, if one has to solve short term problem – increasing consumption of energy, and it is very tempting to solve the problem by moving the easiest way – importing more energy resources. More attention is paid to the short-term solution; less of it is paid to the problem in long-term run – use of RES.

Energy security sometimes has been explained by necessity to build new fossil fuel electric power stations, knowing in advance that it will be only a short-term solution. Seeming security is based on the opportunity to use natural gas from Russia with no justification of sustainability of natural gas sources. Another aspect of utilization of fossil fuel is related to the fact that no high efficiency power plants can be installed, which means that around a half of the valuable natural gas energy would be „thrown out" into the environment [1].

## 2. METHODOLOGY

Within the framework of this work, quantitative and qualitative analysis of existing projects in the area of power industry, for which environmental impact assessment has been prepared, is performed. The work identifies qualitative and quantitative indicators of materiality of effect.

## 3. ROLE AND TASKS OF ENVIRONMENTAL IMPACT ASSESSMENT

Environmental impact assessment is one of tools, which may be used for facilitation of sustainable development of a state.

EIA is focused on implementation of preventive means, since aim of the environmental impact assessment is identification of possible risks and effect as early as possible. Environmental impact assessment provides opportunity to consider potential effects of the designed activity and consider any alternatives in project implementation from different aspects. It aims to identify potential environmental, social and health aspects of the designed activity [2].

Considering that assessment of environmental impact is inter-disciplinary, and it aims by objective consideration to assess benefits and damage, which will be caused by implementation of the project, and to provide decision makers with comprehensive information on possible effects, we may conclude that implementation of environment-relieving measures shall be considered as a complex of measures, which facilitates sustainable development [3].

European and Latvian laws and regulations provide that prior to implementation of projects, which may cause significant environmental impact, environmental impact assessment must be carried out. Environmental impact assessment in Latvia is being performed already for several decades and it allowed reduction of negative effect by the designed activities. There is a system elaborated in Latvia, which established procedure of environmental impact assessment, though, no significant improvements have been made during recent years.

Environmental impact assessment aims not to prohibit performance of polluting activity, but to reduce and eliminate adverse environmental effect caused due to activities by physical and legal entities. As we all know, any action can have both positive and negative consequences. Purpose of environmental impact assessment is to identify possible consequences, and, after careful analysis of such consequences, to consider, if the designed activity shall be implemented, under what conditions and where it shall be implemented.

Thus, considering the procedure of environmental impact assessment, it shall be noted that environmental effect caused by various actions is very diverse both in terms of risk and scale of such effect, and not all activities require performance of environmental impact assessment. Formalizing and simplifying assessment of various activities, they may fall into three groups or three different levels:

1. Activities with insignificant effect, which in no case can cause long-term adverse effect on environment and/or human health, and as such, they require no EIA procedure.
2. Activities, which may cause adverse effect on environment and/or human health, and risk of their impact depends on the implementation of the activity in the chosen site or the applied technology. In this case, initial assessment of potential impact shall be required, and, on the basis of such assessment, decision shall be made, whether application of complete procedure of environmental impact assessment is required.
3. Activities with significant effect on environment and/or human health, to which, in any case, complete procedure of environmental impact assessment shall be applied [3].

Aim of the environmental impact assessment procedure shall not be to suspend or hinder development of national economy and industry in the state; it aims to encourage the use of environmentally friendly technologies, reasonable exploitation of resources, etc.

Environmental impact assessment procedure is expensive, time and work consuming process, thus, it shall be applied for objects of more significant impact or possible cumulative effects. Shall the initial environmental impact assessment prove that environmental impact by the designed activities is insignificant, or the proposed technological solutions and choice of site are optimal, to ensure maximum reduction of environmental impact, and implementation of the designed activities will not cause any social protests, decision on non-application of complete procedure of environmental impact assessment and issuance of technical regulations may be taken. At the same time, in some cases instead of complete procedure of environmental impact assessment, an assessment of possible effect on individual environmental components may be required, which may cause collecting, summarizing and assessment of additional information, as well as performing of individual studies prior to final elaboration of the project and commencement of activity. Such information allows to select best technological solutions, most adequate use of technology and, if necessary, provides basic information for selection of impact reduction measures and environmental monitoring regulations.

Fig. 1 shows distribution of projects, for which the environmental impact assessment has been performed, by areas of economic activity. Till 2010, the main spheres of the environmental impact assessment could be mentioned projects in area of infrastructure and industry, waste management projects, extraction of mineral deposits and energy industry projects.

From analysis of information on environmental impact assessment of the designed activities, it has been concluded that since introduction of the environmental impact assessment procedure in 1997 up to the end of 2010, the environmental impact assessment procedure has been applied to around 200 projects in Latvia. Increase in number of initiated procedures during last 6 years is observed. It may be due to economic growth of the state, use of European funds, as well as increased awareness of governmental institutions in relation to significance and necessity of the environmental impact assessment.

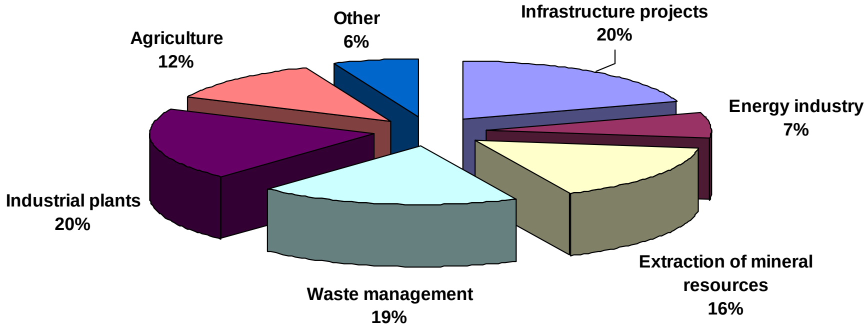

Fig. 1. Areas of application of the environmental impact assessment in Latvia

## 4. REVIEW AND DEVELOPMENT OF POWER ENERGY INDUSTRY IN LATVIA

About 70% of the primary energy sources used within the territory of Latvia in the year 2008 was imported. The largest share of these sources was imported from Russia. The Latvian energy system has a very high dependence on natural gas which constitutes about 28% share in the primary energy supply, and about 80 % of the district heat in Latvia was produced by using natural gas in 2008 [4]. Since there is no fossil fuel mining site in Latvia, oil products, natural gas and coal are being imported. Latvia uses local energy resources, such as biomass (mainly, wood), peat, water and wind. Several hydroelectric power stations are built on the largest river of Latvia, while numerous small hydroelectric power plants are built on small rivers. Wind energy is used less. Use of this type of energy is in its initial stage.

Up to 45% of the entire territory of Latvia is covered with forests, ensuring major part of biomass used. In 2005, imported natural gas and oil products constituted up to 60% of the total primary energy supply. Biomass shall be considered a local source of energy, which covers more than 30% of the primary energy needs. Biomass is mainly used for heat supply, while oil products are used mainly by transport sector. During the recent years, consumption of energy by final consumers was constantly increasing in Latvia, especially, during the period of time from 2002 to 2005. Total capacity of power stations in Latvia has increased from 2090 MW (in 1990); 2165 MW (in 2005) to 2275 MW (in 2010) [5].

The largest power stations are hydroelectric power plants and cogeneration plants. Installed capacity of three hydroelectric power plants is 1531 MW, and that of two largest cogeneration plants is 744 MW. The main fuel used in cogeneration plants is natural gas. Biomass is usually used for heat supply in boiler-houses. District heating mainly uses natural gas and woodchips. However, it uses also wood chips and pellets. Several CHP units also use woodchips.

Latvia had a high share of hydropower (39%) and cogeneration (27%) in the production mix of electricity, and the share of wood fuel used in the boiler plants of district heating systems and sectors of final energy use were 15% and 22 %, respectively. In addition, Latvia exports sustainable amount of wood fuel (8.5% of the final energy use in 2008) which could be used in domestic cogeneration plants and boiler houses [4].

## 5. EIA FOR POWER INDUSTRY OBJECTS IN LATVIA

Recent years in the area of environmental impact assessment have brought new trends, which are related to current global initiatives of national economy development and reorientation of economy in crisis situation. Reflecting guidelines of European Union Policy of Action, global programmes for reduction of climate change impact, as well as Latvian policy for "green" energy purchase strategy, a trend for projects based on socially responsible economy and energy efficient economy initiatives may be observed in Latvia. Thus, number of projects, which provide production of energy from renewable energy resources, including the use of biogas and wind energy for power production, has increased significantly. Particular trend of such project development may be observed along seashore of Baltic Sea, where the strategic EIA, EIA and initial EIA have been proven as tools, using which adverse aspects of impact are being assessed, and establishment of adequate and suitable mechanism for prevention or reduction of such possible adverse effects is being achieved to implement such measures.

The largest projects in Latvia, for which environmental impact assessment has been prepared, are projects in relation to reconstruction and expansion of combined heat and power generation plants, hydroelectric power plant projects, wind power plant construction projects, construction of coal power complex.

### 5.1. Reconstruction projects of combined heat and power generation plants

There are two combined heat and power plants in Latvia, where simultaneous production of thermal energy and electrical power is being performed. Four environmental impact assessments of reconstruction projects of heat-electric generation plants have been performed.

One assessment of reconstruction project has been performed for heat electric power plant TEC-1, while three environmental impact assessments of reconstruction projects have been performed for TEC-2.

Within the framework of TEC-1 reconstruction project, reconstruction of individual buildings and constructions, installation of new steam and gas turbines, recuperative steam generator, as well as modernization of existing water boilers to increase the total thermal capacity up to 380 MW and electric capacity up to 150 MW has been planned in the territory of TEC-1. Natural gas shall be used as fuel in this case.

Environmental impact assessments of reconstruction projects have been performed for TEC-2. During the Stage 1 of reconstruction new power unit in the territory of TEC-2 was constructed, which will operate in co-generation regimen. As a result of reconstruction Stage 2, installation of 2nd power unit with thermal capacity of 270 $MW_{th}$ and electric capacity of 400 $MW_{el}$ has been planned.

At the same time, it shall be noted that, as a result of environmental impact assessments of reconstruction project, the alternative of the use of renewable energy resources or partial use of fossil and renewable energy resources has not even been considered. Furthermore, capacities, installed during the Stage 1 of TEC-2 reconstruction, were not used in co-generation regimen, since thermal power consumption decreases during summer time and it fails to operate in effective cogeneration regimen.

### 5.2. Hydroelectric power plant projects

Environmental impact assessments procedures for hydroelectric power stations of the following capacities have been performed:

1. Small scale hydroelectric station on river Musa. As a result of the designed activity, water reservoir with area of 54.1 ha will be formed. Planned total capacity of hydroelectric power plant – 1020 kW.

2. Construction of hydroelectric station on river Malupe. As a result of the designed activity, water reservoir with area up to 61.5 ha will be formed. Planned total power production capacity of hydroelectric power plant – 1 000 000 kWh/year.
3. Construction of hydroelectric station on river Malupe Planned total power production capacity of hydroelectric power plant – 2 000 000 kWh/year.

### 5.3. Wind power station construction projects

Environmental impact assessments procedures for wind power plants of the following capacities have been performed:

1. Construction of offshore wind farm with total capacity of 200 MW, producing from 590 000 MWh to 910 000 MWh of electricity per year in the Baltic Sea close to Pavilosta. Total amount of 47-80 wind power plants to be installed with capacity from 2.3 kW to 5 MW.
2. Expansion of the existing wind power park by installing another one wind power plant with nominal capacity of 250 kW on the adjacent property close to Pavilosta. This is the only one small scale wind project for witch EIA procedure has been performed.
3. Installation of wind power plant with total capacity of 34 MW in Liepaja town area.

### 5.4. Construction of coal power complex

The company aims to process around 450 000 t of coal per year (or 1233 t per day), which contain 80% of carbon, producing up to 310 000 t of coke per year. During the process of pyrolysis, which lasts for 59 h, obtaining of highly refined coke and combustible gas is expected. Technology to be used – auto-thermal gasification of coke by use of air flow. According to the report, ecological benefit will be based on the neutralization of the products of thermal decomposition of coal mass, which contain hazardous components, burning them entirely behind the area of pyrolysis. The hot combustion gases will be used for generation of steam, which will be used in steam turbine for production of electric power, and part of heat – for production of energy, which shall be transferred to town district heating. The report states that in one year, up to 855000 t of steam will be produced, from which around 182200 MWh of electric power and up to 400300 MWh of thermal power shall be obtained.

The principal motivation for increasing of biomass use in coal electric power plants is assumptions on effect by carbon dioxide on climate changes and efforts by EU to mitigate climate changes. Motivation to produce energy from biomass in wide scale relates to the existing initiative, which encourages the use of biomass. It is based on existing EU emission trade system and national political plans in the area of renewable energy sources. They provide replacement of fossil fuel with biomass, which ensures reduction in $CO_2$ emissions, and this saved volume of $CO_2$ emission can be sold in the respective market. Co-combustion of biomass and coal within the existing fossil fuel energy transformation plants shall be considered dominant method to increase number of energy sources for production of energy.

## 6. CONDITIONS FOR SUSTAINABILITY OF POWER INDUSTRY

Sustainability of power industry is related to constant development of power industry (energy production, energy supply and energy end users). Conditions for sustainability of power industry in Latvia include:

1. Development of renewable energy resources;
2. Increase of energy efficiency in power production;
3. Increase of energy efficiency in energy transformation;
4. Increase of energy efficiency in power use;

Development of systemic energy resources in the country [6]. Table 1 shows summarized data on the potential of available local energy sources in Latvia.

Table 1. Potential of local energy source availability [7]

| **Type of energy source** | **Potential amount of primary energy per year** |
|---|---|
| Biomass | 30 TWh |
| Onshore wind power plants | 600 $MW_{el}$ |
| Offshore wind power plants | 1200 $MW_{el}$ |
| Biogas | 7 TWh |
| Waste | 1.8 TWh |
| Biofuel | 10.5 TWh |

### 6.1. Biomass resources and co-combustion of biomass

Latvia has a high biomass potential. One of the most popular biomass fuel types is wood, which currently is used in large scale in Latvia, and it is likely that power production from solid biomass fuel will reach the volume of 30 TWh/year. One of the ways to implement the use of biomass in power industry is simultaneous combined combustion of wood and the fossil fuel. Current sustainable approach to energy supply defines necessity for more extensive availability of modern and effective bio-energy technologies. Such initiatives are aimed to technologies related to environmentally friendly, technically and economically beneficial use of biomass. It is expected that, in the future, special plants, designed for production of bio-energy, will increase their contribution in this sector.

Incorrect solutions in implementation of co-combustion and related problems in many countries occurred due to insufficient knowledge on technologies available for co-combustion with fossil fuels. The reason was insufficient supply of biomass and inadequate development of biomass market. This, in its turn, arises from insufficient information and incorrect organization of potential biomass market system principles. Thus, despite the lack of knowledge and information, volume of biomass, used for power production in Central and Eastern Europe, increases. This might be even more beneficial for power producers, as well as power saving on national level, if it is based on knowledge in relation to co-combustion technologies.

## 7. INCREASING OF EFFICIENCY IN PROCESS OF POWER PROJECT ASSESSMENT

The concepts of sustainability need methods and tools to evaluate (comparing and measuring) the impacts of human activities for providing of goods and services (generally defined as products). Environmental impacts include those from emissions into the environment and through the consumption of resources associated with the entire life of a certain product from extracting resources till end-of-life. These emissions and consumptions (energy and materials) contribute to several types of impacts (e.g. climate change, stratospheric ozone depletion, tropospheric ozone creation, eutrophication, acidification, toxicological stress on human health and ecosystems, the depletion of resources, water use, land use, and noise). A clear need to decrease this amount with the help of regulatory practices is needed: the life cycle assessment is exactly one of those [8].

When conducting an LCA, the design/development phase is usually excluded, since it is often assumed not to contribute significantly. However, one has to note that the decisions in the design/development phase highly influence the environmental impacts in the other life cycle stages.

LCA can be defined in first instance as methodological framework for estimating and assessing the environmental impacts attributable to the life cycle of a product in which structural pathways in the economic and environmental system are delineated and connected to environmental problems. As such, it can be seen as an extension (or complement) of an energy analysis. The main aim of an LCA is to quantify potential environmental impacts of products over their full life cycle.

Basically the LCA consists of a series of stages running from extraction of raw materials, through design and formulation, processing, manufacturing, packaging, distribution, use, re-use, recycling and, ultimately, waste disposal.

A typical LCA study consists of the following stages: goal and scope definition, life cycle inventory (LCI) definition, potential impact assessment evaluation, interpretation of the results from the previous phases.

More in specific the goal and scope must be stated clearly, together with the intended objectives of the LCA and the system boundary of the process under study. Then the Life Cycle Inventory (LCI) analysis, consisting of the material and energy balance of the product system, aims at the identification and quantification of substances that may be environmentally relevant.

The Life Cycle Impact Assessment is the phase in which the set of results of the inventory analysis (mainly the inventory table) is further processed and interpreted in terms of potential environmental impacts and societal preferences.

In reference to the ISO Standards 14040-44 this phase includes three stages: characterization, normalization and weighting where the last two are not mandatory. This procedure in terms of impact evaluation is fundamental in order to reference each impact categories to a certain emission factor and/or to make comparable the results among all the impact categories (identification of the environmental hot spots).

Interpretation is the last stage of an LCA study, where the results obtained are presented in a synthesis of all stages in the LCA process, in order to check the consistency of the assumptions and the data quality in relation to the goal and scope of the study.

Implementation of LCA principles in the process of assessment of effect by power objects will allow to perform objective assessment and comparison of various types of fuel, for instance, to assess impact caused by fossil and renewable energy resources.

### 7.1. Future plans

Latvia, in collaboration with Poland, Lithuania and Estonia, are intensively working on the development of the future newly-built nuclear power plant (NPP) project. Currently, the management representatives of the power companies involved in the project – Leo LT (Lithuania), Latvenergo (Latvia), Eesti Energia (Estonia) and PGE (Poland) – have been carrying on discussions on the new nuclear power plant construction. LCA must be used for assessment of possible impact of NPP.

## 8. CONCLUSIONS

The aim of Renewable energy sources by 2020 for Latvia can be achieved, if energy efficiency of user energy resources is ensured and energy sources are constructed, where fossil fuel is replaced with the renewable one.

It is necessary to elaborate common approach for EIA of power projects. During the process of impact assessment, principles of LCA should be implemented, which allow to enhance quality and efficiency of EIA.

The use of LCA principles in the process of EIA will allow the assessment of the designed activities and environmental impact by proposed alternatives in a more objective way.

## REFERENCES

1. BLUMBERGA Andra; BLUMBERGA Dagnija; BAZBAUERS Gatis; DAVIDSEN Pal; MOXNES Erling; DZENE Ilze; BARISA Aiga; ZOGLA Gatis; DACE Elina; BERZINA Alise: *Integration of systemic thinking into environmental policy*. Madona: Madonas Poligrafists, 2010. 225 p. ISBN 978-9934-8196-0-5.
2. GLASSON John; THERIVEL Riki; CHADWICK Andrew: *Intoduction to Environmental Impact Assessment, Third Edition*. London: Routledge, 2005. 365 p. ISBN 0-415-33837-9.
3. THERIVEL Riki; MORRIS Peter: *Methods of Environmental Impact Assessment, Third Edition.* London: Routledge. 2009. 559 p. ISBN 0-415-44174-9.
4. Ministry of economics of the Republic of Latvia: *Latvian Energy in figures*. Riga. 2009. p. 35.
5. BLUMBERGA Dagnija; OZOLINA Liga; ROSA Marika; GAJ Henryk; ZUWALA Jaroslaw; LECHAWACKA Malgorzata; KALLASTE Tiit; LAUR Anton; PEREDNIS Eugenius; JAKUBES Jaroslav; TANTAREANU Cristian; PCHELKA Franciszek; WEBER Roman; BRINKER Stefan: *Co-Firing – from Research to Practice: Technology and Biomass Supply Know-How Promotion in Central and Eastern Europe*, 2009. 72 p. ISBN 978-9934-8058-1-3.
6. BLUMBERGA Dagnija: *Sustainable Energy Development in Latvia*. Riga, RTU Publishing House, 2010. 38 p. ISBN 978-9934-10-083-3.
7. PORUBOVA Jekaterina; BAZBAUERS Gatis: Analysis of Long-Term Plan for Energy Supply System for Latvia that is 100 % Based on the Use of Local Energy Resources, *Scientific Journal of Riga Technical University. Environmental and Climate Technologies*, 2010, Vol. 4, p. 82–90.
8. REBITZER, G., EKVALL, T., FRISCHKNECHT, R., HUNKELER, D., NORRIS, G., RYDBERG, T., SCHMIDT, W.P., SUH, S., WEIDEMA, B. P., PENNINGTON, D.W. 2004. Life cycle assessment Part 1: Framework, goal and scope definition, inventory analysis, and applications. *Environment International,* 30 (5): p. 721–739.

CYSENI 2011, May 26–27, Kaunas, Lithuania
ISSN 1822-7554, www.cyseni.com

# LITHUANIA´S NEW STRATEGY IN ENERGY POLICY

**U. Roßegger**
*Brunswick University of Technology*
*Section Public Law and Administrative Sciences*
*Bienroder Weg 87, D-38106 Braunschweig – Germany*
*Phone +49 (0) 531 391 - 2465*
*Email: u.rossegger@tu-bs.de*

ABSTRACT

The closure of Ignalina Nuclear Power Plant of unit I in 2004 and unit II at the end of 2009 was part of the agreement, when Lithuania applied to join the European Union (EU). EU had concerns about the RMBK reactor (Reaktor bolshoy moshchnosti kanalniy means High Power Channel-type Reactor). In 2009, Ignalina NPP unit II has generated 70 percent of Lithuanians electricity. As a result of the shut-down Lithuania has changed its status to an importer, after being a net exporter for more than two decades. The shut-down led to structural changes in the Lithuanian energy mix and shows a strong need for a new energy strategy.

The three Baltic States – Latvia, Estonia and Lithuania – are defined as an "energy island". Among themselves Latvia, Estonia and Lithuania have well developed electricity interconnections, transboundary interconnections to other European countries are limited by the only existing interconnection between Estonia-Finland. For this reason, the integration into the EU internal energy market is one of the main targets Lithuania´s of energy policy. On 17 June 2009, the European Commission with eight participating Baltic Sea states signed the Baltic Energy Market Interconnection Plan (BEMIP). The Baltic electricity market shall be created by 2013 and the common market of Scandinavia and the three Baltic States shall be launched in 2015. According to this plan Lithuania has announced to liberalize half of its energy market in 2014. The prevailing opinion for reaching long-term energy security is to mainly focus on nuclear energy.

The paper discusses the approach how to attain the goal of energy security in conjunction with the target of a fully integrated European electricity market. Finally, the paper aims to clarify, if the building of a new nuclear power plant is the only solution for achieving national energy security.

Keywords: Lithuania, energy policy, national energy security.

## 1. INTRODUCTION

By the reason of the closure of Ignalina Nuclear Power Plant unit II at the end of 2009 Lithuania is up-to-date highly dependent on electricity imports, particularly from Russia. Therefore Lithuania is requested to develop a new strategy in energy policy. In 2008, the European Commission presented the Baltic Energy Market Interconnection Plan (BEMIP) to "end the energy isolation" of the Baltic States [1].

The brief focuses on the three main goals specified through BEMIP as a part to achieve and push a fully integrated European energy market and to support a secured national energy policy [2]:

- the promoting of national energy security;
- the functioning of the energy market and the full integration of the three Baltic States into the European energy market;
- the strengthening of interconnections with their EU neighbouring countries.

According to European Commission president Barroso's statement in Brussels the term of planning is ambitious. Therefore, it is subsequently to push for completing the internal energy market by 2014, while energy islands ought to be non-existent by 2015. The modernization of infrastructure is an important step to achieve the single European energy market [3].

In October 2010 the government of Lithuania affirmed the National Energy (Energy Independence) Strategy [4].

Besides the EU level there is the question how to react on the developments at different levels – namely national energy strategy and future electricity mix in Lithuania. Most important question is about the role of nuclear power in the future and how to reach national energy security.

## 2. EU ENERGY POLICY

In March 2007 the European Union's new energy and environmental policy has been agreed by the European Council. It is part of the aim to complete the Community's core energy objectives [5]:

- Sustainability;
- Competitiveness;
- Security of Supply.

These main targets are linked to the Baltic Energy Market Interconnection Plan. Surplus is gained because of the development of infrastructure while integration of the Baltic Sea region and the diversification are an outcome of this initiative.

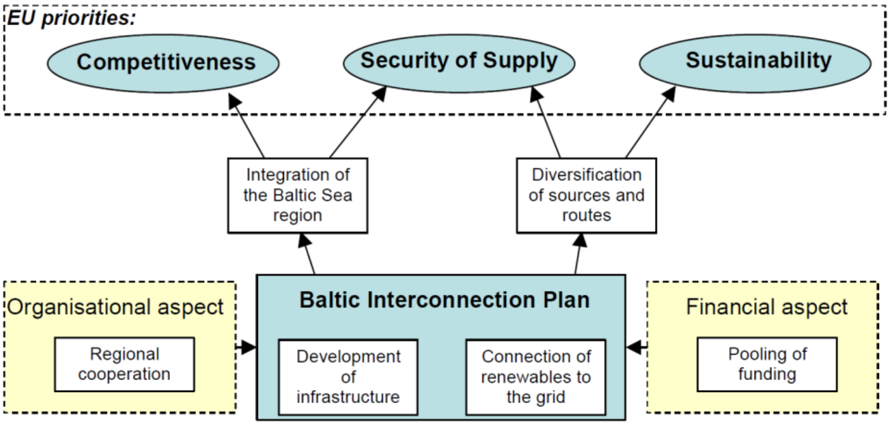

Fig. 1. Baltic Energy Market Plan within the overall EU energy framework (source EC) [6]

As well in 2007, the European Council requested the Commission to prepare a new action plan for the next decade post 2010. In retrospective, the Energy Action Plan of 2007 has shown some results such as the adoption of the third internal energy market package, the energy and climate change package, the Nuclear Safety Directive and the Strategic Energy Technology Plan [7].

Proposals of EU´s new energy policy has been added to the third energy package. The content of Directive 2009/72/EC and 2009/73/EC concerning common rules for the internal market in electricity or rather common rules for the internal market in natural gas.

Most important for the European energy policy is the effectiveness of the legislative framework and therefore it strongly needs to have the implementation in place. This link to an overall implementation of European energy legislation is currently at a low level [8].

The result of the poor implementation is an internal energy market which does not function properly yet. This means that a crucial lever to promote affordable and secure energy and to accompany the transition towards low carbon energy is currently not fully exploited. Well functioning retail and wholesale markets, accompanied by smart regulation, are crucial to ensure that citizens and businesses in Europe can exercise choice with the appropriate tools at their disposal and that competition between suppliers presses prices down and quality of service up [9].

In sum, four challenges have recently addressed to fulfil an integrated energy market. It is necessary to interconnect the various markets in Europe and enforcing market integration. Moreover, conditions should ensure security of supply through appropriate connections with third country supply sources. Renewable energy production sources must be linked with the existing grids. In addition, the development of smart grids for increasing decentralization of energy production and to fully absorb renewable energy must realize too [2].

## 2.1 EU Energy Security and Solidarity Action Plan

The current development process in energy policy is boosted by Commission´s Second Strategic Energy Review package in 2008. With regard to the EU energy security and solidarity action plan the Commission figured out five key areas [2]:

- Infrastructure needs and the diversification of energy supplies;
- External energy relations;
- Oil and gas stocks and crisis response mechanisms;
- Energy efficiency;
- Making the best use of the EU´s indigenous energy resources.

It has to be assumed a highly substantial change in the European energy system over the next decades until 2050. All over Europe the Commission estimates challenges and fundamental changes for the energy system between 2020 and 2050. The main parts of European Commission´s proposal of a wide ranging energy package are to put forward a new strategy to deploy energy solidarity among Member States. It has to be stimulated by investments in energy networks.

Main parts in the European Commission proposal of a wide-ranging energy package are [2]:

- putting forward a new strategy to build up energy solidarity among Member States and a new policy on energy networks to stimulate investment in more efficient, low-carbon energy networks;
- proposing a Energy Security and Solidarity Action Plan to secure sustainable energy supplies in the EU and looking at the challenges that Europe will face between 2020 and 2050;
- adopting a package of energy efficiency proposals aims to make energy savings in key areas, such as reinforcing energy efficiency legislation on buildings and energy-using products.

This approach is supported by definite targets, by reducing greenhouse gas emissions by 20 percent, increasing the share of renewables in the final energy consumption to 20 percent and improving energy efficiency by 20 percent, all of it shall be realized until 2020 (in reference to 2005) [2].

## 2.2 Baltic Energy Market Interconnection Plan

The leading goal of this plan is to integrate the Baltic States into the EU energy market and to overcome the dependency on historical connections with Russia. The Baltic Energy Market Interconnection Plan (BEMIP) is part of the Green paper on energy networks which identifies six strategic initiatives to assure EU´s energy security [10]:

- Baltic Interconnection Plan;
- Mediterranean Energy Ring;

- North-South gas and electricity interconnections with Central and South-East Europe;
- A North Sea Offshore Grid;
- A Southern Gas Corridor;
- Liquefied natural gas (LNG) supplies for Europe.

An effective interconnection of the Baltic region was identified as one of 6 priority energy infrastructure projects in the Second Strategic Energy Review adopted by the Commission in November 2008 [11]:

The BEMIP and the extension of the Nordic electricity market model to the Baltic States are also designated as key projects in the Commission's contribution to the Baltic Sea Region. Eight Baltic Sea member states signed (17 June 2009) a Memorandum of Understanding (MoU) on the Baltic Energy Market Interconnection Plan with European Commission President, José Manuel Barroso. The Baltic Energy Market Interconnection Plan (BEMIP) is the fruit of nine months’ work at the initiative of the Commission to look at concrete measures to connect Lithuania, Latvia and Estonia better to wider EU energy networks.

The electricity network of Lithuania, Estonia and Latvia is currently overweightly linked to the Russian and Belarusian. Three main projects of BEMIP initiative ought to solve missing interconnections of Baltic power system to have an electricity bridge to Western Europe (mainly Poland) and Scandinavia (mainly Sweden) [12].

One special case is the approach to synchronise the network between Poland and Lithuania. This project is the most complicated one because lots of politically, economically and technically issues together with lack of competence and problems of buying land were hindering to come to a result. The motivation is unequal on Lithuania’s and Poland’s site. Poland seems to have not the same amount of political will to build an interconnection as Lithuania has. In general, Poland links this infrastructural project with the building of new nuclear power plant Visaginas as Lithuania has a main interest to have an interconnection to Poland while NPP is not the strongest argument. Therefore Poland has no rush in time to start the project and is waiting until the final agreement on a new NPP is achieved. Besides power networks also gas systems of the Baltic States also need new connections – establishment of a gas interconnection between Poland and Lithuania is still open and no rapid steps are on the way [12].

Nevertheless, European Union’s energy policy is inconsistent by reason that a clear strategy, coherent and better-targeted approach to penetrate energy infrastructure is missing.

European priorities can only become real if a well-interconnected grid between the Baltic States and Continental Europe is achieved soon.

To support the BEMIP by Commission is a logical step for achieving a fully interconnected internal EU energy market and also emits to energy supply security of all Member States. Firstly, BEMIP focuses on the electricity sector, the second priority is gas [12].

On 3 December 2010 ministers of EU member states responsible for energy have discussed the new future Energy Strategy for 2011–2020 and the most effective ways for developing the prospective energy infrastructure in Europe, alongside a council meeting [13]. The elimination of Baltic States’ Energy Island will be only partly finished in 2015 because not all necessary interconnections are online.

As a main problem ACER (Agency for the Cooperation of Energy Regulators) points out that existing cross-border capacity is not used efficiently and regional electricity markets are not integrated. The establishment of a common market has the potential to overcome this situation and to achieve energy security and competition. To come to diversity will help consumers. Current situation leads to benefits for the production companies [14].

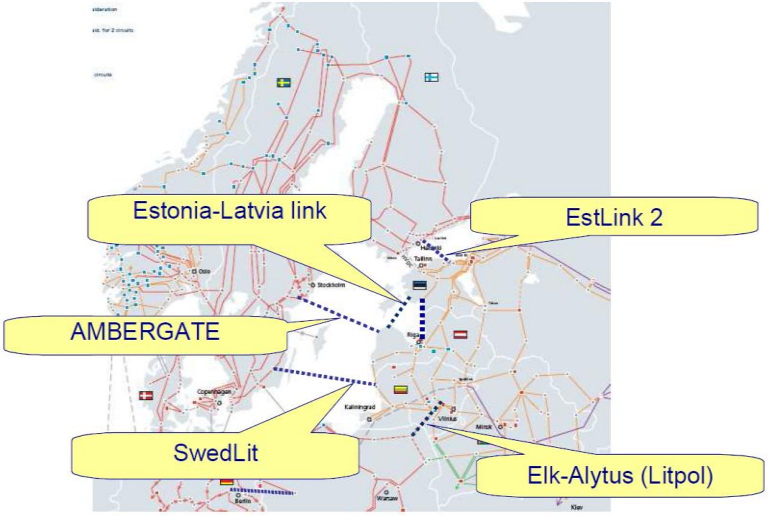

Fig. 2. Interconnection projects between the Baltic Member States and the rest of the EU, including Estonia-Latvia third interconnection [15]

Integrated markets will help to gain a higher value of Lithuanian power plants. Indicator or criterion for an open electricity market is the amount of electricity which is traded under market price for customers.

Three transboundary interconnections are planned for Lithuania[16]:

- NordBalt, former SwedLit (between Lithuania and Sweden) – electricity interconnection;
- LitPol (between Lithuania and Poland) – electricity interconnection;
- Lithuania – Poland gas interconnection.

Since 17 December 2010 NordBalt project is on track when the Swedish and Lithuanian power grid operators signed a EUR 270 million contract with Asea Brown Boveri (ABB) [17]. The project will complete the interconnection from Sweden’s Svenska Kraftnaet and Lithuania's LITGRID Turtas AB, linking the Nordic and Baltic electricity markets. ABB will design, engineer and supply two 700 megawatt converter stations, two 300 kilovolt underwater cables, each 400 kilometres long, as well as land cables in Sweden and Lithuania. This infrastructure project will be supported by European Union funding, to be completed by the end of 2015 [17].

With reference to previous projects ABB has made some experience in that region while they delivered also the Estonia-Finland Estlink, the first interconnection between the Nordic and Baltic energy markets, in 2006.

For the interconnection between Sweden and Lithuania European Union has already contributed a financial support of EUR 175 million to the NordBalt project. The main part of funding, EUR 131 million, will be used for the construction of the link. A left part is for reinforcing the Latvian electricity transmission system. The total value of the NordBalt project is EUR 552 million and the interconnection is scheduled to be available in the beginning of 2016 [18]. The table 1 below shows the current status of network expansion and planning terms.

Table 1. Cross-border lines considered in the project assessment [15] and own additions

| Project | Capacity | Ends | Notes | In operation |
|---|---|---|---|---|
| Estlink | 350 MW | Harku-Espoo | Completed in 2007 | 2006 |
| Estlink 2 | 650 MW | Anttila-Püssi |  | 2014 |
| Ambergate | 700 MW | Norrköping-Ventspils |  | 2014 |
| NordBalt | 700 MW | Nybro-Klaipeda |  | 2015 |
| LitPol | 2 x500 MW | Elk-Alytus | development in stages | 2015 |
| Latvia-Estonia 3rd Interconnection | not decided |  |  | open |

## 3. NATIONAL ENERGY STRATEGY IN CURRENT DEVELOPMENT

From the view of 2011, a lot of objectives defined by the Lithuanian state to adopt the national energy strategy were unreal.

Beforehand, in the late 2006 and early 2007 the issues of energy security were on the top of the agenda besides a highly raising awareness regarding this topic for the public and politicians. One can explain the situation with Russians strong use of Europe´s energy dependence on gas supply for political purposes. Therefore it has been a very strong factor when Lithuanian National Energy Strategy was developed. [19]

Arvydas Sekmokas Minister of Energy stated in his speech to the Energy Council on 3 December 2010:

The goal in 2015 no EU state to be isolated from internal market of Europe is a clear message binding all of us. The implementation of the goal will be a clear success indicator of the European Energy Policy. [20]

Under realistic circumstances the timetable is too short for reaching this target. In the official document the government pointed out as main goal of the strategy to achieve Lithuania´s energy independence before 2020. Overall, the Lithuanian state has defined the main objectives in the energy sector. For implementing the national targets ten or rather twenty years steps are made to complete the strategic initiatives through the years 2020, 2030 and 2050 as seen in Fig. 3.

The most important aim of the National Energy Independence Strategy is to achieving energy independence of Lithuania. Electricity has an accentuated position. In 2020, it is planned that Lithuanian energy sector will be fully independent of energy supply from a single source. Therefore electricity ought to be covered by a new nuclear power plant in Visaginas and the production from renewable energy sources. (2010 Energy strategy Lithuania) The initiative to reach energy independence will cost 11-17 billion LTL public investment and additionally 18-24 billion LTL private investment. The expected outcome of this is Lithuania will benefit from reliable energy supply and more stable energy prices, while each household will on average save 500 LTL per year on heating costs [21]. An overview about the stategic goals in electricity sector can be seen in Table 2 below.

Table 2. Strategic goals in electricity sector

| **Current situation** | **Vision** | **Strategic initiatives till 2020** |
|---|---|---|
| Lack of supply in the Baltic States, at least 1.3. GW of new capacity has to be built until 2020 | Synchronzied with the EU and integrated with other regional systems | *Integration with European electricity networks*<br>- LitPol Link<br>- To íntegrate into the Nordic market (including NordBalt construction)<br>- Synchronous interconnection with European Continental Networks (ECN)<br>- To strengthen internal network<br>- To finalize creation of common Baltic electricity market |
| Production mix heavily dependant on fossil fuels | Sufficient capacities to cover domestic demand | *Self – sufficient generation*<br>- Visaginas nuclear power plant<br>- To finalize other ongoing constructions |
| No electricity link with the EU and thus no possibility to exploit the benefits of single market | Diversified fuel supply | *Increase in production from renewable energy sources* |
| Extensive electricity network requiring investments into modernization | Large share of electricity in energy-mix of Lithuania | *Market liberalization and electricity sector reorganisation* (ownership unbundling) |

Strongest action is given to the implementation of the three-part strategic initiatives as having the essential impacts on increasing national energy independence [22]:

4. Integration to European electric power system:
    - Completion of Lithuania – Poland power interconnection LitPol Link;
    - Completion of Lithuania – Sweden power interconnection NordBalt;
    - Interconnection of Lithuanian, Latvian and Estonian electricity grids for synchronous operation with the European continental electricity grids;
    - Integration into the European electricity markets.
5. Ensuring of adequate electricity generation capacity in order to meet the national electricity demand in 2020 (12–14 TWh annually):
    - Construction of Visaginas nuclear power plant;
    - Increasing of share of renewable generation sources.
6. Implementation of EU Third Energy Package:
    - Separation of generation, transmission and distribution activities;
    - Electricity market liberalization.

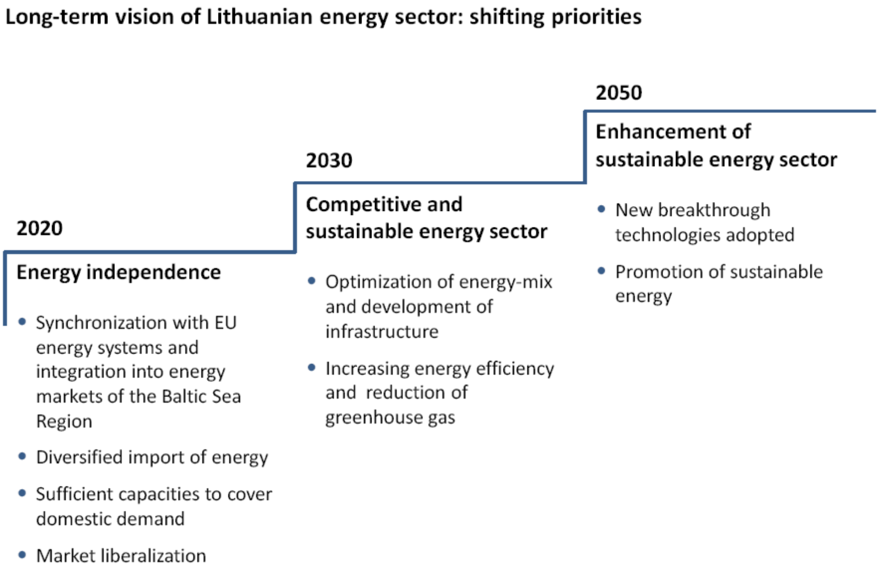

Fig. 3. Strategic vision for Lithuania´s energy policy [23]

The idea of building powerful high-voltage grids to connect Lithuania’s energy network with Sweden and Poland is the most efficient way to basically improve the energy security in the Baltic region. Furthermore it will help Lithuania to join the common Nordic energy market and is concurrently the first significant step in a future of an unified energy system all over Europe. Positive impact of the closure of Ignalina nuclear power plant helps to create a common electricity market of the Baltic region until the range 2015–2020. On 1 January 2010, the Lithuanian electricity power exchange started its activity and is the main driver for opening the electricity market. Moreover, electricity power exchange promotes the necessity to secure the functioning of deregulated electricity prices. The main function of the operator BALTPOOL UAB is to organize the electricity trade at the Lithuanian power exchange and bilateral trade. The Lithuanian power exchange is based on the principles of Scandinavian Nord Pool Spot – the price of electricity is fluctuant and trading has an anonymous mechanism. Due to this development the companies operating in the Lithuanian market gain an opportunity to participate in the wholesale electricity market [24].

In January 2011, the average price in Lithuania decreased to 44.5 EUR/MWh, which was 7.3 percent lower than in November 2010 due to the reason of electricity imports and higher supply. The mechanism of fixing the electricity price for long period has led to high savings of money for customers in Lithuania [25]. While in the first months of 2010 the electricity prices increased about 30 percent in comparison to the closure of Ignalina at the end of 2009 [26/27].

When following J. Vilemas approach, there is a need for a further construction of at least 500 MW of wind power plants in the next years means all together 950 MW additionally. In sum the future availability of interconnectors for importing electricity shows that there is no requirement for extra capacity buildings in large power plants like a nuclear power plant. Vilemas concluded that Lithuania will be able to satisfy all its electricity needs in the short-run until 2015 by using existing generating capacity – under the assumption of average growth in the electricity consumption of 4–5% per year. The import of electricity together with local production in small and mid-scale constructions of new capacities could be a realistic approach. With regard to long term perspective beyond 2020 Vilemas stated that a new nuclear power station becomes the most economically attractive source of electricity, if prices of fossil fuels receive a substantial tax on CO2 emissions [19].

Regarding the construction of a new nuclear power plant in Lithuania time schedule as report in the Lithuanian Energy Strategy of 2007 was unrealistic. Currently, the new date for the building of a nuclear power plant is stated by the government for 2020. Lithuania will not be able to build a NPP without foreign investors. Regarding the BEMIP programme it is foreseen that Lithuania with stakeholders from Poland and the other Baltic states will hold shares in the Visaginas NPP (expected capacity up to 3400 MW) planned site near to Ignalina NPP. Discussions on different scenarios are not on the road while Lithuanian state interrupts critical opinions which question the sense of a new NPP [28].

The current situation is completely insecure, also Poland, Russia and Belarus have plans to build up their own NPP. It is questionable if all projects can be realized and under which circumstances a benefit will be an outcome. The fact is that electricity prices in the Baltic region will get competition, for example from Kaliningrad NPP which has an expected capacity of 2400 MW when it will be build [28]. In Lithuania high-level inter-agency coordination and management in energy issues between relevant departments is taking place. [29]. A complicated situation depending energy security is still a serious challenge of finding a new balance and diversifying the sources to import electricity. A new NPP is the biggest hope for energy security for Lithuania and also for Estonia and Latvia [20].

## 4. LITHUANIAN ENERGY MIX

The Table 2 shows the development of electricity generation and consumption between the years 2007 and 2010. 2010 was the first year without nuclear power. Currently more than half of electricity is imported.

In the field of renewable energy resources Lithuania wants to increase the total energy consumption to achieve the target of 23% of renewable energy in 2020. For the electricity sector this means at least 20% (60% heat; 10% transport). A clear framework should be helpful and the most economically feasible technical solutions.

In particular, the RES-Directive has fixed a renewable energy target for electricity of 7% from gross electricity consumption by 2010.

It is questionable if a new nuclear power plant will be built in Lithuania because of a lot of other plans for new nuclear build in the region. Open question is what´s about continuant support of Estonia, Latvia and Poland. Baltic nuclear power plant in the enclave of Kaliningrad has an estimated capacity of 2300 MW, price is 6 billion USD. The argument to build a new nuclear power plant is the current regional energy deficit and the reason countries' are hurt very much. An important step is also the construction of a new LNG terminal. The plan is to overcome the dependency from Russia and to create an own gas market. Therefore it is strongly needed to build some LNG terminals in the Baltic region. It is yet not sure which location these terminals will have.

Another important issue is to boost renewable energies: one main restriction is that Lithuanian renewables legislation is “lagging behind”. At the moment Lithuanian legislation is not ready yet in this field, in accordance to EU's requirements. In addition, restriction is also existent because of limited financial resources [30].

Lithuania´s Vice-Minister of Energy Svedas claims that there is not a conflict between renewable energies and nuclear power.

The two are complementary. Wind power needs backup power and power mix should be as diverse as possible [30].

Former National Energy Strategy came into force in 2007. It was planned to finalise construction of the new NPP not later than 2015. This time schedule and the building would help Lithuania to become energy independent. The realization of the visional project becomes more and more unrealistic, because Lithuania is up-to-date unable to start construction works of a new NPP (Visaginas Nuclear Power Plant), the regional context is rapidly changing in prejudice of Lithuania. Most important reason is the increasing competition of nuclear energy producers in the region. Updated press releases in the region come to the result that Russian and Belarusian planned units are ready to replace former Lithuanian NPP Ignalina [28].

Table 3. Lithuanian Energy Data 2007–2010 [31]

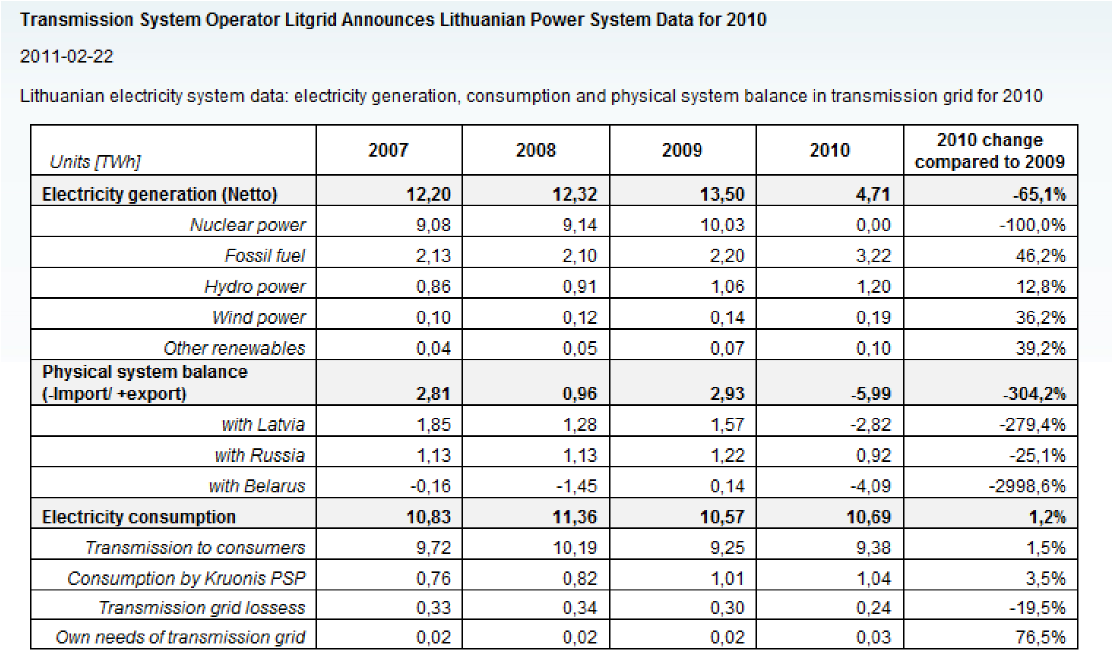

**Transmission System Operator Litgrid Announces Lithuanian Power System Data for 2010**

2011-02-22

Lithuanian electricity system data: electricity generation, consumption and physical system balance in transmission grid for 2010

| *Units [TWh]* | 2007 | 2008 | 2009 | 2010 | 2010 change compared to 2009 |
|---|---|---|---|---|---|
| **Electricity generation (Netto)** | **12,20** | **12,32** | **13,50** | **4,71** | **-65,1%** |
| *Nuclear power* | 9,08 | 9,14 | 10,03 | 0,00 | -100,0% |
| *Fossil fuel* | 2,13 | 2,10 | 2,20 | 3,22 | 46,2% |
| *Hydro power* | 0,86 | 0,91 | 1,06 | 1,20 | 12,8% |
| *Wind power* | 0,10 | 0,12 | 0,14 | 0,19 | 36,2% |
| *Other renewables* | 0,04 | 0,05 | 0,07 | 0,10 | 39,2% |
| **Physical system balance (-Import/ +export)** | **2,81** | **0,96** | **2,93** | **-5,99** | **-304,2%** |
| *with Latvia* | 1,85 | 1,28 | 1,57 | -2,82 | -279,4% |
| *with Russia* | 1,13 | 1,13 | 1,22 | 0,92 | -25,1% |
| *with Belarus* | -0,16 | -1,45 | 0,14 | -4,09 | -2998,6% |
| **Electricity consumption** | **10,83** | **11,36** | **10,57** | **10,69** | **1,2%** |
| *Transmission to consumers* | 9,72 | 10,19 | 9,25 | 9,38 | 1,5% |
| *Consumption by Kruonis PSP* | 0,76 | 0,82 | 1,01 | 1,04 | 3,5% |
| *Transmission grid lossess* | 0,33 | 0,34 | 0,30 | 0,24 | -19,5% |
| *Own needs of transmission grid* | 0,02 | 0,02 | 0,02 | 0,03 | 76,5% |

The question is, which quality energy dependency has. To be dependent from Russia, from oligarchs has a link to the availability of an own energy market and of the possibility to buy energy from competing markets if there wouldn't be a NPP to answer the practical force of Russia to pay more than someone is able to pay. In the opinion of Dalia Grybauskaite, president of the Republic of Lithuania, one has to be more afraid about the inability of the country to demonopolize and establishing the market to combine it with the European network. Furthermore discussion about shutting down INPP was a strong idea of energy clans interests. In the result political elite organisations were able to blockade specific future development in its turn, namely to hamper the investment into the deployment in renewable energies [32].

The Baltic region as a whole has a continued need of importing electricity due to the closure of the Ignalina nuclear power plant, Elering (transmission system operator) noted. Electricity imports from third countries accounted for 14 percent of total consumption in the Baltic region last year.

Most of the electricity imported to the Baltic States went to Lithuania that covered nearly 80 percent of its six terawatt-hour shortage with purchases from Russia and Belarus. Imports from third countries made up 51 percent of electricity consumption in Lithuania [33].

As shown in Table 3, the amount of net electricity generation in 2010 has decreased to 4.71 TWh (2009: 13.5 TWh) means a change of minus 65.1 percent. About 6 TWh had to be imported, almost from Belarus (4.09 TWh) and also through Latvia (2.82 TWh) while small amount (0.92 TWh) has been exported to Russia. The Lithuanian total consumed electricity in 2010 was 52 percent from fossil fuels and about 16 percent (9.6 percent of the consumed electricity) from renewable sources. To consider the fact that in 2009 74 percent in electricity mix was from nuclear power. In particular, the increase of renewables is only relatively and therefore mostly linked to NPP shut-down. For the Lithuanian electricity system imports of 62 percent of the entire electricity demand were necessary. Lithuania had to import 2-3 times more electricity than any other deficit power system in the European Union [31].

Today, Lithuania's most important energy sources are gas and oil, each 42 percent, the full amount out of these sources comes from Russia [1].

Lithuania´s Deputy Minister of Energy Romas Svedas said:

This situation is very serious for us. Perhaps this is not understood in the West [1].

In the time after 2050 Lithuania wants to move towards a fully sustainable, carbon free economy. Electricity production ought to have two main sources, nuclear power and renewable energy, decentralized.

## 5. DEBATE ON NUCLEAR POWER

It has to mention that cooperation between Baltic States in the energy area require to have a strong transparent element. On the Baltic Development Forum in Vilnius on 1–2 June 2010 there were some warnings against nationalistic and politically motivated energy policies in the Baltic region. The current view shows that investment requirements for new generation power have been strongly politicized in some countries of this region [34]. Nevertheless Deputy Minister for Energy Svedas has the opinion of a well-functioning cooperation between the Baltic States. A strong need of working together is resulted in the BEMIP, of course. BEMIP is prepared by the high-level group (HLG). The HLG presented a plan about some projects which are necessary to achieve the full integration of the Baltic energy market in the wider EU market. Transparency is also taking place with regard to Lithuania's behaviour to inform Russia, Belarus and Ukraine about every step Lithuania is taking. [1] Transparent element is not used everywhere, for example in the case of Belarus. Questions about the NPP's environmental impact of planned Belarusian NPP were unacknowledged. [35]

Besides all transparent arguments, concrete incentives to build Visaginas Nuclear Power Plant are low.

New analyses under specific assumptions are strongly needed. Otherwise realization of a new NPP would be highly risky.

Actual development with regard to build a new nuclear power plant is not positive. South Korean company Korea Electric Power Corp. (KEPCO) flipped its bid to become a strategic investor in the construction of the Visaginas nuclear power plant (AE). The current status to build a NPP mentioned by the Energy Ministry of Lithuania was a time horizon until 2020, overly optimistic. Another argument is that country's financial basis is too small to take on the project. [36]

[…] Lithuania does not need the AE not only because of the financial issues, but also because of the fact that there should not be high electricity demand in 2020 in the country, especially because the neighbouring countries are already implementing ambitious nuclear power plant projects. [36]

Financial analyst Rimantas Rudzkis comes to the conclusion that Lithuania has a lot of opportunities to purchase electricity from the neighbouring countries. Therefore it should be clear that cheap electricity without any nuclear power plant in Lithuania is absolutely possible. Question is then, why a risky and expensive building, namely a NPP, in Lithuania. [36] The amount of potential costs depending on the design and vary between EUR 3 billion and EUR 5 billion [37]. It is not for sure to have buyers for electricity possibly generated by Lithuania's intended NPP.

Rudzkis is remarking the following:

[…] Let's build the power plant if we clearly see that we will not manage without it. Now we clearly see that we will survive without it. [36]

In February 2010, Russia has started to construct the Baltiyskaya nuclear power plant (BNPP) in the Kaliningrad region [38]. The first unit should be launched in the year 2016, second unit in 2018. With Russian assistance Belarus is ready for constructing a new NPP in Ostrovets, Grodno region, close to the Lithuanian frontier – first unit shall be online by the end of 2016 or the latest in 2017 [39].

According to Lithuania the projects in Kaliningrad and Belarus are by way of, therefore these nuclear power plants will most likely start delivering energy to the European market much earlier than Visaginas NPP. And it is pretty sure that Lithuanian unit will not able to start operation before 2018. Next restriction is that Lithuania will have some problems to enter the market. Of course, if you come to the details, Belarus is building a NPP to supply for the domestic market, while the Kaliningrad Baltic NPP has export potential and is expected to be a real challenge for Visaginas NPP. Kaliningrad region is not able to consume such large amounts of electricity [28].

There is a strong ambition from Russian site to develop energy links with Poland. The interconnection infrastructural projects of the European Union will also help to open the door for Russian energy to Polish, Central and Eastern European markets, and through the Lithuanian and Swedish link – to the Scandinavian market. If Visaginas NPP will be built once it’s firstly a time lagging with regard to Russia while they are seeking to consolidate its position on the European energy market. The competition could have negative impacts for Lithuania, because their unit would be hardly generate cheaper energy than Baltic NPP. One answer could be to sell energy to neighbouring countries by lower prices in comparison to its production and transmission costs [28].

It has to take into account that Poland also plans to construct two new nuclear power plants. The Polish national nuclear energy program has forced to finalize the construction of the first out of four units in 2022. So therefore competition could be established like to put pressure on Lithuania from the Polish and European energy market. Polish state wants to find a foreign investor by 2013 to help build 3.000 MW nuclear power plant, planned to be operational in 2020 and a second 3.000 MW unit to be ready by 2030 [40]. However, the planning and permission process is not fulfilled yet. Poland has still to choose a location for their domestic nuclear power plant and furthermore appropriate legislation is missing.

The interconnectors between Lithuania and Poland could be an obstacle in solving Visaginas NPP dilemma. When a 3400 MW nuclear power plant will build then Poland could be one market for Lithuania’s surplus energy. The energy network in the northern part of Poland will not withstand the load if Poland uses links to Visaginas and Kaliningrad. Lithuania is strongly pushing Poland for constructing a 1000 MW transmission line Kruonis-Alytus – Elk. There is also dispute about an energy link with Kaliningrad which is negotiated between Moscow and Warsaw. An interconnection from Elk toward the West Poland would open a corridor for the Lithuanian energy to an own market, to Germany as well as to other countries. The extensions of Polish and Lithuanian power grid would be unacceptable for Russia. The companies Enel and Iberdrola are involved in the construction of the Baltic NPP. Only if these companies blockade or refusing to take part in the Russian project, the Baltic NPP could not be finished on time. Additionally, Russia will probably try to suspend the development of energy link Kruonis-Alytus-Elk and hamper Visaginas NPP grid connections. [41]

The 700 MW NordBalt cable is also an important energy transmission corridor – should be online by 2016. Opposite scenario is when Visaginas NPP would not construct. Then NordBalt would become a bridge for exporting Russian energy to the Scandinavian market. Worst scenario would be last one, Russia gets attracted to NordBalt and proceed hindering construction of Visaginas NPP [28].

But there are also increasing scepticism in scientific view in Lithuania, which possibly hampers construction of Visaginas.

Lithuania could do without own nuclear power plant if it manages to find other ways for energy generation. By 2015 eleven Lithuanian power plants will produce in forecast 982 megawatts' [28].

On 8 March 2011 new developments with regard to Baltic NPP are taking place. Full capacity of BNPP is about 2400 MW. Now a deal has been made to export the volume of 1000 MW to Lithuania, expected starting date is 2017. Moreover, there is maybe the possibility of an increase capacity of BNPP in 2019 if the expansion is technically and economically feasible. Restrictively the amount of 1000 MW will supply from BNPP to Lithuania cannot loop up into energy network. The grid connection has a limited capacity of only 750 MW. In comparison, former Ignalina NPP had a performance of 1720 MW [42]. Nevertheless, Inter RAO Lietuvos', a Lithuanian energy company, and its chair Jonas Garbaravicius come to the following statement:

[The power deal] will not be an obstacle to the emergence of the Ignalina nuclear power plant or other energy plan [but rather would help primary energy security and keep prices down for consumers].

## 6. CONCLUSION

Lithuania puts energy independence as a first priority in the setting of national energy strategy. Nevertheless the three principles – energy independence, competitiveness, and sustainability – are not isolated from each other. It has to be pointed out that nuclear energy cannot be sustainable with regard to the storage of nuclear waste. Furthermore, a single nuclear power plant will not help to deploy competition between the energy companies while also de-monopolization of the domestic markets leaves open a lot of questions.

A main issue is that Lithuanian dependency on Russian energy supply would increase if nuclear power will be imported from Baltic nuclear power plant. However, logical approach is to strongly focus on supporting the construction of interconnections. This is an adequate answer to come to a positive impact for the Lithuanian energy system. Some efforts are still needed depending the expansion of electricity grid in the Baltic region – as can be seen in comparison with network capacity between Kaliningrad and Lithuania. Primary these interconnections will help for achieving a competitive, secured energy market and guarantee energy security.

Further effort is to promote small and mid-scale power plants which are useful for reaching flexibility in energy supply.

In the field of renewable energy resources Lithuania wants to increase the total energy consumption to achieve the target of 23% of renewable energy. For the electricity sector this means at least 20%. Regarding renewables Lithuania is lagging behind while only 3 percent of the total capacities are alternative energies. At the moment Lithuanian legislation is not disposed to support renewables, in accordance to EU´s requirements. In addition, restriction is also existent because of limited financial resources.

In 2010 the closure of Ignalina NPP led to an increase in electricity prices in Lithuania about 30 percent and that is a lot for a one year period. Nevertheless, the loss of nuclear power deployed in a positive way the opportunity for a reform of energy market. At same time Ignalina NPP was taken down, new trading exchange BaltPool took off. After first three months electricity trading reached an amount of 60 percent which was used in Lithuania. With regard to the fact that Lithuania trades 40 percent of the power consumers on the exchange, you can see there is a difference between theoretically and practical trades. Lithuanian state expects a duration of 5 to 10 years to finalise the whole process of liberalization and integration. Again, most hampering aspects are the limited interconnections between the neighbouring countries of Lithuania.

In 2020 it is planned to reach fully independency in energy supply from a single source. Therefore electricity demand shall be covered by the use of nuclear power at the basic in Visaginas NPP and through the production from renewable energy sources. While the creation of electricity interconnections with neighbour countries has a high potential to promote a common market, it is questionable if a new nuclear power plant will be built in Lithuania because of a lot of other plans for new nuclear build in the region. Open question is what is about continuant support of Estonia, Latvia and Poland. Baltic nuclear power plant in the enclave of Kaliningrad has an expected capacity of 2400 MW. The argument to build a new nuclear power plant is the current regional energy deficit and the reason that countries´ are hurt very much. To deal with this structure is not simple, but why excluding options, namely electricity supply from Kaliningrad. One can hardly understand the fear about a deep dependence from Russian energy supply. The counter argument is that you have competition if you reach a single energy market for Europe.

Currently, no improvements are on the way for Visaginas NPP. Moreover, a discussion about the reason KEPCO withdraw the bid to construct Lithuanian is only helpful if you come to results. Actual occasions have shown that a deeper scrutiny would be reasonable to analyse the seriousness and necessity of a new NPP building in Lithuania. For that reason the report of Rothschild needs a proof in comparison under current assumptions. It seems to be that the used business model and financing plan for the Visaginas project needs to be revised. At the moment no one is able to make a statement about the question if a new NPP in Lithuania will pay off – the borrowing requirement varies between 3 and 5 billion euros. Firstly, a reliable project planning is needed to come to action. In the short run the project will not help for energy independence and it is questionable if the new NPP is online in 2020. Currently, the NPP project seems to be unrealistic while KEPCO classified the building as non-fundable. If Sekmokas, Lithuanian Minister for Energy, comes to the conclusion that there is no need for Kaliningrad NPP with planned 2500 megawatts, he is may be right. In comparison with his view that political will is the most important condition to build a new nuclear power plant other elements, like essential economical requirements, are completely disregarded.

Boosting investments in renewable energies are useful to achieve long-term energy security. To explore local resources would help to diversify electricity generation. The updated share of Lithuanian renewable energy sources in the final energy consumption reached a level of 15 percent.

The National Energy Strategy also includes increasing the use of renewable energy to 23 % by 2020 and improving energy efficiency. One of the priorities of Lithuania remains to connect the Baltic power grids to the Western European network. The first step is to integrate the three Baltic States in the Nordic countries' electricity market – currently limited by existing Estlink which has a capacity of 350. The strategy calls to complete NordBalt (a connection between Lithuania and Sweden), and LitPol (a connection between Poland with Lithuania) by 2015. Another important step could be the construction of a new LNG terminal. The plan is to overcome the dependency from Russia and to create an own gas market. Therefore it is strongly needed to build some LNG terminals.

Finally, nationalistic and politically motivated energy policies in the Baltic region will help nobody.

## REFERENCES

1. GATERMANN, R. Energy fever in the Baltics, 5 February 2010, European Energy Review. Link to the internet <http://www.europeanenergyreview.eu/index.php?id=1694>

2. COMMISSION. Communication from the Commission to the European Parliament, the Council, the European Economic and Social Committee and the Committee of the Regions - Energy infrastructure priorities for 2020 and beyond – A Blueprint for an integrated European energy network. Link to the internet: <http://www.energy.eu/directives/com-2010-0677_en.pdf>
3. XINHUA. Barroso calls for EU internal energy market by 2014, 4 February 2011. Link to the internet <http://news.xinhuanet.com/english2010/world/2011-02/04/c_13719330.htm>
4. National Energy (Energy Dependence) Strategy, 6 October 2010. Link to the internet: http://www.enmin.lt/en/activity/veiklos_kryptys/strateginis_planavimas_ir_ES/NIS_project_2010_2050.pdf
5. COMMISSION. Communication from the Commission to the European Parliament, the Council, the European Economic and Social Committee and the Committee of the Regions - Second Strategic Energy Review: an EU energy security and solidarity action plan {SEC(2008) 2870} {SEC(2008) 2871} {SEC(2008) 2872}/* COM/2008/0781 final. */. Link to the internet <Communication "Second Strategic Energy Review - An EU Energy Security and Solidarity Action Plan" [COM/2008/0781]>
6. COMMISSION. Report A9017214, Updating T E N-Energy- Invest study (Contract n. TREN/04/ADM/S07.38533/ETU/B2-CESI) with a particular attention paid to the future development of the Energy Market in the Baltic region – Working Group Electricity Interconnections. Phase I: present status of the electricity sector in the EU Member States surrounding the Baltic Sea, including Norway, Belarus, Kaliningrad region and Ukraine; main gaps and bottlenecks, qualitative assessment of new interconnection projects, p. 4. Link to the internet: <http://ec.europa.eu/energy/infrastructure/doc/2009_bemip_a9017214-cesi-interconn-ec-phase_i-final-june_2009.pdf>
7. COMMISSION: Stock taking document. Towards a new Energy Strategy for Europe 2011-2020, p. 1–17. Link to the internet: <www.ec.europa.eu/energy/strategies/consultations/doc/2010_07_02/2010_07_02_energy_strategy.pdf>
8. Ibid., p. 5.
9. Ibid., p. 5–6.
10. Directorate General for Energy and Transport. EU ENERGY SECURITY AND SOLIDARITY ACTION PLAN: SECOND STRATEGIC ENERGY REVIEW, MEMO/08/703, 13 November 2008.
11. COMMISSION. Communication from the Commission to the European Parliament, the Council, the European Economic and Social Committee and the Committee of the Regions - Second Strategic Energy Review: an EU energy security and solidarity action plan, p. 4. See note 5.
12. MAIGRE, M. Energy Security concerns of the Baltic States, March 2010, p. 7. Link to the internet: <http://www.icds.ee/fileadmin/failid/Merle_Maigre-Energy_Security_Concers_of_the_Baltic_States.pdf>
13. Ministry of Energy of the Republic of Lithuania. Year 2015 – the Final Line of Elimination of „Power Islands“, 6 December 2010. Link to the internet: <http://www.enmin.lt/en/news/detail.php?ID=114>
14. EREG. The Regional Initiatives – a major step towards integrating Europe’s national energy markets, March 2010. Link to the internet < http://www.energy-regulators.eu/portal/page/portal/EER_HOME/FS-10-03_RegionalInitiatives_2010-12_v10OK.pdf>

15. COMMISSION. Report A9017214, Updating T E N-Energy- Invest study (Contract n. TREN/04/ADM/S07.38533/ETU/B2-CESI) with a particular attention paid to the future development of the Energy Market in the Baltic region – Working Group "Electricity interconnections” Phase II: methodology for the assessment of new infrastructures and application to the assessment of the interconnection projects already identified in the Baltic area. Link to the internet: <http://ec.europa.eu/energy/infrastructure/doc/2009_bemip_a9017216-interconnections-phase_ii-final-june_2009.pdf>, p. 9
16. SEKMOKAS, A. Changing energy security environment in Lithuania - old challenges and new responses, Expert article 479: *Baltic Rim Economies*, 28.4.2010, p.4. Link to the internet: <http://www.tse.fi/FI/yksikot/erillislaitokset/pei/Documents/BRE2010/BRE_2_2010_Web.pdf>
17. REUTERS. ABB signs 270 mln euro NordBalt power cable deal, 17 December 2010. Link to the internet: <http://uk.reuters.com/article/2010/12/17/abb-nordbalt-idUSWEA820020101217>
18. NUCLEUS. Important stage of NordBalt is Launched, information publication No. 7. Link to the internet: < http://www.vae.lt/files/nucleus_issue_7_en.pdf>
19. VILEMAS, J.: Energy Policy of Lithuania in 1990-2010 and Projections for the Future, Fourth Quarter 2010, International Association for Energy Economics, p. 41. Link to the internet: <http://www.iaee.org/documents/2010FallEnergyForum.pdf>
20. MAIGRE, M. Energy Security concerns of the Baltic States, March 2010, p. 5.See note 12.
21. National Energy (Energy Dependence) Strategy, 6 October 2010, p.5/6. See note 4.
22. LITGRID. Guidelines of national energy independence strategy. Link to the internet: <http://www.litgrid.eu/go.php/eng/Strategic_projects/352/2/514>
23. National Energy (Energy Dependence) Strategy, p. 10. See note 4.
24. BALTPOOL. Market Operator. Link to the internet: http://www.baltpool.lt/go.php/eng/About_us/233/24/373
25. Enefit. Market overview. Electricity market in January 2011. Link to the internet: <https://www.energia.ee/-/doc/pdf/services/Market_overview_January2011.pdf>
26. EESTI ENERGIA GROUP. Eesti Energia Group preliminary results for FY2010, on 28 January 2011. Link to the internet: <https://www.energia.ee/en/business/start/-/asset_publisher/0rFx/content/modalwindow/411876>
27. NATIONAL CONTROL COMMISSION FOR PRICES AND ENERGY. Annual Report on Electricity and Natural
Gas Markets of the Republic of Lithuania
to the European Commission
2010. Link to the internet:http://www.energy-regulators.eu/portal/page/portal/EER_HOME/EER_PUBLICATIONS/NATIONAL_REPORTS/National%20Reporting%202010/NR_En/E10_NR_Lithuania-EN_V2.pdf, p. 14]
28. BAGDONAS, A. New nuclear power plant in Lithuania utopia or realistic project? Geopolitika, 7 February 2011. Link to the internet: <http://www.geopolitika.lt/?artc=4491>
29. MAIGRE, M. Energy Security concerns of the Baltic States, March 2010, p. 9.See note 12.
30. BECKMAN, K. Lithuania trades in Ignalina for BaltPool, 19 Mai 2010. Link to the internet: <http://www.europeanenergyreview.eu/site/pagina.php?id=1996>

31. LITGRID. Transmission System Operator Litgrid Announces Lithuanian Power System Data for 2010, 22 February 2011. Link to the internet: <http://www.litgrid.eu/go.php/eng/Transmission_System_Operator_Litgrid_Ann/78/2>
32. GRYBAUSKAITE, D.: BALTIC NEWS Service. Energy Security Within Baltic Context. Link to the internet:<http://www.eurodialogue.org/Energy-Security-Within-Baltic-Context>
33. EWPA. Electricity consumption in Estonia up 4 percent on year. Link to the internet: <http://www.tuuleenergia.ee/en/2011/02/electricity-consumption-in-estonia-up-4-percent-on-year/>
34. SUSTAINABLE ENERGY SCENARIOS. Energy Perspectives for the Kaliningrad Region as an Integrated Part of the Baltic Sea Region, 2010. Link to the internet: <www.ea-energianalyse.dk/.../1021_Energy_Perspectives_for_the_Kaliningrad_Region_2010.pdf>
35. VAIDA, P. Belarus does not answer Lithuania's questions about NPP’s environmental impact, on 3 March 2011. Link to the internet: http://www.baltic-course.com/eng/energy/?doc=37967
36. VAIDA, P. Rudzkis: does Lithuania need nuclear power plant, on 6 December 2010. Link to the internet: http://www.baltic-course.com/eng/energy/?doc=34605
37. BELLONA. Single Lithuanian nuclear power plant desperately seeking investor, 31 January 2011. Link to the internet: <http://www.bellona.org/articles/articles_2011/single_lithuania>
38. THE VOICE OF RUSSIA. Russia to build nuclear power plant in Kaliningrad region, on 26 February 2011. Link to the internet: http://english.ruvr.ru/2010/02/26/4849931.html
39. TREND. Belarusian nuclear power plant could be operational by 2017, 25 January 2011. Link to the internet: http://en.trend.az/regions/world/ocountries/1817760.html
40. WARSAW BUSINESS JOURNAL. Poland´s nuclear ambitions, 7 March 2011. Link to the internet: http://www.wbj.pl/article-53577-polands-nuclear-ambitions.html
41. REUTERS. Poland´s nuclear works must start by 2014 – GE Hitachi, 1 March 2011. Link to the internet: < http://af.reuters.com/article/energyOilNews/idAFLDE72029820110301>
42. WORLD NUCLEAR NEWS. Import agreement: Baltic to Lithuania, 8 March 2011. Link to the internet:

    <http://www.world-nuclear-news.org/C_Import_agreement_Baltic_to_Lithuania_0803111.html>

CYSENI 2011, May 26–27, Kaunas, Lithuania
ISSN 1822-7554, www.cyseni.com

# INERTIAL PROPERTIES OF THE TACHOMETRIC AIR VELOCITY METER AND THEIR INFLUENCE ON METER'S DYNAMIC ERROR IN PULSING FLOW

**A. Bertašienė, A. Tonkonogovas**
*Lithuanian Energy Institute*
*Breslaujos 3, LT-44403 Kaunas – Lithuania*
*Phone +370 37 401 865*
*Email: agne@mail.lei.lt*

## ABSTRACT

Tachometric velocity meters are widely used for air flow measurements. Their inertial properties and the dynamic error in pulsing flows are investigated insufficiently. We have experimentally studied the response of one of the most common types of this anemometer – cup-shaped one, to a step change in flow velocity. The studies were carried out according to the method that was previously developed and applied to the turbine gas meters.

Experiments have shown that the instantaneous speed of approximation of the tested meter readings to the changing value of flow velocity depends not only on this velocity, but also to some extent on the instantaneous meter readings. In general, the change of the reading is exponential.

By processing of the experiments results, the dependence for the time constant of inertia of the tested meter has been obtained. This dependence has been used to calculate the dynamic error in measuring of the velocity in the pulsing under some lows air flows at different frequencies and amplitudes of pulsations.

The obtained results are useful for selecting the proper size and other parameters of the cup-shaped air velocity meter in a pulsing flows and for estimating of the accuracy of the measurement in pulsing flows.

Keywords: tachometric velocity meters, pulsing flow, air flow measurements, dynamic error.

Nomenclature: $\omega$ – frequency, V – velocity, m/s, Q - flow rate, $m^3/h$, t – time, s, T – inertia index, $s^{-1}$
$\Omega$ – dimensionless excessive rotation frequency.

## 1. INTRODUCTION

Air velocity meters are widely used in industry, the experimental investigations of hydrodynamics, meteorology and environmental protection. There are many different types of meters, whose device and operation are based on different physical principles, and which can be divided into several groups: hydrodynamic, a typical representative is the Pitot tube, thermal, Doppler, mechanical, electromagnetic, ultrasonic and others [1]. Each meter has a certain advantages and disadvantages, which determine the choice of the type under specific conditions.

A special place among the others is occupied by the mechanical velocity meters, first of all, tachometric, i.e. with a rotating sensor. Their main advantages are: simplicity of design, reliability, wide measuring range, ability to measure low velocities, good linearity and sensibility, the possibility to transfer the results of measuring at a distance.

Sensing element is a rotating axial impeller, which wheel generally has (10–20) flat blades to measure small (up to 5 m/s) velocities, or several – usually (3–4) – a semi-circular blades of so-called cup shape. Meters of such type are usually intended for measurement of higher ( > 10 m/s) velocities.

The tachometric meter measures the average velocity across its own cross-section. The less the diameter of the impeller, the higher the measurement locality. In this case, however, the measurement range narrows by reducing the upper limit of measurement, overload capacity and resistance to other off-design influences decrease. To avoid the errors due to wear of bearings the meter must be recalibrated frequently enough.

Measured velocity $V$ and the meter's rotor rotation frequency $\omega$ are related by:

$$\omega = C \cdot V \tag{1}$$

The factor $C$ retains its constancy up to 1% within the measurement range. In the area of the lower limit of measurement it's possible a slightly larger deviation from the nominal value of the factor $C$.

The principles of operation and metrological properties of the tachometric air velocity meters and turbine gas meters (also tachometric), which are widely used for natural gas account, are very close. Because of different reasons, in gas flows always there are pulsations and other flow rate and air velocity changes in the time. Due to meters' rotors inertia their rotation frequency and correspondingly meters' reading always lag from the true momentary value. In the phase of flow rate increasing the lag always bigger than in the phase of decreasing, so the average reading of the meter is always bigger than the true average value. This is the reason of appearing the typical for tachometric meters dynamic error which is always positive.

The problem of the rotation inertia and dynamic error have been studied for turbine gas meters much better than for tachometric air velocity meters. One of the first to evaluate and predicate the dynamic error was W.F.Z. Lee et al. [2]. His studies were developed by N. Lehmann [3], K.N. Atkinson [4], R.J. McKee [5],. B Lee et al. [6]. N. Lehmann got analytical solution for turbine gas meters dynamic error at flow pulsations of rectangular form, which are not occur in practice. The most known are the results of K.N. Atkinson They are obtained for sine flow pulsations and are included into ISO document [7]. Analogical results were presented by R.J. McKee [5]. All obtained results are based on solution of differential equation of turbine meter rotation in the transitional flow, which contains a certain number of hard-to-evaluate parameters. This is the main reason that different investigators results are fragmentary and often disagreed. According to investigations, for example, B Lee et al. [6] in practice the flow pulsation occurs by complex law, for which the results were absent until recently.

Recently J. Tonkonogij et al. proposed and implemented the new method of simulating the turbine gas meter behavior in pulsing flow of arbitrary pulsation law [8]. The combined calculating-experimental method has been developed. The method stipulates the meter inertia time constant as the principal and only characteristic of the meter for the simulation of the meter behavior in transitional flow. The dependence for inertia time constant should be experimentally evaluated by measuring of meter response to the sharp flow rate changing from one value to another. This dependence can be used for calculating the meter response to flow changing by any law.

The main principal difference between tachometric air velocity meter and the turbine gas meter is the design, shape and size of the meters' blades, which perceive the hydrodynamic flow forces. This distinction determines the peculiarities and differences in the dependences for time constant of inertia, response to flow pulsation and dynamic error of the both meters. There are very few investigations of transient processes and dynamic errors in the tachometric air velocity meters. Among them is the work of L.L. Boshniak [9]

The aim of this study was to investigate experimentally the characteristics of the tachometric air velocity meters' inertia and in further to use the results for calculating of the meters' dynamic errors using the developed in [8] method.

## 2. OBJECT OF INVESTIGATION

The cup type anemometer of AP1M2 type has been selected as the object of investigation (Fig. 1). It’s characteristics are given in Table 1.

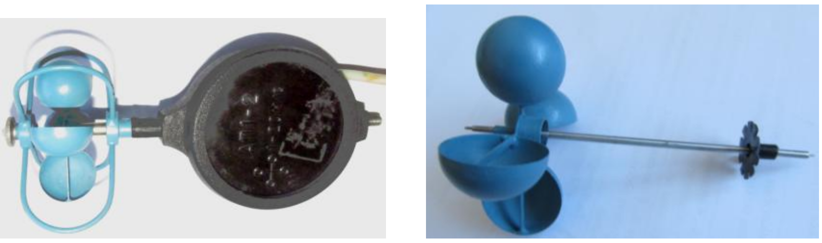

Fig. 1. Anemometer under test: a – general view; b – rotating parts

Table 1. Anemometer’s characteristics

| | |
|---|---|
| Measurement range | (1–20) m/s |
| Maximum permissible error in the range V = (1.5...20) m/s | ±(0.1+0.05V)…±(0.3+0.05V); |
| Number of cups | 4 |
| Cup’s diameter | 21 mm |
| PCD of the cups | 35 mm |
| PCD of the cups’ protection | 81 mm |
| Outer circumference of caps | 56 mm |
| Shaft diameter | 2 mm |
| Shaft length | 90 mm |
| Material of shaft | stainless steel |
| Material of cups | plastic |
| Rotating parts total mass | 9.2 g |
| Number of the pulses per one complete revolution | 10 |

### 2.1. Calibration of the tested meter

Prior to the main research tested velocity meter was calibrated to evaluate dependence of the meter’s rotor rotation frequency on air velocity. Calibration was performed using a standard facility with reference meters for recovery of air flow volume unit. The simplified facility scheme is presented in Fig. 2.

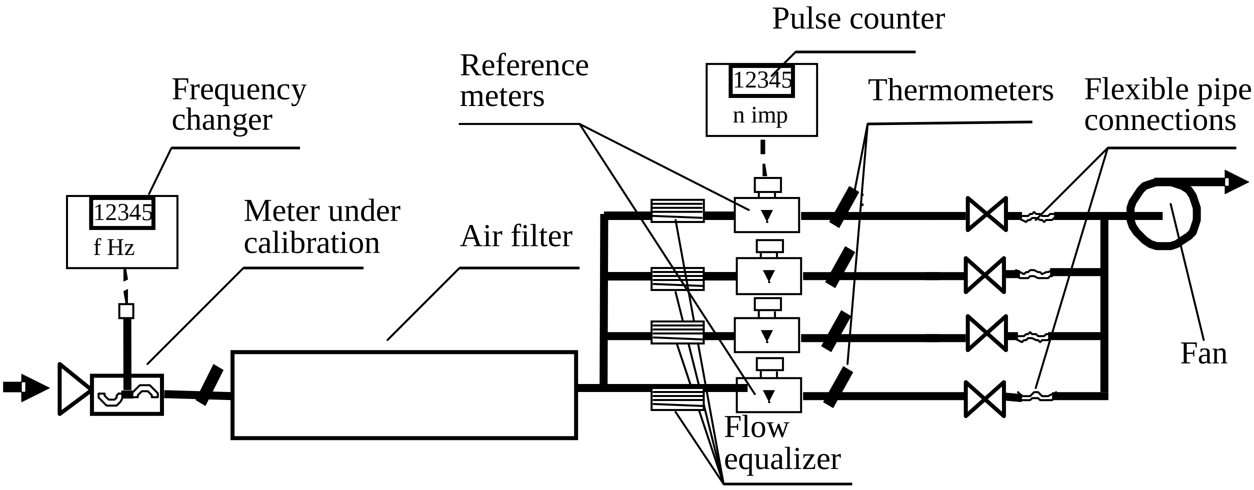

Fig. 2. The simplified scheme of the facility for calibration of the tested air velocity meter

The calibrated velocity meter was installed inside of round tube of inner diameter 100mm. Results of calibration are presented in Fig. 3.

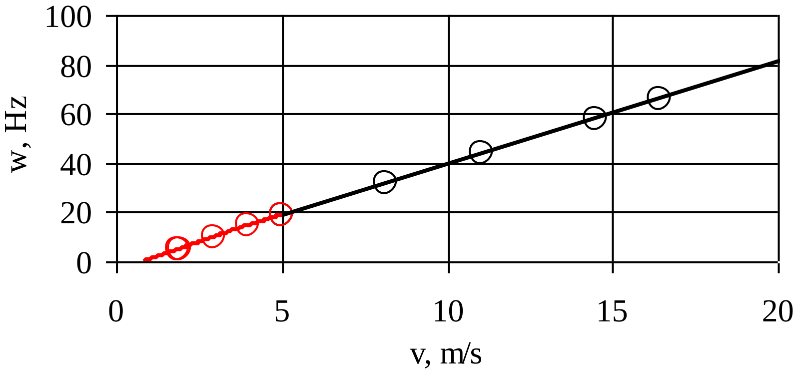

Fig. 3. Calibration dependence for the investigated velocity meter

It has been found two areas of operation of the calibrated meter. For velocity V ≥ 5 m/s, the meters rotation frequency $\omega$ is proportional to air velocity $V$, as must be for the majority of tachometric meters:

$$\omega = 4.124 \cdot V - 1.71\ Hz. \tag{2}$$

For velocity $V < 5$ m/s, rotation frequency $\omega$ and air velocity $V$ are related by the third degree polynomial:

$$\omega = -0.0437V^3 + 0.3112V^2 + 3.9587V - 3.2588,\ Hz. \tag{3}$$

Approximation equations very well describe the experimental data of calibration.

## 2.2. Experimental facility

Experiments were conducted at the facility, previously developed to study the inertia of turbine gas meters [8]. This facility (Fig. 4) ensures possibility of sharp (in shorter time span as in 0.1 s) switching of the tested meter from the line with given initial air flow value $Q_{in}$ into the line with other given finite air flow value $Q_{fin}$ and to measure the meters response – changing rotation frequency during the transient process.

Air flows in every measurement line are provided independently by two fans. Instant switch of the meter under test from one measurement line to another one is ensured by the system of three valves with pneumatic actuators. For air flow rates measurement in each line by flow rate meters of Venturi type have been used. To control the transition process at rapid change of the flow rate pressure drop across the Venturi flow meter in the line of final flow rate was measured by low-inertia diaphragm pressure transducer with a differential transformer.

Change in time of the tested meter rotation frequency has been evaluated from measuring time of receipt pulses from the meter. The pulses have been received and time of each was measured by high accuracy analog-digital converter of ACP 16/16 type which ensures data registration with frequency up to 500 000 records per second.

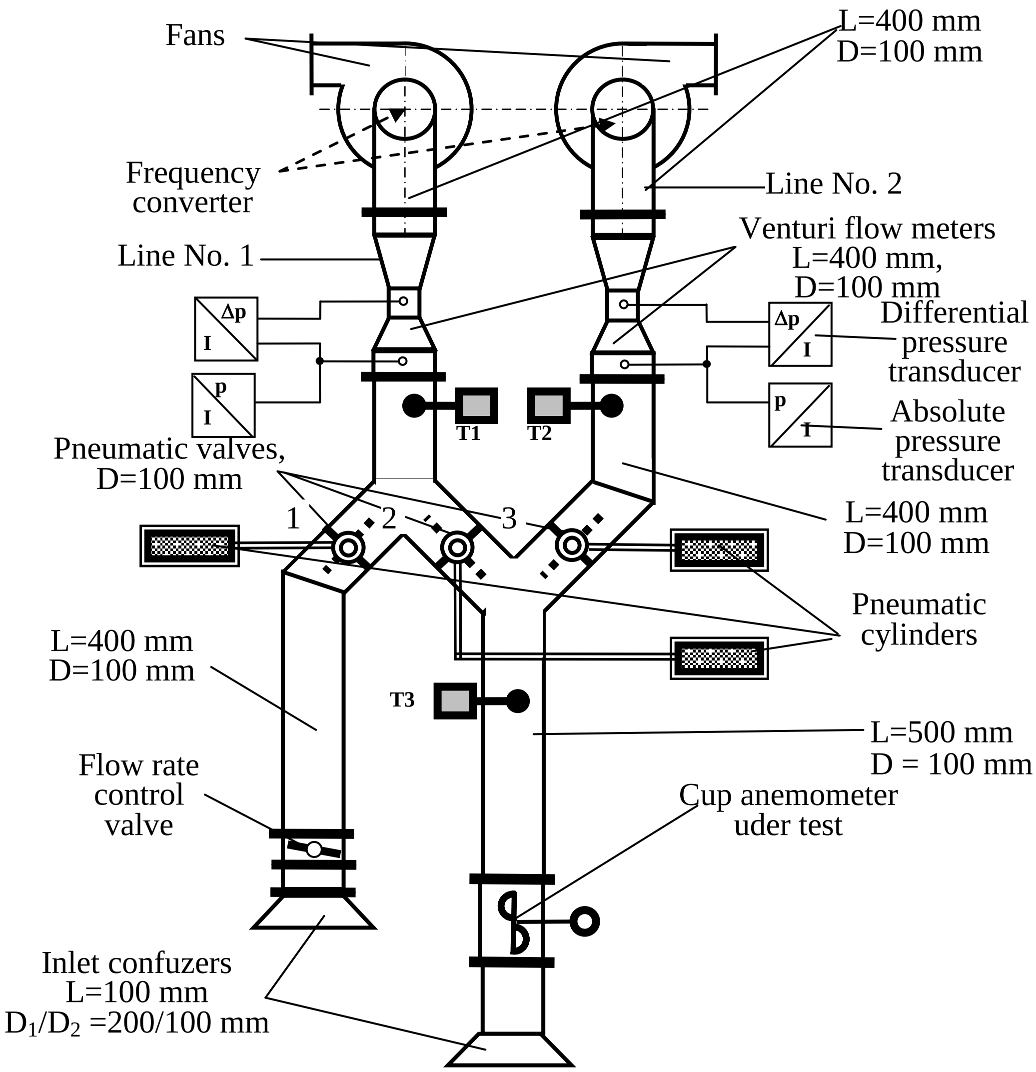

Fig. 4. The simplified scheme of the facility for investigation of tachometric flow meters response to sharp flow change

### 2.3. Program of investigation

Response of the tested velocity meter and its inertia properties have been evaluated for the following four values of the finite air velocity: $V_{fin}$ = 5, 7.5, 10, 15 m/s. It's corresponded to finite meter's rotation frequencies $\omega_{fin}$ = 20, 30, 40, 60 Hz. For each $V_{fin}$ experiments have been carried out for number values of initial velocity from measurement range (1–20) m/s, or (0–80) Hz with a step $\Delta V_{in}$ = (2.5–5) m/s, or $\Delta\omega_{in}$ = (10–20) Hz.

## 3. PROCESSING OF EXPERIMENTAL DATA; RESULTS OF INVESTIGATION

### 3.1. Initial data processing – evaluation of the meter's rotation frequency

For all stored signals from the tested velocity meter (voltage pulse sequence) the time interval between two consecutive pulses has been calculated:

$$\Delta t_i = t_i - t_{i+1}, \text{ s.} \tag{4}$$

For all time values $t_i$ the current rotation frequency has been calculated:

$$\omega_i = 1 / \Delta t_i, \text{ Hz.} \tag{5}$$

Change the rotation frequency in time as a response of the tested meter to the sharp change of air velocity has been plotted. It has been superimposed with a plot of flow rate signal in line of the finite flow rate (Fig. 5).

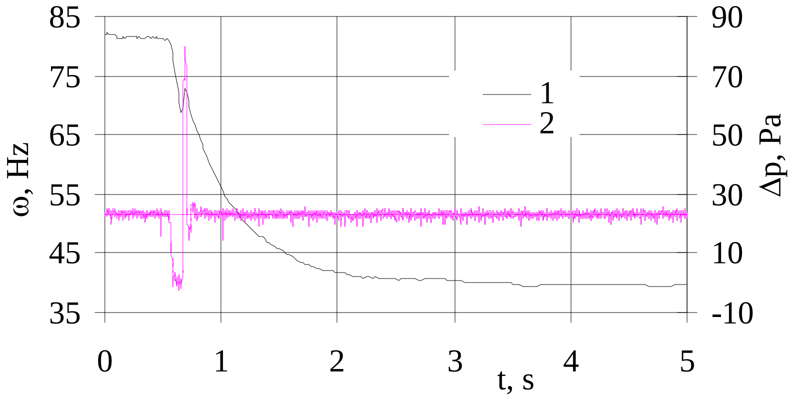

Fig. 5. Change in time of the velocity meter's rotation frequency (1) and of flow rate (pressure drop across the Venturi meter) (2)

On Fig. 5 differential pressure signal from Venturi tube No. 1 is given (2). It shows, that flow rate, that goes through this line is constant before and after shutting valves No. 1 and 3 and opening valve No. 2. Pressure drop shows the moment, when pneumatic valves are openning/shutting, and flow stabilizes after this transitional proceses.

Similar calculations has been performed for all combinations of initial and finite frequencies.

## 3.2. Secondary data processing – evaluation of the meter's index of inertia

As a basic and universal characteristic of inertia of investigated tachometric velocity meter, as well as in the case of turbine gas meters, with reference to [8] was accepted inertia index, or time constant of inertia of the meter *T*. By it, we understand index of the exponential function:

$$\Omega = e^{-\frac{t}{T}}; \tag{6}$$

where $\Omega$ - dimensionless excessive rotation frequency.

$$\Omega = \frac{\omega - \omega_Q}{\omega_{in} - \omega_Q}. \tag{7}$$

This is ratio of difference of current rotation frequency $\omega$ and rotation frequency $\omega_V$, which corresponds to the current flow rate, and initial value of this difference.

In the case, when quantities of $T$ and $\omega_V$ are constant, from dependence (6) it follows that ln($\Omega$) is proportional to time t, and this dependence ln($\Omega$) = f(*t*) is displayed by a straight line, as shown in Fig. 6a.

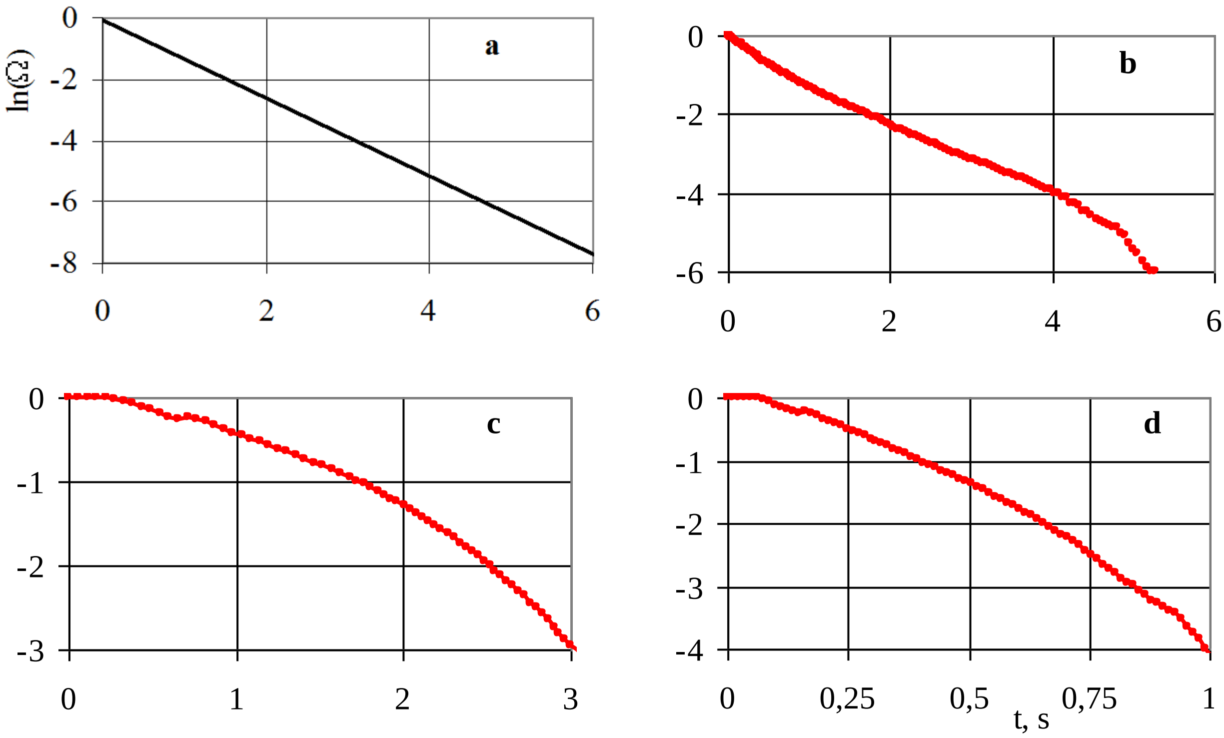

Fig. 6. Change in time of the dimensionless relative rotation frequency at the various values of the current and finite rotation frequencies: a – $T$=const; b – small (< 20 Hz)values of $\Omega_{fin}$; c – moderate (20 – 60 Hz) values; d- high (> 60 Hz) values

Our experiments have shown, that index $T$ does not remain constant even under conditions of constant flow rate $Q$, and significantly changes with the change in time of the difference between the current and finite rotation frequencies. At the same time dependence for different values $\omega_{fin}$ may be as shown in Fig. 6b, c, d.

Considering all the above, the during secondary processing of experimental data the local values of the inertia index T have been evaluated. The current value of the index of $T$ has been determined by numerical differentiation of dependence ln($\Omega$)=f($t$).

## 4. RESULTS OF INVESTIGATION

The main results of the experiments are shown in Fig. 7 as the dependence of the current value of index of inertia of the difference between the current and finite rotation frequencies.

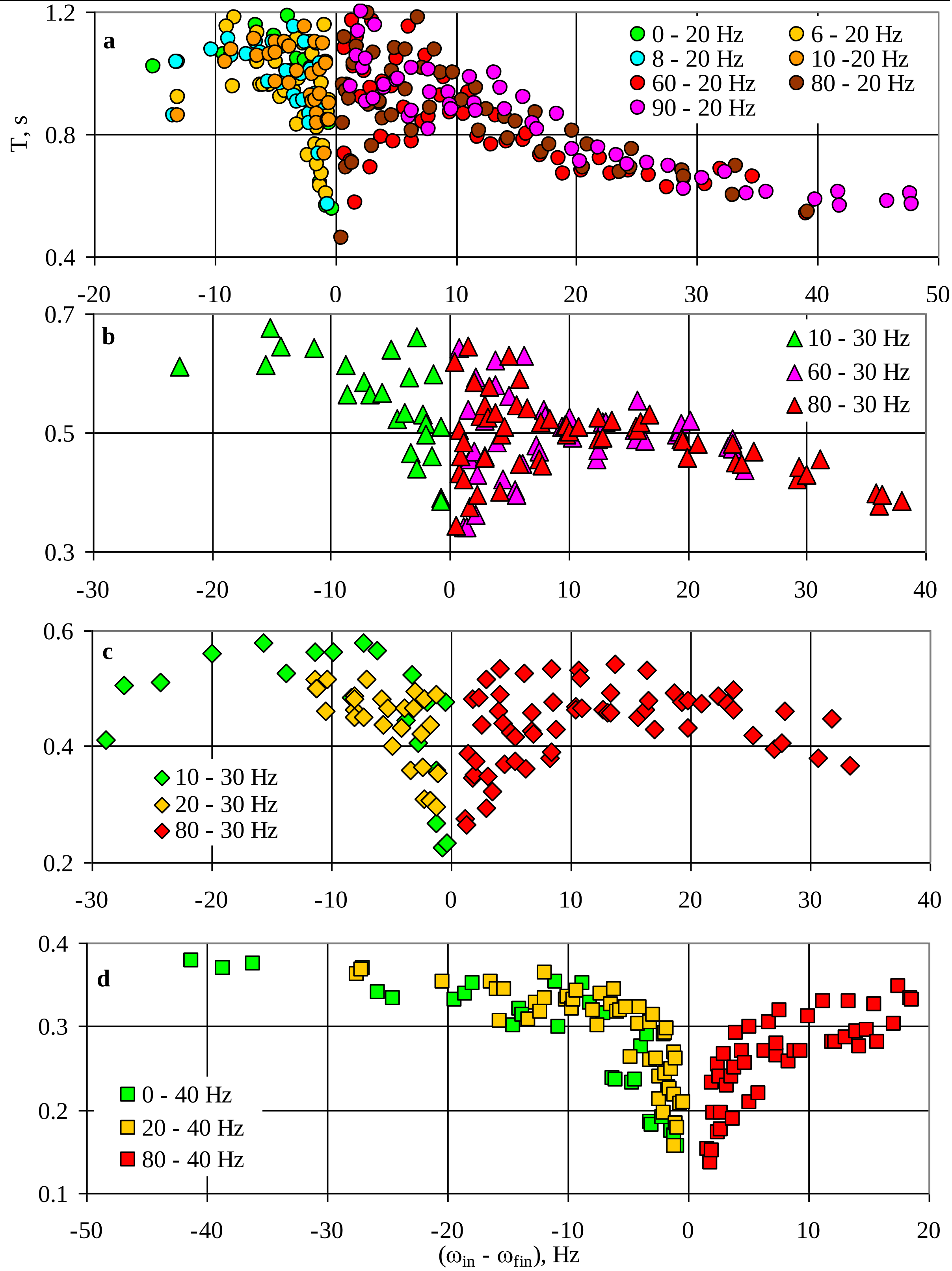

Fig. 7. Dependence of the initial value of the inertia index on the difference of initial and finite rotation frequencies of the tested meter

The character of the influence of the difference of current and finite rotation frequencies on index of inertia is explained by controversial affecting on index of inertia factors the. The first factor is positive and this is hydrodynamic forces aspiring to accelerate the transition process.

The second factor is the braking one; this is discrepancy of current rotation frequency to common hydrodynamic picture.

Analysis of graphs, presented in Fig.7 suggests the following conclusions. Initial rotation frequency of velocity meter does not affect the index of inertia. The last depends on the difference between the current and finite rotation frequencies. Results for different values of the initial frequency coincide at the same current frequency.

It can be assumed that under conditions of changing flow rate the index of inertia will be affected the difference between the current meter's rotation frequency and corresponding to current flow rate frequency. Index of inertia depends strongly on the finite value of rotation frequency.

As seen from Figs. 7, at low values of the difference between the current and finite frequencies greatly increases the scatter of results. It is associated with a significant increase in the error of differentiation and, consequently, increasing the uncertainty of the index of inertia.

At stable flow inertia index depends only on flow velocity (or flow rate, or meter rotation frequency), in our case, on finite velocity. This dependence is presented in Fig. 8.

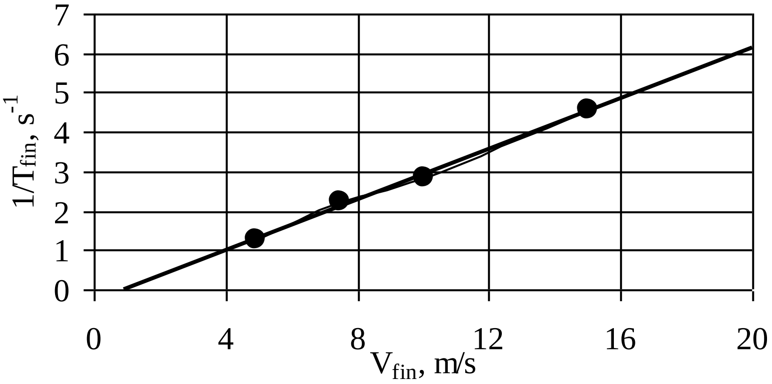

Fig. 8. Dependence of the limit value of the index of inertia of the finite flow velocity

Experimental data for tested air flow velocity meter are described by equation:

$$T_{fin} = 1 / (0.322 V_{fin} - 0.287), s \qquad (8)$$

Finite value of the index of inertia is inversely proportional to air velocity as well as for turbine gas meters.

## 5. CONCLUSIONS

Inertia characteristics of one of representatives tachometric air velocities – a small cup anemometer, have been investigated.

This air velocity meter's calibration showed, that its rotation frequency is proportional to air velocity *V*, when air velocity is > 5 m/s, as must be for the majority of tachometric meters, , but in the range of small velocities (1-5 m/s) rotation frequency and air velocity are related by the third dergee polynome.

It is determined that inertia index *T* does not remain constant even under conditions of constant flow rate *Q*, and significantly changes with the change in time of the difference between the current and finite rotation frequencies. Finite value of the index of inertia is inversely proportional to air velocity.

The obtained results will be used for calculating the dynamic error of the studied class of velocity meters.

## REFERENCES

1. КРЕМЛЁВСКИЙ П.П. *Расходометры и счетчики количества веществ, 5th edition*. Санкт-Петербург: Политехника, 2002, ISBN 5-7325-0410-9.
2. LEE W.F.Z., KIRIK M.J., MILLINGTON B. Gas turbine flow meter measurement in pulsating flow. *Journal of engineering for gas turbines and power.* 1975, Vol. 97, p. 531–539.
3. LEHMANN N. Dynamisches Verhalten von Turbinenradgaszahlern. DAS GAS UND WASSERFACH -GWF-131 1990, Nr. 4, Gas Erdgas, p. 160–167.
4. ATKINSON K. N. A software tool to calculate the overregistration error of a turbine meter in pulsating flow. *Flow measurement and instrumentation,* 1992 Vol. 3 No 3, p. 167–172.
5. *LST ISO/TR 3313:1998*. Measurement of fluid flow in closed conduits – Guidelines on the effects of flow pulsations on flow-measurement instruments.
6. MCKEE R. J. Pulsation effects on single – and two rotor turbine meters. *Flow measurement and instrumentation,* 1992, Vol. 3 No 3, p. 151–166.
7. LEE B. CHEESEWRIGHT R., CLARK C. The dynamic response of small turbine flow meters in liquid flows. *Flow measurement and instrumentation,* 2004, Vol. 15 No 5–6, p. 239-248.
8. TONKONOGIJ J., PEDIŠIUS A., STANKEVIČIUS A. The new semi-experimental method for simulation of turbine flow meters rotation in the transitional flow. World Congress of Science, Engineering and Technology (WCSET 2008), Paris, France. 2008 July 4–6. ISSN 1307-6884, p. 208–212.
9. БОШНЯК Л.Л., БЫЗОВ Л.Н., Оценка динамических свойств турбинно-тахометрических расходомеров. *Приборы и системы управления.* 1967, № 5, с. 15–16.

CYSENI 2011, May 26–27, Kaunas, Lithuania
ISSN 1822-7554, www.cyseni.com

# THERMAL EFFICIENCY OF FORCED DRAFT COOLING TOWER WITH FULL CONE NOZZLES

**A.A. Brin, A.I. Petruchik**
*A. V. Luikov Heat and Mass Transfer Institute*
*National Academy of Sciences of Belarus*
*P. Brovki St. 15, 220072, Minsk, Belarus*
*Phone +375 17 2842222*
*Email: brin@hmti.ac.by*

## ABSTRACT

The mathematical model of the forced draft cooling tower with full cone spray nozzles is proposed. The model represents a boundary-value problem for a system of ordinary differential equations, describing a change in the droplets velocity, its radiuses and temperature, a change in the temperature and density of the water vapour in a mist air in a cooling tower. Heat and mass transfer processes between water and air take place on upward and downward moving droplets. The new simulation data concerning influence of water flow rate, meteorological conditions, water pressure on the spray characteristics and water cooling are obtained. The maximum and minimum values of the droplet radiuses are determined, respectively, by the breaking of large droplets and the carrying away of small ones by the air flow. The dependence of the thermal efficiency of the forced draft cooling tower on the ratio between the mass flow rates of water and air is defined.

Keywords: forced draft, cooling tower, evaporation, thermal efficiency.

## 1. INTRODUCTION

Among the main problems, with which industry is currently faced, is saving the energy resources and decreasing the specific consumption of materials for the equipment. In this connection, the prospects of using the forced draft cooling towers for cooling the circulating water was noted by many authors [1–4]. As of now, the forced draft cooling towers are widely applied in various industrial branches abroad [5–7].

The operating principle of the forced draft cooling tower is shown in Fig. 1.

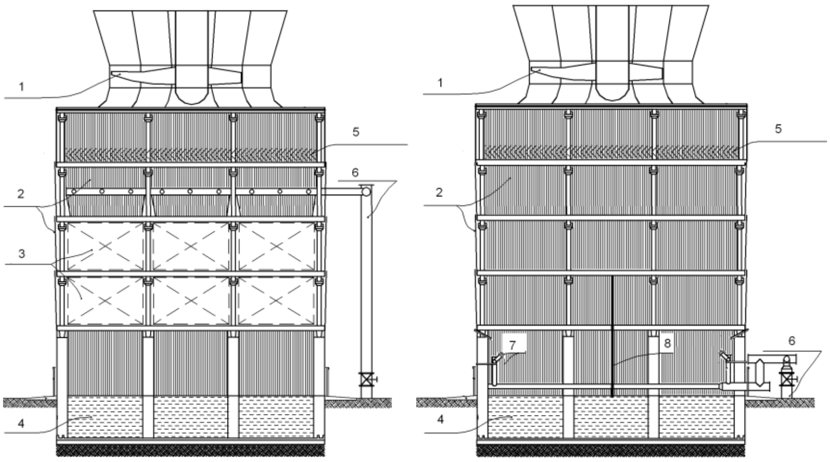

Fig. 1. Schematic of the forced draft cooling tower with fill (left) and nozzles (right): 1 – fan, 2 – wall, 3 – fill, 4 – water pond, 5 – drift eliminator, 6 – supply line, 7 – nozzles, 8 – wind wall

In it, the cooled water is fed under a pressure of 0.05–0.4 MPa to sprayers installed in air-inlet windows. Finely dispersed water drops uniformly occupy the cooling tower space freed from the irrigator. Heat and mass transfer between water and air occurs on a highly developed drop surface. The warm and damp air moves upward, and the cooled water is collected in the catchment basin. Here a high-velocity flow of drops ejects the surrounding air into the cooling tower, producing an additional inflow of the cooling air.

Thus, the forced draft cooling towers can operate without a fan, an irrigator, and other elements, which in some cases allows designing water cooling facilities of simple structure. The advantage of the schemes of such cooling towers with a fan and without it alike lies in the absence of an irrigator, which is essential for plants of metallurgy and oil chemistry. Also, it is established that on transition from free to forced convection the efficiency of the forced draft cooling tower increases by 20–40% depending on the initial water temperature and hydraulic load.

## 2. MATHEMATICAL MODEL

Among the promising methods of studying and calculating the forced draft cooling towers is mathematical modeling. The developed mathematical model is based on the models of evaporative cooling of water drops obtained by the authors previously [8–10]. These models describe, with high accuracy, heat and mass transfer of water drops falling in the air flow. Mathematical modeling of processes in the forced draft cooling tower requires that specifics of hydro- and aerodynamic processes be additionally taken into account.

As in models [8–10], we assume that the axis $z$ is directed vertically downward. Here the value for the velocity of drops moving upward is negative, and for drops moving downward, it is positive. The mathematical model represents a system of ordinary differential equations:

– the equation for variation in the radius of a drop moving upward $R_1(z)$ as a consequence of its evaporation:

$$\frac{dR_1(z)}{dz} = -\frac{\gamma(Re)\left[\rho_s(T_1(z)) - \rho_v(z)\right]}{\rho_w v_1(z)}, \qquad (1)$$

where $\rho_v(z)$ is the density of water vapour in air that is a function of the coordinate $z$;

– the equation for variation in the radius of a drop moving downward $R_2(z)$ as a consequence of its evaporation:

$$\frac{dR_2(z)}{dz} = -\frac{\gamma(Re)\left[\rho_s(T_2(z)) - \rho_v(z)\right]}{\rho_w v_2(z)}, \qquad (2)$$

– the equation for variation in the velocity $v_1(z)$ of a drop moving upward:

$$\frac{dv_1(z)}{dz} = \frac{g}{v_1(z)} - C(Re)\frac{\rho_a[v_1(z) - v_a]^2}{2v_1(z)}\frac{\pi R_1(z)^2}{m}, \qquad (3)$$

– the equation for variation in the velocity $v_2(z)$ of a drop moving downward:

$$\frac{dv_2(z)}{dz} = \frac{g}{v_2(z)} - C(Re)\frac{\rho_a[v_2(z) - v_a]^2}{2v_2(z)}\frac{\pi R_2(z)^2}{m}, \qquad (4)$$

– the equation for variation in the volume-average temperature $T_1(z)$ of a drop moving upward:

$$\frac{dT_1(z)}{dz} = -\frac{3\left\{\alpha(Re)\left[T_1(z) - T_a(z)\right] + \gamma(Re)r\left[\rho_s(T_1(z)) - \rho_v(z)\right]\right\}}{c_w \rho_w R_1(z) v_1(z)}, \qquad (5)$$

- the equation for variation in the volume-average temperature $T_2(z)$ of a drop moving downward:

$$\frac{dT_2(z)}{dz}=-\frac{3\left\{\alpha(Re)\left[T_2(z)-T_a(z)\right]+\gamma(Re)r\left[\rho_s(T_2(z))-\rho_v(z)\right]\right\}}{c_w\rho_w R_2(z)v_2(z)}, \tag{6}$$

- the equation for variation in the temperature of the vapour-air mixture $T_a(z)$ with allowance for heat transfer of drops moving upward and downward alike:

$$\frac{dT_a(z)}{dz}=\frac{4\pi R_1(z)^2N_d}{\rho_a c_a(v_1(z)-|v_a|)}\left[\alpha(Re)\left[T_a(z)-T_1(z)\right]\right]+\frac{4\pi R_2(z)^2N_d}{\rho_a c_a(v_2(z)-|v_a|)}\left[\alpha(Re)\left[T_a(z)-T_2(z)\right]\right], \tag{7}$$

- the equation for variation in the density of water vapour $\rho_v(z)$ in air with allowance for mass transfer of drops moving upward and downward alike:

$$\frac{d\rho_v(z)}{dz}=-\frac{4\pi R_1(z)^2N_d}{v_1(z)-|v_a|}\gamma(Re)\left[\rho_s(T_1(z))-\rho_v(z)\right]-\frac{4\pi R_2(z)^2N_d}{v_2(z)-|v_a|}\gamma(Re)\left[\rho_s(T_2(z))-\rho_v(z)\right], \tag{8}$$

where $\rho_v$ and $\rho_s$ are the water density and the saturated water density in air, respectively $\alpha$(Re) – heat transfer coefficient, $\gamma$(Re) – mass transfer coefficient, C(Re) – drag coefficient [8, 9].

Unlike models [8–10], for the forced draft cooling tower boundary conditions for the system of equations (1)–(8) are specified separately for drops moving upward and downward. The initial velocity of drops moving upward was found with account for the water discharge determined by the water pressure ahead of the sprayer and by the diameter of the sprayer outlet. The initial velocity of falling water drops was taken to be 0.001 m/s. Numerical solution was obtained using an iteration procedure, as a result of which the temperature of water drops at the upper point, the height of the region of drop motion, and the profiles of temperature of the vapour-air mixture and density of water vapour in the heat and mass transfer zone were refined. The solution of the system was implemented in the MathCAD 14 environment using the Runge-Kutta method and was represented as graphs of the dependence of the sought quantities entering into the system of equations (1)–(8) on the vertical coordinate *z*.

## 3. RESULTS

Numerical calculations were performed using the above mathematical model (1)–(8). The efficiency of the cooling tower is defined by the dimensionless parameter:

$$\eta=\frac{T_{w0}-T_{wf}}{T_{w0}-T_{lim}}, \tag{9}$$

where $T_{w0}$ is the water temperature at the inlet to the cooling tower, $T_{wf}$ is the water temperature at the outlet from the cooling tower, and $T_{lim}$ is the wet-bulb temperature. Calculations indicated that thermal efficiency of the forced draft cooling tower, which is characterized by the dimensionless parameter $\eta$, for the given calculation conditions is ~ 0,4 and is a linear function of the ratio $T_{w0}/T_{lim}$.

The efficiency of the forced draft cooling tower $\eta$ as a function of the ratio of specific volumetric flow rates of water and air $q_w/q_a$ is shown in Fig. 2.

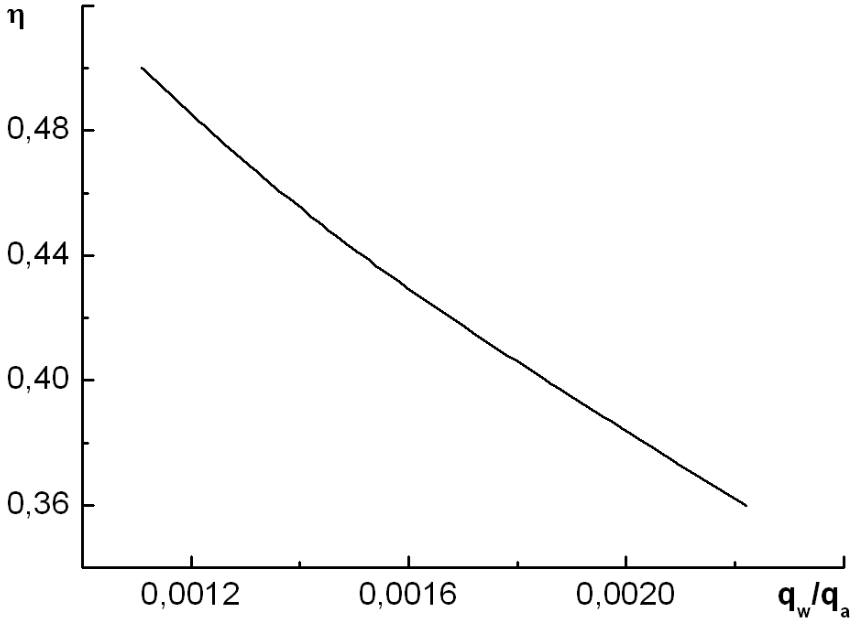

Fig. 2. Efficiency of the cooling tower η as a function of the ratio of volumetric flow rates of water and air $q_w/q_a$

As is seen from Fig. 2, the η dependence on $q_w/q_a$ is a decreasing function, and here the thermal efficiency of the cooling tower with water and air flows organized in it does not tend to unity even with an appreciable increase in the air flow rate or a decrease in the water flow rate. It should be noted that, since the efficiency is defined as the degree to which the temperature of the cooled water approaches the wet-bulb temperature, its higher values correspond to lower values of the initial temperature of water and higher values of the dry- and wet-bulb temperature of air.

In the forced draft cooling tower an irrigator is absent, and a fan and a drop catcher may also be absent. Water is fed to sprayers installed in the air-inlet windows, and the spray cone is directed into the cooling tower perpendicularly to the face. Thus, the problem lies in producing a stable ascending vortex flow of air in the entire internal space of the forced draft cooling tower. It is solved by placing spray nozzles in plan at an angle to the face of the cooling tower rather than perpendicularly to it. Thereby a stable vortex flow of air in the forced draft cooling tower is formed, which is less susceptible to the wind effect, the air discharge through the cooling tower increases, uniformity of the air intake over the irrigation area improves, and irreversible losses of water that are linked with its entrainment in the drop from diminish.

## 4. CONCLUSIONS

It is found that the thermal efficiency of the forced draft cooling tower for design conditions is ~ 0,4 and is a linear function of the ratio $T_{w0}/T_{\mathrm{lim}}$.

It is established that on transition from free to forced convection the efficiency of the forced draft cooling tower increases by 20–40% depending on the initial water temperature and hydraulic load.

The results obtained facilitate the development of a novel method of improving the efficiency of the forced draft cooling tower, which ultimately will significantly increase the economic effect, improve the operation of basic equipment, decrease the ejection of harmful substances into the surroundings, and reduce irreversible losses of water linked with its entrainment in the drop form in the modernization of cooling towers with their conversion to forced draft cooling.

## 5. REFERENCES

1. GALUSTOV, V.S.; CHUFAROVSKII, A.I. Increase of the efficiency of circulating water cooling systems. *Information Bulletin of Water Handling Facilities*, 1984, No. 1, p. 27–31.
2. SVERDLIN, B. L.; BUKINGA, B. V. Experience of introduction of ejection cooling towers in systems of circulating water supply with nonstandard service conditions. *Izv. VNIIG im. B. E. Vedeneeva*, 2000, Vol. 236, p. 219–224.
3. GONCHAROV, A. V. Full-scale investigation of a chimney-type shower cooling tower at the heat and electric plant of the Volzhskii automobile factory. *Izv. VNIIG im. B.E. Vedeneeva*, 2000, Vol. 236, p. 242–247.
4. GALUSTOV, V.S. Direct-flow sprayers in heat power engineering. M.: Energoatomizdat, 1989.
5. YAJIMA, S. Experimental performance of the shower cooling tower in Japan. *Renewable Energy*, 1996, Vol. 10, No. 2–3, p. 179–183.
6. KAISER, A.S.; LUCAS, M. Numerical model of evaporative cooling processes in a new type of cooling tower. *Int. J. Heat Mass Transfer*, 2005, Vol. 48, p. 986–999.
7. QI, X. Performance characteristics of a shower cooling tower. *Energy Conversion and Management*, 2007, Vol. 48, p. 193-203.
8. SOLODUKHIN, A. D.; FISENKO, S. P.; PETRUCHIK, A. I. Simulation of cooling of water droplet and film flows in large natural wet cooling towers. *Inzh.-Fiz. Zh.*, 2001, Vol. 74, No. 1, p. 45–49.
9. FISENKO, S. P.; PETRUCHIK, A. I.; SOLODUKHIN, A. D. Evaporative cooling of water in a natural draft cooling tower. *Int. J. Heat Mass Transfer*, 2002, Vol. 45, p. 4683–4694.
10. BRIN, A. A.; PETRUCHIK, A. I.; FISENKO, S. P. Mathematical modeling of evaporative cooling of water in a mechanical-draft tower. *Inzh.-Fiz. Zh.*, 2002, Vol. 75, No. 6, p. 68–73.

CYSENI 2011, May 26–27, Kaunas, Lithuania
ISSN 1822-7554, www.cyseni.com

# INVESTIGATION OF HEAT EXCHANGE BETWEEN PLANE SURFACE AND TWO PHASE FOAM FLOW

**R. Jonynas**
*Kaunas University of Technology*
*Department of Thermal and Nuclear Energy*
*K. Donelaicio 20, LT–44239 Kaunas – Lithuania*
*Phone +370 37 300445*
*Email: rolandas.jonynas@gmail.com*

ABSTRACT

The main goal of this work is to investigate heat exchange between plane surface and two phase foam flow. Comparing with single phase fluid (gas or liquid), the two phase heat/cool carrier has more advantages – additional potentiality of volumetric void fraction parameter adjustment. By changing this parameter could be changed intensity of heat transfer. During this experimental investigation, two phase foam were generated at the bottom of experimental channel. The flux of upward foam flowed around the plane surface. Surface was heated using direct electric current. Heated experimental section was made of stainless steel with dimensions 0.12 x 0.56 m. Temperature of experimental surface was measured with wired 0.1 mm thermocouples. At the result of this experimental investigation was determined dependence of heat transfer intensity according flow parameters. At flow regime, then Reynolds number of gas ($Re_g$) was enhanced from 190 to 380 (volumetric void fraction $\beta = 0.998$), it was determined that heat exchange rate ($Nu_f$) increased about 30%. Than two phase foam flow was vertical upward comparing plane surface, heat exchange with case of tube bundle (1.5x1.5 in previous investigations) was determined a very notable difference. Using plane surface heat exchange rate ($Nu_f$) is about 5.5 time less (by the same boundary conditions as in case of tube bundle).

Keywords: two phase, flow, foam, plane surface, heat exchange.

## 1. INTRODUCTION

Heat exchange between heated surfaces and two-phase aqueous foam is still on the small scale studied area. In outcome of our previous investigations were defined boundary conditions of foam flow for proper and steady heat exchange process performance.

Statically stable foam keeps its primary structure and dimensions of bubbles for a conditionally long interval of time [1]. This type of coolant was used as heat transfer working fluid.

Heat exchange between tube bundle with various geometry arrays of tubes and upward (and downward) directed aqueous foam flow was investigated in our previous works [2, 3, 4]. It was noticed that value of the heat transfer coefficient between alone heated tube and foam flow was by 21÷42 times higher than by using air flow (single – phase fluid flow) and 6÷11 times less than by using water flow (velocity of water flow was the same as for foam and air). Foam flow velocity was equal to 0.4 m/s and the volumetric void fraction of foam varied from 0.996 to 0.998 for above mentioned case. For comparison a density of the same coolants was equal: 1.2 kg/m$^3$ for air; 3.2 ÷ 5.2 kg/m$^3$ for foam; 998.2 kg/m$^3$ (190÷310 times more than the density of aqueous foam) for water.

Main objective of this work is experimental investigating of heat exchange between plane surface and two phase statically stable foam flow. Results of the investigation compared with previous investigation with tube bundle.

## 2. METHODOLOGY

Experimental facility for investigations was designed and constructed in 2010 yr. and till the end of same year experimental setup was adjusted to proper level.

### 2.1. Experimental equipment

The main experimental equipment consists of: vertical experimental channel with plane surface of stainless steel foil (0.1 mm thickness), gas and liquid control valves, gas and liquid flow meters, liquid storage reservoir, liquid level control reservoir, compressor with receiver, electric current transformer (I and II). Walls of the experimental channel were made from the perspex for visibility of foam flow process. Total length of experimental channel is about 2 m, inner dimensions of cross section – 0.14 x 0.14 $m^2$.

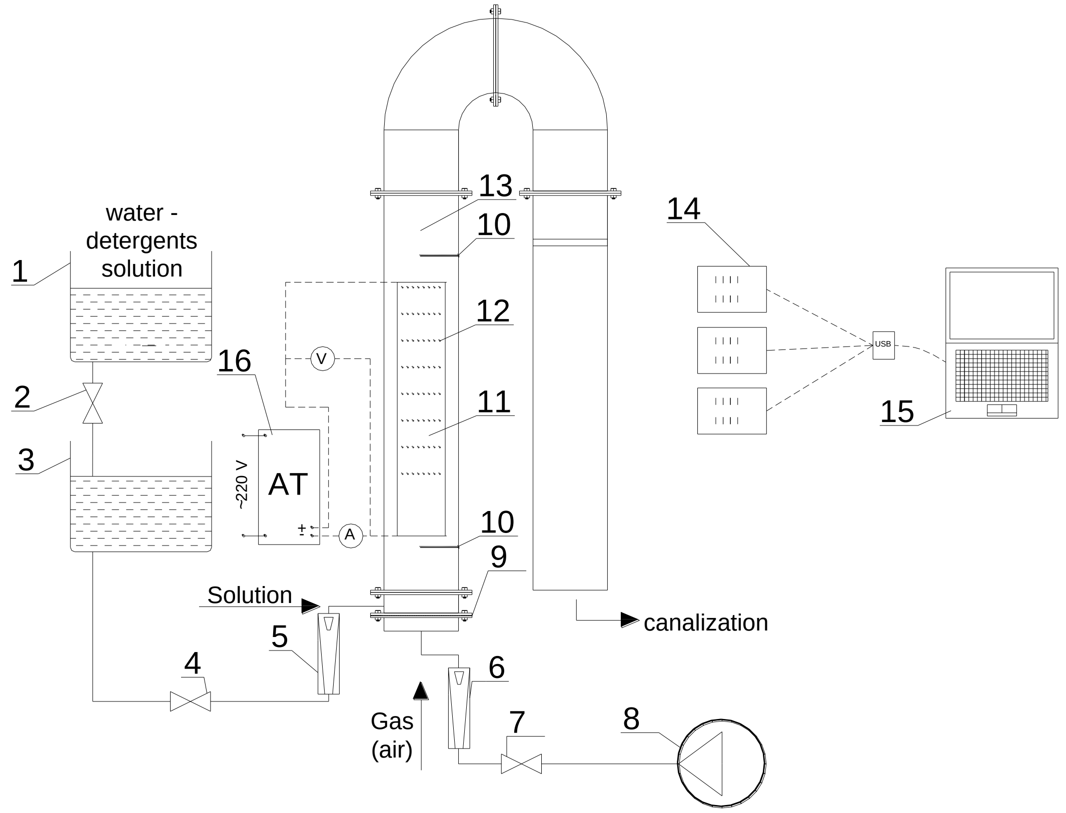

Fig. 1. Principal scheme of experimental setup

There 1 – solution reservoir, 2 – valve, 3 – liquid level control reservoir, 4 – liquid control valves, 5, 6 – flow meter, 7 – gas control valves, 8 – compressor, 9 – foam generation plate, 10 – foam flow temperature sensors (thermocouples), 11 – stainless steel foil (s = 0.1 mm), 12 – copper – constantan thermocouple (0.1 mm), 13 – experimental channel, 14 – data loggers, 15 – laptop, 16 – power source

Statically stable foam was used as a coolant for the experiments. Foam flow was generated from the water solution with detergents. The concentration of detergents was constant at 0.5% level in all the experiments. Solution (water – detergent) was supplied from the reservoir onto the perforated plate. Foam flow was generated during gas and liquid contact. Foam flow parameters control was fulfilled using gas and liquid valves.

The perforated stainless steel plate with a thickness of 2 mm for foam generation was installed at the bottom of the experimental channel; orifices were located in a staggered order with diameter equal to 1 mm.

The calorimeter – electrically heated plane surface was made of 0.1 mm thickness and 0.12x0.56 m dimensions stainless steel foil . At the top and the bottom of stainless steel foil was wired 0.02 m weight copper plates as contacts for electric transformer connection. On the back side of heated plane surface are wired 24 copper – constantan thermocouples. Temperatures were measured with thermocouples and transmitted through data logger to laptop in real-time. During the investigation it was used DC, with electricity parameters: U = 0–2 V, I = 0–80 A.

## 2.2. Estimation of heat exchange

During the experimental investigation the relationship between an average heat transfer coefficient $\alpha$ and gas flow Reynolds number $Re_g$ was obtained:

$Nu_f = f\left(\beta, \mathrm{Re}_g\right)$.(1)

Nusselt number expressed as:

$$Nu_f = \frac{\alpha \cdot d}{\lambda_f}, \tag{2}$$

here $\lambda_f$ is the thermal conductivity of the statically stable foam flow, W/(m·K), computed by the equation:

$$\lambda_f = \beta\lambda_g + \left(1 - \beta\right)\lambda_l . \tag{3}$$

An average heat transfer coefficient was calculated as:

$$\alpha = \frac{\overline{\overline{q_w}}}{\Delta T} . \tag{4}$$

Gas Reynolds number of foam flow was computed by formula:

$$\mathrm{Re}_g = \frac{G_g d}{A \nu_g} . \tag{5}$$

Foam flow volumetric void fraction was expressed by the equation:

$$\beta = \frac{G_g}{G_g + G_l} . \tag{6}$$

Experiments were performed within limits of Reynolds number range for gas ($\mathrm{Re}_g$): 190~440 (laminar flow regime) and foam volumetric void fraction (β): 0.998. Gas velocity for foam flow was changed from 0.14 to 0.32 m/s.

## 3. RESULTS

During the investigation of heat exchange statically stable foam with volumetric void fraction β = 0.998 flows vertically upward.

Heat exchange intensity coefficient was expressed by dependence of $Nu_f$ number from foam flow velocity ($\mathrm{Re}_g$), when β = 0.998 (Fig. 2.). $\mathrm{Re}_g$ was changed from 190 till 380. $Nu_f$ (heat exchange intensity) raised about 30% (from $Nu_f = 60$ till $Nu_f = 78$).

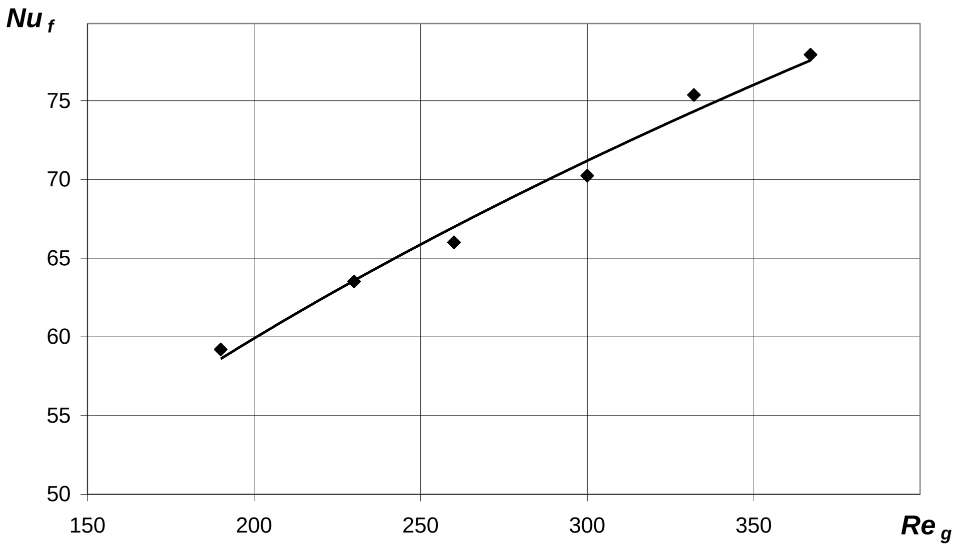

Fig. 2. Plane surface heat exchange intensity dependence from foam‘s $Re_g$ than β=0.998

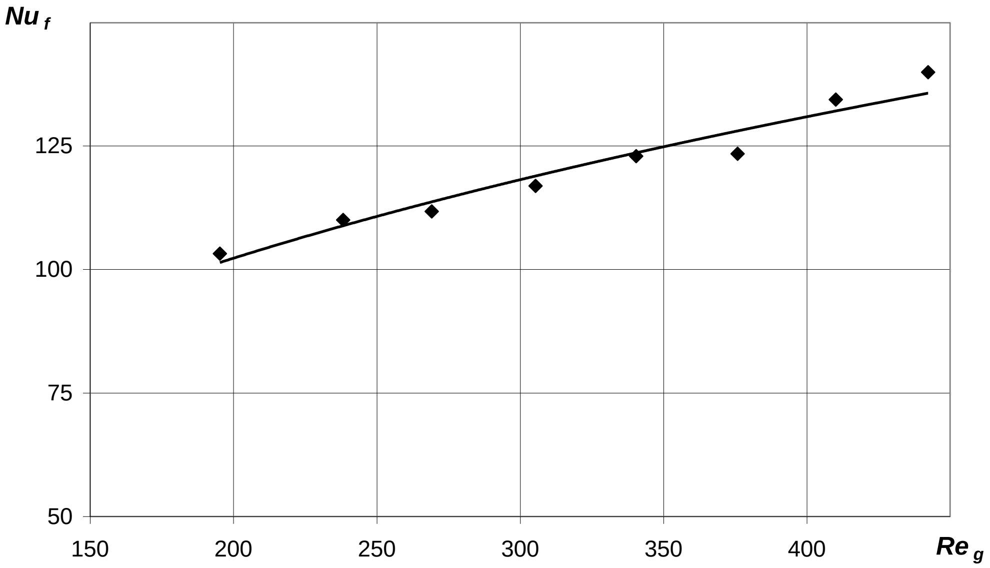

Fig. 3. In-line 1.5x1.5 tube bundle heat exchange intensity dependence from foam‘s $Re_g$ (β = 0.998)

Experimental results of this investigation was compared with previous investigation, when upward statically stable foam crossed 1.5x1.5 in-line tube bundle (β=0.998, Fig. 3.). In this case intensity of heat transfer ($Nu_f$) raised about 66% (from $Nu_f$=298 till $Nu_f$=496). Cooling of in-line tube bundle was 5.5 time more intensive as case of plane surface.

Heat exchange between plane surface and two phase foam flow (β=0.997, β=0.996) investigations takes performance currently.

## 4. CONCLUSIONS

1. Experimentally investigated heat exchange between heated plane surface and two phase aqueous foam than β=0.998.

2. Average heat exchange intensity coefficient value was determined. Valid with boundary conditions: Reg=190 – 380, β=0.998.

3. It was determined that using plane surface heat exchange ($Nu_f$) is about 5,5 time less than in case of tube bundle by the same boundary conditions.

## REFERENCES

1. GYLYS, J. *Hydrodynamics and Heat Transfer Under the Cellular Foam Systems*. Kaunas: Technologija, 1998, p. 50–314.
2. GYLYS, J., ŽDANKUS, T., BABILAS, M., JONYNAS, R., KĖŽELIS, R. Experimental investigation of inline tube bundle cooling with two-phase foam flow. *Power engineering*, 2010, T. 56, No. 2, p. 139–145.
3. GYLYS, J., ŽDANKUS, T., ŠINKŪNAS, S., BABILAS, M., JONYNAS, R. Experimental investigation of the heat transfer process between a tube bundle and an upward aqueous foam flow. Proceedings of Eleventh International Conference on Advanced Computational Methods and Experimental Measurements in Heat and Mass Transfer: Heat transfer 2010. Tallinn, Estonia. Wessex Institute of Technology, UK. 2010 July 14–16.
4. GYLYS, J., ŽDANKUS, T., GYLYS, M., INGILERTAS, A., JONYNAS, R. Heat transfer between non-standard in-line tube bundle and vertically upward aqueous foam flow. CYSENI 2010. Proceedings of the 7th Annual Conference of Young Scientists on Energy Issues. [CD]. Kaunas: Lithuanian Energy Institute. 2010 May 27–28.

CYSENI 2011, May 26–27, Kaunas, Lithuania
ISSN 1822-7554, www.cyseni.com

# RESEARCH OF VISCOSITY INFLUENCE ON THE DENSITY MEASUREMENTS

**M. Kulokas, E. Maslauskas**
*Lithuanian Energy Institute*
*Breslaujos str. 3, LT-44403 Kaunas – Lithuania*
*Phone +370 37 401864*
*Email: kulokas@mail.lei.lt*

ABSTRACT

Measuring systems for different liquids such as petroleum products, liquid biofuels, alimentary liquids, installed in stationary terminals or rail and road tankers, must be regularly calibrated and verified. These works are usually carried out with reference facility. The most important device for measuring liquid volume is positive displacement flow meter. But, it is known; that viscosity of the fluid has influence on accuracy of volume measurement furthermore it is often necessary to convert the volume into a mass or contrary. In this case, it is necessary to know the density of liquids, which is determined by taking samples of liquids for density measurement in the laboratory. This method isn't convenient and accurate, especially now, when there is a need to measure quantity of compressed natural gas, which pressure changes quickly.

These problems can be solved using the Coriolis type mass flow meters (CMF), which directly measures the mass flow and density, and allows justifying universal method for the measurement of liquid or gas. Although the such method isn't new, but the use it as standard measurement tool requires further investigation to determine the influences of viscosity, which changes depend from the fluid type, temperature, pressure, presence of another phase in the flow. Therefore, this method isn't validated for commercial accounts and as reference method. The affect of fluid viscosity to the density measurement accuracy is analyzed in this paper. The density of different viscosity but similar density fluids was measured in experiments. Measurements were executed with CMF and in parallel density and viscosity of experimental liquids control samples were measured with reference devices DMA 5000 and SVM 3000. The results from filling gas cylinders of vehicle with the compressed natural gas in the real situation were analyzed.

Keywords: Coriolis flow meter, viscosity, density, measurement, fluid, calibration, measurement system.

## 1. INTRODUCTION

Most liquids (water, petroleum products, liquid biofuels) and gases (compressed natural gas and synthetic or liquefied petroleum gas) supplied and used in large quantities makes an important part of the country's energy resources therefore raising requirements for accounting system accuracy and legal metrological supervision are foreseen. The same can be said about the widely used chemical and alimentary fluids.

Almost in all cases, the measurement systems consist at least of the following elements [1]:

- flow meter with pulse or current transmitter;
- temperature sensor;
- computer, for processing sensor signals and calculation the actual flowing volume in real and standard conditions;
- filter and air separator for removal of air (gas).

At present the density meter is treated as not mandatory device because fluid properties are determined in the laboratory for each batch and introduced into calculator in advance. Commonly positive displacement flowmeter is used as flow sensor in commercial measuring systems. The liquid portions with the volume equal to the volume of chamber of the rotating rotor are pushed out to the pipeline and counted with calculator. Errors of such devices are setted by amount of leakage through gaps between the rotor and the meter body and alsoinertness. Since the accuracy of most mechanical fluid flow sensor is ± 0.30% [1], so the meter can be used only in a relatively narrow range of viscosity variation [2]. Otherwise, the meter must be calibrated considering the real viscosity ranges of measured fluid.

The calibrations using different liquids in the laboratories require very expensive equipment, because fluid viscosity is changing in quite wide range and it realization isn't economically reasonable in a small country where relatively small amount of measurement systems are installed. Experience shows that there are two solutions of this problem:

- in areas where specific requirements are set more accurate and less inert flow sensors should be installed. It is already going into practice, for example: installation of CMF for accounting produced dehydrated ethyl alcohol, as normative documents require that flow measurement accuracy must be within ± 0.2 %; filling gas cylinders of vehicles with compressed natural gas is measured with accuracy ± 1.0% using low inertia CMF as gas which pressure changes rapidly over short period of time; for similar reasons, CMF is used for natural gas turbine power control in energy objects; more often the electromagnetic flow meters is used for alimentary liquids measurements;
- CMF are rather expensive and have some installation limitation, concerning mechanical affects, overall dimensions and other factors, so it is necessary to pay attention to those factors when CMF is installed in mobile reference facilities. These reference facilities must be accurate and easily transportable to the measurement systems maintenance location. In addition, industrial fluids must be used for calibration. This factor is particularly important to reduce expenses for calibration and to increase accuracy of measurement systems.

In both cases it is advisable to choose mass flow meter as most important element of mobile reference facility and only in certain cases for calibration it is recomended to apply weighing or volumetric methods and instruments .

Fig. 1 block scheme of the oil metering system connected for calibration with mobile reference facility using that is settled in dotted line. Mobile equipment is connected consistently to calibration measuring system.

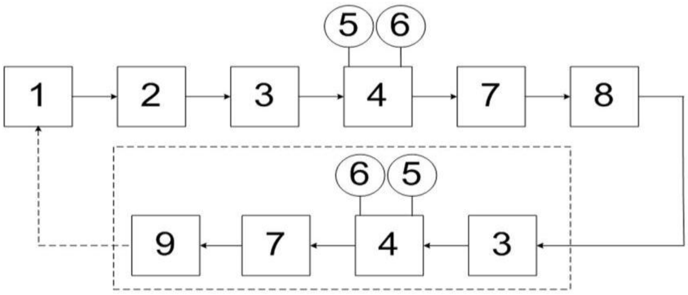

Fig. 1. Scheme of liquid fuel measuring system connected for its calibration to reference mobile facility. 1–8 is elements of the measurement system: the reservoir, operated pump, air separator/filter, meter chamber, thermometer, pressure sensor, fluid density meter. Calibration equipment such as 3–7 is as a measurement system, an intermediate tank, 9 – marked by the dashed line

As it was mentioned earlier, the density of liquid filling systems is often calculated using the American Society for Testing and Materials (ASTM) reference tables [3]. For achievement most accurate measurement results the liquid density is measured using density meters that operates on CMF principles.

Coriolis mass flow meters for liquids and gas flow measurement method based on the Coriolis forces, when the fluid is flowing in vibrating tubes. These forces depend on the fluid mass flow rate and the density.

One or two tubes vibrated perpendicular to the flow direction, electromagnetic actuator mostly operated the center of the pipe. Electromagnetic (sometimes laser) position sensors is received measuring tubes motion. At the absence of flow, and at the empty tube, they vibrate at rezonant frequency. After filling the tube with liquid (gas), weight changes and therefore frequency of tube vibration changes [4].

Coriolis force causes vibratied tube stay behind the front of the tube against the end. Diference of phase between the front and rear is proportional to the mass flow. Such dependence is used often at CMF to simplify the calculation of density:

$$\rho = K_\rho \left( \left( \frac{f_{lt}}{f_{vt}} \right)^2 - 1 \right), \tag{1}$$

here $K_p$ is the density calibration constant, which depends for the pipe geometry, the Young's modulus and other parameters which are fixed for a specific meter, $f_{lt}$ is vibration of empty pipe frequency at measurement temperature $t$, $f_{vt}$ is full pipe frequency. In this case, the temperature effect is eliminated. Flow rate is obtained by:

$$Q_m = K_q \frac{A_c}{A_e} \frac{1}{f_v}. \tag{2}$$

here $A_c/A_e$ is the phase difference between the front and rear of the tube, $K_q$ – the mass flow calibration constant.

## 2. INVESTIGATIONS OF LIQUID VISCOSITY INFLUENCING TO THE DENSITY OF THE LIQUID

### 2.1. Research method and equipment

This study aims to asses the impact on the viscosity of investigated fliud density mesurement results.The research was performed at calibration of the CMF with diferent viscocity and similar density liquids. Two curved pipe type Coriolis mass flow meter was selected for experiments. Its nominal diameter for the connecting line is DN15, working temperature range is $-50 \div +200$ °C and maximum pressure – 4 MPa. The density measurement error is $\Delta\rho = \pm\ 0.001$ g/cm$^3$ and is achieved after calibration of the density in the narrow temperature ranges. Mass flow measurement accuracy is $\delta$ = ±0.1%. Other metrological characteristics of the devices is presented at [5, 6]. This type of meter was chosed not randomly. These CMF’s are more used, probably, befor the other types for both liquid and gas metering, batching in Lithuania. Viscosity and density of experimental liquids was measured with the reference laboratory viscosity and density meter SVM 3000, whose density measurement accuracy is $\Delta\rho = \pm 0.0005$ g/cm$^3$ and viscosity – $\delta_\mu = \pm 0.35\%$. Other characteristics are present in [7].

The analysed fluid density directly depends from temperature, but at the research time is necessary to know the true fluids density value. Temperature gradient between the fluid and the room must by low and room temperature need to maintain stable.

The measurements were performed at atmospheric pressure, to avoid the pressure influence to research. Atmospheric pressure fluctuation almost does not affect fluids density. Influence of pressure to measurements with CMF is described some detail in [8].

In considering to the aforesaid, the density measuring accuracy with CMF includes:

$$\Delta\rho = f(T_f, T_o, P_f, P_o, \mu); \tag{3}$$

here $T_f$ and $T_o$ – the fluid and air temperatures, $P_f$ ir $P_o$ – the excess fluid and air pressure, $\mu$ – viscosity.

If the conditions is: $T_f \approx T_o$, temperature gradient $\Delta T_{fo} \to 0$, $P_f = 0$ and $\Delta\rho_p = f(\Delta P_o) \to 0$, (3) can be rewritten:

$$\Delta\rho = k \cdot f(\mu); \tag{4}$$

here $k = f(T_f, T_o, P_f, P_o) = const$.

Since the CMF density measurement characteristic was corrected in narrow ranges, changes of errors are relatively small, and it can be concluded that the CMF density measurement error varies only of the viscosity of liquids.

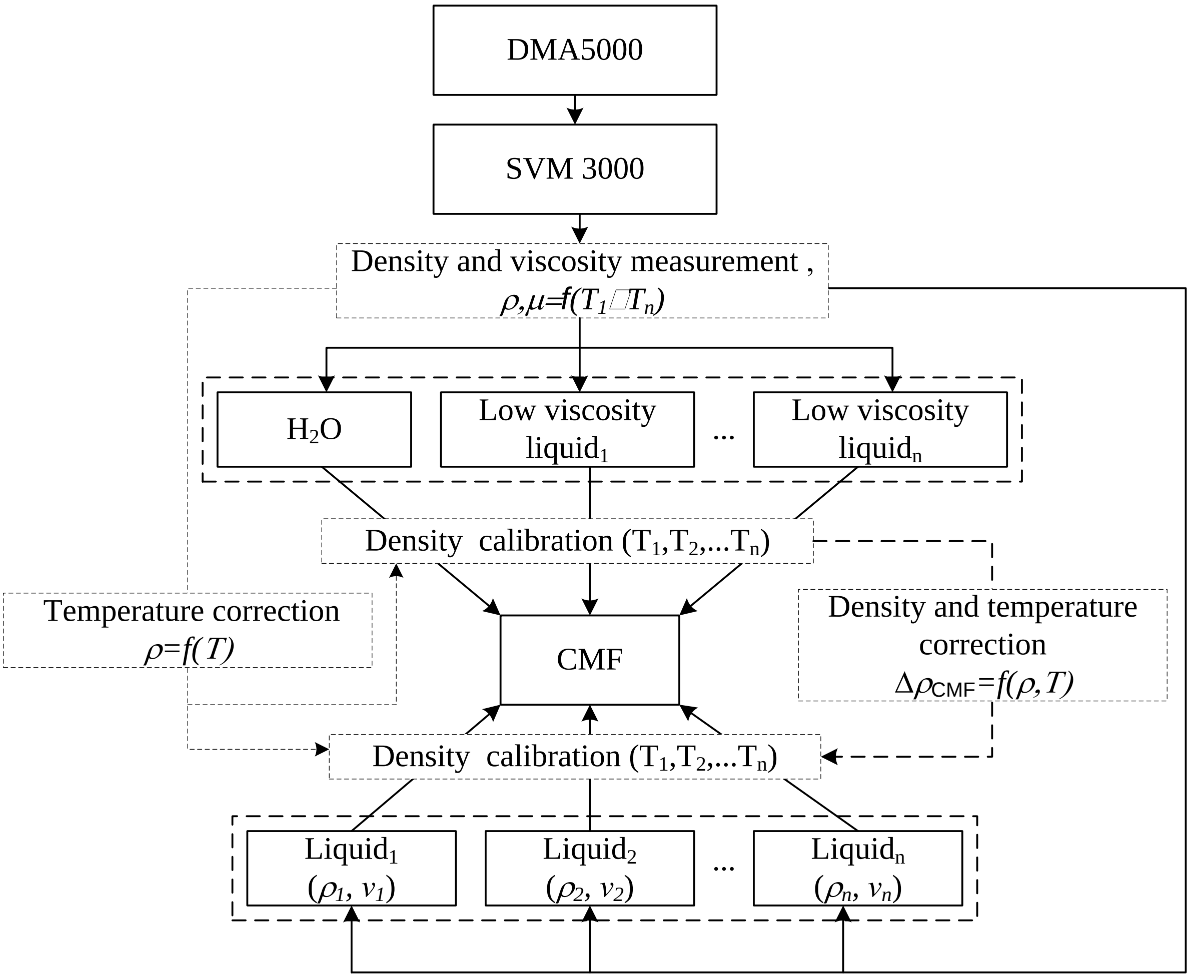

Fig. 2. Research scheme

Density – viscosity research was performed in several phases: density and viscosity measurements of experimental low and high viscosity liquids with density and viscosity meter SVM 3000 in temperature ranges 20÷22 °C; CMF density errors finding with known parameters low viscosity liquids; CMF density errors finding with known parameters high viscosity liquids , liquid density correction of temperature changes and finding additional errors by eliminating with low viscosity liquids errors:

$$\rho_p = \rho_{CMF}(T_x) - \rho_{SVM}(T_x) - \Delta\rho_0, \tag{5}$$

here $\rho_{CMF}(T_x)$ – the high viscosity liquids density, measured with CMF at operating temperature $T_x$, $\rho_{SVM}(T_x)$ – the same fluid density, measured with the reference density meter SVM 3000 at the same temperature $T_x$, $\Delta\rho_0$ – CMF density error, obtained by measuring low viscosity at known parameters fluids.

## 2.2. Results

One of the most important study of preparatory task – study and analysis of the basic fluids parameters. Basic attention was gave on the liquid performance characteristics (wide range of viscosity at the simple density); stability over time at the affect of temperature, pressure, humidity; safety (non-toxic, non-aggressive, low-evaporating). The heat conductivity has the important moment, because the temperature delay trought room and liquid has influence on the measurement.

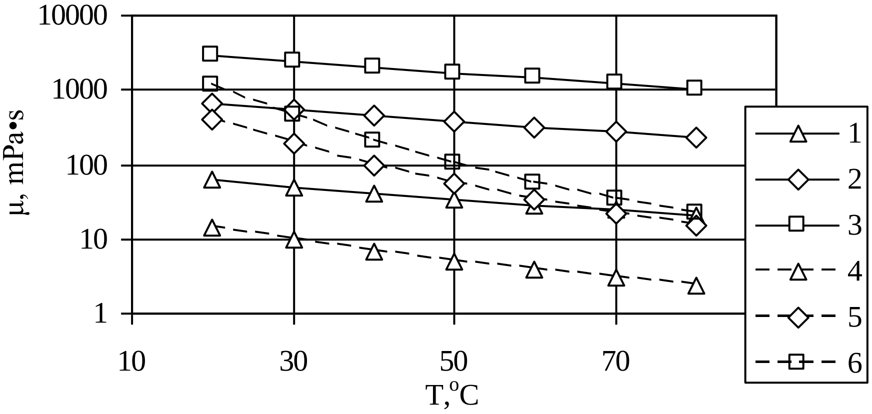

Fig. 3. The temperature influence on vicosity of liquids: 1 – „Dow Corning 200/50“, 2 – „Molyduval Sylo D 500“, 3 – „Molyduval Sylo D 2000“ (1, 2, 3 – silicone oils), 4 – sugar solution in water „1:1“, 5 – sugar solution in water „2:1“, 6 – sugar solution in water „3:1“

The measurements of a different fluids viscosity and density where made. Study of the sugar solution showed that the viscosity change is very high of sugar–water solutions at temperatures of the room and lower (sugar solution 3:1 dynamic viscosity μ dropped from 1.0 to 0.8 Pa • s, at rising temperatures from 22°C to 24°C). Thus, It is necessary to maintain a relatively stable temperatures, when these liquids is used in research. This relation is much smaller for silicone oil. These oils have good physical stability of properties in time at affect of temperature, pressure, etc. It is also important, that the silicone oil densities are similar to each other and similar to the water density. The temperature influence on the density is approximating linear for the all liquids.

Density measurements were performed in some intermediate points with the low viscosity fluids, to determine the CMF density error characteristic. Samples of liquid were ethanol-water solutions and water.

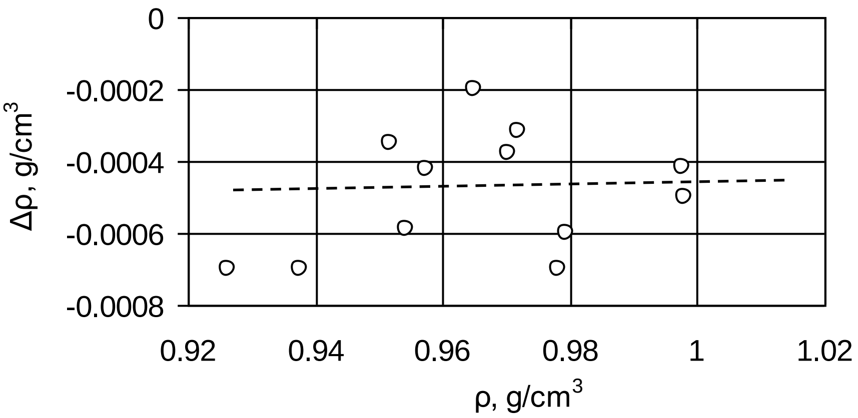

Fig. 4. The density calibration of CMF with low viscosity liquids

It is traced line through error values $\Delta\rho$ = -0.0005 ÷ -0.0004 g/cm$^3$, although the dispersion of the results is quite big (it can be perform linear approximation at the narrow density ranges). The large dispersion is likely influenced by the water-ethanol solutions and their characteristics volatility, and tendency to stratification. The difference of water density measurements (two last points) is 0.0001 g/cm$^3$, and quite well correspondes the passing line.

It had to take actions for removal of air bubbles, and the cleaning of sensor tube at the time replacement of liquids, during the measurements with higher viscosity oils ($\mu$ = 3000 mPa • s).

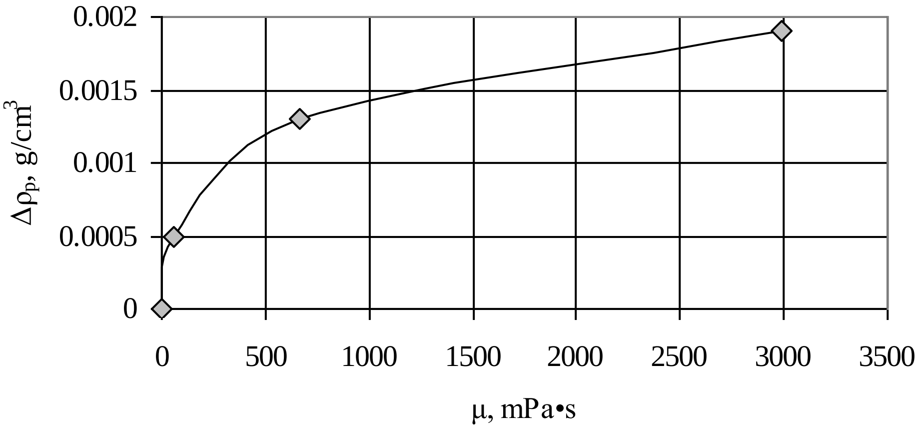

Fig. 5. Additional CMF density measurement error for the viscosity change by changing liquids

It is noted, that the changing of additional error is important, when the fluid viscosity changes from 0.8 to μ = 60 mPa•s and later, when viscosity exceed μ = 3000 mPa•s the aditional density error approach to the constant value. However, the density error changes would still not exceed the tolerance, which is given by the manufacturer's documentation for CMF (at using CMF at narrowed temperature-density ranges, and after density calibration).

The density measurements of A-95 petrol samples was performed with CMF at liquid fuel filling terminals: 1 – AB „ORLEN Lietuva“, 2 – UAB „Lukoil-baltija“ ir 3 – AB „Klaipėdos nafta“. Three density measurements were performed at each of the terminals and the results are presented in Fig. 6. They shows same characteristics of fluid sample density distribution at these terminals.

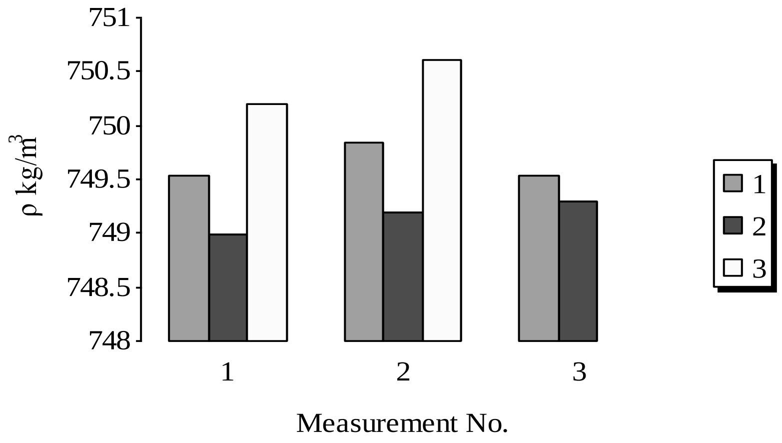

Fig. 6. Density values at temperature 15 °C of the petrol A-95 samples received from liquid fuel filling terminals: 1 – AB „ORLEN Lietuva“, 2 – UAB „Lukoil-baltija“ and 3 – AB „Klaipėdos nafta“

The density values were determined after petrol A-95 sample density measurements at the same liquid fuel filling terminals: 1 – with the CMF, 2 – industrial density meter (L-Dens 427F [9]) and 3 – with the laboratory density meter(DMA 4500 [10]). Absolute errors in table 1 was calculated by comparing measurements results: $\Delta\rho_1 = \rho_{system} - \rho_{CMF}$, $\Delta\rho_2 = \rho_{system} - \rho_{terminal\ lab.}$ and $\Delta\rho_3 = \rho_{terminal\ lab.} - \rho_{CMF}$.

Table 1. Absolute errors of petrol A-95 samples density measurements

| $\Delta\rho_1$ | $\Delta\rho_2$ | $\Delta\rho_3$ |
|---|---|---|
| 0.0003 | -0.0003 | 0.0 |
| 0.0002 | 0.0001 | 0.0003 |
| 0.0004 | - | - |

Performed density measurements showed, that the density difference is constant at each object, but they differ when compared to each other. Such density measurement errors could to procure by changing of the sample properties: stratification, changes in temperature, evaporation.

Accuracy test of compressed gas was performed at the gas-station by filling to the vehicle cylinders, which flow is measured with CMF. Compressor was feed compressed gas to 200 bar into the cylinder, which has been weighed before and after the measurement. CMF readings are compared with the reading of scales. The test was performed at empty cylinder filling and from starting pressure $p_0$ = 100 bar.

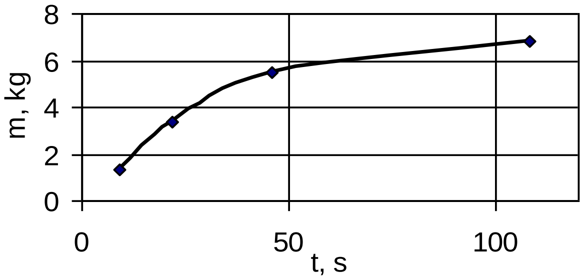

Fig. 7. Cylinder weight change at time

Fig. 7 shows, that weight of cylinder and flow change in logarithmic law. so we can say that, at fill starting from empty bottle and from starting pressure 100 bar, the average flow rate is different.

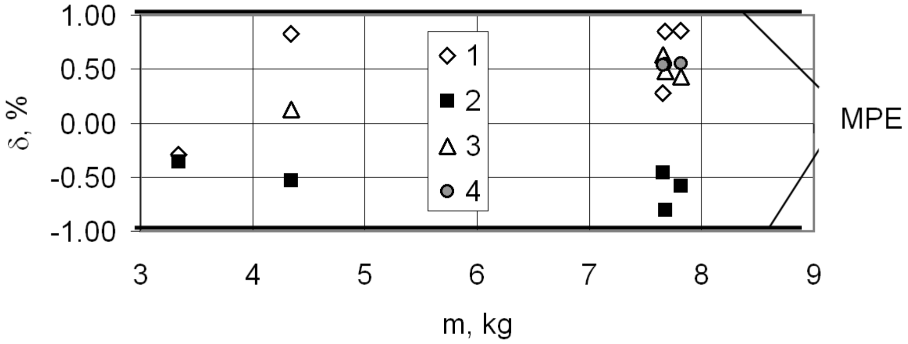

Fig. 8. Errors of compressed natural gas mesurements with CMF at gas station. Filled weight m ≈ 4 kg (equivalent to $p_0 \approx 100$ bar) and m ≈ 7 kg (equivalent to $p_0 \approx 0$ bar)

Fig. 8 shows, that all errors is significantly lower than the maximal permission error (MPE), despite the fact, that the gas pressure and viscosity was changed from begin to the end of measurement in very large range and CMF was calibrated with water.

## 3. CONCLUSIONS

1. Density of different viscosity liquids was measured with CMF. Parameters of liquids were measured with reference density and viscosity meters DMA 5000 and SVM 3000. It was established, that accuracy of density measurement with CMF depends of viscosity. The higher growth of density errors was observed in lower viscosity range. Meanwhile, the use of more viscous fluids ($\mu > 600$ mPa•s), reduced the growth of additional density error. However, the additional error does not exceed the value of $\Delta\rho = \pm 0.0010$ g/cm$^3$ in the all investigated fluids viscosity ranges which comply with the manufacturer's declarations.
2. The density differences of A-95 petrol samples, measured by CMF in several liquid fuels filling terminals did not exceed 0.0004 g/cm$^3$. The repeated density measurements with DMA 5000 of the same liquid samples in the laboratory show the deviation value of 0.0003 g/cm$^3$ which can be explained by air, vapor release from the liquid and stratification.
3. The errors of mass flow accuracy test using CMF in gas-station, was derived lower than the Maximal Permission Error (MPE), despite the fact, that the pressure and viscosity of gas was changed in wide ranges. Therefore CMF calibrated with water could be also used for gas mass flow measurements.

## REFERENCES

1. International Document OIML R 117-1. Dynamic measuring systems for liquids other than water. Paris. Edition 2007, p.126.
2. PEDIŠIUS, N, ZYGMANTAS, G, BONČKUS, A. Tekančių skysčių klampos įtakos tūrio matavimui tyrimas. ENERGETIKA. 2008. T.54, Nr. 4, p. 29–34.
3. Petroleum Measurement Tables. International Library Service, Vol. 8. Link to the internet <http://www.normas.com/ASTM/pmts.html>
4. RASZILLIER H., DURST, F. Coriolis-effeet in mass flow metering. Archive of Applied Mechanics, 1991, No. 61, p. 192–214.

5. Coriolis Flow Measuring System Promass 80/83 F, M. Technical Information TI 053D/24/ae. Endress+Hauser. Link to the internet <http://www.amjequipment.com/eh/Flow/Coriolis%20Mass.htm>
6. PROline promass 83 Coriolis Mass Flow Measuring System. Operating Instructions BA 059D/06/en/01.03. Endress+Hauser. Link to the internet <http://www.amjequipment.com/eh/Flow/Coriolis%20Mass.htm>
7. Stabinger Viscometer SVM 3000 instruction manual. Anton Paar, Austria, 2007, 123 p.
8. KOLAHI, K., SCHRÖDER, T., RÖCK, H. Model-based density measurement with Coriolis flowmeter. *IEEE transactions on instrumentation and measurement,* Vol. 55, No. 4, August 2006.
9. Density transducer L-Dens 427F I instruction manual. Anton Paar, Austria, 2007, 116 p.
10. Density meter DMA 4100/DMA 4500/DMA 5000 instruction manual. Anton Paar, Austria, 2007, 159 p.

CYSENI 2011, May 26–27, Kaunas, Lithuania
ISSN 1822-7554, www.cyseni.com

# METHODOLOGY FOR MEASUREMENT OF WATER TEMPERATURE PROFILES

**D. Laurinavičius**
*Lithuania Energy Institute*
*Laboratory of Nuclear Installation Safety*
*Breslaujos str. 3, LT-44403 Kaunas – Lithuania*
*Phone +370 612 81433*
*Email: darius@mail.lei.lt*

ABSTRACT

The fundamental studies of condensation process are carried out by Lithuanian energy institute for several years. Scientists are trying to find out interdependence between steam momentum to interface and energy transfer. Particular object is the influence of condensation to inter-phase friction. All this studies are aimed to broaden the range of condensation control. A following study, which will be discussed in this paper will examine the two-phase flow (water - steam) in rectangular channel at the different steam and water characteristics.

This article is presenting the water temperature profile measurement methodology using non-intrusive (infrared camera) and intrusive (thermo couples) measurement methods. Using these methods the water temperature profile measurements near the inner wall of the channel were done at the different steam and water flow velocity. The analysis of the experimental results shows, that the temperature measurement method, using infrared camera, is very promising and could be employed for evaluating of water temperature profiles inside the closed channel.

Key words: two-phase flow, condensation, temperature profiles, infrared camera.

## 1. INTRODUCTION

Water like coolant is used in many industrial facilities such as power plants, chemical, nitrogen factories and others. Water like other liquid materials by the certain temperature and pressure conditions changes its state in other words – conversion of phases (water-steam-water) takes place. Therefore is important to understand the dynamic interaction of steam and water. Otherwise, steam condensation and water evaporation may causes serials accidents in the system. In the world are made many studies related to condensation and evaporation. But till now is not developed any universal model which fully explain and predicts all the processes taking place in steam-water system.

At Lithuanian Energy Institute (LEI) the two-phase flow researches are carrying out almost 10 years. Earlier, the condensation implosion event was investigated. Further researches should involve the temperature gradient in the water and interface validity dependence from the steam flowing velocity and condensation. According latter dependences will be created digital thermodynamic model for the phase condensable flux in closed channel model.

Methodology for experimental measurements of temperature profiles in the rectangular channel will be presented in this paper. Investigation performed using fast infrared camera SC-5000 and thermocouples (K type). The work was divided into 3 stages. At first, the temperature profile on the inner rectangular channel wall was measured using infrared camera. In second stage was checked - is the water temperature, measured using infrared camera, correct? For verification, temperature inside of channel was measured using thermocouple and infrared camera. And at the third stage experimentally was checked using infrared camera and thermocouples - is accumulated the heat on the glass of rectangular channel wall?

# 2. METHODOLOGY

## 2.1. Experimental equipment

Experiment measurement of temperature was made in rectangular channel, which is demonstrated in Fig. 1. The channel was made from stainless steal. Inner dimensional characteristics are 1200x100x20 mm (LxHxW). The channel has circular "Spinel" ($MgAl_2O_4$) 100 mm diameter and 7.5 mm width (Fig. 1, 4) window through which water temperature profiles is measured using infrared rays camera SC-5000. Spinel thermal conductivity coefficient is 15 $W/_{m\cdot K}$. The channel is insulated on purpose to decrease heat losses to environment.

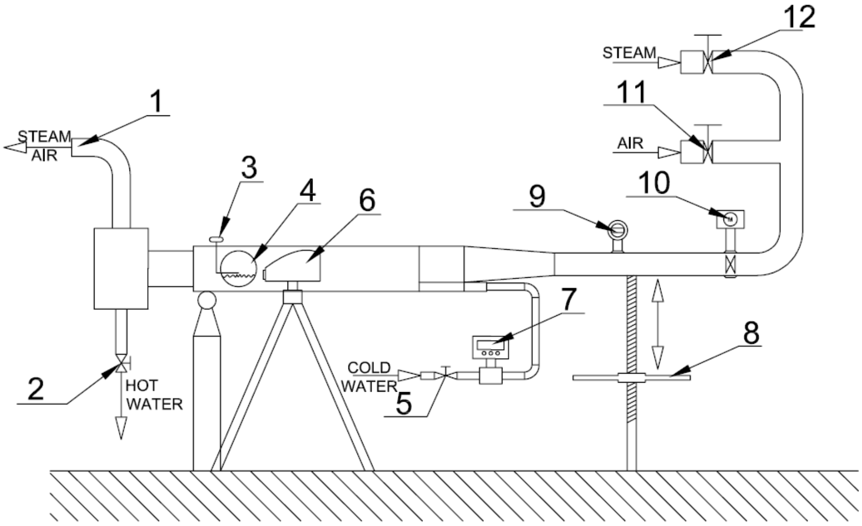

Fig. 1. Schematic view of experimental facility: 1 – steam/air outlet; 2– hot water outlet valve; 3 – thermocouples; 4 - rectangular channel test window (Spinel- $MgAl_2O_4$); 5 – water inlet valve; 6 – infrared rays camera SC-5000; 7 – electromagnetic water flow meter; 8 – channel height regulator; 9 - vortex type steam flow measuring system; 10 – electric linear actuator for steam flow adjustment; 11 - air inlet valve; 12 - steam inlet valve

Spinel glass has good transparency (95%) for the light and infrared rays in 3–5 μm range. This length of wave range is the most suitable for water temperature measurements. And infrared rays camera SC-5000 works in latter range. Water emission coefficient has very high value 0.98 in 3-5 μm range. Camera detects various energy infrared rays, which radiates from hotter sources to environment. If the temperature of source is higher than radiation will be more intensive and camera will measure higher values of temperature. Applying this method is very important, that in thermal camera seeing view will not be any other hot energy source, because it can alter the measurement results. It can be found as serious measurement error. Camera is installed at 10 cm distance from the channel outer glass of Spinel wall. It is the closest distance to channel as possible.

## 2.2. Research Methodology

At the beginning of experiment 12 and 5 valves are opened (Fig. 1). Then the flows of steam (101°C) and of cold water (~8°C) into the channel are supplied. Using 7, 10 flow meters and 5, 10 valves flow mate are regulated. Level of water 2.5 cm in height, and steam (7.5 cm) is above it. Water temperature at the end of the channel is increased (due heat exchange (between steam and water) and is supplying the hot water through outlet valve 2. Water temperature depends from steam and water flowing velocities. Used steam is removing through 1 (Fig. 1) pipe. Before measurements is very important to regulate water level inside channel, because water flow dependent from steam and velocity water level can be changed so for that channel height regulator 8 is used.

Temperature measurements using infrared camera at different steam and water velocities (Table 1) were made. The steam velocities were 4, 6, 8, 10, 12 m/s and the water flow rates were 0, 10, 20, 50, 100 l/h.

Table 1. Matrix of temperature measurement

| | | | | Steam flow velocity | | | | |
|---|---|---|---|---|---|---|---|---|
| | | | | 4 m/s | 6 m/s | 8 m/s | 10 m/s | 12 m/s |
| Water flow rate | 0 l/h | Water flow velocity in channel | 0.00 m/s | + | + | + | + | + |
| | 10 l/h | | $5.56\cdot10^{-3}$ m/s | + | + | + | + | + |
| | 20 l/h | | $1.11\cdot10^{-2}$ m/s | + | + | + | + | + |
| | 50 l/h | | $2.78\cdot10^{-2}$ m/s | + | + | + | + | + |
| | 100 l/h | | $5.56\cdot10^{-2}$ m/s | + | + | + | + | + |

Infrared camera is controlled by computer using ALTAIR software.

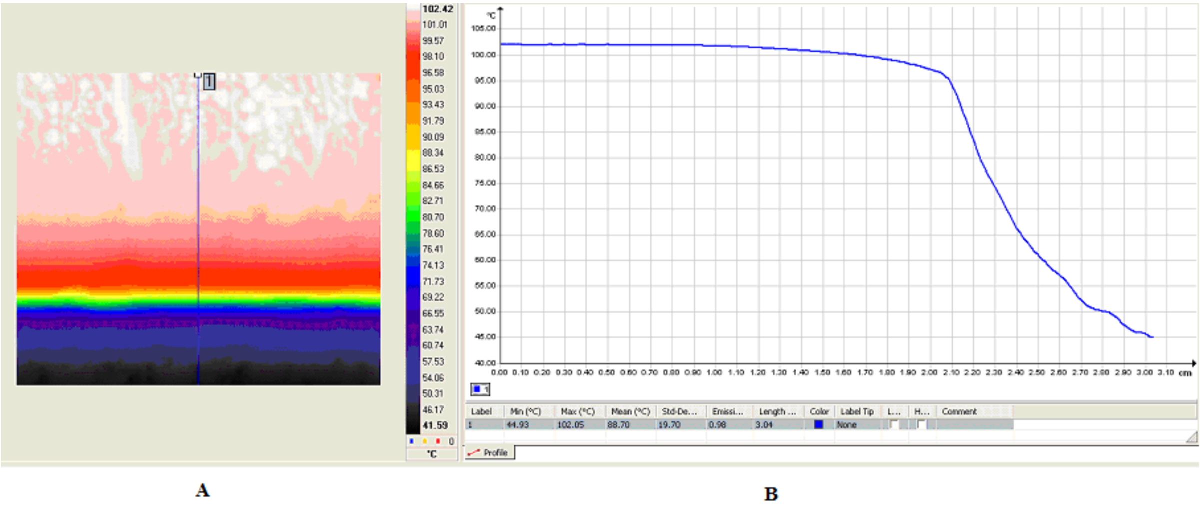

| Label | Min (°C) | Max (°C) | Mean (°C) | Std-De... | Emissi... | Length ... | Color | Label Tip | L... | H... | Comment |
|---|---|---|---|---|---|---|---|---|---|---|---|
| 1 | 44.93 | 102.05 | 88.70 | 19.70 | 0.98 | 3.04 | 🟦 | None | ☐ | ☐ | |

Fig. 2. ALTAIR software results windows

In Fig. 2 two windows A and B are showed. In A window the thermal image of water at the inner wall of rectangular channel is seen. And in B window temperature profile along a window showing vertical line is demonstrated. Infrared camera can see only the water and steam view on the inner window wall, because water is not transparent for thermal radiation.

Purpose at the next research stage to check - is temperature measurements using infrared rays camera correct? Here two temperature measurement methods were used: non intrusive - infrared camera and intrusive control method - thermocouples. Measurements of temperature were made using two latter methods at the same area in the water. The results of temperature measurement were different. So the hypothesis was rose that the temperature inside of the Spinel glass window (in water area) is higher than in the water near the window wall. On purpose to confirm the third research stage was initiated.

The two thermocouples were located on opposite walls of window at the equal positions (Fig. 1, 3, 4). Infrared camera was focused at the same area where thermocouples were installed.

At the beginning of experiment the channel has been heated with steam about 90 min. The temperature in the channel was increased to 101°C. Then steam in flow was stopped (1 Fig. 12 valve) and instead of it the cold (-20°C) air in flow (1 Fig. 1 valve) was supplied. Both thermocouples and infrared camera were used at the same time when steam was swapped by air. The duration was 860 seconds at all this stage measurements. After 700 s, from the measurement begin, the valve 11 was closed (Fig. 1) and air flow was stopped. After that, the measurements of temperatures were made by the natural air convection in the channel.

## 3. RESULTS

A temperature profiles in water is depended from velocities of water and steam. Measurements of water temperature profiles (using infrared camera) was carried out and demonstrated in Fig. 3. In picture is seen, that increasing steam and water velocities increases the temperature difference, between channel bottom and water surface.

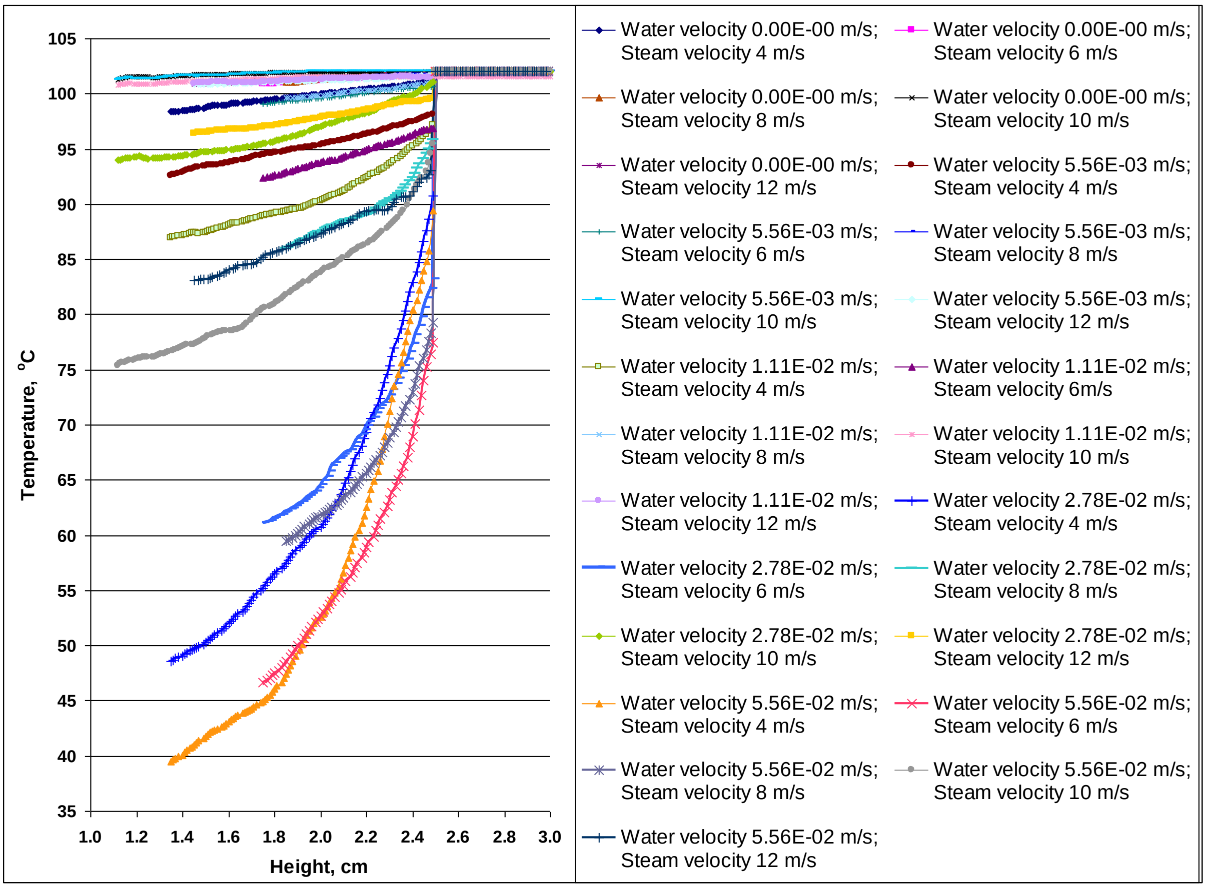

Fig. 3. Temperatures profiles dependence in water from the water and steam velocity

Analyzing these results in detail was obtained that temperature profiles do not have clear distribution. After that was decided to check reliability of the infrared camera results. The same temperature inside of channel was measured using thermocouples and infrared camera. The measurements in all water flow rates were made at the 4 and 6 m/s steam flow velocity. The results showed that measured temperature of water with infrared camera are about 20–40°C higher compared to thermocouple results, when water flowing velocity is larger than $5.56 \cdot 10^{-3}$ m/s (10 l/h). In the steam area the both measurements methods gives the same results.

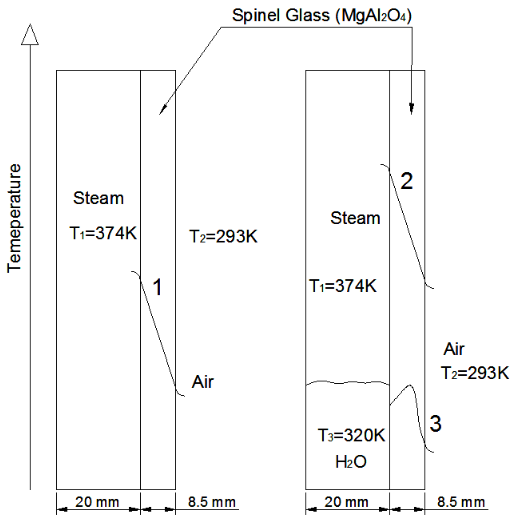

Fig. 4. Schematic temperature profiles within Spinel glass window

This disagreement can be explained by Spinel glass conduction of heat from steam to water and environment. Normally, when only one fluid flows inside the channel, (Fig. 4) infrared camera measures the same temperature as thermocouple, because the temperature of glass is lower than fluid. But in case of two phase flow when temperature is lower (~80°C) then temperature profile in the Spinel window at water region (Fig. 4; 3) will not be linear. So, because Spinel glass conductivity is much higher than water (15 v. s. $0.65\,{}^{W}\!\big/_{m \cdot K}$ [1, 2]) and water velocity is relatively small the glass temperature becomes higher then on water region. Therefore measured peak of temperature inside of glass adds its value positive errors to the water thermal radiation. Aforesaid explanation was checked experimentally in the third research stage. The results are demonstrated in Fig. 5.

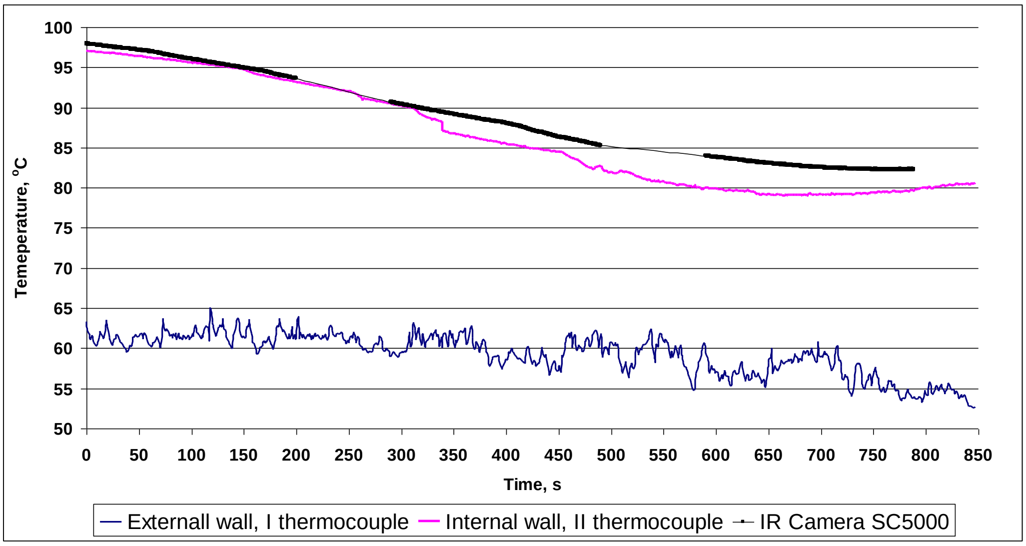

Fig. 5. Temperature measurements on the inner and outer wall of rectangular channel using thermocouples and infrared camera

In Fig. 5 three curves are seen. Black curve represents measured, using infrared camera, temperature on the inner window wall. Pink and blue curves – the temperatures on the inner and outer walls measured with thermocouples. First 700 s the temperature inside of channel is decreased while cold air is supplied. When cold air flows through the channel heat transfer coefficient of Spinel window wall increase and the temperature decrease. After 700 s the temperature inside of channel has begun to increase, after cold air supply termination. Infrared camera records the largest energy source of its visibility area. Accordingly, camera measures the temperature peak (Fig. 4; 3) inside of glass.

The temperature has been decreasing on the external wall of glass all measuring (Fig. 5, external wall).

The last experimental results showed, that infrared camera sees temperature inside the window glass, when it is larger than fluid temperature it changes measurement values by adding positive errors.

## 4. FINAL REMARKS

In this article the methodology which was used to measure the water temperature profiles at the inner wall of the closed rectangular channel was presented,. Measurements were taken at the different steam and water flow regimes. The results of temperature measurements are insufficient yet. The error reaches 20–30°C at the water area. This error arises due to glass thermal radiation, because of higher glass than water temperature. The peak of temperature (Fig. 4; 3) inside of glass adds own value to the water infrared radiation.

The temperature profiles measurements methodology, using infrared camera, is very promising. Very important is to evaluate thickness, conductivity and thermal capacity of window.

In order to apply this methodology for the measurements of water temperature profiles is needed to decrease the temperature of glass, to the same or lower than water.

## 5. REFERENCES

1. DROBAVIČIUS A., GARBARAVIČIUS J. and others, Bendroji šiluminė technika.; Redactor Milenskis N. Vilnius: Mintis, 1974. 555 p.
2. http://atomoptics.en.alibaba.com/product/271309401-203183113/Transparent_Ceramic_spinel_MgAl2O4.html

# INFLUENCE OF RADIATIVE SOURCE TO THERMAL STATE AND PHASE TRANSFORMATIONS OF WATER DROPLETS

**K. Norvaišienė, G. Miliauskas**
*Kaunas University of Technology*
*Department of Thermal and Nuclear Energy*
*K. Donelaičio str. 20, LT-44239 Kaunas – Lithuania*
*Phone +370 37 300437*
*Email: kristina.tiuksaite@stud.ktu.lt*

## ABSTRACT

Modelling is performed using the combined analytical – numerical method to investigate heat and mass transfer in the two-phase droplets-gas flow system. Thermal state of water droplets and intensity of phase transformations is modelled numerically under various heat and mass transfer conditions during their unsteady evaporation. Balance of energy fluxes in the droplet with confidence of one hundredth of percent and using the fastest sinking the droplet surface temperature is selected. Additional radiant energy allows forming unsteady temperature field with negative gradient in droplets and essentially changes the rate of phase transformations and thermal state. The results of investigation are presented in the real time scale and the Fourier number – based time scale.

Keywords: water droplet, radiative source, heat and mass transfer processes.

Nomenclature: a – thermal diffusivity ($m^2/s$), D – mass diffusivity ($m^2/s$), I – index of control time, $I_\omega$ – spectral intensity of radiation (W/m ster), $I_{\omega 0}$ – spectral intensity of radiation of a black body (W/m ster), L – latent heat of evaporation (J/kg), $m_v$ – vapour mass flux density (kg/ $m^2$ s), n – number of the term in infinite sum, p – Pressure (Pa), q – heat flux ($W/m^2$), r – coordinate of a droplet (m), R – radius of a droplet (m), $R_\mu$ – universal gas constant (J/kmol K), t – control time (s), T – temperature (K), η – non-dimensional droplet coordinate, λ – thermal conductivity (W/m K), μ – molecular mass (kg/kmol), ρ – density ($kg/m^3$), τ – time (s), φ – relative humidity (%).

*Subscript:* c – convective, co - condensation regime, e – equilibrium evaporation regime, g – gas, vg – vapor-gas mixture, i – time index in a digital scheme, I – index of control time, j – index of droplet cross-section, J – index of droplet surface, k – conductive, r – radiative, rt - dew point, R - droplet surface, s – saturate, v – vapor, Σ – total, ∞ – far from a droplet, f – phase change.

*Superscript:* + External side of a surface, – Internal side of a surface.

## 1. INTRODUCTION

Droplets are encountered in nature and wide range of science and engineering applications. Droplet properties and deformation characteristics are of interest in liquid-liquid phase separation, emulsion, ink-jet printing and gas-liquid mass transfer applications [1]. Cognition of heat and mass transfer in the systems of liquid droplets, spread in gas, is urgent, because two phase droplets and gas flows are very often met in important thermal technology processes. In processes as: air conditioning systems; air drying or humidification in evaporation chambers; in technologies of optimization of combustion process or reduction of $NO_x$ emission, in contact heat exchangers – recovery of heat from flue gas etc. The effectiveness of the mentioned technologies depends on an intensive energy and mass interaction between liquid and gaseous phases, which is ensured by highly developed interphase contact surface and sensible difference between thermal energy levels of gas and liquid.

The interaction of heat and mass transfer processes determines the thermal state of droplets and phase transformations on their surfaces. This interaction is influenced by many factors: unsteadiness of transfer processes; the Stefan’s hydrodynamic flow; radiative flow absorbed in semitransparent liquid; temperature and pressure drops in the Knudsen layer; the size of droplets and slipping of droplets in gas; turbulence of a two-phase flow surrounding droplets, variable physical properties, etc. These factors are evaluated by researches, known as the “droplet” problem [2–5], and others.

One of the most important factors: influence of the radiant flow. During the primary investigations of sprayed liquid systems, was not taking into account the influence of radiation flow on heat and mass transfer processes. A semitransparent liquid droplet absorbs radiation energy by its entire volume. It is very complicated process because the variable intensity of spectral radiation flow in the droplet determines this process. The energy of radiation source affects the process of droplets heating and evaporation and influences the interaction of transfer processes inside and outside the droplets. It is not possible to neglect interaction of transfer processes when modeling sprayed liquid systems. The methods for calculation of radiation [4, 6–12] allow evaluating the influence of spectral optical characteristics on combined energy transfer in semitransparent liquid droplets. The method presented in [12] allows considering the selectivity of radiation in droplet surroundings. The volumetric heating due to radiation absorption has been computed as a function of radial position for spherical water droplets in black body surrounds in the work [6]: the ray tracing procedure developed for these computations includes polarization, refraction, external reflection, multiple internal reflections, and absorption. The integral equation of local radiant flux in a semitransparent sphere is constructed in the study [13]. For that spectral optical density along freely chosen direction was replaced by optical density along the direction of a semitransparent sphere dimension. The advantage of this method is that liquid radiation emission and dependence of optical spectral properties on liquid temperature is evaluated. In the paper [4] the author by using the integral equation of local radiant flux in a semitransparent sphere (was created in the paper [13]), has developed the calculation method of local radiation flow in the semitransparent liquid volume which is presented in the form of system of integral equations. Mie theory has been used to predict absorption and scattering efficiency factors for monodisperse water droplets [14]. It was found that absorption is approximately proportional to the volume of liquid water present, regardless of the droplet size. In the paper [7] for the first time was presented that radiation absorption can significantly distort temperature field in a semitransparent liquid droplet and even change the direction of temperature field gradient. The fundamental model is presented in the paper [15]: a radiative transfer model based on geometrical optics theory is used to calculate the local volumetric rate of radiation absorption. The authors's of paper [15] to validate the model, the predicted water droplet surface temperatures (the droplet diameter, the equilibrium evaporation rate of a water droplet and others dimensions) were compared with both experimental data cited by and predictions of paper [2] author and they confirmed the results of investigations of the paper [2]. The work [15] have the practical importance, the results of this investigation shows that, the effect of external radiation absorption by a droplet is to cool the ambient atmosphere and can control the fire by water sprays.

The influence of radiation on liquid droplets has been investigated quite widely, but till now has not submited the systematical evaluation of influence of radiation on the thermal state of droplets and the rate of phase transformations on their surfaces, what is presented in this investigation. This paper presents the investigation of warming and evaporation of separate droplets, according to the method of analytical – numerical solution of the “droplet” problem, developed in Kaunas University of technology, where the most important factor taken into account is influence of the radiant flow.

## 2. ANALYTICAL-NUMERICAL METHOD OF INVESTIGATION

The combined analytical numerical method [4, 16] of the ‘‘droplet” problem’s solution is more applicable, when it is necessary to evaluate the interaction of unsteady heat and mass transfer processes and the peculiarities of spectral radiation. The essence of those methods that, the schemes of numerical computation of an unsteady temperature field of a droplet are constructed not for the primary system of nonlinear differential and integral equations, but for its solution – the system of nonlinear algebraic and integral equations. The main advantages of this method are avoidance of the indeterminacies, related to selection of time and coordinate steps and reliable control of numerical research convergence. The temperature of the interphase contact surface is determined when there is a balance of the energy flow’s taken to the surface and taken from the surface of droplet (Fig. 1).

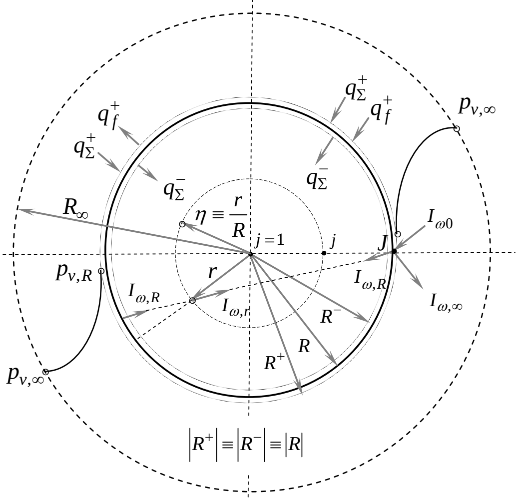

Fig. 1. Layout of energy flows on the droplet surface

Droplet surface temperature determines the mode of droplet’s phase transformations. Water vapor in the gas is condensing on the droplet surface, as long as droplet surface temperature is below temperature of the dew point. As a droplet warms above dew point temperature, the water starts to evaporate.

$$\vec{q}_\Sigma^{\,+}(\tau)+\vec{q}_\Sigma^{\,-}(\tau)+\vec{q}_f^{\,+}(\tau)=0 \tag{1}$$

In the case of combined heating, the total heat flow on the external side of the droplet surface depends on the radiant and convective heat components: $\vec{q}_\Sigma = \vec{q}_c + \vec{q}_r$. Because convective component of total heat flow density is on the droplet surface, radiant component is absorbed inside of semitransparent droplet: therefore influence physics on state of droplet is different. One part of the energy that is supplied to the droplet is used for its heating; another part is used for evaporating. In spectrum of infrared radiation, the complex refractive index of water varies significantly [17], though it is finite. When the surface of water droplet does not absorb the spectral radiation flow, $|q_r^-| \equiv |q_r^+|$. Therefore the condition (1) for the mode of condensing phase transformation of water droplets corresponds to the expression: $q_c^+ + q_f^+ = q_c^-$, and in the evaporative mode the expression is: $q_c^+ - q_c^- = q_f^+$. The density of heat flow of phase transformations:

$$q_f^+ = m_v^+ \cdot L \tag{2}$$

is determined by the density of water vapor flow on the droplet surface, which is described by using the Shorin-Kuzikovsky model [18], which evaluates the influence of the Stefan flow on the mass transfer:

$$m_v^+ = \frac{D_{vg}\mu_v}{T_{R,vg}R_\mu R} p \ln \frac{p - p_{v,\infty}}{p - p_{v,R}} \tag{3}$$

Water vapor and gas mixture temperature is close to the temperature on its surface $T_{R,vg} \equiv T_R$, whereas liquid vapor pressure on droplet surface corresponds to the saturation vapor pressure: $p_{v,R} \equiv p_s(T_R)$, chosen by its temperature. The direction of an external convective flow between gas and a droplet is unambiguously influenced by the temperature difference between gas and the droplet ($T_g - T_R$): the intensity of the convective flow ($q_c^+$) corresponds to the conductive heat flow ($q_k^+$). As a droplet is carried by gas flow without slipping, we have $Nu = 2$; the droplet is heated by conduction: $q_c^+ \equiv q_k^+$.

$$q_c^+ \equiv q_k^+ = \frac{\lambda_{vg}}{R}\left(T_g - T_R\right) \cdot f\left(B_T\right). \tag{4}$$

The function of the Spalding transfer number ($B_T$) evaluates the influence of hydrodynamic Stephan flow. The Nusselt number (*Nu*) for a droplet is described by Abramzon-Sirignano model, as Spalding transfer number is selected using the recommendations presented in [19].

The internal convective flow in a droplet is described by the modified Fourier's law as the effective coefficient of thermal conductivity evaluates the influence of water circulation for heat transfer inside a droplet according to the recommendations presented in [20].

In the case of combined heat transfer in a droplet by conduction and radiation, the unsteady temperature field (5) in a spherically – symmetrical droplet is defined by the method [4] which evaluates the influence of radiation absorption peculiarities in a semi-transparent droplet and the rate the droplet's surface temperature change:

$$T(r,t) = T_R(t) + \frac{2}{r}\sum_{n=1}^{\infty}\sin(n\pi\eta)\int_0^t f_n(\tau)\exp\left[-a\left(\frac{n\pi}{R}\right)^2(t-\tau)\right]d\tau. \tag{5}$$

The function $f_n$ takes into account the influence of the radiant absorption in a droplet and the rate of change of droplet surface temperature on the unsteady temperature field of a droplet. In the case of equilibrium evaporation behaviour of the droplet surface temperature depends on the boundary conditions of heat and mass transfer [2].

Radiation flow is calculated by the equation (6):

$$\begin{aligned} q(r) = 2\pi\int_0^{\infty}\int_0^{\pi/2}\cos\gamma\sin\gamma\Big[I_\omega(R)\exp\left(-\tau_r^R\right) + \int_r^R n_\omega^2 I_{0\omega}\exp\left(-\tau_r^{r^1}\right)d\tau_r^{r^1} - I_\omega(R)\exp\left(-\tau_{r\cdot\sin\gamma}^R - \tau_{r\cdot\sin\gamma}^r\right) \\ - \int_{r\cdot\sin\gamma}^r n_\omega^2 I_{0\omega}\exp\left(-\tau_{r^1}^r\right)d\tau_{r^1}^r - \int_{r\cdot\sin\gamma}^R n_\omega^2 I_{0\omega}\exp\left(-\tau_{r\cdot\sin\gamma}^r - \tau_{r\cdot\sin\gamma}^{r^1}\right)d\tau_r^{r^1}\Big]d\gamma\, d\omega. \end{aligned} \tag{6}$$

When defining the volume variation of a spherically symmetrical droplet, the intensity of the phase transformations on droplet surface and expansion of warming water are evaluated:

$$\rho\frac{\partial R^3}{\partial\tau} = R^3\frac{\partial\rho}{\partial\tau} - 3R^2 m_v^+. \tag{7}$$

Equations system (3–7) can be solved numerically, by the iteration method. Using this method number *J* of a control droplet cross-section is selected freely; the position of the cross-section is defined by dimensionless droplet coordinate $\eta_j$ ($\eta_j = 0$ when $j \equiv 1$; $\eta_j = 1$ when $j \equiv J$). Control time *t* is selected and number *I* of time coordinate change steps is provided ($\tau = 0$

when $i \equiv 1$; $\tau = t$ when $i \equiv I$). The thermal state of water droplets, convectively heated by gas and influenced by additional radiant energy source is calculated numerically, solving the equation (5), as temperature of a warming droplet surface is selected using the method of the fastest descent, requiring accuracy of the balance (1) to be not less than one hundredth percent.

## 3. RESULTS AND DISCUSSION

Warming and phase transformations of water droplets heating in different conditions with the initial temperature $T_{R,0}$ in the gas with temperature $T_{g,0}$ and the initial relative humidity $\varphi_{g,0}$ are modelled using the numerical method. In the case of combined heating, a radiation source with temperature $T_{sr}$, which emits radiant flow, similar to the black body's radiation, is acting additionally. The characteristic lifetime of droplets in the scale, expressed by Fourier number, independent of the water spraying dispersity [21]. This characteristic lifetime of droplets combines the three modes of droplet phase transformations: in the first condensation mode of phase transformations $0 \div Fo_{co,k}$ the droplets are heated by heat from condensing water vapor together with conductive heat from gas; in the second mode of unsteady evaporation $Fo_{co,k} \div Fo_{e,k}$ heat supplied for droplets by conduction not only heats them, but also evaporates water. As droplet warming declines and water evaporation increases, the situation gradually approaches towards an equilibrium evaporation mode, which actually starts, when entire heat supplied to the droplet is used for evaporation of water. At the time instant $Fo \equiv Fo_{co,e}$ droplets warm up till temperature $T_{e,k}$, which ensures the mode of equilibrium evaporation. In the third mode of phase transformations the temperature $T_{e,k}$ remains constant. The existence of the universal curve which defines variation of conductively heated water droplet surface temperature and which is normed in regards to sprayed water temperature and equilibrium evaporation temperature in the scale, based on the ratio of Fourier numbers is verified in [21].

When in the droplets – gas systems there is a small difference of energetically potential between gas and water, therefore the processes of phase transformations are inefficient. To change the intensity of heat and mass transfer processes it would be possible to use additional thermal energy, introduced into heating of water droplets. Radiation sources from hot surfaces or even laser can spread such energy. The external radiant source's energy absorbed into water droplets substantially changes the thermal mode in droplets (Fig. 2). This radiant energy allows forming unsteady temperature field with negative gradient in droplet - the mode of unsteady phase transformations starts after formation of negative gradient temperature field in the droplets and ends, as certain assumptions occur, according to which radiant energy, absorbed in droplets completely takes place in the process of water equilibrium evaporation.

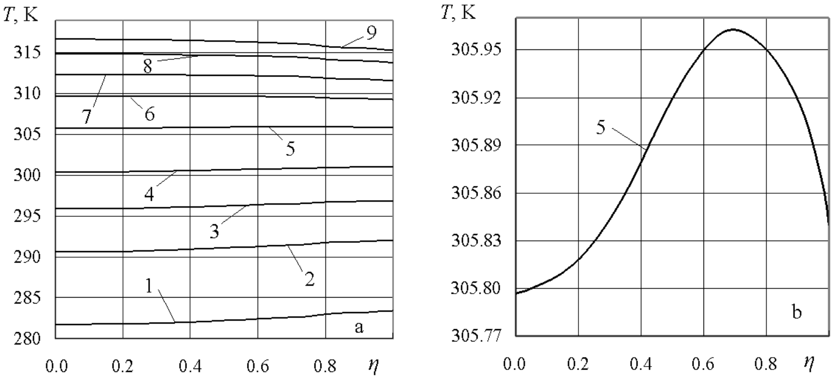

Fig. 2. The influence of an external radiant source on the thermal state of water droplets. *Fo*: (1) 0.153, (2) 0.610, (3) 0.915, (4) 1.220, (5) 1.680, (6) 2.140, (7) 2.600, (8) 3.360, (9) 5.800; $T_{sor} = 1000$K; $T_g = 300$ K; $\varphi = 75\%$; $R = 0.0001$ m

In the initial stage, similarly to the case of conductive heating, as surface layers of the droplets warm intensively, the temperature field of positive gradient (Fig. 3) is being formed.

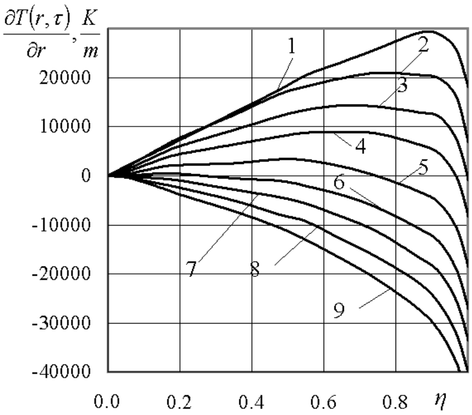

Fig. 3. The influence of the external radiant source on the gradient of unsteady field in water droplets. Nomenclatures the same as in Fig. 2

This temperature field is typical for the first period of the mode of unsteady phase transformation. The condensation mode of phase transformation is possible also in the first period. The second period begins when the internal layers of a droplet get warmer than its surface. During this period the maximum of the unsteady temperature field in droplets gradually shifts from the droplet surface into its center. In the second period, the curve 5 represents the peculiarities of the unsteady temperature field (Fig. 2). During this period the peculiarities of the temperature field's gradients (Fig. 3, curve 5) determine intensive distribution of absorbed radiant energy in the droplets by conduction and ensures that part of this energy already participates in the process of water evaporation. The third period of the mode of unsteady phase transformations starts after formation of negative gradient temperature field in the droplets and ends, as certain assumptions occur, according to which radiant energy, absorbed in droplets completely takes place in the process of water equilibrium evaporation.

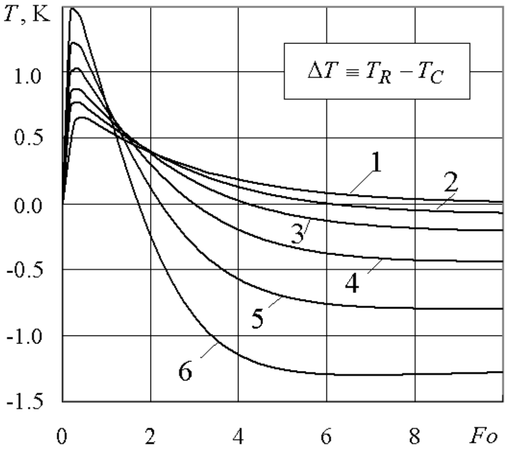

Fig. 4. The influence of the external radiation source's temperature on non-isothermality of water droplets. $T_{sor}$, K: (1) 0, (2) 500, (3) 600, (4) 700, (5) 800, (6) 900; $T_g = 300$ K; $\varphi = 50\%$; $T_0 = 280$K; $R = 0.0001$m

Hence, energy of the additional radiant source appreciably influences the thermal state of water droplets (Fig.4). In the initial stage of the mode of condensation phase transformations non-isothermality of the droplets reaches the first peak due to intensive heating of their surface layers, as $T_R > T_C$. Later non-isothermality of the conductively heated droplets gradually declines, as the equilibrium evaporation mode approaches (Fig.4, curve 1). As the internal layers of the droplets are intensively heated under the influence of the external radiant source, non-isothermality of the droplets decreases significantly. Later on non-isothermality begins to increase again, as a negative gradient temperature field is formed in the droplets and at the beginning of equilibrium evaporation it reaches its second peak, as $T_C > T_R$. Hence, comparing with the case of conductive heating of droplets, introduction of an additional source of radiation, completely changes dynamics of energy flows on the droplets surface.

Droplet evaporation rates, calculated in the case of conductive – radiant heating of water droplets, correlate with the results of the experimental research of water droplet evaporation, presented in the study [22] (Fig. 5). The experiments were performed with 900–2900 μm size water droplets, evaporating in equilibrium conditions in dry air at temperature 673–1073 K. This was achieved by a continuous pumping out of water vapor in velocity, not higher than 0.01 m/s. The constancy of droplet size was ensured by a special capillary system. The authors [22] stated that maximal error of droplet evaporation rate did not exceed 5%.

In the numerical research the calculation of the rate of equilibrium evaporation, was performed with the same equilibrium evaporation conditions as in the above described experimental research in the case, when the diameter of droplet is constant and the heating of droplet is combined conduction and radiation. The results of these experiments are quite well described by the model of radiant-conductive droplet heating, presented in this study, stating that the source of radiation is absolutely black body, the temperature of which equals to that of air, as $p_{v,\infty}/p = 0$. In the case of combined heating in a droplet by conduction and radiation the process of equilibrium evaporation is faster, because droplets reaches equilibrium evaporation warmed up to the higher temperature, than heating only by conduction.

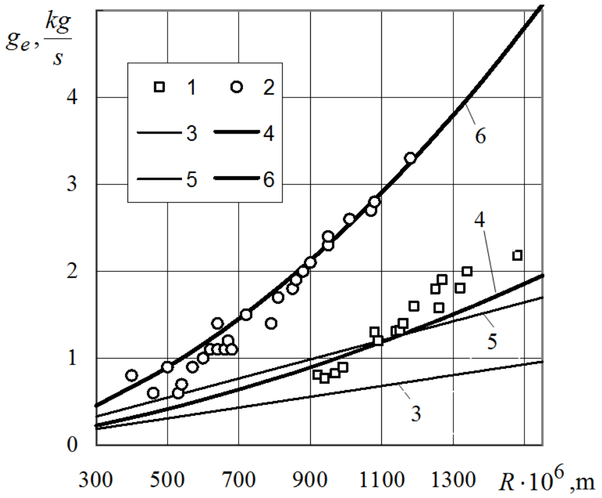

Fig. 5. The rate of water droplet evaporation in the case of different heating mode: (1, 2, 4, 6) combined conduction and radiation heating; (3,5) conduction heating; (1, 2) experiment (V. Ivanov, E. Smirnova) [22], (3–6) numerical research; temperature of dry air $T_g$ (K): (1, 3, 4) 678, (2, 5, 6) 889; temperature of radiant source $T_{sr}$ (K): (1,4) 678, (3,5) 0, (2,6) 889

The radiant flow absorbed in the droplets, depends not only on the external radiant source's temperature, but also on size of the droplets. In larger droplets radiant flow is being absorbed more intensively in the surface layers, whereas in smaller droplets absorption takes place in the central layers, though radiation of the external source penetrates less in smaller droplets, therefore the influence of the radiant source on the thermal state (Fig. 6) and the rate of phase transformations of the droplets is smaller (Fig. 7).

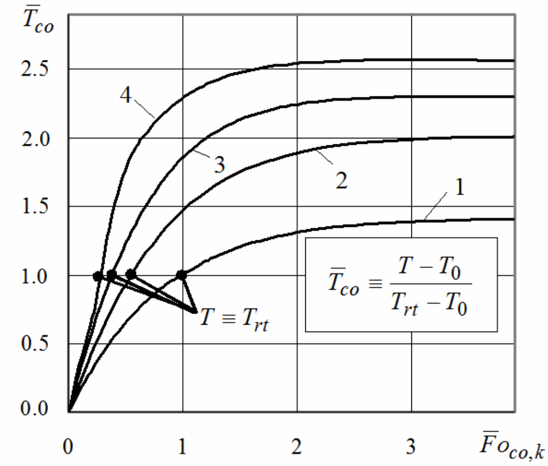

Fig. 6. The influence of water droplet's size, acted by an external radiant source on their heating. $T_{sor}$, K: (1) 0, (2, 3, 4) 700; $R \cdot 10^6$, m: (2) 50, (3) 75, (4) 100; $T_g = 300$ K; $\varphi = 50\%$; $T_0 = 280$K; $R = 0.0001$ m

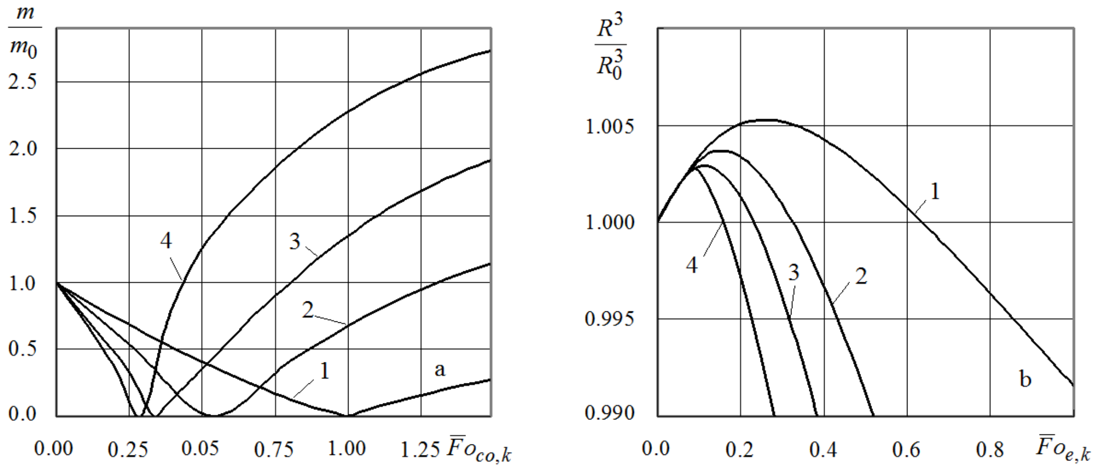

Fig. 7. The influence of water droplet's size, acted by an external radiant source on intensity of phase transformations (a) and variation of droplets volume (b). Nomenclatures the same as in Fig. 6

Larger droplets faster warm up till the dew point under the influence of radiant source (Fig. 6), therefore the condensation mode of phases transformations on their surface gets significantly shorter (Fig. 7 a). Under the influence of the source at 700 K temperature, the condensation mode of phase transformations for 100 micron diameter droplet, comparing with conductive heating case, becomes approximately 2 times shorter and for 200 microns - more than 3 times (Fig. 7 a).

## CONCLUSIONS

1. The research results show that the radiative flow make the essential influence on the heat transfer process interaction in semitransparent liquid droplets. Energy of the additional radiant source distorts the unsteady temperature field in the droplet and makes changes of the direction of the temperature field gradient vector.
2. The influence of radiation source on the droplets thermal state and phase transformations is more pronounced, when temperature of radiation source is higher and droplets are larger.

## REFERENCES

1. LIU, Huimin. *Science and engineering of droplets– fundamentals and applications.* New York: Noyes publications /William Andrew Publishing, 1981. 1 p. ISBN 0-8155-1436-0.
2. MILIAUSKAS, G. Interaction of the transfer processes in semitransparent liquid droplets. *IJ Heat Mass Transfer*, 2003, Vol. 46, No. 21, p. 4119–4138.
3. SAZHIN, S.S. Advanced models of fuel droplet heating and evaporation. *Progress in Energy and Combustion Science*, 2006, Vol. 32, No. 2, p. 162–214.
4. MILIAUSKAS, G. Regularities of unsteady radiative-conductive heat transfer in evaporating semitransparent liquid droplets. *IJ Heat Mass Transfer*, 2001, Vol. 44, No. 4, p. 785–798.
5. ONISHI, Y. The spherical-droplet problem of evaporation and condensation in a vapour-gas mixture. *Fluid Mechanics*, 1986, Vol. 163, p. 171–194.
6. HARPOLE, G.M. Radiative absorption by evaporating droplets. *IJ Heat and mass Transfer*, 1980, Vol. 23, No. 1, p. 17–26.
7. MILIAUSKAS, G. TAMONIS, M., SVENCHIANAS, P. Radiation and combined heat transfer in spherical volume of selective-radiating and absorbing medium (3. Radiative-conductive heat transfer in the presence of external heating sources). Lietuvos TSR Mokslo Akademijos darbai serija B, 1988, Vol. 3, p. 92–102.
8. LAGE, P.L.C., RANGEL, R.H. On the role of internal radiation absorption in single droplet vaporization. *AIAA Pap.*, 1992, Vol. 92-106, p. 1–19.
9. MILIAUSKAS, G. Unsteady heat and mass transfer in the two phase radiating flows 1. Spectral absorption of radiation flux in water droplets. *Energetika*, 1997, Vol. 1, p. 3–10.
10. DOMBROVSKY, L.A. Thermal radiation from non-isothermal spherical particles of a semitransparent material. *IJ Heat and Mass Transfer*, 2000, Vol. 43, No. 9, p. 1661–1672.
11. LIU, L.H., TAN, H.P., YU Q.Z. Internal distribution of radiation absorption in one-dimensional semitransparent medium. *IJ Heat and Mass Transfer*, 2002, Vol. 45, No. 2, p. 417-424.
12. SAITON, T., YAMAZAKI, K., VISKANTA, R. Effect of thermal radiation on transient combustion of a fuel droplet with the finite rate of chemical reaction. *Transactions of the Japan Society of Mechanical Engineers*, 1991, Vol. 57 (536), p.1485–1490.
13. MILIAUSKAS, G., TAMONIS, M., SVENCHIANAS, P. Radiation and combined heat transfer in spherical volume of selectively-radiating and absorbing medium (1. Determination of radiation heat flow). Lietuvos TSR Mokslo Akademijos darbai serija B, 1983, Vol. 6, p. 53–61.
14. BARTLETT, JC. The optical properties of water droplets in the infrared. *Physics: D Applied Physics*, 1985, Vol.18, p.753–764.
15. TSENG, C.C., VISKANTA. R. Enhancement of water droplet evaporation by radiation absorption. *Fire Safety*, 2006, Vol. 41, p. 236–247.
16. SAZHIN, S.S. Modeling of heating, evaporation and ignition of fuel droplets: combined analytical, asymptotic and numerical analysis. Proceedings of international workshop on hystereis and multi-scale assymptotics. [Journal of Physics]. Ireland: Institute of Physics, University College, Cork. 2005, p. 174–193.
17. HALE, G.M., QUERRY, M.R. Optical constants of water in the 200-nm to 200-μm wavelength region. *Applied Optics*, 1973, Vol. 12, No. 3, p. 555-563.
18. KUZIKOVSKIJ, A.V. Dynamic of spherical particle in powerful optical field. Izv. VUZ Fizika, 1970, No.5, p. 89–94.

19. MILIAUSKAS, G., SABANAS, V. Interaction of transfer processes during unsteady evaporation of water droplets. *IJ Heat Mass Transfer*, 2006, Vol. 49, p. 1790–1803.
20. APASHEV, M.D., MALLOV, R.V. Evaporation of various liquid single droplets, as flow passes around the droplets at small Reynolds numbers. Izv. AN SSSR Energetika i Automatika, 1960, Vol. 2, p. 185–191.
21. MILIAUSKAS, G., SINKUNAS S., MILIAUSKAS, G. Evaporation and condensing augmentation of water droplets in flue gas. *IJ Heat Mass Transfer*, 2010, Vol. 53, p. 1220–1230.
22. SHCUKIN, E.P., KRASOVITOV, V.G., JALAMOV, J.I. Evaporation and condensative growth of large and moderately large droplets in gaseous media at any temperature differences, 1991, VINITI 3706-B091, 96 p.

CYSENI 2011, May 26–27, Kaunas, Lithuania
ISSN 1822-7554, www.cyseni.com

# MEASUREMENTS OF METHANE CONCENTRATION IN AN AXIALLY SYMMETRICAL TURBULENT METHANE FLOW USING A TALBOT INTERFEROMETER METHOD

**I.N. Shatan**
*A.V.Luikov Heat and Mass Transfer Institute of National Academy of Sciences of Belarus*
*P. Brouki str. 15, Minsk BY-220072, Republic of Belarus*
*Phone +375(17)2842246*
*Email: inShatan@gmail.com*

## ABSTRACT

The paper presents experimental measurements of averaged values of admixture concentrations in a turbulent flow using a talbot interferometer method. Averaged concentrations throughout the flow field are determined using local light refraction index measurements with a high spatial resolution from a long-exposed (20 s in these experiments) Talbot image of the jet. Current study investigates averaged concentrations of axially symmetrical turbulent methane jet issuing into air space. The methane jet was formed by a nozzle with a critical cross-section diameter 4 mm. Velocity of the flow of methane at the nozzle exit was 12 m/s. In the paper the principles of talbot effect-based technique for analysis optical inhomogenities are discussed. And the posibillity of applying the talbot interferometer method for meassurements of concentration of turbulent flows in binary mixtures is demonstrated. Also optical scheme of the experimental setup for current investigations is described in the article. As the concentration is not directly meassured value in the talbot interferometer method, the paper presents the mathematical apparatus for concentration calculation of axially symmetrical turbulent flows. The paper illustrates that the Talbot effect-based method is a powerful tool for concentration meassurements of turbulent gas flows.

Keywords: talbot effect, shear flow, turbulence, concentration meassurements.

## 1. INTRODUCTION

Of the many diagnostic methods currently available, non-intrusive optical diagnostic methods offer several advantages. The absence of any instrumentation within the flow allows data acquisition to be performed without disrupting the flow in any way. Secondly, very rapid fluctuations can be analyzed with optical techniques and small length scales can be resolved. These advantages make optical diagnostic techniques prime candidates for the analysis of turbulent flow. In this work we apply Talbot interferometer method for concentration measurements of a turbulent, nonpremixed, nonreacting methane-jet flow.

This method is based on the periodical reproduction of intensity structure of a light beam that has been passed through the uniform grating. This phenomenon is easy to observe with the coherent light beam. If uniform grating is placed in such wide aperture monochromatic beam, then, as the result of superposition of diffracted waves, the intensity distribution in some distance from the grating will be the same as directly after it. The distance $z_N$ between grating and $N$ -th imaging plane can be calculated:

$$z_N = \frac{p^2 \cdot N}{2\lambda}, \tag{1}$$

where $z_N$ – location of the imaging plane number $N$, $p$ – period of the grating and $\lambda$ - wavelength of the light beam.

A wavefront sensor based on the Talbot effect was proposed for diagnostic optical inhomogeneous in [1, 2]. Later the Talbot effect-based technique was applied for concentration measurements in axially symmetrical helium flow and in binary mixture two-dimensional flow past cylinder [3, 4]. Averaged and fluctuating characteristics of turbulent flow for two-dimensional submerged jet for the entire flow field were measured in [5, 6].

Optical diagnostic based on the Talbot effect operates by measuring the change in optical phase of a laser beam that has propagated through an optical inhomogeneity. When a laser beam is propagated through an aberration medium, such as turbulent flow, the non-uniformity of the density field distorts the incident phase front. In absence of optical inhomogeneity the intensity field structure in self-imaging plane will be the same as directly after the grating. But after passing the optical inhomogeneity, intensity field structure will be also distorted. The differences (displacements and blurring) in intensity field structure are directly related to the averaged local refracting angles.

The purpose of this work was optical diagnostic of nonpremixed, nonreacting axially-symmetrical methane-jet flow and the following calculating of methane averaged concentration in the flow field of the axisymmetrical jet.

## 2. EXPERIMENTAL SETUP

The experimental setup for optical diagnostic of turbulent jet based on the Talbot effect is comprised of a laser source, optical system, diffraction grating (or Talbot grating) and a receiving camera. As a laser source a cadmium-vapor laser with a wavelength of 441.6 nm was used.

The Talbot grating represented a reflective grating with a system of equally spaced round holes of orthogonal arrangement. The optical density of the reflecting layer was $D = 4$, the period of holes location was $p = 1000$ µm and diameter of each hole was $d = 200$ µm. The pictorial presentation of the grating is shown on the Fig. 1.

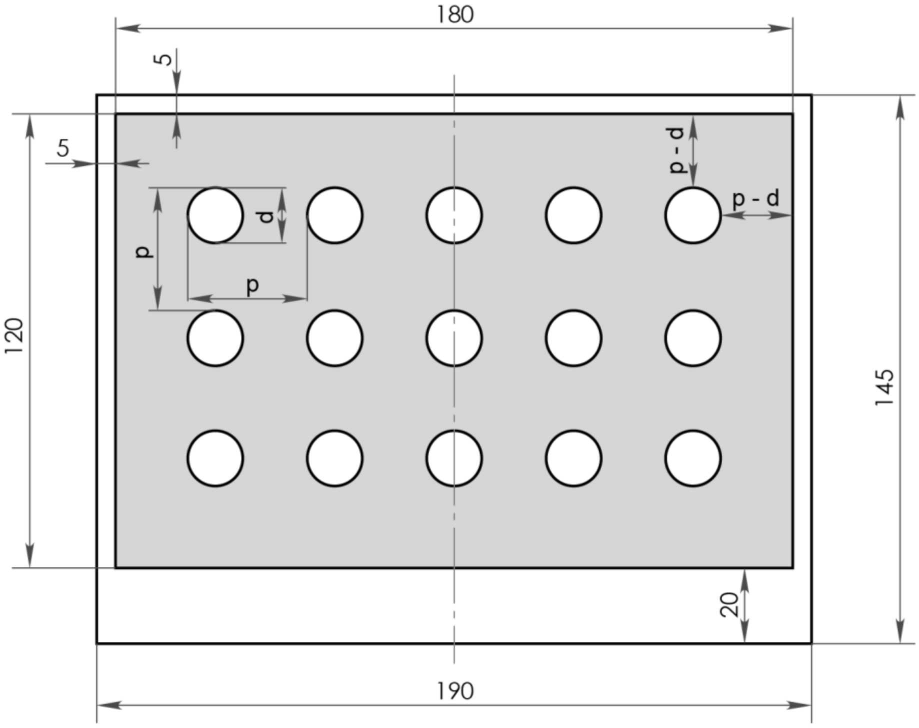

Fig. 1. Geometric parameters of Talbot grating

The optical scheme of the setup for optical diagnostic is shown in Fig. 2. A collimator transforms the He-Cd laser radiation which has passed through an aperture diagram and a neutral filter (which has a constant attenuation across the wide range of wavelengths) into a wide-aperture light beam with an approximately plane wave front. A diameter of this laser beam was approximately 200 mm. Talbot grating was placed into the laser beam region just behind the collimator and was orthogonally arranged to the laser beam. A system forming an axisymmetric methane jet was placed at some distance from the grating (no more than the distance of the first imaging plane $z_1$). The image was projected on the CCD matrix of the camera “Nikon-D700”. The physical dimensions of the photosensitive matrix are 24×36 mm and a number of active pixels are approximately 12.1 MP. Depending on a required sensitivity of the technique, the camera was placed in the corresponding self-imaging plane at the distance $z_N$ from the grating. In order to match the aperture of the CCD matrix the aperture transducer was installed directly in front of the camera. It consisted of two collecting lenses with focal length $F_1$ = 1000 mm and $F_2$ = 180 mm.

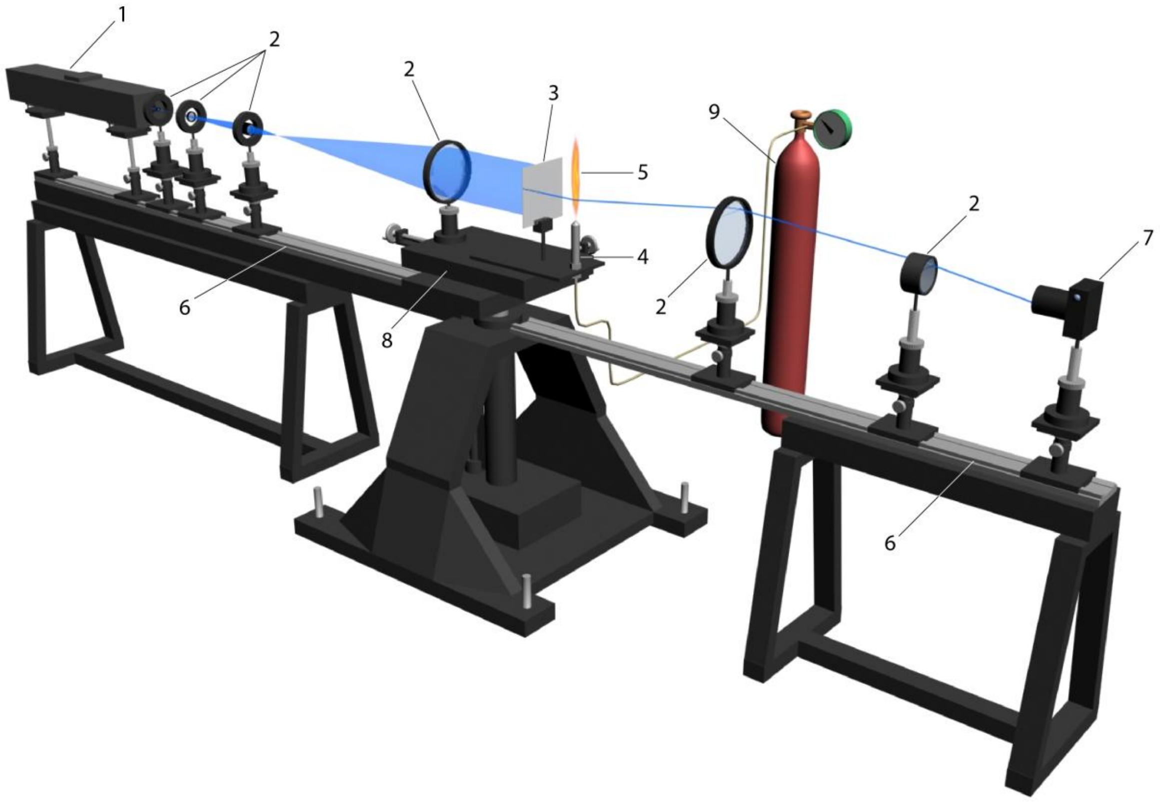

Fig. 2. Experimental setup for the Talbot effect based optical diagnostic of turbulent flows: 1 – He-Cd laser; 2 – optical elements; 3 – Talbot grating; 4 – nozzle; 5 – test object (methane jet in this case); 6 – optical rail; 7 – CCD camera; 8 – optical plate; 9 – tank with methane

An axially symmetrical methane jet was formed by a nozzle with an outlet nozzle cross section equal to 4 mm in diameter. A gas was fed through a receiver with a constant pressure. The velocity of the gas at the nozzle throat was 12 m/s. The difference between reference and distorted Talbot images for this case is shown in Fig. 3.

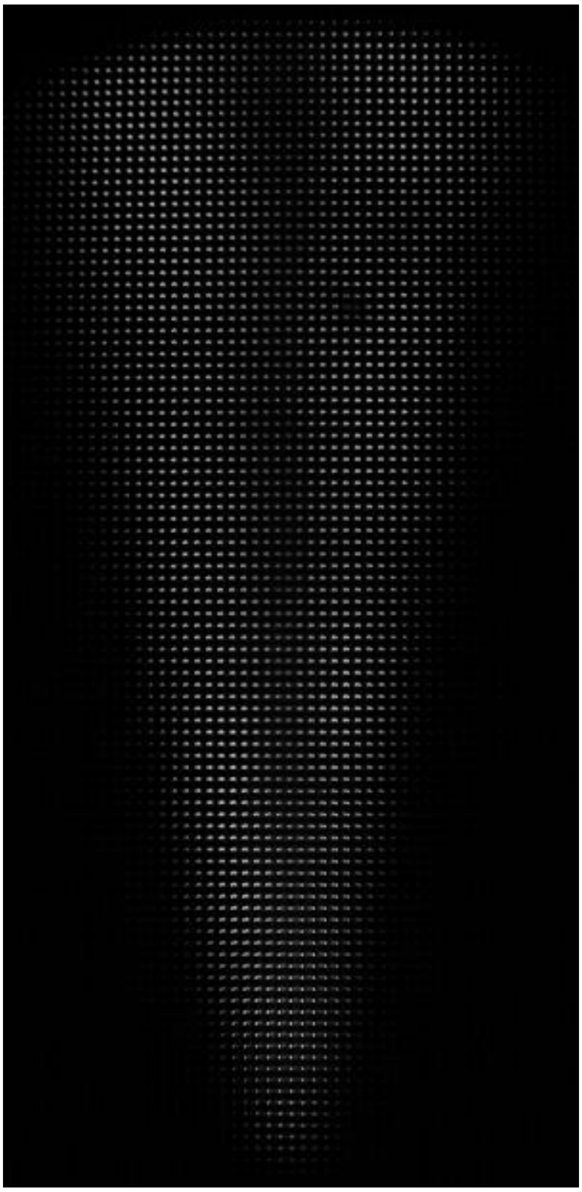

Fig. 3. A difference between reference Talbot image and distorted by an axially symmetrical methane jet Talbot image

## 3. CALCULATIONS OF AVERAGED METHANE CONCENTRATION IN THE FLOW FIELD OF AXIALLY SYMMETRICAL JET.

In our case, the optical axis of the setup matches $z$ coordinate axis. The symmetry axis of turbulent jet is perpendicular to the $z$-axis and codirectioned by $y$ coordinate axis. For this arrangement the Euler equations after substitution of variables for cylindrical coordinates are transformed into the Abel equations [7]:

$$\varepsilon_x = \frac{2}{n_0}\int_x^R \frac{\partial n}{\partial r}\frac{x}{\sqrt{r^2 - x^2}}dr, \qquad \varepsilon_y = \frac{2}{n_0}\int_x^R \frac{\partial n}{\partial y}\frac{r}{\sqrt{r^2 - x^2}}dr, \tag{2}$$

where $\varepsilon_x$ and $\varepsilon_y$ – local refraction angles determined from the difference of the Talbot image, $n$ – refraction index , $n_0$ – refraction index in the point $x = R$, $R$ – radius of the jet and $r$ – cylindrical coordinate.

The three dimensional distribution of local averaged refraction angles $\langle \varepsilon_x \rangle$ and $\langle \varepsilon_y \rangle$ caused by the axisymmetric methane jet are shown in Fig. 4 and 5. In Fig. 6 these variations are shown as a function of $x$ coordinate for distance 10, 15 and 20 jet diameters from the jet exit. Positive and negative values indicate that relative displacement of single Talbot elements in distorted Talbot image was to the left and to the right for $x$-axis, and upwards and downwards for $y$-axis.

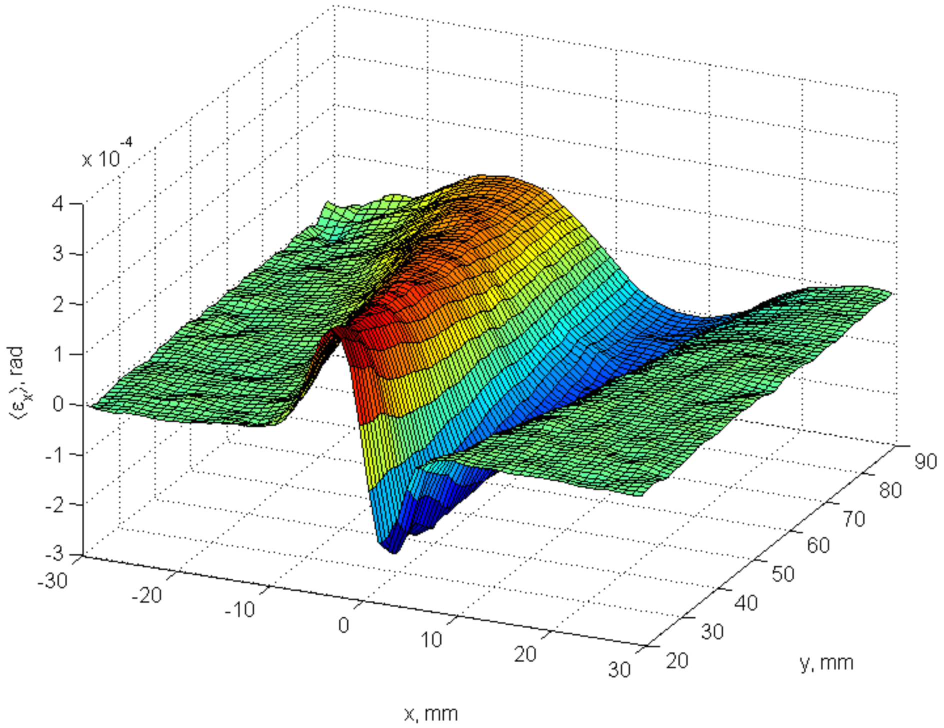

Fig. 4. Distribution $\langle \varepsilon_x \rangle$ of projected on $x$-axis averaged refraction angle

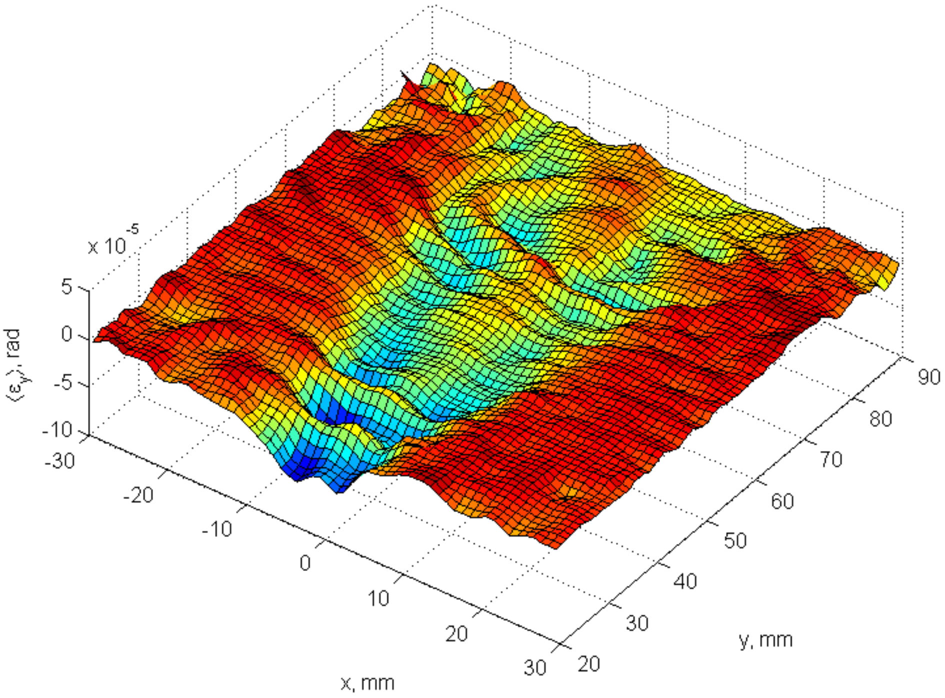

Fig. 5. Distribution $\langle \varepsilon_y \rangle$ of projected on $y$-axis averaged refraction angle

The maximum absolute values of refracted angles along $x$-axis do not exceed $2\cdot10^{-4}$ radian (40″), and along $y$-axis – $5\cdot10^{-5}$ radian (10″). On the axis of symmetry both refracted angles approximately are equal to zero.

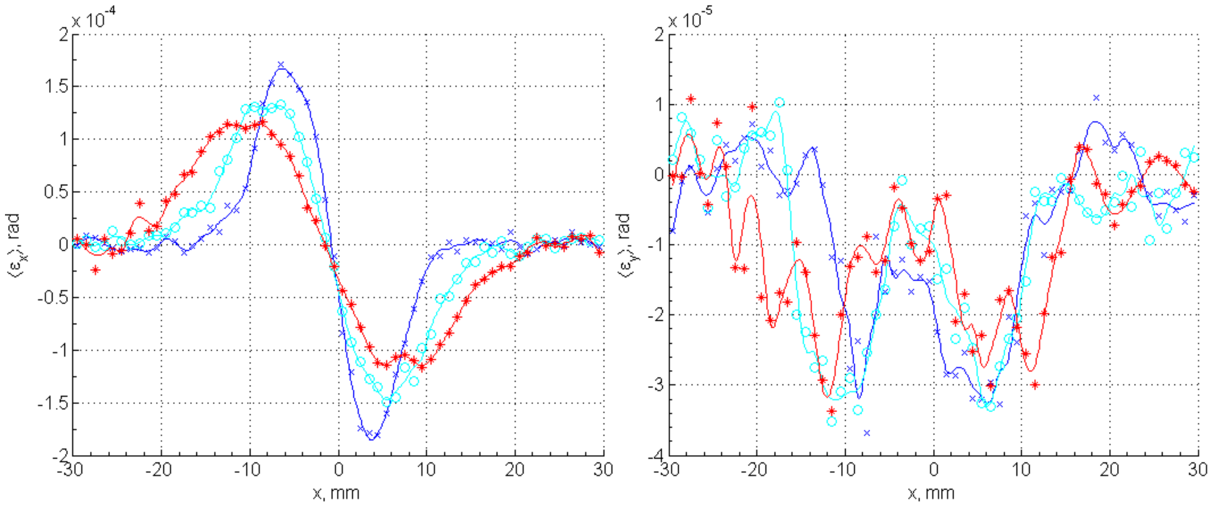

Fig. 6. Distributions of averaged refractions angles $\langle\varepsilon_x\rangle$ and $\langle\varepsilon_y\rangle$ at different distances $y$ from the jet exit: —×— – $y=10D$, —○— – $y=15D$, —✱— – $y=20D$.

The solution for the Abel equations (2) can be written in the following form:

$$\frac{1}{r}\frac{\partial n}{\partial r}=\frac{1}{\pi}\left[\frac{\frac{\varepsilon_x(R)}{R}}{\sqrt{R^2-r^2}}-\int_r^R\frac{\frac{\partial}{\partial x}\left(\frac{\varepsilon_x(x)}{x}\right)}{\sqrt{x^2-r^2}}dx\right],\qquad \frac{\partial n}{\partial y}=\frac{1}{\pi}\left[\frac{\varepsilon_y(R)}{\sqrt{R^2-r^2}}-\int_r^R\frac{\frac{\partial\varepsilon_y(x)}{\partial x}}{\sqrt{x^2-r^2}}dx\right]. \tag{3}$$

By the assumption that light beam is not refracted in $x=R$, where the optical inhomogeneity of the medium is negligible, the equations (3) can be converted to:

$$\frac{1}{r}\frac{\partial n}{\partial r}=-\frac{1}{\pi}\int_r^R\frac{\frac{\partial}{\partial x}\left(\frac{\varepsilon_x(x)}{x}\right)}{\sqrt{x^2-r^2}}dx,\qquad \frac{\partial n}{\partial y}=-\frac{1}{\pi}\int_r^R\frac{\frac{\partial\varepsilon_y(x)}{\partial x}}{\sqrt{x^2-r^2}}dx. \tag{4}$$

After integration of the equation (4) we will obtain:

$$\bar{n}(x)=n_0-\frac{n_0}{\pi}\int_r^R\frac{\bar{\varepsilon}_x(x)}{\sqrt{x^2-r^2}}dx, \tag{5}$$

where $\bar{n}(x)$ – averaged refraction index, and $n_0$ – refraction index in the point $x=R$, corresponding to the refraction index of the air.

For optical diagnostic by means of Talbot-interferometer discrete data set is obtained during the experiment. This set of averaged parameters depends on the period of the Talbot-grating. In the case of axially symmetric problem, the inhomogeneity is automatically divided in to some number of concentric regions. And the integral (5) can be substituted by the sum from first inner region to the last outer one. By using different approximations for the experimentally measured refraction angle distribution, different recurrence formulas can be obtained for calculation of radial profile of refraction index [8]. The distribution of calculated averaged refraction index is shown in Fig. 7.

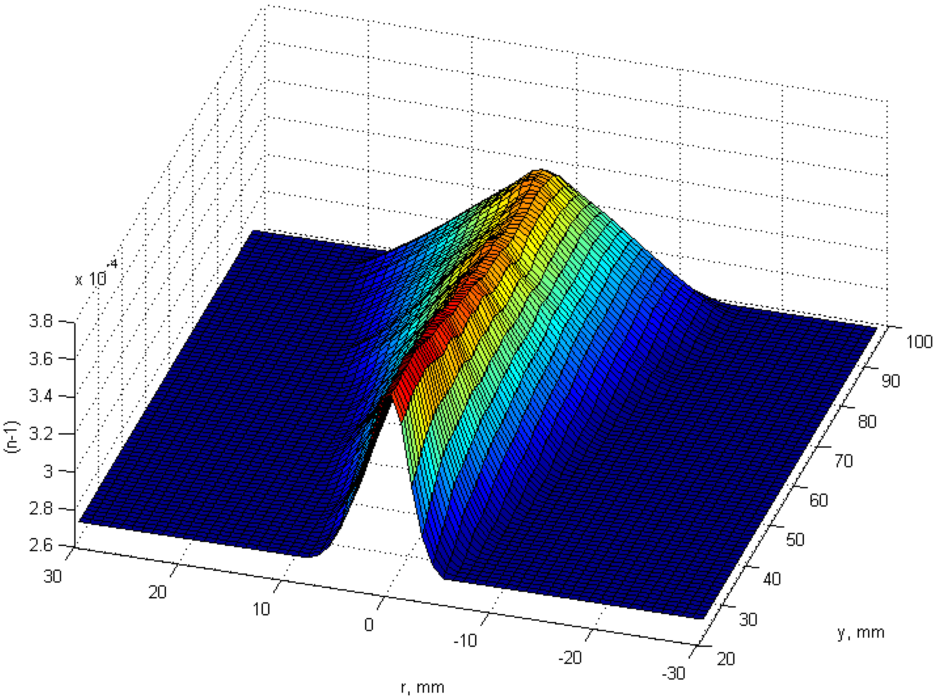

Fig. 7. Distribution of averaged refraction index $\bar{n}(x)$

The obtained distribution of the medium refractive index can be used for calculating an averaged methane concentration. Considering a methane-air mixture as binary and assuming that refractive index values for gas mixtures differ slightly from unity, we write the Lorenz-Lorentz formula [7] in the form of the following system of equations:

$$\begin{array}{l} \overline{n-1} = 2\pi\left(\overline{C_{CH_4}} a_{CH_4} + \overline{C_{air}} a_{air}\right) \\ \overline{C_{CH_4}} + \overline{C_{air}} = \overline{C} \end{array}, \qquad (6)$$

where $\overline{C_{CH_4}}$ and $\overline{C_{air}}$ are the averaged concentrations of methane and air in the jet, while $a_{CH_4}$ and $a_{air}$ are the polarizability of methane and air molecules, respectively.

Figure 8 shows the calculation results of the averaged concentration of methane obtained from the previously calculated data for averaged refractive index distribution (Fig. 7). Fig. 9 represents methane concentrations distributions for flow field cross sections y = 10D, 15D and 20D from jet exit. The maximum of methane concentration is reached on the axis of methane jet. The concentration of methane decreases slowly downstream. In the diagnosed part of flow field a potential core of the jet was not detected.

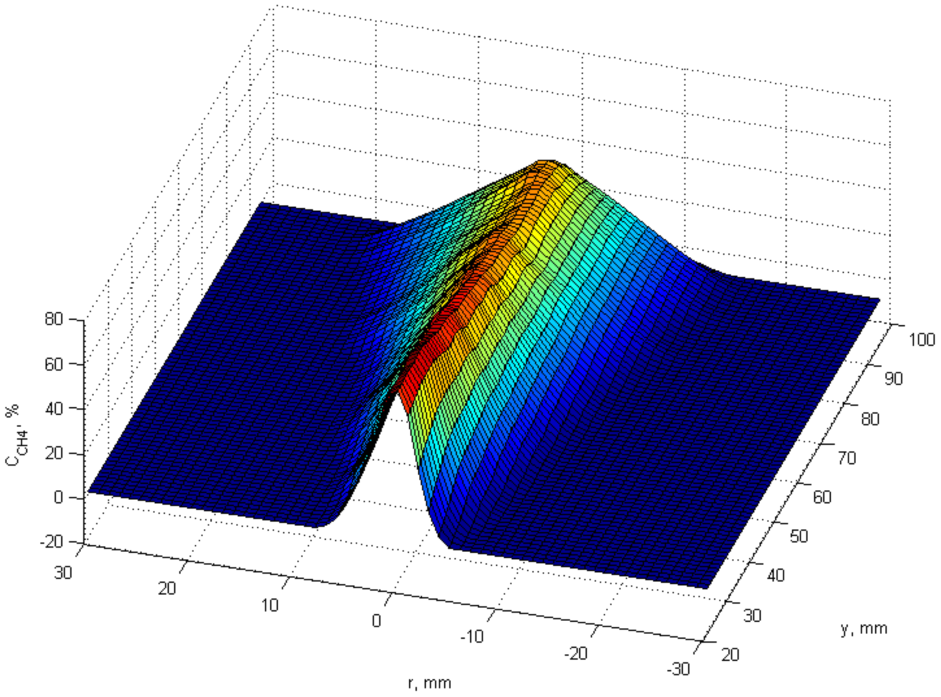

Fig. 8. Distribution of methane concentration in the flow field

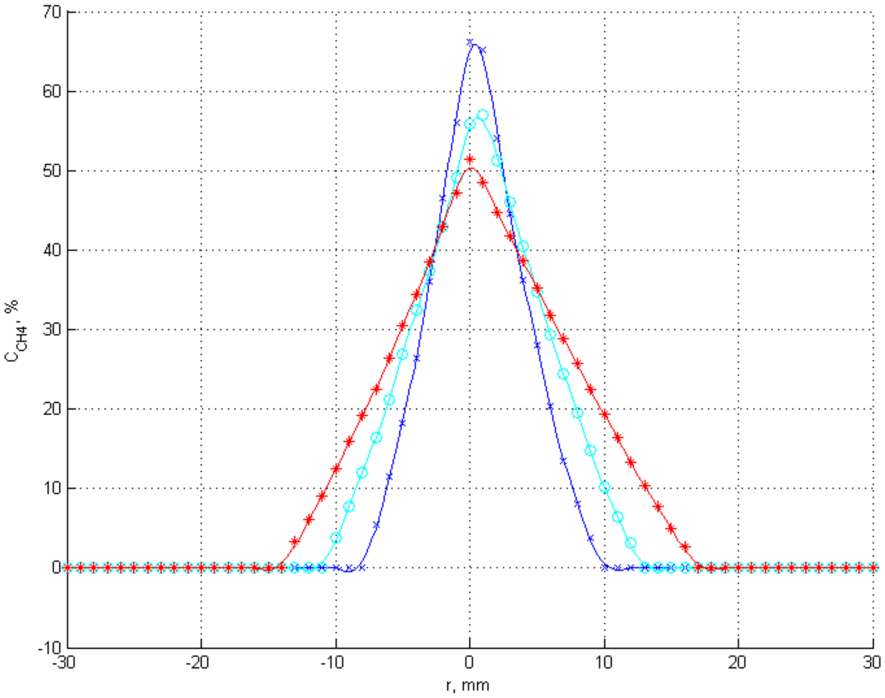

Fig. 9. Distributions of methane concentration in the jet cross section at different distances $y$ from the nozzle throat: —×— – $y = 10D$, —○— – $y = 15D$, —✱— – $y = 20D$

## 4. CONCLUSION

The applied potentialities of the technique based on the Talbot effect are illustrated by the results of averaged concentration measurements for a turbulent, nonpremixed, nonreacting methane jet. The possibility of measuring the spatial distribution of averaged admixture concentration makes this method very promising in investigations of turbulent mixing.

Carried out investigations give reason to conclude that Talbot effect-based technique is a powerful tool for diagnostics of turbulent gas flows. The method is simple to implement, requires no additional optical elements and it is illustrative. Due to the small number of optical elements, it is little prone to external disturbances and can be used in industrial conditions.

## REFRENCES

1. KORYAKOVSKI, A., MARCHENKO, V. Интерферометрия оптических неоднородностей активных сред лазеров на основе эффекта Тальбота. *Квантовая электроника,* 1980, Vol. 7, No 5, p. 1048–1057.
2. KORYAKOVSKI, A., MARCHENKO, V. Датчик волнового фронта на основе эффекта Тальбота. *Журнал Технической Физики*, 1981, Vol. 51, No 7, p. 1432–1438.
3. DOROSHKO, M., PENYAZKOV, O., RENKIN, G., SEVRUK, K., KHRAMTSOV, P., SHIKH, I. Тальбот-интерферометрия в измерениях параметров осесимметричной турбулентной струи. *Инженерно-физический журнал*, 2006, Vol. 79, No 5, p. 94–99.
4. DOROSHKO, M., PENYAZKOV, O., RENKIN, G., SEVRUK, K., KHRAMTSOV, P., SHIKH, I. Исследование обтекания горизонтального цилиндра двумерной турбулентной струей методом тальбот-интерферометрии. *Тепло- и массоперенос–2005,* 2005, p. 210–214.
5. DOROSHKO, M., KHRAMTSOV, P., PENYAZKOV, O., SHIKH, I. Measurements of admixture concentration fluctuations in a turbulent shear flow using an averaged Talbot image. *Experiments in Fluid.* 2008, Vol. 44, p. 461–468.
6. DOROSHKO, M., KHRAMTSOV, P., PENYAZKOV, O., SHIKH, I. Измерение пульсаций концентрации в сдвиговом турбулентном потоке методом осредненных Тальбот-изображений. *Инженерно-физический журнал*, 2008, Vol. 81, No 1, p. 49–54.
7. VASILIEV, Lev A. *Теневые методы*. Moscow: Nauka Press, 1968, UDC535.311
8. DOROSHKO, M., PENYAZKOV, O., KHRAMTSOV, P., SHIKH, I. Влияние методики расчета на значения осредненных параметров осесимметричной турбулентной струи, исследуемой методом тальбот-интерферометрии. *Тепло- и массоперенос–2008*, 2009, p. 254–261.

CYSENI 2011, May 26–27, Kaunas, Lithuania
ISSN 1822-7554, www.cyseni.com

# THE INFLUENCE OF GAS FLOW PULSING ON PERFORMANCE OF THERMAL POWER PLANT

**A. Tonkonogovas, A. Stankevičius**
*Lithuanian Energy Institute*
*Breslaujos g. 3, LT-44403 Kaunas – Lithuania*
*Phone +370 37 401 862*
*Email: andriust@mail.lei.lt, aras@mail.lei.lt*

ABSTRACT

The cogeneration combined-cycle heat power plants are widely implemented in practice due to their high efficiency. Usually the gas pressure in main pipelines is less than required pressure inlet of a gas turbine. To enlarge it, gas is compressed, usually by the compressor of the reciprocating type. Such compressors during operation produce flow pulsations which can cause considerable errors of gas accounting system and strong vibration of adjoining equipment up to its destruction.

The similar problems have appeared at one of Lithuanian heat power plants of such type, soon after its commissioning. The aim of our study was to investigate the problem and suggest the remedy to solve the problem.

During the study, the parameters of gas pressure pulsations and gas consumption balance have been evaluated depending on the power plant load. Gas pressure pulsation frequency, compressor's rotation frequency and frequency of pulsation of turbine gas meter rotation coincide within accuracy of measurements. From that it follows that the compressor is the only source of flow pulsations. Pulsation frequency changing is determined by the mode of regulation of the compressor operation. Specificity of regulation is such that compressor rotation frequency in some points (at some loads) achieves system resonance frequency which value by our estimation is 9 Hz. At resonance the errors of the gas meter increase up to sixty percents.

The calculation predicts that installation of two-staged damper at the compressor input will let to reduce the resonance frequency of the system to the value of 3 Hz, i.e. less then the least compressor rotation frequencies, and in such manner to avoid the resonance, vibration and significantly reduce meter's errors in all power plant's loads range.

Keywords: turbine gas meter, flow pulsation, dynamic error.

## 1. INTRODUCTION

Recently in one of the Lithuanian cities the small cogenerational thermal power plant (TPP) of 30 MW capacity, operating by the combined gas-steam thermodynamic cycle, has been commissioned. At once after TPP putting into operation the problem of consumed natural gas measurement has revealed. Gas is measured by turbine gas meter (TGM), which is the most abundant means of gas accounting at its moderate consumption. Readings of gas meter have been significantly higher than the really consumed gas volume – up to 10%. The difference was even greater at some small TPP loads.

TPP of the considered type are characterized by high power efficiency (electricity generation efficiency reaches 55% and above with additional costless heat generation), and it is advisable to spread them widely. It is important to examine the shortcomings of the pilot station to avoid them in the future.

It has been suggested that the main reason of enlarged gas measuring error is the impact of gas flow pulsation, caused by the reciprocating compressor of TPP gas supply system, on gas meter.

It is known [1–5] that operation of TGM in pulsating flows is always associated with so called dynamic error that appears owing to inertia of the TGM rotor. With increasing pulsation frequency the error grows to a certain limit, later on it remains constant. The amplitude of the pulsation most strongly affects the dynamic error. At large amplitudes the value of error can reach tens of percents. The dynamic error also depends on the time constant of TGM inertia and on the pulsation law as well. As an example, dependence of the dynamic error TGM MZ100 type on the pulsation's parameters according to [5] is presented in Fig. 1 for the pulsation law which is shown in the same figure.

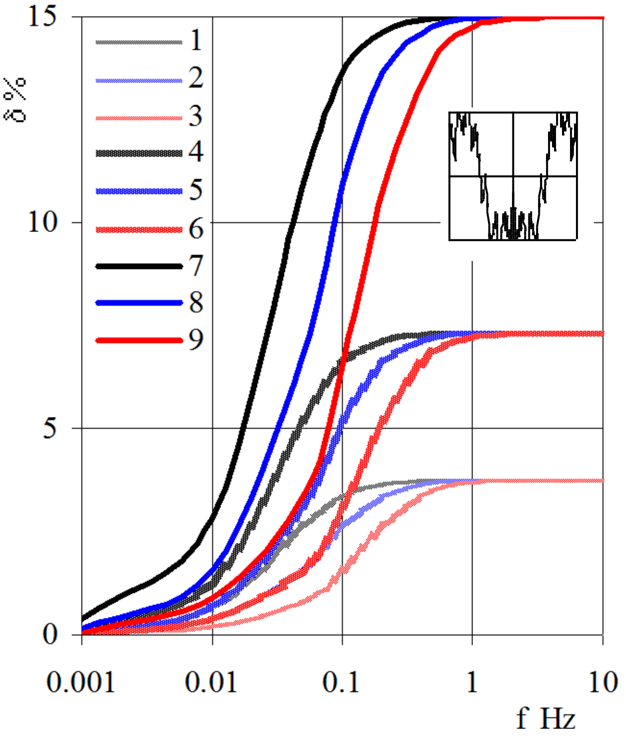

Fig. 1. Dependence of dynamic error of MZ100 type turbine gas meter on the pulsation parameters. 1, 2, 3 – air flow rate = 100, 200, 400 $m^3$/h, respectively, the relative amplitude of flow rate pulsation $\Delta\overline{Q}$ = 0.25; 4, 5, 6 and 7, 8, 9 – the same flow rates at amplitudes $\Delta\overline{Q}$ = 0.35 and 0.5 respectively

The objective of this study was to check this assumption and to investigate the effect of gas flow pulsation on the TGM and TPP operation.

## 2. METHODOLOGY

### 2.1. Power plant‘s gas supply system

Gas to TPP derives from the regional gas measurement station (GMS) of main gas pipelines (MPL) through the pipe DN200 in diameter and length of approximately 3 km. At the distance about 0.3 km from TPP there is a branch from the pipe to GMS of city, where TPP is located. At this GMS gas is accounted by TGM of SM-RI-XL G650 type of INSTROMET production. Further the gas arrives into compressor to enlarge pressure from 1.5 MPa – the largest (for environmental considerations) pressure of gas transportation within the city, to 2.5 MPa – the pressure at which gas should be supplied into gas turbine of TPP. The single-cylinder double-acting reciprocating compressor of V181 130 N2.5 type produced by LMF AG (Austria), of 300 kW power is used. At the inlet and outlet of the compressor there are pulsation dampers of volumetric type, cylindrical shape with two hemispheric caps, the volume of every damper is 0.36 $m^3$.

### 2.2. Measurements

During the experimental investigation gas flow pressure in TGM as well as frequencies of rotation of TGM and of the compressor have been measured. Pressure has been measured by piezoceramic transducer with pressure resolution up to fractions of the Pascal and with time resolution up to 60 μs. Frequency of TGM rotation has been evaluated from time of passage of TGM turbine blades past the high-frequency pulse sensor. The analogical signals of the gauges have been registered and converted by high-frequency 16 digit analog-digital converter. Frequency and amplitude of pressure pulsation have been evaluated by processing of data for pressure changing in time.

By results of the 1st stage of the spent researches the company-manufacturer of the compressor has offered for elimination of the revealed shortages and improvement of pulsations damping quality to install before cylindrical damper at the compressor inlet an orifice of 150/85 mm diameter and realized the offer. After that the 2nd stage of measurements has been carried out.

## 3. RESULTS OF MEASUREMENTS

### 3.1. Analysis of pulsations

In Fig. 2 change in time of gas pressure in TGM and change in time of TGM rotation frequency at different TPP loads (before installation of the orifice) are presented.

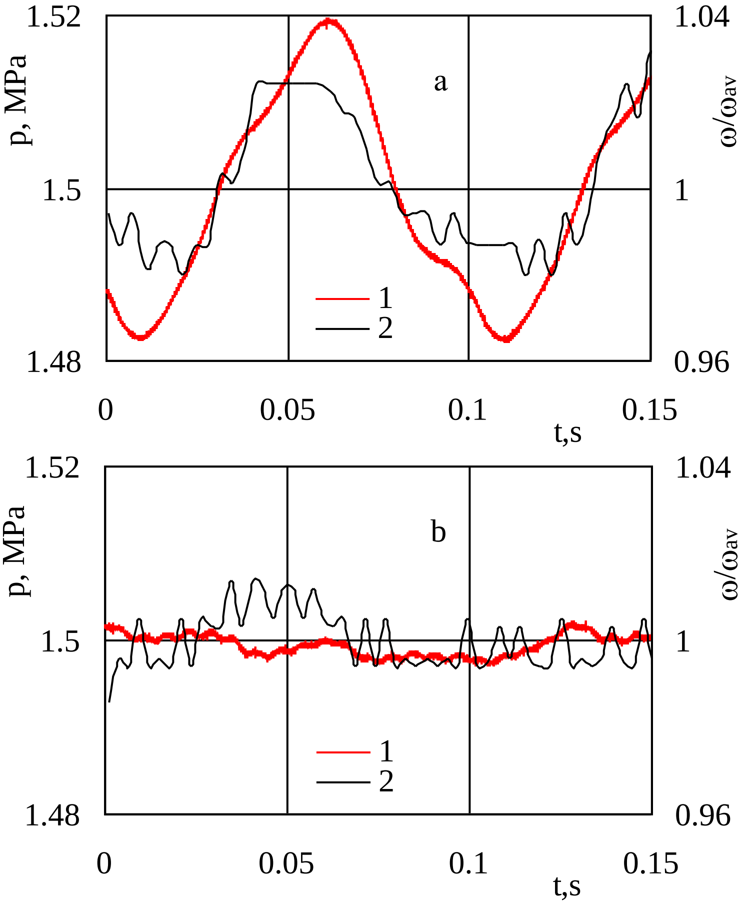

Fig. 2. Change in time of TGM rotation frequency (1) and change in time of gas pressure in TGM (2); a, b – TPP load 16, 30 MW respectively

Good correlation between both curves is observed.

At all TPP loads both parameters significantly pulsate. Therewith pulsations of higher harmonics (2nd and higher) with considerably bigger frequencies and smaller amplitudes are imposed on a pulsation with the biggest amplitude (the 1st harmonic).

In Fig. 3 dependences of frequency and amplitude of pressure pulsation, of a pulsation of frequency of a pulsation of TGM turns, and frequency of the compressor of rotation on TPP loads before and after of the orifice installation are presented.

Dependences of frequency and amplitude of pressure pulsation, frequency of a pulsation of TGM rotation, and frequencies of the compressor rotation on TPP loads before and after the orifice installation are presented in Fig. 3

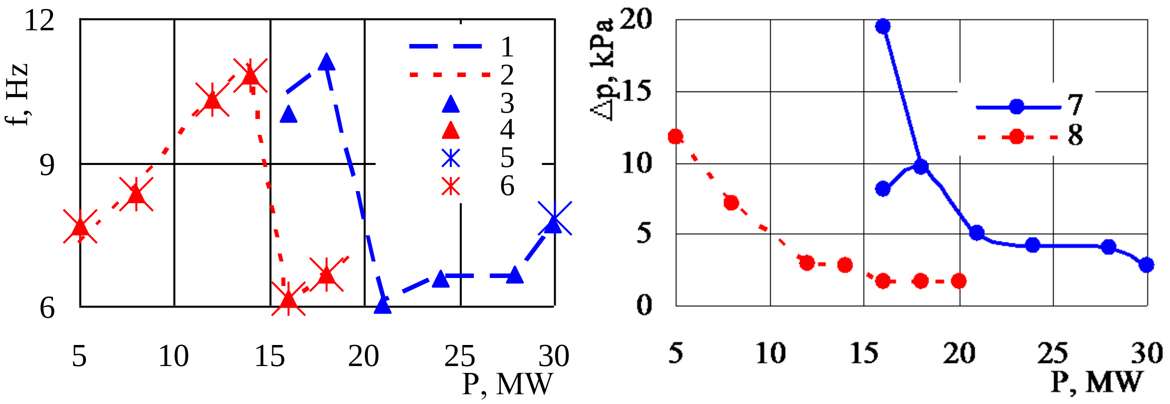

Fig. 3. Dependence of the pulsation parameters on TPP load. 1, 3, 5 – frequencies of pressure pulsation, TGM rotation pulsation and the compressor rotation respectively before orifice installation; 2, 4, 6, the same frequencies after orifice installation; 7, 8 – amplitude of pressure pulsation before and after orifice installation, respectively

Character of change of pulsations frequencies is caused by feature of the compressor operation regulation which is carried out by two ways:

at the raised loads by change of frequency of the compressor crank rotation;

at the lowered loads in addition by change of the compressor valves operating cycle when at reverse motion of the piston receipt of gas in the gas turbine is blocked.

With decrease of TPP load from nominal value of 30 MW frequency of the compressor rotation and accordingly frequencies of pulsations first also decrease a little, but at load below 18 MW they start to grow sharply up to value of 11 Hz. Increasing these frequencies pass through value of the system resonant frequency, by our estimations approximately 9 Hz. As this takes place, a resonance arises, and the amplitude of pulsations sharply increases.

After installation at the compressor input orifice of 80 mm in diameter the quality of pulsations damping has a little improved. Therewith curves of frequency and amplitude of pulsations have displaced to the left, resonant frequency and amplitude of pressure pulsation have a little decreased, however the general picture of processes has remained the same, and the resonance has not been eliminated.

## 3.2. Arising of a resonance

The resonance arises every time when changing due to regulation of the compressor operation actual pulsations frequency becomes equal or close to systems resonant frequency. The scheme of arising of a resonance is shown in Fig. 4.

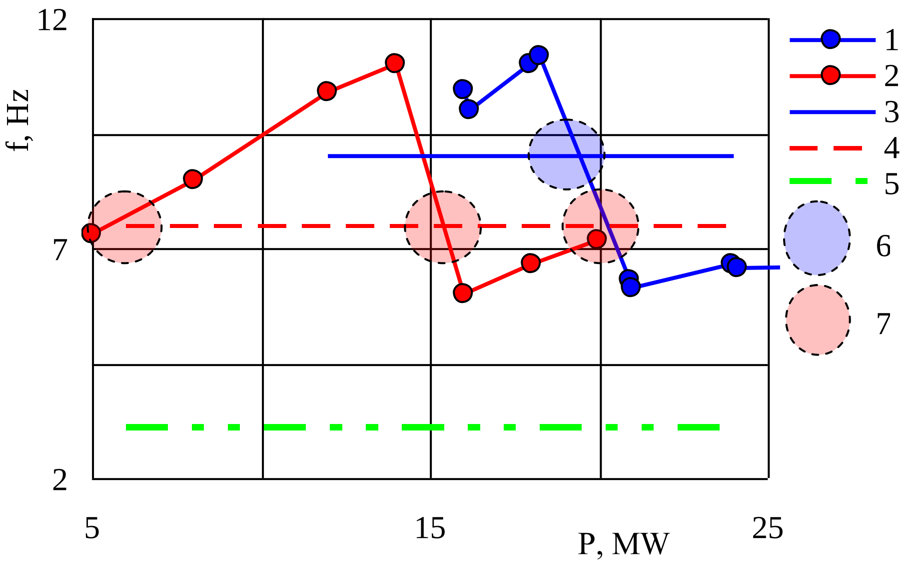

Fig. 4. Scheme of a resonance arising. 1 – frequency of pulsations; 3 – resonant frequencies; 6 – zones of a resonance before installation of orifice; 2, 4 and 7 – the same after installation of orifice; 5 – calculated resonant frequency value at good damping

The curve of actual frequency crosses a line resonant frequency in several points, and in all of them it should be expected arising of a resonance. The resonance is accompanied by sharp increase of amplitude of pulsations and strong, perceptible on hearing and to the touch vibration of the pipeline, able to lead to its destruction.

### 3.3. TGM error. Impact of pulsation on TGM bearings

In Fig. 5 dependence of TGM error on TPP load is presented. Character of this dependence and the dependence of amplitude of a pulsation of pressure on TPP load (Fig 2-b) are very similar, since the enlarged pulsation is the reason of the enlarged error.

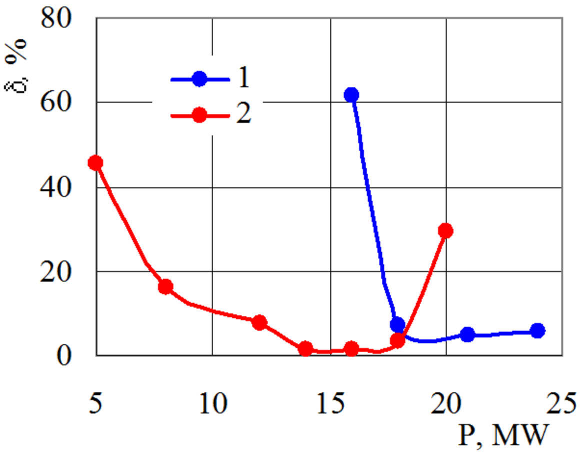

Fig. 5. Dependence of TGM error on TPP load before (1) and after (2) installation of a orifice

At all loads the error is positive. With reduction of load below 18 MW TGM error sharply increases up to value of 62%. At loadings above 18 MW values of an error do not exceed the value of 5% and generally approximately is equal to 2%. Installation of a orifice does not solve a problem up to the end (about it see below).

There is one more unpleasant consequence of pulsations. Repeated change of pressure with the big amplitude and with high frequency creates dangerous sign-altering impact loading on the main parts of TGM – bearings, a gear-box and turbine blades. Here the weakest part – the main bearings of a rotor. Calculation of average speed of pressure change dp/dt according to data of our measurements yields following results. At resonant frequency $f_{res}$=9Hz the greatest amplitude of pressure pulsing $\Delta p_{max} = \pm 20$kPa. Then $(dp/dt)_{max}$ = 720 kPa/s, that is twenty times more than maximum permissible by the European standard [7] speed $(dp/dt)_{max}$ = 35 kPa/s. TGM has no chances to resist to such loading.

## 3.4. Spreading of pulsations beyond of TPP limits. TGM response on flow pulsing at zero total flow

To clarify the question on propagation of pulsations outside of TPP measurements have been made on the GMS of main pipeline, from which gas is supplied to the power plant, as well as o the city's GMS, located on one branch with the power plant's pipeline. At GMS of MPL measurements were taken immediately after the pressure regulator, which reduces the pressure to 1.5 MPa, at the city's GMS – in the TGM, which accounts supplied to with MPL of gas supplying to TPP. Output of TGM was closed with ball valve, so that the resulting flow of gas through the meter was zero. During the measurements pressure changes in time and the TGM readings have been registered. The measurements were carried out at the TPP load about 17 MW, i.e. in the regime of strong resonance. The frequency of pressure pulsations on the city's GMS (1) and MPL GMS (2) is shown in Fig. 6-a, the readings of TGM of city's GMS - in Fig. 6-b.

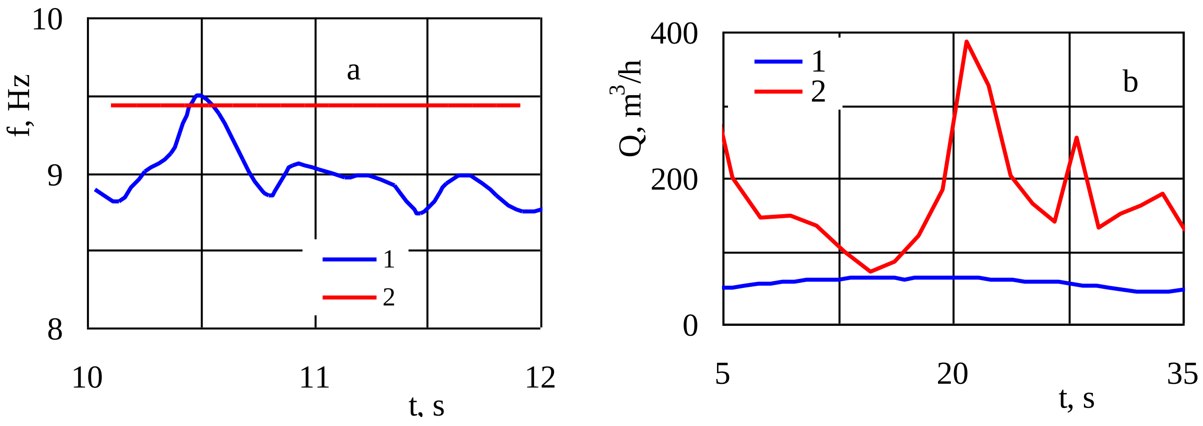

Fig. 6. Change in time of gas pressure pulsing frequency (a) on the city's GMS (1) and on the MPL GMS (2) and TGM readings (b) before orifice installation

Frequencies of pressure pulsations on MPL GMS and on city GMS approximately coincide each with other, differing only due to some instability of TPP load. They also coincide with pulsations frequency on TPP. The greatest observed on both GMS values of pressure pulsation amplitude have reached value of ± (10 – 12) kPa. Pulsation has been accompanied with strong vibrations of gas pipelines and the equipment of both GMS.

So, arising in TPP gas flow pulsations propagates by the pipeline far beyond TPP, causing a resonance and creating danger of equipment destruction.

Propagation of the pulsations distorts the gas account of located on one with TPP branch GMS. At zero summary gas flow through GMS indications TGM are appreciable above zero.

It is connected with features of a design of the used now on majority TGM pulse sensors. The sensor registers passage of turbine's blades past itself, but does not consider a direction of their movement. The electronic device of gas volume converting summarizes all impulses from the sensor in one register and in such a way fixes the sum of "imaginary" and actual volumes of gas. Results of modeling of TGM behavior in a pulsing gas flow at the zero total flow rate, presented in Fig. 7, confirm this fact.

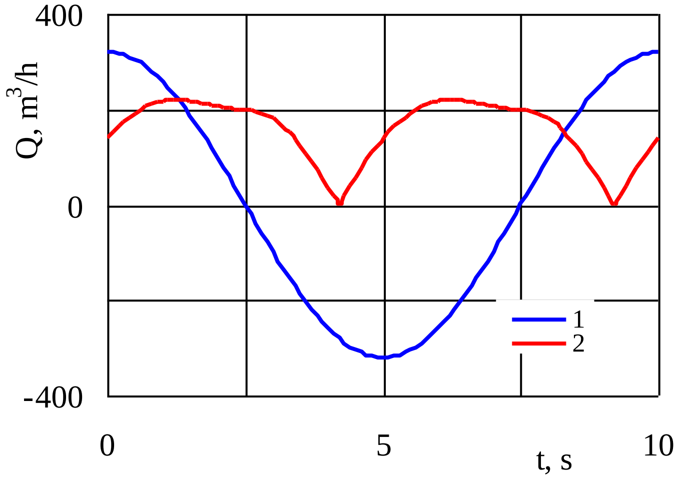

Fig. 7. TGM response on flow pulsing at zero total flow rate. 1 – flow rate; 2 – TGM readings

### 3.5. The estimation of the taken by the manufacturer of compressor measures for an improvement in the quality of damping

The installation of orifice at the compressor impute led to the shift of frequency curved to the left. As before pressure pulsing frequency coincides with the curve of a change in the frequency of the compressor rotation. Resonance frequency and amplitude of the pressure pulsations a little decreased (from 9 to 7 Hz and from 20 to 12 kPa respectively at the resonance). However, resonance and increased pulsations are not removed

The level of dynamic error has been significantly reduced; however, it still exceeds the maximal allowed value. As before pulsations from the compressor are propagates beyond the limits TPP, causing vibration and influencing the accuracy of gas account and the technical state of TGM. Installation of orifice - step in the right direction, but insufficient.

### 3.6. Recommendations on radical removing of the revealed shortages

For the complete avoiding of the vibrations of the gas pipelines and equipment and for the considerable reduction in the intensity of flow pulsations it is necessary to decrease the resonance frequency lower than the smallest value of the frequency of the rotation of compressor. For this it is necessary to improve the device of the suppression of pulsations, increasing its volume and/or hydraulic resistance. In particular, should be equipped entrance and output of compressor with the dual chamber damper of pulsations. As show the carried out calculations [8], if the existing camera was supplemented with the second camera of the same volume and was connected by their pipe with a length of 2 m and with a diameter of 0.04 m, resonance frequency will decrease to the value of 3.1 Hz – it is lower than the actual minimum of operating frequency of the rotation of compressor.

Also should be changed the principle of the control of compressor operation. At decreased TPP loads during the compressor piston back stroke gas should be directed not back in the entrance of compressor, but into the special intermediate damping volume.

If the technical-normative regulations don't forbid it’s reasonable to avoid the use of a compressor and to transport gas to TPP under pressure which is required for gas applying in gas turbine facility  (in considered case it's 2.5 MPa).

In the absence of such possibility instead of the reciprocating compressor should be used the compressor of the type, which creates the pulsation of the smaller intensity, for example, of screw type.

In all cases level of pulsations should be controlled. By use of the proper damping system the flow pulsing should be reduced to the acceptable level on considerations of gas measurement accuracy and as well on considerations of absence of vibrations [1, 6].

## 4. CONCLUSIONS

1. The enlarged positive errors of natural gas account and vibration of TPP gas equipment as well are caused by flow pulsations which are produced by the installed in TPP reciprocating gas compressor. Such dynamic error is typical for turbine gas meters. It arises because of turbine meter rotation inertia.
2. The existing system of the pulsations damping does not satisfy the requirements of international standards and must be improved.
3. Especial danger is associated with resonance phenomena, which impose as a result of superposition of the actual frequency of the rotation of compressor and resonance frequency of the system at some TPP loads. The resonance cause a sharp increasing of the pulsations intensity, sharp increasing of the gas measurement by TGM error and dangerous vibrations of the equipment.
4. Pulsations are extended far beyond limits TES, implying unpleasant the consequences pointed out above.
5. The measures for the control of gas pulsations and their decrease to the acceptable level on accuracy conditions of the calculation of gas and absence of vibrations have been suggested.

## REFERENCES

1. *ISO/TR 3313:1998.* Measurement of fluid flow in closed conduits – Guidelines on the effects of flow pulsations on flow-measurement instruments. 1998
2. ATKINSON K. N. A software tool to calculate the overregistration error of a turbine meter in pulsating flow. *Flow measurement and instrumentation*, 1992 Vol. 3 No 3, p. 167–172.
3. CHEESEWRIGHT R., BISSET D., CLARK C. Factors which influence the variability of turbine flow meter signal characteristics, Flow measurement and instrumentation. *Flow measurement and instrumentation* 1998, Vol. 9 No 2, p. 83–189.
4. LEE W.F.Z., KIRIK M.J., MILLINGTON B. Gas turbine flow meter measurement in pulsating flow. *Journal of engineering for gas turbines and power.* 1975, Vol. 97, p. 531–539.
5. TONKONOGIJ J., PEDIŠIUS A. The errors of gas meters. *Measurement techniques* 2006. Vol. 42. No. 5, p. 458–463.
6. *API standard 618 4th ed.* Reciprocating compressors for petroleum, chemical, and gas industry services. 1995.
7. *European Standard EN 12261:2002*. Turbine gas meters. 2002.
8. ATKINS K. E., PYLE A. S., TYSON J. D. Understanding the pulsation & vibration control concepts in the new API 618 5th edition. *Gas Machinery Conference. Albuquerque, New Mexico.*

CYSENI 2011, May 26–27, Kaunas, Lithuania
ISSN 1822-7554, www.cyseni.com

# LASER *3D* FABRICATION OF POLYMERIC MICRO/NANOSTRUCTURES FOR BIOMEDICAL APPLICATIONS

**P. Danilevičius, M. Malinauskas**
*Laser Research Center, Department of Quantum Electronics*
*Physics Faculty, Vilnius University*
*Saulėtekio Ave. 10, LT-10223 Vilnius – Lithuania*
*Phone +370 5 2366014*
*Email: paulius.danilevicius@ff.stud.vu.lt*

**E. Balčiūnas**
*Vivarium, Institute of Biochemistry, Vilnius University*
*Mokslininkų str. 12, LT-08662 Vilnius – Lithuania*

## ABSTRACT

In this work we present the latest results on Multi-Photon Polymerization (MPP) application for tissue engineering, by fabrication of microstructured artificial 3D scaffolds for stem cell proliferation. Microstructuring of large scale 3D scaffolds is investigated and MPP technique is supplemented by micromolding over large area. Biocompatibility of non-microstructured different polymers and 3D scaffolds fabricated out of them by the MPP has been experimentally tested. Proliferation tests with adult myogenic stem cells proliferation tests show that polymers as well as artificial 3D scaffolds fabricated from acrylate based AKRE, hybrid organic-inorganic ORMOCORE b59, SZ2080 materials and biodegradable PEG-DA-258 photopolymer are applicable for biomedical practice. All these materials have been found at least as biocompatible as glass or polystyrene surfaces for stem cells *in vitro* and as a surgical suture judging by the results of histological examination of tissues surrounding polymer implants *in vivo*. Laboratory animals were rats and rabbits and implantation period was up to 3 weeks. Adhesion of cells was also investigated and obtained results proved the photostructurable polymers to be promising for future works for production of biocompatible 3D scaffolds. Within the limitation of our study, we conclude that the proposed nonlinear direct laser writing technique offers rapid and flexible fabrication of biomedical components with required shape, pore size and general porosity. Applications could target biostable and biodegradable implants applied for bone or tissue replacement as well as drug delivery or release agents.

Keywords: direct laser writing, multi-photon polymerization, micro/nanofabrication, 3D scaffolds, micromolding, biocompatible and biodegradable photopolymers, tissue engineering.

## 1. INTRODUCTION

Multi-Photon Polymerization (MPP) is a promising direct laser writing technique which has gained a lot of attention during the past decade. It is based on tightly focused ultrashort laser pulses initiating polymerization reaction of radicals in a confined region of a photosensitive material. A desirable form of polymeric structure which is insoluble in developer can be created by exposing selectively. After washing unexposed areas, the free standing micro-object with internal nanostructure remains on a cover glass. Due to non-linear multi-photon absorption in a transparent material polymerization reaction is initiated only in a focal volume. This technique allows creating true three-dimensional (3D) structures within the bulk of the material having no geometrical restrictions [1]. A threshold nature of radical polymerization and multi-photon absorption dependence on second or higher powers of light intensity allows working in conditions very close to the photopolymerization threshold and reaching the sub-diffraction resolution up to tens of nanometers [2]. These above mentioned advantages distinguish MPP among the other high spatial resolution fabrication techniques such as UV [3] and electron-beam [4] lithographies, self-organization [5], ink-jet printing [6], laser ablation [7] and laser sintering [8]. Due to its advantages compared to alternative technologies, MPP has already been applied in photonics [9], microoptics [10] and microfluidics [11] as well as biomedicine [12].

Organ and tissue donor problem is very important in medical practice. Synergetic studies of nanotechnologies and stem cell research has already yielded products helping to cure diseases or traumas [13]. Nowadays, complex polymeric matrices for stem cell growth are being designed which could serve as the templates for the controllably forming artificial tissue [14]. Exactly MPP fabrication technique satisfies requirements for these scaffolds, such as a complex geometry, precise control of pores architecture and sub-micron resolution [15]. However, much effort is still needed to improve fabrication by MPP and to understand cell behavior at micro-scale.

The aim of this work was to investigate the opportunities of fabrication of large scale 3D scaffolds and to evaluate biocompatibility of the materials suitable for micro/nanostructuring by MPP.

## 2. METHODOLOGY

### 2.1. Photosensitive materials

In our experiment we have used four different photopolymers: custom made acrylate based material AKRE19 [16], hybrid organic-inorganic SZ2080 (ORganicaly MOdified SILica ORMOSIL, FORTH) [17] and Ormocore b59 (ORganicaly MOdified CERamics ORMOCER, Micro Resist Technology GmbH) [18], biodegradable PEG-DA-258 (PolyEthylenGlycol Di-Acrylate of M.w. = 258, Sigma-Aldrich GmbH) [19]. The monomers were photosensitized adding 1–2 wt. % of 2-Benzyl-2-dimethylamino-1-(4-morpholinophenyl)-butanone-1 photoinitiator (Sigma-Aldrich GmbH). PDMS thermo elastomer (Poly(DiMethyl Siloxane), Dow Corning Corp.) was used producing transparent mask for UV micromolding, it was mixed with matched curing agent (Dow Corning Corp.) using weight ratio 10:1. Chemical formulas and developers of the used materials are given in Table 1.

Table 1. Photosensitive materials used in experiment

| Material | Chemical formula | Developer |
|---|---|---|
| AKRE19 | $C_{18}H_{21}N_3O_9$ | ethyl alcohol |
| SZ2080 | $C_4H_{12}SiZrO_2$ | methyl isobutyl ketone |
| PEG-DA-258 | $C_8H_{10}O_4$ | water |
| Ormocore b59 | $C_4H_{12}Si_2O_2$ | methyl isobutyl ketone |
| PDMS | $C_2H_6SiO$ | methyl isobutyl ketone |

Samples for fabrication were prepared by drop-casting the photopolymer on a cover glass substrate. After laser processing samples were treated with the appropriate organic solvent in order to wash out unexposed material. Photopolymer exposed by light underwent polymerization and became insoluble in the developer. Polymerized features sustained during the development process. In this way, the free-standing structures were fabricated on a glass substrate. Scanning Electron Microscope (SEM) and optical profilometer were applied to evaluate the microstructured scaffolds.

### 2.2. Laser fabrication setup

In this work we used the MPP system which schematic illustration is depicted in Fig. 1 a. Irradiation source was the high-peak-power femtosecond Yb:KGW laser (Pharos, Light

Conversion Co. Ltd.), which parameters were: the repetition rate from 1 to 200 kHz, average power 6W, pulse duration 300 fs, fundamental wavelength 1030 nm (515 nm second harmonics was used in experiment). The laser beam was guided through an optical system to a high numerical aperture objective and focused to a volume of photopolymer. The sample was mounted on a high speed and wide working area XYZ scanning stages. The positioning system consisted of linear motor driven stages (Aerotech, Inc.): XY-ALS130-100, Z-ALS130-50. These stages ensured an overall travelling range of 100 mm into X and Y directions and 50 mm in Z direction and support the scanning speed up to 300 mm/s. Upon irradiation the monomers underwent transition from liquid to solid (or from gel to solid) and resulted to the change in refractive index. It enabled wide-field transmission microscopy to be used for monitoring the manufacturing process in real time. A microscope was built by assembling its main components: a source of red light provided by LED, a CMOS (mvBlueFOX-M102G, Matrix Vision GmbH) camera and a video screen. The ability to image photostructuring while performing MPP is an important feature for successful fabrication process. It is of upmost importance to anchor the microstructures to the substrate in order for them to survive the washing step of the unsolidified resin. Control of all equipment was automated via custom-made software 3D-Poli specially designed for MPP applications. By moving the sample three-dimensionally, the position of laser focus was changed inside the resin and this enabled writing complex 3D structures (Fig. 1 b). Structures can be imported from Computer Aided Design (CAD) files or programmed directly. This MPP system was tested for structuring in various photosensitive materials at large scale [20]. The ability to scale up and speed up the fabrication was ensured by changing laser beam focusing objectives in the range from 100x NA = 1.4 to 10x NA = 0.25, thus at the sacrifice of the resolution from 200 nm to 4 μm [16].

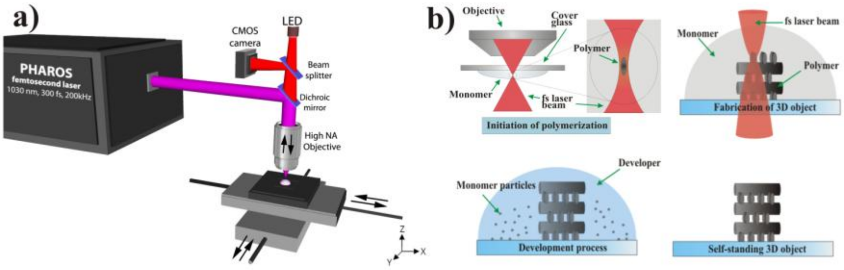

Fig. 1. a) Schematic illustration of MPP fabrication setup. b) Fabrication steps: laser beam was focused inside the resin and initiated radical polymerization reaction; 3D structure was built by scanning the sample; unexposed monomer was washed out by organic developer; in this way polymeric structure was fabricated on a glass substrate

## 3. RESULTS AND DISCUSSIONS

### 3.1. Fabrication of 3D scaffolds

Constructed MPP fabrication setup was used for production of 3D micro-porous scaffolds over the large area in order to have objects of acceptable size for later implantation *in vivo*. SZ2080 photosensitive material, known for its good micro and nanostructuring capabilities, was chosen. Scaffolds were up to 5x5x0.3 $mm^3$ in size, with 30-40 μm pores and ~40 % of general porosity. The pore size of the scaffolds should be around twice as large as a single cell, and for mammals it should correspond to tens of micrometers [21]. Precise control of the pore size, their homogeneity and interconnection is believed to be beneficial for cell proliferation [22]. Also, scaffold stiffness and biodegradability depends on inner architecture and filling factor ($V_{material}/V_{scaffold}$) [23].

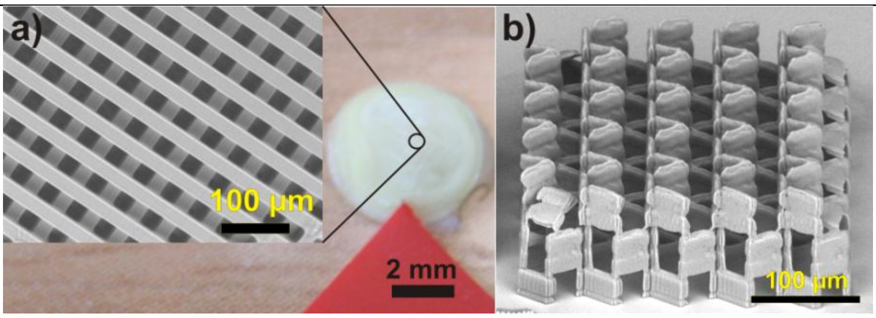

Fig. 2. a) 3D scaffold for artificial tissue growth fabricated from biocompatible photopolymer SZ2080 (size 5x5x0.3 mm$^3$). Inset shows internal microstructure with 40 % of porosity. Objective 40x NA = 0.65, laser average power 1 mW, scanning speed 10 m/s were used. b) Complex geometry 3D scaffold with 40 µm pores fabricated from the same material. Objective 40x NA = 0.65, laser average power 0.5 mW, scanning speed 2 m/s were used

### 3.2. Large scale micromolding of 2D scaffolds

Replica molding by PDMS soft lithography (Fig. 3 a) is a low cost, high throughput and a simple to operate fabrication method [24]. For repeated cell growth experiments, there is demand on many equal scaffolds. In such case fabrication with the MPP system is rather expensive and time-consuming process. As an alternative method, micromolding can be used for rapid production of a series of equal samples.

Compared to other fabrication techniques, like MPP, PDMS soft lithography is attractive because its fabrication time is independent of dimensions of the structure (Fig. 3 b, Eq. 1) and it has a relatively low cost/quality ratio. Fabrication time using the MPP system can be expressed as:

$$t \propto \frac{h \times w \times l}{v}, \tag{1}$$

where $t$ – time needed to fabricate a structure, $h$ – height, $w$ – width, $l$ – length, $v$ – velocity of serial writing (it is specific for each monomers being used).

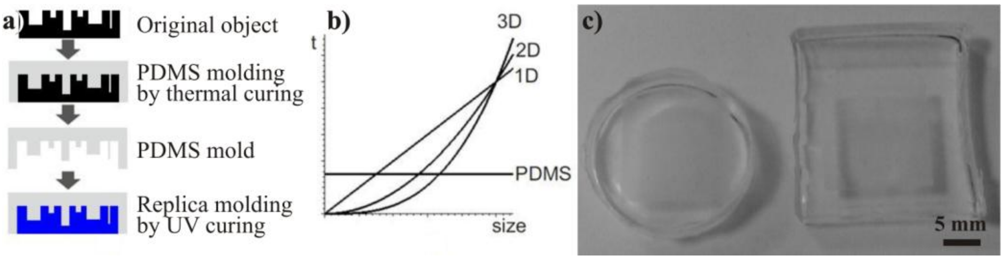

Fig. 3. a) Schematic illustration of micro/nano-structured object replication using PDMS. b) Replication by PDMS soft lithography is independent of structure dimensions, because it is cured all at once. Fabricating a structure using multi-photon polymerization requires time-consuming serial writing: 1D structure fabrication time linearly depends on the structure size, 2D structure – quadratic, 3D – cubic. c) A photograph of PDMS molds with negative structure of the master substrate: a 15x15 mm scaffold for stem cell growth

PDMS is a substantial elastomer and molds made of it may be used up to tens times without significant loss of quality. Furthermore, micromolding technique allows fabrication of other materials, that would otherwise not be susceptible to structuring, e.g. thermo-polymers. There is a wide spectrum of other applications which would benefit from this replica molding technique, such as microfluidics, microelectronics, photonic components, functional coatings [24–27].

The elastomer for replica molding was prepared by mixing PDMS with a thermo-initiator at 10:1 weight ratio, respectively. The mixture was degassed in a vacuum chamber until all air bubbles were removed. It was then poured onto a microstructured master substrate (fabricated by using MPP) and heated for 1 hour at 100°C. After that, the PDMS mold was carefully peeled off from the master substrate (Fig. 3 c). Biodegradable photopolymer (PEG-DA-258) was poured onto a cover glass and the mold was applied on top. UV curing was applied using a femtosecond laser (40 mW average power, 10 Hz repetition rate) for three minutes.

Using this technique, we have successfully replicated scaffolds for stem-cell growth (Fig. 4), reducing fabrication time twenty times. We have showed that using this technique we can reproduce surface roughness with 2% difference.

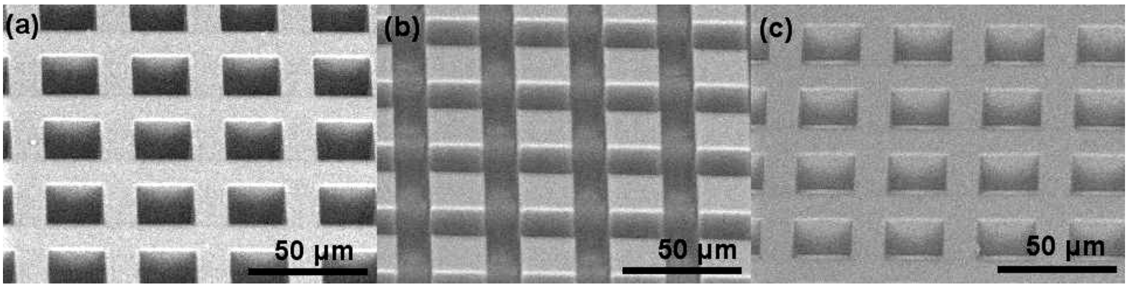

Fig. 4. a) SEM micrograph of a scaffold out of SZ2080 photopolymer, fabricated using multi-photon polymerization; b) PDMS mold, made using a SZ2080 master; c) Replica of the laser fabricated SZ2080 scaffold, made out of PEG-DA-258 polymer

### 3.3. Biocompatibility test of polymeric materials

Biocompatibility of four different photosensitive materials, which were found suitable for MPP processing, such as acrylate AKRE19, biodegradable PEG-DA-258, hybrid organic-inorganic SZ2080 and Ormocore b59, was tested *in vitro* and *in vivo*. Adult myogenic stem cells derived from rabbit muscle were seeded on non-structured polymeric films *in vitro* for 48 h and their viability was registered by staining with dye-mix solution (Fig. 5 a). Results demonstrated that polymers were as biocompatible as control polystyrene and glass surfaces. Biocompatibility of polymeric samples manufactured as shapeless granules were tested *in vivo*. For comparison of tissue response, surgical suture was taken as a control sample. After three weeks of implantation all tested materials were found as biocompatible as surgical suture, showing them to be suitable for biomedical practice (Fig. 5 b).

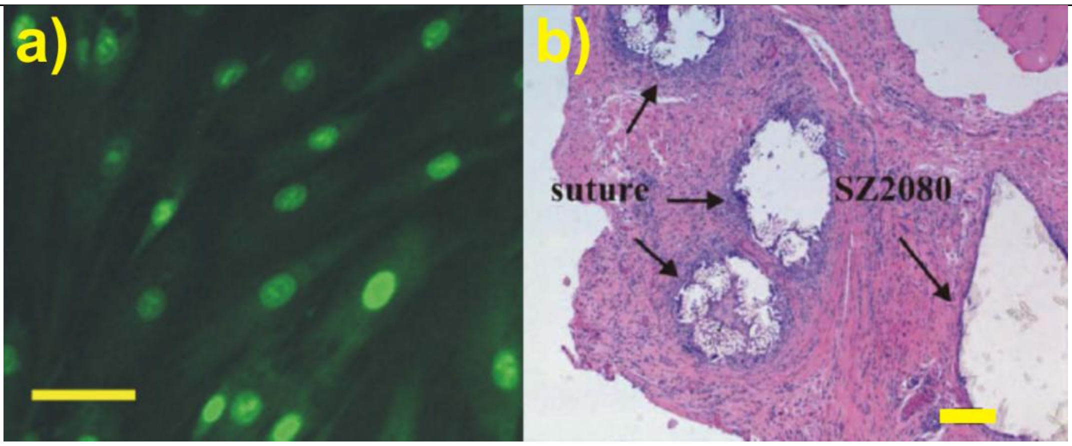

Fig. 5. a) Green adult stem cells grown on tested polymeric films showing their viability. The scale bar is 50 μm. b) Histological cross-section of stained tissue surrounding SZ2080 and surgical suture after 3 weeks of implantation. The scale bar is 200 μm

## 4. CONCLUSIONS

We applied the MPP system for the high resolution and large scale fabrication of 3D scaffolds for tissue engineering applications. PDMS micromolding over the large area was incorporated in order to increase fabrication throughput. Stem cell growth on the photostructurable polymeric materials was tested *in vitro*, and the results were supported by the biocompatibility tests *in vivo*. Experimental results showed that four different polymeric materials are applicable for biomedical practice and our approach to tissue engineering offers good perspectives. However, future work on investigation of stem cell proliferation on 3D scaffolds, its biodegradability and design with suitable mechanical properties is still in progress.

## REFERENCES

1. JUODKAZIS, S., MIZEIKIS, V., MISAWA, H. Three-dimensional structuring of resists and resins by direct laser writing and holographic recording. *Adv. Polym. Sci.*, 2008, Vol. 213, p. 157-206.
2. QI, F., LI Y., TAN D., YANG H., GONG Q. Polymerized nanotips via two-photon Photopolymerization. *Opt. Expr.*, 2007, Vol. 15, No. 3, p. 971–976.
3. NAULLEAU, P.P., ANDERSON, C.N., CHIU, J., DENHAM, P., GEORGE, S., GOLBERG, K.A., GOLDSTEIN, M., HOEF, B., HUDYMA, R., JONES, G., KOH, C., FONTAINE, B.L., MA,A., MONTGOMERY, W., NIAKOULA, D., PARK, J.O., WALLOW, T., WURM, S. 22-nm half-pitch extreme ultraviolet node development at the sematech berkeley microfield exposure tool. *Microelectron. Eng.*, 2009, Vol. 86, No. 4–6, p. 448–455.
4. SUNE, G. R. Electron beam lithography for nanofabrication. PhD thesis, University of Barcelona, 2008.
5. ROUSSET, S., ORTEGA, E. Self-organized nanostructures. *J. Phys. Condens. Matter*, 2006, Vol. 18, No. 13.
6. WALTHER, M., ORTNER, A., MEIER, H., LOFFELMANN, U., SMITH, P.J., KORVINK, J.G. Terahertz metamaterials fabricated by inkjet printing. *Appl. Phys. Lett.*, 2009, Vol. 95, No. 25, p. 251107–251103.

7. LIM, Y.C., BOUKANY, P.E., FARSON, D.F., LEE, L.J. Direct-write femtosecond laser ablation and DNA combing and imprinting for fabrication of a micro/nanofluidic device on an ethylene glycol dimethacrylate polymer. *J. Micromech. Microeng.*, 2011, Vol. 21, No. 1, p. 015012.
8. KUMAR, S. Selective laser sintering: A qualitative and objective approach. *JOM*, 2003, Vol. 55, No 10, p. 43–47.
9. SUN, Q., JUODKAZIS, S., MURAZAWA, N., MIZEIKIS, V., MISAWA, H. Freestanding and movable photonic microstructures fabricated by photopolymerization with femtosecond laser pulses. *J. Micromech. Microeng.*, 2010, Vol.20, No. 3, p. 035004.
10. MALINAUSKAS, M., GILBERGS, H., ŽUKAUSKAS, A., PURLYS, V., PAIPULAS, D., GADONAS, R. A femtosecond laser induced two-photon photopolymerization technique for structuring microlenses. *J. Opt.*, 2010, Vol. 12, No. 3, p. 035204.
11. WU, D., CHEN, Q.D., NIU, L.G., WANG, J.N., WANG, J., WANG R., XIA, H., SUN H.B. Femtosecond laser rapid prototyping of nanoshells and suspending components towards micro fluidic devices. *Lab Chip*, 2009, Vol. 9, No. 16, 2391–2394.
12. OVSIANIKOV, A., SCHLIE, S., NGEZAHAYO, A., HAVERICH, A., CHICHKOV, B.N., Two-photon polymerization technique for microfabrication of CAD-designed 3D scaffolds from commercially available photosensitive materials. *J. Tiss. Eng. Regen. Med.*, 2007, Vol. 1, No. 6, p/ 443–449.
13. GRIFFITH, L. G., NAUGHTON, G. Tissue engineering: current challenges and expanding opportunities. *Sci.*, 2002, Vol. 295, No. 5557, p. 1009–1014.
14. RINGE, J., KAPS, C., BURMESTER, G.-R., SITTINGER, M. Stem cells for regenerative medicine: advances in the engineering of tissues and organs. *Naturwissenschaften*, 2002, Vol. 89, No. 8, p. 338–351.
15. MALINAUSKAS, M., DANILEVIČIUS, P., BALTRIUKIENĖ, D., RUTKAUSKAS, M., ŽUKAUSKAS, A., KAIRYTĖ, Ž., BIČKAUSKAITĖ, G., PURLYS, V., PAIPULAS, D., BUKELSKIENĖ, V., GADONAS, R. 3D artificial polymeric scaffolds for stem cell growth fabricated by femtosecond laser. *Lith. J. Phys.*, 2010, Vol. 50, No. 1, p. 75–82.
16. MALINAUSKAS, M., PURLYS, V., RUTKAUSKAS, M., GAIDUKEVIČIŪTĖ, A., GADONAS, R. Femtosecond visible light induced two-photon photopolymerization for 3D micro/nanostructuring in photoresists and photopolymers. *Lith. J. Phys.*, 2010, Vol. 51, No. 2, p. 201–207.
17. OVSIANIKOV, A., VIERTL, J., CHICHKOV, B., OUBAHA, M., MACCRAITH, B., SAKELLARI, I., GIAKOUMAKI, A., GRAY, D., VAMVAKAKI, M., FARSARI, M., FOTAKIS, C. Ultra-low shrinkage hybrid photosensitive material for two-photon polymerization microfabrication. *ACS Nano*, 2008, Vol. 2, No. 11, p. 2257–2262.
18. SCHLIE, S., NGEZAHAYO, A., OVSIANIKOV, A., FABIAN, T., KOLB, H.A., HAFERKAMP, H., CHICHKOV, B.N. Three-dimensional cell growth on structures fabricated from Ormocer by two-photon polymerization technique. *J. Biomater. Appl.*, 2007, Vol. 22, No. 3, p. 275–287.
19. OVSIANIKOV, A., MALINAUSKAS, M., SCHLIE, S., CHICHKOV, B., GITTARD, S., NARAYAN, R., LOBLER, M., STERNBERG, K., SCHMITZ, K. P., HAVERICH, A. Three-dimensional laser micro- and nano-structuring of acrylated poly(ethylene glycol) materials and evaluation of their cytoxicity for tissue engineering applications. *Acta Biomater.*, 2011, Vol. 7, No. 3, p. 967–974.
20. MALINAUSKAS, M., PURLYS, V., RUTKAUSKAS, M., GADONAS, R. Two-photon polymerization for fabrication of three-dimensional micro- and nanostructures over a large

area. Proceedings Vol. 7204 of conference of Micromachining and Microfabrication Process Technology XIV. San Jose, CA, USA. 2009 February 13.

21. CHACHQUES, J.C., TRAININI, J.C., LAGO, N., CORTES-MORICHETTI, M., SCHUSSLER, O., CARPENTIER, A. Myocardial assistance by grafting a new bioartificial upgraded myocardium magnum trial: Clinical feasibility study. *Ann. Thorac. Surg.*, 2008, Vol. 85, No. 3, p. 901–908.
22. WENG, J., WANG. M. Producing chitin scaffolds with controlled pore size and interconnectivity for tissue engineering. *J. Mater. Sci. Lett.*, 2001, Vol. 20, No. 15, p. 1401–1403.
23. HOLLISTER, S. J., MADDOX, R. D., TABOAS, J. M. Optimal design and fabrication of scaffolds to mimic tissue properties and satisfy biological constraints. *Biomater.*, 2002, Vol. 235, No. 20, p. 4095–4103.
24. XIA, Y, WHITESIDES, G. M. Soft Lithography. *Annu. Rev. Mater. Sci.*, 1998, Vol. 28, p. 153–184.
25. PAN, Y.J., YANG, R.J. Fabrication of UV epoxy resin masters for the replication of PDMS-based microchips. *Biomed. Microdevices*, 2007, Vol. 9, No. 4, p. 555–563.
26. QU, S., CHEN, X., CHEN, D., YANG, P., CHEN, G. Poly (methyl methacrylate) CE microchips replicated from poly(dimethylsiloxane) templates for the determination of cations. *Electrophoresis*, 2006, Vol. 27, No. 24, p. 4910–4918.
27. CHOI, C.H., LEE, M.W., O,B. H., LEE, S.G., PARK, S G., LEE, E.H. Fabrication of micro-photonic devices using embossing technique. *Microelectron. Eng.*, 2006, Vol. 83, p. 1336–1338.

CYSENI 2011, May 26–27, Kaunas, Lithuania
ISSN 1822-7554, www.cyseni.com

# COMPARISON OF COPPER ZINC TIN SELENIDE FORMATION IN MOLTEN POTASSIUM IODIDE AND SODIUM IODIDE AS FLUX MATERIALS

**I. Leinemann, J. Raudoja, M. Grossberg, M. Altosaar, D. Meissner**
*Institute of Materials Science, Tallinn University of Technology,*
*Ehitajate tee 5, EE-19086 Tallinn, Estonia*
*Phone +3726203362*
*Email:* ingaklav@inbox.lv

**R. Traksmaa**
*Centre for Materials Research, Tallinn University of Technology,*
*Ehitajate tee 5, EE-19086 Tallinn, Estonia*
*Phone +3726203150*
*Email:* rainer@staff.ttu.ee

**T. Kaljuvee**
*Laboratory of Inorganic Materials, Tallinn University of Technology,*
*Ehitajate tee 5, EE-19086 Tallinn, Estonia*
*Phone +3726203362*
*Email:* tiidu@staff.ttu.ee

## ABSTRACT

The aim of the present study is to describe the formation of $Cu_2ZnSnSe_4$ in molten sodium iodide. The study deals with the possible chemical reactions associated between the binary precursor compounds CuSe, SnSe, ZnSe and NaI. Differential thermal analysis (DTA) runs were used to determine the thermal effects. The phase composition in mixtures of binary precursors and flux materials were studied by X-ray diffraction (XRD) and Raman spectroscopy. It is found that despite the fact that $Cu_2SnSe_3$ and $Cu_2ZnSnSe_4$ were detectable by Raman in the mixtures of precursors already at temperatures lower than $400^oC$ the extensive formation process of $Cu_2ZnSnSe_4$ starts close to the melting point of flux (KI or NaI). It is found that NaI can be used as a flux material for the synthesis of $Cu_2ZnSnSe_4$.

Keywords: $Cu_2ZnSnSe_4$, solution growth, XRD, Raman and DTA.

## 1. INTRODUCTION

A molten phase between the solid particles can act as a contracting or repelling agent depending on its amount. It is well known that the presence of a liquid phase in an amount that forms an adhesive attraction assists the growth of big crystallites and even the formation of continuous compact thin films. On the other hand, an isothermal recrystallization of semiconductor polycrystalline powders in the presence of a liquid phase of a suitable solvent material such as KI or NaI, called flux, in an amount sufficient for repelling the initial crystallites, leads to the formation and growth of semiconductor powder materials with single-crystalline grain structure and narrow-disperse granularity, so-called monograin powders. The driving force in this growth process is the differences in surface energies of crystals of different sizes. The growth of single-crystalline powder grains takes place at temperarures higher than the melting point of the used flux material – much lower than the melting point of the semiconductor compound [1]. The liquid phase of a solvent material is also usable for the synthesis of complicated multicomponent semiconductor compounds such as $Cu_2ZnSnS_4$ and $Cu_2ZnSnSe_4$ used as absorber materials in solar cells [2]. As a rule, the synthesis of $Cu_2ZnSnSe_4$ (CZTSe) monograin materials in molten fluxes results in homogeneous material [3]. Conventionally, the flux materials should have low melting temperatures and high solubilities in water, making the separation of powders from the flux easier. There are several suitable flux materials, such as KI, NaI and $CdI_2$, available for the synthesis and monograin growth or recrystallization of these $Cu_2ZnSnS_4$ and $Cu_2ZnSnSe_4$ absorber materials. In the previous papers [4, 5], we presented the results of studies of the formation of $Cu_2ZnSnSe_4$ in molten $CdI_2$ and KI. The present study deals with the possible chemical reactions between the binary precursor compounds – CuSe, SnSe, ZnSe – in molten NaI comparing them with the similar processes in KI. Differential thermal analysis (DTA) runs were used for determining the thermal effects. The phase compositions in mixtures of binary precursors and flux materials were determined by X-ray diffraction (XRD) and Raman spectroscopy. In this paper, we present the results of the $Cu_2ZnSnSe_4$ formation in NaI and compare them with findings obtained in the previous investigations using KI as flux. The aim is to find suitable preparation conditions for the synthesis of $Cu_2ZnSnSe_4$, starting from binary chalcogenides.

## 2. METHODOLOGY

The $Cu_2ZnSnSe_4$ powder materials were synthesized from CuSe, ZnSe and SnSe precursors in molten KI or NaI in sealed quartz vacuum ampoules. For determining the temperatures of phase changes and the interactions between the initial binaries and the flux material, DTA setups were used. According to the thermal effects found in DTA curves, the samples of mixtures (NaI+CuSe+ZnSe+SnSe and KI+CuSe+ZnSe+SnSe) were prepared. The samples were kept for prolonged periods at slightly higher temperatures than the thermal changes observed in the DTA curves, and then steeped in water. The mass ratio of the binary precursor compounds and the flux material was kept equal to 1:1. The precursors were mixed by grinding in a mortar and sealed into degassed quartz ampoules. As a reference for DTA, an identical empty quartz ampoule was used. The applied heating/cooling rate was 5ºC per minute.

Room temperature Raman spectra were recorded for phase analysis using a Horiba's LabRam HR high-resolution spectrometer equipped with a multichannel CCD detection system in the backscattering configuration. In micro Raman measurements, the incident laser light with a wavelength of 532 nm can be focused on a 1 μm diameter spot of the studied sample and the composition of the surface can be analysed. XRD measurements were performed using a Bruker D5005 diffractometer (Bragg-Brentano geometry) Cu Kα1 radiation with λ=1.5406 Å at 40 kV, 40 mA and graphite monochromator. For composition determination, the ICDD PDF-4 + 2009 database was used.

## 3. RESULTS AND DISCUSSIONS

### 3.1. Differential thermal analysis (DTA)

The DTA heating/cooling curves of a KI/CuSe/ZnSe/SnSe and a NaI/CuSe/ZnSe/SnSe mixtures are presented in Fig. 1 (parts a and b). As a reference, the DTA heating/cooling curves of a KI/empty ampoule and a NaI/empty ampoule are also presented (c and d parts of Fig. 1). The endothermic peak around 377ºC occurring in both heating curves (and corresponding exothermic peak at 410ºC in the cooling curve of NaI/CuSe/ZnSe/SnSe) was seen also in quasi-binary system of CuSe/KI [5]. Therefore, we attribute this peak to the peritectic temperature of 377ºC – phase transformation of CuSe to $Cu_{2-x}Se$+Se – as shown in the phase diagram of Cu-Se [6]. The peak at 522ºC in the cooling curve of

KI/ZnSe/CuSe/SnSe can correspond to the monotectic point of Cu-Se phase diagram ( 51.2 at.% Se by T. Gödecke et al.)) [7]. In the vicinity of the melting temperatures of pure KI (686ºC) and NaI (658ºC) [5], but at a slightly lower temperatures, endothermic effects at 676 and 652ºC (melting processes) can be seen followed by intense exothermic effects at 685 and 661ºC. In the same temperature region, the cooling curves of both systems studied show endothermic peaks (662 and 639ºC). The peaks of cooling curves at 649 and 626ºC are attributable to the solidification processes of the molten phases of KI and NaI with the other compounds dissolved in them.

It was established in [8] that $Cu_2ZnSnSe_4$ melts incongruently at 788ºC leaving ZnSe:Cu:Sn in the solid phase. Therefore, the peaks at 788ºC in the heating curve and at 777ºC in the cooling curve of KI/ZnSe/CuSe/SnSe can be attribeted to the melting/solidification of CZTSe and are in good agreenment with reference data [8]. Similar peaks in the heating/cooling curves of NaI/ZnSe/CuSe/SnSe – at 778ºC/770ºC respectively are slightly shifted in comparision with KI/ZnSe/CuSe/SnSe curves. This shift could be connected with the formation of a sodium containing quaternary compound similar to CZTSe ($Na_2SnSe_3$ as precursor for it was found in the XRD pattern of the NaI/ZnSe/CuSe/SnSe mixture heated at and quenched at 790ºC (see Fig. 3).

The peak at 604ºC in the cooling curve of NaI/ZnSe/CuSe/SnSe may belong to the melting point of CuI ($T_m$ = 606ºC) [9] found by XRD studies (see Fig. 3).

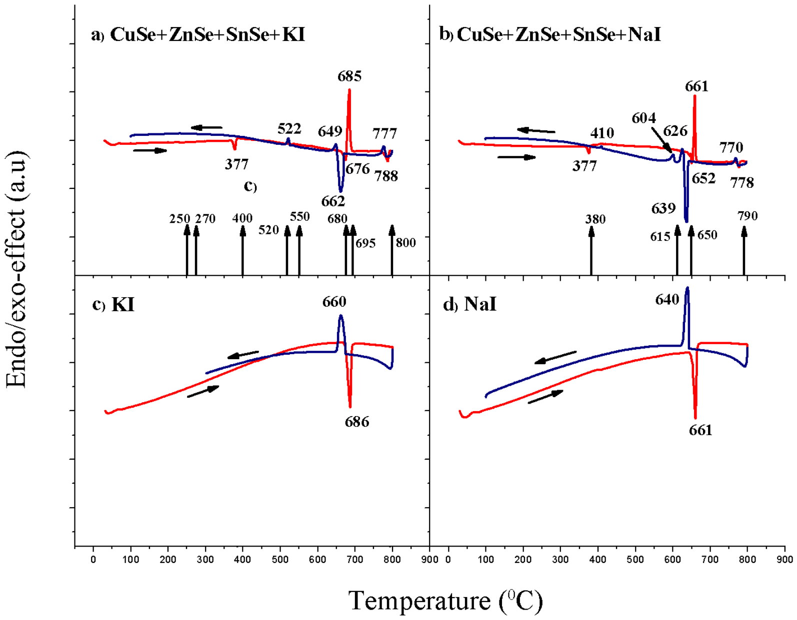

Fig. 1. DTA curves of KI, NaI and the mixtures for synthesis of quaternary CZTSe. Heating/cooling rate was 5ºC/min (heating corresponds to the red plot; cooling – blue). Using arrows on the x axes, the temperatures of prolonged heating of the samples for Raman and XRD analyses are marked

## 3.2. Raman analysis

In order to get the true average results for every sample, at least 5 Raman spectra were recorded. The experimental data are presented in Table 1. We also measured the Raman spectra of $NaI \cdot 2H_2O$ powder. Experimentally recorded Raman peaks of $NaI \cdot 2H_2O$ were found at 95, 107, 122, 160, 167, 189, 194 and 225 $cm^{-1}$. $NaI \cdot 2H_2O$ was detected in every

CuSe/ZnSe/SnSe/NaI sample since NaI is very hygroscopic and NaI·2H$_2$O is easily formed. KI peaks were detected at 90, 95, 102, 106 cm$^{-1}$.

From the experimental Raman data, it is observed that only the binary compounds CuI, ZnSe, CuSe, SnSe and SnSe$_2$ can be found in the mixtures heated at low temperatures (250-270ºC), see in Table 1. The formation of CuI indicates the chemical interaction of KI and NaI with CuSe. In Raman spectra of samples heated up to 380–400ºC, the most intensive Raman peak is characteristic to the ternary compound Cu$_2$SnSe$_3$ at 180 cm$^{-1}$ together with Raman peaks of CZTSe at 171 and 195 cm$^{-1}$ [3]. In NaI CZTSe can be formed already at 380ºC. The appearance of elemental Se indicates the decomposition of CuSe. CuI and elemental Se can be found by their characteristic peaks at 139 [11] and 240 cm$^{-1}$ [12], correspondingly. The samples quenched at 790ºC (slightly higher than the melting temperature of CZTSe) show again Raman spectra of different binary compounds. Besides the spectra of CZTSe with peaks at 195 and 171 cm$^{-1}$, there are spectra with intensive peaks at 178, 240, 251 and 262 cm$^{-1}$ belonging to Cu$_2$SnSe$_3$, Se, ZnSe and CuSe, respectively (see Fig. 2). It was found in [8] that Cu$_2$ZnSnSe$_4$ melts incongruently at 788ºC leaving ZnSe in the solid phase. Due to the non-equilibrium cooling of the mixture (quenching), the formation of CZTSe is incomplete in the cooling process and therefore the Raman spectra show the characteristic peaks of Cu$_2$SnSe$_3$, ZnSe, CuSe and Se. Overpressure of Se avoids the decomposition of CuSe [6].

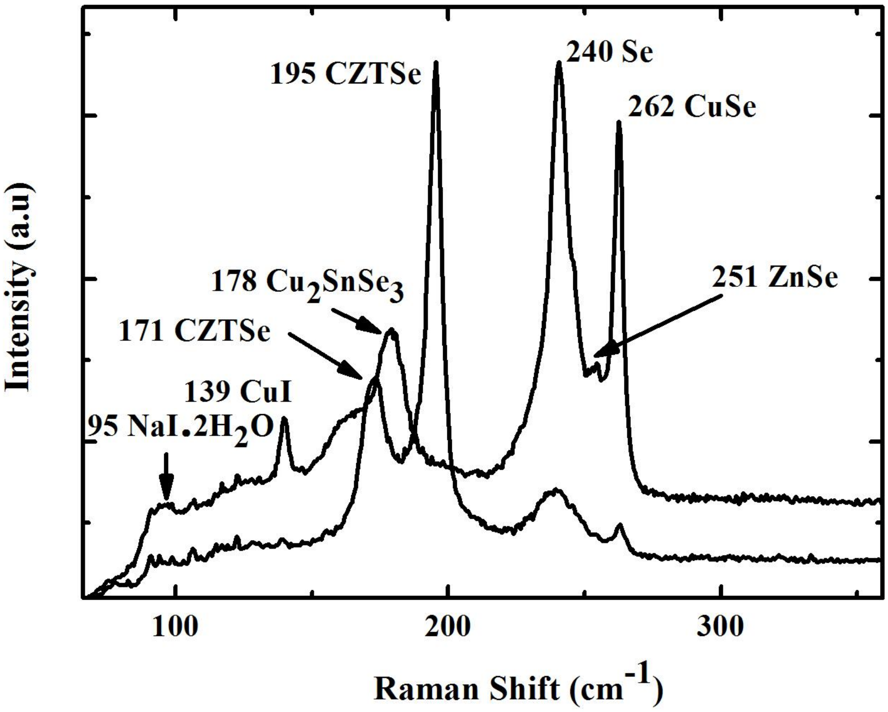

Fig. 2. Raman spectra taken from different places of the CuSe/ZnSe/SnSe/NaI sample quenched at 790ºC

Table 1. The phases detected by Raman analyses in the mixtures of CuSe/ZnSe/SnSe/KI and CuSe/ZnSe/SnSe/NaI annealed at different temperatures (selected annealing temperatures are based on the DTA results)

| CeSe/ZnSe/SnSe/KI | | | | CuSe/ZnSe/SnSe/NaI | | | |
|---|---|---|---|---|---|---|---|
| Annealing temp., ºC | Raman peaks, cm$^{-1}$ | Compon. | Reference | Annealing temp., ºC | Raman peaks, cm$^{-1}$ | Compon. | Reference |
| 250, 270 | 263 | CuSe | Experim. and [3] | 380 | 263 | CuSe | Experim. and [3] |
| | 187 | $SnSe_2$ | [10] | | 181 | $Cu_2SnSe_3$ | [3] |
| | 139 | CuI | [11] | | 139 | CuI | [11] |
| | 204, 252 | ZnSe | Experim. and [3, 14] | | 254 | ZnSe | Experim. and [3, 14] |
| | | | | | 240 | Elemental Se | [12] |
| | | | | | 81, 170, 191, 231 | CZTSe | [3] |
| 400 | 263 | CuSe | Experim. and [3] | 615 | | | |
| | 180 | $Cu_2SnSe_3$ | [3] | | 186 | $SnSe_2$ | [10, 13] |
| | 171, 195, 234 | CZTSe | [3] | | 171, 194, 236 | CZTSe | [3] |
| | 205, 251 | ZnSe | Experim. and [3, 14] | | 251 | ZnSe | Experim. and [3, 14] |
| 520 | 205, 250 | ZnSe | Experim. and [3, 14] | 650 | 249 | ZnSe | Experim. and [3, 14] |
| | 171, 195, 220, 234 | CZTSe | [3] | | 171, 194, 232 | CZTSe | [3] |
| 680 | 107, 127, 149 | SnSe | [10] | 790 | 139 | CuI | [11] |
| | 187 | $SnSe_2$ | [9, 13] | | 178 | $Cu_2SnSe_3$ | [3] |
| | 81, 171, 195, 233 | CZTSe | Experim. and [3] | | 171, 195 | CZTSe | [3] |
| | 250 | ZnSe | Experim. and [3, 14] | | 240 | Elemental Se | [12] |
| | | | | | 251 | ZnSe | Experim. and [3, 14] |
| | | | | | 262 | CuSe | Experim. and [3] |

### 3.3. XRD analysis

*CuSe/ZnSe/SnSe/KI*: XRD phase analysis data are presented in Fig. 3. All the samples also contain crystalline KI, not shown in Fig. 3. From the XRD data, the route of the CZTSe formation can be drawn. In some samples heated at 250ºC, $Cu_{1.85}Se$ was found. $SnSe_2$ was detected in samples heated at 400ºC. Se, released from CuSe, reacts with SnSe forming $SnSe_2$. Reaction of $Cu_2Se$ with $SnSe_2$ results in the formation of $Cu_2SnSe_3$, as it was already proposed by F. Hergert and R. Hock [15]. $Cu_2SnSe_3$ was found in samples heated at 520ºC. At 680ºC (a little below the melting point of KI), $Cu_2ZnSnSe_4$ is formed from $Cu_2SnSe_3$ and ZnSe. This provides some evidence that the formation of the liquid phase of the flux material is the main mediator for the synthesis of CZTSe. Micro XRD measurements done from individual grains of the sample quenched at 790ºC gave the information that in the molten phase CZTSe decomposes to $Cu_2SnSe_3$ and to $Cu_2Se$, $SnSe_2$ and ZnSe binary phases.

*CuSe/ZnSe/SnSe/NaI:* The XRD results confirm the formation of $Cu_2ZnSnSe_4$ in NaI already at 380ºC. The formation of CZTSe starts also with the release of Se from CuSe and through the formation of $SnSe_2$, as it was the case in the KI flux. No $Cu_2SnSe_3$ was found by XRD. Se-rich phase $Cu_{0.87}Se$ coexists with the $Cu_{1.82}Se$ at very low temperatures of synthesis, giving information that CuSe precursor has not been homogeneous single phase material and more attention has to be payed to the phase composition of precursors got from different producers. All samples also contain CuI. The particularity of using NaI flux is the formation of different phases containing Na and oxygen ($Na_2SnSe_3$, $Na_2Cu(OH)_4$, $Na_2SeO_4$), as found by XRD in all samples investigated. All sodium containing compounds are well soluble in water and can be separated, except CuI, because CuI is poorly soluble in water (0.00042 g/L at 25ºC), but it dissolves in the presence of NaI or KI to give the linear anion $[CuI_2]^-$. Dilution of such solutions with water re-precipitates CuI [16]. The by-products such as $NaI·2H_2O$, $Na_2SeO_4$, $Na_2Cu(OH)_4$, CuI and $Na_2SnSe_3$ can be separated from CZTSe absorber by washing it with distilled water. The hydroscopic nature of NaI makes the syntheses process complicated and requires the preparation of samples in a glove box, because the formation of $NaI·2H_2O$ as a result of the NaI hydrolysis process is detected.

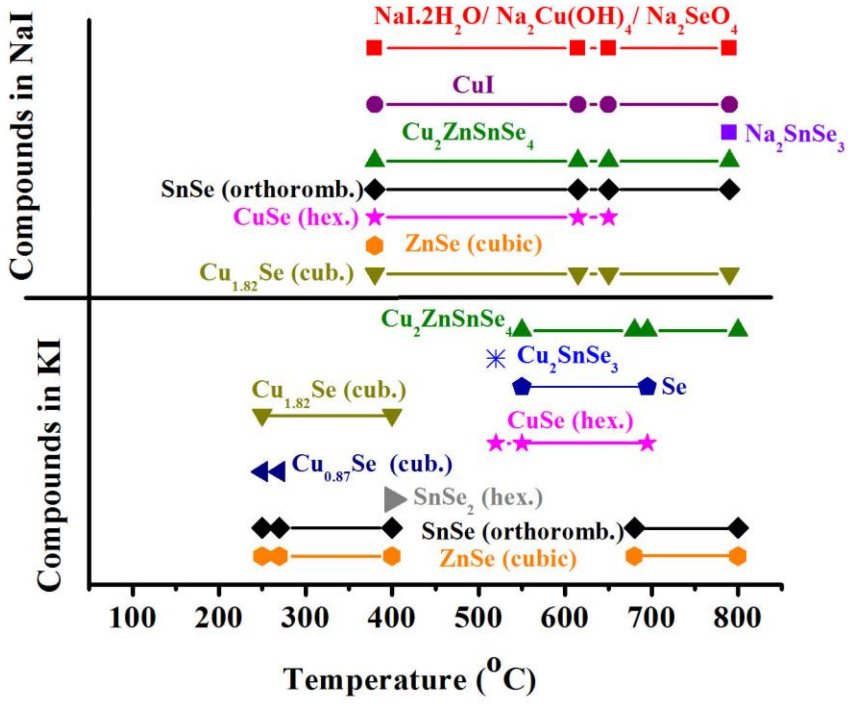

Fig. 3. The formed phases in CuSe/ZnSe/ SnSe/KI (lower part) and CuSe/ZnSe/SnSe/NaI (upper part) mixtures annealed at different temperatures and detected by XRD

On the basis of the Raman and the XRD results obtained from the mixtures CuSe/ZnSe/SnSe/NaI and CuSe/ZnSe/SnSe/KI, it can be derived that Se, released in the decomposition of CuSe to $Cu_{1.8}Se$, reacts with SnSe forming $SnSe_2$. However, CuSe does not completely decomposes due to the formation of Se overpressure in closed ampoules as CuSe was detected by Raman and XRD measurements in all samples. The formation of CZTSe in KI involves intermediate reaction steps where the formation of $Cu_2Se$, $SnSe_2$ and the ternary compound $Cu_2SnSe_3$ from the formers can be derived. Raman measurements show that $Cu_2SnSe_3$ and CZTSe already form at temperatures lower than 400ºC. However, they are not yet detectable in XRD measurements due to the lower sensibility of XRD. At lower temperatures, CZTSe formation is more intensive in NaI. Most likely, some sodium containing compound is involved in the chemical route. The extensive formation process of CZTSe starts close to the melting point of flux (KI or NaI). Comparison of the DTA curves reveals that melting of the mixtures starts even at lower temperatures than the melting of pure KI or NaI. The occurrence of an intensive exothermic peak right after an endothermic peak due to the melting process suggests a strong chemical interaction between the precursors.

## 3. CONCLUSIONS

By DTA, XRD and Raman spectroscopy data, it can be concluded that in the presence of solid KI or NaI, the formation of CZTSe is inhibited. The chemical interactions are induced by the formation of the liquid phase in the mixture of materials for the synthesis of the quaternary compound. The melting and extensive formation process of CZTSe starts close to the melting point of flux (KI or NaI). NaI as flux material is preferable, due to the possibility to reduce the synthesis temperature. The hygroscopic nature of NaI requires the preparation of samples in a glove box.

The phase in-homogeneity of the used precursors was revealed and has to be carefully studied.

## ACKNOWLEDGEMENTS

This research was supported by the Doctoral Studies and Internationalization Program DoRa of the European Social Funds, the Estonian Ministry of Education and Research Contract No. SF0140099s08, and the EAS project EU29713.

## REFERENCES

1. MELLIKOV, E., HIIE, J., ALTOSAAR, M. Powder materials and technologies for solar cells. *International Journal of Materials & Product Technology*, 2007, Vol. 28, No. 3, 4, p. 291–311.
2. CHOPRA, K., PAULSON, P., DUTTA, V. Thin film solar cells: an owerview. *Progress in Photovoltaics*, 2004, Vol. 12, p. 69–92.
3. ALTOSAAR, M., RAUDOJA, J., TIMMO, K., DANILSON, M., GROSSBERG, M., KRUSTOK, J., MELLIKOV, E. $Cu_2Zn_{1-x}Cd_xSn(Se_{1-y}S_y)_4$ solid solutions as absorber materials for solar cells. *Physica Status Solids*, 2008, Vol. 205, No. 1, p. 167–170.
4. KLAVINA, I. CZTS ($Cu_2ZnSnSe_4$) crystal growth and use in monograin membrane solar cells. CYSENI 2010. Proceeding of annual conference of young scientists on energy issues. [CD]. Kaunas: Lithuanian Energy Institute. 2010 May 27–28.
5. KLAVINA, I., KALJUVEE, T., TIMMO, K., RAUDOJA, J., TRAKSMAA, R., ALTOSAAR, M., MEISSNER, D. Study of $Cu_2ZnSnSe_4$ monograin formation in molten KI starting from binary chalcogenides. *Thin Solid Films*, 2011, doi: 10.1016/j.tsf.2011.01.365.
6. GLAZOV, V., PASHINKIN, A., FEDOROV, V. Phase Equilibria in the Cu-Se system. *Inorganic Materials*, 2000, Vol. 36, No. 7, p. 641–652.
7. GÖDECKE, T., METALLKD, Z. *Phase equilibria of Cu-In-Se II.* 2000, p. 637.

8. DUDCHAK, I., PISKACH, L. Phase equilibria in the $Cu_2SnSe_3$-$SnSe_2$-ZnSe system. *Journal of Alloys and Compounds*, 2003, Vol. 351, p. 145–150.
9. NÖLTING, J., WIEGERT, F., PUSCHMANN, E. The Phase-Diagram CuI — $HgI_2$. *Berichte der Bunsengesellschaft für physikalische Chemie*, Vol. 93, No. 11, p. 1335–1339.
10. BOSCHER, N., CARMALT, J., PALGRAVE, R., PARKIN, I. Atmospheric pressure chemical vapour deposition of SnSe and $SnSe_2$ thin films on glass. *Thin Solid Films*, 2008, Vol. 516, No. 15, p. 4750–4757.
11. SERRANO, J., CARDONA, M., RITTER, T., WEINSYEIN, B., RUBIO, A., LIN, C. Pressure and Temperature Dependence of the Raman Phonons in Isotopic $\gamma$-CuI. *Physical Review*, 2002, Vol. 66, No. B, p. 245202-245214.
12. RAMDANI, O., GUILLEMOLES, J. One-step electrodeposited $CuInSe_2$ thin films studied by Raman spectroscopy. *Thin solid films*, 2007, Vol. 515, p. 5909–5912.
13. SMITH, A., MEEK, P., LIANG, W. Occurrence of polytypism in $SnSe_2$. *Solid State Physics*, 1977, Vol. 55, No. 2, p. 395–397.
14. VENKATACHALAMA, S., YOSHINORI, K., MANGALAJARB, D., NARAYANDASSB, S. Effect of boron ion implantation on the structural, optical and electrical properties of ZnSe thin films. *Physica*, 2007, Vol. 390, No. B, p. 71–78.
15. HERGERT, F., HOCK, R. Predicted formation reactions for the solid-state sytheses of the semiconductor materials $Cu_2SnX_3$ and $Cu_2ZnSnX_4$ (X = S, Se) starting from binary chalcogenides. *Thin Solid Films*, 2007, Vol. 515, No. 15, p. 5953–5956.
16. KAUFFMAN, B., FANG, Y. Purification of Copper (I) Iodide. *Inorganic Syntheses*, 1983, Vol. 22, p. 101–103.

CYSENI 2011, May 26–27, Kaunas, Lithuania
ISSN 1822-7554, www.cyseni.com

# CHANGES OF STOICHIOMETRIC AND NON-STOICHIOMETRIC NANOPOWDERS OF LITHIUM ORTHOSILICATE UNDER THERMAL TREATMENT AND ACTION OF MOISTURE

**A. Zarins, G. Kizane, L. Avotina, A. Supe**
*Laboratory of Radiation Chemistry of Solids*
*Institute of Chemical Physics*
*University of Latvia*
*Kronvalda blvd. 4, Riga, LV-1586, Latvia*

**A. Berzins**
*Department of Chemistry*
*University of Latvia*
*Kr. Valdemara street 48, Riga, LV-1013, Latvia*

**I. Steins**
*Laboratory of Plasma Processes*
*Institute of Inorganic Chemistry*
*Riga Tehnical university*
*Miera street 34, Salaspils, LV-2169, Latvia*

ABSTRACT

Nanopowders of $Li_4SiO_4$ are very perspective materials as well sorbent of $CO_2$ as well as fusion reactors tritium breeding material. During the research changes of composition of stoichiometric and non-stoichiometric nanopowders of lithium orthosilicate under heat treatment and action of moisture on the ground of thermal gravimetric and X-ray diffraction analysis are determined. Nanopowders of $Li_4SiO_4$, synthesized by plasma technology and protractedly holded at room temperature with moisture 10–12%, contain 7% of $H_2O$ and $CO_2$. Reflexes of $Li_4SiO_4$, $LiOH\cdot H_2O$, $Li_2SiO_3$ and $Li_2CO_3$ are observed in X-ray diffractogramms of the stoichiometric and non-stoichiometric nanopowders.
Thermaly treating nanopowders, concentration of $CO_2$ and $H_2O$ decreases up to 1%. Only reflexes of $Li_4SiO_4$ and $Li_2SiO_3$ are observed in the X-ray diffractogramms. Curves of the thermal gravimetric analyses show that in air atmosphere $H_2O$ of nanopowders desorbs at intervals of 30–90°C and 250-300°C temperature. At the temperature 90-300°C nanopowders absorb extra $CO_2$ that desorbs at temperature 450–600°C. Changes of structure of nanopowders are investigated after 258 h action of 10.5 and 77.6% of moisture at room temperature. At 10.5% of moisture stoichiometric nanopowders adsorb 15% and non-stoichiometric – 11% of $CO_2$ and $H_2O$ both together. While at 77.6% moisture stoichiometric nanopowders absorb 32% and non-stoichiometric 28% of $H_2O$ and $CO_2$, respectively. By increasing of moisture increases concentration of $Li_2SiO_3$, $LiOH\cdot H_2O$ and $Li_2CO_3$, concentration of $Li_4SiO_4$ reduces.

Keywords: Stoichiometric and non-stoichiometric nanopowders of lithium orthosilicate, thermal treatment, moisture.

## 1. INTRODUCTION

Nowadays global warming is a large problem and it is very important to solve it as soon as possible. One of the main causes of the global warming is increase of the emision of carbon dioxide ($CO_2$) that produces as by-product in power plants that generates electricity and in factories. Therefore it is very important to separate and accumulate carbon dioxide from factories and power plants produced gases in solid state for example carbonates [1]. For this purpose most perspective are high temperature sorbents lithium zirconate ($Li_2ZrO_3$) and lithium orthosilicate ($Li_4SiO_4$) [2].

Lithium orthosilicate as one of the most promising carbon dioxide sorbents makes a relatively high and fast absorption (up to 36.7%), high thermal resistance (melting temperature is 1255°C) and selective high temperature reaction with $CO_2$. Chemisorption reaction of carbon dioxide is reversible at temperature higher than 450°C and that makes lithium orthosilicate recoverable [3].

$$Li_4SiO_{4\,(s)} + CO_{2\,(g)} \leftrightarrow Li_2SiO_{3\,(s)} + Li_2CO_{3\,(s)} \qquad (1)$$

Several researchers have reported that wet environment can affect the carbon dioxide sorption process and composition of lithium orthosilicate. Under dry conditions in room and high temperatures on layer of lithium orthosilicate particles due to carbon dioxide chemisorption process a thin layer of lithium carbonate forms and chemisorption process is hindered. But if atmosphere is with humidity – layer of lithium carbonate is dissouluted and promote $CO_2$ capture again. By-product of reactions speedes up chemisorption of carbon dioxide [4].

Other problem for carbon dioxide sorbents is to obtain maximal absorption which is close to theoretical value (36.7%). Some researchers offer that ceramics of $Li_4SiO_4$, for example pebbles, capacity of sorption probably can be improved by production of pebbles from nanopowders with high specific area and small particle diameter [5]. While the mechanical stability of the ceramics can be improved by adding a small amounts (~2%) of fine $SiO_2$.

Stoichiometric and non-stoichiometric nanopowders of lithium orthosilicate can be synthesised in high temperature plasma stage. This type of nanopowders have very high specific area and they are more reactive than powders with higher particle size [6]. It is very important to study changes of composition of nanopowders of lithium orthosilicate under action of several factors – moisture, carbon dioxide, thermal tratment etc.

Aim of the reseach was to determine changes of composition of the stoichiomeric and non-stoichiometric nanopowders of lithium orthosilicate depending on heat treatment and air humidity on ground of thermal gravimetric, differencial thermal and X-ray diffraction analysis.

## 2. SYNTHESIS AND RESEARCH METHODS OF NANOPOWDERS OF LITHIUM ORTHOSILICATE

Stoichiometric nanopowders of lithium orthosilicate with particle size 100±10 nm and specific area 24 $m^2 \cdot g^{-1}$ were synthesized in high temperature plasma of nitrogen. In plasma stream of nitrogen were injected composition of fine lithium carbonate and silica in stoichiometric - 2:1, rations. Resulting product was extra oxidized with oxygen. Synthesized nanopowder additionaly was thermaly treated at temperature 620°C for 4 hours in air atmosphere [6]. Summar reaction of synthesis was:

$$2Li_2CO_3 + Si + O_2 \rightarrow Li_4SiO_4 + 2CO_2 \qquad (2)$$

Non-stoichiometric nanopowders with size 100±10 nm and specific area 24 $m^2 \cdot g^{-1}$ were made from stoichiometric nanopowders – adding 2% of fine $SiO_2$.

After synthesis stoichiomettric and non-stoichiometric nanopowders of lithium orthosilicate were placed in atmosphere with reduced (~12%) moisture for long time and then thermaly treated for 2 hours, temperature 600°C in air atmosphere. 1–1.5 g of thermal treated samples of each nanopowder were placed in atmosphere with reduced (10.5±0.5%) and elevated (77.5±0.5%) humidity in isothermal (19.5±0.5°C) conditions for 256 hours (10.75 days).

Before and after each step of research – sythesis, action of air, thermal tratment and action reduced and elevated moisture, nanopowders of lithium orthosilicate were investigated by thermogravimetric (TG), differential thermal analysis (DTA) and powder X-ray diffractometry (XRD). TG and DTA were made on derivatograph EXSTAR 6000 TG/DTA 6300 with heat rate $2^{o}C \cdot min^{-1}$ up to temperature $600^{o}C$ in air atmosphere. XRD of nanopowders were measured on a Bruker D8 Advanced XRD spectrometer (source: CuKα, $\lambda$=0.15418 nm) in 2theta interval $10–60^{o}$.

## 3. RESULTS AND DISCUSION

### 3.1. Chemical properties of nanopowders of lithium orthosilicate under action of air moisture

In high temperature plasma synthesized stoichiometric and non-stoichiometric nanopowders of lithium orthosilicate main phase is lithium orthosilicate ($Li_4SiO_4$), but minor phase is lithium metasilicate ($Li_2SiO_3$). In X-ray diffractogramms of synthesised nanopowders (Fig. 1.) main phase – $Li_4SiO_4$ marked with ○, but minor phase – $Li_2SiO_3$ with □.

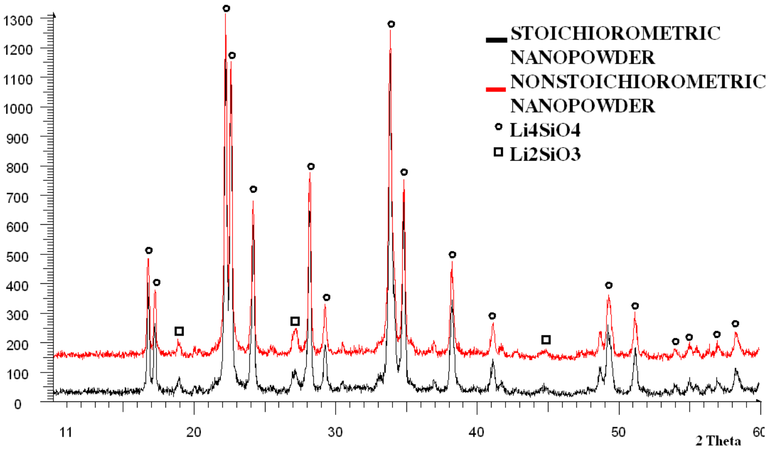

Fig. 1. XRD of synthesized stoichiometric and nonstoichiometric nanopowders of lithium orthosilicate

Formation of lithium metasilicate in “stoichiometric” nanopowder could be explaned by producing of lithium metasilicate as by-product of plasma stage synthesis:

$$Li_2CO_{3\,(s)} + Si_{(s)} + O_{2(g)} \rightarrow Li_2SiO_{3(s)} + CO_{2(g)}. \qquad (3)$$

Low concentration of lithium metasilicate in nanopowders after synthesis can be explaned with thermal treatment of nanopowders. In “stoichiometric” nanopowders at temperature $620^{o}C$ lithium carbonate reacts with lithium metasilicate forming lithium orthosilicate and carbon dioxide [1]:

$$Li_2CO_{3(s)} + Li_2SiO_{3(s)} \rightarrow L_4SiO_{4(s)} + CO_{2(g)}. \qquad (4)$$

In action with atmosphere air and humidity nanopowders of lithium orthosilicate relatively rapidly react with the gases of air – water and carbon dioxide, forming lithium metasilicate ($Li_2SiO_3$) [2], lithium hydroxide hydrate ($LiOH \cdot H_2O$) [4], lithium carbonate ($Li_2CO_3$) [2] and silanol group (≡Si-O-H) [4]. In stoichiometric and non-stoichiometric nanopowders these compounds were detected with X-ray diffraction, except silanol groups.

At X-ray diffractogramm of nanopowders after action of moisture (Fig. 2.) phase of lithium orthosilicate marked with ○, lithium metasilicate with □, lithium carbonate – ■ and lithium hydroxide monohydrate – ●.

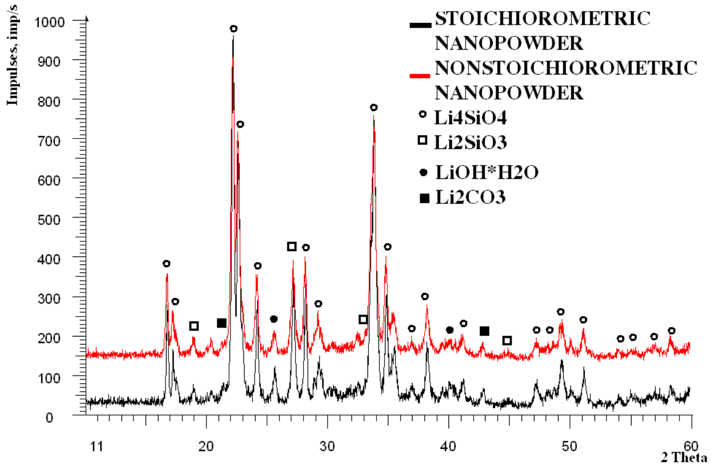

Fig. 2. XRD of nanopowders of lithium orthosilicate after action of 10–12% moisture at room temperature

In air atmosphere in first order on surface of particle of nanopowders water molecules physicaly adsorb. Then absorbed water slowly chemisorbs in volume of particle of nanopowder forming lithium hydroxide and silanol group [4].

$$\equiv\text{Si-O-Li}_{(s)} + \text{H}_2\text{O}_{(g)} \rightarrow \text{LiOH}_{(s)} + \equiv\text{Si-O-H}_{(s).} \qquad (5)$$

Majority of hygroscopic lithium hydroxide forms on surface of particle of nanopowders. Lithium hydroxide reacts with water of atmosphere forming lithium hydroxide monohydrate. $LiOH\cdot H_2O$ is thermaly stable compound and dissociates at temperature above $500^{o}$C.

$$\text{LiOH}_{(s)} + \text{H}_2\text{O}_{(g)} \rightarrow \text{LiOH}\cdot\text{H}_2\text{O}_{(s)}. \qquad (6)$$

Instead of water, molecules of carbon dioxide react with lithium orthosilicate and lithium hydroxide. In reaction with lithium orthosilicate carbon dioxide forms lithium carbonate and lithium metasilicate [2].

$$\text{Li}_4\text{SiO}_{4(s)} + \text{CO}_{2(g)} \rightarrow \text{Li}_2\text{SiO}_{3(s)} + \text{Li}_2\text{CO}_{3(s)}. \qquad (7)$$

Lithium hydroxide that was formed on nanopowders particle layer, increases the rate of reaction between lithium hydroxide and carbon dioxide. The products of chemisorbtion are lithium carbonate and water [4].

$$2\text{LiOH}_{(s)} + \text{CO}_{2(g)} \rightarrow \text{Li}_2\text{CO}_{3(s)} + \text{H}_2\text{O}_{(vol)}. \qquad (8)$$

Carbon dioxide absorption reactions product – water, after reaction diffuses into volume of paricle. It reacts with lithium orthosilicate forming lithium hydroxide and silanol group.

$$\equiv\text{Si-O-Li}_{(s)} + \text{H}_2\text{O}_{(vol)} \rightarrow \text{LiOH}_{(s)} + \equiv\text{Si-O-H}_{(s).} \qquad (9)$$

During thermal treatment of stoichiometric and non-stoichiometric nanopowders of lithium orthosilicate, which were exposed to air atmosphere up to temperature $600^{o}$C for 2 hours, rapid $CO_2$ and $H_2O$ desorbtion and rapid mass reducement in samples of nanopowders is observed.

After thermal treatment of stoichiometric and non-stoichiometric nanopowders of lithium orthosilicate in powder X-ray diffractogramms only characteristic reflexes of main phase – $Li_4SiO_4$ and little reflexes of minor phase – $Li_2SiO_3$ are observed. X-ray diffractogramms of thermaly treated stoichiometric and nonstoichiometric nanopowder of lithium orthosilicate coresponds to XRD of bouth synthesised nanopowders (Fig. 1.).

### 3.2. Impact of thermal treatment on nanopowders of lithium ortosilicate composition

Thermal treating of synthesized stoichiometric and non-stoichiometric nanopowders of lithium orthosilicate up to temperature 620°C with heat rate $2^{o}C\cdot min^{-1}$ in air atmosphere generates mass exchanging processes with several stages. In first of two stages mass raises, but during four next stages the reduction of mass of samples is observed (Fig. 3.).

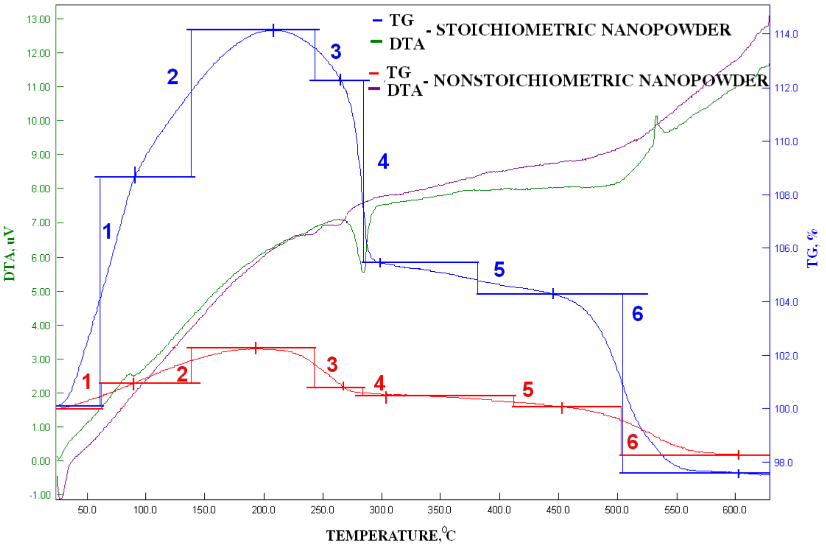

Fig. 3. TG and DTA of synthesized stoichiometric and non-stoichiometric nanopowders of lithium orthosilicate

In the 1st stage at temperature 30–90°C from the air on surface of nanopowders adsorbs water and then it chemisorbs in nanopowders reacting with lithium orthosilicate forming lithium hydroxide and silanol group.

$$\equiv Si\text{-}O\text{-}Li_{(s)} + H_2O_{(g)} \rightarrow LiOH_{(s)} + \equiv Si\text{-}O\text{-}H_{(s)}. \quad (10)$$

At the 2nd stage nanopowders at temperature 90–200°C carbon dioxide chemisorbs in nanopowders forming lithium carbonate and lithium metasilicate.

$$Li_4SiO_{4(s)} + CO_{2(g)} \rightarrow Li_2CO_{3(s)} + Li_2SiO_{3(s)}. \quad (11)$$

Carbon dioxide chemisorbtion is speeded up with reaction with layer of lithium hydroxide on particle surface. In same time at 2nd stage in lithium hydroxide reaction with carbon dioxide formed water diffuse in nanopowders particle volume and reacts with lithium orthosilicate forming lithium hydroxide and silanol group.

$$2LiOH_{(s)} + CO_{2(g)} \rightarrow Li_2CO_{3(s)} + H_2O_{(vol)}. \quad (12)$$

$$\equiv Si\text{-}O\text{-}Li_{(s)} + H_2O_{(vol)} \rightarrow LiOH_{(s)} + \equiv Si\text{-}O\text{-}H_{(s)} \quad (13)$$

Continuing thermal treatment at the 3rd and the 4th stage at temperature 200–300°C water rapidly desorbs from nanopowders, but at the 6th stage at temperature 450–600°C carbon dioxide rapidly desorbs from nanopowders.

$$LiOH_{(s)} + \equiv Si\text{-}O\text{-}H_{(s)} \rightarrow \equiv Si\text{-}O\text{-}Li_{(s)} + H_2O_{(g)}. \quad (14)$$

$$Li_2CO_{3(s)} + Li_2SiO_{3\,(s)} \rightarrow Li_4SiO_{4\,(s)} + CO_{2(g)}. \quad (15)$$

In nanopowders after heat treatment main phase is $Li_4SiO_4$, but minor phase - impurities of $Li_2SiO_3$. X-ray diffractogramms of thermaly treated stoichiometric and non-stoichiometric nanopowders of lithium orthosilicate match to XRD of synthesised soichiometric and non-stoichiometric nanopowders (Fig. 1.).

Particular should be highlighted that the stoichiometric nanopowders of lithium orthosilicate faster and much more (up to 14% of prime weigt of sample) sorb water and carbon dioxide than non-stoichiometric nanopowders at elevated temperatures. It could be explained with that in non-stoichiometric nanopowders of lithium orthosilicate at synthesis stage by adding 2% of fine silicon dioxide forms layer of it.

Silicon dioxide layer on surface of particle disturbs water chemisorbtion reactions with lithium orthosilicate. At same time the concentration of water chemosrbtion reactions product – lithium hydroxide, is very low and this affects carbon dioxide chemisorbtion. That could be the reason why weigt of bouth chemisorbed gases (water and carbon dioxide) in non-stoichiometric nanopowders of lithium orthosilicate, compearing with stoichiometric nanopowders, decreases.

### 3.3. Impact of moisture on nanopowders of lithium orthosilicate composition

Thermaly treated (600°C for 2 hours) stoichiometric and non-stoichiometric nanopowders of lithium orthosilicate in atmosphere with a reduced (10.5%) and elevated (77.6%) humidity in isothermal conditions 19$^{o}$C up to 10.75 days gradually sorb airborne atmospheric gases – $H_2O$ and $CO_2$. From previsory results folows that absorbed gases in nanopowders of lithium orthosilicate accumulates, forming lithium hydroxide monohydrate, lithium metasilicate, silanol groups and lithium carbonate.

In atmosphere with low humidity (10.5%) stoichiometric nanopowders sorb 10% of $H_2O$ and 5% of $CO_2$ of samples prime weigt. But non-stoichiometric nanopowders sorbs 7% of $H_2O$ and 4% of $CO_2$. These results confirms that reaction rate of stoichiometric nanopowders is higher than for non-stoichiometric nanopowders. And water reaction rate with lithium orthosilicate in room temperature is much more higher than carbon dioxide reaction rate.

Raising temperature from 25 to 150$^{o}$C, in nanopowders, who were exposed to atmosphere with reduced humidity, on surface selectively chemisorbs $CO_2$. It can be explained with that nanopowders particle surface consists of majority of LiOH. As well that indicates that the maximum amount of absorbed gas has not yet been reached in nanopowders.

By contrast, in atmosphere with 77.6% of moisture, stoichiometric nanopowders sorb 16% of $H_2O$ and 16% of $CO_2$. But non-stoichiometric nanopowders sorb 13% of $H_2O$ and 15% of $CO_2$. These results indicates that air humidity affects and accelerate carbon dioxide chemisorbtion reaction. Raising the temperature to 90$^{o}$C, the surface absorbed $H_2O$ desorbs, this indicates that the nanopowders have absorbed close to the maximum quantity of gas – 36.7%.

Results of stoichiometric and non-stoichiometric nanopowders of $Li_4SiO_4$ could be explained with layer of $SiO_2$ on particles of non-stoichiometric nanopowder. Silicon dioxide layer on nanopowders particles forms at synthesis stage – when to stoichiometric nanopowders of lithium orthosilicate adds fine $SiO_2$. It disturbs water chemisorbtion reaction with lithium orthosilicate and so at same time carbon dioxide chemisrobtion. In general it could be the main reason why non-stoichiometric nanopowders of lithium orthosilicate are more stable at action of moisture than stoichiometric nanopowders.

## 4. CONCLUSIONS

Stoichiometric and non-stoichiometric nanopowders of $Li_4SiO_4$ with particle size 100±10 nm and a specific area of 24 $m^2 \cdot g^{-1}$ synthesized by using high temperature plasma of nitrogen in temperature range 150-250°C selectively react with carbon dioxide, forming lithium carbonate and lithium metasilicate. Reaction is reversible at 450–650°C temperature.

Stoichiometric nanopowder of lithium orthosilicate can sorb up to 32% of air atmosphere gases – water and carbon dioxide. Stoichiometric nanopowders of lithium orthosilicate are much more attractive material for production of multiple-recyclable high temperature carbon dioxide sorbents than non-stoihiometric nanopowders.

## 5. REFERENCES

1. TOGASHI, N., OKOMURA, T., OH-ISHI, K. Synthesis and $CO_2$ absorption property of $Li_4TiO_4$ as a novel $CO_2$ absorbent, *Journal of the Ceramic Society of Japan*, 2007, Vol. 115, No. 5, p. 324–328.
2. YAMAGUCHI, T., NITSUMA, T., NAIR, B.N., NAKAGAWA, K. Lithium silicate based membranes for high temperature $CO_2$ separation. *Journal of Membrane Science*, Vol. 294, No.1–2, p. 16–21.
3. KATO, M., NAKAGAVA, K., ESSAKI, K., etc. Novel $CO_2$ absorbents using lithium-containing oxide. *International Journal of Applied Ceramic Technology*, 2005, Vol. 2, No. 6, p. 467–475.
4. ORTIZ-LANDEROS, J., MARTINEZ-DLCRUZ, L., Gomez-YANEZ, C., PFEIFFER, H. Towards understanding the thermoanalysis of water sorption on lithium orthosilicate ($Li_4SiO_4$). *Thermochimica Acta*, 2011, Vol. 515, No. 1–2, p. 73–78.
5. ORLOV, A., HEIDEMANE, G., GRABIS, J., JANKOVICA, D. Synthesis of lithium silicate powders by plasma chemical method. *Latvian Journal of Physics and Technical Sciences*, 2006, Vol. 1., p. 44–50.
6. NAIR, B. N., BURWOOD, R.P., GOH, V. J., etc. Lithium based ceramic materials and membranes for high temperature $CO_2$ separation. *Progress in Material science*, 2009, Vol. 54, p. 511–541.

CYSENI 2011, May 26–27, Kaunas, Lithuania
ISSN 1822-7554, www.cyseni.com

# FEMTOSECOND LASER DIRECT WRITING OF MICROOPTICAL AND PHOTONIC MICROSTRUCTURES OF NOVEL HYBRID PHOTOPOLYMERS

**A. Žukauskas, M. Rutkauskas and M. Malinauskas**
*Laser Research Center, Department of Quantum Electronics, Physics Faculty*
*Vilnius University*
*Saulėtėkio Ave. 9, LT-10222 Vilnius, Lithuania*
*Phone +370 678 40432*
*Email: albertaszukauskas@ff.stud.vu.lt*

## ABSTRACT

In this report we present results of micro- and nanostructuring of novel hybrid sol-gel materials containing metal isopropoxides-silica by the femtosecond direct laser writing technique, and apply it for the fabrication of various microoptical/nanophotonic components. This approach enabled us to photostructure the true three-dimensional objects with controlled sub-100 nm spatial definition. Due to self-smoothing effects, surface roughness below 30 nm was achieved making this technique promising for the fabrication of microoptical/nanophotonics devices for visible and near infra-red wavelengths. We successfully produced microoptical components such as aspheric and Fresnel lenses. Furthermore, we demonstrated the flexibility and reproducibility of direct laser writing to fabricate custom shaped elements on a tip of the optical fiber, thus producing integrated microoptical devices. The measured focal length and profile of the micro-optics components were in close coincidence to the predicted values. Potential fields of applications cover: light guiding, coupling/extraction, trapping, signal processing and transmitting, microscopy, biology.

Keywords: laser 3D micro/nanofabrication, microoptics, multifunctional devices, fiber optics, hybrid polymers, integrated systems, optofluidics.

## 1. INTRODUCTION

Improvement of the structuring resolution, increase in the fabrication speed, reduction of the costs and truly three-dimensional (3D) manufacturing are the driving forces for the development of micro- and nanostructuring technologies. One of the currently emerging direct laser writing (DLW) technologies is the femtosecond laser two-photon polymerization (FLTPP). Since its invention [1, 2], the technique finds numerous applications in fabrication of various micro- and nanostructures for photonics [3], micro-optics [4, 5], bio-applications [6], micro-electro-mechanical (MEMS) and micro-electro-optical-mechanical systems (MEOMS) [7]. The advantages of the FLTPP method over other lithography or DLW technologies are determined by the ability to fabricate truly 3D structures and to achieve the sub-100 nm spatial resolution using special post-thermal treatment technique [8]. Phenomenon of two-photon polymerization (TPP) is based on the localized chemical reaction initiated in the volume of the photoresist due to simultaneous absorption of two photons of the same frequency. Besides two-photon absorption (TPA) is the stochastic process respectively to the laser intensity, TPA is initiated only in the vicinity of the tightly focused laser focus area where photons flux is above the irreversible photomodification threshold, thus allowing to improve spatial resolution and overcome the diffraction limit [9]. The direct writing of 3D structures is carried out by the point-to-point exposition of the photoresist by moving the laser focus position. As a result, the light exposed photoresist undergoes polymerization and becomes insoluble in the developer, meanwhile unexposed photoresist is washed out and the free-standing structure is obtained on the glass substrate.

Up to date, several acrylate and epoxy materials have been used for the FLTPP [10, 11]. The drawback of these materials is the distortion of the fabricated microstructures due to the shrinkage [12]. To avoid this effect, novel hybrid sol-gel organic-inorganic materials were employed [13]. Transparency in visible (VIS) and near-infrared (NIR) ranges, tunable refraction index by varying material’s inorganic content, high optical quality, postprocessing chemical and electrochemical inertness, good mechanical and chemical stability made hybrid materials suitable candidates for the production of micro-optics components (MOC) [14]. Germanium dioxide, known as material having high refraction index and low optical dispersion, is used for the fabrication of optical fiber cores as an impurity in the silica. Use of *Ge* containing hybrid material allows fabricating MOC on the tip of the optical fiber from the similar material as the fiber core itself. Rapid prototyping and high reproducibility level allows to fabricate Fresnel zone plates or large arrays of microlenses for high resolution imaging [15, 16]. Several groups have demonstrated further extension of MOC integration by the fabricating microlenses on the tip of the optical fiber using electron beam lithography [17], focused ion-beam milling [18] and TPP [19, 20]. The possibility to generate photonic bandgaps in wave frequency [21] attracted a lot of attention since the new micro- and nanostructuring technologies emerged for the fabrication of photonic crystals (PhC). Lately, it has been found out the modification of the spatial dispersion inside PhC [22]. One example of spatial manipulation of light is a self-collimation of the beam due to the appearance of flat segments on the spatial dispersion curves [23, 24]. Notwithstanding these achievements, the field of integrated MOC and PhC is still not explored applying FLTPP technique.

In this paper we present experimental results on fabrication of aspheric and Fresnel lenses, microlenses on the tip of the optical fiber and PhC.

## 2. METHODOLOGY

### 2.1 Materials

In our experiments, we used hybrid sol-gel materials based on organic-inorganic components. A copolymer methacryloxypropyl trimethoxysilane (MAPTMS) was used as an organic content and two metal isopropoxides, zirconium *n*-propoxide (ZPO, 70 % in propanol, Sigma-Aldrich GmbH) and germanium isopropoxide (GIP, 97%, Sigma-Aldrich GmbH), together with alkoxysilane groups of MAPTMS were used to form an inorganic network respectively to zirconium (*Zr*) and germanium (*Ge*) containing materials. Michler‘s ketone (4,4′ – bis (diethylamino) benzophenone, Sigma-Aldrich GmbH) was added as a photoinitiator (PI) at 2 wt. % concentration to the final solution for the *Zr* containing material and at 1 wt. % concentration to the MAPTMS for the *Ge* containing material. *Zr* containing samples were prepared for the photo-polymerization by drop-casting the photoresist on a glass substrate and drying on a hotplate at 90 °C for 1 hour and *Ge* containing samples were drop-cast and dried in ambient conditions for the 48 hours. After the photopolymerization, samples were developed in the pure 4-methyl-2-pentanone (Acros Organics) for one hour for the *Zr* containing material and at least four hours for the *Ge* containing material in order to wash out the unexposed photoresist.

### 2.2 Experimental setup

Practical implementation and basic principles of the FLTPP technology used in this work are illustrated by the optical setup shown in Fig. 1 a. Mainly, it consists from three parts: an excitation source, an optical section and the positioning system. As an excitation source, a femtosecond Ti:sapphire oscillator (Super Spitfire, Spectra Physics) was used with a 800 nm central wavelength, 80 fs pulse width and 80 MHz repetition rate. The intensity, required for the qualitative fabrication of the microstructures in our experiments, was in 0.4 – 0.9 TW/cm$^2$ range. Optical section was designed as follows. λ/2 waveplate combined with polarizer (not shown in Fig.1) were used for the intensity attenuation of the oscillator and a 100x (NA = 1.4) immersion oil microscope objective (SplanApo, Olympus Corp.) was used for the tight focusing of laser beam into a sample. The red-light LED source combined together with the microscope objective, beam splitter and CMOS camera (mvBlueFOXM102G, Matrix Vision GmbH) worked as an transmission microscope and was used for the real time monitoring of the fabrication process ensuring easy anchoring of the microstructures to the glass or fiber. For the adjustment of exposure time, the homemade shutter with the response time of 5 ms was made. High accuracy positioning system was employed in the optical setup, to exploit high-resolution fabrication due to TPA. It was built from the three-axis piezo stage (Nanocube, Physik Instrumente GmbH) having the step resolution of 1 nm and a 100 μm travel range in three perpendicular (XYZ) directions. The drawback of the used piezo stage was the limited overall processing area. Therefore, the piezo stage was mounted on positioning stage with a step motor and micrometer accuracy (Standa Ltd.) with a step resolution of 1 μm, 2.5 μm and 1.25 μm and travel range of 100 mm, 100 mm and 30 mm respectively to X, Y and Z directions. For the fabrication of MOC, the sample was fixed directly on the piezo stage, and for the fabrication on the tip of the optical fiber, the custom-made fiber holder was used. Tip of the optical fiber was immersed in the photopolymer in such a way, that the tip was near to the cover glass. Later, the fiber holder was fixed to the piezo stage. The fabrication process was controlled by custom-made software “3D Poli” especially designed for the fabrication. It provided possibility to import and fabricate structures from computer aided design (CAD) files or to design and fabricate desired 3D features by the software directly.

The geometry and surface roughness of microstructures were characterized by scanning electron microscopy (SEM, TM-1000, Hitachi), optical profilometer (PLμ 2300, Sensofar) and atomic force microscopy (AFM, Scanning Probe AFM Dimension 3100, Digital Instruments).

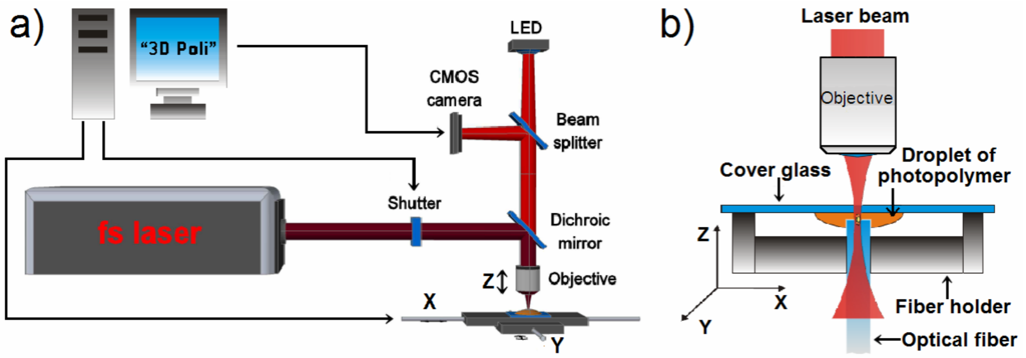

Fig. 1. The optical setup of FLTPP technology (a) and the sketch up for the installation of the optical fiber into setup for the fabrication on the tip (b)

## 3. RESULTS AND DISCUSIONS

### 3.1 Micro-optics components

### *3.1.1 Aspheric lenses*

Spherical lenses, used for the light flow control, are characterized by spherical aberrations and therefore cannot focus collimated beam of monochromatic light into diffraction limited spot. Potential approach to reduce or eliminate spherical aberrations is to use aspheric lenses instead of spherical ones. The curvature radius of surface profile of an aspheric lens depends on the distance from its optical axis, but it still keeps the rotational symmetry. Moreover, aspheric lenses provide possibility to produce smaller and lighter elements and replace multi-lens systems with the one element eliminating losses caused by internal reflections from the multiple surfaces in the optical system.

The aspheric lens, fabricated from the *Ge* containing hybrid material, is shown in Fig. 2. The surface profile of lens is defined by:

$$h(r) = \frac{1}{n^2}\left(F - n\sqrt{R^2+F^2} - \sqrt{(n\sqrt{R^2+F^2}-F)^2 - (1-n^2)(r^2-R^2)}\right), \qquad (1)$$

where $n$ is refraction index of the used sol-gel material, $F$ – focal length, $R$ – lens radius and $r$ – lens curvature radius. Designed and measured surface profile of aspheric lens is shown in Fig. 2 a. Calculated root mean square error (RMSE) is 2.5 %. Mainly, the error is caused by the polymerized tip in the centre of the lens because of the overexposure (Fig. 2. b). The radii of the circles at the center are smaller than in periphery and the sol-gel is exposed much longer at the tip because the next radii are still in the focus while fabricating the next one. Instead of polymerizing the whole volume of 25 μm radius and 50 μm focal length aspheric lens, it was fabricated in successive manner: firstly, only the outer shell of the lens was polymerized using angular scanning method with constant steps between the radii of the circles; secondly, nonfunctional sol-gel was removed from sample during the development procedure and finally, the volume of sol-gel, covered by outer shell, was polymerized by UV exposure. Therefore, the fabrication time of the lens was decreased by a factor $\sim (2-4)\times 10^2$. The lens surface consists of multitude overlapping voxels with the 500 nm diameter, however the measured surface roughness $R_s$ with an AFM was below λ/20 and it satisfied one of the key parameter of micro-optics ($R_s \leq \lambda/10$) for the VIS and NIR spectral region due to self-smoothing [25] and self-polymerization effects [26].

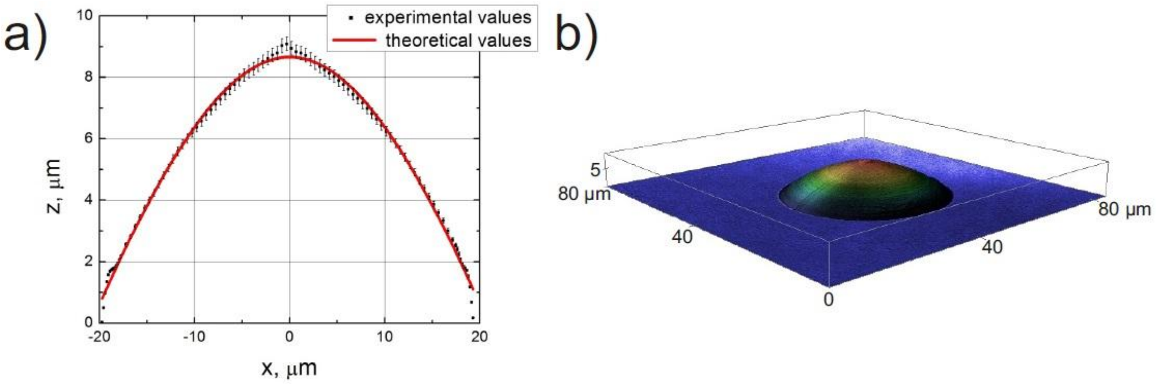

Fig. 2. Aspheric lens fabricated of *Ge* containing hybrid material: designed and measured profile (a) and 3D profile (b)

### 3.1.2 Fresnel lenses

Mostly for all of the integrated micro-optics systems used in MEMS and MEOMS, an important element is focussing MOC. For the effective imaging and compact size, it is preferred that volume of the focussing element should be as small as possible. Compared with the bulk MOC, such as spherical lens, the volume of the Fresnel lens, also known as kinoform, is reduced significantly due to its complex geometry. It consists from a series of concentric circular zones with radii defined by:

$$r_m = \sqrt{2\lambda f m + (\lambda m)^2}\ , \tag{2}$$

and the height defined by:

$$d(r) = \frac{\lambda(m+1)}{n-1} - \frac{\sqrt{f^2 + r^2} - f}{n-1}, \tag{3}$$

where $r_m$ – the radii of the Fresnel lens zones, $\lambda$ – wavelength of the light, $f$ – focal length of the lens, $m$ – number of the Fresnel zone (1, 2. 3…) and $n$ – refraction index of material [27]. Designed Fresnel lens profile consists of the five zones with the radii: 11.3 µm, 16 µm, 19.6 µm, 22.7 µm and 25.3 µm, respectively to $m$ = 1, 2, 3, 4 and 5 order (Fig. 3 a). The SEM image of Fresnel lens (radius 50 µm, height 1.4 µm) fabricated from the designed CAD file is shown in Fig. 3 b. It can be seen that Fresnel lens has smooth contours in each zone as and designed lens. Zone radii measured from SEM pictures were 11 µm, 15.4 µm, 19.3 µm, 22.2 µm and 25.6 µm. Calculated deviation from the theoretical values was 1.5 % and it is caused by assumption that the dimensions of the voxel are infinitely small.

Imaging properties of Fresnel lens were tested using microscope section from the same optical setup as for the fabrication procedure. For this measurement, the text mask "VU LRC" (corresponding to Vilnius University Laser Research Center) was made by laser ablation of a gold layer film sputtered on a glass substrate. Fresnel lens and text mask were mounted together on the positioning stage with the 6 mm distance between text mask and sample and were illuminated with a red LED (650 nm) from the bottom. Images were captured using NA = 0.65 and 40x magnification microscope objective (Nikon) by scanning the stage in $z$ direction starting from the Fresnel lens until the sharp image of the text mask was achieved. Distance, between Fresnel lens and sharp image corresponded to the focal length. Designed and measured Fresnel lens focal lengths were 100 µm and 97.4 ± 2.3 µm respectively and they are close to each other.

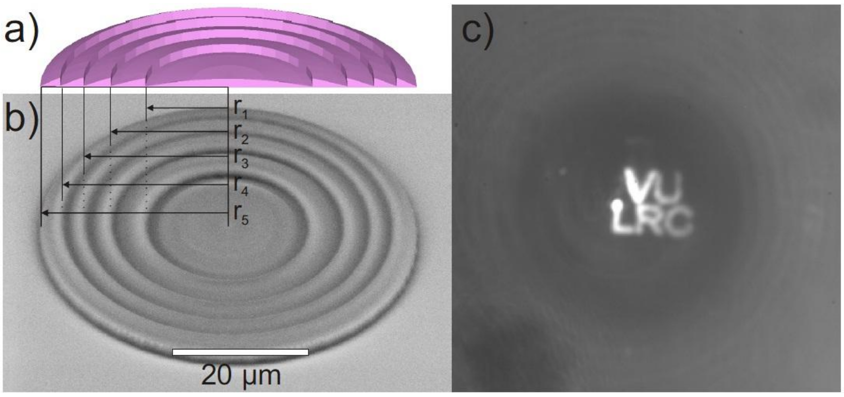

Fig. 3. Fresnel lens and its imaging properties: generated CAD file (a), SEM image tilted 45 deg (b) and image of text mask taken with Fresnel lens (c)

## 3.2 Integrated micro-optics components

In the previous sections, possibility of the FLTPP technology to manufacture complex geometry MOC with the desired optical functions was explored. To demonstrate integrity of the MOC as well as FLTPP technology flexibility and versatility, aspheric lens (radius 25 µm) from a *Zr* containing hybrid material was fabricated on the tip of single mode optical fiber

(460HP, Thorlabs) (Fig. 4 b). The 3D profile reveals the residues of the developed sol-gel on the tip of optical fiber and the lens itself. The designed profile of aspheric lens (Fig. 4 a) is the same as and for the aspheric lens depicted in the previous section. Calculated RMSE is smaller by 1% from the RMSE of the aspheric lens fabricated from the *Ge* containing materials and is equal to the 1.5%. The difference is caused by the use of larger amount of the germanium isopropoxide in the final solution of the hybrid material that the used amount of zirconium *n*-propoxide.

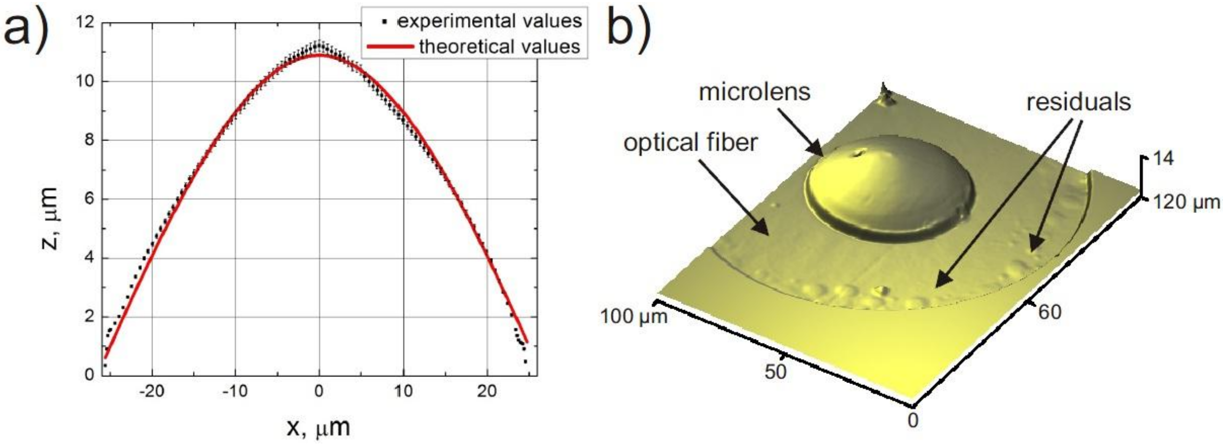

Fig. 4. Aspheric lens fabricated of *Ge* containing hybrid material on the tip of the optical fiber: designed and measured profile (a) and 3D profile (b)

For the quantitative analysis of the aspheric lenses on the tip of optical fiber, the focal length was measured with the custom-built setup. It consisted of the microscope elements fixed on the positioning stage with a step motor and micrometer accuracy for the scanning of the focal plain of the microscope through the focus of the microlenses. Afterwards, the images were taken with a CCD beam profiler (BeamOn HR, Duma Optronics Ltd.) and images were analyzed by fitting the acquired spatial light distribution to a Gaussian function. The width *d* of the Gaussian beam was evaluated, and distance to the minimal diameter indicated the focal position. The same setup was also used to analyse of light propagation from the fiber without the microlens on the tip (more detailed description can be found in [28]). The measured focal lengths for the 18 µm and 25 µm radii aspheric lenses were ~22 µm and ~32 µm, respectively. Results of measurements are presented in Fig 5 a. .The beam diameters are normalized to a maximum value in each measurement sets. Fiber tip was used as a reference position for the experiments and the misalignment in determination of the fiber tip led to the measurement inaccuracy, which is seen in the initial stage of the fiber without microlens curve. Fig. 5 b and c presents two-dimensional (2D) light propagation distribution from the fiber without microlens and with the microlens (radius 37 µm) on the tip. Fiber tip, before focus, focus and after focus labels corresponds to the distance from the fiber tip, respectively 0 µm, 10 µm, 20 µm and 30 µm. As it can be seen, the beam diameter for the fiber without microlens is always increasing as the light is propagating further from the fiber tip, meanwhile for the fiber with microlens, the beam diameter is decreasing and is smallest at focal position. A dashed line corresponds to the eye guidelines and indicates the diffraction and focusing of the light for the fiber without lens and with the lens on top, respectively.

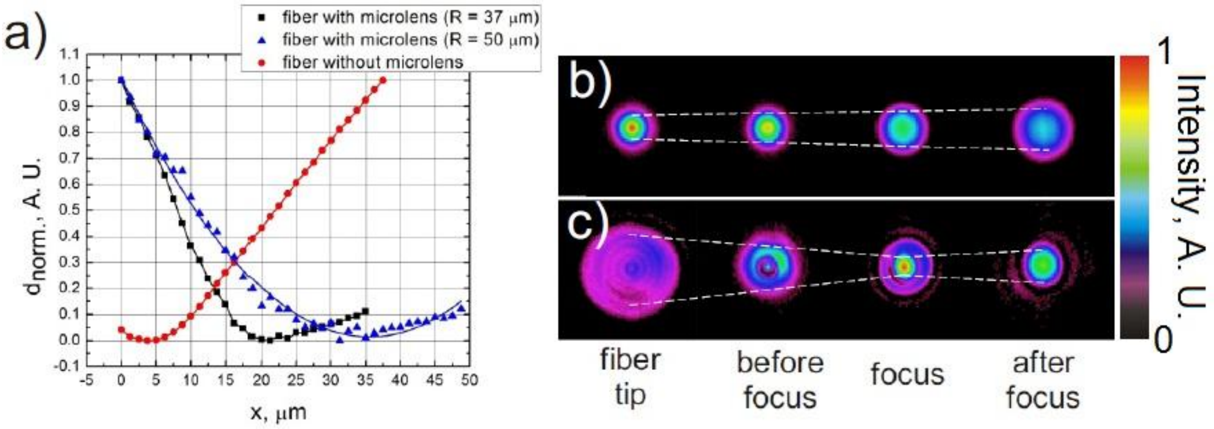

Fig. 5. Diameter of the light distribution for the fiber with 18 μm and 25 μm radii aspheric lenses and without (a) and light propagating distribution from the fiber without microlens (b) and from the fiber with the microlens on top (c). A dashed line corresponds to the eye guidelines for the diffraction and focussing

### 3.3 Photonic components

Since the spatial propagation effects of the light inside the PhC are characterized, the PhCs were fabricated out of the *Zr* containing hybrid material for the evaluation of spatial distribution behind the crystal (Fig. 6). The PhC was fabricated as woodpile geometry structure with the 1 μm transverse and 7.8 μm longitudinal period. It contained of 12 longitudinal periods and each consists of 4 layers. Every layer starting from the glass substrate consists of parallel rods and every adjacent layer was shifted by the value of the half transverse period and was rotated by 90 deg relatively to the previuos layer. The transverse dimensions of the fabricated PhC was 90 μm and the height was 93.6 μm. Low contrast refractive index sample was prepared by filling the voids inside PhCs with an unexposed liquid-state *Zr* containing material after the sample development procedure.

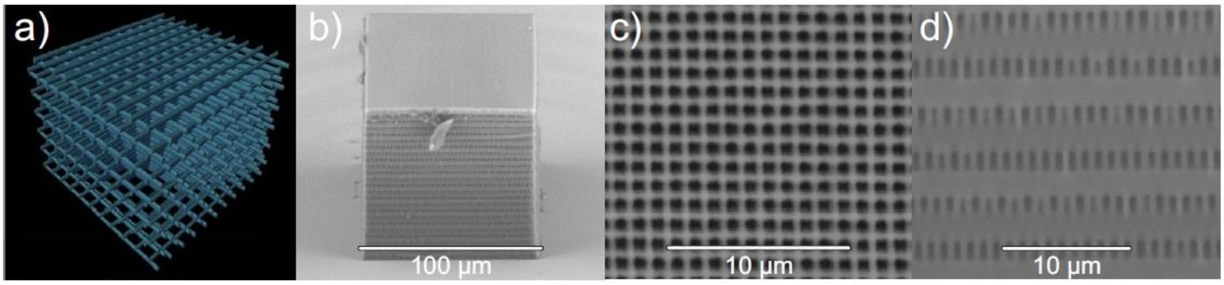

Fig. 6. Schematic illustration of PhC (a) and intensity distribution of transmitted light through the PhC (b). Narrow spot at the center indicates collimated beam and circles indicates the four first order diffraction maxima. SEM image PhC tilted 45 deg (c). Top inset demonstrates transversal period and lower inset demonstrates longitudinal period of PhC

## 4. CONCLUSIONS

In summary, we fabricated aspheric and Fresnel lenses of the novel hybrid materials containing *Zr* and *Ge* using FLTPP technology. The focal lengths of MOC were measured and the experimental results were in good agreement with design value. The surface roughness of MOC was measured and it satisfied $R_s \leq \lambda/10$ condition. Estimated RMSE of the aspheric lenses was below 3% and it is tolerated for the technological processes. We demonstrated integrity to manufacture microstructures in already existing platforms as well as FLTPP technology flexibility and versatility by fabricating aspheric lenses on the tip of optical fiber. Finally, we manufactured low contrast refractive index chirped PhC. To minimize the geometrical imperfections of the MOC the scanning trajectory influence to the MOC profile should be evaluated and the dimensions of the voxel should be incorporated to the design of the MOC. Further research in the measurement of minimal clusters formations during fabrication process in the *Zr* and *Ge* containing hybrid materials is carried out.

## ACKNOWLEDGEMENTS

This work was financially supported by EC’s Seventh Framework Programme (LASERLAB-EUROPE, grant agreement No. 228334, OPTOBIO).

## REFERENCES

1. MARUO, S., NAKAMURA, O., KAWATA, S. Three-dimensional microfabrication with two-photon-absorbed photopolymerization. *Optics Letters*, 1997, Vol. 22, p. 132–134.
2. MIWA, M., JUODKAZIS, S., KAWAKAMI, T., MATSUO, S., MISAWA, H. Femtosecond two-photon stereolithography. *Applied Physics A*, 2001, Vol. 73, p. 561–566.
3. SERBIN, J., EGBERT, A., OSTENDORF, A., CHICHKOV, B. N., HOUBERTZ, R., DOMANN, G., SCHULZ, J., CRONAUER, C., FROHLICH, L., POPALL, M. Femtosecond laser-induced two-photon polymerization of inorganic-organic hybrid materials for applications in photonics. *Optics Letters*, 2003, Vol. 28, No. 5, p. 301–303.
4. WU, D., CHEN, Q.-D., NIU, L.-G., JIAO, J., XIA, H., SONG, J.-F., SUN, H.-B. 100% fill-factor aspheric microlens arrays (AMLA) with sub-20-nm precision. *IEEE: Photonics Technology Letters*, 2009, Vol. 21, No. 20, p. 1535–1537.
5. MALINAUSKAS, M., GILBERGS, H., ŽUKAUSKAS, A., PURLYS, V., PAIPULAS, D., GADONAS, R. A femtosecond laser-induced two-photon photopolymerization technique for structuring microlenses. *Journal of Optics*, 2010, Vol. 12, No. 3, p. 1–8.
6. MALINAUSKAS, M., DANILEVIČIUS, P., BALTRIUKIENĖ, D., RUTKAUSKAS, M., ŽUKAUSKAS, A., KAIRYTĖ, Ž., BIČKAUSKAITĖ, G., PURLYS, V., PAIPULAS, D., BUKELSKIENĖ, V., GADONAS, R. 3D artificial polymeric scaffolds for regenerative medicine fabricated by femtosecond laser. *Lithuanian Journal of Physics*, 2010, Vol. 50, p. 75–82.
7. SUN, H.-B., KAWATA, S. Two-photon laser precision microfabrication and its applications to micro-nano devices and systems. *Journal of lightwave technology*, 2003, Vol. 21, No. 3, p. 624–633.
8. LI, J., JIA, B., GU, M. Engineering stop gaps of inorganic-organic polymeric 3D woodpile photonic crystals with post-thermal treatment. *Optics express*, 2008, Vol. 16, p. 20073–20080.
9. JUODKAZIS, S., MIZEIKIS, V., SEET, K. K., MIWA, M., MISAWA, H. Two-photon lithography of nanorods in SU-8 photoresist. *Nanotechnology*, 2005, Vol. 16, No. 6, p. 846–849.
10. NGUYEN, L., STRAUB, M., GU, M. Acrylate-based photopolymer for two-photon microfabrication and photonic applications. *Advanced Functional Materials*, 2005, Vol. 15, p. 209–216.

11. THIEL, M., FISCHER, J., FREYMANN, G., WEGENER, M. Direct laser writing of three-dimensional submicron structures using a continuous-wave laser at 532 nm. *Applied Physics Letters*, 2010, Vol. 97, p. 221102.
12. OVSIANIKOV, A., SHIZHOU, X., FARSARI, M., VAMVAKAKI, M., FOTAKIS, C., CHICHKOV, B. N. Shrinkage of microstructures produced by two-photon polymerization of Zr-based hybrid photosensitive materials. *Optics Express*, 2009, Vol. 17, No. 4, p. 2143–2148.
13. OVSIANIKOV, A., VIERTL, J., CHICHKOV, B. N., OUBAHA, M., MacCRAITH, B., SAKELLARI, I., GIAKOUMAKI, A., GRAY, D., VAMVAKAKI, M., FARSARI, M., FOTAKIS, C. Ultra-low shrinkage hybrid photosensitive material for two-photon polymerization microfabrication. *ACS Nano*, 2008, Vol. 2, No. 11, p. 2257–2262.
14. FARSARI, M., VAMVAKAKI, M., CHICHKOV, B. N. Multiphoton polymerization of hybrid materials. *Journal of Optics*, 2010, Vol. 12, p. 124001.
15. WU, D., WU, S.-Z., NIU, L.-G., CHEN, Q.-D., WANG, R., SONG, J.-F., FANG, H.-H., SUN, H.-B. High numerical aperture microlens arrays of close packing. *Applied Physics Letters*, 2010, Vol. 97, p. 1–3.
16. LI, Y., YU, Y., GUO, LI., WU, S., CHEN, C., NIU, L., LI, A., YANG, H. High efficiency multilevel phase-type Fresnel zone plates produced by two-photon polymerization of SU-8. *Journal of Optics*, 2010, Vol. 12, p. 1–4.
17. PRASCIOLU, M., COJOC, D., CABRINI, S., BUSINARO, L., CANDELORO, P., TORMEN, M., KUMAR, R., LIBERALE, C., DEGIORGIO, V., GERARDINO, A., GIGLI, G., PISIGNANO, D., Di FABROZIO, E., CINGOLANI, R. Design and fabrication of on-fiber diffractive elements for fiber-waveguide coupling by means of ebeam lithography. *Microlectron Engineer*, 2003, Vol. 67–68, p. 169–174.
18. SCHIAPPELLI, F., KUMAR, R., PRASCIOLU, M., COJOC, D., CABRINI, S., De VITTORIO, M., VISIMBERGA, G., GERARDINO, A., DEGIORGIO, V., Di FABRIZIO, E. Efficient fiber-to-waveguide coupling by a lens on the end of the optical fiber fabricated by focused ion beam milling. *Microlectron Engineer*, 2004, Vol. 73–74, p. 397–404.
19. LIBERALE, C., COJOC, G., CANDELORO, P., DAS, G., GENTILE, F., ANGELIS, F. D., FABRIZIO, E. D. Micro-optics fabrication on top of optical fibers using two-photon lithography. *IEEE: Photonics Technology Letters*, 2010, Vol. 22, p. 474–476.
20. MALINAUSKAS, M., ŽUKAUSKAS, A., PURLYS, V., BELAZARAS, K., MOMOT, A., PAIPULAS, D., GADONAS, R., PISKARSKAS, A., GILBERGS, H., GAIDAKIVIČIŪTĖ, A., SAKELLARI, I., FARSARI, M., JUODKAZIS, S. Femtosecond laser polymerization of hybrid/integrated micro-optical elements and their characterization. *Journal of Optics*, 2010, Vol. 12, p. 124010.
21. YABLONOVITCH, E. Inhibited spontaneous emission in solid-state physics and electronics. *Physics Review Letters*, 1987, Vol. 58, p. 2059–2062.
22. STALIŪNAS, K., SANCHEZ-MORCILLO, V. J. Spatial filtering of light by chirped photonic crystals. *Physics Review A*, 2009, Vol. 79, p. 053807.
23. KOSAKA, H., KAWASHIMA, T., TOMITA, A., NOTOMI, M., TAMAMURA, T., SATO, T., KAWAKAMI, S. Self-collimating phenomena in photonic crystals. *Applied Physics Letters*, 1999, Vol. 74, p. 1212–1214.
24. STALIŪNAS, K., HERRERO, R. Subdiffractive band-edge solitons in Bose-Einstein condensates in periodic potentials. *Physics Review E*, 2006, Vol. 73, p. 016601.

25. TAKADA, K., SUN, H.-B., KAWATA, S. Improved spatial resolution and surface roughness in photopolymerization based laser nanowriting. *Applied Physic Letters*, 2005, Vol. 86, p. 071122.
26. MALINAUSKAS, M., BIČKAUSKAITĖ, G., RUTKAUSKAS, M., PAIPULAS, D., PURLYS, V., GADONAS, R. Self-polymerization of nano-fibers and nanomembranes induced by two-photon absorption. *Lithuanian Journal of Physics*, 2010, Vol. 50, No. 1, p. 135–140.
27. BASS, Michael. *Handbook of Optics*. Optical Society of America, 1995. 1496 p. ISBN 0-07-047974-7.
28. MALINAUSKAS, M., GILBERGS, H., ŽUKAUSKAS, A., BELAZARAS, K., PURLYS, V., RUTKAUSKAS, M., BIČKAUSKAITĖ, G., MOMOT, A., PAIPULAS, D., GADONAS, R., JUODKAZIS, S., PISKARSKAS, A. Femtosecond laser fabrication hybrid micro-optical elements and their integration on the fiber tip. SPIE 2010. Proceedings of micro-optics. Brussels. 2010 May 6.

CYSENI 2011, May 26–27, Kaunas, Lithuania
ISSN 1822-7554, www.cyseni.com

# AUTO-IGNITION AND COMBUSTION BEHAVIOUR OF IRON MICRO POWDERS IN HEATED OXYGEN

**V.V. Leschevich, O.G. Penayzkov**
*Physical and Chemical Hydrodynamics Laboratory*
*Heat and Mass Transfer Institute*
*220072 Minsk – Belarus*
*Phone +375172841520*
*Email: V.Leschevich@dnp.itmo.by*

**J.C. Rostaing**
*L'Air Liquide, Centre de Recherche Claude-Delorme*
*1 chemin de la Porte des Loges*
*Les-Loges-En-Josas 78354 Jouy en Josas – France*

## ABSTRACT

The experiments have been conducted on auto-ignitions of iron powders with particle sizes ranged from 1 μm to 140 μm at oxygen pressures up to 28 MPa and temperatures varied from 550 to 1100 K. Critical conditions at which auto-ignition of iron micro particles resided in layer can occur were determined in dependence of particles sizes, oxygen pressure and temperature. Also some characteristics of ignition and combustion processes like ignition delay time and combustion temperature were studied. Collected experimental database is useful for development and validation of mathematical models describing auto-ignition and combustion phenomena of iron particles in heated oxygen.

Keywords: auto-ignition, combustion, oxygen, iron micro particles.

## 1. INTRODUCTION

Information about ignitibility of metal particles is important for variety of practical applications associated with propulsion, military and industrial safety. In particular, metal particles can be used as catalytic additives that improve the combustion efficiency of conventional fuels and suppression of detrimental emissions from stationary combustion sources [1, 2]. On other hand metal and non-metal elements are often used in industry as powder or dusts, and an evaluation of their possible explosion hazards is important. Therefore numerous experimental studies were connected with the explosibility of metal dusts. A particles cloud is highly reactive medium due to large effective area and high thermal resistance in comparison with solid metal. If the dust is suspended in air it can explode and deflagration-to-detonation transition even can occur due to factors that increase the combustion wave front speed. This phenomenon has been studied in shock tubes [3, 4] and constant volume chambers [5]. The other possible outcome is when the particles reside in layer on a surface. Local ignition causes a slow-acting and smoldering combustion. A rapid energy release can damage surrounding structures and initiate propagation of fire accidents. Simulating this process is a comprehensive physical-chemical problem that combines both kinetic oxidation processes of individual particles and heat transfer processes in particle-particle and particle-gas systems. Development and checking the adequacy of the theoretical models therefore requires input data such as critical parameters of a gas medium, at which auto-ignition occurs, their dependence on particle material and size as well as information about ignition delay time and its dependence on oxygen temperature and pressure. The sufficient amount of experimental data was obtained in this study by means of rapid compression machine (RCM), which was used for generating heated oxygen atmosphere in wide ranges of pressures and temperatures.

## 2. EXPERIMENTAL SETUP

The present RCM consists of a driving and compression cylinders, a pneumohydraulic system of motion control, a driving air tank, and a test chamber. The design of the used RCM has been described in previous works [6-8]. A high compression ratio (up to 80:1) of RCM provides both high pressure and high temperature at the end of compression stroke. Fig. 1 shows the general layout of the compression cylinder and measurement setup. The test chamber (2) is equipped with a high-temperature quartz pressure sensor Kistler 6031U18 (4) combined with a Kistler 5015A charge amplifier (11), a gas inlet/outlet valve (5) with pneumatic actuator and quartz window (6) to the mandrel of which the bifurcated optical fibre light guide was connected for recording the luminescence at auto-ignition and combustion. The neutral filter (optical density D=3.74) was installed in front of photocathode of the first photomultiplier. The second photomultiplier was used without filter. This allows detecting both weak luminescence at local auto-ignition and strong luminescence at combustion of whole particle layer. The gas temperature was calculated using pressure measurements as in other RCM studies [6–8] in assumption that compression is adiabatic and isentropic and heat losses effects only on thin boundary layer.

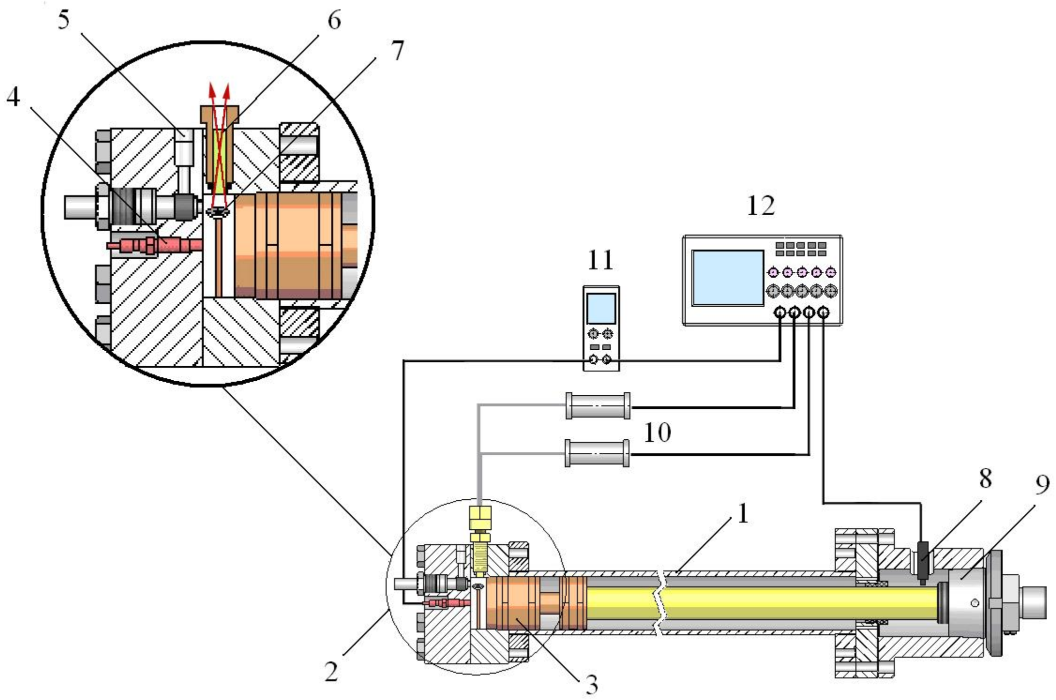

Fig. 1. The layout of the compression cylinder and measurement system: 1 – compression cylinder, 2 – test chamber, 3 – compression piston, 4 – pressure sensor, 5 – inlet gas and vacuum valve, 6 – quartz window, 7 – ceramic cup with particle sample, 8 – optical reflection probe, 9 – conical stopper,10 – photomultipliers, 11 – charge amplifier, 12 – digital oscilloscope

Temperature of burning particles was measured with time resolution of 4 μs by photoemission method based on analysis of photoelectron energy distribution. The essence of this technique has been extensively described in [9, 10]. The applicability of this method was proved by observation of emission spectrum during ignition and combustion. The registered spectrum in 300–600 nm was continuous and similar to emission spectrum of solids. It allowed us to use the preliminary temperature lamps calibration for determining current temperatures during particles auto-ignitions and burning. Moreover, the measured maximal temperature well agrees with colour temperature calculated from spectrum by method described in [11]. The advantage of used method is a possibility of temperature measurements with temporal resolution up to 1 µs.

The experiments has been performed for five iron powders: two metallurgical ultra fine iron powders with main particles fraction 1–3 µm and 1–5 µm, respectively, and three powders separated by sieves 45 µm, 56–63 µm and 80–125 µm. The smallest available mesh size of sieve is 45 µm. Therefore the separated sample was additionally analyzed by the microscope. It was observed that powder generally consists of particles with sizes ranged from 20 to 40 µm. As a very little amount of more fine particles was found their influence were not taken into account in this study. Moreover, all powders were examined by certified picture scanner “Mini-Magiscan”. The results of accurate granulometric analysis are presented in Table 1. It was found that the main fraction of powders consisted of the particles with size ranges lightly different from the sizes of the sieves meshes. Therefore we used the main fraction sizes (the size range of particles generally presented by quantity in powder) as identification of each powder. The particle samples (mass of 0.05 g) were placed in a small ceramic cup (Fig. 1 (7)) mounted in the test chamber of RCM.

Table 1. Results of granulometric analysis for studied powders

| Powder | | Size range (min-max), µm | Main fraction | | | average by quantity size (length/weigh),µm | average by mass size, µm |
|---|---|---|---|---|---|---|---|
| | | | quantity | | mass, µm | | |
| | | | horizontal projection, µm | vertical projection, µm | | | |
| metallurgical ultra fine iron powders | | 0.2–9.2 | 1–3 | 1–3 | 2–4 | 2.59/2.16 | 3.4 |
| | | 0.2–16.4 | 1–5 | 1–3 | 4–5 | 4.01/3.08 | 4.7 |
| powders separated by sieves | 45 | 9.0–98.1 | 20–40 | 30–40 | 30–60 | 42.92/30.56 | 43.8 |
| | 56–63 | 6.7–180.3 | 60–90 | 70–90 | 70–90 | 82.76/59.01 | 80.6 |
| | 80–125 | 32.8–268.1 | 110–140 | 100–110 | 130–160 | 155.48/114.8 | 140.2 |

## 3. RESULTS AND DISCUSSION

Experiments were conducted at oxygen pressures of 0.5–27.8 MPa and temperatures of 550–1100 K. In order to achieve these conditions initial pressure in compression cylinder was varied from 25 kPa to 1098 kPa and compression ratio was changed from 10 to 40 while the initial temperature was equal to room temperature. Results of all experimental runs are plotted on Fig. 2 in terms of oxygen pressure and temperature at the end of compression stroke. The post compression conditions at which ignition was occurred and caused combustion of sufficient amount of particle samples (smouldered fragments were visible by an unaided eye) is marked by filled symbols. Lines on these plots present approximations of critical conditions corresponded to ignition limits. As one can see auto-ignition temperature strongly depends on oxygen pressure and particle size, especially at temperatures lower than 800 K. Moreover the form of this dependence is significantly intensified for powders with smaller particles.

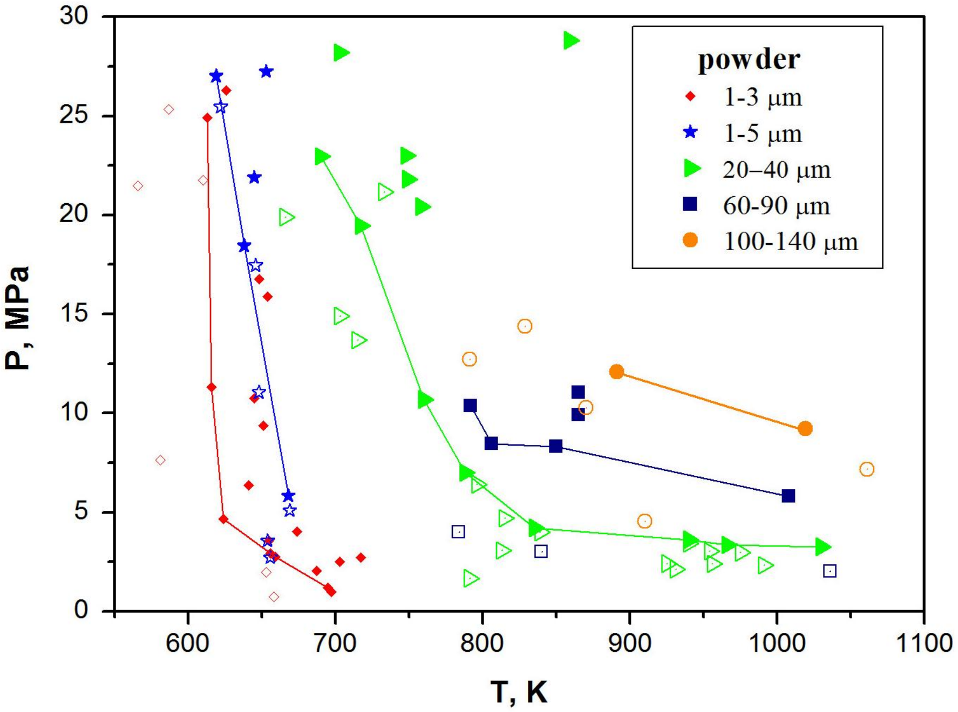

Fig. 2. Critical conditions: oxygen pressures vs. temperatures, at which auto-ignitions of particle domains were and not observed (black and empty symbols, respectively). The main particles fractions in tested micro powders are indicated on the graph

The ignition delay time is usually defined as the time difference between pressure peak at the end of compression stroke and the onset of emission (5% of maximal rise) registered by photomultiplier. The example of pressure and luminescence recorded during compression, ignition and combustion of powder 60–90 μm is presented on Fig 3. The calculated postcompression oxygen temperature was about 790 K. Some problems have appeared with measuring ignition delay time from such signal records. A weak luminescence was always observed at the end of compression event for post compression oxygen temperatures higher then 600 K. This light (marked on Fig. 3 by black ellipse) is not connected with ignition of particle samples. It corresponds to ignition of submicron particle ejected from piston's seals due to friction on cylinder surface during compression stroke. This conclusion was confirmed by experimental runs without any particle samples. The second problem is related to the fact that the powder consist of different size particles. As was shown in Fig. 2 finer particles can be ignited easier than larger one. Since it is impossible to identify what particle has been ignited the measured ignition delay time is the unrepeatable and stochastic value. On other hand the ignition of whole particles layer is more global process which can be repeated with rather good accuracy. That is why in this study ignition delay time was defined as the time difference between pressure peak at the end of compression and the onset of emission which corresponds to ignition of whole particle layer. This time interval is marked on Fig. 3.

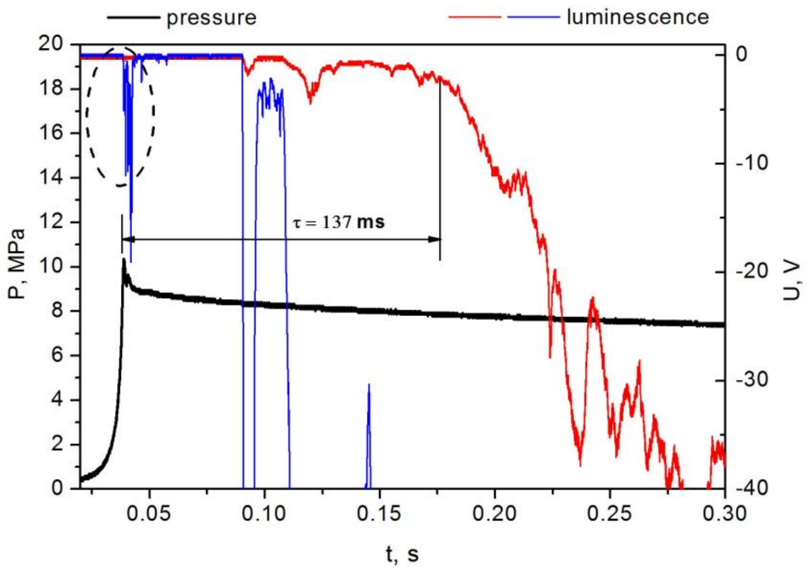

Fig. 3. Signal records during oxygen compression and particles auto-ignition

Ignition of iron powders are strongly depended not only on oxygen temperature but also on oxygen pressure (Fig. 2). Therefore it is expected that ignition time will also depend on oxygen pressure. In order to point out this dependence we collected auto-ignition data on powder 1–3 μm for the same temperatures and different pressures (Fig. 4). It was found that at oxygen temperature of 650 ± 10 K ignition time strongly increases with reducing oxygen pressures to values less than 4 MPa. For higher temperature (700 ± 15) the considerable effect of oxygen pressure on auto-ignition time was observed at pressures less than 2 MPa.

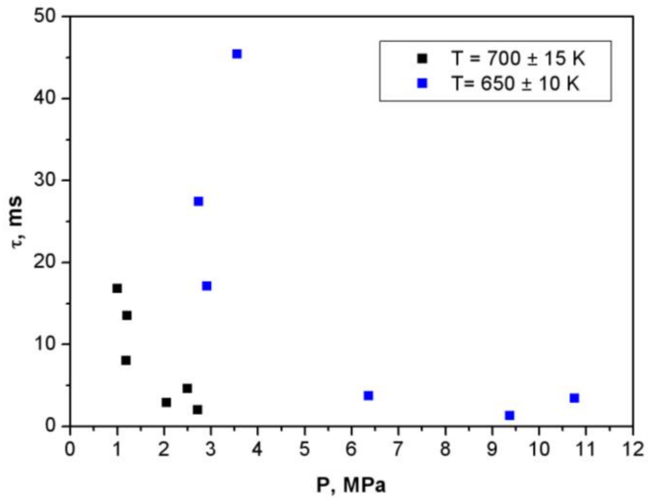

Fig. 4. Pressure dependence of ignition times of iron powder 1–3 μm in oxygen atmosphere at different temperatures

For different particles, the pressure behaviour of ignition times is presented in the Fig.5. The lines on this plot correspond to liner approximations of measured ignition times for specified powder at certain oxygen pressure range. It is seen that lines have similar angle that is why pressure influence on ignition time can be presented by introduction of some coefficient. The plotted dependences are rather coarse and have a big scatter but nevertheless are useful for validation of mathematical models describing auto-ignition of iron particles in heated oxygen. Moreover, this data is useful for safety evaluation of technological processes during which iron micro particles and heated oxygen atmosphere can meet at the same time.

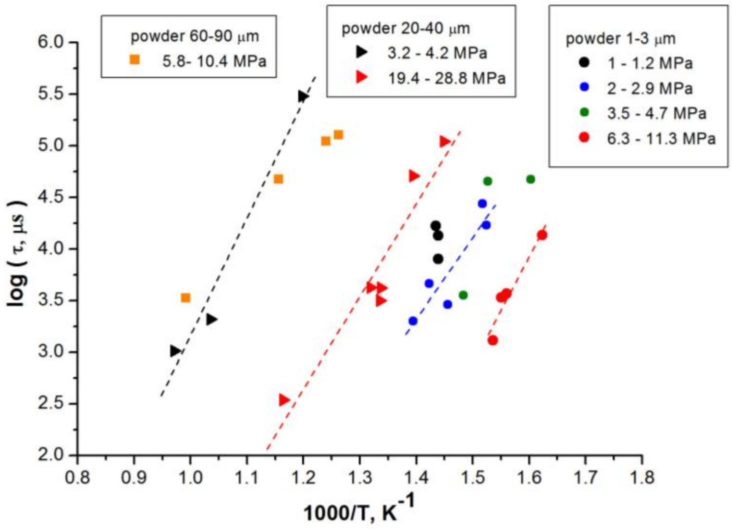

Fig. 5. Ignition times vs. oxygen temperature for studied iron powders and oxygen pressures

Temperature of burning particles was measured with by photoemissive pyrometer connected to the one branch of optical fibre. The one photomultiplier with neutral filter was connected to the second brunch in these experiments. The example of pressure, luminescence and pyrometer's signals recorded during compression, ignition and combustion of is presented on Fig 6.

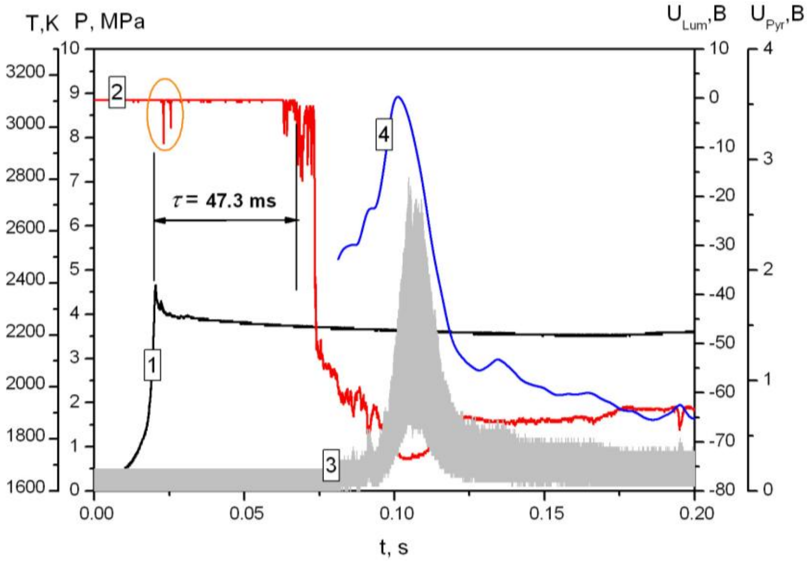

Fig. 6. Signal records during oxygen compression and particles auto-ignition: 1 – oxygen pressure, 2 – luminescence in test volume, 3 – signal of pyrometer and 4 – calculated temperature history

The powder 1-3 μm was tested in this experiment and post compression oxygen temperature was 625 K. The measured in this test ignition delay time is also indicated on graph. The calculated from pyrometer signal temperature of burning particles is presented by line 4 on this graph. The detected temperatures near the onset of particles auto-ignition are varied from 2450 ± 50 K to 3100 ± 50 K and then slow down to the value of 1850 ± 50 K which is close to melting temperatures of iron (1812 K) and iron oxides. The maximal temperature at combustion of iron powder (1–3) didn't exceed value of 3100 K, which is close to iron boiling temperature. Thus, probably the iron boiling limits the maximal temperature, due to high latent vaporization heat of iron.

## CONCLUSIONS

The auto-ignition and combustion of iron micro particles in heated oxygen has been studied by means of rapid compression machine for oxygen pressures varied from 0.5 to 28 MPa and temperatures varied from 550 to 1100 K. The critical conditions that can provoke auto-ignition and combustion were determined for five powders with particle sizes from 1 μm to 140 μm. It was found that iron micro particles can easily ignited in rapidly heated oxygen atmosphere at temperatures much lower than iron boiling temperature. Moreover this critical temperature decreases significantly with increasing oxygen pressure. The influence of oxygen pressure and temperature as well as particle size on ignition delay time of whole powders was established. The received dependences can be easily applied for the prediction of iron micro powders behaviour in the rapidly heated oxygen atmosphere. The variation of temperature developing during iron combustion of powder 1–3 μm was measured with temporal resolution of 4 μs. It was found that the temperature can shortly arise up to 3100 K. The collected data is important for development of new technological processes during which iron micro particles and heated oxygen atmosphere can appear together. Moreover, obtained database is useful for development and validation of mathematical models describing auto-ignition and combustion phenomena of iron particles in heated oxygen.

## ACKNOWLEDGMENTS

This work was sponsored by Air Liquid (France), State Scientific Program “Nanotechnology - US” (Belarus) and WFS (Switzerland).

## REFERENCES

1. ALLEN, C.M., LEE, T. Energetic-nanoparticle enhanced combustion of liquid fuels in a rapid compression machine. Proceedings of 47th AIAA Aerospace Sciences Meeting Including The New Horizons Forum and Aerospace Exposition, 2009: AIAA 2009-227.
2. LISSIANSKI, V.V., MALY P.M., ZAMANSKY V.M., GARDINER W.C. (2001). Utilization of iron additives for advanced control of $NO_x$ emissions from stationary combustion sources, *Industrial and Engineering Chemical Research*, 2001, Vol. 20, No. 3, p. 3287–3293.
3. BOIKO, V.M, PAPYRIN, A.N, WOLINSKI, M., WOLANSKI, P. Dynamics of dispersion and ignition of dust layers by a shock wave. *Progress in Astronautics and Aeronautics*, 1984, Vol. 94, p. 293–301.
4. BORISOV, A.A, GEL’FAND, B.E, TIMOFEEV, E.I., TSYGANOV, S.A., KHOMIC, S.V. Ignition of dust suspensions behind shock waves. *Progress in Astronautics and Aeronautics*, 1984, Vol. 94, p. 332–-339.
5. CASHDOLLAR, K.L, ZLOCHOWER, I.A. Explosion temperatures and pressures of metals and other elemental dust clouds. *J Loss Prevention in the Process Industries*, 2007, Vol. 20, p. 337–348.
6. LESCHEVICH, V.V., MIRONOV, V.N., PENYAZKOV, O.G. Auto-ignition of metal particles in oxygen atmosphere. Proceedings of 22nd International colloquium on the dynamics of explosions and reactive systems, 2009, Minsk, Belarus.
7. LESCHEVICH, V.V. Combustion of metal particles in oxygen atmosphere in rapid compression machine. CYSENI 2009. Proceedings of annual conference of young scientists on energy issues. [CD]. Kaunas: Lithuanian Energy Institute. 2009 May 28–29.

8. LESCHEVICH, V.V., PENYAZKOV, O.G. Auto-ignitions studies of Methane – air mixtures in rapid compression machine. CYSENI 2010. Proceedings of annual conference of young scientists on energy issues. [CD]. Kaunas: Lithuanian Energy Institute. 2010 May 27–28.
9. BARANYSHYN, Y.A., BELAZIORAVA, L.I., KASPAROV K.N., PENYAZKOV, O.G. Photoemission measurements of soot particles temperature at pyrolysis of ethylene. *Nonequilibrium Phenomena: Plasma, Combustion, Atmosphere*, 2009, Moscow: Torus Press Ltd., p. 87–93.
10. BARANYSHYN, Y.A. FISENKO, S.P., PENYAZKOV, O.G. (2010). Heat transfer and growth of nano- and submicron particles of black carbon in nonequilibrium gas mixture. Experiment and simulation. *International Journal of Heat and Mass Transfer*, 2010, Vol. 53: 5465–5471.
11. RYABININ, YU.N., SOBOLEV, N.N., MARKEVICH, A.M., TAMM, I.I. (1952). Optical properties of gases at ultra high pressures. *Journal of Theoretical and Experimental Physics*, 1952, Vol. 23, No. 5, p. 564–575.

# FLOW VELOCITY DEPENDENCE ON PLASMA-CHEMICAL REACTOR OUTLET NOZZLE DESIGN AND EFFECT ON OBTAINED MINERAL FIBRE

**M. Milieška, R. Kėželis, V. Mėčius, V. Grigaitienė**
*Plasma Processing Laboratory*
*Lithuanian Energy Institute*
*Breslaujos str. 3, LT-44403, Kaunas – Lithuania*
*Phone +370 37 401 895*
*Email: milieska@mail.lei.lt*

## ABSTRACT

The aim of this paper is to study the plasma flow velocity dependence on the plasma-chemical reactor outlet nozzle design and its effect on microstructure and quantity of the obtained zeolite microfibre. The zeolite fibres are formed using the kinetic energy of high temperature and velocity air plasma jet. As the fibre formation starts at the end of the reactor, the reactor outlet nozzle diameter has significant role in fibrillation process because the velocity of leaving the reactor plasma flow increases from 980 m/s to 1650 m/s as the outlet nozzle diameter of the reactor decreases from 0.013 m to 0.01 m. The plasma flow velocity exceeds the velocity of sound which is about 1100 m/s for air of plasma temperature. The “shock diamonds” which are typical for supersonic plasma jet are observed in the distance x/d=6 from outlet nozzle of the reactor. The highest quantity of zeolite fibre is reached as the outlet nozzle diameter is 0.011 m. The quality of produced fibre increases decreasing the diameter of the outlet nozzle. Microstructure of the obtained zeolite fibre and visualization of the plasma flow were carried out using SEM and CCD high-speed camera analysis. The plasma flow characteristics were measured or calculated from heat balance.

Keywors: plasma-chemical reactor, mineral fibre, supersonic plasma jet.

## INTRODUCTION

Mineral fibre production assisted by plasma technologies isn’t quite new technology however it is not sufficiently studied so there is a lack of information in worldwide scientific literature about the factors which influences the quality and quantity of obtained fibre.

The properties of obtained mineral fibre using linear plasma-chemical reactor depend on a large number of factors, such as: plasma flow velocity and temperature which are influenced by plasma torch power, plasma forming gas rate and additional gas rates, raw material composition, reactor geometry and etc [1]. The fibre formation is caused by the plasma flow kinetic energy in the reactor which disturbs the melt surface and pulls of elementary jets from it, which are then cooled to solidification [2]. So, the plasma flow velocity is the main factor determining the fibre formation. As the fibre formation takes place at the end of the plasma-chemical reactor the decrease of the outlet nozzle diameter increases the plasma flow velocity [3].

The zeolite powder was used as initial raw material for mineral fibre production. Zeolite is a waste catalyst of oil refinery and petrochemical industries. Waste catalyst can stand the heat of more than 1750 ºC, so it can be used for manufacturing of fire-proof materials, filters and catalysts [4]. Catalysts which are made of solid materials need a higher surface area which has an important effect on the reaction rate. If the catalyst particle size is smaller, the surface area for a given mass of particles is larger [5]. So, the diameter of obtained high quantity mineral fibres must be as small as possible to apply them as catalysts.

The aim of this paper is to study the plasma flow velocity dependence on the plasma-chemical reactor outlet nozzle diameter and its effect on microstructure, quality and quantity of the obtained zeolite microfibre.

## METHODOLOGY

The experiments were performed with plasma-chemical reactor applied for fibrillation raw ceramic materials and developed in Plasma Processing Laboratory of Lithuanian Energy Institute. The plasma-chemical reactor (Fig. 1) consists of plasma torch and 0.24 m. length channel made of stainless steel. The precise description of plasma torch and additional equipment of experimental set-up has been depicted in detail elsewhere [6].

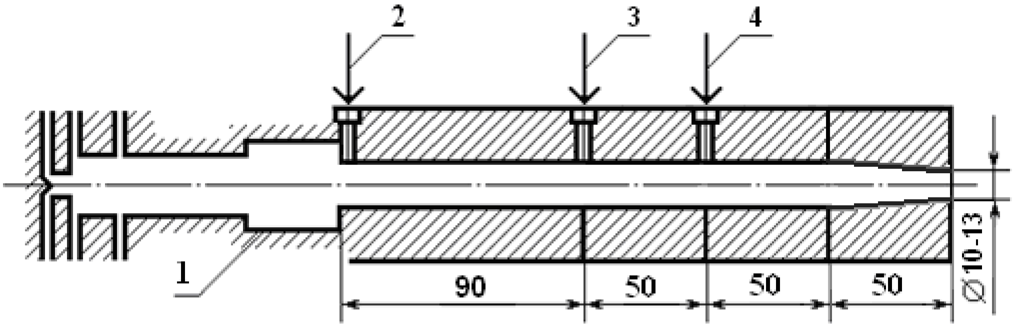

Fig. 1. Plasma-chemical reactor: 1 – plasma torch, 2 – air and dispersed particles, 3 – propane gas, 4 – air

The channel of the plasma-chemical reactor is divided in four sections with 0.015 m inner diameter. The length of first section which is connected to plasma torch is 0.09 m, and other three sections are 0.05 m in length. There are three orifices in the beginning of first three sections for dispersed particle and gas feeding whose importance and influence to the plasma flow temperature was described earlier [7]. The outlet nozzle of fourth section can be changed in the range of $10\text{-}13 \cdot 10^{-3}$ m. The decrease of outlet diameter increases the velocity of leaving the reactor plasma flow.

All sections are cooled with water and insulated from each other, so no heat transfer between the cooling water of each section takes place. Such isolation of sections allows calculating the average plasma mass flow temperature ($T_p$) in each section of the reactor using methodology described in [7]. Using this methodology all plasma flow characteristics can be measured or calculated from the heat balance.

The plasma flow velocity is calculated using equation:

$$w = \frac{4GRT_p}{\pi d^2 p}. \tag{1}$$

Gas flow rate ($G$) and pressure ($p$) in the reactor (with inner diameter $d$) are controlled and measured during the experiments.

The speed of sound in the reactor is equal to:

$$c = \sqrt{\frac{\gamma R T_p}{M}}, \tag{2}$$

where $\gamma$ is the adiabatic index (1.4 for air), $R$ is the molar gas constant (8.3145 J/(mol·K)) and $M$ is the molar mass (0.0289645 kg/mol for dry air).

The microstructure of the mineral fibre was characterized using a SEM (JSM 5600). The high speed MotionPro X4 camera with 512x512 pixel resolution was used for supersonic plasma flow imaging at the rate of 5000 frames per second.

## RESULTS AND DISCUSSIONS

The experiments were performed with four different outlet nozzle diameters of plasma-chemical rector. The Table 1 shows the optimal regimes of plasma-chemical reactor for different outlet nozzle designs.

Such regimes were examined in a big number of experiments as optimal for each plasma-chemical reactor design while melting and fibrillating zeollite powder. As the outlet nozzle diameter decreases, it is very hard to maintain stable melt flow in the reactor because the viscosity of the melt becomes very important. As the melt viscosity is too low, it goes out of the reactor as little drops and no fibre is formed. When the melt viscosity is too high, it can jam the channel.

Table 1. Optimal regimes of plasma-chemical reactor for different outlet nozzle diameters

| **Outlet diameter, m** | 0.01 | 0.011 | 0.012 | 0.013 |
|---|---|---|---|---|
| **Power, kW** | 76.7 | 80.5 | 80.5 | 81.2 |
| **Air flow, g/s** | 21.8 | 23.9 | 23.7 | 21.4 |
| **Propane gas flow, g/s** | 0.95 | 1.03 | 0.95 | 0.94 |
| **Temperature, K** | 2960 | 2990 | 2990 | 3080 |

These optimal conditions are suitable only for zeolite powder because different materials have different properties, for example melting point, viscosity at appropriate temperatures and etc. The chemical composition of zeolite powder in the experiment was (mass %): $Al_2O_3$ − 40.9; $SiO_2$ − 55.2; $Fe_2O_3$ − 0.9; $TiO_2$ − 1.4; CaO − 0.5, MgO − 0.49, $Na_2O$ − 0.2 [1].

The Fig. 2 shows the dependence of the plasma flow velocity on the outlet nozzle diameter of plasma-chemical reactor. The velocity values presented in Fig. 2 was calculated for optimal plasma-chemical reactor regimes.

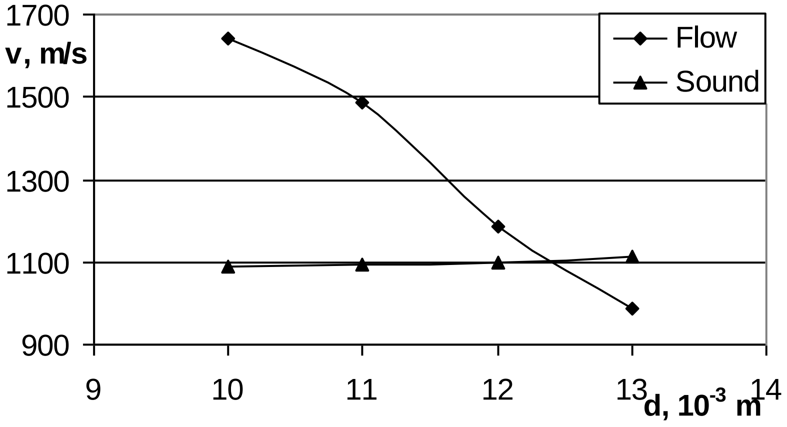

Fig. 2. Plasma flow and sound velocity dependence on plasma-chemical reactor outlet nozzle diameter

In the Fig. 2 it can be seen that the plasma flow velocity exceeds the speed of sound when the outlet nozzle is equal or smaller than $12.4 \cdot 10^{-3}$ m.

The images of high speed camera confirmed that the supersonic multiphase plasma jet was obtained (Fig. 3). The “shock diamonds” which are typical for supersonic plasma jet are observed in the distance x/d=6 from outlet nozzle of the reactor. x/d is the ratio of distance (x) from the reactor outlet nozzle with the inner diameter of the reactor.

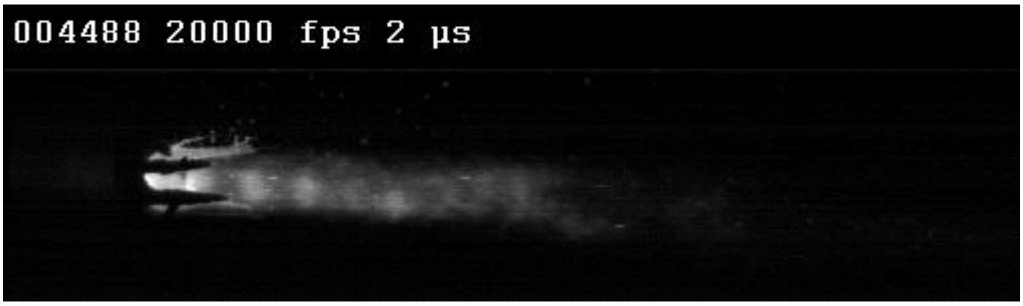

Fig. 3. Supersonic plasma jet with zeolite particles. Outlet nozzle diameter 0.01 m

“Shock diamonds” are a formation of stationary wave patterns that appears when the supersonic jet operated in atmosphere goes through the narrow gap [8].

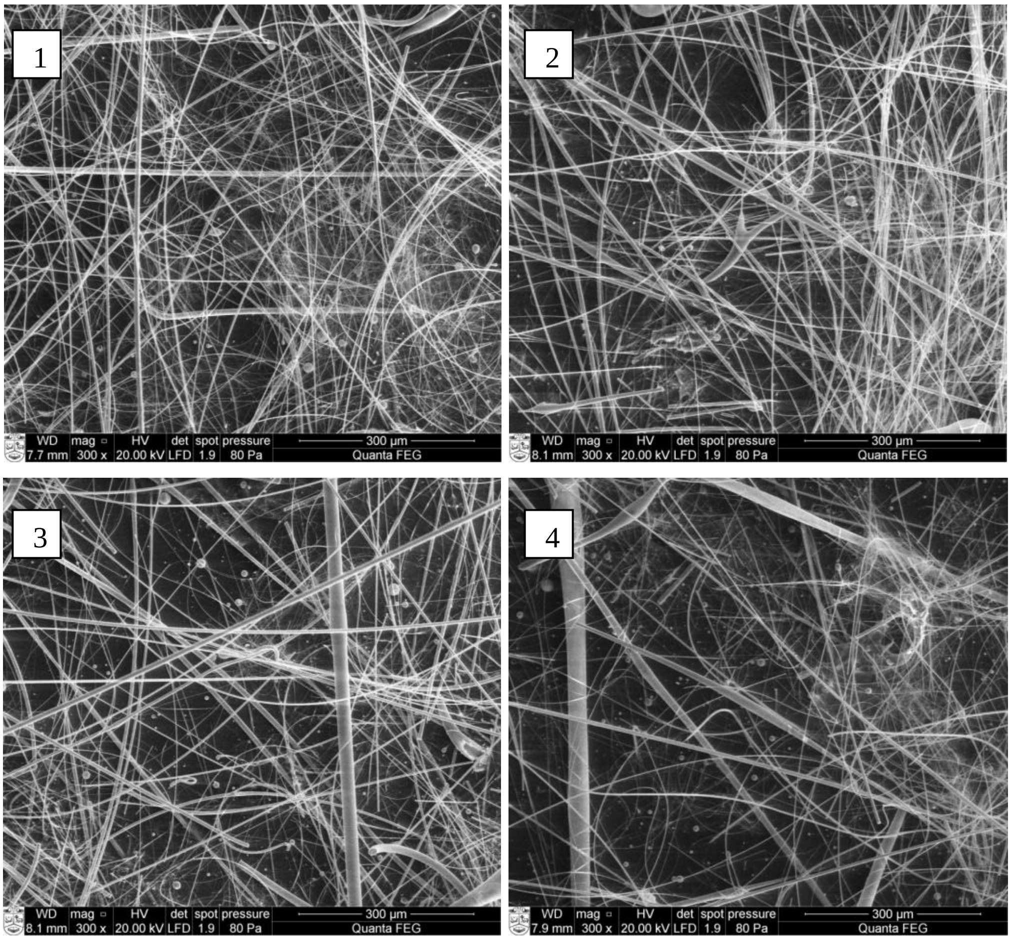

Fig. 4. SEM images of zeolite fibre morphology dependence on outlet diameter: 1 – 0.01 m, 2 – 0.011 m, 3 – 0.012 m, 4 – 0.013 m

Experiments showed that the morphology of fibre, produced by plasma spraying, strongly depends on outlet nozzle diameter (outlet flow velocity). As the outlet nozzle diameter is smaller, the average diameter of obtained mineral fibre is smaller. The dominant diameter of obtained mineral fibre is in the range of 0.5–5 µm, and the length - 50-70 mm. However, the increase of outlet nozzle diameter increases the number of larger (> 20 µm) diameter fibres. It means that the bigger kinetic energy of the flow pulls more elementary jets out of the melt and has more power to stretch them and form a fibre of smaller diameter. As the outlet diameter increases, the amount of microgranules produced simultaneously with fibre increases. The formation of microgranules takes place when the plasma flow kinetic energy is strong enough to pull the drops of the melt but isn't capable to stretch them before solidification.

The dominant diameter of obtained mineral fibre and the quantity of produced microgranules are the most important factors determining the quality of fibre. The smaller diameter of fibres increases the surface area of the product. The big number of produced microgranules significantly reduces the insulation properties of mineral fibre [9].

From Fig. 4 it can be seen that the best quality of obtained mineral fibre is when the outlet nozzle diameter is 0.01 m. However the output of mineral fibre isn't the largest in this case (Fig. 5).

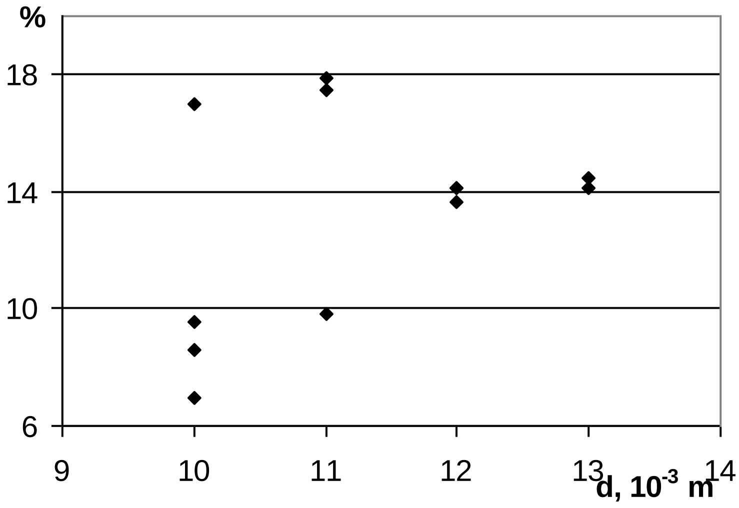

Fig. 5. Fibre output dependence on outlet nozzle diameter

Experimental data shows that fibre output depends on the plasma-chemical reactor outlet nozzle diameter. The output was determined by weighing the initial powder material before injecting it into the reactor and obtained mineral fibre. It can be seen (Fig. 5) that the highest output (around 14%) is obtained when the outlet diameter is 0.011-0.013 m. The decrease of output when the outlet diameter is 0.01 m. is caused by the frequent melt jam in the channel. So, the further decrease of outlet diameter wouldn't make sense.

The highest obtained mineral fibre quality and quantity ratio is when the outlet nozzle diameter of plasma-chemical reactor is 0,011 m because the fibre isn't polluted with granules, the diameter of the fibres is comparatively small and the output is the highest for all used outlet nozzle diameters.

## CONCLUSIONS

1. The decrease of outlet nozzle diameter of plasma-chemical reactor increases the plasma flow velocity. The plasma flow velocity exceeds the speed of sound, when the outlet diameter is equal or smaller than $12.4 \cdot 10^{-3}$ m.
2. The smaller outlet nozzle diameter leads to better quality of obtained mineral fibre. The best quality of obtained mineral fibre was when the outlet nozzle was equal to 0.01 m.
3. The highest quantity of obtained mineral fibre was achieved when outlet diameter was in the range of 0.011-0.012 m.

4. The highest obtained mineral fibre quality and quantity ratio is when the outlet nozzle diameter of plasma-chemical is 0,011 m.

## REFERENCES

1. MILIEŠKA, M., KĖŽELIS, R., KALPOKAITĖ-DIČKUVIENĖ, R., ČĖSNIENĖ, J., BRINKIENĖ, K., MĖČIUS, V. Plazminio metodo taikymas formuojant nanoplaušą iš naftos produktų gamybos proceso atliekų (ceolitų). *Energetika,* 2008, Vol. 54, No. 4 , p. 54–58.
2. LAKTYUSHIN, A., SERGEEV, V. Mathematical description of the process of mineral-fiber formation by the plasma method. *Journal of Engineering Physics and Thermophysics*, 1998, Vol. 71, No. 6, p. 1022–1027.
3. KĖŽELIS, R., VALINČIUS, V., GRIGAITIENĖ, V., MILIEŠKA, M., MĖČIUS, V. Plasma spray recycling of zeolite waste to create micro-and nanostructured mineral fibre // Proceedings of the XVIII international conference on gas discharges and their applications. Greifswald, Germany. 2010 September 5–10.
4. ANTONOVIČ, V., GOBERIS, S., PUNDIENĖ, I., STONYS, R. The effect of waste oil-cracking catalyst on the properties of refractory castable. *Polish Ceramic Bulletin*, 2005, Vol. 88, p. 143–150.
5. KOPER, M., WIECKOWSKY, A. *Fuel Cell Catalysis: A Surface Science Approach*. New York: John Willey & Sons, 2009. 720 p. ISBN 978-0-470-13116-9.
6. VALINČIUS, V., KRUŠINSKAITĖ, V., VALATKEVIČIUS, P., VALINČIŪTĖ, V., MARCINAUSKAS, L. Electric and thermal characteristics of the linear, sectional dc plasma generator. *Plasma sources science and technology*, 2004, Vol. 13, p. 199–206.
7. MILIEŠKA, M., KĖŽELIS, R., MĖČIUS, V. Influence of gas flow rate on the thermal characteristics of plasma-chemical reactor. CYSENI 2010. Proceedings of annual conference of young scientists on energy issues. [CD]. Kaunas: Lithuanian Energy Instityte. 2010 May 27–28.
8. DAVIS, J. R. *Handbook On Thermal Spray Technology*. Thermal spray society and ASM international, 2004. 338 p. ISBN 978-0-87170-795-6.
9. TRDIČ, F., ŠIROK, B., BULLEN, P.R., PHILPOTT, D.R. Motoring mineral wool production using real-time machine vision. *Real-time Imaging*, 1999, Vol. 5, p. 125–140.

CYSENI 2011, May 26–27, Kaunas, Lithuania
ISSN 1822-7554, www.cyseni.com

# STUDY OF WATER VAPOUR PLASMA COMPOSITION BY OPTICAL EMISSION SPECTROSCOPY METHOD

**A. Tamošiūnas, V. Grigaitienė, V. Valinčius**
*Lithuanian Energy Institute*
*Plasma Processing Laboratory*
*Breslaujos str. 3, LT-44403 Kaunas – Lithuania*
*Phone +37062373965*
*Email: tamosiunas@mail.lei.lt*

## ABSTRACT

Since every chemical element has a unique electronic structure, the wavelength of light emitted is a unique property of each individual element. Optical emission spectroscopy (OES), which measures the light emitted from the plasma as a function of wavelength, time and location, is the most commonly used plasma diagnostic probe for plasma processing. Emission lines are registered by the optical emission spectrometer AOS4-1 and analyzed to observe the chemical composition of water vapour plasma jet generated by novel designed direct current (DC) water vapour plasma torch 30-53 kW of power at Lithuanian Energy Institute, Plasma Processing Laboratory. Water vapour ionized by high voltage electric arc dissociates into atomic hydrogen, oxygen and radicals. Hydrogen is very desirable in the formation of high caloric synthetic gas ($CO+H_2$) during thermal plasma gasification of organic materials. Consequently, it is very important to investigate the formation of hydrogen in plasma jet by means of OES, as it non-intrusive, inexpensive and easily applicable for plasma processing. The main goal of this research is a study of water vapour plasma composition by optical emission spectroscopy.

Keywords: water vapour, plasma, optical emission spectroscopy, plasma torch.

## 1. INTRODUCTION

Atmospheric pressure water vapour plasma generated by means of novel designed direct current (DC) water vapour plasma torch at Lithuanian Energy Institute, Plasma Processing Laboratory present a considerable interest for a wide range of applications of plasma technology in the gasification/vitrification for treatment of hazardous waste [1], as well as in pyrolysis/gasification of organic compounds for the production of synthetic fuels [2, 4], in environmental protection for effective destruction of hydrofluorocarbons (HFCs) [5], perfluorcarbons (PFCs) [6], and volatile organic compounds (VOCs) [7]. Plasma technology is also employed for new materials and surface treatment, welding, cutting and etc.

Besides measurements of electrical and thermal characteristics of water vapour plasma generator (PG) and investigation of plasma jet parameters such as temperature and velocity, optical emission spectroscopy (OES) has been used for plasma diagnostics as non-invasive and *in situ* method. It provides valuable information for the determination of the chemical elements and their species, exited atomic and molecular states with a very differing cost performance ratios and time consumption. Also, enables to determine the rotational, vibrational, and electronic excitation temperatures of the plasma and thus the level of non-equilibrium and the gas temperature, and sometimes electron temperature [8, 9]. Reference [10] has investigated the rotational temperature, hydrogen atomic temperature, and electron and excitation temperatures of atmospheric pressure DC microplasma jet (98% Ar-2% $H_2$).

In this research only emission spectra parameters of water vapour plasma jet were investigated in order to understand the behavior and composition of water vapour at high temperatures. Detailed OES characteristics of discharge dynamics usually requires spectrometers equipped with costly ICCD cameras with nanosecond time resolution and very high spectral resolution. Due to technical limitations, the determination of vibrational, rotational and excitation temperatures of active species will not be investigated. The main focus is to carry out and identify species in the emission spectra of ionized water vapour. The identification of species in the emission spectra of atmospheric pressure air and nitrogen plasmas using OES method was reported in [11], radio frequency (RF) cold plasma in [12], DC low pressure discharges in [13].

In this work, the emission spectra of atmospheric pressure plasmas generated by DC electrical arc discharge in water vapour with admixture of argon as shielding gas were carried out, using well-known OES method.

## 2. EXPERIMENTAL SETUP

### 2.1. Water vapour plasma torch

The experimental DC water vapour plasma torch operating at atmospheric pressure is shown in Fig. 1. Plasma torch – is an electric arc gas heater in which electric energy is converted into thermal energy by means of Joule heat in the discharge [14]. The electric arc in the PG of a linear design is stabilized with gas-water vapour vortex. The torch is 30–53 kW of power with button type hot tungsten cathode working as electron emitter and step-formed copper anode. The operational parameters of PG and plasma jet are given in Table 1.

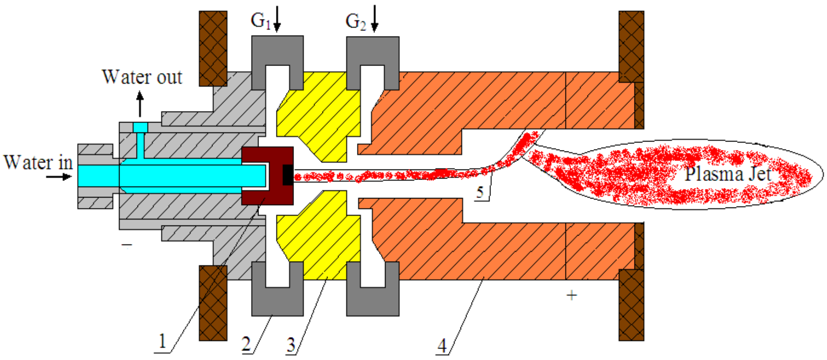

Fig. 1. A scheme of water vapour plasma torch. 1 – cathode, 2 – insulating rings, 3 – neutral section, 4 – anode, 5 – electric arc

It is impossible to generate plasma by means of separate plasma torch. Consequently, complex subsystems are required to enable stable work of PG. The subsystems are as following: power supply and control, torch cooling by water $0.1 \cdot 10^{-3}$ kg · $s^{-1}$, gas feeding $5.2 \cdot 10^{-4}$ kg · $s^{-1}$, water vapour generation $1.48–4.48 \cdot 10^{-3}$ kg · $s^{-1}$ and system of water vapour overheating (to 450 K). The combined operation between mentioned systems allows generating plasma with stable parameters. Electrodes of plasma torch are separated by insulating rings avoiding a short circuit. The rings have the inlet holes for tangential supply of shielding and plasma forming gas.

Argon (Ar) has been used as shielding gas, protecting tungsten cathode form erosion; whereas overheated water vapour (up to 450 K) was used as plasma forming gas produced using 5 bar of pressure water steam generator.

Table 1. The experimental parameters of plasma torch and plasma jet

| | |
|---|---|
| Arc current (A) | 130–210 |
| Arc voltage (V) | 230–330 |
| Arc power (kW) | 30–53 |
| Power loss to the cooling water (kW) | 8–18 |
| Output power (kW) | 24–36 |
| Plasma torch efficiency, η | 0.58–0.78 |
| Argon gas flow rate, $G_1$ ($10^{-4}$ kg · $s^{-1}$) | 5.2 |
| Water vapor flow rate, $G_2$ ($10^{-3}$ kg · $s^{-1}$) | 1.48–4.48 |
| Total mass flow rate, G ($10^{-3}$ kg · $s^{-1}$) | 2–5 |
| Mean temperature of plasma jet at the torch outlet nozzle (K) | 2300–2900 |
| Mean velocity of plasma jet at the torch outlet nozzle (m · $s^{-1}$) | 340–700 |

Water vapour is ionized by high voltage electric arc in the discharge chamber of the plasma torch, i.e. dissociates into atoms, molecules and radicals.

### 2.2. Optical emission spectrometer

The emission spectra of exhaust water vapour plasmas jet at the exit nozzle of PG was measured by means of AOS4-1 spectrometer. The experimental set-up is shown in Fig. 2. The spectrometer with the spectral resolution of 0.05 nm (at 250 nm) and 0.5 nm (at 800 nm) is able to measure radiation emitted from a light source in near UV-VIS spectral range of 250–800 nm wavelength. Time resolution of the spectrometer can vary within the limits from 5 to 100 ms. The AOS4-1 measurement head consists of RF-synthesizer, RF-amplifier with cooler, crystal monochromator, fiber optic-collimator (ø 0.2 mm) and photo detector with detector cable. The spectrometer is controlled via standard USB 2.0 interface from laptop. The "IntelliSpec" software is used for measurements and manipulation of obtained emission spectra.

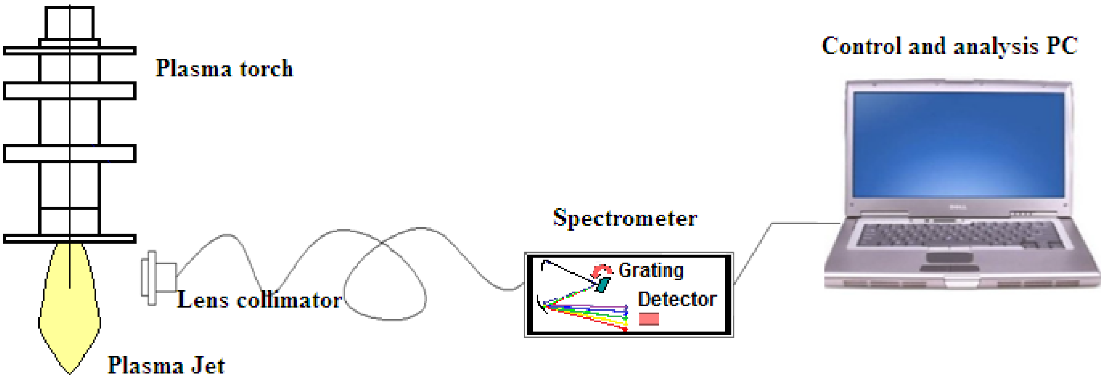

Fig. 2. A scheme of experimental set-up for optical emission spectroscopy

In contrast with conventional spectrometers, in which the spectral dispersion of a broadband optical signal is performed by diffraction gratings, prisms or Fourier Transforming methods, an acousto-optic tunable filter (AOTF) made of quartz ($SiO_2$) crystal is used as a narrow band fast tunable wavelength filter, ensuring calibration of optical system. That's why it is not necessary to have an entrance slit and it is possible to use two dimensional apertures. That means the AOS4-1 allows detecting extremely small amounts of light.

An optical fiber with a lens collimator was placed in front of the plasma region to collect light emission. The focal distance was 0.05 m. The emitted light from plasma jet was deflected by means of lens collimator via optical fiber aperture to the crystal monochromator of the spectrometer, where a photomultiplier (PMT) converted photons into electrical signal. The electrical signal was processed by the software "IntelliSpec".

## 3. RESULTS AND DISCUSSION

The emission spectra of DC electric arc discharge in the argon-water vapour mixture were measured in the range of wavelength from 300 to 800 nm. Figs. 3 and 4 present the optical emission spectrum measured for the argon-water vapour (15% Ar / 85% water vapour) plasma jet at the 5 mm distance from the nozzle exhaust of anode. The experiment conditions in emission spectra measuring (Fig. 3) were the following: the power of plasma torch 31.8 kW, argon flow rate $5.2 \cdot 10^{-4}$ kg · $s^{-1}$ and water vapor flow rate $2 \cdot 10^{-3}$ kg · $s^{-1}$. In the second case (Fig. 4), the power of the torch and flow rate of water vapour have been increased to 36.2 kW and $2.63 \cdot 10^{-3}$ kg · $s^{-1}$, respectively, in order to examine the dependence of active species formation in the emission spectra. The main species observed in Ar/water vapour plasma were: Ar (I), Ar (II) OH, H, O (I), O (II), Cu (I), Cu (II). The emission spectra also showed the peaks of $H_\alpha$ (656.2 nm), $H_\beta$ (486.1 nm) and $H_\gamma$ (434.1 nm), which belong to Balmer series of $H_2$. Visually, the $H_\alpha$ line tends not to be seen well due to human's eye's lack of sensitivity in the deep red part of the spectrum, but the $H_\beta$ line tends to come fairly intense. The emission intensities of obtained peaks are quite low, because of the low energies of exited hydrogen atoms at the atmospheric pressure conditions. In consequence, the temperature of plasma jet at the nozzle exhaust of the plasma torch is high, due to the intense collisions between molecules, but the energies of exited species are low, because the mean free path is short.

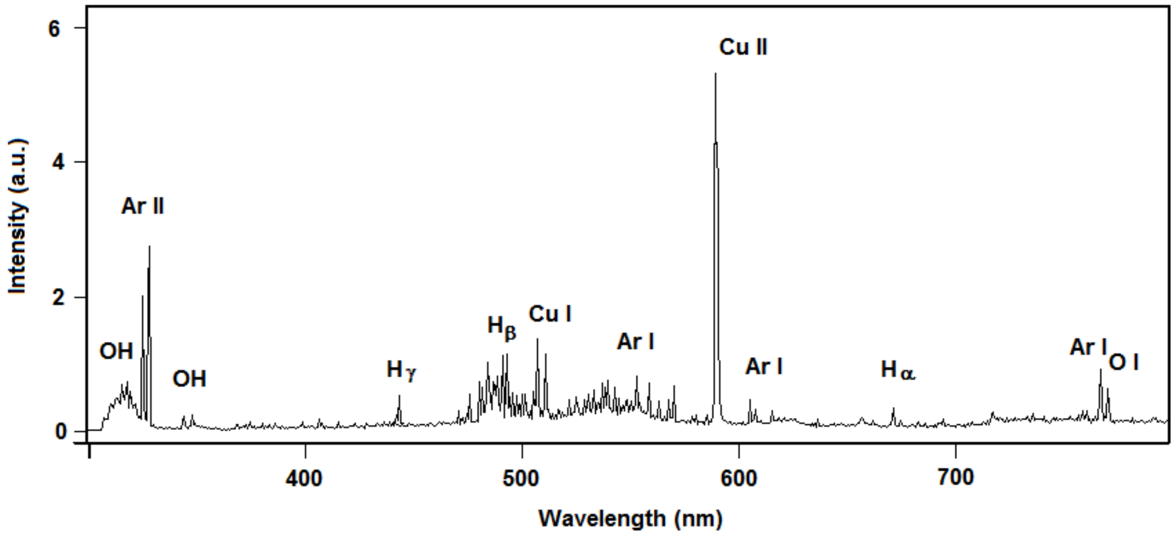

Fig. 3. Optical emission spectra of Ar/water vapour plasma jet at 31.8 kW, flow rate of water vapour $G_2=2 \cdot 10^{-3}$ kg · $s^{-1}$

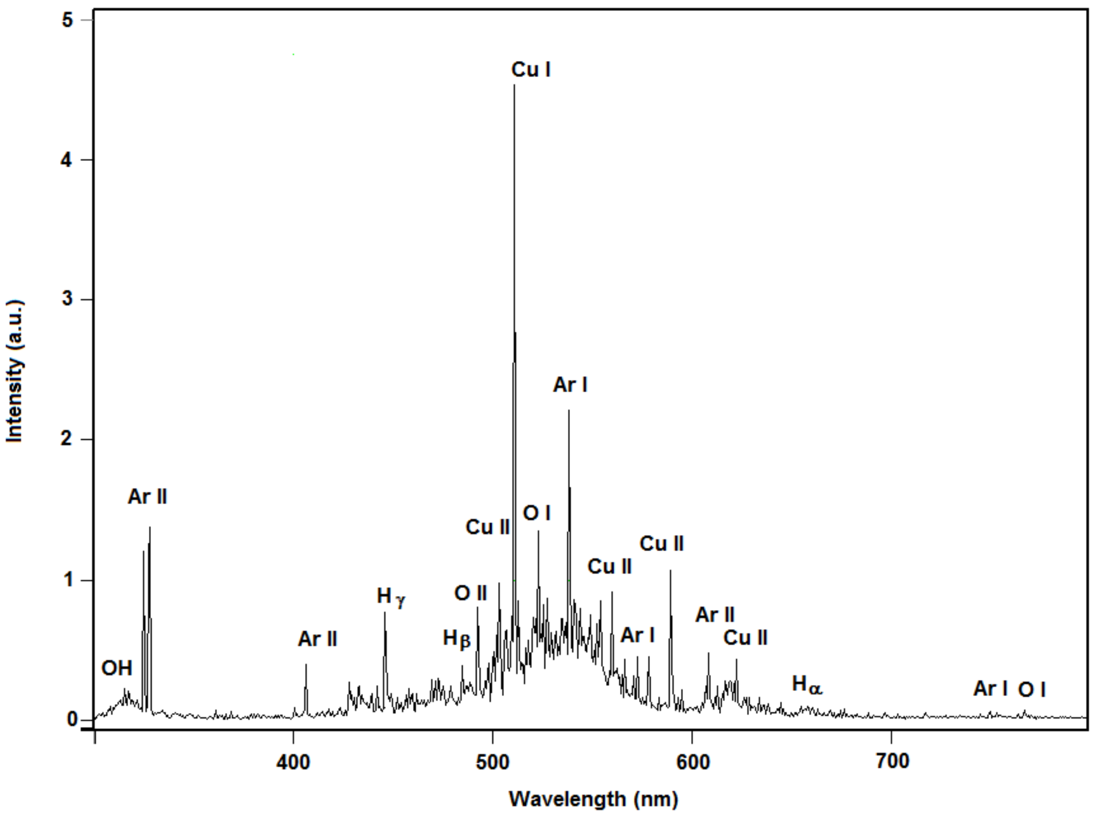

Fig. 4. Optical emission spectra of Ar/water vapour plasma jet at 36.2 kW, flow rate of water vapour $G_2$=2.63 · $10^{-3}$ kg · $s^{-1}$

The intensity of copper (Cu) was much higher compared to the rest species detected. It is considered that copper anode is emitting Cu radicals in the plasma, due to the erosion of the electrode, occurring in the discharge chamber where the electric arc spot burns. The presence of reactive atomic oxygen O (I), which forms during ionization of water vapour, amplifies the negative erosion process also. This could be explained by the fact that oxygen molecule is much heavier compared to hydrogen and tries to settle down to the periphery of the anode, where interacts with inner wall forming copper oxide (CuO).

The obtained hydrogen peaks in the emission spectra where compared to the emission spectra measured in the DC microplasma jet [10], radio frequency plasma [15] and dielectric barrier discharge (DBD) $CH_4$ plasmas [16]. Despite the fact that the intensities of hydrogen peaks are quite low in the measured emission spectra, it didn‘t induced any difficulties to compare it with other works. It was found that the peaks of $H_\alpha$, $H_\beta$ and $H_\gamma$ are situated at the same wavelength of 656.2 nm, 486.1 nm and 434.1 nm, respectively. The peaks of Ar I (565.0 nm), Ar I (603.2 nm) and Cu I (510.5 nm) are also in a good agreement. But, none references have reported on OES applied for plasmas generated by DC electric arc discharge. Lack of information in the literature disables the comparison of results between the same technologies used.

Therefore, the performed emission spectra measurements confirmed that water vapour was decomposed into H, O and OH radicals by high voltage DC electric arc. Beside these important groups of spectral lines, the spectrum contains a large number of other lines with variable intensities, making the plasma emission spectrum rather complicated.

## 4. CONCLUSIONS

The OES has been used to study the emission spectra of Ar/water vapour plasma generated by DC plasma torch at atmospheric pressure. The performed optical emission spectra measurements of the Ar/water vapour plasma jet by means of AOS4-1 spectrometer confirmed that water vapour was decomposed into H, O and OH radicals by high voltage DC electric arc. Beside these important groups, the emission spectrum contains other emission lines such as Ar (I), Ar (II), Cu (I) and Cu (II).

The emission intensities of obtained species were sensitive to the changes in the flow rate of water vapour and the power of the plasma torch. The spectra also showed the peaks of $H_\alpha$ (656.2 nm), $H_\beta$ (486.1 nm) and $H_\gamma$ (434.1 nm), which belong to the Balmer series describing the spectral line emissions of the hydrogen atoms.

## REFERENCES

1. MOUSTAKAS, K., FATTA D., MALAMIS S., HARALAMBOUS K., LOIZIDOU M. Demonstration plasma gasification/vitrification system for effective hazardous waste treatment. *Journal of Hazardous Materials*, 2005, No. B123, p. 120–126.
2. VAN OOST, G., HRABOVSKY, M., KOPECKY, V., KONRAD, M., HLINA, M., KAVKA, T. Pyrolysis/gasification of biomass for synthetic fuel production using a hybrid gas-water stabilized plasma torch. *Vacuum*, 2009, No. 83, p. 209–212.
3. VAN OOST, G., HRABOVSKY, M., KOPECKY, V., KONRAD, M., HLINA, M., KAVKA, T., CHUMAK, A., BEECKMAN, E., VERSTRATEN, J. Pyrolysis of waste using hybrid argon-water stabilized torch. *Vacuum*, 2006, No. 80, p. 1132–1137.
4. NISHIKAWA, H., MASAAKI, I., TANAKA, M., TAKEMOTO, T., USHIO, M. Effect of DC steam plasma on gasifying carbonized waste. *Vacuum*, 2006, No. 80, p. 1311–1315.
5. WATANABE, T., TSURU, T. Water plasma generation under atmospheric pressure for HFC destruction. *Thin Solid Films*, 2008, No. 516, p. 4391–4396.
6. KIM, D. Y., PARK, D. W. Decomposition of PFCs by steam plasma at atmospheric pressure. *Surface and Coatings Technology*, 2008, No. 202, p. 5280–5283.
7. ODA, T. Non-thermal plasma processing for environmental protection: decomposition of dilute VOCs in air. *Journal of Electrostatics*, 2003, No. 57, p. 293–311.
8. LAUX, C.O., SPENCE, T.G., KRUGER, C.H., ZARE, R.N. Optical diagnostics of atmospheric pressure air plasmas. *Journal of Plasma Sources Science and Technology*, 2003, No. 12, p. 125–138.
9. BROEKAERT, Jose A. C. *Analytical Atomic Spectroscopy with Flames and Plasmas*. Wiley-VCH Verlag GmbH & Co, 2002. 347 p. ISBN 3-527-60062-0.
10. SISMANOGLU, B.N., AMORIM, J., SOUZA-CORREA, J.A., OLIVEIRA, C., GOMES, M.P. Optical emission spectroscopy diagnostics of an atmospheric pressure direct current microplasma jet. *Spectrochimica Acta Part B*, 2009, No. 64, p. 1287–1293.
11. MACHALA, Z., JANDA, M., HENSEL, K., JEDLOVSKY, I., LEŠTINSKA, L., FOLTIN, V., MARTIŠOVITŠ, V., MORVOVA, M. Emission spectroscopy of atmospheric pressure plasmas for bio-medical and environmental applications. *Journal of Molecular Spectroscopy*, 2007, No. 243, p. 194–201.
12. KIM, J. H., KIM, Y. H., CHOI, Y. H., CHOE, W., CHOI, J. J., HWANG, Y. S. Optical measurements of gas temperatures in atmospheric pressure RF cold plasmas. *Surface and Coatings Technology*, 2003, No. 171, p. 211–-215.

13. JAMROZ, P., ZYRICKI, W. Optical emission spectroscopy study for nitrogen-acetylene-argon and nitrogen-acetylene-helium 100 kHz and dc discharges. *Vacuum*, 2010, No. 84, p. 940–946.
14. ZHUKOV, M. F; ZASYPKIN, I. M. *Thermal Plasma Torches: Design, Characteristics, Applications*. Cambridge International Science Publishing Ltd, 2007. 600 p. ISBN-13: 978-1-904602-02-6.
15. MILLS, R. L., DHANDAPANI, B., ARHTAR, K. Excessive Balmer α broadening in capacitively coupled rf water-plasmas. *Journal of Hydrogen Energy*, 2008, No. 33, p. 802–815.
16. LIU, D., XU, Y., YANG, X., YU, SH., SUN, Q., ZHU, A., MA, T. Diagnostics of dielectric barrier discharge $CH_4$ plasmas for diamond-like carbon film deposition. *Diamond and Related Materials*, 2002, No. 11, p. 1491–1495.

CYSENI 2011, May 26–27, Kaunas, Lithuania
ISSN 1822-7554, www.cyseni.com

# LCA-BASED COMPARISON OF SIMULTANEOUS $SO_2$ AND $NO_X$ REMOVAL FROM FLUE GAS BY PLASMA AND CONVENTIONAL END-OF-PIPE METHODS

**V. Abromaitis, V. Ochmanaitė, G. Denafas, D. Martuzevičius**
*Department of Environmental Engineering*
*Faculty of Chemical Technology*
*Kaunas University of Technology*
*Radvilėnų road 19, C-505, LT-50254 Kaunas – Lithuania*
*Phone: +370 37 351008*
*Email: daimart@ktu.lt*

## ABSTRACT

The number of experimental and industrial applications of non-thermal plasmas for environmental pollution control is rapidly growing. The simultaneous removal of $SO_2$ and $NO_x$ from flue gas is usually expensive process which requires substantial investments and usage of the large-scale equipment. Generally, conventional end-of-pipe techniques such as wet scrubbing with integrated catalytic reduction device are employed for the removal of $SO_2$ and $NO_x$ from flue gas. In turn, plasma-based Electron Beam Flue Gas Treatment (EBFGT) technology, based on electron beam irradiation was proved to be highly efficient and capable in destruction of $SO_2$ and $NO_x$. The environmental performance of both technologies were compared by life cycle analysis (LCA), which took into account the usage of materials, waste generation and energy consumption. The EBFGT technology was superior with respect acidification and human toxicity potential, but was less favourable with respect to global warming potential, eutrophication potential and ozone layer depletion.

Keywords: Non-thermal plasma, EBFGT, Flue gas, Life cycle assessment.

## 1. INTRODUCTION

Plasmas (both thermal and non-thermal) are employed for various environmental applications. These applications mostly include fields of air pollutant treatment, wastewater and drinking water decontamination, and thermal disposal of solid waste. The non-thermal plasmas used for environmental applications are mainly high-pressure discharges [1]. An increasing number of investigations are devoted to the decomposition of nitrogen and sulphur oxides in flue gases, emanating from various industrial processes, especially energy sector. Electron beam flue gas treatment (EBFGT) technology is a dry-scrubbing process of simultaneous $SO_2$ and $NO_x$ removal, where irradiation of stack gases with an electron beam induce chemical reactions that make removal of $SO_2$ and $NO_x$ easier [2].

Among the conventional technologies for flue gas treatment aimed at $SO_2$ and $NO_x$ emission control are wet, dry and semi-dry flue gas desulphurization (FGD) and selective catalytic reduction (SCR). Basically, the main additives used for the flue gas desulfurization are lime and limestone, while the selective catalytic reduction process uses ammonia as a supplement. Generally, for flue gas treatment, FGD and SCR are used in separate ways, thus, relatively high pollutant removal efficiencies can be achieved. Combined $SO_2$/$NO_x$ removal processes are considered as fairly complex and costly.

Plasma-related processes are usually associated with high energy demand, thus raising a question regarding their overall environmental performance through the entire life cycle. The eco-efficiency of the plasma and non-plasma exhaust treatment technologies may be compared by means of life cycle assessment (LCA) tool. LCA is an environmental assessment methodology that considers the entire life cycle of a product or technology, from raw material extraction and acquisition, through energy and material production and manufacturing, to use and end of life treatment and final disposal. Life cycle assessment is an iterative technique. The individual phases of a LCA use results of the other phases. The iterative approach within and between the phases contributes to the comprehensiveness and consistency of the study and the reported results [3].

The aim of this study was to carry out preliminary assessment of plasma-based and “conventional” end of pipe technologies for the treatment of combustion exhausts. Particularly, electron beam flue gas treatment and wet flue gas desulphurization plus selective catalytic reduction were compared by the life cycle assessment technique.

## 2. METHODS

### 2.1. Electron Beam Flue Gas Treatment

Electron beam flue gas treatment (EBFGT) technology is a non-equilibrium plasma process. It is based on the principle that the energy of incident electron beam is absorbed by components of stack gas in proportion to their mass fraction. The main components of stack gas are $N_2$, $O_2$, $H_2O$ and $CO_2$, with much lower concentration of $SO_2$ and $NO_x$. Electron energy is consumed in the ionization, excitation and dissociation of the molecules and finally in the formation of active free radicals - *OH, $HO_2$*, O, N and H. These radicals oxidize $SO_2$ and NO to $SO_3$ and $NO_2$ which in reaction with water vapour, present in the stack gas, form $H_2SO_4$ and $HNO_3$, respectively. These acids subsequently react with added ammonia (injected to the stack gas before its inlet to the process vessel) to form ammonium sulphate ($(NH_4)_2SO_4$) and ammonium sulphate-nitrate ($(NH_4)_3(SO_4)(NO_3)$). These salts are recovered as a dry powder using a conventional particle collector. The collected powder can be marketed as an agricultural fertilizer or as a component of the commercial nitrogen, phosphorus, potassium (NPK) or nitrogen, phosphorus, potassium, sulphur (NPKS) fertilizers [2].

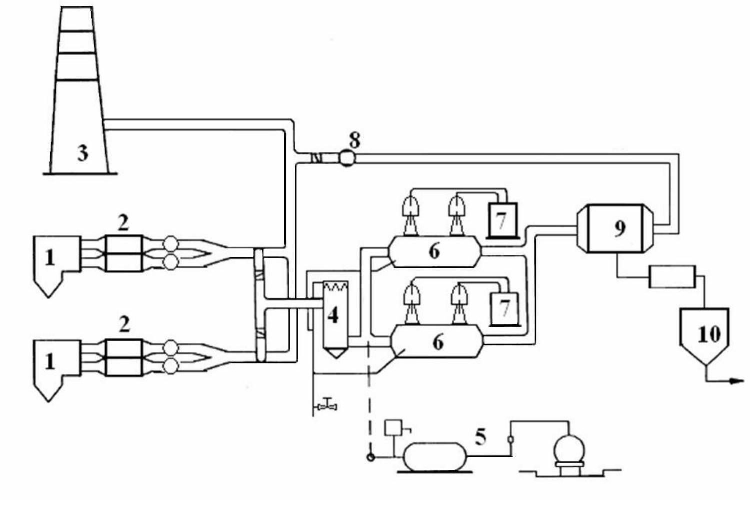

Fig. 1. Scheme of industrial EBFGT plant: 1 – Boilers, 2 – Electrostatic precipitator (ESP) for particulate matter, 3 – Stack, 4 – Spray cooler, 5 – Ammonia storage and dosing unit, 6 – Irradiation, 7 – Electron beam accelerators, 8 – Auxiliary fan, 9 – ESP for fertilizers, 10 – Fertilizer bunker [2]

A scheme of an industrial plant is shown in Fig. 1. The main components of industrial EBFGT plant are: flue gas conditioning system, reaction unit, ammonia storage and dosing system, by-product collecting and storage system.

## 2.2. Wet Flue Gas Desulphurization and Selective Catalytic Reduction

Wet FGD technology is a simultaneous $NO_x/SO_x$ removal process, which is based on using limestone or lime as a reagent. It is a wet scrubbing process and has been the FGD technology most frequently selected for sulphur dioxide ($SO_2$) reduction from coal-fired utility boilers [4]. Typical scheme of coal-fired power plant with integrated wet limestone FGD and SCR modules is shown in Fig. 2.

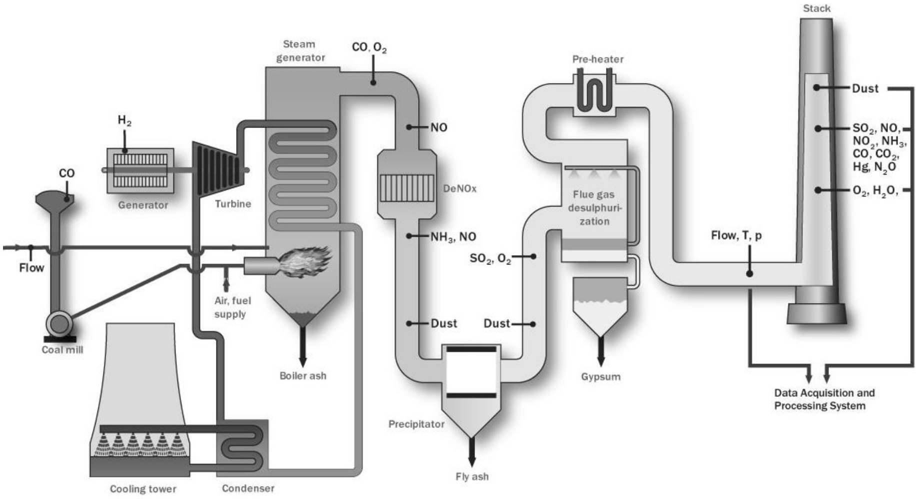

Fig. 2. Coal-fired power plant with integrated flue gas treatment system: wet limestone FGD and SCR devices [5]

The Wet FGD system is typically located after a baghouse or an electrostatic precipitator employed for the removal of particulate matter from flue gas. The treated exhaust gas is discharged to the stack. The gaseous pollutants such as $SO_2$ are solved in the liquid and react with the liquid to form calcium sulphite or sulphates which are removed by dewatering and settling into a thickener [4].

In the SCR process, $NH_3$ is injected into the flue gas within a temperature range of about 588 to 673 K, upstream of a catalyst. Subsequently, as the flue gas contacts the SCR catalyst, NOx, which predominantly is NO in combustion devices, is chemically reduced to nitrogen. Any unreacted $NH_3$ released from the SCR system, known as $NH_3$ slip, is undesirable because it may combine with sulphur dioxide ($SO_2$) and sulphur trioxide ($SO_3$) in the flue gas to generate ammonium sulphate and bisulphate compounds that may cause fouling of downstream equipment, especially the air preheater [6].

## 2.3. Life Cycle Assessment methodology

### *2.3.1. Goal and scope definition*

The scope of this study was to compare two different flue gas treatment technologies: Electron beam flue gas treatment and Wet flue gas desulphurization with integrated selective catalytic reduction module. The technologies were assumed to be installed in coal-fired boilers. The functional unit was set as 1000 $Nm^3$ of treated flue gases, that is, all inputs and outputs of the processes were normalized to the above quantity of exhaust gas. This was done in purpose to normalize the obtained operational data and to make an adequate comparison of these technologies. The initial concentration of pollutants in exhaust gas was selected equal. The remaining concentrations after treatment were considered as potential impact factors and evaluated during LCA modelling.

### *2.3.2. System boundaries*

The qualitative and quantitative data for inclusion in the inventory should be collected for each unit process that is included within the system boundary. The collected data, whether measured, calculated or estimated, are utilized to quantify the inputs and outputs of a unit process [7].

In this study system boundary was set to the processes of the flue gas treatment technologies. The materials needed for transportation of supplements and by-product elimination were not included due to the extensive amount of data. Moreover, the materials used for manufacturing the flue gas treatment devices were not evaluated too. The main attention was paid to process material consumption, energy (electricity), emissions to atmosphere and deposition of by-products. System boundaries and input/output flow schemes are represented in Fig. 3.

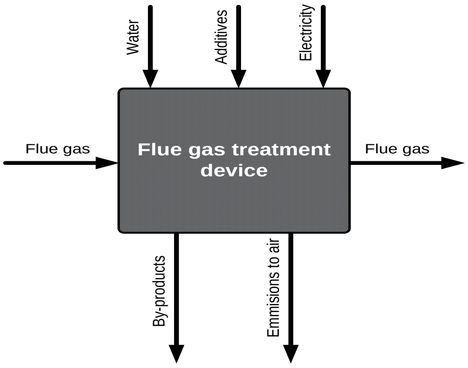

Fig. 3. System input/output flow scheme in a flue gas treatment device

### *2.3.3. Inventory analysis*

The data, obtained for LCA of flue gas treatment technologies, were collected using special made-up technological questionnaires, which were sent to PlasTEP project and industrial companies. The questionnaires consist of 2 chapters: general information, and engineering data. The first chapter included the information of main parameters (technology scale, its application, flue gas rate, temperature, equipment capacity, plant availability etc.) The data about energy and raw materials consumption, by-products formation, treatment efficiency and pollutant input/output flows were characterised in engineering section.

### *2.3.4. Impact characterization*

Based on similar studies [8, 9], the 5 main impact categories were chosen for evaluation: global warming (GW), ozone layer depletion (OD), acidification (AC), euthrophication (EU) and human toxicity (HT), based on the CML2001 method [10]. GaBi software (Version 4, PE international) equipped with Eco-invent database was employed for modelling process.

## 3. RESULTS

### 3.1. Inventory analysis

Inventory analysis was performed using particular questionnaires. The collected data were normalized – the flue gases flows and pollutant concentrations, entering the process, were equalised. The data, used for life cycle assessment of EBFGT and Wet FGD + SCR, are listed below, in Table 1.

Table 1. Normalised data for LCA

| **Parameter** | | **Flue gas treatment method** | |
|---|---|---|---|
| | | **EBFGT** | **Wet FGD + SCR** |
| **Inlets** | | | |
| $SO_2$ | kg | 1.172 | 1.172 |
| $NO_x$ | kg | 0.521 | 0.521 |
| **Outlets** | | | |
| $SO_2$ | kg | 0.023 | 0.117 |
| $NO_x$ | kg | 0.156 | 0.156 |
| **Removal efficiency** | | | |
| $SO_2$ | % | 98 | 90 |
| $NO_x$ | % | 70 | 70 |
| **Additive** | | | |
| Ammonia (solution) | kg | 1.577 | 0.209 |
| Limestone | kg | – | 1.795 |
| Water | l | 15.000 | 7.179 |
| **Power** | | | |
| Power | kWh | 6.67 | 3.27 |
| **By-product** | | | |
| Ammonia salts | kg | 2.014 | – |
| Wastewater | kg | – | 1.026 |
| Gypsum | kg | – | 3.088 |
| $NH_3$ | kg | 0.102 | 0.00418 |
| Water steam | kg | – | 6.154 |

From the data presented in the Table 1, it may be concluded that the ammonia consumption in the EBFGT device is 7.5 times higher compared to the SCR unit. At the same time, it was estimated that the unreacted ammonia emissions with the flue gas from the EBFGT process will comprise 102 g/1000Nm$^3$ of treated flue gas, while in SCR it is 0.4 g. The consumption of water is also higher at EBFGT device (approximately 2 times) than in Wet FGD. In turn, the wet FGD process requires limestone to react with $SO_2$, forming gypsum. The flow of limestone is 1.795 kg/1000Nm$^3$ of treated flue gas.

The by-products forming during the flue gas treatment process depend on the input materials and process chemistry. EBFGT is a dry process, with the main focus of converting $SO_2$ and $NO_x$ to ammonium fertilizers, with the help of $NH_3$. The amount of ammonia salts is equal to 2.014 kg/1000Nm$^3$ of treated flue gas. At the Wet FGD unit, usually, gypsum and wastewater form. The amounts of gypsum and wastewater, estimated at this study, are 3.088 kg and 1.026 kg per 1000Nm$^3$ of treated flue gas, respectively.

## 3.2. Impact characterization

With respect to the global warming potential, EBFGT technology showed higher overall emission of $CO_2$ equivalents, compared to the Wet FGD+SCR process (7.4 vs. 2.5 kg $CO_2$ equiv., Fig. 4). In case of EBFGT, both energy and materials consumption contributed almost equally to the emission of $CO_2$ equivalent. The contribution from energy is equivalent to electricity consumption in both technologies. The higher emission of $CO_2$ equivalent in case materials in EBFGT is caused by the higher usage of ammonia. In case of Wet FGD+SCR, in addition to ammonia, the usage of zeolite had a minor contribution to the global warming potential (0.2 kg $CO_2$ equiv.)

The ozone depletion potential also reflects similar patterns to the global warming potential. The EBFGT shows higher Ozone depletion potential, compared to the Wet FGD+SCR process ($6.0 \cdot 10^{-7}$ vs. $1.3 \cdot 10^{-7}$ kg Freon-11(R11) equiv.) The main difference with a favour to Wet FGD+SCR process is caused by material consumption portion, namely usage of ammonia. In case of wet FGD+SCR, minor contributions are of usage of zeolite and limestone.

With respect to acidification potential, the disposal of gypsum formed in case of wet FGD+SCR process determines the fact that Wet FGD+SCR technology causes much more substantial impact to the environment (511.3 vs. 0.2 kg $SO_2$ equiv.). This is valid in the system boundaries researched here. On the other hand, it was assumed that the formed gypsum will be disposed, that is, permanently stored in a special landfill. This is the most expected option, since the gypsum formed in treatment process of flue gas is contaminated with other pollutants, such as heavy metals. It must be noted that in EBFGT process the formed ammonium salts (sulphate and nitrate) are utilized as fertilizers, thus no potential impact was estimated.

In case of eutrophication potential, the release of ammonia plays major role, determining the overall environmental impact and causing EBFGT to make almost twice higher environmental impact (0.043 vs. 0.022 kg phosphate equiv.). Electricity and material consumption had only a minor contribution.

Human toxicity potential, similarly to acidification potential, was present in case of wet FGD+SCR, while for the EBFGT is was >1000 times lower (5.6 vs. 7581.7 kg Dichlorobenzene (DCB) equiv.).

It must be noted that several important steps in comparison of the two flue gas treatment technologies were omitted. First of these includes evaluating resources needed for the manufacturing of process enclosures. Another step is evaluating the advantage of EBFGT in removal other pollutants, such as volatile organic compounds (VOC's) and Hg (in case of coal combustion). On the other hand, the mechanism of the processes with VOC's and total organic compounds (TOC) in gas during Wet FGD+SCR process is not researched, thus inventory data may be difficult to obtain.

## 4. CONCLUSIONS

The preliminary calculations have revealed that EBFGT performed better from the environmental impact viewpoint with respect to acidification and human toxicity potential, but the Wet FGD and SCR technology was more favourable from the global warming potential, ozone layer depletion and eutrophication potential. Most of the impacts were associated with the utilization of ammonia in both processes. In addition, formation and deposition of gypsum sludge scored low in case of Wet FGD and SCR technology, while the formation of ammonium salts on EBFGT process is controlled in a way that the formed materials are utilized as fertilizers.

Further research directions should include more detailed estimations of process inputs and outputs, and estimation of model uncertainties.

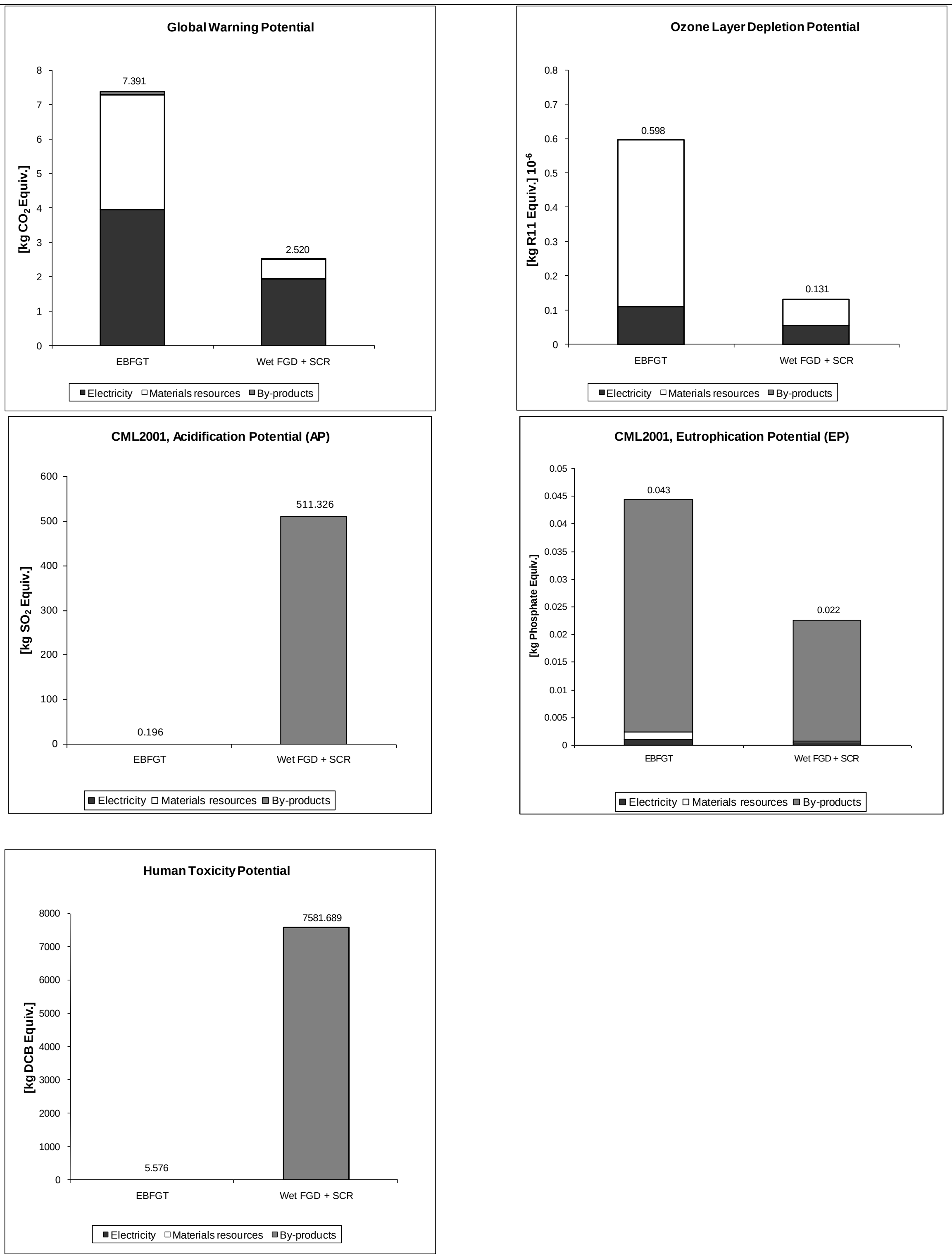

Fig. 4. Comparison of environmental impacts of EBFGT and Wet FGD + SCR technologies

## ACKNOWLEDGEMENTS

The study was part-financed by the European Regional Development Fund, Baltic Sea Region programme 2007–2013 (project No 033, “Dissemination and Fostering of Plasma

Based Technological Innovation for Environment Protection in The Baltic Sea Region”, PlasTEP).

## REFERENCES

1. BOGAERTS A., NEYTS E., GIJBELS R., MULLEN J. *Gas discharge plasmas and their applications.* Spectrochimica Acta Part B, 2002, 57, p. 609–658.
2. CALINESCU I., IGHIGEANU D., MARTIN D., BULEARCA A. *Electron beam technologies for reducing* $SO_2$ *and* $NO_x$ *emissions from thermal power plants*. WEC regional energy forum – Foren 2008.
3. ISO 14040:2006. Environmental management – Life cycle assessment – Principles and framework.
4. GAIKWAD R., BOWARD W. L. *Wet flue gas desulfurization technology evaluation*. Sargent and Lundy, LLC, 2007, prepared for National Lime Association, project number: 11311-000.
5. Power station, SICK Sensor Intelligence. Clean energy production by intelligent analysis, retrieved on October, 2010, from http://www.sick.com/group/en/home/solutions/industries/power_plant/pages/power.aspx
6. FOERTER D., JOZEWICZ W. *Cost of Selective Catalytic reduction (SCR) application for* $NO_x$ *control on Coal-fired boilers*, U.S. Environmental protection agency office of research and development, 2001, EPA-600/R-01-087.
7. ISO 14044:2006. Environmental management – Life cycle assessment – Requirements and guidelines.
8. Society of Environmental Toxicology and Chemistry (SETAC): Guidelines for Life-Cycle Assessment, A "Code of Practice"; SETAC Workshop in Sesimbra 31.03.-03.04.1993, Brüssel, 1993.
9. CADENA, E., COLON, J., ARTOLA, A., SÁNCHEZ, A., and FONT, X. *Environmental impact of two aerobic composting technologies using life cycle assessment*. The International Journal of Life Cycle Assessment, 2009, 14, p. 401–410.
10. Institute of Environmental Sciences, Leiden University, The Netherlands: Handbook on impact categories "CML 2001".

CYSENI 2011, May 26–27, Kaunas, Lithuania
ISSN 1822-7554, www.cyseni.com

# INVENTORY ANALYSIS FOR LIFE CYCLE ASSESSMENT OF $CO_2$ BINDING BY MINERAL CARBONATION

**A. Babarskaitė, I. Stasiulaitienė, D. Martuzevičius**
*Kaunas University of Technology*
*Radvilėnų pl. 19, LT-50254 Kaunas – Lithuania*
*Phone +370 624 50617*
*Email: agnes.babarskaites@gmail.com*

## ABSTRACT

Carbon dioxide ($CO_2$) capture and storage (CCS) is considered to be one of the main options for reducing $CO_2$ emissions caused by human activities. Mineral carbonation, i.e. $CO_2$ trapping by suitable minerals forming carbonates, could be used as one of the CCS techniques. Such process is more attractive for the countries where more mature techniques to store $CO_2$ (i.e. underground or ocean storage) are unavailable. Advantages of mineral carbonation process include the worldwide abundance of suitable silicate minerals, no need of post-storage monitoring and exothermic overall process.

In order to implement mineral carbonation to an industrial scale process, the environmental and economic aspects must be considered. The environmental impact assessment of the mineral carbonation process must be carried out in order to evaluate the overall environmental performance. This paper describes the inventory analysis of life-cycle assessment (LCA) of the mineral carbonation of $CO_2$. The main issues associated with this process are consumption of energy and release of secondary $CO_2$ during energy production. As a case study, the retrieval of serpentinites distributed in the southeastern part of Lithuania within the Varena geological province of the East Lithuanian domain as potential $CO_2$ binders were analyzed. The modeling scenarios have been designed based on the excavation depth, transporting distance as well as various carbonation process related parameters. Several approaches of setting process boundaries and functional unit are discussed.

Keywords: carbon dioxide, mineral carbonation, storage, life cycle assessment, functional unit, inventory analysis, serpentinite.

## 1. INTRODUCTION

Through the millions of years the temperature of the Earth has constantly varied. At the same time global warming of the recent 50 years is considered to be sudden and it is explained as the intensification of human activities. Carbon dioxide ($CO_2$) has made the greatest impact on the global warming of the all greenhouse gases produced through human activities. The highest amount of $CO_2$ is released by fossil fuels burning.

Some of the changes, at least partly linked to global warming, today is observed both in human life as well as in the wild. These changes such as melting of mountain glaciers, rising of sea level and the amount and pattern of precipitation, may follow, along with increases in the frequency and intensity of extreme weather events [1].

In order to reduce the effects of global warming some measures have been offered. Some of those are already implemented such as limitation of carbon emissions, carbon taxes, renewable energy, use of electric or hybrid cars and others. Carbon dioxide capture and storage occupy an important place among these methods. Since $CO_2$ can remain in the atmosphere for a long time, even if the level of emissions were stabilized, its concentration would continue to grow [2]. The scientists of Canadian Climate Modeling and Analysis Center analysis show that even if carbon dioxide emissions now are totally suspended, the amounts of these gases, that is in the atmosphere, would affect our climate for 1.000 years more [3]. Therefore, it is important to gather as much information as possible about all the

$CO_2$ emissions to the atmosphere and the removal by long-term isolation techniques. One of these methods, which can be applied in Lithuania, is the mineral carbonation. It is considered as one of the most feasible option for storing captured $CO_2$ inside the country. According to the National GHG emission inventory report 2011 of the Republic of Lithuania [4] during 2009, 5.8 Mt of $CO_2$ were emitted in industry sector. Approx 66% of this amount are produced in the 4 biggest installations in Lithuania: JSC "Orlen Lithuania", JSC "Lietuvos elektrinė", JSC "Akmenės cementas" and JSC "Kauno termofikacijos elektrinė" (Fig. 1). These companies are about 100–300 km away from serpentinite extraction site, thus $CO_2$ may be transported by pipelines, which are implemented for natural gas transportation. From the literature review is known that the transportation of $CO_2$ by pipelines is proven, cost-effective technology [5]. Also, there is a high degree of experience in this field, especially in USA and Canada.

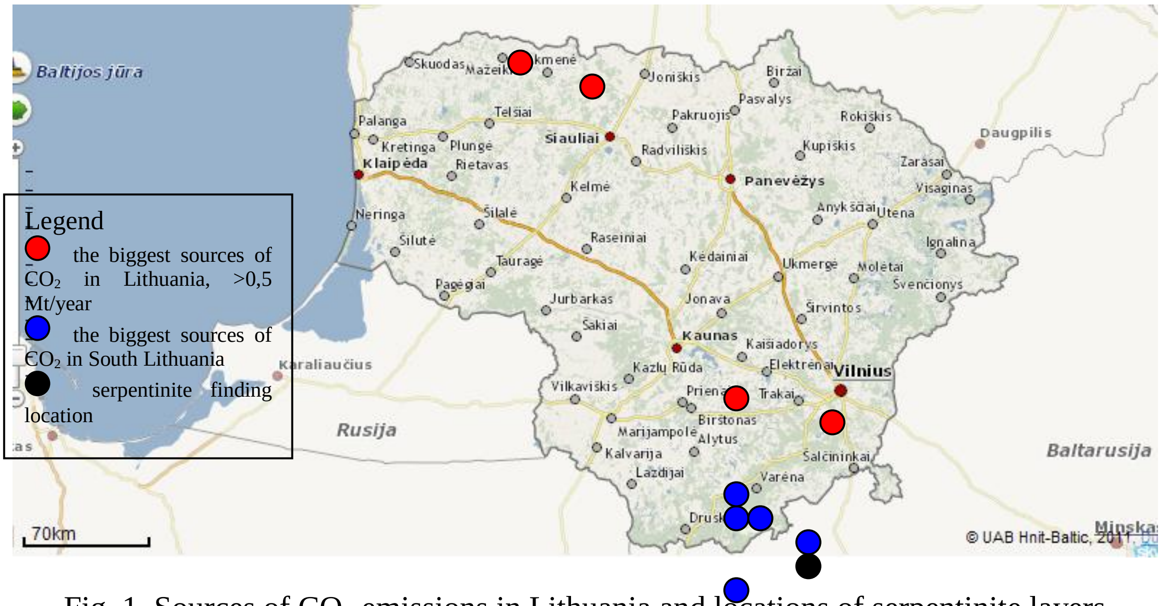

Fig. 1. Sources of $CO_2$ emissions in Lithuania and locations of serpentinite layers

According to the *IPCC report (2005)* mineral carbonation is „the fixation of $CO_2$ using alkaline and alkaline-earth oxides, such as magnesium oxide (MgO) and calcium oxide (CaO), which are present in naturally occurring silicate rocks such as serpentine and olivine“ [6]. One of these rocks – serpentines – is found in southern Lithuania. To determine the overall environmental efficiency of the process it is necessary to assess this process according to life-cycle methodology. This paper focuses on the initial and the most important step - inventory analysis – of the overall environmental assessment according to life-cycle methodology. The reliability of the data which are presented in this step plays a significant role in LCA. For this reason particular attention was paid to collection of data and it was carried out on the basis of concrete works done in this sphere.

## METHODOLOGY

The methodology used in this study is the Life Cycle Assessment (LCA) technique based on the ISO 14040 (International Organization for Standardization (ISO), 1997) [7] series of standards. LCA is an environmental management tool that enables quantification of environmental burdens and their potential impacts over the whole life cycle of a product, process or activity. LCA is mostly performed for products, but increasingly it assess various processes, which could have negative influence for the environment. According to the ISO standard 14 040, LCA is divided into four main phases: goal and scope definition, inventory analysis, impact assessment, and interpretation.

This paper describes one phase of the LCA – inventory analysis (LCIA) for mineral carbonation process. The data gathered for the LCIA were taken from the ref. [8] and are annual. The last stage of the whole CCS process, i.e. the storage of $CO_2$ is researched. The capture process and the transport of $CO_2$ are herewith not modeled, so it is located outside the system boundary. The capture process delivers $CO_2$ in a defined physical state. The compression of $CO_2$ is assumed to take place at the power plant therefore it is not defined as a part of the transport and storage system. The central point is the energy and material requirements associated with storage processes. Fig. 2 shows a simplified schematic view with the system boundary and the inputs of interests from outside.

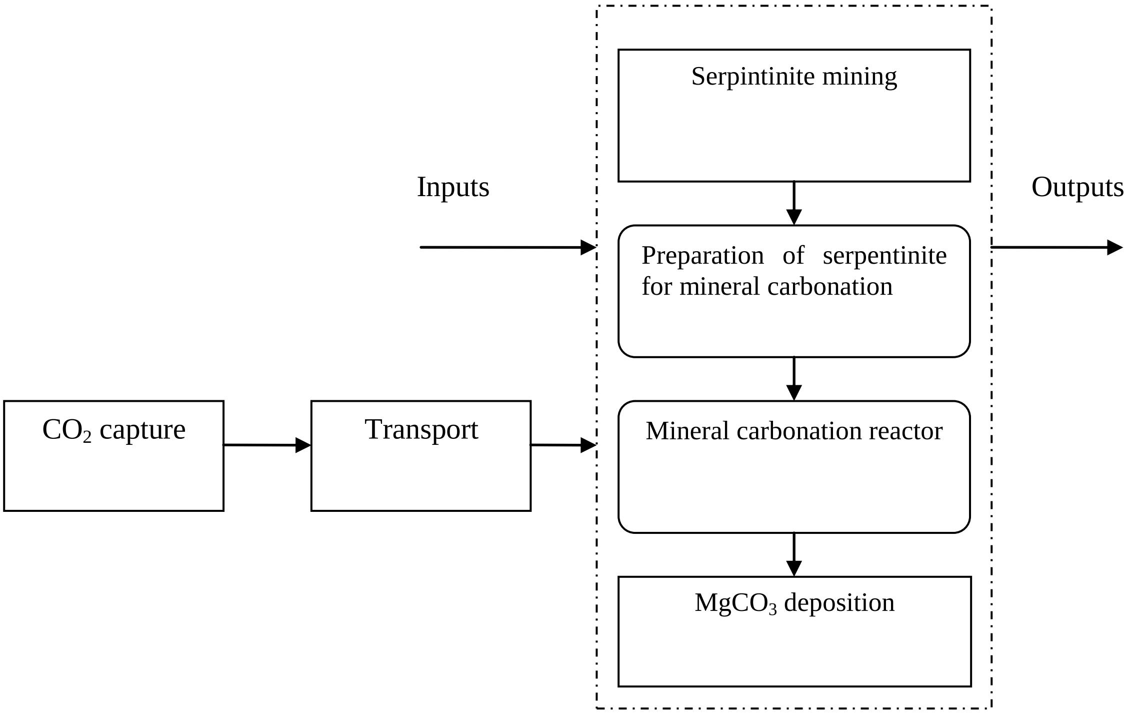

Fig. 2. Principal scheme of the CCS process including system boundaries for LCI analysis

The research of the inventory analysis is divided into identification of the materials and energy flows associated with the following processes:

1. mining activities;
2. preparation of serpentinite for mineral carbonation;
3. mineral carbonation process;
4. transportation of magnesium carbonate to the storage site.

## 3. RESULTS AND DISCUSSION

### 3.1. Identification of materials and energy flows in serpentinite mining processes

This sub-chapter consists of the description of the mining and mineral processing operations. The following processes have been associated with mining of minerals: drilling, blasting, ventilation, dewatering, auxiliary equipment, crushing and grinding processes [8].

Serpentinites are covered by 280–500 m [9] thick platform sediments and the depth of it layers varies from 360 m to 1–1.5 km [10]. Therefore, underground mining technique was chosen. As seen in the Table 1 this technique requires more energy than surface mining with respect to greater requirements for ventilation, hauling, drilling and other operations. It was assumed that copper ore underground mining could be equate to serpentinite used in this study mining [11].

Drilling is the process of making a cylindrical hole with a tool for the purpose of exploration, blasting preparation, or tunneling. Drilling equipment includes explosive loader trucks, diamond drills, rotary drills, percussion drills and drill boom jumbos. Drills are run from electricity, diesel power and to a lesser extent, indirectly from compressed air. The energy is used to power components of the drill that perform tasks such as hammering and rotation. Drilling process requires 0.7 kg diesel for 1 tonne of extracted mineral.

Blasting uses explosives to aid in the extraction or removal of mined material by fracturing rock and ore by the energy released during the blast. The energy consumed in the blasting process is derived from the chemical energy contained in the blasting agents. This sets blasting apart from other processes, which are powered by traditional energy sources, such as electricity and diesel fuel. Blasting process rerquires 0.1 kg of diesel for 1 tonne of extracted mineral. A common explosive used for mining is ammonium nitrate/fuel oil mixture, which amount for 1 tonne of extracted mineral are 0.4 kg. The powder factor is the amount of explosives used per unit of rock blasted, and varies depending on the rock type and strength.  The blast holes are detonated with a nonel (non-electric) device for firing. Blasting frees ore from the host rock and reduces the size of ore before it undergoes crushing and grinding, thereby reducing the energy consumption of crushing and grinding processes. Optimising blasting techniques will therefore produce downstream energy savings.

Ventilation is the process of bringing fresh air to the underground mine workings while removing stale and/or contaminated air from the mine and also for cooling work areas in deep underground mines. The mine ventilation system consists of fans, airways (openings to surface and interconnections in the mine between the openings through the working areas), and control devices for air coursing [12]. The common amount of used electricity for those devices are assumed as 8 kWh/t mineral.

Dewatering is the process of pumping water from the mine workings. Pumping systems are large energy consumers. This study assumes that centrifugal pumps are used for dewatering the mine during ore extraction. It was assumed that pumping system requires 3.8 kWh electricity for 1 tonne of extracted mineral.

On most mine sites, there is other equipment such as dozers, graders, excavators and water tankers. They are used for road construction, maintenance and dust suppression within the mine site. It is assumed that these units use diesel fuel for their operation.

Crushing is the process of reducing the size of run-of-mine material into coarse particles (typically coarser than 5 mm). The efficiency of crushing in mining depends on a number of factors including the efficiency of upstream processes (rock fragmentation due to blasting or digging in the extraction process) that in turn, has a significant effect on downstream processes (grinding or separations).

Grinding is the process of reducing the size of material into fine particles (often below 0.1 mm or 100 mm). As with crushing, the efficiency of grinding is influenced by upstream processes that fragment the rock prior to the grinding stage. In the case of both crushing and grinding, estimates of their energy efficiency in the literature vary widely, with energy efficiencies as low as 1% being reported for grinding. Crushing and grinding plants are usually powered by electric motors, with the electricity often generated onsite using a diesel fuel-based engine and generator. Crushing plants can include primary, secondary and tertiary crushers, while grinding plants can include rod and ball mills.

Crushing and grinding processes consumed 18.5 kWh electricity for 1 tonne of extracted mineral.

Table 1. Inventory data for mining and mineral processing operations used in study [8]

| Ore mined | Mining method | Stage | Inventory | | |
|---|---|---|---|---|---|
| | | | Item | Value | Units |
| Iron ore | Open-cut | Drilling | Diesel | 0.03 | kg/t ore |
| | | Blasting | Explosives[a] | 0.5 | kg/t ore |
| | | Loading and hauling | Diesel | 2.2 | kg/t ore |
| | | Crushing and screening | Electricity | 2.5 | kWh/t ore |
| | | Stacking and reclaiming | Electricity | 0,5 | kWh/t ore |
| | | Rail transport | Diesel | 0.5 | kg/t ore |
| | | Port operations[b] | Electricity | 0.8 | kWh/t ore |
| | | Overall | Water | 0.21 | $m^3$/t ore |
| | | | Diesel[c] | 3.4 | kg/t ore |
| | | | | 135 | MJ/t ore |
| | | | Electricity | 3.8 | kWh/t ore |
| | | | Explosives | 0.5 | kg/t ore |
| | | | Waste rock | 1.3 | t/t ore |
| Copper ore | Underground | Drilling | Diesel | 0.7 | kg/t ore |
| | | Blasting | Diesel | 0.1 | kg/t ore |
| | | | Explosives[a] | 0.4 | kg/t ore |
| | | Loading and hauling | Diesel | 2.0 | kg/t ore |
| | | Ventilation | Electricity | 8 | kWh/t ore |
| | | Dewatering | Electricity | 3.8 | kWh/t ore |
| | | Crushing and grinding | Electricity | 18.5 | kWh/t ore |
| | | Concentrating | Copper ore[f] | 16.2 | t ore/ t concentrate |
| | | | Electricity | 7.5 | kWh/t ore |
| | | | Reagents[g] | 1.7 | kg/t ore |
| | | | Grinding media | 1.4 | kg/t ore |
| | | | Tailings | 37 | t/t concentrate |
| | | Overall | Copper ore | 16.2 | t ore/t concentrate |
| | | | Water | 0.51 | $m^3$/t ore |
| | | | Diesel | 2.8 | kg/t ore |
| | | | | 115 | MJ/t ore |
| | | | Electricity[h] | 46.4 | kWh/t ore |
| | | | Explosives | 0.4 | kg/t ore |
| | | | Reagents | 1.7 | kg/t ore |
| | | | Grinding media | 1.4 | kg/t ore |
| | | | Waste rock | 0.03 | t/t ore |
| | | | Tailings | 2.3 | t/t ore |

a Ammonium nitrate/fuel oil (ANFO) – 94% AN & 6% FO. Production of AN¼ 7.1 MJ/kg, 1.2 kg $CO_2$e/kg; ANFO¼ 6.6 MJ/kg, 1.4 kg $CO_2$e/kg.
b Includes train unloading, stacking, reclaiming & shiploading.
c Includes miscellaneous equipment 0.7 kg/t ore.
d Assumed same as for iron ore.
e Includes miscellaneous/auxillary equipment 0.1 kWh/t bauxite.
f Based on ore grade 1.8% copper, concentrate grade 27.3% copper, 93.7% copper recovery.
g Dependent on ore mineralogy - assumed to comprise 80% lime, 12% xanthate, 8% sodium cyanide.
h Includes miscellaneous/auxillary equipment for underground mining 8.6 kWh/t ore.

## 3.2. Preparation of serpentinite for mineral carbonation

Mineral carbonation mimics a natural rock weathering process, which is naturally very slow. There are various pre-treatment options for acceleration of this process. Generally pre-treatment stage consists of the following processes: size reduction, magnetic separation and thermal treatment.

In order to achieve a reasonable reaction rate the minerals have to be grinded [13]. The reaction rate increases with the surface area. Among others, O'Connor *et al.* examined the influence of the particle size on the conversion to $MgCO_3$. These authors found that a reduction from 106–150 μm to < 37 μm increased the conversion in their experiments from 10% to 90% [14]. Electricity consumptions for size reduction process of the mineral are 13 kWh/t extracted mineral.

The oxidation of iron (magnetite) slows down the carbonation of serpentine due to the formation of a layer of hematite on the mineral surface [15]. To execute the process in a non-oxidising atmosphere complicates the process and increases the costs significantly. Magnetic separation of the iron compounds prior to the carbonation process resolves this complication. Furthermore, a potentially marketable iron ore byproduct is formed.

When a combination of magnetic separation and thermal treatment is used, it is more effective first to conduct the magnetic treatment step.

Serpentine contains up to 13 wt% chemically-bound water. By heating the serpentine to 600–650°C the water is removed and an open structure is created [14]. This significantly improves the reaction kinetics owing to the increase reactive surface. For example heat-treatment of antigorite increased the surface areas from 8.5 $m^2/g$ to 18.7 $m^2/g$ [16].

All processes for mineral preparation require electricity as following: size reduction process – 13 kWh and thermal treatment –- 20–250 kWh for 1 tonne of mineral. Outputs of this process are Fe compounds from magnetic separation, also heat and water vapor from thermal treatment process.

### 3.3. Mineral carbonation process

There are two possible ways to carry out direct mineral carbonation process – aqueous and gas-solid carbonation. The latter method was chosen for the simplicity. During this process, particulate $Mg(OH)_2$ extracted from serpentinite is brought into contact with gaseous $CO_2$. Roughly, the assumed ratio of immobilized $CO_2$ to serpentinite is assumed 1:2 [9], i.e. 2 tonne of serpentinite requires 1 t of $CO_2$. Process conditions are chosen according to the results of direct gas-solid carbonation experiment with Lithuanian serpentinites that are carried out by Stasiulaitienė [10]. Experiment results have shown that the maximum efficiency of the reaction is achieved when the temperature in carbonation reactor is about 500 °C and pressure about 20 bar.

The dry process has the potential of producing high temperature steam or electricity while converting $CO_2$ into carbonates. Process integration with mining activities may be very advantageous from an economic point of view of the cost and energy, possibly allowing for, *e.g.*, higher valuable metal extraction rates as well.

According to the results of investigations of stability of calcium and magnesium carbonate in acidic aqueous environment, we assumed that $MgCO_3$ should be resistant and stable enough to prevent local environmental effects at a mineral carbonate storage site [17].

The overall process flows diagram are presented.

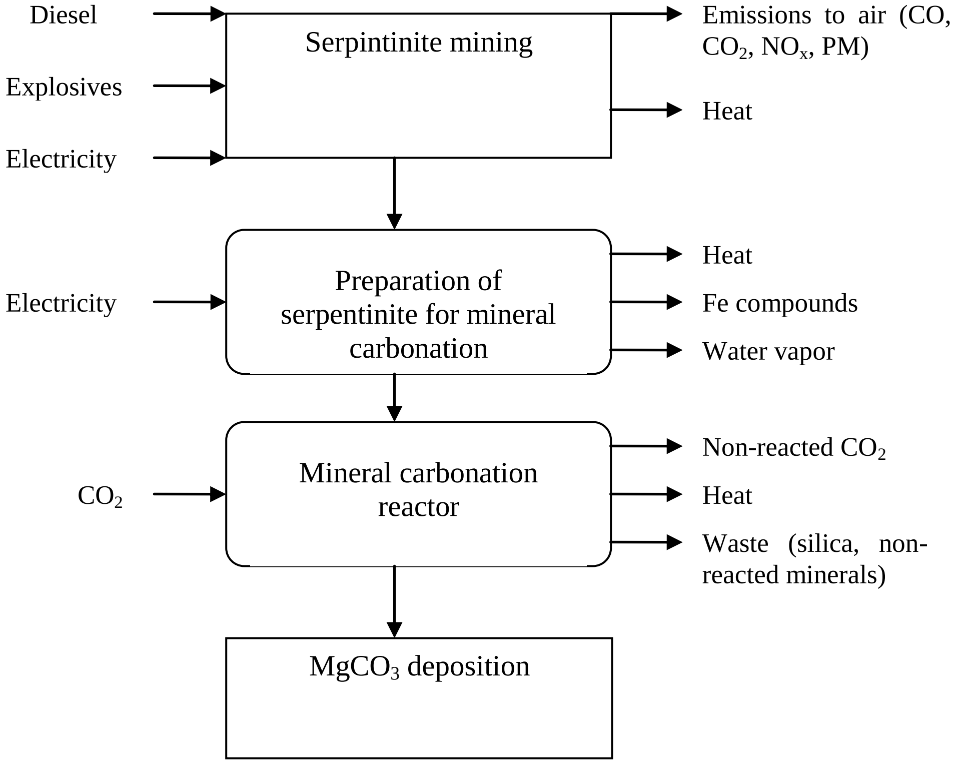

Fig. 4. Flow diagram of processes of mineral carbonation

## 4. CONCLUSION

The inventory analysis of the mineral carbonation process of $CO_2$ has revealed, that the main issues associated with this process are energy consumption. The first step of the process – serpentinite mining - requires 46.4 kWh, mineral pre-treatment – about 300 kWh for 1 tonne of mineral. It is obvious that the most energy required for the second process step – mineral pre-treatment, therefore this process requires the highest running costs. All data was taken from concrete works in this sphere with a purpose to ensure that they are reliable. The first step of the LCA (inventory analysis) sets the goals for the whole environmental impact assessment of the mineral carbonation. Further research directions will include inventory analysis of mineral and $CO_2$ transportation.

## 5. REFERENCES

1. FLORIDES, A. GEORGIOS, CHRISTODOULIDES P. Global warming and carbon dioxide through sciences. Environment International, 2009, Vol. 35, p. 390–401.
2. HOUGHTON, J. Global warming. Reports on Progress in Physics, 2005, Vol. 68, p. 1343–1403.
3. GILLET, N.P.; ARORA, Vivek K.; ZICKFELD, K.; MARSHALL, S.J.; MERRYFIELD, W.J. Ongoing climate change following a complete cessation of carbon dioxide emissions. Nature Geoscience, 2011.
4. National greenhouse gas emission inventory report 2011 of the Republic of Lithuania. Center for environmental policy,Vilnius.
5. WILDBOZ, C. Life cycle assessment of selected technologies for $CO_2$ transport and sequestration. Diploma Thesis. Zurich: Institute of Environmental Engineering.
6. IPCC, 2005. IPCC Special Report on Carbon Dioxide Capture and Storage. Cambridge University Press, Cambridge, United Kingdom and New York, NY, USA.
7. ISO, 2006. International Organization of Standardization 14040: Environmental Management-life Cycle Assessment-principles and Framework. International Organization of Standardization, Geneva.

8. NORGATE, T., HAQUE, N. Energy and greenhouse gas impacts of mining and mineral precessing operations. Journal of Cleaner Production, 2010, Vol. 18, p. 266–274.
9. SHOGENOVA, A., ŠLIAUPA, S., SHOGENOV, K., ŠLIAUPIENĖ, R., POMERANCEVA, R., VAHER, R., UIBU, M., KUUSIK, R. Possibilities for geological storage and mineral trapping of industrial $CO_2$ emissions in the Baltic region. Energy Procedia, 2009, Vol. 1, p. 2753–2760.
10. STASIULAITIENĖ I. (2010). Binding potential of concentrated carbon dioxide using Lithuanian rocks. Doctoral dissertation. Technological Sciences, Environmental Engineering (04T). Kaunas: Kaunas University of Technology.
11. TEIR, S. (2008). Fixation of carbon dioxide by producing carbonates from minerals and steelmaking slags. Doctoral dissertation. Helsinki: Helsinki University of Technology.
12. HAREMAN, Howard L. (1992). SME Mining Engineering book. Printed in the United States of America by Cushing-Malloy, Inc., Ann Arbor, Ml.
13. HUIJGEN, W.J.J.; COMANS, R.N.J. Carbon dioxide sequestration by mineral carbonation. Literature review. Report number ECN-C-03-016. Energy Research Centre of the Netherlands, ECN-Clean Fossil Fuels Environmental Risk Assessment; 2003.
14. O'CONNOR, W. K.; DAHLIN, D. C.; NILSEN, D. N.; WALTERS, R. P.; TURNER, P. C. (2000b). Carbon dioxide sequestration by direct mineral carbonation with carbonic acid, Proceedings, 25th international technical conference on coal utilization and fuel systems, Clearwater, Florida.
15. FAUTH, D. J.; SOONG, Y.; WHITE, C. M. (2002). Carbon sequestration utilizing industrial solid residues, Preprints Symposium, American Chemical Society, Division Fuel Chemistry, p. 37–38.
16. NETL (2001). Proceedings of Workshop NETL Mineral $CO_2$ Sequestration.
17. TEIR, S.; ELONEVA, S.; FOGELHOLM, C.J.; ZEVENHOVEN, R. Stability of calcium carbonate and magnesium carbonate in rainwater and nitric acid solutions. Energy Conversion and Management, 1992, Vol. 38, p. 259–264.

CYSENI 2011, May 26–27, Kaunas, Lithuania
ISSN 1822-7554, www.cyseni.com

# EXTREME VALUE DISTRIBUTIONS FOR PROBABILISTIC ANALYSIS OF EXTREME SNOWFALL

**V. Česnulytė**
*Kaunas University of Technology*
*Faculty of Fundamental Sciences*
*Studentų str. 50, LT-51368 Kaunas – Lithuania*
*Phone +370 625 01055*
*Email: vaida.cesnulyte@ktu.lt*

**R. Alzbutas**
*Lithuanian Energy Institute*
*Laboratory of Nuclear Installation Safety*
*Breslaujos str. 3, LT-44403 Kaunas – Lithuania*
*Phone +370 37 401 945*
*Email: robertas@mail.lei.lt*

## ABSTRACT

Extreme snowfall can do enormous damage to energy systems constructions, power lines, water communications, etc. Accumulation of snow can collapse buildings and knock down power lines. Melting of snow and ice drifts can cause significant seasonal river flooding that may affect the work and safety of hydro power plant. The cost of snow removal, repairing damages, and loss of business can also have large economic impacts.

In order to estimate the possible consequences of extreme snowfall, the probabilistic analysis of the event occurrence has been performed: statistical data have been collected and analyzed, probabilistic model has been built as well as uncertainty of modelling data has been analyzed. The probabilistic analysis of extreme snowfall is based on historical data in Dūkštas territory taken from annals of Lithuanian Hydrometeorological Service and Dūkštas Meteorological Station (MS).

This paper mainly presents the probabilistic analysis of extreme snowfall data. Probabilistic assessment is focused on an application and comparison of Gumbel, Weibull, Frechet and Generalized Extreme Value (GEV) [2, 3, 4, 10] distributions, allowing to single out distribution, which has the best fit for data of extreme snowfall.

Keywords: extreme snowfall, probabilistic analysis, Gumbel model, extreme value distributions.

## 1. INTRODUCTION

Extreme events occur in natural, technical, and societal environments. They may be natural or anthropogenic in origin, or they can arise simply from "chance". Extreme events often entail loss of life and/or materials. They usually occur "by surprise" and therefore often only become the focus of scientific attention after their onset. Knowledge of extreme events is often rather fragmentary, and recorded experience is limited. Indeed, scientists do not really understand *what* causes extreme events, *how* they develop, and *when* and *where* they occur [1].

Extremes in nature occur almost worldwide and cause incalculable human losses, in addition to billions of dollar damages each year (e.g. 622,000 people died in natural disasters in ten year period from 1992). The effects of other weather-related hazards, such as: windstorms, hurricanes, typhoons, and landslides are also known to be severe. Extreme events loss from acts of nature is increasing fast. There has been a rising trend in the number of events and economic and insurance losses from 1960 to 1990 [11].

The study of the statistics of extreme events is the first step in the mitigation of these national disasters. In addition historical records containing observations from the past are usually the only source of information. Using limited samples of the data and imperfect knowlegde of the processes involved, one is expected to develop and to apply statistical techniques in order to estimate the degree of risk involved globally [11].

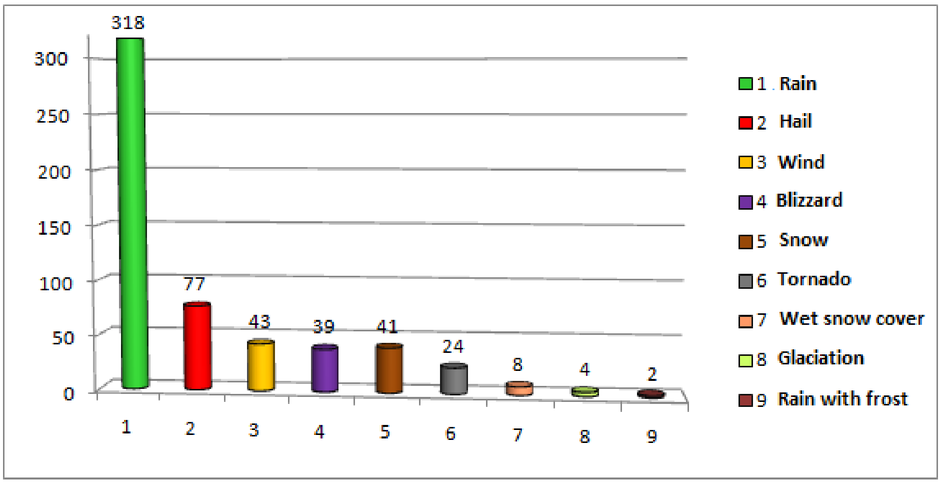

Fig. 1. The number of natural weather phenomena in Lithuania (1961–2009)

The main purpose of this work is to analyse the extreme weight of snow. This natural element is selected because of the high damage in a very short period of time.

In Lithuania 80 percent of all naturally occurring extreme events are caused by weather events. Rain is the most common meteorological phenomenon that can cause extreme events (Fig. 1) [9, 5, 6, 7, 8].

The probabilistic assessment is based on mathematical model which was applied taking into account statistical data from 1992 up to 2009. The weight of snow is used in the probability assessment as the frequency of event of extreme precipitation (snowfall).The Extreme value distribution (Gumbel, Frechet, Weibull, and GEV) laws were used for probability estimation and return period of extreme weight of snow occurrence. Return period is a statistical measurement denoting the average recurrence interval over an extended period of time, and is usually required for risk analysis.

## 2. METHODOLOGY

The proposed methodology takes places in three stages. Firstly, the weight of snow is calculated and the annual maximum value is selected. In this analysis the annual maximum values are considered to be extreme. Then, the Gumbel's, Frechet's, Weibull's, and GEV 's function parameters are determined considering the sample of extreme events. In this step the return period is calculated. Finally, the maximum annual weight of snow is evaluated using the relationship between extreme value distributions and return period.

### 2.1. Extreme Value Distributions

#### *2.1.1. Gumbel distribution*

The Gumbel probability distribution function [2] is

$$F(x;\mu,\sigma) = P(X < x) = e^{-e^{-\left(\frac{x-\mu}{\sigma}\right)}}, \quad -\infty < x < \infty;\ \sigma > 0 \qquad (1)$$

where $\mu$ and $\sigma$ are the constants known as the location and scale parameters, respectively. In this case only two parameters exist, the equality of mean and variance will suffice. The moment equation becomes [2]

$$\bar{x} = \mu - 0.5772\sigma, \tag{2}$$

$$s_x^2 = \frac{\pi^2\sigma^2}{6}, \tag{3}$$

where $\bar{x}$ and $s_x^2$ are the sample mean and quasi-variance. From (2) an (3) we obtain the following moment estimates [2]

$$\sigma = \frac{s_x\sqrt{6}}{\pi}, \tag{4}$$

$$\mu = \bar{x} + 0.5772\sigma. \tag{5}$$

Because of the probability analysis is related to extreme values, the survival function

$$G(x;\mu,\sigma) = P(X > x) = 1 - e^{-e^{-\left(\frac{x-\mu}{\sigma}\right)}}, \quad -\infty < x < \infty;\ \sigma > 0 \tag{6}$$

is used.

It is reasonable to adjust functional expression of Gumbel extreme precipitation distribution, because follow-up analysis will be linked to estimation of mean and standard deviation. The main parameters $\mu$ and $\sigma$ correspondingly are replaced by the estimate of average $\bar{x}$ and standard deviation $s_x$. Hence adjusted Gumbel model is

$$G(x,\bar{x},s_x) = 1 - e^{-e^{-\pi\left(x-\left(\bar{x}-0.5772\frac{s_x\sqrt{6}}{\pi}\right)\right)/s_x\sqrt{6}}}, \tag{7}$$

where $x$ is the level of weight of snow, $\bar{x} = 78.778$ and $s_x = 64.436$.

### *2.1.2. Weibull distribution*

The three-parameter Weibull distribution is given by the distribution function [10]

$$F(x;\mu,\sigma,\beta) = 1 - e^{-\left(\frac{x-\mu}{\sigma}\right)^{\beta}}, \quad x \geq \mu, \tag{8}$$

where $\mu$, $\sigma$, and $\beta$ are the constants known as the location, scale, and shape parameters, respectively and such that $\sigma > 0$ and $\beta > 0$. The main parameters of Weibull distribution are evaluated using threshold parameter. Transforming Weibull cumulative distribution function (henceforth cdf) to

$$\log(x-\mu) = \frac{1}{\beta}\log(-\log(1-p)) + log\sigma \tag{9}$$

again gives a linear relationship between $\log(x-\mu)$ and $\log(-\log(1-p))$ where $\mu$ is a threshold parameter and $p$ is a cumulative probability. Recording threshold parameter and using the least squares we could find shape and scale parameters. We need to maximize the parameter of determination $R^2$ value of a linear regression on the transformed variables $\log(x-c)$ and $\log(-\log(1-p))$ in order to evaluate the location parameter.

### *2.1.3. Frechet distribution*

The Frechet cdf is given by [2]

$$F(x;\mu,\sigma,\beta) = e^{-\left(\frac{\sigma}{x-\mu}\right)^{\beta}}, \quad x \geq \mu, \tag{10}$$

where $\mu$, $\sigma$, and $\beta$ are the constants known as the location, scale, and shape parameters, respectively and such that $\sigma > 0$ and $\beta > 0$. Frechet parameter estimates are obtained with the help of maximum likelihood estimates.

### *2.1.4. Generalized extreme value distribution (GEV)*

The Generalized extreme value distribution (GEV) developed by Jenkinson [3] is a family of continuous probability distributions consisting of Gumbel, Frechet, and Weibull distributions with cdf given by [12]

$$F(x;\mu,\sigma,\beta) = e^{-\left(1+\beta\left(\frac{x-\mu}{\sigma}\right)\right)^{-1/\beta}}, \quad 1+\beta\left(\frac{x-\mu}{\sigma}\right) > 0, \tag{11}$$

where $\mu \in \mathbb{R}$, $\sigma > 0$, and $\beta \in \mathbb{R}$ are the constants known as the location, scale, and shape parameters.

## 2.2. Return period

An extreme event occurs if the random variable $X_i$ is greater or equal to some magnitude $x_T$. The recurrence interval $T$ is defined as the time period between occurrences for the event $X_i \geq x_T$. The return period for the event $X_i \geq x_T$ is the expected value of $T$, denoted by $E(T)$ in this study. The return period for an event of a given magnitude is thus defined as the average reccurence interval between events equaling or exceeding a specific magnitude.

The return period for the event $X_i \geq x_T$ can be related to the probility of occurrence for such events in the following way. It is assumed that the probability of occurrence for the event $X_i \geq x_T$ in any year is $P(X_i \geq x_T)$. $X_i$ is serially independent in the values, the probability that the time interval $T$ between exceedance of a precipitation magnitude $x_T$ equals $n$ is given by [4]:

$$P(T=n) = P(X_1 < x_T)\cdot P(X_2 < x_T)\cdot \ldots \cdot P(X_{n-1} < x_T)\cdot P(X_n \geq x_T) = P(X_1 < x_T)^{n-1}P(X_n \geq x_T). \tag{12}$$

The expected value for $T$ is then given by

$$E(T) = \sum_{n=1}^{\infty} nP(X_{n-1} < x_T)^{n-1}P(P(X_n \geq x_T)) = \frac{1}{P(X_i \geq x_T)} = \frac{1}{1-P(X_i < x_T)}. \tag{13}$$

The above equation is the return period for an extreme event described by a single random variable and based on the annual maximum series. Obviously, the return period depends on the distribution of the selected random variables, that is, the longer the return period, $E(T)$, the less the frequency, $P(X_i \geq x_T)$, and the larger the magnitude of the random variable, $x_T$.

## 3. RESULTS

Load structures formed of the snow depend on both the snow thickness and density. Weight of snow is calculated by multiplying the thickness of snow by the snow density.Weight of snow can be expressed in terms of water reserves in snow.

Extreme weight of snow probability estimates used in the calculation of snow data are derived from annals of Lithuanian Hydrometeorological Service and Dūkštas MS. The snowfall data consist of annual weight of snow values during the period of 1992–2009 in Dūkštas territory . This part of Lithuania is chosen because of importance of Ignalina NPP. The probability of maximum weight of snow and the return period are the main parameters of probability assessment of extreme snow. The time series of these data for the period of 18 years are shown in Fig. 2.

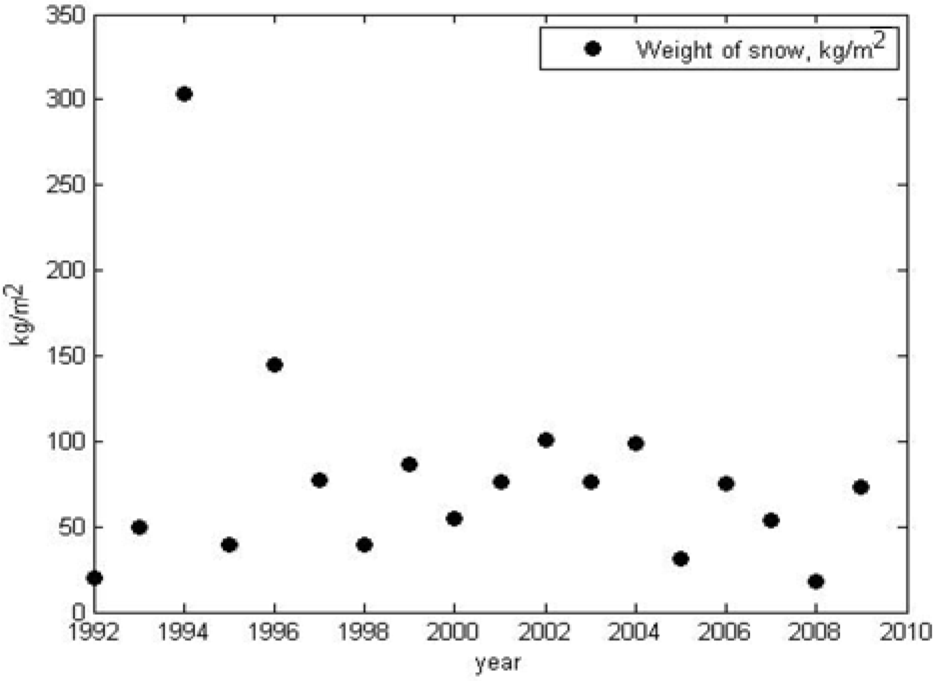

Fig. 2. Annual maximum weight of snow values in Dūkštas MS

We shall assess the dependence of the exceedance probability of extremes on the various extreme value distributions.

Table 1. Location, scale, and shape parameters of extreme value distributions according to Lithuanian annual maximum snowfall series

| | **Gumbel** | **Weibull** | **Frechet** | **GEV** |
|---|---|---|---|---|
| $\mu$ | 49.78 | 13.64 | -66.10 | 50.74 |
| $\sigma$ | 50.24 | 68.34 | 116.84 | 30.40 |
| $\beta$ | - | 1.26 | 3.84 | 0.26 |

Table 1 shows the main parameters of Gumbel, Weibull, Frechet, and GEV distributions that were evaluated using moment method, threshold estimates, and maximum likelihood method.

The probability that extreme weight of snow will exceed more than 50–300 kg/m$^2$ is calculated in consideration of extreme weight of snow frequency and using the model (Table 2).

Table 2. Likelihood estimates of annual extreme weight of snow

| **The annual extreme weight of snow, kg/m$^2$** | **Gumbel** | **Weibull** | **Frechet** | **GEV** |
|---|---|---|---|---|
| 50 | $6.306\cdot10^{-1}$ | $6.360\cdot10^{-1}$ | $6.421\cdot10^{-1}$ | $6.412\cdot10^{-1}$ |
| 70 | $4.877\cdot10^{-1}$ | $4.562\cdot10^{-1}$ | $4.272\cdot10^{-1}$ | $4.267\cdot10^{-1}$ |
| 100 | $3.079\cdot10^{-1}$ | $2.613\cdot10^{-1}$ | $2.283\cdot10^{-1}$ | $2.280\cdot10^{-1}$ |
| 150 | $1.272\cdot10^{-1}$ | $9.23\cdot10^{-2}$ | $9.05\cdot10^{-2}$ | $8.98\cdot10^{-2}$ |
| 200 | $4.905\cdot10^{-2}$ | $2.94\cdot10^{-2}$ | $4.16\cdot10^{-2}$ | $4.14\cdot10^{-2}$ |
| 250 | $1.842\cdot10^{-2}$ | $8.6\cdot10^{-3}$ | $2.05\cdot10^{-2}$ | $2.16\cdot10^{-2}$ |
| 300 | $6.849\cdot10^{-3}$ | $2.3\cdot10^{-3}$ | $1.25\cdot10^{-2}$ | $1.23\cdot10^{-2}$ |

Calculated likelihood estimates of annual extreme weight of snow are shown in Fig. 3. As we can see from Table 2 and Fig. 3 likelihood estimates of Gumbel and Weibull distribution are comparable as well as likelihood estimates of Frechet and GEV distributions respectively.

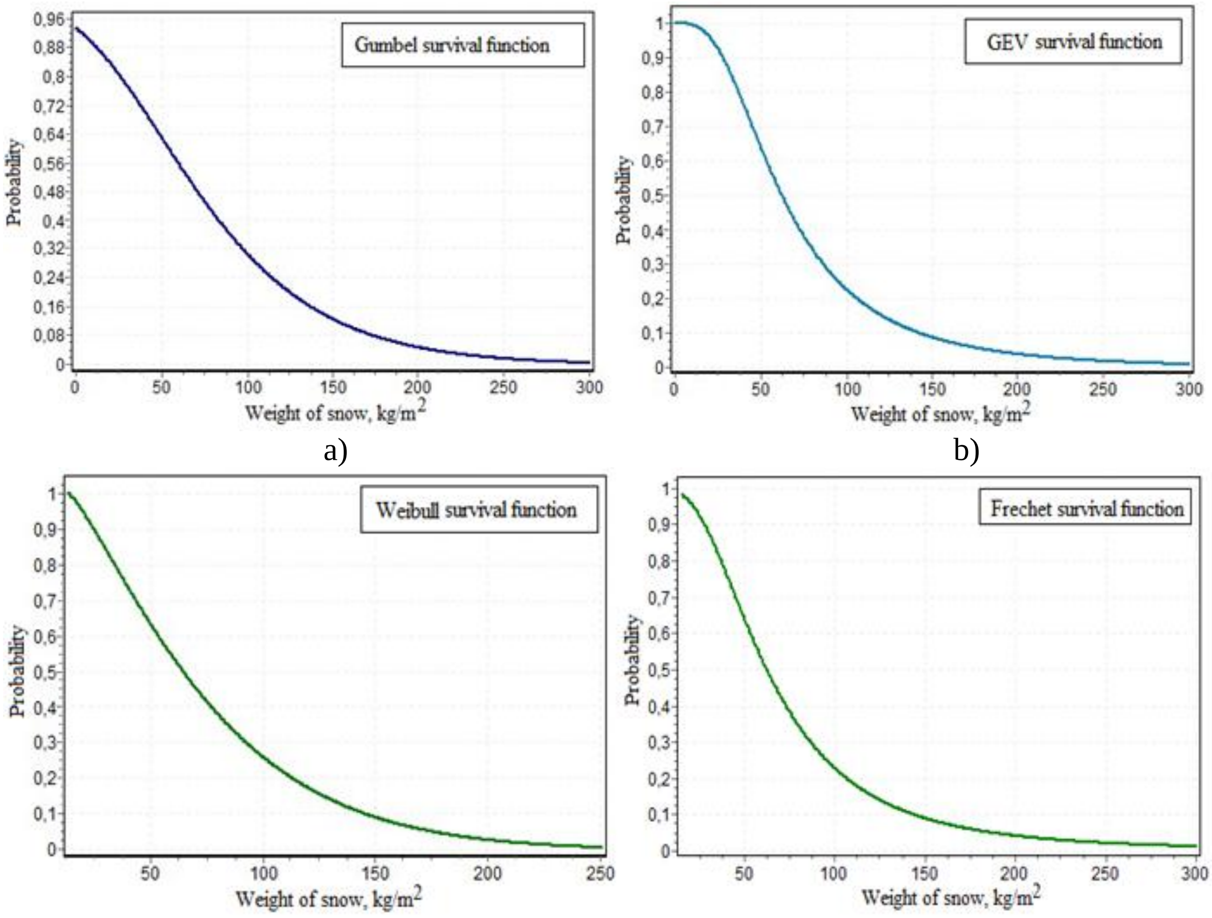

a) b)

c) d)

Fig. 3.Extreme weight of snow occurrence probability per year with: a) Gumbel, b) GEV, c) Weibull, and d) Frechet distributions

In order to estimate extreme values with particular return period, it is necessary to have the relationship between extreme value distribution variables and return period. From Gumbel distribution and from definitions about return period we can write:

$$1 - e^{-e^{-y}} = \frac{1}{T}. \tag{14}$$

Hence

$$y = -\ln(\ln(T) - \ln(T-1)), \text{ where } y = \frac{x-\mu}{\sigma}, \tag{15}$$

$$x_G = \mu + \sigma(-\ln(\ln(T) - \ln(T-1))) \quad (16)$$

According to other relationship between Weibull, Frechet, and GEV distributions and return period we have

$$x_W = \mu + \sigma \cdot (\ln(T) - \ln(T-1))^{1/\beta}, \quad (17)$$

$$x_F = \mu + \frac{\sigma}{(\ln(T)-\ln(T-1))^{\beta}}, \quad (18)$$

$$x_{GEV} = \mu + \frac{\sigma}{\beta(\ln(T)-\ln(T-1))^{\beta}} - \frac{\sigma}{\beta}. \quad (19)$$

Table 3. Periods of extreme recurrence of weight of snow

| **Return period (year)** | **Frequency** | **Maximum annual weight of snow, kg/m$^2$** | | | |
|---|---|---|---|---|---|
| | | **Gumbel** | **Weibull** | **Frechet** | **GEV** |
| 2 | $5\cdot10^{-1}$ | 68.2 | 51.2 | 62.4 | 62.3 |
| 5 | $2\cdot10^{-1}$ | 125.1 | 100.9 | 106.6 | 106.5 |
| 10 | $10^{-1}$ | 162.8 | 138.5 | 143.8 | 143.7 |
| 20 | $5\cdot10^{-2}$ | 199.0 | 176.1 | 187.1 | 186.9 |
| 50 | $2\cdot10^{-2}$ | 245.8 | 225.8 | 256.7 | 256.3 |
| **100** | $\mathbf{10^{-2}}$ | **280.9** | **263.4** | **321** | **320.5** |
| 1 000 | $10^{-3}$ | 396.8 | 388.3 | 639,9 | 638.3 |
| 10 000 | $10^{-4}$ | 512.5 | 513.2 | 1219.9 | 1215.8 |
| 100 000 | $10^{-5}$ | 628.2 | 638.1 | 2276.4 | 2266.7 |
| 1 000 000 | $10^{-6}$ | 743.9 | 763 | 4200.6 | 4179 |

Table 3 shows the maximum annual weight of snow appearance in various return periods. The expected maximum annual weight of snow over 100 years is 280.9 kg/m$^2$ (Gumbel), 263.4 kg/m$^2$ (Weibull), 321 kg/m$^2$ (Frechet), and 320,5 kg/m$^2$ (GEV). Return period of various Extreme value distributions are shown in Fig. 4.

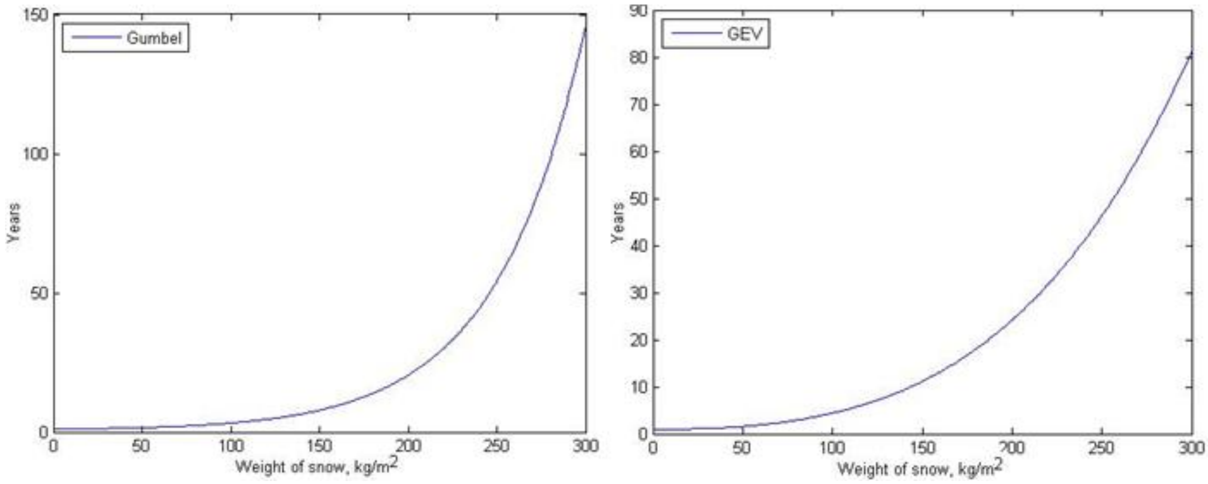

a) b)

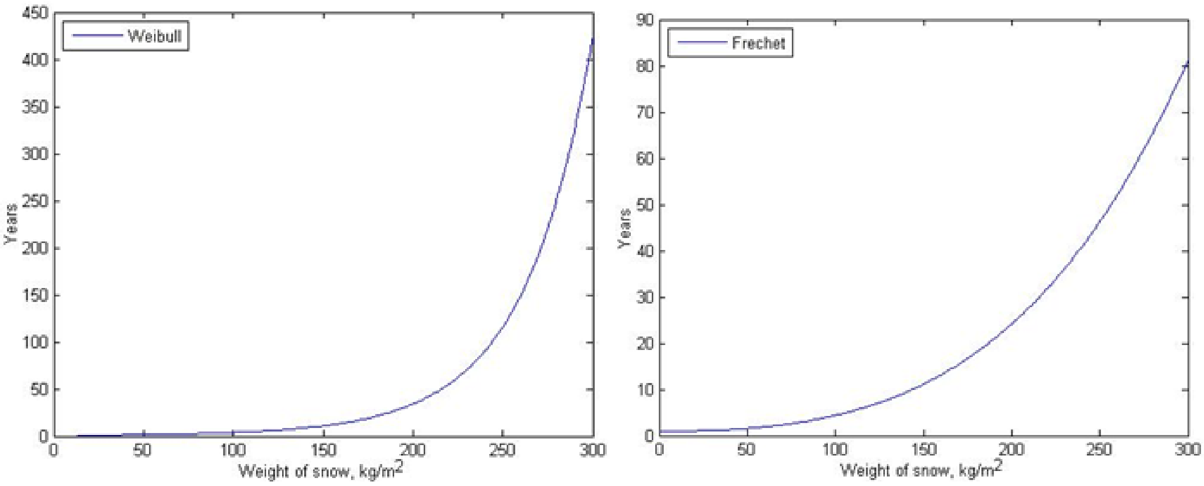

c) d)

Fig. 4. Return period of extreme weight of snow according to a) Gumbel, b) GEV c) Weibull, and d) Frechet distributions

The main disadvantage of graphical analysis is that it is difficult to evaluate the return period of extreme weight of snow (e.g. when *x* is: 50 kg/m$^2$, 100 kg/m$^2$, 200 kg/m$^2$, and 300 kg/m$^2$ (Table 4).

Table 4. Estimated weight of snow for different return periods

| **Gumbel** | | | | |
|---|---|---|---|---|
| Weight of snow, kg/m$^2$ | **50** | **100** | **200** | **300** |
| Probability | $6.306\cdot10^{-1}$ | $3.079\cdot10^{-1}$ | $4.905\cdot10^{-2}$ | $6.849\cdot10^{-3}$ |
| Return period, year | 2 | 3 | 20 | 146 |
| **Weibull** | | | | |
| Probability | $6.360\cdot10^{-1}$ | $2.613\cdot10^{-1}$ | $2.94\cdot10^{-2}$ | $2.3\cdot10^{-3}$ |
| Return period, year | 2 | 4 | 34 | 434 |
| **Frechet** | | | | |
| Probability | $6.421\cdot10^{-1}$ | $2.283\cdot10^{-1}$ | $4.16\cdot10^{-2}$ | $1.25\cdot10^{-2}$ |
| Return period, year | 2 | 4 | 24 | 80 |
| **GEV** | | | | |
| Probability | $6.412\cdot10^{-1}$ | $2.280\cdot10^{-1}$ | $4.14\cdot10^{-2}$ | $1.23\cdot10^{-2}$ |
| Return period, year | 2 | 4 | 46 | 81 |

Return period is 2 years for *x* equal to 50 kg/m$^2$ according to all extreme value distributions. This means that weight of snow exceeding 50 kg/m$^2$ is possible every second year. Actually, the relationship between any extreme weight of snow and return period can be determined according to the presented models and statistics.

Probabilistic modelling may be used further to analyse the uncertainty and sensitivity of calculated estimates of extreme weight of snow. The uncertainty analysis allows to evaluate the uncertainties of extreme value distributions mentioned above. Calculated uncertainty limits may be used for the excretion of distributions that have the best fit for statistical data.

Extreme snowfall can cause disastrous consequences by collapsing buildings and knocking down trees and power lines. Melting of snow and ice drifts can cause significant seasonal riverflooding that may affect the work and safety of hydro power plant.The probabilistic assessment performed in this paper allows further to investigate a risk of extreme events for power systems, energy infrastructure networks, civil buildings, etc.

## CONCLUSIONS

1. The probabilistic assessment is based on mathematical model that was applied taking into account statistical data from 1992 up to 2009. For assessment of the likelihood of extreme weight of snow Gumbel, Weibull, Frechet, and GEV models were chosen that allowed to evaluate the probability of different weight of snow $x$.
2. The return period of 50 kg/m$^2$ weight of snow is 2 years (all distributions under consideration) according to the statistics and relationship between weight of snow and return period. Return period of 100 kg/m$^2$ weight of snow is 3 (Gumbel), 4 (Weibull, Frechet, GEV) years and of 300 kg/m$^2$ weight of snow is 146 (Gumbel), 434 (Weibull), 80 (Frechet), and 81 (GEV) years.
3. Maximum annual weights of snow are calculated. The expected maximum annual weight of snow over 100 years is 280.9 kg/m$^2$ (Gumbel), 263.4 kg/m$^2$ (Weibull), 321 kg/m$^2$ (Frechet), and 320.5 kg/m$^2$ (GEV).
4. This developed methodology may be used in the risk and safety analysis. For such analysis it is necessary to analyze the data in that area and recalculate probabilities of extreme weights of snow, also to assess the implications of the model and the uncertainty of results.

## REFERENCES

1. ALBEVERIO, Sergio; JENTSCH, Volker; KANTZ, Holger. *Extreme Events in Nature and Society*. New York: Springer Berlin Hidelberg, 2006. 1 p.
2. CASTILLO, E. *Extreme Value Theory in Engineering*, Academic Press, Inc (London) Ltd, 1988, p. 184–209.
3. JENKINSON, F.,A.; *The frequency distribution of the annual maxima (or minima values of meteorological elements. Quant. J. Roy. Meteorol*. Soc. 81, 1955, p. 158–171.
4. KOTTEGOTA, N.,T.; *Stochastic Water Resources Technology. Hong Kong:* Mac. Press LTD, 1980.
5. Lietuvos Hidrometeorologijos Tarnyba prie Aplinkos ministerijos. *2006 metų stichinių hidrometeorologinių reiškinių apžvalga.* Vilnius. 2007. 3 p.
6. Lietuvos Hidrometeorologijos Tarnyba prie Aplinkos ministerijos. *2007 metų stichinių hidrometeorologinių reiškinių apžvalga.* Vilnius. 2008. 3 p.
7. Lietuvos Hidrometeorologijos Tarnyba prie Aplinkos ministerijos. *Hidrometeorologinės sąlygos 2008 metais.* Vilnius. 2009.
8. Lietuvos Hidrometeorologijos Tarnyba prie Aplinkos ministerijos. *Hidrometeorologinės sąlygos 2009 metais.* Vilnius. 2010.
9. Lithuanian Hydrometeorological Service. Link to the internet: http://www.meteo.lt/dokumentai/naujienos/20061019/pranesimas.ppt
10. MURTHY, P.N.D.; XIE, M.; JIANG, R. *Weibull Models*. New Jersey: John Willey & Sons, 2004, 9 p. ISBN 0-471-36092-9.
11. SALVADORI, G.; De MICHELE, C.; KOTTEGODA, N. T.; ROSSO, R. *Extremes in Nature. An Approach Using Copulas*. New York: Springer, Dordrecht, 2007, Vol. 56. ISBN 978-1-4020-4415-1.
12. VOVORAS, D.; TSOKOS, P., Ch.; *Statistical analysis and modeling of precipitation data, Nonlinear Analysis: Theory, Methods & Applications*, Volume 71, Issue 12, 15 December 2009, Pages e1169-e1177.

# DISTRIBUTION OF NITROGEN DIOXIDE CONCENTRATION IN KAUNAS AND IN KAUNAS REGION

**D. Laurinavičienė, A. Dėdelė**
*Vytautas Magnus University*
*Vileikos str. 8, LT-44404 Kaunas – Lithuania*
*Phone +370 37 327904*
*Email: dovile@gmf.vdu.lt; a.dedele@gmf.vdu.lt*

## ABSTRACT

The aim of the present study was to assess distribution of nitrogen dioxide concentration in Kaunas city and in Kaunas region (Kaišiadorys, Prienai, Garliava). A passive sampling method was used. $NO_2$ concentrations were measured at 36 sampling points in Kaunas city. In Kaišiadorys, Prienai, Garliava measurements were carried out at 3 sampling points of each town. Study was performed in autumn 2010 and winter 2011. The study results showed that mean of nitrogen dioxide concentration in Kaunas city was 16.6 μg $m^{-3}$. The highest concentration was in Centras district (25.2 μg $m^{-3}$), the lowest in Rokai (10.9 μg $m^{-3}$). Average of nitrogen dioxide concentration in Kaišiadorys was 9.2 μg $m^{-3}$, in Prienai – 9.6 μg $m^{-3}$, in Garliava – 13.1 μg $m^{-3}$.

The results of the study were introduced in the ESRI Geographic Information System software ArcGIS and the extension Geostatistical Analyst was used to obtain maps of dispersion of nitrogen dioxide concentration.

To get a better view of the distribution of pollutant concentration, the obtained values were spatially interpolated using the IDW (Inverse Distance Weighted) method.

Keywords: air pollution, distribution of nitrogen dioxide concentration, map of nitrogen dioxide distribution, interpolation method.

## 1. INTRODUCTION

The attention directed at air quality in Europe is a result of not only the adverse effects on human health from high concentrations of air pollutants in the ambient air, but also of the EU regulations which aim to reduce emissions and to improve air quality [1].

Nitrogen dioxide is one of the most monitored pollutants in ambient air because of this effect on the human respiratory system, his contributions to the acidification of the ecosystems and his role in the formation of photochemical oxidants [2].

Nitrogen dioxide ($NO_2$) is common combustion-related pollutant that is mostly formed from oxidation of nitric oxide (NO) which is produced during high temperature burning of fuel in cars and other road vehicles, heaters and cookers [3]. Large amounts of nitrogen oxides ($NOx = NO + NO_2$) are emitted from mobile and stationary sources [4]. Motor vehicles can be the most important source of nitrogen oxides, especially in areas with few industrial sources [5].

Nitrogen dioxide is considered to be an important atmospheric trace gas pollutant not only because of its effects on health [6] but also because it absorbs visible solar radiation and contributes to impaired atmospheric visibility; as an absorber of visible radiation it could play a potentially direct role in the change in the global climate if its concentrations were to become high enough [7, 8].

Nitrogen dioxide pollution is higher along busy roads compared to background locations. Air pollution in city centres and districts near highways is related to traffic density of the highway, distance of the measuring site to the highway [9, 10, 11].

Air quality is influenced not only by physical and chemical processes but also by synoptical situation and meteorological processes as well as geographical and social factors. Air quality also depends on whether the pollutants will accumulate in the emission place or they will be dispersed in a large area. Thereby poor air quality is influenced by a wide range of factors that include pollutant emission strengths, meteorology and landscape topography [12, 13].

The aim of the present study was to assess nitrogen dioxide concentration in Kaunas city and in Kaunas region (Kaišiadorys, Prienai, Garliava).

## 2. MEASUREMENTS METHODS

For determination of nitrogen dioxide concentration a passive sampling method and triethanolamine as an absorbent was used. The passive sampler has an internal diameter of 25 mm and a depth of 10 mm (Fig. 1). A disc of Whatman 1chr filter paper impregnated with triethanolamine aqueous solution is used as the collecting element. The inside of the passive sampler is protected against wind and dust deposition by a wind screen made of a polypropylene fibre material. After sampling, the content of nitrite ions is determined spectrophotometrically following reaction with Saltzman reagent [14, 15].

This study is the part of project of "Modernization of Lithuanian air quality monitoring system using diffusive samplers". This project covers whole territory of Lithuania. Our measurements cover Kaunas and part of Kaunas region (Kaišiadorys, Prienai, Garliava).

Nitrogen dioxide concentration was measured at 36 sampling points in Kaunas city (Fig. 2). In Kaišiadorys, Prienai, Garliava measurements were carried out at 3 samplings points of each town (Fig. 3). Study was performed in autumn 2010 and winter 2011. We used mean of 2 weeks measurements of nitrogen dioxide concentration to characterize seasonal mean of nitrogen dioxide in Kaunas districts, in the whole city and in Kaunas region.

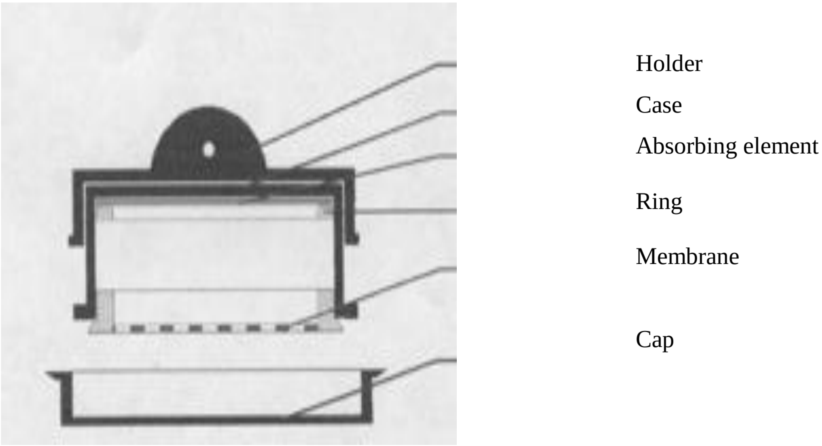

Fig. 1. Passive sampler for determination of nitrogen dioxide concentration

The results of the study were introduced in the ESRI Geographic Information System software ArcGIS and the extension Geostatistical Analyst was used to obtain maps of dispersion of nitrogen dioxide concentration in Kaunas city. To get a better view of the distribution of pollutant concentration, the obtained values were spatially interpolated using the IDW (Inverse Distance Weighted) method.

There were classified five areas, according the yearly limit value (40.0 $\mu g\ m^{-3}$).

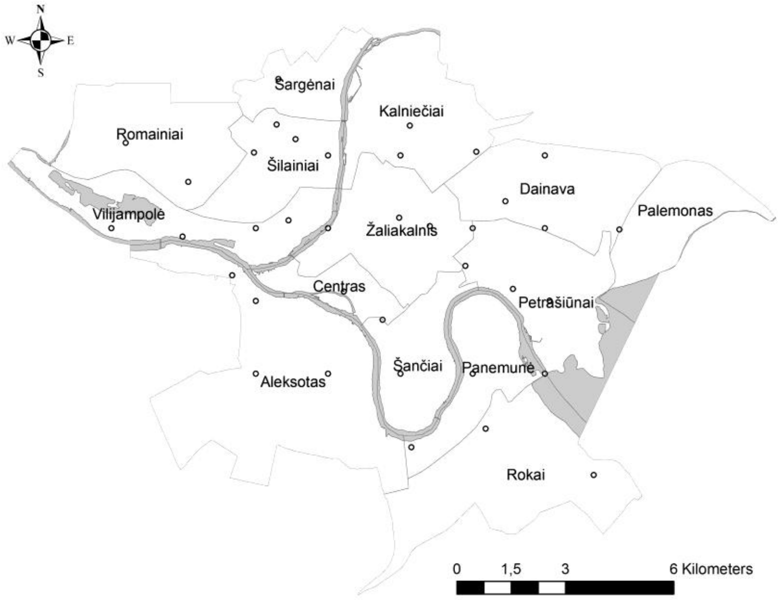

Fig. 2. Nitrogen dioxide concentration measurements points in Kaunas city

Fig. 3. Nitrogen dioxide concentration measurements points in Kaunas region

## 3. RESULTS AND DISCUSSION

The mean of nitrogen dioxide concentration in Kaunas city was 16.6 µg m$^{-3}$, in Kaunas region – 10.7 µg m$^{-3}$ for the study period. Mean of nitrogen dioxide concentration in autumn season in Kaunas city was 15.0 µg m$^{-3}$ in winter season – 18.2 µg m$^{-3}$. In Kaunas region nitrogen dioxide concentration in autumn season was 9.6 µg m$^{-3}$ and 11.7 µg m$^{-3}$ in winter (Fig. 4).

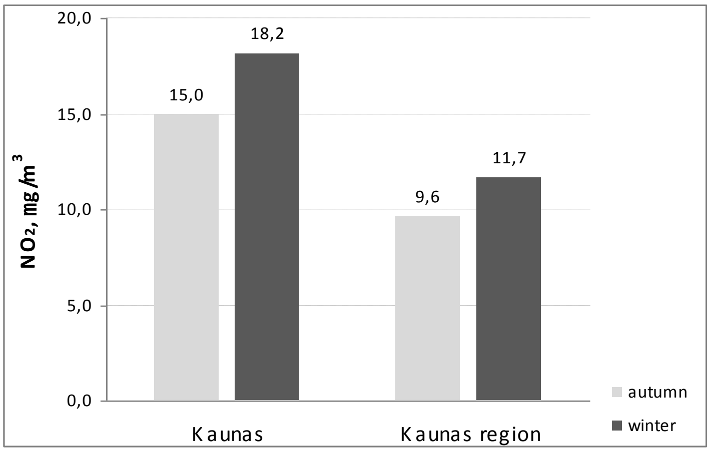

Fig. 4. Mean of nitrogen dioxide concentration in Kaunas city and in Kaunas region in autumn and winter seasons

Fig. 5 presents nitrogen dioxide concentration in Kaunas city and in Kaunas region in autumn season. The highest $NO_2$ concentration was in Kaunas city (15.0 µg m$^{-3}$). Lower nitrogen dioxide concentration was in Kaunas region: 11.5 µg m$^{-3}$ in Garliava, 8.9 µg m$^{-3}$ in Prienai and 8.3 µg m$^{-3}$ in Kaišiadorys.

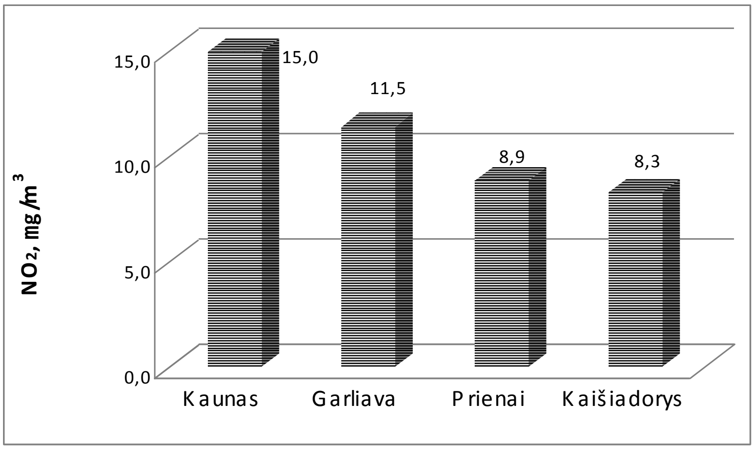

Fig. 5. Nitrogen dioxide concentration in Kaunas city and in Kaunas region in autumn season

There was determined conditionally higher nitrogen dioxide concentration in winter season (Fig. 6). $NO_2$ concentration in Kaunas city was 18.2 µg m$^{-3}$, in Garliava – 14.7 µg m$^{-3}$, in Prienai – 10.3 and in Kaišiadorys – 10.1 µg m$^{-3}$.

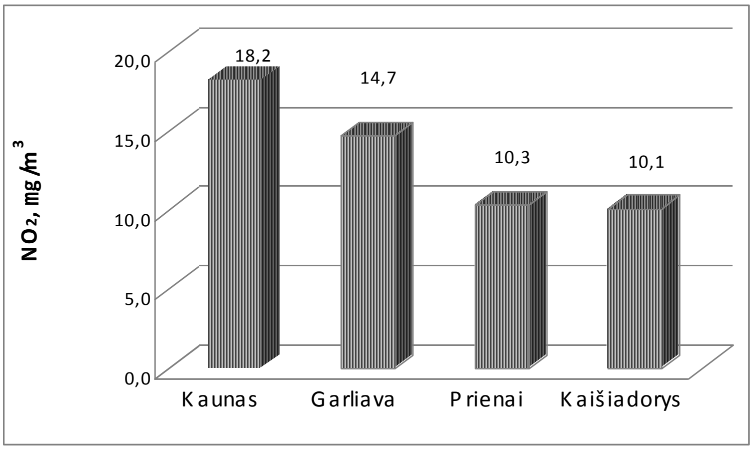

Fig. 6. Nitrogen dioxide concentration in Kaunas city and in Kaunas region in winter season

Distribution of nitrogen dioxide concentration in Kaunas districts in autumn season presented in Fig. 7. The highest nitrogen dioxide concentration was found in Centras district (25.0 µg $m^{-3}$), the lowest in Rokai (9.4 µg $m^{-3}$). Nitrogen dioxide concentration in Centras district was more than 2 times higher than in Rokai. In other districts it ranged from 18.9 µg $m^{-3}$ in Kalniečiai and Žaliakalnis to 11.5 µg $m^{-3}$ in Dainava.

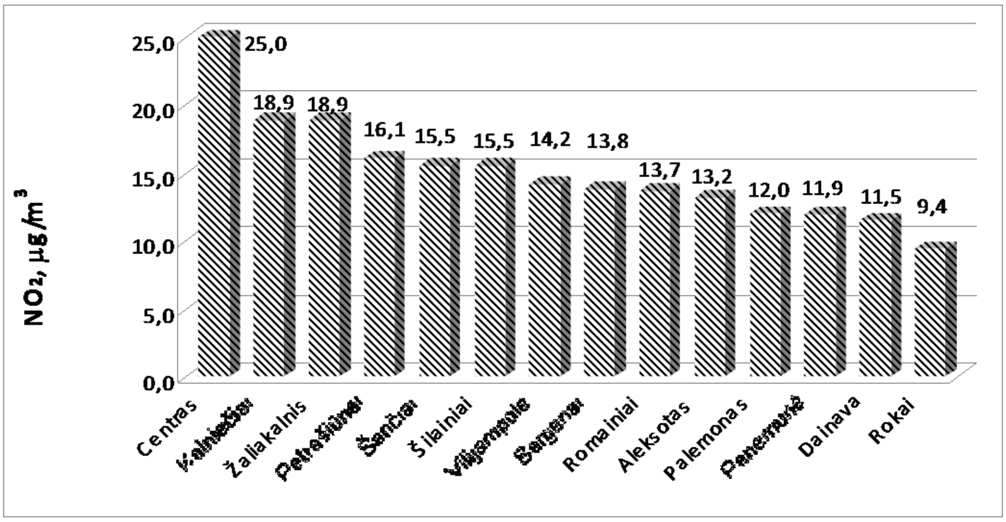

Fig. 7. Nitrogen dioxide concentration in districts of Kaunas city in autumn season

In winter season the highest nitrogen dioxide concentration was in Centras district also (25.4 µg $m^{-3}$), the lowest in Rokai (12.4 µg $m^{-3}$, Fig. 8). In other districts it ranged from 23.5 µg $m^{-3}$ in Palemonas to 14.1 µg $m^{-3}$in Panemunė. In districts which are in central part of the city concentration of nitrogen dioxide was higher than background areas. Similar results reported other authors [16]. The yearly limit value of 40.0 µg $m^{-3}$ for $NO_2$ was not exceeded during the study period in Kaunas and Kaunas region. These results were compared with past years nitrogen dioxide concnetration in Kaunas city. They did not differ significant. 1999–2009 average nitrogen dioxide concentration in Kaunas city was 18.1 µg $m^{-3}$ (e.g. average nitrogen dioxide concnetration in 2008 was 18.1 µg $m^{-3}$, in 2009 – 25.0 µg $m^{-3}$).

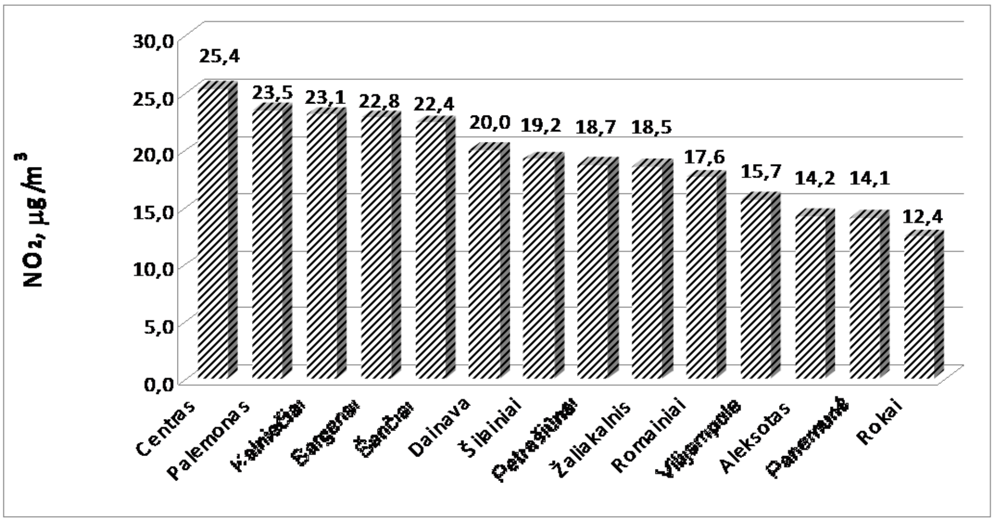

Fig. 8. Nitrogen dioxide concentration in districts of Kaunas city in winter season

Using Arc GIS software maps of nitrogen dioxide concentration dispersion in Kaunas city were plotted (Fig. 9, 10). There were classified five zones of nitrogen dioxide pollution.

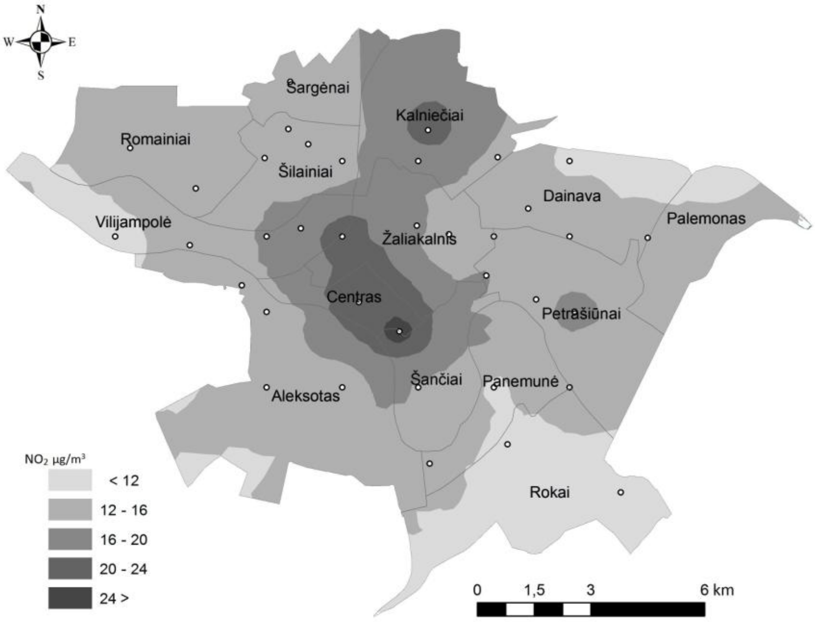

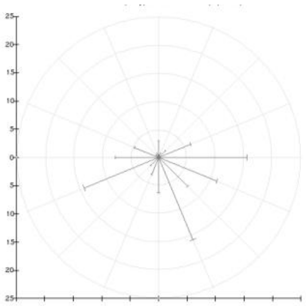

Fig. 9. Dispersion of nitrogen dioxide pollution in Kaunas city in autumn season

In autumn season the lowest nitrogen dioxide concentration was in districts which are located in the periphery of the city (Fig. 9). The highest concentration of nitrogen dioxide was in central or near to centre districts of Kaunas city (Centras, Žaliakalnis, Aleksotas, Šančiai, Kalniečiai).

In winter season the lowest concentration of nitrogen dioxide was in districts which are located in the periphery of the city (Fig. 10). The highest concentration of nitrogen dioxide was in Centras, Žaliakalnis, Šančiai, Kalniečiai, Sargėnai. It is caused by intensive traffic and unfavorable geographical position. In these districts there are more busy roads and more buildings. Centras district is located in a valley; there are unfavourable conditions for pollution dispersion. Similar results were obtained from other authors [17, 18]. Highest concentration of nitrogen dioxide was measured at high-traffic streets, followed by industrial and downtown locations.

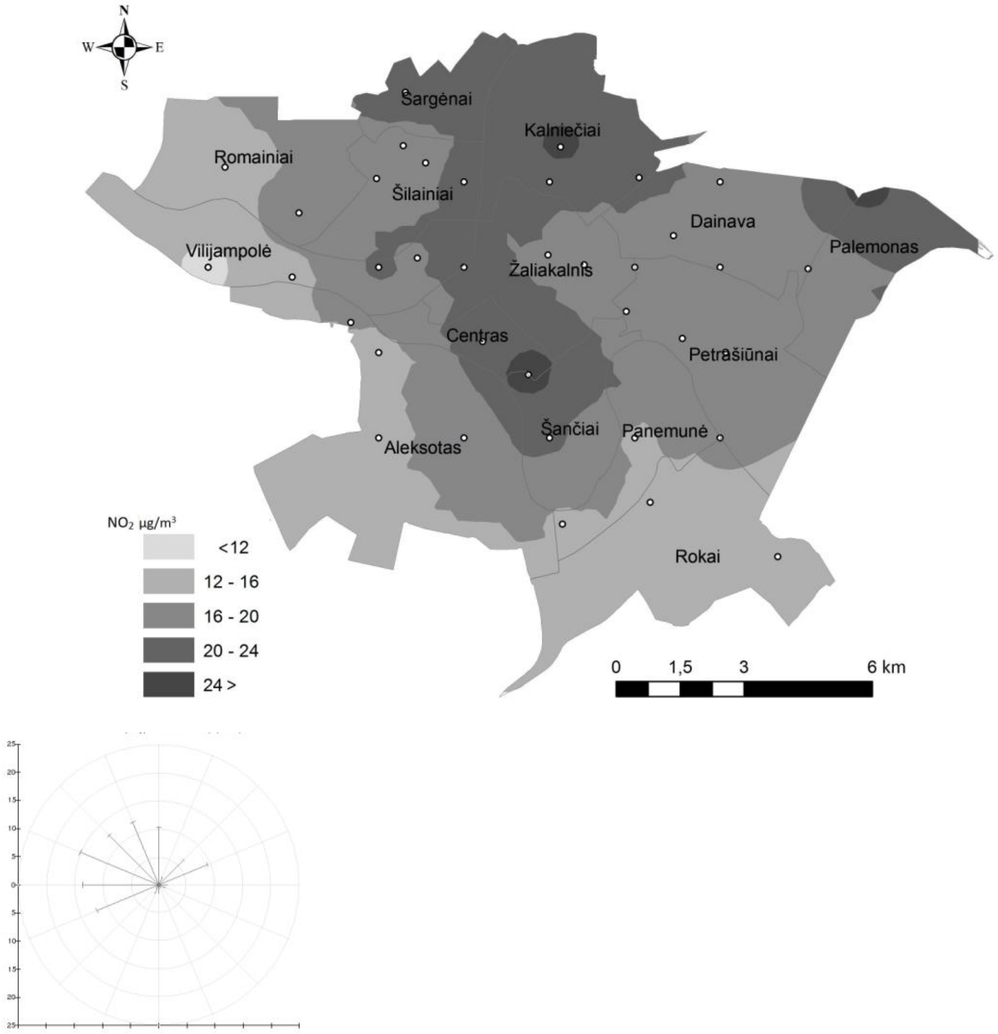

Fig. 10. Dispersion of nitrogen dioxide pollution in Kaunas city in winter season

## 4. CONCLUSIONS

1. Average of nitrogen dioxide concentration in Kaunas city was 16.6 µg $m^{-3}$, in Kaunas region 10.7 µg $m^{-3}$. Average of nitrogen dioxide concentration in Kaišiadorys was 9.2 µg $m^{-3}$, in Prienai – 9.6 µg $m^{-3}$, in Garliava – 13.1 µg $m^{-3}$.

2. Mean of nitrogen dioxide concentration in autumn season in Kaunas city was 15.0 µg $m^{-3}$ in winter season – 18.2 µg $m^{-3}$. In Kaunas region it was 9.6 µg $m^{-3}$and 11.7 µg $m^{-3}$.
3. The highest annual nitrogen dioxide concentration was in Centras district (25.2 µg $m^{-3}$), the lowest in Rokai (10.9 µg $m^{-3}$).
4. Nitrogen dioxide concentration dispersion in Kaunas city area is uneven. Nitrogen dioxide pollution is higher along busy roads compared to the city premises.
5. The yearly limit value of 40.0 µg $m^{-3}$ for $NO_2$ was not exceeded during the study period in Kaunas and Kaunas region.

## REFERENCES

1. VELDERS G.J.M, MATTHIJSEN J. Meteorological variability in $NO_2$ and $PM_{10}$ concentrations in the Netherlands and its relation with EU limit values. *Atmospheric Environment*, 2009, 43, p. 3858–3866.
2. PARRA M. A., ELUSTANDO D., BERMEJO R., SANTAMARIA, J. M. Ambient air levels of volatile organic compounds (VOC) and nitrogen dioxide ($NO_2$) in a medium size city in Northern Spain. *The Science of the Total Environment*, 2009, 407: 999–1009.
3. OZDEN O., DOGEROGLU T., KARA S. Development of a new passive sampler for $NO_2$ and field evaluation in the urban area of Eskisehir, Turkey. *Proceeding of the 9th International Conference on Environmental Science and Technology*, 2005, Rhodes island, Greece, 1–3 September 2005, p. 1144–1149.
4. TSAI W.Y., CHAN L.Y., BLAKE D.R., CHU K.W. Vehicular fuel composition and atmospheric emissions in South China: Hong Kong, Macau, Guangzhou, and Zuhai. *Atmospheric Chemistry and Physics*, 2006, 6, p. 3281–3288.
5. TRAN N. K., STEINBERG S.M., JOHNSON B.J. Volatile aromatic hydrocarbons and dicarboxylic acid concentrations in air at an urban site in the Southwestern US. *Atmospheric Environment*, 2000, 34, p. 1845–1852.
6. OZDEN O., DOGEROGLU T. Field evaluation of a tailor-made new passive sampler for the determination of $NO_2$ levels in ambient air. *Environmental Monitoring and Assessment*, 2008, 142, p. 243–253.
7. WHO. Chapter 7.1. Nitrogen dioxide. Air Quality Guidelines – Second Edition, Copenhaguen, 2000, WHO Regional Office for Europe.
8. DELGADO-SABORIT J.M., ESTEVE-CANO, V. Field study of diffusion collection rate coefficients of a $NO_2$ passive sampler in a Mediterranean coastal area. *Environmental Monitoring and Assessment*, 2006, 120, p. 327–345.
9. BOGO H., GOMEZ D.R., REICH S.L., NEGRI R.M., SAN ROMAN E. Traffic pollution in a down- town of Buenos Aires City. *Atmospheric Environment*, 2001, Vol. 35, p. 1717–1727.
10. BECKERMAN B., JERRETT M., BROOK J.R., VERMA D.K., ARAIN M.A., FINKELSTEIN M.M. Correlation of nitrogen dioxide with other traffic pollutants near a major expressway. *Atmospheric Environment*, 2008, Vol. 42, p. 275–290.
11. CARSLAW D. Evidence of an increasing $NO_2/NO_x$ emissions ratio from road traffic emissions. *Atmospheric Environment*, 2005, Vol. 39, p. 4793–4802.
12. BIMBAITĖ V., GIRGŽDIENĖ R. Evaluation of Lithuanian air quality monitoring data applying synoptical analysis. *Journal of Environmental Engineering and Landscape Management*, 2007, Vol. XV, No 3, p.173–181.
13. SCHNITZHOFER R., BEAUCHAMP J., DUNKL J., WISTHALER A., WEBER A., HANSEL A. Long-term measurements of CO, NO, $NO_2$, benzene, toluene and $PM_{10}$ at a motorway location in an Austrian valley. *Atmospheric Environment*, 2008, Vol. 42, p. 1012–-1024.

14. KROCHMAL D, KALINA A. Measurements of nitrogen dioxide and sulphur dioxide concentrations in urban and rural areas of Poland using a passive sampling method. *Environmental Pollution*, 1997, Vol. 96, No. 3, p. 401–407.
15. GRAZULEVICIENE R., LAURINAVICIENE D. Ambient nitrogen dioxide dispersion in Kaunas and its relation to incidence of myocardial infarction. *Environmental research, engineering and management*, 2001, Vol. 1, No. 15, p.1–6.
16. VELDERS G.J.M., DIEDEREN H.S.M.A. Likelihood of meeting the EU limit values for $NO_2$ and $PM_{10}$ concentrations in the Netherlands. *Atmospheric Environment*, 2009, Vol. 43, p. 3060–3069.
17. COSTABILE F., BERTONI G., DESANTIS F., WANG F., WEIMIN H., FENGLEI L., ALLEGRINI I. A preliminary assessment of major air pollutants in the city of Suzhou, China. *Atmospheric Environment*, 2006, Vol. 40, p. 6380–6395.
18. JO W-K., PARK J-H. Characteristics of roadside air pollution in Korean metropolitan city (Daegu) over last 5 to 6 years: Temporal variations, standard exceedances, and dependence on meteorological conditions. *Chemosphere*, 2005, Vol. 59, p. 1557–1573.

# STATISTICAL ANALYSIS OF THE BALTIC SEA WAVE HEIGHT DATA FOR EVALUATING ENERGY POTENTIAL

**E. Kasiulis**
*Lithuanian University of Agriculture*
*Studentų str. 11, LT-53361 Kaunas – Lithuania*
*Phone +370 62 183 902*
*Email: ukfanas@gmail.com*

ABSTRACT

After the success of hydro, wind and solar energetics searching for the new renewable energy sources began and so oceans and seas have been rediscovered. In our country's conditions, in the Baltic Sea, where periodic tides are inexistent and underwater currents are not powerful, the most important energy can be concentrated into waves. It is already clear that waves carry large amounts of energy and many countries are making efforts to evaluate these resources and to use them to produce electricity. The objective of this article is to assess whether the available data of the Baltic Sea monitoring are sufficient enough for the calculations of wave energy resources by using statistical analysis. Wave height and wind speed are the most important data in monitoring that is required for evaluation of these resources. Still, this investigation also requires a long record, reaching 30 years and more in length. Though wave height observations are usually short term, Klaipėda and Nida gauging stations have long term records of wind speed. First wave height observation data reliability was evaluated in the classical analysis in order to find coherence between hydrological characteristic (wave height) and meteorological characteristic (wind speed). The correlation between wind speed and wave height was verified with the statistical program. Clear correlations between Klaipėda and Nida gauging stations data can be easily used for the extension of wave height time series. When reliability of the data is verified, analogical regression analysis can be used for other gauging stations with short record of wave height data. Thus in this manner all wave height time series data can be prepared for the evaluation of sea wave energy potential.

Keywords: wave energy, data reliability, wave height, wind speed.

## 1. INTRODUCTION

Oceans and seas are an inexhaustible source of energy. In the background of renewable energy development boom in the resent years first commercial projects of wave energy plants are developed. Nevertheless, there are almost no studies of the eastern Baltic Sea energetic potential. The reason for this is not scientific incompetence or lack of knowledge. This is due to the lack of high-quality data.

Very important characteristic to evaluate sea energy potential is wave height. All wave height observations in the eastern Baltic Proper are visual what causes element of subjectivity. Waves are generated by wind, so in this case correlation between these two characteristics can be sought for. Since wind speed observations in Lithuania are instrumental, finding a coherence between wave height and wind speed can serve not only for verifying wave height data reliability, but also for extention of wave height time series.

## 2. METHODOLOGY

### 2.1. The Baltic Sea

National Oceanic and Atmosphere Administrations's National Data Buoy Center (NDBC), located in Washington, in its website explains why there is no linear relationship between wind speed and wave height. Buoys, that are located in the oceans, are recording data not only of waves that are caused by the local wind, but also of waves that are born in storms in distant areas. The wind and wave relationship is not linear because the measured wind speeds are generated locally, but the wave heights include waves generated from various locations.

On the other side, NDBC gives example of Lake Michigan, that is enclosed body of water and swell waves do not occur on such a large scale in these conditions, as they do in the open oceans. Correlation between wind speed and wave height here can be found [1].

It is already known, that wave fields in the Baltic Sea are similar to those on large lakes [2]. Fetch here is too short and wind blows over a short duration for waves to reach fully developed sea state. Extreme storms in the Baltic Sea are very rare.

The Baltic Sea is important for all countries that bound it and so every country has done its part to increase knowledge about this sea in Northern Europe. Currently joint monitoring of the Baltic Sea is carried out in accordance with the Helsinki Convention. But when matter comes to waves, it becomes clear that there is not enough suitable data.

Wave observations in the Baltic Sea extend for more than a 200 years [3]. First observations were carried out in coastal areas with a little knowledge about open sea conditions. Later various buoys were invented, so that wave data could be recorded in deeper and more open sea areas. This sea is very important economically. Because safe shipping was always a priority for all countries in Baltic Sea basin, large number of numerical models, that uses wave height and wind speed data, were developed to forecast sea conditions.

On background of climate change and growing concern about the increasing environmental pollution, new priority emerged – promotion of renewable energy sources. Hydro, wind, solar, biomass energetics are traditionally supported. Recently this group is joined by ocean energy, that includes 3 types of hydrokinetics – wave, current and tidal energy. In our country's conditions, in the Baltic Sea, where periodic tides are trivial and underwater currents are not powerful, the most important energy can be concentrated in waves. In different countries several models were developed to evaluate wave energy potential. Similar to models designed for forecasting sea conditions, these models also use wave height and wind speed data [7, 13].

The analysis of literature relating to wave observations in the Baltic Sea reveals these general sightings. Wave height observations in the eastern part of the Baltic Proper are mostly visual. Instrumentally measured data exist in the northern and western parts of the Baltic Sea, when the highest and longest waves occur in the eastern and north-eastern part of Baltic Proper [4]. Indeed, in the Lithuanian coast of the Baltic Sea west winds prevail. Also they have large enough fetch to produce highest waves in the Baltic Proper (Fig. 1). Evaluating energetic potential of these waves is meaningful.

However, these sightings do not answer all questions. It is not clear is visual observations data plausible to evaluate wave energy potential and are the wind speed and wave height observations sufficient to compute wave energy potential.

## 2.2. Wave height observations

Lithuanian wave observation sites are in Klaipėda, Nida and Palanga. Observation times are at 6:00, 12:00 and 18:00 GMT according to WMO guidelines [5]. As mentioned above all observations are visual.

Visual observations represent only near-coast wave properties, always carry element of subjectivity and are not always homogenous in time. In winter number of observations is always smaller than in summer because of longer dark period in a day.

Still, though in the northern Baltic Sea exists instrumentally measured data and winter dark periods do not have any impact there, big amount of data is still missing because of ice cover. Wave energy converters under these conditions also cannot work and that is regrettable as winter winds generate highest waves throughout the year. Thus, advantage of the Lithuanian part of the Baltic Sea is not only the highest waves with longest periods, but also ice-free sea.

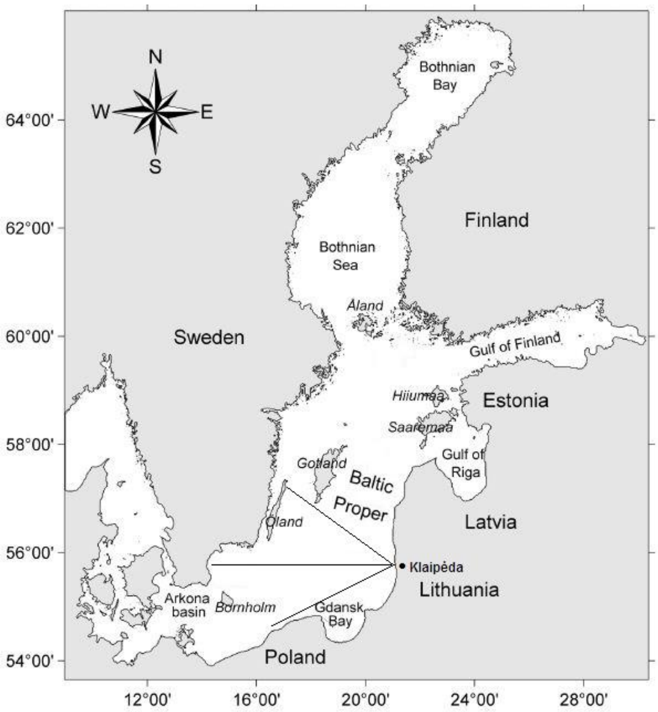

Fig. 1. Fetches generating highest waves in the Baltic Proper

Because the Baltic Sea is lake-type sea and local winds here are more important, than in the open oceans, wave height observations (that are visual) can be verified by wind speed observations (that are instrumental). Previous works on this topic indicate, that wave observations are generally reliable and more or less adequately reflects wave conditions in the Baltic Proper [6].

## 2.3. Wave energy estimation

Wave energy, as the new source of renewable energy, has been taken seriously since 1970's [7]. Virtually at the same time it was clear that simple equations are not suitable for wave energy evaluations. S. Aranuvachapun and J. A. Johnson (1976) in their paper give an example of formula of total energy per unit area in wave record containing M waves:

$$E_M = \frac{1}{8}\rho g \sum_{r=1}^{M} H_r^2 , \qquad (1)$$

where $\rho g$ is the specific weight of the fluid, $H_r$ is the crest-to-trough height of r$^{th}$ wave and warn of the danger of using this simple formula in complex natural sea waves analysis [8].

Describing sea waves in language of mathematics is still a great challenge for scientists. One would inevitably face following terms while going into the question of methodology of wave energetics – zero-crossings, significant wave height, wave energy spectra, etc.

Zero-crossings are used to distinguish between sea surface elevation and waves. In a time record, the surface elevation at any moment in time is the instantaneous elevation of the sea surface. Whereas wave in the same record is the profile of the surface elevation between two successive downward or two successive upward zero-crossings where zero is mean of surface elevations (Fig. 2). A surface elevation can be negative, but a wave cannot [9].

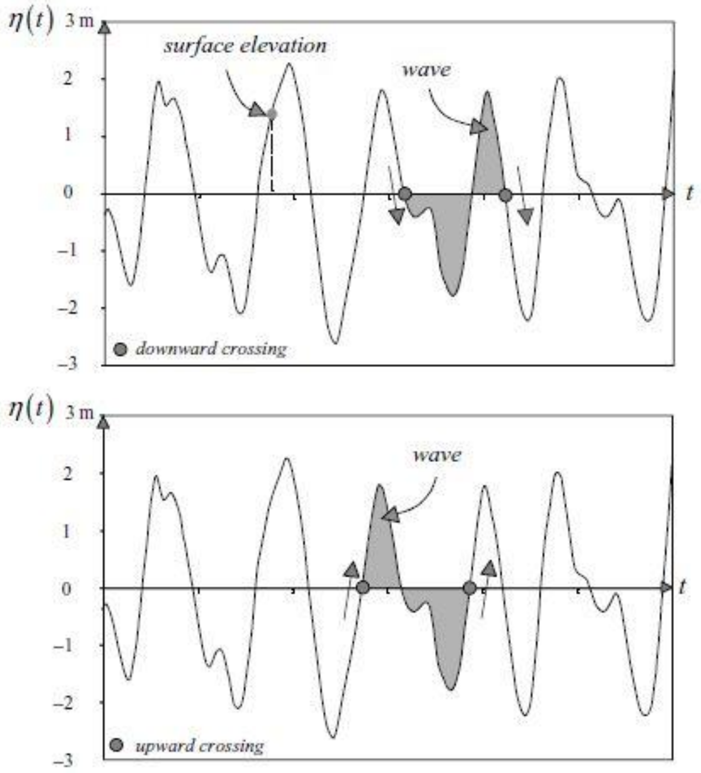

Fig. 2. The definition of wave in a time record of the surface elevation with downward zero-crossings or upward zero-crossings [9]

Visual wave observations procedure reflects the idea of zero crossing method. The observer notes the five highest waves during a 5 minutes time interval with accuracy of 0.25 m for wave heights less than 1.5 m, 0.5 m for wave heights from 1.5 to 4 m, and 1 m for higher waves. The highest single wave and the mean height of these five waves are filed [6,10].

Significant wave height $H_s$ is the most common statistical distribution of sea waves, usually described as the average height $H_{1/3}$ of the highest 1/3 of all waves during certain time interval [3]:

$$H_s = H_{1/3} = \frac{1}{N/3}\sum_{j=1}^{N/3} H_j \,, \tag{2}$$

where $j$ is not the sequence number in the record but the rank number of the wave, based on wave height, i.e. $j = 1$ is the highest wave, $j = 2$ is the second highest wave, etc [9].

This seems like a bizarre way to define characteristic wave height, but significant wave height now is used in numerical wave models, wave energy spectrums, wave climate descriptions, etc. Very useful feature of significant wave height, in our case, is that experience with visual observation showed that observer's visually estimated wave height rather well represents significant wave height [10].

Many wave spectra have been proposed to clarify wind-wave relationship. The simplest of them is by Pierson and Moskowitz. Its essence is that if the wind blew steadily for a long time over a large fetch, the waves come into equilibrium with the wind. And that is the concept of a fully developed sea [11].

The energy of a fully developed sea in the Pierson and Moskowitz wave-wind relationship is function:

$$S(w) = \frac{\alpha g^2}{w^5} \exp\left[ -\beta \left( \frac{w_0}{w} \right)^4 \right] \tag{3}$$

where $w = 2\pi f$, $f$ is the wave frequency in Hertz, $\alpha = 8.1 \cdot 10^{-3}$, $\beta = 0.73$($\alpha$ and $\beta$ are empirically adjusted constants), $w_0 = g / U_{19,5}$ and $U_{19,5}$ is the wind speed at a height of 19.5 m above sea surface [11,12].

It was assumed for a long time that best places to install wave energy converters is open deep sea zones. The reason for this assumption was that in the shallow sea areas waves change their characteristics and because of whitecapping, bottom friction and depth-induced breaking losses large amount of their energy.

Firstly, this theory is overturned by fact that first commercially successful wave energy projects are running in the nearshore and onshore sea zones. Future success of these projects is also approved by recent scientific studies.

Fig. 4 shows the reduction of wave power in sea state with an energy period of 10.0 s and significant wave height 3.2 m. It can be seen, that the wave power loss to water depth of 8 m is relatively small [7]. It is worthy to mention that at Palanga wave observations are made from Palanga Sea Bridge, in about 7 m depth area [6], thus pillars of this bridge can be used to anchor nearshore wave energy converter.

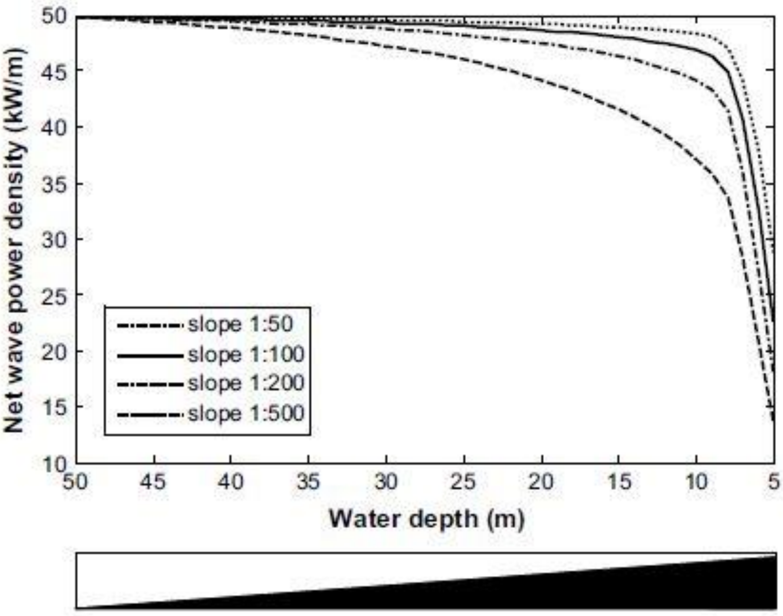

Fig. 3. Shoaling of a 10 s energy period wave propagating orthogonal to depth contours for different seabed slopes [7]

The results of the experiment, carried out on same topic, in Coastal Research Station (CRS) in Lubiatowo, Poland, surprised researchers. CRS is unique in Europe. Measuring devises of the CRS consist of row of cable connected measuring towers stretching 250 m offshore and wave buoy anchored 1 nautical mile offshore. One of main objectives of this experiment was to verify whether the simple formulas of relationships between characteristic wave heights (4, 5, 6), that are basically valid only for deep water waves, can be applied for a coastal zone.

$$H_{rms} = 1.13 H_{mean}, \tag{4}$$

$$H_s = 1.416 H_{rms}, \tag{5}$$

$$H_s = 1.60 H_{mean}, \tag{6}$$

where $H_{rms}$ is root-mean-square wave height and $H_{mean}$ is mean wave height. It is commonly believed that applications of these formulas in coastal zone seems to be a rough approximation.

Unexpectedly, the results revealed a very small differences comparing measured (in coastal zone) and calculated (with simple deep water formulas) characteristic wave heights. It did not exceed 2-5 %. This conclusion allows (4, 5, 6) relationships to be applied not only in deep water areas, but also in complex nearshore conditions.

Another important conclusion, settled in the same work, was that during week and moderate wave conditions, most of the wave energy reaches the shore and dissipates only in the immediate vicinity of the shoreline. High and stormy waves loses their energy at greater water depths and relatively small amount of energy reaches the shoreline area [13].

Hence visually observed data is usually plausible to evaluate nearshore wave energy potential and wind speed and wave height observations are sufficient to compute nearshore wave energy potential. Consequently classical statistical analysis for evaluating energy potential can be made using Klaipėda and Nida gauging stations wind speed and wave height data.

## 3. RESULTS

In this research wind speed and wave height data from Klaipėda and Nida gauging stations, year 1993–2008, was used.

Fig. 4. shows seasonal fluctuations of sea climate. Stronger winds blow in colder period of a year and consequently higher waves occurs. This graph confirms existance of the relationship between wind speed and wave height. Wave height line almost identically repeats the line of wind speed.

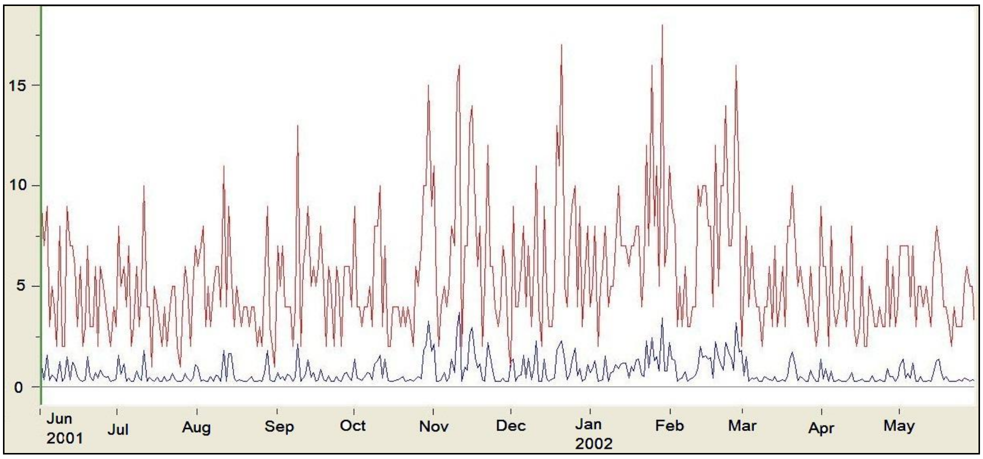

Fig. 4. Seasonal fluctations of wind speed (red line) and wave height (blue line) in Klaipėda

Coherence between these two characteristics was verified by calculating annual correlation coefficients (Table 1). Weak correlation is only in 1996, so it can be inferred that idea of extention of wave height time series by using wind speed time series can be implemented.

These findings were inspected by putting Nida gauging station daily average wind speed and wave height data into one graph (Fig. 5). The obtained correlation coefficient of 0,72 confirms good coherence.

Table 1. Annual correlation coefficients between wind speed and wave height

| | 1993 | 1994 | 1995 | 1996 | 1997 | 1998 | 1999 | 2000 |
|---|---|---|---|---|---|---|---|---|
| Klaipėda | 0.85 | 0.74 | 0.74 | 0.46 | 0.80 | 0.62 | 0.64 | 0.78 |
| Nida | 0.61 | 0.68 | 0.65 | 0.38 | 0.82 | 0.66 | 0.72 | 0.83 |

| | 2001 | 2002 | 2003 | 2004 | 2005 | 2006 | 2007 | 2008 |
|---|---|---|---|---|---|---|---|---|
| Klaipėda | 0.55 | 0.73 | 0.65 | 0.58 | 0.69 | 0.49 | 0.77 | 0.76 |
| Nida | 0.53 | 0.76 | 0.81 | 0.70 | 0.84 | 0.62 | 0.84 | 0.79 |

The statistical analysis rarely can be carried out without probability distributions. In this work probability distribution for Klaipėda 1993-2008 daily average wave height time series was made (Fig. 6). This function indicates that the 50 % probability of wave height is about 0.5 m.

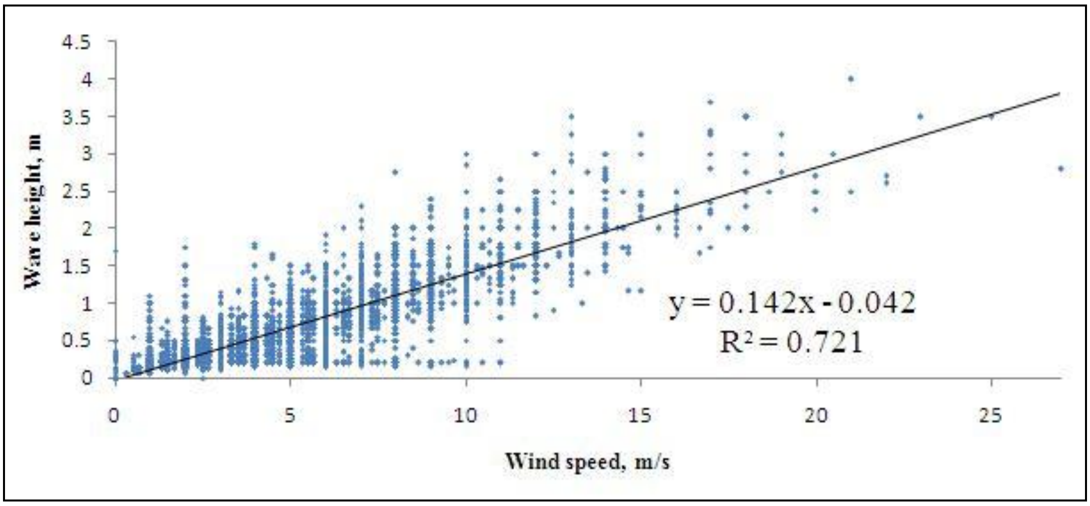

Fig. 5. Correlation between Nida gauging station daily average wind speed and wave height data (1993-2008)

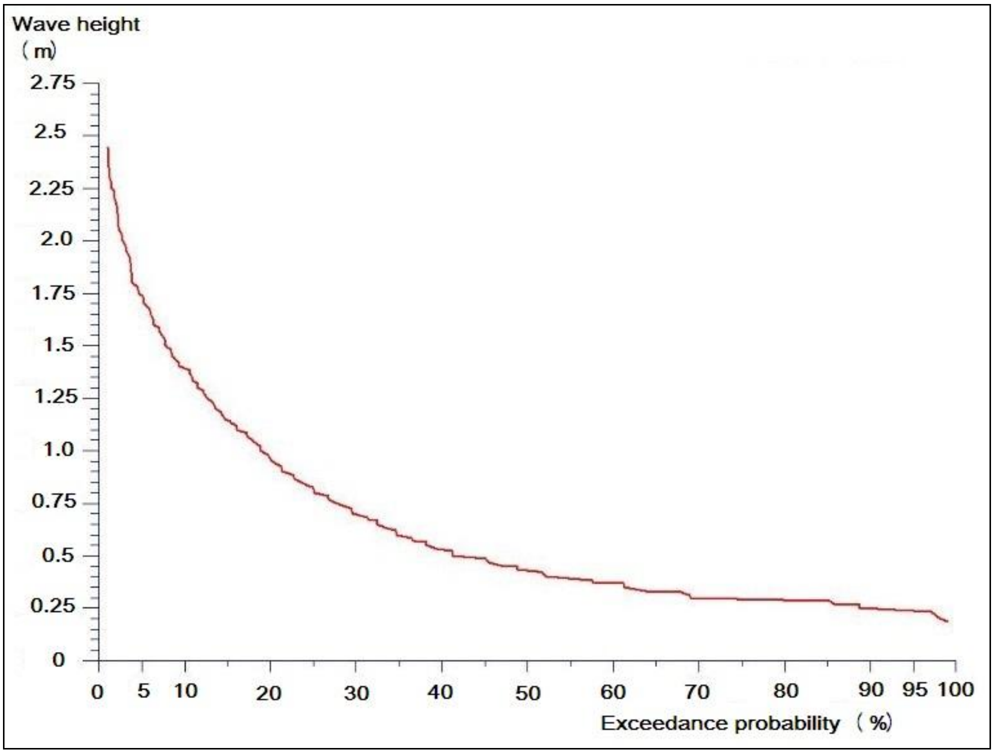

Fig. 6. Probability distribution for Klaipėda gauging station daily average wave heights (1993–2008)

## 4. CONCLUSIONS AND DISCUSSION

Lack of available data is one of the reasons, mentioned by European Ocean Energy Association, that blocks development of wave energetics. Therefore, this problem is important not only in Lithuania. On the other hand, wave climate in the Baltic Proper is different than in northeast Atlantic, where it is believed that wave energetics have the biggest potential.

The Baltic Sea is enclosed water body, lake-type sea and impact of the Atlantic Ocean is minimal here. This imply, that localy generated wind-waves are more reflected in the monitoring data.

This research showed good coherence between visual observed wave height and instrumentally measured wind speed in Klaipėda and Nida gauging stations time series. It proves that wind speed time series can be used to extent wave height time series, which, in turn, can be used for evaluating wave energy potential.

Thus the Baltic Sea do not have energy potential of northeast Atlantic, with more calm conditions it can be potentially handy place for safe and smooth work of wave energy converters.

## REFERENCES

1. LIU, P.C.; SCHWAB, D.J.; BENNETT, J.R. Comparison of a two-dimensional wave prediction model with synoptic measurements in Lake Michigan. *Journal of Physical Oceanography*, 1984, Vol. 14, p. 1514–1518.
2. LEPPARANTA, Matti; MYRBERG, Kai. *Physical Oceanography of the Baltic Sea*. Berlin: Springer, 2009. 378 p. ISBN 978-3-540-79702-9.
3. BROMAN, B.; HAMMARKLINT, T.; RANNAT, K.; SOOMERE, T.; VALDMANN, A. Trends and extremes of wave fields in the north-eastern part of the Baltic Proper. *Oceanologia*, 2006, Vol. 48, p. 165–184.

4. JONSSON, A.; BROMANN, B.; RAHM, L. Variations in the Baltic Sea wave fields. *Ocean Engineering*, 2002, Vol. 30, p. 107–126.
5. *Guide to the Applications of Marine Climatology*. World Meteorological Organization, 1981. Publication 781, Geneva.
6. KELPŠAITĖ, L.; HERRMANN, H.; SOOMERE, T. Wave regime differences along the eastern coast of the Baltic Proper. *Oceanography*, 2008, Vol. 57, No. 4, p. 225–231.
7. FOLLEY, M; WHITTAKER, T. J. T. Analysis of the nearshore wave energy resource. *Renewable Energy*, 2009, Vol. 34, p. 1709–1715.
8. ARANUVACHAPUN, S.; JOHNSON, A. J. Estimating wave energy from a wave record. *Ocean Dynamics*, 1976, Vol. 30, No. 1, p. 26–30.
9. HOLTHUIJSEN, Leo H. *Waves in Oceanic and Coastal Waters*. Cambridge: Cambridge University Press, 2007. 418 p. ISBN-13 978-0-521-86028-4.
10. SOOMERE, T.; ZAITSEVA, I. Estimates of wave climate in the northern Baltic Proper derived from visual wave observations at Vislandi. *Proceedings of the Estonian Academy of Science Engineering*, 2003, Vol. 13, No. 1, p. 48–64.
11. STEWART, Robert H. *Introduction to a Physical Oceanography*. Texas: A&M University, 2008. 354 p.
12. PANDEY, P.C.; GAIROLA, R.M.; GOHIL, B.S. Wind-wave relationship from SEASAT radar altimeter data. *Boundary-Layer Meteorology*, 1986, Vol. 37, No. 3, p. 263–269.
13. PRUSZAK, Z.; SZMYTKIEWICZ, P.; OSTROWSKI, R.; SKAJA, M.; SZMYTKIEWICZ, M. Shallow-water wave energy dissipation in a multi-bar coastal zone. *Oceanologia*, 2008, Vol. 50, No. 1, p. 43–58.

CYSENI 2011, May 26–27, Kaunas, Lithuania
ISSN 1822-7554, www.cyseni.com

# AQUEOUS CARBONATION OF OIL SHALE WASTES FROM ESTONIAN POWER PRODUCTION FOR $CO_2$ FIXATION AND PCC PRODUCTION

**M. Uibu, O. Velts, R. Kuusik**
*Tallinn University of Technology*
*Laboratory of Inorganic Materials*
*Ehitajate tee 5, EE-19086 Tallinn – Estonia*
*Phone +372 620 2812*
*Email: maiuibu@staff.ttu.ee*

ABSTRACT

Atmospheric emissions of greenhouse gas $CO_2$ originating from the fossil fuels based heat and power production are known contributors to global climate change. In Estonia, a local low-grade fossil fuel oil shale is used as a primary energy source. Combustion of oil shale is characterized by elevated specific carbon emissions (29.1 tC/TJ) due to the high content of mineral carbonates in oil shale. In addition to $CO_2$ emissions the power sector is also responsible for producing huge amounts (5–6 Mt annually) of Ca-rich (up to 25% free CaO) waste ash. As Estonia has zero geological storage potential, $CO_2$ sequestration by mineral carbonation considering alkali wastes as $CO_2$ sorbents is a prospective option. The aim of this study was to elaborate the main parameters of $CO_2$ fixation from flue gases via direct (ash suspensions) and indirect (ash leachates) aqueous carbonation of oil shale ash. Direct aqueous carbonation of ash is carried out in two steps by operating the reactors in a series of cascade at different pH levels at room temperature and atmospheric pressure. The water-soluble components such as free lime are carbonated in the first step, and the components of low water-solubility in which Ca is generally bound as silicate ($Ca_2SiO_4$, $Ca_3Mg(SiO_4)_2$), are carbonated in the second step. Indirect aqueous carbonation of oil shale ash is a more complicated multistep process but provides a waste valorization option by production of precipitated $CaCO_3$ (PCC). Obtained PCC contains 94-96% $CaCO_3$ and is characterized by regular rhombohedral crystalline structure, high brightness and mean particles size of 4 - 8 μm.

Keywords: $CO_2$, oil shale ash, mineral carbonation, PCC.

## 1. INTRODUCTION

Atmospheric emissions of $CO_2$ originating from the fossil fuels based heat and power production is a serious problem worldwide. For countries without geological storage sites, mineral carbonation could be considered as a $CO_2$ fixation option. Natural Ca-Mg-silicate (serpentinite, olivine) deposits are sufficient to fix the $CO_2$ that could be produced from the combustion of all fossil fuels resources [1], but the process is currently too slow and energy demanding for practical applications. Utilizing alkaline waste residues [ashes from coal- and oil shale-fired power plants [2–6], steel slags (electric arc furnace slag EAFS, basic oxygen furnace steel slag BOFS, ladle furnace slag LFS, etc) [7–10], municipal solid waste incineration (MSWI) ashes [11–13], air pollution control (APC) residues [14–15], cement kiln dust (CKD) [16], ordinary portland cement (OPC) [17], etc] as $CO_2$ sorbents have some promising advantages. These materials are often associated with $CO_2$ point source emissions and tend to be chemically more active than geologically derived minerals. Consequently, they require not as much of pre-treatment and less energy-intensive operating conditions (lower operating temperature and pressure) to achieve sufficient carbonation rates [7]. Some examples of the $CO_2$ binding potentials ($ThCO_2$ – theoretical extent of carbonation) as well as the process conditions (solid to liquid ratio S/L, temperature t, pressure P, duration τ) of alkaline waste materials are described in table 1. Also, the expensive $CO_2$ sequestration process might become economically feasible in case of upgrading waste materials into products of high commercial value, such as precipitated calcium carbonate or magnesium carbonate [18–20].

In Estonia, the oil shale combustion based power sector is the largest $CO_2$ emitter [21] where the waste ash is also formed in huge quantities (about 5–6 million tons annually) [22, 23]. Ash contains considerable amount of free CaO (10–30%-wt, depending on the combustion technology) as the most active compound and up to 30% of Ca-Mg-silicates ($CaSiO_3$, $Ca_2SiO_4$, $Ca_3Mg(SiO_4)_2$) as potential $CO_2$ binders [24, 25]. Contacting free lime with water leads to elevated pH values (pH > 13) and makes the ash landfilling by hydraulic transportation problematic. Developing methods for abatement of the $CO_2$ emissions as well as for safer deposition and utilization of the liquid and solid oil shale combustion wastes is one of the key environmental challenges in Estonia.

The aim of this study was to elaborate the main parameters (S/L, temperature, pressure, duration, $CO_2$ bound) of $CO_2$ fixation from flue gases via direct (ash suspensions) and indirect (ash leachates) aqueous carbonation (DAC and IAC, respectively) of oil shale ash with the prospect of obtaining PCC as a valuable by-product.

Table 1. Process conditions and $CO_2$ binding potentials of alkaline waste materials

| **Waste** | **CaO$^{total}$** % | **MgO$^{total}$** % | **Th$CO_2$** kg/t | **Process** | **$CO_2$ bound** kg/t | **Ref.** |
|---|---|---|---|---|---|---|
| Coal filter ash (FA) | 5.00 | | 35 | DAC: S/L=0.05-0.15; 100% $CO_2$; t=20-60$^{o}$C; P=10-40 bar | 26 | [5] |
| Lignite FA | 29.28 | 4.47 | 241 | DAC: S/L=1.5; τ=520h | 78 | [6] |
| MSWI FA | 53.02 | | 337 | SDC (semidry carbonation): S/L=25; 100% $CO_2$; τ=240h | 125 | [13] |
| APC | 61.13 | 1.40 | 369 | SDC: S/L=20; 100% $CO_2$; t=30$^{o}$C; P=30 bar; τ=10min | 250 | [15] |
| CKD | 48.03 | 1.39 | 319 | DAC: S/L=0-0.8; 80% $CO_2$; ambient t and P; τ=1-8d | 255 | [16] |
| OPC | 64.50 | 2.90 | 516 | SDC: S/L=0.1; 100% $CO_2$; P=2bar; τ=24h | 290 | [17] |
| EAFS | 32.80 | 10.00 | 366 | DAC: S/L=0.1; 15% $CO_2$, t=20$^{o}$C; τ=24h | 17 | [9] |
| LFS | 58.10 | 6.20 | 522 | | 247 | [9] |
| BOFS | 49.9 | 7.7 | 437 | IAC: extraction with 0.5M $HNO_3$;<br>t=20$^{o}$C; τ=60min | 384 | [10] |
| Red mud | 7.77 | 0.68 | 129 | DAC: S/L=0.1; 15% $CO_2$; t=20$^{o}$C; P=1 bar | 42 | [26] |

## 2. MATERIALS AND METHODS

### 2.1. Characterization methods

Initial pulverized firing oil shale ash sample (PFA) and its carbonation products (cPFA, PCC) were characterized by Total Carbon (TC; ELTRA Carbon/Sulfur Determinator CS-580) and quantitative X-ray diffraction (XRD) analysis as well as by scanning electron microscopy (SEM) methods. Powder XRD analysis was carried out on a Bruker D8 Advanced diffractometer. Scanning electron microscope Jeol JSM-8404A was used for surface observations. The particle size distribution of the PCC samples was determined by laser diffraction analyzer (Beckman Coulter LS 13320). Brightness of the PCC samples was measured according to ISO 2470:1999 [27].

Liquid phase was analyzed for the contents of $Ca^{2+}$ (ISO 6058:1984 [28]) and $SO_4^{2-}$ (spectrophotometer SpectroDirect Lovibond) ions as well as alkalinity (ISO 9963-1:1994 [29]). pH was measured with Mettler Toledo GWB SG2 and conductivity with conductivity meter HI9032.

## 2.2. Experimental setup

### 2.2.1. Direct aqueous carbonation of oil shale ash

The aqueous suspensions of initial samples (Table 2) were treated at S/L = 0.1 with $CO_2$ containing model gas (50 L/h; 15% $CO_2$ in air imitates the $CO_2$ concentration in actual flue gas) in an absorber for 65 minutes (Figure 1, DAC). The solid to liquid ratio was chosen similar to the one used for actual hydrotransport of ash at Narva PP. The carbonation process was carried out at room temperature and atmospheric pressure. After carbonation, the suspension was filtrated (Whatman filter paper "blue ribbon") and the solid phase was dehydrated at 105°C. Solid and liquid phase was analyzed according to Chapter 2.1. Theoretical extent of carbonation (g/100g) was calculated according to Huntzinger et al. [16]:

$$ThCO_2=0.785(\%CaO-0.56\bullet CaCO_3-0.7\bullet\%SO_3)+$$
$$+1.091\bullet\%MgO+0.70\bullet\%Na_2O+0.468(\%K_2O-0.632\bullet\%KCl) \quad (1)$$

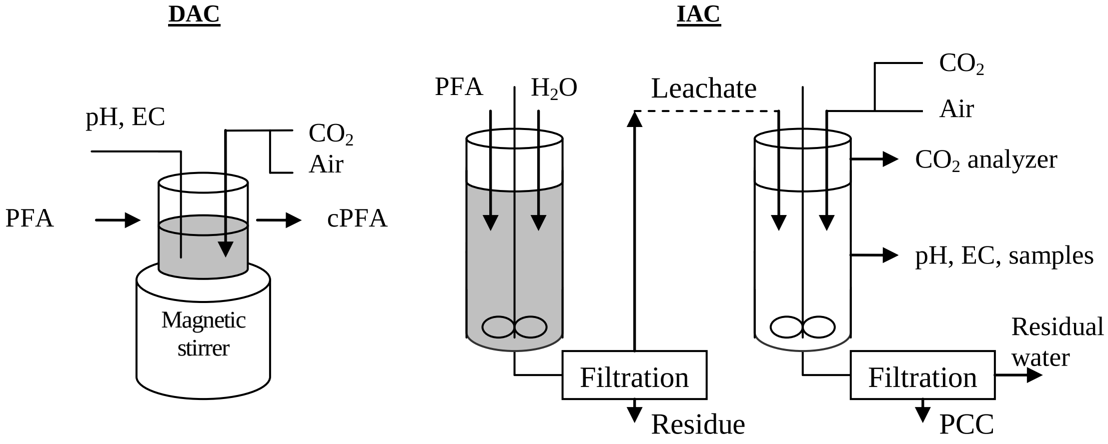

Fig. 1. Laboratory batch setups for DAC and IAC processes

### 2.2.2. Indirect aqueous carbonation of oil shale ash

Oil shale ash leachates were prepared by stirring oil shale ash - distilled water suspension (S/L = 10 w/w) in a 15 L reactor equipped with turbine type impeller for 15 minutes. Then the solid residue was separated by filtration (Fig. 1, IAC). The leachates (10 L) were carbonized in a semi-batch stirred (rotation speed N was 400 or 1000 rpm) reactor at constant gas feed rate of 1000 L/h with a model gas containing 15% $CO_2$ in air (Fig. 1, IAC). pH and electrical conductivity (EC) in the suspension as well as $CO_2$ content in the outgoing gas flow ($CO_2$ IR-analyzer, Duotec) were continuously measured during carbonation experiment. After carbonation, the suspension was filtrated (Whatman filter paper "blue ribbon") and the solid was dehydrated at 105°C. Solid and liquid phase was analyzed according to Chapter 2.1.

## 3. RESULTS AND DISCUSSION

### 3.1. Characterization of the initial sample

PFA contained 51% of total CaO, most of it was in the free form (CaO, $Ca(OH)_2$) or bound into Ca-Mg-silicates ($Ca_2SiO_4$, $Ca_3Mg(SiO_4)_2$, etc) (Table 2). Minor amounts of CaO were bound into sulphates ($CaSO_4$, $CaSO_4{\cdot}2H_2O$) and carbonates ($CaCO_3$, $CaMg(CO_3)_2$). Previous studies about the composition of oil shale ash have shown relatively good correlation between the chemical and quantitative XRD analysis [25]. However, some inconsistencies may occur (content of free CaO, Table 1). The particles of PFA were characterized by irregular as well as regular spherical shapes with smooth surface (Figure 2a).

Table 2. Chemical* and phase composition of PFA

| **Chemical composition** | | | | | |
|---|---|---|---|---|---|
| Component, % | | | | | |
| $CaO^{total}$/$CaO^{free}$ | 51.19 / 22.4 | $SiO_2^{total}$ | 21.90 | $Al_2O_3^{total}$ | 5.25 |
| $MgO^{total}$ | 4.93 | $Fe_2O_3^{total}$ | 3.98 | $CO_2^{total}$ | 5.41 |

| **Phase composition** | | | |
|---|---|---|---|
| Component, % | | $\alpha$-$Ca_2SiO_4$ | 1.99 |
| Calcite, $CaCO_3$ | 9.55 | $\beta$-$Ca_2SiO_4$ | 16.92 |
| Dolomite, $CaMg(CO_3)_2$ | 3.34 | Melilite, $(Ca,Na)_2(Mg,Al)(Si,Al)_3O_7$ | 4.99 |
| Portlandite, $Ca(OH)_2$ | 1.42 | Merwinite, $Ca_3Mg(SiO_4)_2$ | 6.81 |
| Lime, CaO | 29.52 | Wollastonite 2M, $CaSiO_3$ | 3.88 |
| Periclase, MgO | 4.27 | Hematite, $Fe_2O_3$ | 1.19 |
| Anhydrite, $CaSO_4$ | 4.48 | Quartz, $SiO_2$ | 7.38 |
| Gypsum, $CaSO_4{*}2H_2O$ | 0.76 | Orthoclase, $KAlSiO_3$ | 3.51 |

* Chemical analysis performed at the accredited Laboratory of the Geological Survey of Estonia

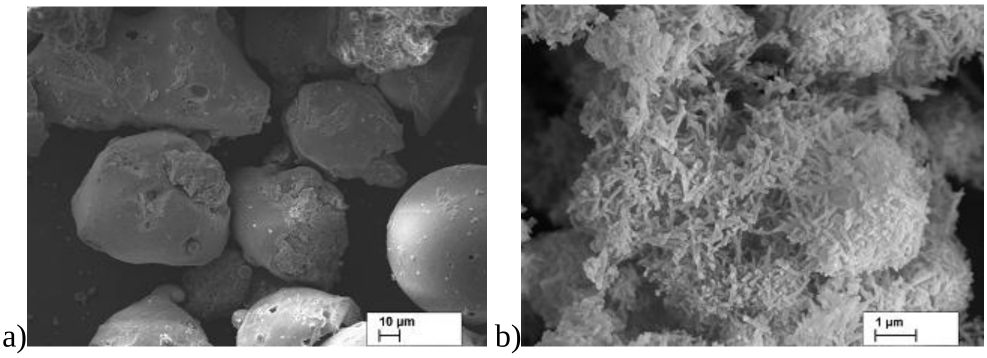

Fig. 2. SEM images of initial (a - PFA) and carbonised (b - cPFA) materials

### 3.2. Direct aqueous carbonation of oil shale ash

When PFA was immersed into water, slaking of lime-containing particles occurred (Eq. 2). The conversion of CaO to $Ca(OH)_2$ was followed by the dissolution of $Ca(OH)_2$ to give $Ca^{2+}$-ions and $OH^-$-ions at the surface of the particles and finally, by the diffusion of $Ca^{2+}$- and $OH^-$-ions into the bulk of solution (Eq. 3). The solution became instantly alkaline (pH ~ 12.9) and oversaturated with $Ca^{2+}$-ions ($Ca^{2+}$ = 1400 – 1500 mg/L). As $CO_2$-containing model gas was bubbled through the ash–water suspension the dissociation of formed $H_2CO_3$ (Eq. 4) and $CaCO_3$ precipitation reactions took place (Eq. 5). During carbonation, the pH and concentration of $Ca^{2+}$-ions in the liquid phase stayed on a high level until almost all free lime was realized. Then the pH of the suspension liquid phase and the concentration of $Ca^{2+}$-ions decreased rapidly until stabilizing at pH ~ 6.5 – 7.5. The $H^+$-ions reacted with the Ca-(Mg)-silicates, liberating $Ca^{2+}$ (and $Mg^{2+}$)-ions (Eq. 6), which in turn reacted with $HCO_3^-$-ions to form solid carbonate (Eq. 7) [30].

$$CaO\ (s) + H_2O\ (l) \leftrightarrow Ca(OH)_2\ (s) \tag{2}$$

$$Ca(OH)_2\ (s) \leftrightarrow Ca^{2+}(aq) + 2OH^-(aq) \tag{3}$$

$$CO_2\ (g) + H_2O\ (l) \rightarrow H_2CO_3\ (aq) \rightarrow H^+\ (aq) + HCO_3^-(aq) \tag{4}$$

$$Ca^{2+}\ (aq) + CO_3^{2-}\ (aq) \leftrightarrow CaCO_3(s) \tag{5}$$

$$Ca/Mg\text{-}silicate\ (s) + 2H^+\ (aq) \rightarrow (Ca/Mg)^{2+}\ (aq) + SiO_2\ (s) + H_2O\ (l) \tag{6}$$

$$(Ca/Mg)^{2+}\ (aq) + HCO_3^-(aq) \rightarrow (Ca/Mg)CO_3\ (s) + H^+\ (aq) \tag{7}$$

The quantitative chemical and phase composition as well as distribution of Ca-compounds for initial (PFA) and treated material (cPFA) was determined (Figure 3). The Ca-compounds consistent in the initial and treated ash were divided into four groups: 1) free CaO (CaO, $Ca(OH)_2$), 2) CaO bound into silicates ($\alpha$-$Ca_2SiO_4$, $\beta$-$Ca_2SiO_4$, $(Ca,Na)_2(Mg,Al)(Si,Al)_3O_7$, $Ca_3Mg(SiO_4)_2$, $CaSiO_3$), 3) CaO bound into sulfates ($CaSO_4$, $CaSO_4{\bullet}2H_2O$), 4) CaO bound into carbonates ($CaCO_3$, $CaMg(CO_3)_2$, $K_2Mg(CO_3)_2$). To compare the $CO_2$-binding efficiency of different groups the quantitative changes were recalculated on the basis of the initial material (PFA).

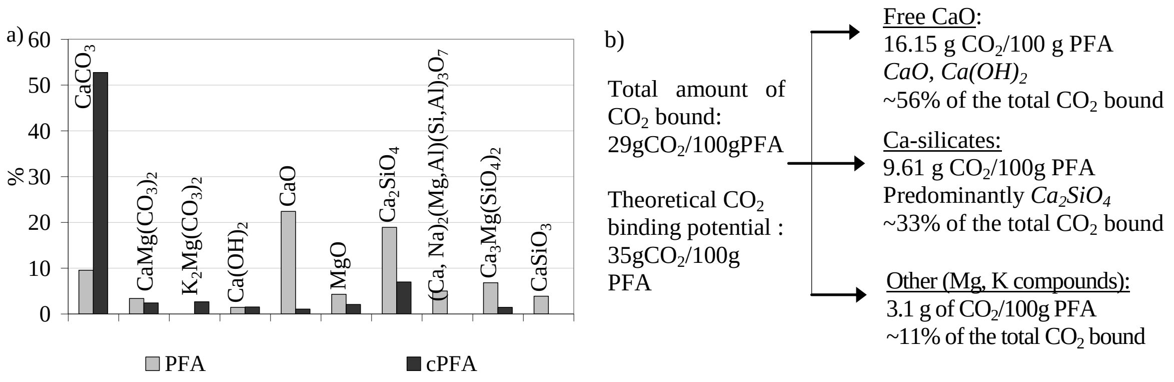

Fig. 3. Distribution of Ca-Mg compounds in the initial (PFA) and treated (cPFA) materials (a) and $CO_2$ bound into different groups of Ca-compounds (b) calculated according to chemical analysis and quantitative XRD measurements

Results of quantitative XRD indicated that the main $CO_2$ binding component of oil shale ash was as expected CaO (16.2 g $CO_2$/100 g PFA) (Figure 3b). An additional amount of $CO_2$ was bound by Ca-silicates (9.6 g $CO_2$/100 g PFA) which formed 33% of the total $CO_2$ bound in DAC of PFA (29 g $CO_2$ /100 g PFA, counting also $CO_2$ bound into $CaMg(CO_3)_2$ and $K_2Mg(CO_3)_2$ by Mg and K compounds). The theoretical extent of carbonation (Eq. 1.) was 35 g $CO_2$/100g PFA.

Carbonation treatment caused significant changes in the structure and surface characteristics of PFA. Hydration of lime caused ash particles to fracture and disintegrate (the molar volumes of $Ca(OH)_2$ and CaO are 33.078 and 16.79 mL/mol, respectively [31]), supporting in that way accessibility of lime to carbonation reactions. The particles of cPFA were covered with porous and permeable product ($CaCO_3$) layer (Fig. 2b).

## 3.3. Indirect aqueous carbonation of oil shale ash

### 3.3.1. Process description

Experiments indicated that alkaline ash leachates reacted readily with $CO_2$ containing model gas decreasing radically the content of $Ca^{2+}$-ions and pH value (Table 3). Contact of $Ca^{2+}$-ions with dissolved $CO_2$ led to precipitation of $CaCO_3$ (~22–24 g of solid product per 10 L ash leachates), which is practically insoluble in the water with pH > 9. At lower pH-values redissolution of $CaCO_3$ occurred and the concentration of $Ca^{2+}$-ions in solution started to increase (Table 3). The concentration of $SO_4^{2-}$ ions decreased moderately (from 870 mg/L to 710–724 mg/L). The concentration of background ions such as $K^+$, $Cl^-$, etc remained unchanged during the treatment, which means that they do not take part in the precipitation process in detectible amount. This finding is important in the context of product purity.

Table 3. IAC of oil shale ash: composition of the liquid and solid phase

| Test No | N | τ | Liquid | | | | | | | | Solid | |
|---|---|---|---|---|---|---|---|---|---|---|---|---|
| | | | pH | $Ca^{2+}$ | $K^+$ | $SO_4^{2-}$ | $Cl^-$ | $OH^-$ | $CO_3^{2-}$ | $HCO_3^-$ | $CaCO_3$ | $d_{mean}$ |
| | rpm | min | | mg/L | | | | meq/L | | | % | µm |
| 1 | 400 | 0 | 12.7 | 1265 | 120 | 874 | 5.0 | 49.0 | 1.0 | 0.0 | 0 | - |
| | | 4 | 9.2 | 244 | - | 732 | - | 0.0 | 0.5 | 1.5 | 94.3 | - |
| | | 15 | 6.45 | 350 | 114 | 734 | 5.2 | 0.0 | 0.0 | 7.5 | 94.7 | 4.89 |
| 2 | 1000 | 0 | 12.8 | 1268 | 124 | 862 | 4.6 | 49.0 | 1.0 | 0.0 | 0 | - |
| | | 3 | 9.2 | 274 | - | 710 | - | 0.0 | 0.2 | 3.6 | 93.6 | - |
| | | 20 | 6.98 | 426 | 124 | 724 | 5.5 | 0.0 | 0.0 | 11.0 | 94.4 | 7.76 |

### 3.3.2. Characterization of the solid product PCC

Formed precipitates were in the form of calcite (according to quantitative XRD analyses 100.0 wt-%) with bright white color, and fine and powdery texture. The TC analysis confirmed that the samples contained predominately $CaCO_3$ (~95 wt-%). Also, a small amount of gypsum (4–5 wt-%) was presumably deposited on the calcite matrix. Washing of the precipitates with distilled water (L/S = 20 w/w) improved the purity of solid products (96 wt-% $CaCO_3$). Main characteristics of the PCC obtained on the basis of PFA are presented in Table 3.

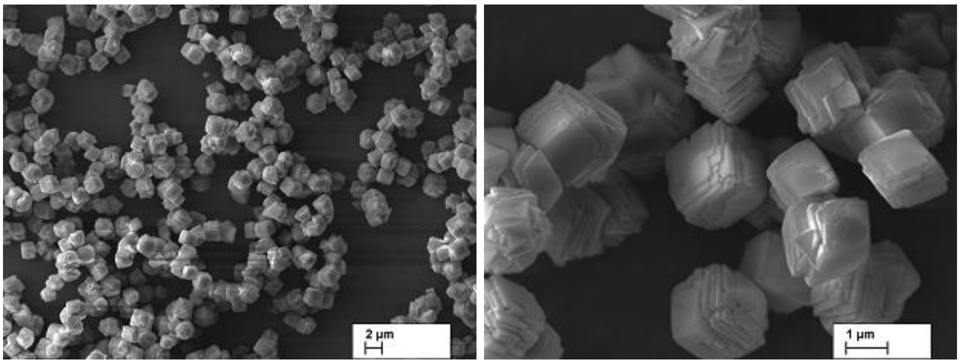

Fig. 4. SEM images of PCC particles (Test 1)

The PCC samples were characterized by a homogeneous particle size and rhombohedral crystal structure. Particle size was influenced by rotation speed N: increasing the rotation speed led to bigger particles ($d_{mean}$ increased from 4.9 to 7.8, Table 3). Shape and surface observations confirmed the results of the particle size distribution analysis (Fig. 4).

Agglomeration of the particles was not detected. In the context of producing PCC as a commercial product, smaller the particle sizes the better. Brightness of the PCC samples was 93%.

### 3.4. Method for eliminating $CO_2$ from flue gases by Ca-containing waste material

Based on recent studies on the carbonation of oil shale ash, a new method for eliminating $CO_2$ from flue gases by Ca-containing waste material was proposed [32]. The process includes contacting the aqueous suspensions of Ca-containing waste material with $CO_2$ containing flue gas in two steps: in the first step (reactor 1) the suspension is bubbled with flue gas keeping the pH levels in the range of 10–12 and in the second step (reactor 2) keeping the pH levels in the range of 7 – 8 (Fig. 5a). The water-soluble components such as free lime are carbonated in the first step and the components of low solubility, in which Ca is generally contained in the form of silicates, are carbonated in the second step. This enables optimal conditions for treating different phases of multicomponent waste materials.

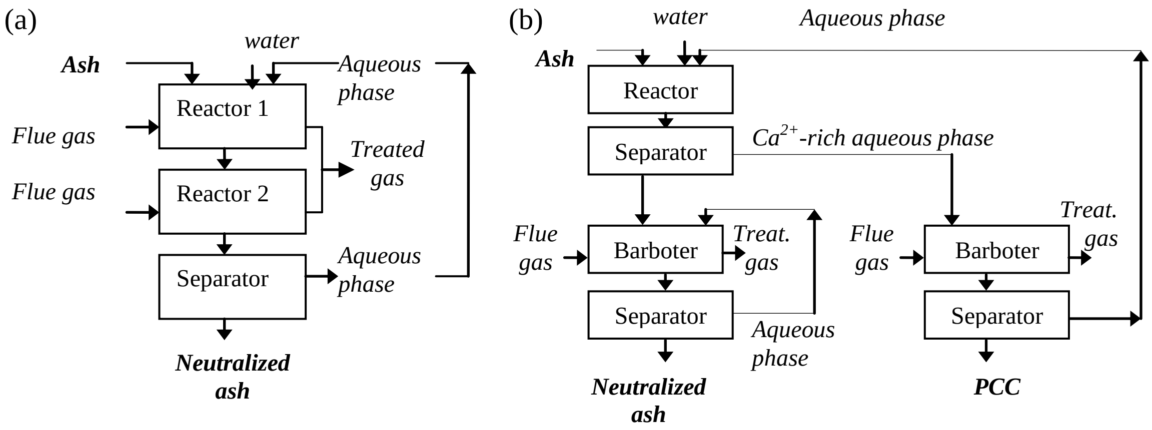

Fig. 5. Process diagrams for continuous mode aqueous carbonation of Ca-containing waste materials

As another process way, the free lime could without difficulty be separated from ash by leaching it into the aqueous solutions in order to produce precipitated calcium carbonate as a commercial product (Fig. 5b). The lime depleted residue is able to bind an additional amount of $CO_2$ on account of residual lime and Ca-silicates.

## 4. CONCLUSIONS

$CO_2$ fixation from model gas via direct and indirect aqueous carbonation of PF oil shale ash was demonstrated. The experiments were carried out at mild operating conditions: room temperature and atmospheric pressure. Comprehensive mineral composition of the initial samples as well as the carbonation products was presented.

Quantitative XRD analysis indicated that the main $CO_2$ binding component of oil shale ash was as expected CaO. An additional amount of $CO_2$ was bound by $Ca_2SiO_4$ and $Ca_3Mg(SiO_4)_2$ as the main $CO_2$ binding low water-solubility components of PFA. The main carbonation product was $CaCO_3$, indicating that Mg-compounds were not in most cases reactive towards $CO_2$ at these mild conditions. The $CO_2$ uptake for PFA was 290 $CO_2$ kg/t PFA (56% bound by lime and 33% bound by Ca-Mg-silicates), which is one of the highest according to table 1.

Indirect aqueous carbonation of oil shale ash provided a waste valorization option by production of precipitated $CaCO_3$. Obtained PCC contained ~95% $CaCO_3$ and was characterized by regular rhombohedral crystalline structure, high brightness and mean particles size of 4–8 µm. Also, the alkaline ash leachates were neutralized during the process.

Based on multifaceted studies related to carbonation of oil shale ash, a new method for eliminating $CO_2$ from flue gases by Ca-containing waste material was proposed. The process includes contacting the aqueous suspensions of Ca-containing waste material with $CO_2$ containing flue gas in two steps: the water-soluble components such as free lime are carbonated in the first step (at pH 10–12) and the components of low solubility in which Ca is generally bound as silicate are carbonated in the second step (at pH 7–8).

## ACKNOWLEDGEMENTS

Authors express their gratitude to Dr. V. Mikli for SEM measurements and to prof. K. Kirsimäe for quantitative XRD analysis. The research was supported by the Estonian Ministry of Education and Research (SF0140082s08) and the Estonian Science Foundation (Grant No 7379).

## REFERENCES

1. IPCC Special Report on Carbon Dioxide Capture and Storage; Intergovernmental Panel of Climate Change: Cambridge University Press, Cambridge, United Kingdom and New York, USA, 2005; 443 p.
2. KUUSIK, R.; VESKIMÄE, H.; UIBU, M. Carbon dioxide binding in the heterogeneous systems formed at combustion of oil shale. 3. Transformations in the system suspension of ash - flue gases. *Oil Shale*, 2002**,** Vol. 19, No. 3, p. 277–288.
3. KUUSIK, R.; UIBU, M.; TOOM, M.; MUULMANN, M.-L.; KALJUVEE, T.; TRIKKEL, A. Sulphation and carbonization of oil shale CFBC ashes in heterogeneous systems. *Oil Shale*, 2005**,** Vol. 22, No. 4 Special, p. 421–434.
4. JIA, L.; ANTHONY, E. J. Pacification of FBC ash in a pressurized TGA. *Fuel*, 2000, Vol. 79, p. 1109-1114.
5. MONTES-HERNANDEZ, G.; PEREZ-LOPEZ, R.; RENARD, F.; NIETO, J.M.; CHARLET, L. Mineral sequestration of $CO_2$ by aqueous carbonation of coal combustion fly-ash. *Journal of Hazardous Materials*, 2009, Vol. 161, p. 1347–1354.
6. ULIASZ-BOCHEŃCZYK, A.; MOKRZYCKI, E.; PIOTROWSKI, Z.; POMYKAŁ, R. Estimation of $CO_2$ sequestration potential via mineral carbonation in fly ash from lignite combustion in Poland. *Energy Procedia*, 2009**,** Vol. 1, p. 4873–4879.
7. HUIJGEN, W. J. J.; COMANS, R. N. J. Carbonation of Steel Slag for $CO_2$ Sequestration: Leaching of Products and Reaction Mechanisms. *Environmental Science and Technology*, 2006, Vol. 40, p. 2790–2796.
8. ELONEVA, S.; TEIR, S.; SALMINEN, J.; FOGELHOLM, C.-J.; ZEVENHOVEN, R. Fixation of $CO_2$ by carbonating calcium derived from blast furnace slag. *Energy*, 2008, Vol. 33, p. 1461–1467.
9. BONENFANT, D.; KHAROUNE, L.; SAUVE, S.; HAUSLER, R.; NIQUETTE, P.; MIMEAULT, M.; KHAROUNE, M. $CO_2$ Sequestration Potential of Steel Slags at Ambient Pressure and Temperature. *Ind. Eng. Chem. Res.*, 2008, Vol. 47, p. 7610–7616.
10. DOUCET, F. J. Effective $CO_2$-specific sequestration capacity of steel slags and variability in their leaching behaviour in view of industrial mineral carbonation. *Minerals Engineering*, 2009, Vol. 23, p. 262–269.

11. RENDEK, E.; DUCOM, G.; GERMAIN, P. Carbon dioxide sequestration in municipal solid waste incinerator (MSWI) bottom ash. *Journal of Hazardous Materials*, 2006, Vol. B128, p. 73–79.
12. VAN GERVEN, T.; VAN KEER, E.; ARICKX, S.; JASPERS, M.; WAUTERS, G.; VANDECASTEELE, C. Carbonation of MSWI-bottom ash to decrease heavy metal leaching, in view of recycling. *Waste Management*, 2005, Vol. 25, p. 291–300.
13. WANG, L.; JIN, Y.; NIE, Y. Investigation of accelerated and natural carbonation of MSWI fly ash with a high content of Ca. *Journal of Hazardous Materials*, 2010, Vol. 174, p. 334–343.
14. COSTA, G.; BACIOCCHI, R.; POLETTINI, A.; POMI, R.; HILLS, C.D.; CAREY, P.J., Current status and perspectives of accelerated carbonation processes on municipal waste combustion residues. *Environ Monitoring Assess*, 2007, Vol. 135, p. 55–75.
15. BACIOCCHI, R.; COSTA, G.; POLETTINI, A.; POMI, R.; PRIGIOBBE, V. Comparison of different reaction routes for carbonation of APC residues. *Energy Procedia*, 2009, – Vol. 1, p. 4851–4858.
16. HUNTZINGER, D.N.; GIERKE, J.S.; KAWATRA, K.; EISELE, T.C.; SUTTER, L.L. Carbon Dioxide Sequestration in Cement Kiln Dust through Mineral Carbonation. *Environ. Sci. Technol.*, 2009, Vol. 43, p. 1986–1992.
17. GUNNING, P.J.; HILLS, C. D.; CAREY, P. J. Production of lightweight aggregate from industrial waste and carbon dioxide. *Waste Management*, 2009, Vol. 29, p. 2722–2729.
18. TEIR, S.; ELONEVA, S.; FOGELHOLM, C.-J.; ZEVENHOVEN, R. Dissolution of steelmaking slags in acetic acid for precipitated calcium carbonate production. *Energy*, 2007, Vol. 32, p. 528–539.
19. KODAMA, S.; NISHIMOTO, T.; YOGO, K.; YAMADA, K. Design and evaluation of a new $CO_2$ fixation process using alkaline-earth metal wastes. GHGT-8 2006. Proceedings of 8-th International Conference of Greenhouse Gas Control Technologies. [CD] Trondheim: Elsevier ltd. 2006, June 19–22.
20. KATSUYAMA, Y.; YAMASAKI, A.; IIZUKA, A.; FUJII, M.; KUMAGAI, K.; YANAGISAWA, Y. Development of a process for producing high-purity calcium carbonate ($CaCO_3$) from waste cement using pressurized $CO_2$. *Environmental Progress*, 2005, Vol. 24, No. 2, p. 162–170.
21. *Greenhouse gas emissions in Estonia 1990-2005. National Inventory report to the UNFCCC secretariat*. Tallinn: Ministry of the Environment, 2007.
22. KAHRU, A.; PÕLLUMAA, L. Environmental hazard of the waste streams of Estonian oil shale industry: an ecotoxicological review. *Oil Shale*, 2006, Vol. 23, No. 1, p. 53–93.
23. Eesti Energia aastaaruanne 2009/2010. Keskkonnaaruanne [referred on the 3rd of March in 2011 y.]. Link to the internet <https://www.energia.ee/c/document_library/get_file?uuid=bb250184-08c8-43f0-8eca-f429fca63656&groupId=10187>
24. UIBU, M.; UUS, M.; KUUSIK, R. $CO_2$ mineral sequestration in oil shale wastes from Estonian power production. *Journal of Environmental Management*, 2009, Vol. 90, p. 1253–1260.
25. KUUSIK, R.; UIBU, M.; KIRSIMÄE, K. Characterization of oil shale ashes formed at industrial scale boilers. *Oil Shale*, 2005, Vol. 22, No. 4 Special, p. 407–420.
26. BONENFANT, D.; KHAROUNE, L.; SAUVE, S. B.; HAUSLER, R.; NIQUETTE, P.; MIMEAULT, M.; KHAROUNE, M. $CO_2$ Sequestration by Aqueous Red Mud Carbonation at Ambient Pressure and Temperature. *Ind. Eng. Chem. Res.*, 2008, Vol. 47, p. 7617–7662.

27. ISO 2470:1999, Paper, board and pulps – Measurement of diffuse blue reflectance factor (ISO brightness).
28. ISO 6058:1984, Water quality – Determination of calcium content - EDTA titrimetric method.
29. ISO 9963-1:1994, Water quality - Determination of alkalinity - Part 1: Determination of total and composite alkalinity
30. O`CONNOR, W.K.; DAHLIN, D.C.; RUSH, G.E.; GERDEMANN, S.J.; PENNER, L. R. Energy and economic considerations for ex-city aqueous mineral carbonation, The Proceedings of the 29-th International Technical Conference on Coal Utilization and Fuel Systems. Clearwater, Florida: Coal Technology Association. 2004, April 18–22.
31. Outokumpu HSC Chemistry for Windows. Chemical Reaction and Equilibrium Software with Extensive Thermochemical database. Version 4.0. License Ser. No. 40050 for Tallinn University of Technology.
32. KUUSIK, R.; UIBU, M.; UUS, M.; VELTS, O.; TRIKKEL, A.; VEINJÄRV, R. Method for eliminating $CO_2$ from flue gases by calcium compounds containing industrial wastes. Patent Application P200900040, 08.06.2009.

CYSENI 2011, May 26–27, Kaunas, Lithuania
ISSN 1822-7554, www.cyseni.com

# EVALUATION OF $NO_2$ AND $NH_3$ CONCENTRATION LEVELS IN KAUNAS USING TWO DIFFERENT PASSIVE SAMPLING METHODS

**J. Žaltauskaitė, G. Sujetovienė, D. Laurinavičienė, I. Šliumpaitė, R. Juknys**
*Vytautas Magnus University*
*Vileikos str.8-223, LT-44404 Kaunas – Lithuania*
*Phone +370 37 327920*
*Email: j.zaltauskaite@gmf.vdu.lt*

## ABSTRACT

The aim of the present study was to evaluate $NO_2$ and $NH_3$ levels in Kaunas and to compare results of nitrogen dioxide concentration measured by two different passive sampling methods. Two different passive sampling methods were used for nitrogen dioxide concentration determination. The first method was developed by M. Ferm (1991), the second one – by D. Krochmal and A. Kalina (1997). $NH_3$ concentration was determined by the same M. Ferm (1991) method. Sampling was carried out in Kaunas city in June of 2010. According to measured concentration comparison of two methods was done. The study results showed that mean nitrogen dioxide concentration in Kaunas city measured by passive method developed by M. Ferm (1991) was 18.7 $\mu g\ m^{-3}$, and 22.6 $\mu g\ m^{-3}$ developed by D. Krochmal and A. Kalina (1997). The highest nitrogen dioxide concentration was determined in city centre, Birštono street, and was quite similar measured by both methods (31.3 $\mu g\ m^{-3}$ by M. Ferm method and 32.2 $\mu g\ m^{-3}$ by D. Krochmal and A. Kalina method). Lowest nitrogen dioxide concentration was determined in recreational zone, J. Basanavičiaus stand, in Vičiūnai district (9.3 $\mu g\ m^{-3}$ measured by M. Ferm method and 11.7 $\mu g\ m^{-3}$ measured by D. Krochmal and A. Kalina method). The range of $NH_3$ concentration was 16.5-32.9 $\mu g\ m^{-3}$ with the mean concentration 22.1 $\mu g\ m^{-3}$. The highest concentration of $NH_3$ was observed in the park near Zoo.

Keywords: air pollution, ammonia concentration, nitrogen dioxide concentration, passive sampling method.

## 1. INTRODUCTION

Atmospheric pollution in urban area is a major issue in many countries all over the world. Air pollution affects human health, animals, damages vegetation, soils, and deteriorates materials, and generally affects not only the large metropolitan areas but also the medium-sized urban areas. Nitrogen oxides ($NO_x$) are one of major pollutants in the ambient atmosphere because of their adverse effects on human health and vegetation, their contributions to the acidification of the environment and role in the formation of photochemical oxidants. $NO_x$ contributes to the build-up of tropospheric ozone ($O_3$) and to the change of the concentration of hydroxyl radical (OH) which determines the lifetime of reactive greenhouse gases, and thus is also a key species for climate change.

Diffusive sampling has been increasingly used for the assessment of concentration of wide range of air pollutants, such as nitrogen dioxide ($NO_2$), ozone ($O_3$), sulphur dioxide ($SO_2$), ammonia ($NH_3$) and volatile organic compounds (VOC) in various environmental conditions [1-6]. The benefits of passive sampling devices include simplicity of sampling, low operating costs, high correlation results as compared to continuous monitors, and deployment in areas where there is no electricity. A large number of units can be used simultaneously, gathering information on the spatial distribution of the pollutants. Diffusive sampling can be used if the average, instead of the real-time, pollutant concentration is adequate for the purpose of monitoring [4].

A wide variety of diffusive samplers has been developed; the first diffusive sampler for carbon monoxide (CO) was patented in 1927 by Gordon and Lowe. Diffusive samplers were not developed further until 1973 when Palmes and Gunnison published a description of the first diffusive sampler for $SO_2$, consisting of a glass cylinder of 1 cm in diameter and 3 cm long, using a diffusion barrier. The diffusive sampler, commonly named Palmes tube, was developed later on and consisted of an acrylic tube 7.1 cm in length and 1.1 cm in diameter, containing a metal mesh coated with triethanolamine as an adsorbent for $NO_2$. Further changes consisted principally in modifications of the sampler dimensions and materials, diffusion barriers and the adsorbent for the gaseous pollutant, though every year sevral modifications of diffusive samplers are reported [7–8].

The aim of the present study was to evaluate nitrogen dioxide ($NO_2$) and ammonia ($NH_3$) levels in Kaunas and to compare results of $NO_2$ concentration measured by two different passive sampling methods.

## 2. MATERIALS AND METHODS

### 2.1. Sampling locations and strategy

Kaunas is the second largest city in Lithuania with the population of more than 415,700 and an area of 156 $km^2$. The mean annual temperature is about 7.6 °C with -1.2 °C in winter and 16.6 °C in summer, the annual rainfall is approximately 744 mm. (the data of 2009). The predominant wind direction is from south-west.

Nitrogen dioxide ($NO_2$) and ammonia ($NH_3$) sampling was carried out 15–22 June, 2010 at 10 points selected at different places of Kaunas city (Fig. 1) regarding their environmental conditions. Those included locations close to emission sources, such as those by main streets of Kaunas with intensive traffic load (Šančiai, Juozapavičiaus av. (1), city centre: K. Mindaugo av., Birštono str., Vasario 16th str. (3-5)) or in residential districts with intensive traffic (Šilainiai, Kuršių str. (7), Dainava, Pramonės av. (8), Žaliakalnis, Kalniečių str. (9), Eiguliai, Ukmergės str. (10)), and others distant from local emission sources, such as those within recreation zones (Vičiūnai (2), Kleboniškis (6)).

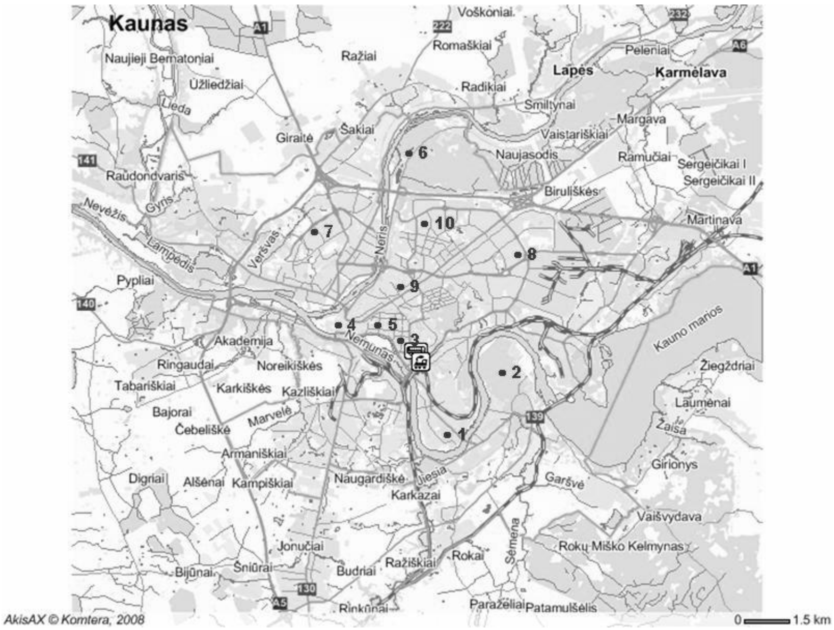

Fig. 1. Nitrogen dioxide sampling locations in Kaunas city

For determination of $NO_2$ concentration two different passive sampling methods were used. One was developed by M. Ferm (1991) [9], another – by D. Krochmal and A. Kalina (1997) [10]. The $NH_3$ sampling was perfomed by means of M. Ferm sampling method.

The chemical analysis of samplers was perfomed in Norwegian Institute for Air Research and Vytautas Magnus university.

## 2.2. Passive sampling method developed by M. Ferm (1991)

Passive sampler developed by M. Ferm is designed as a tube and a concentration gradient is established from the front of the tube to the active surface in the end of the tube [9, 11]. The active surface is normally an efficient absorbent so that the concentration on the surface is close to zero (ideally it should be zero). The concentration gradient over the sampler (the distance from the front to absorbent surface) is equal to the concentration in the surrounding air. The passive sampler has a diameter of 2.0 cm and a length (diffusion path) of 1.0 cm.The gas collection medium in the sample is a paper filter (Whatman 40, 24 mm diameter). A steel net and a teflon membrane filter are placed in the front of the sampler to prevent turbulence inside the sampler and the collection of particles.

For $NO_2$ determination, as an absorbent is used impregnation solution made from NaI and NaOH. After sampling, the content of nitrate and nitrite ions is determined using Gries method [12]. The principle of this method is that nitrate is reduced to nitrite using cadmium treated with copper sulphate as a reducing agent, in presence of ammonium chloride. Nitrite and sulphanilamide form a diazo compound which couples with N-(1-naphtyl)-ethylenediamine-dihydrochloride to form a red azo dye. The concentration in the solution is determined spectrophotometrically at 520 nm.

After sampling, the content of ammonium ions is determined using indophenol blue method [12]. The principle of this method is that in an alkaline solution ammonium ions react with hypochlorite to form monochloramine. In the presence of phenol and an excess of hypochlorite, the monochloramine will form a blue coloured compound, indophenol. The concentration of ammonium is determined spectrophotometrically at 630 nm.

## 2.3. Passive sampling method developed by D. Krochmal and A. Kalina (1997)

The passive sampler developed by D.Krochmal and A.Kalina is a badger type – its internal diameter is equal to 25 mm and depth to 10 mm [10]. A disc of Whatman 1Chr filter paper impregnated with triethanolamine (TEA) aqueous solution is used as the collecting element. The inside of the passive sampler is protected against wind and dust deposition by a wind screen made of a polypropylene fibre material. The reaction product between nitrogen dioxide in the air and TEA, is called - triethanolamine nitrogen oxide:

$$2NO_2 + N(CH_2CH_2OH)_3 + 2OH^- \rightarrow 2NO_2^- + {}^-O^- + N(CH_2CH_2OH)_3 + H_2O \qquad (1)$$

The alcaline medium protects nitrite ions from oxidation. The amount of nitrite which the filter collects depends on nitrogen dioxide concentration in the environment and the length of sampler exposure.

After sampling, the content of nitrite ions is determined spectrophotometrically at 540 nm following reactions with Saltzman reagent. The concentration of $NO_2$ is calculated from the following formula:

$$X = \frac{1.44 \times 10^5 m}{P \times t} \qquad (2)$$

where X is concentration of $NO_2$ , µg $m^{-3}$ at 1,013 x 105 Pa and 20° C; m is mass of $NO_2^-$ found in the sampler (µg); P is empirical coefficient defined as the mass of $NO_2^-$ determined in the sampler after a 24-h exposure in air containing 100 µg of $NO_2$ per 1 $m_3$ , ($NO_2^-$ ) (100 µg ( $NO_2$) $m_3$ 1440 min)$^-$; t is exposure period, min.

The value of the coefficient P for $NO_2$ determination was established using test gas mixtures and through comparisons with reference methods in field conditions. A correction for changes of the coefficient P with temperature is applied for better accuracy. For samplers with Whatman 1 Chr filter paper, the value o the coefficient P is calculated from the formula:

$$P=2.65+0.036xT \qquad (3)$$

where T is the temperature (° C) of the air during sampling.

Nitrogen dioxide measurements by this passive sampling method was used in Kaunas municipal ecological monitoring programme performed by the Departament of Environmental sciences at VMU in 1999–2009.

## 3. RESULTS AND DISCUSSION

The concentration of $NO_2$ in the ambient air measured by different sampling methods are shown in figure 2. The study results showed that mean nitrogen dioxide concentration in Kaunas city measured by M. Ferm method was 18.7 µg $m^{-3}$and varied between 9.3 and 31.3 µg $m^{-3}$. The highest $NO_2$ concentration was determined in the city center (Birštono st.). This site is located in the central part of the city with very high traffic intensity. In other locations which were located in the central part of city, nitrogen dioxide concentration was lower – 21.8 µg $m^{-3}$ (K. Mindaugo av.) and 18.7 µg $m^{-3}$ (Vasario 16th str.). The lowest nitrogen dioxide concentration was determined in the recreation zone – Vičiūnai (9.3 µg/$m^3$) in J. Basanavičiaus stand.

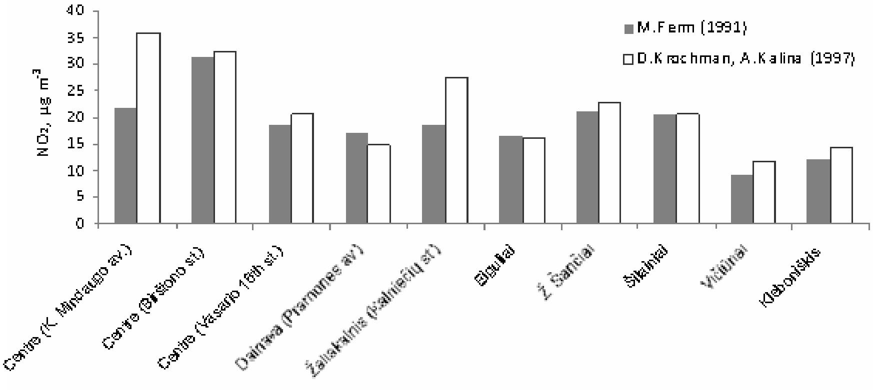

Fig. 2. $NO_2$ concentration measured by different passive sampling methods: the first columns shows $NO_2$ concentration measured by passive sampling method developed by M.Ferm (1991), the second – by D. Krochmal and A. Kalina (1997)

The average $NO_2$ concentration measured by D. Krochmal and A. Kalina method was 21.6 µg $m^{-3}$, and 11.7 µg $m^{-3}$ and 36.0 µg $m^{-3}$ were minimum and maximum values, respectively. The concentration of $NO_2$ in city center exceeded that in peripheral areas by 3 times. The highest concentration of $NO_2$ analysed by this method was also measured in the city centre – K. Mindaugo av. and Birštono str. (36.0 and 32.2 µg $m^{-3}$, respectively).

A good agreement was found between the average concentrations of $NO_2$ measured by different passive sampling methods. If compare the results between the different passive sampling methods, the measured concentrations of nitrogen dioxide was almost in all cases higher analyzing by D. Krochman and A. Kalina method than analyzing by M. Ferm method – 21.6 and 18.7 µg $m^{-3}$, respectively, but differences were statistically insignificant ($p > 0.05$). The $NO_2$ average levels in the largest city in Lithuania – Vilnius, where concentrations were higher – at crossroads it reached 52 µg $m^{-3}$ measured by M. Ferm method [13]. Average nitrogen dioxide concentration in Kaunas in 2003-2007 was 18.1 µg $m^{-3}$, in 2008 – 18.0 µg $m^{-3}$ and the highest concentration was determined in the city centre (2003-2007 – 26.3 µg $m^{-3}$, 2008 – 32.8 µg $m^{-3}$) [14–15]. Measured values agree with the measurement of $NO_2$ in Malaga [4] or in 363 cities of the United Kingdom [16], which shows average concentration levels equal 22.8 and 26.3 µg $m^{-3}$, respectively.

On the base of the measured $NO_2$ concentration, all the sampling sites were classified into 3 groups: city centre (K. Mindaugo av., Birštono str., Vasario 16th str.), residential areas (Šilainiai, Kuršių str., Dainava, Pramonės av., Žaliakalnis, Kalniečių str., Eiguliai, Ukmergės str.) and recreational areas (Vičiūnai, Kleboniškis). The overall average concentration of $NO_2$ for the three pollution groups is shown in Fig. 3.

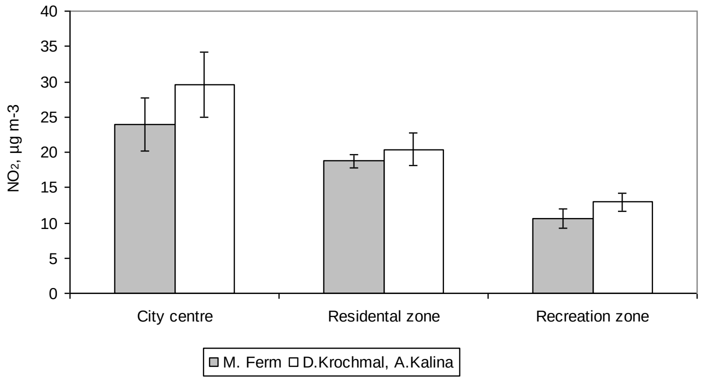

Fig. 3. Concentrations of $NO_2$ sampled in the city centre, residential and recreational zones (measured by M. Ferm (1991) and D. Krochmal and A. Kalina)

These groups were characterized by different $NO_2$ levels as follows: 1) heavily polluted (in the range 20–30 µg $m^{-3}$) (city centre); 2) moderately polluted (in the range 15–20 µg $m^{-3}$) (residential areas); and 3) less polluted (lower than 15 µg $m^{-3}$) (recreational areas). The average values measured in the recreation zone were found to be 55% and 21% lower than the ones detected at the streets with intensive traffic – in the city centre and residential zone, respectively.

The pattern of $NH_3$ concentration in Kaunas was quite different than that of $NO_2$ (Fig. 4). The average $NH_3$ concentration in Kaunas was 22.1 µg $m^{-3}$.

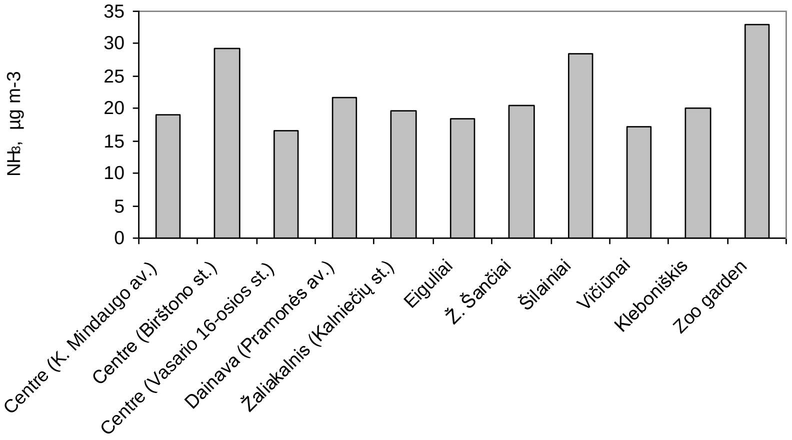

Fig. 4. Concentrations of $NH_3$ in Kaunas city

The highest concentration of $NH_3$ was detected near the Zoo, as the manure of animals is one of the main source of atmospheric ammonia. The lowest concentrations were observed in Vasario 16-osios str., in the districts of Vičiūnai and Eiguliai.

The yearly limit value of 40 μg $m^{-3}$ for $NO_2$ and $NH_3$ was not exceeded during the study period in Kaunas, though it may be presumed that in city center this value in case of $NO_2$ might be exceeded sometimes. The yearly limit value was exceeded in 2008 spring season in three different measurement places in city center: at Birštono st. it was 84.0 μg $m^{-3}$, Laisvės all. and A. Mickevičiaus str. crossroad – 92.8 μg $m^{-3}$, at Vilniaus str. – 72.3 μg $m^{-3}$. In 2009, the yearlu limit value was exceeded in spring and summer seasons. In spring season at Gedimino st. and Grunvaldo str. crossroad near supermarket „Akropolis“, it was 42.5 μg $m^{-3}$, at Vasario 16-osios str. it was 41.0 μg $m^{-3}$. In summer season at Birštono str. and Karaliaus Mindaugo av. crossroad it was 41.4 μg $m^{-3}$. It was caused by intensive traffic, unfavorable geographical position and meteorological conditions. Similar results were obtained from Costabile et al. [17]. Highest concentration of nitrogen dioxide were measured at high-traffic streets, followed by industrial and downtown locations.

## 4. CONCLUSIONS

The study showed that both passive sampling methods developed by M Ferm and D.Krochmal and A. Kalina may be used for the monitoring of $NO_2$ concentration in city territories. The good agreement between the concentration determined by these two methods was obtained in all studied sites.

The average $NO_2$ concentration in Kaunas city was 18.7 μg $m^{-3}$ (by M. Ferm method) and 22.6 μg $m^{-3}$ (by D. Krochmal and A. Kalina method). The highest $NO_2$ concentration was determined in city centre, Birštono street (approximately 31-32 μg $m^{-3}$ ), the lowest concentration was determined in recreational zone (9–12 μg $m^{-3}$).

The range of $NH_3$ concentration was 16.5–32.9 μg $m^{-3}$ with the mean concentration 22.1 μg $m^{-3}$. The highest concentration of $NH_3$ was observed in the park near Zoo garden.

## ACKNOWLEDGEMENTS

The study was funded by common assistance of the Republic of Lithuania and Norwegian Financial Mechanism under the block grant “Transfer of Experience and Strengthening of Cooperation among Local, Regional and Euroregional Partners in Lithuania and Norway”, contract No. 2004-LT0009-TES-1NOR-02-032.

## REFERENCES

1. KIMMEL, V., KAASIK, M. Assessment of urban air quality in south Estonia by simple measures. *Environmental Modeling and Assessment*, 2003, Vol. 8, p. 47–53.
2. SANZ, M.J., CALATAYUD, V., SANCHEZ-Pena, G. Measurements of ozone concentrations using passive sampling in forests of South Western Europe. *Environmental Pollution*, 2007, Vol. 145, p. 620–628.
3. SCHNITZHOFER, R., BEAUCHAMP, J., DUNKL, J., WISTHALER, A., WEBER, A., HANSEL, A. Long-term measurements of CO, NO, $NO_2$, benzene, toluene and $PM_{10}$ at a motorway location in an Austrian valley. *Atmospheric Environment,* 2008, Vol. 42, p. 1012–1024.
4. LOZANO, A., USERO, J., VANDERLINDEN, E., RAEZ, J., CONTRERAS, J., NAVARRETE, B. Air quality monitoring network design to control nitrogen dioxide and ozone, applied in Malaga, Spain. *Microchemical Journal*, 2009, 93, p. 164–172.

5. PARRA, M. A., ELUSTANDO, D., BERMEJO, R., SANTAMARIA, J. M. Ambient air levels of volatile organic compounds (VOC) and nitrogen dioxide ($NO_2$) in a medium size city in Northern Spain. *The Science of the Total Environment*, 2009, Vol. 407, p. 999–1009.
6. BIGI, A., HARRISON, R.M. Analysis of the air pollution climate at a central urban background site. *Atmospheric Environment*, 2010, Vol. 44, p. 2004–2012.
7. HAGENBJÖRK-GUSTAFSSON, A., TORNEVI, A., FORSBERG, B., ERIKSSON, K. Field validation of the Ogawa diffusive sampler for $NO_2$ and $NO_x$ in a cold climate. *Journal of Environmental Monitoring*, 2010, Vol. 12, p. 1315–1324.
8. LIN, C., McKENNA, P., TIMMIS, R., JONES, K.C. Field testing of a new-through directional passive air sampler applied to monitoring ambinet nitrogen dioxide. *Journal of Environmental Monitoring*, 2010, Vol. 12, p. 1430–1436.
9. FERM, M. A sensitive diffusional sampler. IVL-report, 1991, B-1020, IVL, Gothenbourg, Sweden.
10. KROCHMAL, D., KALINA, A. Measurements of nitrogen dioxide and sulphur dioxide concentrations in urban and rural areas of Poland using a passive sampling method. *Environmental Pollution*, 1997, Vol. 96, p. 401–407.
11. RØYSET, O. Comparison passive and active sampling methods for the determination of nitrogen dioxide in urban air. *Fresenius J. of Analytical Chemistry*, 1998, Vol. 360, p. 69–73.
12. EMEP manual for sampling and chemical analysis. 2001. EMEP/CCC-Report 1/95. Norwegian Institute for Air Research. 303 p.
13. PERKAUSKAS, D., MIKELINSKIENĖ, A. Evaluation of $SO_2$ and $NO_2$ concentration levels in Vilnius (Lithuania) using passive diffusion samplers. *Environmental Pollution*, 1998, Vol. 102(1), p. 249–252.
14. LAURINAVIČIENĖ, D. Distribution of nitrogen dioxide conceNtration in Kaunas 2003-2007. *Environmental Research, Engineering and Management*, 2010, Vol. 4 (54), p. 5–13.
15. LAURINAVIČIENĖ, D., JANUŠKAITIENĖ, I. Pollution of nitrogen dioxide in Kaunas in 2008. CYSENI 2010. Proceedings of annual conference of young scientists on energy issues. [CD]. Kaunas: Lithuanian Energy Institute. 2010 May 27–28.
16. CAMPBELL, G.W, STEDMAN, J.R., STEVENSON, K. A survey of nitrogen dioxide concentrations in the United Kingdom using diffusion tubes, July–December 1991. *Atmospheric Environment*, 1994, Vol. 28, p. 477–486.
17. COSTABILE F., BERTONI G., DESANTIS F., WANG F., WEIMIN H., FENGLEI L., ALLEGRINI I. A preliminary assessment of major air pollutants in the city of Suzhou, China. *Atmospheric Environment*, 2006, Vol. 40, p. 6380–6395.

CYSENI 2011, May 26–27, Kaunas, Lithuania
ISSN 1822-7554, www.cyseni.com

# URBAN HEAT ISLAND EFFECT ANALYSIS FOR AKURE, NIGERIA

**I.A. Balogun, A.A. Balogun, Z.D. Adeyewa**
*Department of Meteorology*
*Federal University of Technology*
*PMB 704, 34000 Akure – Nigeria*
*Phone +234-803-919-4212*
*Email: iabalogun@futa.edu.ng*

ABSTRACT

A climatological analysis of the differences in air temperature between rural and urban areas ($\Delta T_{u-r}$) corroborates the existence of an urban heat island (UHI) in Akure (7º 25' N, 5º 20' E), a tropical city in the south western part of Nigeria. The investigations which have been conducted out of a year-long experiment from fixed point observations focus on the description of the climatology of urban canopy heat island in the Akure and the analysis of the results were presented. The results show that the nocturnal heat island was more frequent than the daytime heat island as it exists from less intense to higher intensity categories throughout the study period. Nocturnal heat Island intensity was observed to be stronger during the dry season. Although of lower intensity, daytime heat Island exists throughout the day except for few hours in the months of November and December that exhibits a reverse thermal contrast. The daytime heat Island is observed to be more intense in the wet months than in the dry months, which may be caused by the evaporative cooling of wet surfaces. On the average, the urban/ rural thermal differences are positive, varying from $4^0$C at nocturnal hours during dry months to an approximate of $2^0$C around noon during wet months. This paper explains the aspects of heat islands and their relation to some causative agents such as the sky view factor (SVF) and also discusses its potential impact on energy demand.

Keywords: urban heat island, sky view factor, energy demand.

## 1. INTRODUCTION

The city of Akure has witnessed remarkable growth in its urbanisation in recent years, and its population during the past few decades has more than tripled. Urbanisation has been reported to modifiy local city climates. The resulting UHI is the characteristic warmth of urban areas compared to their outskirts. It is also often referred to as the increase of air temperature in the near-surface layer of the atmosphere within cities relative to their surrounding countryside [1].

Essence of studies of the UHI are not only predicated on the necessity to gain knowledge of its numerous secondary effects when excessive but also its practical needs in town planning, prevention of high concentration of air pollution, creating optimum bioclimatic conditions, etc. [2, 3]. Built-up environment has been found to exacerbate heat stress, particularly at night, during heat waves and provides a preferential site for spread of vector borne diseases [4, 5]. Modification of air temperature by urban areas at roof level has been reported extensively in mid-latitude cities [6, 7], but it has however been noted that transferability of results from knowledge regarding the mid latitude studies is still limited [8]. Lately, the heat-island phenomenon begin to receive attention in tropical environments where cities have been witnessing rapid growth in a chaotic manner [9, 10, 11, 12]. Most of the studies on mid-latitude were undertaken during the summer, when prevailing cloudless skies and calm or light winds allow full development of the phenomenon. Since the above conditions are not often present during winter, with some exceptions [13, 14] rather few studies were attempted to describe the seasonal behavior of the heat island during an annual cycle. Findings regarding relationships between the intensity of the urban heat island and various parameters, meteorological or not (e.g., the population of a city or the so-called sky view factor have been investigated [15, 16, 17].

Urban microclimate studies of tropical regions are still rare, the few that are available in Nigeria have used mean monthly climatological data or 2-3 hourly interval short term manual measurements [10, 11] and these have limited the studies to daytime conditions. This paper intends to provide additional insights on the descriptive aspects of the heat island phenomenon characterizing a tropical urban environment and discuss its relative impact on energy demand of the city and its environs.

## 2. SITE DESCRIPTION AND INSTRUMENTATION

The experiment was conducted from the October 2008 to September 2009. Figure 1 shows the location of the urban and rural stations used. The Oja Oba (meaning King's market), representing the urban site is located at the city centre in a densely mid- rise built-up area characterized with dense population, intense transportation and commercial activity. The rural reference site is situated at the meteorological service observatory of the seldom used local airport located about 15 km east on the outskirt of the city, and is characterized by massive grass-covered open plots, few bungalow office buildings and the control tower.

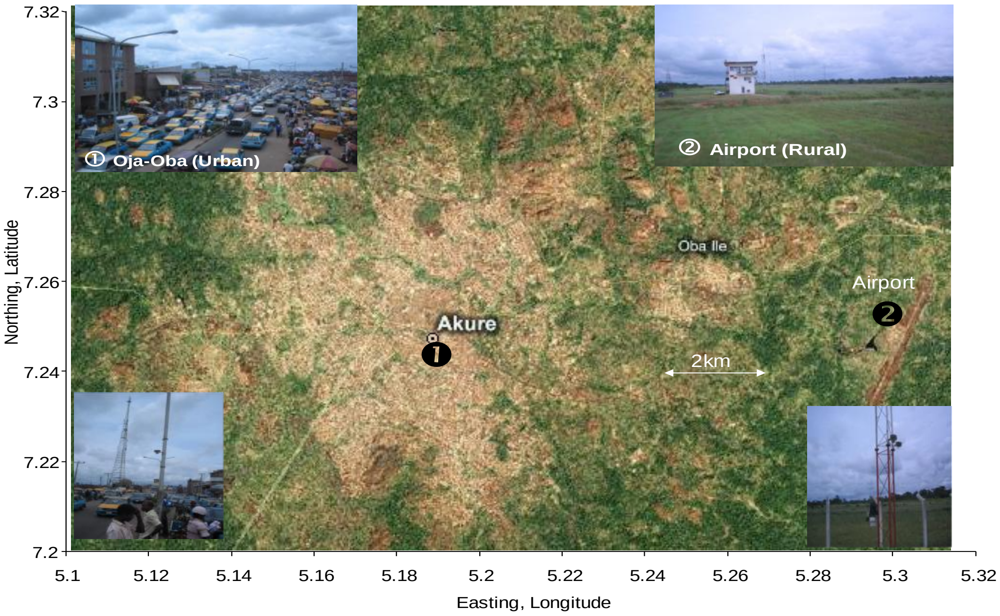

Fig. 1. Google Map of Akure showing the City centre (1) and Airport (2) sites. Inset (left and right) are photos of the sites and measurement systems respectively

The Oja urban site and the rural reference site are classified as Built climate zone (BCZ5) and Agricultural climate zone (ACZ3) respectively [18]. The sites were selected for fixed point observations and data were obtained from shielded portable Lascar EL-USB-2 temperature/humidity data loggers, sampled at 5 minute intervals that were mounted on a lamp post above head height (3 m) in the city urban centre and on a mast at same height in the local Airport. Position of the sensor at the urban site was carefully selected to prevent elevated heat sources such as rooftops. Afternoon air temperatures at 3 m above roof level are about 2°C higher than at 2 m above street level [19]. The difference in temperatures between the city and the out-of-town stations, denoted by ΔTu-r, is the most commonly used index of the intensity of the UHI. In this paper the quantity of this difference is accepted as a measure of the city's influence on thermal conditions. Cooling degree days (CDD) are values compiled daily to assess how much energy may be needed to cool buildings. They are calculated by the following formula; $CDD = \Sigma (ti - T)$ where T is the required room air temperature (25°C). The Hemispherical images are taken using a digital camera (Nikon Coolpix 950 with a 183-degree field of view fisheye lens) and the sky view factor were calculated from the hemispherical images using a method outlined by Chapman [20].

## 3. RESULTS AND DISCUSSION

### 3.1. Diurnal and annual course of the UHI intensity

It is evident that the daily course of the temperature fluctuations between the urban and rural site is a function of the season of the year. The most essential feature of the annual course of urban canopy heat island in the city is that the greatest differences occur in the dry season (November to February) reaching 3.5$^0$C and the smallest difference occurs during the wet season (April to October). The result regarding the urban rural air temperature differences ΔTu-r at both sites is presented in Fig 2. It shows that the UHI exists in Akure throughout the day except in November and December where urban cool island (UCI) is observed for few hours in the afternoon in both months. Daytime heat islands may be positive or negative depending on the particular characteristics of the urban area and their surroundings. Highest UHI values observed in the dry season agrees with Balogun et al [11] that reported UCI at 1500 in October/November and higher UHI values in January/February in Akure. However, results from this study slightly differ as the higher UHI values are observed in November through January but with January recording the highest value in overall. During the wet season, the UHI formed at night is preserved and almost unchanged throughout the day but during the dry season; the UHI formed at night is preserved until the morning hours and significantly drops in intensity or completely vanishes during midday. Annual course of the UHI at the time of the morning observation depends more on the time of sunrise relative to the time of observation, than on any factual dynamics of the weather conditions. The maximum UHI occurs at night between 1800 and 2200 local time having its peak around 2100. The peak period, on the average, might be linked to the release of sensible heat from "rush hour traffic" occurring in the city as a result of closing hours and evening market transactions from about 1800- 2100 thereabout. Thereafter, the heat island continues to develop through the early morning hours due mainly to the rural net radioactive energy loss to an unobstructed sky and less polluted atmosphere prior to sunrise. After this time, the solar heating generates a turbulent mixed layer over both the urban surfaces and the city environs, so thermal contrasts decline until around the end of the afternoon. Our result is however different from earlier reports that indicate that the maximum UHI occurs during the day time. The difference observed in months of highest value of UHI and the disagreement with time of maximum UHI occurrences exists because the earlier studies were restricted to daytime periods using the convectional mercury in glass thermometer. This result therefore provides new information on the diurnal characteristics of the UHI in Akure.

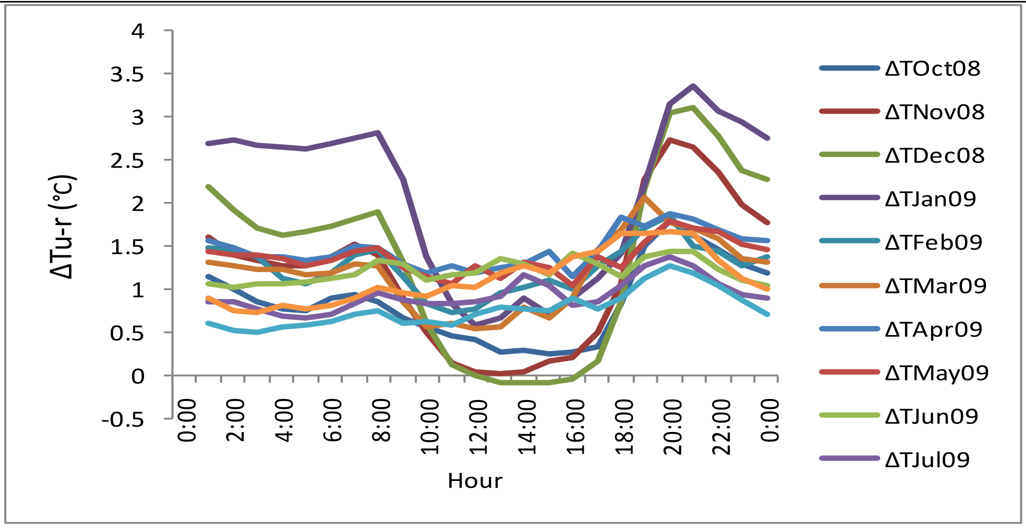

Fig. 2. Diurnal variation of mean monthly urban – rural differences of air temperature

### 3.2 Seasonal Variation of the maximum and minimum UHI

The seasonal variation of the urban/rural thermal contrasts at two critical hours (maximum and minimum) of the day is presented in Fig 3.

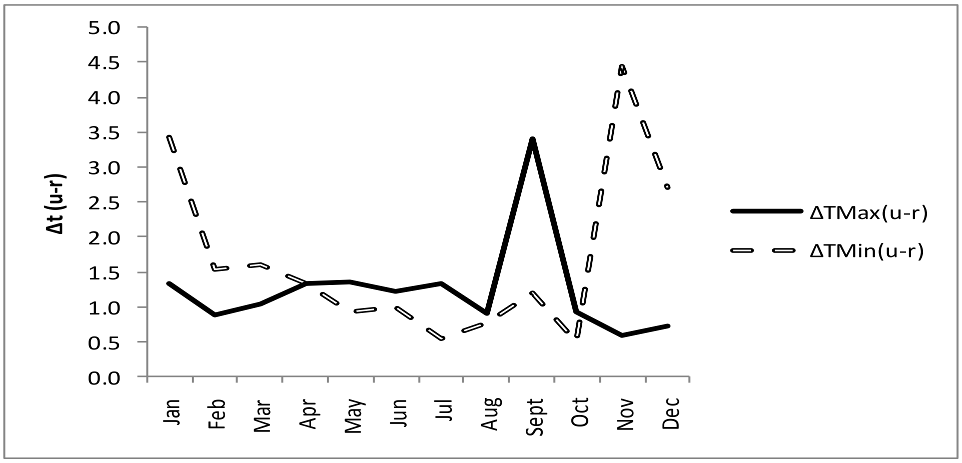

Fig. 3. Seasonal variation of urban heat island using mean monthly differences between maximum and minimum temperatures of both sites for the period of observation (October 2008 – September 2009)

It shows the mean monthly values of thermal contrasts at maximum and minimum temperature time for the study period (October 2008 – September 2009). The variations observed may be a result of different main causes of the UHI phenomenon explained by Oke [7]. Critical properties governing thermal contrasts during the night are the radiation geometry and the surface thermal properties, thermal admittance in particular; while the dominant processes responsible during the day are turbulent sensible heat flux obtained from increased absorption of shortwave radiation and anthropogenic heat sources which are mainly industrial and vehicular.

The distinct seasonal variation which is peculiar to both the nocturnal and daytime phenomena is associated with the seasonality of weather. It ranges from clear, calm nights in the dry season to unstable weather conditions with clouds and rain during the wet seasons (April – October). Therefore, as seen in Fig 3, the largest mean nocturnal heat islands (4.5°C) occur in the dry season when differences in urban/rural thermal admittance are more distinct, declining to a minimum (as low as 0.5°C) during the wet months of July and October when soil in the rural site is near saturation. The mean daytime heat island intensity is less intense reaching a maximum in September (3.5°C) (as a result of rural evaporative cooling from rainstorm), declining to a minimum (0.6°C) in November. The figure gives a clear indication that the urban-rural thermal contrasts, on the average always remain positive throughout the year and at all hours of the day for the 1-year period.

To establish period of pronounced heat island occurrences, we target only days that well marked urban temperature excess of greater than or equals to 1°C are being maintained over several hours. Data within this range were available for 315 days only. Result obtained justify our observation in fig 2 that the nocturnal (1900 to 0600) heat island is far dominant than the daytime heat island (0700–1800) particularly intense during the dry months. It overtakes in all the months except in June and September. However, it is noticed to be weaker and having a very narrow difference with the daytime heat island throughout the wet season (April–October) especially during the monsoon, but prevailing from the transitional month of November through the dry season. The daytime heat islands (0700–1800) were mostly observed during the wet season and almost out of existence in the dry season.

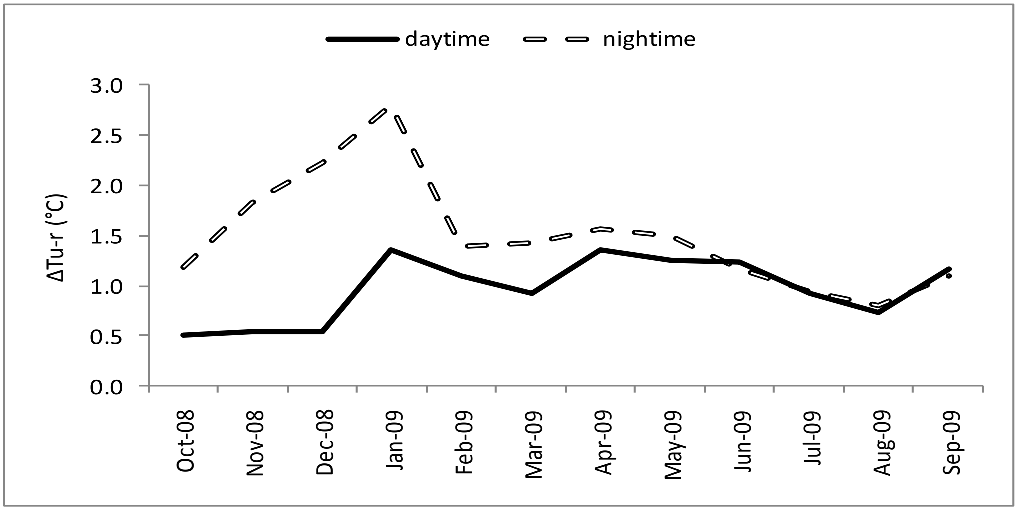

Fig. 4. Average and extreme values of heat island intensity for daytime and nocturnal period in Akure for the period of observation (October 2008 – September 2009)

The average and extreme values of the heat island along the 1 yr period of observations are illustrated in Fig. 4. While the mean heat island intensity for nocturnal events is about 1.5°C, elevating as much as 2.5°C during the dry season and the lowest during wet season (1°C); the mean daytime events have lower intensities in both dry (0.8°C) and wet seasons (1°C) and less variability of extremes. The figure shows that there is hardly existence of daytime heat island from October through December. The average and extreme values of both daytime and nocturnal periods of the day are nearly constant throughout the wet months from June to September (period of the peak rainfall). When they occur, the daytime heat islands have about the same intensities as the night-time.

### 3.3 Cooling Degree Days at the urban and rural sites

Fig. 5 shows the monthly mean numbers of the urban (CDDu) and rural cooling degree days (CDDr). The cooling degree day is clear measure for the comparison of the cooling energy consumption. The cooling season which has two epochs is characterized by significant cooling demand, the first which exists for a very short period in November and the other epoch which begins in February and lasts till May. These periods have peculiarities as they are transitional months, November is the transitional month into harmattan period and February to April are transitional months to the period of summer monsoon The highest cooling demand is observed to peak in March at both sites. The most significant difference appears in January (about $64^0$C of cooling degree higher in the urban than the rural site). Consequently, the effect of the city on the cooling energy demand is stronger than in other period of the cooling season. The months of July, August and September are noticed to exhibit totally different peculiarities as these three months in the both cases were absolutely typical of space heating demand rather than cooling as shown in Fig 5. In this period, the summer monsoon has fully developed, resulting in reduced cooling demand due to cooling effect of monsoon winds. These are the periods discussed in the section above that both daytime and nighttime heat islands exhibit almost the same intensities.

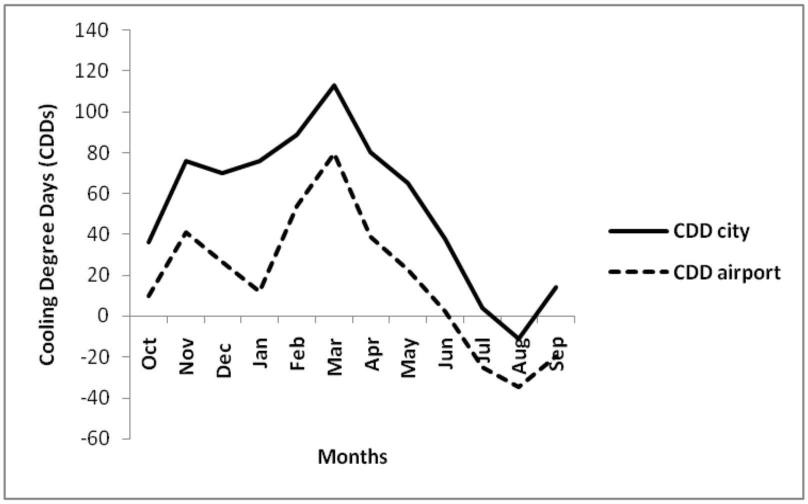

Fig. 5. Seasonal variation of the cooling degree days (CDDs) in the two sites (urban and rural)

### 3.4. The nocturnal heat island

Heat islands in the atmosphere are best expressed at night under calm and clear conditions when differential rates of radioactive cooling are maximized between urban areas and their surroundings, with cities cooling more slowly than their surroundings. Mean hourly development of the heat island for days with clear skies and calm winds during the dry season was investigated and it was observed that average nighttime heat island under such atmospheric conditions reaches its peak maximum value of 4.4°C at about 2100. This is similar to what was obtained in mid-latitude cities where urban/rural diverging cooling rates lead to maximum heat island intensity before midnight [7], but differs from what is observed in the tropical city of Mexico (Jauregui, 1997), where average nocturnal heat island reaches its maximum value at the end of the cooling period at about sunrise (0700-0800).

The Sky view factor (SVF) obtained from the hemispherical images taken at both the urban city core and the rural reference site situated at the old seldom used airport is presented in Fig 6. Facts emanating from the SVF calculation expatiate on why the heat island is more of a nocturnal phenomenon. The SVF is used in urban climatology to characterize radiative properties. By its definition SVF varies from zero when the whole sky is obscured to one when there is no obstruction. It has been proven to be an important concept in studies on radiation and temperature in different research areas. At night time, the rural site that is free from obstructions allows for quick escape of the longwave radiation causing an enhanced radiative cooling; while the city centre with reduced sky view due to its peculiar midrise buildings allows the street canyon to serve as heat storage, thereby causing a much slower radiative cooling from the urban surfaces.

| Site | Eye level photo | Sky view photo | S. V. F |
|---|---|---|---|
| 1. Airport |  |  | 0.98 |
| 2.Oja City |  | 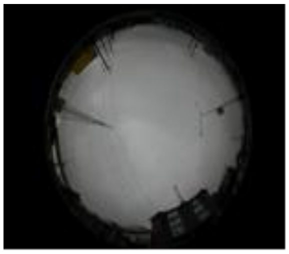 | 0.83 |

Fig. 6. The study sites, its eye level picture, sky view photo and the obtained sky view factor

## 3.5 Daytime heat island

Our results in Fig 2 & 7 show the existence of daytime heat island in the city Akure. The daytime heat island is less intense during the dry season but more pronounced in the wet season (between April and September) on the average of $1.5^{0}$C, and least in August (less than $1^{0}$C) which is the period of the ‘little dry season’ that is peculiar to this region. It revealed that the difference in the air temperature between the city centre and the rural reference site in Akure in some days and particularly during the months of November and December suggests existence of the urban cool Island (UCI). This is similar to some earlier reports in mid latitudes and less continental cities that have been found to be cooler at certain daytime hours in summer [6, 14]. The cool island observed is likely a result of the facts explained by [7].

On the average, the mean intensities are quite small; during the dry season, it revolves around $0.8^{0}$C in the daytime and $2.4^{0}$C overnight, but during the wet season, it is less intense with

$1.1^0$C in daytime and $1.2^0$C at night. The mean night-time intensity is larger than the daytime intensity in each month except for June–September (intense rainfall period. The daytime intensities were generally lower (0–0.9 to 1–$1.9^0$C) than the nighttime that exists within the range (1–1.9 to 3– $3.9^0$C) category. This is clearer in the frequency distribution shown in Fig. 7 below, which covers the total period.

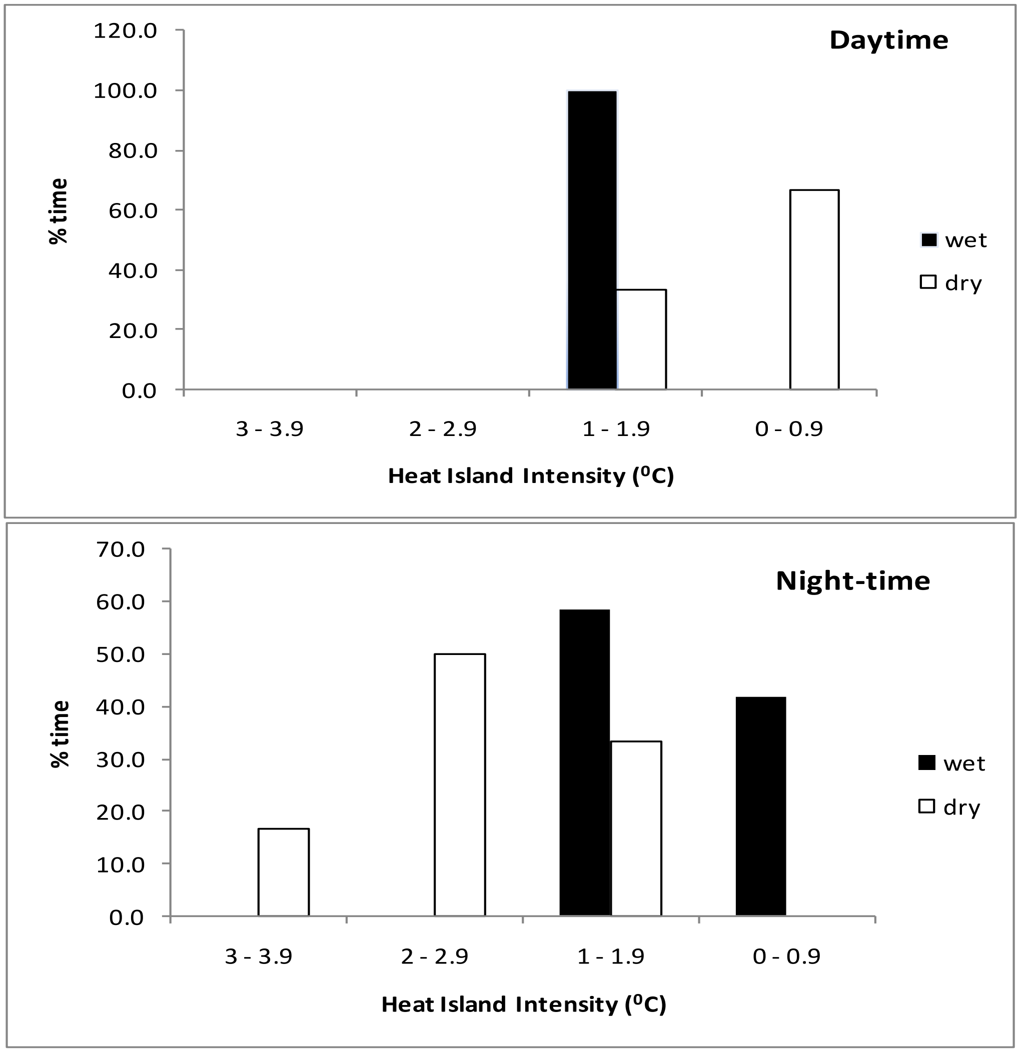

Fig. 7. Frequency distribution of daytime and nighttime heat island intensity for the period of study (October 2008 – September 2009) 1999 in Akure

During the wet season, particularly when the summer monsoon has fully developed (June-September), the frequency of less intense heat island (1- $1.9^0$C) is absolute in prevalence during the daytime and as well high at night. This suggests the observed reduced cooling demand in those periods as presented in figure 5. The dry season is characterized with more intense heat island, ranging as much as 3- $3.9^0$C during the dry season and this also reflects on the cooling demand as presented by the results of the cooling degree day.

## 4. CONCLUSION

The characteristics of urban heat island in Akure have been investigated and results reveal some interesting new findings on the diurnal and seasonal characteristics of the urban heat island in Akure. The urban heat island has been found to occur throughout the day and night except for a few hours in the afternoon of November and December that existence of urban cool island was noticed. The reversed thermal contrast may be as a result of relative abundance of moisture in the city compared to the rural surroundings. Weak daytime heat island exists throughout the wet season and extremely weak during the dry season accounting for reduced energy demand for cooling, but higher frequency of intense heat island at night time during the dry season is an indication of warmer nights capable of increasing the energy required for cooling. Results ascertain that the UHI is more of nocturnal phenomena in the tropical city of Akure as the highest UHI intensity occurs at night from 1800 to 2200 having its maxima at 2100 and also higher in the dry than the wet seasons. The elevation of temperature in the central urban areas at both day and night increases the potential for cooling of buildings. This may therefore lead to increased use of air-conditioning and hence adding more pressure to the electricity grid during peak periods of demand. This result has filled the knowledge gap on the nocturnal status of UHI in Nigeria as earlier studies were restricted to the daytime period due to lack of equipments capable of obtaining nocturnal data and has however supplemented previous attempts to fill knowledge gap of urban effects in tropical urban areas which is still insufficient as compared to the mid latitudes.

## Acknowledgements

The authors are grateful to Dr. Jimmy Adegoke of University of Missouri, Kansas City and Twins & Associates Ltd UK without whom starting this research project would not have been nearly as expeditious. The local airport authorities and the meteorological agency are also appreciated for giving permission for measurement stations to be set up in their premises.

## REFERENCES

1. VOOGT, J.A. Urban heat island. In: Munn, T. (Ed.), *Encyclopedia of Global Change*. Wiley, New York, 2002, p. 660–666.
2. ROSENFELD, A.H., AKBARI, H., ROMM, J.J., POMERANTZ, M. Cool communities: strategies for heat island mitigation and smog reduction. *Energy and Buildings*, 1998, 28: p. 51–62.
3. BALOGUN, A.A., BALOGUN, I.A., ADEYEWA, Z.D. Comparisons of urban and rural heat stress conditions in a hot-humid tropical city. *Global Health Action*, 2010; 3: 5614. DOI: 10.3402/gha.v3i0. 5614.
4. SAMUELS, R. Urban Heat Islands. Australian House of Representative Standing Committee on Environment and Heritage Sustainable Cities 2025 Enquiry, 2004.
5. SVENSSON, D., TARVAINEN, L. The Past and Present Urban Heat Island of Beijing, B416 Projektarbete Goteborg, *Earth Sciences*, 2004, Goteborg University, Sweden.
6. CHANDLER, T. London's urban climate. *Geographical Journal*, 1962, 128, 279–298.
7. OKE, T. R. The energetic basis of the urban heat island. *Quarterly Journal Royal Meteorological Society*, 1982, 108 (45), p. 1–24.
8. OKE, T. R., TAESLER, R., OLSSON L. The tropical urban climate experiment. Energy and Buildings, 1990/91, 15–16, p. 67–74.

9. IMAMURA I. Comparisons between observations at a mid-latitude city and two semiarid tropical cities. Proceedings of the Int. Conf. Tropical Meteorology and Air Pollution, Indian Inst. Tech., Delhi, India. 1988.
10. ADEBAYO, Y.R. Heat island in a humid tropical city and its relationship with potential evaporation. *Theor. Appl. Climatol*, 1991, 43 (3) P. 17–30.
11. BALOGUN, A.A., BALOGUN, I.A., ADEFISAN, A.E., and ABATAN, AA. Observed characteristics of the urban heat island during the harmattan and monsoon in Akure, Nigeria. Proceedings of the Eight Conference on the Urban Environment. AMS 89th Annual Meeting, 11 – 15 January, 2009, Phoenix, AZ. Paper JP4.6, available online – http://ams.confex.com/ams/pdfpapers/152809.pdf
12. BALOGUN, I.A., BALOGUN, A.A., ADEYEWA Z.D. A note on the effect of urbanization on air temperature and humidity of Akure, Nigeria. Proceedings of the seventh International Conference of Urban Climate, 29th June - 3rd July 2009, Yokohama, Japan.
13. MUNN, R.E., HIRT, M.S. and FINDLAY, B.A climatological study of the urban temperature anomaly at Toronto. *Journal Applied Meteorology*, 1969, 8, p. 411–422.
14. UNWIN, D.J. The synoptic climatology of Birmingharn's urban heat island 1965–1974. Weather, 1980, 35(2), p. 43–50.
15. YAMASHITA, S. Some studies of heat island in Japan with special emphasis on the climatological aspects. *Geographical Review of Japan Series B*, 1988, 61, p. 1–13.
16. PARK, H.S., Variations in the urban heat island intensity affected by geographical environments. Environmental Research Center Papers, 1987, Environmental Research Center, the University of Tsukuba, vol. 11, p. 79.
17. TUMANOV, S., STAN-SION, A., SOCI, C., LUPU, A., OPREA, C. Local and mesoscale influences of the metropolitan areas on some meteorological parameters and phenomena to the city of Bucharest. *Romanian Journal of Meteorology*, 1995, 2 (1-2), p. 1–18.
18. STEWART. I., OKE, T.R. Classifying urban climate field sites by “Local climate zones” The case of Nagano, Japan. Proceedings of the seventh International Conference of Urban Climate, 29th June – 3rd July 2009, Yokohama, Japan
19. SAKAIDA, K., SUSUKI, M. Microclimate of an urban canyon with thick street trees. *Geographical Review of Japan*, 1994, 67 Series A8, p. 506–517.
20. CHAPMAN, L., THORNES, J.E., BRADLEY, A.V. “Rapid determination of canyon geometry parameters for use in surface radiation budgets,” Theor. Appl. Climatol., 2001, Vol. 69, No. 1/2, p. 81–89.

# DEPTH PROFILES OF TRITIUM ACCUMULATED IN CARBON FIBRE COMPOSITE DIVERTOR MATERIALS OF JET FUSION REACTOR

**M. Halitovs, G. Kizane, A. Vitins, E. Pajuste, L. Avotina**
*University of Latvia, Institute of Chemical Physics*
*Laboratory of Radiation Chemistry of Solids*
*Kronvalda blvd. 4, LV-1586 – Latvia*
*Phone +371 25963728*
*Email: mihails_halitovs@inbox.lv*

ABSTRACT

Divertor tiles used in different fusion reactors like JET are one of the most important structural parts of whole reactor because they prevent damage to vacuum camera and structural elements that could be damaged by high temperature and intense radiation fluxes. Analysed divertor tiles are made from carbon fibre composites (CFC) that have high mechanical and thermal endurance. Yet these tiles accumulate nuclear fuel – tritium and deuterium – used in fusion reactions. The depth of accumulation depends on energy of nuclei moving towards divertor, erosion of divertor materials and mechanical properties of CFC materials themselves. Therefore it is essential to determine the exact depth profiles of accumulated tritium in toroidal and poloidal directions of divertor tiles.

Analysed tile 14 BWG 4B of MkII type divertor made from CFC material was delivered from JET fusion reactor in Culham, UK after real D + T experiments. The amount and depth profiles of tritium that was accumulated in these tiles was determined with the method of full oxidation and liquid scintillation. General tendencies in results show that up to 98–99% of total accumulated tritium (tritium activity up to $10^6$–$10^8$ Bq·g$^{-1}$) is located in the top layer of about 1 mm thickness of divertor tile. Accumulation of tritium in the bulk of divertor material is constant and does not exceed $10^5$ Bq·g$^{-1}$ in most cases. Increased accumulation of tritium was detected in the lower layers of divertor tile (tritium activity $10^5$–$10^6$ Bq·g$^{-1}$) that is probably due to structural changes of CFC materials and increased diameter of carbon fibres that was shown by SEM analysis.

Keywords: tritium, carbon fiber composites, fusion device, liquid scintilation, divertors, combustion, vance aparatus.

## 1 INTRODUCTION

As fossil energy resources provide the most part of energy used nowadays, it is essential to develop alternative and still effective sources of energy. The most perspective of those for now is fusion. It is planed that by 2030–2040 first commercial fusion device DEMO (DEMOnstration Power Plant) will be constructed and providing electricity. As scientists are trying to replicate processes happening on the Sun, the development of fusion reactor on Earth gets very complicated. Therefore it is important to create materials that would be most efficient for fusion reactors.

Fusion processes simulated on Earth are based on isotopes of Hydrogen – Deuterium and Tritium. Fusion of these two isotopes gives the most energy outcome – up to 17.6 MeV [1]. Described reaction is shown bellow.

$$^{2}H + ^{3}H \rightarrow ^{4}He + 1n + 17.6\ MeV \qquad (1)$$

From 1960s TOKAMAK system has been developed to provide stable fusion reactions in plasma environment. To ensure operation of system, complicated magnetic fields, structural elements and Plasma Facing materials (PFM) have been developed. In order not to cool down plasma and interrupt its stability, materials of small atomic number (i.e. Z) were chosen for PFM. One of the most perspective materials is Carbon Fibre Composites (CFC) that consists of carbon in graphite form.

To ensure protection of fusion device – vacuum camera, structural elements etc. – divertor system is made, consisting of CFC divertor tiles. CFC materials are both thermally and mechanically stable. They do not disrupt plasma stability yet tend to erode noticeably (about 1.2 kg of erosion material during 2001–2004 in Joint European Toros (JET) fusion device [2]) and accumulate a part of nuclear fuel – Deuterium and Tritium.

Tritium is radioactive isotope of hydrogen (half-life time 12.33 years [3]) produced artificially within reactor making it an expensive resource. Therefore it is important to reduce accumulation of tritium. Detecting amount and regions of tritium accumulation is essential for producing the most effective divertor tiles.

## 2 SAMPLES AND RESEARCH METHODS OF ACCUMULATED TRITIUM IN CFC DIVERTOR TILES

### 2.1 Sample preparation for analysis

The analysed samples were taken from MkII-SRP (*Septum Replacement Plate*) type divertor tile 14 BW G4B (Fig. 1) of JET fusion device. Current divertor tile was used in the device from 2001 to 2004. Different parts of divertor are also analysed by members of EURATOM and ITER projects.

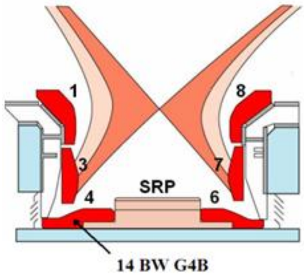

Fig. 1. Scheme of MkII-SRP divertor and position of analysed tile

During this period deuterium (D + D) fusion reactions (2) were realized producing tritium within vacuum vessel.

$$^{2}H + {}^{2}H \rightarrow {}^{3}H + {}^{1}H \tag{2}$$

The above mentioned divertor tile was core- drilled creating cylinders of 2.5÷4.7 cm length (Fig. 2). Cylinders were drilled in the direction of Lawre side of divertor – Cylinder 1 (Cyl 1) being the closest to SRP and Cylinder 11 (Cyl 11) – the most distant to SRP. The position of cylinder is important because divertor tile part closest to SRP has had direct interaction with plasma while part close to Lawre (*shadow part*) had almost no interaction with plasma and accumulated a lot of eroded carbon ash on the top of tile.

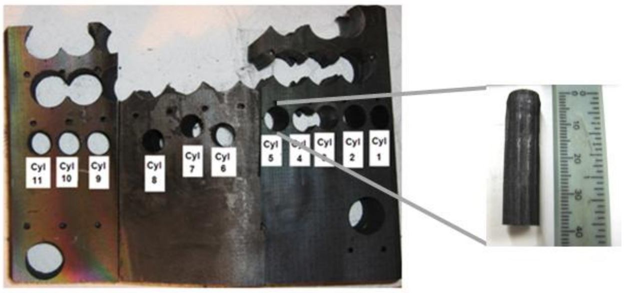

Fig. 2. Divertor tile 14 BW G4B and a close-up of drilled cylinder

A total of 6 lines of cylinders were drilled (showing four first lines in Fig. 3) in the divertor tile. By analysing several parallel cylinders of different lines in the same column (e.g. Cylinders 5 from Line I and Line II) it is possible to obtain 2D accumulation of tritium in different layers of divertor.

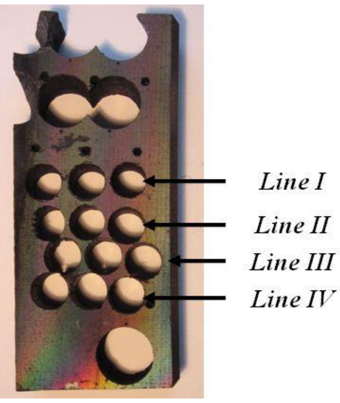

Fig. 3. Cylinder drill- lines I-IV, Lawre part of divertor tile14 BW G4B

To obtain precise 3D imaging of tritium accumulation in the tile, cylinders were cut into 1 mm thin CFC slices (example of slices is shown in Fig. 4). Through these actions it is now possible to get 3D imaging of tritium accumulation in divertor tile.

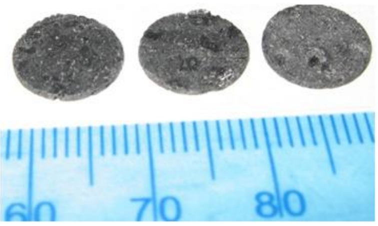

Fig. 4. Samples of analysed CFC slices

## 2.2 Method of analysis

To detect exact amount of accumulated tritium within divertor tile, method of full combustion in the flow of humid air was used. Oxidation products were analysed with liquid scintillation and tritium activity was used to calculate accumulated amount of tritium.

The method of full combustion in flow of humid air was realized in the Vance apparatus [4] (Fig. 5) customized specially for this certain purpose.

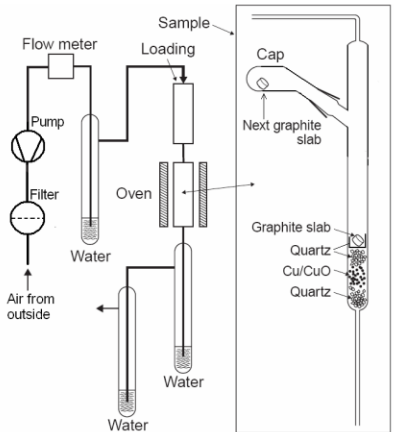

Fig. 5. Scheme of a modified Vance apparatus [4]

Flow of humid air was around $2.5 \cdot 10^{-7}$ $m^3 \cdot s^{-1}$ (15 $mL \cdot min^{-1}$). Humid air is used to optimize the processes of carbon oxidation (3-5).

$$H_2O_{(g)}+C_{(s)} \rightarrow H_{2(g)}+CO_{(g)} \tag{3}$$

$$2\ H_2O_{(g)}+C_{(s)} \rightarrow 2\ H_{2(g)}+CO_{2(g)} \tag{4}$$

$$H_2O_{(g)}+CO_{(s)} \rightarrow H_{2(g)}+CO_{2(g)} \tag{5}$$

Combustion lasts for 4 hours in the temperature around 860 ºC, collecting oxidation products in two chain- connected vials with de-ionised water. After first 4-hour process vials are changed and system is cleaned for 4–16 hours before inserting new CFC slice sample into the Vance apparatus.

To detect radioactivity of tritium in combustion products, a sample of 5 mL or less was taken from each vial with de-ionised water, scintillation cocktail was added and scintillation vials were put into Liquid scintillation counter *Perkin-Elmer* ***TriCarb 2900***.

A freeware programme SRIM (2008.04) was used to calculate the range of tritium ions into graphite. Data was used to compare theoretical calculations with experimental data.

# 3 RESULTS AND DISCUSSION

## 3.1 Tritium accumulation in the upper layer of divertor tiles

As experimental results show the maximal amount of accumulated tritium is located in the top, around 1 mm thick layer of divertor tile. The tritium radioactivity in this layer and next layers differ by a factor of 4÷6.

The average tritium radioactivity in the top layer of different cylinders is in the range of $10^6 \div 10^8$ $Bq \cdot g^{-1}$ (Fig. 6).

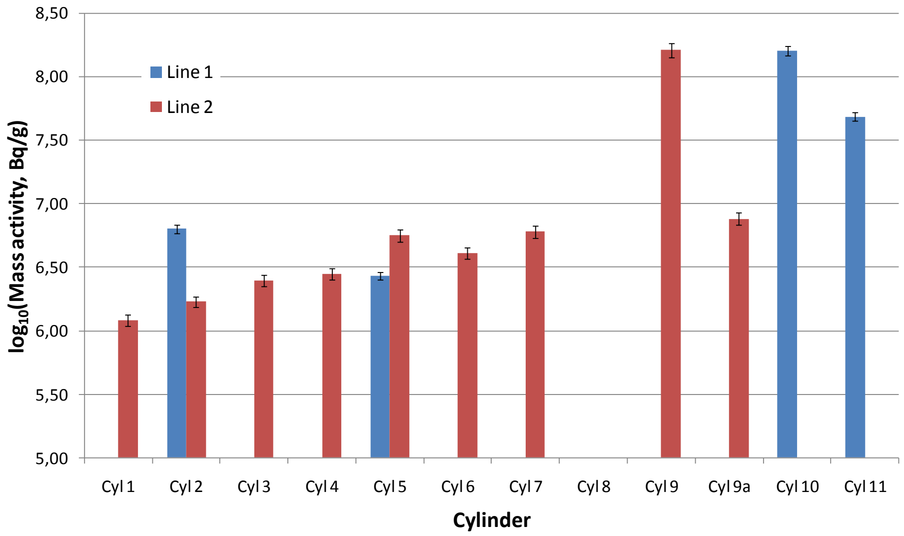

Fig. 6. Mass activity of top slice of Cylinders 1–11 from lines 1, 2; Tile 14 BWG 4B

The difference between tritium activity in different regions of the tile is due to positioning of analysed tile. As it was mentioned earlier in this paper, some regions of divertor tile had more interaction with plasma. Therefore region in the shadowed part of tile (Cyl 10–11) have higher tritium radioactivity because tritium tends to accumulate in ash material of eroded CFC. Part close to SRP was eroded by plasma, thereby accumulated tritium evaporated from the surface of tile in some regions.

Depth of tritium accumulation is also affected by its ion energy. Estimating that tritium ion $T^+$ in fusion reaction has energy around 100 keV, SRIM programme has calculated that maximal depth for tritium accumulating kinetically into graphite is around 9500 Å (~0.001 mm). As experimental method used can analyse samples of only 1 mm thickness, it is hard to determine the exact depth of accumulated tritium and the range of tritium radioactivity in this layer. However it gives an explanation why tritium activity differs noticeably between two analysed layers within 2 mm and proves the theoretical model based on ion energy.

## 3.2 Tritium accumulation in the bulk and bottom layer of divertor tile

Tritium radioactivity in the bulk of divertor tile is mostly defined by diffusion of tritium from the top layer of divertor. It can be verified by the tritium radioactivity in certain regions of tile – radioactivity is even in the bulk not exceeding limits of $10^4 \div 10^5$ Bq·g$^{-1}$.

Comparing the accumulated amount of tritium in different lines of the cylinders of same column (Fig. 7) it is clearly seen that difference between different cylinders does not exceed 15 %. Average difference is in range of 5–7 % that can be considered as insignificant. Thereby it can be concluded that accumulation of tritium within the bulk of divertor tile is mostly regular.

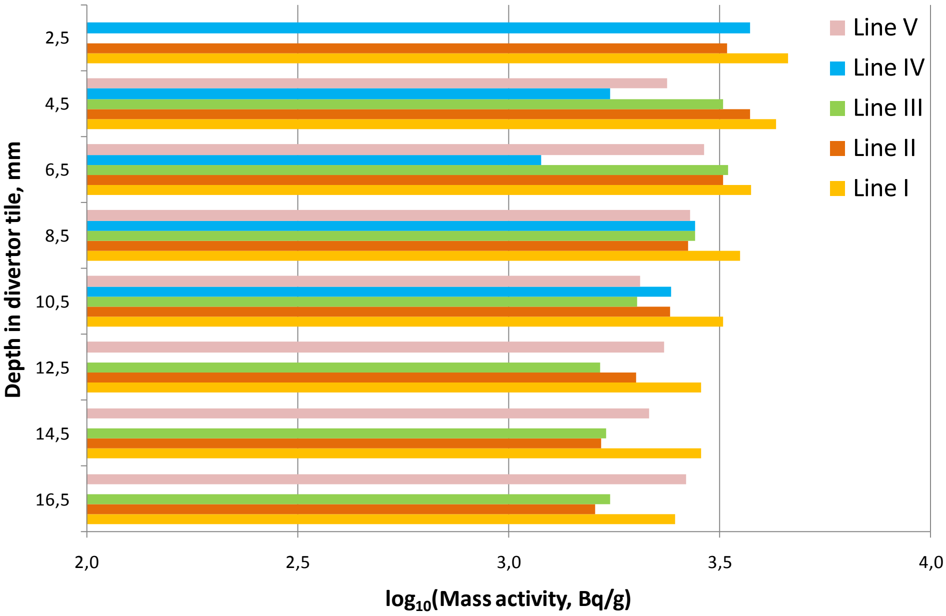

Fig. 7. Tritium accumulation in the bulk of divertor tile,
Cylinder 9 (Lines I–VI); Tile 14 BW G4B

Comparing the results from different lines, the same tendency was detected in several other cylinders – Cyl 10 (lines I–V), Cyl 7 (lines I – III), Cyl 5 (lines I–III). From that we can conclude that tritium diffusion during exploitation in fusion device was stable in both horizontal (Poloidal) and vertical (Toroidal) directions.

While analysing experimental data it was detected that tritium radioactivity is raised in the bottom layer of divertor tile. The tendency of tritium accumulation in various cylinders is similar – it shows a swift increase in the bottom layer of divertor tile. Five cylinders of various lines and columns were compared in Fig. 8, with dotted lines given to highlight tendency of tritium radioactivity. The dotted line does not represent any kind of calculated values, it only shows a tendency of obtained data. Radioactivity in this layer is in range of $10^4$–$10^6$ Bq·g$^{-1}$.

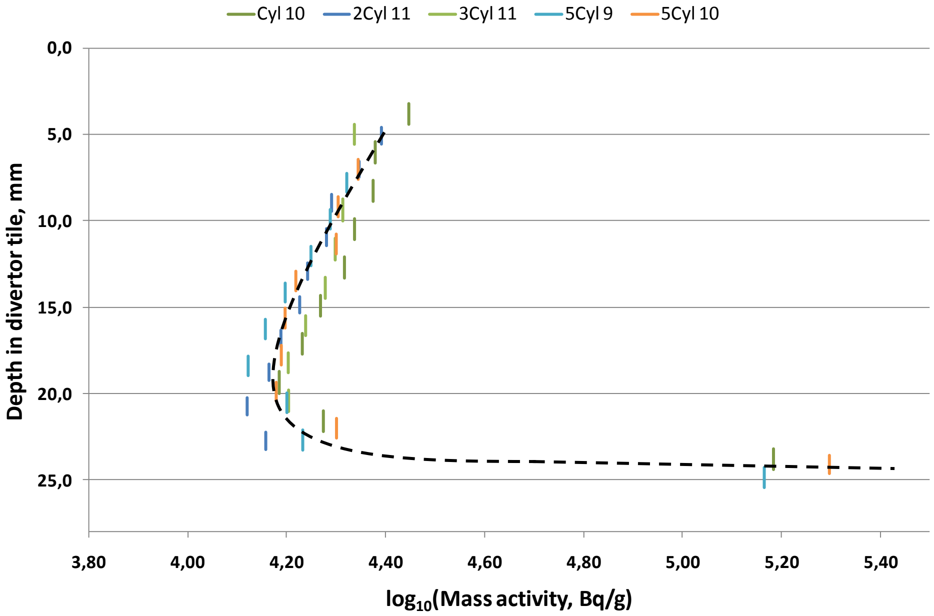

Fig. 8. Tritium mass activity in the bulk and bottom of several cylinders with tendency of activity highlighted; Tile 14 BW G4B

At first the noticed effect is rather surprising as bottom layer of divertor tile has no direct contact with fusion reaction environment. As it was examined, raised tritium radioactivity is present due to increased graphite fibre (Fig. 9) size [5]. That is because of harsh exploitation conditions that led to increased accumulation of tritium.

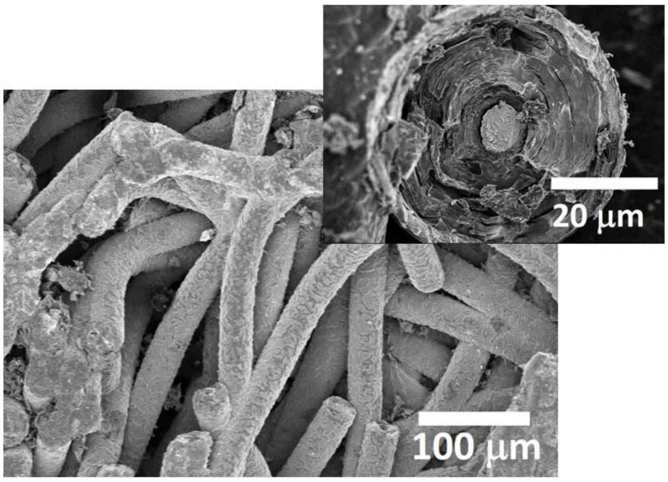

Fig. 9. SEM images of carbon fibres in the bulk of JET divertor tile. Inset shows an expansion of a fibre cross-section [5]

The total uncertainty of the results is calculated to be from 0.64% to 1.01%. The main contribution to the uncertainty is given by statistical error of data gained from scintillation counting and precision of cylinders used for measuring the volume of water in vials for Vance apparatus. Uncertainties of scaling, slice measurement and aliquot volume are negligible.

## 4 CONCLUSIONS

The obtained results show that most amount of tritium is accumulated within top layer of divertor tile. That was theoretically proven by using ion range data obtain from SRIM software and comparing them with experimental results. The exact amount of accumulated tritium in the top layer differs depending on the part of divertor tile examined.

An assumption that accumulation of tritium in the bulk of divertor tile could be greatly different depending on position in 3D coordinates (Poloidal and Toroidal direction) did not prove to be true. Comparison of samples from different lines of the same column cylinders has clearly shown that tritium accumulation within the bulk of divertor tile is mostly regular not exceeding an average of 5 – 7 % difference between different slices. That is explained by the fact that tritium accumulation in the bulk is mostly affected by migration of tritium from the top layers.

As general comparison of samples from different lines does not show any great difference, it can be assumed that tritium accumulation in certain region of divertor could be defined by calculations based on obtained experimental data.

## 5 ACKNOWLEDGMENTS

This work is preformed with the support of European Social Funds and member stuff of Laboratory of Radiation Chemistry of Solids of Institute of Chemical Physics, University of Latvia.

## 6 REFERENCES

1. *International Thermonuclear Experimental Reactor (ITER)* (website). Cadarache, France. Available online: http://www.iter.org/
2. D'AGATA E., OGORODNIKOVA O.V., TIVEYA R., LOWRYB C., SCHLOSSER J. A program to evaluate the erosion on the CFC tiles of the ITER divertor *Fusion Engineering and Design* 2007, p. 1739–1746, 82.
3. LUCAS L. L., UNTERWEGER M. P. Comprehensive Review and Critical Evaluation of the Half-Life of Tritium *Journal of Research of the National Institute of Standards and Technology* 2000, p. 541–549, 105.
4. HAIGH A., BEKRIS N., HELLRIEGEL W., NÄGELE W., NOPPEL H.-E., PEACOCK A., PENZHORN R.-D., ROLLI R., WERLE H., ZIEGLER H., Determination of tritium profiles in tiles from the first wall of fusion machines and development of techniques for their detritiation, *Report JET-P(99)53*, JET Joint Undertaking, Abingdon, Oxfordshire, OX14 3EA, UK, January 2000, 25 p. The paper has been published in J. Nucl. Mater. 279 (2000) 139–152.
5. PAJUSTE E., KIZANE G., COAD J.P., VITINS A., KIRILLOVA A., HALITOVS M. and JET-EFDA Contributors Structural changes and distribution of accumulated tritium in the carbon based JET tiles - *Journal of Nuclear Materials*, 2010, in print.

CYSENI 2011, May 26–27, Kaunas, Lithuania
ISSN 1822-7554, www.cyseni.com

# INTEGRAL ANALYSIS OF THE W7-X FUSION EXPERIMENT WITH ASTEC AND RELAP5 CODES

**T. Kačegavičius, T. Kaliatka**
*Lithuanian Energy Institute*
*Breslaujos g. 3, LT-44403 Kaunas – Lithuania*
*Phone +370 37 401928*
*Email: tomas@mail.lei.lt*

ABSTRACT

Nuclear fusion has the potential to cover a major part of mankind's energy needs under the conditions of ever-increasing population and energy consumption. Wendelstein 7-X (W7-X) is fusion experimental facility of stellarator type, which is currently being built at the Max-Planck-Institute for Plasmaphysics located in Greifswald, Germany. W7-X shall demonstrate that in future the energy could be produced in such type of fusion reactors. This paper presents analyses of processes in the target cooling system with the RELAP5 and ASTEC codes. The numerical analysis of loss-of-coolant accident during the "Baking" operation mode of W7-X (i.e. under the most critical conditions because of the high temperature and pressure applied) is analysed. The simulation using both codes allowed to model the processes in cooling system and plasma vessel. The received results of simulation confirm suitability of safety implements.

Keywords: W7-X, loss-of-coolant accident, ASTEC, RELAP5.

## 1. INTRODUCTION

Fusion power is the power generated by nuclear fusion reactions, i.e. two light atomic nuclei fuse together to form a heavier, more stable nucleus releasing the binding energy. At present, several experimental fusion reactors are under construction, among them ITER, which is built in France, KSTAR in South Korea, Wendelstein 7-X (W7-X) in Germany. W7-X is a stellarator, which shall demonstrate that in the future energy could be produced in such type of fusion reactors. It is presently under construction at the Max-Planck-Institute for Plasmaphysics located in Greifswald, Germany. The superconducting magnet system enables continuous operation, limited only by the plasma exhaust cooling water system whose capacity is designed for 30 minutes full power operation.

Prior to start of the facility operation its safety has to be demonstrated by performance of the safety analysis. The ingress of water during the W7-X no-plasma operation modes "Baking" and "Hot Liner" into the plasma vessel represents one of the most critical failure events, since primary and secondary steam production leads to a rapid increase of the inner pressure in the vessel. It should be noted that in "Baking" mode no plasma in the plasma vessel exists, i.e. no special models for plasma simulation are required. Such event could lead to loss of vacuum condition up to overpressure in the plasma vessel, damage of in-vessel components and diagnostics as well as bellows of the ports. Therefore increase of pressure in excess of 1.1 bar must be avoided by means of active (safety valves) and passive safety devices (burst disk, mass loaded disk).

This paper presents analyses of processes in the target cooling system ofW7-X facility during loss-of-coolant accident (LOCA). Analyses were performed using the RELAP5 and ASTEC codes.

## 2. W7-X TARGET COOLING SYSTEM

The plasma vessel in W7-X facility consists of the five modules having the same configuration and volume (Fig. 1). The one module is composed of two half-modules (divertors) which are divided into two sectors to allow stringing of the innermost coil during assembly. The temperature of the wall surface of the plasma vessel made of steel is 150°C. The thickness of the wall is 17 mm. According to [2] the plasma vessel could be modelled using a simplified geometry of the torus with a major radius of 5.5 m and a minor radius of 1 m with a free volume of 108.5 $m^3$. The weight of the plasma vessel is 32.6 t, the weight of the ports, which are hot too, is 62.5 t. The vessel components consist of the target plates, baffles, panels and heat shields, control coils, cryo-pumps, port protection and special port liners and the complex system of cooling water supply lines [3]. Each divertor unit is assembled from 12 separate horizontal and vertical targets (see Fig. 2). Fig. 2 shows model of one divertor target module with a total plasma facing surface of about 2 $m^2$. Most part of the target can withstand heat loads of up to 10 $MW/m^2$ and the middle part of the horizontal target plate has to withstand only power loads up to 1 $MW/m^2$.

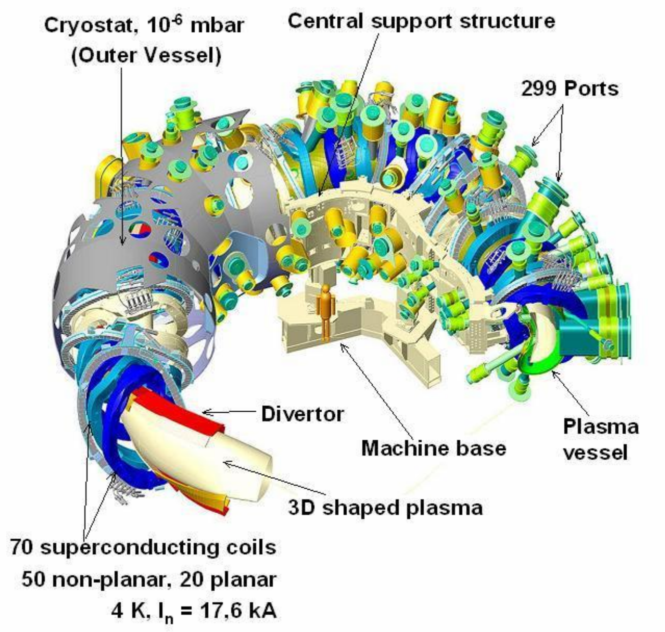

Fig. 1. Fragment of W7-X torus

W7-X facility target cooling system consists of two circuits. One of these is called the Main Cooling Circuit (MCC) and another one the “Baking” circuit. MCC is used for cooling of targets when W7-X facility is on normal operation. Before normal operation and ignition of plasma in plasma vessel the targets and other components must be warmed up. “Baking” circuit mainly is used for this purpose. Both MCC and “Baking” circuits are connected together and supply water to the same targets. During operation of W7-X in “Baking” mode, all target inlet valves of MCC are closed, but contention with “Baking” circuit still exist by bypass. Thus, it is necessary to take into account the whole cooling system.

In the “Baking” mode the maximum water temperature is 160 °C, the water pressure is about 10 bar under the W7-X “Baking” conditions. The corresponding mass flow of water in the “Baking” circuit is 177$m^3$/h (44.6 kg/s), the flow velocity through the cooling tubes of the target elements during “Baking” operation is about 1 m/s [3].

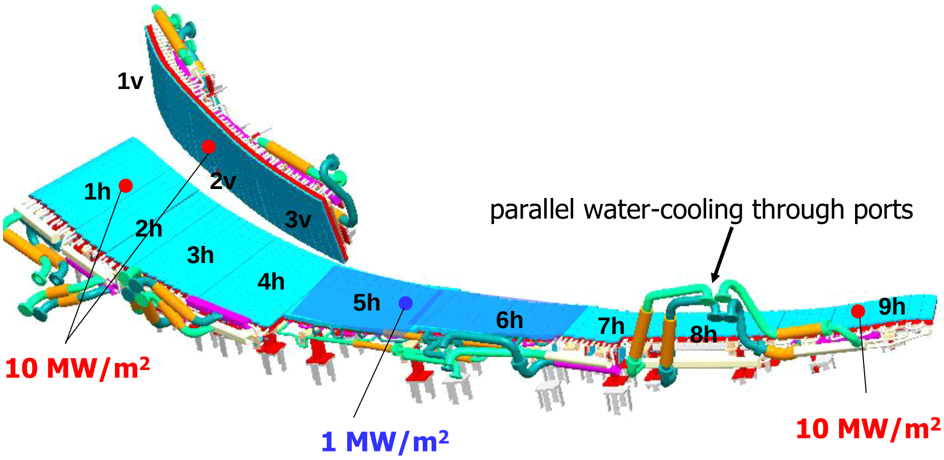

Fig. 2. W7-X divertor target module with horizontal and vertical targets

This analysis assumes a rupture of the 40 mm diameter target module pipe near the flange of the outer vessel, right at the place of the inner surface of the torus, during the vessel “Baking” operation mode. It was qualified as the leading to the one of the most severe consequences [3].

## 2.1. Tools for modelling of W7-X facility

The integral code ASTEC (Accident Source Term Evaluation Code), which is developed by IRSN (France) and GRS mbH (Germany), was used to perform integral analysis of W7-X response to LOCA, i.e. cooling circuit response and plasma vessel pressurisation [5]. ASTEC is an integral code for Light Water Reactors source term severe accident calculation, from the initiating event until radioactive release out of the containment [5]. The main physical phenomena are validated in 20 applications on experiments (validation test-cases), in 26 operationality test-cases and in 16 plant application test-cases. The reactor Cooling system for a 2” cold leg break phenomena was validated in BETHSY 9.1 b test. Now the integral code ASTEC is used for the modelling of the ITER (International Thermonuclear Experimental Reactor) as well. ASTEC code consists of several modules, which are developed for the analysis of separate tasks. In this analysis there were used two modules CESAR and CPA.

CESAR module simulates the whole front-end phase in the vessel (with a simplified core modelling) and in the loops, and then, after the beginning of core degradation phase, two-phase thermal-hydraulics in the loops and in the vessel upper plenum only. The models are based on a thermal-hydraulics simulator code, the physical models of which were derived from the reference thermal-hydraulics code CATHARE [5]. Two phases are considered: water and gas (steam + 1 non-condensable gas). The system is made of 5 scalars mass and energy conservation equations associated with 5 state variables.

CPA module is used for simulation of thermal-hydraulics and aerosol behaviour in containment. Lumped-parameter approach (volumes represented by nodes connected by junctions) in simple or multi-compartment containments (tunnels, pit, dome…) with possible leakages to the environment or to normal buildings, with more or less large openings to the environment [5]. The other modules ICARE, ELSA, SOPHAEROS, RUPUICUV, MEDICIS and IODE are not relevant for the selected accident scenario simulation in the fusion type facility.

RELAP5 [4] – is a ”best estimate” system code suitable for the analysis of all transients and postulated accidents in Light Water Reactor systems, including both large and small-break loss-of-coolant accidents as well as the full range of operational transients. The one dimensional RELAP5 code is based on a non-homogeneous and non-equilibrium model for the two-phase system that is solved by a fast, partially implicit numerical scheme to permit economical calculation of system transients. In addition, RELAP5 can be used to solve many plant thermal-hydraulic problems. The code includes many generic models allowing to simulate general thermal hydraulic systems. The models include pumps, valves, pipes, heat releasing or absorbing structures, reactor point kinetics, electric heaters, jet pumps, turbines, separators, accumulators, and control system logic elements [4]. At the Lithuanian Energy Institute, the RELAP5 code is used since 1993 for Ignalina Nuclear Power Plant licensing purposes (for the analyses of the thermal hydraulic response of the plant to various transients).

## 3. MODELS OF TARGET COOLING SYSTEM AND PLASMA VESSEL

For the modelling of selected accident (40 mm target pipe rupture) in “Baking” operation mode it is enough to develop detail model of “Baking” circuit. Thus, it was decided to develop detailed model of both connected circuits (see

Fig. 3). The geometric characteristics (pipe lengths, elevations, pump parameters, heater power and valves parameters) and configuration of pipes (it is necessary for evaluation of form loss coefficients) were taken from W7-X facility design [6]. The models and geometric characteristics of main cooling circuit and “Baking” circuit are identical for both codes ASTEC and RELAP5.

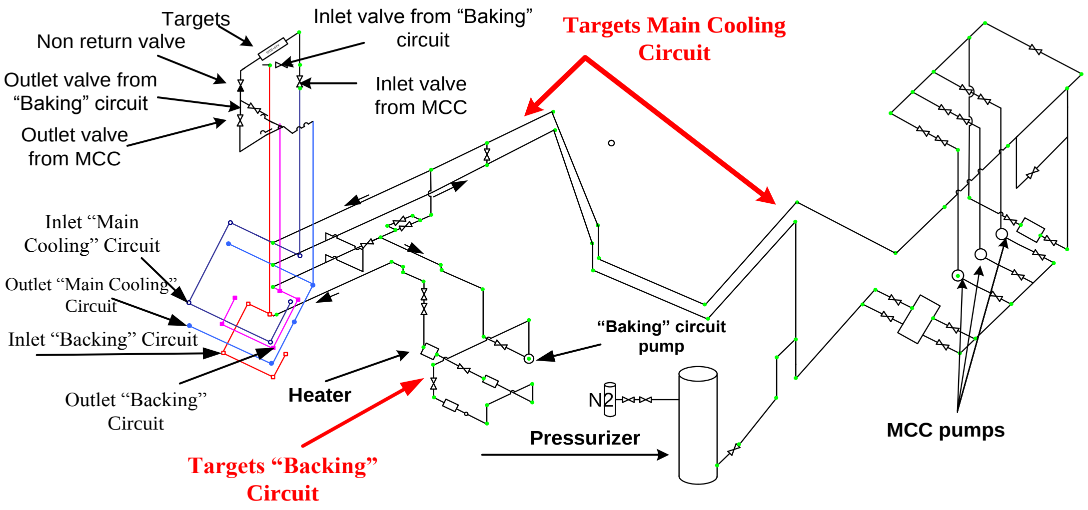

Fig. 3. Nodalisation scheme of W7-X cooling system

The simplified scheme for modelling of targets (nodalisation scheme) was developed (see Fig. 4). Four target modules are modelled as simplified one equivalent element: “F5-F5”, “G5-G5”, “H5-H5”, “J5-J5”. One Target Module “E5-E5” is modelled in more detailed manner. Becouse the rupture assumes in this “E5-E5” module of the 40 mm diameter target upper pipe.

Boundary conditions – whole volume of the plasma vessel, and surface area and mass of vessels structures – are the same for the ASTEC and RELAP5 models and correspond to the available design data, presented in the accident specification:

- inner diameter – 2.016 m;
- inner volume – 108.375 $m^3$;
- inner surface are – 215.337 $m^2$;
- wall thickness – 0.01915 m.

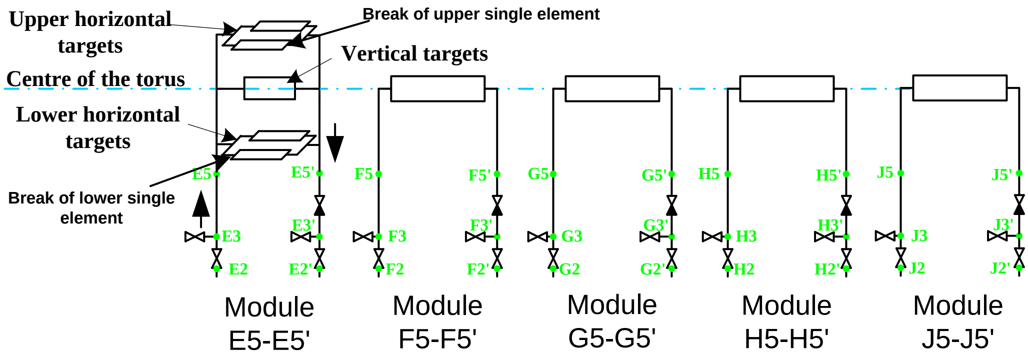

Fig. 4. Modelling of targets (nodalisation scheme)

But nodalization scheme of plasma vessel for ASTEC and RELAP5 codes have some differences. For ASTEC code the model is composed out of five parts with similar configurations, called modules. Each module of the vacuum vessel is subdivided into nine virtual control nodes (zones) in the scheme (Fig. 5), four in the central part of the scheme cross-section (nodes C**), four in the outer part (nodes O**) and one in the bottom part (node BOT), in which released water is collected. Fig. 5 shows cross-section of one module nodalisation scheme. All five modules are simulated in the analysis [1].

All adjacent zones of one module are connected by atmospheric junctions. Areas of these junctions and their lengths are calculated from the cylinder geometry. Corresponding zones of the adjacent modules (e.g., CBL zones of the first and second modules) except BOT zones also are connected by atmospheric junctions, properties of which are calculated from the geometry of cylinder.

INJ zone is the zone into which the water release from the ruptured pipe is simulated. It is defined for the aims of simulation – it helps to more realistically model the water flowing from the ruptured pipe to the wall of the vacuum vessel. INJ zone is present only in one module. Geometric parameters of this zone were selected according to port data and the initial thermodynamic parameters are the same in the whole vacuum vessel. Two zones not presented in the Fig. 5 were also simulated – torus hall and environment.

The former is a 16800 $m^3$ volume hall in which stellarator torus is situated. Conditions in the hall were selected according to planned normal operation of W7-X device. OTL node of the vacuum vessel third module and torus hall node are separated by the simulated burst disk. Burst disk is simulated by defining an atmospheric junction, which is closed at the beginning and opens if pressure difference between the zones it connects reaches indicated value (direction considered). Area of this junction was set equal to the area of the burst disk.

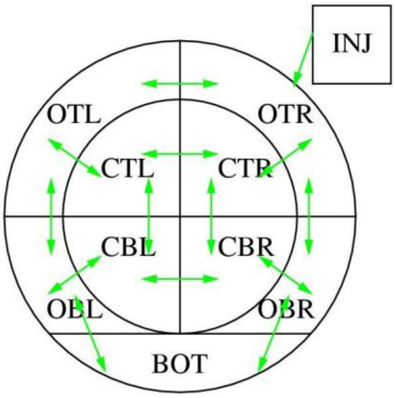

Fig. 5. Cross-section of the developed nodalisation scheme of the vacuum vessel for one module (black – nodalisation nodes, green – atmospheric junctions)

Plasma vessel model for RELAP5 code. Complicated three-dimensional geometry of the Plasma Vessel (PV) volume in the stellarator in the developed model is simplified to the geometry of horizontal cylinder. Ends of the cylinder are open and joined together, simulating closed circle of torus geometry (see Fig. 6).

Device is composed out of five parts with similar configurations, called modules. In the RELAP5 Mod3.3 model Fig. 6 total length of cylinder (PV model) is 33.951 m (length of each out of five module is 33.951 / 5 = 6.8 m). In Fig. 6 the plasma vessel is subdivided into five equal nodes.

One additional small volume was added to the model (0.026 $m^3$). This small volume (element “196”) is the volume into which the water release from the ruptured pipe is simulated. It is defined for the aims of simulation – it helps to more realistically model the steam – water mixture flowing from the ruptured pipe into the volume on back side of target (volume formed with plasma vessel wall and target wall). “196” element is modelled as small pipe with only one node. Geometric parameters of this element were selected according to port data and the initial thermodynamic parameters are the same as in the whole vacuum vessel. The flow area of this “pipe element” in RELAP5 model was assumed equal to 0.026 $m^2$, flow length 1.0 m, hydraulic diameter 0.16 m. It is assumed that the steam water flow at the entrance from this small volume meets some obstructions – the forward (reverse) flow loss coefficient was assumed equal to 1.9.

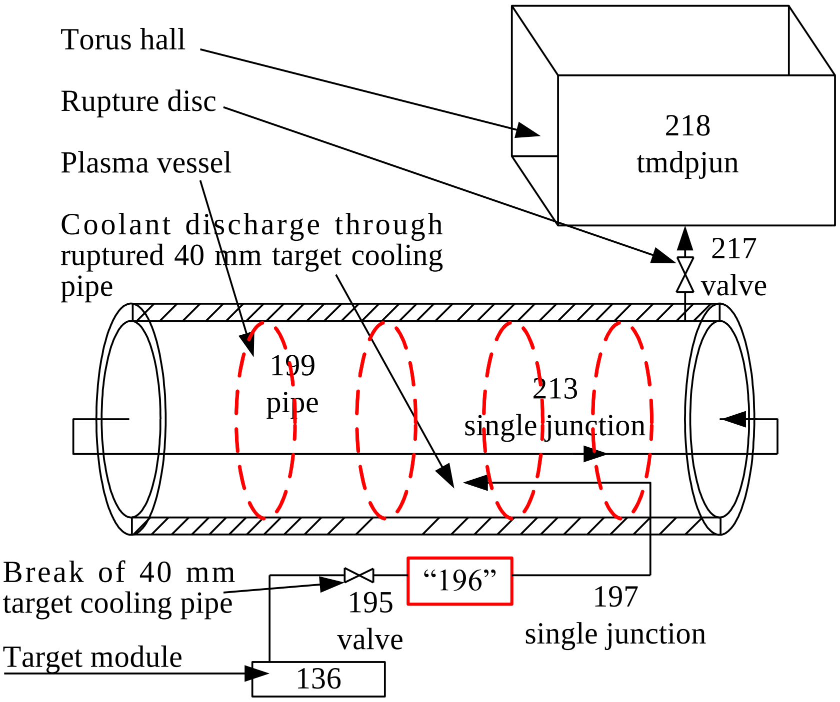

Fig. 6. Nodalization scheme of stellarator module with rupture in 40 mm diameter feeder pipe to upper target and plasma vessel for RELAP5 code

## 4. RESULTS OF ANALYSIS

This section presents the results of analyses of 40 mm pipe rupture, connecting single upper horizontal target. Double ended guillotine rupture of 40 mm pipe in “Baking” mode was modelled with the ASTEC and RELAP5 codes.

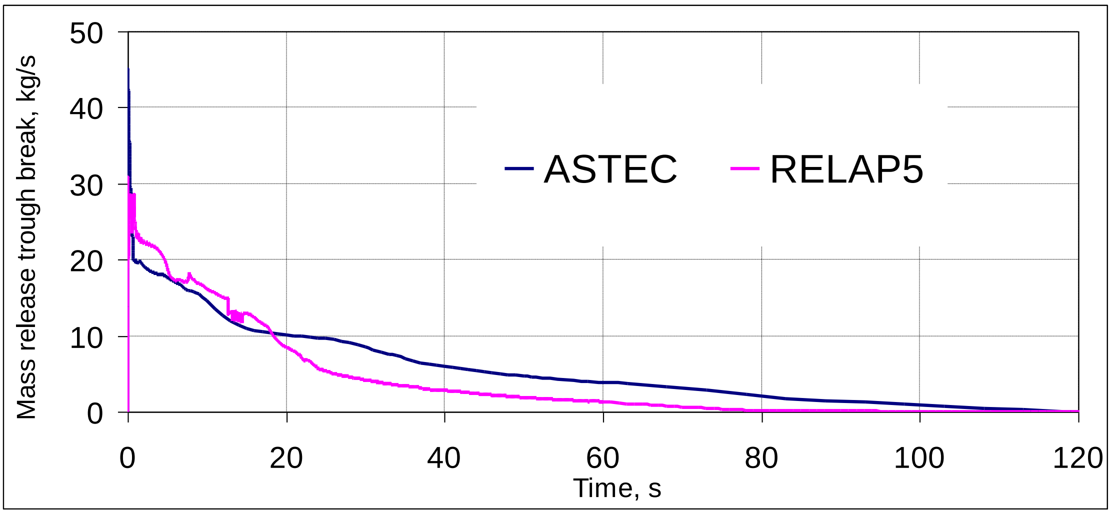

Fig. 7. Mass flow rate through the break

The discharge of the coolant through the ruptured pipe is presented in Fig. 7. After closure of the inlet automatic valves, the discharge of coolant slightly decreases, because the water from other targets in this affected module is discharged until pressure in the affected target decreases down to the pressure in the plasma vessel. Since the inlet automatic valves are closed, the water is discharged only from the affected module. In RELAP5 calculations the discharge of the coolant through the ruptured pipe stops approximately at 80 s after the break, in ASTEC calculations the discharge of the coolant through the ruptured pipe stops in ~110 s, it can be caused by different models of plasma vessel, and differences between RELAP5 and ASTEC calculation results can be explained by the fact, that in the RELAP5 code a non-homogeneous and non-equilibrium models are used for the two-phase system, while in the ASTEC code homogeneous approach is used.

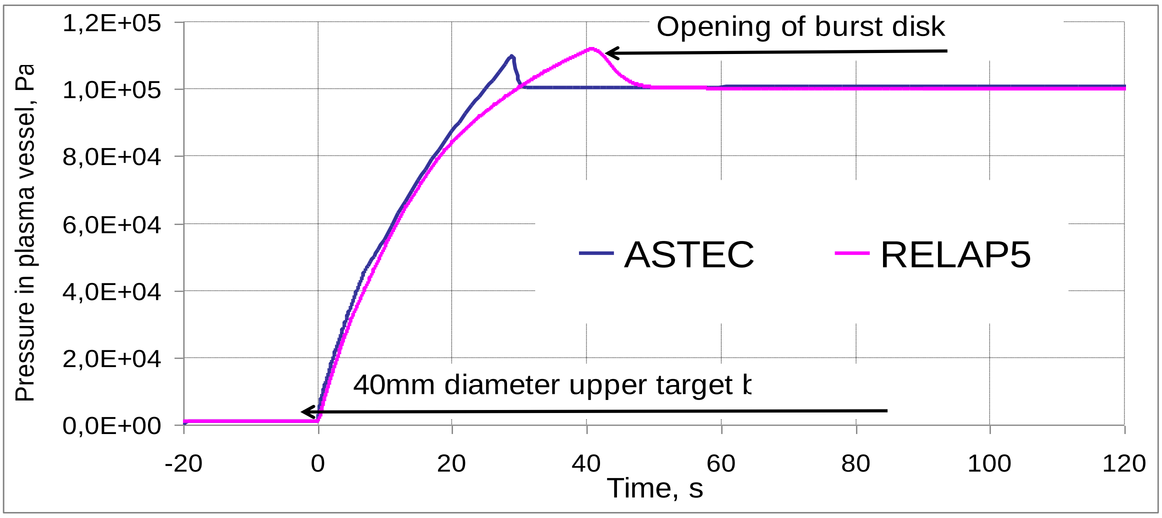

Fig. 8. Pressure in plasma vessel

Pressure increase in the plasma vessel is shown in Fig. 8. ASTEC calculation shows that after 30 s pressure increases up to the set point of safety valve opening (burst disc), which prevents further rise of pressure, respectively in RELAP5 calculation after 41 s. However these results showed that the planned area of the burst disk is sufficient to prevent pressure inside the plasma vessel exceeding 1.1 bar in the case of simulated accident in both calculations. Differences between RELAP5 and ASTEC calculation results can be explained by the fact, that vacuum vessel models (Fig. 5) and (Fig. 6) are different and that the RELAP5 and ASTEC codes have different calculation models for plasma vessel.

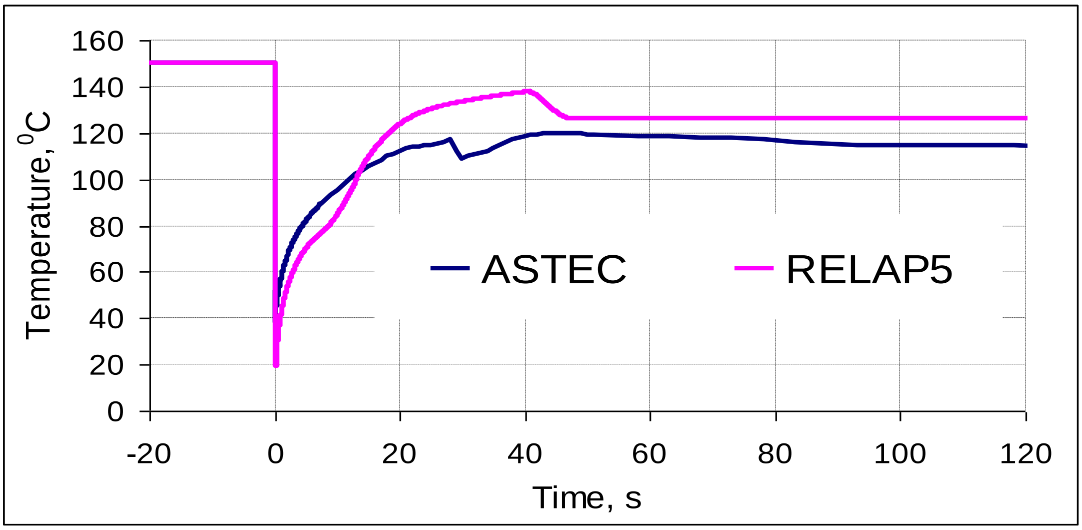

Fig. 9. Steam temperature trend in plasma vessel

The Fig. 9 shows the steam temperature in plasma vessel. The steam temperatures in plasma vessel are very similar, in both codes calculations. At the first seconds after the break water (10 bar. 160 $^{o}$C) from the cooling system releases through the break to the plasma vessel (0.01 bar. 160 $^{o}$C). Due to low pressure in plasma vessel released water evaporates. For the evaporation process energy is required and this energy is taken from released coolant temperature, so steam temperature drops down until ~20 $^{o}$C. After this sharp temperature drop, due to increasing pressure (Fig. 8) in plasma vessel, steam temperature is increasing. Then pressure in plasma vessel become atmospheric – steam temperature settled to the dry saturated steam temperature (~120 $^{o}$C).

## 5. CONCLUSIONS

1 The analysis of processes in targets cooling system of W7-X fusion experiment facility was performed. The break of target feeder pipe and discharge of coolant was analyzed. The models of target module cooling system and plasma vessel in W7-X facility were developed by employing RELAP5 and ASTEC codes. In this paper analysis of the scenario of double ended guillotine break of ~40 mm diameter pipe in upper target module inlet is presented.

2 Obtained results in both calculations showed that the planned area of the burst disk should be sufficient to prevent pressure inside the vacuum vessel exceeding 1.1 bar in the case of simulated accident.

3 RELAP5 and ASTEC codes calculation results of double ended guillotine break of ~40 mm pipe in target module inlet were compared. The presented comparison demonstrated the reasonable agreement: developed models provides an acceptable prediction, all major trends and phenomena are correctly predicted.

## REFERENCES

1. BOSCH, H. S.; DINKLAGE, A.; KLINGER, T.; WOLF, R.; the W7-X Team: Contributions to Plasma Physics, DOI: 10.1002/ctpp.201010101 (2010), in press.
2. STREIBL, B.: Manufacturing of the W7-X divertor and wall protection, Proceedings of 23rd Symposium “Fusion Technology”, Venice, Italy (2004).

3. TOPILSKI, L.: Consequences of the W7X in-vessel coolant pipe break at Baking conditions, Report 1-NBF-T0015, Max-Planck-Institute for Plasma Physics, Greifswald (2006).
4. FLETCHER, C.D., et. al., RELAP5/MOD3 code manual user's guidelines, Report NUREG/CR-5535, Idaho National Engineering Lab (1992).
5. Van Dorsselaere, J.P.; Schings, B.: ASTEC V1.3 rev0 Users Manuals (modules CESAR, DIVA, ELSA, SOPHAEROS and SYSINT) CD (2006).
6. D. NAUJOKS, Initial and Boundary Conditions, 1-NBF-T0008.0, Max-Plank-Institut für Plasma Physik, 2006 p. 2–4.

## 6. ACKNOWLEDGMENTS

This paper was prepared on the basis of work, which was carried out within the framework of the European Fusion Development Agreement and supported by the European Communities. This work is also supported by the Agency for International Science and Technology Development Programmes in Lithuania (at present Agency for Science, Innovation and Technology).

# MEASUREMENT AND ANALYSIS OF (N,X) NUCLEAR REACTION CROSS SECTIONS ON RARE EARTH ELEMENTS WITH D-T NEUTRONS

**A. Kadenko, I. Kadenko**
*Department of Nuclear Physics*
*Taras Shevchenko National University of Kyiv*
*Vasilkovskaya Str.98a, Kyiv – Ukraine*
*Phone +38(044)5213216*
*Email: kadenkoartem@gmail.com*

**N. Dzysiuk**
*Legnaro National Laboratory (INFN), Legnaro*
*35020-Legnaro(PD) – Italy*

ABSTRACT

The Department of Nuclear Physics at the Taras Shevchenko National University of Kyiv is involved in neutron physics research targeted at thorough planning of experiments, irradiation of samples and precise spectroscopic measurements. Particularly this research is devoted to (n,x) nuclear reaction cross section measurements with activation technique based on use of d-t neutrons. In accordance with the main aim to produce new and improve existing nuclear data with their further applications in different fields of knowledge the attention was concentrated on Dy and Er isotopes. Regardless of the fact that up to now many investigations were performed to study (n,x) reactions the problems with inconsistency and discrepancies between available data still remain. One of the main requirements for nuclear data to be utilized is their reliability which may be considered as an acceptable agreement between experimentally obtained and theoretically calculated results. The cross sections of nuclear reactions $^{162,163}$Dy(n,x)$^{162}$Tb, $^{163,164}$Dy(n,x)$^{163}$Tb, $^{166,167}$Er(n,x)$^{166}$Ho, $^{156}$Dy(n,2n)$^{155}$Dy, $^{158}$Dy(n,2n)$^{157}$Dy, $^{170}$Er(n,p)$^{170}$Ho were measured for incident neutron energy of 14.6 MeV. In some cases sufficiently lower uncertainties in comparison with previously reported data were obtained. For reaction $^{162}$Er(n,p)$^{162}$Ho a cross section value was measured for the first time. The samples of natural composition of above mentioned elements were irradiated at own designed and manufactured neutron generator NG-300. Measurements were performed with neutron-activation technique. The $\gamma$-ray spectra of induced activity were measured with HPGe spectrometers. The main sources of uncertainties for cross section values were considered and taken into account. The modelling approach with modern MCNP code was applied in order to achieve an accurate experiment optimization and to enhance the nuclear data reliability. Theoretical calculations of excitation functions for considered reactions in specified energy range were performed with TALYS-1.2 code. Obtained results could be used for verification of nuclear reaction models as well as other practical applications. Measured cross section for $^{162}$Er(n,p)$^{162}$Ho nuclear reaction is to be considered as original data and could be used for nuclear databases updating.

Keywords: cross section, neutron activation technique, neutron generator, time of irradiation, cooling time, time of measurement.

## 1. INTRODUCTION

Currently activation cross sections for (n,x) reactions with (d,t) neutron in input channel are required and useful for different practical applications. Among them is neutron dosimetry of fusion environment. Such data are needed for integral calculations for the first wall, blanket and shield of conceptual fusion power reactors. Furthermore relible experimental data are of considerable importance for refinement of nuclear reaction theory. Although a lot of experimental data on neutron induced cross sections in considered energy range have been reported and great efforts have been devoted to compilation and evaluation of databases, detailed analysis of those data indicates some unsolved problem with their inconsistency. Therefore the main objective was selected in accordance with existing requests for certain cross sections [1,2]. Besides the problem of database inconsistency the discrepancy between those results has been observed as well, what may lead to errors unrecognized during interpolation of experimental data and to influence the quality of estimated data [2, 3]. Based on the analysis of mentioned problems the attention was concentrated on cross section measurements of Dysprosium (Dy) and Erbium (Er) elements.

These elements belong to a group of rare earths (lanthanides) and are characterized by very specific properties interesting and promising nuclear properties. Additional exciting subjects in nuclear physics research of the rare earths are the search for the nuclear limits of stability and proton radioactivity, as well as new reaction channels. The main reason for our choice is that the behaviour of deformed nuclei was not sufficiently studied yet. The increasing number of requests for nuclear data on the rare earths reflects the growth in the number of applications for these elements, including nuclear energy applications.

Another point of interest is the theoretical description of the features of nuclear reactions with such nuclei, which could be performed for verification of theoretical models with reliable experimental data available [4].

Reliable determination of cross sections for (n, x) nuclear reactions is important to evaluate the radiation strength of control rods material for the "VVER-1000" and "RBMK-1000" reactor control and protection systems [5]. Dysprosium has large capture cross section value in the thermal neutron energy range. Since the neutron fission spectrum is continuous with energy extending up to 15 MeV, properties of dysprosium must be investigated in the neutron energy range up to 20 MeV. Erbium may also be considered for utilization in nuclear industry and must be studied thoroughly as well.

Finally, in the field of nuclear astrophysics the cross sections for nuclear reactions with dysprosium isotopes are also required to perform the calculations related to the synthesis of elements and predictions of their abundances in the Universe [4].

## 2. EXPERIMENTAL TECHNIQUE

Cross section measurements were performed using the neutron activation technique [6]. Neutron generator NG-300 was used as a source of neutrons [7] with a maximum neutron flux density of (d, t) neutrons ~ $5.2\cdot10^8$ ($1/cm^2\cdot sec$) which was determined experimentally. Mixed ion beam component ($D^+$-$D_2^+$) with maximum energy ~ 225 keV was used for the neutron generation. To avoid any considerable distortion factors due to neutrons generation, a corresponding neutron spectra incident at specimen were modelled using the MCNP4C code (Fig.1). The samples of dysprosium ($^{156}$Dy - 0.06 %, $^{158}$Dy – 0.1 %, $^{160}$Dy – 2.34 %, $^{161}$Dy – 18.9 %, $^{162}$Dy – 25.5 %, $^{163}$Dy – 24.9 %, $^{164}$Dy – 28.2 %) and Erbium ($^{162}$Er - 0.14 %, $^{164}$Er - 1.61 %, $^{166}$Er - 33.6 %, $^{167}$Er - 22.95 %, $^{168}$Er - 26.8 %, $^{170}$Er - 14.9 %) of natural composition were used. Two dysprosium samples in the shape of disc foils with 15.4 mm diameter, 0.07 mm thickness and 0.132 g mass each were irradiated with (d, t) neutrons. Before irradiation the samples were studied for presence of impurities using mass spectrometry analysis [8], among them the following were reported: Gd – 1.21 %, Sc – 0.039 %, Cu – 0.017 %. The Erbium sample had a shape of parallelepiped with 8.5×7.3×2.1 mm dimensions and mass of 1.022 g. The $\gamma$-ray spectra of induced activity were measured with HPGe spectrometer (detector volume ~ 110 $cm^3$). The energy resolution was 2.0 keV for $\gamma$-rays with energy 1332 keV corresponding to $^{60}$Co decay and 0.9 keV for $\gamma$-rays with energy 122 keV, corresponding to the decay of $^{57}$Co.

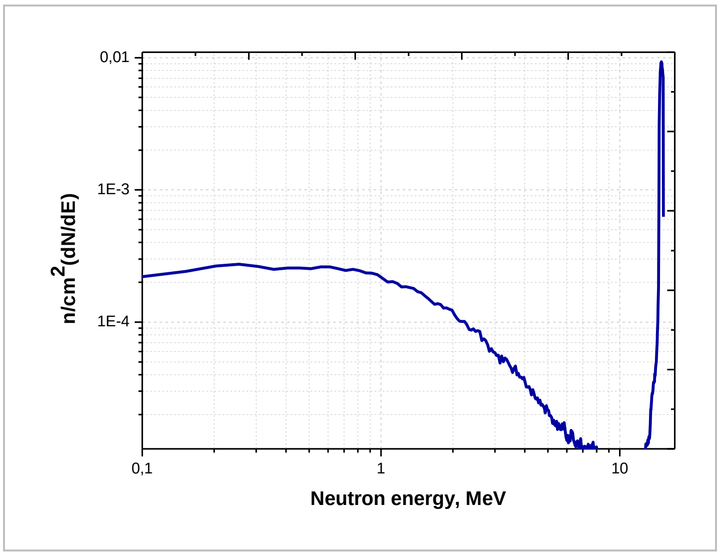

Fig. 1. Simulated spectrum of d-t neutrons

The neutron flux density at the irradiation position was measured using the $^{27}$Al(n,α)$^{24}$Na reaction [15]. The cross sections for each of reaction studied were determined by referring to the standard $^{27}$Al(n,α)$^{24}$Na reaction (ENDF/B-VI). Each specimen was sandwiched between two Al foils with 16 mm diameter and 0.1 mm thickness. During irradiation the neutron flux deviation was kept within ± 5 %. Since neutron spectrum can never be considered as monoenergetic (Fig. 1) due to fast neutron scattering on measurement hall constituents and structural materials, the low-energy component is being observed below (d,t) neutron peak. To take into account the influence of low energy component of incident neutron spectrum the model of neutron generator was developed with the MCNP4C code [9]. Validation of the model was performed by means of (n,γ) reaction on terbium isotope [10].

The fractional contribution (FC) of low-energy neutrons to the total reaction values of interest was calculated by using the following equation:

$$FC = \frac{\int_0^{E_c} S(E)\sigma(E)dE}{\int_0^{E_c} S(E)\sigma(E)dE + \int_{E_c}^{E_{\max}} S(E)\sigma(E)dE}, \qquad (1)$$

where S(E), σ(E), $E_c$, and $E_{max}$ are the distribution of neutrons by energy, the cross section at energy E, the cut-off energy, and the maximum energy (nearly 15 MeV), respectively [11]. A cut-off energy ($E_c$) was set at 10 MeV. The FCs was calculated by using excitation functions from the JENDL-3.3 database [12].

For dysprosium and erbium the angle between the specimen irradiation position and the deuteron beam direction was 0° at 10 mm distance from the Ti-T target. Such geometry corresponds to the following mean energy of emitted neutrons – 14.6 MeV. Values of neutron energy and its spread were determined based on several approaches: kinematic approach (DROSG code) [13] (Fig. 2); model approach based on Monte Carlo calculations; experimental approach [14].

Time of irradiation varied within (20–200) min to guarantee the maximum reaction yield. The specimen “cooling time” after irradiation was minimal to avoid a loss of any useful decay branches.

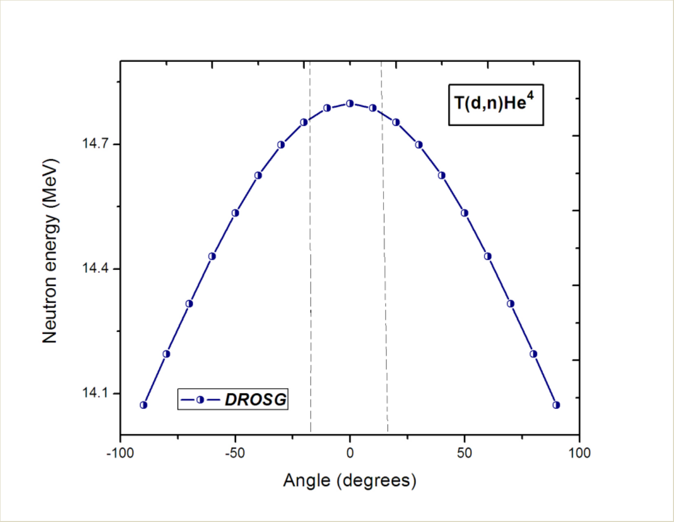

Fig. 2. Angular dependence of the (d,t) neutron energy

To enhance the reliability of measurement results it is necessary to consider some effects which have significant influence on the outcome accuracy. In order to obtain reliable cross section values, all such sources of biases were thoroughly considered. Due to the fact of operation with voluminous irradiated samples the self-absorption effects were taken into account. To address this issue a modeling approach with Monte Carlo simulations was applied using MCNP4C simulations. Equally, the MCNP4C model of the HPGe detector was created and validated by comparison of experimental and calculated efficiencies for different measuring geometries.

Since measurements were performed in condition of close geometry (sample was directly placed on the surface of the detector cryostat), therefore it was necessary to take into account the contribution of γ-rays that emitted at small angles respect to the surface of the detector. For this purpose the model of detector was created in the MCNP4C code (Fig. 3).

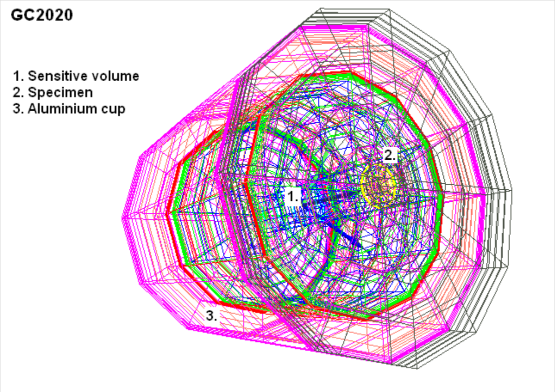

Fig. 3. 3D model of the HPGe detector

Validation of this model was undertaken through a comparison of experimentally measured results of efficiency in various geometries (close and far) with the theoretically predicated values based on the model developed. Correction factor was taken as the ratio of detector efficiency in cases of point and volume radiation sources. Correction factors for coincidence summing effect have been calculated with Nuclide Master+ code [16]. The input parameters for these calculations were the information about nuclear structure from estimated database ENSDF [17] and geometry of measurements.

## 3. RESULTS OF MEASUREMENTS

The neutron induced (n, p), (n, x) and (n,2n) reactions were studied at the average neutron energy 14.6 MeV for the dysprosium and erbium isotopes. Measured cross section values with their denoted uncertainties are summarized in Table 1. Also for comparison data were taken from EXFOR database [2]. Theoretical calculations of excitation function have been performed with the code TALYS-1.2 [18]. Evaluated data have been taken from ENDF B/VII database [2].

Available data for $^{156}$Dy(n,2n)$^{155}$Dy and $^{158}$Dy(n,2n)$^{157}$Dy neutron reactions are presented in a few publications [19-21] only. Based on the available data and corresponding uncertainties it is still difficult to define precisely the corresponding excitation function in considered neutron energy range, namely (14÷15) MeV (Fig. 4).

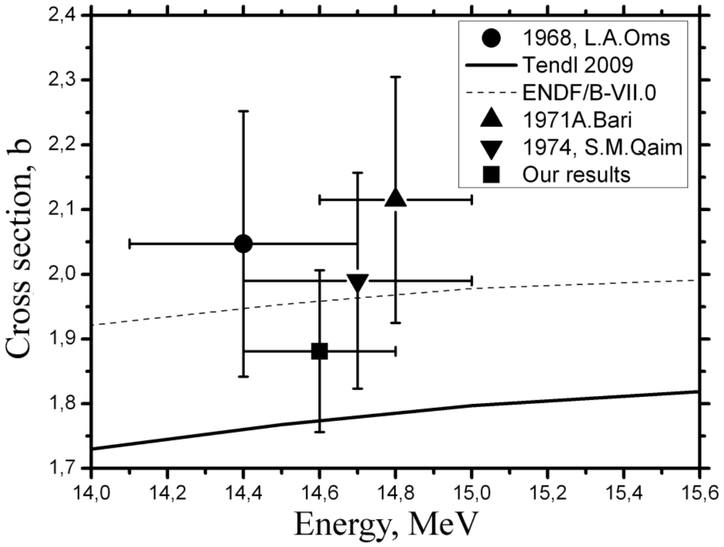

Fig. 4. Comparison of experimental and evaluated data for nuclear reaction $^{158}$Dy(n,2n)$^{157}$Dy

Cross sections for $^{162,163}$Dy(n, x)$^{162}$Tb, $^{163,164}$Dy(n, x)$^{163}$Tb, $^{166,167}$Er(n, x)$^{166}$Ho and $^{170}$Er(n, p)$^{170}$Ho nuclear reactions were specified. Since dysprosium and erbium of natural isotopic abundance contain several stable isotopes, this causes an additional problem to obtain the reliable nuclear data due to occurring interference between possible opened reaction channels and the formation of the same reaction products in the output channels. Nuclear reaction cross section $^{162}$Er(n,p)$^{162m+g}$Ho has been measured for the first time. There is no data presented for this nuclear reaction in a world-wide used database [2]. The γ-line with energy $E_\gamma$ = 1319.3 keV was selected for this cross section determination. After 1.5 min cooling of irradiated specimen a peak area of this γ-line was determined from the instrumental spectrum acquired during 25.9 min.

With the purpose to keep reliability of reaction channel identification procedure the analysis of activation products half-life was applied. The great interest to measure cross section for (n, d+np) reaction is induced by complication of such measurement. Therefore, only limited number of experimental data is available, especially for rare-earth group elements. In this case, we clearly identified gamma peaks, matching the most intense lines of $^{155}$Tb nucleus. We made an assumption about observation of the daughter nucleus from the reaction $^{156}$Dy(n, d+np)$^{155}$Tb. Nucleus $^{155}$Tb has half-life of 5.32 days, which is convenient for the analysis of activity decreasing with time. Thorough intensity consideration of gamma lines shown significant overestimation of the cross section value (~1.4 b), which obviously is not typical for such type of reactions. Then the analysis of all possible ways for this isotope production revealed the following interfering reaction channel:

$$^{156}Dy(n,2n)^{155}Dy \xrightarrow{\beta^{+}} {}^{155}Tb \tag{2}$$

The $^{155}$Dy and $^{155}$Tb nuclei have half-life of 9.9 hours and 5.32 days correspondingly. The production of $^{155}$Tb nuclei in reaction channel (2) through the decay of $^{155}$Dy has been confirmed [22].

Table 1. Cross section for (n, x) reactions with dysprosium and erbium isotopes

| **Nuclear reaction** | **$T_{1/2}$** | **This work** | **Evaluated data [2]** | | **Exfor [2]** |
|---|---|---|---|---|---|
| | | **Cross section, mb** | **Cross section, mb (TALYS-1.2)** | **Cross section, mb (ENDF/B-VII)** | **Cross section, mb** |
| $^{156}$Dy(n,2n)$^{155}$Dy | 9.9 h | 1596 ± 104 | 1670 | 1840 | 1852 ± 143 (14.7 MeV)<br>1982 ± 178 (14.8 MeV)<br>1943 ± 194 (14.4 MeV) |
| $^{158}$Dy(n,2n)$^{157}$Dy | 8.14 h | 1881 ± 125 | 1770 | 1960 | 1990 ± 167 (14.7 MeV)<br>2115 ± 190 (14.8 MeV)<br>2047 ± 205 (14.4 MeV) |
| $^{162,163}$Dy(n,x)$^{162}$Tb | 7.6 min | 3.9 ± 0.3 | 4 | 4 | 3.92 ± 0.4 (14.6 MeV) |
| $^{163,164}$Dy(n,x)$^{163}$Tb | 19.5 min | 3 ± 0.2 | 3.8 | 3.2 | 3.17 ± 0.6(14.6 MeV) |
| $^{156}$Dy(n,d+np)$^{155}$Tb | 5.32 d | * | 2.4 | 2 | - |
| $^{170}$Er(n,p)$^{170}$Ho | 2.76 min | 0.25 ± 0.05 | 2.1 | 2.6 | 0.21 ± 0.02 (14.8 MeV)<br>1.13 ± 0.12 (14.8 MeV)<br>1.8 ± 0.5 (14.8 MeV) |
| $^{162}$Er(n,p)$^{162m+g}$Ho | 15 min | 10.5 ± 3.2 | 15.7 | 11 | - |
| $^{166,167}$Er(n,x)$^{166}$Ho | 26.8 h | 4.7 ± 0.8 | 7.4 | 6.5 | 4.3 ± 0.3 (14.7 MeV)<br>2.3 ± 0.2 (14.8 MeV)<br>6.7 ± 0.9 (14.8 MeV)<br>5.6 ± 0.8 (14.7 MeV) |

* – theoretical calculation of excitation functions performed with TALYS-1.2 code

## 4. ESTIMATION OF THE UNCERTAINTY SOURCES

The principal sources of systematic errors for activation cross-section measurements are the following: nuclear constants ($T_{1/2}$, quantum yield, decay data), interfering reactions, impurities, neutron flux normalization, neutron energy definitions, energy spread ($\Delta E$), instrumental factors (time of irradiation, cooling, and measurements), errors related to the determination of correction factors, errors in time intervals designated for measuring the $\gamma$ - ray spectra. The variation of the neutron flux during irradiation is negligible and was controlled by adjusting the current density of deuterons striking the titanium-tritium target. Precise detector such as boron counter NGD-3 was used to evaluate the relative change in neutron flux density. This counter is surrounded by the moderator of neutrons, and the whole assembly unit is located at the distance of 1.5 m from the target unit. Errors of weighting the sample or monitor are negligible as well (<0.05%). The measurements of several strong $\gamma$-rays with well-defined emission probabilities permit one to reduce the errors due to uncertainties associated with nuclear constants. The estimated and above listed sources of the errors considered in the deduction of cross sections are summarized in Table 2.

Table 2. Principal sources of cross-section errors

| **Parameter** | **Range** |
|---|---|
| Counting rate | (1-48) % |
| Efficiency calibration | (0.6-6.5) % |
| Self-absorption of $\gamma$-ray | (1-5) % |
| Correction for coincidence summing | (1-5) % |
| Constants (mass) | < 0.1 % |
| $\gamma$ -ray intensity error | (0.02-0.09) % |
| Reference cross section for $^{27}$Al(n,$\alpha$)$^{24}$Na | (1÷10) % |
| Average incident neutron energy ($\Delta$) | (170÷269) keV (~1.4%) |

The errors of the half life and $\gamma$-ray intensity were small, the cross sections values are measured with up to (4–7) % uncertainty.

## 5. THEORETICAL CALCULATION AND DISCUSSION

For a discussion about the physical implications of obtained data the model calculations were carried out with the TALYS-1.2 code, which is an often used code system for the prediction and analysis of different nuclear reactions. This code was employed because it contains a wide spectrum of nuclear reaction models that provide qualitative cross section calculations. In the most cases, the nuclear reaction simulations were performed with default input parameters. In these calculations the Hauser-Feshbach (statistical model) and pre-equilibrium exciton model formalisms were employed. In nuclear reactions induced by light projectiles with incident energies higher than 8 MeV the pre-equilibrium processes are dominant therefore for calculations of point-wise measured cross sections (see Table 1) as well as $^{158}$Dy(n,2n)$^{157}$Dy and $^{156}$Dy(n,np)$^{155}$Tb excitation functions (see Fig. 5–7) the two-component exciton model was applied. The formation cross section and the inverse reaction cross section were calculated using the optical model with local and global parameterizations of Koning and Delaroche (OMP) [23]. These are automatically corrected, by reducing the imaginary surface potential, for the deformed nuclides considered here. In most cases the nuclear reaction simulations presented were performed with default input parameters (optical model parameters, level density, etc) except the $^{156}$Dy(n, d(n+p))$^{155}$Tb reaction.

As can be seen in the Table 1 for $^{156}$Dy(n,2n)$^{155}$Dy, $^{158}$Dy(n,2n)$^{157}$Dy and $^{162,163}$Dy(n,x)$^{162}$Tb reactions a rather good agreement between calculated and measured values within their uncertainties was achieved. Likelihood that such agreement could be observed due to big enough (n, 2n) and (n, x) cross section values and possibility to apply the more general approach. From other side the good correspondence between obtained results with theoretically calculated data from evaluated database, and results of other experimental groups could be considered as an indication of applied activation technique correctness. At the same time the rest of cross sections have some deviations independently on similarity of used approach. Evidentially that calculation of cross section has the own approach due to lack of one universal model and in this particular case reveals the problem with availability of reliable cross section data for improving the models for reaction description particularly with heavy nuclei from rare-earth group of elements once again.

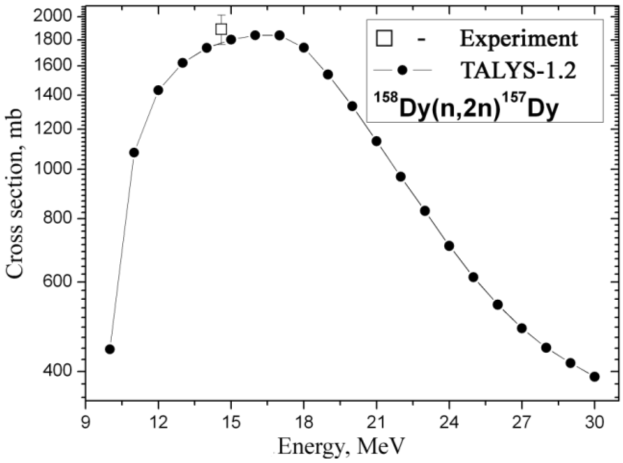

Fig. 5. Excitation function for nuclear reaction $^{158}$Dy(n, 2n)$^{157}$Dy

In this work the attempts to measure $^{156}$Dy(n,d)$^{155}$Tb cross section were done but due to interference between reaction channels it is difficult to say about results reliability yet. That is why taking into account the peculiarities of this reaction the decision to perform the theoretical calculation in order to see the feasibility of such experiment was made.

Fig. 6 and Fig. 7 show the result of theoretical calculations of excitation functions for $^{156}$Dy(n,d)$^{155}$Tb and $^{156}$Dy(n,np)$^{155}$Tb reactions in the energy range (1-30) MeV. The description of nuclear reaction with deuterons in output channel is not simple due to necessity to consider the mechanism of its formation. It is well-known that for nuclear reaction involving deuterons the mechanism like stripping, pickup, breakup, and knockout play an important role and these direct-like reactions are not covered by the exiton model. In TALYS for this reason the special phenomenological model is implemented what allows to calculate the cross sections in accordance with probability of each of mentioned above mechanisms. Practically these contributions can be adjusted with a keyword normalizing the strength of the stripping reaction.

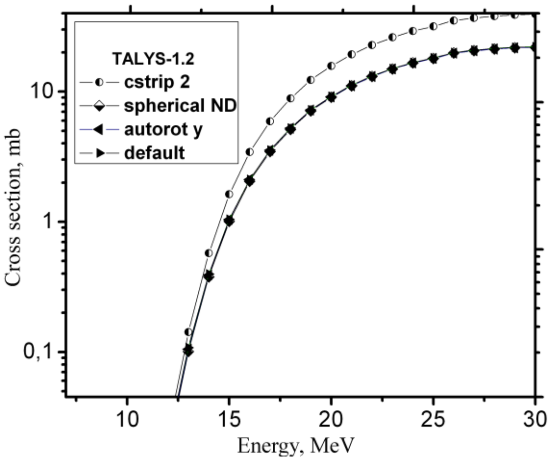

Fig. 6. Excitation function for nuclear reaction $^{156}$Dy(n, d)$^{155}$Tb

In Fig. 6 the calculation for $^{156}$Dy(n, d)$^{155}$Tb reaction using the adjustment parameter (*cstrip*) is presented which guaranteed higher values of the excitation function curve. At the same time the analysis shows that this cross section is unsensitive to the coupled channel consideration (*autorot*) and used optical potential (*spherical*). Currently it is difficult to say about the most probable predications since it requires the further experimental investigations in order to get data for specification an assumption with respect to the most appropriate reaction mechanism.

In Fig. 7 the theoretical calculation of excitation function for the $^{156}$Dy(n, np)$^{155}$Tb nuclear reaction is presented. It is well-known that for nuclei with A>150 the coupled channels description for deformed nuclei is quite influential therefore the corresponding adjustment parameter (*autorot*) was used [24].

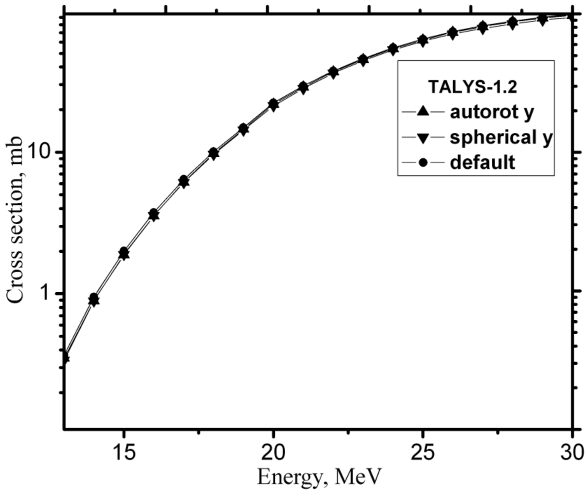

Fig. 7. Excitation function for nuclear reaction $^{156}$Dy(n, np)$^{155}$Tb

Finally based on the analysis of calculated cross section for $^{156}$Dy(n, d+np)$^{155}$Tb reaction, we suggest to perform this measurement allowing further detailed study of the reaction mechanism. This reaction channel is opened within considered energy range ((D-T) neutrons) and could be feasible using the specimen enriched by $^{156}$Dy isotope if combined with the planar geometry detector, operational with the coincidence mode and other high-precision electronics the experiment could be arranged successfully. This possibility is under thorough consideration.

## 6. CONCLUSIONS

In present work the (n, x) nuclear reactions cross sections for dysprosium and erbium isotopes at the neutron energy (14.6 ± 0.2) MeV were measured experimentally.

Nuclear reaction cross sections for $^{162,163}$Dy(n, x)$^{162}$Tb, $^{163,164}$Dy(n, x)$^{163}$Tb, $^{156}$Dy(n,2n)$^{155}$Dy, $^{158}$Dy(n,2n)$^{157}$Dy, $^{166,167}$Er(n, x)$^{166}$Ho and $^{170}$Er(n, p)$^{170}$Ho at the energy of 14.6 MeV were reported.

Theoretical calculation of excitation functions in the neutron energy range (1-30) MeV for the nuclear reaction $^{156}$Dy(n,d+np)$^{155}$Tb was also performed, providing the basis for the detailed study of the formation mechanism of emitted particles in the output channel.

Nuclear reaction cross section $^{162}$Er(n,p)$^{162}$Ho at the neutron energy 14.6 MeV was reported for the first time. Presented results can be utilized in the field of nuclear energy applications as well as in testing of various nuclear reaction models.

## REFERENCES

1. KONING A.J, BLOMGREN J. Nuclear data for sustainable nuclear energy. *JRC Scientific and Tech. Rep*, 2009, Vol. EUR23977EN.
2. Cross section information storage and retrieval system (EXFOR) II National Nuclear Data Center (NNDC), Brookhaven National Laboratory, USA. Link to the internet <http://www.nndc.bnl.gov/index.jsp>

3. FORREST R. A. Data requirements for neutron activation Part I: Decay data. *Fusion Engineering and Design*, 2006, Vol. 81, p. 2143–2156.
4. S.-Y. OH, CH.-S. *CIL Journal of the Korean Nuclear Society*, 2001, Vol. 33, No. 1, p. 46–61.
5. FRIDMAN S. R., RISOVANIY V. D., ZAXAROV A. B, TOPOROVA V. G. Radiation resistance PEL PS SUZ NPP's VVER-1000 with boron carbide. *Problems of Atomic Science and Technology*, 2001, № 2, p. 84–90, (In Rus.).
6. KUZNECOV R.A. *Activation analysis*, Moscow: Atomizdat, 1974, p. 344, (In Rus.).
7. PRIMENKO G.I., MAJDANUK V.K., NEPLUEV V.M. AND OTHER Neutron generator 14 MeV with neutron flux $5{\cdot}10^{11}$ $c^{-1}$ *Instruments and Experimental Techniques,* 1989, № 6, p. 3941, (In Rus.).
8. SAMCHUK A. I. Chemical analysis of rocks and minerals. *Institute of Geochemistry and mineralogy of the ore named Semenenko M.P., Department of Geochemistry and man-made metal ore*, Kiev, 2010, p. 1 (In Rus.).
9. BRIESMEISTER J.F. MCNP – a general Monte Carlo N-particle transport code. *Los Alamos National Laboratory Report*, 1997, Vol. LA-12625-M.
10. DZYSIUK N. C*ross sections for nuclear reactions (n,x) at germanium, terbium and lutetium isotopes with neutron energy about 14 MeV*, Kharkiv National University, Kharkiv, 2008.
11. KAWADE K., SAKANE H., KASUGAI Y., SHIBATA M., IIDA T., TAKAHASHI A., FUKAHORI T. *Nucl. Instrum. Methods*, Phys, 2003, Vol. Res. A 496, p. 183.
12. Janis 3.0, a Java-based nuclear data display program, OECD Nuclear Energy Agency - France, 2007.
13. DROSG. Link to the internet <http://www-nds.iaea.org/drosg2000.html>
14. AGRAWAL H.M., PEPELNIK R. *Nucl. Instrum. and Methods Phys*. Res, 1995, Vol. A366, p. 349.
15. FILATENKOV A. A., CHUVAEV S.V. KHLOPIN RADIEV. Inst. *Leningrad Reports,* 2001, Vol. No. 258.
16. BERLIZOV A., DANILENKO M., KAZIMIROV A., SOLOVYOVA S. At Energy, 2006, 382 p.
17. TULI J. K. Evaluated Nuclear Structure Data File, *A Manual for Preparation of Data Sets*, Brookhaven National Laboratory, 1987, BNL-NCS-51655-Rev.87.
18. KONING A. J., HILAIRE S., DUIJVESTIJN M.C. TALYS-1.2 A nuclear reaction program, *User manual*, 2009, 379 p.
19. QAIM S.M. Nucl Phys.A, 1974, Vol. V224, 319 p.
20. BARI A. Dissertation Abstracts B (Sciences), Vol. 32, p. 5091 (1972), USA.
21. OMS L.A., POLM J.M. Bulletin of the American Physical Society, 1968, Vol. (CA9), No 13, 1699 p.
22. Radioactive equilibrium. The case of no equilibrium. Link to the internet: <http://profbeckman.narod.ru/RH0.files/4_4_2.pdf>
23. KONING A. J., DELAROCHE J. P. Nucl. Phys, 2003, Vol. A713, 231 p.
24. Tamura T., Rev. Mod. Phys. 37, 679 (1965).

CYSENI 2011, May 26–27, Kaunas, Lithuania
ISSN 1822-7554, www.cyseni.com

# THERMAL ANALYSIS OF THE ENGINEERED BARRIERS OF GEOLOGICAL REPOSITORY FOR RBMK-1500 SPENT NUCLEAR FUEL DISPOSAL IN CRYSTALLINE ROCKS

**D. Justinavičius**
*Nuclear Engineering Laboratory*
*Lithuanian Energy Institute*
*Breslaujos str. 3, LT-44403 Kaunas – Lithuania*
*Phone +370 37 401 886*
*Email: justinavicius@mail.lei.lt*

## ABSTRACT

Spent nuclear fuel (SNF) and long-lived high level radioactive wastes (HLW) are best disposed in the geological repositories using a system of engineered and natural barriers. Due to the danger of exposure arising from long-lived radionuclides to humans and the environment, SNF is not allowed to be disposed in the near-surface repositories.

The disposed nuclear waste would release some residual decay heat. Heat is transferred from the canister surface to the bentonite buffer, through the buffer and finally dissipated in the host rock. Heat is transported away through the engineered barriers of a repository by a set of mechanisms (conduction, convection, radiation). The effectiveness of heat removal depends on the properties of the engineered barriers and the conditions existing there. The later can be affected by other processes occurring in the near field such as water flow during buffer resaturation or mechanical deformations due swelling or shrinkage of bentonite. There is a requirement that the surface temperature of the canister cannot exceed 100°C after the emplacement in the repository. Usually pure thermal analysis is being applied for the assessment of the temperature field evolution. However, it is obligatory to confirm the thermal results in respect of coupled thermo-hydro-mechanical models.

In this paper the results of the modelling on the residual decay heat transfer from the geological repository are presented. The axis-symmetric model of the near field of RBMK-1500 SNF repository has been developed and transient calculations for a single canister disposed in the crystalline rocks have been performed. The analysis has been done for 3 different cases: pure thermal (T) analysis and two cases taking into account the coupling with hydraulic (TH) and hydraulic-mechanical processes (THM) analysis. In order to evaluate some uncertainty, three additional sub-cases have been analysed.

Keywords: thermal analysis, geological repository, disposal, crystalline rocks, numerical modelling.

## 1. INTRODUCTION

Many countries are concerned about the safe isolation of nuclear wastes from the biosphere and disposal in a deep geological formation is considered an attractive option [1, 2]. The multiple-barrier concept is the cornerstone in all proposed schemes for the underground disposal of radioactive waste. The concept invokes a series of barriers, both man-made and natural, between the waste and the surface environment. Depending on the waste category and disposal concept, the barriers are: (a) the chemical barrier (conditioned waste), (b) the physical barrier (waste canister), (c) the engineered barrier (clay buffer/backfill, linings, high-integrity seals, etc.) and (d) the geological barrier or low-flow geological environment. The intention of such disposal is to provide sufficient isolation on radioactive waste from human activities and natural processes, securing slow transportation of radioactive nuclides in the geosphere and low concentration eventual release to the biosphere that do not pose a hazard to human health and the natural environment.

Although there is no repository for SNF or HLW operating worldwide, a significant progress has been made on this subject. International nuclear community has conducted extensive research related to deep disposal of HLW over the past few decades. The underground research laboratories (URLs) have been developed in several countries such as Sweden, Finland, Belgium, Germany, Switzerland, USA, Canada and Japan to address the fundamental issues on whether or not a particular rock mass type would be suitable as a repository host rock. Furthermore, the development of more sophisticated models is becoming more important to provide the theoretical background for performance and safety assessment of the waste disposal system. Therefore, several countries are developing a capability to model a wide range of processes including coupling of mechanical stability and groundwater flow through the repository with thermal loading from the decaying waste [3–5].

The results of thermal analysis for a deep geological repository can provide the temperature distribution, which is required for the repository design and for the evaluation of the thermal integrity of the near field materials. The maximum temperature at the outer boundary of canister close to the buffer filling the space between the canister and rock mass is usually considered as the most critical parameter for the repository [6]. The surface temperature of the canister cannot exceed 100 °C. Otherwise unfavourable groundwater chemistry can adversely affect the chemical stability of the bentonite[1] buffer and the conditions can become more aggressive close to the canister surface [7].

The results of thermal analyses for the Swedish KBS-3V (Fig. 1) type nuclear waste repository in granitic rock are presented in this paper. Transient calculations for an axis-symmetric model have been carried out for RBMK-1500 SNF disposal. This study investigates the temperature distribution around one of the boreholes of a transportation tunnel for 200 years after repository closure. Pure thermal analysis for different moisture contents of bentonite and thermal analysis taking into account the coupling with hydraulic and hydraulic-mechanical processes have been performed. For the modelling the finite element code COMPASS (COde for Modelling PArtly Saturated Soil) [8] was used.

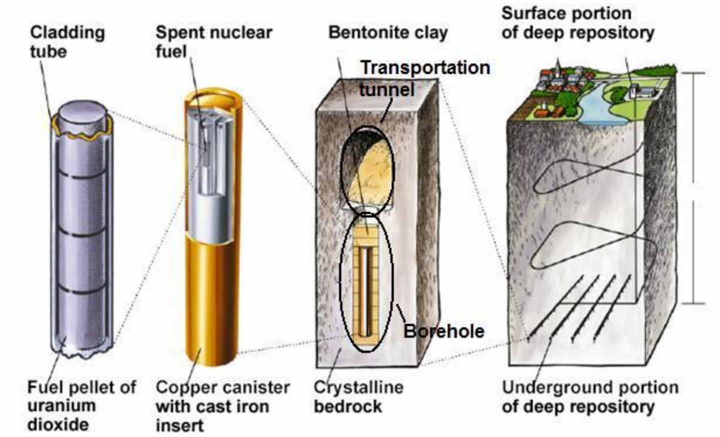

Fig. 1. Illustration of KBS-3V type repository with vertical disposal of the SNF canisters [9]

## 2. PROBLEM DESCRIPTION

Heat generated by radioactive wastes could cause significant effects on the performance of a repository and its multiple-barrier system function. Many of these thermal effects are largely confined to the near field including the buffer/backfill materials and near field rock (excavation disturbed zone).

Once the waste has been disposed in the repository, a transient heat transport starts. Heat transfer through the waste canister and the surrounding materials toward the rock will be

---

[1] Bentonite – a light coloured clay composed essentially of montmorillonite and related mineral of the smectite group. Bentonite is proposed to be as backfill and buffer material in repositories

mainly by conduction. After the backfilling, heat transfer by convection and radiation will be negligible because of low gas and hydraulic conductivity of the surrounding materials.

Heat release from the waste canisters leads to strongly coupled THM processes in clay buffers and fractured rocks surrounding the disposal canisters. The elevated temperature around the waste canister creates a thermal gradient with induced thermal stress and the deformation in the surrounding medium. The temperature gradient causes groundwater movement (by diffusion) within the clay buffer, because the water temperature determines the viscosity and flow properties of the water. At the same time, the clay swells or shrinks as a function of its water content (saturation), causing mechanical deformation and the changes of stress within it. Due to mechanical deformation, the porosity and the apertures of rock pores/fractures could be changed thus will affect the groundwater flow regime. Water flow depends on the material saturation and on the material behaviour under unsaturated conditions as well. Due to affected water pressure gradient, the heat transfer is influenced too. Generally in the case of heat-generating radioactive waste, it is possible to envisage the range of individual and coupled T, H and M processes that can occur. This is illustrated schematically in Fig. 2.

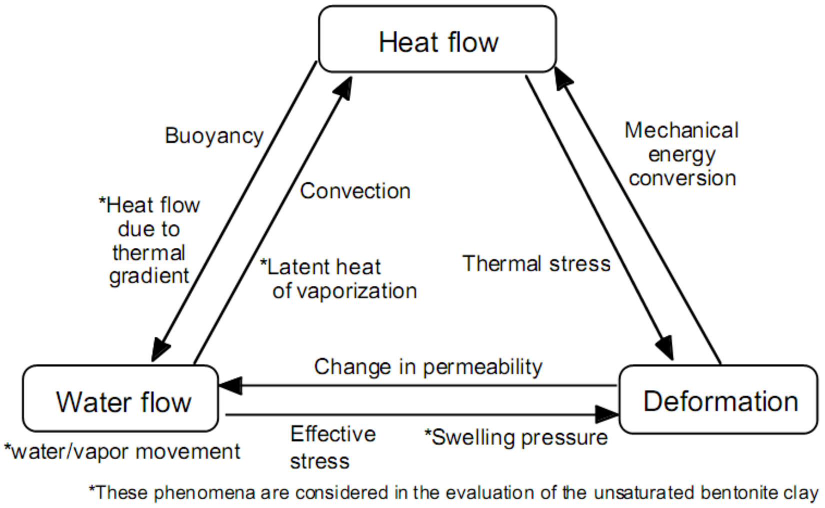

Fig. 2. The illustration of thermo-hydro-mechanical (THM) couplings

The performance of this system is difficult to assess using analytical techniques. Thus a numerical model that is able to simulate coupled and highly nonlinear behaviour of all components (canister, buffer, fractured rock, water) and their interactions has to be applied.

## 3. METHODOLOGY

The temperature evolution in one of the boreholes of a transportation tunnel was modelled using computer code COMPASS, which has been developed at the Cardiff University (UK). COMPASS is a 3D transient finite element code for geotechnical engineering, capable of thermo-hydro-mechanical coupling under unsaturated conditions.

The materials contained within the system being analyzed (buffer, backfill and granite rocks) are assumed to be a three phase porous medium, consisting of solid skeleton, pore-water and pore-air (Fig. 3). In the following formulation the flow of moisture, air and heat energy in a deformable porous medium are considered.

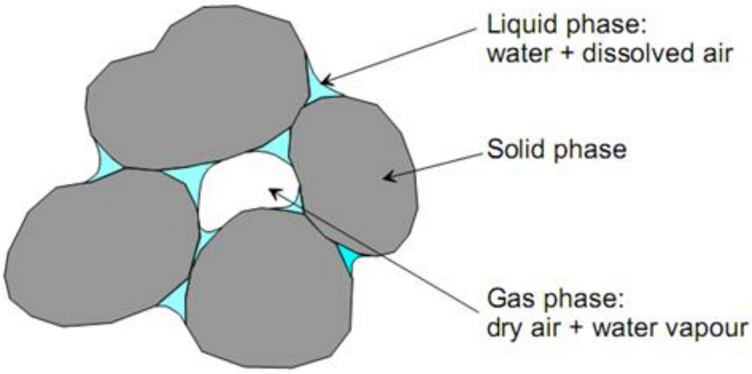

Fig. 3. Schematic representation of unsaturated media

Governing differential equations are solved to assess the flow of moisture, dry air, heat transport and the deformation evolution. Heat transfer is governed by the classical conservation of heat energy:

$$\frac{\partial \Omega_H}{\partial t} = -\nabla Q, \tag{1}$$

here $\Omega_H$ is the heat content of unsaturated soil per unit volume and includes conduction and convection; $Q$ is the heat flux per unit area.

### 3.1. Numerical model

In this study it is assumed that the SNF repository is located at 500 m below the surface in granite rock mass. A part of the transportation tunnel and the single deposition hole (borehole) for the disposal canister with RBMK-1500 SNF are included in model domain. The reference canister for RBMK-1500 SNF disposal in the crystalline rocks is based on Swedish KBS-3 concept and consists of two parts: the outer copper shell and the cast iron insert.

The canister has a length of 4.07 m and a radius of 0.525 m. It is designed for 16 (32 half-assemblies) fuel assemblies of RBMK-1500 SNF. The canister was not modelled itself, it was represented by the means of boundary condition (time dependent heat fluxes). There is 0.35 m thick layer of compacted bentonite around the canister and the bentonite plugs of 1.5 m and 0.5 m height above and below the canister respectively. The height of transportation tunnel is 6 m. After the emplacement of the SNF canister and the bentonite in the deposition hole this tunnel will be backfilled with the mixture of crushed rock and 30% of compacted bentonite.

The single deposition hole is virtually symmetrical therefore an axis-symmetric analysis has been undertaken to reduce computational time. All the mesh contains 925 triangle elements. The discretization of model domain shows that the mesh is more precise in the engineered barriers (bentonite/backfill) of the repository due to higher gradients of the parameters and a finer result resolution required. The geometry and discretized mesh of the model domain is illustrated in Fig. 4.

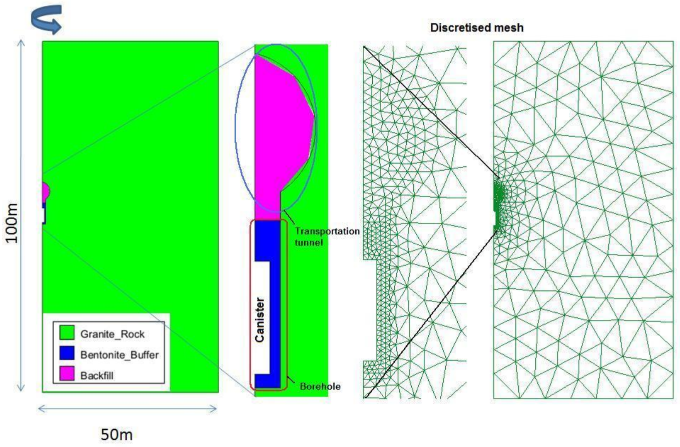

Fig. 4. The geometry and discretized mesh of the model domain

### 3.1.1. *Material properties*

For the development of the model a number of material parameters are required in order to define the behaviour of each individual material. Since there is a lack of geotechnical properties of geological formation and engineered barriers in Lithuania, this information has been obtained from the experimental works performed in the SKB Prototype Repository in the Äspö Hard Rock Laboratory (Sweden) [10].

Heat conductivity and capacity determine the heat transfer process (by conduction) in materials. The thermal conductivity $\lambda$ is the basic parameter for the temperature evolution and distribution. It depends on material liquid saturation $S_l$. The $\lambda$ – values for bentonite, backfill and granite rocks, which have been used in numerical model, are summarized in Fig. 5.

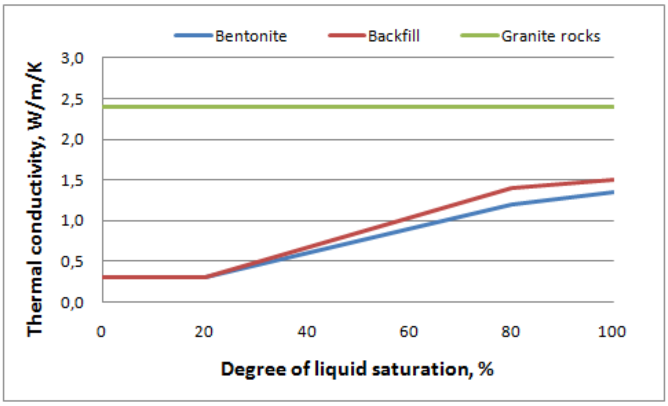

Fig. 5. Thermal conductivity of analyzed materials [10]

A summary of other parameters used in the simulations is given in Table 1.

Table 1. Material parameters used in the analysis

| **Parameter** | **Bentonite** | **Backfill** | **Granite rocks** |
|---|---|---|---|
| Density, $\rho_s$ (kg/m$^3$) | 2700 | 2750 | 2770 |
| Initial porosity, $n$ (-) | 0.4 | 0.39 | 0.005 |
| Specific heat capacity $C_{ps}$(J/kg/K) | 800 | 850 | 750 |
| Coefficient of thermal expansion, $\alpha_T$ (K$^{-1}$)* | $1.5 \cdot 10^{-4}$ | $1.5 \cdot 10^{-4}$ | 0 |
| Initial degree of saturation, $S_l$ (%)* | 85 | 70 | 100 |
| Hydraulic conductivity $K_l$ (m/s)* | $4 \cdot 10^{-14} \div 1.5 \cdot 10^{-13}$ | $5 \cdot 10^{-12} \div 1.5 \cdot 10^{-10}$ | $1 \cdot 10^{-12}$ |

* Used only for TH and THM calculations

### 3.1.2. *Initial and boundary conditions*

The initial 32 °C temperature has been imposed in all modelling domain according the geological data in Lithuania. The temperature evolution of the waste canister was taken from the evaluation using ORIGEN-S [11] code after 50 years of interim storage of RBMK-1500 SNF [12]. The thermal load has been imposed by prescribing the temperature evolution on the inner boundary of the bentonite close to the external surface of the canister. The same conditions were set for both pure thermal and coupled TH, THM analysis.

For TH and THM analysis (thermal analysis considering the coupling with hydraulic and hydraulic-mechanical processes) it was assumed that at the beginning of the simulation the rocks were fully water saturated. The buffer materials were assumed to be partly water saturated at the beginning (Table 1). The initial pore-water pressure of the granite rocks was assumed to be hydrostatic with the water table, which was situated 450 m above the top of the domain. For the assessment of the deformation of the bentonite and backfill initial compressive stresses in x and y directions were set to be equal to 200 kPa and 22 MPa for the granite rock. All model boundaries were restrained in x and y directions.

## 4. RESULTS AND DISCUSSION

Six different cases have been analyzed for the assessment of the temperature distribution around the single deposition hole. All analyzed cases are summarized in Table 2.

The changes of materials water saturation were not modelled in pure thermal analysis. Constant thermal conductivity throughout the simulated period was considered. Bentonite buffer is a primary barrier to heat dissipation in the transportation tunnel and surrounding rock mass. In order to evaluate the uncertainty of bentonite humidity, three sub-cases have been analysed. After the emplacement of the SNF canister and the bentonite in the deposition hole, bentonite will be partially saturated. Cases T1 and T2 represent the “worst” (bentonite will be almost dry) and “realistic” (bentonite will be largely saturated) cases in the point of heat dissipation view, respectively. Incoming water from the rock will re-saturate bentonite within couple years. Case T3 represents the “best” case conditions when bentonite will be fully water saturated.

The changes of materials water saturation were modelled in TH and THM analysis. Thermal conductivity of bentonite and other materials varies with time depending on the water saturation within these materials. Initial thermal conductivity deduced from Table 2 and Fig. 5. In order to evaluate the impact of heat transfer by convection (because of water movement in the bentonite and surrounding materials) on the temperature distribution, additional TH analysis has been performed.

Performing THM analysis the mechanical process (deformations of engineered barriers due swelling or shrinkage) is taken into account besides TH coupling.

Table 2. The modelling cases

| **Case** | **Description** | **Thermal conductivity of bentonite, W/m/K** |
|---|---|---|
| T1 | Pure thermal analysis, the bentonite is almost dry (20 %) | 0.4 |
| T2 | Pure thermal analysis, the bentonite is largely saturated (85 %) | 1.1 |
| T3 | Pure thermal analysis, the bentonite is full saturated (99.9 %) | 1.35 |
| TH1 | TH analysis | varying (1÷1.35) |
| TH2 | TH analysis, taking into account convective flow | varying (1÷1.35) |
| THM | THM analysis | varying (1÷1.35) |

The observation points P1-P4 (Fig. 6.) indicate the locations of analyzed temperature profiles. P1 is a point in the backfill, 2.5 m height above the canister. P2 is a point at the canister radius, it corresponds to the canister surface. P3 is a point outside the bentonite buffer. P4 is a point in the host rock at 2.5 m away from the canister. Additional post-processing option leads to find and fix peak temperatures in whole modelled system at every time step.

## 4.1. Pure thermal analysis

The temperature profiles obtained at various locations around the canister (in the buffer and the granite rock) are presented in Fig. 6. As it could be expected, the peak temperature is reached at the contact with the disposal canister, after ~1–2 years of heat release. Generally the temperature tends to increases when reaches a certain level and start to decrease.

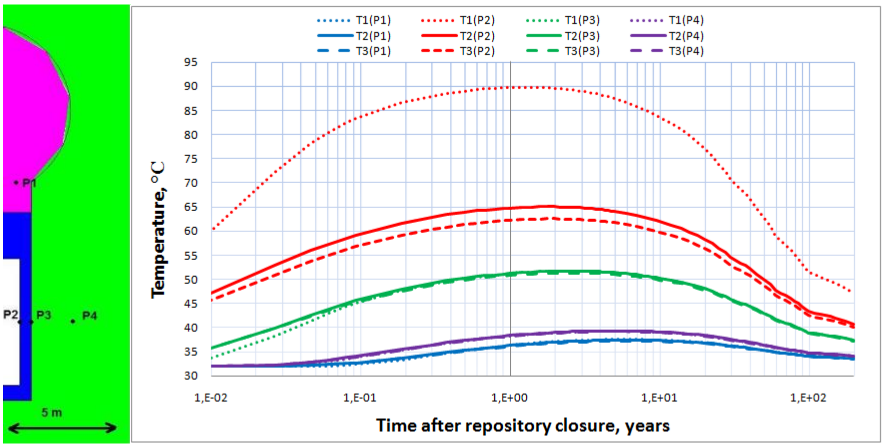

Fig. 6. The temperature profiles at selected points under pure thermal analyses

The results of pure thermal analysis showed that peak temperature near disposal canister (P2) strongly depends on the bentonite saturation (thermal conductivity of bentonite). The peak temperature of pure thermal analysis (~90 °C) was observed in the "worst" (*T1 analysis*) case. The temperatures under realistic conditions (*T2 analysis*) are between "worst" and "best" (*T3 analysis*) cases. The difference of peak temperatures is ~27 °C between the "worst" and the "best" case. The difference of peak temperatures is ~2.5 °C between the "realistic" and the "best" cases.

The temperature profiles at other monitored points are quite similar between the analyzed cases. The difference of peak temperatures at P1, P3, P4 between the "worst" and the "best" cases are ~0.3 °C, ~0.4 °C and ~0.15 °C, respectively.

## 4.2. TH analysis

The thermal gradient induced by the released heat causes a de-saturation close to the heat source (drying of the bentonite). This effect is minor and short-term because the decreasing of residual decay heat and the incoming water from the rock will re-saturate the bentonite. In such way the thermal conductivity of the bentonite/backfill varies with time depending on the bentonite liquid saturation $S_l$. The temperature profiles obtained at P2 under TH analysis (cases *TH1* ant *TH2*) are presented in Fig. 7. For comparative purposes, the temperature profiles under pure thermal analysis ("realistic" *T2* and "best" *T3* cases) are presented too.

The results of coupled thermal-hydraulics analysis showed that the temperatures observed at P2 are lower than in "realistic" case *T2* of pure thermal analysis. On the other hand the estimated temperatures are a slightly higher in comparison to "best" case *T3* of pure thermal analysis. The differences of peak temperatures between *TH1* and *T2*, *T3* are ~2.5 °C and ~0.7 °C, respectively. These discrepancies show that thermal analysis considering the coupling with hydraulic is more precise than only pure thermal analysis (in the point of view real processes and conditions existing in the geological repository view).

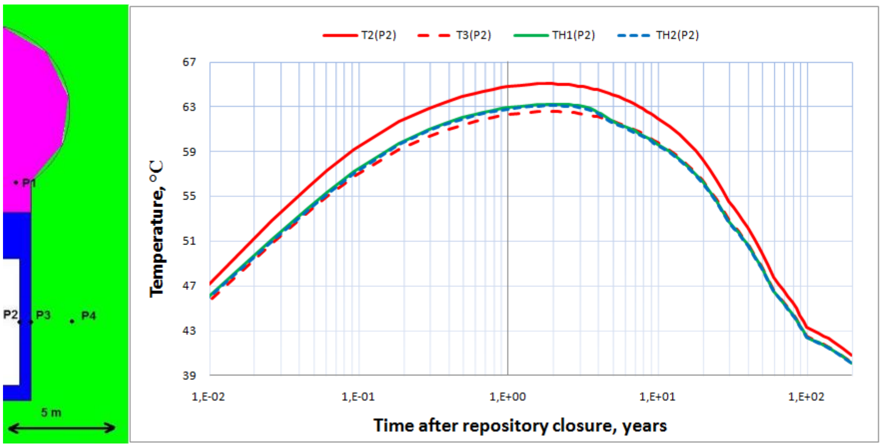

Fig. 7. The temperature profiles observed at P2 under T and TH analyses

The main heat transfer mechanism in the repository conditions is by conduction. In pure thermal and *TH1* analysis the convection heat flow was neglected. The additional analysis case (*TH2*) has been performed in order to evaluate the impact of heat transfer by convection on the temperature distribution. The pore-water movement is very slow due to low hydraulic conductivity of surrounding materials. The results (Fig. 7 and Fig. 8) showed that the temperature distribution at monitored points is insignificantly higher when convective heat transfer has been considered. However convective heat transportation causes a minor effect on the temperature distribution within engineered barriers and the surrounding rocks.

## 4.3. THM analysis

The elevated temperature around the disposal canister creates a thermal gradient with induced thermal stress and the deformation in the surrounding medium. Based on the TH analysis results, the incoming water from the granite rock will increase the saturation of the bentonite/backfill and cause it to swell. Due to the mechanical deformation, the porosity and the apertures of rock pores/fractures could be changed, thus affecting the groundwater flow regime. However groundwater flow influences only heat transfer by convection but has no significant impact on the heat transport by conduction. Thus the results of temperature distribution under THM analyses are very similar to the results considering only TH processes (Fig. 8).

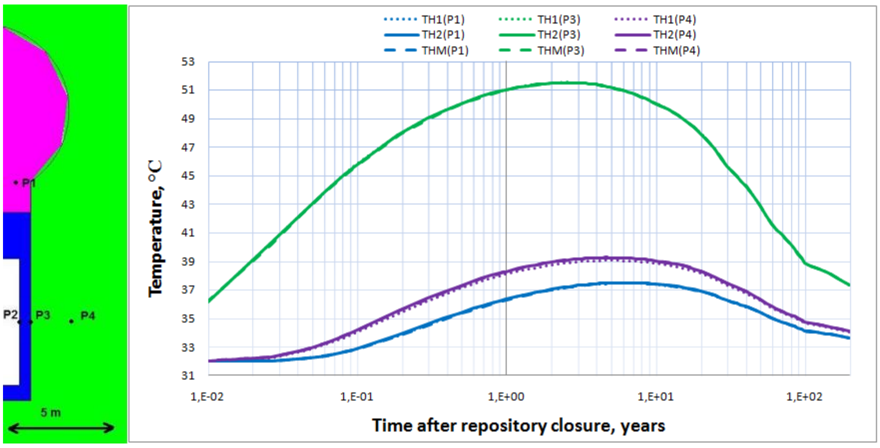

Fig. 8. The temperature profiles observed at selected points under TH and THM analyses

### 4.4. Comparison of the results

The peak temperatures at the monitored points (indicated in the Fig. 6) and in the whole system are presented in Table 3. The peak temperature in the system was observed at different highs of bentonite in contact with SNF canister.

Table 3. The peak temperatures at each monitored point

| **Cases** | **P1** | **P2** | **P3** | **P4** | **Peak temperature in the system, °C** | **Time when peak temperature observed, y** |
|---|---|---|---|---|---|---|
| T1 | 37.55 | 89.80 | 51.73 | 39.27 | 93.92 | 1.2 |
| T2 | 37.42 | 65.03 | 51.42 | 39.24 | 64.38 | 1.8 |
| T3 | 37.23 | 62.54 | 51.34 | 39.19 | 62.72 | 1.8 |
| TH1 | 37.47 | 63.06 | 51.51 | 39.26 | 64.97 | 1.4 |
| TH2 | 37.50 | 63.21 | 51.50 | 39.25 | 65.01 | 1.4 |
| THM | 37.47 | 63.01 | 51.50 | 39.16 | 64.82 | 1.4 |

The peak temperature reached at the contact with the disposal canister was ~94 °C in the “worst” case under pure thermal analysis. There is a requirement that the surface temperature of the canister cannot exceed 100 °C [7]. The results of temperature assessment around the canisters loaded with 32 RBMK-1500 SNF half-assembly showed that the disposal canister with such heat output would satisfy the temperature constrain.

The character of thermal evolution under pure thermal analysis correlates quite well comparing with the results achieved using computer code FLUENT [13] (do not taking consideration of different SNF disposal type). But there are no results for comparison yet of scientific investigations for RBMK-1500 SNF disposal in crystalline rocks in respect of coupled thermo-hydro-mechanical models.

## 5. CONCLUSIONS

1. A numerical model has been developed to simulate temperature distribution in one of the boreholes of a transportation tunnel for RBMK-1500 SNF disposal in the crystalline rocks.
2. The results of temperature modelling under pure thermal analysis illustrate the importance of the bentonite thermal conductivity (bentonite saturation) on the peak temperature in the system (difference is ~27 °C between “worst” and “best” case). Since bentonite water content is varying under the repository conditions it is highly recommended to perform coupled thermo-hydro analysis for more reliable temperature estimation.
3. The main heat transfer mechanism is conduction; heat transfer by convection is a second order process.
4. In comparison to the coupled TH analyses the consideration of mechanical processes in the computational model do not cause any significant changes of the thermal distribution and peak temperature around a single deposition hole.
5. It was determined that the largest peak temperature within modelled system was ~94 °C (pure thermal analysis, “worst” case). The results of temperature assessment showed that the disposal canister with such heat output would satisfy the temperature constrain under all cases which had been analyzed.

## REFERENCES

1. IAEA. Scientific and Technical Basis for the Geological Disposal of Radioactive Wastes. Technical Report Series No. 413. Vienna: IAEA. 2003.
2. WITHERSPOON P.A. Introduction to second world wide review of geological problems in radioactive waste isolation. Geological Problems in Radioactive Waste Isolation. LBNL-38915. 1996, p. 1–4.
3. RUTQVIST J., BORGESSON L., CHIJIMATSU M. et al. Coupled thermo-hydro-mechanical analysis of a heater test in fractured rock and bentonite at Kamaishi Mine – compassion of field results to predictions of four finite element codes. *International Journal of Rock Mechanics and Mining Sciences*. 2001. Vol. 38, p. 129–142.
4. HUDSON. J.A., STEPHANSSON. O., ANDERSSON. J., TSANG. C.-F., JING. L. Coupled T-H-M issues relating to radioactive waste repository design and performance. *International Journal of Rock Mechanics and Mining Sciences*. 2000. Vol. 38, p. 143–161.
5. THOMAS H.R., CLEALL P.J. Inclusion of expansive clay behaviour in coupled thermo hydraulic mechanical models. *Engineering Geology*. 1999. Vol. 54, p. 93–108.
6. PARK J.H., KUH J.E., KWON S., KANG C.H. Thermal analysis of high level radioactive waste repository using a large model. *Journal of the Korean Nuclear Society*. 2000. Vol. 32, p. 244–253.
7. Design premises for canister for spent nuclear fuel. SKB Technical Report TR-98-08. 1998. Swedish Nuclear Fuel and Waste Management Company (SKB). Stockholm. Sweden.
8. THOMAS H.R., HE Y. A coupled heat-moisture transfer theory for deformable unsaturated soil and its algorithmic interpretation. *International Journal for Numerical Methods in Engineering*. 1997. Vol. 40. p. 3421-3441.
9. Interim Main Report of the Safety Assessment SR-Can. SKB Technical Report TR-04-11. 2004. Swedish Nuclear Fuel and Waste Management Company (SKB). Stockholm. Sweden.
10. Äspö Hard Rock Laboratory. Annual report 2008. SKB Technical Report TR-09-10. 2009. Swedish Nuclear Fuel and Waste Management Company (SKB). Stockholm. Sweden.
11. HERMANN. O. W., WESTFALL R. M. ORIGEN-S: SCALE System Module to Calculate Fuel Depletion. Actinide Transmutation. Fission Product Build-up and Decay and Associated Radiation Source Terms. Rev.5. Oak Ridge National Laboratory. March 1997.
12. POŠKAS. P., BRAZAUSKAITĖ. A., NARKŪNAS. E., ŠMAIŽYS. A., SIRVYDAS. A. Generic repository concept for RBMK-1500 spent nuclear fuel disposal in crystalline rocks in Lithuania. ENS Conference TopSeal 2006 Transaction. [CD]. Olkiluoto. 2006 September 17–20.
13. SIRVYDAS. A., POŠKAS. P. Panaudoto RBMK-1500 branduolinio kuro, palaidoto konceptualiame kapinyne, temperatūros kitimo modeliavimas. Energetika. 2010. T. 56, Nr. 3–4, p. 260–266.

CYSENI 2011, May 26–27, Kaunas, Lithuania
ISSN 1822-7554, www.cyseni.com

# UNCERTAINTY AND SENSITIVITY ANALYSIS OF AEROSOL BEHAVIOUR IN PHEBUS CONTAINMENT DURING FPT2 TEST

**A. Kontautas, E. Urbonavičius**
*Lithuanian Energy Institute*
*Breslaujos g. 3, LT-44403 Kaunas – Lithuania*
*Phone +370 37 401983*
*Email: aurkon@mail.lei.lt*

ABSTRACT

PHEBUS-FP is a multi-national collaborative programme comprising four integral and one debris bed melting and fission product release experiments. The integral experiments simulate the heat-up, degradation and fission product release and transport, thermal hydraulic response, aerosol behaviour and iodine chemistry in the containment. The PHEBUS-FP consists of five in-pile experiments being successfully performed during the period from 1993 to 2004. The experiments demonstrated new characteristics of core degradation, fission product and iodine chemistry and accident integral behaviour. This paper is related to uncertainty and sensitivity analysis of aerosol and fission product behaviour modelling for FPT-2 experiment. The analysis of processes in the PHEBUS containment was performed with lumped-parameter code COCOSYS. There were selected 15 input parameters for uncertainty and sensitivity analysis, which was performed with SUSA software. There were performed 100 runs with randomly selected parameter values as input. Results of this sensitivity analysis indicate that the main experimental measurements lie within the uncertainty range of the corresponding calculated values.

Keywords: sensitivity and uncertainty analysis, containment, COCOSYS, SUSA.

## 1. INTRODUCTION

The PHEBUS-FP programme was intended for severe accident progression analysis in a Light Water Reactor (LWR). The PHEBUS facility stands in the French Atomic Energy Commission (CEA) center at Cadarache. The main objective of the PHEBUS-FP programme is to study the release, transport and retention of aerosols and fission products in an in-pile facility under conditions representative of a severe accident in a LWR. The secondary objective is to validate models used in the existing source term codes.

The analysis of processes in the PHEBUS containment was performed with lumped-parameter code COCOSYS. The main purpose of performed analysis is to calculate the distribution and retention of airborne aerosols and to estimate what parameters have the largest influence on the aerosols deposition in the containment. There were selected 15 input parameters for uncertainty and sensitivity analysis, which was performed with SUSA software. The state of knowledge on parameter’s tolerance was taken into account by subjective probability distribution and considering the experience received in previous analyses: average aerosol density and solubility influence on aerosol deposition in FPT-1test [1], analyses of mass median diameter and aerosol dynamic shape factor in FPT-3 [2], and influence of diffusive layer and aerosol density in FPT-1 [3]. All of these analyses investigated influence or sensitivity of the results to separate investigated parameter or modelling approach. In this paper the analysis is performed to investigate not only sensitivity to modelling parameters, but to determine the uncertainty range of the results and determine the most important parameters that give the largest influence on the results.

## 2. DESCRIPTION OF EXPERIMENT FPT-2

### 2.1. Geometric conditions

The PHEBUS containment vessel is a 10 $m^3$ tank (see Fig. 1), made of electro-polished stainless steel (AISI 316L), in which aerosols and gases conveyed through the experimental circuit during the test are collected. Height of containment is 5 m with an inner diameter of 1.8 m. The altitude of containment vessel is shown in Fig. 1.

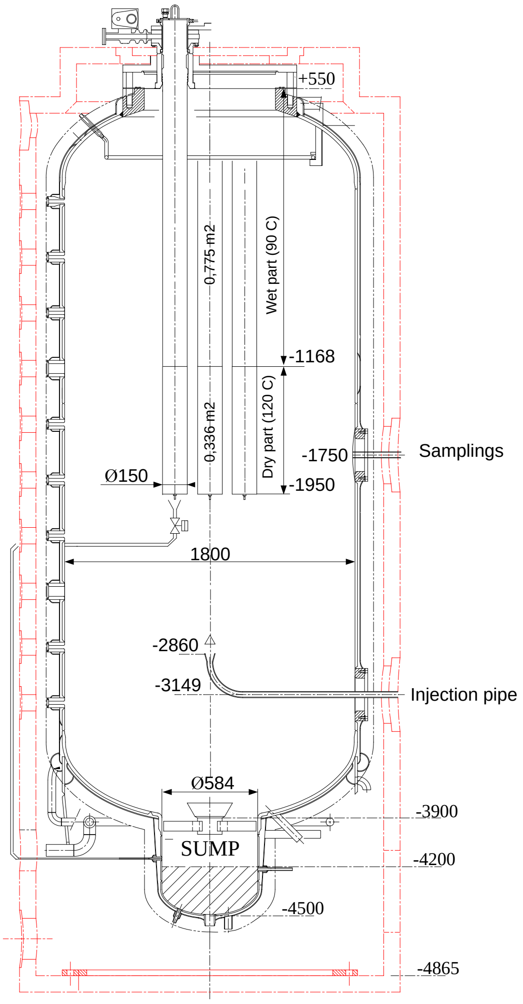

Fig. 1. Schematic view of PHEBUS containment

The containment wall represents a surface of about 25 $m^2$. The containment has cylindrical form with rounded bottom and top. The outer vessel walls were heated to avoid steam condensation and subsequent aerosol deposition on the containment top vault and vertical walls during the test. The top vault is equipped with a group of three condensers, which are designed to control heat transfer, steam condensation and thus simulate the cold structures of a containment building. Total surface area of condensers is 3.333 $m^2$. The condenser surface is divided into two parts: the cooled condensing or “wet” condenser surface (area: 0.775 $m^2$ per condenser) and the non-condensing or “dry” condenser surface (area: 0.336 $m^2$ per condenser). The lower part of each condenser is kept dry by heaters and contains equipment to collect condensate from the upper cooled part. When the collection device is full, the condensate is automatically drained into the sump. The cooled surfaces of condensers are covered with epoxy paint as a source for organic iodine formation. The sump is a lower vessel part closed by a curved bottom structure with volume of 0.1 $m^3$. The sump has a diameter of 0.584 m and height is 0.6 m in order to reproduce a representative atmosphere-water exchange surface. The sump was initially filled with 120 l water. The injection pipe tag to the containment of steam, hydrogen and aerosols is located at elevation of – 2.86 m. Pipe tag is in the centre of containment and is pointed to the condensers.

## 2.2. Initial and boundary conditions

The containment atmosphere consists of condensable gases (i.e., steam) and non-condensable gases (i.e., $H_2$, $O_2$, $N_2$ and He). During the test preparation phase the nitrogen is injected into containment to avoid any explosion hazards with the possible hydrogen injection during experiment. As a result initial pressure in containment increases to 1.95 bar, the average atmosphere temperature is 108 $^oC$ and average relative humidity – 51.48 % [4]. Measured steam and hydrogen flow rates into the containment are shown in Fig. 2. Steam injection to containment also started during test preparation phase. The steam flow rate to containment is 0.47 g/s and corresponds to coolant flow rate through the reactor core. The PHEBUS FPT-2 experiment initial “degradation” phase started at 0 s. In the course of performed test the core temperature increases and the fuel cladding starts oxidising due to zirconium and steam interaction. In this chemical reaction the hydrogen is generated and together with steam is released to the containment. Therefore during the course of test the steam flow rate decreases when the hydrogen flow rate increases. The first fuel-clad failure in the reactor was recorded at about 5630 s and ~3000 s later (8730 s) the control rod failed. As a consequence, aerosols arrived to containment after ~9000 s (see Fig. 3). The total injected mass of aerosols is 44.69 g.

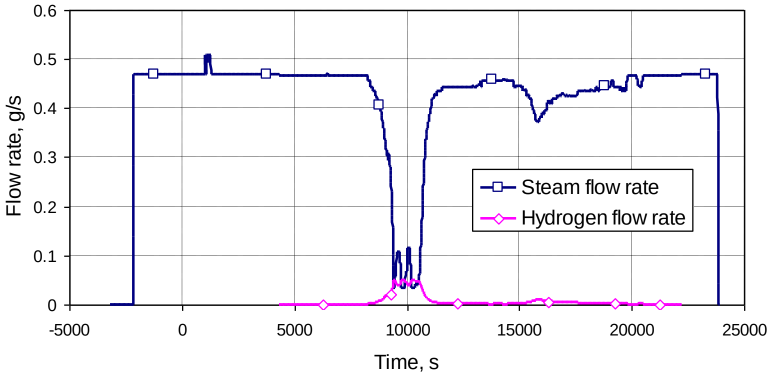

Fig. 2. Steam and hydrogen flow rates to containment during FPT-2

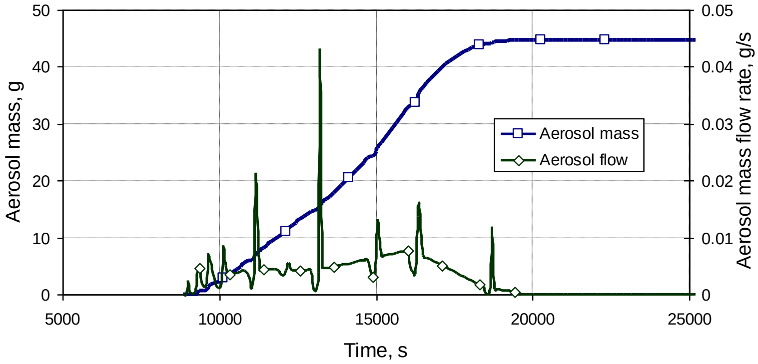

Fig. 3. Injected aerosol mass and flow rate to containment during FPT-2

Sequential samplings devoted to analysis of gases and aerosols characterisation are implemented in the containment and detailed description of sampled volumes with thermal hydraulic conditions is given in FPT-2 test Final report [4].

During the whole test period the temperature of containment walls in contact with the gas phase was 110 °C, temperature of the "wet" condensers 90 °C, temperature of the "dry" condensers 120 °C, and temperature of walls in contact with the sump 90 °C. The containment vessel boundary conditions are chosen to limit the relative humidity to from about 50 up to 70% during the transient, in order to prevent steam condensation on the external containment. Steam condensation in the containment was controlled by the cooled condensing surfaces of the condensers. More detailed description of thermo-hydraulic conditions is given in paper [5].

## 3. MODEL OF PHEBUS CONTAINMENT

For simulation of the aerosol and fission product transport in the PHEBUS containment a model of 16 nodes for COCOSYS code was developed. The nodalization scheme of the model is shown in

Fig. 4. In the model the radial subdivision of the containment consists of two rings in close level above the sump. There is a centre node R1H1 and node R2H1 that simulates the bottom part of the vessel. Above -3350 mm and below 0 mm levels there are three almost equal area rings. The diameter of the radial subdivision was defined in such way that the flow areas are similar. Such approach to nodalization gives similar flow velocities. A ring close to the external containment walls is 175 mm width. At the top vault of the vessel there is one additional node. Simulation of the top vault by single node gives the well-mixed conditions at the top of facility. Similar approach is used at the bottom of facility. Above the SUMP nodes are defined in such way, that there are two junctions to the SUMP. Such approach ensures better mixing and allows avoiding dead-end node, which is not recommended for lumped parameter codes [6].

In the model there are defined 11 structures for the simulation of heat exchange with the containment walls. As well there are defined structures for the simulation of heat exchange between the condensers and containment atmosphere. All PHEBUS containment surfaces and condensers are made of stainless steel, additionally the condenser surfaces are covered with epoxy paint. The reason of the paint is further investigation of the iodine chemical interaction with painted surfaces, but it is out of the scope of this paper.

For simulation of the gas flows between the nodes there are defined atmospheric junctions with real geometric areas. Also, there are defined junctions for simulation of the water drainage from the "wet" condenser to the sump.

In the developed model the initial and boundary conditions (e.g. initial pressure, temperature, humidity, etc.) are defined according to FPT–2 test specification and described in Section 2.2 of report [4].

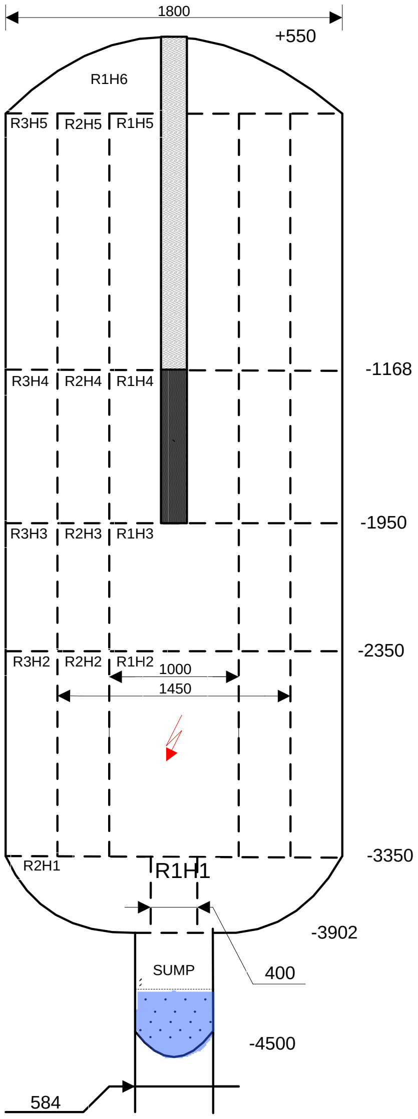

Fig. 4. Nodalization scheme of PHEBUS containment

The aerosols diameter range is assumed $10^{-8}$–$10^{-4}$ m. The models of gravitational, diffusive and diffusiophoretic deposition mechanisms are considered in the model. It is assumed that aerosols could be washed down from the vertical walls by condensate flow and slip through the vertical junctions. Aerosol particles are assumed to be spherical. The soluble (Cs, Rb and I) and non-soluble (Ce, Te, Zr, Ru, Sn, In, Ag, W, U, Ba, Mo, Cd, Re and Tc) aerosols are defined in the model. The composition of elements detected in containment is given in Final test report [4]. It was assumed, that the solubility factor for soluble elements is 1.73 and for non-soluble is 1.0.

## 4. UNCERTAINTY AND SENSITIVITY ANALYSIS

The probabilistic uncertainty and sensitivity analysis was performed with the SUSA software [7]. Table 1 shows the list of 12 parameters with expected values and probabilistic range. Parameters investigated with the Normal (Gaussian) probabilistic distribution. Table 2 shows the list of 3 parameters that are assumed to be changing with discrete distribution. Thus, total number of 15 parameters were chosen for analysis. These modelling parameters are directly related the aerosol behaviour.

Table 1. Parameters of uncertainty and sensitivity analysis

| Nr. | Parameter | Expected value | Min. value | Max. value |
|---|---|---|---|---|
| 1 | Solubility factor of soluble aerosols | 1.73 | 1.56 | 1.90 |
| 2 | Dynamic shape factor | 1.0 | 0.8 | 1.2 |
| 3 | Particle sticking probability factor | 1.0 | 0.8 | 1.2 |
| 4 | Geometric standard deviation | 2.0 | 1.8 | 2.2 |
| 5 | Material structure thickness, m | $1.5\cdot10^{-2}$ | $1.35\cdot10^{-2}$ | $1.65\cdot10^{-2}$ |
| 6 | Molecular weight of soluble components, g/mol | 118 | 106.2 | 129.8 |
| 7 | Molecular weight of nonsoluble components, g/mol | 114 | 102.6 | 125.4 |
| 8 | Thickness of diffusive boundary layer, m | $1.0\cdot10^{-4}$ | $1.0\cdot10^{-3}$ | $1.0\cdot10^{-5}$ |
| 9 | Particle slip coefficient | 1.37 | 1.23 | 1.51 |
| 10 | Average water film thickness, m | $3.0\cdot10^{-4}$ | $2.7\cdot10^{-4}$ | $3.3\cdot10^{-4}$ |
| 11 | Molecular weight of gas, g/mol | 20.35 | 18.315 | 22.385 |
| 12 | Turbulence dissipation rate, $m^2/s^3$ | 0.02 | 0.018 | 0.022 |

Table 2. Parameters of uncertainty and sensitivity analysis

| Nr. | Parameter | Point (prob.) | Point (prob.) | Point (prob.) | Point (prob.) | Point (prob.) | Point (prob.) |
|---|---|---|---|---|---|---|---|
| 1 | Average aerosol density, $kg/m^3$ | 3000.0<br>(40%) | 4000.0<br>(20%) | 5000.0<br>(20%) | 6000.0<br>(20%) | -<br>- | -<br>- |
| 2 | Mass median diameter, m | $2.02\cdot10^{-6}$<br>(40%) | $1.75\cdot10^{-6}$<br>(20%) | $1.57\cdot10^{-6}$<br>(20%) | $1.43\cdot10^{-6}$<br>(20%) | -<br>- | -<br>- |
| 3 | Aerosol size classes | 20<br>(30%) | 18<br>(20%) | 16<br>(15%) | 14<br>(15%) | 12<br>(10%) | 10<br>(10%) |

## 5. RESULTS OF ANALYSIS

The calculated airborne aerosol mass is shown together with the corresponding measured data in Fig. 5. The measured data are shown in red thick line with white squares. The results of all 100 runs are presented in the figure. Aerosol injection to the containment starts after ~9000 s. Most of the investigated time the measured airborne aerosol mass lies in the uncertainty band of the calculated results, but in the long-term after 25000 s the measured mass is below the uncertainty band. It shows that still some parameters that could affect the deposition rate are not identified, or the uncertainty range of some parameters could be expanded.

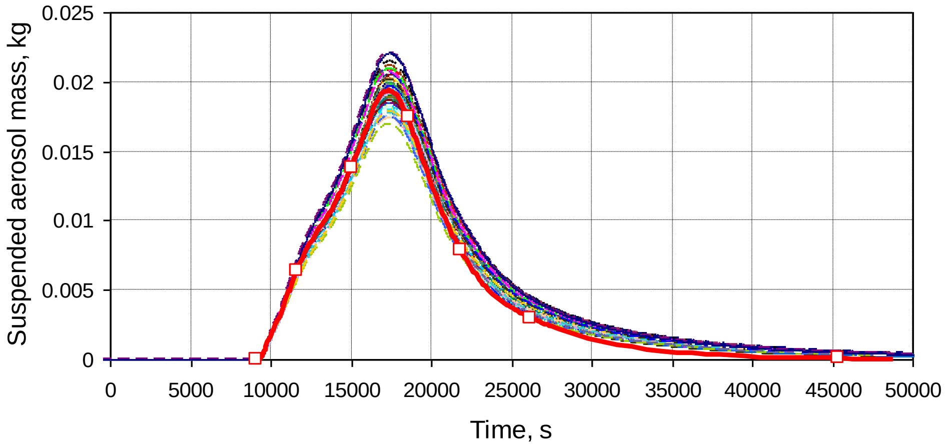

Fig. 5. Suspended aerosol mass in PHEBUS containment

As well, it should be mentioned that in the performed analysis the thermal-hydraulic parameters were not included, which could also affect the results. The sensitivity analysis showed that the largest influence on the airborne aerosol mass comes from the dynamic shape factor, agglomeration shape factor and particle sticking probability. These are the parameters that directly influence the particle deposition rate. In paper [8] is shown that these parameters have a significant influence on the aerosol concentration in containment of VANAM test facility.

Fig. 6 shows aerosol deposition on the elliptic containment bottom received in all 100 runs. Aerosol deposition on the bottom is the largest deposition in the containment. After 50000 s the total deposited mass is between 0.032 – 0.038 kg and it varies in range of 15% of the total deposition on containment bottom. The sensitivity analysis showed that the largest influence on the aerosol deposition on the bottom has dynamic shape factor, agglomeration shape factor and particle sticking probability, plus turbulence dissipation rate and particle slip coefficient. These results agree well with the results published in paper [8].

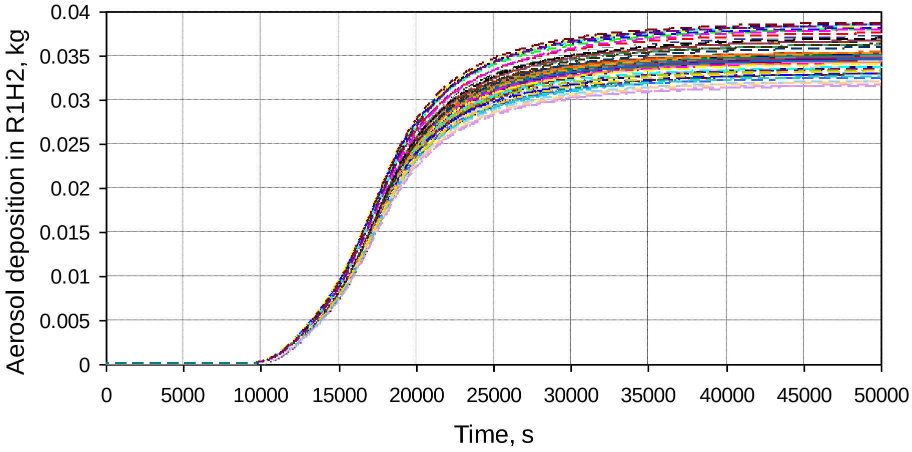

Fig. 6. Deposited aerosol mass on PHEBUS containment bottom

Fig. 7 presents the measured and calculated results of aerosol average geometric mass median diameter in containment atmosphere. The measured data are shown in blue thick line with white squares. According to measured results, the structure of the aerosol particles is predominantly ball shaped, with sizes typically ranging from 0.5 to 1 μm.

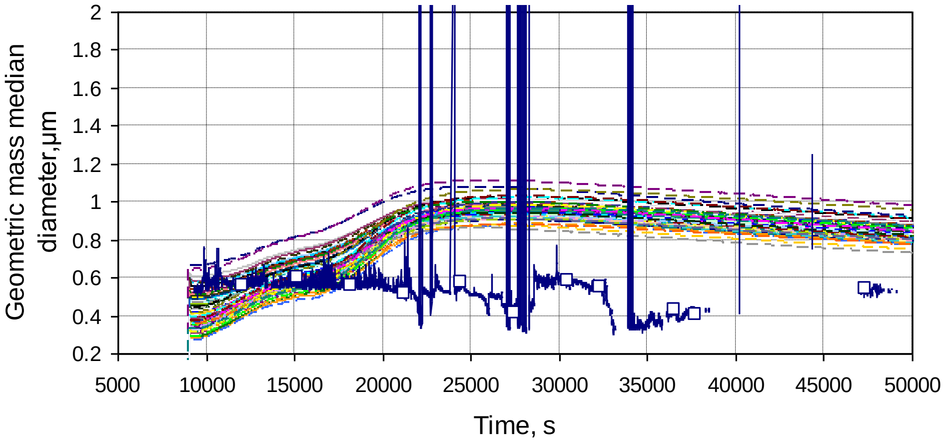

Fig. 7. Aerosol geometric mass median diameter in PHEBUS containment

Observations showed that these very fine particles might be agglomerated to form particles of size up to 20 μm [4]. From the received 100 analyses results, geometric mass median diameter varies in range from 0.3 to 1.1 μm. As it is known there are two principal mechanisms of aerosol growth, as opposed to aerosol formation, the condensation upon an initially existing particle, and agglomeration. Since in containment atmosphere the relative humidity is in the range from 50% to 70% and strong condensation is not observable, so as and observed from calculated results, diameter mostly dependents on particle sticking probability, dynamic shape factor and geometric shape factor.

Distribution of aerosol deposition on different surfaces in containment is shown in **Klaida! Nerastas nuorodos šaltinis.**. The largest aerosol deposition is on the containment floor around the sump, where 74% of aerosols is deposited. On the condensers and in the sump there are deposited 14% of aerosol mass, while on the vertical containment walls and removed by the sampling 12%. The results received with SUSA program shows range from minimum till maximum values of aerosol deposition on different surfaces. Particles deposition on the containment bottom varies in range from 71.44% till 86.88% and depends mainly on sticking probability, dynamic and geometric shape factors. Deposition on the condenser surfaces and sump varies in range from 11.28% till 16.28% and estimated deposition on the containment walls varies from 0.42% till 0.9%. Range of deposition on the condenser surfaces mainly depends on previously mentioned factors plus slip factor. Particles deposition on the containment walls is conversely proportional to particle diameter and directly to diffusion boundary layer, but the observed deposition is less than in measured.

Table 3. Distribution of aerosol deposition

| | Floor of containment | Condenser surfaces and sump | Containment walls + samplings |
|---|---|---|---|
| Experiment | 74.0% | 14.0% | 12.0% |
| Calculated Min | 71.44% | 11.28% | 0.42% |
| Calculated Max | 86.88% | 16.28% | 0.9% |

The expected high influence of the uncertainty related to dynamic shape factor, agglomeration shape factor and particle sticking probability confirms with results in the paper [4]. Additionally, but less importance can be dedicated to parameters: diffusion boundary layer thickness, average aerosol density and geometric median diameter. These analysis results gives answers where could be improved the state of knowledge on parameter level for selected aerosol and fission product model results.

## 6. CONCLUSIONS

The uncertainty and sensitivity analysis of aerosol behaviour in PHEBUS containment during FPT–2 test was performed using SUSA software. The parameters, which have the largest influence on the aerosol deposition processes are identified.

The uncertainty of the suspended aerosol mass in containment atmosphere depends mostly on: dynamic shape factor, agglomeration shape factor and particle sticking probability, which has influence on main agglomeration and deposition processes.

Deposition of particles on the containment bottom depends on: dynamic shape factor, agglomeration shape factor and particle sticking probability; while the deposition on the condenser surfaces depends additionally on slip factor; and the deposition on containment walls depends conversely proportional to particle diameter and directly to diffusion boundary layer, but the observed deposition rate is less than in measured results.

All results of this uncertainty and sensitivity analysis are well understood and confirms with theoretical knowledge. In future uncertainty parameters quantity will be extended and thermal hydraulic parameters will be included.

## REFERENCES

1. KONTAUTAS, A., URBONAVIČIUS, E. Solubility and density parameters influence to aerosol deposition and distribution in PHEBUS FPT-1 experiment. 5th annual conference of young scientists on energy issues CYSENI 2008. Proceedings of annual conference of young scientists on energy issues. [CD]. Kaunas: Lithuanian Energy Institute. 2008 May 29.
2. KONTAUTAS A., URBONAVIČIUS E. Preliminary analysis of aerosol deposition and distribution in PHEBUS containment under FPT-3 experiment conditions. 6th annual conference of young scientists on energy issues CYSENI 2009. Proceedings of annual conference of young scientists on energy issues. [CD]. Kaunas: Lithuanian Energy Institute. 2009 May 28–29.
3. KONTAUTAS, A., URBONAVIČIUS, E. Influence of diffusive layer and aerosol density on aerosol deposition in PHEBUS FPT-1 experiment. International conference Nuclear Energy for New Europe 2008, Portorož, Slovenia, September 8–11, 2008. Ljubljana: Nuclear Society of Slovenia, 2008. ISBN 978-961-6207-30-0, p. 410.1–410.8.
4. GREGOIRE, A.C.; MARCH, P.; PAYOT, F.; RITTER, G.; ZABIEGO, M.; BRENAECKER, A.; BIARD, B.; GREGOIRE, G.; SCHLUTIG, S. Final report FPT2. IRSN and Commission of the European Union Institute for Energy, 2008. 1968 p. Batiment N$^0$250 - P 111-BP N03.
5. KONTAUTAS, A., URBONAVIČIUS, E., RIMKEVIČIUS, S, Influence of the nodalisation and modelling parameters on the results calculation of aerosols deposition in PHEBUS experimental facility. Energetika, 2007, ISSN 0235-7208. T. 53, Nr. 4, p. 16-27.
6. ALLELEIN, H.-J., ARNDT, S., KLEIN-HEßLING, W., SCHWARZ, S., SPENGLER, C., WEBER, G., COCOSYS: Status of development and validation of the German containment code system. Nuclear Engineering and Design 238 (2008) 872–889.HOFER,
7. KLOOS, M., HOFER, E., SUSA users guide and tutorial. Version 3.5. 2008 February.
8. HOFER, E., KRZYKACZ, B., LANGHANS, J., WEBER. G. Uncertainties and sensitivities in aerosol calculations – an analysis of a FIPLOC-M application to the experient VANAM M-2. 1994 Jan

CYSENI 2011, May 26–27, Kaunas, Lithuania
ISSN 1822-7554, www.cyseni.com

# UNCERTAINTY AND SENSITIVITY ANALYSIS OF $^{129}$I RELEASE FROM THE ENGINEERED BARRIERS OF THE GEOLOGIC REPOSITORY FOR RBMK-1500 SPENT NUCLEAR FUEL DISPOSAL

**A. Narkuniene**
*Lithuanian Energy Institute*
*Breslaujos str. 3, LT-44403 Kaunas – Lithuania*
*Phone +370 37 401 886*
*Email: asta@mail.lei.lt*

ABSTRACT

After the final shutdown of Ignalina nuclear power plant approximately 22 thousands of the spent nuclear fuel (SNF) assemblies of RBMK-1500 type have been accumulated. According to Lithuanian Radioactive Waste Management Strategy approved by the Government of Republic of Lithuania it is foreseen to store the assemblies with spent nuclear fuel in the interim storage facilities for about 50 years till the decision on its final disposal option will be made. The international consensus exists that SNF is best to be disposed in geologic repositories using the concept of the multi-barrier system.

Numerical modelling is an essential component of any radioactive waste management programme. Modelling of radionuclide transport helps to analyze the possibilities of radionuclide release from the repository and its distribution, to assess its radiological consequences and the impact of various factors on radionuclide migration as well. The modelling of radionuclide transport from the near field of generic repository for RBMK-1500 SNF disposal in the crystalline rocks has been performed for canister defect scenario in previous studies. It was observed that the radionuclide $^{129}$I is one of the dominant radionuclides in the release from the engineered barriers. The results of the uncertainty and sensitivity analysis of $^{129}$I release are presented in this paper. The analysis was performed using probabilistic and deterministic methods and computer code AMBER (United Kingdom).

Keywords: RBMK-1500, spent nuclear fuel, disposal, crystalline rocks, geologic repository, engineered barriers, uncertainty, sensitivity analysis.

## 1. INTRODUCTION

The long-term management of high-level and long-lived radioactive waste remains one of the most critical issues faced by the nuclear sector. Disposal in deep geological formations is considered by the international community as an appropriate solution to manage these wastes. Most of the European countries with nuclear power launched programmes to study the feasibility of geological disposal in their country. For geological disposal of SNF and other high level radioactive waste (HLW) the concept of the multi-barrier system has been proposed. The multibarrier system consists of the engineered barriers (waste packages, buffer, backfill and other structural materials) and the natural barriers provided by the surrounding geological structures. Principal drawing of typical geological repository is shown in Fig. 1.

Before the initiation of the licensing and implementation of the repository, a number of studies have to be performed in order to evaluate and demonstrate the safety and performance of such facility. Numerical modelling is an essential component of any radioactive waste management programme. Modelling of radionuclide transport helps to analyze the possibilities of radionuclide release from the repository and its distribution, to assess its radiological consequences and the impact of various factors on radionuclide migration as well.

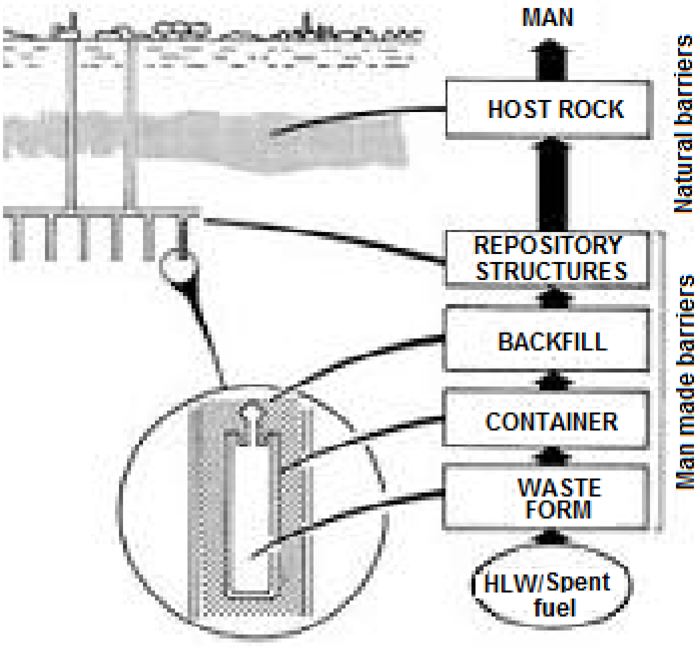

Fig. 1. Scheme of typical geological repository [1]

During 2002-2005 the assessment of possibilities for disposal of the SNF in Lithuania was performed with the support of Swedish experts. Potential geological formations for disposal of the SNF were selected, disposal concept was developed and preliminary generic safety assessment was performed. Disposal concept for RBMK-1500 SNF in crystalline rocks in Lithuania is based on Swedish KBS-3 concept with SNF emplacement into the copper canister with cast iron insert. The bentonite and its mixture with crushed rock are also foreseen as buffer and backfill material. Detailed description of the disposal concept for RBMK-1500 SNF in crystalline rocks in Lithuania is presented [2].

The modelling of radionuclide transport from the near field (engineered barriers) of proposed generic repository for RBMK-1500 SNF disposal in the crystalline rocks in Lithuania was performed for canister defect scenario in previous studies [3, 4]. It was observed that the radionuclides $^{129}$I and $^{226}$Ra (in the long-term) are the dominant radionuclides in the release from the engineered barriers. In this paper the results of the uncertainty and sensitivity analysis of $^{129}$I release are presented. The analysis was performed using probabilistic and deterministic methods. The information about the impact of various factors on the radionuclide release is important and forms the background for the recommendations for further investigations.

## 2. PROBLEM DESCRIPTION

Analysing the radionuclide release from the SNF repository within the context of the repository safety, the possibilities of radionuclide transport from untight canister have to be evaluated. Although the intact SNF disposal canisters will be disposed of in the repository, the possibility of the canister with small initial defect still remains. The canister with small initial defect in the wall could pass the quality control by non-destructive control methods and be emplaced in the repository. The small initial defect is going to increase due to various processes in the vicinity of the canister and the radionuclide transport from the canister is related to it.

The results of previous deterministic and probabilistic transport analysis for canister defect scenario [3, 4] showed that the uncertainty of the diffusivity in bentonite and instant release fraction are the most important parameters for the maximum iodine release rate from the engineered barriers. Uncertainty and sensitivity analysis were carried out with an assumption that the canister defect had been increased at certain time after the repository closure ($2 \cdot 10^5$ years). Different assumptions on the canister defect evolution and radionuclide release start are accepted within the context of repository safety assessment. Based on [5] the most reasonable time for defect enlargement and radionuclide release start is $2 \cdot 10^5$ years after the repository closure, while in the pessimistic case the radionuclide release start after 300 years and the defect enlargement after $2 \cdot 10^4$ years are expected. As indicated in [6] the enlargement of defect and radionuclide release start are not expected before $10^5$ years after the repository closure.

However, the time when the defect becomes large and does not limit the groundwater ingress into the canister is very uncertain as it strongly depends on the thermal, hydraulic, mechanical, etc. processes in the near field and the canister itself. The initial size of small defect in the canister wall is not expected to be very important as the maximum release rate is observed after the defect enlargement when the defect does not form any resistance for transport. Thus, the main aim of this work is to assess the uncertainty of release of $^{129}$I from the engineered barriers considering the uncertainty of defect enlargement time.

## 3. METHODOLOGY

For a complex problem such as the analysis of the future evolution and performance of a geological repository and its environment, it must be acknowledged that exact predictions can never be achieved and that some level of uncertainty can be tolerated provided the uncertainties do not compromise safety [7]. The simplest kind of uncertainty analysis consists of making calculations using bounding values of parameters in order to estimate maximum and minimum results. If an input parameters are described in the terms of probability distribution function (PDF) one common method of uncertainty analysis is random sampling (Monte Carlo) approach (probabilistic approach). For the sensitivity the OAT (one variable at a time) sensitivity analysis could be performed and sample based sensitivity analysis as well. The types of uncertainties, their handling are discussed in more details in [4]. For the parameter sensitivity analysis within the context of geological disposal the standardized linear regression, correlation analysis is used widely [8-15]. The standardized regression coefficients (SRC), correlation coefficients (Pearson, partial correlation coefficients), Spearman rank correlation coefficients (SRCC) could serve as sensitivity measures [15]. Stepwise regression method is used as well.

General steps of the methodology used in this work were:

1) model development;
2) definition of the input parameters (probability distribution function, nominal values);
3) generation of the parameter values sets ($R_i$) for a number of simulations (N);
4) model simulation with parameter set $R_i$ till i =N;
5) analysis of the model output results (uncertainty and sensitivity analysis).

**Radionuclide release model.** The radionuclide transport analysis was performed for the RBMK-1500 SNF with initial enrichment of 2.8 % $^{235}$U and 0.6 % $Er_2O_3$. The SNF burnup is app. 29 MWd/kgU, the radionuclide inventory was assessed by computer code SAS2H (computer code system SCALE 5) [16]. The conceptual model of radionuclide transport through the engineered barriers is presented in Fig. 2.

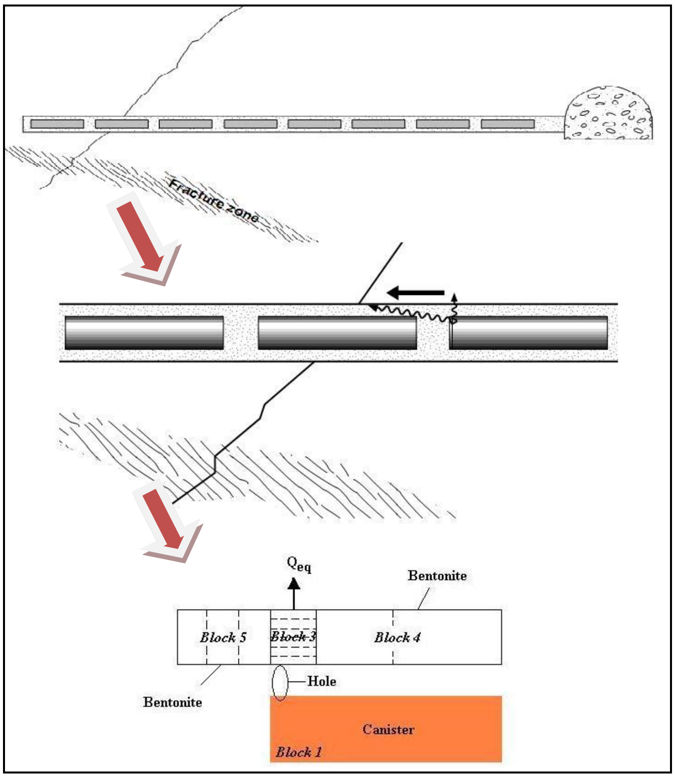

Fig. 2. Conceptual representation of the radionuclide transport in the near field region

As the contaminants diffuse out of the engineered barriers, they could be dispersed in the surrounding geological barriers and transported towards the biosphere. The main assumptions considered during the assessment of $^{129}$I migration in the near field region are as follows:

- when the defect becomes large the entire void space within the canister is filled by water (app. 0.5 m$^3$);
- the structural parts of the SNF assemblies (such as fuel rods, spacer grids, etc.) are not a barrier for the radionuclide release from them, i. e. the release of radionuclides from these parts starts as soon as the canister is filled with water;
- the release of $^{129}$I from the SNF occurs by couple mechanisms: instant release of a part of inventory and congruent release from degrading SNF matrix;
- sorption on the inner parts of disposal canister, the structural parts of SNF assemblies and the concentration gradient within the canister are disregarded due to large uncertainty;
- bentonite barrier is fully water saturated by the time of the radionuclides release start;
- dissolved radionuclides are transported from the canister mainly by diffusion;
- radionuclides transported through the outer boundary of the bentonite barrier diffuse into the flowing water in the fracture intersecting the deposition hole.

Radionuclide transport analysis was performed using the computational model comprising the near field (engineered barriers) of the repository for RBMK-1500 SNF disposal in the crystalline rocks in Lithuania, which is realized in the computer code AMBER [17]. Model developed previously [3, 4] has been updated to take into account the probabilistic nature of the defect enlargement time and associated defect size change.

The following processes were modelled during the iodine release assessment: instant release of a part of $^{129}$I inventory, congruent release of $^{129}$I from degrading SNF matrix, diffusive transport through the engineered barriers and out of the near field region. For the generation of parameter values Monte Carlo method was employed. Taking into consideration the computation time a large sample size has been selected. For a large (1000 and more) sample size a reliable estimation of the statistical characteristics of the modelling results could be made [18]. In total 1000 simulations were performed.

**Input parameters.** As indicated in [19], during the first 1000 years after the repository closure the radionuclide release through the small initial canister defect is not expected. Due to the number of various processes (thermal, mechanical, hydraulic, chemical, etc.) occurring in the environment of the repository, the canister defect could become large at any time between $10^3$-$10^5$ years after the repository closure. However, based on [19] it is the most probable that the enlargement would occur 10 000 years after the repository closure. The time for defect enlargement could be defined by triangular probability distribution function (PDF) within the limits of $10^3$-$10^5$ years and $10^4$ years as a mode [19]. Performing the uncertainty analysis using the probabilistic approach besides the canister defect enlargement time variation ($T_{large}$), the other parameters (SNF dissolution rate, instant release fraction, effective diffusivity, equivalent flow rate) were varied also. These parameters and their PDF data are summarized in Table 1. If no information about the parameter PDF was available, the discrete PDF was assumed based on the recommendations presented in [5, 7]. If SNF or site specific data was not available yet the parameter values were based on the scientific literature. As the data on the parameters and their distribution functions become available in the future (for SNF disposal systems in foreign countries or Lithuania as well) the probabilistic assessment of the radionuclide release is to be extended.

Table 1. Summary of input data for $^{129}$I release modelling

| Parameter | PDF data | | | PDF type |
|---|---|---|---|---|
| | Nominal value (reference, most probable value) | Lower limit | Upper limit | |
| Radionuclide release start (years) | $10^3$ | - | - | - |
| Defect size enlargement time $T_{plarge}$ (years) [19] | $10^4$ | $10^3$ | $10^5$ | Triangular |
| Defect size ($m^2$) [19] | - | $1 \cdot 10^{-5}$ ($t<T_{large}$) | $3 \cdot 10^{-1}$ ($t \geq T_{large}$) | - |
| SNF dissolution rate SNF DR (1/year) [20] | $10^{-7}$ | $10^{-8}$ | $10^{-6}$ | Triangular |
| Instant release fraction IRF (%) [20] | 2 | 0 | 5 | Triangular |
| Effective diffusivity in bentonite $D_e$ ($m^2/s$) [21] | $1 \cdot 10^{-11}$ | $3 \cdot 10^{-12}$ (P=0.15)<br>$1 \cdot 10^{-11}$ (P=0.7)<br>$3 \cdot 10^{-11}$ (P=0.15) | | Discrete |
| Equivalent groundwater flow rate $Q_{eq}$ ($m^3$/year) [22] | $9 \cdot 10^{-4}$ | $9 \cdot 10^{-4}$ (P=0.9)<br>4 (P=0.1) | | Discrete |

**Uncertainty and sensitivity analysis.** Analyzing the results of probabilistic assessment of radionuclide release the comparison to the results obtained with nominal parameter values has been made also. The results about the impact of various factors on the radionuclide release strongly depends on the repository construction, the properties of engineered and natural barriers, prevailing conditions and associated transport parameter values, the repository evolution scenarios, etc..

Besides the probabilistic parameter sensitivity by the means of regression and correlation analysis (SRC, SRRC, SRCC), the deterministic assessment has been performed too. According to [23], varying the parameters' values in a deterministic way, the impact on the results could be assessed by the relative change of the maximum release rate:

$$Ratio = Q_{\max}\left(p_i\right) / Q_{\max}\left(p_{nom}\right), \tag{1}$$

$$p_i = p_{nom} \cdot VF(p_i), \tag{2}$$

here $Q_{max}(p_i)$ – radionuclide maximum release rate when parameter $i$ obtain value $p$; $Q_{max}(p_{nom})$ – radionuclide maximum release rate when parameter $i$ has nominal value; $VF$ – variability factor of parameter $i$.

Based on [24], parameter sensitivity index (SI) could also be assessed by the following expression for the analysis of the impact of particular parameter variation:

$$SI = \left(1 - \frac{Q_{\max}(p_{nom})}{Q_{\max}(p_i)}\right) \Big/ P_I\ , \tag{3}$$

here $P_I$ is defined as $[1-(p_i/p_{nom})]$, if parameter‘s $i$ value $p$ is lower than the nominal value, and as $[1-(p_{nom}/p_i)]$, if parameter‘s value is larger than the nominal one; $p_i$ – parameter’s $i$ value $p$, obtained by multiplication or division the nominal value by its variability factor.

## 4. RESULTS AND DISCUSSION

As the model output to be analyzed the release rate of iodine has been selected. Maximum release rate would correspond to the largest activity (and peak dose subsequently) of this radionuclide flux during the analyzed time period.

Deterministic assessment (using nominal parameter values) of $^{129}$I release from the generic repository for RBMK-1500 SNF disposal has shown that maximum release rate and the largest activity of radionuclide flux is expected after the defect enlargement (at 10000 years) and is observed approximately 11400 years after the repository closure.

### 4.1. Uncertainty analysis

Large number of simulations performed allows assessing the distribution of the maximum release rate due to various combinations of the parameter values. The observed distribution in the form of CDF[1] was compared to the maximum release rate observed with a nominal parameter values (deterministic assessment) (Fig. 3).

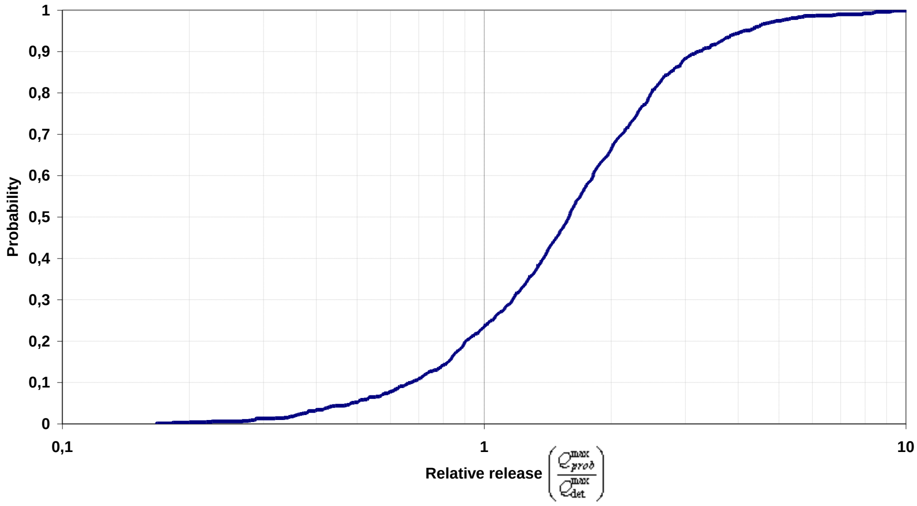

Fig. 3. Relative maximum release rate of $^{129I}$ from the engineered barriers

The uncertainty analysis shows that the maximum release rate of $^{129}$I will be higher up to four times than that observed with nominal parameters’ values with a probability of 95 %. In other words it means that with a probability of 95 %, the maximum release observed by

---

[1] CDF – cumulative distribution function

deterministic analysis and using the nominal parameter values would increase up to 4 times due to variation of transport parameters and defect enlargement time in the defined ranges.

Based on the probabilistic assessment of the radionuclide release the mean release of $^{129}$I ($Q(t)$) has also been determined (Fig 4, normalized to maximum release rate from the deterministic analysis).

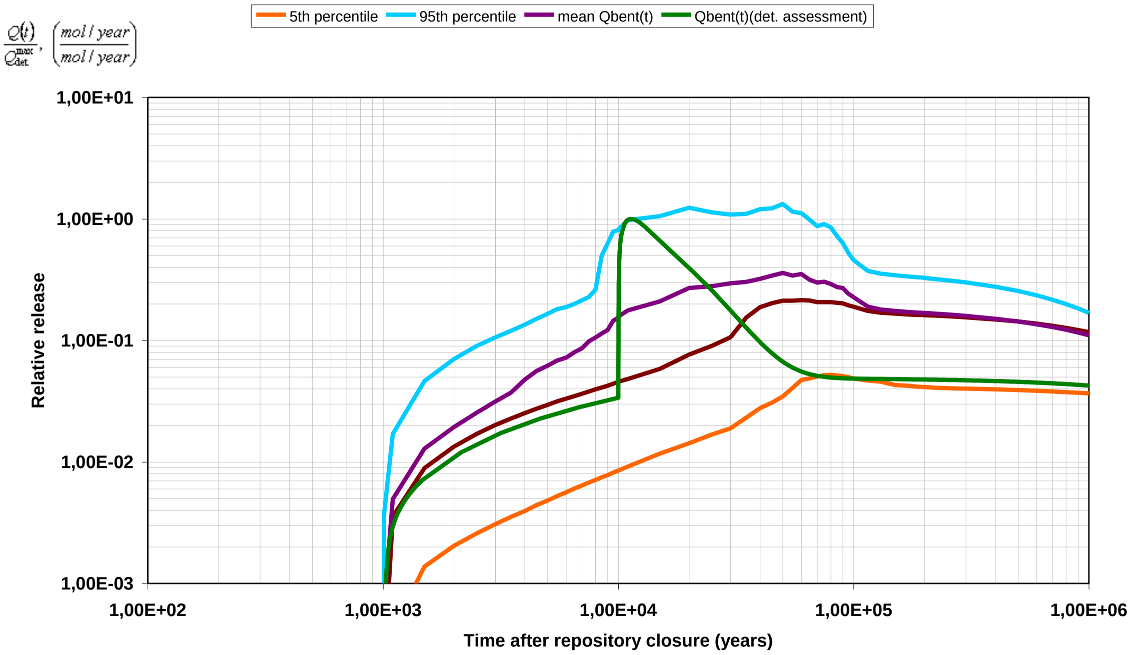

Fig. 4. Mean release of $^{129}$I from the engineered barriers over the analyzed time period

The 5th, 50th and 95th percentile of the modelling results are presented also. Large differences between these dependences during the time period of $10^3$–$10^5$ years after the repository closure were observed. This supposes to be determined by the variations of the beginning of more intensive radionuclide release which is related to the uncertainty of the defect enlargement time. This also explains why the mean release curve is different than that obtained with the nominal parameter values set (deterministic assessment, see Fig 4). It was observed that the maximum of mean release of $^{129}$I is lower than the maximum release rate from the deterministic analysis approximately by a factor of 2.7. The largest mean release rate is expected later, app. after 48700 years after the repository closure.

Summarizing the results it could be concluded that the uncertainty of defect enlargement time and other parameters has a significant impact on the mean release of $^{129}$I from engineered barriers. The largest value of the mean release is expected to be lower than observed using the nominal parameter values (~2.7 times lower) and it would be achieved after the longer time period following the repository closure.

## 4.2. Sensitivity analysis

In order to assess the impact of the defect enlargement time on the maximum release rate of $^{129}$I, the sensitivity analysis has been carried out. The coefficient of determination $R^2$ for the regression analysis on raw data was 0.77, supposing the nonlinear dependency of the maximum release and transport parameters. Using the rank transformed data for the regression analysis, $R^2$ was observed to be 0.89. This also indicates the nonlinearity of the model output being analyzed. The calculated coefficients (standardized regression coefficients, Spearman rank correlation coefficients and standardized rank regression coefficients) for the parameters being analyzed are presented in Fig. 5. The coefficient values were used for the qualitative rather than for the quantitative analysis for the indication of the most important parameters.

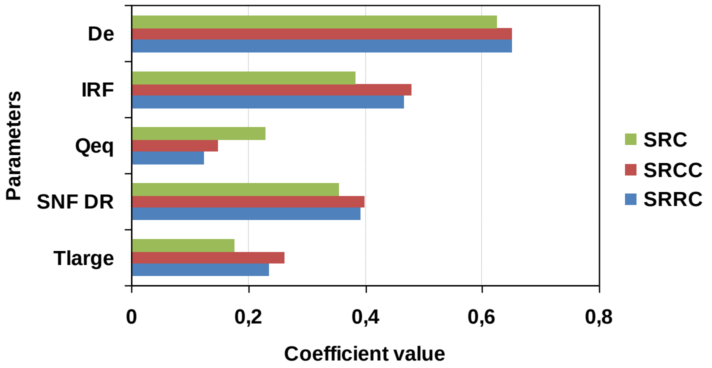

Fig. 5. The results of probabilistic parameter sensitivity analysis for $^{129}$I

The regression and correlation analysis on the transformed data show a good agreement and indicates the same importance of parameter. The coefficient SRC from regression analysis on raw data which is shown for the comparison purposes presents slightly different importance for couple parameter and this should be addressed to the model nonlinearity. It is highly valuable to perform sensitivity analysis using different methods/approaches and to compare the results for more reliable conclusions.

As it is shown in the Fig. 5, the effective diffusivity in the bentonite ($D_e$) and the instant release fraction (IRF) could be indicated as the most important parameters for the maximum release of $^{129}$I from the near field. The variations in SNF dissolution rate (SNF DR), defect enlargement time ($T_{large}$) or equivalent flow rate ($Q_{eq}$) are less relevant for the uncertainty of iodine maximum release. The outcomes of sensitivity analysis using the deterministic approaches are summarized in Fig. 6 and Table 2.

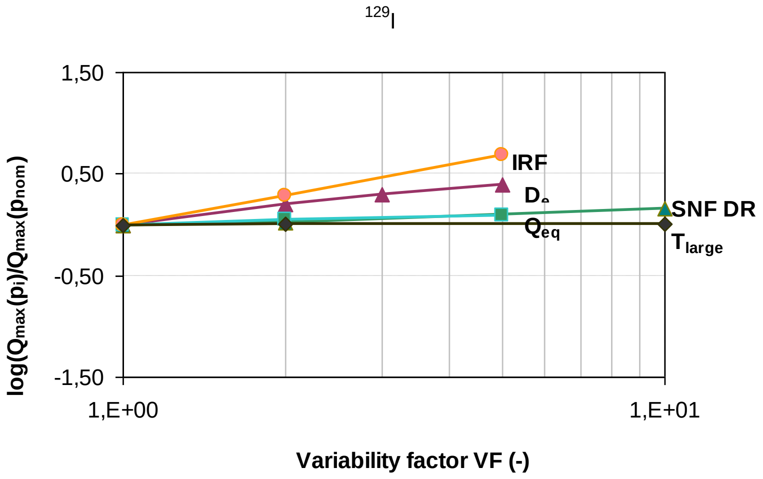

Fig. 6. The results of deterministic parameter sensitivity analysis for $^{129}$I

Table 2. The SI of the main parameter related to the $^{129}$I release from the near field

| Parameter | Largest variability factor | Change of parameter value in comparison to the nominal value | Sensitivity index SI |
|---|---|---|---|
| Effective diffusion coefficient in bentonite $D_e$ | 5 | Increased | 0.7 |
| | | Decreased | -3.7 |
| SNF dissolution rate SNF DR | 10 | Increased | 0.3 |
| | | Decreased | -0.1 |
| Equivalent groundwater flow rate $Q_{eq}$ | 5 | Increased | 0.2 |
| | | Decreased | -1.1 |
| Instant release fraction IRF | 5 | Increased | 1.0 |
| | | Decreased | -4.0 |
| Defect size enlargement time $T_{large}$ | 10 | Increased | 0.0 |
| | | Decreased | 0.0 |

According to the results presented in **Table 2**, the SI for the increased and decreased parameters' values are not the same and this indicate the nonlinear dependency on the parameters and the model output (maximum release rate) [24]. The positive or negative value of SI means the impact of changed (increased or decreased) parameter's value on the results. In case of positive SI, iodine maximum release rate is increased and vice versa. Based on the SI values it is clear that the maximum release of $^{129}$I strongly depends on the variation of IRF (SI = -4) and effective diffusivity. Those results are in agreement with the graphical results (Fig. 6), obtained using the methodology presented in [16]. According to the deterministic analysis, the uncertainties of SNF dissolution rate, $Q_{eq}$ and $T_{large}$ are less important for the maximum release of iodine isotope under consideration. Thus they could be fixed to their nominal values with no real loss of information on the system.

The comparison of the sensitivity analysis using the probabilistic and deterministic approaches showed that the most relevant parameters identified are the same – IRF and $D_e$. However, the conclusions about less important parameters (and $T_{large}$ as well) are slightly different. During the variation of $T_{large}$ in a deterministic way and setting its values equal to the lower and upper limits of $T_{large}$ PDF ($10^3$ and $10^5$ years), the observed maximum release of $^{129}$I was almost the same as for the base case (with nominal values). Thus subsequently the SI and the ratio of maximum release rates were equal to zero. This means that during the probabilistic simulations maximum release rate is not determined by the changes of $T_{large}$, but depends on the set of values of remaining parameters. Summarizing the results, the defect size enlargement time should be indicated as parameter, which does not have a significant impact on the maximum release rate of $^{129}$I from the near field. However it is important for the time when the maximum release is expected, as there is a strong correlation (Pearson correlation coefficient is 0.97) between these times.

## 5. CONCLUSIONS

During the analysis of $^{129}$I transport through the engineered barrier of the generic repository for RBMK-1500 SNF disposal in the crystalline rocks it was observed that:

- with a probability of 95% the maximum release observed by deterministic analysis and using the nominal parameter values would increase up to 4 times due to variation of transport parameters and defect enlargement time in the defined ranges;
- the uncertainty of defect enlargement time has no significant impact on the maximum release rate of $^{129}$I from the engineered barriers;

- due to the uncertainty of defect enlargement time and other transport parameters, the peak of $^{129}$I mean release is expected to be lower app. by a factor of 2.7 than that determined with nominal parameter values.

## REFERENCES

1. European Commission, Research and innovation. [referred 2011-03-04]. Link to the internet <http://ec.europa.eu/research/energy/euratom/fission/microscope /disposal/ index_en.htm>
2. BRAZAUSKAITĖ, A., POŠKAS, P. Radionuklidų sklaida iš kristalinėse uolienose įrengto geologinio kapinyno RBMK-1500 panaudotam branduoliniam kurui laidoti. 1. Kapinyno koncepcija. *Energetika*. ISSN 0235-7208. 2005. Nr. 3, p. 70–78.
3. BRAZAUSKAITĖ, A., POŠKAS, P. Radionuklidų sklaida iš kristalinėse uolienose įrengto geologinio kapinyno RBMK-1500 panaudotam branduoliniam kurui laidoti 3. Radionuklidų sklaida artimojo lauko aplinkoje. *Energetika*. ISSN 0235-7208. 2007. Nr. 1, p. 15–22.
4. BRAZAUSKAITĖ, A. Uncertainty analysis of the modeling of radionuclide releases from the near field of reference repository for RBMK-1500 spent nuclear fuel disposal in crystalline rocks. 5th conference of young scientists on energy issues CYSENI 2008, Kaunas, Lithuania, 29 May, 2008. [CD]. Kaunas: LEI, 2008. ISSN 1822-7554, p. 1–10.
5. *SR 97. Radionuclide transport calculations*: SKB Technical Report TR-99-23. Stockholm: SKB, 1999, 83 p.
6. VIENO, T., NORDMAN, H. *Safety assessment of spent fuel disposal in Hästholmen, Kivetty, Olkiluoto and Romuvaara, TILA-99*. POSIVA Report 99-07. Helsinki: Posiva Oy, 1999.
7. *Project Opalinus Clay: Safety report. Demonstration of disposal feasibility for spent fuel, vitrified high-level waste and long-lived intermediate-level waste (Entsorgungsnachweis)*: Nagra Technical Report NTB 02-05. Wettingen: NAGRA, 2002, 360 p.
8. ALBRECHT, A.; MIQUEL, S. Extension of sensitivity and uncertainty analysis for long term dose assessment of high level nuclear waste disposal sites to uncertainties in the human behaviour. *Journal of Environmental Radioactivity*, 2010, Vol. 101, Issue 1, p. 55–67.
9. AGUERO, A. Performance assessment model development and parameter acquisition for analysis of the transport of natural radionuclides in a Mediterranean watershed. *Science of the Total Environment*, 2005, Vol. 348, Issues 1–3, p. 32–50.
10. AGUERO, A.; et al. Application of the Spanish methodological approach for biosphere assessment to a generic high-level waste disposal site. *Science of the Total Environment*, 2008, Vol. 403, Issues 1–3, p. 34-58.
11. AGUERO, A.; et al. Spanish methodological approach for biosphere assessment of radioactive waste disposal. *Science of the Total Environment*, 2007, vol. 384, Issues 1–3, p. 36–47.
12. ARNOLD, B. W.; KUZIO, S. P.; ROBINSON, B. A. Radionuclide transport simulation and uncertainty analyses with the saturated-zone site-scale model at Yucca Mountain, Nevada. *Journal of Contaminant Hydrology*, 2003, Vol. 62–63, p. 401–419.
13. HEDIN, A. Probabilistic dose calculations and sensitivity analyses using analytic models. *Reliability Engineering & System Safety*, 2003, Vol. 79, Issue 2, p. 195–204.
14. MANACHE, G.; MELCHING, C. S. Identification of reliable regression- and correlation-based sensitivity measures for importance ranking of water-quality model parameters. *Environmental Modelling & Software*, 2008, Vol. 23, Issue 5, p. 549–562.

15. HELTON, J. C.; DAVIS, F. J.; JOHNSON, J. D. A comparison of uncertainty and sensitivity analysis results obtained with random and Latin hypercube sampling. *Reliability Engineering & System Safety*, 2005, Vol. 89, Issue 3, p. 305–330.
16. NARKŪNAS, E. Radionuclides inventory modeling in RBMK-1500 spent fuel assembly. Proc. of Symposium during XVIII International Youth Nuclear festival Dysnai, July 2–9, 2005 Lithuania.
17. *AMBER 4.4. Getting started. Version 1.0/ Users manual*. UK: Enviros Quanitsci, 2002, 94 p.
18. KOPUSTINSKAS, V.; ALZBUTAS, R.; AUGUTIS, J. Matematinių modelių parametrų jautrumo ir rezultatų neapibrėžtumo statistiniai tyrimo metodai. *Energetika*, 2007. T. 53. Nr. 3, p. 10–15.
19. L*ong-term safety for KBS-3 repositories at Forsmark and Laxemar – a first evaluation. Main Report of the SR-Can project:* SKB Technical Report TR-06-09. Stockholm: SKB, 2006, 613 p.
20. *Spent fuel performance under repository conditions: A model for use in SR-Can:* SKB Technical Report TR-04-19. Stockholm: SKB, 2004, 34 p.
21. *Data and uncertainty assessment. Migration parameters for the bentonite buffer in the KBS-3 concept*: SKB Technical Report TR-04-18. Stockholm: SKB, 2004, 159 p.
22. NORDMAN, H.; VIENO, T. *Equivalent flow rates from canister interior into the geosphere in a KBS-3H type repository*: Posiva working report 2004-06. Helsinki: Posiva Oy, 2004. 14 p
23. ROMERO, L.; et al. Sensitivity of the radionuclide release from a repository to the variability of materials and other properties. *Nuclear Technology*, 1996, Vol. 113, p. 316–326.
24. NAIR, R. N., KRISHNAMOORTHY, T. M. Probabilistic safety assessment model for near surface radioactive waste disposal facilities. *Environmental Modelling and Software*, 1999, Vol. 14, Issue 5, p. 447–460.

CYSENI 2011, May 26-27, Kaunas, Lithuania
ISSN 1822-7554, www.cyseni.com

# NUMERICAL ANALYSIS OF EXPERIMENTS PERFORMED IN THE FRAME OF SARNET2 PROJECT HYDROGEN DEFLAGRATION BENCHMARK

**M. Povilaitis**
*Lithuanian Energy Institute*
*Breslaujos str. 3, LT-44403 Kaunas – Lithuania*
*Phone +370 37 401 920*
*Email: mantas@povilaitis.eu*

ABSTRACT

During a hypothetical severe accident involving degradation of the core of a light water reactor the hydrogen could be generated and released into the containment atmosphere posing a deflagration or even an explosion hazard. In case of deflagration, the integrity of the containment would be threatened by the increase of the containment atmosphere pressure and temperature. If turbulent flames developed it would cause high pressure pulses, shock waves, etc. For simulation of such processes a reliable numerical codes are needed. Hydrogen combustion processes have been largely studied in case of a homogeneous hydrogen distribution in the containment atmosphere, however there are still unresolved issue of flame acceleration due to turbulence generated by the obstacles in the flame path. Moreover, in the EURSAFE program, the flame acceleration and quenching have been identified as unresolved hydrogen combustion issues. These problems are even more pronounced in the case of lumped-parameter modelling approach, since lumped-parameter codes generally lack information on turbulence inside modelled volumes and scales of these volumes are large compared to the flame scale. These topics were addressed in the ongoing FP-7 project SARNET2 (Severe Accident Research NETwork 2) hydrogen deflagration benchmark. This article presents numerical analysis performed for this benchmark using integral lumped parameter code ASTEC of the hydrogen and air mixture deflagration experiments. Brief experiment description, used nodalisation schemes of the test facility ENACCEF and obtained numerical results are presented.

Keywords: ASTEC, modelling, hydrogen deflagration, lumped-parameter.

## 1. INTRODUCTION

During a hypothetical severe accident involving degradation of the core of a light water reactor the large amount of hydrogen is expected to be generated and released into the containment atmosphere. Hydrogen – air mixtures are highly flammable and may be even detonable, therefore hydrogen presence in the containment atmosphere is a risk to its integrity, which can be damaged by pressure and temperature increases caused by deflagration or shock waves caused by turbulent flames.

Reliable numerical codes are needed for simulation of hydrogen combustion processes. Hydrogen combustion have been largely studied in case of a homogeneous hydrogen distribution in the containment atmosphere, however there are still unresolved issue of flame acceleration due to turbulence generated by the obstacles in the flame path. Moreover, in the EURSAFE program, the flame acceleration and quenching have been identified as unresolved hydrogen combustion issues. These problems are even more pronounced in the case of lumped-parameter modelling approach, since lumped-parameter codes generally lack information on turbulence inside modelled volumes and scales of these volumes are large compared to the flame scale. These topics were addressed in the ongoing project SARNET2 (Severe Accident Research NETwork 2) hydrogen deflagration benchmark. This article presents numerical analysis performed for this benchmark using integral lumped parameter code ASTEC of the hydrogen and air mixture deflagration experiments. Brief experiment description, used nodalisation schemes of the test facility ENACCEF and obtained numerical results are presented.

## 2. EXPERIMENTS

### 2.1. ENACCEF facility

Simulated experiments were performed in the ENACCEF facility (Orleans, France) by the French National Centre for Scientific Research (CNRS) in the frame of collaboration with the Radio-protection and Nuclear Safety Institute (IRSN).

ENACCEF facility is a vertical stainless steel structure (Fig. 1). It is composed of two parts with different geometry, resulting in different conditions for flame propagation. The lower part of the facility is a long narrow tube called "the acceleration tube". The height of this part is 3.2 m, inner diameter is equal to 154 mm. The total volume of the acceleration tube is 62.1 l. Various repeated obstacles can be inserted into this tube. The tube is open at the upper end, where it connects with the upper part of the facility. The lower end of the acceleration tube ends with a bottom cap. Electrodes used for the flammable mixture ignition are situated at the bottom of the tube.

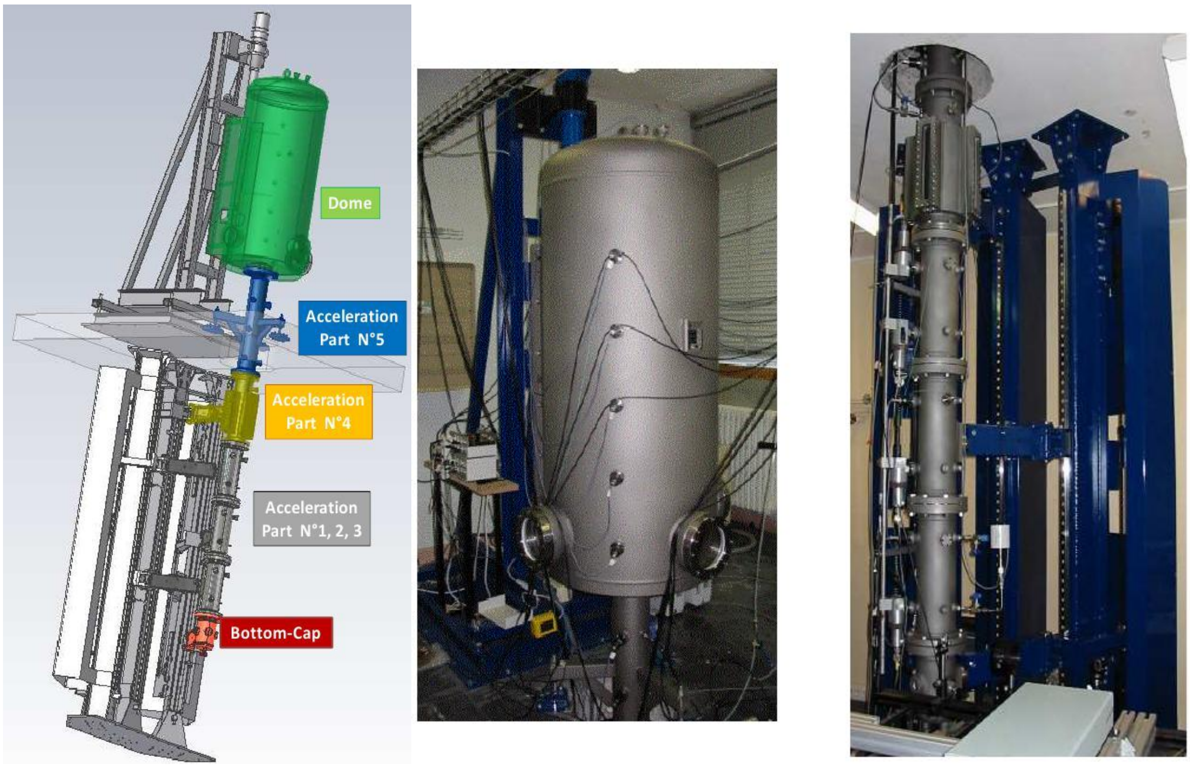

Fig. 1. Scheme and view of ENACCEF facility [1, 2]

The upper part of the facility has a shape of a closed cylinder. It has an opening to the acceleration pipe at the centre of its bottom. This upper part of the facility is called "the dome". The height of the dome is 1.7 m, inner diameter is 738 mm. The total volume of the dome is 658 l.

To generate turbulence and instabilities for the flame, two types of the obstacles can be inserted into the acceleration tube – annular obstacles of various blockage ratios (BR) and hexagonal mesh grids.

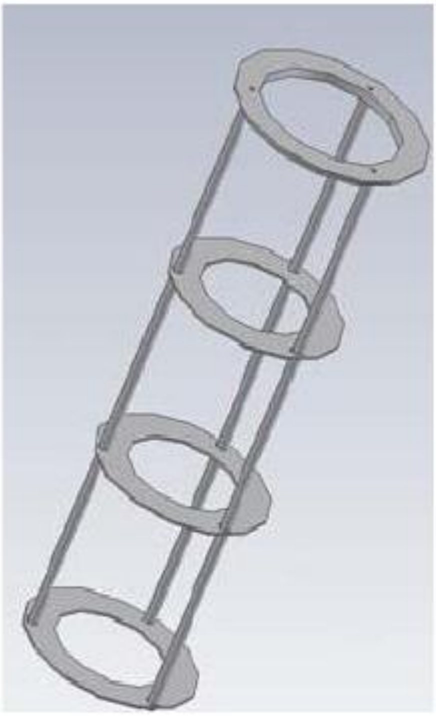

Fig. 2. Example of annular obstacles used in the simulated experiments [1, 2]

Blockage ratio of an obstacle is defined as a ratio of obstructed cross-section area and total cross-section area of the pipe:

$$BR = 1 - \left( \frac{d}{D} \right)^2 ,$$

where d is the inner diameter of the obstacle and D is the diameter of the pipe. The thickness of the obstacle is about 2 mm.

One type of obstacles – annular – was used in the simulated experiments. Nine obstacles were inserted into the acceleration tube. They were arranged at equal distances of 0.154 m. The lowest of the obstacles was inserted at the height of 0.638 m.

Flame positions during deflagration were derived from the photomultiplier records of flame luminosity. There are 16 UV-sensitive photomultiplier tubes mounted across silica windows in order to detect the flame as it propagates in the ENACCEF facility (5 photomultiplier tubes are located along the dome and 11 along the acceleration tube). The flame position is known with an uncertainty of 8 mm [2].

Several high speed pressure transducers record pressure variations in the tube and pressure build-up in the dome as the flame propagates in the facility.

The composition of gas is obtained by the gas chromatography of the samples taken with glass bulb from the facility.

Ignition system of the facility consists of two thin tungsten electrodes of 2 mm diameter situated at the bottom of the facility. Delivered energy is estimated to be about 10 to 20 mJ.

More detailed description of the facility, including its systems and instrumentation, is given by Chaumeix and Bentaib [1, 2].

### 2.2. Description of the experiments

Three experiments performed in the ENACCEF facility were presented for simulations in the SARNET2 H2 benchmark. Initial conditions were the same for all three experiments. The purpose of the benchmark was to evaluate codes' abilities to model flame acceleration due to obstacles; therefore the parameter which was varied between experiments was blockage ratio of the used obstacles. The first experiment was performed without any obstacles in the acceleration tube (BR = 0), the second used obstacles with BR = 0.33 and the third with BR = 0.63.

All three experiments were started at ambient temperature and normal pressure (23 °C and 100000 Pa). Premixed homogeneous flammable hydrogen – dry air mixture was used to fill vacuumed down (to 1 Pa) facility. Hydrogen concentration in the mixture was 13 %vol.

In all three experiments flame propagated upwards from the ignition point at the bottom of the facility. After encountering obstacles flame accelerates in the tube, and decelerates when reaching the dome.

In all three experiments practically full combustion of hydrogen was reached – remaining hydrogen concentration was lower than 0.3 %vol.

## 3. SIMULATIONS

### 3.1. Hydrogen deflagration modelling in ASTEC code

Simulations were performed using integral severe accident analysis code ASTEC (Accident Source Term Evaluation Code) V2.0 [3]. ASTEC code is developed by the IRSN (France) and GRS (Germany) with the aim of creating an analysis tool capable to simulate an entire severe accident sequence from the initiating event through to release of radioactive elements out of the containment. This diversity of simulated processes is achieved by modular structure of the code.

Described simulations were performed using two ASTEC modules: containment thermal-hydraulic module CPA and additional newly-developed CPA-FRONT module for hydrogen combustion simulation.

CPA module is a lumped-parameter code, therefore ENACCEF facility had to be described using nodalisation scheme, in which it is divided into homogeneous zero-dimensional “zones” (also called “nodes” or “control volumes”) connected by one-dimensional “junctions” for gas flows and flame propagation.

In the CPA-FRONT module propagation of the flame front is described by the laminar burning velocity $S_L$, calculated using Liu – MacFarlane correlation [4] and the turbulence velocity (flamelet model by Peters [5]). Since CPA is a lumped-parameter code, there is turbulence information missing, therefore in the FRONT model this information is estimated from the Reynolds number *Re*:

$$u' = C u_{gas} Re^n$$

where $u'$ is turbulence intensity, $u_{gas}$ is gas velocity, $C$ and $n$ are parameters fitted to provide the best results in all experiments available to code developers.

Turbulent burning velocity then is calculated according to Peters model:

$$S_T = S_L(1+\sigma)$$
$$0 = \sigma^2 + 0.39\frac{l}{l_f}\sigma - 0.78\frac{u'l}{S_L l_f},$$

where $l$ is integral time scale, $l_f$ – flame thickness.

The total flame front velocity $U_F$ is the sum of the gas velocity in the junction and turbulent burning velocity:

$$U_F = S_T + u_{gas}$$

### 3.2. Nodalisation scheme

In order to simulate performed experiments using lumped-parameter CPA module of ASTEC, nodalisation scheme of the ENACCEF facility was developed. The view of this scheme is presented in Fig. 3.

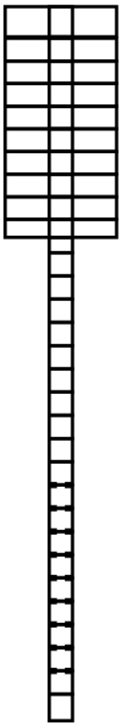

Fig. 3. Nodalisation scheme of the ENACCEF used in the calculations

Developed scheme consists of 31 vertical layers with 41 zones in them. Acceleration tube is divided into layers with one zone in each of them. There are 21 zones in the acceleration tube. Layers in the dome have two zones each – one (inner) in the radial central part of the layer and another one (outer), ring-shaped, around central one. There are 10 layers and 20 zones in the dome. Acceleration tube zones and inner dome zones have the shape of vertical cylinder. Its diameter is equal to the inner diameter of acceleration tube. The height of the zones in the acceleration tube is chosen to be equal to the distance between inserted obstacles – 0.154 m. The height of the zones in the dome is the same, only rounded to 0.15 m. The mass transfers and flame propagation in model is simulated by using one-dimensional connections between zones, called atmospheric junctions. The area of these junctions is set equal to the geometric cross-section area of the connected zones in vertical connection case and to the geometrical side area of inner zone in the horizontal connection case. Obstacles are also simulated using these junctions – since obstacles in the model are located at the zone borders, reducing of the junction area according to the used obstacle blockage ratio effectively simulates the obstacle.

Heat losses to the environment are simulated using “structures” in the model. These structures correspond to the facility walls. Model takes into account their composition and thickness. Environment is simulated as an additional zone with large volume at ambient conditions.

## 4. RESULTS

Fig. 4 presents comparison of experimental and numerical average flame speeds along the height of the facility in the case of smooth acceleration tube (*BR* = 0). Experimental results show that in this case flame speed varies stochastically between 5 m/s and 45 m/s. Such behaviour was not obtained from the calculations. Flame speed values obtained from calculations are between 5 m/s and 10 m/s for the most part of the facility height. Exception to this occurs only just after the ignition – flame accelerates to ~25 m/s. Conclusion can be drawn that laminar flame speed was underestimated in the calculations. This underestimation may be the consequence of inadequate nodalisation scheme of the facility or the used laminar flame speed model, however to establish the cause further studies are needed.

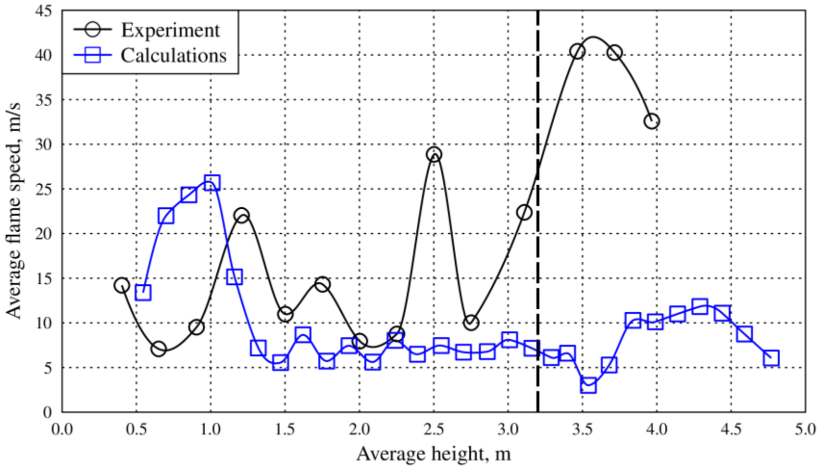

Fig. 4. Comparison of simulated and experimental average flame speeds with *BR*=0 (vertical bold dashed line marks the end of the acceleration tube)

Fig. 5 presents comparison of experimental and numerical average flame speeds along the height of the ENACCEF facility in the case of obstacles with blockage ratio *BR* = 0.33. Experimental results show that, as expected, obstacles in the flame path create turbulence and accelerate flame. Compared to smooth tube case, maximum flame speed increased more than 10 times. However numerical results predict significantly slower flame. Additional reason for this compared to the smooth tube case numerical speed deficit could be inadequate turbulence modelling in the CPA or turbulent flame speed modelling in CPA-FRONT.

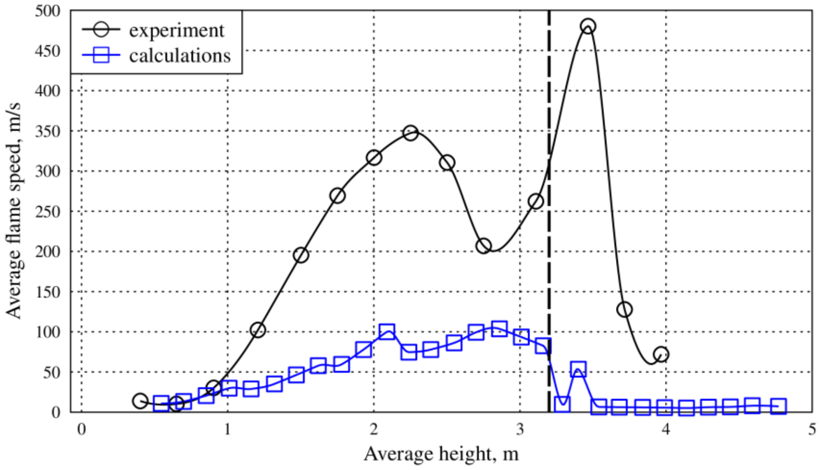

Fig. 5. Comparison of simulated and experimental average flame speeds with *BR*=0.33 (vertical bold dashed line marks the end of the acceleration tube)

Fig. 6 shows comparison of experimental and numerical average flame speeds along the height of the ENACCEF facility in the case of obstacles with blockage ratio BR = 0.63. Experiment results show even bigger flame acceleration than in the previous case, which is expected and should be caused by more intense turbulence which, in turn, is caused by larger blockage ratio of used obstacles. However, in this case code qualitatively predicted flame acceleration. With increased turbulence, code prediction accuracy improved and this leads to conclusion that the source of inaccuracies should be in the nodalisation scheme or laminar flame speed velocity related code part, not in the turbulence related part.

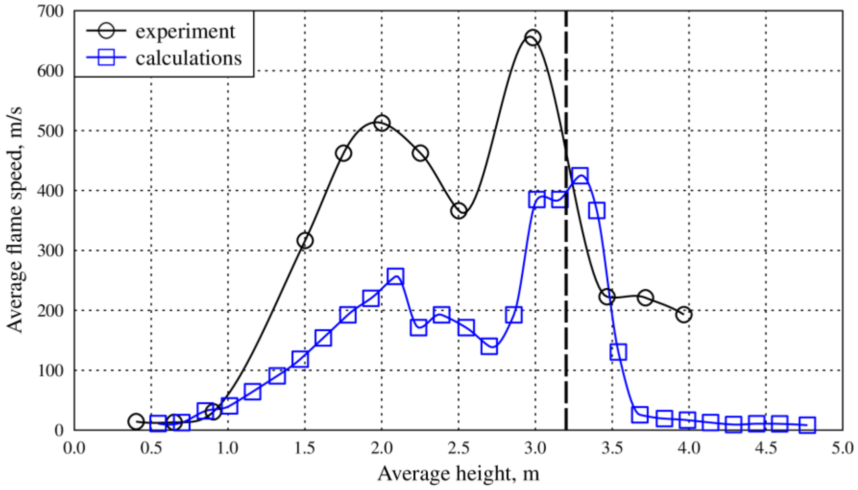

Fig. 6. Comparison of simulated and experimental average flame speeds with BR=0.63 (vertical bold dashed line marks the end of the acceleration tube)

Fig. 7 shows comparison of experimental and numerical pressure evolutions in the ENACCEF facility in the case of obstacles with blockage ratio *BR* = 0. Experimental results show rapid pressure increase caused by hydrogen deflagration, followed by slower depressurization, caused by heat losses to the environment. Code predicts pressurization behaviour quite well, qualitatively agreeing with experimental results, quantitative differences being lower pressure peak predicted (by less than 0,5 bar) and slower pressure increase, which could be caused by low rate of deflagration obtained from the calculations.

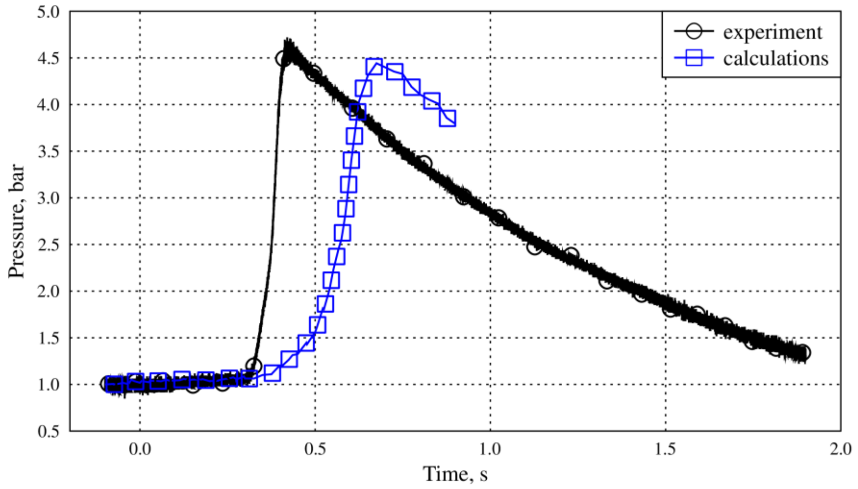

Fig. 7. Comparison of simulated and experimental pressure evolutions with *BR*=0

Fig. 8 shows comparison of experimental and numerical pressure evolutions in the ENACCEF facility in the case of obstacles with blockage ratio *BR* = 0.33. Experimental results are similar as in the previous case, but the pressurization is faster. Numerical results also show more rapid pressure increase than in the previous case, however the rate increase is too small. This can be caused by big numerical flame speed deficit compared to the experimental flame speed.

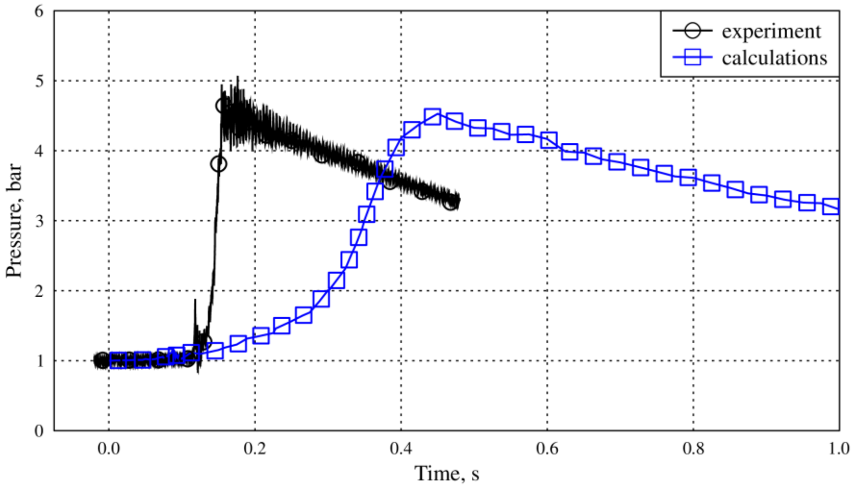

Fig. 8. Comparison of simulated and experimental pressure evolutions with BR=0.33

Fig. 9 shows comparison of experimental and numerical pressure evolutions in the ENACCEF facility in the case of obstacles with blockage ratio *BR* = 0.63. Experimental results are similar as in the previous case. Numerical results are more accurate compared to previous ones; the cause for this may be more accurate flame speed simulation in this case.

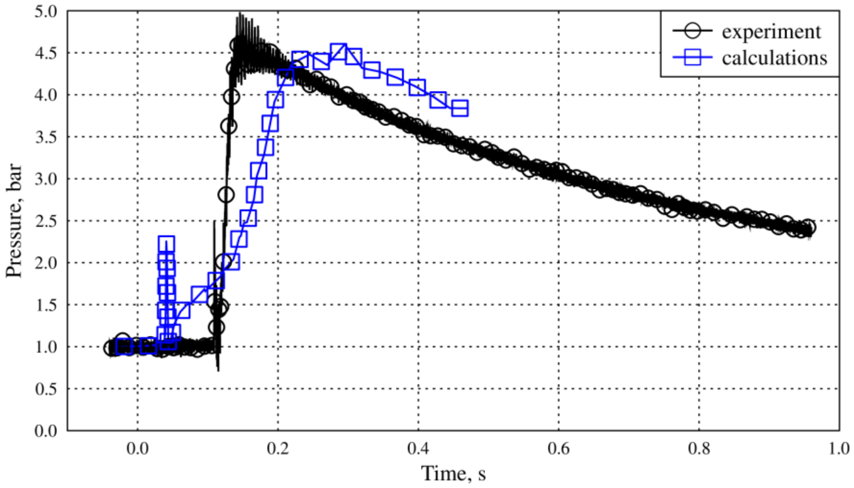

Fig. 9. Comparison of simulated and experimental pressure evolutions with *BR* = 0.63

## 5. CONCLUSIONS

This paper presented simulations of the hydrogen deflagration experiments performed in the ENACCEF test facility in the frame of SARNET2 project hydrogen deflagration benchmark. Simulations were performed using integral severe accident simulation code's ASTEC containment thermo-hydromechanics lumped-parameter module CPA and its hydrogen deflagration module CPA-FRONT.

1. Hydrogen deflagration rates obtained in all performed simulations were lower than experimental ones. The difference was lowest in the case with blockage ratio of used obstacles *BR* = 0.63 (the highest of used obstacles). This suggests that simulation

inaccuracies are less related to turbulence modelling than to nodalisation impact or laminar flame speed modelling.

2. In all performed simulations pressure evolution of facility's atmosphere was qualitatively predicted, quantitative differences are mainly caused by not enough accurate heat losses modelling (could be related to nodalisation) and too slow calculated hydrogen deflagration.
3. Presented conclusions require further simulations to study nodalisation impact on the results, this is planned for future work.

## ACKNOWLEDGEMENT

Author acknowledges the support of Agency for International Science and Technology Development Programmes in Lithuania and the European Commission for preparation of this paper.

## REFERENCES

1. CHAUMEIX, N., BENTAIB, A., 2009, DSR/SAGR 40.
2. CHAUMEIX, N., BENTAIB, A., 2010, DSR/SAGR 102.
3. VAN DORSSELAERE, J.-P., SEROPUAN, C., CHATELARD, P., JACQ, F., FLEUROT, J., GIORDANO, P., REINKE, N., SCHWINGES, B., ALLELEIN, H.J., LUTHER, W., 2009, Nuclear Technology 165, p. 293–307.
4. LIU, D.D.S., MACFARLANE, R., 1983, Combustion and Flame, Volume 49, Issues 1-3, p. 59–71.
5. N. PETERS, 1988, Symposium on Combustion, Volume 21, Issue 1, p. 1231–1250.

CYSENI 2011, May 26–27, Kaunas, Lithuania
ISSN 1822-7554, www.cyseni.com

# VOID REACTIVITY VARIATION IN INNOVATIVE BWR ASSEMBLY

**A. Slavickas**
*Lithuanian Energy Institute*
*Breslaujos str. 3, LT-44403 Kaunas – Lithuania*
*Phone +370 37 401920*
*Email: andriussl@mail.lei.lt*

ABSTRACT

Void reactivity variation in full 0-100% range of void fraction are studied using SCALE code for different design of boiling water reactor (BWR) fuel assemblies. The fuel depletion impact on void reactivity variations is estimated. Westinghouse SVEA-96+ fuel assembly is chosen to investigate void reactivity variations for modern fuel design. Results of investigation were compared with benchmark study results for this modern fuel assembly.

In addition, the evaluation of void reactivity variation in BWR assemblies suggested for innovative fuel designs is performed. These BWR assemblies contain such fissile material and such loading to ensure mean discharge burnup of up to 70 GWd/MTU. The investigation of void reactivity variation for these assemblies is performed for two cases – when assembly is loaded with $UO_2$ and MOX fuel.

The study of void reactivity variations dependence on void fraction and fuel burnup shows main issues related with innovative fuel design taking into account void reactivity effects.

Keywords: void reactivity effect, void reactivity coefficient, innovative fuel, BWR.

## INTRODUCTION

The coolant develops two-phase flow regime in BWR core. As the reactor power is raised to the point, where the steam void start to form, void displaces moderator from the coolant channels within the core. This displacement reduces the moderator-to-fuel ratio and result significant reactivity changes. Therefore void reactivity coefficient, which defines these changes in reactivity due void formations, is prime importance safety parameter during operation of BWR.

Void reactivity effect and coefficient for BWR fuel had been studied for void fractions selected at typically 0%, 40% and 70% [1, 2]. These conditions are overpassed in the current-day BWR power plants. Void fraction is varying till 100% void in BWRs during several transient such like loss of coolant accident. Thereby the investigation of void reactivity variation in full 0–100% range of void fraction is chosen for innovative design fuel.

Modern BWR fuel assemblies differ from old design fuel assemblies since their have such features like high enrichment fuel, wide spread of uranium enrichments, burnable poison and water canal in their centres. These implements ensure better safety and fuel burnup features in comparison with old design assemblies. However there are suggested innovative design assemblies with purpose to improve these features.

The most important feature of modern and innovative design assemblies is higher burnup of discharged assemblies. Many parameters of fuel assembly related with safety are varying since fuel isotopic composition is changing during fuel depletion. Prime importance parameter for BWR assembly in this case is void reactivity coefficient [3, 4]. Therefore fuel burnup impact on void reactivity effect is studied additionally in this paper.

# 1. CALCULATIONAL MODELS AND METHODOLOGY

## 1.1. Westinghouse SVEA-96+ BWR assembly

Fresh Westinghouse SVEA-96+ BWR fuel lattice [5, 6 and 7] had been used as the basis for a benchmark study of the void reactivity coefficient at assembly level in the full void range. In this benchmark study different codes combined with different cross sections libraries were used to obtain void reactivity effect and coefficient values. It is possible to evaluate suitability of SCALE code for such analysis by comparing calculations results with results obtained by other codes and different cross sections referenced at [5]. Thereby this assembly is chosen as modern BWR assembly for this study.

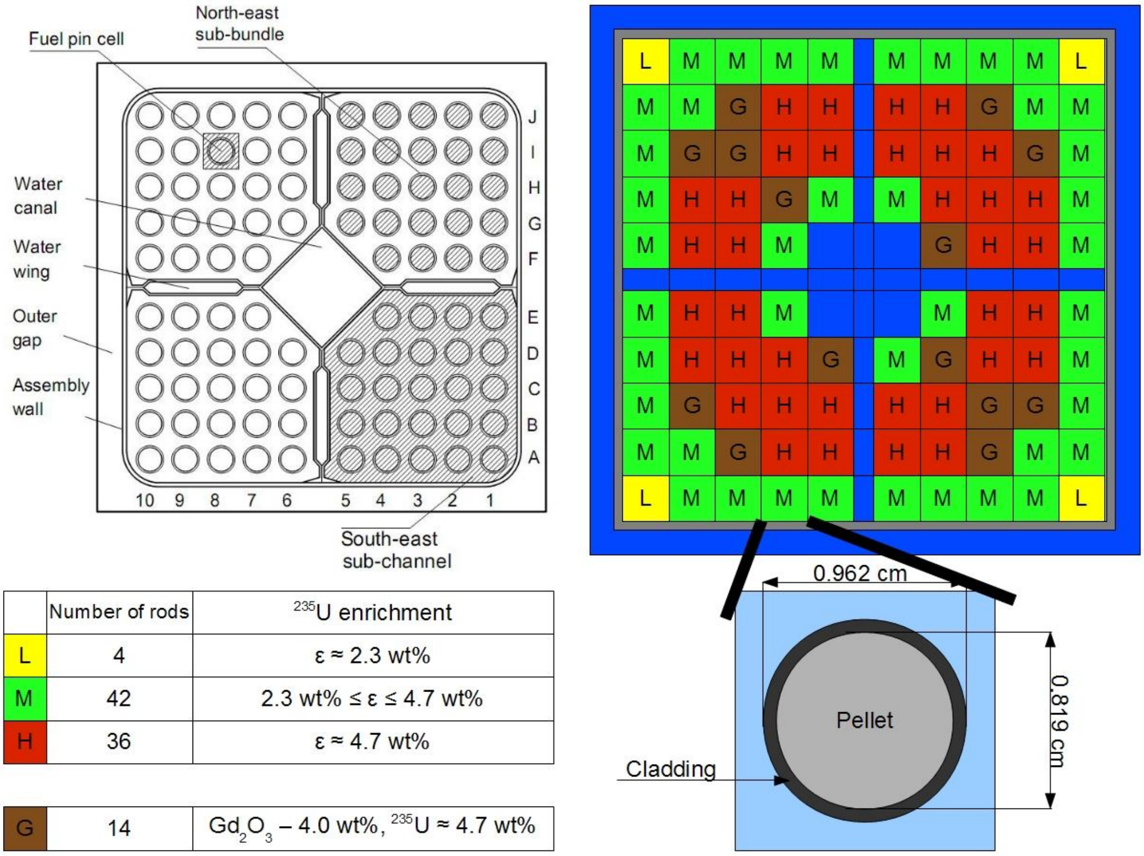

| | | | | | | | | | |
|---|---|---|---|---|---|---|---|---|---|
| L | M | M | M | M | M | M | M | M | L |
| M | M | G | H | H | H | H | G | M | M |
| M | G | G | H | H | H | H | H | G | M |
| M | H | H | G | M | M | H | H | H | M |
| M | H | H | M | | | G | H | H | M |
| M | H | H | M | | | M | H | H | M |
| M | H | H | H | G | M | G | H | H | M |
| M | G | H | H | H | H | H | G | G | M |
| M | M | G | H | H | H | H | G | M | M |
| L | M | M | M | M | M | M | M | M | L |

| | Number of rods | $^{235}$U enrichment |
|---|---|---|
| L | 4 | $\varepsilon \approx 2.3$ wt% |
| M | 42 | 2.3 wt% $\leq \varepsilon \leq$ 4.7 wt% |
| H | 36 | $\varepsilon \approx 4.7$ wt% |
| G | 14 | $Gd_2O_3$ – 4.0 wt%, $^{235}$U ≈ 4.7 wt% |

Fig. 1. SVEA-96+ assembly geometry and macro-regions layout in SCALE nodalisation

SVEA-96+ fuel lattice has high heterogeneity since lattice has all features typical for modern BWR assemblies. It has wide spread of $^{235}$U enrichment, fuel pins with burnable poison gadolinium, water canal in the assembly centre. This assembly is depicted in Fig. 1. SVEA-96+ fuel lattice comprises a bundle of 96 fuel pins contained in four sub-bundles, which are limited by the outer assembly wall and by inner by-pass region consisted of a diamond–shaped central water channel and water wings, which enhances the neutron moderation and flatten the pin power distribution. In the inner by-pass region, water flows like in the outer by-pass region which bases in outer gap. Water remains in pure liquid phase when it flows through core in these by-pass regions. However water transits from pure liquid to liquid and steam mixture when it flows through core in the sun-bundles areas. Therefore two-phase flow of a coolant is restricted only to the sub-bundles areas. Macro-regions with water in pure liquid phase are depicted in dark blue colour. Macro-regions with two-phase water are depicted in light blue colour (fuel pins nodes).

### 1.2. BWR assemblies for innovative $UO_2$ and MOX fuels

A benchmark problem suite for studying the physics of next-generation fuels of light water reactors (LWRs) is stated at reference [2]. This benchmark problem suite should be the verification of prediction capability in which no actual verification data such as critical experiments or core tracking exist. The target discharge burnup of the next generation fuel was set to 70 GWd/MTU in benchmark problem suite taking consideration that the increasing trend in discharge burnup of LWR fuels exists. The discharge burnup of current high burnup fuels for PWR and BWR are less than 70 GWd/MTU [2, 8]. Therefore this benchmark problem suite is suitable for void reactivity variation investigation for innovative assembly with high burnup.

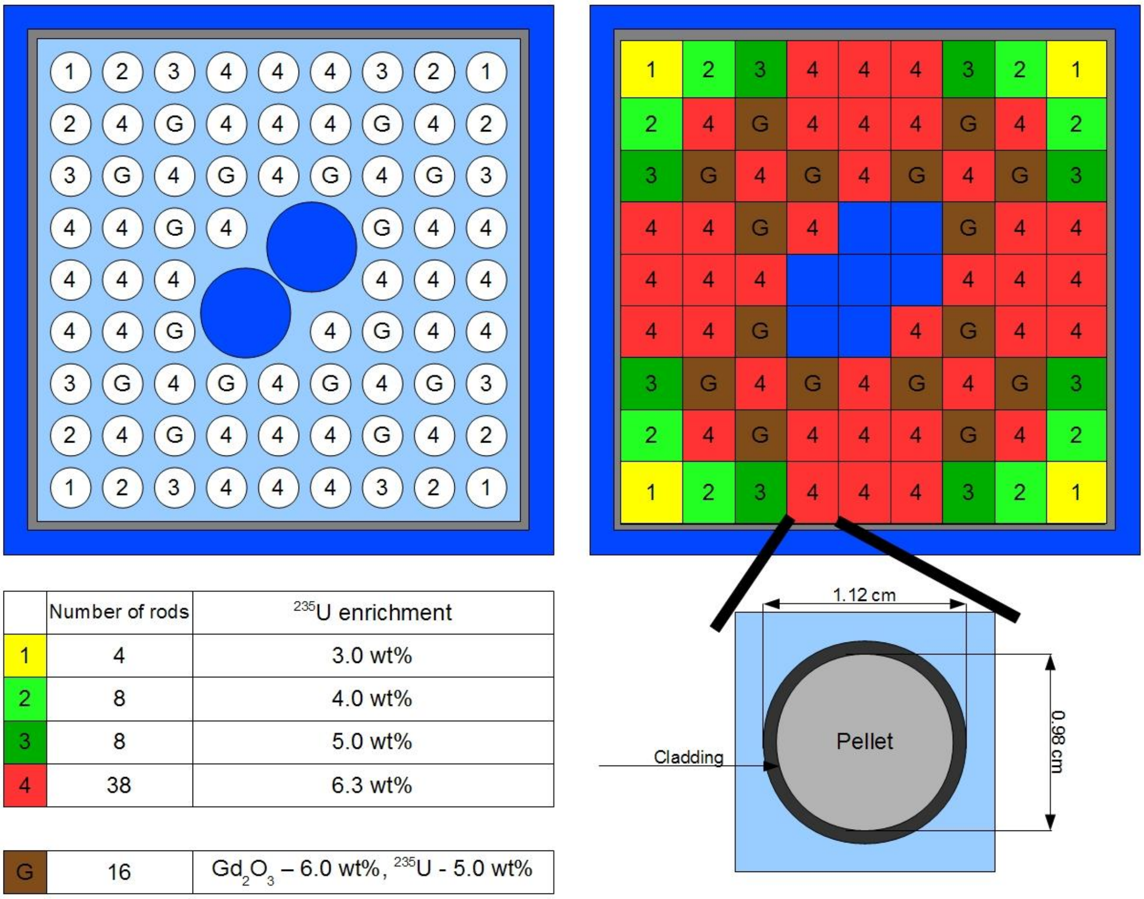

| | | | | | | | | |
|---|---|---|---|---|---|---|---|---|
| 1 | 2 | 3 | 4 | 4 | 4 | 3 | 2 | 1 |
| 2 | 4 | G | 4 | 4 | 4 | G | 4 | 2 |
| 3 | G | 4 | G | 4 | G | 4 | G | 3 |
| 4 | 4 | G | 4 | | | G | 4 | 4 |
| 4 | 4 | 4 | | | | 4 | 4 | 4 |
| 4 | 4 | G | | | 4 | G | 4 | 4 |
| 3 | G | 4 | G | 4 | G | 4 | G | 3 |
| 2 | 4 | G | 4 | 4 | 4 | G | 4 | 2 |
| 1 | 2 | 3 | 4 | 4 | 4 | 3 | 2 | 1 |

| | Number of rods | $^{235}$U enrichment |
|---|---|---|
| 1 | 4 | 3.0 wt% |
| 2 | 8 | 4.0 wt% |
| 3 | 8 | 5.0 wt% |
| 4 | 38 | 6.3 wt% |
| G | 16 | $Gd_2O_3$ – 6.0 wt%, $^{235}$U - 5.0 wt% |

Fig. 2. Geometry and macro-regions layouts in SCALE nodalisation of innovative BWR assembly with $UO_2$ fuel

The $UO_2$ and MOX fuels are included in the benchmark specifications for BWRs. The different design of fuel assemblies are suggested for $UO_2$ and MOX fuel. Assembly with $UO_2$ fuel is the same geometrical configuration as a modern 9 x 9 BWR assembly design (Fig. 2). This assembly has features typical for all modern fuel assemblies such like high heterogeneity due various enrichments of fuel pins and inner water channel for enhanced moderation. Assembly contains 5 types of fuel: 4 types with $^{235}$U enrichment and one type with uranium-gadolinium fuel. These fissile contents ensure mean discharge burnup of up to 70 GWd/MTU for 18 months operation. Bypass region with pure liquid water in assembly consists of outer gap and two inner water channels (macro-regions with dark blue colour). Meanwhile two-phase flow forms only in fuel macro-regions (light blue colour).

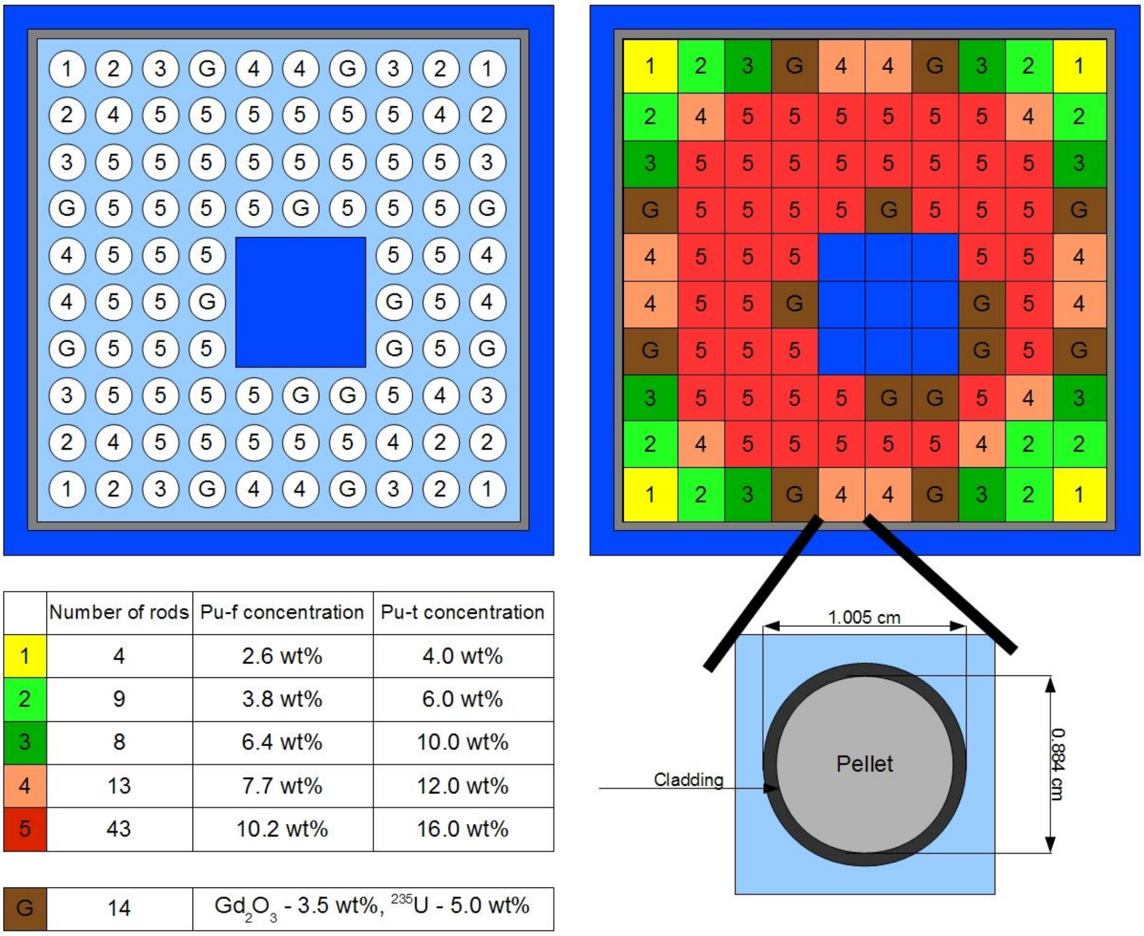

| | | | | | | | | | |
|---|---|---|---|---|---|---|---|---|---|
| 1 | 2 | 3 | G | 4 | 4 | G | 3 | 2 | 1 |
| 2 | 4 | 5 | 5 | 5 | 5 | 5 | 5 | 4 | 2 |
| 3 | 5 | 5 | 5 | 5 | 5 | 5 | 5 | 5 | 3 |
| G | 5 | 5 | 5 | 5 | G | 5 | 5 | 5 | G |
| 4 | 5 | 5 | 5 | | | | 5 | 5 | 4 |
| 4 | 5 | 5 | G | | | | G | 5 | 4 |
| G | 5 | 5 | 5 | | | | G | 5 | G |
| 3 | 5 | 5 | 5 | 5 | G | G | 5 | 4 | 3 |
| 2 | 4 | 5 | 5 | 5 | 5 | 5 | 4 | 2 | 2 |
| 1 | 2 | 3 | G | 4 | 4 | G | 3 | 2 | 1 |

| | | | | | | | | | |
|---|---|---|---|---|---|---|---|---|---|
| 1 | 2 | 3 | G | 4 | 4 | G | 3 | 2 | 1 |
| 2 | 4 | 5 | 5 | 5 | 5 | 5 | 5 | 4 | 2 |
| 3 | 5 | 5 | 5 | 5 | 5 | 5 | 5 | 5 | 3 |
| G | 5 | 5 | 5 | 5 | G | 5 | 5 | 5 | G |
| 4 | 5 | 5 | 5 | | | | 5 | 5 | 4 |
| 4 | 5 | 5 | G | | | | G | 5 | 4 |
| G | 5 | 5 | 5 | | | | G | 5 | G |
| 3 | 5 | 5 | 5 | 5 | G | G | 5 | 4 | 3 |
| 2 | 4 | 5 | 5 | 5 | 5 | 5 | 4 | 2 | 2 |
| 1 | 2 | 3 | G | 4 | 4 | G | 3 | 2 | 1 |

| | Number of rods | Pu-f concentration | Pu-t concentration |
|---|---|---|---|
| 1 | 4 | 2.6 wt% | 4.0 wt% |
| 2 | 9 | 3.8 wt% | 6.0 wt% |
| 3 | 8 | 6.4 wt% | 10.0 wt% |
| 4 | 13 | 7.7 wt% | 12.0 wt% |
| 5 | 43 | 10.2 wt% | 16.0 wt% |

| | | |
|---|---|---|
| G | 14 | $Gd_2O_3$ - 3.5 wt%, $^{235}U$ - 5.0 wt% |

Fig. 3. Geometry and macro-regions layouts in SCALE nodalisation of innovative BWR assembly with MOX fuel

A BWR MOX fuel assembly is the same geometrical configuration as Framatome ANP assembly ATRIUM-10. This assembly is modern 10 x 10 type design assembly (Fig. 3). Assembly has typical feature for modern fuel assemblies like large internal water structure and various enrichment fuel pins too. Assembly contains 5 types of plutonium concentration with depleted uranium and one type of enriched uranium with burnable gadolinium. Plutonium in MOX fuel consists of $^{238}Pu$, $^{239}Pu$, $^{240}Pu$, $^{241}Pu$, $^{242}Pu$ and $^{241}Am$ isotopes. Only $^{239}Pu$ and $^{241}Pu$ isotopes are considered as fissile material (Pu-f concentration) from total plutonium content (Pu-t concentration). However such fissile contents ensure mean discharged burnup of 70 GWd/MTU. Macro-regions in which pure liquid water exist are selected with dark blue colour. Meanwhile macro-regions in which two-phase flow forms are selected with light blue colour.

### 1.3. Methodology for calculations of void reactivity variations

Regular 5% step was chosen in the investigation of void fraction influence on reactivity. Totally 21 cases with different void fraction were analyzed. Therefore void fraction was fixed to range from pure liquid (0% void, density of 0.738 g/cm$^3$) to pure steam (100% void, density of 0.073 g/cm$^3$) in fuel macro-regions where two-phase flow forms. The inner and outer bypass regions were fixed with pure liquid water. In benchmark calculations reference at [5] identical void fraction nodalisation and data had been used.

Infinite medium multiplication factor $k_{\text{inf}}$ were obtained for each of the 21 void fraction values $v_i$ since reflected boundary conditions were given for all fuel lattice. System reactivity $\rho_{inf}$ values from multiplication factor $k_{\text{inf}}$ values were derived as in formula (1):

$$\rho_{\text{inf}} = 1 - \frac{1}{k_{\text{inf}}(v_i)}. \tag{1}$$

Void reactivity variation can be defined by void reactivity effect $\Delta\rho_{inf}$, which accordingly defines reactivity difference between the reactivity of single-phase moderated system ($\rho_{inf}(0)$) and two-phase moderated system ($\rho_{inf}(v)$):

$$\Delta\rho_{inf}(v) = \rho_{inf}(v) - \rho_{\text{inf}}(0). \tag{2}$$

Void reactivity coefficient $\alpha_i$ defines changes of reactivity due changes of void fraction. This coefficient more clearly shows void reactivity variation in void fractions steps since void reactivity effect defines only total effect on reactivity. Values of void reactivity coefficient were calculated by using a central difference scheme:

$$\alpha_i = \alpha\left(\frac{v_{i+1}+v_i}{2}\right) \approx \frac{\Delta\rho_{inf}(v_{i+1}) - \Delta\rho_{inf}(v_i)}{v_{i+1} - v_i}. \tag{3}$$

## 2. CALCULATIONS RESULTS

### 2.1. Benchmark calculations

The codes CASMO-4, HELIOS, PHOENIX, BOXER and MCNP4C have been used with different cross section libraries to study the sensitivity of the void reactivity effect and coefficient to the nuclear data and group structures in the void reactivity coefficient benchmark for modern SVEA-96+ assembly referenced at [5]. Additionally, there are differences in assembly material and geometry data depiction for each code, e.g. the BOXER code performs only two-dimensional transport and depletion calculations in Cartesian geometry. Therefore SVEA-96+ fuel assembly described in Fig. 1 had been modeled using material and geometrical approximation typical for each code. Differences in void reactivity calculations appear due different used cross sections libraries too.

Results of void reactivity variations calculated by SCALE code with ENDF/B-V cross section library were added to compare with results calculated by other used codes for void reactivity coefficient benchmark in case of fresh fuel assembly. The compares of calculated results of SCALE code and others codes are shown in Fig. 4 and Fig. 5. Void reactivity effect and void reactivity coefficient dependences on void fraction, correspondingly, are depicted in Fig. 4 and Fig.5.

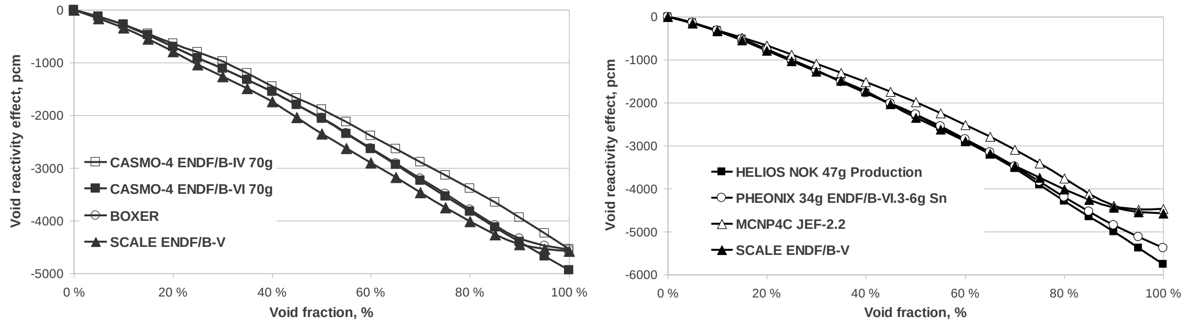

Fig. 4. Void reactivity effect dependence on void fraction. The comparison of SCALE results with [5] data

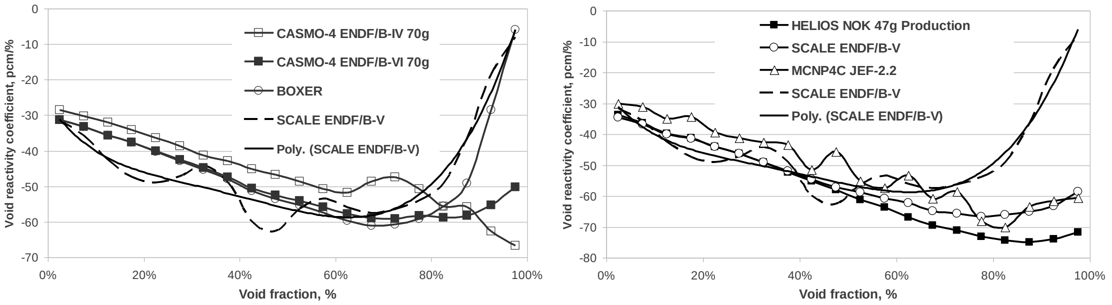

Fig. 5. Void reactivity coefficient dependence on void fraction. The comparison of SCALE results with [5] data

Void reactivity effect variations due void formation $\Delta\rho_{inf}$(v) depict the clearly tendency of the voiding effect value decrease. It means the reactivity decrease in case of void formation. Significant reactivity decrease is obtained in case of pure steam formation (100% void): from 4467 pcm for MNCP4C code till 5756 pcm HELIOS code (22% discrepancy). A significant discrepancy between codes results appears when void fraction is over 40% since void reactivity effects calculated by using different codes and cross sections libraries is varying with different quickness during void formation. This discrepancy conditionally is almost not varying during void formation to 80% (16% in case of void fraction is 40%, and 21% in case of void fraction is 80%). However in case of void formation above 80%, different natures of void reactivity effects variations are obtained. Void reactivity effect values calculated by SCALE and BOXER codes are decreasing not so significant in 80–100% void fraction in comparison with others codes results.

Void reactivity coefficient variations due to void fraction changes $\alpha_i$ (($v_{i+1}$-$v_i$)/2) have the same kind agreement between codes results like in case of void reactivity effect. Only coefficient value variations calculated for void reactivity coefficient in 70–100% void fraction range by SCALE and BOXER codes are different from other codes results since they are approaching to zero at this void range. Discrepancies are more significant since void reactivity coefficient is fluxion of void reactivity effect. Calculated negative void reactivity coefficient values are increasing for all others codes in 70–100% void fraction range, except for value calculated by CASMO-4 code with ENDF/B-IV cross section libraries. Only they are increasing not so significantly (their don’t reach -50 pcm/% margin).

The matches between calculation results of void reactivity effect and coefficient in case of SCALE and other codes uses for void reactivity coefficient benchmark comparisons are no worse that agreement between codes. Therefore SCALE code using described methodology is suitable for the estimation of void reactivity in modern fuel lattices.

## 2.2. Void reactivity dependence on irradiation

SVEA-96+ assembly have features like high $^{235}$U enrichment (average ~4%) and use of burnable poison (Gd$_2$O$_3$). These features ensure higher burnup level of discharged fuel assemblies. Void reactivity effect becomes more important characteristic for modern fuel assemblies taking account higher burnup level of them since fuel depletion influences voiding effect. Thereby study on void reactivity dependence on fuel irradiation was performed for SVEA-96+ assembly.

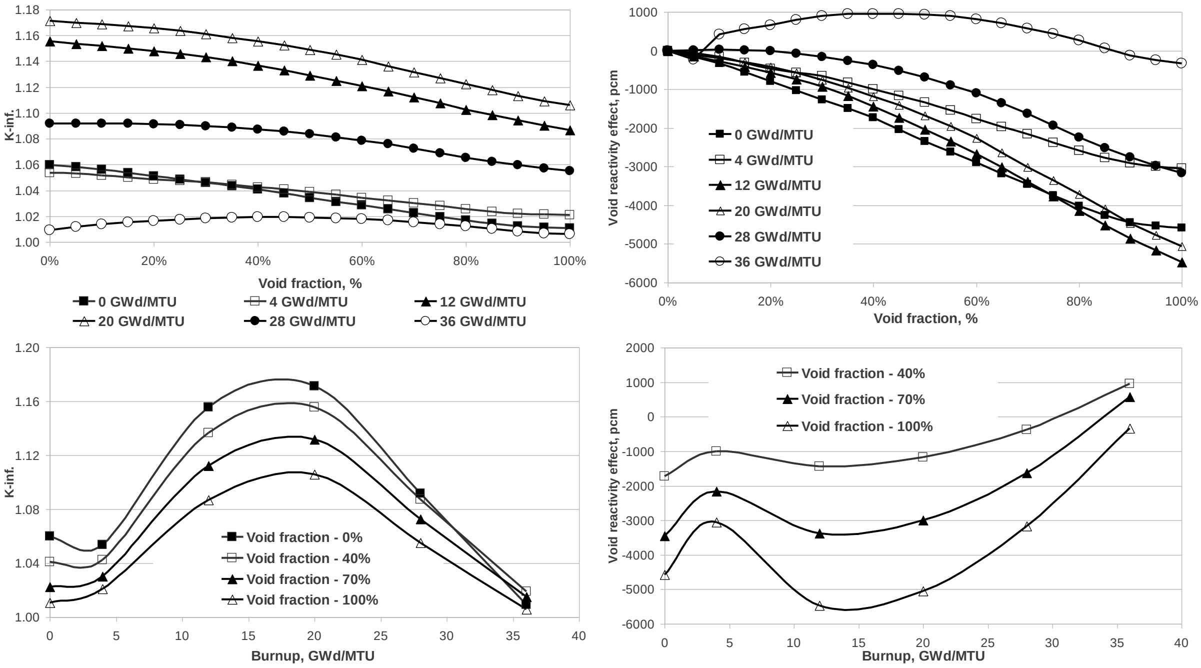

Fig. 6. Calculations results for SVEA-96+ fuel lattice: k-inf. (left) and void reactivity (right) variations vs. void fraction (top) and burnup (bottom)

$K_{\text{inf}}$ and void reactivity effect dependencies on fuel burnup calculated by SCALE code for SVEA-96+ fuel lattice are depicted in Fig. 6. $K_{\text{inf}}$ values are increasing with fuel burnup in 0-20 GWd/MTU interval and decreasing in remaining of interval. This saltatory variation could be explained by rapid $Gd_2O_3$ burning since neutron excess exists in conditionally fresh fuel assembly. Burnable poisons are decreasing reactivity with absorbing excess neutrons in begin of fuel irradiation cycle, what allows higher reactivity in remaining irradiation cycle. It is seen clear neutron multiplication factor decrease with void formation, except for fuel burnup values at the end of fuel irradiation cycle. Therefore reactivity is increasing in case of void formation at the end of fuel assembly depletion.

Primarily, the increase, secondary, the decrease of negative void reactivity effect value is seen in 0-12 GWD/MTU fuel burnup interval. It could be explained by effect of burnable poison $Gd_2O_3$. Meanwhile uniform decrease of negative void reactivity effect value is seen in remaining interval of fuel burnup. In right column figures, clear positive effect of void formation on reactivity it is seen in case of high depletion of fuel assembly (30–36 GWd/MTU burnup interval). However the positive void reactivity is decreasing with void formation over 50% and becomes negative over 85% of void fraction. Therefore the reactivity would decrease in case of complete loss of coolant accident in the full interval of fuel burnup.

## 2.3. Innovative BWR lattices results

Void reactivity variations for innovative BWR assemblies design with $UO_2$ and MOX fuels were evaluated using SCALE code with ENDF/B-V cross section library. These assemblies are described in Section 2. Fissile contents in these assemblies are such that ensure mean discharged burnup of 70 GWD/MTU. Higher discharged burnup and use of higher enrichments fissile materials than in modern assemblies have significant impact on void reactivity variations for innovative assemblies. Thereby void reactivity variations differ between innovative and modern design fuel assemblies.

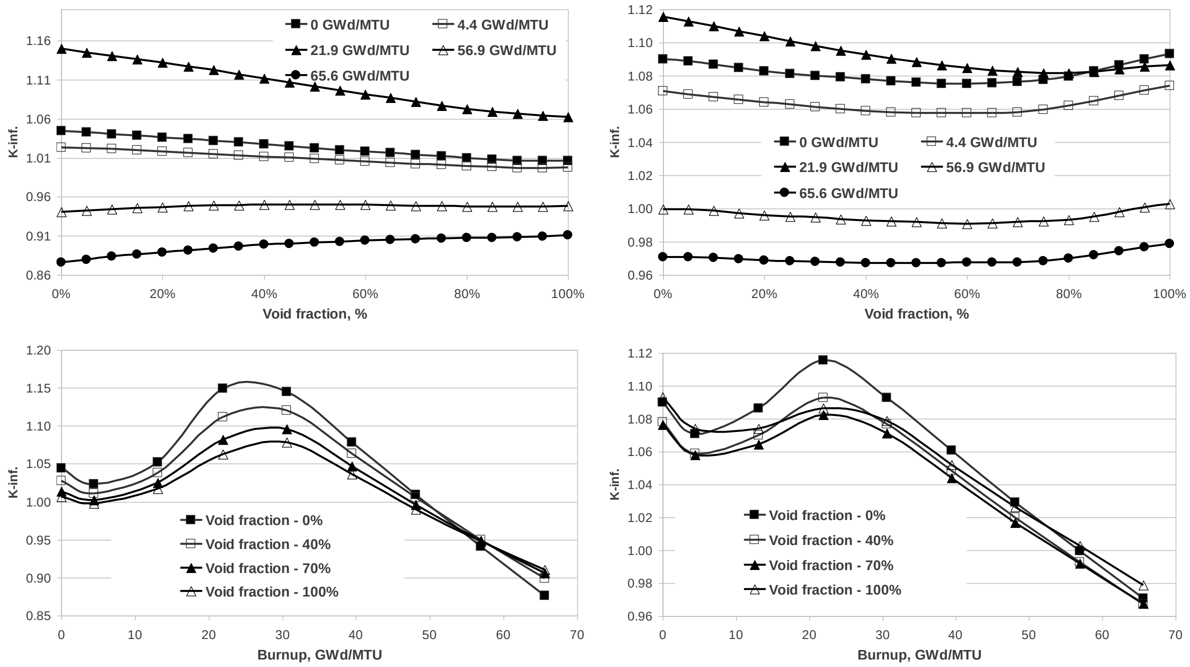

Fig. 7. Calculations results for BWR lattice with innovative fuel ($UO_2$ – left, MOX – right): k-inf. variations vs. void fraction (top) and burnup (bottom)

Fig. 7 depicts $k_{inf}$ variations due to void formation and fuel depletion. $k_{inf}$ values increases at begin of fuel irradiation cycle is obtained in figure. This $k_{inf}$ values varying is obtained for both $UO_2$ and MOX fuels. This varying is due to the same burnable poison gadolinium effect obtained in SVEA-96+ assembly results. Meanwhile neutron multiplication factor varying due to void formation differs for $UO_2$ and MOX fuels. For assembly with $UO_2$ fuel clear $k_{inf}$ values decreases with void formation, except for burnup values at end of fuel irradiation cycle, are obtained in figure. Meanwhile $k_{inf}$ values varying in case of assembly with MOX is more complex since varying is uniform. $k_{inf}$ values decrease at begin of void formation and increase at end of void formation. However bottom row figures show that neutron multiplication factor values for pure steam is higher than multiplication factor values for no voiding case only for high burnup values for both type of fuels. Therefore reactivity increases during loss of coolant accident could be registered only for almost burned fuel.

Additionally, it has to be noticed that $\mathrm{k}_{inf}$ value is varying in smaller range for assembly with MOX fuel than for assembly with $UO_2$ fuel: (0.96÷1.12) for MOX fuel in comparison with (0.87÷1.15) for $UO_2$ fuel. Therefore reactivity excess is smaller at begin of cycle and higher reactivity exist at the end of fuel cycle. Since reactivity is varying in narrow range during void formation reactor core loaded by MOX fuel assemblies could be considered as more stable.

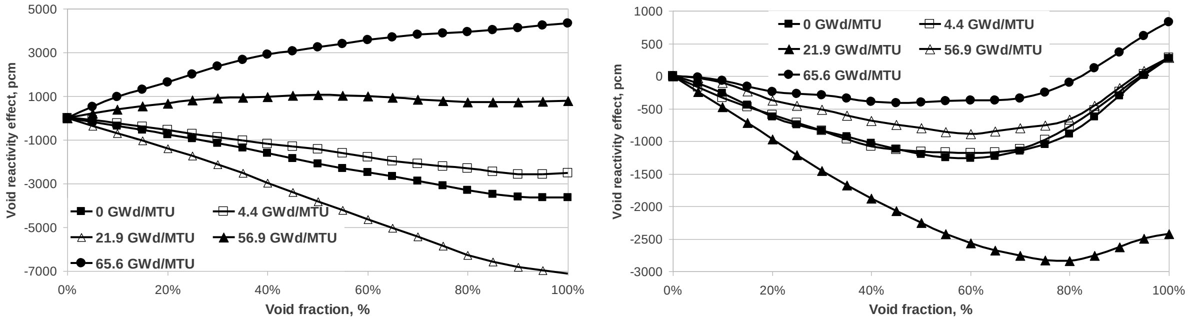

Fig. 8. Void reactivity effect variation due to void fraction for $UO_2$ (left) and MOX (right) fuels

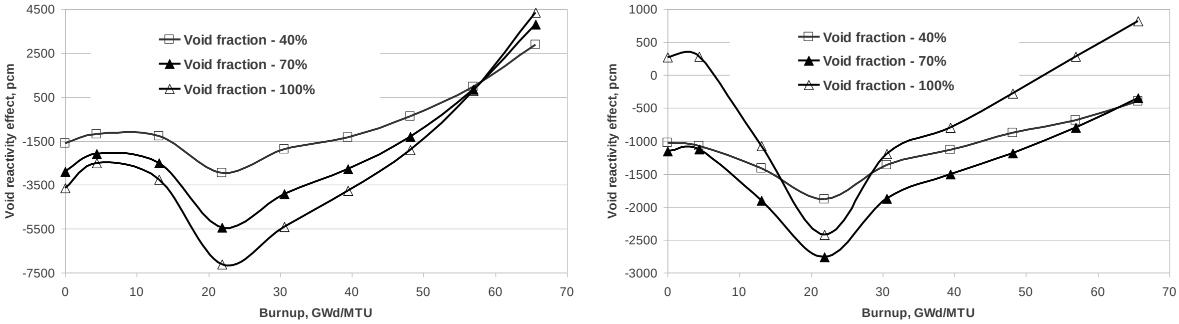

Fig. 9. Void reactivity effect variation due to fuel burnup for $UO_2$ (left) and MOX (right) fuels

Fig. 8 and Fig. 9 depict void reactivity effect variations due void formation and fuel depletion. Primarily, the increase, secondary, the decrease of void reactivity effect values are seen in 0-22 GWd/MTU fuel burnup interval. This effect could be explained with burnable poison gadolinium. Clear positive void reactivity effects are seen in figures for both $UO_2$ and MOX fuels. For assembly with $UO_2$ fuel positive void reactivity effects obtained only for high depleted fuel. These effects are considerably significant and varying till almost 4500 pcm. Meanwhile positive void reactivity effects obtained in assembly with $UO_2$ fuel exist not only for high burnup fuel, but also and for fresh fuel. However positive void reactivity effect values are considerably small and don't reach 1000 pcm. Additionally, it has to be noted, that positive void reactivity effect values in case of MOX fuel are reached in high values of void fraction. In case of $UO_2$ fuel positive void reactivity effect values exist in full range of void fraction. Thereby positive void reactivity effect needs major consideration for assembly with MOX fuel in case of loss of coolant accident only. During normal operation MOX fuel assemblies could be considered more stable and safer than $UO_2$ fuel assemblies since they have negative void reactivity effect and are varying in narrower interval.

## 3. CONCLUSIONS

A detailed study on void reactivity variations has been performed by using SCALE code. Investigation included void reactivity variations due to void formation in full range 0–100% of void fraction and due to fuel depletion during fuel cycle. Three BWR fuel assemblies design were chosen for investigation: modern SVEA-96+ fuel assembly and two innovative BWR fuel assemblies with high burnup.

SCALE code results were compared with other codes results from the void reactivity coefficient benchmark for SVEA-96+ fuel assembly. The comparison showed that SCALE results are within band of other codes discrepancies. Therefore it was showed that created model for SCALE code and described methodology are suitable for the investigation of void reactivity variations in modern fuel lattices.

The study on void reactivity dependency on fuel burnup showed, that the void reactivity effect can become positive in cases then burnup reach discharged fuel burnup level in all investigated cases. For modern SVEA-96+ fuel assembly this effect is relative not significant, but for innovative fuels with high burnup this effect is more significant and needs considerations.

The physical explanation of differences of void reactivity effects for various fuels and assemblies requires an isotopic decomposition analysis of void reactivity variations. The author intends to extend study by implying such analysis.

## REFERENCE

1. GOLTSEV, A.O., MARTYNOV, D.N., MARIN, S.V., LEKOMSTEV, A.A. The impact of the steam–water mixture heterogeneity on the results of boiling water reactor cell calculations. *Nuclear Technology*, 2000, Vol. 131, No. 2, p. 153–158.
2. YANAMOTO, A., IKEHARA, T., ITO, T., SAJI, E., 2. Benchmark problem suite for reactor physics study of LWR next generation fuels. *Nuclear Science and Technology*, 2002, Vol. 39, No.8, p. 900–912.
3. LE TELLIER, R., MARLEAU, G., HEBERT, A., ROUTSOV D., ALTIPARMAKOV, D., IRISH, D. Burnup dependence of coolant void reactivity for ACR-1000 cell. Proceedings of international conference on reactor physics, Nuclear Power: A Sustainable Resource. [CD]. Casino-Kursaal conference center, Interlaken, Switzerland. 2008 September 14–19.
4. PRODEA. I., RIZOIU, A., PRISECARU, I., DUPLEAC, D. Void reactivity evaluation using hafnium absorber in advanced CANDU fuel cells. *Scientific bulletin*, 2010, Series C, Vol. 72, Iss. 2.
5. JATUFF, F., PERRET, G., MURPHY, M.F., GIUST, F., CHAWLA, R. Void reactivity coefficient benchmark results for a 10 x 10 BWR assembly in the full 0–100% void fraction range. *Annals of nuclear energy*, 2009, Vol. 36, p. 853–858.
6. JATUFF, F., GIUST, F., KROUTHEN, J., HELMERSSON, S., CHAWLA, R. Effects of void uncertainties on the void reactivity coefficient and pin power distributions for a 10 x 10 BWR assembly. *Annals of nuclear energy*, 2005, Vol. 33, p. 119–125.
7. TANI, F., JATUFF, F., CHAWLA, R. Study of spectral heterogeneities for the interpretation of calculation trends in predicting pin power distributions in a SVEA-96+ BWR assembly. *Annals of nuclear energy*, 2006, Vol. 33, p. 490–498.
8. *Fuel review: fuel design data*. Nuclear engineering international, 2004 September – [referred on the 9th of March in 2011 y]. Link to the internet < http://www.neimagazine.com/journals/Power/NEI/September_2004/attachments/NEISept04p26-35.pdf >.

CYSENI 2011, May 26–27, Kaunas, Lithuania
ISSN 1822-7554, www.cyseni.com

# ANALYSIS OF PROCESSES IN RBMK-1000 FUEL RODS DURING REACTIVITY INITIATED ACCIDENT USING FEMAXI-6 CODE

**T. Kaliatka, M. Trepulis**
*Lithuanian Energy Institute*
*Laboratory of Nuclear Installation Safety*
*Breslaujos str. 3, LT-44403 Kaunas – Lithuania*
*Phone +370 37 401 911*
*Email: tadas@mail.lei.lt*

## ABSTRACT

In 2006 LEI specialists started to model processes in fuel rods of Ignalina NPP (RBMK-1500). The FEMAXI-6 code, which is designed for BWR and PWR type reactors, is used for the modelling. To gain the experience employing FEMAXI-6 code for the analyses of processes in fuel rods the Studsvik R2 reactor test has been simulated. The comparison of calculated and measured values of fuel rod parameters demonstrated good agreement. FEMAXI-6 code was adopted for modeling of RBMK fuel rods. In this article, using experience gained from previous investigations in RBMK-1500 and BWR power ramp benchmark, analyses of processes in RBMK-1000 fuel rod during short-term power peak due to spurious withdrawal of single control rod is presented. The information obtained during this work allows to conclude that in case of reactivity initiated accidents in RBMK-1000, the fuel rods remain intact and no phenomena occurred that would preclude to the resumption of normal operation after termination of the event.

Keywords: RBMK-1000, FEMAXI-6, reactivity initiated accident.

## 1. INTRODUCTION

The analyses of processes in RBMK fuel rods generally is preparing by Russian specialists of Research and Development Institute of Power Energy (RDIPE- general designer of RBMK) and Kurchatov Institute using Russian in-house codes. However, Lithuanian Energy Institute (LEI) in 2006 started to model processes accruing in fuel rods of Ignalina NPP (RBMK-1500). The FEMAXI-6 code is used for the modelling. Comparing the RBMK with the vessel-type (BWR) reactors it is seen that these reactor types are quite similar in power per fuel quantity or fuel rod length, but big differences appear when comparing reactor power per core volume [1]. The specific power per core volume of the RBMK reactors is somewhat less, while the core heat capacity in RBMK is high. This is due to a large amount of graphite. These parameters have a certain impact on the operation of the reactor during accidents and transients. The fuel and cladding materials and design of fuel rods in RBMK also have differences comparing to vessel type light water reactors. The length of the active region is much higher for the RBMK NPP's. The fuel assembly of RBMK is fit into a circular fuel channel and composed from two fuel bundles one above other. Each fuel bundle includes 18 fuel rods placed in two circles around the carrying rod. In order to decrease the neutron escape from the reactor core in the axial direction the screen pellets of 0.7% $U^{235}$ enrichment are included at the end close to the gag of fuel rod. The plenum of fuel rod from the upper bundle located in the upper part and for the fuel rod from the lower bundle is an opposite. These differences are taken into account during the development of a model.

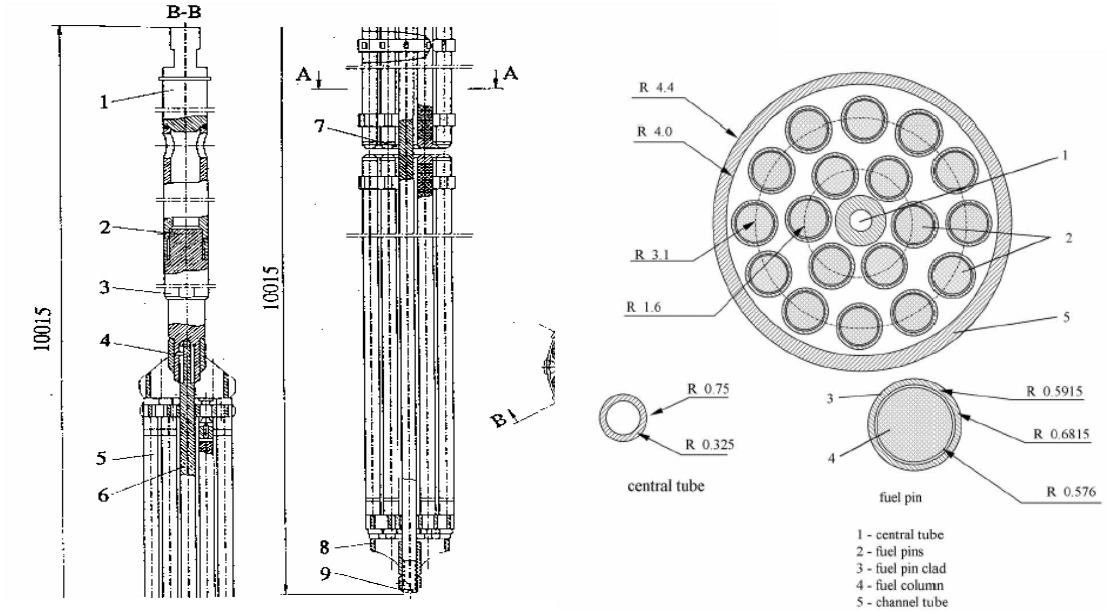

Fig. 1. Fuel assembly and fuel rod of RBMK-1000 [2]

This article contains the information about FEMAXI-6 code validation for RBMK-1000 type reactors and analysis of processes in RBMK-1000 fuel rods during reactivity initiated accident. However, first of all to gain the experience by employing FEMAXI-6 code for the analysis of the processes in fuel rods, the Studsvik R2 reactor (BWR) test has been chosen. The model of BWR fuel rod was developed and calculations have been provided. Obtained calculation results were compared with measurements provided during Studsvik R2 reactor test. RBMK-1500 and RBMK-1000 have differences comparing to vessel type reactors, therefore the FEMAXI-6 code was adopted [3] and model of RBMK-1000 was developed and validated applying “code to code” method (FEMAXI-6 code calculation results were compared to RELAP5-3D code calculation results). After FEMAXI-6 model validation, using experience gained from previous investigations in RBMK-1500 [4], analyses of processes in RBMK-1000 fuel rod during short-term power peak due to spurious withdrawal of single control rod was performed.

## 2. FEMAXI-6 CODE

In the world there are few codes that are used for the modeling of processes in fuel rods, e.g., FEMAXI, TESPA-ROD, FUELSIM, TRANSURANUS, etc. These codes are widely used for the analysis of the thermal and mechanical processes that occur in fuel rods during operation and transients.

In our case FEMAXI-6 code was used, because this code allows producing more detailed calculations, and is able to predict the thermal and mechanical behaviour of a light water reactor fuel rod during normal operation and transient conditions. Also the usage of code is quite simple (short input file and good manual) and open-source is available, what is significant reason of choosing this code. FEMAXI-6 code can analyze the integral behaviour of a whole fuel rod throughout its life as well as the localized behavior of a small part of fuel rod. FEMAXI-6 consists of two main parts (Fig. 2): one for analyzing the temperature distribution, thermally induced deformation, and a fission product gas release, etc., and the other for analyzing the mechanical behaviour of the fuel rod. Temperature distribution, radial and axial deformations, fission gas release, and inner gas pressure are calculated as a function of irradiation time and axial position. Stresses and strains in the pellet and cladding are calculated and pellet-cladding mechanical interaction analysis is performed. Also, thermal conductivity degradation of pellet and cladding waterside oxidation are modeled. Elasto-plasticity, creep, thermal expansion, pellet cracking and crack healing, relocation, densification, swelling, hot pressing, heat generation distribution, fission gas release, pellet-cladding mechanical interaction, cladding creep and oxidation can be modeled by the code [5].

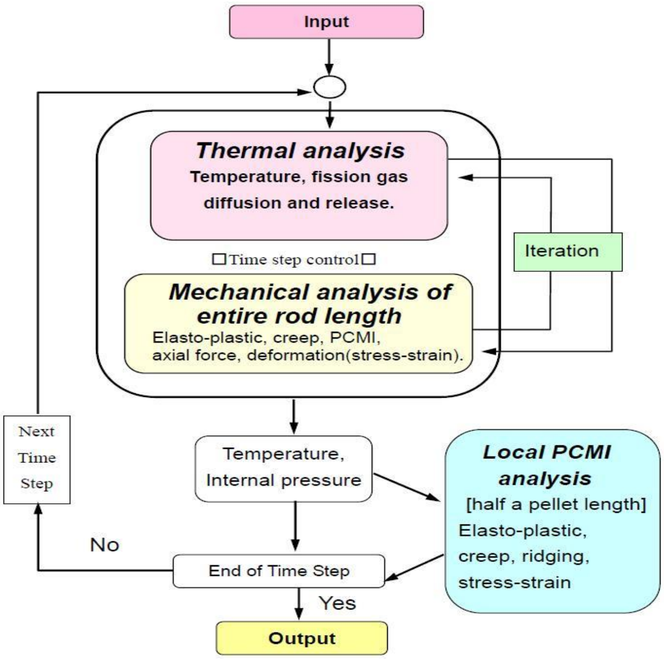

Fig. 2. Entire code structure of FEMAXI-6 [5]

FEMAXI-6 code has an internal structure, in which the finite element method mechanical analysis of entire fuel rod length and thermal analysis have a coupled solution using iteration in each time step for an accurate prediction of fuel behaviour, particularly in high burnup region; i.e. the temperature and fission gas calculation use the gap size and contact pressure, which have been obtained by the mechanical analysis of entire fuel rod length. FEMAXI-6 code can perform a local pellet-cladding mechanical interaction analysis, such as pellet ridging as an optional process [5]. However, in this article presented analysis conducts the entire fuel rod length analysis only.

## 3. TESTING OF CODE USING BWR POWER RAMP MEASURES

FEMAXI-6 code is designed for vessel type reactors. To gain the experience by employing FEMAXI-6 code the Studvik R2 reactor (BWR) test has been simulated [6]. The considered test conducted on a Westinghouse 10x10 SVEA-96S fuel assembly, base irradiated in the Barseback 2 BWR in Sweden, during 1999-2002, to an assembly exposure about 32MW/kgU (Fig. 3). A tested fuel rod of length 570 mm with $UO_2$ fuel pellets was disassembled from the original fuel assembly. Geometrical data of fuel rod used for power ramp test presented in Fig. 3. Cooling conditions are adequate to BWR (9MPa, 558 K) [6].

Using fuel rod geometrical data of Studvik R2 reactor, the FEMAXI-6 model was developed (Fig. 3). In the model fuel rod length is divided into 10 equal segments (47.2 mm for each). The top volume of fuel rod was modelled as separate segment. This volume is used for the plenum of fuel rod and spring. Other fuel rod parts (extension plenum, steam snorkel, water reservoir, etc.) are not involved in the model.

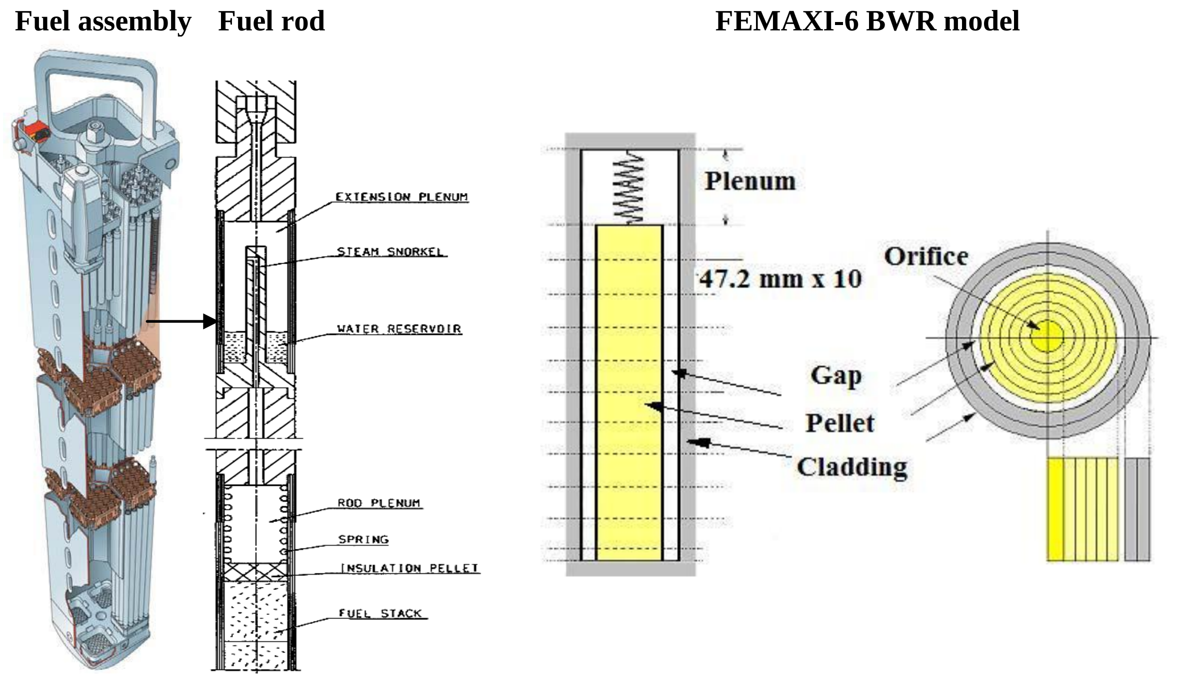

| **Fuel rod** | | **Cladding** | With ZrSn liner | **Fuel pellet** | As-fabricated |
|---|---|---|---|---|---|
| Fill gas | Helium | Material | RXA Zircaloy-2 | Material | $UO_2$ |
| Fill pressure | 0.4 MPa | Outer diameter | 9.63 mm | Diameter | 8.25 mm |
| Active length | 472 mm | Wall thickness | 0.635 mm | Length | 10 mm |
| Plenum volume | 1560 $mm^2$ | | | Density | 10600 $kg/m^3$ |
| | | | | U235 content | 4.2 wt% |

Fig. 3. Studvik R2 reactor fuel assembly [7], fuel rod [8] and model developed using FEMAXI-6 code

The fuel rod was subjected to irradiation in R2 by first raising the linear power from zero to 120 W/cm very rapidly (few seconds). This initial power step was followed by a slow power increase during a period of 25 minutes until liner power reaches 225 W/cm. Fuel rod reaches a state of thermo - mechanical equilibrium at a constant liner power after a sufficient period of time; in this case about 12 h. Later the fuel rod was subjected to a few successive power ramps, where a ramp set height of around 50 W/cm and step duration of 1 h were utilized. The step ramp rate was about 64 W/cm/min. Moreover, the liner power was around 565 W/cm. Power was held at ramp terminal level for about 12 h, and then liner power was finally reduced to 70 W/cm within 50 minutes, after which the irradiation was terminated [6]. Fig. 4 shows fuel rod power history during the ramp test.

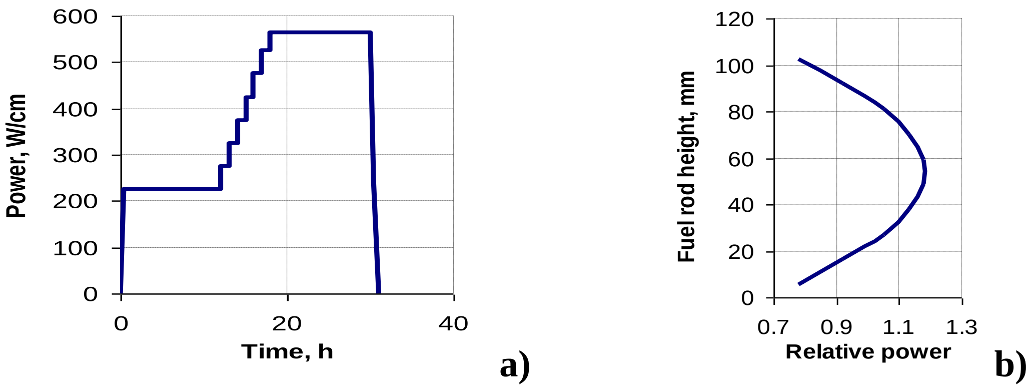

Fig. 4. a) Power ramp history, b) axial distribution along the fuel rod [6]

The increase of power leads to fuel rod temperature increase. During the heating processes the diameter of fuel pellet and cladding is also increasing. The diameter of fuel pellet increases faster than cladding, so the gap between pellet and cladding decreases and the pellet and cladding interaction is possible. Pellet and cladding interaction could be cause of cladding failure. Thus, only gap between pellet and cladding and cladding outer diameter was analyzed. Measured data received form Studsvik R2 test [6] was compared with FEMAXI-6 code calculation results (Fig. 5, Fig. 6). With FEMAXI-6 code calculated values of gap between pellets and cladding and cladding outer diameter has shown qualitative agreement with measured data. This demonstrated the capability of code to model processes in fuel rods.

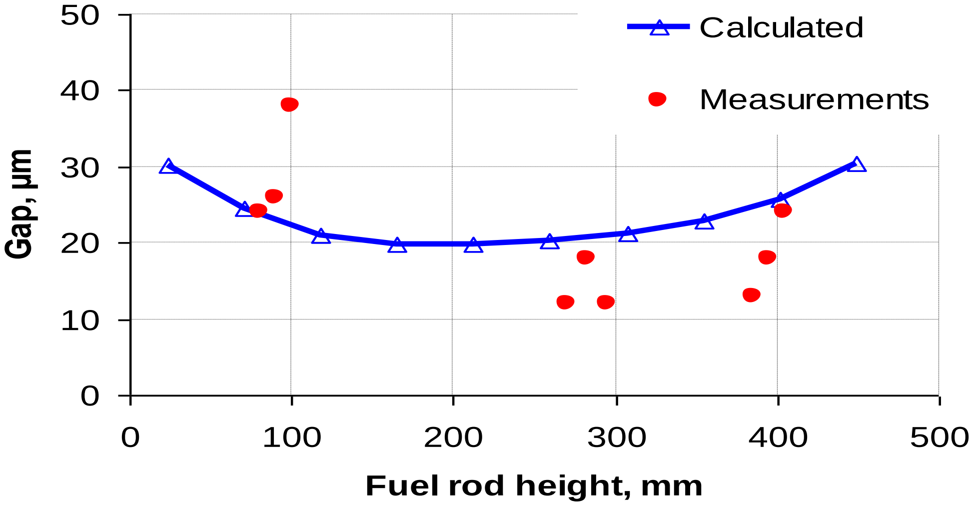

Fig. 5. Comparison between measured [6] and calculated gap between pellet and cladding along the fuel after the ramp

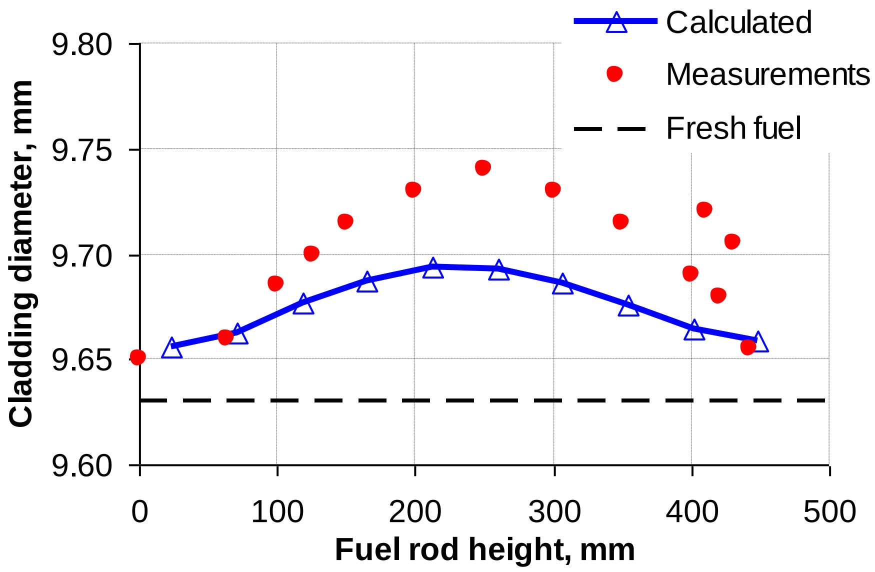

Fig. 6. Comparison between measured [6] and calculated cladding outer diameter along the fuel after the ramp

## 4. MODELLING OF PROCESSES IN RBMK-1000 FUEL ROD DURING REACTIVITY INITIATED ACCIDENT

As it was already mentioned, FEMAXI-6 code is designed for BWR type reactors. Materials of fuel and cladding and design of fuel rods in RBMK-1000 have differences comparing to other vessel type reactors, therefore the FEMAXI-6 code was adopted, by incorporating thermal properties of fuel rod pellets and cladding [3].

The model of RBMK-1000 fuel rod was developed using FEMAXI-6 code, according to the model of RBMK-1500 fuel rod [9]. In both models length is divided into 12 segments, one of which describes screen pellets (Fig. 7). The bottom volume of fuel rod was modelled as separate segment. This volume contains the clamp, compressing column of pellets. The geometrical data of RBMK-1000 fuel pellets and fuel rod cladding are also defined in detail in Fig. 7.

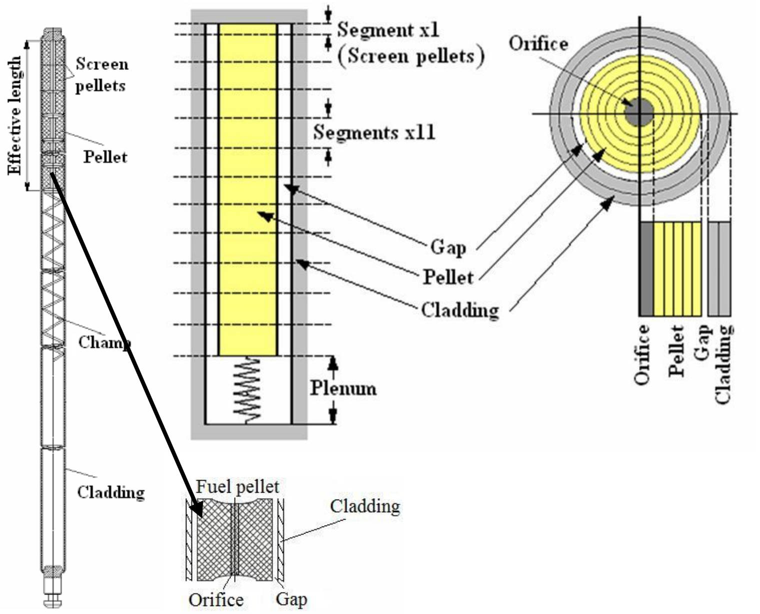

| Length of fuel rod, mm | 3640 | Outside fuel pellet diameter, mm | 11.48 |
|---|---|---|---|
| Active length of fuel rod, mm | 3410 | Pellet central orifice diameter, mm | 2 |
| Height of screening pellets, mm | 30 | Fuel enrichment in $U^{235}$, % | 2.4 |
| Length of plenum, mm | 170 | Edge pellet enrichment, % | 0.7 |
| Outside diameter of fuel rod, mm | 13.63 | Fuel pellet density, g/cm$^3$ | 10.55 |
| Inside cladding diameter, mm | 11.90 | Mass of fuel within fuel rod, g | 3500 |
| Initial pressure of gases in the fresh fuel rod at cold conditions, MPa | | | 0.5 |

Fig. 7. Model of RBMK-1000 fuel rod (bottom bundle), developed using FEMAXI-6 code [9]

### 4.1. FEMAXI-6 code validation for the modelling of RBMK-1000 transients

FEMAXI-6 code is designed for BWR and PWR type reactors and validation for the fuel rod of these type reactors was provided by code developers [5]. Fuel rods of RBMK type reactors are different with their construction and particularly thermal properties of materials. FEMAXI-6 code was adopted by incorporating fuel and cladding specific heat and thermal conductivity properties of RBMK fuel rod. In this case it is very important to test adopted FEMAXI-6 code for the modelling of heat transfer processes. For this purpose FEMAXI-6 calculation results were compared with results observed with RELAP5-3D code in order to validate adopted FEMAXI-6 code and developed fuel rod model.

In this chapter the results of failure of one control rod system is presented. Control rod moved from full inserted position during the control rod withdrawal. The neighbor fuel channel power trend and power distribution along the fuel rod are presented in Fig. 8.

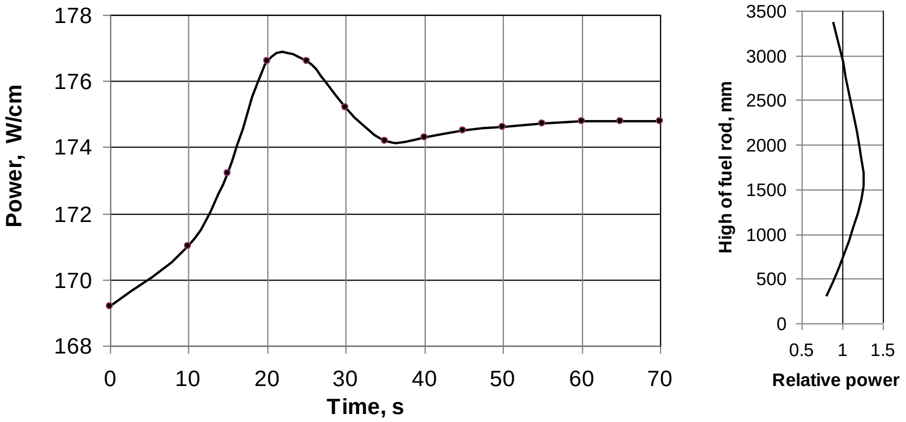

Fig. 8. Power history of the RBMK-1000 fuel rod [2] and the axial power distribution along the fuel rod

Temperatures trend of cladding, of fuel pellets center line, calculated with RELAP5-3D and FEMAXI-6 codes, are presented in Fig. 9.

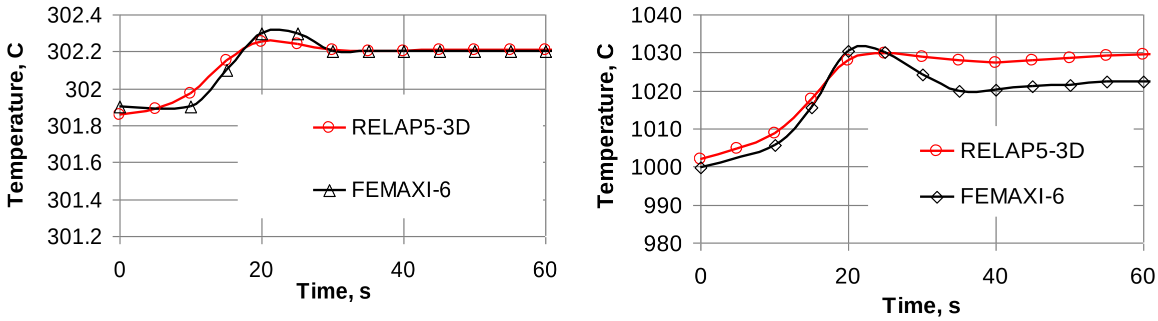

Fig. 9. Comparision of calculation results: Cladding and fuel temperatures

In Fig. 9 presented comparison demonstrated the reasonable agreement between both used codes, all major trends are correctly predicted. So it can be concluded that adopted FEMAXI-6 code and developed model of fuel rod are suitable for the analyses of RBMK-1000 fuel rod. Also all values showed a not critical behavior during this trend raised from the failure of one control rod.

## 4.2. Analysis of reactivity initiating accident in RBMK-1000

Validated, adopted for RBMK type reactors, FEMAXI-6 code was used to analyze processes in fuel rod during reactivity initiating accident (withdrawal of one control rod from the central part of reactor core) which rises to reactor shutdown. In this case control rod is withdrawn with the speed 40 cm/s. These leads to local power increase in reactor core and after 8.7 s scram signal is occurred.

The extraction of control rod from the core results in increase of power in the fuel channels, located around this effected control rod. The power increase is especially strong in channels, which are located in the vicinity of an control rod. For the investigations of power increase the channels ET1 and ET2, which are close to the control rod were chosen. These two channels are different with their initial power: ET1 – 98W/cm, ET2 – 120W/cm. Change of axial power distribution in channel ET1 depending on time is shown in Fig. 10. It is clear from the figure that power increases faster in the bottom part of the channel, according to control rod ejection from the core. The abrupt reduction of reactor power as a whole and in separate channels occurs after scram [2].

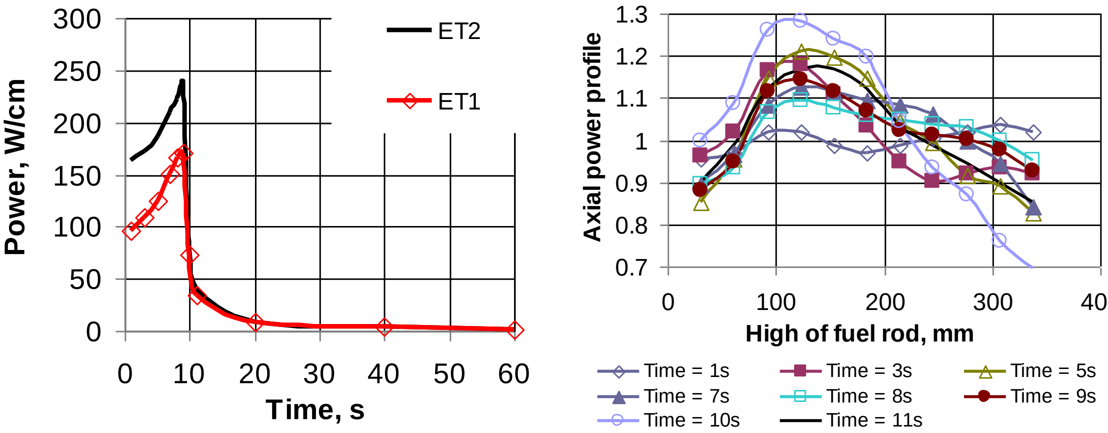

Fig. 10. Power history of reactivity initiating event and the axial power distribution along the fuel rod [2]

The behaviour of fuel rod parameters calculated using the FEMAXI-6 model is presented in Fig. 11 – Fig. 15. In these figures, the parameters are presented only for segment No. 5 (153.5 mm from the bottom of fuel rod), i.e. the segment where the axial power distribution is higher. The peak temperatures of the fuel rod increases due to sudden increase of the power and decrease then reactor is shutting down, but 40s after full reactor shutdown the cladding temperature remains ~295$^{o}$C (Fig. 11) close to the temperature of water in fuel channels.

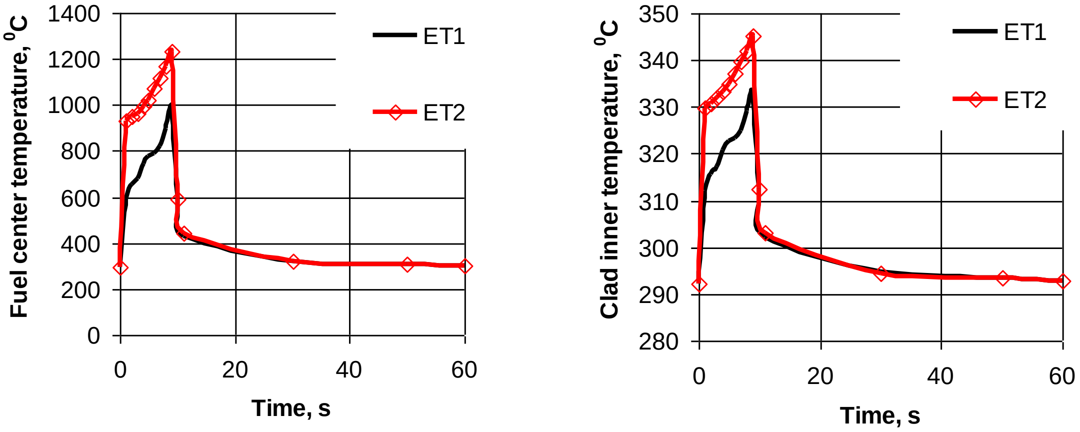

Fig. 11. Fuel center and cladding inner temperatures in channels ET1 and ET2

During the sudden power increase gap between pellet and cladding is decreasing (Fig. 13), but it is far from the cladding and pellet contact; the total volume of gases decreases also, so gas pressure in the fuel rod is increasing (Fig. 12). Fraction of gas mixture in both channels remains stable (~98% - He, 0.03% - Kr and 0.2% – Xe) for all accident time. Radius of fuel grain is also constant (~5 µm) in both channels for all accident time. Fig. 14 presents that the radius of fuel pellets increased during the increase of reactor power. This fact also had influence on the decrease of gap. After reactor shutdown, the radial dimensions of fuel rod and radial gap between fuel pellet and cladding returned back close to the initial conditions. The stresses of fuel rod cladding are presented in Fig. 15. As it is seen from the picture, highest circumferential compression stresses were in the range of ~43 MP. These stresses were increased in accordance with increase linear power. According to the literature [10], the yield stress for Zr+1%Nb alloy is 180-220 MPa for 300 °C temperature. After exceeding this limit of yield stresses, the fuel cladding would be affected by plastic deformation, which leads to cladding failure. In our case, the calculated maximal value of circumferential compression stress in the cladding is much lower than the yield stress. Thus, the fuel cladding remains intact. The values of all analyzed fuel rod parameters showed a not critical behaviour during this reactivity initiating accident.

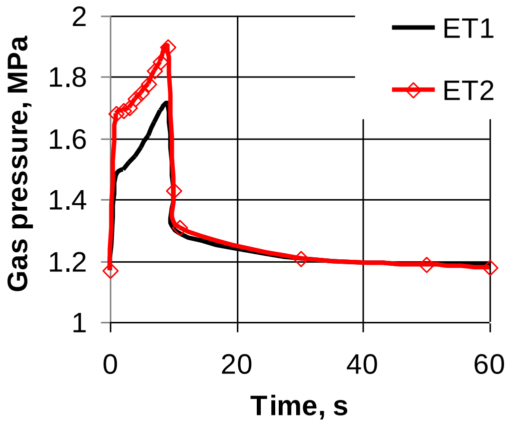

Fig. 12. Gas pressure in fuel rod from the ET1 and ET2 channels

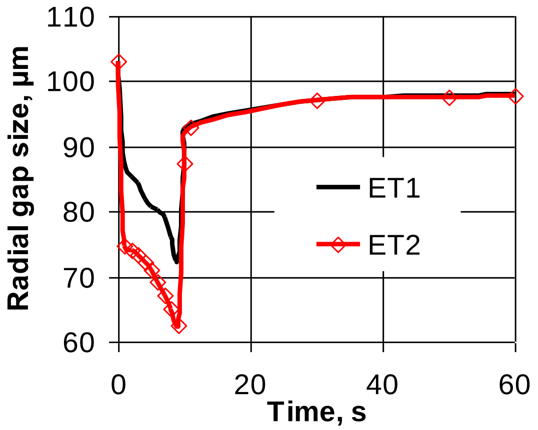

Fig. 13. Radial size of gap between pellet and cladding

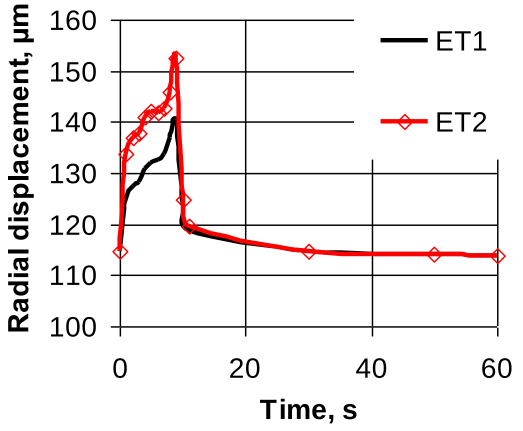

Fig. 14. Fuel pellet radial displacement

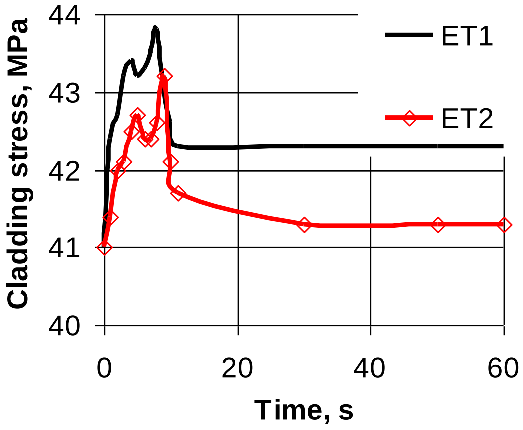

Fig. 15. Stress in fuel rod cladding

## 5. CONCLUSIONS

1. The FEMAXI-6 code capacity was tested using Studvik R2 reactor test measured data. The experience of employment of FEMAXI-6 code was gained by performing BWR power ramp benchmark. The Studvik R2 reactor test measurements are adequate to FEMAXI-6 calculation results. This demonstrated the capability of code to model processes in fuel rods.
2. The model of RBMK-1000 fuel rod was created using experience gained from previous investigations of RBMK-1500.
3. Validation of adopted FEMAXI-6 code and developed RBMK-1000 fuel rod model for heat transfer processes was performed comparing FEMAXI-6 code calculation results with results received from RELAP5-3D code calculations.

4. The performed analysis of reactivity initiating accident in RBMK-1000 due to spurious withdrawal of one control rod in the central part of core showed that the gap between fuel pellet and cladding in the fuel assemblies, located close to the affected control rod remains open. Maximal stresses of fuel rod cladding and fuel pellets are few times lower than the yield stresses. This leads to the conclusion that the safety barrier is sustained – the fuel rods remains intact.

## REFERENCES

1. ALMENAS, K., KALIATKA, A., USPURAS, E., 1998, Ignalina RBMK-1500. A Source Book. Extended and Updated Version, Lithuanian Energy Institute, Kaunas, Lithuania.
2. D'AURIA, F., et al, Development of a Code System for Severe Accident Analysis in RBMK Final Technical Report for TACIS Project R2.03/97, part B, December 2005.
3. KALIATKA, T. Adaptation of FEMAXI-6 Code for Modelling of RBMK-1500 Fuel Rod, CYSENI 2008. Proceedings of annual conference of young scientists on energy issues. [CD] Kaunas: Lithuanian Energy Institute. 2008 May 28–29.
4. PABARČIUS, R., KALIATKA, A., MARAO, A. Analysis of fuel rod behaviour during limiting RIA in RBMK plants, Kerntechnik. ISSN 0932-3902. 2010, Vol. 75, No. 6, p. 329–336.
5. SUZUKI, M. Light Water Reactor Fuel Analysis Code FEMAXI-6 (Ver. 1), Japan Atomic Energy Research Institute, 2005.
6. MASSIH, A. R., JERNKVIST, L. O., LINDBACK, J. E., ZHOU, G. Analysis of Pellet-Clad Interaction of LWR Fuel Rods During Power ramps, SMiRT 18. 18th International Conference on Structural Mechanics in Reactor Technology, SMiRT18-C03-3, Beijing, China 2005.
7. www.westinghousenuclear.com
8. GROUNES, M., GRASLUND, C., LYSELL, G., et al, BWR fuel R&D programs at Studsvik, Studsvik Nuclear AB, Nykoping, Sweden, XA9846753.
9. JUSEVIČIŪTĖ, A., KALIATKA, T., UŠPURAS E. Usage of FEMAXI-6 code for RBMK-1500, Proceedings of the 7th international conference on nuclear option in countries with small and medium electricity grids. Croatian Nuclear Society: IAEA, 2008. ISBN 978-953-55224-1-6, p. 1–15, Dubrovnik, Croatia, May 25–29, 2008.
10. ANTIKAIN, P. A. Metals of equipment and pipe lines for Nuclear power plants, Moscow, 1984.

CYSENI 2011, May 26–27, Kaunas, Lithuania
ISSN 1822-7554, www.cyseni.com

# PROBABILISTIC ANALYSIS OF MULTIPLE ROOMS AREA EVENT CONSIDERING SPURIOUS OPERATION OF IGNALINA NPP FIRE EXTINGUISHING SYSTEM

**R. Voronov**
*Lithuanian Energy Institute*
*Laboratory of Nuclear Installation Safety*
*Breslaujos str. 3, LT-44403 Kaunas – Lithuania*
*Email: roman@mail.lei.lt*

ABSTRACT

Such events as fires and floods, that impact one or several compartments of a nuclear power plant (NPP) and may disable all safety equipment present in that compartments, are subject to area event (AE) analysis which is normally a part of probabilistic safety assessment (PSA) of NPP. Normally safety systems of NPPs have multiple separated trains that makes them well protected against area events. In such case a fire or flood in a single room, although being an undesirable event, may not cause serious danger to reactor safety. Only area event in multiple compartments might be dangerous.

Automatic fire extinguishing systems are important for ensuring the fire safety of nuclear object by protecting NPP compartments and the safety systems from fires. On the other hand automatic water and foam fire fighting systems are possible source of flooding in case of spurious activation acting as a “Troyan horse”. Once such case of spurious activation caused the shutdown of power unit during Ignalina NPP operating history. An event that might cause the spurious activation of fire extinguishing systems in several rooms with safety equipment located would seriously jeopardize NPP safety. A possible scenario is the ingress of smoke from external fire (e.g. forest fire) and it’s distribution by ventilation system to multiple compartments causing the activation of fire fighting systems and a flooding as a consequence.

This paper presents possible approach to analyze such event using NPP PSA model. The collection of necessary data, PSA modelling and the analysis of external event impact on multiple trains of a safety system are discussed.

The application of such approach could be important for PSA of the nuclear power plants and could be of interest of the safety assessment of other objects where spurious operation of automatic fire extinguishing could damage important equipment.

Keywords: multiple rooms area event analysis, external hazards, spurious operation, automatic fire extinguishing.

## 1. INTRODUCTION

An important part of ensuring safety of nuclear object is its protection against the events like fires and floods. Such events may have impact on the safety equipment in both ways: by direct damage and indirectly by damaging power and control cables of that equipment. The later cause a failure to operate and control e.g. pumps and valves of the safety systems. Therefore the fire safety of nuclear objects is of high importance and priority. The safety systems of nuclear power plants are highly redundant, i.e. include more safety trains that are required for the successful completion of their safety functions. In order to keep such redundancy in case of fire the cables and electrical equipment of different safety trains are physically separated, i.e. laid out in different compartments separated by fire resistant walls and doors. Following this principle allows keeping the safety system operable even in the worst case when fire destroys all equipment in a single room.

The fire safety of Ignalina Nuclear Power Plant (INPP) was analysed and confirmed by a number of studies, including Fire Hazard Analysis and Safety Case. Safety Analysis Report of Ignalina NPP also proves the plant safety to such natural external events as floods and fires.

However the combination of external and internal hazards may have effects which were not analysed before.

## 2. DEFINITION OF THE PROBLEM

### 2.1. Impact of area events on INPP safety

In probabilistic safety analysis (PSA) the events like fires and floods that impact multiple equipment in the same area are considered by area event (AE) analysis. Normally NPP safety systems are highly redundant and a failure of one of the components does not affect the safety function of the system. The main hazard imposed by AE to NPP perspective is that such events lead to a failure of several redundant trains or even several safety systems. From this point of view the compartments where power supply and control cables for different safety systems are concentrated are highly important for NPP safety.

A number of studies, including Fire Hazard Analysis and Safety Case were carried out and confirmed the fire safety of Ignalina Nuclear Power Plant. Fire Hazard Analysis showed the adequacy of INPP fire protection [3]. Area Event analysis that was an integral part of Probabilistic Safety Analysis did not identify any fire or flooding scenario, including events in several neighbouring rooms, which would be crucial for the plant safety and could jeopardize a safe reactor shutdown and core cooling. A significant impact on the plant safety is possible only if a number of rooms with the safety system equipment or cables was affected. However the defence against the event such as fire propagation is provided by the fire barriers (walls, doors and isolating valves in ventilation ducts) and no credible scenarios for such events were found.

### 2.2. Spurious operation of fire extinguishing

On 31st July 2000 a short circuit in the control cable damaged by maintenance works in the control cabinets' room had caused an activation of Automatic Fire Fighting System (AFFS) at Unit 2 of Ignalina NPP. Two Main Circulating Pumps were flooded by foam and failed. Unit 2 was shut down for 47 hours. This event could serve as a good example of how the system designed for the protection may cause failure.

Each room protected with AFFS has a potential source of flooding and the equipment of that room in case of fire may be damaged either by fire or by extinguishing the fire. Smoke detectors used in AFFS are very sensitive and a false alarm or false fire extinguishing may be caused even by dust or smoke from welding or cutting works during repairs. A number of such false alarms were experienced during INPP operating. Potentially fire in one compartment might cause the flooding in other compartments due to smoke spread via common ventilation duct and a false fire extinguishing in neighbouring room. Such scenarios are unlikely as special isolating valves in the ventilation ducts prevent the propagation of fire and smoke between rooms. The valves are closed automatically by the fire detection system signal at the same time as the fire alarm is initiated.

### 2.3. Secondary effects of external fire

Despite of this there is still a scenario when spurious operation of fire extinguishing systems in multiple rooms is possible: the ingress of smoke from the external source may cause such event.

The analysis of external events showed that external fire does not pose a hazard to INPP [1], [2]. It is indicated that the smokescreen can disturb an operation and also cause some difficulties for the personnel [2]. However, the secondary effects of smoke ingress to the ventilation system were not analysed in details previously. Presumably, one possible effect of smoke spread to a number of rooms could be the initiation of automatic fire extinguishing and subsequent damage of the safety equipment or cables by water or foam. This scenario is possible as the venting system takes a fresh air from the outside of NPP and has no protecting sensors for the outside smoke [2]. A possible sequence of events is presented schematically in Fig. 1.

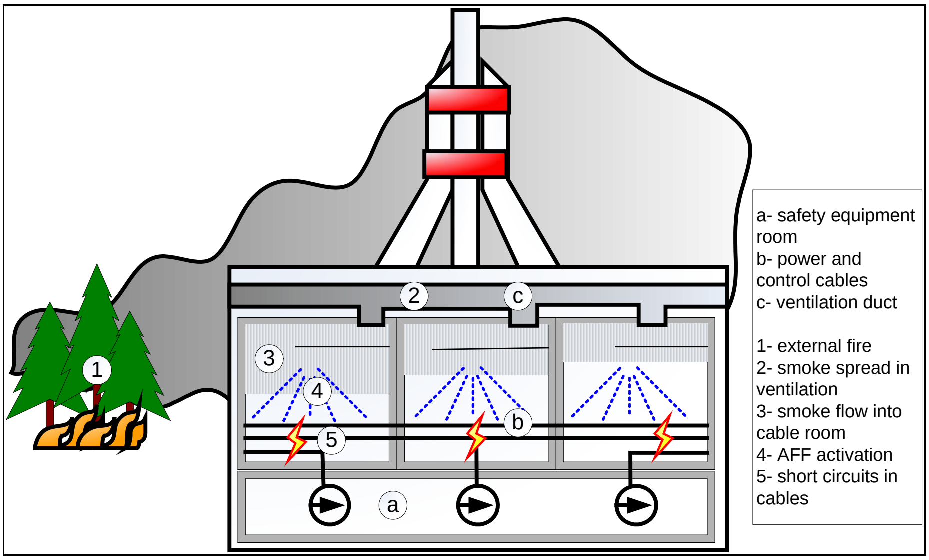

Fig. 1. Secondary effects of external fire

From the engineering judgement such event seems to be almost impossible. High voltage cables have good insulation and are protected by fire protective coating. On the other hand insulation may have cracks or damages due to aging. Thorough analysis of such event should include both the probabilistic and deterministic approaches. The task for deterministic analysis would be to model and estimate the phenomena, i.e. smoke distribution and density, the effect of water sprinklers on the cables and the possibility of short circuits and subsequent damage on high voltage. The probabilistic analysis using complex model of plant safety system interactions may identify the areas where a multi-compartment flooding would be the most dangerous for NPP nuclear safety and allow to estimate the effect on core damage frequency.

At the very first stage PSA can be used for the preliminary analysis of the events defining the bottlenecks – the combinations of compartments where AE are most dangerous for nuclear safety.

This paper presents the application of PSA for the identification of the most important combination of rooms.

## 3. METHODOLOGY FOR THE ANALYSIS OF MULTIPLE ROOMS AREA EVENT

This section in 3.1 and 3.2 shortly describes “traditional” AE analysis methodology when already known AE scenarios are analysed using PSA methods. For the analysis of multiple AE the same methods are used mostly. However at some stage of investigations they could not be used as the scenarios are not explicitly defined. The reasons are described in 3.3. The proposed approach to resolving such problem is provided in 3.4.

### 3.1. Assumptions and screening

It is assumed that AE leads to one of the initiating events considered in PSA model. Usually a manual shutdown or manual shutdown with the unavailability of some important systems is anticipated. This allows the application of existing PSA model for AE analysis. Next assumption is that the equipment vulnerable to the event is affected only. Normally this is related to electrical or electromechanical equipment like cabinets, cables, motors of pumps and motor driven valves. Pipes and heat exchangers are assumed to withstand the area events. It is also assumed that all affected equipment becomes unavailable. This conservative approach helps to save time and efforts by screening out all rooms which have no significant influence on reactor core damage.

The first stage of AE analysis is data collection and a qualitative screening of the compartments. The compartments are defined as areas having adequate barriers against AE spread and are not always the same as the rooms in the common sense. If the neighbouring rooms have no barrier between them (e.g. doors are open or the walls are not fire resistant) they are treated as single compartment. The compartments that do not contain any safety related equipment or have no potential for AE (ignition or flood source) are excluded from the analysis.

The second stage of the analysis is a quantitative screening. AE for each compartment is evaluated using PSA model and a conditional core damage probability (CCDP) is calculated. CCDP, also called a safety barrier, is core damage probability due to the initiating event. Then for the initiating event $i$ the core damage frequency $CDF_i$ is a product of initiating event frequency $F_i$ and $CCDP_i$:

$$CDF_i = F_i \cdot CCDP_i \,. \tag{1}$$

Scenarios with CCDP below predefined threshold are excluded from the further analysis. The compartments that remain after both qualitative and quantitative screening are a subject to detailed analysis at the third stage.

### 3.2. Fault tree modelling

At the quantitative screening and detailed analysis stages the plant PSA model is used for the evaluation of fire impact on the safety systems. There are several methods for adoption of PSA model for AE analysis: surrogate event method, damage term insertion method, fire event insertion method, and house event propagation method [4]. Jung et al. propose JSTAR method for the quantification of fire scenarios [4]. For the illustrative purpose a hypothetical case is presented in Fig. 2.

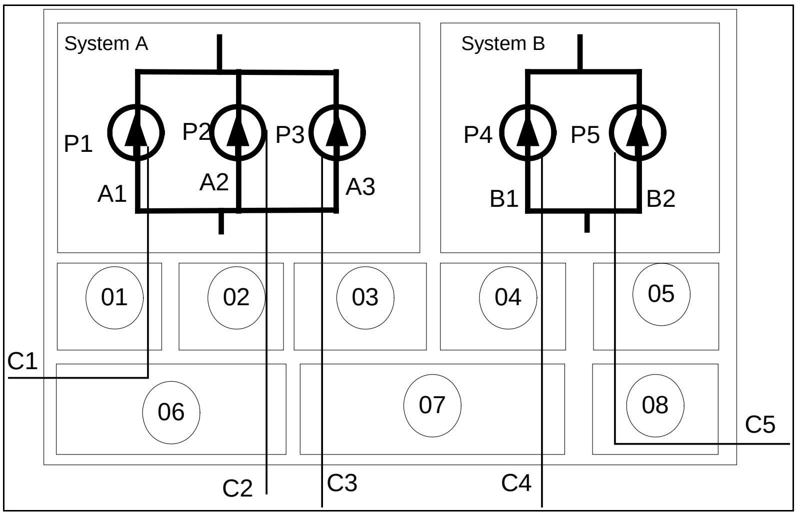

Fig. 2. Hypothetical safety systems and cable layouts

Let’s say that the systems A and B provide a reactor cooling. The systems contain five pumps P1-P5 where P1-P3 belong to the system A and P4-P5 belong to the system B. Either two out of three trains (A1-A3) of the system A or one out of two trains (B1-B2) of the system B are required for the safe cooling. Each pump P1-P5 has a corresponding power cable C1-C5. A failure of the cable leads to a failure of the pump. The fault tree (FT) which models the core damage due to loss of both A and B systems is developed in accordance with the standard procedure [5], [6] and presented in Fig. 3.

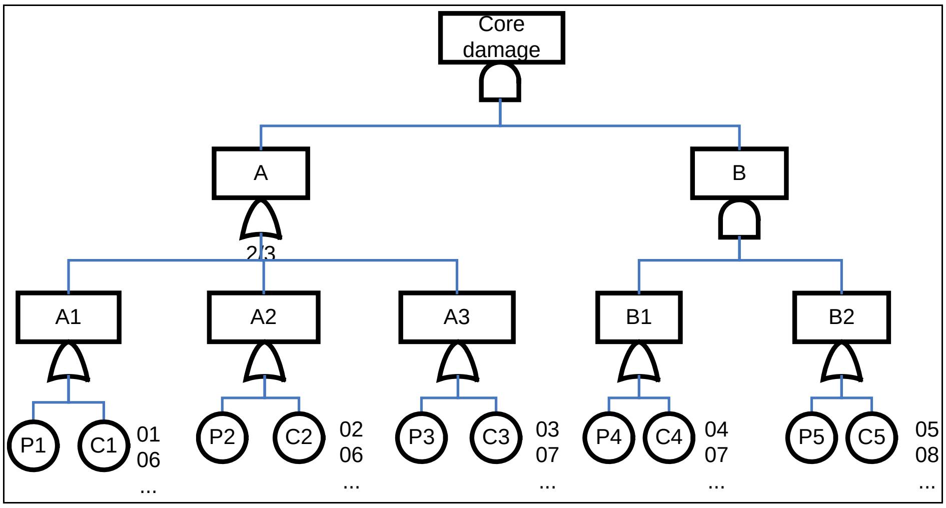

Fig. 3. Fault tree of the hypothetical safety systems

As a result of the fault tree analysis minimal cut sets (MCS) are generated. Minimal cut set is a set of basic events which, if occurred, definitely lead to the top event, i.e. to core damage in our case. Minimal cut set is a cut set such that after removal of any basic events from it is no more a cut set. For the considered case minimal cut sets include failures of pumps, failures of cables and failures of both pumps and cables, for example:

$$\begin{aligned} &P1\times P2\times P4\times P5+\\ &+P1\times P2\times P4\times P5+\\ &+C1\times P2\times P4\times P5+,\\ &+C1\times C3\times C4\times C5 \end{aligned} \tag{2}$$

where *P1..P5* are pump failure basic events; *C1..C5* are cable failure basic events.

The cables C1-C5 are located in the compartments 01-08. It is conservatively assumed that the AE in a compartment leads to a failure of all cables located in that compartment. In the presented example there are no AE scenarios which directly lead to core damage. Really, even when two cables are damaged in case of AE in the compartment 06 leading to a failure of the system A, the system B remains in the operation and in case of AE in the compartment 07 the trains A3 and B1 fail, but both systems A and B are still operable. Usually for the AE analysis the fault tree is modified replacing corresponding equipment failure basic events by basic event representing single area event. An example is provided in Fig. 4.

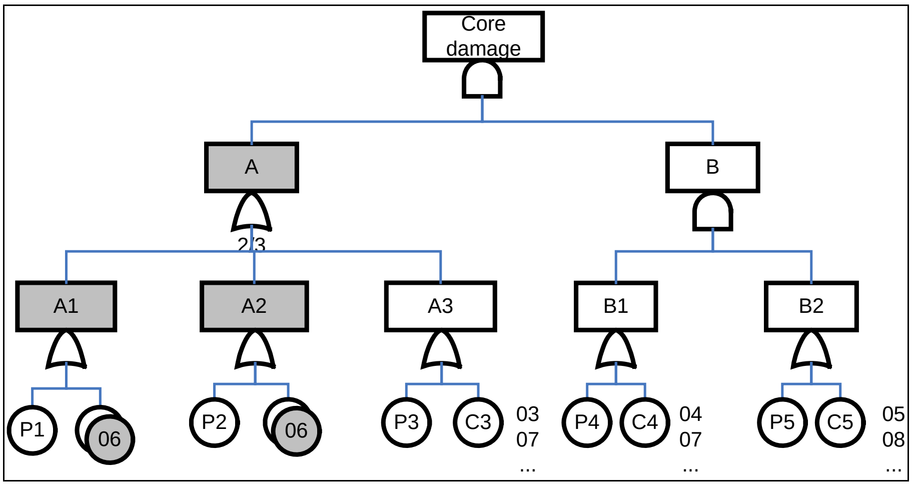

Fig. 4. Using exchange events for single AE analysis

In case of AE in the compartment 06 the corresponding basic event and the fault tree nodes are set to TRUE (shaded nodes). Minimal cut sets in this case are:

$$\begin{aligned} &AE06 \times P4 \times P5 + \\ &AE06 \times C4 \times P5 + \\ &AE06 \times P4 \times C5 + \\ &AE06 \times C4 \times C5 \end{aligned}, \qquad (3)$$

where *AE06* is a basic event which models AE in the compartment 06, *P4,P5* are pump failure basic events; *C4,C5* are cable failure basic events.

This shows that the core damage is possible only if the area event is accompanied by at least two failures of the equipment of trains B1 and B2. In order to analyse area events in other compartments the model should be changed for each scenario.

### 3.3. Scenario identification problem for multiple AE analysis

The approach described above works well for the analysis of single compartment AE. For multiple AE scenarios their identification becomes more complicated. The main problem is related to the selection of the most important or most hazardous scenarios, i.e. such sets of compartments where multiple area events would lead to reactor damage with higher probability. For the provided hypothetical example this is obvious just from the figure that scenarios *AE06×AE07×AE08* or *AE06×AE07×AE05* are the most important as all safety cables are affected. For real NPP where each cable passes several compartments and each compartment contains tens of cables a qualitative selection of scenarios is impossible. Changing the model for each scenario becomes overwhelming work as the number of scenarios $N_S$ is equal to the number of possible compartment combinations:

$$N_S = \sum_{k=2}^{k_{\max}} C_n^k = \sum_{k=2}^{k_{\max}} \frac{n!}{k!(n-k!)}, \tag{4}$$

where $n$ – the total number of compartments, $k$ – a number of compartments included in the scenario and $k_{max}$ is a maximum number of compartments to be included in a single scenario. Even for the hypothetical example there are 28 two-compartment AEs and 56 three-compartment AEs against 8 single-compartment AEs. For the considered INPP case with tens of compartments being analysed the number of scenarios is enormous.

### 3.4. Application of fault trees for the identification of multiple AE scenarios

For the analysed event as the fire barriers and distance are no more an obstacle for smoke spread any combination of AE in compartments is possible. In order to identify the most important scenarios it is proposed by the author to apply fault tree method further developing the existing fault trees. As a cable may fail due to area event in any room where it is located the fault tree may be complemented with OR-gate:

$$F_c = AE_1 \cup AE_2 \cup \ldots \cup AE_n = \bigcup_{i=1}^{n} AE_i, \tag{5}$$

where $F_c$ – cable failure; $AE_i$ – area event in a room $i$ where the cable is located, $1..n$ – cable path.

Modified fault tree is presented in Fig. 5.

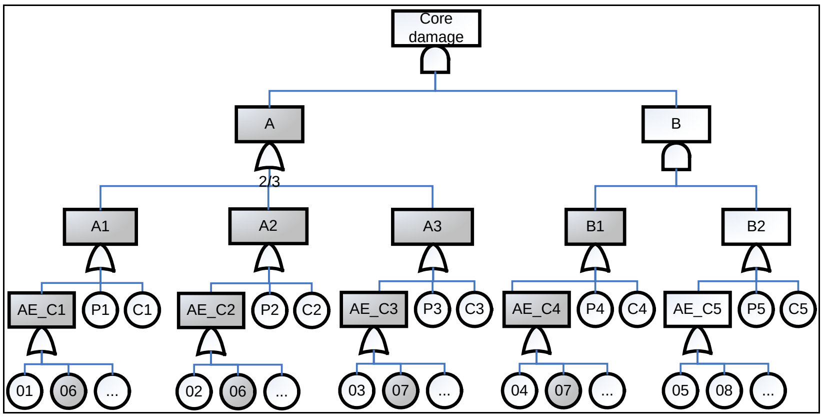

Fig. 5. Core damage FT complemented with AE nodes

In case of AE in the compartments (for example, 06 and 07) the corresponding basic events and the fault tree nodes become TRUE (shaded nodes). Minimal cut sets for such fault tree contain basic events representing both area events and equipment failures:

$$\begin{aligned} &AE06 \times AE07 \times AE08 + \\ &AE06 \times AE07 \times P5 + \\ &AE06 \times AE07 \times C5 \end{aligned} \tag{6}$$

This shows that in case of AE in the compartments 06 and 07 the safety barrier still exists, but there is no safety barrier against the AE in three compartments 06, 07 and 08.

An advantage of such approach is that minimal cut sets are generated by PSA software based on the fault tree information.

In order to identify the multiple AE scenarios with no or minimal safety barrier a high probability is assigned to the AE basic events. Minimal cut sets containing such basic events obtain the higher probability and "floats up" in the minimal cut set list.

## 4. ANALYSIS OF MULTIPLE ROOMS AREA EVENT AT INPP

### 4.1. PSA model update

The analysis provided in this paper was limited to the block D2 of INPP main building only. For this particular case the compartments with cables of the safety systems are identified. The INPP PSA model and cable paths data collected for the AE analysis are used as information source. A list of the compartments protected with AFFS system, i.e. having AFFS as a potential flooding source, is compiled. The compartments which are indicated in both lists are included in the further analysis. In the considered case in total 56 compartments were chosen for the further analysis.

INPP PSA model is developed using RiskSpectrum PSA® software. Cable failures are modelled as the basic events and the information about cable paths is stored in the model database as the basic events attributes where each attribute corresponds to a room number. There are totally 114 basic events related to selected 56 compartments. Based on these information 114 fault trees representing cable failures due to AE were developed. The original fault trees are then complemented by transfer to AE fault tree (Fig. 6).

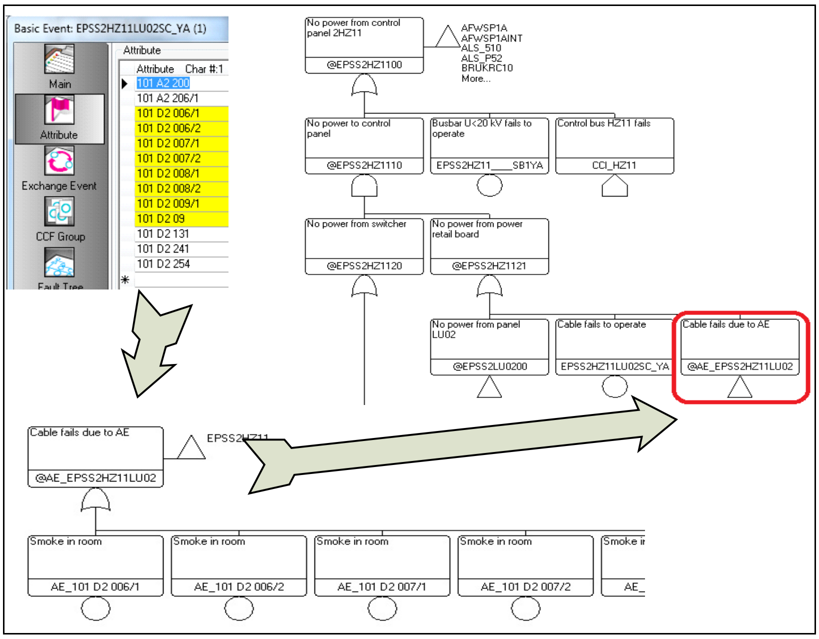

Fig. 6. INPP PSA model update for multiple AE analysis

Event tree for manual shutdown initiating event (IE) was used for the analysis as it was assumed that in case of multiple AE the operators will manually shut down the reactor due to loss of the safety systems.

### 4.2. Analysis results

When the fault trees are structured, the MCS generations is made by PSA software. Basically, the generation of cut sets is made according to a top-down algorithm that starts by creating a cut set with the top gate as the only element. This top gate is then substituted by its inputs. If the gate is an AND-gate, all its inputs are added to the cut set, thus increasing the number of elements in the cut set. If the gate is an OR-gate, new cut sets are created, one for each input to the OR-gate. These new cut sets are similar to the original one but with the OR-gate substituted by one of its inputs. This substitution process is carried out until all cut set elements are either basic events or modules. The cut set list is then reduced by eliminating non-minimal and repeating cut sets. A cut-off procedure is also applied in order to reduce computational time. MCS which probabilities are below predefined cut-off value (either absolute or relative) are excluded [6].

As a result of modified INPP PSA model analysis above 900 minimal cut sets were generated. Top 20 MCS are presented in Table 1. Last characters in BE code replace the actual numbers of INPP cable rooms. Due to understandable reasons the actual room numbers cannot be presented.

Table 1. List of minimal cutsets (excerpt from the list generated)

| No | Probability | % | IE | BE 1 | BE 2 | BE 3 | BE 4 |
|---|---|---|---|---|---|---|---|
| 1 | 1.0E-04 | 0.4 | IE_EF | AE_D2_C | AE_D2_AA | AE_D2_CC | AE_D2_X |
| 2 | 1.0E-04 | 0.4 | IE_EF | AE_D2_F | AE_D2_BB | AE_D2_CC | AE_D2_X |
| 3 | 1.0E-04 | 0.4 | IE_EF | AE_D2_C | AE_D2_CC | AE_D2_M | AE_D2_X |
| 4 | 1.0E-04 | 0.4 | IE_EF | AE_D2_B | AE_D2_C | AE_D2_M | AE_D2_Y |
| 5 | 1.0E-04 | 0.4 | IE_EF | AE_D2_C | AE_D2_E | AE_D2_CC | AE_D2_X |
| 6 | 1.0E-04 | 0.4 | IE_EF | AE_D2_D | AE_D2_CC | AE_D2_G | AE_D2_Y |
| 7 | 1.0E-04 | 0.4 | IE_EF | AE_D2_BB | AE_D2_CC | AE_D2_G | AE_D2_Y |
| 8 | 1.0E-04 | 0.4 | IE_EF | AE_D2_C | AE_D2_CC | AE_D2_G | AE_D2_X |
| 9 | 1.0E-04 | 0.4 | IE_EF | AE_D2_CC | AE_D2_G | AE_D2_H | AE_D2_X |
| 10 | 1.0E-04 | 0.4 | IE_EF | AE_D2_A | AE_D2_AA | AE_D2_BB | AE_D2_CC |
| 11 | 1.0E-04 | 0.4 | IE_EF | AE_D2_C | AE_D2_G | AE_D2_Z | AE_D2_AB |
| 12 | 1.0E-04 | 0.4 | IE_EF | AE_D2_AA | AE_D2_CC | AE_D2_H | AE_D2_Y |
| 13 | 1.0E-04 | 0.4 | IE_EF | AE_D2_AA | AE_D2_BB | AE_D2_CC | AE_D2_Z |
| 14 | 1.0E-04 | 0.4 | IE_EF | AE_D2_B | AE_D2_C | AE_D2_AA | AE_D2_Y |
| 15 | 1.0E-04 | 0.4 | IE_EF | AE_D2_C | AE_D2_CC | AE_D2_G | AE_D2_Z |
| 16 | 1.0E-04 | 0.4 | IE_EF | AE_D2_C | AE_D2_G | AE_D2_N | AE_D2_Y |
| 17 | 1.0E-04 | 0.4 | IE_EF | AE_D2_C | AE_D2_F | AE_D2_Z | AE_D2_AB |
| 18 | 1.0E-04 | 0.4 | IE_EF | AE_D2_D | AE_D2_E | AE_D2_CC | AE_D2_X |
| 19 | 1.0E-04 | 0.4 | IE_EF | AE_D2_D | AE_D2_F | AE_D2_CC | AE_D2_X |
| 20 | 1.0E-04 | 0.4 | IE_EF | AE_D2_E | AE_D2_BB | AE_D2_CC | AE_D2_Z |

The results showed that multiple AE scenarios, when INPP has no safety barriers, exist. The events which would cause damage of all equipment in any of the presented combinations of rooms would lead to reactor core damage without any possibility to recover the situation. In order to understand the influence of each room on the total risk the importance and sensitivity analyses were performed. The importance measures are [6]:

The Fussell-Vesely (FV) importance for a basic event is the ratio between the unavailability based only on all MCSs where the basic event *i* is included and the nominal top event unavailability:

$$I^{FV}{}_{i} = \frac{Q_{TOP}(MCS_{including}\, i)}{Q_{TOP}}, \qquad (7)$$

where $I^{FV}{}_{i}$ – FV importance; $Q_{TOP}$ – nominal top event unavailability; $Q_{TOP}(MCS\ including\ i)$ – unavailability based only on MCSs where the basic event *i* is included.

The risk decrease factor (RDF) calculated as:

$$I^D{}_i = \frac{Q_{TOP}}{Q_{TOP}(Q_i = 0)}, \tag{8}$$

where $I^D{}_i$ – RDF;
$Q_{TOP}(Q_i=0)$ – top event unavailability where unavailability of the basic event *i* is set to zero.

The risk increase factor (RIF) calculated as:

$$I^I{}_i = \frac{Q_{TOP}(Q_i = 1)}{Q_{TOP}}, \tag{9}$$

where $I^I{}_i$ – RIF;
$Q_{TOP}(Q_i=1)$ – top event unavailability where unavailability of the basic event *i* is set to one.

The fractional contribution (FC) calculated as:

$$I^F{}_i = 1 - \frac{1}{I^D{}_i}. \tag{10}$$

The sensitivity *S* is calculated as [6]:

$$S = \frac{Q_{TOP,U}}{Q_{TOP,L}}, \tag{11}$$

where $Q_{TOP,U}$ – top event results where unavailability of the basic event *i* is multiplied by a sensitivity factor (normally equal to 10);
$Q_{TOP,L}$ – top event results where unavailability of the basic event *i* is divided by the sensitivity factor.

The results of importance and sensitivity analyses are presented in Table 2.

Table 2. Importance and sensitivity analysis results

| **No** | **BE** | **Value** | **FV** | **FC** | **RDF** | **RIF** | **S** |
|---|---|---|---|---|---|---|---|
| 1 | AE_D2_CC | 0.2 | 6.45E-01 | 5.42E-01 | 2.18E+00 | 2.19E+00 | 4.23E+00 |
| 2 | AE_D2_C | 0.2 | 4.83E-01 | 3.78E-01 | 1.61E+00 | 1.97E+00 | 2.97E+00 |
| 3 | AE_D2_BB | 0.2 | 3.31E-01 | 2.44E-01 | 1.32E+00 | 1.72E+00 | 2.21E+00 |
| 4 | AE_D2_M | 0.2 | 2.50E-01 | 1.78E-01 | 1.22E+00 | 1.57E+00 | 1.87E+00 |
| 5 | AE_D2_F | 0.2 | 2.45E-01 | 1.74E-01 | 1.21E+00 | 1.56E+00 | 1.85E+00 |
| 6 | AE_D2_AA | 0.2 | 2.45E-01 | 1.74E-01 | 1.21E+00 | 1.56E+00 | 1.85E+00 |
| 7 | AE_D2_X | 0.2 | 2.44E-01 | 1.74E-01 | 1.21E+00 | 1.56E+00 | 1.85E+00 |
| 8 | AE_D2_Z | 0.2 | 2.44E-01 | 1.74E-01 | 1.21E+00 | 1.56E+00 | 1.85E+00 |
| 9 | AE_D2_Y | 0.2 | 2.44E-01 | 1.73E-01 | 1.21E+00 | 1.56E+00 | 1.85E+00 |
| 10 | AE_D2_N | 0.2 | 1.84E-01 | 1.28E-01 | 1.15E+00 | 1.44E+00 | 1.62E+00 |
| 11 | AE_D2_G | 0.2 | 1.74E-01 | 1.20E-01 | 1.14E+00 | 1.41E+00 | 1.58E+00 |
| 12 | AE_D2_E | 0.2 | 1.70E-01 | 1.17E-01 | 1.13E+00 | 1.41E+00 | 1.57E+00 |
| 13 | AE_D2_H | 0.2 | 1.35E-01 | 9.24E-02 | 1.10E+00 | 1.33E+00 | 1.45E+00 |
| 14 | AE_D2_D | 0.2 | 1.35E-01 | 9.24E-02 | 1.10E+00 | 1.33E+00 | 1.45E+00 |
| 15 | AE_D2_AB | 0.2 | 1.27E-01 | 8.64E-02 | 1.09E+00 | 1.31E+00 | 1.42E+00 |
| 16 | AE_D2_B | 0.2 | 1.19E-01 | 8.10E-02 | 1.09E+00 | 1.29E+00 | 1.39E+00 |

Considering the assumptions accepted, the provided results are certainly very conservative. More detailed analysis using both deterministic and probabilistic approaches would provide more realistic picture. The presented results could be the first step for such work indicating the areas where such analysis should be concentrated.

### 4.3. Conclusions

An approach for the probabilistic multiple compartment AE analysis was proposed and is based on the application of modified fault trees. Proposed approach was tested using Ignalina NPP PSA model. The application of this method allows to identify the combinations of the compartments which are the most important for NPP safety. This allows focusing the further analyses and the safety improvement measures on the identified rooms thus reducing the cost and increasing the efficiency. The analysis showed that considered event of multiple AFFS actuations due to smoke spread via ventilation system might jeopardize even nuclear safety of the plant and if INPP would be in operation a special measures should have been taken.

The proposed approach may be applied for the analysis of the area events and external events – both natural and human-induced. Taking into account the last years' climate changes and a number of forest fires happening in the latest years in Europe and Russia such analysis may be of current concern to a number of nuclear objects and could be of interest of the safety assessment of other objects where spurious operation of automatic fire extinguishing could damage important equipment.

## ACKNOWLEDGEMENT

The author would like to dedicate this paper to his father, Sergey Voronov, who devoted all his experience and knowledge to improvement of fire safety of INPP and who first proposed the idea of the presented work.

## REFERENCES

1. KUPČIŪNIENĖ K., ALZBUTAS R. Updated probabilistic analysis of external events data and safety of the nuclear power plant in Lithuania. ICONE 17. Proceedings of 17th international conference on nuclear engineering. Brussels. Belgium. 2009 July 12–16.
2. ALZBUTAS R., AUGUTIS J., URBONAS R. Risk and sensitivity analysis in relaxation to external events. Proceedings of International Conference Nuclear Energy in Central Europe 2001. Portorož. Slovenia. 2001 September 10–13.
3. POŠKAS P., ŠIMONIS R., ZUJUS R., KILDA R., SIRVYDAS A., KOLESNIKOVAS J. Fire hazard analysis at Ignalina nuclear power plant. *Kerntechnik,* 2005, Vol. 70, No. 4, p. 207–212.
4. JUNG W. S., LEE Y-H., YANG J-E. Development of a new quantification method for a fire PSA. *Reliability Engineering and System Safety,* 2009, Vol. 94, p. 1650–1657.
5. BEDFORD, Tim, COOKE, Roger. *Probabilistic Risk Analysis Foundations and Methods*. Cambridge: Cambridge University Press, 2001. 393 p. ISBN 0 521 77320 2.
6. RiskSpectrum Analysis Tools. Theory Manual. Relcon Scandpower AB. Version 3.0.0.

# TRITIUM LOCALIZATION IN THE BULK OF NEUTRON IRRADIATED BERYLLIUM PEBBLES

**V. Zubkovs, E. Pajuste, G. Ķizāne, A. Vītiņš, A. Matīss**
*LU Institute of Chemical Physics*
*Laboratory of Radiation Chemistry of Solids*
*Kronvalda blvd. 4, LV-1586 Riga – Latvia*
*Phone +371 67033883*
*Email: vitaly.zubkov@gmail.com*

ABSTRACT

Beryllium pebbles will be used as a neutron multiplier in a solid tritium breeding blanket for fusion reactors. Tritium inventory in beryllium as a result of neutron-induced transmutations is a significant safety and technological issue for the operation of the breeding blanket. That is why investigation of tritium accumulation process and behaviour in the beryllium pebbles after neutron irradiation in fusion reactor is of a great importance.

In this study beryllium pebbles irradiated with neutrons in the PBA (Pebble Bed Assembly) experiment have been investigated. PBA irradiation experiment had been performed in the frame of the European Programme for development of the helium cooled pebble bed (HCPB) in the High Flux Reactor HFR in Petten (Netherlands). Its purpose was to test thermo-mechanical behaviour of breeder pebble-beds under conditions relevant to the ones in the fusion reactor. The issue of beryllium neutron-induced transmutations is tritium production and accumulation in the bulk of metal. Tritium is localised in beryllium in forms of the gas $T_2$, radicals $T^o$ and ions $T^+$. In order to determine the abundance ratios of chemical forms, the method of beryllium dissolution with and without presence of chemical scavengers has been used. Dominant chemical form of the tritium accumulated in beryllium pebbles is gas molecules $T_2$. Gaseous tritium could be trapped in a technological void at pebble centre and in the pores, located in the bulk of pebbles. Pebbles of a ~1 mm diameter have been analysed and difference in tritium distribution has been observed.

Keywords: beryllium, tritium inventory, chemical forms of tritium, beryllium structure.

## 1. INTRODUCTION

Secure and sustainable energy sources are required to maintain economical, environmental and political stability. Researchers worldwide are working on development of a range of safe, efficient and sustainable energy production technologies. Nuclear fusion of hydrogen isotopes is one of the most promising ones (1). This is the process that powers the Sun and other stars and can take place in a fusion reactor on the Earth. Released energy can be used for generation of electricity. Research on solving fundamental and technological problems in development of fusion reactor is carried out worldwide.

$$^{2}H + {}^{3}H \rightarrow {}^{4}He + n + 17.6\ MeV \qquad (1)$$

Deuterium is the stable isotope of hydrogen that can be extracted from the sea water. Whereas tritium is radioactive isotope with relatively short half-life (12.3 years) and has to be produced artificially by interaction of neutrons with lithium isotopes, according to reactions (2.3). Tritium could be produced in reaction of $^{6}$Li with low energy thermal neutrons, the cross-section of the reaction – 940.4 barns. $^{7}$Li can also take part in generation of tritium, but reaction requires neutrons with higher energy and its cross-section is considerably smaller (0.3 barns).

$$^{6}Li + n\ \ (thermal) \rightarrow {}^{4}He + {}^{3}H \qquad 940.4\ b \qquad (2)$$

$$^{7}Li + n\ \ (E > 17MeV)\ \rightarrow {}^{4}He + {}^{3}H + n \qquad 0.026\ b \qquad (3)$$

The European Helium-Cooled Pebble Bed (HCPB) is one of the tritium breeder blanket concepts that will be tested in ITER (first nuclear-grade fusion machine in the world) as a test blanket modules [1]. Furthermore, the breeding blanket is one of the most important components in the DEMO (first fusion machine that will produce electricity). DEMO blanket has to withstand neutron flux typically 15–30 dpa/year under continuous operation [2]. Therefore, development of blanket structural and breeding materials is essential in the blanket construction for the DEMO. Test programmes for the blanket breeder are directed on in the fields of electromagnetic processes, neutronics, thermo mechanic properties of pebbles beds and tritium handling.

In the HCPB blanket neutron multiplier and breeder material are arranged in pebble beds between flat cooling plates (Fig. 1.). As the tritium breeder was selected lithium containing ceramic pebbles (2; 3), whereas beryllium pebbles are foreseen as a neutron multiplier (4).

$$ {}^{9}Be + n\ (>2\ MeV) \rightarrow 2\,{}^{4}He + 2n \qquad 0.580\ b \tag{4}$$

$$ \left. \begin{array}{lll} {}^{9}Be + n\ (4\text{-}10\ MeV) & \rightarrow {}^{10}Be & 0.010\ b \\ {}^{9}Be + n\ (2\text{-}4\ MeV) & \rightarrow {}^{10}Be & 0.085\ b \\ {}^{9}Be + n\ (1\text{-}2\ MeV) & \rightarrow {}^{10}Be & 0.020\ b \end{array} \right\} \rightarrow {}^{4}He + {}^{6}He \tag{5}$$

$$ {}^{6}He \rightarrow {}^{6}Li + \beta^{-} \qquad 0.8\ sec \tag{6}$$

$$ {}^{6}Li + n\ (thermal) \rightarrow {}^{4}He + {}^{3}H \qquad 0.950\ b \tag{7}$$

Tritium inventory in the beryllium as a result of neutron-induced transmutations (5; 6; 7) is a significant safety and technological issue for the operation of the breeding blanket. Tritium release is governed by several mechanisms: diffusion, surface desorption, trapping. In order to describe and predict tritium behaviour in the beryllium during fusion reactor operation pebbles were irradiated in high neutron flux reactor at the similar to fusion reactor blanket modules conditions.

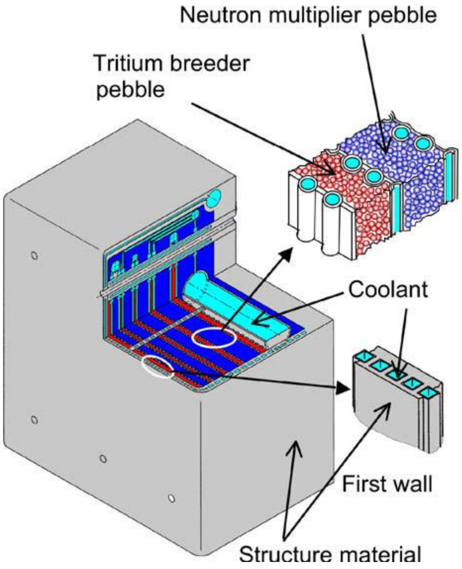

Fig. 1. Principle view of the typical pebble bed type blanket [2]

In this study, produced and accumulated tritium amount in the beryllium pebbles after neutron irradiation in the test-element HCPB Pebble-Bed Assembly has been measured and its distributions in the bulk of the pebbles and the abundance ratios of chemical forms of tritium $T^{o}$, $T^{+}$ and $T_2$ investigated.

## 2. METHODOLOGY

### 2.1. Samples

Beryllium pebbles for HCPB Pebble-Bed Assembly (further in the paper mentioned as PBA pebbles) experiment have been produced by the improved Rotating Electrode Process (REP) method that has been patented in 1999 by NGK, Inc [3]. Production method is based on making an arc between plasma dissoluble electrode and a rotating cylindrical beryllium consumable electrode, both of which being disposed in a closed container filled with an inert gas as an atmosphere. Beryllium droplets cool and solidify during their flight in helium.

Pebbles have been irradiated in the High Flux Reactor (HFR, Petten, the Netherlands) in the flux of fast neutron $3\text{-}4{\cdot}10^{25}$ $n{\cdot}m^{-2}$ ($E > 0.1$ MeV) during 294 full work days. Description of the samples and irradiation conditions are summarized in the Table 1.

Table 1. Description of the PBA beryllium pebbles

| | |
|---|---|
| **Manufacturer** | NGK Insulators Ltd., Handa City, Japan |
| **Production process** | Rotating Electrode Process (REP) |
| **Pebble diameter** | 0.9–1.1 mm |
| **Main impurities** | 2300 ppm BeO, 300 ppm Mg |
| **Irradiation time** | 294 days |
| **Neutron fluence (E>0.1 MeV)** | $3\text{–}4 \times 10^{25}$ $m^{-2}$ |
| **Irradiation temp.** | 420–820 K |
| **$^4$He content** | 300–600 appm |
| **Year of end of irradiation** | 2004 |

### 2.2. Chemical scavenger and dissolution method

In order to determine total tritium activity, bulk distribution and abundance ratios of chemical forms ($T_2$,$T^0$,$T^+$) in irradiated beryllium pebbles, chemical scavenger and dissolution method has been used. Pebbles were dissolved in the solutions of 2 mol·L$^{-1}$ $H_2SO_4$ and 2 mol·L$^{-1}$ $H_2SO_4$ + 0.5 mol·L$^{-1}$ $Na_2Cr_2O_7$ in a special setup [4]. Radical acceptor solvent (2 mol·L$^{-1}$ $H_2SO_4$ and 2 mol·L$^{-1}$ $H_2SO_4$ + 0.5 mol·L$^{-1}$ $Na_2Cr_2O_7$) is used for trapping in the solution radical form of tritium $T^0$ as chemically bonded ionic tritium $T^+$ (2. Table.). Hydrogen recombination rate is 2.6 times lower than hydrogen and chromate reactivity rate [5]. It allows to use chemical scavenger method for calculations of tritium chemical forms.

Table 2. Scheme of irradiated beryllium chemical dissolution

| **Dissolution processes in the 2 mol·L$^{-1}$ $H_2SO_4$ solvent**: |
|---|
| $Be_s + 2H^+_{aq} \rightarrow Be^{2+}_{aq} + 2H^0_{aq}$; recombination of radicals: $2H^0_{aq} \rightarrow H_{2\,g}$<br>$T^0_s \rightarrow T^0_{aq}$; recombination of radicals: $T^0_s + H^0_{aq} \rightarrow \mathbf{TH_g}$<br>$T^+_s \rightarrow \mathbf{T^+_{aq}}$; $T_{2\,s} \rightarrow \mathbf{T_{2\,g}}$ |
| **Dissolution processes in the 2 mol·L$^{-1}$ $H_2SO_4$ + 0.5 mol·L$^{-1}$ $Na_2Cr_2O_7$ solvent:** |
| $Be_s + 2H^+_{aq} \rightarrow Be^{2+}_{aq} + 2H^0_{aq}$; radical accepting: $14H^0_{aq} + Cr_2O_7^{2-}{}_{aq} \rightarrow 2Cr^{3+}_{aq} + 7H_2O_{aq}$<br>$T^0_s \rightarrow T^0_{aq}$; radical accepting*: $7T^0_{aq} + 7H^0_{aq} + Cr_2O_7^{2-}{}_{aq} \rightarrow 2Cr^{3+}_{aq} + \mathbf{THO_{aq}}$<br>$T^+_s \rightarrow \mathbf{T^+_{aq}}$; $T_{2\,s} \rightarrow \mathbf{T_{2\,g}}$ |
| Designations: T – tritium; s – in solid state; aq – in aqua solution; g – in gaseous form;<br>* – principle of reaction |

Molecular tritium $T_2$ and TH was measured with tritium monitor TEM 2100A with a proportional gas flow-through detector DDH 32 of the operating volume 300 cm$^2$. The tritium activity released into a gas phase at dissolution in the pure acid, $A_{T\ gas\ (acid)}$, is a sum of the activities of $T^2$ and $T^0$ (8). Activity of dissolved ionic tritium $T^+$ was measured with liquid scintillation method (9).

$$A_{T\ gas\ (acid)} = A_{T2} + A_{T0} \tag{8}$$

$$A_{T\ aqua\ (acid)} = A_{T+} \tag{9}$$

$$A_{T\ gas\ (dichromate)} = A_{T2} + x \cdot A_{T0} \tag{10}$$

$$A_{T\ aqua\ (dichromate)} = A_{T+} + (1 - x) \cdot A_{T0} \tag{11}$$

Acid with a scavenger of hydrogen decreases the radical hydrogen release by 90%. Then the activity of the tritium released into a gas phase and retained in the solution in the following mechanisms (10;11) (x has experimentally acquired and find to be 0.1). The contents of $T_2$, $T^0$, $T^+$ in a sample were determined separately from the corresponding differences in the activities. More detailed information about this method has been published previously [6].

### 2.3. Measuring of tritium distribution

Dissolution of beryllium pebbles was carried out in a special setup with carrier gas flow (Ar). During beryllium dissolution in acid solution hydrogen molecules that have been released were measured with a catarometer (catarometer is a detector based on the substantial difference in the thermal conductivity of the hydrogen and a carrier gas). The dissolution rate of beryllium and hereby the thickness of dissolved layer can be calculated from the hydrogen measurements. The catarometer is connected with tritium monitor TEM 2100A which measure tritium in the gas mixture flow. This chain connected equipment allows measure released tritium in real time of experiment and calculate gaseous ($T_2$+HT) tritium amount in dissolved layer of pebble. Distribution of gaseous tritium from surface to centre of pebble was calculated and visualised.

## 3. RESULTS AND DISCUSSIONS

### 3.1. Tritium chemical forms in the neutron irradiated beryllium

Tritium is produced in fast neutron induced transmutation of beryllium atoms (5; 6; 7). Tritium initial state is a non-equilibrium solution in the bulk of pebble. High temperature (for PBA pebbles irradiation temperature was 420–820 K depending on the location in the irradiation container) allows tritium atoms to rapidly diffuse. Diffusion of tritium is also influenced by the presence of thin oxide surface layer and of intragranular precipitates of BeO. Those atoms can either form gaseous tritium molecules $T_2$, be trapped by structure traps (such as intragranular He bubbles, closed porosity, grain boundaries etc.) or react with BeO to form $Be(OT)_2$.

The chemical scavenger method (described in chapter 2.2) allows distinguishing and measuring $T_2$, $T^0$ and $T^+$ tritium chemical forms in a solid beryllium matrix. In the PBA pebbles tritium is mostly accumulated in the molecular form $T_2$ 96±4% (Fig. 2.). Tritium can be trapped as $Be(OT)_2$. During dissolution the tritiated beryllium hydroxide ($Be(OT)_2$) reacts with an acid and tritium stays in solution as ionic form $T^+$. In the PBA specimens this form content is 3±2%. Nearly 1% of atomic tritium $T^0$ has been detected in the samples. It proves fact of the easy formation of gaseous tritium molecules in bulk of the pebbles.

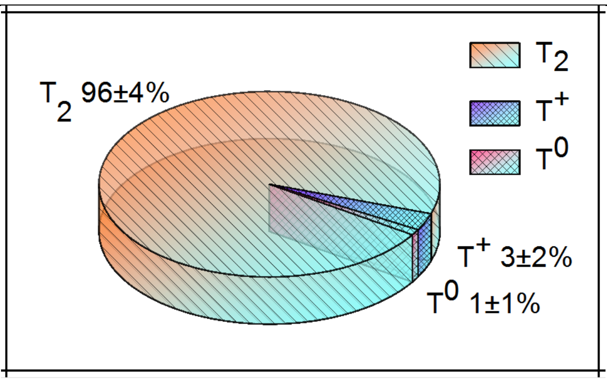

Fig. 2. Chemical forms of accumulated tritium in the PBA beryllium pebbles

### 3.2. Tritium distribution in a bulk of beryllium pebbles

Initially tritium distribution is even due to similar probability of neutron reaction throughout all the bulk of pebble. Further it is assumed to migrate to reach energetically more favourable locations, i.e. chemical traps, pores or surface, where it releases as a gas. These processes have already occurred during neutron irradiation and in a post-irradiation period might continue.

Tritium in the PBA beryllium pebbles (irradiated pebbles) mostly is accumulated as gas molecules $T_2$ (see chapter 3.1.). Determination of $T_2$ during dissolution allows obtain more detailed information on tritium location in the bulk of pebbles. Typical tritium distribution in a bulk of beryllium pebble is given in the Fig. 3. Tritium content has been given as radioactivity units (Bequerels - decays per second) per square centimetres in the dissolved layer of pebble.

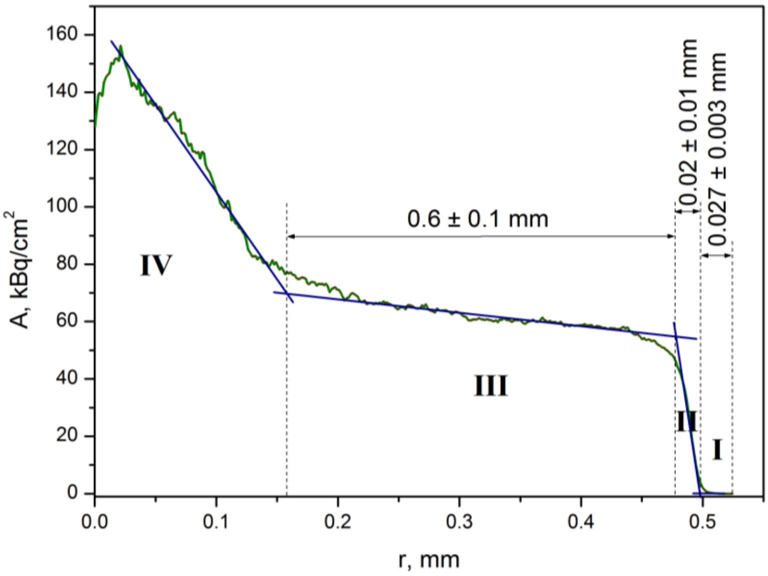

Fig. 3. Tritium distribution in the bulk of the PBA pebble

Investigation of tritium distribution in the bulk of the PBA pebbles shows that gaseous tritium is distributed uneven. Distribution was calculated by measuring tritium activity in the gas phase released during the dissolution. Therefore distribution of chemically bonded tritium $T^+$ was not determined (more likely most of it is in the surface oxide layer and in the oxide inclusions in the bulk) [6]. From the surface layer of pebbles (0.027±0.003 mm) gaseous tritium has been escaped (Fig. 3. sector I). This layer probably is mechanically damaged in the pebble-packing processes; therefore, it might contain lot of small cracks which allow tritium easy to diffuse. In the sector II (Fig. 3.) rapid decrease of tritium in the direction to the surface was observed. It could be caused by diffusion of the tritium to the surface of the pebble where it desorption occurs. In the sector III (main part of the pebble) tritium is evenly localised. Large fraction of gaseous species is trapped also in the technical void (technological formation fabricated by REP method [7]) in the centre of PBA pebble (sector IV). This void prevents swelling of the metallic beryllium pebble since gaseous species are accumulated there instead of lattice [3]. The experimental data (Fig. 4.) shows that gaseous tritium has tendency to accumulate in this part of pebble. Technical void in the centre of pebble stores gaseous tritium and might delay detritiation (beryllium cleaning from tritium) of beryllium pebbles.

The values of total accumulated tritium inventory in each of the PBA pebble is fluctuating between 4–8 GBq/g. It is due to position of the pebble in the irradiation container during the neutron irradiation process (the temperature is graduating between 420–820 K and neutron flux is not homogeneous). Structure of the pebble also is significant factor influencing tritium distribution. Nevertheless, overall tendencies of gaseous tritium distribution in irradiated pebbles can be estimated (Fig. 4.).

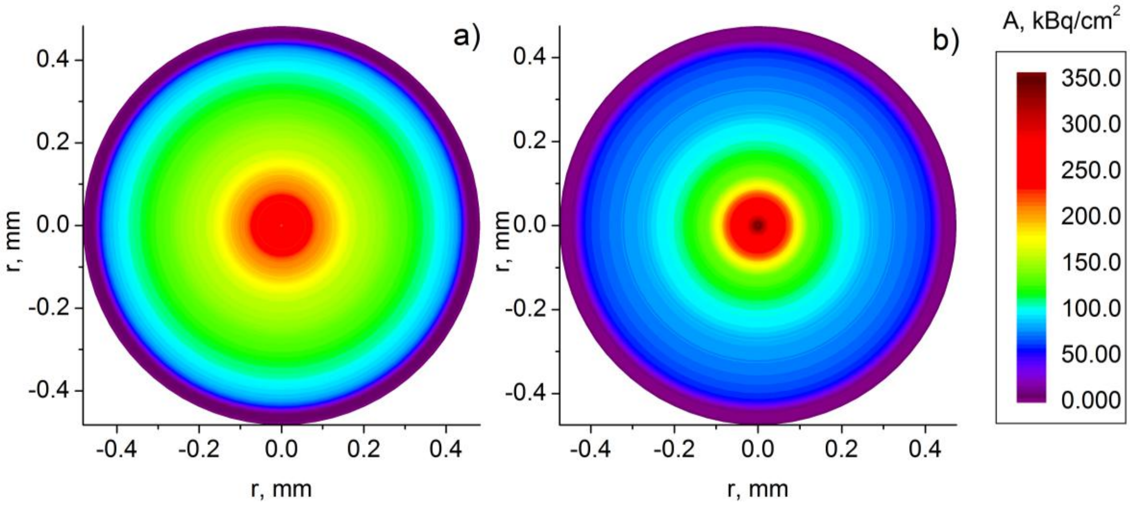

Fig. 4. Tritium distribution in bulk of the PBA pebbles in two examples: a) tritium is gradually distributed in the bulk of the pebble; b) tritium is trapped in the technical void

## 4. CONCLUSIONS

In beryllium pebbles irradiated in the PBA experiment tritium is mainly localised as gaseous tritium $T_2$. Abundance ratios of ionic $T^+$ and radical $T^0$ tritium forms are 3% and 1%, respectively.

Gaseous tritium has escaped from ~0.027 mm depth surface layer of the pebbles. But in the main part of the pebbles it is uniformly distributed due to tritium diffusion process.

Technical void in the centre of the pebble stores gaseous tritium and therefore can delay the detritiation process.

## 5. ACKNOWLEDGMENTS

This work is performed with the Europe social found support and the member stuff of LU institute of chemical physics laboratory of radiation chemistry of solids is also gratefully acknowledged.

## REFERENCES

1. BOCCACCINI, L. V., SALAVY, J. F., BEDE, O., NEUBERGER, H., RICAPITO, I., SARDAIN, P., SEDANO, L. The EU TBM systems: Design and development programme. *Fusion Engineering and Design*, 2009, Vol. 84, p. 333 – 337.
2. NISHITANI, T., TANIGAWA, H., JITSUKAWA, S., NOZAWA, T., HAYASHI, K., YAMANISHI, T., TSUCHIYA, K., MÖSLANG, A., BALUC, N., PIZZUTO, A., HODGSON, E. R., LAESSER, R., GASPAROTTO, M., KOHYAMA, A., KASADA, R., SHIKAMA, T., TAKATSU, H., ARAKI, M. Fusion materials development program in the broader approach activities. *Journal of Nuclear Materials*, 2009, Vol. 386–388, p. 405–410.
3. ISHITSUKA, E., KAWAMURA, H., SAKAMOTO, N., NISHIDA, K. Process for preparing metallic beryllium pebbles. U.S. Pat. 5958105, 1999; EU Pat. EP0872851B1, 1998.
4. TILIKS, J., KIZANE, G., VITINS, A., KOLODISKA, E. Mangetic field effects on tritium release from neutron-irradiated beryllium pebbles. *Nuclear Technology*, 2007, Vol. 159, No. 3, p. 245–249.
5. ANBAR, M., ROSS, A.B., ROSS, F. *Selected specitic rates of reactions of transients from water in aqueous solution. II. Hydrogen atom*. Washington: U.S. Government printig office, 1975. 56 p. NSRDS-NBS 51.
6. PAJUSTE, E., VITINS, A., KIZANE, G., ZUBKOVS, V., BIRJUKOVS, P. Tritium distribution and chemical forms in the irradiated beryllium pebbles before and after thermoannealing. *Fusion Engineering and Design*, 2011, In press.
7. NISHIDA, K., SAKAMOTO, N. Metallic beryllium pebble. Japanese Pat. JP1993000017553, 1994.

CYSENI 2011, May 26–27, Kaunas, Lithuania
ISSN 1822-7554, www.cyseni.com

# SEPARATION OF URANIUM FROM POST-LEACHING SOLUTIONS BY SOLVENT EXTRACTION

**G. Zakrzewska-Trznadel, B. Zielińska, K. Frąckiewicz, I. Herdzik-Koniecko,**
**A. Miśkiewicz, K. Szczygłów, P. Biełuszka, Ł. Steczek, E. Chajduk**
*Institute of Nuclear Chemistry and Technology*
*16 Dorodna str., 03-195 Warsaw – Poland*
*Phone +48 22 504 1214*
*Email: g.zakrzewska@ichtj.waw.pl*

**S. Wołkowicz**
*Polish Geological Institute-National Research Institute,*
*4 Rakowiecka Street, 00-975 Warszawa – Poland*

ABSTRACT

This article is related to the research on the possibility of uranium extraction from domestic resources. Studies are carried out under the project realized by Institute of Nuclear Chemistry and Technology and Polish Geological Institute and concern the development of effective technology of uranium extraction from low-grade ores and finally production of pure yellow cake - $U_3O_8$. First step of the procedure of uranium extraction from the bedrock is leaching by sulphuric acid. The liquid-liquid extraction of post-leaching solutions followed by ammonia precipitation can be employed to obtain final product, yellow cake – $U_3O_8$.

The effect of the different parameters like extractants, sulphuric acid and uranium concentrations affecting the recovery of uranium was investigated. The use of different reagents as strip solutions of the loaded uranium in organic phase was also investigated.

An alternative method to traditional methods of extraction i.e., the technique of extraction with application of membrane contactors with possible concurrent or counter current flows of two phases – water and organic will be examined.

Keywords: uranium ores, post-leaching solutions, solvent extraction, extractants.

## 1. INTRODUCTION

Uranium, the heaviest element occurring in nature, is of great importance as a key element and a basic raw material for nuclear reactor fuels. It occurs in numerous minerals such as uraninite ($UO_2$+$UO_3$), carnotite ($K_2(UO_2)_2(VO_4)_2 \cdot 2H_2O$), uranophane $(H_3O)Ca[UO_2][SiO_4]_2 \cdot 3H_2O$, brannerite ($UTi_2O_6$), coffinite ($USiO_4 \cdot nH_2O$), autinite $(Ca(UO_2)_2(PO_4)_2 \cdot 10\text{-}12H_2O$. It is also found in phosphate rock, lignite, monazite sands and can be recovered commercially from these sources [1]. The treatment procedures commonly used to recover uranium from the bedrock comprise the preconcentration of the ore followed by a leaching process to bring uranium into solution. The leaching of the ore is usually carried out either by sulphuric acid or sodium carbonate. The recovery of U(VI) from the uranium-bearing solutions after leaching can be carried out by ion-exchange, solvent extraction, direct precipitation and other techniques [1, 2].

Development of Polish Nuclear Power Programme and the start-up of the first nuclear power plant in the country enforce the necessity of the identification of domestic uranium resources and the assessment of their exploitation possibilities. The project realized by Institute of Nuclear Chemistry and Technology concerns the development of effective technology of uranium extraction from low-grade indigenous ores and finally production of pure yellow cake – $U_3O_8$.

Main uranium resources in Poland are summarized in Table 1. Analysis of uranium bearing ores showed that Lower Triassic sandstones from Peribaltic syneclise and Lower Ordovician Dictyonema shale from North-East Poland (e.g. Rajsk Deposits) are the most perspective formations with high uranium concentration, locally reaching even 1.5%U (recent analysis of archivic samples). The uranium deposits of dictyonemic shales in Podlasie region are spread out on the large area with the thickness up to 2 m however uranium concentrations in these ores are rather low.

Table 1. Uranium ore resources in Poland (resource prognostic are those situated deeper than 1000 m) according to OECD NEA Red Book, 2008 [3].

| **Region** | **Identified resources $U_{nat}$ [ton]** | **Prognostic resources $U_{nat}$ [ton]** | **Uranium content in ore [ppm]** | **Deposit type** |
|---|---|---|---|---|
| Rajsk | 5320 | 88850 | 250 | Black shales |
| Okrzeszyn | 940 | ? | 500–1100 | other |
| Grzmiąca | 790 | ? | 500 | Sandstone tabular |
| Wambierzyce | 220 | 2000 | 236 | Black shales |
| Baltic region | ? | 10000 | ? | Sandstone tabular |
| Grand total | 7270 t U > 45 y NPP 1000 MW | 100000 t U 625 y NPP 1000 MW | | |

Areas promising for uranium deposits prospecting in Poland are shown in Fig. 1. where the map shows the uranium ore occurrences (exhausted, identified and promising). Low quality of identified uranium resources and their deep location make their utilization would be possible if considerable progress will be gained in uranium recovery from such lean ores.

The valuable source of uranium can be the tailings from phosphate fertilizers plants [5]. In the present work at the beginning of the extraction process, uranium was leached from the ground ore by solid-liquid extraction using sulphuric acid. The post-leaching solution was separated from the leached ore by filtering and washing and then concentrated and purified using solvent extraction or ion exchange resins. Nowadays, the literature reports a great variety of extractants that have been used for the extraction of uranium from its ores [5–10]. Of the extractants studied to date, the neutral organophosphorus extractant tri-n-butylphosphate (TBP) has probably received the most attention and the use of it on a commercial scale for the recovery of uranium (VI) from its ores and spent nuclear fuel is well known [6]. However, the selectivity of TBP is not high, as well as its radiolytic stability. Therefore, it is necessary to search for and develop some new extractants. Other organophosphorus extractants, including bis-2-ethylhexyl phosphoric acid (HDEHP) have also been examined for the extraction of uranium from different samples [5]. Daoud et al. have reported the increase of U(IV) extraction by HDEHP with the increase of the extractant concentration and the decrease of phosphoric acid concentration.

Fig. 1. Areas promising for uranium deposits prospecting in Poland [4]: 1 – exhausted uranium ores; 2 – uranium deposits of lean ores; 3 – area of occurrence of uranium bearing dictyonema shales; 4 – uranium ore occurrence in Triassic sandstones; 5 – area promising for uranium deposits prospecting

Recently the use of calixarenes, which are macrocyclic products of phenol-formaldehyde condensations, as extractants for many kinds of metal ions has been reported. In addition to calixarenes resorcinarenes as new extractants for the extraction of metals were studied. A solvent extraction separation of uranium with a new calix [4] resorcinarene bearing eight hydroxamic acid groups (C4RAHA) has been investigated by Jain [7]. The newly synthesized calix[4]resorcinarene-hydroxamic acid (C4RAHA) has shown high affinity and specificity for uranium(VI) in presence of large quantities of associated metal ions. Quantitative extraction of uranium was possible in ethyl acetate solution of C4RAHA at pH 8.0. Mohanty et al. have reported the extraction of uranium(VI) with LIX-860 (a mixture of 5-dodecylsalicylaldoxime and 3-nonyl acetophenone oxime in kerosene) and its mixture with Versatic 10 (alkyl mono carboxylic acids) in various diluents [8]. It was observed that the percentage of extraction increases with increase in equilibrium pH. Maximum extraction was obtained (93.7%) with 10% (v/v) LIX 860 in kerosene at equilibrium pH 4,6. Quantitative extraction was achieved with the mixture of 2% (v/v) LIX860 and 0,5% (v/v) Versatic 10 in kerosene at equilibrium pH 4.85. The distribution constant of uranium(VI) was found to be maximum with 2% LIX 860 in kerosene as compared to that in other studied diluents. The extraction of U(IV) by bis(2.4,4-trimethylpentyl) monothiophosphinic acid (CYANEX 302) in kerosene from nitric acid solution has been investigated by Rahman [9]. The extraction of U(IV) by CYANEX 302 in kerosene from nitrate medium was found to increase with the extractant and uranium concentrations. The increase in hydrogen ion and nitrate ion concentrations in the medium were found to decrease the extraction process while the variation in nitric acid concentration had nearly no effect. Sulfoxides have been considered as potential extractants for use in nuclear applications for many years. Yan-Zhao et al. have studied the liquid-liquid extraction bahaviour of 2-ethylhexyltolylsulfoxide (EHTSO) towards uranium (VI) contained in nitric acid aqueous solution [10]. It was found that the extraction increases with increasing nitric acid concentration up to 5.0 mol/L and then decreases and also increases with increasing extractant concentration.

The aim of these studies was a selection of the extracting agents appropriate for the recovery of uranium from post-leaching solutions. The raw extractants, like e.g.: tributylphosphate (TBP), di(2-ethylhexyl) phosphoric acid (D2EHPA), trioctylphosphine oxide (TOPO), triethylamine (TEA), tri-n-octylamine (TnOA), etc. were tested and the partition coefficients of uranium were determined. The effect of extractants, sulphuric acid and uranium concentrations on the extraction process from model solutions containing uranium was investigated. An alternative method to traditional methods of extraction i.e., the technique of extraction with application of the membrane contactors with concurrent or countercurrent flows of two phases – water and organic will be examined after selection of the appropriate extracting agents for the membrane process.

The use of different reagents as strip solutions of the loaded uranium in organic phase was also investigated. It is described in the literature that uranium can be re-extracted from solutions of extractants by contacting with sodium carbonate solution, ammonium carbonate solution, hydrochloric, sulphuric or fluoric acids [5, 11].

## 2. EXPERIMENTAL

### 2.1. Procedures

#### *2.1.1. Extraction experiments*

Uranium solutions were prepared by direct dissolution of a certain amount of uranyl nitrates in sulphuric acid to obtain a solution containing 0.2 and 0.5 g/l of uranium respectively. Liquid-liquid extraction experiments were performed by slow mechanical shaking of the tubes with two liquid phases at ambient temperature for various time intervals (from 2 to 45 min). In extraction experiments the organic: aqueous phase ratio was fixed at 1:1. After centrifugation and phase separation, a suitable volume of the aqueous phase has been analysed for uranium content. The concentration of U(VI) ion in the aqueous phase was measured by ICP-MS (Inductively Coupled Plasma Mass Spectrometry) after diluting with $H_2O$ and $HNO_3$ to the concentration suitable for ICP-measurement.

#### *2.1.2. Stripping experiments*

The recovery of uranium from loaded extractant solutions in kerosene was also investigated. The stripping of U(VI) extracted by TOPO, TnOA or HDEHP was tested by different strip solutions, namely, sulphuric acid, hydrochloric acid and sodium carbonate. Studies were performed according to the procedure described above.

## 3. RESULT AND DISCUSSION

In order to determine the extraction kinetics for different extractants, the time dependence of the extraction efficiency of uranium was investigated and the results are plotted in Fig. 2. As can be seen the effect of shaking time on the extraction of U(VI) by variuos extractants from $H_2SO_4$ acid solution investigated in the range 2–30 minutes showed that the extraction equilibrium was accomplished after 15 minutes. Table 2 presents the distribution ratios of uranium for different TnOA, sulpuric acid and uranium concentrations. The results showed that the distribution ratios increase with the increase of extractants concentrations while they decrease with the increase of sulphuric acid concentration. The observed effect of decreased distribution ratios with increased acid concentration and increased distribution ratios with increased extractants (like e.g.: TBP, HDEHP) concentration was also reported previously [12].

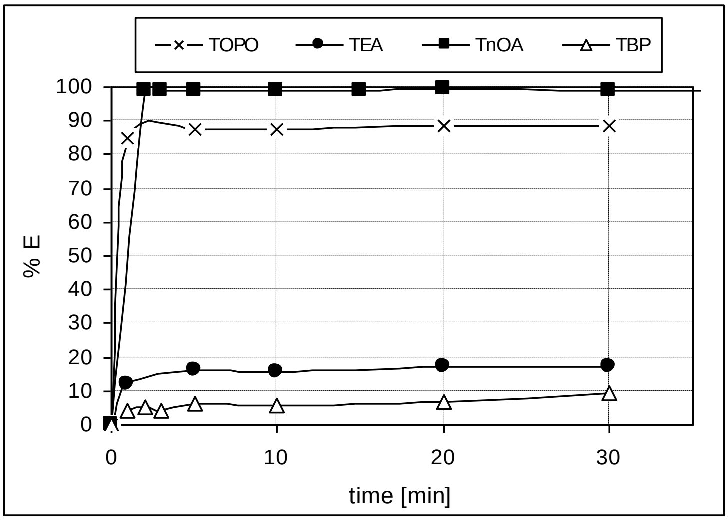

Fig. 2. Time dependence of the extraction efficiency of U in the systems: 0.2 M ( TOPO, TEA, TBP, TnOA); 0.2 g U/l in 5% $H_2SO_4$

Increasing sulphuric acid concentration from 5% up to 10% was found to have the effect on the recovery of uranium from aqueous solutions as it is plotted in Fig. 3. 5% $H_2SO_4$ may be considered as the appropriate concentration from which uranium can be extracted. Tri-n-octylamine and di(2-ethylhexyl)phosphoric acid were found to be most favourable extractants for the uranium extraction efficiency, giving almost 100% recovery of uranium from 5% sulphuric acid solution. The use of TOPO for the extraction of uranium is worth also to be taken into consideration as its extraction efficiency was found to be almost 90%.

Table 2. Effect of sulphuric acid, extractant concentration on the distribution ratios (logD) of uranium in TnOA in kerosene system

| **[TnOA]/[U]** <br> **[$H_2SO_4$][%]** | **0.2M/0.2g/l** | **0.4M/0.2g/l** | **0.2M/0.5g/l** | **0.4M/0.5g/l** |
|---|---|---|---|---|
| 5 | 2.244±0.009 | 3.069±0.001 | 1.397±0.002 | 2.456±0.004 |
| 7.5 | 0.927±0.004 | 1.599±0.010 | 0.834±0.008 | 1.532±0.012 |
| 10 | 0.565±0.001 | 1.193±0.006 | 0.324±0.012 | 1.007±0.009 |

Table 3. Efficiency (%) of stripping of the loaded uranium in organic phase

| **Extractant** | **[$H_2SO_4$] %** | | **5% $Na_2CO_3$** |
|---|---|---|---|
| | **20** | **30** | |
| D2EHPA | 6.22±0.44 | 24.10±0.56 | emulsion |
| TnOA | 2.95±0.66 | 4.24±0.08 | 5.09±0.16 |
| TOPO | 7.78±0.91 | 6.63±0.59 | - |

Very preliminary results on stripping of uranium from the loaded extractant solution by sulphuric acid at the different concentration are shown in Table 3. It can be seen that 30% sulphuric acid is insufficient for the re-extraction of uranium from organic solvents and further studies using more concentrated sulphuric acid solutions and other stripping agents need to be carried out.

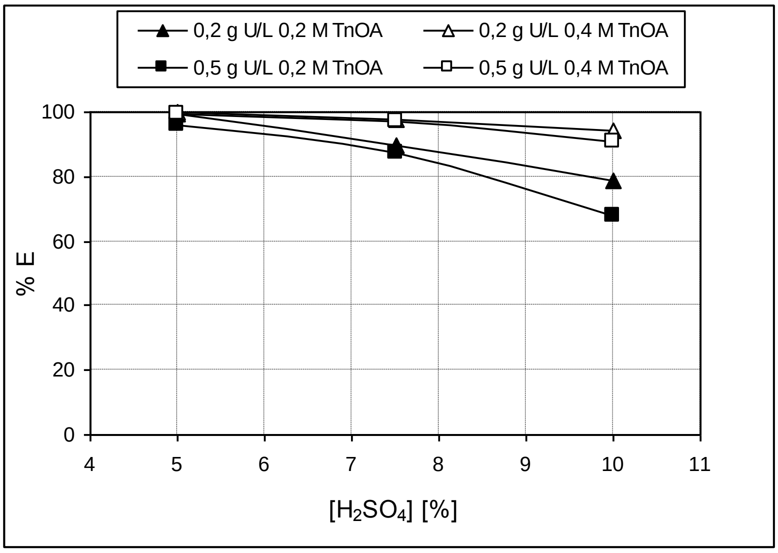

Fig. 3. Effect of sulphuric acid concentration on the extraction of U(VI) by TnOA in kerosene from $H_2SO_4$

## 4. CONCLUSION

The results obtained showed that the extraction increases with the increase of extractants concentrations while it decreases with the increase of sulphuric acid concentration. It was found that 15 minutes of shaking is sufficient for quantitative extraction of uranium from sulphuric acid solutions. Tri-n-octylamine and di(2-ethylhexyl)phosphoric acid were found to be most favourable extractants for the uranium extraction efficiency. Very preliminary studies on stripping of uranium from the loaded extractant solution by sulphuric acid at different concentration showed that more concentrated sulphuric acid solutions and other stripping agents need to be tested.

## Acknowledgement

The studies were supported by the POIG project, No 01.01.02-14-094-09-00 “Analysis of the possibility of uranium supply from domestic resources”.

## REFERENCES

1. EDWARDS, C.R., OLIVER, A.J. Uranium processing: A review of current methods and technology. *JOM*, 2000, Vol. 52, No. 9, p. 12–20.
2. SINGH, S., CHAKRAVORTTY, V., DASH, K.C., Solvent Extraction of Uranium(VI) by LIX-54 and its Mixtures. *Journal of Radioanalytical Nuclear Chemistry. Articles*, 1988, Vol. 122, No. 1, p. 137–142.
3. Uranium 2007: Resources, Production and Demand, A Joint Report by the OECD Nuclear Energy Agency and the International Atomic Energy Agency OECD, Paris, 2008
4. NIEĆ, M., Występowanie rud uranu i perspektywy ich poszukiwań w Polsce. Polityka Energetyczna, 2009, Tom 12, Zeszyt 2/2, p. 435–451.
5. DAOUD, J.A., ZEID, M.M., ALY, H.F. Tetravalent uranium extraction by HDEHP in kerosene from phosphate medium. *Solvent Extraction and Ion Exchange*, 1997, Vol. 15, No. 2, p. 203-217.
6. MUSIKAS, C., Schulz, W.W., RYDBERG, J., CHOPPIN, G.R. Principles and Practices of Solvent Extraction. New York, Marcel Dekker, 1992, p. 413–447.
7. JAIN, Vinod K., PILLAI, Shibu G., PANDYA, Rujul A., AGRAWAL, Yaduvendra K., SHRIVASTAV, Pranav S., Molecular octopus: octa functionalized calyx[4]resorcinarene-hydroxamic acid[C4RAHA] for selective extraction, separation and preconcentration of U(VI). *Talanta*, 2005, Vol. 65, p. 466–475.
8. MOHANTY, S.P., MOHANTY, I., MISHRA, S., CHAKRAVORTTY, V., Extraction of uranium (VI) with a binary mixture of LIX-860 and Versatic-10. *Journal of Radioanalytical Nuclear Chemistry*, 1998, Vol. 227, No. 1–2, p. 99–103.
9. RAHMAN, N.A., DAOUD, J.A., ALY, H.F., Mechanism of uranium(IV) extraction with CYANEX 302 in kerosene from nitric medium. *Journal of Radioanalytical Nuclear Chemistry*, 2003, Vol. 25, No. 3, p. 597–603.
10. YAN-ZHAO, Y., SI-XIU, S., SHENG-YU, F., Liquid-liquid extraction of uranium(VI) Liquid-liquid extraction of uranium(VI) with 2-ethylhexyltolylsulfoxide (EHTSO). *Journal of Radioanalytical Nuclear Chemistry*, 2002, Vol. 251, No. 3, p. 503–506.
11. KHORFAN, S., SHINO, O., WAHOUD, A., DAHDOUH, A., Stripping of uranium from D2EHPA/TOPO solvent by ammonium carbonate solutions. *Periodica Polytechnica Ser. Chem. Eng.*, 2000, Vol. 44, No. 2, p. 123–132.
12. GINDLER, J.E., The radiochemistry of Uranium. Nuclear Science Series, NAS-NS-3050, 1962. Link to the internet http://www.osti.gov/bridge/purl.cover.jsp?purl=/5392883-Tl3fMD/.

CYSENI 2011, May 26–27, Kaunas, Lithuania
SSN 1822-7554, www.cyseni.com

# SOLID-LIQUID EXTRACTION OF URANIUM FROM POLISH ORES

**G. Zakrzewska-Trznadel, K. Frąckiewicz, I. Herdzik-Koniecko, B. Zielińska,**
**A. Miśkiewicz, K. Szczygłów, P. Biełuszka, Ł. Steczek, E. Chajduk**
*Institute of Nuclear Chemistry and Technology*
*Dorodna Street 16, 03-195 Warsaw – Poland*
*Email: g.zakrzewska@ichtj.waw.pl*

**S. Wołkowicz**
*Polish Geological Institute*
*Rakowiecka Street 4, 00-975 Warsaw – Poland*

## ABSTRACT

Exploration of possibilities of the uranium production from Polish low-grade ores and ore processing methods are the main subjects of the project entitled “Analysis of the possibility of uranium supply from domestic resources”. The paper presents current status and development of the project with special emphasis on the solid-liquid extraction of the uranium ores. The experiments showed high extraction of uranium; the average efficiency of the acid leaching was in the range of 64–81%.

Keywords: uranium ore, solid-liquid extraction.

## 1. INTRODUCTION

Nuclear energy will continue to play an important role in the world energy demand for the future. To guarantee an adequate supply of uranium for nuclear reactors, the new production facilities will have to be opened. Many countries developing nuclear power are therefore interested in exploiting their uranium resources for domestic consumption (in connection with their own nuclear power programmes) [1]. Around the year 2020 the first nuclear power plant in Poland is expected to be put in operation (Fig. 1) [2, 3]. On 25 of January 2011 the Council of Ministers adopted the information on Polish Nuclear Power Programme, which is to be accepted by the end of June 2011. According to this Programme determination of the location and conclusion of the contract for construction of the first nuclear power plant will be done by the year 2013. Implementation of nuclear power is a long process, that need various coordinated actions concerning not only technology selection and siting process, but also legislation work and social involvement activities. Successful implementation of Polish Nuclear Power Programme (PNPP) implicates a need of precise analysis of uranium resources in the country and the assessment of their exploitation possibilities. According to OECD-NEA Red Book identified uranium resources in Poland count 7270 T and speculative exceed even 100 000 T [4]. The uranium occurrence in Poland shows great diversity. Uranium is usually accompanied by other valuable metals such as Th, V, Mo, Cu, Co, Zn, Pb, La that can be recovered in technological process to improve the economy of the venture. For development of effective technology of uranium extraction from low-grade ores, the knowledge about chemical composition of the bedrock, uranium speciation and their combination with the rock constituents is necessary. Petrographic, mineralogical and chemical studies will allow elaborating the optimal processing technology and selecting the appropriate methods for uranium extraction. Institute of Nuclear Chemistry and Technology and Polish Geological Institute take an action to realise the new project concerning uranium supply from low-grade ores [5, 6]. The successful implementation of the project results for the production of uranium concentrates is costly and complex. It requires a good knowledge of current technology for uranium exploration, ore body development, estimation of ore reserves, mining and ore processing. It is expected that the project will give the answer to the question whether indigenous resources can be considered as a potential reserve of uranium for Polish nuclear reactors in future. The aim of the present project is also to lower the costs of uranium extraction technology with reduction of its environmental impact.

## 2. THE TECHNOLOGY OF URANIUM EXPLORATION AND EXTRACTION FROM LOW-GRADE ORES

### 2.1. Uranium deposits and ore reserves estimation

Analysis of uranium bearing ores showed that Lower Triassic sandstones from Peribaltic Syneclise and black shales from the north-east part of Poland (Rajsk Deposits) (Fig. 1) are the most perspective formations with high uranium concentration, locally reaching 1.5%U (recent analysis of archivic samples) [7]. Petrographic, mineralogical and chemical studies will allow elaborating the optimal processing technology and selecting the appropriate methods for uranium extraction from the ores.

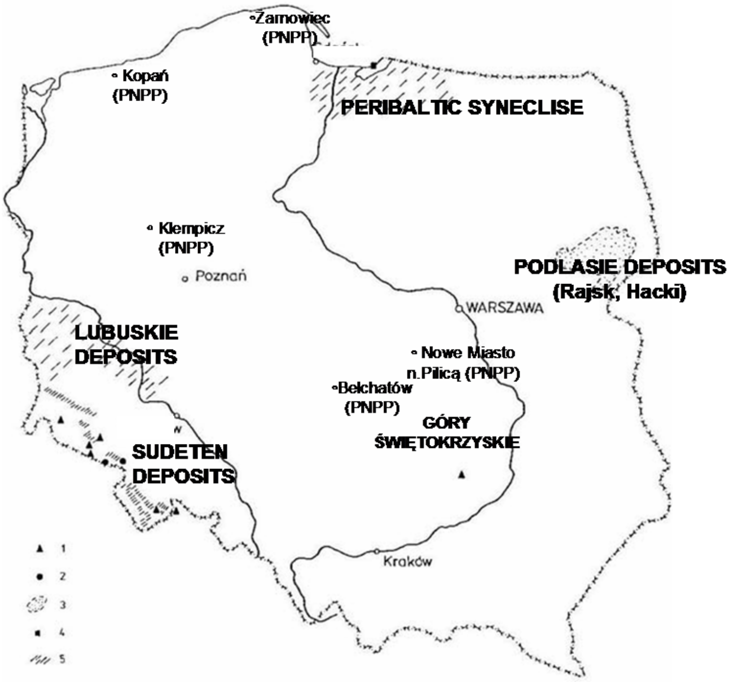

Fig. 1. Deposits of the uranium ores in Poland; 1 – exhausted uranium ores (in independent uranium deposits and in deposits of other ores), 2 – uranium deposits of lean ores, 3 – area of occurrence of uranium bearing dictyonema shales, 4 – uranium ore occurrence in Triassic sandstones, 5 – area promising for uranium deposits prospecting [8]; (PNPP) – Polish Nuclear Power Plant – considered localizations [9]

The uranium deposits of Dictyonema shale in Podlasie Depression are spread out of the large area with the thickness up to 2 m; however uranium content in these ores is rather low [8]. The concentrations do not exceed significantly 100 ppm. The most intense uranium mineralisation occurs in black shales with high content of organics; nevertheless, elevated concentrations in brown shales are also observed. As a rule, the most of uranium content in the black shales is bound with the organic substance, sometimes with the clay materials. The uranium occurrences in domestic resources show great variety. Uranium is combined with several other metals such as Th, V, Mo, Cu, Co, Zn, Pb, La and with different gangue materials such like black and brown shales or sandstones. This variety means that a great assortment of treatment processes will be required to extract uranium from the ores.

## 2.2. Uranium ore processing

### *2.2.1. Leaching in the mixing tank*

The most common equipment used in the solid-liquid extraction process is the mixer-settler system [10–12]. This arrangement is used in laboratory experiments, as well as in larger scale industrial installations. All investigations described in the paper were carried out in the laboratory at Institute of Nuclear Chemistry and Technology in Warsaw.

In present experiments the simple glass vessel with an agitator is applied. The preliminary laboratory tests are performed with the primary purpose of the assessment of the technical and economic feasibility of processing the ore. At this stage it is necessary to evaluate the capability of the subsequent processes applied in the technological scheme: size reduction, leaching, solvent extraction and ion exchange. If it is possible to dissolve most of the uranium present in the samples and if it is possible to obtain a clear pregnant liquor it will generally be feasible to purify and concentrate this liquor and to obtain a uranium concentrate of good quality [13]. At the beginning of extraction process, uranium ore is crushed and grinded to a suitable range of particle size (in the range of 0.1–1.0 mm) required for effective leaching and to produce a material that can be slurried. Then, each fraction is calcinated in the oven at temperature ca. 550°C for 5 hours. For chemical analysis the sample is pulverized and melted with $Na_2O_2$, then dissolved in 5M $HNO_3$. Simultaneously, uranium is leached from the ground ore by solid-liquid extraction using sulphuric acid solution (10% $H_2SO_4$) with heating. Acid leaching is carried out at temperature of 80°C at atmospheric pressure for 8 hours in mechanically agitated vessels with the addition of an oxidant (e.g. manganese dioxide). The pregnant liquor is separated from the leached ore by filtering and successive washing by distilled water. It contains a very low concentration of uranium and other metals, as well as some impurities. It must therefore be concentrated and purified using solvent extraction or ion exchange resins. Uranium ores are analysed for uranium and other elements by ICP-MS (Inductively Coupled Plasma Mass Spectrometry). The recovery of a uranium from the leaching ore is in the range of 64–81% (Table 1). The accuracy of the analyses is in the range of 5–20%.

Table 1. Efficiency of the acid leaching of selected metals in 5 different samples

| **Sample notation** | **Deposit notation** | **U [%]** | **V [%]** | **Mo [%]** | **Cu [%]** | **La [%]** | **Th [%]** |
|---|---|---|---|---|---|---|---|
| 3224 | Rajsk JG-1 | 72 | 33 | 66 | 33 | 60 | 80 |
| 3227 | Rajsk JG-1 | 64 | 30 | 51 | 29 | 59 | 78 |
| 3226 | Rajsk JG-1 | 68 | 44 | 78 | 52 | 62 | 77 |
| 3233 | Rajsk JG-1 | 78 | 25 | 59 | 41 | 66 | 67 |
| 3276 | Hacki JG-5 | 81 | 52 | 33 | 28 | 31 | 76 |

### *2.2.2. Leaching in the autoclave*

Leaching of the uranium ore can be done also in the autoclave with very good efficiency [14]. This apparatus gives the possibility of parameters adjustment in a wide range, thus enables to carry experiments with the aim of process optimisation.

In present experiments, acid leaching of uranium ores is carried out for 2 hours at different pressure of 3, 5 and 7 bar in the autoclave. The leaching parameters: temperature, quantity of sulphuric acid and manganese dioxide, and concentration of sulphuric acid are adjusted by use of the results of the previous laboratory tests with mechanically agitated vessel. It was concluded that leaching of the uranium ore for 2 hours at 80 °C and at different pressure with the reagent additions indecated in the previous experiments would be effective.

The pregnant liquor is analysed for uranium and other elements by the ICP-MS method. The concentration of such metals like U, V, Mo, Cu, Zn, Ni, La and Th was determentd in the samples. The recovery of uranium and other metals from the ores is in the range of 60–80% and V and Cu about 30 % (Fig. 2). It is evident that apart from uranium the other metals occuring in the ores in large concentrations can be recovered by appropriate design of technological scheme, especially those more valuable like molybdenum and vanadium. Very intersting is lanthanum or other lanthanides that are also present in the ores and will be analysed during leaching procedure. The possibility of recovering all of these metals will be assessed in scope of the project to improve the economy of the whole venture.

The influence of pressure in the experimental range was not significant, however the best leaching results were obtained at pressure of 5 bars. In this condition the leaching efficiency of uranium is about 65%, molybdenum 60%, vanadium over 30% and lanthanum – ca. 65%.

The influence of ore grinding was tested in 0.1–1.0 mm particle size range. As experiments showed the influence of particle size on leaching efficiency was not evident in the studied size range (Fig. 3). It can be concluded, that even though during crusching and grinding the total surface area of the leached material increases, it is not necessary in technological process to grind the ores below 1.0 mm.

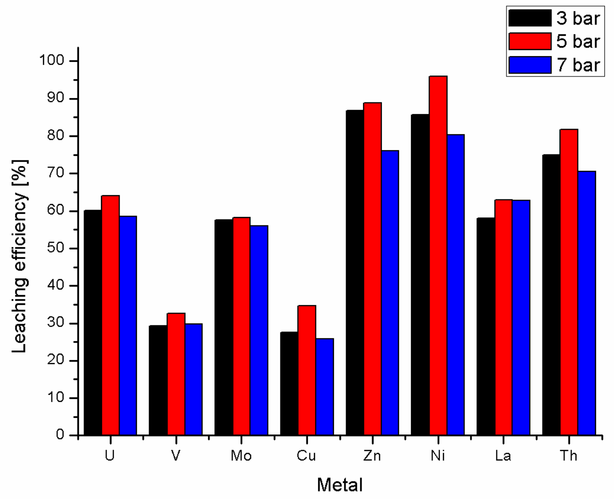

Fig. 2. Efficiency of the acid leaching of selected metals in the autoclave

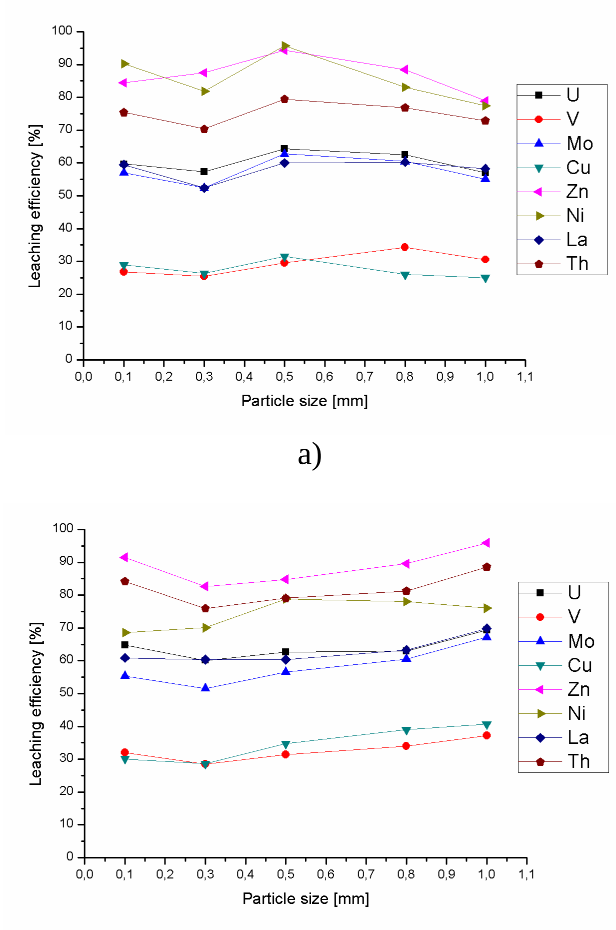

a)

b)

Fig. 3. Efficiency of the acid leaching of selected metals for various particle sizes of grinded uranium ore; a) pressure 3 bar; b) pressure 5 bar

## 3. CONCLUSIONS

The experiments that have preliminary character showed high extraction of uranium from the ores; the average efficiency of acid leaching was in the range of 60–81%. The other metals present in the ores were extracted with similar to uranium efficiency. Only 30% of vanadium and copper were recovered with acidic leaching by use of sulfuric acid. The influence of pressure was rather moderate and it was attributed to more intense mixing in the reaction vessel. It is expected that the influence of temperature will be more noticeable and relevant experiments are planned.

There was no effect of particle size in the range 0.1–1.0 mm on extraction efficiency of uranium ores.

The experiments with the autoclave allowed the variation of the parameters: pressure and temperature. By changing the parameters and assessing their infleuce on leaching efficiency one can easy optimise the process. The next studies of the uranium extraction from the bedrock will be leaching by alkaline solutions, which may be preferred for carbonate-reach ores. The kinetic studies of the uranium ore leaching are also planned. An ion exchange method will be used to concentrate uranium from low concentrated uranium solution such as a uranium poor pregnant liquid and washing water.

In relation to Polish Nuclear programme implementation there is a need of precise analysis of uranium domestic resources in Poland and the assessment of their exploitation possibilities. One part of the assessment is evaluation of technological feasibility of low-grade ores from the resources existing in the country. Although the present exploitation of Polish uranium deposits would not prove to be economic, the situation could change in future with further developement of nuclear energy and exhausting world resources of uranium. Polish resources of uranium can be considered as a reserve and the evident for the country autarchy.

## 4. ACKNOWLEDGEMENTS

The studies were supported by the Operative Programme – Innovative Economy, POIG entitled "Analysis of the possibility of uranium supply from domestic resources" (PO IG 01.01.02-14-094-09-00).

## 5. REFERENCES

1. International status and prospects of nuclear power, 2010 Edition, International Atomic Energy Agency, Vienna, 2011, http://www.iaea.org/books
2. KŁÓDKIEWICZ, M., Pierwsza elektrownia jądrowa w Polsce ruszy w 2020 r., http://*www.elektrownia-jadrowa.pl/Artykuly-3.html*
3. CHOJNACKI, J., PGE bada sześć lokalizacji elektrowni atomowej, www.wnp.pl
4. Uranium 2007:Resources, Production and Demand, A Joint Report by the OECD Nuclear Energy Agency and International Atomic Energy Agency, OECD, Paris, 2008 – ISBN 978-92-64-04766-2.
5. ZAKRZEWSKA-TRZNADEL, G., MIŚKIEWICZ, A., The possibility of uranium supply from domestic resources in Poland, Technical Meeting on Low Grade Uranium Ore, 29–31 March 2010, IAEA Headquarters, Vienna, Austria, available at: http://www.iaea.org/OurWork/ST/NE/NEFW/nfcms_rawmaterials-TMLGUO-presentations.html
6. BIEŁUSZKA, P., ZAKRZEWSKA-TRZNADEL, G., HARASIMOWICZ, M., Analysis of uranium extraction from indigenous sources, XXVth International Symposium on Physico-Chemical Methods of Separation "Ars Separatoria 2010". July 4–7, 2010, Toruń, Poland. in: Proceedings of the XXVth International Symposium on Physico-Chemical Methods of Separation "Ars Separatoria 2010", Wydawnictwo Naukowe Uniwersytetu Mikołaja Kopernika, Editors: Izabela Koter and Stanisław Koter, Toruń 2010, p. 295–299.
7. REJMAN, W., Kopalnie uranu w Polsce, *Wiedza i Życie*, 1996, Nr 9.
8. NIEĆ, M., Występowanie rud uranu i perspektywy ich poszukiwań w Polsce, *Polityka energetyczna*, 2009,Tom 12, Zeszyt 2/2
9. POLSKA GRUPA ENERGETYCZNA SA, Lokalizacja elektrowni jądrowej w Polsce, http://www.elektrownia-jadrowa.pl/Lokalizacja-elektrowni-jadrowej-w-Polsce-2.html
10. EDWARDS, C.R., OLIVER, A.J., Uranium Processing: A Review of Current methods and Technology, *JOM*, 2000, p. 12–20.
11. REIMAN, T., Sizing Up In-Situ Leaching, *Canadian Mining Journal*, 1990, 111(12), p. 19–22.
12. HUNTER, J., Highland In-Situ Leach Mine, *Mining Magazine*, 1991, 165(2), p. 58–63
13. SMIRNOV, I.P, MATVEEV, A.A., Scientific principles, technology, and equipment for hydrometallurgical processing of uranium and complex ores, *Atomic Energy*, 2001, Vol. 91, No. 4, p. 815–823.
14. SHATALOV, V.V., PIRKOVSKI, S.A., SMIRNOV, K.M., Oxidation of pyrite by oxygen and concurrent leaching of uranium from ore under the conditions of an autogenous autoclave process, *Atomic Energy*, 2007, Vol. 102, No. 2, p. 147–150.

# General sponsor:

Lithuanian
Energy
Institute

# Sponsors:

PlasTEP
Baltic Sea Region
Programme 2007-2013
Part-financed by the European Union
(European Regional Development Fund)

HIA
HYDROGEN
IMPLEMENTING
AGREEMENT

AB KAUNO ENERGIJA

BEA

**CALL FOR PAPERS:**
www.cyseni.com

Lithuanian Energy Institute
Young Scientists Association
Breslaujos str. 3, LT—44403 Kaunas,
Lithuania
www.lei.lt, jms.lei.lt